frontiers | Research Topics

Advancements in biomechanical modeling of injuries, diseases, diagnoses, and treatments of lower extremities

Edited by
Chih-Hsiu Cheng, Mohammad Nikkhoo, Lizhen Wang and Ching-Chi Hsu

Published in
Frontiers in Bioengineering and Biotechnology

ISSN 1664-8714
ISBN 978-2-8325-2242-4
DOI 10.3389/978-2-8325-2242-4

About Frontiers

Frontiers is more than just an open access publisher of scholarly articles: it is a pioneering approach to the world of academia, radically improving the way scholarly research is managed. The grand vision of Frontiers is a world where all people have an equal opportunity to seek, share and generate knowledge. Frontiers provides immediate and permanent online open access to all its publications, but this alone is not enough to realize our grand goals.

Frontiers journal series

The Frontiers journal series is a multi-tier and interdisciplinary set of open-access, online journals, promising a paradigm shift from the current review, selection and dissemination processes in academic publishing. All Frontiers journals are driven by researchers for researchers; therefore, they constitute a service to the scholarly community. At the same time, the *Frontiers journal series* operates on a revolutionary invention, the tiered publishing system, initially addressing specific communities of scholars, and gradually climbing up to broader public understanding, thus serving the interests of the lay society, too.

Dedication to quality

Each Frontiers article is a landmark of the highest quality, thanks to genuinely collaborative interactions between authors and review editors, who include some of the world's best academicians. Research must be certified by peers before entering a stream of knowledge that may eventually reach the public - and shape society; therefore, Frontiers only applies the most rigorous and unbiased reviews. Frontiers revolutionizes research publishing by freely delivering the most outstanding research, evaluated with no bias from both the academic and social point of view. By applying the most advanced information technologies, Frontiers is catapulting scholarly publishing into a new generation.

What are Frontiers Research Topics?

Frontiers Research Topics are very popular trademarks of the *Frontiers journals series*: they are collections of at least ten articles, all centered on a particular subject. With their unique mix of varied contributions from Original Research to Review Articles, Frontiers Research Topics unify the most influential researchers, the latest key findings and historical advances in a hot research area.

Find out more on how to host your own Frontiers Research Topic or contribute to one as an author by contacting the Frontiers editorial office: frontiersin.org/about/contact

Advancements in biomechanical modeling of injuries, diseases, diagnoses, and treatments of lower extremities

Topic editors

Chih-Hsiu Cheng — Chang Gung University, Taiwan
Mohammad Nikkhoo — Islamic Azad University, Iran
Lizhen Wang — Beihang University, China
Ching-Chi Hsu — National Taiwan University of Science and Technology, Taiwan

Citation

Cheng, C.-H., Nikkhoo, M., Wang, L., Hsu, C.-C., eds. (2023). *Advancements in biomechanical modeling of injuries, diseases, diagnoses, and treatments of lower extremities*. Lausanne: Frontiers Media SA. doi: 10.3389/978-2-8325-2242-4

Table of contents

frontiers | Frontiers in Bioengineering and Biotechnology

TYPE Editorial
PUBLISHED 11 April 2023
DOI 10.3389/fbioe.2023.1178336

OPEN ACCESS

EDITED AND REVIEWED BY
Yih-Kuen Jan,
University of Illinois at Urbana-Champaign, United States

*CORRESPONDENCE
Chih-Hsiu Cheng,
chcheng@mail.cgu.edu.tw

RECEIVED 02 March 2023
ACCEPTED 03 April 2023
PUBLISHED 11 April 2023

CITATION
Nikkhoo M, Wang L, Hsu C-C and Cheng C-H (2023), Editorial: Advancements in biomechanical modeling of injuries, diseases, diagnoses, and treatments of lower extremities. *Front. Bioeng. Biotechnol.* 11:1178336. doi: 10.3389/fbioe.2023.1178336

Editorial: Advancements in biomechanical modeling of injuries, diseases, diagnoses, and treatments of lower extremities

Mohammad Nikkhoo[1,2,3], Lizhen Wang[4], Ching-Chi Hsu[5] and Chih-Hsiu Cheng[1,2]*

[1]School of Physical Therapy and Graduate Institute of Rehabilitation Science, College of Medicine, Chang Gung University, Taoyuan, Taiwan, [2]Bone and Joint Research Center, Chang Gung Memorial Hospital, Linkou, Taiwan, [3]Department of Biomedical Engineering, Science and Research Branch, Islamic Azad University, Tehran, Iran, [4]School of Biological Science and Medical Engineering, Beihang University, Beijing, China, [5]Department of Mechanical Engineering, National Taiwan University of Science and Technology, Taipei, Taiwan

KEYWORDS

biomechanics of lower extremities, mathematical musculoskeletal modeling, finite element modeling, hip biomechanics, knee biomechanics, leg injuries, footwear

Editorial on the Research Topic
Advancements in biomechanical modeling of injuries, diseases, diagnoses, and treatments of lower extremities

The musculoskeletal system is a complex multi-articular structure which provides a relative range of motion for functional activities. It seems similarities between the joint biomechanics of the upper and the lower extremities. However, the upper extremity is more specialized for daily activities with greater ranges of motion, and the lower extremity structures are well prepared for locomotion and its weight-bearing (Yan et al., 2015). The basic principles of lower limb biomechanics focus on understanding the mechanical response and performance, the effect of injuries or diseases, and movement optimization in hope of finding effective rehabilitation procedures. Nevertheless, there is still a lack of knowledge in this research field, particularly at the level of injury risk factors, muscle functions, control, and instability. Hence, studying the biomechanical response of healthy, diseased, and treated lower extremities has been of great interest to clinicians and researchers. Numerous experimental, theoretical, as well as computational biomechanical studies have been conducted in the hope of understanding the underlying mechanisms involved in lower limb biomechanics. While some studies have been geared toward the prevention of injuries, others deal with more effective diagnostic and treatment modalities. Experimental clinical studies, using both *in-vitro* and *in-vivo* platforms, have the ability to provide relevant information regarding the biomechanical behavior and response of the lower extremities. Incidentally, these studies are essential but could be costly and limited by their inability to estimate the detailed microstructural phenomenon.

In the past few decades, different mathematical and computational methodologies of modeling [such as musculoskeletal and finite element (FE) modeling] have emerged as powerful and practical tools for non-invasive biomechanical investigations. These modeling approaches can explore the various aspects of the lower extremities, from the response of the

health conditions in different movements, to evaluations of the effects of different pathologies and injuries, and to relevant treatment modalities and techniques. The current Research Topic presents a collection of cutting-edge studies which enhance our knowledge about biomechanical investigations of lower extremities and stimulate deliberations for the improvement of research techniques used for the development of relevant studies for injuries, diseases, diagnoses, and treatments.

Three studies focused on investigating the kinematics and kinetics of the whole lower extremity. Li et al. have quantified the kinetic and kinematic features of pedestrian active and avoidance behaviors in dangerous impact scenarios and pedestrian-vehicle interaction in the pre-crash phase using immersive virtual reality technology. They confirmed that the pedestrian kinetics and kinematics at the instant of occurrence of a collision were significantly influenced by their active avoidance behavior. In addition, the physical conditions, sufficient time, and a safe distance are required for effective avoidance motion. This study provided comprehensive experimental data which can be utilized as a valuable reference for developing and validating the FE models and multi-body simulations for lower limbs. Herrera-Valenzuela et al. have used a novel mathematical methodology behind the Gait Deviation Index (GDI) proposed by Schwartz and Rozumalski (2008) to a dataset of adults with spinal cord injury (SCI). Using the motion capture system on the lower limb, this novel index is calculated using 21-feature vectorial basis derived from gait data of the population with SCI. They have reported that implementation of the original GDI in population with SCI may result in an overestimation of gait function, but the new proposed index (SCI-GDI) could be more sensitive to larger gait impairment than the GDI. Prasad et al. proposed a simulation-based generalized framework for modelling and evaluation of cable-driven mobile lower limb exoskeleton is proposed which can be used for rehabilitation procedures. Simulation of the conceptual configurations in this study indicated that the 4-cable configuration is an encouraging design option for a lower limb rehabilitation exoskeleton based on tracking performance, component forces exerted on the lower limb, and motor power requirements.

During routine activities of daily living, the hip joint plays a crucial role in the mobility and stability of the lower extremities as the primary link between the upper and lower limbs. Hence, investigation of the hip biomechanics principles can be beneficial for the enhancement of the knowledge of the pathological mechanisms, diagnosis, and treatment techniques (Polkowski and Clohisy, 2010). Jiang et al. conducted a retrospective investigation for patients with femoral neck fractures (FNF) to comprehensively study the effect of vertical and oblique inclinations on fracture stability and reoperation risks using an innovative multivariant model. It was shown that fracture inclination in vertical and oblique planes is closely related to reoperation outcomes and evaluating the fracture stability using this methodology may be a beneficial complement to the classic Pauwels technique (van Embden et al., 2011). Chen et al. used the FE modeling to study the influence of anterior center-edge angle (ACEA) on stress distribution of the hip joint, which could enhance the clinical diagnosis of the severity of hip dysplasia. This study showed that in the patients with lower ACEA, the area ratio of high stress increased. They concluded that for cases with borderline developmental dysplasia of the hip, both the ACEA and the area of facies lunata played critical roles in characterizing the severity of hip dysplasia. Vega et al. used a patient-specific neuro-musculoskeletal model and direct collocation optimal control to estimate the impact of ipsilateral psoas muscle strength on gait cycle following internal hemipelvectomy surgery with prosthesis reconstruction. The results showed that when post-surgery psoas strength was increased, stance width and stride length returned to pre-surgery values. Hence, this study suggests that retention and strengthening of the psoas muscle on the operated side may be vital for maximizing post-surgery post-surgery gait function. Alexander et al. developed personalized musculoskeletal models to study lower limb kinematics and kinetics during gait in pediatric and adolescent patients with increased, isolated femoral anteversion compared to typically developing controls. The contribution of this study was to identify the specific subgroups of patients who may have a higher risk of joint overloading as a consequence of both altered morphology and kinematics. In conclusion, it was shown that the altered femoral morphology does not always result in an increased risk of joint overloading. However, personalized kinematics should be considered for better judgment.

Five studies focused on the pathological mechanism and surgical techniques for the treatment of fractures in Femur and Tibia. Cen et al. developed multiscale FE models of the proximal femur for both the elderly and young population to evaluate the mechanical responses at the tissue and cell scales in the mid-stance of gait. Mechanical responses of cortical bone and osteocytes in different quadrants of the mid-femoral neck were studied in the mid-stance of gait. It was confirmed that the mass and bone mineral density of femoral neck cortical bone could be correlated to the mechanical response of osteocytes. This could be valuable to adopt novel treatment techniques based on the improvement of cortical bone quality by stimulating osteocytes. In addition, quadrantal differences in bone quality in the mid-femoral neck might be deliberated to improve fracture risk prediction in future investigations. Wang et al. used a combination of the experimental study, topological optimization analyses, and FE modeling to evaluate the performance of a novel strategy for a minimally invasive plate osteosynthesis of distal tibia fractures. They showed that this technique which is called bionic lightweight design plating. It was shown that the application of FE simulation analyses combined with a topology optimization algorithm could improve the capacity of soft tissue protection by reducing the volume of the implant. They concluded that a smaller plate volume results in decreasing the excessive mechanical stimulation of soft tissues caused by the implants. Three of these investigations were focused on tibial plateau fractures (TPF) which are among the most common fractures in knee trauma. Ren et al. developed a novel plate through an anterolateral approach for posterolateral TPF and assessed the biomechanical performance of six different groups by the biomechanical experimental testing and FE simulations. This study concluded that the proposed patented plate had a proper biomechanical advantage for posterolateral TPF including balanced stress distribution which can reduce the risk of fixation failure. Moufid et al. measured the mechanical effects of cement injection on adjacent bone structures for stabilizing the TPF using the combination of the *in-vitro* experimental studies and FE analyses. They concluded that cement can provide proper

reduction and primary stabilization, permitting the patient to undergo rehabilitation with active and passive mobilization. However, it is suggested that no weight-bearing would be authorized while the cortical bone is not stabilized. Vendeuvre et al. performed *in-vitro* experiments to comprehensively compare different minimally invasive fixations in association with balloon reduction based on the tuberoplasty method. They evaluated the primary structural strength of the TPF fixation regarding the separation and depression components and tested the mechanical influence of injectable bone cement filling on three different types of percutaneous screws. It was determined that cement filling during tuberoplasty could be a promising approach in association with percutaneous osteosynthesis to provide a better surgical outcome.

The knee, as the main lower limb motor joint, is comprising four bones and an extensive network of ligaments and muscles. Knee diseases, including musculoskeletal and neurological disorders, and the relevant treatment strategies may extremely affect the knee biomechanical response. Five studies were focused on knee biomechanics and the treatment modalities in this Research Topic. Guo et al. provided a systematic review and performed a meta-analysis on the impact of anterior cruciate ligament (ACL) defects and ACL integrity on clinical outcomes. They determined that no differences were observed in the primary clinical outcomes such as postoperative revision, and Tegner activity score and Oxford Knee Score in ACL deficient and unicondylar knee arthroplasty intact patients. Chen et al. performed experiments and developed a validated musculoskeletal model to evaluate the ACL biomechanics and the variation between the knee joint variables in three landing test actions. This study showed minimal differences in knee valgus, knee valgus moment, and ACL forces between the aforementioned landing actions. Nonetheless, it was reflected that knee flexion angle, knee extension moments sagittal factors, and quadriceps and gastrocnemius forces are the main risk factors for ACL injury. Cheng et al. developed a validated 3D FE model of a healthy cadaveric knee to find the optimal femoral drilling angle for ACL reconstruction with the anteromedial (AM) portal technique. It was presented that the femoral tunnel drilling angle could directly affect both the strain and stress distribution on the femoral tunnel, tibial tunnel, and ACL graft. A femoral tunnel drilling angle of 45° coronal/45° sagittal represented the lowest peak stress, maximum strain on the femoral and tibial tunnel entrance, and the lowest peak stress on the ACL graft. Ren et al. adapted a gait perturbation process induced the mechanism of human falls and quantified the lower limb response to examine the compensatory strategies of patients with knee osteoarthritis (KOA). It was found that patients with KOA have a higher risk of falling in response to a backward slip perturbation compared with healthy older individuals. Patients with KOA have a better focus on the strength and activation of the muscles that play a critical role in hip extension during gait. Lin et al. used a custom-made knee extension force measurement system to evaluate the effect of cycling training with a central fatigue challenge resistance on individuals with Parkinson's disease (PD). This study confirmed that this training methodology could be beneficial, efficient, and feasible for patients with early-stage PD in strengthening both central and peripheral components of knee extensor forces and can be considered for developing rehabilitation interventions for these patients.

Studying foot and ankle biomechanics is another major field in lower extremities research investigations which focuses on the function of the foot and ankle in the normative, pathologic, and clinically treated states (Towers et al., 2003). Jiang et al. developed a multi-rigid body modeling technique to analyze the kinetics and kinematics of the lower limb in the half-squat parachuting landing to evaluate the protective effects of an ankle brace. It was found that this ankle brace might provide more effective protection for the lower-extremity joints in the half-squat parachuting landing with a backpack than no backpack landing. Zeng et al. developed a 3D fracture line mapping methodology to define the distribution of fracture lines throughout the ankle joint to describe a novel classification for the fibular and tibial fracture lines. They have classified 228 patients with ankle fractures using this methodology and claimed that this technique can include fracture types that cannot be identified by both AO and Lauge-Hansen (LH) classification. Rebelo et al. utilized a validated lower limb FE model of underbody blast (UBB) to estimate the effect of stature on injury risk. This study showed that there is a higher risk of calcaneal injury associated with short statures than medium and tall statures. In addition, they found that shorter individuals are at a higher risk of leg injury compared to taller ones. A combat boot and a floor mat were revealed to have a variable attenuating efficiency depending on the UBB loading characteristics. Funaro et al. developed a personalized FE model which contained the sub-tendons structure and their relative sliding to study the impact of rehabilitation maneuvers and different twists on Achilles tendon (AT) strains. It was shown that the rehabilitation maneuvers ranking was independent of the AT twist. However, the findings in this study could provide a better guide for clinicians to prescribe rehabilitation exercises for different twists on AT strains. Lv et al. utilized a 3D FE model of foot with a calcaneal fracture to assess the biomechanical performance of double-point fixation (DPF) compared to the three-point fixation technique. They concluded that DPF fixation by volar distal radius plates revealed favorable and sufficient fixation stability with a lower risk of postoperative stress fracture, which may possibly assist surgeons in planning a new fixation modality. Li et al. used a foot multi-segmental modeling to explore the kinematics and GRFs in marathon-experienced recreational runners before, during, and after long-distance running. It was found that excessive foot motion after 5 km of running may hypothetically increase the risks of running-related injuries (IRR). Moreover, the forefoot space of footwear may affect the biomechanical response of foot in long-distance running. In addition, Matias et al. studies the biomechanical-related risk factors for RRI and stated the effects of the 8-week foot-core exercise training program. They observed that changes in foot-joint kinematics resulting from the foot-core training program could be in charge of the reduction in RRI incidence. Xiao et al. measured the foot muscle strength, passive ankle kinesthesia, and postural control to examine the effects of 4 weeks of foot core exercise and multi-session high-definition transcranial direct current stimulation (HD-tDCS). The achieved results showed that HD-tDCS might increase the metatarsophalangeal joint flexor strength and the passive kinesthesia thresholds of ankle inversion and eversion. Footwear is generally designed to provide protection, assist in motion control

and stability, and treat musculoskeletal deformities and injuries (Barton et al., 2009). Henceforward, numerous investigations are dedicated to this field of lower extremity biomechanics. Chen et al. used a validated musculoskeletal model to identify the immediate effects of worn shoes on the kinematics and kinetics of the lower limb. The outcomes of this research suggested that aging shoes are not appropriate. Attrition in the heel can raise the balance risk. Attrition shoes may affect the gait pattern and result in discomfort. Yu et al. studied the effects of heel-to-toe drops (HTD) and running speed on the biomechanical response of lower limb biomechanics using the inverse kinematics algorithm. This investigation showed that shoes with −8 mm HTD possibly will have a better ability to store and return energy that was related to running performance. Wang et al. combined the FE simulations with musculoskeletal modeling to study the effect of heel height on the strain distribution of plantar fascia. The results from the present research could reveal the strain variation on the plantar fascia and facilitate understanding of potential causes of plantar fasciitis induced by using high-heel shoes. In addition, this study claimed that the findings found that heel elevation as a treatment recommendation for plantar fasciitis could be questionable. Peng et al. used a detailed flatfoot orthosis FE model combined with Taguchi methodology to calculate the effect of design combinations on the response of foot-ankle biomechanics. It was shown that the foot orthosis with higher arch support and medial inclination angle could be more effective in reducing the peak plantar pressure. Besides, adding the medial forefoot posting may modify the forefoot deformity and forefoot pressure. Zhang et al. and Su et al. used a high-speed dual fluoroscopic imaging system to investigate the alterations of the first metatarsophalangeal joint (MTPJ) and medial longitudinal arch's (MLA) kinematics between shod and barefoot running. Zhang et al. determined that shoe-wearing could limit the extension and joint translation of the first MTPJ and increase the horizontal adduction angle. This conclusion revealed that shoemakers would increase the capacity of the forefoot movement to reduce the injury risk factors. Su et al. presented that shoe-wearing may limit the partial movements of the MLA which may affect the storage and release of elastic energy during running.

Collectively, 31 peer-reviewed papers presented in this Research Topic tackle different challenges in the topic of biomechanical investigations of injuries, diseases, diagnoses, and treatments of lower extremities. The outputs of these studies could be generally utilized to either understand the causes of musculoskeletal system disorders, predict the risk factors, or enhance the effectiveness of certain treatment management strategies. Every study in this Research Topic reports its potential and existing limitations of the established technique and highlights the progress in its relevant research area. Hence, we believe that the current Research Topic could be fundamental to enhance understanding of lower limb biomechanics which may be used for clinical applications. However, various studies and clinical observations may need to be considered in the future to see these methodologies used routinely. As guest editors, and contributors, we hope this Research Topic can serve as state-of-the-art research investigations which may be beneficial for the design and development of new and more effective interventions for lower limb disorders.

Author contributions

MN and C-HC have prepared the draft of the editorial manuscript and all other authors have critically revised it. All authors have read and agreed to the published version of the manuscript.

Conflict of interest

The authors declare that the research was conducted in the absence of any commercial or financial relationships that could be construed as a potential conflict of interest.

Publisher's note

References

Barton, C. J., Bonanno, D., and Menz, H. B. (2009). Development and evaluation of a tool for the assessment of footwear characteristics. *J. Foot Ankle Res.* 2, 10. doi:10.1186/1757-1146-2-10

Polkowski, G. G., and Clohisy, J. C. (2010). Hip biomechanics. *Sports Med. Arthrosc. Rev.* 18 (2), 56–62. doi:10.1097/JSA.0b013e3181dc5774

Schwartz, M. H., and Rozumalski, A. (2008). The gait deviation index: A new comprehensive index of gait pathology. *Gait Posture* 28 (3), 351–357. doi:10.1016/j.gaitpost.2008.05.001

Towers, J. D., Deible, C. T., and Golla, S. K. (2003). Foot and ankle biomechanics. *Semin. Musculoskelet. Radiol.* 7 (1), 67–74. doi:10.1055/s-2003-41086

van Embden, D., Roukema, G. R., Rhemrev, S. J., Genelin, F., and Meylaerts, S. A. (2011). The Pauwels classification for intracapsular hip fractures: Is it reliable? *Injury* 42 (11), 1238–1240. doi:10.1016/j.injury.2010.11.053

Yan, T., Cempini, M., Oddo, C. M., and Vitiello, N. (2015). Review of assistive strategies in powered lower-limb orthoses and exoskeletons. *Robotics Aut. Syst.* 64, 120–136. doi:10.1016/j.robot.2014.09.032

frontiers in Bioengineering and Biotechnology

ORIGINAL RESEARCH
published: 03 November 2021
doi: 10.3389/fbioe.2021.782001

The Effect of Vertical and Oblique Inclinations on Fracture Stability and Reoperation Risks in Femoral-Neck Fractures of Nongeriatric Patient

Dajun Jiang, Shi Zhan, Hai Hu, Hongyi Zhu, Changqing Zhang and Weitao Jia**

Department of Orthopedic Surgery and Orthopedic Biomechanical Laboratory, Shanghai Jiao Tong University Affiliated Sixth People's Hospital, Shanghai, China

Background: For nongeriatric patients with femoral neck fractures (FNFs), preoperative evaluation of fracture three-dimensional inclination is essential to identify fracture stability, select appropriate fixation strategies, and improved clinical prognoses. However, there is lack of evaluation system which takes into account both vertical and oblique inclinations. The purpose of this study was to comprehensively investigate the effect of vertical and oblique inclinations on fracture stability and reoperation risks.

Methods: We retrospectively reviewed the medical records of 755 FNFs patients with over 2 years follow-up. The 3-D inclination angle in vertical (α) and oblique plane (β) were measured based on CT images. The optimal threshold for unstable 3-D inclination were identified by seeking the highest Youden Index in predicting reoperation and validated in the biomechanical test. According to the cut-off value proposed in the diagnostic analysis, forty-two bone models were divided into seven groups, and were all fixed with traditional three parallel screws. Interfragmentary motion (IFM) was used for comparison among seven groups. The association between reoperation outcome and 3-D inclination was analysed with a multivariate model.

Results and Conclusion: The overall reoperation rate was 13.2%. Unstable 3-D inclination angles with an optimally determined Youden index (0.39) included vertical (α > 70°) and oblique (50°<α < 70° and β > 20°/β < –20°) types. Biomechanical validation showed these fractures had significantly greater (p < 0.05) interfragmentary motion (1.374–2.387 mm vs. 0.330–0.681 mm). The reoperation rate in 3-D unstable group (32.7%) is significantly (p < 0.001) higher than that in 3-D stable group (7.9%). Multivariate analysis demonstrated that 3-D inclination angle was significantly (OR = 4.699, p < 0.001) associated with reoperation. FNFs with α > 70°; 50°<α < 70° and β > 20°/β < –20° are real unstable types with significantly worse interfragmentary stability and higher reoperation risks. Fracture inclination in vertical and oblique planes is closely related to reoperation outcomes and may be a useful complement to the way FNFs are currently evaluated.

Keywords: femoral neck fracture (hip fracture), nongeriatric patients, fracture inclination, fracture stability, reoperation, three-dimensional measurement and analysis

OPEN ACCESS

Edited by:
Lizhen Wang,
Beihang University, China

Reviewed by:
Wenbo Wang,
First Affiliated Hospital of Harbin Medical University, China
Yuancheng Li,
Dalian Medical University, China

****Correspondence:***
Weitao Jia
jiaweitao@shsmu.edu.cn
Changqing Zhang
zhangcq@sjtu.edu.cn

Specialty section:
This article was submitted to Biomechanics, a section of the journal Frontiers in Bioengineering and Biotechnology

Received: *23 September 2021*
Accepted: *19 October 2021*
Published: *03 November 2021*

Citation:
Jiang D, Zhan S, Hu H, Zhu H, Zhang C and Jia W (2021) The Effect of Vertical and Oblique Inclinations on Fracture Stability and Reoperation Risks in Femoral-Neck Fractures of Nongeriatric Patient. Front. Bioeng. Biotechnol. 9:782001. doi: 10.3389/fbioe.2021.782001

INTRODUCTION

Femoral neck fractures (FNFs) in patients younger than 60 years old frequently result from high-energy impact and remain a clinical challenge to treat (Slobogean et al., 2015; Anne et al., 2018). Internal fixation treatment is generally preferred over arthroplasty for these patients, but healing complications and reoperations are particularly common (Slobogean et al., 2015; Anne et al., 2018). Avascular necrosis (AVN) rate is most common (14.3%) (Slobogean et al., 2015), followed by rates of 9.3% for non-unions (NU) (Slobogean et al., 2015), and 13.0% reoperation rate (Anne et al., 2018). FNFs in nongeriatric patients are difficult to treat because of the high-energy violent nature of the insult, unfavorable biomechanical environment, tenuous vasculature, and inappropriate treatment strategies. An improved understanding of fracture morphology and the underlying stability is the prerequisite to select an appropriate internal fixation and rehabilitation plan in order to maximally reduce the high risks of complications. However, for years, debate has continued about what the optimal internal fixation is for these patients, a controversy that is exacerbated by a lack of a satisfactory principle to evaluate fracture stability and predict clinical prognosis accurately.

Currently, for nongeriatric patients, Pauwels classification, based on two-dimensional (2-D) X-ray, is a relatively widely used system to evaluate fracture stability and guiding internal fixation choice. Typically, the Pauwels angle reflects vertical inclination in the vertical plane. But recent analysis of fracture morphology (Collinge C A et al., 2014; Sarfani et al., 2021) revealed that the fracture surface in axial oblique plane was not always sagittally oriented. Increasing evidences indicated that fixation stability is influenced by both of the fracture's vertical and oblique inclinations (Collinge C A et al., 2014; Wright_et al., 2020; Wang et al., 2021), but Pauwels angle is insensitive to the latter important parameter. To date, the effect of axial obliquity on fracture stability and clinical outcome has not been thoroughly studied in all FNF types. Consequently, there is still necessary to draw a more complete picture of fracture stability which takes into account both vertical and oblique inclinations.

With a large scale of nongeriatric patients with all FNF types, the purpose of the current study was to comprehensively describe the 3-D inclination angle in both vertical and oblique planes, and to investigate the combined effect of fracture inclinations in multiple planes on fracture stability and reoperation risks.

MATERIALS AND METHODS

Patient Recruitment

From January 2013 to December 2018, we conducted a retrospective search for patients with FNFs in ten orthopaedic wards of one general hospital, which is the second largest medical centre in this country with over 51,000 operations annually. According to our inclusion/exclusion criteria, a convenience sample of 755 patients were finally included in the analysis (**Figure 1**). All subjects were given written informed consent to participate, and the study was approved by the local institutional ethics review board (No. 2016-143). The essential parameters of each case such as age, gender, smoking history, number of follow-up months, displacement degree, comminution, reduction quality, and fixation strategy were documented as baseline information.

Radiographic Measurement

The CT images of the 755 patients were analysed using the novel quantitative analysis system using MIMICS and MATLAB software. Three-dimensional bone models were reconstructed based on their CT scans. Outlines of the fracture were drawn along the cortical edges of distal fragment models (**Figure 2A**). In order to quantify the 3-D inclination angle, we used a coordinate system based on the contralateral femur for

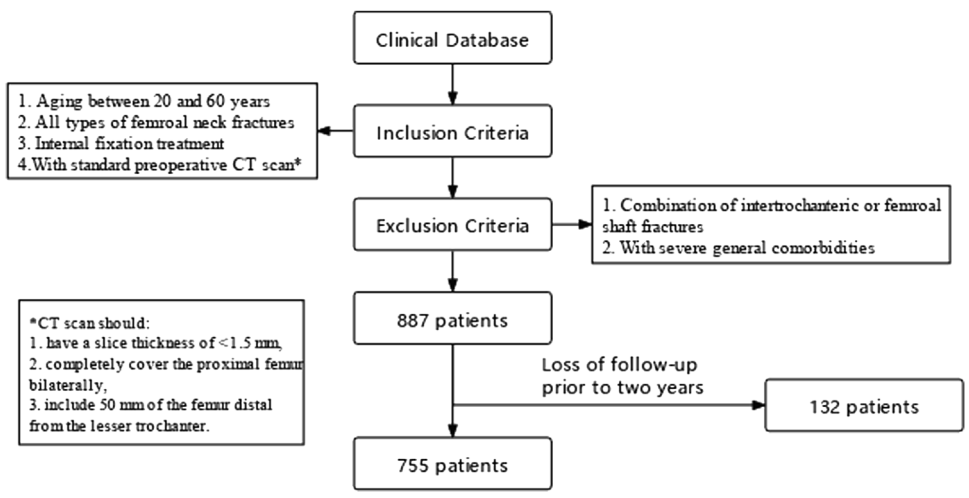

FIGURE 1 | Patient selection process.

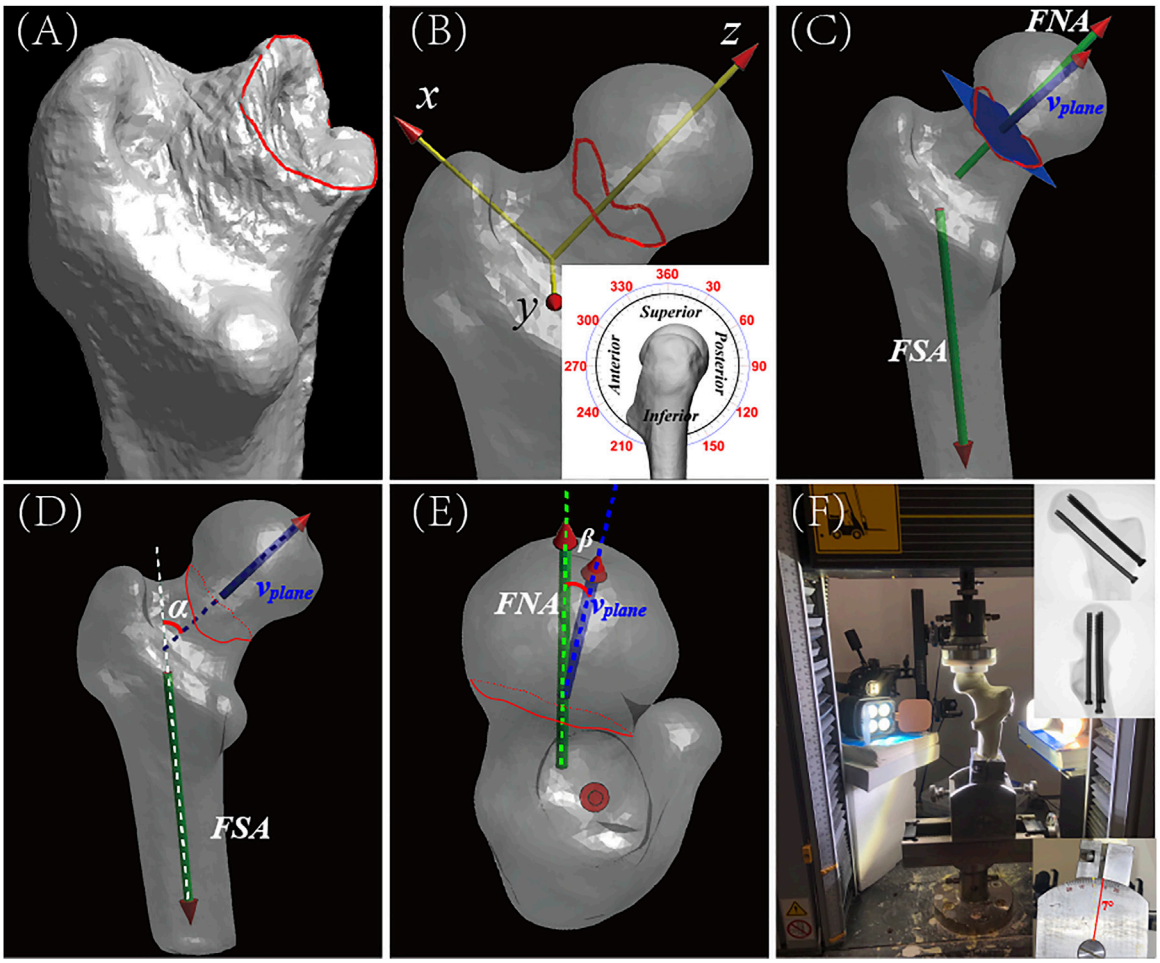

FIGURE 2 | The measurement of Fracture inclination in multiple planes from CT images, and the setup for the biomechanical validation study. **(A)** Anteroposterior (AP) view of reconstructed distal fragment of proximal femur and neck showing position of FNF. The fracture line (red) was manually traced along the cortical edges of the distal fragment in 3-Matics® software. Proximal fragment is hidden in this image. For orientation purposes, lesser trochanter occupies the lower foreground. **(B)** Local coordinate axes (X, Y, Z) overlaid on complete 3-D reconstruction. Local coordinate axes (X, Y, Z) overlaid on complete 3-D reconstruction. Fracture line was divided into equal sections or degrees using the classical clock-face system (inset, lateral view). For orientation, 0°/360° (i.e., 12 o'clock) points toward the superior part of the femoral head and 180° (i.e., 6 o'clock) points toward its inferior part. The clock-face system was then digitally transposed onto the custom proximal femoral coordinate system. **(C)** AP view of reconstructed proximal femur showing orientation of the fracture plane, which is represented by the blue-colored rectangle. v_{plane} represents the normal vector of the fracture plane. FSA, femoral shaft axis; FNA, femoral neck axis. **(D)** AP view of the reconstructed proximal femur showing how proposed classification parameters were determined. α (red) is defined as the angle between v_{plane} (blue, projected on vertical plane) and the FSA (white dotted line). **(E)** Axial view of the reconstructed femur showing femoral head and determination of proposed classification parameters. β is defined as the angle between v_{plane} (blue, projected on coronal plane) and the FNA (green dotted line). β is a measure of the axial obliquity of a fracture. **(F)** Photograph of the biomechanical test setup showing a simulated FNF in a Synbone®. In the biomechanical test, a simulated fracture was made in a Synbone®, the fracture was fixed with standard cannulated orthopaedic screws, and the femoral shaft was fixed in the Instron testing instrument at a shaft adduction angle of 7° (lower inset photograph). Interfragmentary motion (IFM) was then recorded using a VIC-3D 9 system (Correlated Solutions, Inc.). As progressively greater downward force was applied to the fixed Synbone®, high-speed digital images were acquired of the Synbone® and stored for later analysis. The digital images were imported into MATLAB software, and IFM was calculated for each of the seven groups of simulated FNFs. Top inset shows postoperative radiograph of fixation screws in Synbone®.

reference (Dolatowski et al.;Dimitriou et al., 2016). This reference coordinate system was mirrored and best-fit aligned with the distal fragment using the iterative closest points (ICP) method (Dimitriou et al., 2016). In the coordinate system, the fracture line was divided equally into 360 points according to the classic clock-face system (Lavigne et al.;Lazaro et al., 2015) (**Figure 2B**). Although the contour of the fracture line is a complex shape, a representative fracture plane is necessary for calculating the inclination angle. Current morphological studies (Collinge C A et al., 2014) typically have only calculated fracture inclination in just one slice of each CT plane, which cannot accurately describe the overall orientation of a complex fracture line. In order to solve this problem more scientifically and quantitively, a best-fitting plane based on the 360 points on the fracture line was created using the least-squares method, and the normal vector (v_{plane}) of the plane was defined as its 3-D orientation (**Figure 2C**). This method is a classic technique in geology for accurately determining the orientation of a rock

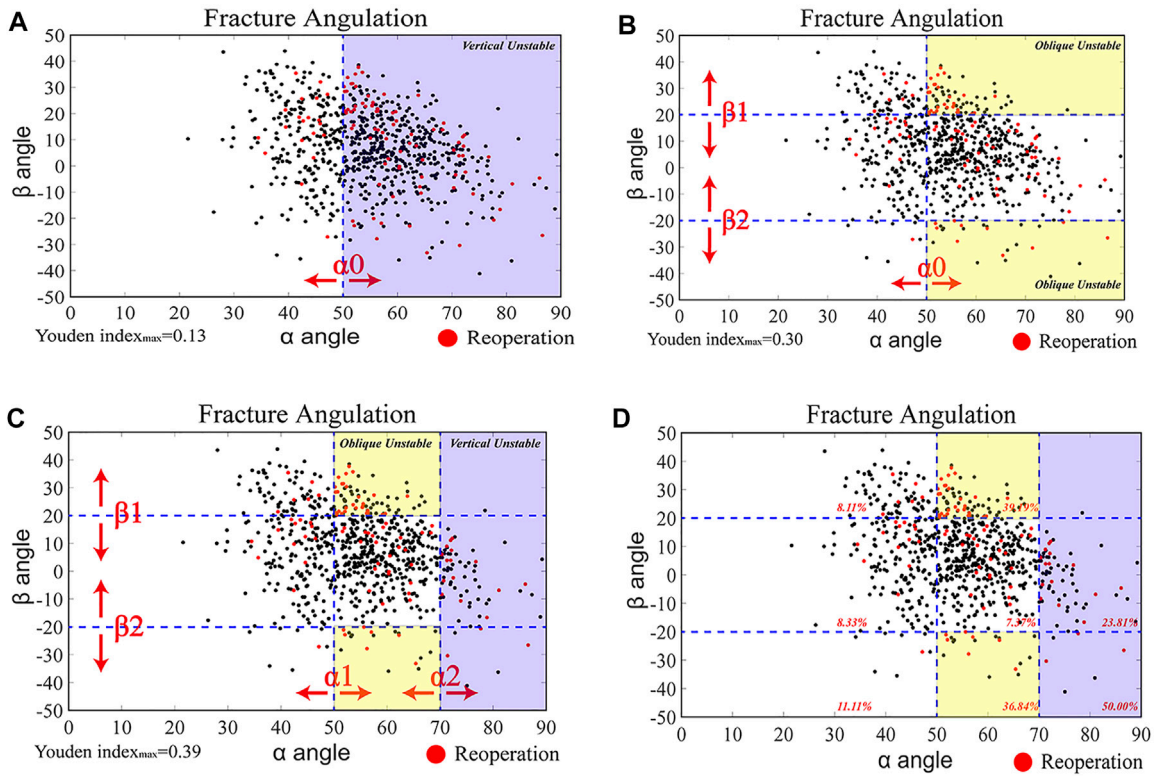

FIGURE 3 | Identification of Three-Dimensional Unstable Inclination angles based on clinical prognosis analyses **(A–C)** Scatterplots of 3-D inclination angles of all FNFs (n = 755) (black dots). Reoperated cases (red dots) are overlaid. The identification of 3-D unstable inclination angles was based on the 755 reoperation cases (n = 100; See **Supplementary Table S2**) and their associated α and β angles calculated from the 3-D reconstructions of their proximal femur and FNFs. Three grouping principles were tested in the diagnostic test: (1) vertical unstable [**(A)**, purple-colored region); (2) oblique unstable [**(B)**, yellow-colored region]; and (3) both vertical and oblique unstable [**(C)**, purple-colored and yellow-colored regions]. **(D)** The optimal threshold values (α0, α1, α2, β1, β2) were identified by calculating the maximum Youden index among over 12,160 possible combinations. The combined vertical ($\alpha > 70^{\circ}$) and oblique ($50^{\circ} < \alpha < 70^{\circ}$ and $\beta > 20^{\circ}/< -20^{\circ}$) unstable types had the highest Youden index (0.39). The reoperation rate percentages (red) are shown in each region.

fracture surface in 3-D (Feng et al., 2001), a problem that shares the same basic parameter space as accurately determining the orientation of a bone fracture in 3-D. The fracture's 3-D inclination angle was quantified by measuring the angulation of fracture orientation with femoral shaft axis (FSA) in the coronal plane (α, **Figure 2D**) and that with femoral neck axis (FNA) in axial plane (β, **Figure 2E**).

Clinical Outcomes

The primary endpoint was relevant reoperation due to the advantage of absolute objectivity, which has been extensively applied in clinical studies (Slobogean et al., 2017; Anne et al., 2018). All complications were recorded as secondary outcomes; these included nonunion, femoral neck shortening (Zlowodzki et al., 2008) (>10 mm), and avascular necrosis.

Clinical Analysis of 3-D Unstable Inclination Angles

We identified 3-D unstable inclination angles based on inclination angles and the corresponding reoperation outcome (yes or no, See **Supplementary Table S1**) for each of the 755 cases. Based on clinical and biomechanical considerations, three grouping principles were evaluated in the "diagnostic test": 1) only vertical unstable (**Figure 3A**); 2) only oblique unstable (**Figure 3B**); and 3) both vertical and oblique unstable (**Figure 3C**). We calculated the Youden index YI (Habibzadeh et al., 2016) (YI = Specificity + Sensitivity − 1) for all possible combinations of α and β angles to determine the optimal threshold in predicting reoperation outcome. After identifying the optimal cut-off value, the association between 3-D inclination angles and reoperation outcome was analysed using a multivariant model. Complications and reoperation risks in 3-D unstable groups were compared with those in the stable group.

Biomechanical Validation

The 3-D unstable fractures were validated by setting up a biomechanical test using commercially available realistic bone simulants. Forty-two Synbone models (model # 2200, Synbone®; Zizers, Switzerland) were divided into seven groups for the biomechanical test. According to the cut-off value proposed in

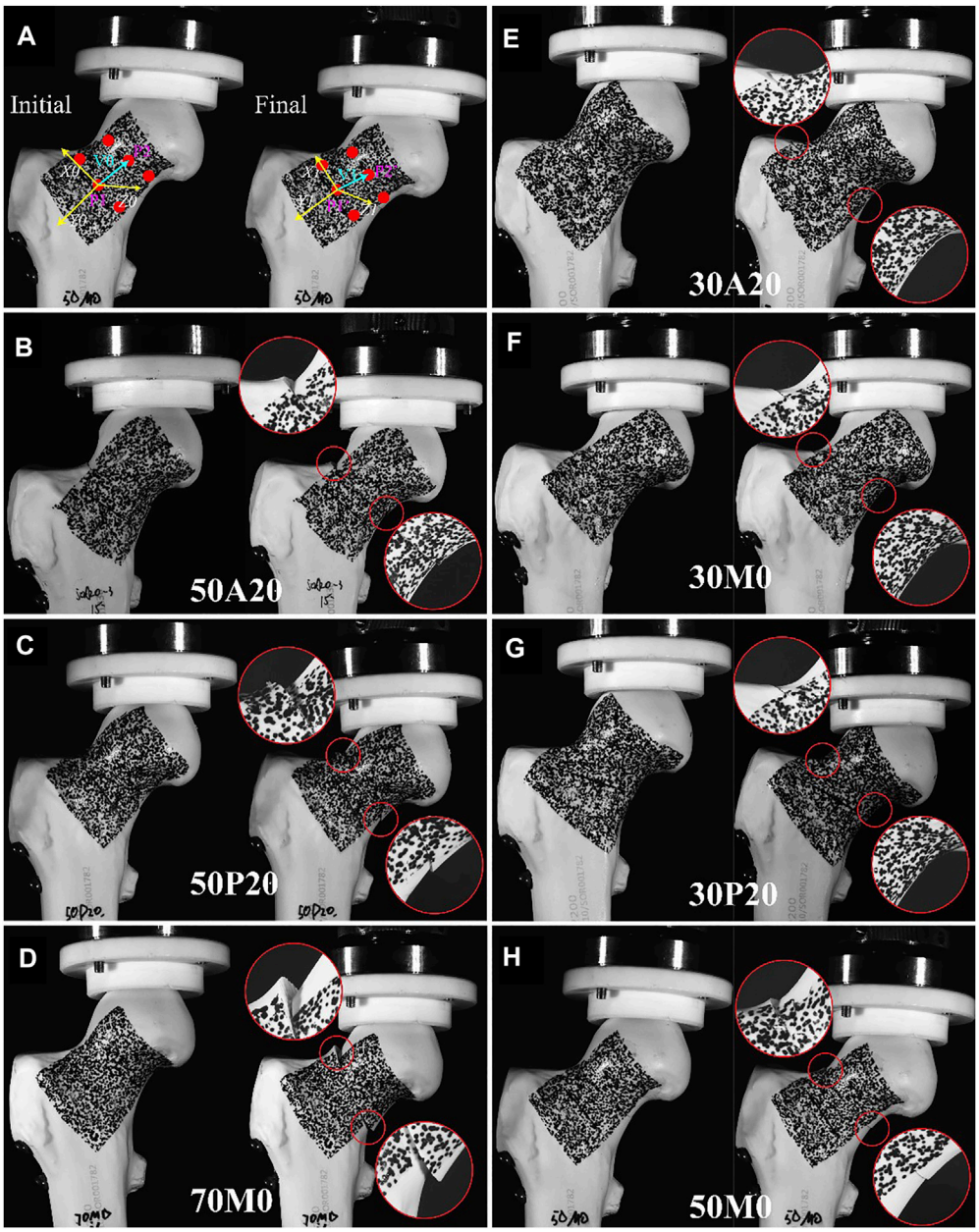

FIGURE 4 | Validation of 3-D unstable inclination angles in a biomechanical test. Illustrating the calculation and results of interfragmentary motion. Interfragmentary motion (IFM) was calculated according to the location of the three paired points (red dotted) in proximal and distal fragments, and the local coordinate system **(A)**. According to the photograph obtained with the VIC-3D, IFM was more severe in unstable groups **(B–D)** compared to stable groups **(E–H)**.

the diagnostic analysis, the fractures plane in each group had the following α and β values: 1) 30A20 ($\alpha = 30^{\circ}$, $\beta = -20^{\circ}$); 2) 30M0 ($\alpha = 30^{\circ}$, $\beta = 0^{\circ}$); 3) 30P20 ($\alpha = 30^{\circ}$, $\beta = 20^{\circ}$); 4) 50A20 ($\alpha = 50^{\circ}$, $\beta = -20^{\circ}$); 5) 50M0 ($\alpha = 50^{\circ}$, $\beta = 0^{\circ}$); 6) 50P20 ($\alpha = 50^{\circ}$, $\beta = 20^{\circ}$); and 7) 70M0 ($\alpha = 70^{\circ}$, $\beta = 0^{\circ}$). All fractures were fixed with three cannulated screws positioned in a classic inverted triangle configuration. The 3-D printed guiding plate was applicated to guarantee the accuracy of fracture orientation and screws position (Jiang et al., 2021c). Prior to being mounted on an Instron® system test apparatus, the model bones were speckled with black paint for VIC-3D to identify each spot and document its position during deformation (**Figure 4**). After that, all models were tested using an Instron load test system, set to a maximum 2000 N vertical loading load angled 7°(Zhang et al., 2018) relative to the FSA (**Figure 2F**). The main outcome variable for this part of the study was Inter-fragmentary motion (IFM).

IFM was calculated according to the location of the points recorded by the VIC-3D (XR-9M; Correlated Solutions Inc., Irmo, SC, United States). Three paired points from superior, medial, and inferior parts of the femoral neck were selected for

TABLE 1 | Demographic and selected clinical characteristics of the study population.

Variable	Total	Reoperation	OR (95% CI)	*p* Value
Participants	755	100 (13.3%)	—	—
Age	47.14 ± 10.68	46.00 ± 10.85	0.988 (0.966–1.010)	0.281
Sex				
Male	410	57 (13.9%)	1	—
Female	345	43 (12.5%)	1.321 (0.760–2.296)	0.324
Smokers	210	29 (13.8%)	1.109 (0.614–2.003)	0.731
Follow-up time	47.89 ± 18.84	50.34 ± 19.25	1.007 (0.995–1.019)	0.256
Displacement degree[c]				
Non-displaced	201	7 (3.5%)	1	—
Displaced	554	93 (16.8%)	3.774 (1.667–8.544)	0.001[b]
Comminution				
No	333	32 (9.60%)	1	—
Yes	422	68 (20.2%)	1.599 (0.979–2.610)	0.061
Reduction quality[d]				
Excellent-Good	639	72 (11.3%)	1	—
Fair-Poor	116	28 (24.1%)	2.117 (1.233–3.635)	0.007[b]
Fixation strategy[e]				
3 cannulated screws	611	69 (11.3%)	1	—
4 cannulated screws	108	20 (18.5%)	1.547 (0.846–2.829)	0.156
Other	36	11 (30.6%)	2.500 (1.096–5.704)	0.029[b]
3-D inclination Angle[f]				
Stable	593	47 (7.9%)	1	0
Unstable	162	53 (32.7%)	4.699 (2.949–7.486)	<0.001[b]

[a]*CI, confidence interval.*
[b]*Significant.*
[c]*Displacement degree is evaluated by Garden classification.*
[d]*Reduction quality was assessed according to the method of Haidukewych and colleagues.*
[e]*Other fixation strategies included 32 dynamic hip screws and four buttress plate technique.*
[f]*3-D unstable inclination angles were identified in the current study and were defined as $\alpha > 70^{\circ}$; $50^{\circ} < \alpha < 70^{\circ}$ and $\beta > 20^{\circ}$ or $< -20^{\circ}$.*

analysis. The algorithm used to calculate the IFM was based on vector rather than scalar values. As showed in (**Figure 4A**), V0 and V1 represent the vectors of two target points at the initial and final state, respectively. Both V0 and V1 were projected into X (V0X, V1X); Y (V0X, V1X); and Z (V0X, V1X) axes (**Figure 4A**). The two coordinate systems, X0Y0Z0 and X1Y1Z1, were constant in relation to the distal fragment. IFM was calculated based on the formula below. The mean IFM of the three paired nodes was defined as the IFM of the fracture model.

$$IFM = \sqrt[2]{\left|\overrightarrow{V1X} - \overrightarrow{V0X}\right|^2 + \left|\overrightarrow{V1Y} - \overrightarrow{V0Y}\right|^2 + \left|\overrightarrow{V1Z} - \overrightarrow{V0Z}\right|^2}. \quad (1)$$

Statistical Statistics

All calculations were conducted using SAS software (version 9.4 for Windows; SAS Institute, Cary, NC, United States). Categorical variables were compared using the chi-squared test, expressing as frequencies. Continuous variables are presented as means and standard deviations, and were checked for normality firstly using Kolmogorov-Smirnov test. Multiple-group comparisons of parametric continuous variables in the biomechanical validation test were performed using one-way ANOVA. The possible relationship between 3-D inclination angles with reoperation risks was evaluated using a binary logistic regression model. The 3-D inclination angles were regarded as exposure variables and was converted into a binary variable (stable = 0; unstable = 1). Other possible confounding parameters documented as baseline information were also entered as variables into the regression models. Statistical significance was set at $p < 0.05$.

RESULTS

From January 2013 through the end of December 2018, a total of 755 patients with a mean age of 47.14 ± 10.68 years was included in this study as participants (**Table 1**). The mean values for α, β were, respectively, 54.91° ± 10.91°, 6.96° ± 14.65° with ICCs (95% CI) values of 0.78 (0.75–0.80), 0.85 (0.82–0.87).

Among the included patients, 100 (13.2%) cases underwent relevant reoperation for the reasons of non-union (n = 12, 7 with arthroplasty, 4 with re-osteosynthesis, 1 with vascularized fibular grafting), avascular necrosis (n = 67, 58 with arthroplasty, 9 with vascularized fibular grafting) and screw withdrawal or protruding (n = 21, Removal of implants).

Among the 12,160 possible combinations of cut-off values, 3-D unstable inclination angles with an optimal Youden index (0.39) were identified in fractures having an $\alpha > 70^{\circ}$ (vertical) and $50^{\circ} < \alpha < 70^{\circ}$ and $\beta > 20^{\circ}$/< -20° (oblique) (**Figure 3D**).

Binary logistic regression models indicated that reoperation was significantly associated with fracture's 3-D inclination angle (OR = 4.699 (95%CI 2.949–7.486), p-value <0.001). The reoperation rate in 3-D unstable group (32.7%) is significantly ($p < 0.001$) higher than that in 3-D stable group (7.9%). Apart from reoperation risks, complications including non-union, femoral neck shortening and avascular

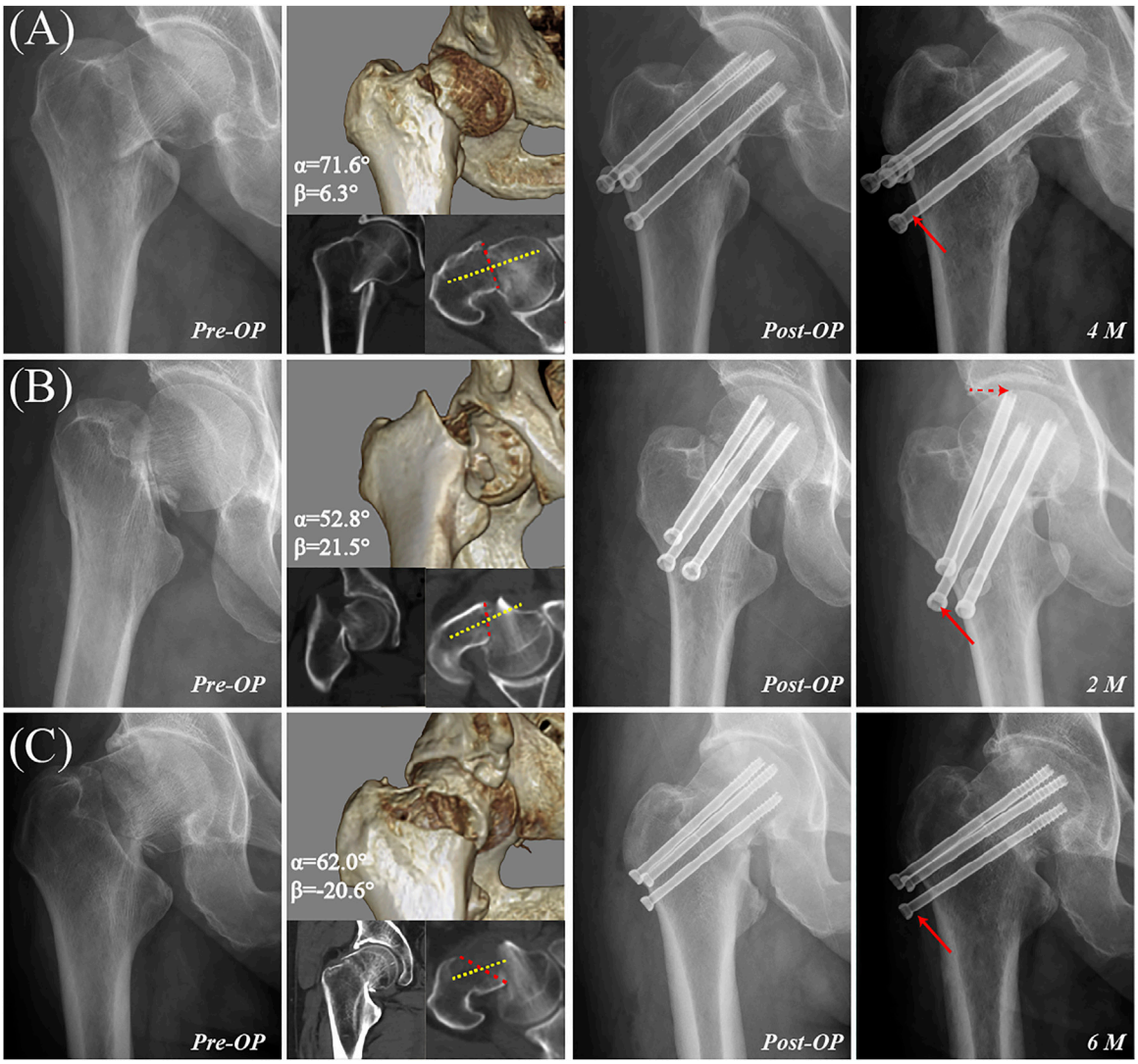

FIGURE 5 | Examples of femoral neck fractures with 3-D unstable inclination angle. **(A)** A 46-year-old male with a vertical unstable inclination angle (α = 71.6° and β = 6.3°) was treated with three cannulated screws. Radiography taken 4 months postoperatively revealed severe screw withdrawal (red arrow) as well as femoral neck shortening, varus collapse, and delayed union. **(B)** A 46-year-old female with retroversion oblique unstable inclination angle (α = 52.8° and β = 21.5°) was treated by three cannulated screws with a fair reduction quality. Radiography taken 2 months postoperatively revealed severe screw withdrawal (solid red arrow) as well as femoral neck shortening, varus collapse, screw penetration of the joint capsule (dotted red arrow), and delayed union. **(C)** A 59-year-old male with anteversion oblique unstable inclination angle (α = 62.0° and β = −20.6°) was treated with three cannulated screws. Radiography taken 6 months postoperatively revealed severe screw withdrawal (red arrow) as well as femoral neck shortening, varus collapse, and delayed union.

necrosis were all significantly lower (p-value <0.05) in fractures designated as 3-D unstable inclinations (**Figures 5**, **6**) (**Table 2**).

In the combined biomechanical validation test (**Figure 7**), the IFM was significantly greater ($p < 0.05$) in the 70M0 ($\alpha = 70^{\circ}$, $\beta = 0^{\circ}$; 2.387 ± 0.532 mm); 50P20 ($\alpha = 50^{\circ}$, $\beta = 20^{\circ}$; 1.963 ± 0.406 mm); and 50A20 ($\alpha = 50^{\circ}$, $\beta = -20^{\circ}$; 1.374 ± 0.491 mm) groups than that in any other group of α and β combinations. The IFMs of the remaining groups (50M0 ($\alpha = 50^{\circ}$, $\beta = 0^{\circ}$; 0.699 ± 0.327 mm), 30M0 ($\alpha = 30^{\circ}$, $\beta = 0^{\circ}$; 0.330 ± 0.184 mm), 30A20 ($\alpha = 30^{\circ}$, $\beta = -20^{\circ}$; 0.456 ± 0.104 mm), and 30P20 ($\alpha = 30^{\circ}$, $\beta = 20^{\circ}$; 0.681 ± 0.184 mm) were not significantly different.

DISCUSSION

In the present study, we calculated 3-D fracture inclinations of a comprehensive set of FNFs in 755 patients using 3-D digitally reconstructed models from CT scans. We analysed and identified unstable types of 3-D inclinations based on the patient's clinical prognosis, and validated these types in a biomechanical experiment. Thereby, the effect of fracture inclination in both vertical and oblique planes were firstly clarified in the current study. The 3-D evaluating method presented as a useful complement to the classic Pauwels method. Fractures with $\alpha > 70^{\circ}$, or $50^{\circ} < \alpha < 70^{\circ}$ and $\beta > 20^{\circ}/\beta < -20^{\circ}$ were real unstable fracture

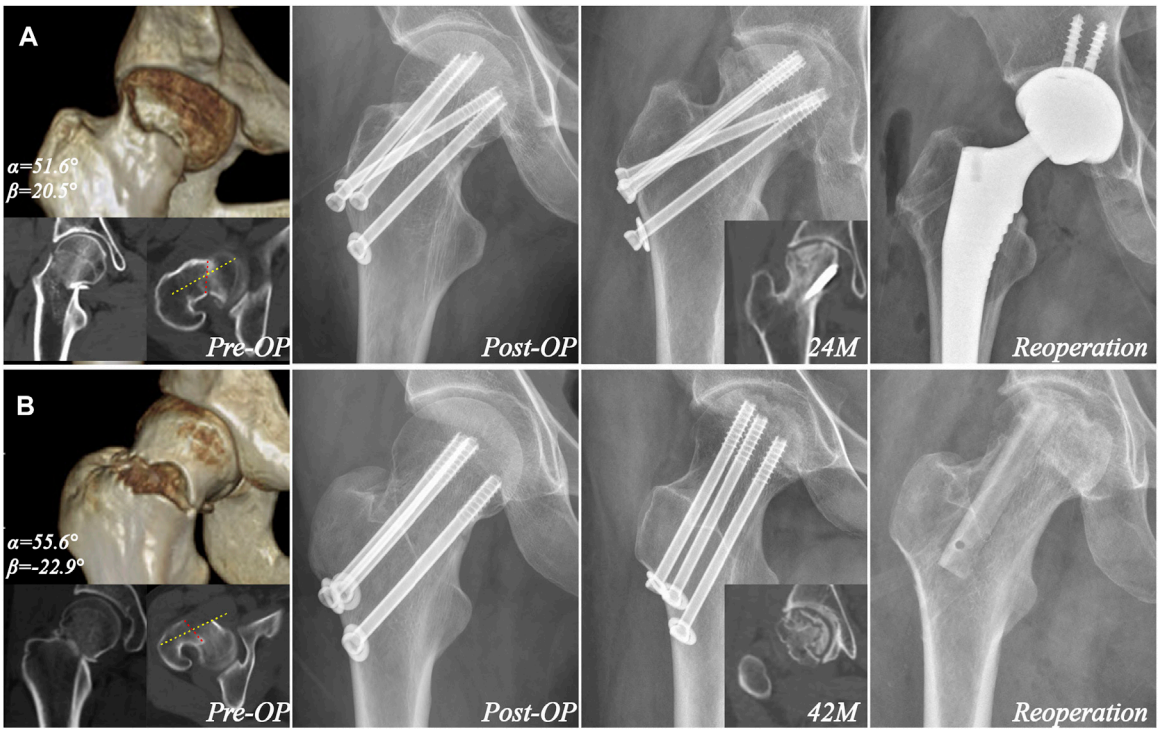

FIGURE 6 | Examples of avascular necrosis in cases with oblique unstable inclination. **(A)** A 42-year-old female with retroversion oblique unstable inclination angle (α = 51.6° and β = 20.5°) was treated with four cannulated screws. Radiography taken 24 months postoperatively revealed avascular necrosis, which was treated with arthroplasty. The yellow and red line showed the femoral neck axis and fracture orientation in one CT plane. **(B)** A 32-year-old female with anteversion oblique unstable inclination angle (α = 55.6° and β = −22.9°) was treated with three cannulated screws. Radiography taken 42 months postoperatively revealed avascular necrosis, which was treated with free vascularized fibular grafting. The yellow and red line showed the femoral neck axis and fracture orientation in CT plane.

types in 3-D view, with significantly higher IFM and higher reoperation and complication risks.

With the 3-D inclination measurement, apart from vertical angulation, severe fracture obliquity axially ($\beta > 20^{\circ}$ or $\beta < -20^{\circ}$) was observed in 24.11% patients. Variability in axial obliquity may be related to a combination of shear and rotational forces (Augat et al., 2019), patients experienced upon the traumatic impact and the position of the lower limb during the impact. Previous studies have confirmed that fracture obliquity reduces fracture stability (Collinge C A et al., 2014; ;Wright et al., 2020), but the concept of an oblique instability, has not been routinely considered in current preoperative evaluations. The present study is the first to quantitatively illustrate the influence of 3-D inclinations in both of vertical and oblique planes on fracture stability and clinical prognosis.

What is an "unstable" fracture after fixation? It can be defined as a fracture that has a large motion of the two fragments at the fracture site when under physiological load (An, 2018), even with anatomic reduction and standard internal fixation. Therefore, compared with construct stability, interfragmentary stability is more consistent with clinical prognosis (Jiang et al., 2021a). In this study, fractures with 3-D inclination angles having $\alpha > 70^{\circ}$; $50^{\circ}<\alpha < 70^{\circ}$ and $\beta > 20^{\circ}/\beta < -20^{\circ}$ should be demonstrated as the real unstable types because of significantly greater IFM than other α and β angle combinations of fractures assessed in the biomechanical test. Most of the unstable fractures with $\alpha > 70^{\circ}$ were the "centered" type (i.e., $-20^{\circ}<\beta < 20^{\circ}$), indicating that they were likely the result of predominantly violent vertical forces, while those with $50^{\circ}<\alpha < 70^{\circ}$ and $\beta > 20^{\circ}/\beta < -20^{\circ}$ were produced by a combination of vertical and rotational forces (Augat et al., 2019). Fracture obliquity affected stability only to a certain extent. Either anteversion or retroversion over 20° significantly reduced stability in fractures with $50^{\circ}<\alpha < 70^{\circ}$, while no such effect on stability was observed in fractures with $\alpha < 50^{\circ}$.

Higher rates of non-union, femoral neck shortening and avascular necrosis resulted in a higher reoperation rate in 3-D unstable fractures. Excess IFM, especially in the shear direction, may lead to osteoclastogenesis (Ma et al., 2019) and bone resorption, which may eventually result in femoral neck

TABLE 2 | Comparison of complications between 3-D stable and unstable groups.

	3-D stable	3-D unstable	*p*
N	593	162	—
Reoperation	47 (7.9%)	53 (32.7%)	<0.001
Non-union	23 (3.8%)	13 (8.02%)	0.028
Femoral neck shortening	86 (14.5%)	51 (31.5%)	<0.001
Avascular necrosis	113 (19.1%)	46 (28.4%)	0.010
Complication	158 (23.8%)	67 (45.1%)	0.008

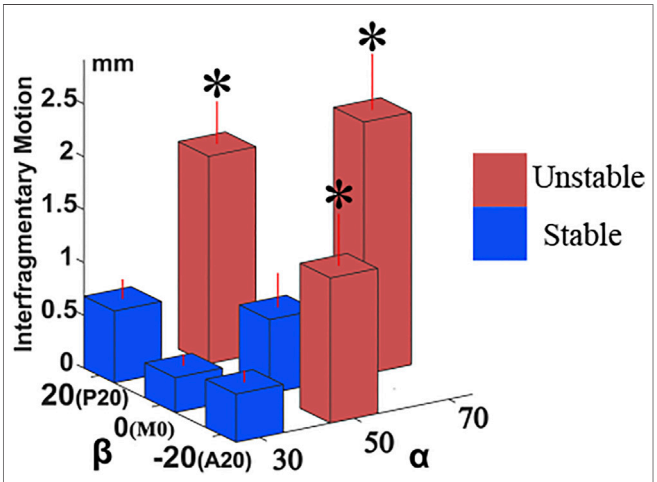

FIGURE 7 | The comparison of interfragmentary motion in biomechanical test. IFM plots as a function of α and *β* angles in the biomechanical validation test. Synbone® fracture groups with combinations of α = 70°; α = 50° and β = 20°; and α = 50° and β = 20° had significantly greater IFMs than groups with combinations of α = 30° (<50°), and α = 50° and β = 0°. These outcomes of simulated FNFs in Synbones® correspond well with clinical findings. Asterisks indicate significance as evaluated by one-way ANOVA. Extent of group (*n* = 5) variability is standard deviation (SD) shown by red-colored vertical lines.

shortening (Zlowodzki et al., 2008). Severe shortening of the femoral neck will lead to abductor moment reduction and irritation from protruding screws, which significantly decreases functional scores of patients (Slobogean et al., 2017; Felton et al., 2019). In the present study, there was a significantly (p = 0.02) higher incidence of avascular necrosis in fractures with 50°<α < 70° and β > 20°/β < -20° (See **Supplementary Table S2**), probably due to a difficulty of vessel reconstruction in these fractures.

Identifying the exact fracture type of a femoral neck fracture is prerequisite to develop appropriate treatment and rehabilitation plans, which can maximally reduce the potentially high risks of complications, and thus halt or delay the progression to arthroplasty. In clinical practice, surgeons should be aware of the inherent high risks of complications in fractures with unstable inclination angles, and handle these patients more prudently and schedule closer follow-ups. Because of the unstable nature, apart from achieving an acceptable reduction, a more biomechanically beneficial fixation strategy such as sliding hip screws (Bhandari and Swiontkowski, 2017; Augat et al., 2019), Buttress plate (Zhan et al., 2020; Jiang et al., 2021c), Alpha fixation (Jiang et al., 2021b; Jiang et al., 2021c) or the Tragon locking plate system (Bliven et al., 2020) were more recommended for these fractures compared with traditional three parallel screws. However, clinical evidence of the optimal internal fixation selection for the real unstable femoral neck fractures is still absent. Current available clinical studies such as the FAITH trail (Slobogean et al., 2017) all evaluated fracture stability according to Pauwels classification. The Pauwels angle based on 2-D radiography cannot reflect the real vertical inclination angle, which is subjective and inconsistent among observers (Embden et al., 2011). Therefore, further multicentric prospective or randomized controlled trials are still required to clarify the optimal internal fixation selection for the unstable femoral neck fractures identified in the current prognostic study. Finally, due to the tendency of re-displacement postoperatively in these fractures, a relatively conservative rehabilitation plan such as prolonging the time in bed or postponing weight-bearing exercise is preferred.

The current study had some limitations. Currently, CT scan is not a clinical routine, and there is no internationally uniform standard for identifying to whom CT scan should apply. Whether the cases in our hospital received CT scans is determined by the surgeon's own experience, rather than patient's specific condition or fracture severity, but a potential selection bias may still exist in the analysis. Although the 3-D inclination angle of FNFs showed a close association with reoperation outcome, the practical measurement of 3-D inclination angle needs to be simplified for convenience in order to be applied routinely in clinical applications. Nevertheless, the measurement of 3-D inclination angle is not beyond the abilities of most modern radiology departments, and given the potential long-term benefits, may well be worth the effort. Additionally, this study mainly concentrated on fracture inclination. Fracture comminution is another important factor determining interfragmentary stability, which should be analysed as a separate topic in future studies.

Internal fixation for femoral neck fractures of nongeriatric patients poses a clinical challenge, one with dissimilar prognoses for different fracture types. Evaluating fracture stability from both vertical and oblique planes in 3-D view could be a useful complement to the classic Pauwels method. Apart from vertical inclination, severe obliquity (β > 20°/β < -20°) was observed in 24.11% of all cases, a previously underappreciated rate. FNFs with particular combinations of α and β angles (α > 70°; 50°<α < 70° and β > 20°/β < −20°) produce worse fracture stability, higher complication rate, and reoperation risks. For these unstable FNFs, fixation with traditional three parallel screws showed a significantly greater interfragmentary motion across fracture site, thus a more mechanically stable internal fixation and conservative rehabilitation schedule are required in order to achieve a successful treatment outcome, improve life quality and reduce the burdensome healthcare costs of treating complications after suboptimal treatment.

DATA AVAILABILITY STATEMENT

The raw data supporting the conclusion of this article will be made available by the authors, without undue reservation.

ETHICS STATEMENT

The studies involving human participants were reviewed and approved by Shanghai Sixth People's Hospital. The patients/participants provided their written informed consent to

participate in this study. Written informed consent was obtained from the individual(s) for the publication of any potentially identifiable images or data included in this article.

AUTHOR CONTRIBUTIONS

DJ: Design the study, Biomechanical validation, Analysis the results, Draft the manuscript. SZ: Evaluate the results and technical support HH: Supervised the study Evaluate the results; HZ: Evaluate the results; CZ: Supervised the study, Revise the manuscript. WJ: Design the study, Supervised the study, Biomechanical validation, Revise the manuscript.

FUNDING

This work was supported by Science popularization project funds of Shanghai Science and Technology Commission (No. 20DZ2310300); Shanghai Municipal Education Commission—Gaofeng Clinical Medicine Grant Support (20172026); Interdisciplinary Program of Shanghai Jiao Tong University (YG2017QN14).

SUPPLEMENTARY MATERIAL

The Supplementary Material for this article can be found online at: https://www.frontiersin.org/articles/10.3389/fbioe.2021.782001/full#supplementary-material

REFERENCES

An, S. (2018). AO Principles of Fracture Management. *Acta Chirurgica Belgica* 118, 269. doi:10.1080/00015458.2018.1467124

Augat, P., Bliven, E., and Hackl, S. (2019). Biomechanics of Femoral Neck Fractures and Implications for Fixation. *J. Orthop. Trauma* 33 (Suppl. 1), S27–s32. doi:10.1097/bot.0000000000001365

Bhandari, M., and Swiontkowski, M. (2017). Management of Acute Hip Fracture. *N. Engl. J. Med.* 377, 2053–2062. doi:10.1056/NEJMcp1611090

Bliven, E., Sandriesser, S., Augat, P., von Rüden, C., and Hackl, S. (2020). Biomechanical Evaluation of Locked Plating Fixation for Unstable Femoral Neck Fractures. *Bone Jt. Res.* 9, 314–321. doi:10.1302/2046-3758.96.bjr-2019-0331.r1

Collinge, C. A., Mir, H., and Reddix, R. (2014). Fracture Morphology of High Shear Angle "Vertical" Femoral Neck Fractures in Young Adult Patients. *J. Orthopaedic Trauma* 28, 270–275. doi:10.1097/BOT.0000000000000014

Dimitriou, D., Tsai, T.-Y., Yue, B., Rubash, H. E., Kwon, Y.-M., and Li, G. (2016). Side-to-side Variation in normal Femoral Morphology: 3D CT Analysis of 122 Femurs. *Orthopaedics Traumatol. Surg. Res.* 102, 91–97. doi:10.1016/j.otsr.2015.11.004

Dolatowski, F. C., Temmesfeld, M. J., Pierre-Jerome, C., Borthne, A., and Hoelsbrekken, S. E. (2018). Bilateral Symmetrical Comparison of the Proximal Femur Using 3D-CT Models. *Surg. Radiol. Anat.* 40, 507–513. doi:10.1007/s00276-018-1968-6

Felton, J., Slobogean, G. P., Jackson, S. S., Della Rocca, G. J., Liew, S., Haverlag, R., et al. (2019). Femoral Neck Shortening after Hip Fracture Fixation Is Associated with Inferior Hip Function: Results from the FAITH Trial. *J. Orthop. Trauma* 33, 487–496. doi:10.1097/bot.0000000000001551

Feng, Q., Sjögren, P., Stephansson, O., and Jing, L. (2001). Measuring Fracture Orientation at Exposed Rock Faces by Using a Non-reflector Total Station. *Eng. Geology.* 59, 133–146. doi:10.1016/s0013-7952(00)00070-3

Habibzadeh, F., Habibzadeh, P., and Yadollahie, M. (2016). On Determining the Most Appropriate Test Cut-Off Value: the Case of Tests with Continuous Results. *Biochem. Med.* 26, 297–307. doi:10.11613/bm.2016.034

Jiang, D., Zhan, S., Cai, Q., Hu, H., and Jia, W. (2021a). Enhanced Interfragmentary Stability and Improved Clinical Prognosis with Use of the off-axis Screw Technique to Treat Vertical Femoral Neck Fractures in Nongeriatric Patients. *J. Orthop. Surg. Res.* 16, 473. doi:10.1186/s13018-021-02619-8

Jiang, D., Zhan, S., Cai, Q., Hu, H., and Jia, W. (2021b). Long-term Differences in Clinical Prognosis between Crossed- and Parallel-Cannulated Screw Fixation in Vertical Femoral Neck Fractures of Non-geriatric Patients. *Injury*. doi:10.1016/j.injury.2021.07.014

Jiang, D., Zhan, S., Wang, L., Shi, L. L., Ling, M., Hu, H., et al. (2021c). Biomechanical Comparison of Five Cannulated Screw Fixation Strategies for Young Vertical Femoral Neck Fractures. *J. Orthop. Res.* 39, 1669–1680. doi:10.1002/jor.24881

Lavigne, M., Kalhor, M., Beck, M., Ganz, R., and Leunig, M. (2005). Distribution of Vascular Foramina Around the Femoral Head and Neck Junction: Relevance for Conservative Intracapsular Procedures of the Hip. *Orthop. Clin. North America* 36, 171–176. doi:10.1016/j.ocl.2005.02.002

Lazaro, L. E., Klinger, C. E., Sculco, P. K., Helfet, D. L., and Lorich, D. G. (2015). The Terminal Branches of the Medial Femoral Circumflex Artery. *Bone Jt. J.* 97-B, 1204–1213. doi:10.1302/0301-620X.97B9.34704

Ma, Q., Ma, Z., Liang, M., Luo, F., Xu, J., Dou, C., et al. (2019). The Role of Physical Forces in Osteoclastogenesis. *J. Cel Physiol* 234, 12498–12507. doi:10.1002/jcp.28108

Nyholm, A. M., Palm, H., Sandholdt, H., Troelsen, A., and Gromov, K. (2018). Osteosynthesis with Parallel Implants in the Treatment of Femoral Neck Fractures:. *J. Bone Jt. Surg.*, 100, 1682, 1690 Volume.doi:10.2106/JBJS.18.00270

Sarfani, S., Beltran, M., Benvenuti, M., and Collinge, C. (2021). Mapping of Vertical Femoral Neck Fractures in Young Patients Using Advanced 2 and 3-Dimensional Computed Tomography. *J. Orthop. Trauma*, Publish Ahead of Print.doi:10.1097/bot.0000000000002102

Slobogean, G. P., Sprague, S. A., Scott, T., and Bhandari, M. (2015). Complications Following Young Femoral Neck Fractures. *Injury* 46, 484–491. doi:10.1016/j.injury.2014.10.010

Slobogean, G. P., Stockton, D. J., Zeng, B.-f., Wang, D., Ma, B., and Pollak, A. N. (2017). Femoral Neck Shortening in Adult Patients under the Age of 55 Years Is Associated with Worse Functional Outcomes: Analysis of the Prospective Multi-center Study of Hip Fracture Outcomes in China (SHOC). *Injury* 48, 1837–1842. doi:10.1016/j.injury.2017.06.013

van Embden, D., Roukema, G. R., Rhemrev, S. J., Genelin, F., and Meylaerts, S. A. G. (2011). The Pauwels Classification for Intracapsular Hip Fractures: Is it Reliable? *Injury* 42, 1238–1240. doi:10.1016/j.injury.2010.11.053

Wang, K., Ni, M., Liao, P., Dou, B., Yan, X., Lv, L., et al. (2021). Fracture Morphology and Biomechanical Characteristics of Pauwels III Femoral Neck Fractures in Young Adults. *Injury*. doi:10.1016/j.injury.2021.08.025

Wright, D. J., Bui, C. N., Ihn, H. E., Mcgarry, M. H., Lee, T. Q., and Scolaro, J. A. (2020). Posterior Inferior Comminution Significantly Influences Torque to Failure in Vertically Oriented Femoral Neck Fractures: A Biomechanical Study. *J. Orthopaedic Trauma* 34, 644–649. doi:10.1097/BOT.0000000000001846

Zhan, S., Jiang, D., Xu, J., Ling, M., Yang, K., Li, Y., et al. (2020). Influence of the Proximal Screws of Buttress Plates on the Stability of Vertical Femoral Neck Fractures: a Finite Element Analysis. *BMC Musculoskelet. Disord.* 21, 842. doi:10.1186/s12891-020-03853-7

Zhang, B., Liu, J., Zhu, Y., and Zhang, W. (2018). A New Configuration of Cannulated Screw Fixation in the Treatment of Vertical Femoral Neck Fractures. *Int. Orthopaedics (Sicot)* 42, 1949–1955. doi:10.1007/s00264-018-3798-x

Zlowodzki, M., Brink, O., Switzer, J., Wingerter, S., Woodall, J., Jr., Petrisor, B. A., et al. (2008). The Effect of Shortening and Varus Collapse of the Femoral Neck

on Function after Fixation of Intracapsular Fracture of the Hip. *The J. Bone Jt. Surg. Br. volume* 90-B, 1487–1494. doi:10.1302/0301-620x.90b11.20582

Conflict of Interest: The authors declare that the research was conducted in the absence of any commercial or financial relationships that could be construed as a potential conflict of interest.

Publisher's Note: All claims expressed in this article are solely those of the authors and do not necessarily represent those of their affiliated organizations, or those of the publisher, the editors and the reviewers. Any product that may be evaluated in this article, or claim that may be made by its manufacturer, is not guaranteed or endorsed by the publisher.

frontiers in Bioengineering and Biotechnology

ORIGINAL RESEARCH
published: 25 November 2021
doi: 10.3389/fbioe.2021.783003

Kinetic and Kinematic Features of Pedestrian Avoidance Behavior in Motor Vehicle Conflicts

*Quan Li, Shi Shang, Xizhe Pei, Qingfan Wang, Qing Zhou and Bingbing Nie**

State Key Lab of Automotive Safety and Energy, School of Vehicle and Mobility, Tsinghua University, Beijing, China

The active behaviors of pedestrians, such as avoidance motions, affect the resultant injury risk in vehicle–pedestrian collisions. However, the biomechanical features of these behaviors remain unquantified, leading to a gap in the development of biofidelic research tools and tailored protection for pedestrians in real-world traffic scenarios. In this study, we prompted subjects ("pedestrians") to exhibit natural avoidance behaviors in well-controlled near-real traffic conflict scenarios using a previously developed virtual reality (VR)-based experimental platform. We quantified the pedestrian–vehicle interaction processes in the pre-crash phase and extracted the pedestrian postures immediately before collision with the vehicle; these were termed the "pre-crash postures." We recorded the kinetic and kinematic features of the pedestrian avoidance responses—including the relative locations of the vehicle and pedestrian, pedestrian movement velocity and acceleration, pedestrian posture parameters (joint positions and angles), and pedestrian muscle activation levels—using a motion capture system and physiological signal system. The velocities in the avoidance behaviors were significantly different from those in a normal gait ($p < 0.01$). Based on the extracted natural reaction features of the pedestrians, this study provides data to support the analysis of pedestrian injury risk, development of biofidelic human body models (HBM), and design of advanced on-vehicle active safety systems.

Keywords: pedestrian safety, active behavior, kinematics, biomechanics, integrated safety, volunteer testing

OPEN ACCESS

Edited by:
Lizhen Wang,
Beihang University, China

Reviewed by:
Francesco Travascio,
University of Miami, United States
Harry M. C. Choi,
University of Maryland School of Medicine, United States

****Correspondence:***
Bingbing Nie
nbb@tsinghua.edu.cn

Specialty section:
This article was submitted to Biomechanics, a section of the journal Frontiers in Bioengineering and Biotechnology

Received: *25 September 2021*
Accepted: *05 November 2021*
Published: *25 November 2021*

Citation:
Li Q, Shang S, Pei X, Wang Q, Zhou Q and Nie B (2021) Kinetic and Kinematic Features of Pedestrian Avoidance Behavior in Motor Vehicle Conflicts. Front. Bioeng. Biotechnol. 9:783003. doi: 10.3389/fbioe.2021.783003

1 INTRODUCTION

Road traffic injuries remain a major global health issue, resulting in the loss of 310,000 pedestrian lives each year and representing 23% of all road traffic deaths (WHO, 2018). Pedestrian pre-impact posture significantly influences the risks and severity of injury outcomes (Li et al., 2015; Zou et al., 2020). Understanding the active avoidance behavior of pedestrians in dangerous traffic scenarios is necessary to develop advanced pedestrian safety systems that can reduce the risk of injury. The traditional survey method used to investigate accidents involves collecting detailed information (such as the vehicle trajectory and injury distribution) after a collision and then reconstructing the scenario. However, it is not realistic to collect accurate information on pedestrian avoidance behavior using this method (Fredriksson et al., 2010). By watching and analyzing real-world accident video records, researchers have recently observed the emergency postures and kinematics of pedestrians in dangerous impact scenarios (Zou et al., 2020; Wu et al., 2021). However, the pedestrian avoidance behavior has not been quantified.

Pedestrian avoidance behavior affects the impact posture, which then affects the subsequent impact condition and injury risk variables (Simms and Wood, 2006; Tang et al., 2016). In previous studies, common methods for investigating pedestrian injuries have included traffic accident database analyses (Shang et al., 2018), cadaver impact tests (Shang et al., 2020), human surrogate crash tests (Konosu et al., 2005), and mathematical analyses based on numerical pedestrian models (Forman et al., 2015; Nie and Zhou, 2016). Understanding the active behavior of pedestrians during traffic conflicts is vital for predicting pedestrian injury risk under complex impact conditions. However, several previous studies have focused on analyzing pedestrian injuries under stationary or normal walking postures, while ignoring the influence of active pedestrian behaviors (EEVC, 1994); therefore, the conventional computational methods (e.g., multi-body (MB)/finite element (FE) modeling) in the field of vehicle safety does not fully represent the actual collision conditions. Some recent studies have investigated the influence of pedestrian avoidance behavior on injury risk through volunteer tests and simulations (Holdgrin et al., 2018). However, the biomechanical features of pedestrians, such as the kinetics and kinematics, during active avoidance remain unidentified.

Pedestrian will perform activation behavior such as acceleration forward or deceleration backward to avoid danger when they notice the upcoming vehicle in traffic conflicts. If the pedestrian does not notice the danger, they will keep walking with a constant velocity. Thus, the avoidance behavior of pedestrians affects the subsequent trajectories, which shall be considered by the on-vehicle active safety system. Previous studies have focused on predicting normal pedestrian walking trajectories in safe traffic scenarios owing to the limited sample size for dangerous-scenario datasets (Rasouli et al., 2018). The randomness of pedestrian avoidance behavior remains a major challenge for vehicle awareness systems in real-world accidents (Zhang et al., 2019). Therefore, analyzing and quantifying pedestrian avoidance behaviors in dangerous scenarios is an important research topic in the context of advanced vehicle safety systems (Sportillo et al., 2018). Accordingly, the aims of this study are to 1) identify and quantify the kinetic and kinematic features of pedestrian active behavior in dangerous impact scenarios, 2) analyze and quantify pedestrian avoidance reactions to dangerous scenarios, and 3) quantify the pedestrian–vehicle interaction in the pre-crash phase.

2 MATERIALS AND METHODS

2.1 Experimental Platform and Design

We developed a pedestrian natural response experimental platform and recruited volunteers to determine the kinetic and kinematic features of the subjects' ("pedestrians") active avoidance behavior. The experimental platform comprised three modules: a virtual reality (VR) test platform, a kinetic capture system, and an electromyogram (EMG) signal capture system. Specifically, the VR test platform (51VR High Technology Co., Ltd.) generated a near-real immersive VR traffic scene. The peripheral auditory functions, sense of distance, and interactions of the subjects immersed in the virtual traffic environment functioned as normal. The subjects performed the action of crossing the road in the VR traffic scene, while a dangerous scenario was created to produce a natural reaction in the subjects. For representing typical conflict scenes between pedestrians and vehicles in real-world (Han et al., 2017) and stimulating pedestrians to respond naturally, one of two emergent near-real car–pedestrian conflict scenarios (traffic scene A (TSA) and traffic scene B (TSB)) was created by the experimenter immediately after the subject entered the road. Detailed information on the experimental platform can be found in our previous studies (Li et al., 2020; Nie et al., 2021). To record the natural responses of the pedestrians and eliminate the influence of vigilance on crossing behavior caused by repeated experiments, each subject participated only once per scene. An experiment video is accessible through the following link: https://github.com/QuanLI-21/Pedestrian-avoidance-behavior-dataset-PABD.

2.2 Subjects and Ethical Statement

The experimental procedures were approved by the Institutional Review Board (IRB) of Tsinghua University. The procedures were performed according to the approved guidelines. Informed consent was obtained from each subject before conducting the experiments. A total of n = 24 subjects were recruited, conforming to the inclusion criteria for this study. However, due to the calibration error of the motion capture system and the wireless connection failure of the VR glasses, only n = 34 experiments (involving 19 subjects) were recorded completely and used in the final data analysis. The human body information for the subjects is provided in **Supplementary Table S1.**

2.3 Feature Extraction of the Pedestrian Avoidance Behavior

2.3.1 Coordinates of the Pedestrian and Vehicle

The dynamic relative positions of the pedestrian and vehicle during the interaction were extracted using a motion capture system. The pedestrian moved in the vehicle coordinate system, and the pedestrian's local coordinate system was located on the pelvis (**Figure 1**).

2.3.2 Pedestrian Kinetics and Kinematics

The pedestrian kinetic and kinematic features include the relative locations of the vehicle and pedestrian, the pedestrian's movement velocity and acceleration, their posture (joint positions and angles), and their muscle activation levels. The data were recorded and extracted using the 12 cameras (100 Hz) of the motion capture system (No. Mars 2H; Beijing Nokov Science and Technology Co., Ltd.) by tracking 54 markers. In addition, 11 joints were used to describe the pedestrian posture (Arnold et al., 2010) (**Supplementary Figure S1**). The pedestrian kinematics were inversed using OpenSim and the "Full Body Model" (Rajagopal et al., 2016).

The EMG signals of the lower limb surface muscles were recorded using a physiological signal system (16 channels, DELSYS Trigno wireless system). The EMG signals of the

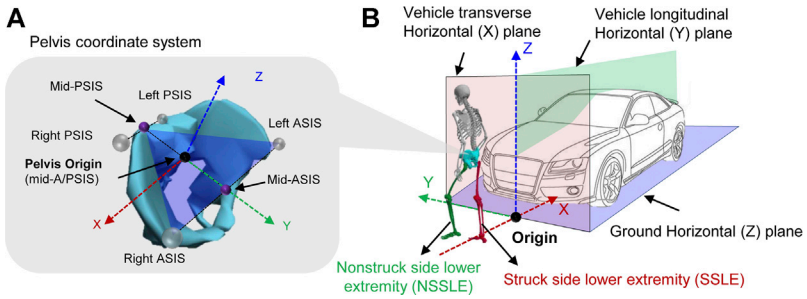

FIGURE 1 | Illustration of the locations of the coordinate system; **(A)** pedestrian local coordinate system, **(B)** vehicle coordinate system.

lower extremities were measured using eight separate electrical signal sensors (sampling frequency: 2000 Hz). Considering the relationship between the lower limb muscles and motion, the rectus femoris (RF), vastus lateralis (VL), vastus medialis (VM), biceps femoris (BF), gastrocnemius medial head (GMH), gastrocnemius lateral head (GLH), soleus (SO), and tibialis anterior (TA) muscles were selected for testing (**Supplementary Figure S2**). The raw EMG signals were band-pass-filtered (20–500 Hz), full-wave-rectified, and smoothed with a 25 ms root mean square window. The muscle activation levels were calculated based on the normalized EMG signals through a parallel experimental process based on maximum voluntary contraction (MVC) signals. The experimental approach for the MVC calculation is illustrated in **Supplementary Figure S3**.

In addition, data analysis was performed using MATLAB 2019b. The Kruskal–Wallis test was used to detect differences in pedestrian avoidance behaviors.

3 RESULTS

We categorized four representative pedestrian behaviors based on the direction of the avoidance motion. The avoidance processes of pedestrians in vehicle–pedestrian conflicts are illustrated in detail through case studies. We fitted the average velocities, pre-crash postures, acceleration of pedestrians, and relative locations of the vehicle and pedestrian. These results can assist in understanding and quantifying the kinetics and kinematics of pedestrian active avoidance behaviors. The experimental data, such as the EMG, kinematics, and video recordings, are available online at Github repositories (link in **section 2.1**).

3.1 Representative Reaction Categories in Vehicle–Pedestrian Conflicts

The test subjects exhibited representative avoidance behaviors to avoid the "bullet vehicle" in car–pedestrian conflicts. The "bullet vehicle" refers to a vehicle which would suddenly appear and virtually crash into the pedestrian. The results of the conflicts and pedestrian reactions in all cases are summarized in **Supplementary Table S2**. In our previous study, the actions were classified into four categories based on the perception of the "bullet vehicle" and the relative motion vector: (1) backward avoidance (BA), (2) forward avoidance (FA), (3) oblique stepping (OS; startled response), and (4) walking/no avoidance reaction (NAR; not noticing the approaching vehicle). Based on the avoidance behavior categories, we discuss the kinetic and kinematic features of pedestrian avoidance behaviors in detail through case studies.

3.2 Case Studies

To explain pedestrian kinetic and kinematic features in avoidance behavior, we randomly selected and analyzed one collision case from each of the three avoidance behavior categories. We considered the relative locations of the vehicle and pedestrian, posture, kinematics, and EMG signals in the process of the avoidance behavior. The three representative avoidance processes in the VR environment and in-lab environment are shown in **Supplementary Figure S4**. In addition, one case in which the pedestrian walked normally (NAR case, **Supplementary Figure S5**) was compared with the cases in the other categories (**Figures 3–5**) to illustrate the differences in the kinetics and kinematics.

3.2.1 Backward Avoidance Case

In this case (subj019_TSB), the subject entered the vehicle lane before the collision and started to step back to avoid the impending collision upon noticing the "bullet vehicle"; the collision occurred in the process of the subject stepping backward (**Figure 2**; **Supplementary Figure S4A**). According to the analysis of the trajectory of the subject (**Figures 2A,B**), the subject exhibited an avoidance behavior of stopping and moving backward. The velocity, acceleration, and myoelectric signals of normal pedestrian walking are presented in **Figures 2C,D**. Eventually, the subject rotated 22° toward the vehicle (Y-direction of the pelvis and vehicle coordinate system) and collided with the vehicle at y = -0.6 m (left side of the vehicle) from the vehicle's center axis (**Table 1**). In this avoidance process, the subject initially decelerated forward and then accelerated backward; and the peak values of the pelvis deceleration and acceleration in the Y-direction were −10.9 and 6.4 m/ s^2, respectively, which is significantly higher than the peak acceleration observed during the normal walking test (**Figure 2C**). Time histories (t_1, t_2, t_3, t_4) of the posture information for subjects are provided in **Supplementary Table S3.**

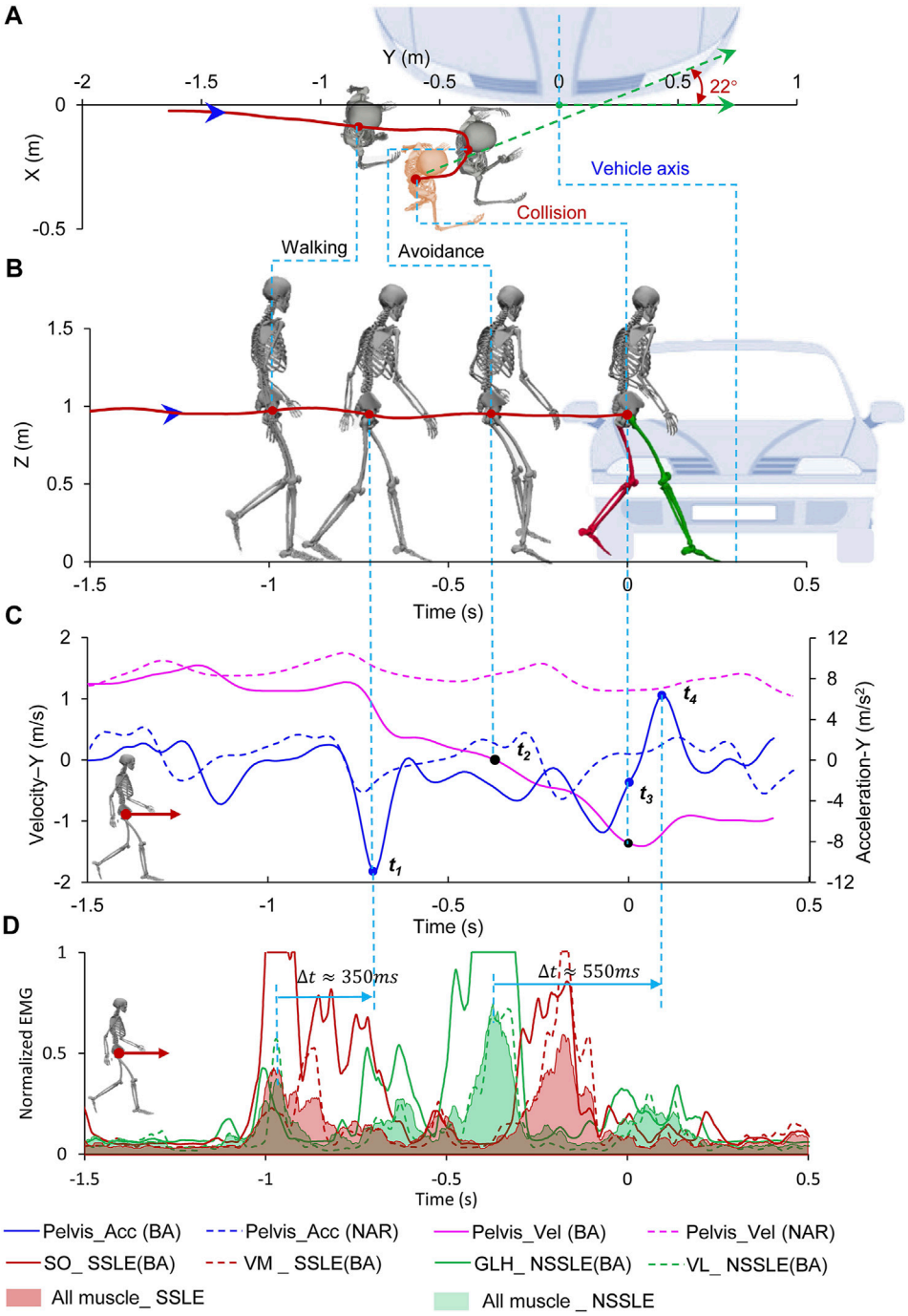

FIGURE 2 | Pedestrian backward avoidance behavior. **(A)** Top view of relative location of pedestrian and vehicle; **(B)** Side view of relative location of pedestrian and vehicle; **(C)** Pedestrian's acceleration and velocity during avoidance, the dotted line represents the process of the pedestrian walking normally (Supplementary Figure S5); **(D)** Muscle activation level of pedestrian during avoidance. Time = 0 s represents the collision time. The location of the vehicle at the collision time is shown. Negative times represent the time before the virtual collision.

With regard to the kinetics, the lower limb muscles contract and control the foot striking the ground to gain momentum and drive the pelvis motion. Thus, myoelectric signals can represent muscle activation and capture the pelvis motion features. The muscle activation time histories of the four most activated muscles are shown in **Figure 2D**. In the process of BA behavior, the SO and VM of the struck-side lower extremity (SSLE) as well as the GLH and LV of the non-struck-side lower extremity (NSSLE) showed higher activation states. Physiologically, the generation of movement was delayed

TABLE 1 | Pelvis kinematics at the instant of collision in the case studies.

Pelvis kinematics	Backward avoidance	Forward avoidance	Oblique steeping avoidance
Vel_x (m/s)	-0.1	-0.8	-1.5
$vel_y \cdot$ (m/s)	-1.4	2.8	0.9
Vel_z (m/s)	0.2	0.3	0.1
Acc_x (m/s^2)	-1.2	-4.3	-0.9
Acc_y (m/s^2)	-2.1	-2.1	6.4
Acc_z (m/s^2)	-5.9	-10.2	4.2

Vel_x, Vel_y, Vel_z, Acc_x, Acc_y, and Acc_z represent the velocity and acceleration of the pelvis in the X-, Y-, and Z-directions, respectively.

compared with that of the muscle force, which, in turn, was delayed compared with that of the myoelectric signals. The delay time is affected by several factors, such as individual differences and movement characteristics (De Luca, 1997). Therefore, the delay times between the myoelectric signals and corresponding movement show significant discrepancies between individuals and motions. In this study, to facilitate the determination of lower limb muscle activation, the myoelectric signals measured from the SSLE and NSSLE were summed and normalized, respectively, and were significantly higher than the myoelectric signals recorded during normal walking; this indicate that the scenarios were effective. The delay times between the peak value of the myoelectric signals and the peak pelvis acceleration were approximately 350 and 550 ms in the processes of deceleration and acceleration, respectively.

The time interval also varies with individual differences and response behaviors. As it is difficult to determine the accurate time interval by single muscle or muscle group, the presented time intervals serve as a reminder and demo. It reminds that it is necessary to consider proper time intervals when using the EMG signal to characterize the muscle activation state and kinematics at a certain moment.

3.2.2 Forward Avoidance Case

In this case (subj014_TSB), the subject entered the vehicle lane before the collision and chose to avoid collision by accelerating across the road upon noticing the "bullet vehicle"; the collision occurred in the process of acceleration (**Figure 3**; **Supplementary Figure S4B**; **Supplementary Table S4**). According to the motion trajectory of the subject (**Figures 3A,B**), the subject performed a forward avoidance motion exhibiting a trend of moving away from the vehicle in the direction of vehicle movement. Eventually, in a running posture, the subject collided with the vehicle at y = 0.4 m (right side of the vehicle) from the vehicle's center axis (**Figure 3B**; **Table 1**). In the process of forward avoidance, the subject underwent two accelerations through the NSSLE and SSLE striking the ground to gain a driving force, and the peak values of the pelvis acceleration in the Y-direction were 5.5 and 7.3 m/ s^2, respectively (**Figure 3C**). In terms of the muscle activation state, the VL and VM of the SSLE and NSSLE showed higher activation levels, and the muscle activation level of the thighs was higher than that of the shank (**Figure 3D**). The myoelectric signals reached their peaks approximately 180 and 330 ms earlier than the pelvis accelerations did during the two accelerations. The peak values of the myoelectric signals and pelvis acceleration and deceleration were significantly higher than those observed in the normal walking test.

3.2.3 Oblique Stepping Avoidance Case

In this case (subj016_TSA), the subject entered the vehicle lane before the collision and raised his hands in an attempt to stop the vehicle upon noticing the impending danger. The collision occurred in the process of oblique stepping avoidance (**Figure 4**; **Supplementary Figure S4C**; **Supplementary Table S5**). According to the trajectory of the subject's motion (**Figures 4A,B**), the subject first underwent a forward deceleration and then turned to face the front of the vehicle while simultaneously moving away from the vehicle to avoid the collision. Eventually, while in a stepping posture rotated 117° toward the vehicle (Y-direction of the pelvis and vehicle coordinate system), the subject collided with the vehicle at y = 0.3 m (right side of the vehicle) from the vehicle's central axis (**Figure 4B**; **Table 1**). In the OS avoidance process, the subject underwent a deceleration because of the SSLE striking the ground first, followed by the NSSLE striking the ground to create an oblique acceleration; the peak values of the pelvis deceleration and acceleration in the Y-direction were −7.3 and 8.4 m/ s^2, respectively (**Figure 4C**). The four muscles with the highest activation levels during the OS behavior were the LV and SO of the SSLE and the GMH and TA of the NSSLE (**Figure 4D**). The peak values of the myoelectric signals occurred approximately 210 and 250 ms after the peak value of the pelvis acceleration during the acceleration and deceleration, respectively. Similar to the previous case results, the peak values of the myoelectric signals, pelvis acceleration, and deceleration were significantly higher than those of normal walking.

In addition, we used the Kruskal–Wallis test to detect differences in the kinematic features between different avoidance behaviors and normal walking. The results showed that the velocities were significantly different between the avoidance behaviors and normal gait ($p < 0.01$ for BA, FA, and OS vs. NAR).

3.3 Kinetic and Kinematic Features of the Pedestrian

Vehicle–pedestrian collisions usually occur with a process of pedestrian avoidance, which results in a highly random pedestrian impact posture. The average kinetic and kinematic features of the pedestrian "pre-crash postures" corresponding to the peak values of the pedestrian pelvis acceleration during the

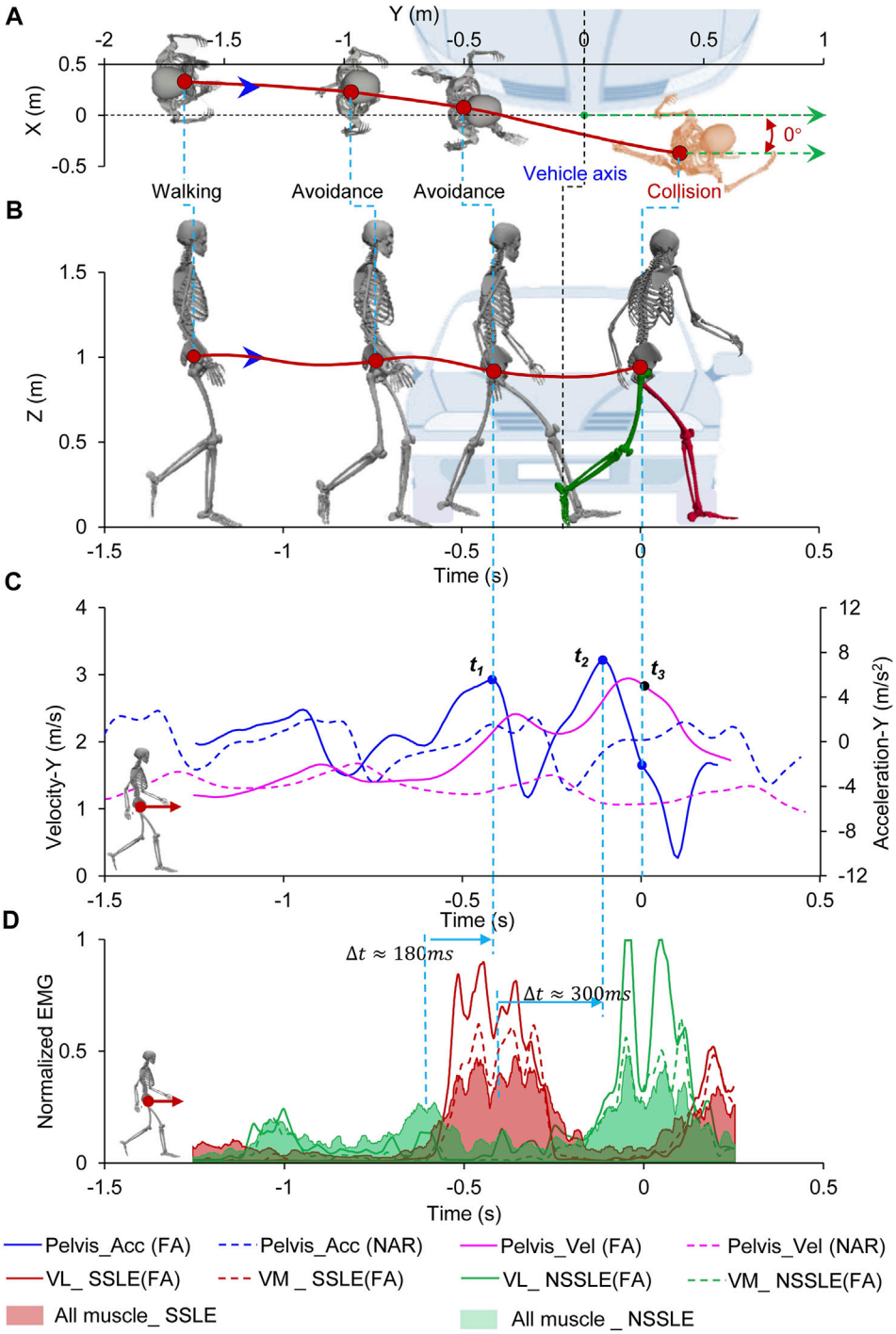

FIGURE 3 | Pedestrian forward avoidance behavior process. **(A)** Top view of relative location of pedestrian and vehicle; **(B)** Side view of relative location of pedestrian and vehicle; **(C)** Pedestrian's acceleration and velocity during avoidance, the dotted line represents the process of the pedestrian walking normally (Supplementary Figure S5); **(D)** Muscle activation level of pedestrian during avoidance. Time = 0 s represents the collision time. The location of the vehicle at the collision time is shown. Negative times represent the time before the collision.

motion were extracted. With regard to the kinematic features of the pedestrian "pre-crash posture," the overall kinematics of the pedestrian's body were represented by the pelvis motion and posture information, which included the time histories of the velocity and acceleration, joint angles, and joint coordinates. The kinetic features of the pedestrian avoidance behavior were extracted from the EMG signal of the lower limb muscles to represent the muscle activation and exertion.

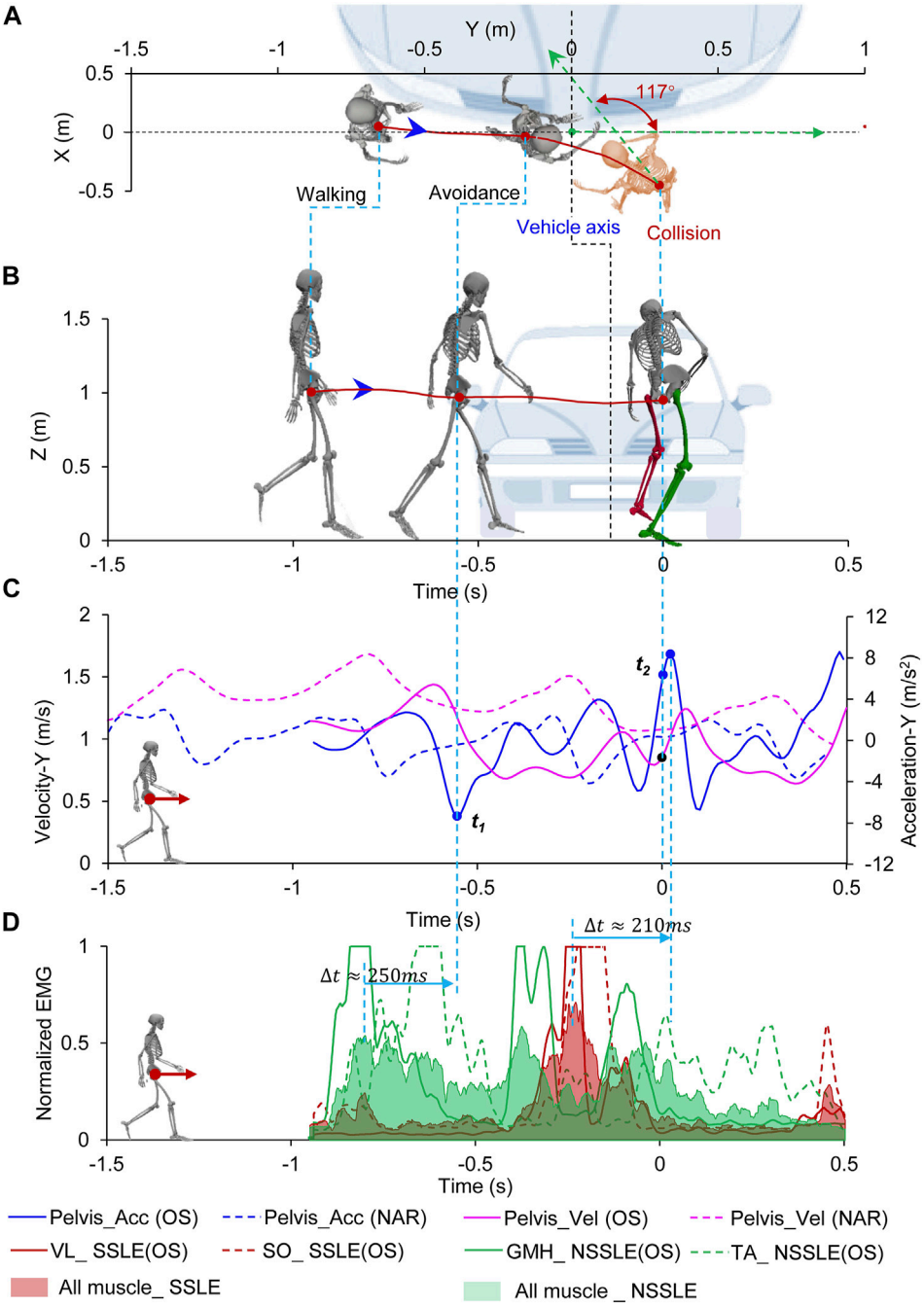

FIGURE 4 | Pedestrian oblique stepping avoidance behavior process. **(A)** Top view of relative location of pedestrian and vehicle; **(B)** Side view of relative location of pedestrian and vehicle; **(C)** Pedestrian's acceleration and velocity during avoidance, the dotted line represents the process of the pedestrian walking normally (Supplementary Figure S5); **(D)** Muscle activation level of pedestrian during avoidance. Time = 0 s represents the collision time. The location of the vehicle at the collision time is shown. Negative times represent the time before the collision.

3.3.1 Average Kinematic Features and "Pre-crash Postures" of Pedestrians

The BA behavior had a two-phase motion: deceleration to stop followed by backward acceleration (**Figure 5A**). The subjects required approximately 1.0 s to decelerate from the initial velocity of approximately 1 m/ s to the backward velocity of 1 m/ s. The braking and backing postures at the occurrence of the peak accelerations during deceleration (t_1) and acceleration (t_2) were extracted as the "pre-crash postures." The FA behavior included a consistent forward acceleration motion from the initial velocity of approximately 1 m/ s to a forward velocity of 2 m/ s (**Figure 5B**). The acceleration posture at the occurrence of the

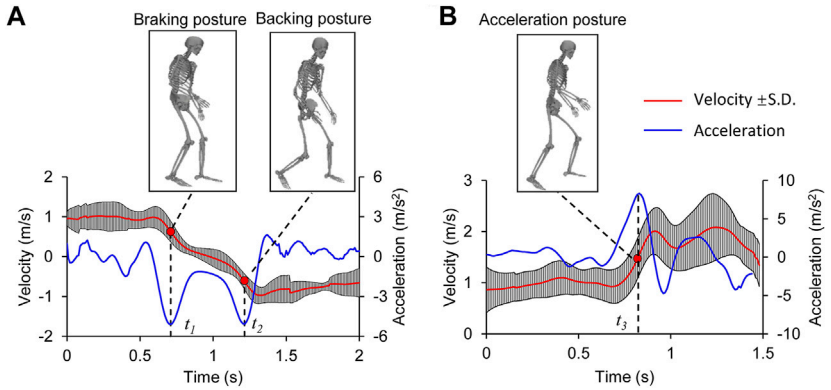

FIGURE 5 | Pelvis velocity corridors and "pre-crash postures" for different motion categories; **(A)** backward avoidance, **(B)** forward avoidance; t_1, t_2, and t_3 are the moments of peak acceleration in the processes of braking, backing, and acceleration, respectively. The peak acceleration occurrence was defined as a time alignment standard for the participants under the same motion category.

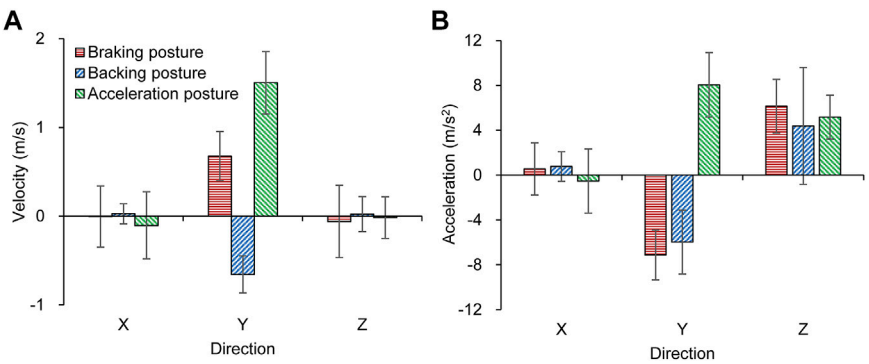

FIGURE 6 | Peak values of the kinematic indicators for the "pre-crash postures"; **(A)** Pedestrian pelvis velocity, **(B)** Pedestrian pelvis acceleration.

peak acceleration during acceleration (t_3) was extracted. The "pre-crash posture" was normalized by the cases with the same motion categories and illustrated with the joint angles of the human body (**Eq. 1**); the joint angles of the three "pre-crash postures" are listed in **Supplementary Table S6**.

$$AJ_i = \frac{1}{n}\sum_{j=1}^{n} J_{ij}, \tag{1}$$

where AJ_i denotes the average angle of subject joint i, J_{ij} denotes the angle of subject joint i in case j, and n denotes the number of cases.

Corresponding to the three aforementioned "pre-crash postures," the average peak velocities in the Y-direction for the braking posture, backing posture, and acceleration posture were −0.7 m/ s, 0.7 m/ s, and 1.5 m/ s, respectively (**Figure 6A**). The velocities of the pedestrian in the X-direction and Z-direction were approximately 0 m/ s. The average peak accelerations of the braking posture, backing posture, and acceleration posture in the Y-direction were −6.0 m/ s^2, −7.1 m/ s^2, and 8.1 m/ s^2, respectively (**Figure 6B**). In addition, the three "pre-crash postures" exhibited a positive acceleration in the Z-direction, with average peak values of 6.2, 4.4, and 5.2 m/ s^2, respectively.

3.3.2 Muscle Activation Levels for "Pre-crash Postures"

Different muscle groups were activated on the SSLE and NSSLE. For the three average pre-crash postures mentioned before, the muscle activation levels of the lower limbs were normalized based on the results of the MVC tests. (Soni et al., 2013b) (**Figure 7**). For the braking posture, the NSSLE struck the ground to gain momentum for braking, and the SSLE stopped swinging forward. The muscles in both the SSLE and NSSLE were activated to varying degrees. Similarly, for the backing posture, the NSSLE, as the supporting leg, struck the ground to gain momentum for backward avoidance, and the muscle activation level was higher than that of the SSLE. For the acceleration posture, the NSSLE struck the ground, and the SSLE swayed forward rapidly.

3.3.3 Pedestrian Trajectory During Vehicle Interaction

The pedestrian trajectories relative to the "bullet vehicle" during the collisions are shown in **Figure 8**. The vertical axis represents the distance between the pedestrian and the vehicle lane, and the horizontal axis represents the time when the vehicle reached the potential collision location. According to the average values of the

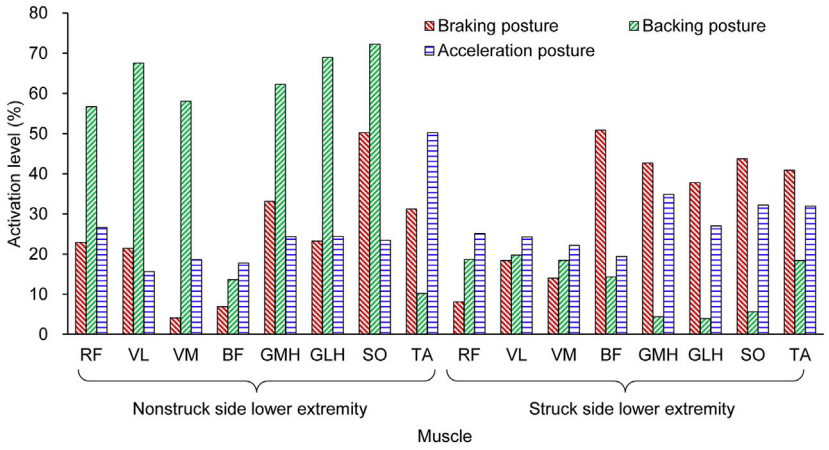

FIGURE 7 | Muscle activation levels in pedestrian avoidance postures.

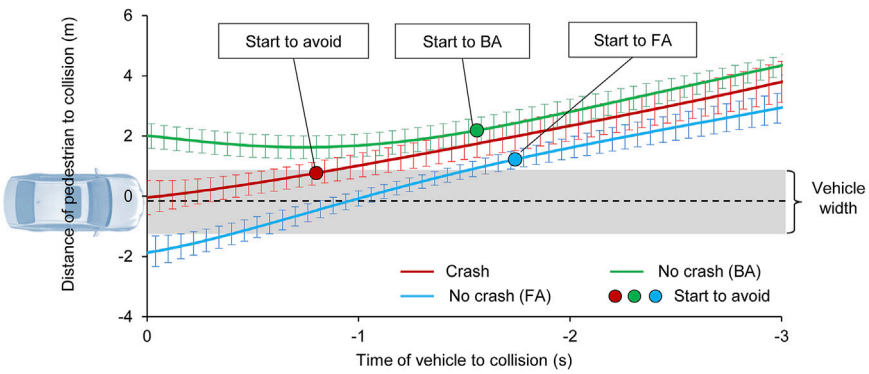

FIGURE 8 | Relative locations of the vehicle and pedestrian during the interactions. The red curve represents the crash cases, in which the pedestrian noticed the coming vehicle but failed to avoid the virtual collision. The green curve indicates that the pedestrian successfully avoided the collision through backward avoidance. The blue curve indicates that the pedestrian successfully avoided the collision through forward avoidance. The standard deviation of the data is also shown.

experiment results, when the pedestrian noticed the "bullet vehicle," 1) if the subject was located 2.2 m (SD 0.25) away from the vehicle center lane and the time to collision (TTC) was longer than 1.6 s (SD 0.38), the collision could be avoided by stepping backward; 2) if the subject was located approximately 1.2 m (SD 0.97) away from the vehicle center lane and the vehicle TTC was more than 1.8 s (SD 0.64), the collision could be avoided by performing the forward avoidance motion. In the collision cases, the subjects noticed the "bullet vehicle" too late to avoid collision in a short time window.

4 DISCUSSION

We investigated and quantified the kinetic and kinematic features of active pedestrian behaviors in virtual dangerous impact scenarios. The observed natural avoidance behaviors were similar to those in real-world accidents (Schachner et al., 2020). The results can thus represent natural pedestrian behaviors, help us better understand the pedestrian behavior features in real-world accidents, and facilitate development of an advanced integrated safety system that combines active and passive functions.

4.1 Kinetic and Kinematic Features of Pedestrian Avoidance Behavior

Pedestrians are individuals with active behavior abilities and awareness; their active avoidance behavior will be activated when they notice an approaching vehicle with a potential collision risk. Consequently, pedestrians will exhibit forward, backward, jumping, and other non-standing behaviors when facing danger. However, the existing warning systems for pedestrian safety only focus on vehicle avoidance behavior (Matsui et al., 2013) and default pedestrians to uniform movement or stationary positions; thus such systems fail to consider active pedestrian behaviors (Hamdane et al., 2015). To predict the collision risk as a follow-up study, two key

points are addressed: 1) quantifying pedestrian avoidance abilities in a broad range of conditions, and 2) identifying the impact conditions of pedestrians and vehicles during inevitable collisions. This study provides a new viewpoint for evaluating collision risk from the perspective of pedestrians. The minimum reaction time of pedestrians who avoided collision was less than 1.6 s in BA behaviors and 1.8 s in FA behaviors when they noticed the approaching vehicle in advance (**Figure 8**). Active behavior usually relies on surrounding visual and auditory information (Koh et al., 2014). Therefore, when emphasizing the improvement of vehicle collision risk prediction and avoidance capabilities, measures to activate pedestrian avoidance capabilities, such as automatic whistles, are needed.

Predicting the trajectory of a pedestrian in a real-world environment is challenging because of the randomness of natural human reactions. The active behavior of pedestrians depends on whether they notice the vehicle, as well as the relative locations of the vehicle and pedestrian, and identifying this active behavior is vital for advanced pedestrian safety warning systems. Pedestrian active avoidance behaviors were characterized in this study and can provide a reference for further pedestrian behavior prediction.

4.2 Influence of Pedestrian Avoidance Behavior on Potential Injury Risk

We collected kinetic and kinematic data for natural pedestrian avoidance reactions in vehicle conflicts, and the vehicle–pedestrian interaction processes were analyzed in detail using case studies. A previous study identified several influencing factors for the injury risk of pedestrians with a normal gait in vehicle crashes, such as stature, impact posture, orientation, and obesity (Elliott et al., 2012; Tang et al., 2020b). However, the posture, kinetics, and kinematics of the pedestrians at the time of collision were significantly different from those of the normal gait (**Supplementary Figure S4**). Such difference would result in different injury risks between the pedestrians with active avoidance posture and normal gait if the collision occurs. In the BA case (**Figure 2B**; **Table 1**), the subject's NSSLE on the front was almost straight, and the SSLE at the back was bent by 48° (additional information can be found in **Supplementary Table S3**, t_3), and the struck-side elbow was raised and bent. If only the influence of the impact posture on the injury risk is considered, the NSSLE at the back may cause the body to rotate and result in more severe injury (Tang et al., 2020a). Pedestrians with a flexed knee in the pre-crash phase exhibit a lower injury risk (Li et al., 2015). In addition, an impact on the elbow influences head rotation, and the head undergoes rotational acceleration toward the vehicle (Paas et al., 2012). The pedestrian's backward velocity (Vel_y) affects the impact location with the vehicle and further affects the risk of injury (Elliott et al., 2012). The vertical acceleration (Acc_y) of the pedestrian affects the load distribution on the lower limbs as well as the injury risk. In the FA case (**Figure 3**; **Table 1**), the pedestrian exhibited a running posture and had a higher forward velocity and vertical acceleration than that in the normal gait. The pedestrian head may directly collide with the ground over the vehicle front due to the high forward velocity, resulting in increased injury risk to the head. In such case, knee flexion in a running posture may reduce the injury risk of the leg (Li et al., 2015). In the case of OS avoidance (**Figure 4**; **Table 1**), the pedestrian faced the approaching vehicle and stepped backward; the impact posture and direction were thus different from those in the other cases. Since the pedestrian is usually facing with the vehicle in OS cases, the impact directions between the human body (head, chest, lower limbs et.) and the vehicle are unlike the side-impact under the normal gait, which causes the injury risks are different.

The joint angles, velocities, and accelerations of the pedestrians were accurately captured by the motion capture system. The peak value of the EMG signal corresponded to the peak value of acceleration in the process of avoidance behavior and was significantly higher than the EMG signal captured during a normal gait (**Figures 2D**, **3D**, **4D**; **Supplementary Figure S4D**). However, the influence of kinetic characteristics on pedestrian injury risk remains unclear. Pedestrian avoidance behavior is complex in terms of kinetic and kinematic features, which causes the impact conditions to be highly diverse and uncertain and also influences the pedestrian injury risk in vehicle collisions.

In addition, previous studies have not focused on the process of pedestrian avoidance behaviors (Soni et al., 2013a). When collisions occur during the process of pedestrian avoidance, the pedestrian's posture, kinematics, and muscle activity will affect the risk of injury. Therefore, the influence of pedestrian avoidance behaviors on injury risk cannot be ignored. It is important to highlight the effect of pedestrian posture on the level of injury suffered from potential collisions. The data for pedestrian avoidance behaviors provided in this study can be used to analyze pedestrian injury mechanisms with a high-precision human numerical model (Golman et al., 2014). In addition, it can elucidate pedestrian injury characteristics in real-world accidents and provide data for predicting pedestrian trajectories and injury risks.

4.3 Application in HBM Development and Integrated Active and Passive Safety Systems

The presented kinematics and EMG data describe the pedestrian avoidance process completely. These data can serve as a reference for the development of more advanced biofidelic human models to predict pedestrian injury risk. For example, researchers can define the activation state of pedestrian muscles to develop an active human body model and analyze the influence of the muscle response on impact injuries.

In addition, the results of this study can facilitate the development of integrated active and passive safety systems from two aspects: collision risk assessment and potential injury prediction. Existing research has indicated that the development of vehicle active safety systems can improve the effectiveness of passive safety systems (Habibovic and Davidsson, 2012). To predict the potential injury risk of pedestrians, this study analyzed the pedestrian avoidance behaviors in detail and

extracted three representative pedestrian pre-crash postures via normalization. As a database, these results can be used to input the collision condition into a numerical model to predict pedestrian injury risk and establish an injury risk prediction system. The pedestrian prediction system of a vehicle can currently only predict pedestrian behavior under normal walking states (Rasouli et al., 2018). This study describes the kinematic features of pedestrians, including the changes in velocity and acceleration and differences in posture relative to a normal gait that are essential information for quantitating pedestrian avoidance abilities and judging changes in pedestrian intentions.

4.4 Limitations

It should be noted that this study has several limitations. First, the scope was limited to the given representative traffic scenarios, which cannot represent all vehicle–pedestrian crash scenarios. Second, this study only focused on the behavioral characteristics of men aged 18–30 years; the behavioral characteristics of women, the elderly, and children need to be investigated in a future study. Third, although the current sample size could quantify pedestrian avoidance behaviors, a larger experimental sample size is necessary to predict the collision risk more accurately. Moreover, a follow-up study will focus on elucidating the relationship between pedestrian avoidance behaviors and the corresponding injury risks and severities. Furthermore, additional factors that influence pedestrian avoidance behaviors, such as age, gender, and stature, will be considered. A larger databank that includes a broad range of pedestrian active behavior characteristics in dangerous scenarios will be generated to predict the risk of collision more accurately.

5 CONCLUSION

This study identified pedestrian active avoidance behaviors and interaction processes with a vehicle in near-real traffic conflict scenarios using immersive VR technology. The time histories of kinetic and kinematic features of the pedestrian, such as velocity, acceleration, joint angles, EMG, and the relative location with the vehicle, were extracted to quantify and characterize the avoidance behaviors (all of the experimental data are available on an open-source platform). Pedestrian kinetics and kinematics at the instant of occurrence of collision were strongly influenced by the active avoidance behavior; for example, the pedestrian collision postures in the backward avoidance and forward avoidance behaviors were clearly and significantly different than that in the normal gait. In addition to the influence of individual physical conditions, sufficient time and a safe distance are also necessary for the pedestrian to perform a complete and effective avoidance motion. The minimum reaction time of pedestrians who successfully avoided collision was 1.6 s for BA behavior and 1.8 s for FA behavior. When investigating the effect of avoidance behaviors on injury risk and severity, the experimental data from this study can serve as a valuable reference for developing an FE/MB human model and simulating the pedestrian injury risk during collisions.

DATA AVAILABILITY STATEMENT

The datasets presented in this study can be found in online repositories. The names of the repository/repositories and accession number(s) can be found below: https://github.com/QuanLI-21/Pedestrian-avoidance-behavior-dataset-PABD.

ETHICS STATEMENT

The studies involving human participants were reviewed and approved by Institutional Review Board of Tsinghua University. The patients/participants provided their written informed consent to participate in this study.

AUTHOR CONTRIBUTIONS

BN designed the experiments and coordinated the working project; QL conducted the experiments and data analysis; BN and QL wrote the paper; SS contributed to the discussion of the results and implications; XP and QW contributed to the revision work; QZ contributed to the discussion of the experiment design and results. All authors reviewed the manuscript.

FUNDING

This work was in part supported by the National Natural Science Foundation of China (52072216, 51705276) and the Tsinghua University-Toyota Joint Research Fund.

SUPPLEMENTARY MATERIAL

The Supplementary Material for this article can be found online at: https://www.frontiersin.org/articles/10.3389/fbioe.2021.783003/full#supplementary-material

REFERENCES

Arnold, E. M., Ward, S. R., Lieber, R. L., and Delp, S. L. (2010). A Model of the Lower Limb for Analysis of Human Movement. *Ann. Biomed. Eng.* 38 (2), 269–279. doi:10.1007/s10439-009-9852-5

De Luca, C. J. (1997). The Use of Surface Electromyography in Biomechanics. *J. Appl. Biomech.* 13 (2), 135–163. doi:10.1123/jab.13.2.135

Eevc, E. E. V. C. W. G. o. P. P. (1994). *Proposals for Methods to Evaluate Pedestrian protection for Passenger Cars: Final Report*.

Elliott, J. R., Simms, C. K., and Wood, D. P. (2012). Pedestrian Head Translation, Rotation and Impact Velocity: The Influence of Vehicle Speed, Pedestrian

Speed and Pedestrian Gait. *Accid. Anal. Prev.* 45, 342–353. doi:10.1016/j.aap.2011.07.022

Forman, J. L., Lopez-Valdes, F. J., Duprey, S., Bose, D., del Pozo de Dios, E., Subit, D., et al. (2015). The Tolerance of the Human Body to Automobile Collision Impact - a Systematic Review of Injury Biomechanics Research, 1990-2009. *Accid. Anal. Prev.* 80, 7–17. doi:10.1016/j.aap.2015.03.004

Fredriksson, R., Rosén, E., and Kullgren, A. (2010). Priorities of Pedestrian protection-A Real-Life Study of Severe Injuries and Car Sources. *Accid. Anal. Prev.* 42 (6), 1672–1681. doi:10.1016/j.aap.2010.04.006

Golman, A. J., Danelson, K. A., Miller, L. E., and Stitzel, J. D. (2014). Injury Prediction in a Side Impact Crash Using Human Body Model Simulation. *Accid. Anal. Prev.* 64, 1–8. doi:10.1016/j.aap.2013.10.026

Habibovic, A., and Davidsson, J. (2012). Causation Mechanisms in Car-To-Vulnerable Road User Crashes: Implications for Active Safety Systems. *Accid. Anal. Prev.* 49, 493–500. doi:10.1016/j.aap.2012.03.022

Hamdane, H., Serre, T., Masson, C., and Anderson, R. (2015). Issues and Challenges for Pedestrian Active Safety Systems Based on Real World Accidents. *Accid. Anal. Prev.* 82, 53–60. doi:10.1016/j.aap.2015.05.014

Han, Y., Li, Q., He, W., Wang, F., Wang, B., and Mizuno, K. (2017). "Analysis of Vulnerable Road User Kinematics Before/During/After Vehicle Collisions Based on Video Records," in Proceedings of 2017 International Research Council on the Biomechanics of Injury, Antwerp, Belgium, 13–15 September 2017.

Holdgrin, T., Doric, I., Brandmeier, T., Fuchs, T., Mihlbauer, J., Steinert, P., et al. (2018). *A Virtual Reality Based Approach for Researching Pedestrian to Vehicle Collisions*.

Koh, P. P., Wong, Y. D., and Chandrasekar, P. (2014). Safety Evaluation of Pedestrian Behaviour and Violations at Signalised Pedestrian Crossings. *Saf. Sci.* 70, 143–152. doi:10.1016/j.ssci.2014.05.010

Konosu, A., Issiki, T., and Tanahashi, M. (2005). *Development of a Biofidelic Flexible Pedestrian Leg-form Impactor (Flex-PLI 2004) and Evaluation of its Biofidelity at the Component Level and at the Assembly Level*. SAE Technical Papers. doi:10.4271/2005-01-1879

Li, G., Yang, J., and Simms, C. (2015). The Influence of Gait Stance on Pedestrian Lower Limb Injury Risk. *Accid. Anal. Prev.* 85, 83–92. doi:10.1016/j.aap.2015.07.012

Li, Q., Zhou, Q., Chen, W., Deng, G., Wei, X., Zhang, F., et al. (2020). "*In Vivo* Pedestrian Behaviour upon Motor Vehicle Conflicts: Experimental Framework and Initial Results," in Proceedings of IRCOBI Asia Conference, 1–2 June 2021 (online) (Beijing, China).

Matsui, Y., Hitosugi, M., Doi, T., Oikawa, S., Takahashi, K., and Ando, K. (2013). Features of Pedestrian Behavior in Car-To-Pedestrian Contact Situations in Near-Miss Incidents in Japan. *Traffic Inj. Prev.* 14, S58–S63. doi:10.1080/15389588.2013.796372

Nie, B., Li, Q., Gan, S., Xing, B., Huang, Y., and Li, S. E. (2021). Safety Envelope of Pedestrians upon Motor Vehicle Conflicts Identified via Active Avoidance Behaviour. *Sci. Rep.* 11 (1), 3996. doi:10.1038/s41598-021-82331-z

Nie, B., and Zhou, Q. (2016). Can New Passenger Cars Reduce Pedestrian Lower Extremity Injury? A Review of Geometrical Changes of Front-End Design before and after Regulatory Efforts. *Traffic Inj. Prev.* 17 (7), 712–719. doi:10.1080/15389588.2016.1143096

Paas, R., Davidsson, J., Masson, C., Sander, U., Brolin, K., and Yang, J. (2012). "Pedestrian Shoulder and Spine Kinematics in Full-Scale PMHS Tests for Human Body Model Evaluation," in 2012 IRCOBI Conference, Dublin, Ireland, 12–14 September, 2012 (Dublin, Ireland).

Rajagopal, A., Dembia, C. L., DeMers, M. S., Delp, D. D., Hicks, J. L., and Delp, S. L. (2016). Full-Body Musculoskeletal Model for Muscle-Driven Simulation of Human Gait. *IEEE Trans. Biomed. Eng.* 63 (10), 2068–2079. doi:10.1109/TBME.2016.2586891

Rasouli, A., Kotseruba, I., and Tsotsos, J. K. (2018). Understanding Pedestrian Behavior in Complex Traffic Scenes. *IEEE Trans. Intell. Veh.* 3 (1), 61–70. doi:10.1109/TIV.2017.2788193

Schachner, M., Sinz, W., Schneider, B., and Klug, C. (2020). "Extracting Quantitative Descriptions of Pedestrian Pre-crash Postures from Real-World AccidentVideos," in *International Research Council on Biomechanics of Injury (IRCOBI)* (Munich, Germany.

Shang, S., Masson, C., Teeling, D., Py, M., Ferrand, Q., Arnoux, P.-J., et al. (2020). Kinematics and Dynamics of Pedestrian Head Ground Contact: A Cadaver Study. *Saf. Sci.* 127, 104684. doi:10.1016/j.ssci.2020.104684

Shang, S., Otte, D., Li, G., and Simms, C. (2018). Detailed Assessment of Pedestrian Ground Contact Injuries Observed from In-Depth Accident Data. *Accid. Anal. Prev.* 110, 9–17. doi:10.1016/j.aap.2017.10.011

Simms, C. K., and Wood, D. P. (2006). Effects of Pre-impact Pedestrian Position and Motion on Kinematics and Injuries from Vehicle and Ground Contact. *Int. J. Crashworthiness* 11 (4), 345–355. doi:10.1533/ijcr.2005.0109

Soni, A., Robert, T., Rongiéras, F., and Beillas, P. (2013b). Observations on Pedestrian Pre-crash Reactions during Simulated Accidents. *Stapp Car Crash J.* 57, 157–183. doi:10.4271/2013-22-0006

Soni, A., Robert, T., and Beillas, P. (2013a). Effects of Pedestrian Pre-crash Reactions on Crash Outcomes during Multi-Body Simulations. IRCOBI Conference Proceedings - International Research Council on the Biomechanics of Injury, Gothenburg, Sweden, 11–13 September 2013, 762–776.

Sportillo, D., Paljic, A., and Ojeda, L. (2018). Get Ready for Automated Driving Using Virtual Reality. *Accid. Anal. Prev.* 118, 102–113. doi:10.1016/j.aap.2018.06.003

Tang, J., Zhou, Q., and Chen, W. (2020a). "Intrinsic Relationship between Anatomy, Kinematics and Injuries of Knee Joint under Various Vehicle-To-Pedestrian Impact Orientations," in Proceedings of IRCOBI Asia Conference, 1"2 June 2021 (online) (Beijing, China).

Tang, J., Zhou, Q., Nie, B., and Hu, J. (2020b). Obesity Effects on Pedestrian Lower Extremity Injuries in Vehicle-To-Pedestrian Impacts: A Numerical Investigation Using Human Body Models. *Traffic Inj. Prev.* 21 (8), 569–574. doi:10.1080/15389588.2020.1821195

Tang, J., Zhou, Q., Nie, B., Yasuki, T., and Kitagawa, Y. (2016). Influence of Pre-impact Pedestrian Posture on Lower Extremity Kinematics in Vehicle Collisions. *SAE Int. J. Trans. Saf.* 4 (2), 278–288. doi:10.4271/2016-01-1507

Who (2018). *Global Status Reports on Road Safety*.

Wu, H., Han, Y., Pan, D., Wang, B., Huang, H., Mizuno, K., et al. (2021). The Head AIS 4+ Injury Thresholds for the Elderly Vulnerable Road User Based on Detailed Accident Reconstructions. *Front. Bioeng. Biotechnol.* 9 (525), 682015. doi:10.3389/fbioe.2021.682015

Zhang, C., Chen, F., and Wei, Y. (2019). Evaluation of Pedestrian Crossing Behavior and Safety at Uncontrolled Mid-block Crosswalks with Different Numbers of Lanes in China. *Accid. Anal. Prev.* 123, 263–273. doi:10.1016/j.aap.2018.12.002

Zou, T., Zha, A., Liu, Q., and Simms, C. (2020). Pedestrian Gaits Observed from Actual Pedestrian-Vehicle Collisions. *Int. J. Crashworthiness*, 1–23. doi:10.1080/13588265.2020.1769455

Conflict of Interest: The authors declare that the research was conducted in the absence of any commercial or financial relationships that could be construed as a potential conflict of interest.

frontiers in Bioengineering and Biotechnology

ORIGINAL RESEARCH
published: 26 November 2021
doi: 10.3389/fbioe.2021.797389

The Femoral Tunnel Drilling Angle at 45° Coronal and 45° Sagittal Provided the Lowest Peak Stress and Strain on the Bone Tunnels and Anterior Cruciate Ligament Graft

Rongshan Cheng[1,2†], *Huizhi Wang*[1,2†], *Ziang Jiang*[1,2], *Dimitris Dimitriou*[3], *Cheng-Kung Cheng*[1,2*] *and Tsung-Yuan Tsai*[1,2*]

[1]School of Biomedical Engineering & Med-X Research Institute, Shanghai Jiao Tong University, Engineering Research Center of Digital Medicine and Clinical Translation, Ministry of Education, Shanghai, China, [2]Shanghai Key Laboratory of Orthopaedic Implants & Clinical Translation R&D Center of 3D Printing Technology, Department of Orthopaedic Surgery, Shanghai Ninth People's Hospital, Shanghai Jiao Tong University School of Medicine, Shanghai, China, [3]Department of Orthopedics Balgrist University Hospital, Forchstrasse, Zürich, Switzerland

OPEN ACCESS

Edited by:
Ching-Chi Hsu,
National Taiwan University of Science and Technology, Taiwan

Reviewed by:
Wenxin Niu,
Tongji University, China
Yun Peng,
NuVasive, United States

***Correspondence:**
Cheng-Kung Cheng
ckcheng2020@sjtu.edu.cn
Tsung-Yuan Tsai
tytsai@sjtu.edu.cn

[†]These authors have contributed equally to this work

Specialty section:
This article was submitted to Biomechanics, a section of the journal Frontiers in Bioengineering and Biotechnology

Received: 18 October 2021
Accepted: 08 November 2021
Published: 26 November 2021

Citation:
Cheng R, Wang H, Jiang Z, Dimitriou D, Cheng C-K and Tsai T-Y (2021) The Femoral Tunnel Drilling Angle at 45° Coronal and 45° Sagittal Provided the Lowest Peak Stress and Strain on the Bone Tunnels and Anterior Cruciate Ligament Graft. Front. Bioeng. Biotechnol. 9:797389. doi: 10.3389/fbioe.2021.797389

Purpose: The aims of this study were to 1) investigate the effects of femoral drilling angle in coronal and sagittal planes on the stress and strain distribution around the femoral and tibial tunnel entrance and the stress distribution on the graft, following anterior cruciate ligament reconstruction (ACLR), 2) identify the optimal femoral drilling angle to reduce the risk of the tunnel enlargement and graft failure.

Methods: A validated three-dimensional (3D) finite element model of a healthy right cadaveric knee was used to simulate an anatomic ACLR with the anteromedial (AM) portal technique. Combined loading of 103.0 N anterior tibial load, 7.5 Nm internal rotation moment, and 6.9 Nm valgus moment during normal human walking at joint flexion of 20° was applied to the ACLR knee models using different tunnel angles (30°/45°/60° and 45°/60° in the coronal and sagittal planes, respectively). The distribution of von Mises stress and strain around the tunnel entrances and the graft was calculated and compared among the different finite element ACLR models with varying femoral drilling angles.

Results: With an increasing coronal obliquity drilling angle (30° to 60°), the peak stress and maximum strain on the femoral and tibial tunnel decreased from 30° to 45° and increased from 45° to 60°, respectively. With an increasing sagittal obliquity drilling angle (45° to 60°), the peak stress and the maximum strain on the bone tunnels increased. The lowest peak stress and maximum strain at the ACL tunnels were observed at 45° coronal/45° sagittal drilling angle (7.5 MPa and 7,568.3 μ-strain at the femoral tunnel entrance, and 4.0 MPa and 4,128.7 μ-strain at the tibial tunnel entrance). The lowest peak stress on the ACL graft occurred at 45° coronal/45° sagittal (27.8 MPa) drilling angle.

Conclusions: The femoral tunnel drilling angle could affect both the stress and strain distribution on the femoral tunnel, tibial tunnel, and graft. A femoral tunnel drilling angle

of 45° coronal/ 45° sagittal demonstrated the lowest peak stress, maximum strain on the femoral and tibial tunnel entrance, and the lowest peak stress on the ACL graft.

Keywords: femoral tunnel drilling angle, femoral and tibial tunnel, bone tunnel enlargement, graft failure, anterior cruciate ligament reconstruction, finite element analysis

INTRODUCTION

Anterior cruciate ligament (ACL) rupture is one of the most common ligamentous injuries of the knee joint (Griffin et al., 2006). ACL reconstruction (ACLR) is the commonly treatment for ACL injuries, with a success rate of up to 90% in knee function at short-term follow-ups (Oiestad et al., 2010). However, long-term follow-up studies have reported several complications following ACLR. Neblung et al. (Nebelung et al., 1998) reported that 72% patients demonstrated enlargement of the femoral tunnel and 38% patients demonstrated enlargement of the tibial tunnel following ACLR, respectively. Xu et al. (Xu et al., 2011) found that the rates of tunnel enlargement were 41% around the femoral side and 35% around the tibial side. Sonnery-Cottet et al. (Sonnery-Cottet et al., 2017) found that 10.77% of ACLR patients with quadrupled hamstring tendon graft and 16.77% with bone-patellar-tendon-bone (BPTB) graft suffered a graft rupture in a 4-years follow-up study. Furthermore, previous studies (Weber et al., 2015; Wang et al., 2020a) reported that tunnel enlargement and graft fatigue failure occurred at the bone tunnel aperture, which might be due to high contact stress or strain between the bone tunnel aperture and the graft. Hence, tunnel enlargement and graft fatigue failure raise relevant concerns following ACLR.

Several studies (Schechtman and Bader, 1997; Jagodzinski et al., 2005; Yao et al., 2014; Srinivas et al., 2016; Srinivas et al., 2016) have investigated the factors that might cause tunnel enlargement and graft failure. Srinivas et al. (Srinivas et al., 2016) found that the enlargement of femoral tunnel and tibial tunnel varied with different methods of fixation. L'Insalata et al. (L'Insalata et al., 1997) showed tunnel enlargement was significantly greater following ACL reconstruction using hamstring (HS) autograft than in those using bone-patellar-tendon-bone (BPTB) autograft. Schechtman et al. (Schechtman and Bader, 1997) reported a linear relationship between the stress and the number of cycles of tendons to fatigue failure. Few studies demonstrated that tunnel orientation might influence tunnel enlargement and graft failure (Jagodzinski et al., 2005; Yao et al., 2014). Specifically, Yao et al. (Yao et al., 2014) quantified the effects of tibial tunnel drill-guide angle on the stress redistribution at the tibial tunnel aperture after ACLR, which potentially contributed to the tibial tunnel widening. A cadaver study (Jagodzinski et al., 2005) reported that the bone tunnel angle might affect the redirecting force between the femoral tunnel and the graft. It may be an essential factor causing tunnel enlargement and graft failure. However, to the best of our knowledge, no study has determined the optimal femoral drilling angle to provide a better mechanical environment for the bone tunnel and the graft to prevent tunnel enlargement and graft failure.

The aims of this study were to 1) investigate the effects of femoral drilling angle in coronal and sagittal planes on the stress and strain distribution around the bone tunnels and the stress distribution of the graft, following anterior cruciate ligament reconstruction (ACLR), 2) to identify the optimal femoral drilling angle to reduce the risk of the tunnel enlargement and ACL graft failure. It was hypothesized that the femoral tunnel drilling angle in coronal and sagittal planes could affect the stress and strain distribution around the femoral and tibial tunnel entrance and the graft.

METHODS

Finite Element Model of the Knee Joint

A three-dimensional (3D) FE model of a healthy right cadaveric knee (male, 45 years) was reconstructed and validated in a

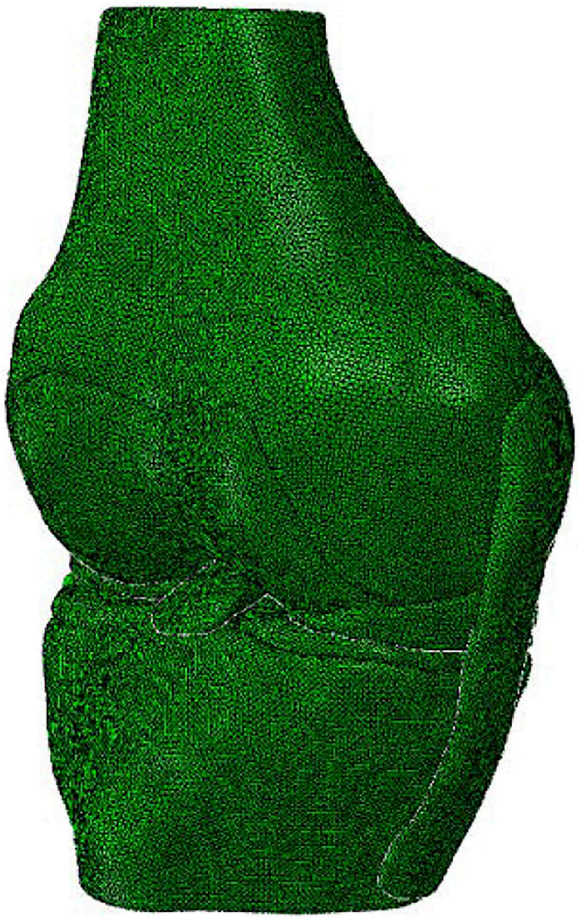

FIGURE 1 | A three dimensional **(3D)** finite element model of the knee joint was reconstructed using Abaqus/CAE 6.14.

TABLE 1 | Material properties of the tissues in the knee model (Wang et al., 2020b).

Tissue	*Material type*	*Parameters*
Bone	Isotropic elastic	Young's modulus = 0.4 GPa, Poisson's ratio v = 0.33
Cartilage	Isotropic elastic	Young's Modulus = 5 MPa, Poisson's ratio v = 0.46
Menisci	Orthotropic elastic	E_θ = 125 MPa, $E_R = E_Z$ = 27.5 MPa, $G_{\theta R} = G_{\theta Z}$ = 2 MPa, G_{RZ} = 10.34, $V_{\theta R} = V_{\theta Z}$ = 0.1, V_{RZ} = 0.33
ACL	Isotropic hyperelastic	Veronda-Westmann: α = 0.3 MPa, β = 12.20
PCL	Isotropic hyperelastic	Veronda-Westmann: α = 0.18 MPa, β = 17.35
MCL and LCL	Isotropic hyperelastic	Mooney-Rivlin: C1 = 30.1 MPa, C2 = – 27.1 MPa

TABLE 2 | Anterior tibial translation, valgus rotation and internal rotation of tibial, and ACL *in-situ* force obtained from robotic testing and FE model under the loading conditions 1) 134 N anterior tibial load; 2) 10 Nm valgus moment; 3) 10 Nm internal moment at a joint flexion angle of 30° (Wang et al., 2020b).

	134 N Anterior tibial load		**10 Nm valgus moment**		**10 Nm internal moment**	
	Anterior tibial translation (mm)	**ACL *in-situ* force (N)**	**Anterior tibial translation (mm)**	**ACL *in-situ* force (N)**	**Anterior tibial translation (mm)**	**ACL *in-situ* force (N)**
Experimental (robotic)	5.1	124	5	42	22 ± 3	41 ± 21
Computational (FE)	5.2	123	4	41	19	62

published study using software ABAQUS 6.14 (Simulia Inc., United States) (Wang et al., 2020a; **Figure 1**). Details about the construction and validation of the knee FE model were shown as follows. The cadaveric knee was imaged using magnetic resonance imaging (MRI) (SIEMENS MAGNETOM Skyra, SIEMENS, Germany) with a 0.2 mm resolution (TE/TR = 26.3 and 53 ms). 3D model of the knee was reconstructed from the MRI images and consisted of ligaments [ACL, posterior cruciate ligament (PCL), medial and lateral collateral ligament (MCL and LCL)], bones, cartilage, and menisci. The mechanical characteristics of the bone and the tissues were defined from the literature (Wang et al., 2020b; **Table 1**). A pre-strain of 3% was defined for the ACL (Song et al., 2004). A frictionless sliding contact was established among the femoral and tibial cartilage and the meniscus (Wang et al., 2020b). A tie contact was defined between the ligaments and the bone insertions (Wang et al., 2020b). The model was meshed in ABAQUS software using 4-node tetrahedron elements. To optimize the element size of the model, we used a mesh convergence test, whereby the element size was determined until the result for ACL *in-situ* force (under a 2.5 mm translational load at full extension) converged with a calculation difference within 0.5 N (Wang et al., 2020a). The resulting validated element size was 1 mm. Validation of the knee FE model: the differences between the results of robotic testing and the FE model were within 0.1 mm, 1° and 1 N for anterior tibial translation, rotation of valgus, and ACL *in-situ* force, respectively (Wang et al., 2020b) (**Table 2**).

Simulation of ACLR

To simulate the anatomic ACLR, we removed the native ACL from the model. The positions of the bone tunnels were determined at 110° knee flexion (Alentorn-Geli et al., 2010). The femoral and tibial tunnels were drilled through the center of ACL insertion sites (Forsythe et al., 2010; Ziegler et al., 2011; Bae et al., 2016). According to the previous studies (Loh et al., 2003; Seon et al., 2011; Warme et al., 2012; Takeda et al., 2013; Zhang et al., 2013; Tomihara et al., 2014), the femoral tunnel was drilled through the anteromedial (AM) portal technique in a coronal obliquity angle of 30°,45°, and 60° and a sagittal obliquity angle of 45° and 60° (**Figure 2**). The tibial tunnel was created at a tibial angle of 20° in the coronal plane and 60° in the sagittal plane (Alentorn-Geli et al., 2010; Yao et al., 2014). Numbers of studies (Asif et al., 2016; Goyal et al., 2016; Kang et al., 2019; Alomar et al., 2021) reported a graft diameter ≥7 mm was associated with significantly lower ACLR failure rates than a graft diameter <7 mm. A 4-strand hamstring tendon graft was simulated as cylindrical with a diameter of 7 mm (Goyal et al., 2016; Snaebjörnsson et al., 2017; Alomar et al., 2021) and Young's modulus of 144.8 MPa (Wilson et al., 1999). Titanium endoscrews with a diameter of 7 mm (Young's modulus / Poisson's ratio v = 100Gpa and 0.35) (Herbort et al., 2007; Hung et al., 2014; Shen et al., 2018) used in anatomical ACLR were used to secure the graft. The bottom surface of the endoscrews was tied to the ends of the graft, and the outer surface of the endoscrews was connected to the tunnel wall. The screw and the tunnel were concentric.

According to the methods described by Wang et al. (Wang et al., 2020a), the entrances of the femoral and tibial tunnel were split into four zones to describe the stress distribution around the bone tunnel entrances: anterior and posterior (A and Po), proximal and distal (Pr and D) zone for the femoral tunnel entrance, and anterior and posterior (A and P), medial and lateral (M and L) zone for the tibial tunnel entrance (**Figure 3**).

Loading and Boundary Conditions

The maximum anterior tibial load (103 N, 15% body weight), internal tibial moment (7.5 Nm, 1.1% body weight), and valgus tibial moment (6.9 Nm, 1% body weight) during normal human walking (Kutzner et al., 2010; Wang et al., 2020a; Wang et al., 2020b) were applied to the ACLR model using different tunnel angles at a joint flexion angle of 20° (Wang et al., 2020b). This loading condition represented a worst-case outcome for the ACL during walking (Kutzner et al., 2010). The von Mises stress and strain distribution around the bone tunnel entrances and the graft was calculated and compared among different

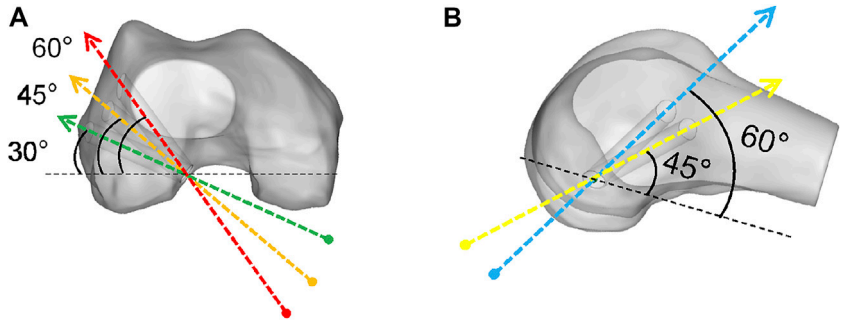

FIGURE 2 | Right knee flexed at 110°, demonstrating the femoral tunnel created by the. anteromedial portal technique at **(A)** a coronal obliquity angle of 30° (green arrow), 45° (orange arrow) and 60° (red arrow), **(B)** a sagittal obliquity angle of 45° (yellow arrow) and 60° (blue arrow), starting at the native femoral ACL center (green circle).

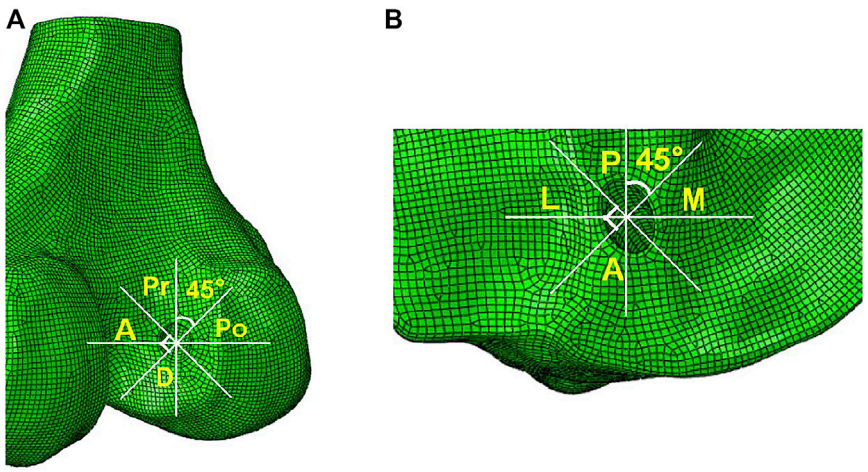

FIGURE 3 | Femoral and tibial tunnel entrances divided into four zones. The two white lines divided the femoral tunnel entrance into four zones: anterior and posterior (A and Po), proximal and distal (Pr and D) zone for the femoral tunnel entrance, and anterior and posterior (A and P), medial and lateral (M and L) zone for the tibial tunnel entrance.

finite element ACLR models with varying femoral drilling angles in coronal and sagittal planes.

RESULTS

On the femoral side, with an increasing coronal obliquity drilling angle (30° to 60°), the peak stress and maximum strain decreased from 30° to 45° and increased from 45° to 60°, respectively. With an increasing sagittal obliquity drilling angle (45° to 60°), the peak stress and the maximum strain on the bone tunnels increased. The peak stress and the maximum strain in the ACLR knee occurred at the anterior and distal zone of the femoral tunnel entrance (**Figures 4**, **5**) at all angles. The lowest peak stress of the femoral tunnel entrance was 7.5 MPa and occurred in 45° coronal/ 45° sagittal, whereas the highest peak stress with 12.1 MPa occurred in 60° coronal/ 60° sagittal (**Table 3**). The lowest maximum strain of the femoral tunnel entrance was 7,568.3 μ-strain in 45° coronal/ 45° sagittal, whereas the highest maximum strain with 13,570.8 μ-strain occurred in 60° coronal/ 60° sagittal (**Table 4**).

On the tibial side, the trend of the peak stress and maximum strain on the tibial tunnel entrance with coronal and sagittal angle changes was consistent with that on the femoral tunnel entrance. The peak stress and the maximum strain in the ACLR knee occurred at the posterior zone of the tibial tunnel entrance (**Figure 6**; **Figure 7**) at all angles. The lowest peak stress of the tibial tunnel entrance was 4.0 MPa and occurred in 45° coronal/ 45° sagittal. In contrast, the highest peak stress with 5.5 MPa occurred in 30° coronal/ 60° sagittal (**Table 3**). The lowest maximum strain of the tibial tunnel entrance was 4,128.7 μ-strain in 45° coronal/ 45° sagittal, whereas the highest maximum strain with 5,424.4 μ-strain occurred in 60° coronal/ 60° sagittal (**Table 4**).

The peak stress found on the ACL graft was located close to the entrance of the femoral tunnel (**Figure 8**). Following ACLR, the highest peak stress on the ACL graft was 30.69 MPa and occurred in 60° coronal/ 60° sagittal. The lowest peak stress on the ACL graft was 27.8 MPa and appeared in 45° coronal/ 45° sagittal.

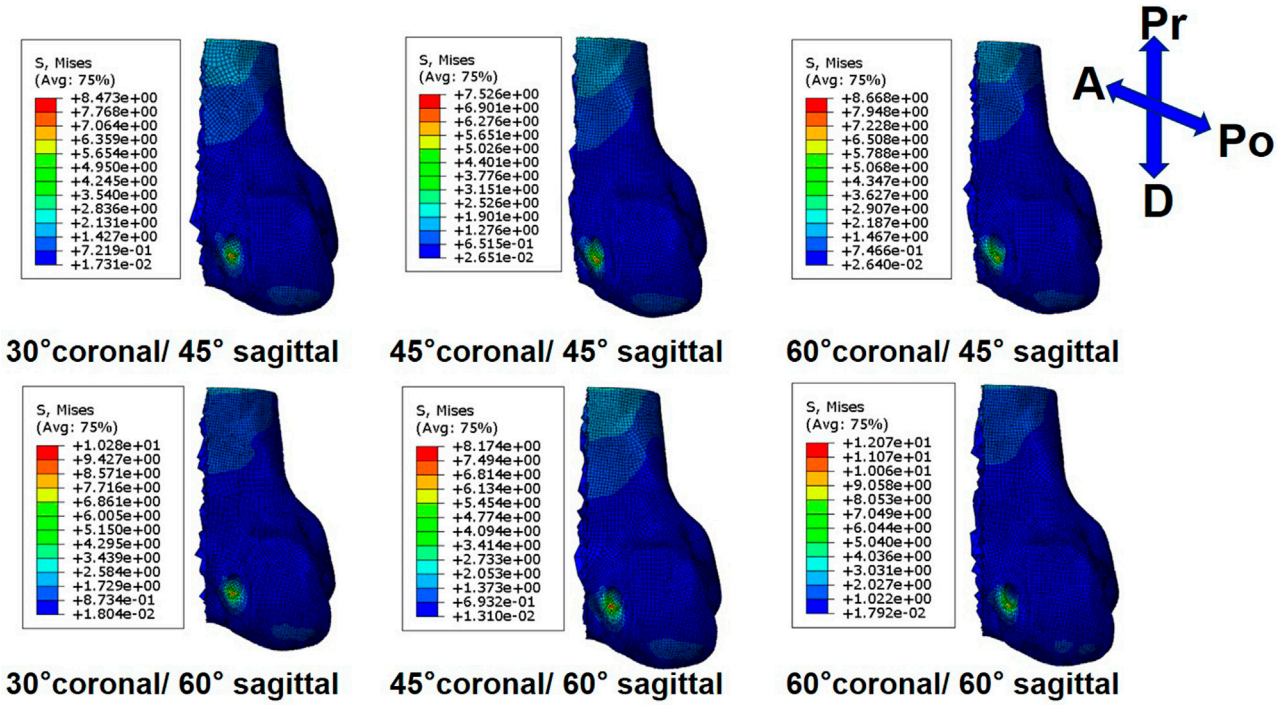

FIGURE 4 | Stress distribution around femoral tunnel entrance following ACLR.

DISCUSSION

The most important finding of the present study was that the femoral tunnel drilling angle could affect the stress and strain distribution on both tunnel entrances and the ACL-graft. A femoral tunnel drilling angle of 45° coronal/ 45° sagittal demonstrated the lowest peak stress, maximum strain at both femoral and tibial tunnel entrances, and the lowest peak stress on the ACL graft following ACLR.

The femoral tunnel angle could influence the enlargement of the femoral tunnel (Segawa et al., 2003; Jagodzinski et al., 2005). Jagodzinski et al. (Jagodzinski et al., 2005) found that the bone tunnel angle could affect the force between the bone tunnel and the graft at the entrance of the bone tunnel, which might cause the "bungee effect" and "windshield–wiper effect" of the ACL graft at the tunnel entrances which may be related to the tunnel enlargement. Segawa et al. (Segawa et al., 2003) reported that an acute femoral tunnel angle in the sagittal plane might increase mechanical stress on the margin of the femoral tunnel, resulting in bone tunnel enlargement. Similarly, the present study results demonstrated that the peak stress and the maximum strain at the femoral tunnel entrance increased with an increase in the sagittal obliquity angle. In addition, the peak stress and the maximum strain at the femoral tunnel entrance decreased from 30° to 45° and increased from 45° to 60° in the coronal plane. Previous studies (Wiskott and Belser, 1999; Cheng et al., 2021) showed a critical factor determining the bone loss or formation in response to mechanical loading was the strain value inside the bones. Bone resorption (bone density) was predicted for strain values below the effective strain level (100 μ-strain) or above the low strain level (4,000 μ-strain), whereas bone formation was predicted for strain values between 2000 μ-strain and 4000 μ-strain, and an imbalance between bone resorption and formation was predicted in the strain values range from 100 μ-strain to 2000 μ-strain (Wiskott and Belser, 1999). Our results showed the strain of the distal zone and anterior zone of the femoral tunnel entrance in several coronal and sagittal obliquity angles exceeded 4,000 μ-strain, which could cause an enlargement of the femoral tunnel. In line with our data, a clinical follow-up study (Tachibana et al., 2015) reported that tunnel enlargement occurred in the anterior and distal directions at the femoral tunnel entrance. Therefore, to reduce the femoral tunnel enlargement at the distal zone and anterior zone of the tunnel entrance, a femoral tunnel drilling angle in 45° coronal/ 45° sagittal might be recommended.

The present study is the only available literature to describe the effects of femoral tunnel angle on tibial tunnel enlargement. Our results showed that the trends of change in peak stress and maximum strain at the tibial tunnel entrance in several femoral tunnel drilling angles were consistent with that at the femoral tunnel entrance. Although the trend was consistent, the strain exceeding 4,000 μ-strain only occurred at the posterior zone of the tibial tunnel entrance. Xu et al. (Xu et al., 2011) reported the tunnel enlargement was more evident in the femoral side than in the tibial side, which was in concordance with the current study. The maximum strain at the tibial tunnel entrance was smaller than that at the femoral tunnel entrance. Moreover, Fink et al. (Fink et al., 2001) found that tibial tunnel enlargement was larger in the sagittal plane than that in the coronal plane. This observation was also consistent with our

TABLE 3 | Maximum von Mises stress (MPa) at different zones of the tunnel entrances following ACLR by AM portal technique in several coronal and sagittal obliquity angles.

	Femoral tunnel entrance				Tibial tunnel entrance			
	A zone	D zone	Pr zone	Po zone	A zone	M zone	P zone	L zone
ACLR (30° coronal / 45° sagittal)	5.06	8.47	0.55	2.02	0.82	2.24	4.11	0.53
ACLR (45° coronal / 45° sagittal)	5.68	7.53	0.83	1.04	0.75	2.28	3.98	0.44
ACLR (60° coronal / 45° sagittal)	4.98	8.67	1.51	0.84	0.89	1.95	4.01	0.49
ACLR (30° coronal / 60° sagittal)	7.69	10.28	0.54	3.4	1.14	1.64	5.49	0.61
ACLR (45° coronal / 60° sagittal)	4.99	8.17	0.75	1.97	0.67	2.24	4.45	0.51
ACLR (60° coronal / 60° sagittal)	7.36	12.07	1.26	1.44	1.18	2.02	5.48	0.45

TABLE 4 | Maximum strain (μ-strain) at different zones of the tunnel entrances following ACLR by AM portal technique in several coronal and sagittal obliquity angles.

	Femoral tunnel entrance				Tibial tunnel entrance			
	A zone	D zone	Pr zone	Po zone	A zone	M Zone	P Zone	L Zone
ACLR (30° coronal/45° sagittal)	6896.94	8300.45	1350.07	4217.28	2067.39	3014.44	4429.76	1340.97
ACLR (45° coronal/45° sagittal)	6873.11	7568.32	2070.74	2619.67	1889.14	2893.54	4128.73	759.77
ACLR (60° coronal/45° sagittal)	6941.73	7891.13	3731.91	2142.78	2255.56	3803.60	4571.03	1237.60
ACLR (30° coronal/60° sagittal)	10296.30	11699.20	1611.68	6928.15	2454.41	3433.40	5383.89	1511.62
ACLR (45° coronal/60° sagittal)	9921.03	10327.50	1842.31	4707.57	1715.97	2941.94	4702.43	1287.82
ACLR (60° coronal/60° sagittal)	10454.35	13570.80	3138.72	3678.64	2642.13	3149.21	5424.38	1135.21

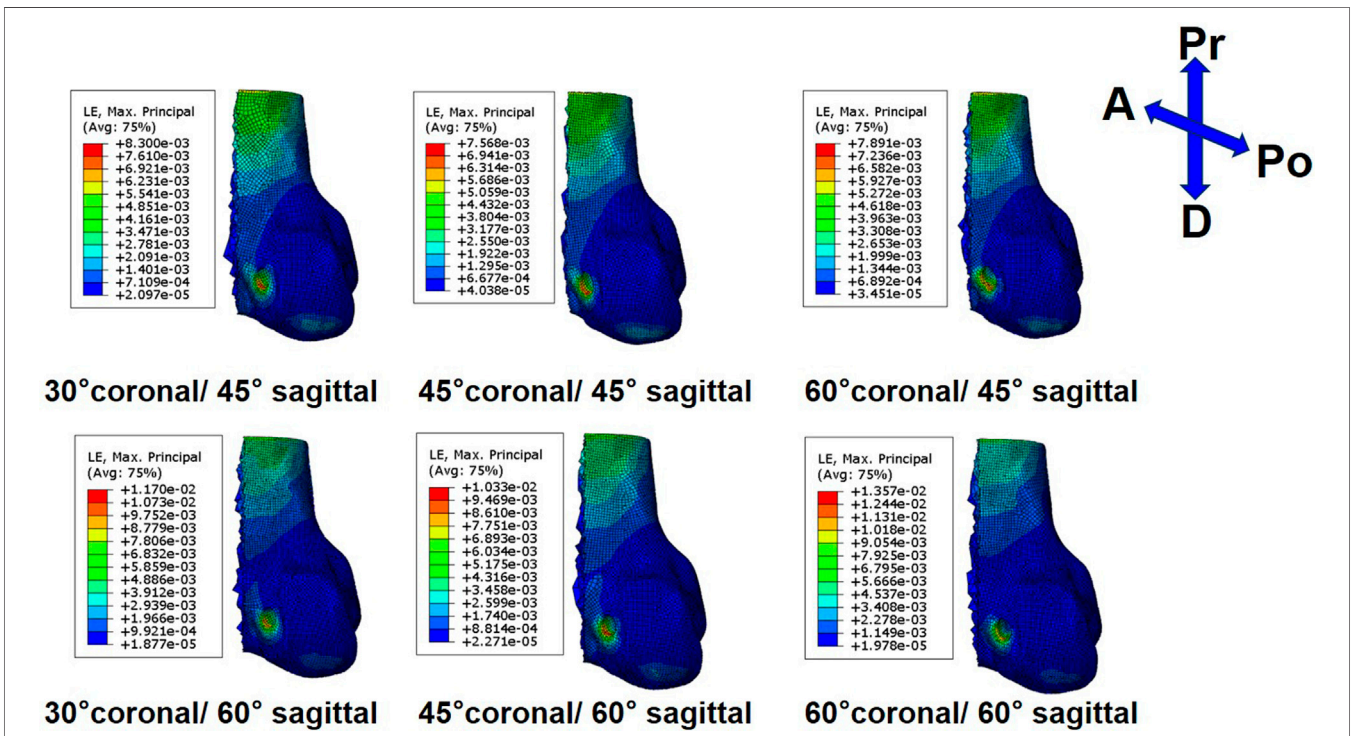

FIGURE 5 | Strain distribution around femoral tunnel entrance following ACLR.

results, as the maximum strain occurred at the posterior zone of the tibial tunnel entrance.

Previous studies (Schechtman and Bader, 1997; Adeeb et al., 2004; Lipps et al., 2013; Purevsuren et al., 2017) reported a high cyclic loading or stress might decrease the number of cycles to cause fatigue failure of ligament and tendon and result in a faster rupture. Our data showed the cyclic stress on the graft following ACLR by AM portal technique in 45° coronal/ 45° sagittal was

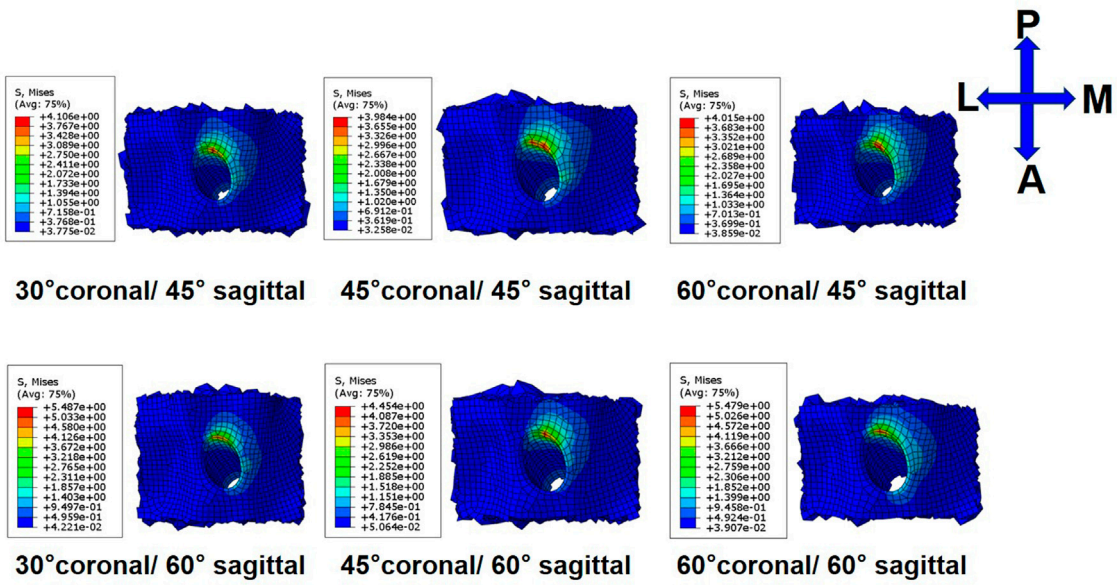

FIGURE 6 | Stress distribution around tibial tunnel entrance following ACLR.

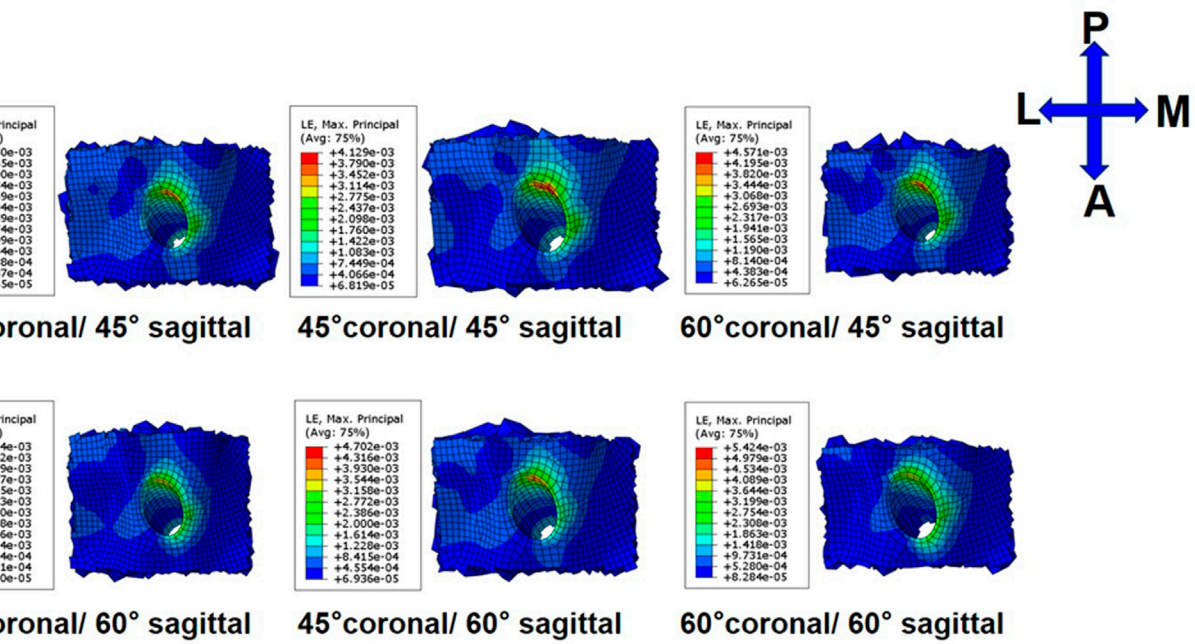

FIGURE 7 | Strain distribution around tibial tunnel entrance following ACLR.

lowest among several coronal and sagittal obliquity angles, leading to the largest number of cycles to cause a fatigue failure of the graft over time. A cadaver study (Purevsuren et al., 2017) demonstrated the number of cycles for the failure of the ligament and tendon could be predicted by the magnitude of the applied cyclic peak stress [percentage of the ultimate tensile stress (UTS)]. This present study demonstrated that a femoral tunnel drilling angle of 45° coronal/ 45° sagittal showed the lowest peak stress. Therefore, our results showed the femoral tunnel drilling angle at 45° coronal/ 45° sagittal might be optimal to reduce the risk of graft failure. Furthermore, A previous study (Guidoin et al., 2000) showed that most grafts failed at the junction between the femoral tunnel entrance and the graft, which might be caused by the stress concentration. This observation was consistent with our results, as the peak stress on the graft was concentrated at the junction.

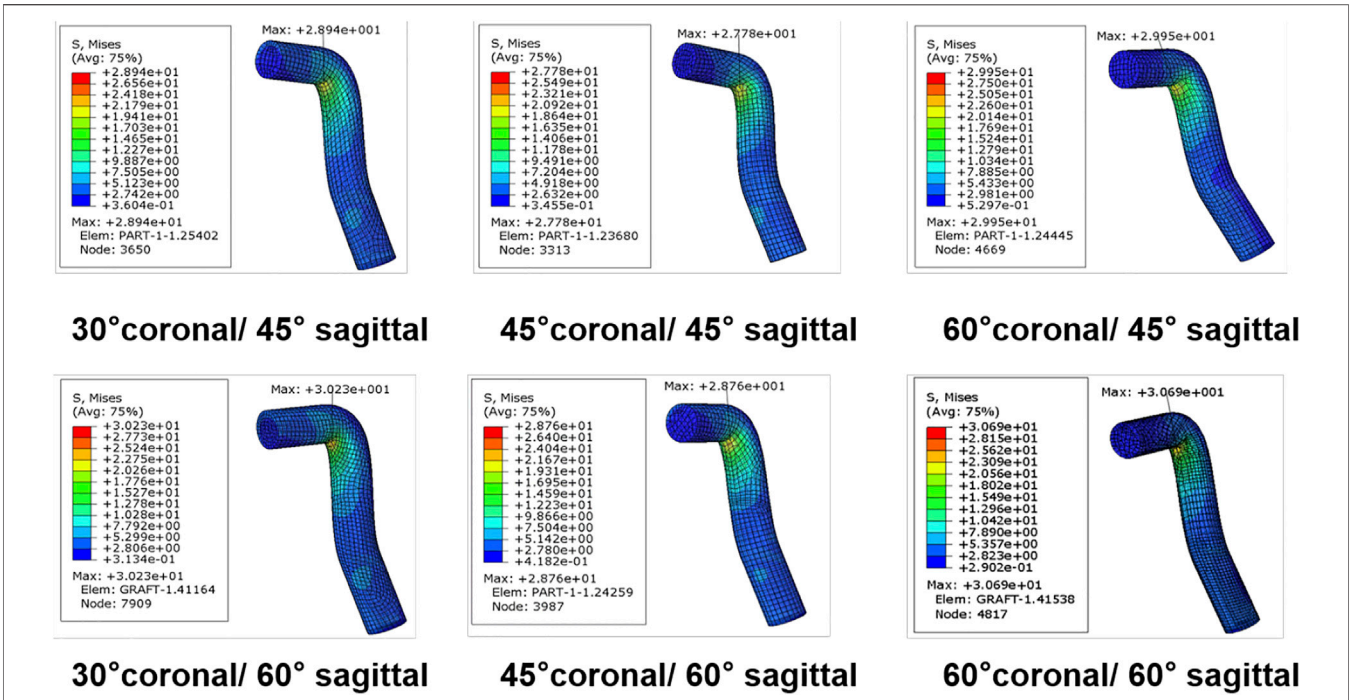

FIGURE 8 | Stress distribution around the ACL graft following ACLR.

The current study should be interpreted in light of its potential limitations. First, a static load was used in this study, and the maximum combined loadings on the ACL during walking were applied to the model. However, different loading conditions may cause different stress environments at the tunnel entrances and the ACL graft. Thus, the influence of different daily activities around the tunnel entrances and the ACL graft may be considered in future studies. Second, several studies (Jagodzinski et al., 2005; Wang et al., 2020a) showed the process leading to tunnel enlargement was thought to be complex and multifactorial. These studies evaluated tunnel enlargement from a biomechanical perspective. In contrast, biological factors may also lead to tunnel enlargement (Yue et al., 2020), which were not considered in this study. In the future, the influence of biological factors on tunnel enlargement and graft fatigue should be quantitatively studied to reinforce our understanding of the mechanism of these complications following ACLR. Third, the present study only focused on the bone tunnel entrances. However, a previous study (Tachibana et al., 2015) showed the tunnel enlargement was more severe at the entrance because the more significant interaction appeared at this location between the tunnel and the graft than that between screw and graft inside the bone tunnel.

CONCLUSION

The femoral tunnel drilling angle could affect both the stress and strain distribution on the femoral tunnel, tibial tunnel, and graft. A femoral tunnel drilling angle of 45° coronal/ 45° sagittal demonstrated the lowest peak stress, maximum strain on the femoral and tibial tunnel entrance, and the lowest peak stress on the ACL graft.

DATA AVAILABILITY STATEMENT

All datasets generated for this study are included in the article/ supplementary material.

AUTHOR CONTRIBUTIONS

RC: Designing the study, Finishing the model calculation, Analyzing the data, Writing and editing the manuscript, Approving the manuscript. HW: Assisting with model calculation, Editing the manuscript, Approving the manuscript. ZJ: Analyzing the data, Editing the manuscript. DD: Reviewing the literature, Editing the manuscript. C-KC: Reviewing and approving the manuscript. T-YT: Designing and supervising the study, Reviewing and approving the manuscript.

FUNDING

This project was sponsored by the National Natural Science Foundation of China (31972924 and 31771017), the Science and Technology Commission of Shanghai Municipality (16441908700), the Innovation Research Plan supported by the Shanghai Municipal Education Commission (ZXWF082101), the National Key R&D Program of China (2019YFC0120600), and the Interdisciplinary Program of Shanghai Jiao Tong University (ZH2018QNA06).

REFERENCES

Adeeb, S. M., Zec, M. L., Thornton, G. M., Frank, C. B., and Shrive, N. G. (2004). A Novel Application of the Principles of Linear Elastic Fracture Mechanics (LEFM) to the Fatigue Behavior of Tendon Tissue. *J. Biomech. Eng.* 126 (5), 641–650. doi:10.1115/1.1800556

Alentorn-Geli, E., Samitier, G., Álvarez, P., Steinbacher, G., and Cugat, R. (2010). Anteromedial portal versus Transtibial Drilling Techniques in ACL Reconstruction: a Blinded Cross-Sectional Study at Two- to Five-Year Follow-Up. *Int. Orthopaedics (Sicot)* 34 (5), 747–754. doi:10.1007/s00264-010-1000-1

Alomar, A. Z., Nasser, A. S. B., Kumar, A., Kumar, M., Das, S., and Mittal, S. (2021). Hamstring Graft Diameter above 7 Mm Has a Lower Risk of Failure Following Anterior Cruciate Ligament Reconstruction. *Knee Surg. Sports Traumatol. Arthrosc*, 1–10. doi:10.1007/s00167-021-06503-0

Asif, N., Ranjan, R., Ahmed, S., Sabir, A. B., Jilani, L. Z., and Qureshi, O. A. (2016). Prediction of Quadruple Hamstring Graft Diameter for Anterior Cruciate Ligament Reconstruction by Anthropometric Measurements. *Indian J. Orthop.* 50 (1), 49–54. doi:10.4103/0019-5413.173521

Bae, J. Y., Kim, G.-H., Seon, J. K., and Jeon, I. (2016). Finite Element Study on the Anatomic Transtibial Technique for Single-Bundle Anterior Cruciate Ligament Reconstruction. *Med. Biol. Eng. Comput.* 54 (5), 811–820. doi:10.1007/s11517-015-1372-x

Cheng, R., Jiang, Z., Dimitriou, D., Gong, W., and Tsai, T.-Y. (2021). Biomechanical Analysis of Personalised 3D-Printed Clavicle Plates of Different Materials to Treat Midshaft Clavicle Fractures. *J. Shanghai Jiaotong Univ. (Sci.)* 26 (3), 259–266. doi:10.1007/s12204-021-2291-7

Fink, C., Zapp, M., Benedetto, K. P., Hackl, W., Hoser, C., and Rieger, M. (2001). Tibial Tunnel Enlargement Following Anterior Cruciate Ligament Reconstruction with Patellar Tendon Autograft. *Arthrosc. J. Arthroscopic Relat. Surg.* 17 (2), 138–143. doi:10.1053/jars.2001.21509

Forsythe, B., Kopf, S., Wong, A. K., Martins, C. A., Anderst, W., Tashman, S., et al. (2010). The Location of Femoral and Tibial Tunnels in Anatomic Double-Bundle Anterior Cruciate Ligament Reconstruction Analyzed by Three-Dimensional Computed Tomography Models. *The J. Bone Jt. Surgery-American Volume* 92 (6), 1418–1426. doi:10.2106/jbjs.I.00654

Goyal, S., Matias, N., Pandey, V., and Acharya, K. (2016). Are Pre-operative Anthropometric Parameters Helpful in Predicting Length and Thickness of Quadrupled Hamstring Graft for ACL Reconstruction in Adults? A Prospective Study and Literature Review. *Int. Orthopaedics (Sicot)* 40 (1), 173–181. doi:10.1007/s00264-015-2818-3

Griffin, L. Y., Albohm, M. J., Arendt, E. A., Bahr, R., Beynnon, B. D., DeMaio, M., et al. (2006). Understanding and Preventing Noncontact Anterior Cruciate Ligament Injuries. *Am. J. Sports Med.* 34 (9), 1512–1532. doi:10.1177/0363546506286866

Guidoin, M.-F., Marois, Y., Bejui, J., Poddevin, N., King, M. W., and Guidoin, R. (2000). Analysis of Retrieved Polymer Fiber Based Replacements for the ACL. *Biomaterials* 21 (23), 2461–2474. doi:10.1016/s0142-9612(00)00114-9

Herbort, M., Weimann, A., Zantop, T., Strobel, M., Raschke, M., and Petersen, W. (2007). Initial Fixation Strength of a New Hybrid Technique for Femoral ACL Graft Fixation: the Bone Wedge Technique. *Arch. Orthop. Trauma Surg.* 127 (9), 769–775. doi:10.1007/s00402-006-0217-3

Hung, C.-C., Chen, W.-C., Yang, C.-T., Cheng, C.-K., Chen, C.-H., and Lai, Y.-S. (2014). Interference Screw versus Endoscrew Fixation for Anterior Cruciate Ligament Reconstruction: A Biomechanical Comparative Study in Sawbones and Porcine Knees. *J. Orthopaedic Translation* 2 (2), 82–90. doi:10.1016/j.jot.2014.02.001

Jagodzinski, M., Foerstemann, T., Mall, G., Krettek, C., Bosch, U., and Paessler, H. H. (2005). Analysis of Forces of ACL Reconstructions at the Tunnel Entrance: Is Tunnel Enlargement a Biomechanical Problem? *J. Biomech.* 38 (1), 23–31. doi:10.1016/j.jbiomech.2004.03.021

Kang, H., Dong, C., and Wang, F. (2019). Small Hamstring Autograft Is Defined by a Cut-Off Diameter of 7 Mm and Not Recommended with Allograft Augmentation in Single-Bundle ACL Reconstruction. *Knee Surg. Sports Traumatol. Arthrosc.* 27 (11), 3650–3659. doi:10.1007/s00167-019-05475-6

Kutzner, I., Heinlein, B., Graichen, F., Bender, A., Rohlmann, A., Halder, A., et al. (2010). Loading of the Knee Joint during Activities of Daily Living Measured *In Vivo* in Five Subjects. *J. Biomech.* 43 (11), 2164–2173. doi:10.1016/j.jbiomech.2010.03.046

L'Insalata, J. C., Klatt, B., Fu, F. H., and Harner, C. D. (1997). Tunnel Expansion Following Anterior Cruciate Ligament Reconstruction: a Comparison of Hamstring and Patellar Tendon Autografts. *Knee Surg. Sports Traumatol. Arthrosc.* 5 (4), 234–238. doi:10.1007/s001670050056

Lipps, D. B., Wojtys, E. M., and Ashton-Miller, J. A. (2013). Anterior Cruciate Ligament Fatigue Failures in Knees Subjected to Repeated Simulated Pivot Landings. *Am. J. Sports Med.* 41 (5), 1058–1066. doi:10.1177/0363546513477836

Loh, J. C., Fukuda, Y., Tsuda, E., Steadman, R. J., Fu, F. H., and Woo, S. L.-Y. (2003). Knee Stability and Graft Function Following Anterior Cruciate Ligament Reconstruction: Comparison between 11 O'clock and 10 O'clock Femoral Tunnel Placement. *Arthrosc. J. Arthroscopic Relat. Surg.* 19 (3), 297–304. doi:10.1053/jars.2003.50084

Nebelung, W., Becker, R., Merkel, M., and Ropke, M. (1998). Bone Tunnel Enlargement after Anterior Cruciate Ligament Reconstruction with Semitendinosus Tendon Using Endobutton Fixation on the Femoral Side. *Arthrosc. J. Arthroscopic Relat. Surg.* 14 (8), 810–815. doi:10.1016/s0749-8063(98)70015-5

Øiestad, B. E., Holm, I., Aune, A. K., Gunderson, R., Myklebust, G., Engebretsen, L., et al. (2010). Knee Function and Prevalence of Knee Osteoarthritis after Anterior Cruciate Ligament Reconstruction. *Am. J. Sports Med.* 38 (11), 2201–2210. doi:10.1177/0363546510373876

Purevsuren, T., Kwon, M. S., Park, W. M., Kim, K., Jang, S. H., Lim, Y.-T., et al. (2017). Fatigue Injury Risk in Anterior Cruciate Ligament of Target Side Knee during golf Swing. *J. Biomech.* 53, 9–14. doi:10.1016/j.jbiomech.2016.12.007

Schechtman, H., and Bader, D. L. (1997). *In Vitro* fatigue of Human Tendons. *J. Biomech.* 30 (8), 829–835. doi:10.1016/s0021-9290(97)00033-x

Segawa, H., Koga, Y., Omori, G., Sakamoto, M., and Hara, T. (2003). Influence of the Femoral Tunnel Location and Angle on the Contact Pressure in the Femoral Tunnel in Anterior Cruciate Ligament Reconstruction. *Am. J. Sports Med.* 31 (3), 444–448. doi:10.1177/03635465030310032001

Seon, J. K., Park, S. J., Lee, K. B., Seo, H. Y., Kim, M. S., and Song, E. K. (2011). *In Vivo* stability and Clinical Comparison of Anterior Cruciate Ligament Reconstruction Using Low or High Femoral Tunnel Positions. *Am. J. Sports Med.* 39 (1), 127–133. doi:10.1177/0363546510377417

Shen, X. Z., Qu, F., Li, C. B., Qi, W., Lu, X., Li, H. L., et al. (2018). Comparison between a Novel Human Cortical Bone Screw and Bioabsorbable Interference Screw for Graft Fixation of ACL Reconstruction. *Eur. Rev. Med. Pharmacol. Sci.* 22 (1 Suppl. l), 111–118. doi:10.26355/eurrev_201807_15372

Snaebjörnsson, T., Hamrin Senorski, E., Ayeni, O. R., Alentorn-Geli, E., Krupic, F., Norberg, F., et al. (2017). Graft Diameter as a Predictor for Revision Anterior Cruciate Ligament Reconstruction and KOOS and EQ-5D Values: A Cohort Study from the Swedish National Knee Ligament Register Based on 2240 Patients. *Am. J. Sports Med.* 45 (9), 2092–2097. doi:10.1177/0363546517704177

Song, Y., Debski, R. E., Musahl, V., Thomas, M., and Woo, S. L.-Y. (2004). A Three-Dimensional Finite Element Model of the Human Anterior Cruciate Ligament: a Computational Analysis with Experimental Validation. *J. Biomech.* 37 (3), 383–390. doi:10.1016/s0021-9290(03)00261-6

Sonnery-Cottet, B., Saithna, A., Cavalier, M., Kajetanek, C., Temponi, E. F., Daggett, M., et al. (2017). Anterolateral Ligament Reconstruction Is Associated with Significantly Reduced ACL Graft Rupture Rates at a Minimum Follow-Up of 2 years: A Prospective Comparative Study of 502 Patients from the SANTI Study Group. *Am. J. Sports Med.* 45 (7), 1547–1557. doi:10.1177/0363546516686057

Srinivas, D. K., Kanthila, M., Saya, R. P., and Vidyasagar, J. (2016). Femoral and Tibial Tunnel Widening Following Anterior Cruciate Ligament Reconstruction Using Various Modalities of Fixation: A Prospective Observational Study. *Jcdr* 10 (11), Rc09–rc11. doi:10.7860/jcdr/2016/22660.8907

Tachibana, Y., Mae, T., Shino, K., Kanamoto, T., Sugamoto, K., Yoshikawa, H., et al. (2015). Morphological Changes in Femoral Tunnels after Anatomic Anterior Cruciate Ligament Reconstruction. *Knee Surg. Sports Traumatol. Arthrosc.* 23 (12), 3591–3600. doi:10.1007/s00167-014-3252-6

Takeda, Y., Iwame, T., Takasago, T., Kondo, K., Goto, T., Fujii, K., et al. (2013). Comparison of Tunnel Orientation between Transtibial and Anteromedial portal Techniques for Anatomic Double-Bundle Anterior Cruciate Ligament Reconstruction Using 3-dimensional Computed Tomography. *Arthrosc. J. Arthroscopic Relat. Surg.* 29 (2), 195–204. doi:10.1016/j.arthro.2012.08.020

Tomihara, T., Yoshida, G., Hara, Y., Taniuchi, M., and Shimada, N. (2014). Transparent 3-dimensional CT in Evaluation of Femoral Bone Tunnel Communication after ACL Double-Bundle Reconstruction: Comparison between Outside-In and Transportal Technique. *Knee Surg. Sports Traumatol. Arthrosc.* 22 (7), 1563–1572. doi:10.1007/s00167-013-2594-9

Wang, H., Zhang, M., and Cheng, C. K. (2020b). A Novel protection Liner to Improve Graft-Tunnel Interaction Following Anterior Cruciate Ligament Reconstruction: a Finite Element Analysis. *J. Orthop. Surg. Res.* 15 (1), 1–10. doi:10.1186/s13018-020-01755-x

Wang, H., Zhang, B., and Cheng, C.-K. (2020a). Stiffness and Shape of the ACL Graft Affects Tunnel Enlargement and Graft Wear. *Knee Surg. Sports Traumatol. Arthrosc.* 28 (7), 2184–2193. doi:10.1007/s00167-019-05772-0

Warme, B. A., Ramme, A. J., Willey, M. C., Britton, C. L., Flint, J. H., Amendola, A. S., et al. (2012). Reliability of Early Postoperative Radiographic Assessment of Tunnel Placement after Anterior Cruciate Ligament Reconstruction. *Arthrosc. J. Arthroscopic Relat. Surg.* 28 (7), 942–951. doi:10.1016/j.arthro.2011.12.010

Weber, A. E., Delos, D., Oltean, H. N., Vadasdi, K., Cavanaugh, J., Potter, H. G., et al. (2015). Tibial and Femoral Tunnel Changes after ACL Reconstruction. *Am. J. Sports Med.* 43 (5), 1147–1156. doi:10.1177/0363546515570461

Wilson, T. W., Zafuta, M. P., and Zobitz, M. (1999). A Biomechanical Analysis of Matched Bone-Patellar Tendon-Bone and Double-Looped Semitendinosus and Gracilis Tendon Grafts. *Am. J. Sports Med.* 27 (2), 202–207. doi:10.1177/03635465990270021501

Wiskott, H. W. A., and Belser, U. C. (1999). Lack of Integration of Smooth Titanium Surfaces: a Working Hypothesis Based on Strains Generated in the Surrounding Bone. *Clin. Oral Implants Res.* 10 (6), 429–444. doi:10.1034/j.1600-0501.1999.100601.x

Xu, Y., Ao, Y., Wang, J., Yu, J., and Cui, G. (2011). Relation of Tunnel Enlargement and Tunnel Placement after Single-Bundle Anterior Cruciate Ligament Reconstruction. *Arthrosc. J. Arthroscopic Relat. Surg.* 27 (7), 923–932. doi:10.1016/j.arthro.2011.02.020

Yao, J., Wen, C. Y., Zhang, M., Cheung, J. T.-M., Yan, C., Chiu, K.-Y., et al. (2014). Effect of Tibial Drill-Guide Angle on the Mechanical Environment at Bone Tunnel Aperture after Anatomic Single-Bundle Anterior Cruciate Ligament Reconstruction. *Int. Orthopaedics (Sicot)* 38 (5), 973–981. doi:10.1007/s00264-014-2290-5

Yue, L., DeFroda, S. F., Sullivan, K., Garcia, D., and Owens, B. D. (2020). Mechanisms of Bone Tunnel Enlargement Following Anterior Cruciate Ligament Reconstruction. *JBJS Rev.* 8 (4), e0120. doi:10.2106/jbjs.rvw.19.00120

Zhang, C., Xu, H., Li, X., Wang, Y., Zhang, Q., and Zhu, Q. (2013). Oblique Femoral Tunnel or Oblique Graft? A Modified Anteromedial portal Technique to Obtain Vertical Femoral Tunnel and Oblique Graft in Anatomic Anterior Cruciate Ligament Reconstruction. *Eur. J. Orthop. Surg. Traumatol.* 23 (6), 731–735. doi:10.1007/s00590-012-1046-4

Ziegler, C. G., Pietrini, S. D., Westerhaus, B. D., Anderson, C. J., Wijdicks, C. A., Johansen, S., et al. (2011). Arthroscopically Pertinent Landmarks for Tunnel Positioning in Single-Bundle and Double-Bundle Anterior Cruciate Ligament Reconstructions. *Am. J. Sports Med.* 39 (4), 743–752. doi:10.1177/0363546510387511

Conflict of Interest: The authors declare that the research was conducted in the absence of any commercial or financial relationships that could be construed as a potential conflict of interest.

Publisher's Note: All claims expressed in this article are solely those of the authors and do not necessarily represent those of their affiliated organizations, or those of the publisher, the editors and the reviewers. Any product that may be evaluated in this article, orclaim that may be made by its manufacturer, is not guaranteed or endorsed by the publisher.

frontiers in Bioengineering and Biotechnology

ORIGINAL RESEARCH
published: 09 December 2021
doi: 10.3389/fbioe.2021.790595

Protection by Ankle Brace for Lower-Extremity Joints in Half-Squat Parachuting Landing With a Backpack

*Tianyun Jiang[1], Shan Tian[1], Tianhong Chen[1], Xingyu Fan[2], Jie Yao[1] and Lizhen Wang[1]**

[1]Key Laboratory of Biomechanics and Mechanobiology (Beihang University), Ministry of Education, Beijing Advanced Innovation Center for Biomedical Engineering, School of Biological Science and Medical Engineering, Beihang University, Beijing, China, [2]College of Bioengineering, Chongqing University, Chongqing, China

Half-squat parachuting landing is a kind of activity with high impact force. Injuries on lower-extremity joints are common in half-squat parachuting landing and would be increased with a backpack. An ankle brace was used to prevent ankle injuries in landing. However, few quantitative studies reported about the protection of an ankle brace for lower-extremity joints in half-squat parachuting landing with a backpack. This study focused on evaluating the protective effects of an ankle brace in half-squat parachuting landing with a backpack. Seven male participants landed from 120 cm with a backpack and an ankle brace. Each participant performed three landing trials on every experimental condition. Kinetics and kinematics of the hip, knee, and ankle were analyzed. It was found that the ankle brace did not significantly affect the ground reaction force with backpack but increased the ground reaction force from 14.7 ± 2.0 bodyweight to 16.2 ± 1.9 bodyweight ($p = 0.017$) without the backpack. The ankle brace significantly ($p < 0.05$) decreased the angular displacement, angular velocity, and angular acceleration of the ankle both without and with the backpack. In conclusion, the ankle brace could restrict ankle motion and significantly increase ground reaction force without the backpack. However, the ankle brace did not significantly influence ground reaction force and still restricted ankle motion with the backpack. Therefore, the ankle brace was more effective in half-squat parachuting landing with the backpack than no-backpack landing.

Keywords: ankle brace, lower-extremity joints, backpack, injury prevention, half-squat parachuting landing

OPEN ACCESS

Edited by:
Zhi-Yong Li,
Southeast University, China

Reviewed by:
Jia Yu,
Soochow University, China
Zhan Liu,
Sichuan University, China

****Correspondence:***
Lizhen Wang
lizhenwang@buaa.edu.cn

Specialty section:
This article was submitted to Biomechanics, a section of the journal Frontiers in Bioengineering and Biotechnology

Received: *07 October 2021*
Accepted: *25 October 2021*
Published: *09 December 2021*

Citation:
Jiang T, Tian S, Chen T, Fan X, Yao J and Wang L (2021) Protection by Ankle Brace for Lower-Extremity Joints in Half-Squat Parachuting Landing With a Backpack. Front. Bioeng. Biotechnol. 9:790595. doi: 10.3389/fbioe.2021.790595

INTRODUCTION

Parachuting landing, one kind of landing with high impact force, was common in military and civil activities. Injuries, such as ankle fracture, ankle sprains, and hip contusions, occurred on lower-extremity joints (i.e., hip, knee, and ankle) due to the high impact force on the lower extremity (Ekeland, 1997; Knapik et al., 2011; Zakowski et al., 2019). Half-squat parachuting landing is one kind of parachuting landing in China, in which the left and right knees and ankles hug each other and the feet are in parallel with the ground (Niu et al., 2010). Injuries on the lower-extremity joints were commonly seen in the half-squat parachuting landing (Li et al., 2013). This study would focus on decreasing injuries of the lower-extremity joints in the half-squat parachuting landing.

An ankle brace was developed to decrease injuries in parachuting landing by restricting the excessive motion of the ankle (Knapik et al., 2008; Knapik and Steelman, 2016; Tamura et al., 2017). It was reported that inversion ankle sprains were decreased by the ankle brace from 0.379% to 0.055%

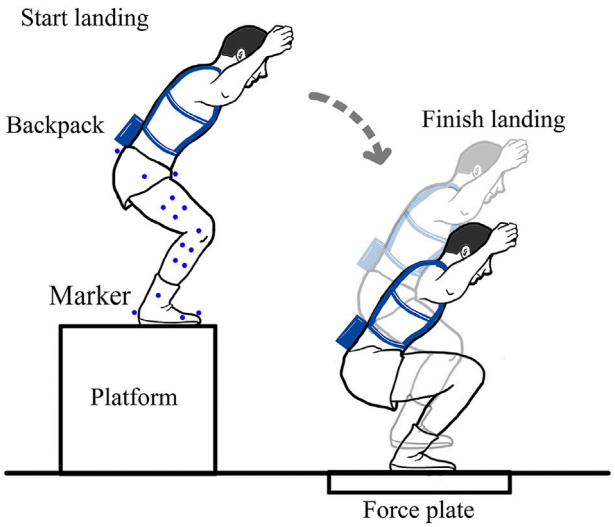

FIGURE 1 | The schedule of the half-squat parachuting landing experiment.

FIGURE 2 | The ankle brace in this study.

(Schmidt et al., 2005). Kinetic and kinematic parameters of the lower-extremity joints, including ground reaction force, joint moment, joint energy absorption, angular displacement, angular velocity, and angular acceleration, were used as indicators in injury evaluation of the lower-extremity joints and the protective effects of ankle brace (Gardner et al., 2012; Tamura et al., 2016; Wu et al., 2018; Sato et al., 2019).

The ankle brace, on one hand, could restrict ankle motion, decrease the angular displacement and the angular velocity of the ankle, and increase stabilization of the ankle in the half-squat parachuting landing (Niu et al., 2011; Wu et al., 2018). However, on the other hand, the ankle brace could also increase the ground reaction force in the half-squat parachuting landing (Niu et al., 2011), which was the negative effect of the ankle brace protection. In the drop landing, the joint moment of the ankle was not significantly influenced with the ankle brace (Zhang et al., 2012; Maeda et al., 2019). The joint energy absorption of the ankle was decreased by the ankle brace (Gardner et al., 2012). The angular displacement of the ankle was also decreased by the ankle brace (Cordova et al., 2010; Zhang et al., 2012; Kuni et al., 2016; Mason-Mackay et al., 2016). However, in the half-squat parachuting landing, the effects of an ankle brace on the joint moment, joint energy absorption, and angular acceleration of the ankle were not clear.

In our previous study, the multi-joint protection for the hip, knee, and ankle in the half-squat parachuting landing was found to be provided by a knee brace, which was another type of protective device (Jiang et al., 2020). For motion of the knee and hip in the drop landing, it was reported that the angular displacement of the knee and the hip was not significantly influenced by the ankle brace in the previous study (Cordova et al., 2010; Agres et al., 2019; Maeda et al., 2019). It was meaningful for protecting the lower-extremity joints if an ankle brace could provide the multi-joint protection for the hip, knee, and ankle. However, in the half-squat parachuting landing, there were few studies on whether an ankle brace could provide the multi-joint protection for the hip, knee, and ankle. This study would analyze kinetics and kinematics of the hip, knee, and ankle in the half-squat parachuting landing to evaluate the protective effects of an ankle brace.

A backpack, containing the necessities for military missions and living, was carried in parachuting landing, which would increase injuries by approximate 160% (Knapik and Steelman, 2016). Ankle sprain and ankle fracture were increased by 71% and 179% by the backpack, respectively (Knapik et al., 2008). In the half-squat parachuting landing with a backpack, there were a few studies about injury evaluation. In the drop landing with a 15 kg backpack, the peak vertical ground reaction force was significantly increased by 0.27 bodyweight (BW) (Sell et al., 2010). It was suggested that a backpack could increase the impact force and injuries of the lower-extremity joints. However, there were few studies about the protective effects of an ankle brace on the hip, knee, and ankle in half-squat parachuting landing with a backpack.

The purpose of this study was to evaluate the protective effects of an ankle brace on lower-extremity joints in half-squat parachuting landing with a backpack by analyzing kinetics and kinematics of the hip, knee, and ankle. Participants would be

recruited for the experiment. The hypothesis was that the ankle brace could protect the lower-extremity joints in the half-squat parachuting landing with the backpack.

MATERIALS AND METHODS

Participants

Seven participants (male; 22.0 ± 3.0 years old; 176.2 ± 4.2 cm height; 67.6 ± 6.2 kg weight; no injury history since 1 year ago) were recruited. The studies involving human participants were reviewed and approved by the Science and Ethics Committee of School of Biological Science and Medical Engineering in Beihang University, China (no. BM201900121). The participants provided their written informed consent to participate in this study.

Equipment

Thirteen passive infrared reflex markers were attached to the bony landmarks of the participant: the left anterior superior iliac spines, the left posterior superior iliac spines, the right anterior superior iliac spines, the right posterior superior iliac spines, the greater trochanter, the lateral knee, the medial knee, the lateral ankle, the medial ankle, the heel, the fifth metatarsal, the second toe, and the first toe, as shown in **Figure 1**. Eight markers were attached to the surface of the thigh and the shank, respectively.

A 5 kg sports vest was regarded as the backpack because the markers on the pelvis could be conveniently attached and traded. The ankle brace in this study was made of terylene, spandex, and elastic fiber, as shown in **Figure 2**. A bar made of aluminum alloy and a spring bar made of no. 72A spring steel were put into two sides of the ankle brace near the lateral ankle and the medial ankle, respectively. The two bars were shaped to be suitable for the anatomic structure of the lateral ankle and the medial ankle, respectively. A soft pad was placed on the bottom of the ankle brace under the heel to improve comfort.

Procedure

The experimental conditions were group 1: no backpack + no brace (without the backpack and without the ankle brace), group 2: backpack + no brace (with the backpack and without the ankle brace), group 3: no backpack+ ankle brace (without the backpack and with the ankle brace), and group 4: backpack+ ankle brace (with the backpack and with the ankle brace). The three-dimensional displacements of the markers were measured by using a three-dimensional motion capture system (VICON, Oxford Metrics, UK) at the sample frequency of 200 Hz. The ground reaction force was measured by using the force plate (900 mm × 600 mm× 100 mm, AMTI, United States) at the sample frequency of 1,600 Hz. All participants had already trained the half-squat parachuting landing technique before trials. Before landing, the participant stood straightly and unbent two arms with the palms toward the body to get the static calibration of the markers. Then, the participant dropped from a 120 cm high platform and landed on the force plate, as shown in **Figure 1**. Each participant performed three trials for each experimental condition.

Data Analysis

A multi-rigid-body model including the pelvis and right lower-extremity was developed based on the static calibration of markers by using the Visual3D software (C-Motion Inc., United States). The center of the hip was estimated based on the markers on the left anterior superior iliac spines, the left posterior superior iliac spines, the right anterior superior iliac spines, the right posterior superior iliac spines, and the greater trochanter. The center of the knee was defined as the middle point between the markers on the lateral and medial knee. The center of the ankle was defined as the middle point between the markers on the lateral and medial ankle.

The angular displacement and the joint moment of the hip, knee, and ankle on sagittal plane and frontal plane were computed by using the Visual3D software. The angular velocity and angular acceleration of the hip, knee, and ankle on sagittal plane and frontal plane were computed based on the angular displacement and the numerical differential formula. The joint energy absorption was computed by integrating the joint moment over the angular displacement. The ground reaction force, the joint moment, and the joint energy absorption were normalized with BW.

The peak vertical ground reaction force and the joint moment, the joint energy absorption, the angular displacement, the angular velocity, and the angular acceleration of the hip, knee, and ankle on sagittal plane and frontal plane were analyzed by using ANOVA by SPSS v19.0 software. The level of significant difference was $p < 0.05$. The study power was analyzed using G*Power based on the data of angular displacement of the knee, assuming an alpha of 0.05. The statistical power (1-beta) was equal to 1.0, larger than 0.8. The Kolmogorov–Smirnov method was used to test that all outcomes conformed to normal distribution. The one-way repeated measures ANOVA was used to test the repeatability of the three trials based on the angular displacement of the hip, knee, and ankle on sagittal plane and the peak ground reaction force in the four experimental groups, and there was a good repeatability of the three trials ($p > 0.05$).

RESULTS

Kinetics

The peak vertical ground reaction force was increased by the backpack from 14.7 ± 2.0 to 16.0 ± 1.6BW ($p = 0.012$), as shown in **Table 1**. The peak vertical ground reaction force was significantly increased from 14.7 ± 2.0 to 16.2 ± 1.9 BW ($p = 0.017$) by the ankle brace in the landing without the backpack. There was a significant difference in the interaction ($p = 0.009$) between the backpack and the ankle brace in the peak vertical ground reaction force.

The joint moment of the hip, knee, and ankle on sagittal plane and frontal plane was not significantly affected ($p > 0.05$) with the backpack as well as the ankle brace, as shown in **Table 1**. There were no significant differences in the interaction ($p > 0.05$) between the backpack and the ankle brace in the joint moment of the hip, knee, and ankle on sagittal plane and frontal plane.

TABLE 1 | The peak vertical ground reaction force, the joint moment, and the joint energy absorption.

		Group 1: no backpack + no brace	Group 2: backpack + no brace	Group 3: no backpack + ankle brace	Group 4: backpack + ankle brace
Peak vertical ground reaction force (BW)[a,b]		14.7 ± 2.0	16.0 ± 1.6	16.2 ± 1.9	15.3 ± 2.0
Joint moment on sagittal plane (BW)	Hip	1.77 ± 0.51	1.67 ± 0.50	1.97 ± 0.42	1.58 ± 0.36
	Knee	0.86 ± 0.27	0.84 ± 0.22	0.89 ± 0.54	0.73 ± 0.18
	Ankle	0.36 ± 0.11	0.31 ± 0.08	0.37 ± 0.11	0.29 ± 0.07
Joint moment on frontal plane (BW)	Hip	0.62 ± 0.18	0.59 ± 0.27	0.69 ± 0.17	0.56 ± 0.18
	Knee	0.31 ± 0.08	0.28 ± 0.13	0.35 ± 0.18	0.24 ± 0.08
	Ankle	0.11 ± 0.08	0.09 ± 0.03	0.11 ± 0.03	0.08 ± 0.03
Joint energy absorption (BW)	Hip[a]	0.11 ± 0.04	0.14 ± 0.05	0.12 ± 0.02	0.13 ± 0.04
	Knee[a]	0.41 ± 0.07	0.49 ± 0.07	0.45 ± 0.19	0.47 ± 0.06
	Ankle[a,b,c]	0.10 ± 0.02	0.11 ± 0.02	0.08 ± 0.03	0.09 ± 0.02

[a]*Significant difference (p < 0.05) between group 1 and group 2.*
[b]*Significant difference (p < 0.05) between group 1 and group 3.*
[c]*Significant difference (p < 0.05) between group 2 and group 4.*

TABLE 2 | The angular displacement, the angular velocity, and the angular acceleration.

		Group 1: no backpack ± no brace	Group 2: backpack + no brace	Group 3: no backpack + ankle brace	Group 4: backpack + ankle brace
Angular displacement on sagittal plane (°)	Hip[a]	52.6 ± 7.2	60.1 ± 8.2	53.6 ± 9.6	65.1 ± 9.1
	Knee[a]	102.1 ± 9.3	110.1 ± 9.3	104.2 ± 17.6	105.3 ± 16.0
	Ankle[a,b]	45.2 ± 7.8	53.8 ± 5.1	36.0 ± 10.9	48.0 ± 5.5
Angular velocity on sagittal plane (°/s)	Hip[a]	438.9 ± 71.4	482.2 ± 54.1	410.0 ± 90.0	483.4 ± 101.3
	Knee[a]	808.9 ± 54.4	855.9 ± 65.3	795.1 ± 78.0	865.0 ± 79.4
	Ankle[a,b]	508.7 ± 105.9	594.0 ± 99.5	332.0 ± 104.2	471.3 ± 110.4
Angular acceleration on sagittal plane (°/s^2)	Hip[a]	8,165.9 ± 1,920.6	9,810.8 ± 1,478.1	7,605.9 ± 2,029.0	10,506.6 ± 1,920.6
	Knee[a]	12,791.7 ± 1,266.5	14,025.1 ± 1,979.6	13,151.5 ± 2,637.2	13,327.7 ± 1,407.1
	Ankle[a,b]	10,813.6 ± 2,179.3	13,099.7 ± 2,280.0	7,764.4 ± 2,542.5	11,077.1 ± 1,703.4
Angular displacement on frontal plane (°)	Hip	6.9 ± 3.3	8.2 ± 3.7	7.6 ± 2.5	8.2 ± 3.8
	Knee	12.5 ± 2.4	14.5 ± 2.3	9.9 ± 2.3	13.0 ± 3.8
	Ankle[b]	13.1 ± 3.6	14.5 ± 4.7	9.4 ± 4.8	11.5 ± 3.5
Angular velocity on frontal plane (°/s)	Hip	67.6 ± 15.8	69.6 ± 17.0	59.8 ± 15.1	72.7 ± 13.9
	Knee	165.5 ± 36.1	181.3 ± 42.4	131.1 ± 40.2	167.3 ± 34.4
	Ankle[b]	159.4 ± 37.5	180.5 ± 56.1	115.9 ± 48.6	151.7 ± 30.1
Angular acceleration on frontal plane (°/s^2)	Hip	2,061.5 ± 636.0	2,182.7 ± 558.1	2,068.1 ± 574.4	2,186.7 ± 511.5
	Knee	5,271.0 ± 1,424.5	5,195.0 ± 1,042.7	5,985.3 ± 1,228.7	5,534.2 ± 1,468.0
	Ankle[b]	3,895.2 ± 792.1	3,997.8 ± 670.6	3,075.4 ± 972.4	3,515.3 ± 738.8

[a]*Significant difference (p < 0.05) between group 1 and group 2.*
[b]*Significant difference (p < 0.05) between group 1 and group 3 and between group 2 and group 4.*

As shown in **Table 1**, the joint energy absorption of the hip, knee, and ankle was increased by the backpack from 0.11 ± 0.04 BW, 0.41 ± 0.07 BW and 0.10 ± 0.02 BW to 0.14 ± 0.05 BW (p = 0.037), 0.49 ± 0.07 BW (p = 0.001) and 0.11 ± 0.02 BW (p = 0.045) respectively. The joint energy absorption of ankle was decreased by the ankle brace from 0.10 ± 0.02 BW to 0.08 ± 0.03 BW (p = 0.037) without the backpack, and was decreased from 0.11 ± 0.02 BW to 0.09 ± 0.02 BW (p < 0.001) with the backpack. There was no significant difference in the interaction (p > 0.05) between the backpack and the ankle brace in the joint energy absorption of the hip, knee, and ankle.

Kinematics

As shown in **Table 2**, the angular displacement of the hip, knee, and ankle on sagittal plane was increased from 52.6 ± 7.2°, 102.1 ± 9.3° and 45.2 ± 7.8° to 60.1 ± 8.2° (p = 0.006), 110.1 ± 9.3° (p = 0.009) and 53.8 ± 5.1° (p < 0.001) respectively by the backpack. The angular displacement of ankle on sagittal plane was decreased from 45.2 ± 7.8° to 36.0 ± 10.9° (p = 0.005) by the ankle brace without the backpack, and was decreased from 53.8 ± 5.1° to 48.0 ± 5.5° (p = 0.001) by the ankle brace with the backpack. There was no significant difference in the interaction (p > 0.05) between the backpack and the ankle brace in the angular displacement of the hip, knee, and ankle on sagittal plane.

As shown in **Table 2**, the angular velocity of the hip, knee, and ankle on sagittal plane was increased from 438.9 ± 71.4°/s, 808.9 ± 54.4°/s, and 508.7 ± 105.9°/s to 482.2 ± 54.1°/s (p = 0.037), 855.9 ± 65.3°/s (p = 0.022), and 594.0 ± 99.5°/s (p = 0.014), respectively, by the backpack. The angular velocity of the ankle on sagittal plane was decreased from 508.7 ± 105.9°/s to 332.0 ± 104.2°/s (p < 0.001) by the ankle brace without the

backpack and was decreased from 594.0 ± 99.5°/s to 471.3 ± 110.4°/s ($p = 0.001$) by the ankle brace with the backpack. There were no significant differences in the interaction ($p > 0.05$) between the backpack and the ankle brace in the angular velocity of the hip, knee, and ankle on sagittal plane.

As shown in **Table 2**, the angular acceleration of the hip, knee, and ankle on sagittal plane was increased from 8,165.9 ± 1,920.6°/s^2, 12,791.7 ± 1,266.5°/s^2, and 10,813.6 ± 2,179.3°/s^2 to 9,810.8 ± 1,478.1°/s^2 ($p = 0.003$), 14,025.1 ± 1,979.6°/s^2 ($p = 0.021$), and 13,099.7 ± 2,280.0°/s^2 ($p = 0.002$), respectively, by the backpack. The angular acceleration of the ankle on sagittal plane was decreased from 10,813.6 ± 2,179.3°/s^2 to 7,764.4 ± 2,542.5°/s^2 ($p < 0.001$) by the ankle brace without the backpack and was decreased from 13,099.7 ± 2,280.0°/s^2 to 11,077.1 ± 1,703.4°/s^2 ($p = 0.002$) by the ankle brace with the backpack. There were no significant differences in the interaction ($p > 0.05$) between the backpack and the ankle brace in the angular acceleration of the hip, knee, and ankle on sagittal plane.

As shown in **Table 2**, the angular displacement of the ankle on frontal plane was decreased from 13.1 ± 3.6° to 9.4 ± 4.8° ($p = 0.017$) by the ankle brace without the backpack and was decreased from 14.5 ± 4.7° to 11.5 ± 3.5° ($p = 0.026$) by the ankle brace with the backpack. There were no significant differences in the interaction ($p > 0.05$) between the backpack and the ankle brace in the angular displacement of the hip, knee, and ankle on frontal plane.

As shown in **Table 2**, the angular velocity of the ankle on frontal plane was decreased from 159.4 ± 37.5°/s to 115.9 ± 48.6°/s ($p = 0.005$) by the ankle brace without the backpack and was decreased from 180.5 ± 56.1°/s to 151.7 ± 30.1°/s ($p = 0.043$) by the ankle brace with the backpack. There were no significant differences in the interaction ($p > 0.05$) between the backpack and the ankle brace in the angular velocity of the hip, knee, and ankle on frontal plane.

As shown in **Table 2**, the angular acceleration of the ankle on frontal plane was decreased from 3,895.2 ± 792.1°/s^2 to 3,075.4 ± 972.4°/s^2 ($p = 0.009$) by the ankle brace without the backpack and was decreased from 3,997.8 ± 670.6°/s^2 to 3,515.3 ± 738.8°/s^2 ($p = 0.032$) by the ankle brace with the backpack. There were no significant differences in the interaction ($p > 0.05$) between the backpack and the ankle brace in the angular acceleration of the hip, knee, and ankle on frontal plane.

DISCUSSION

In this study, kinetic and kinematic parameters of the hip, knee, and ankle were analyzed to evaluate the protective effects of an ankle brace for the lower-extremity joints in the half-squat parachuting landing with a backpack. It was found that the ankle brace could provide more effective protection in the half-squat parachuting landing with the backpack than that without the backpack.

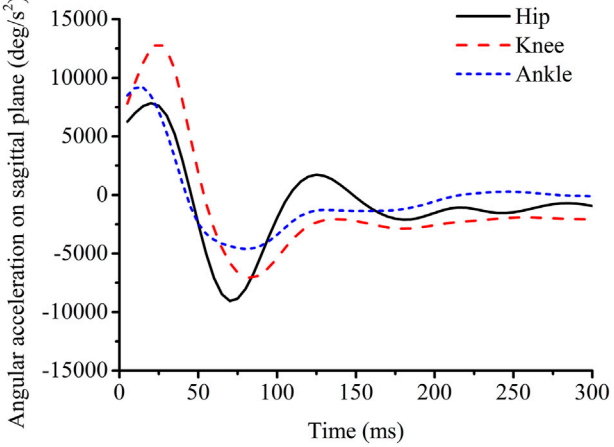

FIGURE 3 | Angular acceleration of the hip, knee, and ankle on sagittal plane.

The Effects of the Backpack

The peak vertical ground reaction force was increased by the backpack, as shown in **Table 1**. The joint energy absorption of the hip, knee, and ankle was significantly increased with the backpack, as shown in **Table 1**. These were because the additional weight and the gravity potential energy of the participant were increased by the backpack. Similar results in the drop landing with the backpack were shown in a previous study, in which the peak vertical ground reaction force was increased, and the increase of the ground reaction force indicated more injuries of the lower extremity (Sell et al., 2010). The higher ground reaction force could induce higher angular acceleration of the hip, knee, and ankle (**Table 2**). Therefore, one purpose of designing an ankle brace was to decrease the ground reaction force. With the backpack, the lower-extremity joints absorbed more impact energy to prevent injuries, which was the instinct of body. The knee absorbed more impact energy than the hip and ankle, which was the same as the results in a previous study (Lee et al., 2018).

The joint moment of the hip, knee, and ankle was not significantly affected by the backpack, as shown in **Table 1**. The angular displacement and the angular velocity of the hip, knee, and ankle on sagittal plane were significantly increased with the backpack, as shown in **Table 2**. A similar outcome was reported that the angular displacement of the knee was increased with the backpack in the drop landing (Sell et al., 2010). The increase of the angular displacement of lower-extremity joints on sagittal plane would decrease the landing stabilization and increase injuries (Wu et al., 2017). With the higher angular velocity, stress on soft tissues of the joints might be increased due to the viscoelasticity of the soft tissues (Jiang et al., 2020). The increase of the angular velocity could increase injuries of the joints. The higher angular acceleration of the knee was also an indicator of the non-contact injury of the anterior cruciate ligament in single-leg drop landing (Tamura et al., 2016). Therefore, designing an ankle brace should decrease angular displacement, angular velocity, and angular acceleration. It

could be found that there were two directions of angular acceleration on sagittal plane: positive direction, which is the same to the direction of angular displacement and angular velocity, and negative direction (**Figure 3**). The positive direction represented that the impact force flexed the joints, while the negative direction represented that lower-extremity joints were counterbalanced by the muscle activation of the lower extremity to keep stability and absorb the impact energy. No significances in the joint moment, angular displacement, angular velocity, and angular acceleration of the hip, knee, and ankle on frontal plane were found with the backpack, as shown in **Tables 1** and **2**. The half-squat parachuting landing posture required that the left and right knees and ankles hugged each other, and the joints' motion on the coronal plane might be restricted.

The Effects of the Ankle Brace

The peak vertical ground reaction force was increased with the ankle brace in the landing without the backpack (**Table 1**), possibly because the joint energy absorption of the lower-extremity joints was significantly decreased with the ankle brace (**Table 1**). Similar results were reported in a previous study that the peak vertical ground reaction force was increased by the ankle brace in the half-squat parachuting landing (Niu et al., 2011). The increase in the ground reaction force could increase injuries, which was the negative effect of the ankle brace because it increased the ground reaction force. The protective effect of the ankle brace could be decreased. However, the negative effect of the ankle brace was lost in the half-squat parachuting landing with the backpack. With the backpack, the ground reaction force was not significantly influenced by the ankle brace (**Table 1**). The reason might be that the impact energy was absorbed by other joint motions of the body such as trunk flexion, except for the lower-extremity joint motion in the landing with the backpack. It could be suggested that the ankle brace could provide better protection in the half-squat parachuting landing with the backpack than without the backpack. For the half-squat parachuting landing in military area, a backpack was commonly carried. It was meaningful to use an ankle brace in the half-squat parachuting landing especially with a backpack.

The joint moments of the hip, knee, and ankle were not significantly influenced by the ankle brace in the landing both without and with the backpack. This outcome was similar to that in the drop landing (Zhang et al., 2012). The angular displacement, the angular velocity, and the angular acceleration of the ankle on sagittal plane were decreased with the ankle brace in the landing both without and with the backpack, as shown in **Table 2**. The outcomes in this study were satisfactory for protection. The ankle brace could still restrict ankle motion and provide protective effects for the ankle without the backpack, even though there was as negative effect that the ankle brace increased the ground reaction force without the backpack as shown in **Table 1**. The angular displacements and the angular velocities of the hip and knee on sagittal plane were not significantly influenced with the ankle brace, as shown in **Table 2**. A similar outcome was reported that the ankle brace did not significantly influence the angular displacement of the hip on sagittal plane in the drop landing (Cordova et al., 2010). One plausible reason was that the ankle brace did not restrict the angular displacement and the angular velocity of the ankle sufficiently enough to significantly influence the angular displacement and the angular velocity of the hip and knee (Simpson et al., 2013).

The motion of the ankle on frontal plane was another factor of ankle sprain injury (Niu et al., 2011). Injuries of the ankle could be induced by greater angular displacement and angular velocity of the ankle on frontal plane (Bhaskaran et al., 2015; Sinsurin et al., 2017; Hanzlikova et al., 2019). Ankle sprain would be prevented by the decrease in the angular displacement of the ankle on frontal plane (Klem et al., 2017). The angular displacement, the angular velocity, and the angular acceleration of the ankle on frontal plane were decreased by the ankle brace, as shown in **Table 2**. The ankle motion on frontal plane was restricted by the ankle brace, which would even benefit users whose ligaments on the ankle have been injured before (Choisne et al., 2019).

Multi-Joint Protection

In this study, the ankle brace did not significantly influence the ground reaction force with the backpack but increased the ground reaction force without the backpack. In our previous study, the multi-joint protection of a knee brace for the hip, knee, and ankle was provided in the half-squat parachuting landing without the backpack, but the knee brace could only protect the knee in the half-squat parachuting landing with the backpack (Jiang et al., 2020). Different from the knee brace, the ankle brace could not provide multi-joint protection because the ankle brace could only protect the ankle in the half-squat parachuting landing both without and with the backpack. However, it was not suggested that the ankle brace was useless. In the real-life half-squat parachuting landing, paratroopers commonly carried heavy backpacks. The injury risk of the ankle was 36%, higher than that of the knee (18%) (Ekeland, 1997). The knee brace could not protect the ankle in the half-squat parachuting landing with the backpack. Therefore, the ankle brace was necessary for ankle protection.

Limitations

One limitation of this study was that the sample size of the participants was limited due to the cost. Each participant performed three trials to enlarge the sample size. The G*Power software was used to analyze the study power of the sample size. Only male participants were recruited in this experiment because the injury risk of male paratroopers was higher than that of females (Fer et al., 2021). Another limitation was that the experimental design could not fully simulate the real-life half-squat parachuting landing. The backpack load was lighter than the real weight due to safety. Besides, it was hard to use the real backpack, which would shade markers on the pelvis, and there were few experimental studies on the real backpack. Even with these limitations, we still found a trend that the backpack

affected the kinematic and kinetic parameters of the hip, knee, and ankle.

CONCLUSION

The ankle brace could restrict ankle motion and protect the ankle in the half-squat parachuting landing both without and with the backpack. The ankle brace significantly increased the ground reaction force, which thus decreased the protective effects of the ankle brace. The ankle brace did not significantly increase the ground reaction force but could still maintain the protective effects with a backpack. The ankle brace could provide more effective protection for the lower-extremity joints in the half-squat parachuting landing with a backpack than no-backpack landing.

DATA AVAILABILITY STATEMENT

The original contributions presented in the study are included in the article/Supplementary Material; further inquiries can be directed to the corresponding author.

ETHICS STATEMENT

The studies involving human participants were reviewed and approved by the Science and Ethics Committee of School of Biological Science and Medical Engineering in Beihang University, China. The patients/participants provided their written informed consent to participate in this study.

AUTHOR CONTRIBUTIONS

TJ, TC, JY, and LW contributed to the conception and design of the study and performed the experiment and the statistical analysis. TJ, ST, XF, and LW wrote sections of the manuscript. All authors contributed to the article and approved the submitted version.

FUNDING

This work was supported by the National Natural Science Foundation of China (11822201) and 111 Project (B13003).

REFERENCES

Agres, A. N., Chrysanthou, M., and Raffalt, P. C. (2019). The Effect of Ankle Bracing on Kinematics in Simulated Sprain and Drop Landings: A Double-Blind, Placebo-Controlled Study. *Am. J. Sports Med.* 47 (6), 1480–1487. doi:10.1177/0363546519837695

Bhaskaran, D., Wortley, M., Chen, Q., Milner, C. E., Fitzhugh, E. C., and Zhang, S. (2015). Effect of a Combined Inversion and Plantarflexion Surface on Ankle Kinematics and EMG Activities in landing. *J. Sport Health Sci.* 4 (4), 377–383. doi:10.1016/j.jshs.2014.10.005

Choisne, J., McNally, A., Hoch, M. C., and Ringleb, S. I. (2019). Effect of Simulated Joint Instability and Bracing on Ankle and Subtalar Joint Flexibility. *J. Biomech.* 82, 234–243. doi:10.1016/j.jbiomech.2018.10.033

Cordova, M. L., Takahashi, Y., Kress, G. M., Brucker, J. B., and Finch, A. E. (2010). Influence of External Ankle Support on Lower Extremity Joint Mechanics during Drop Landings. *J. Sport Rehabil.* 19 (2), 136–148. doi:10.1123/jsr.19.2.136

Ekeland, A. (1997). Injuries in Military Parachuting: a Prospective Study of 4499 Jumps. *Injury* 28 (3), 219–222. doi:10.1016/s0020-1383(96)00185-4

Fer, C., Guiavarch, M., and Edouard, P. (2021). Epidemiology of Skydiving-Related Deaths and Injuries: a 10-years Prospective Study of 6.2 Million Jumps between 2010 and 2019 in France. *J. Sci. Med. Sport* 24 (5), 448–453. doi:10.1016/j.jsams.2020.11.002

Gardner, J. K., McCaw, S. T., Laudner, K. G., Smith, P. J., and Stafford, L. N. (2012). Effect of Ankle Braces on Lower Extremity Joint Energetics in Single-Leg Landings. *Med. Sci. Sports Exerc.* 44 (6), 1116–1122. doi:10.1249/mss.0b013e318240d564

Hanzlíková, I., Richards, J., Hébert-Losier, K., and Smékal, D. (2019). The Effect of Proprioceptive Knee Bracing on Knee Stability after Anterior Cruciate Ligament Reconstruction. *Gait & Posture* 67, 242–247. doi:10.1016/j.gaitpost.2018.10.026

Jiang, T., Tian, S., Fan, X., Chen, T., Luo, C., Yao, J., et al. (2020). Kinematics and Kinetics of Lower-Extremity Joints in Parachuting landing with Backpack and Knee Brace. *Med. Eng. Phys.* 86, 1–7. doi:10.1016/j.medengphy.2020.10.009

Klem, N.-R., Wild, C. Y., Williams, S. A., and Ng, L. (2017). Effect of External Ankle Support on Ankle and Knee Biomechanics during the Cutting Maneuver in Basketball Players. *Am. J. Sports Med.* 45 (3), 685–691. doi:10.1177/0363546516673988

Knapik, J. J., Darakjy, S., Swedler, D., Amoroso, P., and Jones, B. H. (2008). Parachute Ankle Brace and Extrinsic Injury Risk Factors during Parachuting. *Aviat Space Environ. Med.* 79 (4), 408–415. doi:10.3357/asem.2218.2008

Knapik, J. J., Steelman, R., Grier, T., Graham, B., Hoedebecke, K., Rankin, S., et al. (2011). Military Parachuting Injuries, Associated Events, and Injury Risk Factors. *Aviat Space Environ. Med.* 82 (8), 797–804. doi:10.3357/asem.3061.2011

Knapik, J., and Steelman, R. (2016). Risk Factors for Injuries during Military Static-Line Airborne Operations: a Systematic Review and Meta-Analysis. *J. Athletic Train.* 51 (11), 962–980. doi:10.4085/1062-6050-51.9.10

Kuni, B., Mussler, J., Kalkum, E., Schmitt, H., and Wolf, S. I. (2016). Effect of Kinesiotaping, Non-elastic Taping and Bracing on Segmental Foot Kinematics during Drop landing in Healthy Subjects and Subjects with Chronic Ankle Instability. *Physiotherapy* 102 (3), 287–293. doi:10.1016/j.physio.2015.07.004

Lee, J., Song, Y., and Shin, C. S. (2018). Effect of the Sagittal Ankle Angle at Initial Contact on Energy Dissipation in the Lower Extremity Joints during a Single-Leg landing. *Gait & Posture* 62, 99–104. doi:10.1016/j.gaitpost.2018.03.019

Li, Y., Wu, J., Zheng, C., Huang, R. R., Na, Y., Yang, F., et al. (2013). The Effect of landing Surface on the Plantar Kinetics of Chinese Paratroopers Using Half-Squat landing. *J. Sports Sci. Med.* 12 (3), 409–413.

Maeda, N., Urabe, Y., Sasadai, J., Numano, S., Fujishita, H., Morikawa, M., et al. (2019). Effect of Soft and Semi-rigid Ankle Braces on Kinematic and Kinetic Changes of the Knee and Ankle Joints after Forward and Lateral Drop landing in Healthy Young Women. *Isokinetics Exerc. Sci.* 27, 219–225. doi:10.3233/ies-192150

Mason-Mackay, A. R., Whatman, C., Reid, D., and Lorimer, A. (2016). The Effect of Ankle Bracing on landing Biomechanics in Female Netballers. *Phys. Ther. Sport* 20, 13–18. doi:10.1016/j.ptsp.2015.11.002

Niu, W., Wang, Y., He, Y., Fan, Y., and Zhao, Q. (2010). Biomechanical Gender Differences of the Ankle Joint during Simulated Half-Squat parachute landing. *Aviat Space Environ. Med.* 81 (8), 761–767. doi:10.3357/asem.2725.2010

Niu, W., Wang, Y., Yao, J., Zhang, M., Fan, Y., and Zhao, Q. (2011). Consideration of Gender Differences in Ankle Stabilizer Selection for Half-Squat parachute landing. *Aviat Space Environ. Med.* 82 (12), 1118–1124. doi:10.3357/asem.3128.2011

Sato, N., Nunome, H., Hopper, L. S., and Ikegami, Y. (2019). Ankle Taping Can Reduce External Ankle Joint Moments during Drop Landings on a Tilted Surface. *Sports Biomech.* 18 (1), 28–38. doi:10.1080/14763141.2017.1375552

Schmidt, M. D., Sulsky, S., and Amoroso, P. (2005). Effectiveness of an Outside-The-Boot Ankle Brace in Reducing Parachuting Related Ankle Injuries. *Inj. Prev.* 11 (3), 163–168. doi:10.1136/ip.2004.006304

Sell, T. C., Chu, Y., Abt, J. P., Nagai, T., Deluzio, J., Mcgrail, M. A., et al. (2010). Minimal Additional Weight of Combat Equipment Alters Air Assault Soldiers' landing Biomechanics. *Mil. Med.* 175 (1), 41–47. doi:10.7205/milmed-d-09-00066

Simpson, K. J., Yom, J. P., Fu, Y.-C., Arnett, S. W., O'Rourke, S., and Brown, C. N. (2013). Does Wearing a Prophylactic Ankle Brace during Drop Landings Affect Lower Extremity Kinematics and Ground Reaction Forces? *J. Appl. Biomech.* 29 (2), 205–213. doi:10.1123/jab.29.2.205

Sinsurin, K., Srisangboriboon, S., and Vachalathiti, R. (2017). Side-to-side Differences in Lower Extremity Biomechanics during Multi-Directional Jump landing in Volleyball Athletes. *Eur. J. Sport Sci.* 17 (6), 699–709. doi:10.1080/17461391.2017.1308560

Tamura, A., Akasaka, K., Otsudo, T., Sawada, Y., Okubo, Y., Shiozawa, J., et al. (2016). Fatigue Alters Landing Shock Attenuation during a Single-Leg Vertical Drop Jump. *Orthop. J. Sports Med.* 4 (1), 2325967115626412. doi:10.1177/2325967115626412

Tamura, K., Radzak, K. N., Vogelpohl, R. E., Wisthoff, B. A., Oba, Y., Hetzler, R. K., et al. (2017). The Effects of Ankle Braces and Taping on Lower Extremity Running Kinematics and Energy Expenditure in Healthy, Non-injured Adults. *Gait & Posture* 58, 108–114. doi:10.1016/j.gaitpost.2017.07.041

Wu, D., Zheng, C., Wu, J., Hu, T., Huang, R., Wang, L., et al. (2018). Prophylactic Ankle Braces and the Kinematics and Kinetics of Half-Squat parachute landing. *Aerospace Med. Hum. Perform.* 89 (2), 141–146. doi:10.3357/amhp.4950.2018

Wu, D., Zheng, C., Wu, J., Wang, L., Wei, X., and Wang, L. (2017). Protective Knee Braces and the Biomechanics of the Half-Squat Parachuting landing. *Aerospace Med. Hum. Perform.* 88 (12), 1–6. doi:10.3357/amhp.4872.2017

Zakowski, B., Wagner, I., and Domzalski, M. (2019). Analysis of a Military Parachutist Injury - A Retrospective Review of over 37,000 Landings‡. *Mil. Med.* 184 (1-2), e261–e265. doi:10.1093/milmed/usy315

Zhang, S., Wortley, M., Silvernail, J. F., Carson, D., and Paquette, M. R. (2012). Do ankle Braces Provide Similar Effects on Ankle Biomechanical Variables in Subjects with and without Chronic Ankle Instability during landing? *J. Sport Health Sci.* 1 (2), 114–120. doi:10.1016/j.jshs.2012.07.002

Conflict of Interest: The authors declare that the research was conducted in the absence of any commercial or financial relationships that could be construed as a potential conflict of interest.

Publisher's Note: All claims expressed in this article are solely those of the authors and do not necessarily represent those of their affiliated organizations, or those of the publisher, the editors, and the reviewers. Any product that may be evaluated in this article, or claim that may be made by its manufacturer, is not guaranteed or endorsed by the publisher.

frontiers in Bioengineering and Biotechnology

ORIGINAL RESEARCH
published: 20 December 2021
doi: 10.3389/fbioe.2021.791238

The Influence of Heel Height on Strain Variation of Plantar Fascia During High Heel Shoes Walking-Combined Musculoskeletal Modeling and Finite Element Analysis

Meizi Wang[1,2], *Shudong Li*[2], *Ee-Chon Teo*[3]*, *Gusztáv Fekete*[4] *and Yaodong Gu*[1]*

[1]Faculty of Sports Science, Ningbo University, Ningbo, China, [2]Faculty of Health and Safety, Óbuda University, Budapest, Hungary, [3]School of Mechanical and Aerospace Engineering, Nanyang Technological University, Singapore, Singapore, [4]Savaria Institute of Technology, Eötvös Loránd University, Budapest, Hungary

OPEN ACCESS

Edited by:
Ching-Chi Hsu,
National Taiwan University of Science and Technology, Taiwan

Reviewed by:
Zimi Sawacha,
University of Padua, Italy
Panagiotis Chatzistergos,
Staffordshire University, United Kingdom

***Correspondence:**
Ee-Chon Teo
eechon-teo@e.ntu.edu.sg
Yaodong Gu
guyaodong@hotmail.com

Specialty section:
This article was submitted to Biomechanics, a section of the journal Frontiers in Bioengineering and Biotechnology

Received: 08 October 2021
Accepted: 26 November 2021
Published: 20 December 2021

Citation:
Wang M, Li S, Teo E-C, Fekete G and Gu Y (2021) The Influence of Heel Height on Strain Variation of Plantar Fascia During High Heel Shoes Walking-Combined Musculoskeletal Modeling and Finite Element Analysis. Front. Bioeng. Biotechnol. 9:791238. doi: 10.3389/fbioe.2021.791238

The therapeutic benefit of high heel shoes (HHS) for plantar fasciitis treatment is controversial. It has been suggested that plantar fascia strain can be decreased by heel elevation of shoes which helps in body weight redistribution throughout the length of the foot. Yet it is a fact that the repetitive tension caused by HHS wearing resulting in plantar fasciitis is a high-risk disease in HHS individuals who suffer heel and plantar pain. To explore the biomechanical function on plantar fascia under HHS conditions, in this study, musculoskeletal modeling (MsM) and finite element method (FEM) were used to investigate the effect of heel height on strain distribution of plantar fascia. Three-dimensional (3D) and one-dimensional (1D) finite element models of plantar fascia were generated to analyze the computed strain variation in 3-, 5-, and 7-cm heel heights. For validation, the computed foot contact pressure was compared with experimental measurement, and the strain value on 1D fascia was compared with previous studies. Results showed that the peak strain of plantar fascia was progressively increased on both 3D and 1D plantar fascia as heel elevated from 3 to 7 cm, and the maximum strain of plantar fascia occurs near the heel pain site at second peak stance. The 3D fascia model predicted a higher strain magnitude than that of 1D and provided a more reliable strain distribution on the plantar fascia. It is concluded that HHS with narrow heel support could pose a high risk on plantar fasciitis development, rather than reducing symptoms. Therefore, the heel elevation as a treatment recommendation for plantar fasciitis is questionable. Further studies of different heel support structures of shoes to quantify the effectiveness of heel elevation on the load-bearing mechanism of plantar fascia are recommended.

Keywords: high heel shoes, finite element model, musculoskeletal modeling, plantar fascia, plantar fasciitis

1 INTRODUCTION

The plantar fascia is a rather complex and important structure, which has different biomechanical functions in gait, such as supporting transverse and longitudinal arch, facilitating force transmission between foot and ground, balancing weight-bearing distribution on foot, cushioning ground reaction force, and preventing the foot from injury (D'Ambrogi et al., 2003; Wearing et al., 2007; Mahowald

et al., 2011; Stecco et al., 2013; Chen et al., 2015). However, any injury of plantar fascia inevitably affects the biomechanical function of the foot. In the United States, approximately two million people experience symptoms of heel and plantar pain due to plantar fascia injury yearly (Chen et al., 2015). Known as plantar fasciitis, it is caused by excessive repetitive loading of the plantar fascia leading to microtears and inflammation of the calcaneal adhesions (Luffy et al., 2018; Trojian and Tucker, 2019), and it is a common complaint among women, especially those wearing high heel shoes (HHS) regularly (López-López et al., 2018).

It is evidence that wearing HHS adversely affects the musculoskeletal system, altering ankle–foot complex function, changing the force transmission pattern of muscle tendon, and interfering in load distribution of the foot (Di Sipio et al., 2018; Wiedemeijer and Otten, 2018; Wan et al., 2019). The length of the calcaneus to metatarsals is shortened, accompanied by arch rising under HHS conditions, leading to a change in arch morphology, transferring a greater portion of weight-bearing to the forefoot, and reducing the plantar contact area of the midfoot, leading to increased contraction and tension force on the plantar fascia (Sun et al., 2017). Khodair and Younes investigated the relationship between the plantar fascial pathology and HHS wearing in 40 female patients with resulting heel pain; they reported that 30 patients had fascial edema at calcaneal insertion and the plantar fascia thickened; the signal intensity in plantar fascia increased in 21 patients, which are characteristic signals of plantar fasciitis (Khodair and Younes, 2019).

On the contrary, there are different opinions about the effect of HHS on plantar fascia strain. Some investigators have suggested that the appropriate heel elevation was beneficial in the treatment of plantar fasciitis on account of the plantar fascia tension could be temporarily reduced by heel raising (Kogler et al., 2001; Marshall, 1988). It was believed that the angle discrepancy between the hindfoot and metatarsus decreased under HHS, which allowed more movement of the forefoot in the plantar-flexion position and reduced the fascia tension (Kogler et al., 2001). Recently, Yu et al. investigated the influence of heel height on strain stress on the plantar fascia using finite element method (FEM); its total tension force was reduced by 77.3% as heel height rose from 0 to 5.08 cm during balanced standing (Yu et al., 2016). However, the plantar fascia in this research was simply represented by the 1D linear truss element, which may overestimate its elastic modulus resulting in an inaccurate plantar fascia strain (Erdemir et al., 2004; Chen et al., 2015).

Accordingly, to address the controversial views of tension force in plantar fascia as the main crucial biomechanical concern in foot pathology in the HHS population to further understand the influence of the heel height on plantar fascia tension, a solid 3D plantar fascia modeling is established. In this study, the effects of HHS of three different heel heights (3, 5, 7 cm) on the strain–stress variation of 3D plantar fascia were observed by using a combination of FEM and musculoskeletal modeling. A comparison of 3D and 1D digitization of the plantar fascia, with 1D of plantar fascia created by linear truss elements that simply connect the heel and five proximal phalanxes, was carried out.

2 METHODS

In this study, a healthy female (age: 26 years old; height: 165 cm; weight: 53 kg) with no sign of musculoskeletal pathology and lower-limb injury was recruited. For data acquisition, gait capturing 3D motions of the subject wearing HHS in three different heel heights (3, 5, 7 cm) and each gait corresponding relevant muscle forces and strain distribution in plantar fascia were computed using musculoskeletal modeling (MsM) and FEM, respectively.

The protocol was approved by Ningbo University following the declaration of the ethical committee. The subject has informed all contents regarding the test with written consent before the experiment. The workflow of the study is shown in **Figure 1**.

2.1 Gait Analysis

The gait analysis was used to drive MsM and FEM. A Vicon motion capture system (Oxford Metrics Ltd., Oxford, UK) consisting of eight cameras and two AMTI force platforms (Watertown, MA, USA) was utilized to capture the kinematic and kinetic lower extremities during HHS gait. The kinematic and kinetic data were measured synchronously at frequencies of 100 and 1,000 Hz, respectively. The marker set was placed on the subject's various lower-extremity key points according to generic GaitModel 2,392 in Opensim. One static standing trial and six successful waking trials were captured on each heel height condition. For walking trail data acquisition, the subject walked through the motion capture area in a straight direction at their self-pace with both feet stepping entirely at the force platforms. The captured representative data of six trials of each heel height were selected for MsM analysis.

2.2 MsM Analysis

To calculate the relevant muscle forces in the lower limbs, GaitModel 2,392 as a generic MsM was selected in Opensim. GaitModel 2,392 has 10 main rigid body segments, 23 degrees of freedom, and 92 musculotendon actuators to represent 76 muscles in the lower limbs and torso (Kainz et al., 2016). Three major extrinsic muscle groups of lower extremities—gastrocnemius (GC), soleus (SL), and tibialis anterior (TA)—for foot movement were digitized. GC and SL play important roles in ankle plantar flexor, and TA produces major dorsiflexion moment to the ankle during gait (Hwang et al., 2006).

The kinematic data and ground reaction force (GRF) in 3-, 5-, and 7-cm heel height conditions were converted into Opensim from the V3D to calculate the muscle forces. A three-step process was performed in Opensim: firstly, the selected MsM was scaled to accommodate the height and mass of the test subject with adjusting muscle attachments and length. Then, the kinematic data was loaded into the Opensim gait model. Secondly, the residual reduction algorithm was applied to match the coordinates of the model more dynamically consistent with the measured GRF and movement which drive the generalized coordination of the dynamic musculoskeletal model toward the desired kinematic trajectory. Finally, the computed muscle

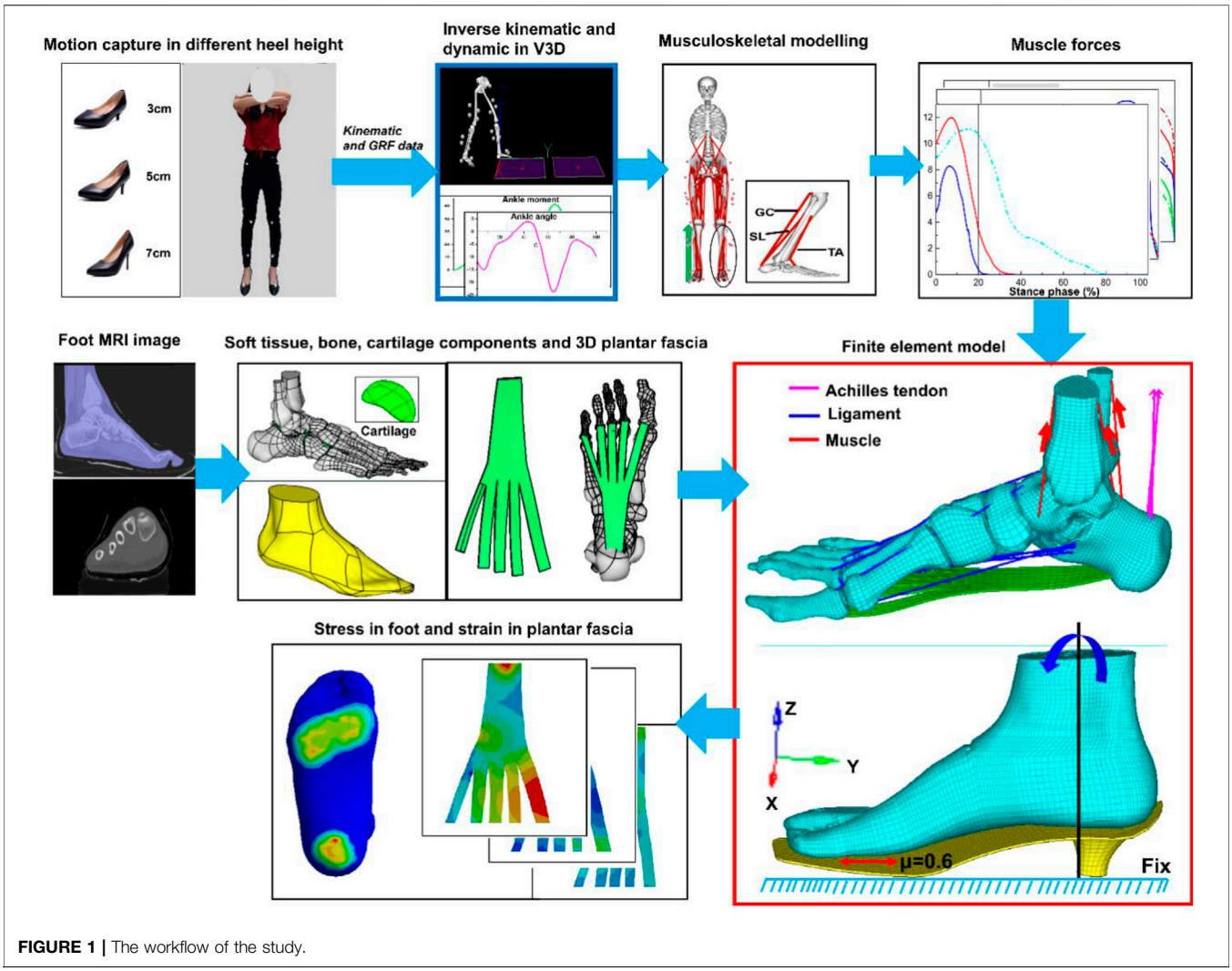

FIGURE 1 | The workflow of the study.

control algorithm was applied to calculate muscle activations and muscle forces in three heel height conditions. These peak muscle forces obtained from Opensim were validated against electromyography (EMG) data acquired from the previous studies (**Figure 2**) (Hwang et al., 2006; Son et al., 2008), and these validated muscle forces were assigned as boundary and loading conditions for the FEM analysis.

2.3 FEM Analysis

2.3.1 Model Construction and Material Property

MRI scan was performed on one subject using a 3.0-T Siemens MRI system; the foot ankle was fixed at a neutral position using a brace during the CT scan, and the images of the sagittal and coronal plane were collected (repetition time: 4.11 s; slice thickness: 1 mm; and matrix: 320 × 260). The geometrical shapes of the right foot model were segmented based on magnetic resonance images of the participant using Mimics 18.0 (Materialise, Leuven, Belgium). The 28 anatomical segmented bones and one encapsulated soft tissue together with cartilages were generated based on areas of two adjacent segmented bones using SolidWorks (SolidWorks Corporation, MA, USA) to create the solid model. The muscles and 1D plantar fascia were created in Hypermesh. Three muscle groups GC, TA, and SL and 20 ligaments and Achilles tendon together with the plantar fascia connecting the corresponding points between the calcaneal tubercle and five proximal phalanges were modeled as 1D linear truss elements. The 1D plantar fascia and ligament elements were given a cross-sectional area to present strain response. For the 3D plantar fascia, a thickness of 2 mm was generated in SolidWorks according to the anatomical atlas (Hedrick, 1996). The FEM of HHS based on the subject's shoe size (37 EU size) of 3-, 5-, and 7-cm heel height shoes were generated in SolidWorks, respectively. **Table 1** shows the material property of shoes, bone, muscle, plantar fascia, cartilage, ligament, Achilles tendon, and encapsulated soft tissue, as previously reported (Lemmon et al., 1997; Pailler-Mattei et al., 2008; Siegler et al., 1988; Gu et al., 2010a). All elements were idealized as linearly elastic materials, except that the encapsulated soft tissue was defined as hyperelastic material properties (Gu et al., 2010b).

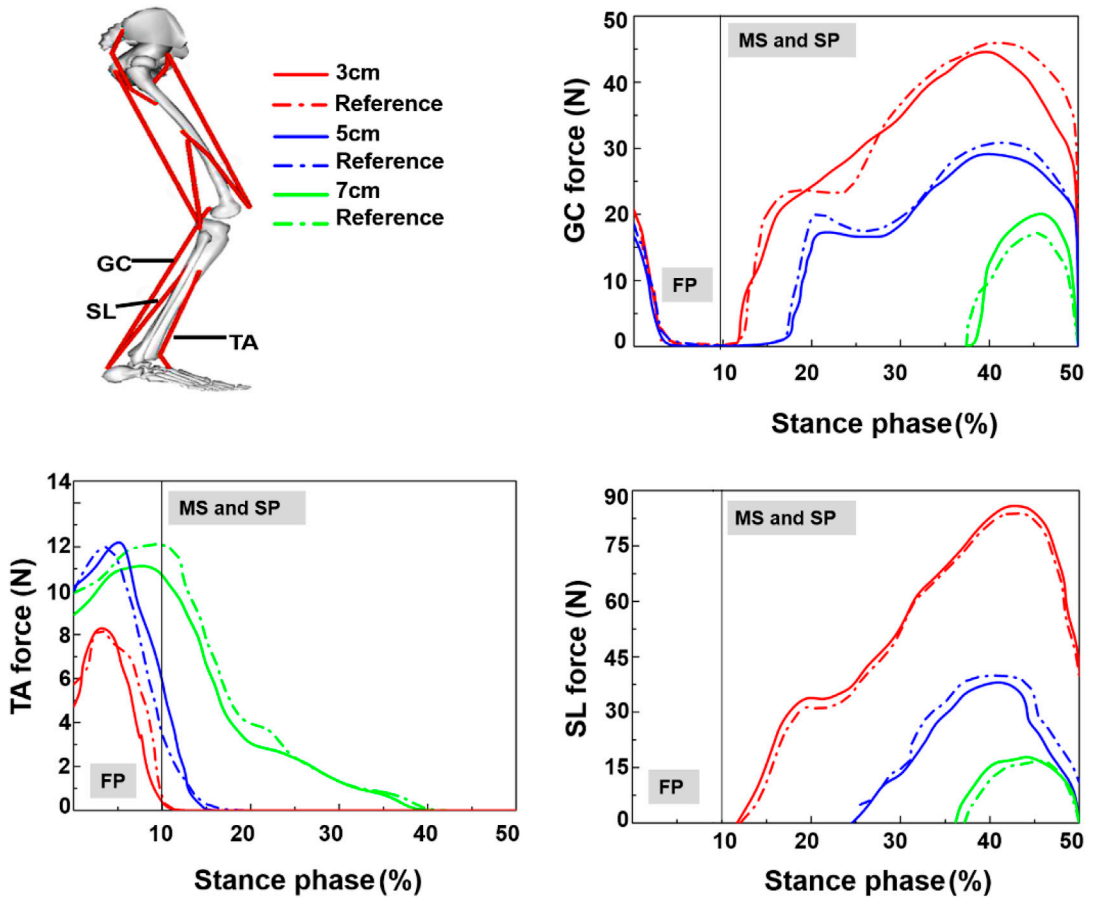

FIGURE 2 | Muscle force in stance phase, TA = tibialis anterior; GC = gastrocnemius; SL = soleus; FP = first peak; MS = mid-standing; SP = second peak (Hwang et al., 2006; Son et al., 2008).

TABLE 1 | Material properties of the components in the finite element model.

	Elastic modules (MPa)	Poisson ratio	Cross section (mm^2)	Mass density ρ (kg/m^3)
Bulk soft tissue	Second-order polynomial strain hyperelastic model (C_{10} = 0.8556, C_{01} = 0.05841, C_{20} = 0.03900, C_{11} = 0.02319, C_{02} = 0.00851, D_1 = 3.65273)		—	
Bone	7,300	0.30	—	1,500
Sole	200,000	0.42	—	7,800
Ligaments	260	—	18.4	-
Cartilage	1	0.40	—	1,050
3D plantar fascia	350	0.45	—	—
1D plantar fascia	350	—	58.6	—

2.3.2 Boundary and Loading Condition

The loading condition during walking in FEM simulation was determined from experimental data of the participant. Three instants [the GRF first peak (25% stance phase), the GRF valley (45% stance phase), and the GRF second peak (60% stance phase)] of the stance phase were used to drive the foot model.

The generated foot solid model comprised of the foot bony components and 3D plastic fascia embedded in the encapsulated soft tissue. Prior to the simulation runs, with the sole of shoes fully restrained, the foot model was placed as heel strike position with an angle between the plantar and sole set at 20°, which was the angle acquired in experimental data between the sole of the shoe and the ground. With the tibia set as the axis of rotation defined by the load joint option in Ansys (ANSYS, Inc., Canonsburg, PA, USA), an inclination angle of the tibia relative to the ground of 0° was set as the initial first peak stance condition. The tibia was further rotated about the *X*-axis from 0° to 25° relative to the vertical ground axis

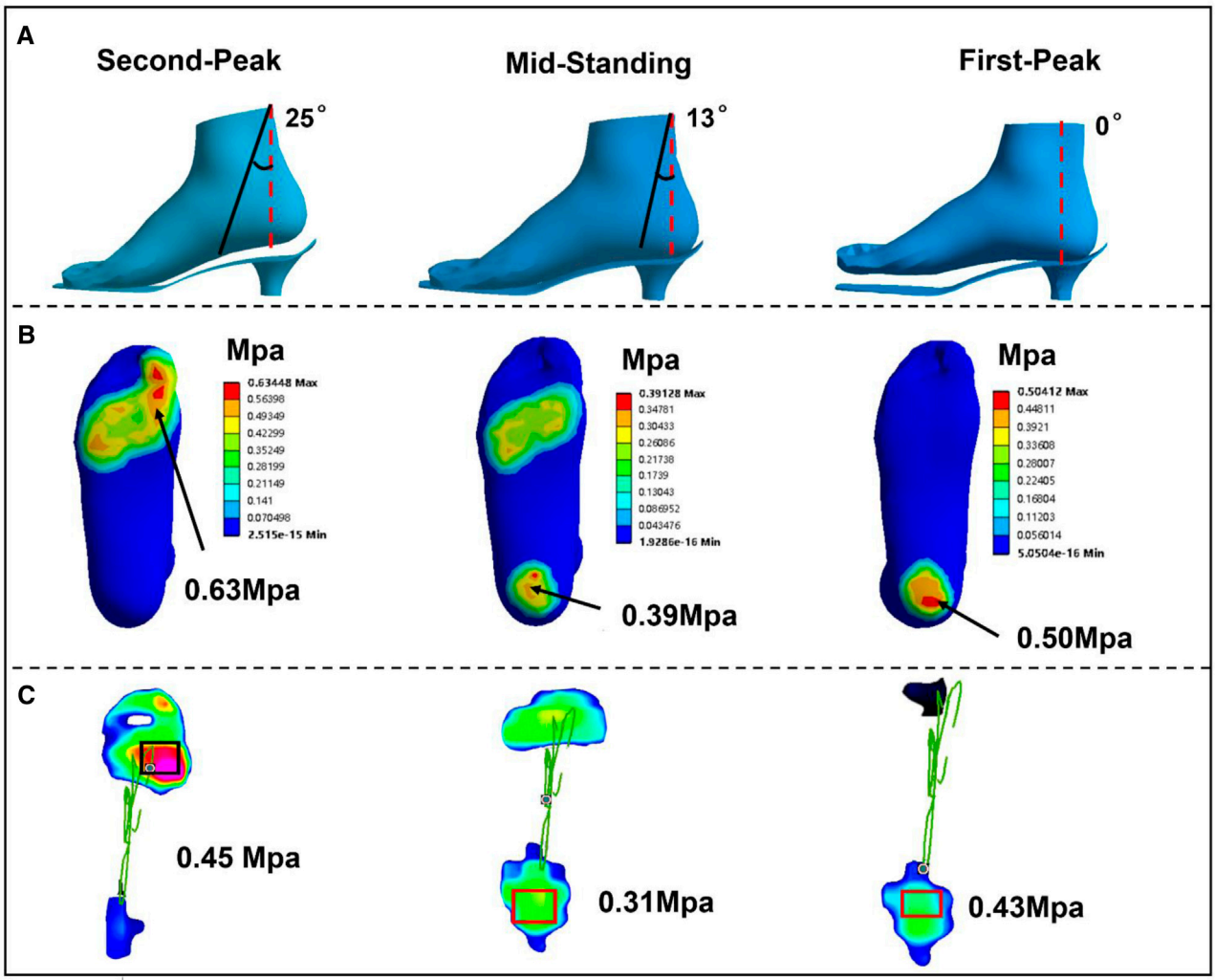

FIGURE 3 | (A) The different stance phase of the foot relative to the sole of shoes during simulation in 3-cm heel height. **(B)** FEM predicted. **(C)** Plantar contact pressure in experimental measurement.

(**Figure 3A**) to define the mid-standing stance and second-peak stance conditions, and the rotation moment function described by ankle moment in the sagittal plane. In the analysis, the foot FEM model translation and rotation in coronal and transverse planes were not considered. For the surface between the sole and the forefoot, a friction coefficient of 0.6 was defined (Yu et al., 2013), and the respective GC, SL, and TA force acquired from the MsM (**Figure 2**) at three stances were applied, with Achilles tendon forces obtained from previous research applied (Yu et al., 2013). The Transient Solver was selected in Ansys to avoid convergence problems.

2.3.3 Geometry Mesh

The foot model was predominately meshed with hexahedral elements with less than 5% of tetrahedral elements in Hypermesh (14.0). The irregular bony and soft tissue parts were sectioned and re-meshed manually to improve the quality of the mesh with an aspect ratio of 3D element close to 1 and Jacobi ratio of 0.6 (Li et al., 2017). Simple loading and boundary conditions were applied to investigate the mesh sensitivity of the whole foot structure based on computed results of the soft tissue, bony component, location of plantar in the soft tissue, anterior and posterior ends of the plantar fascia, and the connection region between bones and cartilages in Ansys. The element sizes were gradually reduced until the variation of force displacement is less than 3% between the two size meshes (Li et al., 2017), with the final model consisting of 279,037 elements.

2.3.4 FEM Validation

The validation was conducted by comparing the plantar pressure of the experimental measurements and FEM predictions in the three different stance phases of three different heel height conditions. Firstly, the plantar pressure was measured by an in-shoe system (Novel Pedar-X System, Novel GmbH, Munich, Germany, www.novel.de) during the HHS gait in each heel height condition with each corresponding

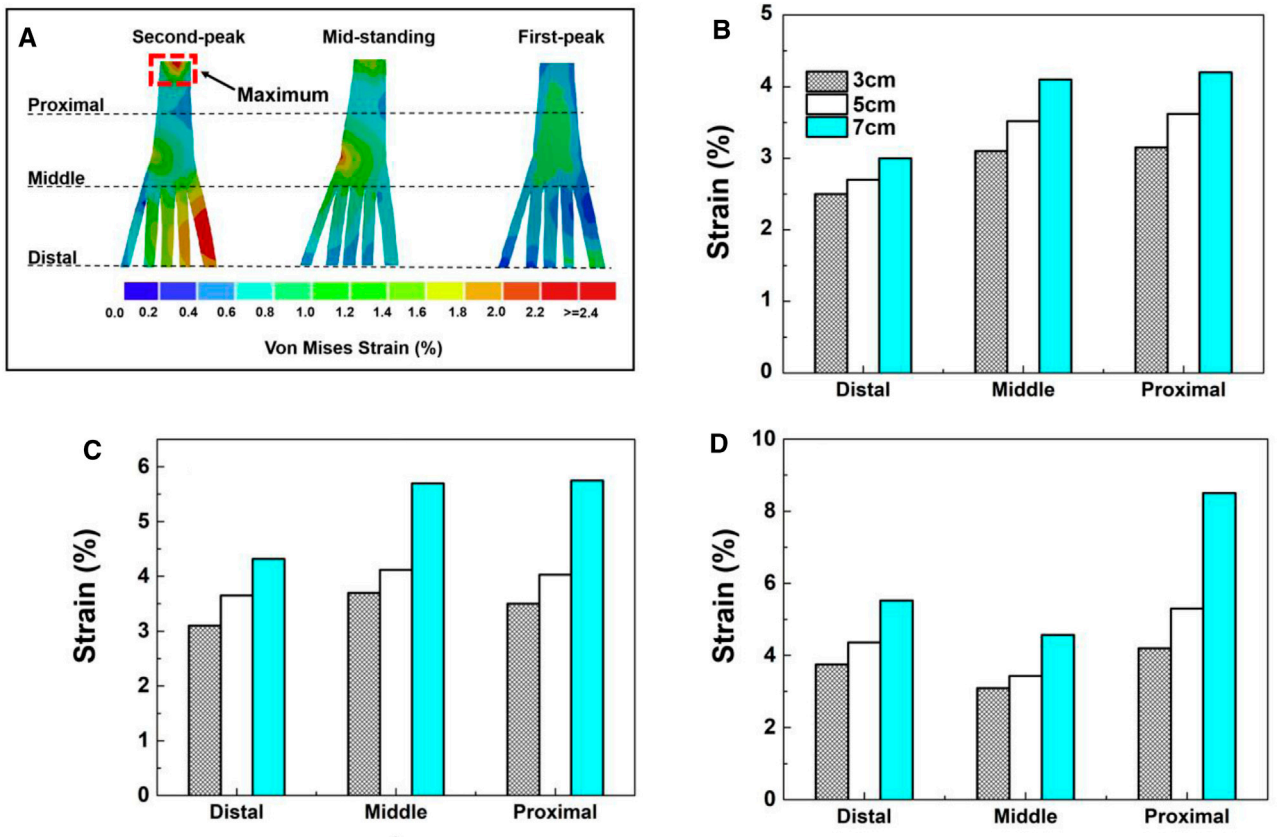

FIGURE 4 | (A) The peak 3D fascia strain for three heel heights in three gait events. **(B)** First-peak phase. **(C)** Mid-standing phase. **(D)** Second-peak phase.

peak contact pressure recorded. The plantar insole in this study was selected based on the shoe size as well as foot size of the subject to minimize the extent of deformation, while the pressure insole was calibrated before the test to reduce the error. Secondly, both experimental and predicted maximum contact pressures in nine plantar regions (big toe, other toes, three equally divided regions in the forefoot, lateral and medial of midfoot and rearfoot) were collected. Then by applying the Pearson correlation, |r|, the agreement between predictions and experimental measurements of 18 data pairs was compared. Values of $|r| \leq 0.35$, $0.36 \leq |r| \leq 0.67$, and $0.68 \leq |r| \leq 1.0$ represent weak, moderate, and strong correlation, respectively (Taylor, 1990). The predicted tension of the 1D plantar fascia was compared with existing research, as well as muscle force in GC, SL, and TA.

3 RESULTS

3.1 Validation

Figures 3B,C show the plantar pressure distribution of the 3-cm heel height condition obtained from the FEM prediction and the experimental measurement in three stance phases. Correlation analysis showed a high linear relationship between the FEM prediction and measurement (r = 0.83; confidence interval: 95%, 0.57–0.90; $p < 0.002$). The differences between the experimentally measured and computationally estimated values are 14% in the first peak, 20.5% in mid-standing, and 28.6% in the second peak. **Figure 2** shows the muscle forces calculated by Opensim compared with previous studies; the graphs show similar corridor trends (Son et al., 2008; Hwang et al., 2006). Lastly, the variation range of predicted strain in 3D and 1D plantar fascia models at mid-standing is 3%–5.7%, which was consistent with previous measurements (Kogler et al., 2001). Based on these validation results, our simulation results are considered to be reliable.

3.2 Changing of the Strain Value on Plantar Fascia Among Different Heel Heights

As predicted, strain distributions of plantar fascia from FEM simulations showed similar patterns for three different heel heights in three different stances; **Figure 4A** shows the typical strain distribution pattern on the plantar fascia in the 5-cm heel height condition. The two end portions of the 3D plantar fascia tied to the bones at the proximal and distal regions were excluded to avoid excessive deformation, and the remaining region of the 3D fascia was divided equally into proximal, medial, and distal regions. FEM prediction results showed that heel height had a significant effect on the strain level of fascia in three stance phases.

For the strain level of plantar fascia, irrespective of heel heights, at the first peak and mid-standing phases, the middle and proximal regions experience a similar level of higher peak strain on the fascia than in the distal region. At the second-peak phase, the plantar fascia strain presents the highest value in the proximal region, followed by the distal region with the lowest strain in the middle region.

For different heel heights, the simulations predicted different plantar fascia strain distributions at different regions irrespective of stance phases. **Figure 4D** shows that the highest plantar fascia strain occurred in the second peak stance phase. In this stance phase, in the proximal region, the peak strain increased by 102% for heel heights of 3–7 cm. For heel heights raised from 3 to 5 cm, the fascia strain increased by 26.1%, and there is a sharp increase by 60.3% from 5 to 7 cm of heel height.

However, for the model with fascia modeled as 1D truss elements, there are no distinct three regions as defined for 3D fascia. The peak strain in 1D fascia is smaller than that in 3D fascia in all three different heel heights in all different stance phases.

4 DISCUSSION

Due to the complex interaction between foot movement and internal components, it is difficult to investigate the biomechanical mechanism of the plantar fascia *in vitro* measurements. Therefore, establishing a realistic plantar fascia simulation method is the premise to understand the biomechanical response of plantar fascia under HHS conditions. In this study, a combination method of FEM and MsM was used to evaluate the strain characteristics of the plantar fascia during HHS walking in three different heel heights.

The opinions on heel elevation as a treatment approach for plantar fasciitis are questionable based on the results of this study. The plantar fascia strain progressively increased in both 3D and 1D modeling when heel height was elevated from 3 to 7 cm. The highest strain was found at the 7-cm heel height, the lowest was found at the 3-cm heel height, and there was a sharp increase by 60.3% from 5 to 7 cm of heel height. However, the findings differ from previous reports (Yu et al., 2016). Yu et al. indicated that the average tension force and strain on the plantar fascia decreased from 151.0 N (strain: 0.74%) to 59.6 N (strain: 0.28%), which reduced by 60.5% and 62.2%, respectively, when the heel height elevated from 0 to 5.08 cm during balanced standing with HHS, then there was a remarkably increase from 5.08 to 7.62 cm of heel height. They suggested that the strain of the plantar fascia could be decreased by an appropriate heel height. According to Yu et al., the 1D element of the plantar fascia was used in their simulation; this simplification did not take into account the complex relationship between ligaments and articular surfaces. In terms of foot structural complexity, the biomechanical response of the plantar fascia under loading is different in the lateral and medial aspects, and it may be responsible for limiting the predicted loading result in an abnormal plantar fascia strain when it is depicted as a 1D truss (Hedrick, 1996). Therefore, a more comprehensive 3D modeling could provide insight into the biomechanical response of the plantar fascia variation under HHS conditions. In our study, 3D fascia modeling shows a higher average strain than that of 1D fascia at all heel heights, and the strain variation of the entire 3D fascia structure can be demonstrated. The peak strain of the plantar fascia in the proximal region was larger than that of the middle and distal portions in three different heel heights, especially at the second peak phase. The results were consistent with previous reports that stress and strain were concentrated on the medial calcaneus tubercle, close to the site of heel pain (Peng et al., 2021). However, this strain response does not appear in the current 1D fascia model or the previous linear fascia model.

Meanwhile, the predicted results of this study are different from previous cadaver experiments, in which plantar fascia strain decreased gradually from a heel height of 2–6 cm (Kogler et al., 2001). According to cadaver investigation, the heel elevation was achieved by a contoured platform with a shank profile located in the mid-region, simulates the inner weight-bearing surface of shoes, and provides complete support for the foot arch. The decreased plantar fascia strain was induced by an extended shank profile from under the calcaneus to the cuboid; this may be enough to relieve severe symptoms of plantar fasciitis (Kogler et al., 2001). Researchers have suggested that the load transmission pattern could be changed by shoe interface configuration, further affecting the strain response of the plantar fascia (Alexander et al., 1990; Kogler et al., 2001; Speksnijder et al., 2005). Differently, in our study, the stiletto shoes with a narrow base support were used which could lead to plantar pressure concentrating on the hindfoot and forefoot as well as reduce the contact area on the mid-foot (Chevalier et al., 2010). Furthermore, the arch is raised passively and reached its limit of flattening with a toe flexion that requires greater muscle force to keep body posture stability under stiletto shoe conditions. However, maintaining the posture under HHS conditions demands a higher-level activity on intrinsic muscles that becomes inadequate, especially in terms of a long period using HHS that muscles are easily prone to fatigue (Mika et al., 2011). Thus, the plantar fascia is more likely to experience tightness and obtain a higher tension force. The appropriate heel elevation may contribute to a strain relief on the plantar fascia, but it certainly does not refer to HHS with a narrow heel base support. In further research, the influence of different sole structures of shoes on plantar fascia strain and tension force should be investigated.

On the other hand, the peak strain on the plantar fascia reaches the maximum at the second peak stance compared with the first peak and valley stance phase. Under HHS conditions, the metatarsophalangeal joints (MPJ) are kept in a dorsiflexion angle which progressively increased with heel elevation. Healey and Chen demonstrated that the increased MPJ dorsiflexion as a result of the elevated hindfoot is a compensation mechanism to stabilize the body posture (Healey and Chen, 2010). However, the larger dorsiflexion angle of the toes could increase the tension force on the plantar fascia due to the "windlass mechanism," which has been well described by Hicks in 1954 (Hicks, 1954). During the push-off phase, the toes are forced into an extended position as toe-standing; the plantar pad is pulled forward, then it moves the attached fascia anterior, contributing a relatively shorter longitudinal arch.

Therefore, the plantar fascia will be subjected to a greater tension force when the forefoot makes a push on the ground during the gait. In a cadaver model test, Erdemir et al. observed that plantar fascia tension gradually increased during stance and reached the maximum at the late stance phase (Erdemir et al., 2004).

Certain limitations in this research should be discussed. Firstly, the realistic simulation of the mechanical behavior of the plantar fascia is important for plantar fascia biomechanics response and effect of pathological conditions (Behforootan et al., 2017). However, the material properties of ligament, cartilages, and plantar fascia were idealized as linearly elastic, in order to compare simulation results with the previous one (Yu et al., 2016); thus, the same material properties were adopted and the hyperelastic or viscoelastic behavior was ignored here. Although this consideration could reduce computational costs and complexity, the simplified material properties may negatively affect internal strain distribution on plantar fascia. As for how different material models may affect the strain distribution of the plantar fascia in specific applications, such as HHS conditions, further research is needed. Secondly, only extrinsic muscle forces were involved in this simulation, while other intrinsic muscles were not considered. Similar to the flexor digitorum brevis muscle that was longitudinally adhered by the central plantar fascia, its absence may adversely affect the accuracy of the fascia strain value. Thirdly, FEM analysis is always limited to a specific subject and does not take into account differences in individual foot morphology. Lastly, the more the ModelGait 2,392 we used here limits DOFs at the ankle joint, the more detailed should be the foot model used in future research to evaluate the foot function related to pathology.

5 CONCLUSION

A 3D FEM model of plantar fascia has been established to explore the effect of heel elevation on plantar fascia internal loading during HHS walking, and a 1D plantar fascia model was created for comparison. The results from the present research could reveal the strain variation on the plantar fascia and facilitate understanding of potential causes of plantar fasciitis induced by using HHS. According to this study, 3D plantar fascia could reflect the entire biomechanical change on the plantar fascia than 1D and provide a reliable strain distribution on the plantar fascia under HHS conditions. The strain on the plantar fascia in this study was progressively increased instead of reduced as heel height rose from 3 to 7 cm. The trend of increased strain on the plantar fascia under HHS conditions is more in line with the "windlass mechanism." Meanwhile, the higher strain on the proximal region of the fascia provides evidence for plantar fasciitis development in the HHS population. Proper heel elevation may help to relieve plantar fascia tension, but it certainly does not refer to HHS with narrow heel support. Therefore, the HHS as a treatment recommendation for plantar fasciitis is questionable. Considering the foot morphology as a determinant factor in load transmission patterns that can be shaped by footwear, the variation sole structure of shoes should be investigated in the future to quantify the effect of different force transmission patterns on the plantar fascia.

DATA AVAILABILITY STATEMENT

The original contributions presented in the study are included in the article/supplementary material; further inquiries can be directed to the corresponding authors.

ETHICS STATEMENT

The study was approved by the Ethics Committee of Ningbo University (protocol code RAGH 20200612). The patients/participants provided their written informed consent to participate in this study.

AUTHOR CONTRIBUTIONS

MW and YG developed the concept. MW organized the structure of the manuscript and wrote the manuscript. WM and SL created the simulation model. E-CT and GF revised the manuscript and approved the final version.

FUNDING

This study was supported by the ÚNKP-21-5 New National Excellence Program of the Ministry for Innovation and Technology from the source of the National Research, Development and Innovation Fund and the János Bolyai Research Scholarship of the Hungarian Academy of Sciences (BO/00047/21/6). Key R&D Program of Zhejiang Province China (2021C03130), Zhejiang Province Science Fund for Distinguished Young Scholars (R22A021199).

REFERENCES

Alexander, I. J., Chao, E. Y. S., and Johnson, K. A. (1990). The Assessment of Dynamic Foot-To-Ground Contact Forces and Plantar Pressure Distribution: a Review of the Evolution of Current Techniques and Clinical Applications. *Foot Ankle* 11, 152–167. doi:10.1177/107110079001100306

Behforootan, S., Chatzistergos, P., Naemi, R., and Chockalingam, N. (2017). Finite Element Modelling of the Foot for Clinical Application: a Systematic Review. *Med. Eng. Phys.* 39, 1–11. doi:10.1016/j.medengphy.2016.10.011

Chen, Y.-N., Chang, C.-W., Li, C.-T., Chang, C.-H., and Lin, C.-F. (2015). Finite Element Analysis of Plantar Fascia during Walking. *Foot Ankle Int.* 36, 90–97. doi:10.1177/1071100714549189

Chevalier, T. L., Hodgins, H., and Chockalingam, N. (2010). Plantar Pressure Measurements Using an In-Shoe System and a Pressure Platform: A Comparison. *Gait Posture* 31, 397–399. doi:10.1016/j.gaitpost.2009.11.016

D'Ambrogi, E., Giurato, L., D'Agostino, M. A., Giacomozzi, C., Macellari, V., Caselli, A., et al. (2003). Contribution of Plantar Fascia to the Increased Forefoot Pressures in Diabetic Patients. *Diabetes Care* 26, 1525–1529. doi:10.2337/diacare.26.5.1525

Di Sipio, E., Piccinini, G., Pecchioli, C., Germanotta, M., Iacovelli, C., Simbolotti, C., et al. (2018). Walking Variations in Healthy Women Wearing High-Heeled

Shoes: Shoe Size and Heel Height Effects. *Gait Posture* 63, 195–201. doi:10.1016/j.gaitpost.2018.04.048

Erdemir, A., Hamel, A. J., Fauth, A. R., Piazza, S. J., and Sharkey, N. A. (2004). Dynamic Loading of the Plantar Aponeurosis in Walking. *J. Bone Jt. Surg.* 86, 546–552. doi:10.2106/00004623-200403000-00013

Gu, Y., Li, J., Ren, X., Lake, M. J., and Zeng, Y. (2010a). Heel Skin Stiffness Effect on the Hind Foot Biomechanics during Heel Strike. *Skin Res. Technol.* 16, 291–296. doi:10.1111/j.1600-0846.2010.00425.x

Gu, Y. D., Ren, X. J., Li, J. S., Lake, M. J., Zhang, Q. Y., and Zeng, Y. J. (2010b). Computer Simulation of Stress Distribution in the Metatarsals at Different Inversion landing Angles Using the Finite Element Method. *Int. Orthopaedics (SICOT)* 34, 669–676. doi:10.1007/s00264-009-0856-4

Healey, K., and Chen, K. (2010). Plantar Fasciitis: Current Diagnostic Modalities and Treatments. *Clin. Podiatric Med. Surg.* 27, 369–380. doi:10.1016/j.cpm.2010.03.002

Hedrick, M. R. (1996). The Plantar Aponeurosis. *Foot Ankle Int.* 17, 646–649. doi:10.1177/107110079601701012

Hicks, J. H. (1954). The Mechanics of the Foot. II. The Plantar Aponeurosis and the Arch. *J. Anat.* 88, 25–30.

Hwang, S. J., Choi, H. S., Choi, H. H., Kim, H. S., and Kim, Y. H. (2006). The Evaluation of the Lower Extremity Joint Moments and Muscle Force during Various High-Heel Walking. *Kem* 326-328, 755–758. doi:10.4028/www.scientific.net/kem.326-328.755

Kainz, H., Modenese, L., Lloyd, D. G., Maine, S., Walsh, H. P. J., and Carty, C. P. (2016). Joint Kinematic Calculation Based on Clinical Direct Kinematic versus Inverse Kinematic Gait Models. *J. Biomech.* 49, 1658–1669. doi:10.1016/j.jbiomech.2016.03.052

Khodair, S. A. Z., and Younes, R. L. (2019). Wearing High Heels and Plantar Fasciitis; MRI Evaluation. *Imaging* 8, 1–5. doi:10.11648/j.ijmi.20200801.11

Kogler, G. F., Veer, F. B., Verhulst, S. J., Solomonidis, S. E., and Paul, J. P. (2001). The Effect of Heel Elevation on Strain within the Plantar Aponeurosis: *In Vitro* Study. *Foot Ankle Int.* 22, 433–439. doi:10.1177/107110070102200513

Lemmon, D., Shiang, T. Y., Hashmi, A., Ulbrecht, J. S., and Cavanagh, P. R. (1997). The Effect of Insoles in Therapeutic Footwear-A Finite Element Approach. *J. Biomech.* 30, 615–620. doi:10.1016/s0021-9290(97)00006-7

Li, S., Zhang, Y., Gu, Y., and Ren, J. (2017). Stress Distribution of Metatarsals during Forefoot Strike versus Rearfoot Strike: A Finite Element Study. *Comput. Biol. Med.* 91, 38–46. doi:10.1016/j.compbiomed.2017.09.018

López-López, D., Marañon-Medina, J., Losa-Iglesias, M. E., Calvo-Lobo, C., Rodríguez-Sanz, D., Palomo-López, P., et al. (2018). The Influence of Heel Height Related on Quality of Life on the Foot in a Sample of Women. *Revista da Associação Médica Brasileir* 64, 324–329. doi:10.1590/1806-9282.64.04.324

Luffy, L., Grosel, J., Thomas, R., and So, E. (2018). Plantar Fasciitis. *JAAPA* 31, 20–24. doi:10.1097/01.JAA.0000527695.76041.99

Mahowald, S., Legge, B. S., and Grady, J. F. (2011). The Correlation between Plantar Fascia Thickness and Symptoms of Plantar Fasciitis. *J. Am. Podiatr Med. Assoc.* 101, 385–389. doi:10.7547/1010385

Marshall, P. (1988). The Rehabilitation of Overuse Foot Injuries in Athletes and Dancers. *Clin. Sports Med.* 7, 175–191. doi:10.1016/s0278-5919(20)30966-2

Mika, A., Oleksy, Ł., Mikołajczyk, E., Marchewka, A., and Mika, P. (2011). Changes of Bioelectrical Activity in Cervical Paraspinal Muscle during Gait in Low and High Heel Shoes. *Acta Bioeng. Biomech.* 13, 27–33.

Pailler-Mattei, C., Bec, S., and Zahouani, H. (2008). *In Vivo* measurements of the Elastic Mechanical Properties of Human Skin by Indentation Tests. *Med. Eng. Phys.* 30, 599–606. doi:10.1016/j.medengphy.2007.06.011

Peng, Y., Wong, D. W.-C., Wang, Y., Chen, T. L.-W., Zhang, G., Yan, F., et al. (2021). Computational Models of Flatfoot with Three-Dimensional Fascia and Bulk Soft Tissue Interaction for Orthosis Design. *Med. Novel Techn. Devices* 9, 100050. doi:10.1016/j.medntd.2020.100050

Siegler, S., Block, J., and Schneck, C. D. (1988). The Mechanical Characteristics of the Collateral Ligaments of the Human Ankle Joint. *Foot Ankle* 8, 234–242. doi:10.1177/107110078800800502

Son, J., Choi, H., and Kim, Y. (2008). "Analysis of Changes in Muscle Length of Lower Limbs during High-Heeled Walking Based on the Musculoskeletal Model," in 2008 International Conference on BioMedical Engineering and Informatics, May 27–30, 2008, 809–812. doi:10.1109/BMEI.2008.342

Speksnijder, C. M., vd Munckhof, R. J. H., Moonen, S. A. F. C. M., and Walenkamp, G. H. I. M. (2005). The Higher the Heel the Higher the Forefoot-Pressure in Ten Healthy Women. *The foot* 15, 17–21. doi:10.1016/j.foot.2004.10.001

Stecco, C., Corradin, M., Macchi, V., Morra, A., Porzionato, A., Biz, C., et al. (2013). Plantar Fascia Anatomy and its Relationship with Achilles Tendon and Paratenon. *J. Anat.* 223, 665–676. doi:10.1111/joa.12111

Sun, D., Gu, Y., Mei, Q., Shao, Y., Sun, J., and Fernandez, J. (2017). Effect of Heel Heights on Female Postural Control during Standing on a Dynamic Support Surface with Sinusoidal Oscillations. *J. Mot. Behav.* 49, 281–287. doi:10.1080/00222895.2016.1191423

Taylor, R. (1990). Interpretation of the Correlation Coefficient: a Basic Review. *J. Diagn. Med. Sonography* 6, 35–39. doi:10.1177/875647939000600106

Trojian, T., and Tucker, A. K. (2019). Plantar Fasciitis. *Am. Fam. Physician* 99, 744–750.

Wan, F. K. W., Yick, K.-L., and Yu, W. W. M. (2019). Effects of Heel Height and High-Heel Experience on Foot Stability during Quiet Standing. *Gait Posture* 68, 252–257. doi:10.1016/j.gaitpost.2018.12.004

Wearing, S. C., Smeathers, J. E., Sullivan, P. M., Yates, B., Urry, S. R., and Dubois, P. (2007). Plantar Fasciitis: Are Pain and Fascial Thickness Associated with Arch Shape and Loading? *Phys. Ther.* 87, 1002–1008. doi:10.2522/ptj.20060136

Wiedemeijer, M. M., and Otten, E. (2018). Effects of High Heeled Shoes on Gait. A Review. *Gait Posture* 61, 423–430. doi:10.1016/j.gaitpost.2018.01.036

Yu, J., Cheung, J. T.-M., Wong, D. W.-C., Cong, Y., and Zhang, M. (2013). Biomechanical Simulation of High-Heeled Shoe Donning and Walking. *J. Biomech.* 46, 2067–2074. doi:10.1016/j.jbiomech.2013.05.009

Yu, J., Wong, D. W.-C., Zhang, H., Luo, Z.-P., and Zhang, M. (2016). The Influence of High-Heeled Shoes on Strain and Tension Force of the Anterior Talofibular Ligament and Plantar Fascia during Balanced Standing and Walking. *Med. Eng. Phys.* 38, 1152–1156. doi:10.1016/j.medengphy.2016.07.009

Conflict of Interest: The authors declare that the research was conducted in the absence of any commercial or financial relationships that could be construed as a potential conflict of interest.

Publisher's Note: All claims expressed in this article are solely those of the authors and do not necessarily represent those of their affiliated organizations, or those of the publisher, the editors, and the reviewers. Any product that may be evaluated in this article, or claim that may be made by its manufacturer, is not guaranteed or endorsed by the publisher.

frontiers in Bioengineering and Biotechnology

ORIGINAL RESEARCH
published: 28 January 2022
doi: 10.3389/fbioe.2021.821530

Acute Effects of Heel-to-Toe Drop and Speed on Running Biomechanics and Strike Pattern in Male Recreational Runners: Application of Statistical Nonparametric Mapping in Lower Limb Biomechanics

Peimin Yu[1,2,3], *Yuhuan He*[1], *Yaodong Gu*[1,2,3]*, *Yuwei Liu*[1,2,3], *Rongrong Xuan*[4]* and *Justin Fernandez*[1,2,3,5]

[1]Faculty of Sports Science, Ningbo University, Ningbo, China, [2]Research Academy of Grand Health, Ningbo University, Ningbo, China, [3]Auckland Bioengineering Institute, The University of Auckland, Auckland, New Zealand, [4]Obsterical Department, The Affiliated Hospital of Medical School of Ningbo University, Ningbo, China, [5]Department of Engineering Science, The University of Auckland, Auckland, New Zealand

OPEN ACCESS

Edited by:
Mohammad Nikkhoo,
Islamic Azad University, Iran

Reviewed by:
Masoud Abdollahi,
Rochester Institute of Technology, United States
Wenxin Niu,
Tongji University, China
Lin Wang,
Shanghai University of Sport, China

***Correspondence:**
Yaodong Gu
guyaodong@nbu.edu.cn
Rongrong Xuan
fyxuanrongrong@nbu.edu.cn

Specialty section:
This article was submitted to Biomechanics, a section of the journal Frontiers in Bioengineering and Biotechnology

Received: 24 November 2021
Accepted: 20 December 2021
Published: 28 January 2022

Citation:
Yu P, He Y, Gu Y, Liu Y, Xuan R and Fernandez J (2022) Acute Effects of Heel-to-Toe Drop and Speed on Running Biomechanics and Strike Pattern in Male Recreational Runners: Application of Statistical Nonparametric Mapping in Lower Limb Biomechanics. Front. Bioeng. Biotechnol. 9:821530. doi: 10.3389/fbioe.2021.821530

With the increased popularity of running, many studies have been conducted into footwears that are highly related to running performance and running-related injuries. Previous studies investigated different shoe types and running shoes with different heel-to-toe drops (HTDs). However, no research was found in investigating shoes with negative values with HTD. Therefore, the aim of this study was to determine the acute effect of HTD and running speed on lower limb biomechanics and strike pattern in recreational runners. Thirteen male recreational runners wearing shoes with two different HTDs (–8 and 8 mm) performed running at three different speeds (preferred speed [PS], 90% of PS, 110% of PS). Lower extremity kinematics and ground reaction forces were synchronously captured *via* Vicon motion analysis system and AMTI force platform. Strike index (SI), vertical average loading rate (VALR), vertical instantaneous loading rate (VILR), excursion, eversion duration, joint angles, and range of motion (ROM) of metatarsophalangeal (MTP), ankle, knee, and hip joints were calculated. Joint angles during the entire stance phase were analyzed applying the statistical nonparametric mapping (SnPM) method. SI and VILR in shoes with –8 mm HTD significantly increased by 18.99% and 31.836 BW/s compared to those with 8 mm HTD (SI: $p = 0.002$; VILR: $p < 0.001$). Significant alterations of ROM occurred in the MTP, ankle, and knee joints ($p < 0.05$), and HTD factor primarily accounted for these changes. Joint angles (MTP, knee, and hip) during the entire stance phase altered due to HTD and speed factors. Running speed primarily influenced the kinematics parameters of knee and hip joints, increasing knee angles in the frontal plane and hip angle in the horizontal plane at PS ($p > 0.05$). Compared to shoes with 8 mm HTD, shoes with –8 mm HTD may be useful to storage and return energy because of the increased ROM of MTP in the sagittal plane. Besides, forefoot strike gait retraining was recommended before transition from normal running shoes to running shoes with –8 mm HTD.

Keywords: heel-to-toe drop, strike index, statistical nonparametric mapping, loading rate, footwear

1 INTRODUCTION

Running, as one of the convenient, low-cost, and beneficial sports, is widely welcomed by people of all age groups among the world (Haskell et al., 2007; Fields et al., 2010). Accompanied with the popularity of running, more people were involved in running, and the risk of skeletal muscle injuries is also increased. Almost a half of runners would have a history of running-related injuries each year (Fields et al., 2010). Among all running-related injuries, the most common injury types are patellofemoral pain syndrome, iliotibial band friction syndrome, plantar fasciitis, meniscal injuries of the knee, and patellar tendinopathy (Taunton et al., 2002). To reduce the risk of running-related injuries, different types of running shoes were designed, which are minimalist, maximalist, and traditional running shoes (Chan et al., 2018; Mo et al., 2020; Mo et al., 2021). Both minimalist and maximalist running shoes had a shared feature of low heel-to-toe drop (HTD) compared to traditional running shoes (Malisoux et al., 2016; Mo et al., 2021). Over a period, maximalist running shoes were supposed to reduce the impact loading *via* the highly cushioned midsole (O'Leary et al., 2008). However, it remained controversial whether enhancing the shock absorption performance of running shoes could reduce the running-related injuries (Yan et al., 2013).

The foot strike patterns could be divided into forefoot strike (FFS), midfoot strike (MFS), and rearfoot strike (RFS), which would result in difference of the vertical loading rate, and thus influence the running-related injury risk (Daoud et al., 2012). Habitually barefoot runners usually adopted the FFS pattern, while habitually shod runners maintained the RFS pattern during running (Lieberman et al., 2010; de Almeida et al., 2015). Minimalist running shoes were produced to imitate the barefoot running pattern, since the idea that barefoot running might be beneficial to reduce the risk of running-related injuries was put forward (Lieberman et al., 2010). Minimalist running shoes took characteristic as low midsole stack height, high flexibility, and low HTD and weight (Esculier et al., 2015). In some studies, it is found that wearing minimalist running shoes could imitate the running biomechanics of barefoot running (Squadrone and Gallozzi 2009; Sinclair et al., 2013b; Paquette et al., 2013), or that it could approximate the barefoot running pattern after certain practice and adaptation (Rixe et al., 2012), while others held the opinion that the biomechanical characteristics of the lower limb were similar between minimalist running shoes and traditional running shoes (Bonacci et al., 2013; Frank et al., 2013; Bergstra et al., 2015). The differences of these studies might be caused by the usage of various types of minimalist running shoes, since HTD of minimalist running shoes varied from 0 to 8 mm (Horvais and Samozino 2013). HTD, as a main feature of shoe design, was associated with alterations of lower limb biomechanics. Reduced HTD led to a transition of the foot strike pattern from RFS to FFS or MFS and changes of ankle and knee joints kinematics and kinetics (Horvais and Samozino 2013; Lee et al., 2013; Richert et al., 2019). As for the injury risk, although the injury risk among all runners was not changed, lower HTD shoes were associated with the lower injury risk among occasional runners, but the higher injury risk among regular runners (Malisoux et al., 2016).

Running speed is also one of the factors that influence the foot strike pattern and lower limb biomechanics of runners (Mo et al., 2021). Cheung et al. found that the proportion of FFS and MFS patterns increased with the increasing of the running speed (Cheung et al., 2017), whereas in the study of Fredericks et al., the foot strike pattern was not obviously influenced by the running speed (Fredericks et al., 2015). As for the kinematics of the lower limb, the influence of running speed mainly focused on the knee joint, resulting in the increase of the flexion angle at the initial contact (Bishop et al., 2006). Moreover, with the running speed increasing, the peak values of hip flexion and extension increased. With regard to the ankle joint, the dorsiflexion angle increased at the initial contact, and the peak plantar flexion angle increased during the early swing phase (Orendurff et al., 2018). With regard to the kinetics of the lower limb, the vertical instantaneous loading rate (VILR) increased when running speed increased (Breine et al., 2019).

To date, there is a lack of information about the effects of negative HTD on foot strike pattern and lower limb biomechanics in recreational runners. Furthermore, the influence of running speed was controversial because of different values of speeds. More information was required to illustrate the relationship among running speed, HTD, and lower limb biomechanics. Therefore, the aim of the current study was to investigate the effects of HTD and running speed on lower limb biomechanics and strike pattern in recreational runners. It is hypothesized that 1) running shoes with the negative value of HTD would alter the lower limb biomechanics and the foot strike pattern of runners, the proportion of FFS and MFS might increase; 2) increasing running speed would mainly affect the loading rates and kinematics of the lower limb rather than the foot strike pattern.

2 METHODS

2.1 Participants

Prior to the study, the sample size of the current study was calculated *via* G*Power 3.1.9.7 (effect size = 0.4, α value = 0.05, power value = 0.8) (Kang 2021). A total of 13 male recreational runners (age 23.67 ± 1.21 years, height 169 ± 5.59 cm, weight 60.83 ± 5.87 kg, body mass index 21.27 ± 1.32 kg/m^2, shoe size 41 EU) were involved in this study. The definition of recreational runners was based on the previous study, which required runners ran less than 3 times per week and less than 10 km per trail (Yu et al., 2021). All participants were rearfoot strikers with the right limb as the dominant limb, defined as the leg used to kick a ball. Individuals with any foot deformity or lower limb injuries in the previous 6 months were excluded from participation. Besides, all participants had no previous running experience in the running shoes with negative value of HTD. To avoid adjusting the foot strike pattern subjectively, participants were not informed of the study aim. Before the experiment, all individuals were given the inform consent, and the ethical approval was granted by the Ningbo University Ethics Committee.

FIGURE 1 | Illustration of shoe types (left side: running shoes with the −8 mm HTD; right side: running shoes with the 8 mm HTD).

2.2 Shoe Conditions

All participants conducted this study in shoes with a positive and a negative value of HTD, respectively (**Figure 1**). These two types of shoes were produced by the same footwear company. The shoe size of these two shoes was 41 EU, midsole material was ethylene-vinyl acetate (EVA), and the outsole material was rubber. Taking the traditional running shoes was the control shoes with the HTD 8 mm, and the height of the sole at the heel and forefoot region was 30 and 22 mm (D8). HTD of the experimental running shoes was −8 mm, and the height of the sole at the heel and forefoot region was 15 and 23 mm (D-8).

2.3 Testing Procedure

All participants were given 5 min to warm up and be familiar with the study environment. The preferred speed (PS) of each subject was recorded *via* Brower timing light (Brower Timing System, Draper, UT, United States). Based on the PS, 90% of the PS was denoted as comparatively slower speed (90% PS), and 110% of the PS was denoted as comparatively quicker speed (110% PS) (Van Oeveren et al., 2017). Participants were required to wear these two types of running shoes to conduct running tasks with three different running speeds (90% PS, 100% PS, 110% PS) in the laboratory. Each subject conducted three successful trials of running test under the different running speeds and shoes. Average values of these three trails were used to minimize the inter-trail error. To avoid the influence of fatigue, each trial was required 30 s interval. The sequence of the shoe types and running speeds was random.

Lower extremity kinematics was captured *via* the 8-camera motion analysis system (Oxford Metrics Ltd., Oxford, United Kingdom) with a frequency of 200 Hz. All subjects were required to wear tight-fitting pants, and 24 reflective markers with a diameter of 12 mm were used to define the motion axis and the center of the lower limb joint (Zhu et al., 2020). The reflective markers were attached unilaterally (right limb) except the pelvis segment, using double side tape to attach on the following anatomical landmarks (**Figure 2**): left/right iliac crest, left/right anterior superior iliac spine, left/right posterior–superior iliac spine, left/right greater trochanter (Cen et al., 2021), three thigh tracking targets, femoral lateral/medial epicondyle, three shank tracking targets, lateral/medial malleolus, three heel tracking targets, first and fifth metatarsal heads, and toe. Based on the previous studies, the metatarsophalangeal (MTP) joint angle referred to the angle between the forefoot and the rearfoot coordinate system, and the rotation axis referred to the center of the first and fifth metatarsal heads and the conjunction between the reflective markers of the first and fifth distal metatarsals (Zhu et al., 2020; Cen et al., 2021). The

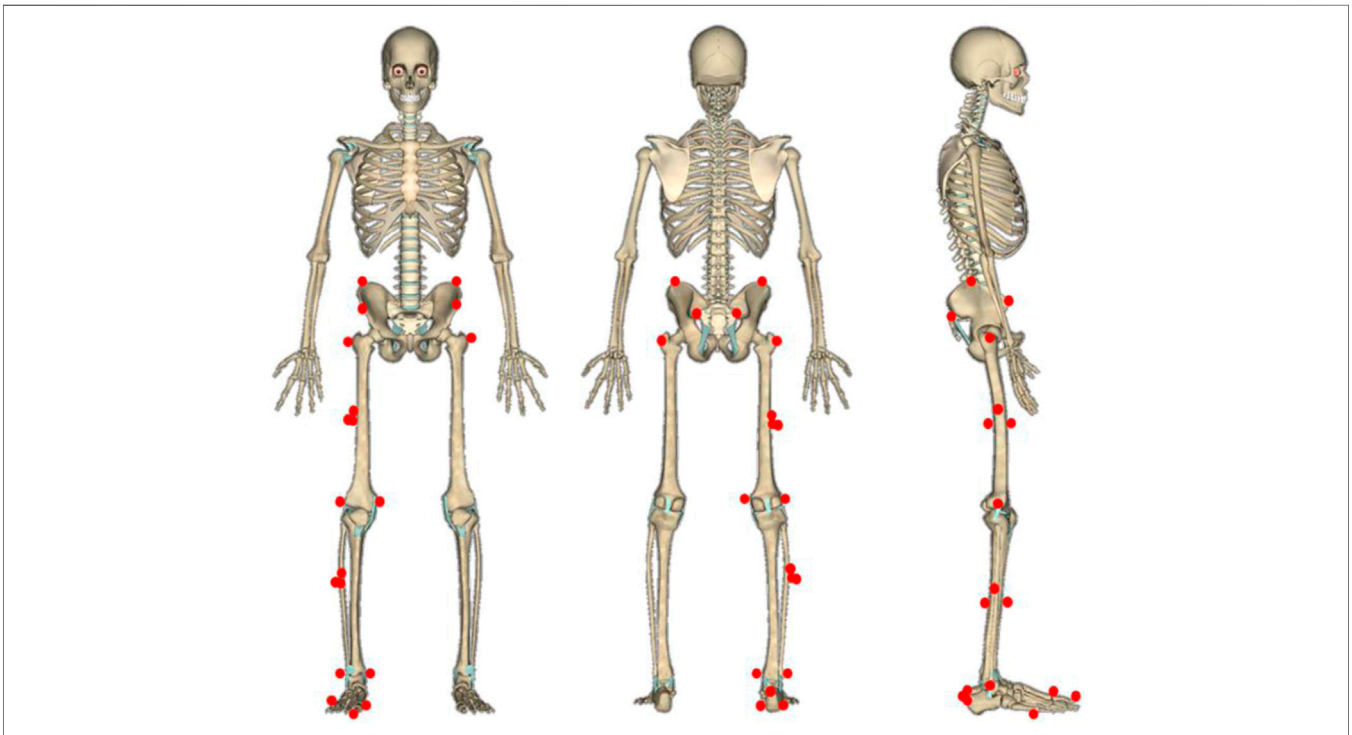

FIGURE 2 | Illustration of reflective markers on subjects. From left to right: front view, rear view, and right side view.

TABLE 1 | Strike pattern, ground reaction force, and kinematic data for the two shoes under different running speeds.

		D-8			D8		–		
		90% PS	100% PS	110% PS	90% PS	100% PS	110% PS	Interaction	HTD	Speed
Strike index (%)		42.43 (24.83)	42.28 (26.04)	40.47 (25.02)	16.10 (7.80)	22.17 (18.56)	30.05 (26.93)	0.269	0.002[a]	0.198
Ground reaction forces										
VILR (BW/s)		102.20 (32.22)	116.04 (44.95)	119.98 (35.35)	83.35 (23.20)	81.36 (23.90)	78.00 (21.92)	0.242	<0.001[a]	0.466
ROM (°)										
MTP	Sagittal	28.14 (10.86)	5.47 (2.55)	27.54 (13.00)	34.09 (13.81)	30.67 (14.53)	30.33 (13.61)	0.001[b]	–	–
	Frontal	14.68 (7.88)	16.68 (7.96)	13.50 (5.67)	9.86 (5.68)	10.92 (7.09)	10.81 (6.99)	0.001[b]	–	–
Ankle	Frontal	16.87 (7.87)	17.86 (5.62)	15.11 (6.67)	12.40 (4.72)	13.09 (5.77)	13.47 (6.26)	0.069	0.001[a]	0.078
Knee	Horizontal	9.77 (5.08)	9.70 (6.19)	9.14 (5.46)	12.25 (6.72)	11.19 (6.55)	9.72 (6.06)	0.003[b]	–	–
	Sagittal	22.88 (3.77)	20.93 (4.75)	19.75 (4.38)	23.50 (2.75)	23.89 (2.90)	22.17 (4.14)	0.285	0.007[a]	0.027[c]
	Horizontal	10.22 (2.78)	10.88 (2.72)	9.52 (2.48)	11.04 (2.29)	11.57 (2.83)	12.03 (3.30)	0.456	0.018[a]	0.018[c]
Excursion (°)		16.03 (9.93)	12.76 (8.89)	15.60 (6.82)	9.47 (3.17)	12.17 (5.87)	13.62 (6.46)	0.094	0.106	0.026[c]

Notes: PS, preferred speed; HTD, heel-to-toe drop; D-8, shoes with the −8 mm HTD; D8, shoes with the 8 mm HTD; VILR, vertical instantaneous loading rate; ROM, range of motion; MTP, metatarsophalangeal joint.

[a]Indicates the significant main effect of heel-to-toe drop.

[b]Indicates a statistically significant interaction.

[c]Indicates the significant main effect of running speed.

AMTI force platform (Advanced Mechanical Technology, Inc., Watertown, MA, United States) was used to synchronously capture the ground reaction forces (GRFs) with a sample frequency of 1,000 Hz. Prior to the data collection, the force platform was zero-leveled, and the stance phase was defined through the vertical GRF with the threshold set to 20 N.

2.4 Data Processing

Experimental data of each trail during the stance phase were processed and analyzed in the current study *via* Visual3D software (version 3.26; C-motion Inc., Germantown, MD, United States). The trajectory of reflective markers was filtered by a low-pass filter with a cut-off frequency of 10 Hz (Yu et al., 2020). The joint angles were calculated *via* an inverse kinematics algorithm in Visual3D and normalized to 100 frames. Stance phase was defined as the period when the value of vertical GRF surpassed 20 N. Kinematic data of interest included the joint angles (MTP, ankle, knee, hip) in the three planes (sagittal, frontal, transverse) during the stance phase. Range of motion (ROM) was defined as the difference between the maximum and minimum joint angles during the stance phase. Besides, excursion of the ankle joint was also included, which was defined as the difference between the angle at the initial contact and the maximum joint angle (Hannigan and Pollard 2020). The eversion duration was referred to the percentage of the stance phase in which the foot was in an everted position. Kinetic variables included the vertical average loading rate (VALR) and VILR that were calculated based on the previous studies (Milner et al., 2006; Law et al., 2019). When the impact peak was undetectable or absent, the vertical GRF at 13% stance phase was defined as the impact peak (Blackmore et al., 2016). Strike index (SI) was used to classify the foot strike pattern, calculated based on the following equation (Cavanagh and Lafortune 1980).

$$SI = \frac{D_{COP-heel}}{foot\ length} \times 100\%$$

Where the $D_{\text{cop-heel}}$ refers to the distance from the location of the center of pressure at the initial contact to the heel along the foot long axis. The SI of 0%–33% presents the RFS pattern, between 34% and 67% is classified as the MFS pattern, and 68%–100% is defined as the FFS pattern (Cavanagh and Lafortune 1980).

2.5 Statistical Analysis

Normal distribution was checked for all discrete values. Mean and standard deviation (SD) were applied to describe the discrete values of ROM, excursion, eversion duration, SI, AVLR, and IVLR. These parameters were evaluated by the two-factor repeated measures ANOVA followed by Bonferroni post hoc test for multiple comparisons. Analysis was conducted in SPSS (version 25; SPSS, Chicago, IL, United States). Due to the one-dimensional time-varying characteristic of the joint angle, the two-factor repeated measures ANOVA in open-source factorial statistical nonparametric mapping (SnPM) was employed, which is based on label permutation tests (Nichols and Holmes 2001; Trama et al., 2021). Bonferroni correction was used to adjust the post hoc tests alpha risk (Trama et al., 2021). Factorial SnPM was

conducted in MATLAB R2018a (The MathWorks, MA, USA). The significance level was set as 0.05.

3 RESULTS

Results that had no significant differences between two factors were presented in the Supplementary Material.

3.1 Strike Index

As is shown in **Table 1**, there was no significant interaction between running speed and HTD on the SI ($p = 0.269$). There was no significant main effect of running speed on foot SI, while the main effect of HTD on foot SI was significant (F (1,12) = 15.040, $p = 0.002$). The foot strike pattern in D-8 shifted anteriorly to 18.99% compared to that in D8 (95% CI: 8.31%–29.61%, $p = 0.002$).

3.2 Ground Reaction Forces

As for the VILR (**Table1**), there was no significant interaction between running speed and HTD ($p = 0.242$). There was no significant main effect of running speed on VILR (F (2,24) = 0.674, $p = 0.519$), while the main effect of HTD on the VILR was significant (F (1,12) = 33.847, $p < 0.001$). The VILR in D-8 significantly increased by 31.836 BW/s compared to that in D8 ($p < 0.001$).

3.3 Discrete Kinematic Data

All discrete kinematic data with significant differences are presented in **Table 1**. For the ROM of MTP in the sagittal plane, there was a significant interaction between running speed and HTD ($p = 0.001$). At the 90% and 100% of PS, the ROMs in D-8 significantly reduced by 5.910° and 25.206° compared to those in D8 (F (1,12) = 6.202, $p = 0.028$; F (1,12) = 30.485, $p < 0.001$). As for the frontal plane, there was also a significant interaction between running speed and HTD ($p = 0.001$). At each group of running speed, the ROMs in D-8 significantly increased (90% PS: F (1,12) = 11.821, $p = 0.005$; 100% PS: F (1,12) = 46.663, $p < 0.001$; 110% PS: F (1,12) = 5.873, $p = 0.032$). In D-8, there was a significant simple main effect of running speed (F (2,24) = 3.475, $p = 0.047$), while the post hoc tests revealed no significant differences between groups ($p > 0.05$). In D8, there was no significant simple main effect of running speed (F (2,24) = 0.598, $p = 0.468$).

For the ROM of the ankle joint in the frontal plane, there was no significant interaction between running speed and HTD ($p = 0.069$). There was no significant main effect of running speed on the ROM (F (2,24) = 2.840, $p = 0.078$), while the main effect of HTD was significant (F (1,12) = 35.097, $p < 0.001$). The ROM in D-8 was significantly greater than that in D8 ($p < 0.001$). As for the horizontal plane, there was a significant interaction between two factors ($p = 0.003$). The significant differences only existed in groups of 90% and 100% of PS, and the ROMs in D-8 significantly reduced by 2.480° and 1.485° compared to those in D8 (F (1,12) = 8.717, $p = 0.012$; F (1,12) = 6.585, $p = 0.025$). As for the ankle excursion, no HTD * speed interaction effect or main effect of HTD was observed ($p = 0.094$, $p = 0.106$). The main effect of running speed was significant (F (2,24) = 4.278, $p = 0.006$). The ankle excursion at 100% of PS significantly reduced by 2.142° compared to that at 110% of PS ($p = 0.016$).

For the ROM of the knee joint in the sagittal plane, there was no significant interaction between running speed and HTD ($p = 0.285$). There was a significant main effect of HTD on the ROM (F (1,12) = 10.454, $p = 0.007$), and the ROM in D-8 significantly reduced by 1.999° ($p = 0.007$). Besides, there was a significant main effect of running speed on the ROM (F (2,24) = 4.665, $p = 0.027$). The ROM at 90% of PS was significantly greater than that at 110% of PS ($p = 0.032$). As for the horizontal plane, no HTD * speed interaction effect was observed ($p = 0.456$). The significant difference only existed in the HTD group; ROM in D-8 significantly reduced by 0.884° ($p = 0.018$).

3.4 Joint Angles During the Entire Stance Phase

No HTD * speed interaction effects were observed for MTP angles in the sagittal plane during the entire stance phase (**Figure 3**). There was an "HTD" effect, with an F-value above the significant threshold of 5.95 during the entire stance phase. There were significant main effects of running speed for MTP angles in the sagittal plane during 86%–100% of the stance phase, with the F-value above the threshold of 4.08. During that phase, MTP angles at 110% of PS were significantly greater than those at 100% of PS. As for the horizontal plane, no HTD * speed interaction effects or main effects of speed were observed for MTP angles during the entire stance phase (**Figure 4**). There was an "HTD" effect, with an F-value above the significant threshold of 3.69 during the entire stance phase.

No HTD * speed interaction effects or main effects of HTD were observed for knee angles in the frontal plane during the entire stance phase (**Figure 5**). There were significant main effects of running speed for knee angles in the frontal plane during 0%–21% of the stance phase. Knee angles at 100% of PS were significantly greater than those at 90% of PS.

No HTD * speed interaction effects or main effects of HTD were observed for hip angles in the horizontal plane during the entire stance phase (**Figure 6**). There were significant main effects of running speed for hip angles in the horizontal plane during 15%–24% of the stance phase. Hip angles at 100% of PS were significantly greater than those at 110% of PS.

4 DISCUSSION

The primary aim of the current study was to explore the effects of HTD (−8 and 8 mm) and running speed (90% of PS, 100% of PS, 110% of PS) on lower limb biomechanics and strike patterns in recreational runners. Differences in SI were observed between two different HTDs, and no differences were seen in different running speeds, which did support our hypothesis. Both VALR and VILR were not influenced by running speed, but VILR in D-8 reduced compared to D8, which did not support our initial hypothesis. Running speed or HTD mainly affected the ROM of MTP, ankle, and knee joints. Besides, during the entire stance

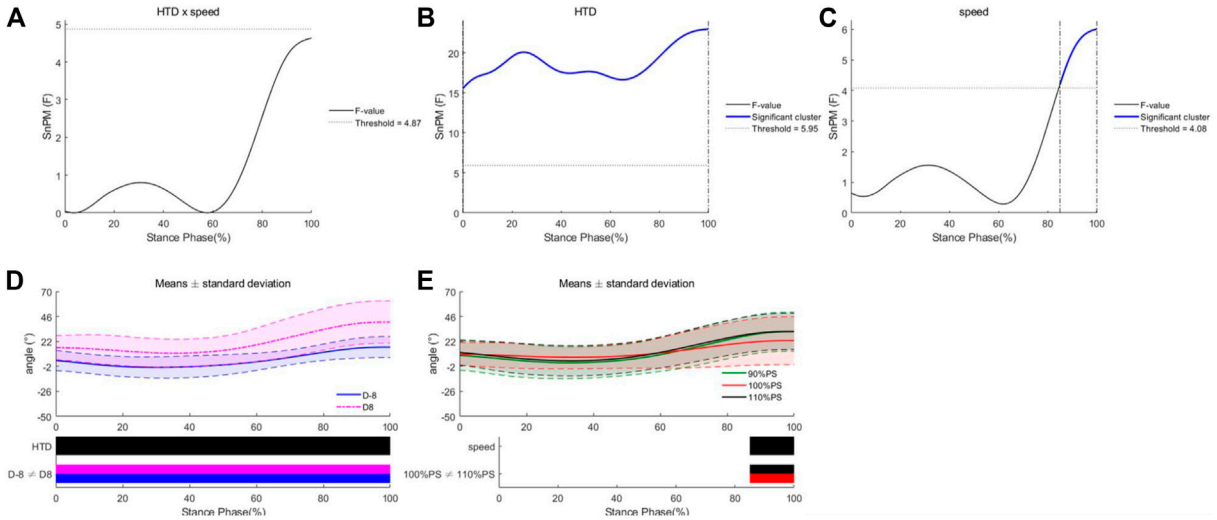

FIGURE 3 | Differences of MTP angles in the sagittal plane under different HTDs and running speeds. Interaction **(A)**, main effects of HTD **(B)** and speed **(C)**, post hoc test for HTD **(D)**, and post hoc test for speeds **(E)**.

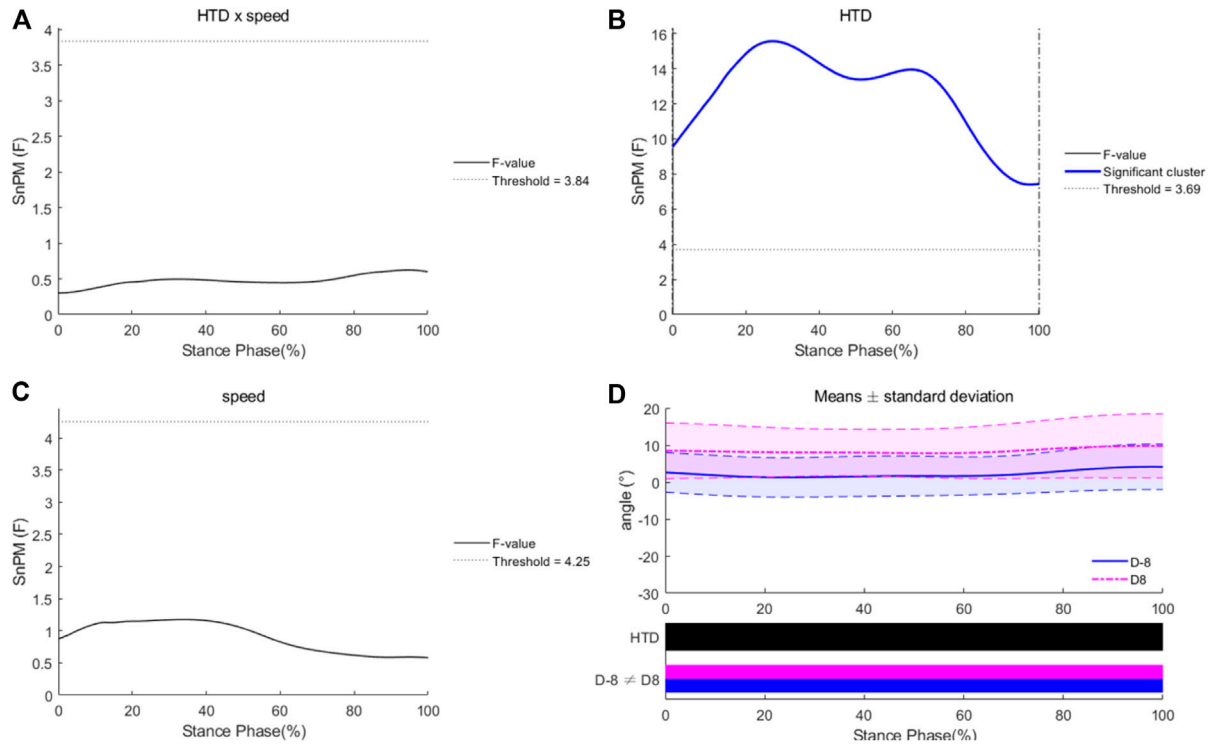

FIGURE 4 | Differences of MTP angles in the horizontal plane under different HTDs and running speeds. Interaction **(A)**, main effects of HTD **(B)** and speed **(C)**, and post hoc test for HTD **(D)**.

phase, angles of ankle joint did not change significantly. These findings partially supported our hypothesis.

The influence of running speed on the strike pattern was controversial. While some studies found that the proportion of FFS and MFS patterns increased with the increase of running speed (Breine et al., 2014; Cheung et al., 2017; Jiang 2020), other studies found that it did not change (Fredericks et al., 2015; Lai et al., 2020). The disagreement between these studies might be

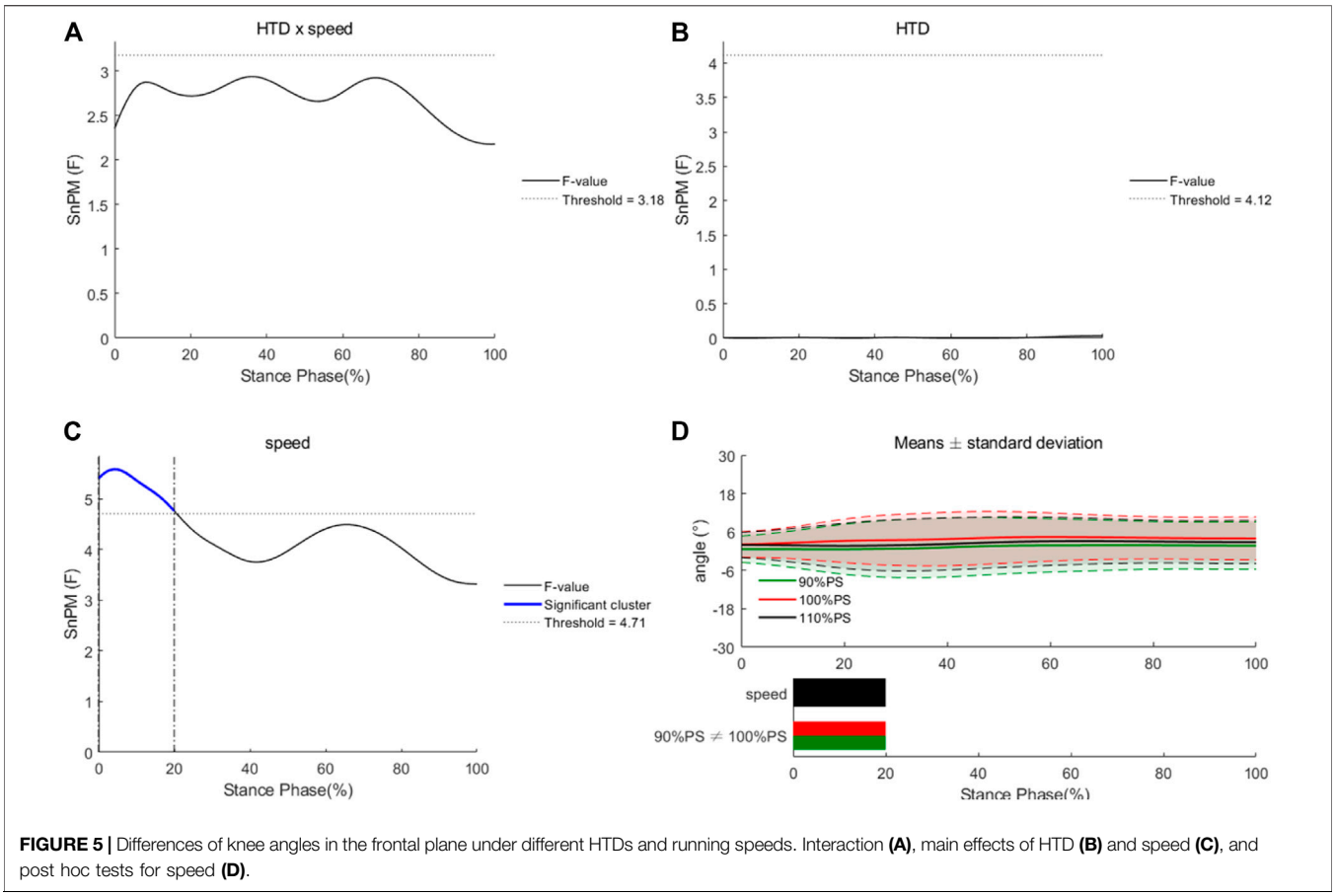

FIGURE 5 | Differences of knee angles in the frontal plane under different HTDs and running speeds. Interaction **(A)**, main effects of HTD **(B)** and speed **(C)**, and post hoc tests for speed **(D)**.

attributed to different ranges of running speeds, where relatively slow running speed might not influence the strike pattern of runners. The running speeds of the current study were set at 90%, 100%, and 110% of PS. Besides, PS of individuals was relatively slow because this study was conducted in the laboratory environment. Strike pattern, therefore, did not alter with the running speed in the current study. As for the HTD that is a critical feature of the shoe design, it was related with the foot strike pattern (Fredericks et al., 2015; Dempster et al., 2021). To a certain extent, a lower HTD might result in the greater proportion of FFS and MFS patterns according to the previous studies (Hollander et al., 2015; Cheung et al., 2017). Previous studies mainly focused on the comparisons between traditional, minimalist, and maximalist running shoes, all of which have positive values of HTD. In this study, experimental running shoes increased the thickness of forefoot midsole and reduced the thickness of heel midsole, resulting in the −8 mm HTD. Accordingly, the proportion of FFS and MFS patterns increased. Although not all runners used the FFS/MFS pattern, the foot strike pattern shifted anteriorly compared to traditional running shoes.

No significant effects of running speed and HTD were found in VALR. VILR, however, increased in shoes with −8 mm HTD compared to that in 8 mm HTD. GRFs and loading rates (including VALR and VILR) have been applied to investigate the mechanisms of running-induced injuries (Milner et al., 2006; Phan et al., 2017; Breine et al., 2019; Malisoux et al., 2021). Although habitually barefoot runners who commonly adopted the FFS pattern had lower impact peak of GRF and loading rates than habitually shod runners (Lieberman et al., 2010), acute transition to the FFS or MFS pattern in habitually shod runners increased impact peaks and loading rates (De Wit et al., 2000; Willson et al., 2014; Willy and Davis 2014; Hannigan and Pollard 2020). Consistent with the previous studies, VILR in shoes with −8 mm HTD was significantly greater, and even the overall strike pattern shifted anteriorly. The characteristics of participants and shoe design could account for this phenomenon. All participants included in this study were accustomed to the RFS pattern when running. And experimental shoes with −8 mm HTD encouraged an FFS pattern because of the thickness of forefoot midsole. Although the proportion of a non-RFS pattern increased, runners adopted an RFS pattern in some trails of the experiment. To reduce the potential risk of running-induced injuries, FFS gait retraining would be of great importance (Futrell et al., 2020).

The MTP joint, as an essential contributor to lower limb energetics, has also received widespread attention in recent years (Stefanyshyn and Nigg 2000; Roy and Stefanyshyn 2006; Smith et al., 2014). Previous studies have found that MTP

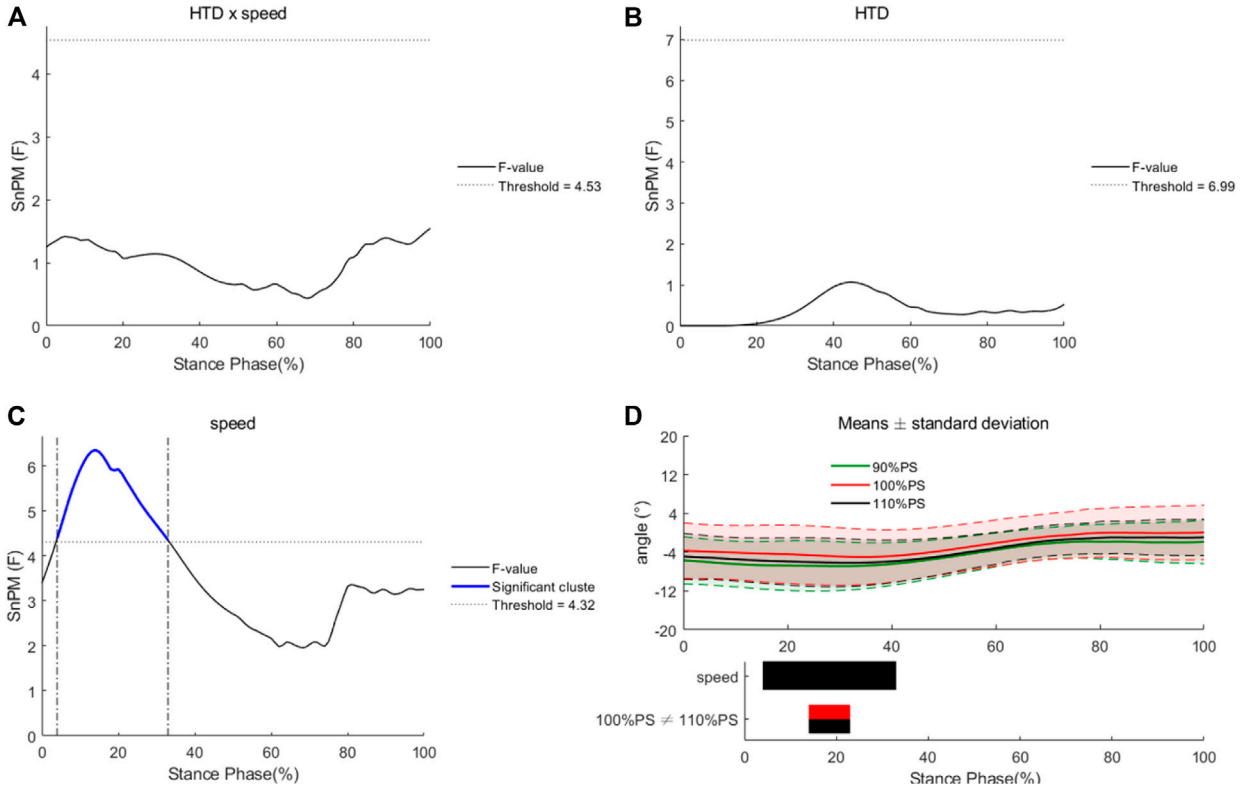

FIGURE 6 | Differences of hip angles in the horizontal plane under different HTDs and running speeds. Interaction **(A)**, main effects of HTD **(B)** and speed **(C)**, and post hoc tests for speed **(D)**.

joint was a large dissipater of energy, absorbing energy and generating no or very little energy before take-off (Roy and Stefanyshyn 2006; Smith et al., 2014). This could be attributed to dorsiflexion of MTP at the majority phase of the stance and plantar flexion at the end of the stance (Stefanyshyn and Nigg 2000; Willwacher et al., 2013). In this study, MTP angles in the sagittal plane reduced significantly in shoes with −8 mm HTD. The increased thickness of forefoot midsole and decreased thickness of heel midsole promoted runners to perform plantar flexion movement at the stance phase, which was supposed to transfer energy appropriately. When running at 90% and 100% of PS, the ROM of MTP in the sagittal plane in shoes with −8 mm HTD reduced significantly. But the increased ROM of MTP might be beneficial to storage and return energy (Willwacher et al., 2013). More evidence was still required to identify the effects of HTD on energy absorption or production of MTP.

During the entire stance phase, there were no differences of ankle angles between different HTDs or speeds. Consistent with the previous studies, running speed did not significantly influence the ankle angles, which supported the idea that power did not mainly be generated from the ankle joint (Pink et al., 1994; Lohman et al., 2011). In the frontal plane, ROM of ankle joint in shoes with −8 mm HTD was greater than that with 8 mm HTD. That could surmise that shoes with −8 mm HTD produced excessive ankle motion in the frontal plane, which might indicate increased instability of shoes with −8 mm HTD. When running at 90% and 100% of PS, ROM of ankle joint in the horizontal plane decreased when wearing shoes with −8 mm HTD. Besides, dorsiflexion excursion increased at 110% of PS compared to that at 100% of PS. No differences were seen in eversion duration, which has been associated with injury risk of Achilles tendinopathy and medial tibia stress syndrome (Becker et al., 2017).

In the sagittal plane, ROM of knee joint in shoes with −8 mm HTD reduced compared to that with 8 mm HTD. Additionally, the internal–external ROM of knee joint reduced in shoes with −8 mm HTD. During the stance phase, reduced knee ROM was associated with better running economy that was strongly related to running performance (Sinclair et al., 2013a; Moore 2016). Additionally, flexion–extension ROM of knee joint at 110% of PS was greater than that at 90% of PS. In the frontal plane, knee angles at 100% of PS were greater than those at 90% of PS from the first contact to 21% of the stance phase. During that period, runners went from initial contact to loading response. Hip angles in the horizontal plane at 100% of PS were significantly greater than those at 110% of PS during 15%–24% of the stance phase (from heel strike to mid stance). Consistent with the previous studies, knee and hip joints changed with difference running

speeds (Pink et al., 1994; Lohman et al., 2011). It could be assumed that knee and hip joints are the main source of power in running rather than ankle joint.

Some limitations of the current study should be noticed. Firstly, although SnPM provided a good approach to compute ANOVA and post hoc tests, the post hoc tests with Bonferroni correction were only approximate and conservative. Furthermore, only immediate effects of HTD and running speed on lower limb biomechanics and strike pattern were compared in this study. The long-term effects of these two factors remained uncertain, which should be considered in the future studies. Finally, participants of this study were all rearfoot strikers, so conclusions might not be appropriate to apply to naturally forefoot or midfoot strikers.

5 CONCLUSION

This study assessed the immediate effects of both HTD and speed on running biomechanics and strike pattern in recreational runners. Foot strike pattern shifted anteriorly when wearing shoes with −8 mm HTD. In addition, VILR in shoes with −8 mm HTD increased, which would increase the risk of injury risks. The influence of HTD on the kinematic parameters mainly happened on the MTP joint, especially resulting in greater joint angles in the sagittal plane. These alterations make storage and return energy effectively compared to shoes with 8 mm HTD. Running speed primarily influenced knee and hip joints that may be the main source of power in running. The results of this study indicated that shoes with −8 mm HTD may have better ability to storage and return energy that was related to running performance. But according to higher VILR in shoes with −8 mm HTD, FFS gait retraining was suggested before transition from normal running shoes to running shoes with −8 mm HTD.

DATA AVAILABILITY STATEMENT

The original contributions presented in the study are included in the article/supplementary material. Further inquiries can be directed to the corresponding authors.

ETHICS STATEMENT

The studies involving human participants were reviewed and approved by the Ethics Committee of Ningbo University. The patients/participants provided their written informed consent to participate in this study.

AUTHOR CONTRIBUTIONS

PY, RX, and YG developed the concept; PY, YG, and JF organized the structure of the manuscript and wrote the manuscript, YL, RX, and YH created the biomechanical model. YG and JF revised the manuscript and approved the final version.

FUNDING

This study was supported by Zhejiang Province Medical and Health Science and Technology Plan Project (No. 2018KY710), Ningbo Public Welfare Science and Technology Plan Project (No. 2019C50095), Health Youth Technical Talent Cultivation Special Fund Project (2020SWSQNGG-01), Ningbo Medical Science and Technology Plan (2020Y14), Young Cultivation Fund Project of The Affiliated of School of Medicine of Ningbo University (FYQM-KY-202003), Open Fund Project of Institute of Human Biomechanics of Ningbo University (CJ-HBIO202112), and K.C. Wong Magna Fund in Ningbo University.

REFERENCES

Becker, J., James, S., Wayner, R., Osternig, L., and Chou, L.-S. (2017). Biomechanical Factors Associated with Achilles Tendinopathy and Medial Tibial Stress Syndrome in Runners. *Am. J. Sports Med.* 45, 2614–2621. doi:10.1177/0363546517708193

Bergstra, S. A., Kluitenberg, B., Dekker, R., Bredeweg, S. W., Postema, K., Van den Heuvel, E. R., et al. (2015). Running with a Minimalist Shoe Increases Plantar Pressure in the Forefoot Region of Healthy Female Runners. *J. Sci. Med. Sport* 18, 463–468. doi:10.1016/j.jsams.2014.06.007

Bishop, M., Fiolkowski, P., Conrad, B., Brunt, D., and Horodyski, M. (2006). Athletic Footwear, Leg Stiffness, and Running Kinematics. *J. Athl. Train.* 41, 387–392.

Blackmore, T., Willy, R. W., and Creaby, M. W. (2016). The High Frequency Component of the Vertical Ground Reaction Force Is a Valid Surrogate Measure of the Impact Peak. *J. Biomech.* 49, 479–483. doi:10.1016/j.jbiomech.2015.12.019

Bonacci, J., Saunders, P. U., Hicks, A., Rantalainen, T., Vicenzino, B. T., and Spratford, W. (2013). Running in a Minimalist and Lightweight Shoe Is Not the Same as Running Barefoot: A Biomechanical Study. *Br. J. Sports Med.* 47, 387–392. doi:10.1136/bjsports-2012-091837

Breine, B., Malcolm, P., Frederick, E. C., and De Clercq, D. (2014). Relationship between Running Speed and Initial Foot Contact Patterns. *Med. Sci. Sports Exerc.* 46, 1595–1603. doi:10.1249/MSS.0000000000000267

Breine, B., Malcolm, P., Galle, S., Fiers, P., Frederick, E. C., and De Clercq, D. (2019). Running Speed-Induced Changes in Foot Contact Pattern Influence Impact Loading Rate. *Eur. J. Sport Sci.* 19, 774–783. doi:10.1080/17461391.2018.1541256

Cavanagh, P. R., and Lafortune, M. A. (1980). Ground Reaction Forces in Distance Running. *J. Biomech.* 13, 397–406. doi:10.1016/0021-9290(80)90033-0

Cen, X., Lu, Z., Baker, J. S., István, B., and Gu, Y. (2021). A Comparative Biomechanical Analysis during Planned and Unplanned Gait Termination in Individuals with Different Arch Stiffnesses. *Appl. Sci.* 11, 1–10. doi:10.3390/app11041871

Chan, Z. Y. S., Au, I. P. H., Lau, F. O. Y., Ching, E. C. K., Zhang, J. H., and Cheung, R. T. H. (2018). Does Maximalist Footwear Lower Impact Loading during Level Ground and Downhill Running?. *Eur. J. Sport Sci.* 18, 1083–1089. doi:10.1080/17461391.2018.1472298

Cheung, R. T. H., Wong, R. Y. L., Chung, T. K. W., Choi, R. T., Leung, W. W. Y., and Shek, D. H. Y. (2017). Relationship between Foot Strike Pattern, Running Speed, and Footwear Condition in Recreational Distance Runners. *Sports Biomech.* 16, 238–247. doi:10.1080/14763141.2016.1226381

Daoud, A. I., Geissler, G. J., Wang, F., Saretsky, J., Daoud, Y. A., and Lieberman, D. E. (2012). Foot Strike and Injury Rates in Endurance Runners. *Med. Sci. Sports Exerc.* 44, 1325–1334. doi:10.1249/MSS.0b013e3182465115

de Almeida, M. O., Saragiotto, B. T., Yamato, T. P., and Lopes, A. D. (2015). Is the Rearfoot Pattern the Most Frequently Foot Strike Pattern Among Recreational Shod Distance Runners?. *Phys. Ther. Sport* 16, 29–33. doi:10.1016/j.ptsp.2014.02.005

De Wit, B., De Clercq, D., and Aerts, P. (2000). Biomechanical Analysis of the Stance Phase during Barefoot and Shod Running. *J. Biomech.* 33, 269–278. doi:10.1016/S0021-9290(99)00192-X

Dempster, J., Dutheil, F., and Ugbolue, U. C. (2021). The Prevalence of Lower Extremity Injuries in Running and Associated Risk Factors: A Systematic Review. *Phys. Activity Health* 5 (1), 133–145. doi:10.5334/paah.109

Esculier, J.-F., Dubois, B., Dionne, C. E., Leblond, J., and Roy, J.-S. (2015). A Consensus Definition and Rating Scale for Minimalist Shoes. *J. Foot Ankle Res.* 8, 1–9. doi:10.1186/s13047-015-0094-5

Fields, K. B., Sykes, J. C., Walker, K. M., and Jackson, J. C. (2010). Prevention of Running Injuries. *Curr. Sports Med. Rep.* 9, 176–182. doi:10.1249/JSR.0b013e3181de7ec5

Frank, N. S., Callaghan, J. P., and Prentice, S. D. (2013). Lower Limb Kinematic Variability Associated with Minimal Footwear during Running. *Footwear Sci.* 5, 171–177. doi:10.1080/19424280.2013.797505

Fredericks, W., Swank, S., Teisberg, M., Hampton, B., Ridpath, L., and Hanna, J. B. (2015). Lower Extremity Biomechanical Relationships with Different Speeds in Traditional, Minimalist, and Barefoot Footwear. *J. Sports Sci. Med.* 14, 276–283.

Futrell, E. E., Gross, K. D., Reisman, D., Mullineaux, D. R., and Davis, I. S. (2020). Transition to Forefoot Strike Reduces Load Rates More Effectively Than Altered Cadence. *J. Sport Health Sci.* 9, 248–257. doi:10.1016/j.jshs.2019.07.006

Hannigan, J. J., and Pollard, C. D. (2020). Differences in Running Biomechanics between a Maximal, Traditional, and Minimal Running Shoe. *J. Sci. Med. Sport* 23, 15–19. doi:10.1016/j.jsams.2019.08.008

Haskell, W. L., Lee, I.-M., Pate, R. R., Powell, K. E., Blair, S. N., Franklin, B. A., et al. (2007). Physical Activity and Public Health. *Med. Sci. Sports Exerc.* 39, 1423–1434. doi:10.1249/mss.0b013e3180616b27

Hollander, K., Argubi-wollesen, A., Reer, R., and Zech, A. (2015). Comparison of Minimalist Footwear Strategies for Simulating Barefoot Running: A Randomized Crossover Study. *PLoS One* 10, e0125880–11. doi:10.1371/journal.pone.0125880

Horvais, N., and Samozino, P. (2013). Effect of Midsole Geometry on Foot-Strike Pattern and Running Kinematics. *Footwear Sci.* 5, 81–89. doi:10.1080/19424280.2013.767863

Jiang, C. (2020). The Effect of Basketball Shoe Collar on Ankle Stability: A Systematic Review and Meta-Analysis. *Phys. Activity Health* 4 (1), 11–18. doi:10.5334/paah.48

Kang, H. (2021). Sample Size Determination and Power Analysis Using the G*Power Software. *J. Educ. Eval. Health Prof.* 18, 17–12. doi:10.3352/JEEHP.2021.18.17

Lai, Y. J., Chou, W., Chu, I. H., Wang, Y. L., Lin, Y. J., Tu, S. J., et al. (2020). Will the Foot Strike Pattern Change at Different Running Speeds with or without Wearing Shoes?. *Int. J. Environ. Res. Public Health* 17, 1–9. doi:10.3390/ijerph17176044

Law, M. H. C., Choi, E. M. F., Law, S. H. Y., Chan, S. S. C., Wong, S. M. S., Ching, E. C. K., et al. (2019). Effects of Footwear Midsole Thickness on Running Biomechanics. *J. Sports Sci.* 37, 1004–1010. doi:10.1080/02640414.2018.1538066

Lee, J., Lee, K., and Kim, J. (2013). Effect of Shoe Heel to Toe Drop and Strike Patterns in Sole Angle. *Footwear Sci.* 5, S48–S49. doi:10.1080/19424280.2013.799548

Lieberman, D. E., Venkadesan, M., Werbel, W. A., Daoud, A. I., D'Andrea, S., Davis, I. S., et al. (2010). Foot Strike Patterns and Collision Forces in Habitually Barefoot versus Shod Runners. *Nature* 463, 531–535. doi:10.1038/nature08723

Lohman, E. B., Balan Sackiriyas, K. S., and Swen, R. W. (2011). A Comparison of the Spatiotemporal Parameters, Kinematics, and Biomechanics between Shod, Unshod, and Minimally Supported Running as Compared to Walking. *Phys. Ther. Sport* 12, 151–163. doi:10.1016/j.ptsp.2011.09.004

Malisoux, L., Chambon, N., Urhausen, A., and Theisen, D. (2016). Influence of the Heel-To-Toe Drop of Standard Cushioned Running Shoes on Injury Risk in Leisure-Time Runners. *Am. J. Sports Med.* 44, 2933–2940. doi:10.1177/0363546516654690

Malisoux, L., Delattre, N., Meyer, C., Gette, P., Urhausen, A., and Theisen, D. (2021). Effect of Shoe Cushioning on landing Impact Forces and Spatiotemporal Parameters during Running: Results from a Randomized Trial Including 800+ Recreational Runners. *Eur. J. Sport Sci.* 21, 985–993. doi:10.1080/17461391.2020.1809713

Milner, C. E., Ferber, R., Pollard, C. D., Hamill, J., and Davis, I. S. (2006). Biomechanical Factors Associated with Tibial Stress Fracture in Female Runners. *Med. Sci. Sports Exerc.* 38, 323–328. doi:10.1249/01.mss.0000183477.75808.92

Mo, S., Lam, W.-K., Ching, E. C. K., Chan, Z. Y. S., Zhang, J. H., and Cheung, R. T. H. (2020). Effects of Heel-Toe Drop on Running Biomechanics and Perceived comfort of Rearfoot Strikers in Standard Cushioned Running Shoes. *Footwear Sci.* 12, 91–99. doi:10.1080/19424280.2020.1734868

Mo, S., Chan, Z. Y. S., Lai, K. K. Y., Chan, P. P.-K., Wei, R. X.-Y., Yung, P. S.-H., et al. (2021). Effect of Minimalist and Maximalist Shoes on Impact Loading and Footstrike Pattern in Habitual Rearfoot Strike Trail Runners: An In-Field Study. *Eur. J. Sport Sci.* 21, 183–191. doi:10.1080/17461391.2020.1738559

Moore, I. S. (2016). Is There an Economical Running Technique? A Review of Modifiable Biomechanical Factors Affecting Running Economy. *Sports MedMed* 46, 793–807. doi:10.1007/s40279-016-0474-4

Nichols, T. E., and Holmes, A. P. (2001). Nonparametric Permutation Tests for Functional Neuroimaging: a Primer with Examples. *Hum. Brain Mapp.* 15, 1–25. doi:10.1002/hbm.1058

O'Leary, K., Vorpahl, K. A., and Heiderscheit, B. (2008). Effect of Cushioned Insoles on Impact Forces during Running. *J. Am. Podiatr. Med. Assoc.* 98, 36–41. doi:10.7547/0980036

Orendurff, M. S., Kobayashi, T., Tulchin-Francis, K., Tullock, A. M. H., Villarosa, C., Chan, C., et al. (2018). A Little Bit Faster: Lower Extremity Joint Kinematics and Kinetics as Recreational Runners Achieve Faster Speeds. *J. Biomech.* 71, 167–175. doi:10.1016/j.jbiomech.2018.02.010

Paquette, M. R., Zhang, S., and Baumgartner, L. D. (2013). Acute Effects of Barefoot, Minimal Shoes and Running Shoes on Lower Limb Mechanics in Rear and Forefoot Strike Runners. *Footwear Sci.* 5, 9–18. doi:10.1080/19424280.2012.692724

Phan, X., Grisbrook, T. L., Wernli, K., Stearne, S. M., Davey, P., and Ng, L. (2017). Running Quietly Reduces Ground Reaction Force and Vertical Loading Rate and Alters Foot Strike Technique. *J. Sports Sci.* 35, 1–7. doi:10.1080/02640414.2016.1227466

Pink, M., Perry, J., Houglum, P. A., and Devine, D. J. (1994). Lower Extremity Range of Motion in the Recreational Sport Runner. *Am. J. Sports Med.* 22, 541–549. doi:10.1177/036354659402200418

Richert, F. C., Stein, T., Ringhof, S., and Stetter, B. J. (2019). The Effect of the Heel-To-Toe Drop of Standard Running Shoes on Lower Limb Biomechanics. *Footwear Sci.* 11, 161–170. doi:10.1080/19424280.2019.1630016

Rixe, J. A., Gallo, R. A., and Silvis, M. L. (2012). The Barefoot Debate. *Curr. Sports Med. Rep.* 11, 160–165. doi:10.1249/JSR.0b013e31825640a6

Roy, J.-P. R., and Stefanyshyn, D. J. (2006). Shoe Midsole Longitudinal Bending Stiffness and Running Economy, Joint Energy, and EMG. *Med. Sci. Sports Exerc.* 38, 562–569. doi:10.1249/01.mss.0000193562.22001.e8

Sinclair, J., Taylor, P. J., Edmundson, C. J., Brooks, D., and Hobbs, S. J. (2013a). The Influence of Footwear Kinetic, Kinematic and Electromyographical Parameters on the Energy Requirements of Steady State Running. *Mov Sport Sci/sci Mot.* 80, 39–49. doi:10.1051/sm/2012025

Sinclair, J., Greenhalgh, A., Brooks, D., Edmundson, C. J., and Hobbs, S. J. (2013b). The Influence of Barefoot and Barefoot-Inspired Footwear on the Kinetics and Kinematics of Running in Comparison to Conventional Running Shoes. *Footwear Sci.* 5, 45–53. doi:10.1080/19424280.2012.693543

Smith, G., Lake, M., and Lees, A. (2014). Metatarsophalangeal Joint Function during Sprinting: A Comparison of Barefoot and Sprint Spike Shod Foot Conditions. *J. Appl. Biomech.* 30, 206–212. doi:10.1123/jab.2013-0072

Squadrone, R., and Gallozzi, C. (2009). Biomechanical and Physiological Comparison of Barefoot and Two Shod Conditions in Experienced Barefoot Runners. *J. Sports Med. Phys. Fitness* 49, 6–13.

Stefanyshyn, D. J., and Nigg, B. M. (2000). Influence of Midsole Bending Stiffness on Joint Energy and Jump Height Performance. *Med. Sci. Sports Exerc.* 32, 471–476. doi:10.1097/00005768-200002000-00032

Taunton, J. E., Ryan, M. B., Clement, D. B., McKenzie, D. C., Lloyd-Smith, D. R., and Zumbo, B. D. (2002). A Retrospective Case-Control Analysis of 2002 Running Injuries. *Br. J. Sports Med.* 36, 95–101. doi:10.1136/bjsm.36.2.95

Trama, R., Hautier, C., and Blache, Y. (2021). fctSnPM: Factorial ANOVA and post-hoc Tests for Statistical nonParametric Mapping in MATLAB. *Joss* 6, 3159. doi:10.21105/joss.03159

Van Oeveren, B. T., De Ruiter, C. J., Beek, P. J., and van Dieën, J. H. (2017). Optimal Stride Frequencies in Running at Different Speeds. *PLoS One* 12, e0184273–13. doi:10.1371/journal.pone.0184273

Willson, J. D., Bjorhus, J. S., Williams, D. S. B., Butler, R. J., Porcari, J. P., and Kernozek, T. W. (2014). Short-Term Changes in Running Mechanics and Foot Strike Pattern after Introduction to Minimalistic Footwear. *PM&R* 6, 34–43. doi:10.1016/j.pmrj.2013.08.602

Willwacher, S., König, M., Potthast, W., and Brüggemann, G.-P. (2013). Does Specific Footwear Facilitate Energy Storage and Return at the Metatarsophalangeal Joint in Running?. *J. Appl. Biomech.* 29, 583–592. doi:10.1123/jab.29.5.583

Willy, R. W., and Davis, I. S. (2014). Kinematic and Kinetic Comparison of Running in Standard and Minimalist Shoes. *Med. Sci. Sports Exerc.* 46, 318–323. doi:10.1249/MSS.0b013e3182a595d2

Yan, A. F., Sinclair, P. J., Hiller, C., Wegener, C., and Smith, R. M. (2013). Impact Attenuation during Weight Bearing Activities in Barefoot vs. Shod Conditions: A Systematic Review. *Gait & Posture* 38, 175–186. doi:10.1016/j.gaitpost.2012.11.017

Yu, P., Gong, Z., Meng, Y., Baker, J. S., István, B., and Gu, Y. (2020). The Acute Influence of Running-Induced Fatigue on the Performance and Biomechanics of a Countermovement Jump. *Appl. Sci.* 10, 1–15. doi:10.3390/app10124319

Yu, P., Liang, M., Fekete, G., Baker, J. S., and Gu, Y. (2021). Effect of Running-Induced Fatigue on Lower Limb Mechanics in Novice Runners. *Thc* 29, 231–242. doi:10.3233/THC-202195

Zhu, Z., Fu, W., Shao, E., Li, L., Song, L., Wang, W., et al. (2020). Acute Effects of Midsole Bending Stiffness on Lower Extremity Biomechanics during Layup Jumps. *Appl. Sci.* 10, 1–10. doi:10.3390/app10010397

Conflict of Interest: The authors declare that the research was conducted in the absence of any commercial or financial relationships that could be construed as a potential conflict of interest.

Publisher's Note: All claims expressed in this article are solely those of the authors and do not necessarily represent those of their affiliated organizations, or those of the publisher, the editors, and the reviewers. Any product that may be evaluated in this article, or claim that may be made by its manufacturer, is not guaranteed or endorsed by the publisher.

frontiers in Bioengineering and Biotechnology

ORIGINAL RESEARCH
published: 09 February 2022
doi: 10.3389/fbioe.2022.824297

Effects of Attrition Shoes on Kinematics and Kinetics of Lower Limb Joints During Walking

Shane Fei Chen[1], *Yan Wang*[1,2], *Yinghu Peng*[1] *and Ming Zhang*[1,2]*

[1]Department of Biomedical Engineering, Faculty of Engineering, The Hong Kong Polytechnic University, Hong Kong, Hong Kong SAR, China, [2]Hong Kong Polytechnic University Shenzhen Research Institute, Shenzhen, China

Shoe attrition is inevitable as wearing time increases, which may produce diverse influences on kinematics and kinetics of lower limb joints. Excessive attrition may change support alignment and lead to deleterious impacts on the joints. The study identifies the biomechanical influences of aging shoes on lower limb joints. The shoes in the experiment were manually worn in the lateral heel. Nineteen healthy participants, including thirteen males and six females, were recruited to conduct walking experiments wearing attrition shoes (AS) and new shoes (NS) with a random order. A Vicon motion analysis system was used to collect kinematic data and ground reaction force. Kinematic and kinetic parameters of the hip, knee, and ankle joints were calculated using the Anybody Musculoskeletal Model and compared between the two conditions, AS and NS. The results showed that wearing an attrition shoe decreased the plantarflexion angle and plantarflexion moment of the ankle joint, while significantly increasing the magnitude of the first peak of the knee adduction moment and hip abduction moment and hip internal rotation moment ($p < .05$). The results of the study implied that wearing attrition shoes is not recommended for those people with knee problems due to increase in medial loading.

Keywords: attrition shoes, lower extremity, multibody calculation, motion analysis, joint biomechanics

OPEN ACCESS

Edited by:
Lizhen Wang,
Beihang University, China

Reviewed by:
Qichang Mei,
Ningbo University, China
Yaodong Gu,
Ningbo University, China

***Correspondence:**
Ming Zhang
ming.zhang@polyu.edu.hk

Specialty section:
This article was submitted to Biomechanics, a section of the journal Frontiers in Bioengineering and Biotechnology

Received: *29 November 2021*
Accepted: *17 January 2022*
Published: *09 February 2022*

Citation:
Chen SF, Wang Y, Peng Y and Zhang M (2022) Effects of Attrition Shoes on Kinematics and Kinetics of Lower Limb Joints During Walking. Front. Bioeng. Biotechnol. 10:824297. doi: 10.3389/fbioe.2022.824297

INTRODUCTION

Footwear is designed to protect humans from injuries in different environments (Barton et al., 2009) and provide assistance in motion control and attenuation of impact forces in daily activities. Shoes affect kinematics with a limitation of eversion and inversion range of motion of lower limb joints during walking (Morio et al., 2009; Sun et al., 2020; Dempster et al., 2021). However, aging attrition shoes (Moghaddam et al., 2019) change the plantar support surface and may affect the kinematics and kinetics of the lower limb, which might be related to joint injuries (Taunton et al., 2003; Ramsey et al., 2019). Compared with new shoes, worn shoes with decreasing cushioning capability lead to an increase of stance time and kinematic adaptational changes (Kong et al., 2009). Worn shoes were also demonstrated to increase energy cost and risk of injuries (Ramsey et al., 2018) and decrease lower limb stability (Saito et al., 2007). Footwear was found to reduce the external loading rate to protect lower limbs from injuries (Altman and Davis, 2016) and designed to reduce the knee adduction moment (Fisher et al., 2007; Peng et al., 2020) to relieve medial knee pain. Lateral-wedged insoles or shoes with a certain degree of inclination to the medial were normally adopted to be the interventions to decrease the first peak knee adduction moment that was beneficial to patients with medial knee osteoarthritis (Radzimski et al., 2012; Felson et al., 2019; Sinclair and Stainton, 2019).

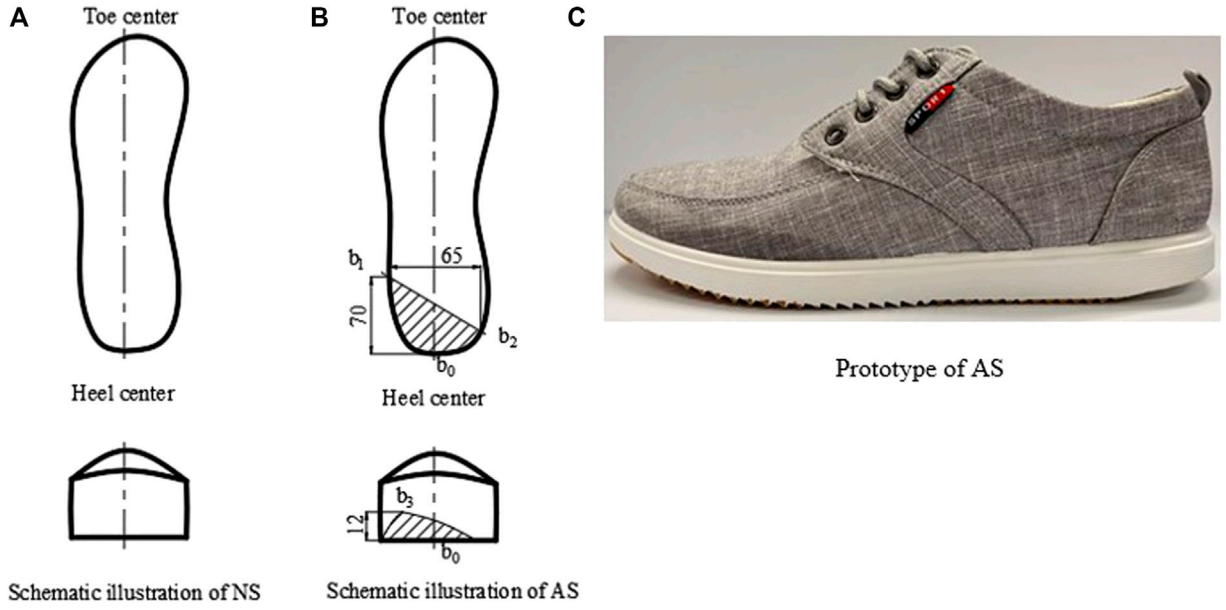

FIGURE 1 | Scheme of shoe conditions. **(A)** Schematic illustration of NS. **(B)** Schematic illustration of AS. **(C)** Prototype of AS.

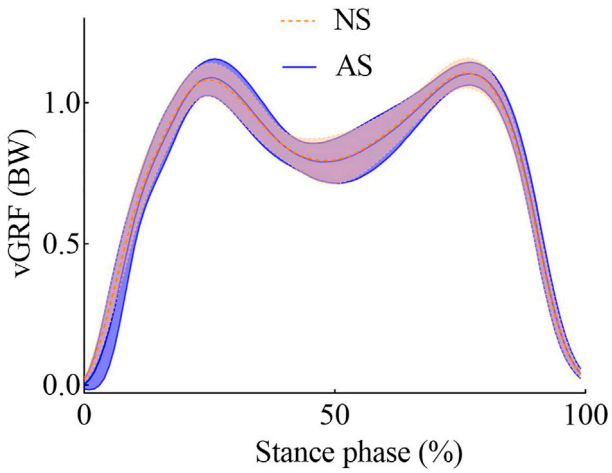

FIGURE 2 | Vertical GRF for NS and AS during stance.

TABLE 1 | Peak angles of lower limb joints for NS and AS during stance (°).

Parameter	NS mean (SD)	AS mean (SD)	*p*-values	P*
Hip				
flexion	26.199 (3.639)	26.270 (3.672)	0.761	0.027
extension	−14.587 (3.246)	−14.611 (3.509)	0.923	0.041
external	14.284 (4.211)	14.313 (4.330)	0.947	0.050
rotation				
internal rotation	4.708 (6.133)	5.283 (6.782)	0.141	0.014
abduction	3.199 (2.468)	3.235 (2.326)	0.822	0.032
adduction	−4.384 (2.091)	−4.372 (1.861)	0.946	0.045
Knee				
flexion	45.461 (5.358)	45.357 (4.665)	0.864	0.036
Ankle				
eversion	−5.213 (11.201)	−6.053 (10.003)	0.230	0.018
inversion	−23.019 (11.700)	−23.415 (11.626)	0.578	0.023
dorsiflexion	24.499 (2.534)	25.651 (3.339)	0.057	0.009
plantarflexion	−2.466 (2.506)	−0.828 (3.336)	0.027	0.005

Significant difference at p-value < P* *when walking with AS was compared with walking with NS.*

Patterns of shoe attrition could be classified into lateral, medial, and central degradation (Baumfeld et al., 2015). Lateral heel degradation was found to be the most popular pattern according to a measurement of over 200 shoes, with an average shoe age of almost a year (Sole et al., 2014). In an assessment of 76 participants (Finestone et al., 2012), most of the outsole abrasion presented a posterolateral pattern with an average of 12° and 5 cm^3 abrasion volume. There is lack of studies to understand the biomechanical effects of shoe abrasion on lower limb biomechanics.

This study aimed to identify the immediate effects of worn shoes on kinematics and kinetics of the lower limb. As the most popular worn pattern, lateral heel attrition with mediolateral asymmetry was set as the experimental condition. It is hypothesized that lateral heel attrition would increase the knee adduction moments.

METHODS

Participants

Nineteen participants were recruited to participate in the study. This sample size was estimated using G*power 3.0.10, Universität

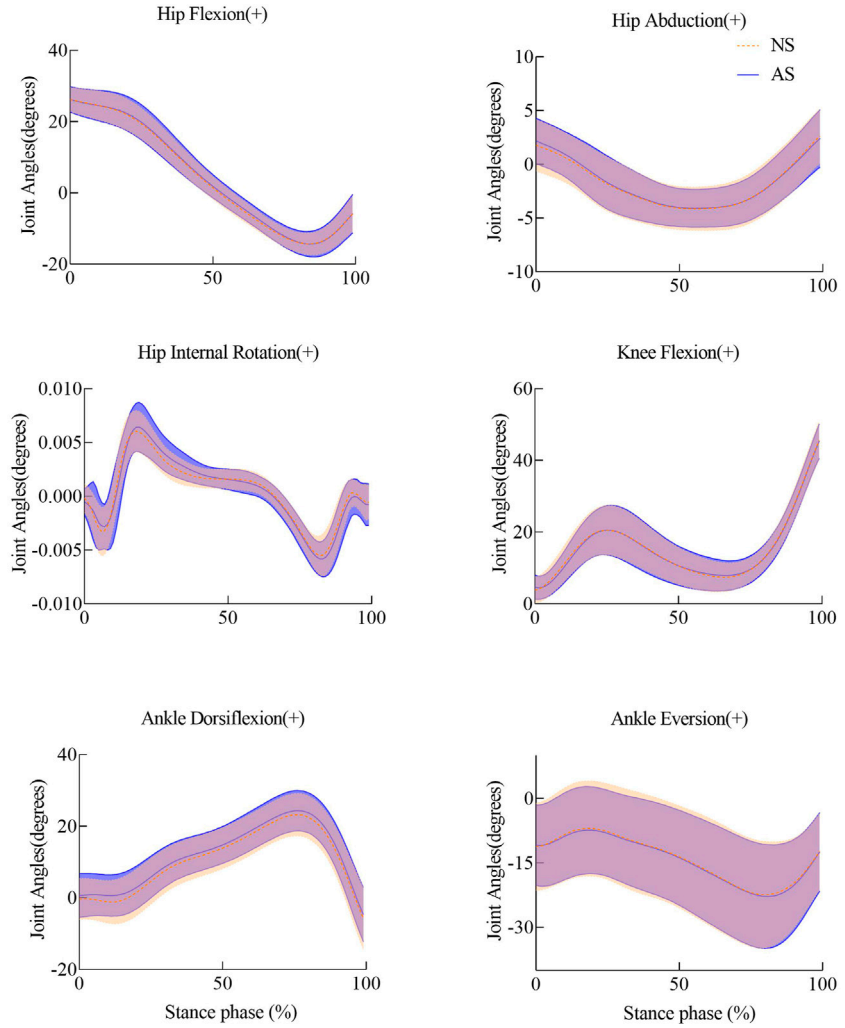

FIGURE 3 | Joint angles of lower extremities with shade ± 1 std for NS and AS during the stance phase.

Düsseldorf, Germany, and the minimum sample size was 15 with a significant level of 0.05 and a statistical level of 0.8. The medium effect size of 0.8 was adopted in the sample size calculation. The average age of participants was 25 ± 5 years. The means and standard deviations of body mass and height were 69.5 ± 12.2 kg and 173.6 ± 9.3 cm, respectively. All participants had no histories of lower extremity injuries during the experiments. This study was approved by the Human Participants Ethics Sub-Committee of The Hong Kong Polytechnic University (Number: HSEARS20150121003). Informed consent was obtained from all participants before experiments.

Footwear Conditions

Canvas shoes were adopted for the preparation of non-attrition (new shoes, NS) and attrition shoes (attrition shoes, AS). Attrition shoes (AS) with lateral worn heels were adopted, which is the most popular attrition pattern (Finestone et al., 2012; Sole et al., 2014). As shown in **Figure 1B**, the degree of attrition was measured by the length of two lines, where one is the line connecting the lateral attrition point b_1 and heel center b_0 and the other is the line connecting the lateral attrition point b_1 and the other attrition point b_2. The maximum attrition position is at point b_3 in the lateral heel portion, as shown in **Figure 1B**. A prototype of AS is shown in **Figure 1C**.

Experiment Setup and Procedure

A Vicon motion capture system with eight cameras (Vicon, Oxford Metrics Ltd., Oxford, England) was used to collect motion data at 150 Hz, and two force platforms (OR6, AMTI, Watertown, United States) were used to measure the ground reaction force (GRF) at 1000 Hz. The participants wore tight-fitting clothes, and reflective markers were attached on bony landmarks to define the lower limb into seven segments. The marker set followed a previous study (Peng et al., 2020). The participants were required to walk for a few minutes to accommodate each pair of shoes in random order. They were required to walk at their natural walking speed during the walking trials. Each participant completed three successful trials with each condition of shoes.

TABLE 2 | Peak moments of lower limb joints for NS and AS during stance (BW and·BH).

Parameter	NS mean (SD)	AS mean (SD)	*p*-value	P*
Hip				
flexion rotation	0.044 (0.012)	0.043 (0.012)	0.443	0.039
extension rotation	−0.035 (0.012)	−0.038 (0.014)	0.130	0.022
external rotation	0.006 (0.002)	0.007 (0.002)	0.062	0.017
internal rotation	−0.005 (0.002)	−0.006 (0.002)	0.000[1]	0.003
first abduction	0.046 (0.008)	0.047 (0.008)	0.049	0.014
second abduction	0.043 (0.008)	0.045 (0.008)	0.004[1]	0.006
Knee				
Flexion	0.033 (0.016)	0.034 (0.015)	0.286	0.033
extension	−0.015 (0.009)	−0.014 (0.009)	0.064	0.019
external rotation	0.001 (0.001)	0.001 (0.001)	0.982	0.050
internal rotation	−0.002 (0.001)	−0.002 (0.001)	0.186	0.028
first adduction	−0.024 (0.004)	−0.026 (0.004)	0.006[1]	0.008
second adduction	−0.020 (0.006)	−0.021 (0.005)	0.310	0.036
Ankle				
eversion	0.018 (0.007)	0.019 (0.008)	0.173	0.025
inversion	−0.005 (0.001)	−0.005 (0.001)	0.816	0.044
external rotation	0.003 (0.001)	0.003 (0.001)	0.452	0.042
internal rotation	−0.008 (0.002)	−0.008 (0.002)	0.926	0.047
dorsiflexion	0.090 (0.008)	0.089 (0.007)	0.233	0.031
plantarflexion	−0.008 (0.002)	−0.007 (0.003)	0.011[1]	0.011

[1]*Significant difference at* p-*value < P* when walking with AS was compared with walking with NS.*

Musculoskeletal Model

The lower limb musculoskeletal (MSK) model using the Anybody Modeling System (version 6.0.3, AnyBody Technology, Aalborg, Denmark) was used in this study. The generic MSK model was based on the anthropometric database of the Twente Lower Extremity Model (TLEM 1.1) (Klein Horsman et al., 2007). The experimental data provided input for the MSK model to calculate the kinematics and kinetics of the lower extremity joints (Peng et al., 2018). The marker trajectory data and anthropometrics for each participant were used to optimize the MSK model, and then, kinematic parameters of the lower limb joints were calculated. After the kinematical calculation, inverse dynamic calculation was conducted to obtain kinetics of the joints.

Statistical Analysis

SPSS (Version 22.0, IBM, Chicago, IL, United States) was used to perform statistical analysis. Peak values of angles and moments of ankle, knee, and pelvis joints and vertical GRF were extracted for statistical analysis of the two conditions. The joint moments were normalized with body weight and body height (BW and·BH) (Peng et al., 2020). Mean values of all variables were calculated from three successful trials of each shoe condition for each participant. The data distribution was testified to be normal when the Shapiro–Wilk test with significance level 0.05 was performed. Post hoc paired t-tests with Benjamini–Hochberg adjustment (P*) were conducted to determine the relationship between the two conditions with a significance level of 0.05.

RESULTS

Figure 2. shows the mean vertical GRF during the stance phase. The vertical GRFs were normalized by the body weight. Mean vertical GRF for different shoe conditions was calculated and showed no statistical difference with $p > .05$.

The mean and standard deviation (SD) of peak angles of lower extremity joints for the two conditions for all participants are listed in **Table 1**. Joint angles of lower extremities showed no significant difference during the stance phase shown in **Figure 3**.

The joint moments were normalized by dividing the body weight and body height (BW and·BH) of each participant. Details of joint moments are shown in **Table 2**. The amplitudes of the hip internal rotation moment and the second hip abduction moment increased significantly in the AS group. The first peak of the knee adduction moment for the AS group revealed an increase of 8.3% compared with that of the NS group. The peak moments of the ankle joint showed a slight decrease. Joint moments during the stance phase are shown in **Figure 4**.

DISCUSSION

In this study, the effects of attrition shoes on lower limb joints were revealed by comparing them with those of new shoes during walking. Joint angles showed no significant effects, but some of joint moments of the lower limb displayed significant changes. The amplitudes of the ankle plantarflexion moment decrease significantly in the AS group as compared to those of the NS group. However, the amplitudes of the second hip abduction moment and internal rotation moment increased significantly when participants wore attrition shoes. Meanwhile, the first peak of the knee adduction moment revealed a significant increase of 8.3% when the AS group was compared with the NS group.

For the ankle joint, though the amplitude of the plantarflexion angle showed no significant effects, it tends to decrease while walking in worn shoes. Meanwhile, the amplitude of the plantarflexion moment showed a slightly significant decrease. AS lack one wedge part in the lateral heel, which prolongs the onset of heel strike. Thus, it leads to a shortening time for the plantarflexion. The duration of the plantarflexion is decreased, which makes the foot dorsiflexion quick. However, during the loading phase, the plantarflexion of the ankle joint provides eccentric contraction for the tibialis anterior muscle (Jafarnezhadgero et al., 2020). The reduction of the plantarflexion would cause the tibialis anterior muscle to provide less contraction force, which results in larger landing impact. The lateral heel attrition shifts the contact center anteriorly, which reduces the lever arm that lowers. The reduction of the lever led to decrease of the peak of the plantarflexion moment as shown in **Figure 4**. Insufficient plantarflexion moment may generate a more flattening longitudinal arch (Kirby, 2017), which would lead to an increase of tensional force in the plantar fascia that has been reported to be one of the causes of ankle pain (Kogler et al.,

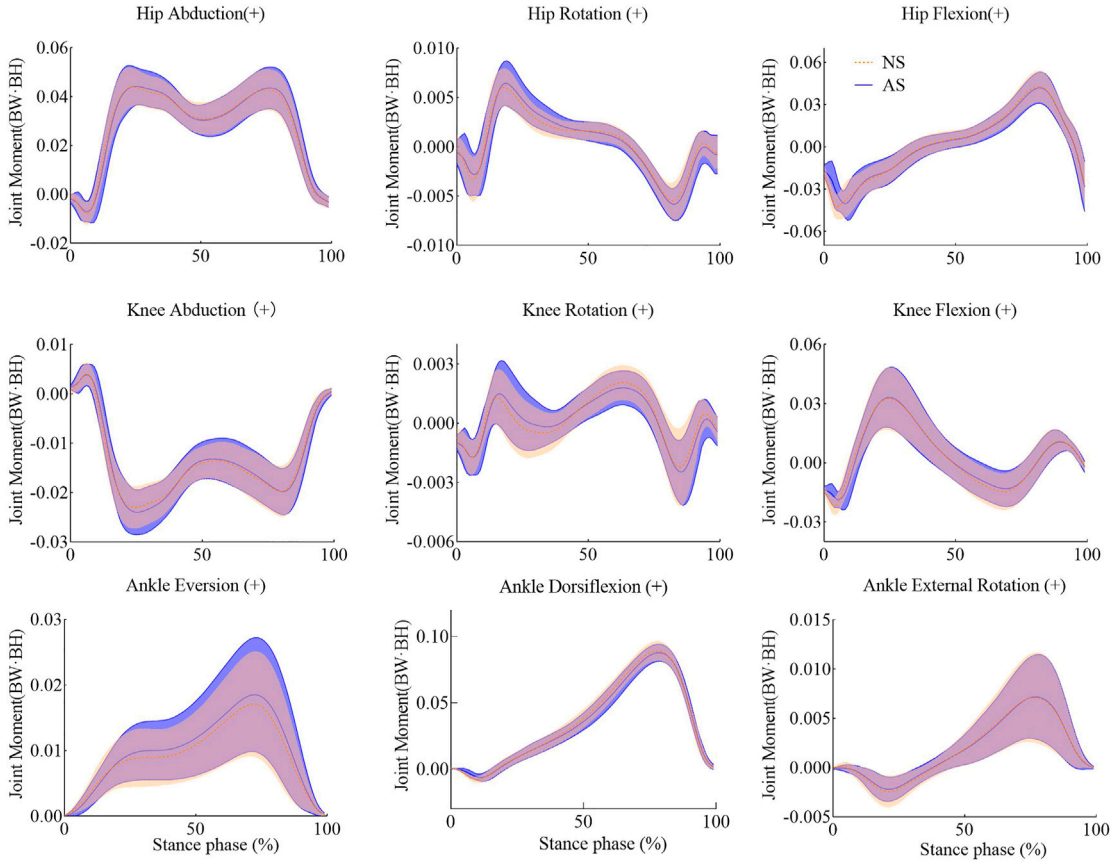

FIGURE 4 | Joint moments of lower extremities with shade ± 1 std for NS and AS during the stance phase.

1996). Furthermore, the plantarflexion moment plays an important role in counterbalance (Kirby, 2017). Previous studies have indicated that plantarflexors regulate whole-body angular momentum in the sagittal plane during balance control (Neptune and Mcgowan, 2011), and fallers created a decreased plantarflexion moment compared to non-fallers (Barak et al., 2006). Consequently, the lack of plantarflexion moment in the AS group may also cause problems in balance.

Kinematic parameters of knee joints show no significant differences between the NS group and AS group. However, the first peak of the knee adduction moment increases by 8.3% with a significant level of p = .006, as shown in **Table 2** and **Figure 4**. Since the attrition concentrates on the lateral heel, there is no significant effect in the second peak of the knee adduction moment. Wedge soles are often adopted as interventions for knee osteoarthritis (OA) (Desmyttere et al., 2018). Although the attrition outsole in this study is not exactly like wedge outsoles, the heel of AS displays the same appearance with medial wedges to a certain degree. The increase of the amplitude of the knee adduction moment agrees with that found in the previous studies (Lewinson et al., 2013; Peng et al., 2020), which illustrates that the peak knee adduction moment increases as the wedge develops from lateral to medial. On the contrary, lateral wedges are beneficial for participants with medial knee OA patients because they can reduce the peak of the knee adduction moment; the AS is disagreeable for them as it increases the knee adduction moment. Higher knee adduction moment has also been reported to have a relationship with the development of knee pain (Mai and Willwacher, 2019). Consequently, the aging shoes are also not suitable for participants with knee pain.

Aging shoes make an impact on the kinetics of the hip joint. For the AS group, the peak moments of the hip internal rotation and abduction increase significantly when compared with the NS group as illustrated in **Table 2** and **Figure 4**. Aging shoes were found to lower activities of the vastus medialis and rectus femoris muscles and strengthen the activity of the gluteus medius muscle during the loading phase while walking (Jafarnezhadgero et al., 2020). The activities of these muscles may lead to increase of hip internal rotation and abduction moments. Furthermore, the increase of the hip internal rotation moment may cause abnormal hip motions (Weidow et al., 2006), which may change the rotational alignment of other segments in the lower limb.

A few limitations in the study should be discussed. The present study examines the immediate effect of shoe degradation on

lower limb joints. However, the wear of shoes was a persistent behavior, of which impact is gradual. Canvas shoes with flat outsoles were adopted in this study, but other types of shoes were not explored. The lateral heel of shoes was worn mechanically, which may have slight differences with naturally worn shoes. The sample size in the study was another limitation. The generalizability of the findings should be noted. Additionally, further research should identify the gender difference in shoe attrition. The effects of other attrition patterns on the lower limb joints require further research.

CONCLUSION

Lateral heel attrition in outsoles is the most common degeneration pattern of shoes. The attrition shoes have significant impacts on the kinematics and kinetics of the lower limb joints. The peak plantarflexion angle and moment of the ankle joint decrease, and the first knee adduction moment and hip internal and abduction moments increase during walking for the AS group. Our findings in this study imply that aging shoes are not desirable, especially for those people with knee problems. Attrition in the heel also raises balance risk. Although the exact abrasion amount in aging shoes is not demonstrated for a shoe change, attrition shoes influence the walking pattern and result in discomfort.

DATA AVAILABILITY STATEMENT

The raw data supporting the conclusion of this article will be made available by the authors, without undue reservation.

ETHICS STATEMENT

The studies involving human participants were reviewed and approved by the Human Participants Ethics Sub-Committee of The Hong Kong Polytechnic University (Number: HSEARS20150121003). The patients/participants provided their written informed consent to participate in this study.

AUTHOR CONTRIBUTIONS

SC: project conception, manuscript draft, and revising. YW: manuscript revising. YP: project conception and manuscript draft. MZ: manuscript revising and supervision.

FUNDING

This study was supported by the National Science Foundation of China (NSFC) (Numbers: 11732015 and 11972315).

REFERENCES

Altman, A. R., and Davis, I. S. (2016). Prospective Comparison of Running Injuries between Shod and Barefoot Runners. *Br. J. Sports Med.* 50, 476–480. doi:10.1136/bjsports-2014-094482

Barak, Y., Wagenaar, R. C., and Holt, K. G. (2006). Gait Characteristics of Elderly People with a History of Falls: a Dynamic Approach. *Phys. Ther.* 86, 1501–1510. doi:10.2522/ptj.20050387

Barton, C. J., Bonanno, D., and Menz, H. B. (2009). Development and Evaluation of a Tool for the Assessment of Footwear Characteristics. *J. Foot Ankle Res.* 2, 1–12. doi:10.1186/1757-1146-2-10

Baumfeld, D., Raduan, F. C., Macedo, B., Silva, T. A. A., Baumfeld, T., Favato, D. F., et al. (2015). Shoe Heel Abrasion and its Possible Biomechanical Cause: a Transversal Study with Infantry Recruits. *J. Orthop. Surg. Res.* 10, 1–5. doi:10.1186/s13018-015-0319-0

Dempster, J., Dutheil, F., and Ugbolue, U. C. (2021). The Prevalence of Lower Extremity Injuries in Running and Associated Risk Factors: A Systematic Review. *Phys. Activity Health* 5, 133–145. doi:10.5334/paah.109

Desmyttere, G., Hajizadeh, M., Bleau, J., and Begon, M. (2018). Effect of Foot Orthosis Design on Lower Limb Joint Kinematics and Kinetics during Walking in Flexible Pes Planovalgus: A Systematic Review and Meta-Analysis. *Clin. Biomech.* 59, 117–129. doi:10.1016/j.clinbiomech.2018.09.018

Felson, D. T., Parkes, M., Carter, S., Liu, A., Callaghan, M. J., Hodgson, R., et al. (2019). The Efficacy of a Lateral Wedge Insole for Painful Medial Knee Osteoarthritis after Prescreening: A Randomized Clinical Trial. *Arthritis Rheumatol.* 71, 908–915. doi:10.1002/art.40808

Finestone, A. S., Petrov, K., Agar, G., Honig, A., Tamir, E., and Milgrom, C. (2012). Pattern of Outsole Shoe Heel Wear in Infantry Recruits. *J. Foot Ankle Res.* 5, 1–7. doi:10.1186/1757-1146-5-27

Fisher, D. S., Dyrby, C. O., Mündermann, A., Morag, E., and Andriacchi, T. P. (2007). In Healthy Subjects without Knee Osteoarthritis, the Peak Knee Adduction Moment Influences the Acute Effect of Shoe Interventions Designed to Reduce Medial Compartment Knee Load. *J. Orthop. Res.* 25, 540–546. doi:10.1002/jor.20157

Jafarnezhadgero, A. A., Anvari, M., and Granacher, U. (2020). Long-term Effects of Shoe Mileage on Ground Reaction Forces and Lower Limb Muscle Activities during Walking in Individuals with Genu Varus. *Clin. Biomech.* 73, 55–62. doi:10.1016/j.clinbiomech.2020.01.006

Kirby, K. A. (2017). Longitudinal Arch Load-Sharing System of the Foot. *Revista Española de Podología* 28, e18–e26. https://docs.vicon.com/pages/viewpage.action?pageId=50888852. doi:10.1016/j.repod.2017.03.003

Klein Horsman, M. D., Koopman, H. F. J. M., Van Der Helm, F. C. T., Prosé, L. P., and Veeger, H. E. J. (2007). Morphological Muscle and Joint Parameters for Musculoskeletal Modelling of the Lower Extremity. *Clin. Biomech.* 22, 239–247. doi:10.1016/j.clinbiomech.2006.10.003

Kogler, G., Solomonidis, S., and Paul, J. (1996). Biomechanics of Longitudinal Arch Support Mechanisms in Foot Orthoses and Their Effect on Plantar Aponeurosis Strain. *Clin. Biomech.* 11, 243–252. doi:10.1016/0268-0033(96)00019-8

Kong, P. W., Candelaria, N. G., and Smith, D. R. (2009). Running in New and Worn Shoes: a Comparison of Three Types of Cushioning Footwear. *Br. J. Sports Med.* 43, 745–749. doi:10.1136/bjsm.2008.047761

Lewinson, R. T., Fukuchi, C. A., Worobets, J. T., and Stefanyshyn, D. J. (2013). The Effects of Wedged Footwear on Lower Limb Frontal Plane Biomechanics during Running. *Clin. J. Sport Med.* 23, 208–215. doi:10.1097/jsm.0b013e31826b7c83

Mai, P., and Willwacher, S. (2019). Effects of Low-Pass Filter Combinations on Lower Extremity Joint Moments in Distance Running. *J. Biomech.* 95, 109311. doi:10.1016/j.jbiomech.2019.08.005

Moghaddam, S. R. M., Hemler, S. L., Redfern, M. S., Jacobs, T. D. B., and Beschorner, K. E. (2019). Computational Model of Shoe Wear Progression: Comparison with Experimental Results. *Wear* 422-423, 235–241. doi:10.1016/j.wear.2019.01.070

Morio, C., Lake, M. J., Gueguen, N., Rao, G., and Baly, L. (2009). The Influence of Footwear on Foot Motion during Walking and Running. *J. Biomech.* 42, 2081–2088. doi:10.1016/j.jbiomech.2009.06.015

Neptune, R. R., and Mcgowan, C. P. (2011). Muscle Contributions to Whole-Body Sagittal Plane Angular Momentum during Walking. *J. Biomech.* 44, 6–12. doi:10.1016/j.jbiomech.2010.08.015

Peng, Y., Wong, D. W.-C., Wang, Y., Chen, T. L.-W., Tan, Q., Chen, Z., et al. (2020). Immediate Effects of Medially Posted Insoles on Lower Limb Joint Contact Forces in Adult Acquired Flatfoot: A Pilot Study. *Ijerph* 17, 2226. doi:10.3390/ijerph17072226

Peng, Y., Zhang, Z., Gao, Y., Chen, Z., Xin, H., Zhang, Q., et al. (2018). Concurrent Prediction of Ground Reaction Forces and Moments and Tibiofemoral Contact Forces during Walking Using Musculoskeletal Modelling. *Med. Eng. Phys.* 52, 31–40. doi:10.1016/j.medengphy.2017.11.008

Radzimski, A. O., Mündermann, A., and Sole, G. (2012). Effect of Footwear on the External Knee Adduction Moment - A Systematic Review. *The Knee* 19, 163–175. doi:10.1016/j.knee.2011.05.013

Ramsey, C. A., Cury Ribeiro, D., Lamb, P., Sole, C. C., and Sole, G. (2018). Reliability of the Footwear Total Asymmetry Score Tool. *Footwear Sci.* 10, 119–128. doi:10.1080/19424280.2018.1478888

Ramsey, C. A., Lamb, P., Kaur, M., Baxter, G. D., and Ribeiro, D. C. (2019). "How Are Running Shoes Assessed? A Systematic Review of Characteristics and Measurement Tools Used to Describe Running Footwear". *J. Sports Sci.* 37, 1617–1629. doi:10.1080/02640414.2019.1578449

Saito, S., Muraki, S., and Tochihara, Y. (2007). Effects of Worn-Out Soles on Lower Limb Stability, Shock Absorption and Energy Cost during Prolonged Walking. *J. Physiol. Anthropol.* 26, 521–526. doi:10.2114/jpa2.26.521

Sinclair, J., and Stainton, P. (2019). Effects of Medial and Lateral Wedged Orthoses on Knee and Ankle Joint Loading in Female Runners. *Kinesiology (Zagreb, Online)* 51, 189–197. doi:10.26582/k.51.2.9

Sole, C. C., Milosavljevic, S., Sole, G., and Sullivan, S. J. (2014). Patterns of Mediolateral Asymmetry in Worn Footwear. *Footwear Sci.* 6, 177–192. doi:10.1080/19424280.2014.913694

Sun, D., Fekete, G., Baker, J. S., and Gu, Y. (2020). Foot Motion Character during Forward and Backward Walking with Shoes and Barefoot. *J. Mot. Behav.* 52, 214–225. doi:10.1080/00222895.2019.1605972

Taunton, J. E., Ryan, M. B., Clement, D. B., Mckenzie, D. C., Lloyd-Smith, D. R., and Zumbo, B. D. (2003). A Prospective Study of Running Injuries: the Vancouver Sun Run "In Training" Clinics. *Br. J. Sports Med.* 37, 239–244. doi:10.1136/bjsm.37.3.239

Weidow, J., Tranberg, R., Saari, T., and Kärrholm, J. (2006). Hip and Knee Joint Rotations Differ between Patients with Medial and Lateral Knee Osteoarthritis: Gait Analysis of 30 Patients and 15 Controls. *J. Orthop. Res.* 24, 1890–1899. doi:10.1002/jor.20194

Conflict of Interest: The authors declare that the research was conducted in the absence of any commercial or financial relationships that could be construed as a potential conflict of interest.

frontiers in Bioengineering and Biotechnology

ORIGINAL RESEARCH
published: 21 February 2022
doi: 10.3389/fbioe.2022.820921

Optimal Design and Biomechanical Analysis of a Biomimetic Lightweight Design Plate for Distal Tibial Fractures: A Finite Element Analysis

Mian Wang[1,2†], Yuping Deng[1,2,3†], Pusheng Xie[1,4], Jinchuan Tan[1], Yang Yang[1,3], Hanbin Ouyang[1,5], Dongliang Zhao[2,6], Gang Huang[3] and Wenhua Huang[1,3,4]**

[1]National Key Discipline of Human Anatomy, Guangdong Provincial Key Laboratory of Medical Biomechanics, Guangdong Engineering Research Center for Translation of Medical 3D Printing Application, School of Basic Medical Sciences, Southern Medical University, Guangzhou, China, [2]Institute of Biomedical Engineering, Shenzhen Bay Laboratory, Shenzhen, China, [3]Department of Orthopedics and Traumatology, Integrated Hospital of Traditional Chinese Medicine, Southern Medical University, Guangzhou, China, [4]Guangdong Medical Innovation Platform for Translation of 3D Printing Application, The Third Affiliated Hospital of Southern Medical University, Guangzhou, China, [5]Orthopaedic Center, Affiliated Hospital of Guangdong Medical University, Guangdong Medical University, Zhanjiang, China, [6]Drug Discovery Center, State Key Laboratory of Chemical Oncogenomics, School of Chemical Biology and Biotechnology, Peking University Shenzhen Graduate School, Shenzhen, China

OPEN ACCESS

Edited by:
Lizhen Wang,
Beihang University, China

Reviewed by:
Ginu Unnikrishnan,
Intelligent Automation, United States
Yongchang Gao,
Chang'an University, China
Zhongmin Jin,
Southwest Jiaotong University, China

***Correspondence:**
Gang Huang
huanggang@smu.edu.cn
Wenhua Huang
Orthobiomech@163.com

[†]These authors have contributed equally to this work and share first authorship

Specialty section:
This article was submitted to Biomechanics, a section of the journal Frontiers in Bioengineering and Biotechnology

Received: 23 November 2021
Accepted: 27 January 2022
Published: 21 February 2022

Citation:
Wang M, Deng Y, Xie P, Tan J, Yang Y, Ouyang H, Zhao D, Huang G and Huang W (2022) Optimal Design and Biomechanical Analysis of a Biomimetic Lightweight Design Plate for Distal Tibial Fractures: A Finite Element Analysis. Front. Bioeng. Biotechnol. 10:820921. doi: 10.3389/fbioe.2022.820921

The treatment of fractures of the distal tibia can be problematic due to the insubstantial soft-tissue covering this part of the anatomy. This study investigates a novel strategy for minimally invasive plate osteosynthesis of distal tibia fractures called bionic lightweight design plating. Following the structure of the animal trabecular bone, we utilized topological mathematical methods to redesign the material layout of the internal fixation device to fulfill the desired lightweight design within given boundary conditions. The results showed that this method can maintain the same stability of the construct as the original plate after a reduction in the original volume by 30%, and the differences in strain energy of plates and maximum node displacement of constructs between the constructs [RP construct *vs.* LP construct] were not statistically significant ($p > 0.05$). In the safety assessment of the constructs, the peak stress of plates between constructs was found to not be statistically significantly different under a doubled physiological load ($p > 0.05$). The average stress of the plates' elements exceeding the allowable stress was analyzed, and no statistically significant differences were found between the two constructs under axial compression stress conditions ($p > 0.05$). The average stress of the plates' elements in the redesigned plating construct under torsional stress conditions was 3.08% less than that of the locked plating construct ($p < 0.05$). Under the double physiological load condition, 89% of the elements of the plate in the redesigned plating construct and 85% of the elements of the plate in the locked plating construct were lower than the maximum safe stress of the plate, which was 410 MPa (secondary allowable stresses). That reminds us the topology optimization offer a possible way to improve the capacity of soft tissue protection while ensuring the safety of the RP construct by reducing the volume of the implants.

Keywords: distal tibial fractures, internal fixation, low-profile, plate topology optimization

INTRODUCTION

The incidence of distal tibia fracture is high, and it is one of the most common long bone fractures (Court-Brown and McBirnie, 1995; Weiss et al., 2009; Vaienti et al., 2019). Such fractures usually lead to the stripping of the periostea, poor soft-tissue blood supply, and severe trauma to the surrounding soft tissue structures because of its relative thinness. Open reduction and internal fixation (ORIF) surgery is suitable for most types of fractures and fracture types that require fine reduction, at the cost of more extensive soft tissue dissection and blood supply effects. In cases of unhealthy soft tissue at the anterior tibia, ORIF surgery on the tibia distal segment can cause increased rates of nonunion, deep infections (Sirkin et al., 2004), and surgical wound dehiscence (Teeny and Wiss, 1993; Sheerin et al., 2006; Vidović et al., 2015). This is true even in a staged approach, which is considered to be an effective way of handling soft tissues (Sheerin et al., 2006; Chan et al., 2017) for distal tibia fractures through temporized treatment. Such techniques protect the affected tissue from iatrogenic trauma through delayed or elective surgery; however, they can also lead to poor outcomes due to the necrosis of the edges of the operative wounds and higher rates of infection following surgical delays greater than 7 days (Mont et al., 1992). However, the timing of surgery in the setting of fractures still largely relies on the experience of the orthopedist (Chou and Lee, 2009).

Work has been underway to develop plating technologies for soft tissue protection (Krackhardt et al., 2005; Pallister and Iorwerth, 2005; Namazi and Mozaffarian, 2007; Cheng et al., 2011; Zhou et al., 2015). However, these efforts have not yielded clinically viable solutions. For example, a minimally invasive plate osteosynthesis (MIPO) technique, based on the less invasive stabilization system and the locking compression plate system, has been developed that enables indirect reduction and stable fixation with minimal surgical trauma relative to ORIF (Vidović et al., 2015). MIPO provides indirect reduction of and minimizes trauma to the soft tissue and maintains the periosteal blood supply, so it should provide undisturbed union and a low rate of complications. However, in distal tibial fractures, reports of delayed union, malunion, skin impingement, and saphenous nerve and vein injury continue to appear with the use of MIPO (Khoury et al., 2002; Lau et al., 2008; Cheng et al., 2011). Further, to minimize the surgical trauma, it is nearly impossible to emphasize an anatomic reduction of the articular surface of a distal fracture of the tibia with intra-articular fractures, which are necessary for the treatment of these distal tibial fractures.

The present study established a theoretical model for evaluating the impact of internal fixation on surrounding soft tissues and investigated a novel strategy for the MIPO of distal tibia fractures called here bionic lightweight design plating. Bionic lightweight design plates utilize topological mathematical models of the number and density of the animal trabecular bone structure changing with the stress distributions which redesign the material layout of the address area of the internal fixation device to develop a lightweight design that would be desirable under a series of boundary conditions. Using finite element (FE) methods, the designer can access a wealth of valuable information for use in medical implant redesign with minimal expense of material resources and funds. Although the topological optimization associated with the FE method can generate a new, customized, and optimized plate design for tibia distal fractures, this has not yet been utilized or reported on. We hypothesized that bionic lightweight design optimization plates will reduce the compression of the implant on the soft tissue by reducing the implant volume while retaining construct strength relative to standard locking plates.

MATERIALS AND METHODS

Geometrical Modelling

A tibia structure model was reconstructed using Mimics 14.0 software (Materialise, Leuven, Belgium) from a series of computed tomography images (Optima CT660, GE medical systems, USA) of a healthy 27-year-old male volunteer (with fully understand the purpose of the data and sign the informed consent document). The whole tibia, distal femoral condyle, and proximal talar condyle were scanned. The slice thickness was 1.25 mm and the plane resolution was 512 × 512 pixels. All procedures were approved by the Ethical Inspection Committee of Integrated Hospital of Traditional Chinese Medicine. This model was imported into the Unigraphics NX 8.5 software (Siemens, Munich, Germany) to build an AO-43C3 type distal tibial fracture according to the clinical fracture classification of association for the study of internal fixation. The tibia was divided into two major fragments with a fracture gap of 3 mm. The gap was located 40 mm above the tibiotalar joint.

The computer aided design model of a general six-hole locking plate (LP) is 3.2 mm thick (LCP Distal Tibia Plates, 6-Hole, Synthes) and uses 3.5 mm diameter screws to fix the LP to the tibia. As this LCP distal tibia plates are most commonly used in clinic to treat AO-43C3 type tibial fracture. We adopted this LP construct as a prototype and optimized on this basis.

Following previous biomechanical studies, we mimic the experimental setup with the proximal tibia embedded centrally in an embedding box with 10-mm diameter loading disks to validate the simulation model (Hoegel et al., 2012; Högel et al., 2012). The positional relationship between the implant and the tibia and the boundary conditions of whole model are shown in (**Figure 1B**).

The two models were imported into Abaqus 2017 (Dassault Systems, Velizy-Villacoublay, France) for FE modelling. The mesh densities were settled to 1.1 mm for the LP model followed convergence analyses within the capacity of the available computers. Then 10-node tetrahedral elements were used to discretize all of the parts of the bone-implant system. The details of these elements are given in **Table 1**.

Mechanical Environment Theoretical Model Analyses of Post-operation Soft Tissue

The structural distribution of each part after the placement of the implants is presented in **Figure 2**. The original position of the entire soft tissue is occupied by the implant, and the relative

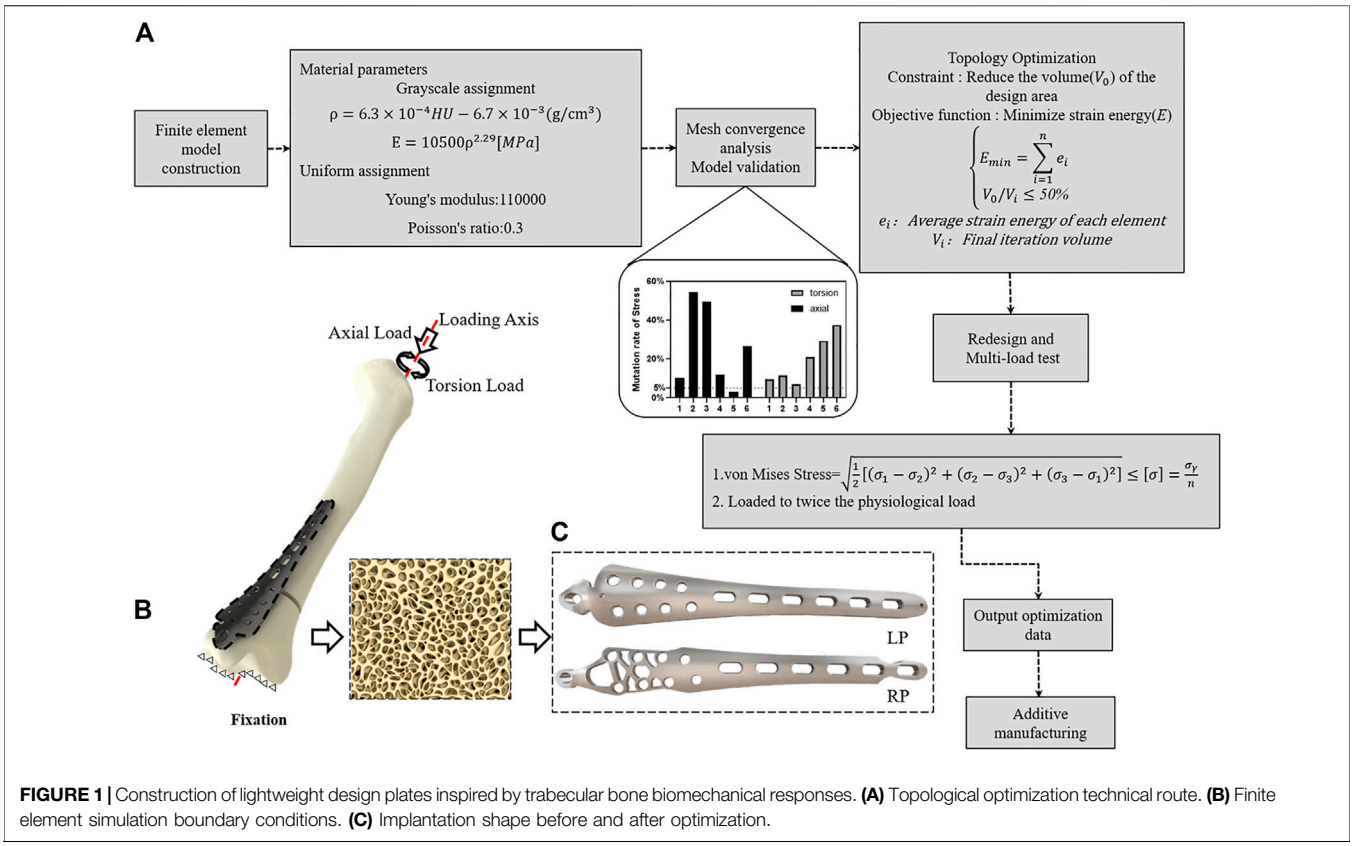

FIGURE 1 | Construction of lightweight design plates inspired by trabecular bone biomechanical responses. **(A)** Topological optimization technical route. **(B)** Finite element simulation boundary conditions. **(C)** Implantation shape before and after optimization.

TABLE 1 | Types of elements, number of nodes, and number of elements in each part of the model.

Parts	Element type	Number of elements	Number of nodes
Tibia	C3D10	56,804	84,837
Screw	C3D10	269,041	175,364
Locking Plate	C3D10	142,407	215,871
Redesigned Plate	C3D10	419,629	624,277

position of the soft tissue changes (**Figures 2B,C**). Assuming that the soft tissue is a beam model, the implantation of the internal fixation causes the beam to be stretched; specifically, the equivalent volume of the internal fixation implant V can be calculated with the following equation:

$$V = L \times S \tag{1}$$

where S represents the cross-sectional area of internal fixation, and L represents the unit thickness of the internal fixation; the mechanical effect on the soft tissue after implantation is approximated as a stretch model, and the strain of the strain direction ε can be expressed as follows:

$$\varepsilon = \frac{\Delta V}{L \times S} \tag{2}$$

where ΔV represents the volume change with or without internal fixation. The following equation represents the tissue tensile balance force:

$$F = \sigma \times A \tag{3}$$

where F is the tensile force on the section, σ represents the stress on the section, and A represents the cross-sectional area of the soft tissue, which can also be written as:

$$F = E \times \varepsilon \times A \tag{4}$$

Combining **Eq. 4** with **Eq. 2** gives:

$$F = E \times A \times \frac{\Delta V}{L \times S} \tag{5}$$

where in **Eqs 4**, **5** the E represents the soft tissue elastic modulus. On the other hand, Poisson's ratio γ in the theoretical model can be written as:

$$\gamma = -\frac{\varepsilon^{\#}}{\varepsilon} \tag{6}$$

And therefore can be written as:

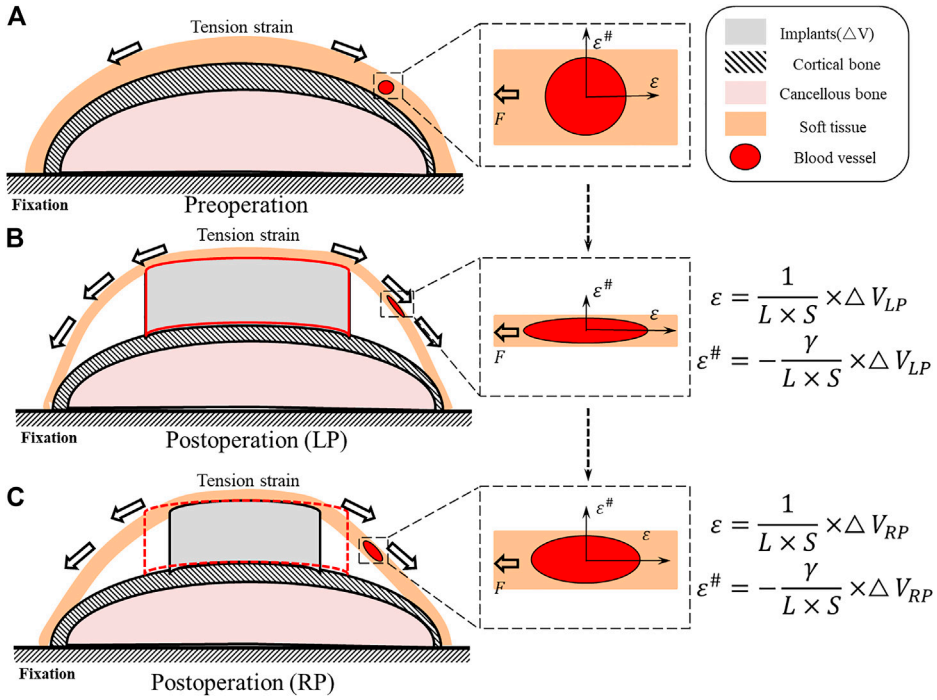

FIGURE 2 | Schematic diagram of the internal implantation of the distal tibia fracture implant. **(A)** The relative position and morphology of the tibia and the soft tissue of the skin and the blood vessels passing through it under physiological conditions. **(B)** The strain increases after LP implantation and causes the strain of the strain direction ε to increase and the strain in the vertical direction $\varepsilon^{\#}$ to increase. This leads the soft tissue and blood vessels to stretch with the affected blood the supply. **(C)** After implantation, with smaller ΔV, the strain of the strain direction ε is reduced, and the strain in the vertical direction $\varepsilon^{\#}$ is reduced, and the deformation of the soft tissue and blood vessels is reduced.

$$\varepsilon^{\#} = -\gamma \times \varepsilon \tag{7}$$

Combining **Eq. 7** with **Eq. 2** gives:

$$\varepsilon^{\#} = -\frac{\gamma}{L \times S} \times \Delta V \tag{8}$$

Where $\varepsilon^{\#}$ represents the strain in the vertical direction; **Eqs 2**, **3** can be combined with (**Eq. 4**) to be written as a formula for σ:

$$\sigma = \frac{E}{L \times S} \times \Delta V \tag{9}$$

Material Properties

The tibia was modeled as an elastic and non-homogenous material by assigning specific Young's modulus values to each element using Mimics. To calculate each element's modulus of elasticity, the Hounsfield unit was extracted from CT images and calculated at the centroid of each element. Formulas 10 and 11 were used in previous studies (Chen et al., 2010; Nourisa and Rouhi, 2016; Xie et al., 2020) to find the apparent density (ρ) and Young's modulus (E) of each element.

$$\rho = 6.3 \times 10^{-4} HU - 6.7 \times 10^{-3} \left[\frac{g}{cm^3}\right] \tag{10}$$

$$E = 10500\rho^{2.29} [MPa] \tag{11}$$

The materials of the LP and the screws were assumed to be titanium alloy (Ti6Al4V). Both the embedding box and loading disk were considered rigid during the analysis.

Boundary and Loading Conditions

Previous work (Cristofolini and Viceconti, 2000; Stoffel et al., 2004; Hoegel et al., 2012) has fully constrained the distal tibialis-articular surface, and the proximal tibia was bonded with the embedding box. The engagement of the screw-plate interface was completely bonded to all screws and to the screw-bone interface. The direction of the loading was along the tibial mechanical axis.

For optimization, the construct was simulated in the two-leg stance, in which the patient tries to load both sides equally. We considered a load equal to 50% of the body weight of a 70 kg person (F = 350 N), and we set a torque of 3500 Nmm along the internal direction of rotation of the tibial mechanical axis as the physiological loading condition (Hoegel et al., 2012; Högel et al., 2012).

To test the stability and safety of the bionic lightweight design constructs, a series of loads were placed in succession on the loading disk. For axial compression stress, loads ranged from 50 to 700 N with increments of 50 N, and for torsion stress, the loads ranged from 1000 to 7000 N·mm at increments of 500 N·mm (Snow et al., 2008) (**Table 2**).

Optimization of the Tibia Locking Plate

The optimization of the distal tibia plate occurred in two steps: topology optimization and plate redesign. Initially, the LP model served as a template for topology optimization. Then, design variable, objective function, and constraints were predefined as essential parameters. In this study, the strategy of topology optimization was to minimize the strain energy of the LP model to achieve maximal fixation stiffness as the objective function. The optimal solution is determined by iteratively changing the element density within predetermined constraints (Ouyang et al., 2017). The 50% volume of LP was fixed as the optimization constraint of the redesigned plate (RP). The optimization strategy minimizes the structural compliance of the plate while satisfying the volume of the structure and can be stated as:

$$\begin{cases} E_{min} = \sum_{i=1}^{n} e_i \\ V_0/V_i \le 50\% \end{cases} \tag{12}$$

e_i: Average strain energy of each element.

V_i: Final iteration volume.

Several iterations of the optimization of the material layout were performed with the goal of maximizing the performance of the system for use as the basis for the design of the RP. The RP was designed to have the same thickness and load and to be in the same configuration as in the LP model. Subsequently, the RP model was analyzed and compared to the LP construct (**Figure 1C**).

Statistical Methods

To qualify the stability and safety of the topological optimization and the plate redesign, we compared the differences in biomechanical behavior between 15 loads on the plates in the LP constructs and the RP constructs, particularly in terms of fixed stability, including 1) the strain energy of the fixation models 2) and the construct stiffness of the plate fixation system for each load. The safety assessment included 1) the von Mises stress distribution and peak and average values of the plates in both the LP and the RP constructs and 2) the von Mises stress distribution ratio of all elements of the plates in the RP and the LP constructs.

All of the data were collected from the plate elements of the RP and LP constructs. The software SPSS Statistics v. 20 (IBM, Armonk, NY, USA) was used to statistical analysis. The box plots (**Figures 4B,D**) represent the mean, and the error bars indicate maximum and minimum values. Descriptive statistics and independent-sample t tests were used in the analyses to compare the means. For all statistical analyses, $^*P < 0.05$ was considered to indicate significance.

RESULTS

Theoretical Model Analysis

The positive correlation between F and ΔV can be obtained using **Eq. 5**. Additionally, without considering the change in A, the deformation of extension is also positively correlated with ΔV. Further, it can be concluded from **Eq. 8** that $\varepsilon^{\#}$ increases with the increase of ΔV.

TABLE 2 | Loading conditions and load values corresponding to each construct of LP and RP e.g., LP-A350 means the LP construct uses 350 N as the load value under axial compression loading conditions.

Axial compression			Torsion		
Load (N)	LP	RP	Load (N·mm)	LP	RP
50	LP-A50	RP-A50	1000	LP-T100	RP-T100
100	LP-A100	RP-A100	1500	LP-T150	RP-T150
150	LP-A150	RP-A150	2000	LP-T200	RP-T200
200	LP-A200	RP-A200	2500	LP-T250	RP-T250
250	LP-A250	RP-A250	3000	LP-T300	RP-T300
300	LP-A300	RP-A300	3500	LP-T350	RP-T350
350	LP-A350	RP-A350	4000	LP-T400	RP-T400
400	LP-A400	RP-A400	4500	LP-T450	RP-T450
450	LP-A450	RP-A450	5000	LP-T500	RP-T500
500	LP-A500	RP-A500	5500	LP-T550	RP-T550
550	LP-A550	RP-A550	6000	LP-T600	RP-T600
600	LP-A600	RP-A600	6500	LP-T650	RP-T650
650	LP-A650	RP-A650	7000	LP-T700	RP-T700
700	LP-A700	RP-A700	—	—	—

The RP construct and the LP construct volume as ΔV_{RP} = 3159.61 mm^3 and ΔV_{LP} = 4481.82 mm^3 are placed into formula (2). **Eqs 8**, **9** can represent the relationship between ΔV and the strain in the vertical direction $\varepsilon^{\#}$; the strain in the direction of strain ε and the stress on the section σ are described in **Table 3**.

Fixation Stability

In the FE simulation, the strain energy represented the carrying capability of the entire structure. **Figure 3** shows the strain energy curves of all constructs as the load increases. No statistical difference is seen in strain energy as the axial compression load ($P > 0.05$) and the torsion load increase ($P > 0.05$) between the LP and the RP constructs. **Figures 4A,C** shows the maximal value of the nodal displacement of each construct under all loads. There were no statistical differences in maximal nodal displacement ($P > 0.05$) as the axial compression load increased (0.99 and 1.04 mm in RP fixation and LP fixation under the axial loading condition of 700 N, respectively); similar results were obtained for torsion load ($P > 0.05$) with maximal nodal displacements of 3.84° and 3.91° under 7000 N·mm torque, respectively. The stiffness of the RP construct was 4.23% lower than that of the LP construct (1984.22 N·mm compared to 2071.85 N·mm; **Figure 4B**). The torsional rigidity of the RP construct was 12.6% higher than that of the LP construct (6.34 Nm/deg compared to 5.63 Nm/deg; **Figure 4D**). For model validation, the stiffness derived from the FE model was highly consistent with the experimental stiffness found in previous studies. (Cristofolini and Viceconti, 2000; Stoffel et al., 2004; Snow

TABLE 3 | Relationship between stress strain and volume in theoretical model.

σ	ε	$\varepsilon^{\#}$
ΔV_{LP} $\sigma = \frac{E}{L \times S} \times 4481.82$	$\varepsilon = \frac{1}{L \times S} \times 4481.82$	$\varepsilon^{\#} = -\frac{\gamma}{L \times S} \times 4481.82$
ΔV_{RP} $\sigma = \frac{E}{L \times S} \times 3159.61$	$\varepsilon = \frac{1}{L \times S} \times 3159.61$	$\varepsilon^{\#} = -\frac{\gamma}{L \times S} \times 3159.61$

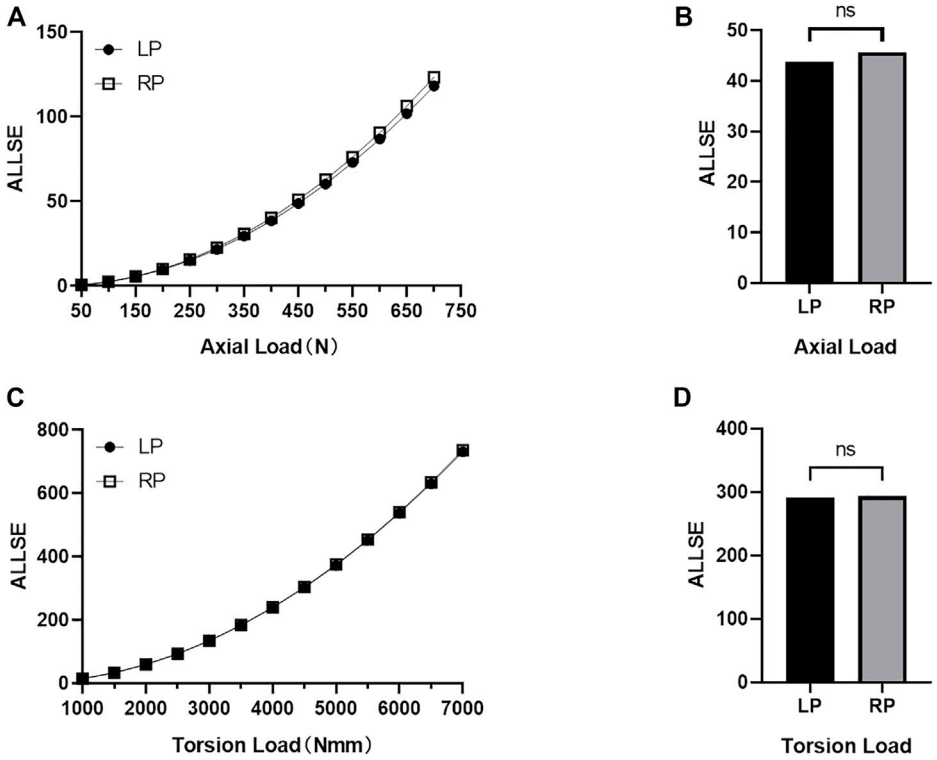

FIGURE 3 | The strain energy (ALLSE) of whole the LP and RP construct changes with the load under axial compression load conditions and torsional load conditions. **(A)** Change in ALLSE in the LP and RP constructs under different axial compression load values **(B)** Statistical analyses of ALLSE for the LP and RP constructs under all axial compression load values ($p > 0.05$) **(C)** Change in ALLSE in the LP and RP constructs under different torsional load values **(D)** Statistical analyses of ALLSE for the LP and RP constructs under all torsion load values ($p > 0.05$).

et al., 2008; Gardner et al., 2010; Yenna et al., 2011; Liu et al., 2017; MacLeod et al., 2018).

Construct Safety Assessment

The comparison of the plate designs of the RP and LP constructs is shown in **Figure 1C**. The volume of the plate in RP construct was 3159.61 mm^3 and that in the LP construct was 4481.82 mm^3. The average stress on the plates generated by the RP construct under maximum axial compression loading conditions was 31.57 MPa, and under maximum torsion, 80.03 MPa. The average stress of the plates generated by the LP construct was 27.63 and 122.49 MPa, respectively, under maximum axial compression and torsional loads.

The peak values of the von Mises stresses on the plates under all loads are presented in **Figure 5**. The maximal stresses of the plates in the RP and LP constructs were 558.30 and 356.57 MPa ($P > 0.05$) in the axial compression and 1125.18 and 1182.40 MPa ($P > 0.05$) in the torsional loading conditions, respectively.

Nevertheless, when the axial compression load was less than or equal to the physiological load (350 N), the observed peak stress of the plates in the constructs was much smaller than the yield stress of the Ti6Al4V material. Under the torsional physiological load (3500 N·mm), the peak stress of the plate in the RP construct was 562.6 MPa, and the peak stress of the plate in the LP construct was 591.2 MPa. In the transmission of the axial compression load, when the load increased to 700 N, the element stress of plates was still much lower than three-quarters of the yield stress of the Ti6Al4V material (**Figures 5E,F**).

Furthermore, the allowance stress of the titanium alloy was adopted for safety assessment, following previously published work. (Yuping Deng, 2020). The allowance stress can be calculated by $[\sigma] = \frac{\sigma_y}{n}$, and we selected two allowable stresses according to the material characteristics, strict $[\sigma_1] = 275\,MPa$ and secondary $[\sigma_2] = 410\,MPa$, as the max-safe stress and min-safe stress of the plate, respectively—that is, the reference for the allowable stress. Statistical analyses were performed on the part of the plates' element stress exceeding 275 MPa in the LP and the RP constructs under doubled physiological load groups (**Figure 6**). For the elements of the plate within the allowed stress range, the average stress of the elements in the LP construct was 322.68 MPa, and in the RP construct, it was 337.48 MPa ($P > 0.05$). The average stress of the elements of the plate in the LP construct and the RP construct under torsion conditions was 375.12 and 364.21 MPa, respectively ($P > 0.05$) (**Figure 6F**).

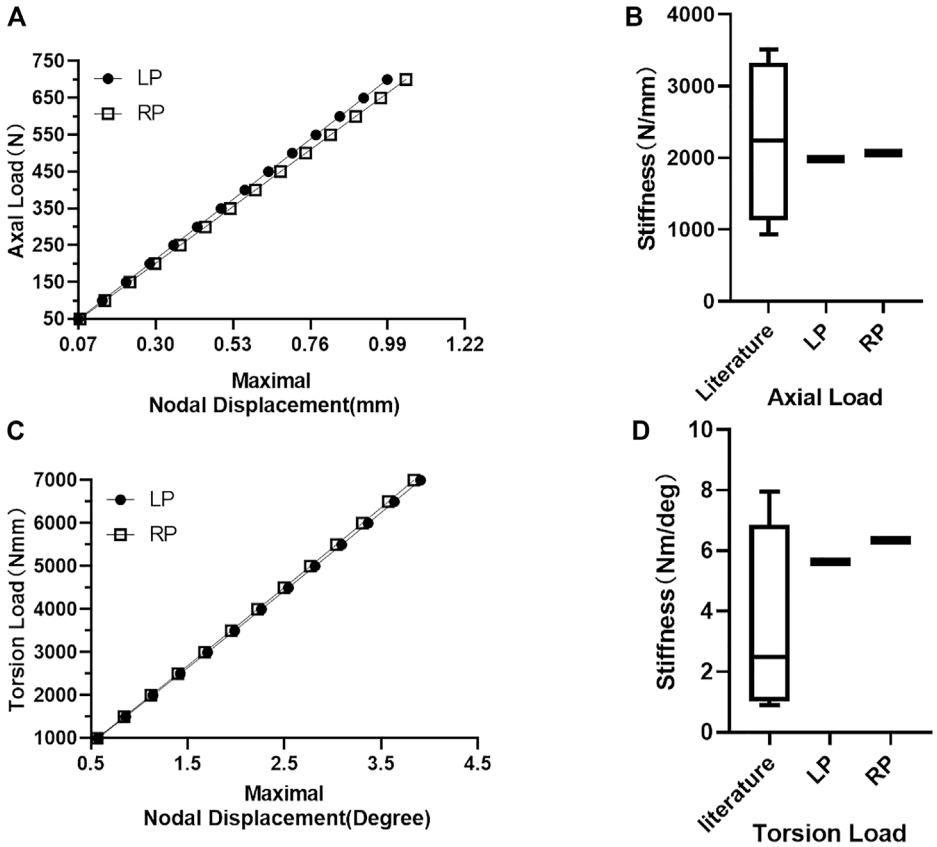

FIGURE 4 | Maximum node displacement and construct stiffness. **(A)** Constructs' maximum nodal displacement increases with load under axial compression load conditions. **(B)** Comparison of LP and RP construct axial compression stiffness with the stiffness values reported in the literature. **(C)** Constructs' maximum nodal displacement increases with load under torsional load conditions. **(D)** Comparison of the torsional stiffness of LP and RP construct with the stiffness of previous studies.

DISCUSSION

Due to fractures, surgery, and plate implantation, the soft tissue conditions around blood vessels change, which leads to changes in the external mechanical environment and increasing stress on the blood vessels (Liu et al., 2016). On the other hand, changes in the vascular diameter can cause changes to the hemodynamics as well as vascular endothelial damage (Hinderliter et al., 2002; Jou et al., 2005; Liu et al., 2016; Cuomo et al., 2017). Mechanical factors work together inside and outside of the blood vessels, activating the endothelial cells and smooth muscle cells, leading to further changes in blood vessel morphology (Pfisterer et al., 2014; Cuomo et al., 2017). This is consistent with commonly observed adverse events during the clinical treatment of fractured distal tibia, such as poor wound healing, delayed wound healing, and delayed fracture healing (Guo and DiPietro, 2010; Gantwerker and Hom, 2012).

We developed an iterative topological optimization algorithm to design an optimized plate that reduced the overall plate volume by 30% compared to the prototype plate without changing the maximum thickness. According to our analyses of the theoretical model (**Figures 2B,C**), the method of continuum structure optimization reduced the volume of the subcutaneous space occupied by the internal implant, specifically LP. This method can reduce the strain of the tension direction ε and that in the vertical direction $\varepsilon^{\#}$ of the soft tissue, which in theory causes decreased stress acting on the blood vessels in soft tissue. As the effect on the vascular diameter decreases, the effects on blood flow velocity, flow rate, and strain on the vascular elements caused by these changes in hemodynamics also decreases (Liu et al., 2001; Berman et al., 2020). Clinical research reports on the treatment effects of lightweight design plates are in good agreement with the theoretical analyses found in the present study (Carter et al., 1998; Borens et al., 2009; Chen et al., 2021), namely, that the impact of the internal plant on the soft tissues around the surgical area is alleviated. Due to the large differences in load-bearing capacity, mechanical behavior, and stress conduction of the various components of the skin and soft tissues of the distal tibia under physiological conditions, opinions on the distal tibia of the soft tissues and blood fluid-solid coupling simulation have always been based on algorithms and theoretical models that are almost impossible to perfectly validate (Alberto Figueroa et al., 2009; Krittian et al., 2010; Liu et al., 2020; Humphrey, 2021) and are almost irreproducible in the laboratory. On other hand, there are many factors that affect fracture healing, and the fixation effects of the implant on the fracture block are considered the primary relevant factor (Davis et al., 1990; Norris et al., 2018; Hu et al., 2019; Li et al., 2020).

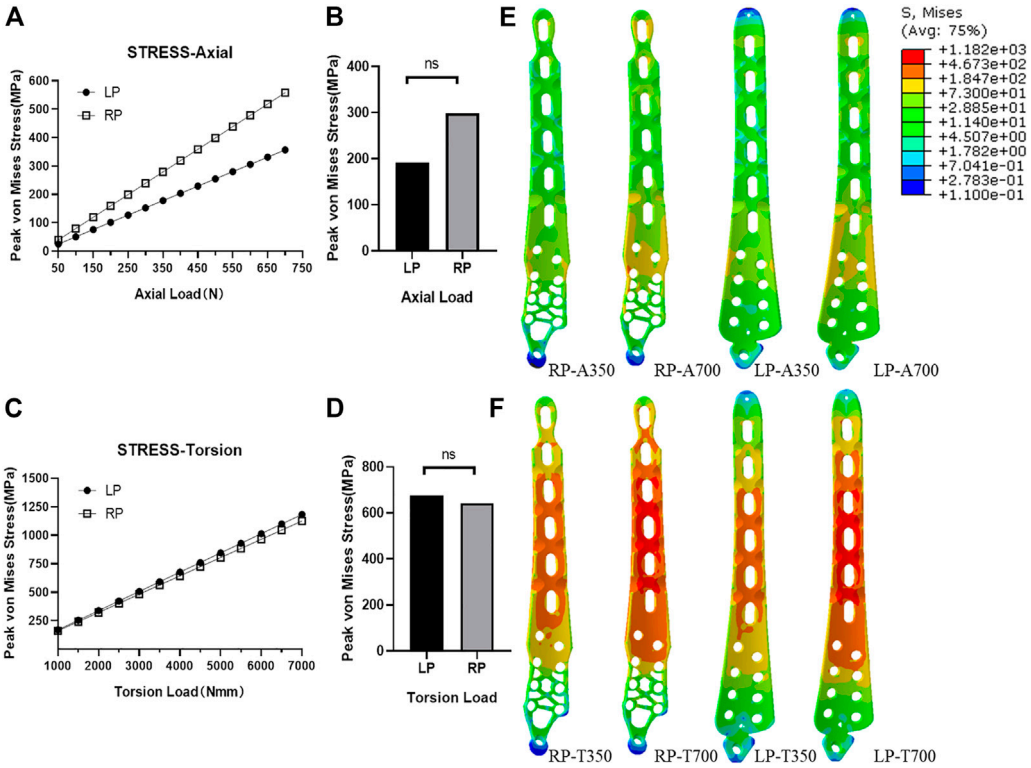

FIGURE 5 | Plate stress analyses. **(A)** Peak stress with difference load values for two kinds of plates under axial compression conditions. **(B)** Statistical analyses of peak stress of the load values of LP and RP plate under axial compression conditions ($p > 0.05$). **(C)** Peak stress with difference load values for two kinds of plates under torsion conditions. **(D)** Statistical analyses of peak stress of the load values of LP and RP plate under torsion conditions ($p > 0.05$). **(E)** Stress distribution of LP and RP plate under axial compression load conditions with a standard physiological load and twice that in the physiological load case. **(F)** Stress distribution of LP and RP plate under torsional conditions with a standard physiological load and twice that in the physiological load case.

What's more, we investigated the constructs' maximum nodal displacement and overall construct stiffness at different loads under axial compression and torsional to find out that the difference in fixation effect between RP structure and LP structure is not statistically significant. We assessed that the RP and LP construct are consistent in their ability to fix the fracture block and limit the displacement of the fracture end. On the other hand, in previous research and in clinical practice, it has been found that the damage severity of the implants was closely related to strain energy and stress (Duan et al., 2011; Guastaldi et al., 2020). This study evaluated the stress and strain energy for RP and LP as an evaluation of the safety of the optimized plate (Walker et al., 2020; Zeng et al., 2020). We found no statistically significant differences between the LP and RP plates in terms of model strain energy and maximum nodal displacement. In summary, we have shown that, after topology optimization and redesign, RP reduces volume by 30%, while the effectiveness and safety remain basically unchanged.

We used an effective method that incorporates strength theory and is suitable for metal materials, allowing strict and secondary allowable stresses to estimate the fatigue failure of the internal fixation under loose and strict allowable stress requirements. In the result, the stress of the plates' elements is greater than the strictly allowable stress ($[\sigma_1] = 275\,MPa$) and does not statistically significantly differ in the axial compression conditions between the LP and the RP construct, but the torsion does differ. We believe that this result shows that as the load gradually exceeds twice the physiological loading area, a difference is seen in the safety of implants in torsion conditions between the optimized construct RP and the prototype construct LP (**Figures 6E,F**). In our analyses of the proportions of different stress elements of the plates in the constructs, we found that the overall stress under physiological load in axial compression stress conditions was lower than the secondary allowable stresses ($[\sigma_2] = 410\,MPa$) (**Figures 6A,B**), while under torsional stress conditions, the physiological load may be higher than 410 MPa. When the load increases to twice that of the natural physiological load, under torsion conditions, the element stresses of the LP and RP constructs are 85 and 89% below 410 MPa (**Figures 6C,D**). Combined with the stress cloud diagram (**Figures 5E,F**), we believe that the stress distribution of RP is more uniform than that of LP. Through experimental analyses of the stress distribution of the plate elements (**Figures 6C,D**), we conclude that the number of elements exceeding the secondary allowable stress under the torsion load condition accounts for a larger proportion of the total number of elements. According to the fatigue life S-N curve theory, we have reason to believe that the RP construct is expected to obtain a longer fatigue life due to its smaller number of high-stress elements.

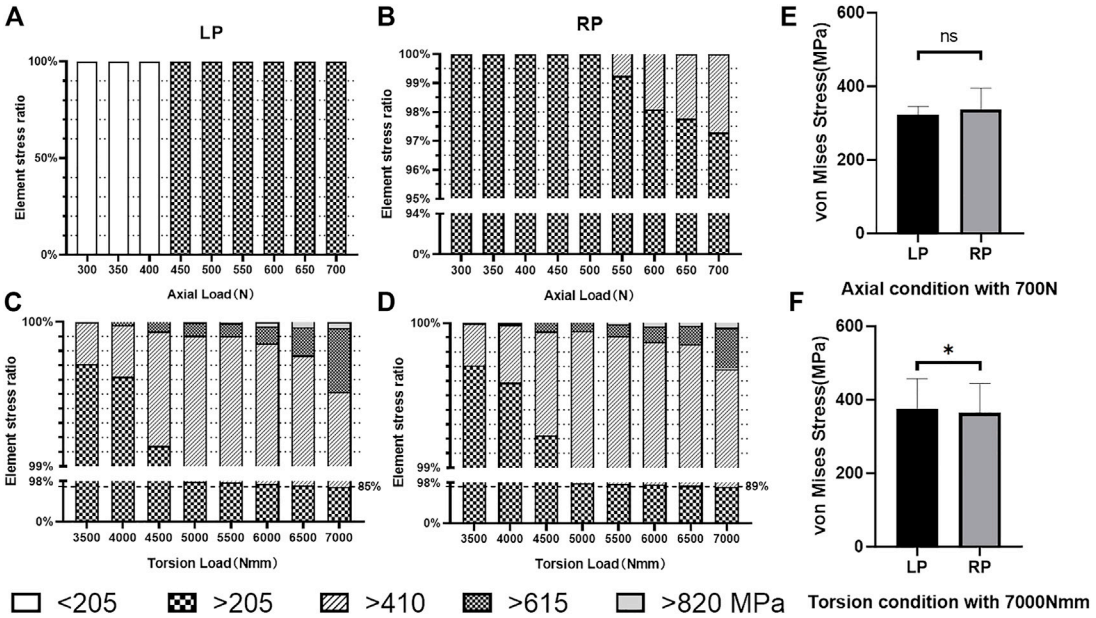

FIGURE 6 | Elemental stress distribution. **(A)** Stress distribution under load values of the LP plate element in axial compression load conditions. **(B)** Stress distribution under load values of the RP plate element in axial compression load conditions. **(C)** Stress distribution under load values of the LP plate element in torsional load conditions. **(D)** Stress distribution under load values of the RP plate element in torsional load conditions. **(E)** Number of the elements which exceeds the allowable stress of 275 MPa under axial compression conditions in twice that of the physiological load case ($p > 0.05$). **(F)** Number of elements which exceeds the allowable stress of 275 MPa under torsion conditions in twice that of the physiological load case ($p < 0.05$).

The limitations of this study are as follows: Because the structural and mechanical properties of soft tissues under physiological conditions are still controversial, and the changes in the aforementioned conditions under trauma are not clear, this study's analyses were only theoretical, based on an idealized model of the soft tissue force. The focus of the next stage of our research will be supplementary mechanical analyses based on the nonlinear material properties of soft tissues, and the theory will be verified through existing methods.

Second, this three-dimensional structure, created using optimization algorithms (which is a better scheme regarding the thickness of the plate structure), is still difficult to manufacture through traditional subtractive manufacturing, and further research on additive manufacturing is required.

In general, these experimental results show that use of finite element simulation analysis combined with topology optimization can improve the capacity of soft tissue protection by reducing the volume of the implant while ensuring the safety of RP by leaving only the necessary structure and generating a more uniform stress distribution. We infer that a smaller plate volume could reduce the excessive mechanical stimulation of soft tissues caused by the implants, and the occurrence rate of adverse prognostic events caused by poor mechanical stimulation may decrease.

DATA AVAILABILITY STATEMENT

The original contributions presented in the study are included in the article/**Supplementary Material**, further inquiries can be directed to the corresponding authors.

AUTHOR CONTRIBUTIONS

MW completed the experiment and wrote the manuscript. YD directed the design test and repaired manuscript. The rest of the authors were put forward valuable opinions in the whole subject design. All authors contributed to the article and approved the submitted version.

FUNDING

Science and Technology Planning Project of Guangdong Province (2018B090944002). Sanming Project of Medicine in Shenzhen (SZSM201612019). Shenzhen Bay Laboratory Initial Funding (21300021). The Third Affiliated Hospital of Southern Medical University Youth Research Startup Fund (QN2020010). Southwest Medical University High-Level Talents (Zhong Shizhen Team) Special Support Program. National Natural Science Foundation of China (21773199). National Natural Science Foundation of China (31972915). Basic and Applied Basic Research Foundation of Guangdong Province (2020B1515120001).

SUPPLEMENTARY MATERIAL

The Supplementary Material for this article can be found online at: https://www.frontiersin.org/articles/10.3389/fbioe.2022.820921/full#supplementary-material

REFERENCES

Alberto Figueroa, C., Baek, S., Taylor, C. A., and Humphrey, J. D. (2009). A Computational Framework for Fluid-Solid-Growth Modeling in Cardiovascular Simulations. *Comp. Methods Appl. Mech. Eng.* 198 (45-46), 3583–3602. doi:10.1016/j.cma.2008.09.013

Berman, D. J., Schiavi, A., Frank, S. M., Duarte, S., Schwengel, D. A., and Miller, C. R. (2020). Factors that Influence Flow through Intravascular Catheters: the Clinical Relevance of Poiseuille's Law. *Transfusion* 60 (7), 1410–1417. doi:10.1111/trf.15898

Borens, O., Kloen, P., Richmond, J., Roederer, G., Levine, D. S., and Helfet, D. L. (2009). Minimally Invasive Treatment of Pilon Fractures with a Low Profile Plate: Preliminary Results in 17 Cases. *Arch. Orthop. Trauma Surg.* 129 (5), 649–659. doi:10.1007/s00402-006-0219-1

Carter, P. R., Frederick, H. A., and Laseter, G. F. (1998). Open Reduction and Internal Fixation of Unstable Distal Radius Fractures with a Low-Profile Plate: a Multicenter Study of 73 Fractures. *J. Hand Surg.* 23 (2), 300–307. doi:10.1016/S0363-5023(98)80131-7

Chan, D. S., Balthrop, P. M., White, B., Glassman, D., and Sanders, R. W. (2017). Does a Staged Posterior Approach Have a Negative Effect on OTA 43C Fracture Outcomes? *J. Orthop. Trau.* 31 (2), 90–94. doi:10.1097/BOT.0000000000000728

Chen, G., Schmutz, B., Epari, D., Rathnayaka, K., Ibrahim, S., Schuetz, M. A., et al. (2010). A New Approach for Assigning Bone Material Properties from CT Images into Finite Element Models. *J. Biomech.* 43 (5), 1011–1015. doi:10.1016/j.jbiomech.2009.10.040

Chen, M. J., Frey, C. S., Salazar, B. P., Gardner, M. J., and Bishop, J. A. (2021). Low Profile Fragment Specific Plate Fixation of Lateral Tibial Plateau Fractures - A Technical Note. *Injury* 52 (4), 1089–1094. doi:10.1016/j.injury.2020.12.037

Cheng, W., Li, Y., and Manyi, W. (2011). Comparison Study of Two Surgical Options for Distal Tibia Fracture-Minimally Invasive Plate Osteosynthesis vs. Open Reduction and Internal Fixation. *Int. Orthopaedics (Sicot)* 35 (5), 737–742. doi:10.1007/s00264-010-1052-2

Chou, L. B., and Lee, D. C. (2009). Current Concept Review: Perioperative Soft Tissue Management for Foot and Ankle Fractures. *Foot Ankle Int.* 30 (1), 84–90. doi:10.3113/FAI.2009.0084

Court-Brown, C., and McBirnie, J. (1995). The Epidemiology of Tibial Fractures. *The J. Bone Jt. Surg. Br. volume* 77-B (3), 417–421. doi:10.1302/0301-620x.77b3.7744927

Cristofolini, L., and Viceconti, M. (2000). Mechanical Validation of Whole Bone Composite Tibia Models. *J. Biomech.* 33 (3), 279–288. doi:10.1016/S0021-9290(99)00186-4

Cuomo, F., Roccabianca, S., Dillon-Murphy, D., Xiao, N., Humphrey, J. D., and Figueroa, C. A. (2017). Effects of Age-Associated Regional Changes in Aortic Stiffness on Human Hemodynamics Revealed by Computational Modeling. *PLoS One* 12 (3), e0173177. doi:10.1371/journal.pone.0173177

Davis, T., Sher, J., Horsman, A., Simpson, M., Porter, B., and Checketts, R. (1990). Intertrochanteric Femoral Fractures. Mechanical Failure after Internal Fixation. *J. Bone Jt. Surg.* 72-B (1), 26–31. doi:10.1302/0301-620x.72b1.2298790

Deng, Y., Ouyang, H., Xie, P., Wang, Y., Yang, Y., Tan, W., et al. (2020). Biomechanical Assessment of Screw Safety between Far Cortical Locking and Locked Plating Constructs. *Comp. Methods Biomech. Biomed. Eng.* 24, 663–672. doi:10.1080/10255842.2020.1844882

Duan, Y., Zhang, H., Min, S.-x., Zhang, L., and Jin, A.-m. (2011). Posterior Cervical Fixation Following Laminectomy: a Stress Analysis of Three Techniques. *Eur. Spine J.* 20 (9), 1552–1559. doi:10.1007/s00586-011-1711-z

Gantwerker, E. A., and Hom, D. B. (2012). Skin: Histology and Physiology of Wound Healing. *Clin. Plast. Surg.* 39 (1), 85–97. doi:10.1016/j.cps.2011.09.005

Gardner, M. J., Nork, S. E., Huber, P., and Krieg, J. C. (2010). Less Rigid Stable Fracture Fixation in Osteoporotic Bone Using Locked Plates with Near Cortical Slots. *Injury* 41 (6), 652–656. doi:10.1016/j.injury.2010.02.022

Guastaldi, F. P. S., Martini, A. P., Rocha, E. P., Hochuli-Vieira, E., and Guastaldi, A. C. (2020). Ti-15Mo Alloy Decreases the Stress Concentration in Mandibular Angle Fracture Internal Fixation Hardware. *J. Maxillofac. Oral Surg.* 19 (2), 314–320. doi:10.1007/s12663-019-01251-8

Guo, S., and DiPietro, L. A. (2010). Factors Affecting Wound Healing. *J. Dent. Res.* 89 (3), 219–229. doi:10.1177/0022034509359125

Hinderliter, A. L., Sherwood, A., Blumenthal, J. A., Light, K. C., Girdler, S. S., McFetridge, J., et al. (2002). Changes in Hemodynamics and Left Ventricular Structure after Menopause. *Am. J. Cardiol.* 89 (7), 830–833. doi:10.1016/s0002-9149(02)02193-8

Hoegel, F. W., Hoffmann, S., Weninger, P., Bühren, V., and Augat, P. (2012). Biomechanical Comparison of Locked Plate Osteosynthesis, Reamed and Unreamed Nailing in Conventional Interlocking Technique, and Unreamed Angle Stable Nailing in Distal Tibia Fractures. *J. Trauma Acute Care* 73 (4), 933–938. doi:10.1097/TA.0b013e318251683f

Högel, F., Hoffmann, S., Weninger, P., Bühren, V., and Augat, P. (2012). Biomechanical Comparison of Two Locking Plate Systems for the Distal Tibia. *Eur. J. Trauma Emerg. Surg.* 38 (1), 53–58. doi:10.1007/s00068-011-0123-4

Hu, L., Xiong, Y., Mi, B., Panayi, A. C., Zhou, W., Liu, Y., et al. (2019). Comparison of Intramedullary Nailing and Plate Fixation in Distal Tibial Fractures with Metaphyseal Damage: a Meta-Analysis of Randomized Controlled Trials. *J. Orthop. Surg. Res.* 14 (1), 30. doi:10.1186/s13018-018-1037-1

Humphrey, J. D. (2021). Constrained Mixture Models of Soft Tissue Growth and Remodeling - Twenty Years after. *J. Elast* 145 (1-2), 49–75. doi:10.1007/s10659-020-09809-1

Jou, L. D., Wong, G., Dispensa, B., Lawton, M. T., Higashida, R. T., Young, W. L., et al. (2005). Correlation between Lumenal Geometry Changes and Hemodynamics in Fusiform Intracranial Aneurysms. *AJNR Am. J. Neuroradiol* 26 (9), 2357–2363.

Khoury, A., Liebergall, M., London, E., and Mosheiff, R. (2002). Percutaneous plating of distal tibial fractures. *Foot Ankle Int.* 23 (9), 818–824. doi:10.1177/107110070202300908

Krackhardt, T., Dilger, J., Flesch, I., Höntzsch, D., Eingartner, C., and Weise, K. (2005). Fractures of the Distal Tibia Treated with Closed Reduction and Minimally Invasive Plating. *Arch. Orthop. Trauma Surg.* 125 (2), 87–94. doi:10.1007/s00402-004-0778-y

Krittian, S., Janoske, U., Oertel, H., and Böhlke, T. (2010). Partitioned Fluid-Solid Coupling for Cardiovascular Blood Flow. *Ann. Biomed. Eng.* 38 (4), 1426–1441. doi:10.1007/s10439-009-9895-7

Lau, T. W., Leung, F., Chan, C. F., and Chow, S. P. (2008). Wound complication of minimally invasive plate osteosynthesis in distal tibia fractures. *Int. Orthop.* 32 (5), 697–703. doi:10.1007/s00264-007-0384-z

Li, J., Qin, L., Yang, K., Ma, Z., Wang, Y., Cheng, L., et al. (2020). Materials Evolution of Bone Plates for Internal Fixation of Bone Fractures: A Review. *J. Mater. Sci. Techn.* 36, 190–208. doi:10.1016/j.jmst.2019.07.024

Liu, J., Yang, W., Lan, I. S., and Marsden, A. L. (2020). Fluid-structure Interaction Modeling of Blood Flow in the Pulmonary Arteries Using the Unified Continuum and Variational Multiscale Formulation. *Mech. Res. Commun.* 107, 103556. doi:10.1016/j.mechrescom.2020.103556

Liu, W., Yang, L., Kong, X., An, L., Hong, G., Guo, Z., et al. (2017). Stiffness of the Locking Compression Plate as an External Fixator for Treating Distal Tibial Fractures: a Biomechanics Study. *BMC Musculoskelet. Disord.* 18 (1), 26. doi:10.1186/s12891-016-1384-1

Liu, X., Zhang, H., Ren, L., Xiong, H., Gao, Z., Xu, P., et al. (2016). Functional Assessment of the Stenotic Carotid Artery by CFD-Based Pressure Gradient Evaluation. *Am. J. Physiology-Heart Circulatory Physiol.* 311 (3), H645–H653. doi:10.1152/ajpheart.00888.2015

Liu, Y., Lai, Y., Nagaraj, A., Kane, B., Hamilton, A., Greene, R., et al. (2001). Pulsatile Flow Simulation in Arterial Vascular Segments with Intravascular Ultrasound Images. *Med. Eng. Phys.* 23 (8), 583–595. doi:10.1016/S1350-4533(01)00088-1

MacLeod, A., Simpson, A. H. R. W., and Pankaj, P. (2018). Experimental and Numerical Investigation into the Influence of Loading Conditions in Biomechanical Testing of Locking Plate Fracture Fixation Devices. *Bone Jt. Res.* 7 (1), 111–120. doi:10.1302/2046-3758.71.BJR-2017-0074.R2

Mont, M. A., Sedlin, E. D., Weiner, L. S., and Miller, A. R. (1992). Postoperative radiographs as predictors of clinical outcome in unstable ankle fractures *J. Orthop. Trau.* 6 (3), 352–357. doi:10.1097/00005131-199209000-00014

Namazi, H., and Mozaffarian, K. (2007). Awful Considerations with LCP Instrumentation: a New Pitfall. *Arch. Orthop. Trauma Surg.* 127 (7), 573–575. doi:10.1007/s00402-007-0343-6

Norris, B. L., Lang, G., Russell, T. A., Rothberg, D. L., Ricci, W. M., and Borrelli, J. (2018). Absolute versus Relative Fracture Fixation: Impact on Fracture

Healing. *J. Orthop. Trauma* 32 (3), S12–S16. doi:10.1097/BOT.0000000000001124

Nourisa, J., and Rouhi, G. (2016). Biomechanical Evaluation of Intramedullary Nail and Bone Plate for the Fixation of Distal Metaphyseal Fractures. *J. Mech. Behav. Biomed. Mater.* 56, 34–44. doi:10.1016/j.jmbbm.2015.10.029

Ouyang, H., Deng, Y., Xie, P., Yang, Y., Jiang, B., Zeng, C., et al. (2017). Biomechanical Comparison of Conventional and Optimised Locking Plates for the Fixation of Intraarticular Calcaneal Fractures: a Finite Element Analysis. *Comp. Methods Biomech. Biomed. Eng.* 20 (12), 1339–1349. doi:10.1080/10255842.2017.1361938

Pallister, I., and Iorwerth, A. (2005). Indirect Reduction Using a Simple Quadrilateral Frame in the Application of Distal Tibial LCP-Technical Tips. *Injury* 36 (9), 1138–1142. doi:10.1016/j.injury.2005.02.023

Pfisterer, L., König, G., Hecker, M., and Korff, T. (2014). Pathogenesis of Varicose Veins - Lessons from Biomechanics. *Vasa* 43 (2), 88–99. doi:10.1024/0301-1526/a000335

Sheerin, D. V., Turen, C. H., and Nascone, J. W. (2006). Reconstruction of Distal Tibia Fractures Using a Posterolateral Approach and a Blade Plate. *J. Orthop. Trau.* 20 (4), 247–252. doi:10.1097/00005131-200604000-00003

Sirkin, M., Sanders, R., DiPasquale, T., and Korff, D. J. (2004). A staged protocol for soft tissue management in the treatment of complex pilon fractures. *Orthop Trauma* 18 (8), S32–S38. doi:10.1097/00005131-200409001-00005

Snow, M., Thompson, G., and Turner, P. G. (2008). A Mechanical Comparison of the Locking Compression Plate (LCP) and the Low Contact-Dynamic Compression Plate (DCP) in an Osteoporotic Bone Model. *J. Orthop. Trauma* 22 (2), 121–125. doi:10.1097/BOT.0b013e318160c84c

Stoffel, K., Stachowiak, G., and Kuster, M. (2004). Open Wedge High Tibial Osteotomy: Biomechanical Investigation of the Modified Arthrex Osteotomy Plate (Puddu Plate) and the TomoFix Plate. *Clin. Biomech.* 19 (9), 944–950. doi:10.1016/j.clinbiomech.2004.06.007

Teeny, S. M., and Wiss, D. A. (1993). Open reduction and internal fixation of tibial plafond fractures. Variables contributing to poor results and complications. *Clin. Orthop. Relat. Res.* 292, 108–117.

Vaienti, E., Schiavi, P., Ceccarelli, F., and Pogliacomi, F. (2019). Treatment of Distal Tibial Fractures: Prospective Comparative Study Evaluating Two Surgical Procedures with Investigation for Predictive Factors of Unfavourable Outcome. *Int. Orthopaedics (Sicot)* 43 (1), 201–207. doi:10.1007/s00264-018-4121-6

Vidović, D. M. P., Matejčić, A. M. P., Ivica, M. M. P., Jurišić, D. M., Elabjer, E. M. P., and Bakota, B. M. P. (2015). Minimally-invasive plate osteosynthesis in distal tibial fractures: Results and complications. *Injury* 46, S96–S99. doi:10.1016/j.injury.2015.10.067

Walker, R., Castaneda, P., Putnam, J. G., Schemitsch, E. H., and McKee, M. D. (2020). A Biomechanical Study of Tuberosity-Based Locked Plate Fixation Compared with Standard Proximal Humeral Locking Plate Fixation for 3-Part Proximal Humeral Fractures. *J. Orthop. Trauma* 34 (7), e233–e238. doi:10.1097/BOT.0000000000001744

Weiss, R. J., Montgomery, S. M., Ehlin, A., Dabbagh, Z. A., Stark1, A., and Jansson, K.-A. (2009). Decreasing Incidence of Tibial Shaft Fractures between 1998 and 2004: Information Based on 10,627 Swedish Inpatients. *Acta Orthopaedica* 79 (4), 526–533. doi:10.1080/17453670710015535

Xie, P., Deng, Y., Tan, J., Wang, M., Yang, Y., Ouyang, H., et al. (2020). The Effect of Rotational Degree and Routine Activity on the Risk of Collapse in Transtrochanteric Rotational Osteotomy for Osteonecrosis of the Femoral Head-A Finite Element Analysis. *Med. Biol. Eng. Comput.* 58 (4), 805–814. doi:10.1007/s11517-020-02137-5

Yenna, Z. C., Bhadra, A. K., Ojike, N. I., ShahulHameed, A., Burden, R. L., Voor, M. J., et al. (2011). Anterolateral and Medial Locking Plate Stiffness in Distal Tibial Fracture Model. *Foot Ankle Int.* 32 (6), 630–637. doi:10.3113/FAI.2011.0630

Zeng, W., Liu, Y., and Hou, X. (2020). Biomechanical Evaluation of Internal Fixation Implants for Femoral Neck Fractures: A Comparative Finite Element Analysis. *Comp. Methods Programs Biomed.* 196, 105714. doi:10.1016/j.cmpb.2020.105714

Zhou, Y., Wang, Y., Liu, L., Zhou, Z., and Cao, X. (2015). Locking Compression Plate as an External Fixator in the Treatment of Closed Distal Tibial Fractures. *Int. Orthopaedics (Sicot)* 39 (11), 2227–2237. doi:10.1007/s00264-015-2903-7

Conflict of Interest: The authors declare that the research was conducted in the absence of any commercial or financial relationships that could be construed as a potential conflict of interest.

Publisher's Note: All claims expressed in this article are solely those of the authors and do not necessarily represent those of their affiliated organizations, or those of the publisher, the editors and the reviewers. Any product that may be evaluated in this article, or claim that may be made by its manufacturer, is not guaranteed or endorsed by the publisher.

frontiers in Bioengineering and Biotechnology

ORIGINAL RESEARCH
published: 01 March 2022
doi: 10.3389/fbioe.2022.840052

Contribution of Minimally Invasive Bone Augmentation With PMMA Cement in Primary Fixation of Schatzker Type II Tibial Plateau Fractures

*T. Vendeuvre [1,2], C. Koneazny [2], C. Brèque [1], P. Rigoard [1,3], M. Severyns [1,4] and A. Germaneau [1]**

[1]Institut Pprime UPR 3346, CNRS, ISAE-ENSMA, Université de Poitiers, Poitiers, France, [2]Department of Orthopaedic Surgery and Traumatology, University Hospital, Poitiers, France, [3]PRISMATICS Lab, Department of Spine Surgery and Neuromodulation, University Hospital, Poitiers, France, [4]Department of Orthopaedic Surgery and Traumatology, University Hospital, Martinique, France

OPEN ACCESS

Edited by:
Ching-Chi Hsu, National Taiwan University of Science and Technology, Taiwan

Reviewed by:
Rui B. Ruben, Polytechnic Institute of Leiria, Portugal
Kuo-Chih Su, Taichung Veterans General Hospital, Taiwan

***Correspondence:**
A. Germaneau
arnaud.germaneau@univ-poitiers.fr

Specialty section:
This article was submitted to Biomechanics, a section of the journal Frontiers in Bioengineering and Biotechnology

Received: *20 December 2021*
Accepted: *02 February 2022*
Published: *01 March 2022*

Citation:
Vendeuvre T, Koneazny C, Brèque C, Rigoard P, Severyns M and Germaneau A (2022) Contribution of Minimally Invasive Bone Augmentation With PMMA Cement in Primary Fixation of Schatzker Type II Tibial Plateau Fractures. Front. Bioeng. Biotechnol. 10:840052. doi: 10.3389/fbioe.2022.840052

Background: The most common type of fracture of the lateral tibial plateau is the Schatzker type II split-depressed fracture. Minimally invasive surgery using balloon reduction appears to be very promising compared to the gold standard using a bone tamp. This surgery aims to have the best reduction and stabilization to benefit from an early passive and active rehabilitation to avoid stiffening and muscle wasting. Using a balloon for fracture reduction has allowed the use of semi-liquid Injectable Bone Cement (IBC) fillers. These fillers can be phosphocalcic or polymethyl methacrylate (PMMA). The latest recommendations on these IBCs in spinal surgery increasingly rule out phosphocalcic fillers because of their low mechanical strength.

Questions/purposes: 1) What is the mechanical influence of IBC filling (PMMA) regarding the split and depression components of a Schatzker type II fracture? 2) What is the mechanical influence of osteosynthesis regarding the split and depression components of a Schatzker type II fracture with or without PMMA filing in three different kinds of percutaneous fixations?

Methods: This biomechanical study was performed on 36 fresh frozen tibia/fibula specimens. Six groups were formed according to the type of percutaneous osteosynthesis or possible PMMA filling. Mechanical strength tests were carried out using a Unicompartmental Knee prosthesis and displacement components were measured on either side of the separation on the anterolateral facet by optical method.

Results: We found a significant difference between cementless and cemented osteosynthesis for depression fracture stabilization (difference –507.56N with 95% confidence interval [–904.17; –110.94] (p-value = 0.026)). The differences between the different types of osteosynthesis were not significant (p-value = 0.58). There was a significant difference between osteosynthesis without cement and osteosynthesis with cement on separation (difference –477.72N [–878.52; –76.93] (p-value = 0.03)). The

differences between the different types of fixations were not significant regarding separation (p-value = 0.99).

Conclusion: PMMA cement significantly improves primary stability, regardless of the type of osteosynthesis for a Schatzker type II plateau fracture. Filling with PMMA cement during tuberoplasty seems to be a very promising strategy in association with percutaneous osteosynthesis to allow rapid recovery after surgery.

Keywords: tibial plateau fracture osteosynthesis, tuberoplasty, percutaneous osteosynthesis, injectable bone cement, optical methods, biomechanics

INTRODUCTION

The most common type of fractures of the lateral tibial plateau is the Schatzker type II split-depressed fracture (Schatzker et al., 1979; Zeltser and Leopold, 2013). Minimally invasive surgery using balloon reduction appears to be very promising compared to the gold standard using a bone tamp (Ollivier et al., 2016; Doria et al., 2017). This surgery aims to have the best reduction and stabilization to benefit from an early passive and active rehabilitation to avoid stiffening and muscle wasting (Wang et al., 2018). The goal is also to achieve early weight-bearing for rapid recovery and minimize the risk of complications related to decubitus (Wang et al., 2018; Vendeuvre and Gayet, 2021). Using a balloon for fracture reduction has allowed the use of semi-liquid Injectable Bone Cement (IBC) fillers. These fillers can be phosphocalcic or polymethyl methacrylate (PMMA). The latest recommendations on these IBCs in spinal surgery increasingly rule out phosphocalcic fillers because of their low mechanical strength (Singh et al., 2019). PMMA is the injectable filler that offers the best mechanical properties in compression (Wittenberg et al., 1993; Kayanja et al., 2006). It is regularly used in orthopedic surgery for filling vertebral fractures or for arthroplasty (Lieberman and Reinhardt, 2003; Singh et al., 2019; Sebastian et al., 2020).

Minimally invasive plate osteosynthesis systems have been developed with a mindset similar to percutaneous screw fixation. These systems allow for optimal positioning of the screws under the depressed part of the fracture to have a mechanical strut while controlling the separation (Mauffrey et al., 2014). This use of minimally invasive plates is often referred to as MIPPO (Minimal Invasive Percutaneous Plating Osteosynthesis). Percutaneous screws are the most widely used because their ease of use and modern plating systems allow for optimized screw positioning and locking to the plate.

There are two main locking techniques for plating systems: direct locking by screw head threads or secondary locking by caps. These designs offer differences in the number of screws positioned in the epiphysis and the screw diameters. Our study compares the NCB® percutaneous plate, which uses Caps locking, with the VA-LCP® percutaneous plate, which uses screw head thread locking and fixation using percutaneous screw alone.

The main goal of this study was to compare different minimally invasive fracture fixations in association with balloon reduction using the tuberoplasty technique. We compared the primary structural strength of the fracture fixation regarding the separation and depression components. We also tested the mechanical influence of IBC filling on these three types of percutaneous fixations.

METHODS

Preparation of the Parts

This biomechanical study was performed on 36 fresh frozen tibia/fibula specimens collected at the ABS Lab laboratory of the University of Poitiers (Ministry of Education and Research No. DC-2008-137). They were divided into six groups, each with six randomized specimens, homogeneous in age, sex, and laterality (**Table 1**).

In order to address the different issues, the six groups were formed as follows:

- Group 1 was reduced using a balloon and osteosynthesis with a Zimmer® plate and filled with PMMA cement;
- Group 2 was reduced by balloon then osteosynthesis by Zimmer® plate without filling;
- Group 3 was reduced by balloon then osteosynthesis by two Maconor® screws with washers without filling;
- Group 4 was reduced by balloon then osteosynthesis by two Maconor® screws with washers and PMMA cement filling;
- Group 5 was reduced with a balloon and then osteosynthesis with a Synthes® plate and PMMA cement filling;
- Group 6 was reduced with a balloon and then osteosynthesis with a Synthes® plate without filling.

Specimen preparation and fracture pattern were performed according to Vendeuvre et al. (Vendeuvre et al., 2018).

Specimens were prepared using the proximal tibia and fibula up to the middle diaphysis. They were fixed in a rigid polyurethane resin base (Allrim®) and stabilized in an anatomical position.

The Schatzker type II fracture pattern was made in a standardized and reproducible matter.

Post-fracture CT analysis was performed to confirm the Schatzker type II fracture. All fractures were validated, and, at this stage of the study, no specimens were excluded.

Fracture Reduction and Fixation

Fractures were reduced by tuberoplasty with a 20-mm Medtronic Sofamor Expender 2 kyphoplasty® balloon using an anterior MIS approach (Vendeuvre et al., 2013).

TABLE 1 | Distribution of anatomical parts according to age, sex, and laterality.

	G1	G2	G3	G4	G5	G6
Sex (M/F)	3/3	3/3	3/3	3/3	3/3	3/3
Laterality (R/L)	3/3	3/3	3/3	3/3	3/3	3/3
Age (Years ± DS)	85 ± 8.10	85 ± 8.1	78.8 ± 6.2	74.6 ± 11.4	77.3 ± 12.4	77.6 ± 12.1

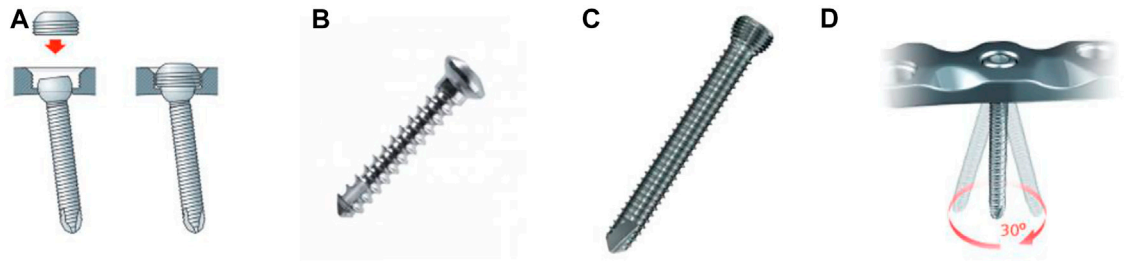

FIGURE 1 | Three differents kind of screw fixation. **(A)** Caps used for locking screws in NCB Zimmer® plates, **(B)** Maconor® bicortical screw without plate, **(C)** Epiphysial screw with a 30° range in the Synthes® plate, and **(D)** 30° variable axis for the tool locking system.

The Different Materials

- Percutaneous osteosynthesis

The choice of fixation techniques was: 1) percutaneous system, 2) placement of polyaxial screws. We then selected three types of osteosynthesis (**Figure 1**).

- Two Maconor (Howmedica®) bicortical screws, 4.5 mm in diameter, for groups 3 and 4 (**Figure 1B**).

Fracture fixation was performed in both groups using two 4.5 mm diameter Maconor (Howmedica®) bicortical screws and a 13 mm stainless steel washer. The trajectory was prepared with a 3.4-mm drill bit, and the screws were positioned with a lateral entry point located below the most distal part of the depression. The configuration of the osteosynthesis screws was the same for both groups.

- Zimmer® NCB Proximal Tibia Plate + Screws for Groups 1 and 2 (**Figure 1A**).

In this study, we used a lateral anatomical plate compatible with a percutaneous minimally invasive ancillary. This plate has three 4.5 mm epiphyseal screws with spherical heads locked secondarily with caps (**Figure 1A**). Screws can be oriented in a 30° radius. The shortest plate, 132 mm long, was used, as well as three bi-cortical diaphyseal screws. The system allows the placement of polyaxial screws (30°) with subsequent locking of the screws and use of locking caps.

- Synthes®VA-LCP Proximal Tibial Plate 3.5 for Groups 5 and 6 (**Figure 1C**).

In this study, we chose a lateral anatomical plate that could be used with a percutaneous ancillary. Two models were available, allowing a choice between two radii of curvature (Small Bend and Large Bend) and adapting to the anatomy of each subject. This plate has four 3.5 mm diameter epiphyseal screws with self-locking threads. They are adjustable and can be positioned within a 30° radius (**Figure 1D**). We chose the shortest plate, 87 mm long, which was more than sufficient for our fracture model. Three bi-cortical screws were systematically positioned at the diaphyseal level.

- Medtronic® balloon

We used a Medtronic Sofamor® balloon kyphoplasty Xpander® IBT 20 mm long and a capacity of 10 ccs or 350 PSI.

- PMMA cement

We chose to fill the gaps in groups 1, 4, and 6 with PMMA KyphX HV-R® Kyphon® cement, whose composition is as follows:

- Barium sulfate
- Benzoyl peroxide
- Methyl methacrylate
- N, N-dimethyl-p-toluidine
- Hydroquinone

The role of the cement is to increase the mechanical strength of the fixation with which it may be associated, thus allowing for early active rehabilitation and a faster return to weight-bearing. As shown in the management of

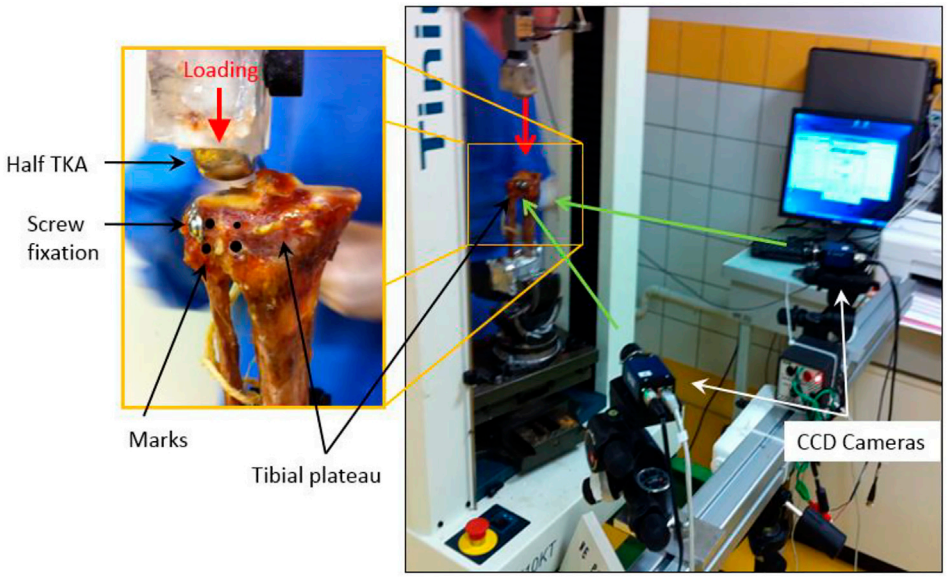

FIGURE 2 | Mechanical strength tests were carried out using a Unicompartmental Knee prosthesis positioned on the lateral tibial plateau (Vendeuvre et al., 2018).

spinal fractures, we did not use phosphocalcic cement, which has a lower mechanical strength (Blattert et al., 2009). In addition, a tibia has to bear a greater weight than a vertebra.

Biomechanical Tests

Mechanical strength tests were carried out using a Zimmer Unicompartmental Knee High Flex® prosthesis, size 48 mm, positioned on the Tinius Olsen® compression machine (able to provide up to 10kN loading), positioned on the lateral tibial plateau (**Figure 2**) (Vendeuvre et al., 2018).

The loading rate was set at 5 mm/min. The compression force on the tibial plateau was measured by a load cell (up to 10kN) located between the mobile span and the unicompartmental knee prosthesis. Four marks were placed on either side of the separation on the anterolateral facet of the specimen to measure the distance between the fracture line by 3D mark tracking. These four marks were used to characterize the separation of bone fragments after stabilization and during the loading. The depression fracture was characterized by measuring the displacement of the unicompartmental knee prosthesis according to loading.

The mark tracking allowed us to study the bone deformations in compression and separation as a function of the applied force and determine the force's value necessary to cause plastic deformation of the upper end of the tibia, corresponding to the assembly's failure.

The characterization of the mechanical response of the stabilization systems was carried out by identifying the limiting force **Fe** determining the transition from linear response to a non-linear response corresponding to the transition from an elastic bone deformation to plastic deformation.

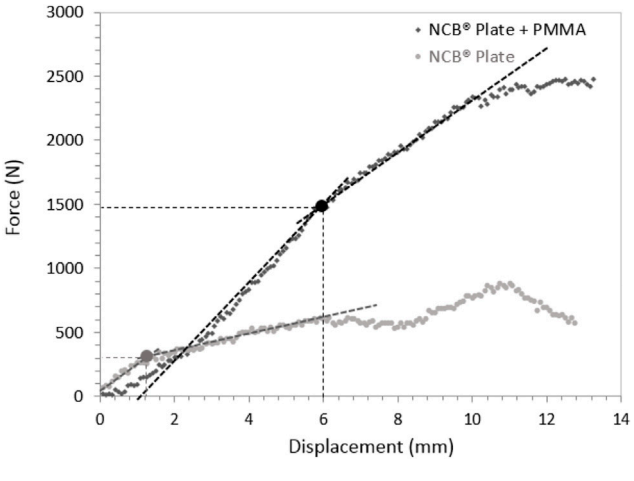

FIGURE 3 | Example of load-displacement curves for depression analysis for specimens stabilized with NCB® plates, with and without PMMA filling.

Statistical Analysis

All measured data was computerized and analyzed using R 3.0.1™ statistical software. Comparisons between groups (for quantitative mechanical parameters) were performed using a non-parametric Wilcoxon Man Whitney test. A Tukey test was also used to compare the groups. Finally, the influence of PMMA was calculated using a multivariate analysis of variance (MANOVA) with two factors: osteosynthesis and PMMA.

TABLE 2 | Statistical results of the comparisons of the measured limiting force values between the different groups (Wilcoxon Mann Whitney test).

Comparison of the different assemblies (2 by 2)	Depression *p*-value	Separation *p*-value
Screw:Cement/Plate VA-LCP:Cement	0.9999	0.9220
Plate NCB:Cement/Plate VA-LCP:Cement	0.9071	0.8166
Plate NCB:Cement/Screw:Cement	0.8097	0.9998
Plate VA-LCP:No Cement/Plate VA-LCP:Cement	0.6547	0.9999
Screw:No Cement/Screw:Cement	0.8935	0.2333
Plate NCB:No Cement/Plate NCB:Cement	0.3942	0.4765
Screw:No Cement/Plate VA-LCP:No Cement	0.9998	0.8198
Plate NCB:No Cement/Plate VA-LCP:No Cement	0.9907	0.9959
Plate NCB:No Cement/Screw:No Cement	0.9991	0.9763

TABLE 3 | Comparison of the measured limiting forces between the different fixations with and without PMMA cement regarding separation and depression (Tukey test).

Groups	Depression			Separation		
	Mean (N)	STD (N)	*p*-value	Mean (N)	STD (N)	*p*-value
G1–NCB® + PMMA	1864.7	947.4	0.394	1519.7	894.0	0.476
G2–NCB®	1209.3	491.2		897.7	442.5	
G3–Screw	1088.7	397.2	0.893	645.8	411.9	0.233
G4–Screw + PMMA	1444.8	222.0		1430.7	273.0	
G5–VA-LCP®	1010.0	525.3	0.654	1068.5	565.5	0.999
G6–VA-LCP® + PMMA	1521.2	644.1		1094.8	757.3	

RESULTS

For each group sample, we obtained a value of elastic limit on the depression and separation components.

Then, we studied the influence of the different types of osteosynthesis and PMMA filling on the Schatzker II fractures.

Results on the Depression Fracture

Figure 3 shows the load vs. displacement (of the knee prosthesis) curves for the depression component for two representative specimens of the NCB® plate group (with and without PMMA filling). This graph illustrates the mechanical response of the fracture fixation under compressive loading with a specimen that a linear behavior can approximate. Elastic limit forces are measured at the transition between the linear and the other part of the curve.

We found a significant difference between cementless and cemented osteosynthesis for depression fracture stabilization (difference −507.56 N with 95% confidence interval [−904.17; −110.94] p-value = 0.026). The differences between the different types of osteosynthesis were not significant (p-value = 0.58).

A two-factor MANOVA analysis showed that only the addition of cement had an influence on the depression (p = 0.013) and that neither the type of synthesis nor the interaction between the type of osteosynthesis (p = 0.43) and cement influenced the depression (p = 0.82).

Results on Separation

There was a significant difference on the separation component (measured from the marks disposed on either side of the fracture) between osteosynthesis without cement and osteosynthesis with cement on separation (difference −477.72N with 95% confidence interval [−878.52; −76.93] p-value = 0.03). The differences between the different types of fixations were not significant regarding separation (p-value = 0.99) (**Tables 2**, **3**).

A two-factor MANOVA analysis showed that only the addition of cement had an influence on separation (p = 0.023) and that neither the type of synthesis nor the interaction between the type of osteosynthesis (p = 0.77) and cement influenced separation (p = 0.28) (**Figure 4**).

DISCUSSION

The most important finding of this study was that PMMA cement significantly improves the primary stability in case of Schatzker type II tibial plateau fractures. And the multivariate analysis of variance confirms that PMMA, independent of the type of osteosynthesis used, strengthens the fixation.

Mechanical Influence of PMMA Filling

This fracture pattern is the most common tibial plateau fracture, and minimally invasive surgical management is increasingly used (Vendeuvre and Gayet, 2021). The balloon reduction technique has already been studied without filling and provides better

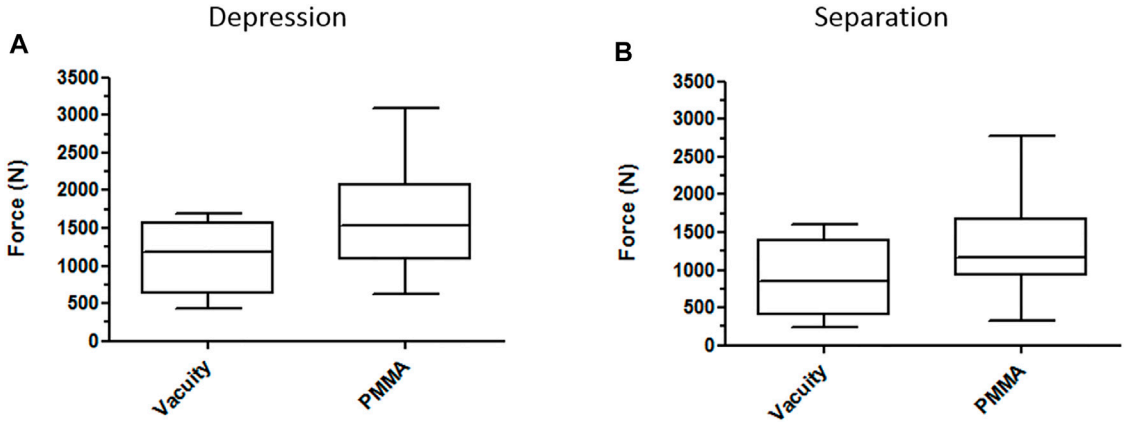

FIGURE 4 | Box plots on the contribution of PMMA in the stabilization of depression **(A)** and separation **(B)** components on all types of fixations.

mechanical stabilization than the bone tamp technique (Vendeuvre et al., 2018). Using a balloon to reduce tibial plateau fractures offers the possibility of using a semi-liquid filler such as PMMA. PMMA has also previously shown efficacy on pull-out tests on pedicle screws. A previous biomechanical study with a finite element method has shown that the cement filling of the tibial depression fracture may increase implant stability and decrease the loss of depression reduction, while the presence of the cement in the healed model renders the load distribution uniform (Belaid et al., 2018). Different clinical studies also did not report loss of reduction (Gosling et al., 2005; Evangelopoulos et al., 2010; Ollivier et al., 2016; Cuzzocrea et al., 2018). When reducing the fracture, the balloon compacts the cancellous bone and thus avoids the risk of cement leakage. The semi-liquid injection is then secured. Due to the proximity to the cartilage, no cement leakage can be allowed because polymerization is done at 80°C. Polymerization at 90°C can induce a risk of cartilage, skin, nerve, and vascular burns (Verlaan et al., 2003). However, bone vitality appears to remain intact according to SPECT/CT analysis after cement-augmented balloon tibioplasty (Jentzsch et al., 2015) when technical principles and indications are strictly respected (Mauffrey et al., 2014; Vendeuvre and Gayet, 2021).

Mechanical Influence of Osteosynthesis Regarding the Split and Depression Components

The Schatzker fracture has two components: separation and depression (Schatzker et al., 1979; Zeltser and Leopold, 2013). The purpose of fixation for these fractures is to control these two parameters. Therefore, screws must be positioned below the depression to control the separation. It is also necessary to increase the contact to the cortical bone by using washers or plates to decrease the stress for better control of the separation (Mauffrey et al., 2014). The new plating systems meet this requirement: screws that can be angled (30°) to position themselves under the bone recess and an anatomical shape to fit the shape of the bone best and thus increase the external contact surface for separation control. The NCB® Zimmer plate offers a medium curvature, and the Synthes VA-LCP® plate offers the advantage of two possible curvatures to accommodate individual variability best. We used the latest minimally invasive locked plates, therefore being consistent with Boisrenoult's study (Boisrenoult et al., 2000), which showed no difference between non-locked plates and screw fixation. At the time of this previous study, it was impossible to use MIPPO mini-invasive plates; therefore, mini-invasive reduction fixation under arthroscopy was done using only screws. Nowadays, plating systems have changed and been perfected, using locked screws, but the conclusion remains the same. Our study confirms the absence of significant difference between the three kinds of percutaneous osteosynthesis.

The fixation system one uses is a matter of habit and depends on its possibility to stabilize the reduced fracture. Indeed, a fracture in which separation pattern is dominant will be more easily reduced and stabilized using a plate, which is not the case if the depression is preponderant.

We created a reproducible cadaveric Schatzker type II fracture for this study (Belaid et al., 2018). However, many variations for this type of fracture can be seen, the separation can be preponderant, or the depression can be. If the separation is predominant, then its control can be much simpler with an anatomically shaped plate with a console-type fixation on the reduction obtained by ligamentotaxis. If the depression pattern is predominant, screw fixation is simpler and sufficient (Vendeuvre and Gayet, 2021).

Impact on Postoperative Rehabilitation

Results from our study allow for optimistic outcomes regarding postoperative rehabilitation and may lead to early return to full weight-bearing. In 1970, Morrison observed that walking requires 200–300% of the bodyweight (a percentage that increases when standing and going down the stairs) (Morrison, 1970), corresponding to 1570–2360N for an 80 kg patient. In our study, we observed fixation failure with fracture displacement at an average of 1609.6 N when fixation was done after balloon reduction with PMMA filling, and 1102.3 N in the group without

filling. Patients weighing less than 80 kg could thus resume full weight-bearing, protected by two crutches, immediately after surgery.

Strengths of the Study

The use of mark tracking technique highlights in an original way, without degrading the material, the stabilization of the split component of the fracture. We noticed that the elastic limit value reached the fastest for each group was the value for the split element. Fixation failure regarding split-depressed fractures would therefore be primarily due to the split component. Therefore, it seems necessary that this fracture component is correctly studied. The study of the load impact from the unicompartmental knee prosthesis shows the effect on controlling the depression element of the fracture. With a confidence interval of 95%, we increase by 500 N the bearable load allowed by PMMA. This mechanical contribution is beneficial for both components of these fractures, depression, and separation.

The high number of specimens used in this study with a reproducible and validated fracture model.

Study Limitations

The patient's age was not representative of the young, non-osteoporotic subject; there were few specimens per subgroups of 6. Our study tended towards the superiority of the MIS plates, which was not significant because of this small number of specimens. The main limitations of our study may lie in the lack of dynamic cyclic testing, which is particularly indicative of *in vivo* conditions, and the fact that we used a unicompartmental and not a total knee prosthesis to apply the load. That said, *in vivo* conditions were not sought in this study, and using a total knee prosthesis would not have allowed for an even distribution of compressive forces on the lateral tibial plateau. In future works, dynamic cyclic testing will be considered for the development of a specific loading setup combining experimental procedures with a finite element modeling (Aubert et al., 2021).

CONCLUSION

In a Schatzker type II plateau fracture, the use of a balloon for fracture reduction has been shown to increase the primary stability of the fixation when compared to bone stamp reduction alone. In addition, the balloon allows the use of a semi-liquid filler such as injectable PMMA bone cement. PMMA cement significantly improves primary stability, regardless of the type of osteosynthesis. The choice regarding which fixation system to use can therefore be left to the surgeons' appreciation. Filling with PMMA cement seems to be a very promising strategy in association with percutaneous osteosynthesis to allow rapid recovery after surgery.

DATA AVAILABILITY STATEMENT

The raw data supporting the conclusions of this article will be made available by the authors, without undue reservation.

AUTHOR CONTRIBUTIONS

Conceptualization: TV, MS, and AG; methodology: TV, CK, CB, MS, and AG; software: AG, TV, and CK; validation: AG, CB, and TV; resources: AG, CB, PR, and TV; writing—original draft preparation: TV, CK, MS, and AG; writing—review and editing: TV, CK, CB, PR, MS, and AG; supervision: AG, CB, TV, and PR; project administration: AG, CB, and TV. All authors have read and agreed to the published version of the manuscript.

REFERENCES

Aubert, K., Germaneau, A., Rochette, M., Ye, W., Severyns, M., Billot, M., et al. (2021). Development of Digital Twins to Optimize Trauma Surgery and Postoperative Management. A Case Study Focusing on Tibial Plateau Fracture. *Front. Bioeng. Biotechnol.* 9, 856. doi:10.3389/fbioe.2021.722275

Belaid, D., Vendeuvre, T., Bouchoucha, A., Brémand, F., Brèque, C., Rigoard, P., et al. (2018). Utility of Cement Injection to Stabilize Split-Depression Tibial Plateau Fracture by Minimally Invasive Methods: A Finite Element Analysis. *Clin. Biomech.* 56, 27–35. doi:10.1016/j.clinbiomech.2018.05.002

Blattert, T. R., Jestaedt, L., and Weckbach, A. (2009). Suitability of a Calcium Phosphate Cement in Osteoporotic Vertebral Body Fracture Augmentation. *Spine* 34, 108–114. doi:10.1097/BRS.0b013e31818f8bc1

Boisrenoult, P., Bricteux, S., Beaufils, P., and Hardy, P. (2000). Screws versus Screw-Plate Fixation of Type 2 Schatzker Fractures of the Lateral Tibial Plateau. Cadaver Biomechanical Study. Arthroscopy French Society. *Rev. Chir Orthop. Reparatrice Appar Mot.* 86, 707–711.

Cuzzocrea, F., Jannelli, E., Ivone, A., Perelli, S., Fioruzzi, A., Ghiara, M., et al. (2018). Arthroscopic-Guided Balloon Tibioplasty in Schatzker III Tibial Plateau Fracture. *Joints* 06, 220–227. doi:10.1055/s-0039-1697607

Doria, C., Balsano, M., Spiga, M., Mosele, G. R., Puddu, L., and Caggiari, G. (2017). Tibioplasty, a New Technique in the Management of Tibial Plateau Fracture: A Multicentric Experience Review. *J. Orthopaedics* 14, 176–181. doi:10.1016/j.jor.2016.12.002

Evangelopoulos, D. S., Heitkemper, S., Eggli, S., Haupt, U., Exadaktylos, A. K., and Benneker, L. M. (2010). Percutaneous Cement Augmentation for the Treatment of Depression Fractures of the Tibial Plateau. *Knee Surg. Sports Traumatol. Arthrosc.* 18, 911–915. doi:10.1007/s00167-009-1003-x

Gosling, T., Schandelmaier, P., Muller, M., Hankemeier, S., Wagner, M., and Krettek, C. (2005). Single Lateral Locked Screw Plating of Bicondylar Tibial Plateau Fractures. *Clin. Orthopaedics Relat. Res.* 439, 207–214. doi:10.1097/00003086-200510000-00036

Jentzsch, T., Fritz, Y., Veit-Haibach, P., Schmitt, J., Sprengel, K., and Werner, C. M. L. (2015). Osseous Vitality in Single Photon Emission Computed Tomography/computed Tomography (SPECT/CT) after Balloon Tibioplasty of the Tibial Plateau: a Case Series. *BMC Med. Imaging* 15, 56. doi:10.1186/s12880-015-0091-y

Kayanja, M., Evans, K., Milks, R., and Lieberman, I. H. (2006). The Mechanics of Polymethylmethacrylate Augmentation. *Clin. Orthop. Relat. Res.* 443, 124–130. doi:10.1097/01.blo.0000200243.60426.57

Lieberman, I., and Reinhardt, M. K. (2003). Vertebroplasty and Kyphoplasty for Osteolytic Vertebral Collapse. *Clin. Orthopaedics Relat. Res.* 415, S176–S186. doi:10.1097/01.blo.0000093841.72468.a8

Morrison, J. B. (1970). The Mechanics of the Knee Joint in Relation to normal Walking. *J. Biomech.* 3, 51–61. doi:10.1016/0021-9290(70)90050-3

Ollivier, M., Turati, M., Munier, M., Lunebourg, A., Argenson, J.-N., and Parratte, S. (2016). Balloon Tibioplasty for Reduction of Depressed Tibial Plateau Fractures: Preliminary Radiographic and Clinical Results. *Int. Orthopaedics (Sicot)* 40, 1961–1966. doi:10.1007/s00264-015-3047-5

Roberts, G., Cuellar, D., Herbert, B., Hak, D., and Mauffrey, C. (2014). Balloon Tibioplasty: Pearls and Pitfalls. *J. Knee Surg.* 27, 031–038. doi:10.1055/s-0033-1363516

Schatzker, J., McBroom, R., and Bruce, D. (1979). The Tibial Plateau Fracture. The Toronto Experience 1968--1975. *Clin. Orthop. Relat. Res.* 138, 94–104.

Sebastian, S., Liu, Y., Christensen, R., Raina, D. B., Tägil, M., and Lidgren, L. (2020). Antibiotic Containing Bone Cement in Prevention of Hip and Knee Prosthetic Joint Infections: A Systematic Review and Meta-Analysis. *J. Orthopaedic Translation* 23, 53–60. doi:10.1016/j.jot.2020.04.005

Singh, V., Mahajan, R., Das, K., Chhabra, H. S., and Rustagi, T. (2019). Surgical Trend Analysis for Use of Cement Augmented Pedicle Screws in Osteoporosis of Spine: A Systematic Review (2000-2017). *Glob. Spine J.* 9, 783–795. doi:10.1177/2192568218801570

Vendeuvre, T., Babusiaux, D., Brèque, C., Khiami, F., Steiger, V., Merienne, J.-F., et al. (2013). Tuberoplasty: Minimally Invasive Osteosynthesis Technique for Tibial Plateau Fractures. *Orthopaedics Traumatol. Surg. Res.* 99, S267–S272. doi:10.1016/j.otsr.2013.03.009

Vendeuvre, T., and Gayet, L.-É. (2021). Percutaneous Treatment of Tibial Plateau Fractures. *Orthopaedics Traumatol. Surg. Res.* 107, 102753. doi:10.1016/j.otsr.2020.102753

Vendeuvre, T., Grunberg, M., Germaneau, A., Maloubier, F., Faure, J.-P., Gayet, L.-E., et al. (2018). Contribution of Minimally Invasive Bone Augmentation to Primary Stabilization of the Osteosynthesis of Schatzker Type II Tibial Plateau Fractures: Balloon vs Bone Tamp. *Clin. Biomech.* 59, 27–33. doi:10.1016/j.clinbiomech.2018.08.004

Verlaan, J.-J., Oner, F. C., Verbout, A. J., and Dhert, W. J. A. (2003). Temperature Elevation after Vertebroplasty with Polymethyl-Methacrylate in the Goat Spine. *J. Biomed. Mater. Res.* 67B, 581–585. doi:10.1002/jbm.b.20002

Wang, J.-Q., Jiang, B.-J., Guo, W.-J., Zhang, W.-J., Li, A.-B., and Zhao, Y.-M. (2018). Arthroscopic-assisted Balloon Tibioplasty versus Open Reduction Internal Fixation (ORIF) for Treatment of Schatzker II-IV Tibial Plateau Fractures: Study Protocol of a Randomised Controlled Trial. *BMJ Open* 8, e021667. doi:10.1136/bmjopen-2018-021667

Wittenberg, R. H., Lee, K.-S., Shea, M., White, A. A., and Hayes, W. C. (1993). Effect of Screw Diameter, Insertion Technique, and Bone Cement Augmentation of Pedicular Screw Fixation Strength. *Clin. Orthopaedics Relat. Res.* 296, 278–287. doi:10.1097/00003086-199311000-00045

Zeltser, D. W., and Leopold, S. S. (2013). Classifications in Brief: Schatzker Classification of Tibial Plateau Fractures. *Clin. Orthop. Relat. Res.* 471, 371–374. doi:10.1007/s11999-012-2451-z

Conflict of Interest: The authors declare that the research was conducted in the absence of any commercial or financial relationships that could be construed as a potential conflict of interest.

Publisher's Note: All claims expressed in this article are solely those of the authors and do not necessarily represent those of their affiliated organizations, or those of the publisher, the editors, and the reviewers. Any product that may be evaluated in this article, or claim that may be made by its manufacturer, is not guaranteed or endorsed by the publisher.

frontiers in Bioengineering and Biotechnology

ORIGINAL RESEARCH
published: 01 March 2022
doi: 10.3389/fbioe.2022.823557

Role of the Anterior Center-Edge Angle on Acetabular Stress Distribution in Borderline Development Dysplastic of Hip Determined by Finite Element Analysis

Songhao Chen[1†], *Liqiang Zhang*[2,3†], *Yuqian Mei*[1,4], *Hong Zhang*[5], *Yongcheng Hu*[6*] and *Duanduan Chen*[1*]

[1]School of Life Science, Beijing Institute of Technology, Beijing, China, [2]Tianjin Medical University, Tianjin, China, [3]Department of Orthopaedics, Shanxi Children's Hospital, Taiyuan, China, [4]School of Medical Imaging, North Sichuan Medical College, Sichuan, China, [5]Department of Orthopaedics, The Fourth Medical Centre of PLA General Hospital, Beijing, China, [6]Department of Bone and Soft Tissue Oncology, Tianjin Hospital, Tianjin, China

OPEN ACCESS

Edited by:
Mohammad Nikkhoo, Islamic Azad University, Iran

Reviewed by:
Kamran Hassani, Islamic Azad University, Iran
Elango Natarajan, UCSI University, Malaysia

***Correspondence:**
Yongcheng Hu
yongchenghu@163.com
Duanduan Chen
duanduan@bit.edu.cn

[†]*These authors share first authorship*

Specialty section:
This article was submitted to Biomechanics, a section of the journal Frontiers in Bioengineering and Biotechnology

Received: *27 November 2021*
Accepted: *17 January 2022*
Published: *01 March 2022*

Citation:
Chen S, Zhang L, Mei Y, Zhang H, Hu Y and Chen D (2022) Role of the Anterior Center-Edge Angle on Acetabular Stress Distribution in Borderline Development Dysplastic of Hip Determined by Finite Element Analysis. Front. Bioeng. Biotechnol. 10:823557. doi: 10.3389/fbioe.2022.823557

Background: The joint with hip dysplasia is more likely to develop osteoarthritis because of the higher contact pressure, especially in the socket. The lateral center-edge angle (LCEA) is the major indicator for hip dysplasia *via* radiography. However, the pathological conditions of LCEA angles in the range of 18°–25° are still controversial, which challenges precise diagnosis and treatment decision-making.

Objective: The purpose of this study is to investigate the influence of anterior center-edge angle (ACEA) on the mechanical stress distribution of the hip joint, *via* finite element analysis, to provide insights into the severity of the borderline development dysplasia.

Methods: From 2017 to 2019, there were 116 patients with borderline developmental dysplasia of the hip (BDDH) enrolled in this research. Based on the inclusion criteria, nine patients were involved and categorized into three LCEA groups with the maximal ACEA differences. Patient-specific hip joint models were reconstructed from computed tomography scans, and the cartilages, including the labrum, were established *via* a modified numerical method. The finite element analysis was conducted to compare the stress distributions due to the different ACEA.

Results: As ACEA decreased, the maximum stress of the acetabulum increased, and the high stress area developed toward the edge. Quantitative analysis showed that in the cases with lower ACEA, the area ratio of high stress increased, and the contact facies lunata area significantly affected the stress distribution.

Conclusion: For patients with BDDH, both the ACEA and the area of facies lunata played essential roles in determining the severity of hip dysplasia and the mechanical mechanism preceding osteoarthritis.

Keywords: borderline developmental dysplasia of the hip, cartilage of hip joint, finite element analysis, stress distribution, hip joint

1 INTRODUCTION

The hip joint is the most critical structure for stability and weight-bearing in the joint formation between the acetabulum and the femoral head (Zhao et al., 2010). Developmental dysplasia of the hip (DDH) is a common orthopedic disease and a complex developmental disorder. The anatomical features usually manifest as incomplete wrap of the acetabulum into the anterior and lateral parts of the femoral head, reducing the coverage area of the contact in the hip joint (Murphy et al., 1990). This disease can lead to structural instability of the hip joint and thus result in osteoarthritis (Klaue et al., 1991; Weinstein et al., 2003). From a biomechanical perspective, the reduction in load transfer area contributes to the increased contact pressure distribution in the dysplastic hip joint in daily life (Russell et al., 2006; Henak et al., 2013). Pathologically, because of the cumulative effect of time in the areas of high stress concentration and the discontinuous distribution over articular cartilage (Henak et al., 2014), it will eventually cause acetabular labrum and cartilage damage, accelerating the hip degradation (Murphy et al., 1995).

The diagnosis of DDH mainly relies on the structural characteristics of the hip joint based on X-ray image measurements (Chosa et al., 1997). Wiberg initially proposed an index named the lateral center-edge angle (LCEA), which is the angle formed by a line connecting the center of the femoral head perpendicular to the transverse axis of the pelvis and the line connecting the center of the femoral head and the uppermost lateral point of the acetabular sclerosis weight-bearing area in the anterior and posterior view of the pelvis in standing position (Wiberg, 1939). According to this definition, LCEA <18° is defined as hip dysplasia, whereas LCEA >25° is defined as the normal state. However, when LCEA is between 18° and 25°, the pathological status of the hip is uncertain and is defined as critical dysplasia. A few researches defined the hip with the LCEA in the range of 18°–25° as the borderline developmental dysplasia of the hip (BDDH) (Domb et al., 2013; Chandrasekaran et al., 2017; Hatakeyama et al., 2018) and indicated that the hip joint under this condition is in a state of mild dysplasia (Fukui et al., 2015; Matsuda et al., 2017; Ricciardi et al., 2017). Recent researches also suggest that the LCEA alone might not be adequate to evaluate the severity of hip dysplasia (Jessel et al., 2009; Fujii et al., 2010). Multiple morphological features, such as the anterior center-edge angle (ACEA), the acetabular wall indices (Siebenrock et al., 2012), the femoral epiphyseal acetabular roof, and the Tönnis angle (Lequesne and de SEZE, 1961), should be involved. In particular, the ACEA can assess the anterior coverage of the femoral head, which can significantly affect the magnitude and distribution of stress in the hip joint (Lequesne, 1961a; Ganz et al., 2003). The parameter is the angle formed by a vertical line passing through the center of the femoral head and the line passing through the center point of the femoral head and the most anterior point of the acetabular sourcil on a pseudosection radiograph.

With the rapid development of interdisciplinary research in the medical field, numerical computing technology has made significant contributions to medical problem analysis and risk prediction in the study of pathological mechanisms. Finite element analysis (FEA) is an effective tool to reveal biomechanics (Kaku et al., 2004) and has been widely applied to investigate the biomechanical behavior of spine and tibia bone with good agreement with experimental measurements (Dalstra et al., 1995; Anderson et al., 2008; Anderson et al., 2010). Tan et al. conducted numerical study of bone healing process of a transverse fractured tibia (Tan et al., 2021). Kosalishkwaran et al. applied this technique to the spine, proposing an innovative method for calculating RoM (Kosalishkwaran et al., 2019). Furthermore, Schuller et al. first used the FEA technique to study the dysplasia of the hip (Schuller et al., 1993), and the subsequent researches mainly focused on the mechanical evaluation of different LCEAs and Bernese periacetabular osteotomy treatment.

In this study, specifically targeting the BDDH, we aimed to investigate the mechanical influence of ACEA by establishing detailed models of the hip joint, including the acetabulum, the femoral head, the acetabular cartilage, and the femoral head cartilage. The spatial stress distributions of the acetabulum and acetabular cartilage were analyzed in detail to assist the clinical diagnosis of the severity of hip dysplasia.

2 METHODS

2.1 Patients

This retrospective research collected 116 patients (144 hips) diagnosed with BDDH in the Fourth Medical Center of PLA General Hospital from July 2017 to May 2019 at the outpatient service. Informed consent was obtained for the studies with human subjects.

For the purpose of this study, inclusion criteria included the following: (1) the LCEA was in the range of 18°–25°; (2) the ACEA was less than 25°; (3) the pseudosection radiographs and standing anteroposterior pelvic and computed tomography (CT) scanning data were well preserved; (4) the Tönnis osteoarthritis grade less than or equaled to 1. The patients were excluded according to the following: (1) the patients had an operation history of the hip disease; or (2) the patients had a medical history of neuromuscular diseases, such as cerebral palsy or poliomyelitis.

Eventually, nine hips with borderline dysplasia were included in our study. The study was approved by the institutional review board. All enrolled patients who agreed to participate in this study and publish the results of the study signed an informed consent form. The average age of patients was 35.33 years (range = 24–48 years), and the relevant patient information is listed in **Table 1**. The LCEA, ACEA, and Tönnis angle were all measured three times by two experienced orthopedic surgeons independently, and the averaged values were set as the ultimate results. As the ACEA is changing with the LCEA in the same hip joint model, the use of idealized models to form different LCEAs and ACEAs by rotating the acetabulum and femoral head is not applicable to this study. The ACEA greater than 25° was considered as a physiological condition that was excluded in this research. Eventually, as shown in **Figure 1**, nine hips with the available LCEAs, ranging from 18° to 20°, satisfying the condition

TABLE 1 | Clinical data of patients with borderline developmental dysplasia of the hip.

Patients	A_1	A_2	A_3	B_1	B_2	B_3	C_1	C_2	C_3
Hip affected	Left	Left	Right	Left	Right	Right	Right	Left	Left
Gender	Female	Female	Female	Female	Female	Female	Female	Female	Female
Age (years)	35	34	24	31	42	41	39	48	24
LCEA (°)	18.1	18.1	18.2	18.9	19.1	19.1	20.1	20	19.9
ACEA (°)	21.6	15.7	13.9	24.8	19.8	−7.5	21	18.5	12.8
TONNIS (°)	10.6	15.2	11.3	10.8	13.5	11.1	11	15	13.1

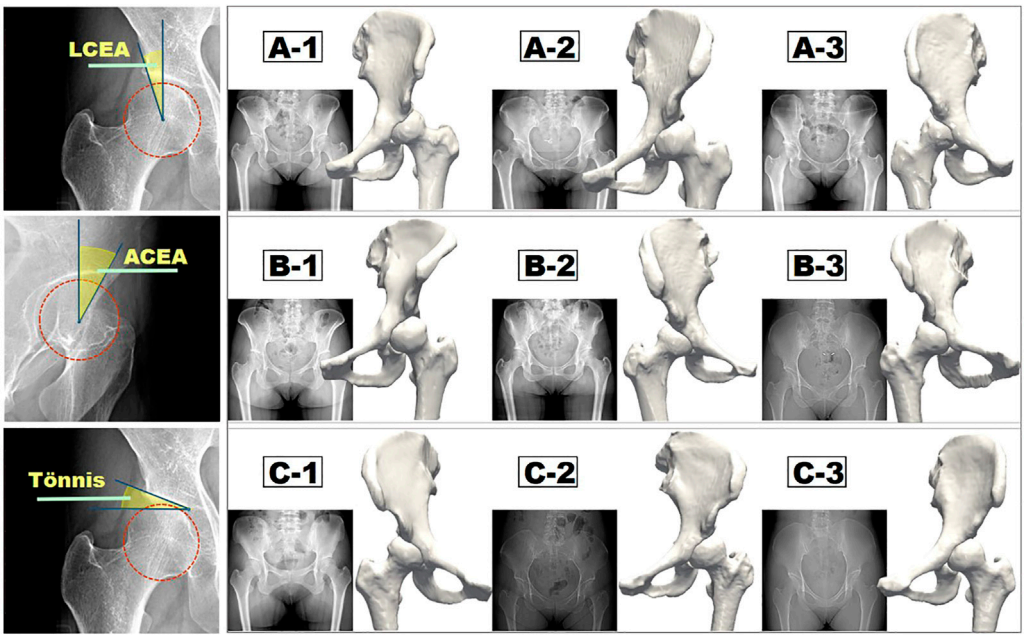

FIGURE 1 | Measurement methods of three major morphological indices (LCEA, ACEA, and Tönnis angle) and the corresponding three groups of reconstructed hip joint models.

of ACEA <25°, were divided into three groups (A, B, C) with various ACEAs with a maximal difference. Because of the interdependent relationship between LCEA, ACEA, and Tönnis angle, the otherness of Tönnis angle was not considered temporary in this research.

2.2 Construction of Three-Dimensional Model of Hip Joint

The patient-specific three-dimensional (3D) models of the hip joint (bony structure, i.e., acetabulum and femur) were constructed from the CT cross-sectional images (GE Medical Systems, United States). Scanning parameters were as follows: voltage: 120 kV; slice thickness: 1.3 mm; kilovolt peak (kVp): 120 kVp; spacing between slices: 5 mm. The DICOM data of enrolled hips were loaded into the Mimics (Materialise, Belgium), and regions of femur and acetabulum were extracted by thresholding, region growing, and manual editing. Surgeons confirmed the final mask, and reconstructed 3D models were carefully improved by executing the smooth operation to reconstruct the original surface profile.

Cartilage structure and cartilage interface are significant factors in computing the stress distribution of the hip joint (Anderson et al., 2005). Currently, the commonly used techniques for cartilage construction include spherical cartilage modeling, uniform thickness cartilage modeling, and midline cartilage modeling (Anderson et al., 2005). The contact stress of the hip joint predicted by the first spherical cartilage modeling method is continuous, and the peak value is lower, which is closer to the physiological state (Li et al., 2018). For this reason, the spherical cartilage modeling method was used in this research.

The schematic diagram of the cartilage construction method is shown in **Figure 2**, and the cartilages included the acetabular cartilage, the cartilage of the femoral head, and the labrum. First, the center point $\boldsymbol{O}$ of the femoral head was calculated and used as the shared center point of the minimal circumscribed sphere ($\boldsymbol{S_A}$) of the femoral head with a radius of $\boldsymbol{r_1}$, shown by the light blue circle in **Figure 2A**. Second, the maximal inscribed sphere of the acetabular fossa ($\boldsymbol{S_B}$) was built based on the center point O, and

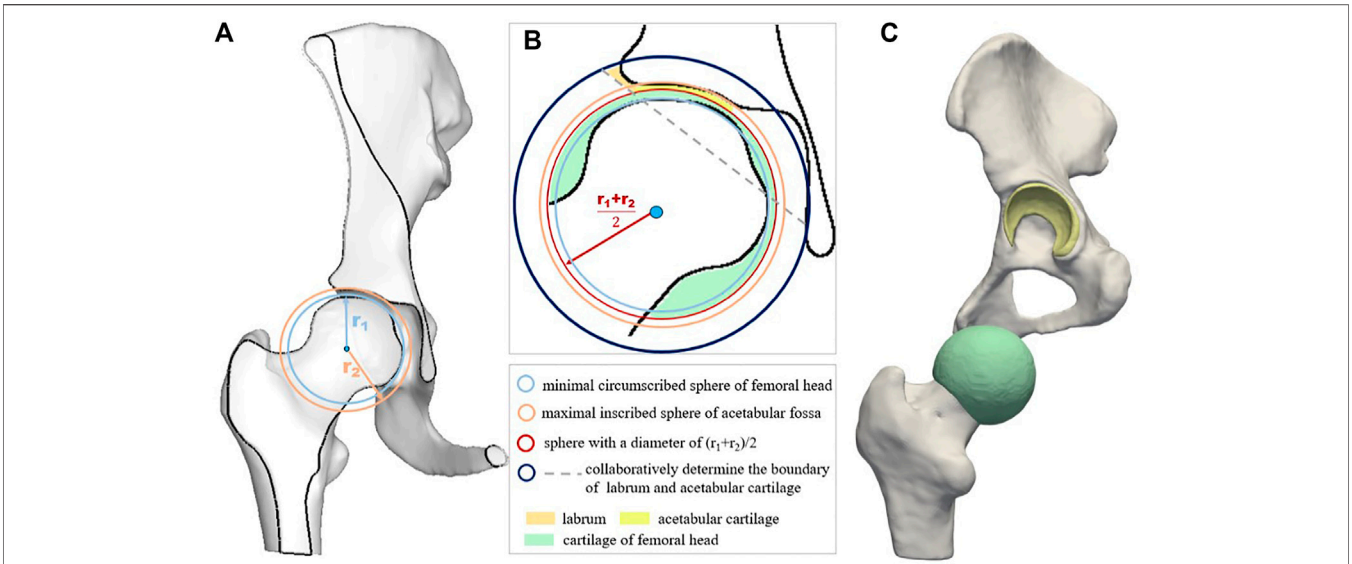

FIGURE 2 | Schematic diagram of cartilage construction method including acetabular cartilage, cartilage of femoral head, and the labrum. **(A)** displays the minimal circumscribed sphere of the femoral head and the maximal inscribed sphere of the acetabular fossa; **(B)** is the schematic diagram of cartilage construction method; and **(C)** shows the geometric models of the cartilage layers.

the corresponding radius was denoted as r_2 (**Figure 2A**, orange circle). The homocentric sphere S_C with radius $(r_1 + r_2)/2$ was generated. It was the interface boundary between the acetabular cartilage and the cartilage of the femoral head, as shown in the red circle in **Figure 2B**. The cartilage of the femoral head was then obtained by subtracting the femoral head volume using the sphere S_C *via* the Boolean operation. Another homocentric sphere S_D with a larger radius was established to build the labrum considering its high mechanical impact (**Figure 2B**, dark blue circle). The acetabular cartilage and labrum combination was calculated by S_D minus S_C and then cut by the dotted gray line concerning the labrum thickness and deleted the part connected to the acetabular fossa. The constructed femoral head cartilage and the acetabular cartilage and labrum were built and represented by green and yellow in **Figure 2C**.

2.3 Mesh Generation and Material Property Assignment

The reconstructed acetabulum and femoral head were discretized with tetrahedral grid in all of the hip models. The average cell numbers of the acetabular tetrahedral units, femoral tetrahedral units, and tetrahedral cartilage units were 251,068, 52,720, and 3,837, respectively. Grid independency analysis was conducted before the computations of all the hip models, which confirmed that the baseline grid assignment was adequate for the current research. Detailed information regarding the mesh validation is presented in the Supporting Document.

The contact parts between models were treated as common nodes. All discretized models were imported back to Mimics (Materialise) to assign material properties according to the spatial gray value in CT scans. The Young's modulus of the cartilage tissue was set as 10.35 MPa (Ike et al., 2015), whereas that for the bone tissue was calculated based on the relationship between the element-specific gray value in the CT images and the elasticity property of the material (Lequesne, 1961b). The Poisson ratio of all bone tissues and cartilage tissues was set as 0.4. By applying the formulas presented in **Table 2**, the spatial material attributes could be assigned in the center of each element.

2.4 Boundary Conditions

Previously, Bergeman et al. used sensors to detect the change in the direction of stress between the acetabulum and the femoral head of ordinary people in various activities of daily life (**Figure 3A**) (Bergmann et al., 2010). In the current study, the state in which the acetabulum experienced the most significant stress throughout gait was investigated. An averaged body weight of 60 kg was considered. Based on measurements of the curve in **Figure 3A**, the magnitudes of the load in the *X*, *Y*, and *Z* directions were 307.29, −189.22, and 1,326.12 N, respectively, (Bergmann et al., 2010), and the force acting site was at the center of the femoral head (**Figure 3B**). The sacroiliac joint and the

TABLE 2 | Formulas describing the transformation from gray value to elastic modulus.

Gray value	Bone density (g/cm^3)	Young's modulus (MPa)
HU ≤ −1	$\rho = 0$	0.001
HU > −1	$\rho = (HU + 1.4246) \times 0.001/1.058$	
	$0 < \rho \leq 0.27$	$33900\rho^{2.20}$
	$0.27 < \rho < 0.6$	$5307\rho + 469$
	$0.6 \leq \rho$	$10200\rho^{2.01}$

HU, Hounsfield units.

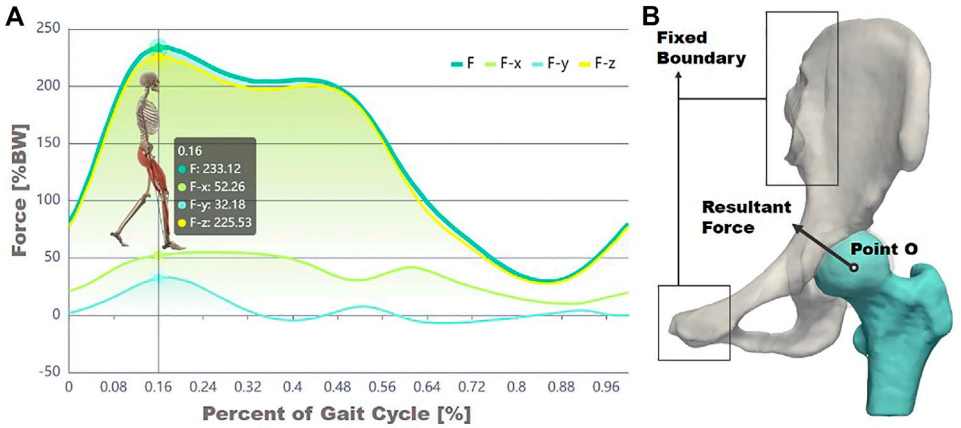

FIGURE 3 | Experimental data of force decomposition over a gait cycle **(A)** and the illustration of forces and constraint boundary conditions **(B)**.

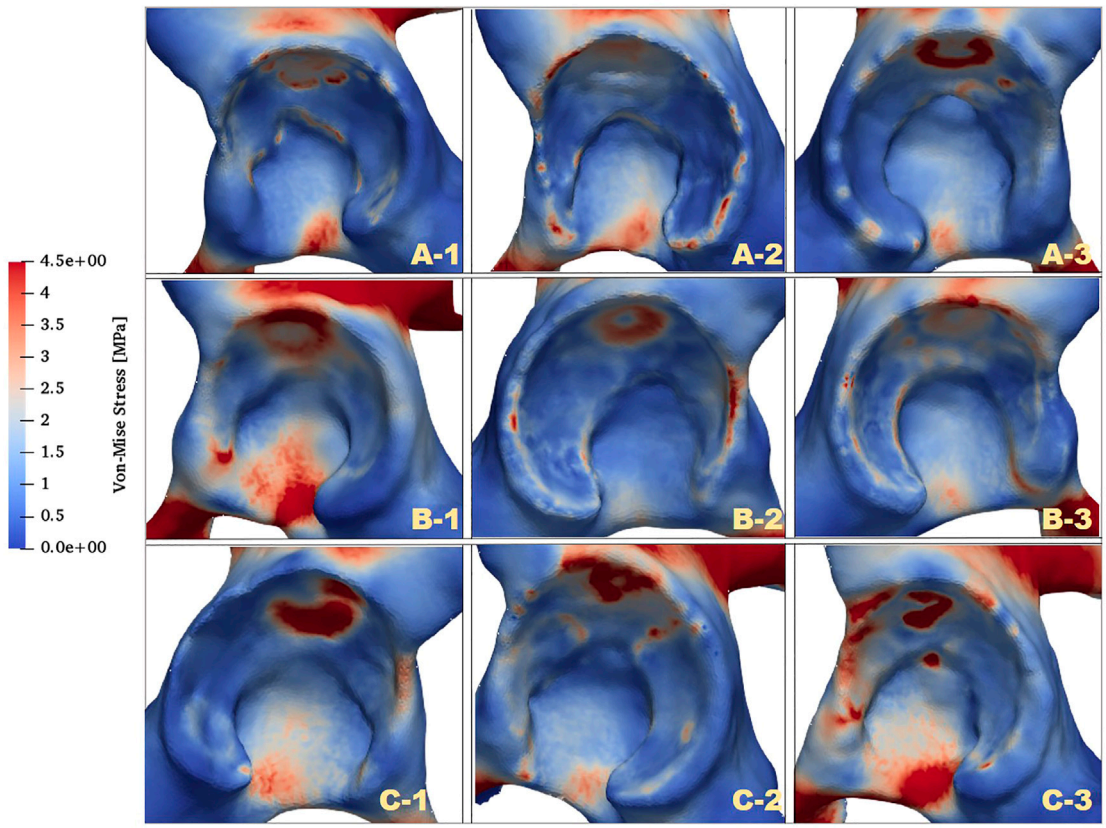

FIGURE 4 | Comparison of stress distributions of the acetabulum at different LCEA and ACEA angles.

pubic symphysis were set with constraint condition of zero displacements. The acetabular cartilage and the acetabulum, the femoral cartilage, and the femoral were set as the bound state. Considering that the nonlinear contact between the femoral head and the acetabulum might bring uncertainty to the entire solution process, this study used a constraint equation to constrain the contact surface between the two cartilages, transforming the nonlinear contact problem into a linear

TABLE 3 | Quantitative stress analysis on acetabulum and local facies lunata.

Patients		A_1	A_2	A_3	B_1	B_2	B_3	C_1	C_2	C_3
Maximum stress of the acetabulum [MPa]		5.08	5.43	6.31	6.67	6.87	10.31	5.88	6.42	6.75
Contact area [mm^2]		2,236	2,416	2,021	1,763	2,047	1,830	2,352	2,287	1,990
Area percentage [%]	[0–1) MPa	72.57	61.2	49.64	75.4	82.1	76.07	73.67	52.07	38.64
	[1–2) MPa	22.47	30.6	32.03	19.64	14.02	19.68	17.63	32.27	38.25
	[2–3) MPa	4.41	7.5	9.17	3.67	3.18	3.92	5.15	9.43	19.92
	[3–4) MPa	0.48	0.6	3.36	0.9	0.58	0.12	2.04	3.47	6.62
	[4–5) MPa	0.05	0.09	3.57	0.29	0.12	0.14	0.96	1.92	2.61
	[5–6) MPa	0	0	2	0.11	0	0.05	0.55	0.59	0.8
	[6–7) MPa	0	0	0.24	0	0	0	0	0.24	0.14

contact problem, in order to ensure the stability of the solution process.

2.5 Computation Modeling and Results Analysis

A finite element solver (ANSYS Inc., 2019) was applied to numerically solve the structural mechanics equations. According to the fourth strength theory (the von Mises theory or shape change–specific energy density theory), the von Mises equivalent stress was selected as the reference standard. The maximum stress values and quantitative stress distributions were analyzed by selecting regions of interest (ROIs). We mainly focused on the acetabulum and the contact surface of acetabular cartilage and acetabulum, that is, the facies lunata, through the equivalent stress program provided by the finite element solution.

3 RESULTS

3.1 Global Acetabular Stress Analysis

The distributions of von Mises stress (simplified as stress below) of the acetabulum in the three groups are plotted in **Figure 4**. In all cases, a high-stress area was located at the acetabular labrum with various degrees and positions. This phenomenon was consistent with the statement proposed by Hanak et al., which reported that the labrum in dysplastic hips supported more of the load transferred across the joint than in normal hips (Henak et al., 2011; Henak et al., 2014). With reduction of the ACEA, the high-stress concentration region was moving from the side near the acetabular fossa to the labrum side. For case C_1, the stress on the labrum was relatively low with a significantly smaller area compared with the other cases. This might be because the LCEA and ACEA of this model (LCEA of 20.1° and ACEA of 21°) were closer to the standard values than other models.

Apart from the stress distribution, the maximum stress of the acetabulum for all models was also extracted, and the highest stress magnitudes were listed in **Table 3**. It was clearly shown that the maximal stress value increased with the decline of ACEA in the same group. Notably, the maximum stress in group B was higher than that in groups A and C. The contact area between the acetabulum and acetabular cartilage was measured for all cases and recorded in **Table 3**. Results revealed that the average contact area in group B was 1,871 mm^2, which was much lower than that in group A (2,224 mm^2) and group C (2,209 mm^2). Therefore, the relatively high stress in group B might be related to the smaller contact area.

3.2 Quantitative Stress Distribution of Facies Lunata

To further investigate the mechanics of the acetabulum, the stress distributions of the local facies lunata for each case were extracted, as shown in **Figure 5**. Compared with the stress distribution on the global acetabulum, **Figure 5** displays that the high-stress area gradually moved toward the edge and increased on the local labrum with the decline of ACEA. This mechanical behavior was recognizable, especially in group C, where the area contact region decreased monotonic, indicating that the contact area played an essential role on the mechanical distribution. Furthermore, the extracted stress data were divided by an interval of 1 MPa, and the corresponding area ratio was calculated for each interval. The area ratio of each stress interval at different ACEAs was compared.

The area ratios of each stress interval were calculated and are listed in **Table 3** and shown as a histogram in **Figure 6**. Most stress values were located between 0 and 1, and the average number was 64.6% of all cases. Results presented a declined trend of area ratio with the rise of stress magnitude. Especially for the higher stress interval, that is, 5–7 MPa, the area percentage was significantly limited, which accounted for only a smaller proportion of the total area of the acetabular contact. The area decreased in groups A and C in the first interval, whereas it increased in other stress intervals as the ACEA declined, indicating the smaller ACEA leading to an incline to higher stress and corresponding larger area. In group B, there was no coincident tendency affected by the ACEA as shown in groups A and C. In fact, the area of the acetabular fossa of the B_1 model was 3,898 mm^2, which was the smallest compared with the other models (≥4,000 mm^2), and the B_1 model also had the lowest contact area (1,736 mm^2), as shown in **Table 3**.

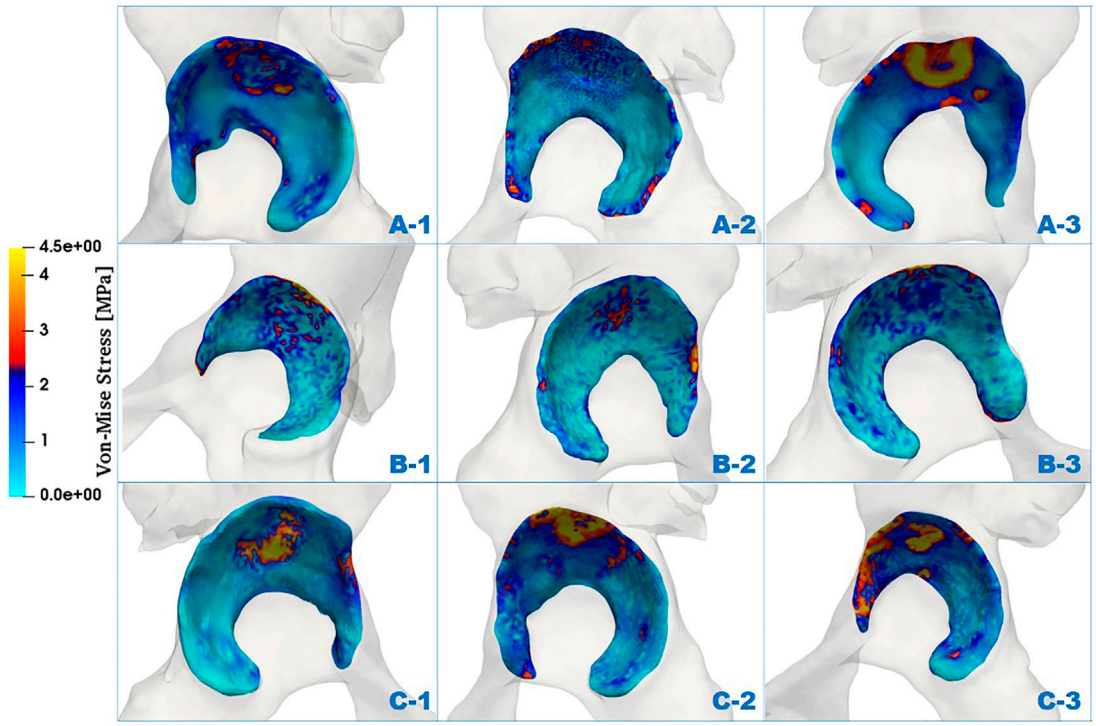

FIGURE 5 | Comparison of von Mises stress distributions of facies lunata at different LCEA and ACEA angles for all models.

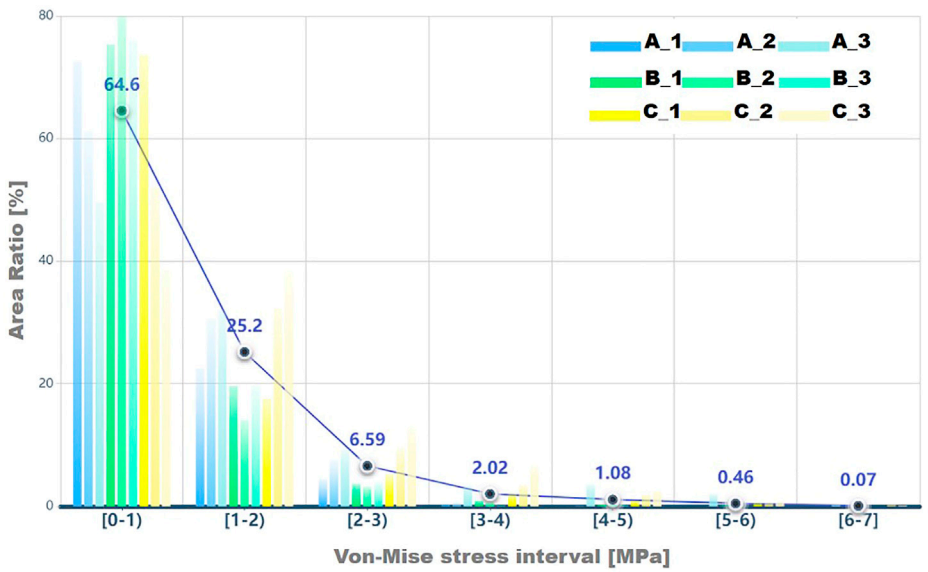

FIGURE 6 | The area ratio in each von Mises stress interval for results on facies lunata is displayed, and a circle icon represents the average percent value for each stress interval.

4 DISCUSSION

Accurate diagnosis of hip dysplasia is of great significance for the subsequent decision-making of the treatment strategy, that is, conservation therapy or surgery. Current diagnosis and the severity evaluation mainly rely on the morphologic information, such as the LCEA, the ACEA, the Tönnis angle, and so on, which were provided by medical imaging. It has been

reported that the LCEA could be considered as a reliable index because it is closely related to other radiographic markers and is highly associated with cartilage damage and osteoarthritis severity (Zhang et al., 2020). Moreover, it has been extensively used for the clinical diagnosis of DDH. However, when LCEA falls into the range of 18°–25°, physicians might face the challenge to precisely determine the dysplasia status and the severity. Therefore, to reveal other related morphological indicators and to understand the underlying mechanisms are needed. In this study, the influence of the ACEA on the mechanical effects of the hip was quantitatively studied. Together with LCEA, the results preliminarily confirmed the rationality of adding ACEA as the indication to refine the severity evolution of BDDH.

In order to obtain the stress variation accurately in the acetabulum with the change of ACEA angle, a new method was proposed in the operation of cartilage reconstruction. The thick articular cartilage layer in the hip joint helps to slow down the tremendous force passing through the hip joint, which can significantly influence the study of the mechanical behavior of the hip joint. Cartilage layer can be observed in magnetic resonance imaging (MRI) but not available in CT scans unless contrast is injected (Harris et al., 2012; Li et al., 2018; Wesseling et al., 2019). However, the majority of BDDH patients in outpatient experienced only the X-ray and ordinary CT scans. In this research, the cartilage was constructed based on the model reconstructed from CT images (Anderson et al., 2010), and resultant cartilage morphology was comparable to the data reported in previous studies (Ng, 2017). More importantly, a higher percentage of the load was transferred to the labrum in the dysplastic model because the femoral head achieved equilibrium near the lateral edge of the acetabulum (Henak et al., 2011). Therefore, we proposed a new acetabular cartilage construction method that combined the labrum into the cartilage (**Section 2.2**). Previous studies have demonstrated that the maximum stress value is mainly concentrated in the middle and upper part of the lunar surface of the acetabulum (Zhao et al., 2010; Ghosh et al., 2015; Liu et al., 2015). Our results revealed that the labrum region presented a concentrated high-stress area. This area moved toward the edge side with the decrease in ACEA, indicating that the labrum suffered from increasing stress at a smaller ACEA. This was consistent with the measurement conducted by Henak et al. (2011), who suggested that the labrum played a more significant role in load transfer and joint stability in hips with acetabular dysplasia than in hips with standard acetabular geometry. A more detailed comparison had been made and attached in the Supporting Document. This confirmed the rationality of the current model and the reported mechanical distribution in this study. As to the bone material, we spatially assigned anisotropic material characteristics based on the Hounsfield unit values in CT images, which was an advantage compared with the uniform assignment of the bone material (Dopico-González et al., 2010; Ghosh et al., 2012). According to the force magnitude and direction of the hip joint in the whole gait range obtained by Bergmann et al. (2010), the maximum contact force of the hip joint in the single supporting phase of normal walking mode was selected as the load condition of this study, to simulate the mechanical conditions in the ROIs in the acetabulum.

By solving the finite element models of the hip joint, the qualitative and quantitative analyses were performed on the global acetabulum and the contact region between the acetabulum and acetabular cartilage locally. Results showed that the maximum stress on the acetabulum increased as the ACEA decreased. Furthermore, quantitative analysis on the contact region revealed that the area ratio of higher stress intervals (>2 MPa) increased with the decline of ACEA. These two key results presented a good agreement in groups A and C. However, they did not fully fit in group B. Combined with the geometric analysis, the higher maximum stress in the B_3 model was postulated because of the smaller ACEA and the lower area of facies lunata. The area ratio in the range of 0–2 MPa was also smaller for the B_1 model, with a maximum ACEA in group B. It should be noted that the B_1 model presented the smallest area of both facies lunata acetabular fossa among all groups. This extraordinary phenomenon in group B suggests that, apart from the ACEA angle, the surface area of facies lunata and acetabular fossa was also an important factor in the mechanical distribution of the hip joint.

This study also implicated that the finite element model could be used as a valuable tool to assist the evaluation of the severity of BDDH. The contact area of BDDH was mainly limited to the upper half, and the stress concentration area was also in the upper part of the acetabulum, which was similar to the prediction by Anderson et al. (Kaku et al., 2004). However, a portion of the acetabular concentration predicted by our analysis was located in the acetabular fossa because of the dysplastic acetabulum poor coverage of the femoral head.

The present study suffered from several limitations, which should be further improved in the future. First, the impact of the Tönnis angle was not considered, which might also play a role in the acetabular mechanical behavior. Because the LCEA, ACEA, and Tönnis angle were interdependent, the idealized model was not applicable in the current study. Because of the strict inclusion criteria, the influence of the Tönnis angle could not be studied in the current research. Second, the cartilage construction was not established based on MRI or enhanced CT. The modified reconstructed methods were proposed by this study, which was able to generate relatively realistic models of the cartilage based on ordinary CT images. Future studies could be improved when multimodality data were available for each patients. Third, a single loading state was analyzed in the current study. Dynamic analysis of a complete gait cycle with various load patterns should be achieved in the future.

5 CONCLUSION

This study investigated the relationship between ACEA and the mechanical behavior of the acetabulum of BDDH. By establishment of comprehensive finite element models of the

hip joint, this study revealed that the high-stress concentration area increased as the ACEA declined. The contact region of facies lunata was also a significant factor influencing the stress distribution. This research confirmed the effectiveness of the ACEA in determining the severity of BDDH, which might facilitate precise evaluation of the disease when LCEA was in the range of 18°–25° and thus contribute to wise decision-making of the subsequent treatment.

DATA AVAILABILITY STATEMENT

The data that support the findings of this study are available on request from the corresponding authors. They are not publicly available due to privacy or ethical restrictions.

AUTHOR CONTRIBUTIONS

SC and YM carried out the finite element computations, data analysis and drafted the manuscript. LZ and HZ carried out the image segmentation and 3D model reconstruction and participated in mechanical analysis of the models. YH and DC designed this study, directed the mechanical simulations, and helped to draft the manuscript.

FUNDING

This study is supported by the Beijing Natural Science Foundation (L212049, L212067 and 7222298).

ACKNOWLEDGMENTS

The authors would like to thank Shukun (Beijing) Network Technology Co., Ltd. for providing additional computing resources and Bejing Infervision Technology Co., Ltd. for the technical support in medical image processing.

SUPPLEMENTARY MATERIAL

The Supplementary Material for this article can be found online at: https://www.frontiersin.org/articles/10.3389/fbioe.2022.823557/full#supplementary-material

REFERENCES

Anderson, A. E., Ellis, B. J., Maas, S. A., Peters, C. L., and Weiss, J. A. (2008). Validation of Finite Element Predictions of Cartilage Contact Pressure in the Human Hip Joint. *J. Biomech. Eng.* 130 (5), 051008. doi:10.1115/1.2953472

Anderson, A. E., Peters, C. L., Tuttle, B. D., and Weiss, J. A. (2005). Subject-specific Finite Element Model of the Pelvis: Development, Validation and Sensitivity Studies. *J. Biomech. Eng.* 127 (3), 364–373. doi:10.1115/1.1894148

Anderson, A. E., Ellis, B. J., Maas, S. A., and Weiss, J. A. (2010). Effects of Idealized Joint Geometry on Finite Element Predictions of Cartilage Contact Stresses in the Hip. *J. Biomech.* 43 (7), 1351–1357. doi:10.1016/j.jbiomech.2010.01.010

Bergmann, G., Graichen, F., Rohlmann, A., Bender, A., Heinlein, B., Duda, G. N., et al. (2010). Realistic Loads for Testing Hip Implants. *Biomed. Mater. Eng.* 20 (2), 65–75. doi:10.3233/bme-2010-0616

Chandrasekaran, S., Darwish, N., Martin, T. J., Suarez-Ahedo, C., Lodhia, P., and Domb, B. G. (2017). Arthroscopic Capsular Plication and Labral Seal Restoration in Borderline Hip Dysplasia: 2-Year Clinical Outcomes in 55 Cases. *Arthrosc. J. Arthroscopic Relat. Surgeryofficial Publ. Arthrosc. Assoc. North America Int. Arthrosc. Assoc.* 33 (7), 1332–1340. doi:10.1016/j.arthro.2017.01.037

Chosa, E., Tajima, N., and Nagatsuru, Y. (1997). Evaluation of Acetabular Coverage of the Femoral Head with Anteroposterior and False Profile Radiographs of Hip Joint. *J. Orthopaedic Sci.* 2 (6), 378–390. doi:10.1007/bf02488925

Dalstra, M., Huiskes, R., and van Erning, L. (1995). Development and Validation of a Three-Dimensional Finite Element Model of the Pelvic Bone. *J. Biomech. Eng.* 117, 272–278. doi:10.1115/1.2794181

Domb, B. G., Stake, C. E., Lindner, D., El-Bitar, Y., and Jackson, T. J. (2013). Arthroscopic Capsular Plication and Labral Preservation in Borderline Hip Dysplasia. *Am. J. Sports Med.* 41 (11), 2591–2598. doi:10.1177/0363546513499154

Dopico-González, C., New, A. M., and Browne, M. (2010). Probabilistic Finite Element Analysis of the Uncemented Hip Replacement—Effect of Femur Characteristics and Implant Design Geometry. *J. Biomech.* 43 (3), 512–520.

Fujii, M., Nakashima, Y., Yamamoto, T., Mawatari, T., Motomura, G., Matsushita, A., et al. (2010). Acetabular Retroversion in Developmental Dysplasia of the Hip. *The J. Bone Jt. Surgery-American Volume* 92 (4), 895–903. doi:10.2106/jbjs.i.00046

Fukui, K., Briggs, K. K., Trindade, C. A. C., and Philippon, M. J. (2015). Outcomes after Labral Repair in Patients with Femoroacetabular Impingement and Borderline Dysplasia. *Arthrosc. J. Arthroscopic Relat. Surg.* 31 (12), 2371–2379. doi:10.1016/j.arthro.2015.06.028

Ganz, R., Parvizi, J., Beck, M., Leunig, M., Nötzli, H., and Siebenrock, K. A. (2003). Femoroacetabular Impingement: a Cause for Osteoarthritis of the Hip. *Clin. Orthop. Relat. Res.* 417, 112–120. doi:10.1097/01.blo.0000096804.78689.c2

Ghosh, R., Gupta, S., Dickinson, A., and Browne, M. (2012). Experimental Validation of Finite Element Models of Intact and Implanted Composite Hemipelvises Using Digital Image Correlation. *J. Biomech. Eng.* 134 (8), 081003. doi:10.1115/1.4007173

Ghosh, R., Pal, B., Ghosh, D., and Gupta, S. (2015). Finite Element Analysis of a Hemi-Pelvis: the Effect of Inclusion of Cartilage Layer on Acetabular Stresses and Strain. *Comput. Methods Biomech. Biomed. Eng.* 18 (7), 697–710. doi:10.1080/10255842.2013.843674

Harris, M. D., Anderson, A. E., Henak, C. R., Ellis, B. J., Peters, C. L., and Weiss, J. A. (2012). Finite Element Prediction of Cartilage Contact Stresses in normal Human Hips. *J. Orthop. Res.* 30 (7), 1133–1139. doi:10.1002/jor.22040

Hatakeyama, A., Utsunomiya, H., Nishikino, S., Kanezaki, S., Matsuda, D. K., Sakai, A., et al. (2018). Predictors of Poor Clinical Outcome after Arthroscopic Labral Preservation, Capsular Plication, and Cam Osteoplasty in the Setting of Borderline Hip Dysplasia. *Am. J. Sports Med.* 46 (1), 135–143. doi:10.1177/0363546517730583

Henak, C. R., Anderson, A. E., and Weiss, J. A. (2013). Subject-specific Analysis of Joint Contact Mechanics: Application to the Study of Osteoarthritis and Surgical Planning. *J. Biomech. Eng.* 135 (2), 021003. doi:10.1115/1.4023386

Henak, C. R., Abraham, C. L., Anderson, A. E., Maas, S. A., Ellis, B. J., Peters, C. L., et al. (2014). Patient-specific Analysis of Cartilage and Labrum Mechanics in Human Hips with Acetabular Dysplasia. *Osteoarthritis and cartilage* 22 (2), 210–217. doi:10.1016/j.joca.2013.11.003

Henak, C. R., Ellis, B. J., Harris, M. D., Anderson, A. E., Peters, C. L., and Weiss, J. A. (2011). Role of the Acetabular Labrum in Load Support across the Hip Joint. *J. Biomech.* 44 (12), 2201–2206. doi:10.1016/j.jbiomech.2011.06.011

Ike, H., Inaba, Y., Kobayashi, N., Yukizawa, Y., Hirata, Y., Tomioka, M., et al. (2015). Effects of Rotational Acetabular Osteotomy on the Mechanical Stress within the Hip Joint in Patients with Developmental Dysplasia of the Hip. *Bone Jt. J.* 97-B (4), 492–497. doi:10.1302/0301-620x.97b4.33736

Jessel, R. H., Zurakowski, D., Zilkens, C., Burstein, D., Gray, M. L., and Kim, Y.-J. (2009). Radiographic and Patient Factors Associated with Pre-radiographic Osteoarthritis in Hip Dysplasia. *J. Bone Jt. Surgery-American Volume* 91 (5), 1120–1129. doi:10.2106/jbjs.g.00144

Kaku, N., Tsumura, H., Taira, H., Sawatari, T., and Torisu, T. (2004). Biomechanical Study of Load Transfer of the Pubic Ramus Due to Pelvic Inclination after Hip Joint Surgery Using a Three-Dimensional Finite Element Model. *J. Orthopaedic Sci.* 9 (3), 264–269. doi:10.1007/s00776-004-0772-9

Klaue, K., Durnin, C., and Ganz, R. (1991). The Acetabular Rim Syndrome. A Clinical Presentation of Dysplasia of the Hip. *The J. Bone Jt. Surg. Br. volume* 73-B (3), 423–429. doi:10.1302/0301-620x.73b3.1670443

Kosalishkwaran, G., Parasuraman, S., Singh, D. K. J., Natarajan, E., Elamvazuthi, I., and George, J. (2019). Measurement of Range of Motions of L3-L4 Healthy Spine through Offsetting Reflective Markers and In Silico Analysis of Meshed Model. *Med. Biol. Eng. Comput.* 57 (10), 2305–2318. doi:10.1007/s11517-019-02026-6

Lequesne, M., and de Seze (1961). False Profile of the Pelvis. A New Radiographic Incidence for the Study of the Hip. Its Use in Dysplasias and Different Coxopathies. *Rev. Rhum Mal Osteoartic* 28, 643–652.

Lequesne, M. (1961). Le faux profile de bassin. Nouvelle incidence radiographique pour l'etude de la hanche. Son utilite dans les differentes coxopathies. *Rev. Rhem Malosteoartic* 28, 643–652.

Lequesne, M. (1961). Le faux-profil du bassin. *Rev. Rhum* 28, 643–652.

Li, F. E. I., Chen, H., Mawatari, T., Iwamoto, Y., Jiang, F. E. I., and Chen, X. (2018). Influence of Modeling Methods for Cartilage Layer on Simulation of Periacetabular Osteotomy Using Finite Element Contact Analysis. *J. Mech. Med. Biol.* 18 (02). doi:10.1142/s0219519418500185

Liu, L., Ecker, T., Xie, L., Schumann, S., Siebenrock, K., and Zheng, G. (2015). Biomechanical Validation of Computer Assisted Planning of Periacetabular Osteotomy: A Preliminary Study Based on Finite Element Analysis. *Med. Eng. Phys.* 37 (12), 1169–1173. doi:10.1016/j.medengphy.2015.09.002

Matsuda, D. K., Gupta, N., Khatod, M., Matsuda, N. A., Anthony, F., Sampson, J., et al. (2017). Poorer Arthroscopic Outcomes of Mild Dysplasia with Cam Femoroacetabular Impingement versus Mixed Femoroacetabular Impingement in Absence of Capsular Repair. *Am. J. Orthop. (Belle Mead Nj)* 46 (1), E47–E53.

Murphy, S. B., Kijewski, P. K., Millis, M. B., and Harless, A. (1990). Acetabular Dysplasia in the Adolescent and Young Adult. *Clin. Orthop. Relat. Res.* 261 (261), 214–223. doi:10.1097/00003086-199012000-00023

Murphy, S. B., Ganz, R., and Müller, M. E. (1995). The Prognosis in Untreated Dysplasia of the Hip. A Study of Radiographic Factors that Predict the Outcome. *J. Bone Jt. Surg.* 77 (7), 985–989. doi:10.2106/00004623-199507000-00002

Ng, K-C. G. (2017). *The Effects of Cam Femoroacetabular Impingement on Mechanical Hip Joint Loading*. Ottawa: Université d'Ottawa/University of Ottawa.

Ricciardi, B. F., Fields, K. G., Wentzel, C., Nawabi, D. H., Kelly, B. T., and Sink, E. L. (2017). Complications and Short-Term Patient Outcomes of Periacetabular Osteotomy for Symptomatic Mild Hip Dysplasia. *Hip Int.* 27 (1), 42–48. doi:10.5301/hipint.5000420

Russell, M. E., Shivanna, K. H., Grosland, N. M., and Pedersen, D. R. (2006). Cartilage Contact Pressure Elevations in Dysplastic Hips: a Chronic Overload Model. *J. Orthop. Surg. Res.* 1 (1), 6. doi:10.1186/1749-799x-1-6

Schuller, H., Dalstra, M., Huiskes, R., and Marti, R. (1993). Total Hip Reconstruction in Acetabular Dysplasia. A Finite Element Study. *J. Bone Jt. Surg. Br. volume* 75-B (3), 468–474. doi:10.1302/0301-620x.75b3.8496225

Siebenrock, K. A., Kistler, L., Schwab, J. M., Büchler, L., and Tannast, M. (2012). The Acetabular wall index for Assessing Anteroposterior Femoral Head Coverage in Symptomatic Patients. *Clin. Orthopaedics Relat. Research®* 470 (12), 3355–3360. doi:10.1007/s11999-012-2477-2

Tan, J., Natarajan, E., Lim, W., Ramesh, S., Ang, C., Parasuraman, S., et al. (2021). Effects of Bone-Plate Materials on the Healing Process of Fractured Tibia Bone under Time-Varying Conditions: a Finite Element Analysis. *Mater. Res. Express* 8 (9), 095308. doi:10.1088/2053-1591/ac24f8

Weinstein, S. L., Mubarak, S. J., and Wenger, D. R. (2003). Developmental Hip Dysplasia and Dislocation. *J. Bone Jt. Surgery-American Volume* 85 (9), 1824–1832. doi:10.2106/00004623-200309000-00028

Wesseling, M., Van Rossom, S., Jonkers, I., and Henak, C. R. (2019). Subject-specific Geometry Affects Acetabular Contact Pressure during Gait More Than Subject-specific Loading Patterns. *Comput. Methods Biomech. Biomed. Eng.* 22 (16), 1323–1333. doi:10.1080/10255842.2019.1661393

Wiberg, G. (1939). The Anatomy and Roentgenographic Appearance of a normal Hip Joint. *Acta Chir Scand.* 83 (Suppl. 58), 7–38.

Zhang, D., Pan, X., Zhang, H., Luo, D., Cheng, H., and Xiao, K. (2020). The Lateral center-edge Angle as Radiographic Selection Criteria for Periacetabular Osteotomy for Developmental Dysplasia of the Hip in Patients Aged above 13 Years. *BMC Musculoskelet. Disord.* 21 (1), 493. doi:10.1186/s12891-020-03515-8

Zhao, X., Chosa, E., Totoribe, K., and Deng, G. (2010). Effect of Periacetabular Osteotomy for Acetabular Dysplasia Clarified by Three-Dimensional Finite Element Analysis. *J. Orthopaedic Sci.* 15 (5), 632–640. doi:10.1007/s00776-010-1511-z

Conflict of Interest: The authors declare that the research was conducted in the absence of any commercial or financial relationships that could be construed as a potential conflict of interest.

Publisher's Note: All claims expressed in this article are solely those of the authors and do not necessarily represent those of their affiliated organizations, or those of the publisher, the editors and the reviewers. Any product that may be evaluated in this article, or claim that may be made by its manufacturer, is not guaranteed or endorsed by the publisher.

frontiers in Bioengineering and Biotechnology

ORIGINAL RESEARCH
published: 02 March 2022
doi: 10.3389/fbioe.2022.829772

Effects of Lower Limb Cycling Training on Different Components of Force and Fatigue in Individuals With Parkinson's Disease

*Yen-Po Lin[1], Rou-Shayn Chen[2,3,4], Vincent Chiun-Fan Chen[5], Chun-Hsien Liu[6], Hsiao-Lung Chan[4,7] and Ya-Ju Chang[4,6,8]**

[1]School of Medicine, Chung-Shan Medical University, Taichung, Taiwan, [2]Department of Neurology, Chang Gung Memorial Hospital, Linkou, Taoyuan, Taiwan, [3]School of Medicine, College of Medicine, Chang Gung University, Taoyuan, Taiwan, [4]Neuroscience Research Center, Chang Gung Memorial Hospital, Linkou, Taoyuan, Taiwan, [5]Engineering Program, Loyola University Chicago, Chicago, IL, United States, [6]School of Physical Therapy and Graduate Institute of Rehabilitation Science, College of Medicine, Chang Gung University, Taoyuan, Taiwan, [7]Department of Electrical Engineering, College of Engineering, Chang Gung University, Taoyuan, Taiwan, [8]Healthy Aging Research Center, Chang Gung University, Taoyuan, Taiwan

The strength of lower extremity is important for individuals to maintain balance and ambulation functions. The previous studies showed that individuals with Parkinson's disease suffered from fatigue and strength loss of central origin. The purpose of this study was to investigate the effect of lower extremities' cycling training on different components of force and fatigue in individuals with Parkinson's disease. Twenty-four individuals (13 males, 11 females, mean age: 60.58 ± 8.21 years) diagnosed with idiopathic Parkinson's disease were randomized into training and control groups. The maximum voluntary contraction (MVC) force, voluntary activation level (VA), and twitch force of knee extensors were measured using a custom-made system with surface electrical stimulation. The general, central, and peripheral fatigue indexes (GFI, CFI, and PFI) were calculated after a fatiguing cycling protocol. Subjects received 8 weeks of low resistance cycling training (training group) or self-stretching (control group) programs. Results showed that MVC, VA, and twitch force improved ($p < 0.05$) only in the training group. Compared to the baseline, central fatigue significantly improved in the training group, whereas peripheral fatigue showed no significant difference in two groups. The cycling training was beneficial for individuals with Parkinson's disease not only in muscle strengthening but also in central fatigue alleviation. Further in-depth investigation is required to confirm the effect of training and its mechanism on central fatigue.

Keywords: Parkinson's disease, central fatigue, activation level, cycling exercise, low intensity exercise, fatigue, maximal voluntary contraction

OPEN ACCESS

Edited by:
Lizhen Wang,
Beihang University, China

Reviewed by:
Wenxin Niu,
Tongji University, China
Yaodong Gu,
Ningbo University, China

****Correspondence:***
Ya-Ju Chang
yjchang@mail.cgu.edu.tw

Specialty section:
This article was submitted to Biomechanics, a section of the journal Frontiers in Bioengineering and Biotechnology

Received: *06 December 2021*
Accepted: *31 January 2022*
Published: *02 March 2022*

Citation:
Lin Y-P, Chen R-S, Chen VC-F, Liu C-H, Chan H-L and Chang Y-J (2022) Effects of Lower Limb Cycling Training on Different Components of Force and Fatigue in Individuals With Parkinson's Disease. Front. Bioeng. Biotechnol. 10:829772. doi: 10.3389/fbioe.2022.829772

INTRODUCTION

Parkinson's disease (PD) is a neurodegenerative disease and affects 1–2 per 1000 of the population at any time. PD prevalence increases with age, and PD affects 1% of the population above 60 years (Tysnes and Storstein, 2017). The typical features of individuals with Parkinson's disease are bradykinesia, resting tremor, rigidity, and postural instability (Jankovic, 2008). In addition to the cardinal motor symptoms, there are also nonmotor symptoms, including fatigue, pain, sleep

problems, autonomic nervous system problems, and cognitive problems. Among these nonmotor symptoms, fatigue is considered as an independent nonmotor symptom which appears early and persists throughout the disease course. A recent meta-analysis study showed that the prevalence of fatigue was up to 50% in PD (Siciliano et al., 2018). Fatigue was moderately associated with several negative health outcomes, such as apathy, anxiety, daytime somnolence, sleep disturbances, and poor quality of life (Siciliano et al., 2018).

The cause and the expression of fatigue are complicate. Studies showed that fatigue might be related to depression, but others showed fatigue also occurred in patients without depression (Finsterer and Mahjoub, 2014; Ferraz et al., 2018; Ghanean et al., 2018). According to the site of fatigue, fatigue can be divided into central and peripheral components. Central fatigue is attributed to the processes within the central nervous system (CNS) that reduce the neural drive to the exercising muscle and lead to a decrease in the voluntary activation (VA) level and subsequently its performance (Taylor et al., 2016; Sidhu et al., 2018). Peripheral fatigue, i.e., muscle fatigue, is attributed to neuromuscular transmission, excitation–contraction coupling, or muscle bioenergetics (Gandevia, 2001; Chang et al., 2008; Boyas and Guevel, 2011; Chen et al., 2014; Huang et al., 2017). In healthy aging subjects, the time to fatigue was longer; however, the percentage of central vs. peripheral fatigue was similar to young subjects (Mademli and Arampatzis, 2008). In the past, clinical measurements of fatigue in PD patients relied on subjective measurements and exercise-induced fatigue. However, our previous studies showed that exercise-induced fatigue had different impacts on central or peripheral origin fatigue and suggested that fatigue and muscle weakness in PD are pathologically central-originated which is different from fatigue in the normal aging process. PD patients suffered more central origin than peripheral origin muscle weakness and fatigue. This makes the alleviation of central fatigue in PD important (Huang et al., 2017). Since the mechanism of fatigue in PD is not similar to that of exercise-induced fatigue that occurs in non-PD population, strategies of alleviating fatigue, such as those suggested by the American College of Sports Medicine (ACSM), may not be suitable for PD-related fatigue. This would make a clinical prescription of the fatigue-alleviating program in PD patients distinctively different.

For fatigue in PD patients, especially central-originated fatigue, there is no clinical treatment with satisfactory results (Kluger et al., 2013). The effect of levodopa on fatigue is controversial (Schifitto et al., 2008). Exercise training is a common non-drug intervention for individuals with PD suggested in the study by Fisher et al. (2008), 8 weeks of treadmill training showed improvements in walking speed with a prolonged central silent period (CSP) observed. Alberts et al. (2011) showed that cycling training could produce a levodopa-like effect, which reduced tremors during off-stage. Cycling training also showed various beneficial effects on symptoms, such as tremor, cognitive function, and walking speed, in PD (Nadeau et al., 2016) even with low intensity (Chang et al., 2018). These studies showed that cycling exercise is beneficial to PD patients. However, whether cycling training altered the fatigue status, especially the central origin fatigue, is not clear.

TABLE 1 | The characteristics of subjects.

	Training	Control	*p* value
Gender (M:F)	8:4	5:7	—
Age (yr)	61.5 ± 5.65	60.58 ± 8.21	0.05
H&Y (score)	1.625 ± 0.33	1.42 ± 0.36	0.71
Duration (yr)	5.5 ± 1.73	5.50 ± 2.28	0.29
MoCA (score)	27.17 ± 0.94	27.75 ± 0.62	0.25
FSS (score)	5.18 ± 0.68	4.70 ± 0.55	0.28

Cycling training is a common endurance training for healthy populations, which could increase joint mobility, muscle strength and endurance, prevent muscle atrophy, and improve cardiorespiratory fitness (Bourne et al., 2018; Ferraz et al., 2018; Silveira et al., 2018; Chavarrias et al., 2019; Ahmed and Babakir-Mina, 2021). Cycling training also has an improved effect on patients with central fatigue. For patients with multiple sclerosis, 8 weeks of cycling training improved not only the walking speed but also the maximum exercise times (Cakt et al., 2010). Cycling training is a potential strategy. However, none of the previous studies has reported success in alleviating Parkinson-related central fatigue. This was probably due to the cycling protocol, in terms of the resistance level and dosage, which was not designed specifically for central fatigue.

In exercise training, the training program has to be specific and relevant to the targeted activities or sports in order to produce the desired effect. Our recent study showed that the level of resistance of cycling exercise is critical in the mechanisms of fatigue. With an equivalent dosage, cycling at a lower resistance level could challenge the center fatigue-related mechanism more (Hsu et al., 2020). It is plausible to hypothesize that cycling training in this central fatigue challenging resistance could alleviate Parkinson-related fatigue, but its evidence has never been obtained. In addition, whether the alleviation of central fatigue was related to the severity of subjective fatigue of PD patients was not clear. Therefore, the purpose of our study employed a randomized control design to evaluate the effect of cycling training with a central fatigue challenge resistance on individuals with PD. In order to identify the candidate most likely to benefit from cycling training, our secondary purpose is to evaluate the correlation between the training gain, if there is any, and the baseline feature of patients.

MATERIALS AND METHODS

Participants

Twenty-four individuals (13 males, 11 females, mean age: 60.58 ± 8.21 years) diagnosed with idiopathic PD, according to the United Kingdom Brain Criteria, were recruited from the outpatient clinics. The sample size was estimated by G*Power software according to the pilot study with the effect size f = 0.5, α = 0.05, and power = 80%. Considering the potential dropout rate, twenty-four subjects were recruited. The inclusion criteria

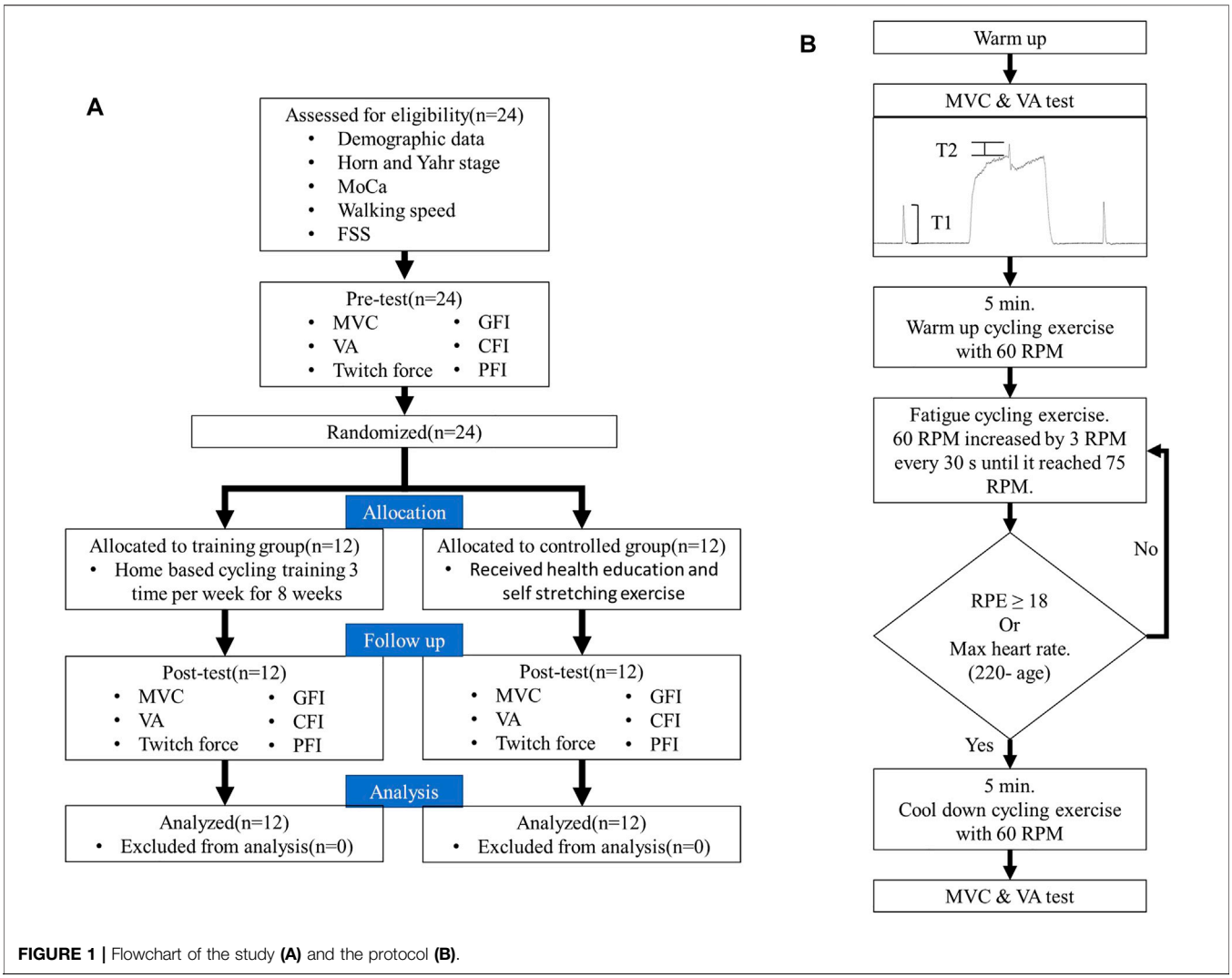

FIGURE 1 | Flowchart of the study **(A)** and the protocol **(B)**.

include 1) Hoehn and Yahr stages II-III, 3) stable medication usage, and 4) mini-mental state examination score ≥24. Patients who had tremors when on medication or during recording and those with other central or peripheral neurological diseases or musculoskeletal injuries of the lower limbs were excluded from the study. Included individuals were further randomized into training and control groups (**Table 1**). All tests and training were performed during the clinical "ON" status. Written informed consent was obtained before participation. This study was approved by the Institutional Review Board.

Baseline Evaluation

After inclusion, the basic data including demographic data (age and gender), Hoehn and Yahr stages, MoCa, fatigue severity scale (FSS), and walking speed were obtained for post-training comparison. FSS (Herlofson and Larsen, 2002) is a questionnaire commonly used to assess patients' subjective grading of fatigue on their daily living.

Subjects then moved to a stationary bike with a custom-made knee extension force measurement system with a force transducer (AWU, Genisco Technology, CA, United States) coupled to a transducer amplifier (Gould Inc., Valley View, OH, United States). Data were sampled at 1000 Hz *via* (InstruNet Model 200 PCI controller, United States) and recorded on a computer for offline analysis. This system can measure the knee isometric extension force at 90 degrees of flexion after biking without changing the position with a good reliability. For further details, please refer to the previous study (Hsu et al., 2020).

Electrical stimulation (stimulator model DS7A, Digitimer Ltd.; Hertfordshire, United Kingdom) with surface electrodes (9 × 12 cm) was used for measuring the VA and twitch force of quadriceps. The electrodes were placed on the muscle belly of the quadriceps. The induced force was monitored simultaneously with an oscilloscope (TDS220, Tektronix Inc., Beaverton, OR, United States). The force signal was digitized using an analog-to-digital converter with 16-bit resolution (InstruNet Model 200 PCI controller, United States) at 1000 Hz.

After the warm-up contractions, participants performed three maximal voluntary contractions (MVCs), each sustained for 5 s. After the MVC test, the VA was evaluated by the interpolated twitch technique (ITT) (**Figure 1A**). During this test, the

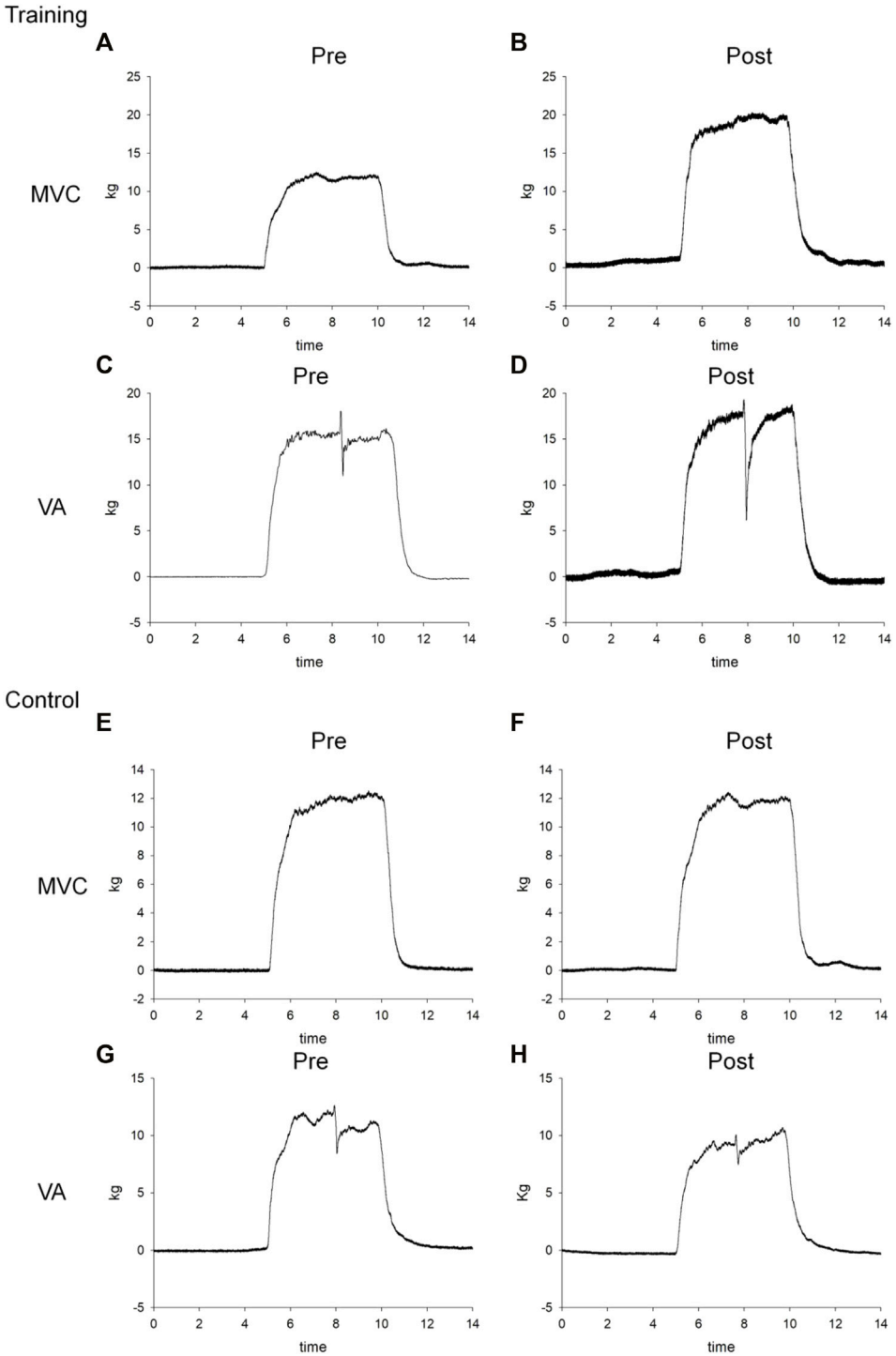

FIGURE 2 | Representative force–time curves of the MVC and VA for one training patient **(A–D)** and one control subject **(E–H)** before (pre) and after (post) 8-week cycling training.

supramaximal electrical stimulation (200 μs duration with 120% of the maximum intensity) was applied under relax and during knee extensor MVCs to obtain the resting twitch (T_1) and interpolated twitches (T_2). The resting twitch represents the peripheral component of force whereas the interpolated twitch represents the force generated from spared motor units that failed

to be activated by the CNS (Huang et al., 2010; Chang et al., 2011; Huang et al., 2017; Chuang et al., 2019; Tang et al., 2020). The resting twitch was averaged from the twitch elicited before and after the MVC to avoid the variation caused by force potentiation. The VA was calculated by the following formula.

$$VA = (1 - T_2/T_1) \times 100\%.$$

Cycling Protocol for Inducing Fatigue

After the measurements of MVC, VA, and twitches, subjects received a cycling protocol to induce fatigue. The cycling protocol was adapted from the previous study with an intensity found to predominantly induce central fatigue (Hsu et al., 2020). This protocol included a 5-min warm-up by cycling at 60 revolutions per minute (RPM) with no resistance. After warming up, the cycling speed increased by 3 RPM every 30 s until it reached 75 RPM. The target resistance was 70 W, which corresponded to 25% MVC. During the testing session, the rate of perceived exertion (RPE) was reported by the participants every 1 min. Once the participants' RPE reached 18 or the participants' maximum heart rate (maximum = 220 minus the age), the cycling test was terminated, and 5 min of cool-down was provided (**Figure 1B**). The parameters of the cycling protocol were recorded for each subject for the ensuing training protocol and for post-training testing. This protocol complied with the exercise guideline for safety suggested by the ACSM to prevent blood pooling in lower extremities and facilitate venous return (American College of Sports Medicine, 2016). After the cycling protocol, MVCs, VA, and resting twitches were measured again to evaluate general fatigue, central fatigue, and peripheral fatigue (**Figure 1**). Representative data for the MVC and interpolated twitch force are shown in **Figure 2**.

The ratio of post-fatigue MVC to pre-fatigue MVC was calculated as the general fatigue index (GFI). The ratio of the post-fatigue VA to pre-fatigue VA was calculated as the central fatigue index (CFI). The ratio of the post-fatigue twitch force to the pre-fatigue twitch force was calculated as the peripheral fatigue index (PFI) (Chien et al., 2008; Ju et al., 2011). A higher fatigue index indicates less fatigue.

Training Protocol

Subjects in the training group then received home-based cycling training three times per week for 8 weeks. The intensity and speed were determined individually based on the baseline cycling protocol described previously. Subjects in the control group received health education and self stretching exercise.

One week after the last training, the subjects returned to the laboratory for post-training evaluation of the MVC, VA, twitch, GFI, CFI, and PFI. The evaluation procedures were the same as in baseline evaluation.

Data Reduction and Statistical Analysis

Two-way (group by time) repeated measures of ANOVA with the *post hoc* Tukey test were used to analyze the MVC, VA, twitch force, GFI, CFI, and PFI. Once a significant interaction was detected, one-way ANOVA was applied for individual groups. The Spearman correlation coefficient was used to estimate the correlation between the training-induced gain and the baseline condition of patients. The significance level was set at $p < 0.05$. Statistical analyses were performed using SAS (version 9.4; SAS Institute, Cary, NC, United States).

RESULTS

Strength

Two-way repeated measures of ANOVA showed significant group x time interaction in the MVC, VA, and twitch forces (**Table 2**). In the training group, the MVC, VA, and twitch force significantly increased from 82.96 ± 48.69 to 107.17 ± 50.75 kg ($p = 0.002$), 64.32 ± 9.60 to 74.36 ± 12.85% ($p = 0.046$), and 2.97 ± 2.17 to 4.06 ± 2.09 kg ($p = 0.001$) after 8 weeks of cycling training, respectively (**Figure 3**). In the control group, none of the MVC, VA, or twitch changed after 8 weeks ($p > 0.05$).

This suggested that the muscle force increased in both central and peripheral origins after training. In contrast, the muscle forces did not change in the control group ($p > 0.05$) after 8 weeks.

Fatigue

For fatigue indexes, two-way repeated ANOVA showed significant group x time interaction only in the CFI ($p < 0.001$) but not in the GFI ($p = 0.08$) or PFI ($p = 0.216$). Compared to the baseline, the CFI significantly increased from 66.96 ± 14.88 to 93.21 ± 6.70 ($p = 0.0001$) in the training group, whereas the CFI did not change in the control group. (CFI = 57.02 ± 10.63 and 55.68 ± 7.81 before and after 8 weeks, $p = 0.72$). For the GFI and PFI, no group x time interaction ($p > 0.05$), or main effect in time ($p > 0.05$) or group ($p > 0.05$), was found. These results indicated that cycling training minimized the degree of central fatigue (**Table 2**) (**Figure 3**).

Correlation With the Baseline Status

The Spearman correlation coefficient showed that the Hoehn and Yahr stage has moderate negative correlation with training-induced improvement in the VA ($r = -0.69$ $p = 0.01$) but not the MVC ($r = -0.31$ $p = 0.33$) or twitch force ($r = -0.04$ $p = 0.9$). The CFI improvement was not correlated with the baseline status of FSS. ($r = -0.22$ $p = 0.50$) (**Figure 4**).

DISCUSSION

We conducted a randomized control trial investigating the effects of cycling training on 24 PD patients who were classified into the training and control groups. The main finding was that using a central fatigue-challenging intensity, the cycling training group improved in the MVC, VA, and twitch force more than the control group in patients with PD. Furthermore, a significant difference in the CFI index was found between the two groups after intervention. To our knowledge, this is the first study to prove that a cycling training at a central fatigue-challenging resistance could improve strength and alleviate central fatigue in individuals with PD. In addition, the training effect is better for earlier stage PD patients, but not influenced by the severity of subjective fatigue in the baseline.

TABLE 2 | The mean, standard deviation, and results of ANOVA of the maximal voluntary contraction (MVC), voluntary activation level (VA), twitch force, central fatigue index (CFI), peripheral fatigue index (PFI), and general fatigue index (GFI) before (pre) and after (post) 8-week cycling training in two groups. The main effect is not shown if the interaction is significant (p <0 .05).

	Pre (mean ± standard deviation)		Post (mean ± standard deviation)		2 way ANOVA (p-value)		
	Training	Control	Training	Control	Interaction	Main effect time	Main effect group
MVC	82.96 ± 48.69	82.32 ± 41.86	107.17 ± 50.75[a]	80.99 ± 36.09	0.0006[b]	—	—
VA	64.32 ± 9.60	71.75 ± 14.11	74.36 ± 12.85[a]	69.40 ± 12.19	0.0194[b]	—	—
Twitch force	2.97 ± 2.17	2.53 ± 0.93	4.06 ± 2.09[a]	2.49 ± 0.77	0.0027[b]	—	—
CFI	66.96 ± 14.88	57.02 ± 10.63	93.21 ± 6.70[a]	55.68 ± 7.81	0.0001[b]	—	—
PFI	107.69 ± 51.74	78.88 ± 14.12	80.46 ± 16.23	76.57 ± 37.56	0.2162	0.1454	0.1057
GFI	69.96 ± 22.88	73.08 ± 15.07	83.63 ± 7.31	69.31 ± 15.78	0.08	0.3089	0.2376

[a]*Significant (p < 0.05) difference in comparison to pre-training conditions.*
[b]*Significant interaction (p < 0.05) between time and group.*

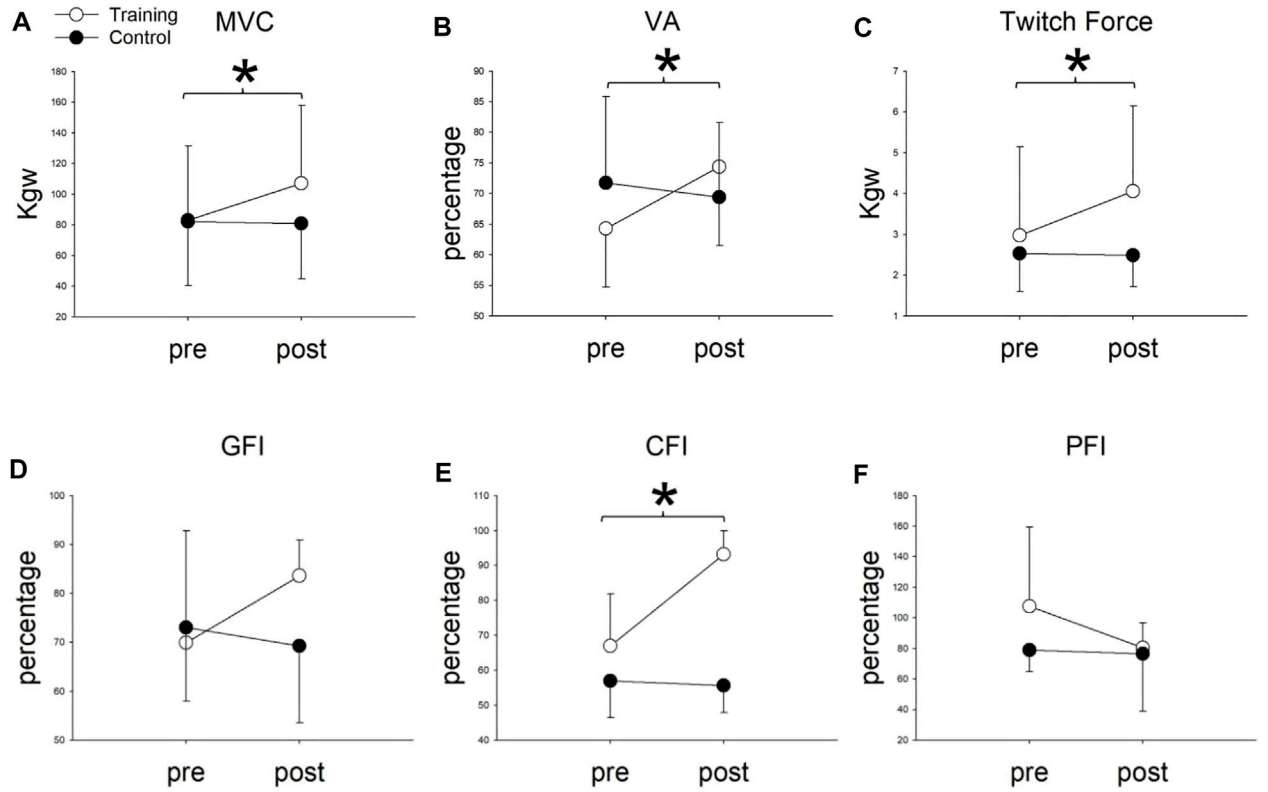

FIGURE 3 | (A) Maximal voluntary contraction (MVC), **(B)** voluntary activation (VA), **(C)** twitch Force, **(D)** general fatigue index (GFI), **(E)** central fatigue index (CFI), and **(F)** peripheral fatigue index (PFI) before (pre) and after (post) 8-weeks cycling training between training and control groups. *Significant difference between pre- and post-8-week cycling training in the training group (p < 0.05).

Bicycle endurance training is a common treatment in clinical practice. Its main functions include maintaining or increasing joint mobility, muscle strength and endurance, preventing muscle atrophy, and improving walking function (Kubukeli et al., 2002; Katz-Leurer et al., 2006). Although it is already known that bicycle training improves the motor function of patients with PD, its neural mechanism and how training affects the fatigue of patients with PD are not clear. Fatigue management of PD is always a challenge for clinicians partially due to the complicated etiology per se (Kostic et al., 2016). The reason why previous studies failed to show the effect of training intervention on fatigue in PD may be due to its complicated etiology and the clinically subjective measurements. The subjective fatigue measurement required individuals to sensibly respond to the feeling of fatigue which would be influenced by the subjects' other daily activity levels. It only reflects subjective aspects of the effects of fatigue on subjects' daily activities. Therefore, the aim of our study is to offer more objective and quantitative results. Since PD is a long-term

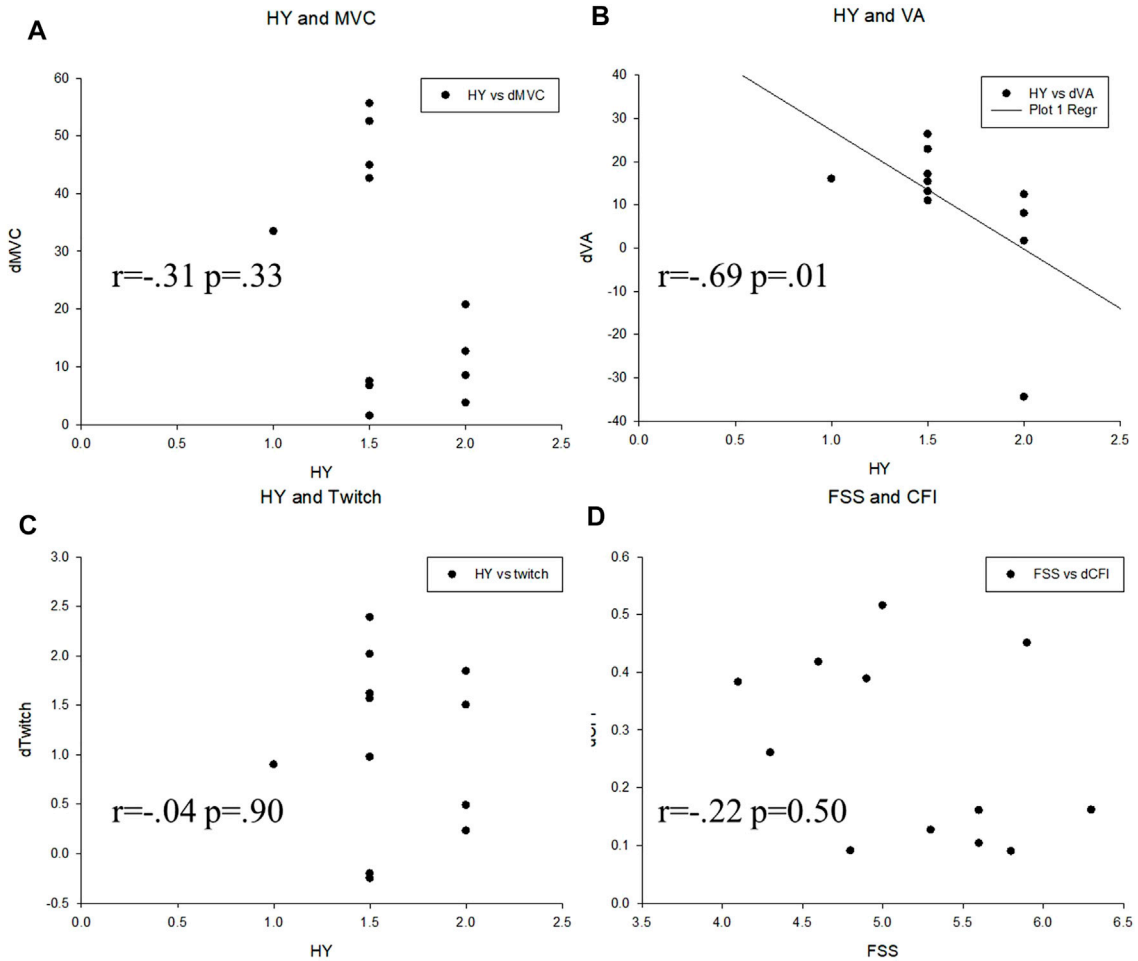

FIGURE 4 | Correlation analysis between variables in the two groups. **(A)** Hoehn and Yahr scale (HY) and maximal voluntary contraction (MVC), **(B)** Hoehn and Yahr scale (HY) and voluntary activation (VA), **(C)** Hoehn and Yahr scale (HY) and twitch force (Twitch), **(D)** Fatigue severity scale (FSS) and central fatigue index (CFI).

degenerative disease, early intervention and patients' adherence to continuing exercise regimen are essential (Salgado et al., 2013). Therefore, different from previous studies, milder PD patients with stable medication were included in our study (Ridgel et al., 2011).

The major finding in our study, as predicted, is that the MVC, VA, and twitch force improved in the training group. These findings agree with previous studies indicating that PD patients whose proprioceptors are continuously activated by riding a bicycle may be vital for the recovery of motor functions (Ridgel et al., 2015). There were no previous studies that reported improved central fatigue by cycling exercise in PD patients. Although the etiology of central fatigue in patients with multiple sclerosis is not identical to that in PD, Cakt et al. (2010) showed that after 8 weeks of cycling training for patients with multiple sclerosis, the exercise tolerance increased, and the subjective fatigue feelings decreased. Both are regarded as indicators of fatigue alleviation. Our study not only provided evidence of cycling training in PD patients but also specified the training effects on central and peripheral components of lower extremity strength and central origin fatigue. Alberts et al. (2011) offered more information regarding the effects of 8-week bicycle training intervention on slowing down the progress of PD. In our study, the subjects were under medication control while showing improvements through cycling training. This indicates that cycling training improves motor function in patients with PD concomitantly under medication.

We further use the CFI and PFI to explore and compare the changes in central fatigue and peripheral fatigue before and after cycling training intervention in patients with PD. Notably, the intervention group had significantly better improvement than the control group (**Figure 3E**) in the CFI. It is known that peripheral fatigue is produced by changes at nerve branches, neuromuscular junction, or distal to these structures. Central fatigue originates from the central nervous system, which decreases the neural drive to the muscle (Davis, 1995). Currently, it is recognized that central fatigue is more pronounced in PD patients, which means that the alleviation of central fatigue can possibly enhance the functional activities of daily living in PD patients (Huang et al., 2017). Ferraz et al. (Juvet et al., 2017; Ferraz et al., 2018) have also outlined the high prevalence of subjective fatigue

in PD patients. Our study is novel in using an RCT design to show the effect of cycling training, especially on central fatigue in PD patients. The result may apply to other diseases, such as joint hypermobility syndrome and multiple sclerosis that share similar central fatigue symptoms (Chang et al., 2011; To et al., 2019).

The fatigue of PD patients is puzzling and poorly understood. There are several mechanisms which have been proposed to explain improvements related to physical training. Bicycle training on PD patients with mild-to-moderate severity is reported to have better activation in the putamen of the basal nucleus and the globus pallidus (Alberts et al., 2011). Similar studies also report coordination training or motor fitness training to be promising means to increase the basal ganglia volume which is related to coordinative aspects of fitness and partially explained the cognitive performance (Niemann et al., 2014). Other proposed mechanisms, for example, the brain-derived neurotrophic factor (BDNF), which is induced by aerobic exercise, may possibly explain the relationship between central fatigue and cycling training. The BDNF not only enhances synaptic GABA clearance (Boyne et al., 2019) but also potentiates normal central nervous system myelination in development and enhances recovery after myelin injury (Fletcher et al., 2018). Another possible and direct reason may be that central fatigue has been suggested to be related to neurotransmitters such as serotonin and dopamine (Dobryakova et al., 2015). In previous studies, dopamine has been shown to increase during exhausting exercise (Fisher et al., 2004; Petzinger et al., 2007), and a reduced level of dopamine was reported in fatigued rats (Meeusen et al., 2010). In addition, Petzinger et al. have shown that exercise may influence activity-dependent processes in the basal ganglia through alterations in dopaminergic neurotransmission and have demonstrated that exercise-induced behavioral benefits may be due to changes in cortical hyper-excitability normally observed in the dopamine-depleted state (Petzinger et al., 2010). Although the afore mentioned studies provide basic evidence, the unclear mechanisms of PD-related central fatigue phenomena still require further studies to investigate the potential interaction between exercise, neurotransmitter, and neuronal activation.

Our study showed that the training-induced gain were not correlated with the baseline FSS, suggesting that patients in different subjective statuses would be benefitted from this training. However, the negative correlation between the improvement of the VA to Hoehn and Yahr stages suggests that the training effect would be better in earlier stages. Patients are suggested to receive training in earlier stages to receive better effects.

There are some limitations while applying the results of this study in clinical settings. First, only patients with Hoehn and Yahr stages II-III with stable medication were enrolled in this study. The optimal training setting for more advanced PD patients remains to be investigated. Second, to avoid interference of tremors on the resting twitch force measurement, subjects with obvious tremors and subjects who had tremors during recording were excluded. Enhanced twitch activation during muscle training was merely recorded for analysis. The training effects on tremor-dominant patients require future in-depth investigation. Finally, we did not use gender stratification when recruiting. Based on previous studies that have compared fatigue between elderly women and men, there is no significant difference in gender (Hicks and McCartney, 1996; Ekman and Ehrenberg, 2002). Thus, we consider that gender differences are not a significant interfering factor in our study. Future studies with gender stratification design are suggested to further clarify the potential gender issue.

CONCLUSION

The present study confirmed that cycling training is efficient, beneficial, and feasible for patients with early-stage PD in strengthening both central and peripheral components of knee extensor forces. Moreover, this is also the first study to show that cycling training at a low resistance alleviates central fatigue, especially for patients with pronounced central fatigue. The training effects could be shown on individuals with PD who have different baseline levels of subjective fatigue. These findings provide important insights which will be useful for the development of rehabilitation interventions for PD and suggest that progressive cycling training could serve as a new treatment for early-stage PD.

DATA AVAILABILITY STATEMENT

The raw data supporting the conclusion of this article will be made available by the authors, without undue reservation.

ETHICS STATEMENT

The studies involving human participants were reviewed and approved by the Chang Gung Medical foundation Institutional Review Board. The patients/participants provided their written informed consent to participate in this study.

AUTHOR CONTRIBUTIONS

Y-PL, R-SC, VC-FC, C-HL, H-LC, and Y-JC conceived, designed, and coordinated the study. C-HL, R-SC, and Y-JC acquired data. Y-PL, R-SC, VC-FC, and Y-JC analyzed and interpreted the data and were major contributors in writing the manuscript. All authors read and approved the final manuscript.

FUNDING

This study was supported by the Ministry of Science and Technology, Taiwan (MOST 110-2221-E-182-018), the Chang Gung Medical Foundation (CMRPD1L0311 and BMRP610), and the Healthy Aging Research Center, Chang Gung University (EMRPD1L0411).

ACKNOWLEDGMENTS

We specially thank the Neuroscience Research Center of Chang Gung Memorial Hospital, Linkou, and Dr. Ying-Zu Huang, the neurologist of Chang Gung Medical Foundation.

REFERENCES

Ahmed, H. M., and Babakir-Mina, M. (2021). Population-level Interventions Based on Walking and Cycling as a Means to Increase Physical Activity. *Phys. Activity Health* 5, 55–63. doi:10.5334/paah.87

Alberts, J. L., Linder, S. M., Penko, A. L., Lowe, M. J., and Phillips, M. (2011). It Is Not about the Bike, it Is about the Pedaling. *Exerc. Sport Sci. Rev.* 39, 177–186. doi:10.1097/jes.0b013e31822cc71a

American College of Sports Medicine (2016). *ACSM's Guidelines for Exercise Testing and Prescription*. Philadelphia, PA: Lippincott, Williams & Wilkins.

Bourne, J. E., Sauchelli, S., Perry, R., Page, A., Leary, S., England, C., et al. (2018). Health Benefits of Electrically-Assisted Cycling: a Systematic Review. *Int. J. Behav. Nutr. Phys. Act* 15, 116. doi:10.1186/s12966-018-0751-8

Boyas, S., and Guével, A. (2011). Neuromuscular Fatigue in Healthy Muscle: Underlying Factors and Adaptation Mechanisms. *Ann. Phys. Rehabil. Med.* 54, 88–108. doi:10.1016/j.rehab.2011.1001.1001

Boyne, P., Meyrose, C., Westover, J., Whitesel, D., Hatter, K., Reisman, D. S., et al. (2019). Exercise Intensity Affects Acute Neurotrophic and Neurophysiological Responses Poststroke. *J. Appl. Physiol.* 126, 431–443. doi:10.1152/japplphysiol.00594.2018

Cakt, B. D., Nacir, B., Genç, H., Saraçoğlu, M., Karagöz, A., Erdem, H. R., et al. (2010). Cycling Progressive Resistance Training for People with Multiple Sclerosis: a Randomized Controlled Study. *Am. J. Phys. Med. Rehabil.* 89, 446–457. doi:10.1097/PHM.0b013e3181d3e71f

Chang, H.-C., Lu, C.-S., Chiou, W.-D., Chen, C.-C., Weng, Y.-H., and Chang, Y.-J. (2018). An 8-Week Low-Intensity Progressive Cycling Training Improves Motor Functions in Patients with Early-Stage Parkinson's Disease. *J. Clin. Neurol.* 14, 225–233. doi:10.3988/jcn.2018.14.2.225

Chang, Y.-J., Hsu, M.-J., Chen, S.-M., Lin, C.-H., and Wong, A. M. K. (2011). Decreased central Fatigue in Multiple Sclerosis Patients after 8 Weeks of Surface Functional Electrical Stimulation. *Jrrd* 48, 555–564. doi:10.1682/jrrd.2010.03.0038

Chang, Y.-J., Liu, C.-C., Lin, C.-H., Tsaih, P.-L., and Hsu, M.-J. (2008). Using Electromyography to Detect the Weightings of the Local Muscle Factors to the Increase of Perceived Exertion during Stepping Exercise. *Sensors* 8, 3643–3655. doi:10.3390/s8063643

Chavarrias, M., Carlos-Vivas, J., Collado-Mateo, D., and Pérez-Gómez, J. (2019). Health Benefits of Indoor Cycling: A Systematic Review. *Medicina (Kaunas)* 55. doi:10.3390/medicina55080452

Chen, S.-W., Liaw, J.-W., Chan, H.-L., Chang, Y.-J., and Ku, C.-H. (2014). A Real-Time Fatigue Monitoring and Analysis System for Lower Extremity Muscles with Cycling Movement. *Sensors* 14, 12410–12424. doi:10.3390/s140712410

Chien, M.-Y., Wu, Y.-T., and Chang, Y.-J. (2008). Assessment of Diaphragm and External Intercostals Fatigue from Surface EMG Using Cervical Magnetic Stimulation. *Sensors* 8, 2174–2187. doi:10.3390/s8042174

Chuang, Y.-F., Chen, C.-C., Hsu, M.-J., Huang, N.-J., Huang, Y.-Z., Chan, H.-L., et al. (2019). Age Related Changes of the Motor Excitabilities and central and Peripheral Muscle Strength. *J. Electromyogr. Kinesiol.* 44, 132–138. doi:10.1016/j.jelekin.2018.12.007

Davis, J. M. (1995). Central and Peripheral Factors in Fatigue. *J. Sports Sci.* 13, S49–S53. doi:10.1080/02640419508732277

Dobryakova, E., Genova, H. M., Deluca, J., and Wylie, G. R. (2015). The Dopamine Imbalance Hypothesis of Fatigue in Multiple Sclerosis and Other Neurological Disorders. *Front. Neurol.* 6, 52. doi:10.3389/fneur.2015.00052

Ekman, I., and Ehrenberg, A. (2002). Fatigue in Chronic Heart Failure - Does Gender Make a Difference. *Eur. J. Cardiovasc. Nurs.* 1, 77–82. doi:10.1016/s1474-5151(01)00016-0

Ferraz, D. D., Trippo, K. V., Duarte, G. P., Neto, M. G., Bernardes Santos, K. O., and Filho, J. O. (2018). The Effects of Functional Training, Bicycle Exercise, and Exergaming on Walking Capacity of Elderly Patients with Parkinson Disease: A Pilot Randomized Controlled Single-Blinded Trial. *Arch. Phys. Med. Rehabil.* 99, 826–833. doi:10.1016/j.apmr.2017.12.014

Finsterer, J., and Mahjoub, S. Z. (2014). Fatigue in Healthy and Diseased Individuals. *Am. J. Hosp. Palliat. Care* 31, 562–575. doi:10.1177/1049909113494748

Fisher, B. E., Petzinger, G. M., Nixon, K., Hogg, E., Bremmer, S., Meshul, C. K., et al. (2004). Exercise-induced Behavioral Recovery and Neuroplasticity in the 1-Methyl-4-Phenyl-1,2,3,6-Tetrahydropyridine-Lesioned Mouse Basal Ganglia. *J. Neurosci. Res.* 77, 378–390. doi:10.1002/jnr.20162

Fisher, B. E., Wu, A. D., Salem, G. J., Song, J., Lin, C.-H., Yip, J., et al. (2008). The Effect of Exercise Training in Improving Motor Performance and Corticomotor Excitability in People with Early Parkinson's Disease. *Arch. Phys. Med. Rehabil.* 89, 1221–1229. doi:10.1016/j.apmr.2008.01.013

Fletcher, J. L., Murray, S. S., and Xiao, J. (2018). Brain-Derived Neurotrophic Factor in Central Nervous System Myelination: A New Mechanism to Promote Myelin Plasticity and Repair. *Int. J. Mol. Sci.* 19. doi:10.3390/ijms19124131

Gandevia, S. C. (2001). Spinal and Supraspinal Factors in Human Muscle Fatigue. *Physiol. Rev.* 81, 1725–1789. doi:10.1152/physrev.2001.81.4.1725

Ghanean, H., Ceniti, A. K., and Kennedy, S. H. (2018). Fatigue in Patients with Major Depressive Disorder: Prevalence, Burden and Pharmacological Approaches to Management. *CNS Drugs* 32, 65–74. doi:10.1007/s40263-018-0490-z

Herlofson, K., and Larsen, J. P. (2002). Measuring Fatigue in Patients with Parkinson's Disease - The Fatigue Severity Scale. *Eur. J. Neurol.* 9, 595–600.

Hicks, A. L., and Mccartney, N. (1996). Gender Differences in Isometric Contractile Properties and Fatigability in Elderly Human Muscle. *Can. J. Appl. Physiol.* 21, 441–454. doi:10.1139/h96-039

Hsu, M.-J., Chan, H.-L., Huang, Y.-Z., Lin, J.-H., Hsu, H.-H., and Chang, Y.-J. (2020). Mechanism of Fatigue Induced by Different Cycling Paradigms with Equivalent Dosage. *Front. Physiol.* 11, 545. doi:10.3389/fphys.2020.00545

Huang, Y.-M., Hsu, M.-J., Lin, C.-H., Wei, S.-H., and Chang, Y.-J. (2010). The Non-linear Relationship between Muscle Voluntary Activation Level and Voluntary Force Measured by the Interpolated Twitch Technique. *Sensors* 10, 796–807. doi:10.3390/s100100796

Huang, Y. Z., Chang, F. Y., Liu, W. C., Chuang, Y. F., Chuang, L. L., and Chang, Y. J. (2017). Fatigue and Muscle Strength Involving Walking Speed in Parkinson's Disease: Insights for Developing Rehabilitation Strategy for PD. *Neural Plast.* 2017, 1941980. doi:10.1155/2017/1941980

Jankovic, J. (2008). Parkinson's Disease and Movement Disorders: Moving Forward. *Lancet Neurol.* 7, 9–11. doi:10.1016/s1474-4422(07)70302-2

Ju, Y.-Y., Liu, Y.-C., Cheng, H.-Y. K., and Chang, Y.-J. (2011). Rapid Repetitive Passive Movement Improves Knee Proprioception. *Clin. Biomech.* 26, 188–193. doi:10.1016/j.clinbiomech.2010.09.015

Juvet, L. K., Thune, I., Elvsaas, I. K. Ø., Fors, E. A., Lundgren, S., Bertheussen, G., et al. (2017). The Effect of Exercise on Fatigue and Physical Functioning in Breast Cancer Patients during and after Treatment and at 6 Months Follow-Up: A Meta-Analysis. *The Breast* 33, 166–177. doi:10.1016/j.breast.2017.04.003

Katz-Leurer, M., Sender, I., Keren, O., and Dvir, Z. (2006). The Influence of Early Cycling Training on Balance in Stroke Patients at the Subacute Stage. Results of a Preliminary Trial. *Clin. Rehabil.* 20, 398–405. doi:10.1191/0269215505cr960oa

Kluger, B. M., Krupp, L. B., and Enoka, R. M. (2013). Fatigue and Fatigability in Neurologic Illnesses: Proposal for a Unified Taxonomy. *Neurology* 80, 409–416. doi:10.1212/wnl.0b013e31827f07be

Kostic, V. S., Tomic, A., and Jecmenica-Lukic, M. (2016). The Pathophysiology of Fatigue in Parkinson's Disease and its Pragmatic Management. *Mov Disord. Clin. Pract.* 3, 323–330. 10.1002/mdc3.12343.

Kubukeli, Z. N., Noakes, T. D., and Dennis, S. C. (2002). Training Techniques to Improve Endurance Exercise Performances. *Sports Med.* 32, 489–509. doi:10.2165/00007256-200232080-00002

Mademli, L., and Arampatzis, A. (2008). Effect of Voluntary Activation on Age-Related Muscle Fatigue Resistance. *J. Biomech.* 41, 1229–1235. doi:10.1016/j.jbiomech.2008.01.019

Meeusen, R., Nederhof, E., Buyse, L., Roelands, B., De Schutter, G., and Piacentini, M. F. (2010). Diagnosing Overtraining in Athletes Using the Two-Bout Exercise Protocol. *Br. J. Sports Med.* 44, 642–648. doi:10.1136/bjsm.2008.049981

Nadeau, A., Lungu, O., Duchesne, C., Robillard, M. È., Bore, A., Bobeuf, F., et al. (2016). A 12-Week Cycling Training Regimen Improves Gait and Executive Functions Concomitantly in People with Parkinson's Disease. *Front. Hum. Neurosci.* 10, 690. doi:10.3389/fnhum.2016.00690

Niemann, C., Godde, B., Staudinger, U. M., and Voelcker-Rehage, C. (2014). Exercise-induced Changes in Basal Ganglia Volume and Cognition in Older Adults. *Neuroscience* 281, 147–163. doi:10.1016/j.neuroscience.2014.09.033

Petzinger, G. M., Fisher, B. E., Van Leeuwen, J. E., Vukovic, M., Akopian, G., Meshul, C. K., et al. (2010). Enhancing Neuroplasticity in the Basal Ganglia: the

Role of Exercise in Parkinson's Disease. *Mov Disord.* 25 Suppl 1 (Suppl. 1), S141–S145. doi:10.1002/mds.22782

Petzinger, G. M., Walsh, J. P., Akopian, G., Hogg, E., Abernathy, A., Arevalo, P., et al. (2007). Effects of Treadmill Exercise on Dopaminergic Transmission in the 1-Methyl-4-Phenyl-1,2,3,6-Tetrahydropyridine-Lesioned Mouse Model of Basal Ganglia Injury. *J. Neurosci.* 27, 5291–5300. doi:10.1523/jneurosci.1069-07.2007

Ridgel, A. L., Muller, M. D., Kim, C.-H., Fickes, E. J., and Mera, T. O. (2011). Acute Effects of Passive Leg Cycling on Upper Extremity Tremor and Bradykinesia in Parkinson's Disease. *The Physician and Sportsmedicine* 39, 83–93. doi:10.3810/psm.2011.09.1924

Ridgel, A. L., Phillips, R. S., Walter, B. L., Discenzo, F. M., and Loparo, K. A. (2015). Dynamic High-Cadence Cycling Improves Motor Symptoms in Parkinson's Disease. *Front. Neurol.* 6, 194. doi:10.3389/fneur.2015.00194

Salgado, S., Williams, N., Kotian, R., and Salgado, M. (2013). An Evidence-Based Exercise Regimen for Patients with Mild to Moderate Parkinson's Disease. *Brain Sci.* 3, 87–100. doi:10.3390/brainsci3010087

Schifitto, G., Friedman, J. H., Oakes, D., Shulman, L., Comella, C. L., Marek, K., et al. (2008). Fatigue in Levodopa-Naive Subjects with Parkinson Disease. *Neurology* 71, 481–485. doi:10.1212/01.wnl.0000324862.29733.69

Siciliano, M., Trojano, L., Santangelo, G., De Micco, R., Tedeschi, G., and Tessitore, A. (2018). Fatigue in Parkinson's Disease: A Systematic Review and Meta-Analysis. *Mov Disord.* 33, 1712–1723. doi:10.1002/mds.27461

Sidhu, S. K., Weavil, J. C., Thurston, T. S., Rosenberger, D., Jessop, J. E., Wang, E., et al. (2018). Fatigue-related Group III/IV Muscle Afferent Feedback Facilitates Intracortical Inhibition during Locomotor Exercise. *J. Physiol.* 596, 4789–4801. doi:10.1113/jp276460

Silveira, R. a. D., Trippo, K. V., Duarte, G. P., Gomes, M., Oliveira, J., and Ferraz, D. D. (2018). The Effects of Functional Training and Stationary Cycling on Respiratory Function of Elderly with Parkinson Disease: a Pilot Study. *Fisioterapia em Movimento* 31, 1–8. doi:10.1590/1980-5918.031.ao19

Tang, W. T., Hsu, M. J., Huang, Y. M., Hsu, Y. T., Chuang, L. L., and Chang, Y. J. (2020). Low-intensity Electrical Stimulation to Improve the Neurological Aspect of Weakness in Individuals with Chronic Anterior Cruciate Ligament Lesion. *Biomed. Res. Int.* 2020, 7436274. doi:10.1155/2020/7436274

Taylor, J. L., Amann, M., Duchateau, J., Meeusen, R., and Rice, C. L. (2016). Neural Contributions to Muscle Fatigue. *Med. Sci. Sports Exerc.* 48, 2294–2306. doi:10.1249/mss.0000000000000923

To, M., Strutton, P. H., and Alexander, C. M. (2019). Central Fatigue Is Greater Than Peripheral Fatigue in People with Joint Hypermobility Syndrome. *J. Electromyogr. Kinesiol.* 48, 197–204. doi:10.1016/j.jelekin.2019.07.011

Tysnes, O.-B., and Storstein, A. (2017). Epidemiology of Parkinson's Disease. *J. Neural Transm.* 124, 901–905. doi:10.1007/s00702-017-1686-y

Conflict of Interest: The authors declare that the research was conducted in the absence of any commercial or financial relationships that could be construed as a potential conflict of interest.

Publisher's Note: All claims expressed in this article are solely those of the authors and do not necessarily represent those of their affiliated organizations, or those of the publisher, the editors, and the reviewers. Any product that may be evaluated in this article, or claim that may be made by its manufacturer, is not guaranteed or endorsed by the publisher.

frontiers in Bioengineering and Biotechnology

ORIGINAL RESEARCH
published: 04 March 2022
doi: 10.3389/fbioe.2022.833774

Effect of Long-Distance Running on Inter-segment Foot Kinematics and Ground Reaction Forces: A Preliminary Study

Jialin Li[1,2], Yang Song[3,4,5], Rongrong Xuan[1,2], Dong Sun[3], Ee-Chon Teo[3]*, István Bíró[4,5] and Yaodong Gu[3]**

[1]The Affiliated Hospital of Medical School, Ningbo University, Ningbo, China, [2]Ningbo University School of Medicine, Ningbo University, Ningbo, China, [3]Research Academy of Human Biomechanics, Ningbo University, Ningbo, China, [4]Doctoral School on Safety and Security Sciences, Óbuda University, Budapest, Hungary, [5]Faculty of Engineering, University of Szeged, Szeged, Hungary

Long-distance running has gained massive popularity in recent years, yet the intra-foot adaptations during this event remain unclear. This study aimed to examine the kinematic and ground reaction force alterations induced within the foot following a 5 and 10 km run using the Oxford Foot Model Ten marathon-experienced recreational runners participated in this study. Five-kilometer running led to more rearfoot dorsiflexion, rearfoot eversion, and rearfoot rotation while less forefoot plantarflexion during the stance phase. Increased rearfoot plantarflexion, while decreased forefoot plantarflexion, supination, adduction, and hallux plantarflexion were observed at 10 km. In addition, the forefoot space of footwear was found to play a role in hallux kinematics. Concerning GRFs, only a lesser propulsive force was presented after a 10 km run. Findings of this study showed that 5 km of running would induce excessive foot motion while 10 km of running may gradually change the foot posture and lead to reduced propulsive forces, which could potentially increase the risks of running-related injuries (RRI) due to overuse or fatigue. Nevertheless, further research is warranted, and this study could be used as a preliminary reference to evaluate and predict foot running-related injuries.

Keywords: long-distance running, foot kinematics, kinetics, multi-segment foot model, running-related injuries

OPEN ACCESS

Edited by:
Lizhen Wang,
Beihang University, China

Reviewed by:
Alessandra Bento Matias,
University of São Paulo, Brazil
Chi-Wen Lung,
Asia University, Taiwan

****Correspondence:***
Rongrong Xuan
fyxuanrongrong@nbu.edu.cn
Ee-Chon Teo
eechon-teo@e.ntu.edu.sg
Yaodong Gu
guyaodong@hotmail.com

Specialty section:
This article was submitted to "Biomechanics", a section of the journal Frontiers in Bioengineering and Biotechnology

Received: *12 December 2021*
Accepted: *27 January 2022*
Published: *04 March 2022*

Citation:
Li J, Song Y, Xuan R, Sun D, Teo E-C, Bíró I and Gu Y (2022) Effect of Long-Distance Running on Inter-segment Foot Kinematics and Ground Reaction Forces: A Preliminary Study. Front. Bioeng. Biotechnol. 10:833774. doi: 10.3389/fbioe.2022.833774

1 INTRODUCTION

As one of the most accessible sports to achieve better physical health and prevent diseases, running, especially long-distance running, has attracted extensive participation worldwide (Kim et al., 2018; Mei et al., 2018). It has been reported that the number of runners has doubled, and the number of marathon finishers has shown an exponential increase over the past decade (Nikolaidis et al., 2021; van Poppel et al., 2021). For instance, at least 344,000 marathon runners finished the "New York City Marathon" from 2010 to 2017, which is more than 10 times compared to ~25,000 in 1970–1979 (Vitti et al., 2020). In China, a total of 2.8 million people participated in long-distance running races across the country in 2016, which hit a record high at the time (ChinaDaily, 2016). Unfortunately, broad participation in long-distance repetitive exercise may also bring in a higher rate of running-related injuries (RRI), particularly to the lower extremities and the foot (Van Gent et al., 2007; Hulme et al., 2017; Mei et al., 2019).

As the primary interface of the lower limb with the external environment, the foot has been previously demonstrated to be a common injury site (Kindred et al., 2011; Zhou et al., 2019; Dempster et al., 2021). In addition, some foot biomechanical changes during running may further potentially increase the risk of RRI of the lower limbs (Mei et al., 2018; Takabayashi et al., 2018; Mei et al., 2019; Matias et al., 2020). For example, increased foot pronation during running would contribute to a significantly higher medical knee contact force, consequently increasing knee injury risks (Mei et al., 2019). Different landing techniques, i.e., rearfoot strike and forefoot strike, would lead to relatively distinct foot joint rotations and bone orientations, which may further be associated with different RRI (Matias et al., 2020). Moreover, excessive rearfoot eversion angles exhibited during running would further result in excessive dorsiflexion of midfoot due to kinematic coupling. This abnormal foot motion has been proved to be a risk factor for lower limb RRI (Takabayashi et al., 2018). The above evidence clearly showed that the human foot is a particularly deformable and vulnerable structure during long-distance running. Further analysis of the foot biomechanics is therefore of great importance. At this time, numerous foot models are available for gait analysis. However, it is assumed that, based on previous studies, a multi-segment foot model is required for the in-depth foot kinematics analysis (Wolf et al., 2008; Dixon et al., 2011). The Oxford Foot Model (OFM), which divides the foot into several rigid segments, has shown robust reliability on inter-segmental angles through the gait cycle (Milner and Brindle, 2016; Balsdon and Dombroski, 2018). It has been extensively applied to explore the biomechanical properties of the foot during different movement tasks, such as walking (Sun et al., 2018), running (Xiang et al., 2020a), and jumping (Xiang et al., 2020b). Nevertheless, information concerning the influence of prolonged running activities on foot inter-segment kinematics is still limited.

Kinetic gait parameters, such as ground reaction forces (GRFs) and the corresponding impact loading rate exhibited strong correlations with running distance (Derrick et al., 2002; Morin et al., 2011; Degache et al., 2013). Decreased vertical GRFs and lower vertical average loading rate (VALR) were detected after long-distance running, which was speculated as an indicator that the runner tends to shift the running style toward a smoother pattern to alleviate the increased mechanical stresses and avoid RRI (Morin et al., 2011). Since the OFM is a kinematics-only model, a combination of kinetics with this multi-segment foot model shall yield more insight into foot function during long-distance running. Therefore, the purpose of this study was to investigate the differences in inter-segment foot kinematics and GRFs before (baseline test (0 km)), during (interval test after 5 km), and after (final test after 10 km) long-distance running. It was hypothesized that: 1) the inter-segment foot kinematics would change after 5 and 10 km of running, and that 2) the vertical GRFs and VALR would decrease as running distance increased and some differences may also be detected on horizontal GRFs after 5 and 10 km of running.

2 MATERIALS AND METHODS

2.1 Participants

A total of 10 marathon-experienced recreational runners (demographic information: age, 25.63 ± 2.88 years; height, 171.88 ± 3.64 cm; weight, 64.73 ± 5.68 kg; BMI, 21.99 ± 2.75 kg/m^2; training status: running experiences, 4.25 ± 1.81 years; running frequency, 3.13 ± 0.64 times/week; running distance: 7.88 ± 3.76 km per time) were recruited to participate in this study. All of them have regularly joined in the half or full marathon race within 3 years and they were free from any lower limb and foot injuries at least 6 months before this experiment. All runners prefer a rear-foot strike at the beginning of long-distance running and the dominant leg was confirmed to be the right one based on the kicking test. Informed written consent was obtained and this study was approved by the Ethics Committee in Ningbo University (RAGH20201013).

2.2 Experimental Protocol and Procedure

A Vicon motion capture system (Oxford Metrics Ltd., Oxford, United Kingdom) with 8 infrared cameras was applied to collect the foot inter-segment kinematics during running at 200 Hz. A total of 30 spherical reflective markers with 9 mm in diameter were attached to the corresponding bony landmarks through the hole cut in the shoes based on a previously established protocol (Song et al., 2020), and three markers (LD1M, LMMA, and LCPA) were removed after the static calibration trials (**Figure 1**). GRFs data and gait cycle were obtained using an AMTI force platform (Advance Mechanical Technology Inc, Watertown, United States) embedded in the middle of a 20-m indoor walkway at a frequency of 1000 Hz. The Vicon Nexus software (Version 1.8.5, Oxford Metrics Ltd., Oxford, United Kingdom) was used to record the kinematics and kinetics data synchronously. The same pants and running shoes were provided and participants were required to wear them while running at least 1 week before the test for adaptation.

The baseline data were first collected during the test day after a 10-min basic warm-up and environment familiarization. Participants were instructed to run on the 20-m indoor track at 3.3 m/s (equal to 12 km/h), with the above motion capture system and force platform used to record data and a timing gate to monitor the running speed. After that, participants were asked to run for 10 km on a treadmill at 12 km/h. This running protocol was chosen because a running distance of 10 km is long enough to initiate changes, and 12 km/h corresponds to the average moderate running speed for recreational runners (Kim et al., 2018). The marker and GRFs data were again measured immediately after 5 km of running. After the interval test, participants kept running for another 5 km and did the final 10-km test.

2.3 Data Collection and Processing

Demographic information and training experience were collected and calculated before the test. Gait data were first labelled and run in Vicon Nexus. An experienced technician further checked the traces and removed all the inconsistent trials. Five successful trials

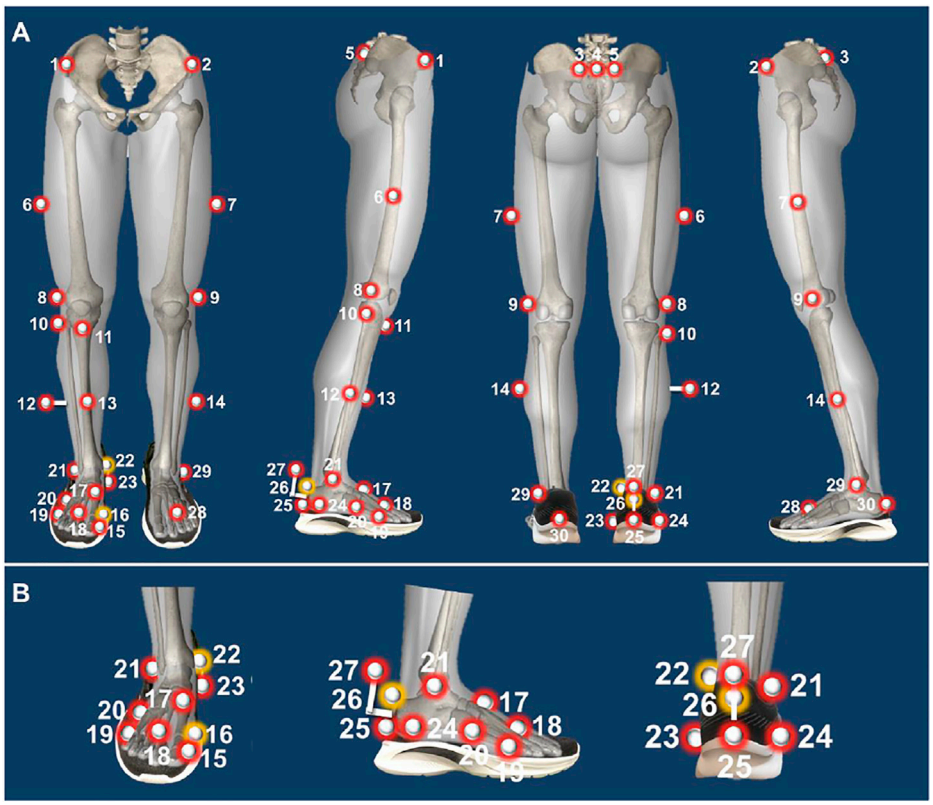

FIGURE 1 | Illustration of Oxford Foot Model marker placement protocol (**(A)**: Lower limb model; **(B)**: Foot multi-segmental model). Note: 1, RASI: right anterior superior iliac spine; 2, LASI: left anterior superior iliac spine; 3, LPSIS: left posterior superior iliac spine; 4, SACR Sacral marker; 5, RPSIS: right posterior superior iliac spine; 6, RTHI: right thigh marker; 7, LTHI: left thigh marker; 8, RKNE: right lateral knee; 9, LKNE: left lateral knee; 10, RHFB: right lateral head of fibula; 11, RTUB: right tibial tuberosity; 12, RTIB: right tibial marker; 13, RSHN: right anterior aspect of the shin; 14, LTIB: left tibial marker; 15, RHLX: right hallux; 16, RD1M: right 1st metatarsal, distal medial; 17, RP1M: right 1st metatarsal, proximal dorsal; 18, RTOE: right toe; 19, RD5M: right 5th metatarsal, distal lateral; 20, RP5M: right 5th metatarsal, proximal lateral; 21, RANK: right ankle; 22, RMMA: right medial malleoli; 23, RSTL: right sustaniculum tali; 24, RLCA: right lateral calcaneus; 25, RHEE: right heel; 26, RPCA: right posterior calcaneus proximal; 27, RCPG: right peg marker; 28, LTOE: left toe; 29, LANK: left ankle; 30, LHEE: left heel; The yellow markers were removed after static calibration.

for each participant were extracted for further analysis. The dominant foot inter-segment kinematics, including forefoot with respect to hindfoot angles (FFHFA) and hindfoot with respect to tibia angles (HFTBA) in the sagittal, frontal, and transverse planes, as well as hallux with respect to forefoot angle (HXFFA) in the sagittal plane, were measured. Angle values at initial contact (IC) and toe-off (TO), as well as peak values and range of motion (ROM) in the stance phase, were then derived. For GRFs parameters, the 1st and 2nd vertical GRFs, peak propulsive, and breaking GRFs in the stance phase, together with the 1st and 2nd VALR, were extracted. The peak propulsive and breaking GRFs refer to the peak positive and negative GRF in *X*-axis (anteroposterior direction), and VALR were calculated by dividing the corresponding vertical GRF with the time from IC. All kinetic parameters were normalized to body weight for further analysis.

2.4 Statistical Analysis

For peak variables analysis, one-way repeated-measures analysis of variance (ANOVA) through SPSS 17.0 software (SPSS, Chicago, IL, United States) was taken to examine the significance of foot inter-segment kinematics and GRFs at critical points between the baseline condition, 5 km, and 10 km of running. The Shapiro-Wilk test was first performed to assess data normality and data were presented as mean ± SD (standard deviation). The mean differences (confidence intervals (95%CI)) among groups were also calculated. Moreover, ANOVA of one-dimensional statistical parametric mapping (SPM1d) was also conducted to further observe foot kinematics changes over the stance phase by using MATLAB 2019b software (The MathWorks, Natick, MA, United States). The statistical significance level was set at $p < 0.05$.

3 RESULTS

3.1 Foot Inter-segment Kinematics

The time-series data of foot inter-segment kinematics and the corresponding SPM1d analysis during the stance phase among three conditions are shown in **Figure 2**. **Table 1**, **Table 2**, **Table 3**

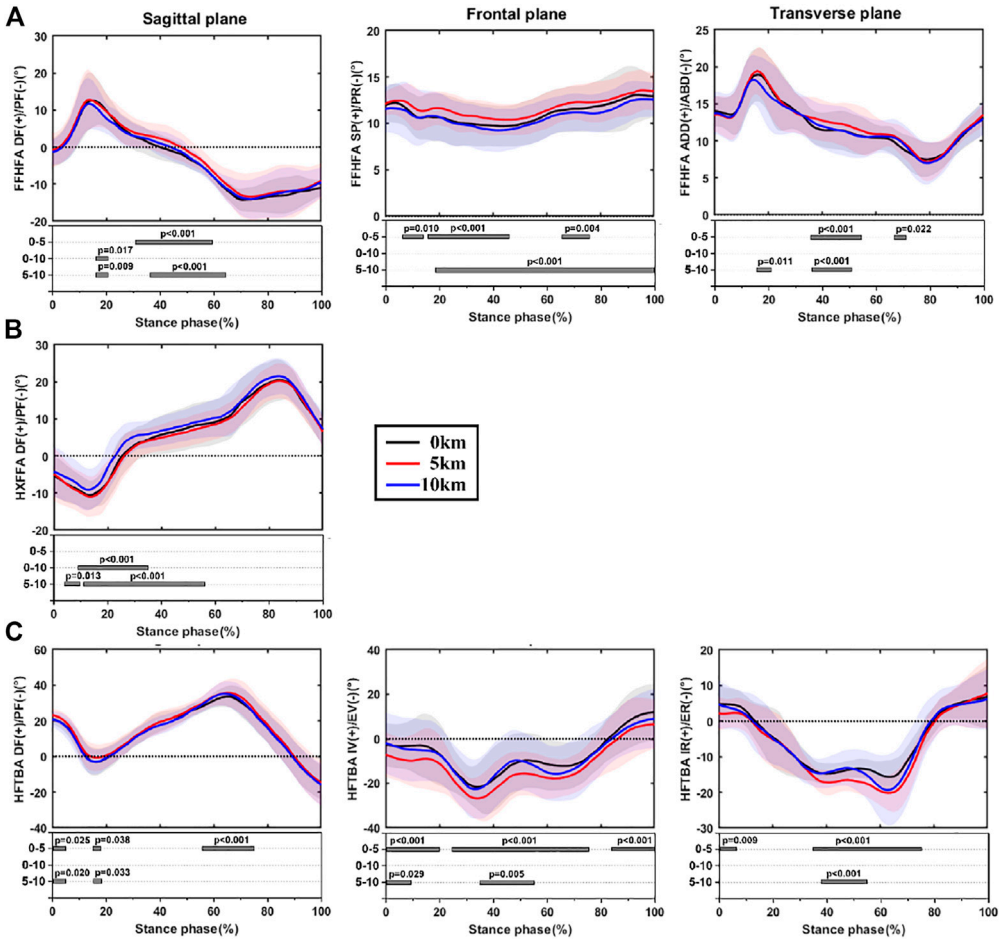

FIGURE 2 | The time-series data and SPM1d analysis of foot inter-segment kinematics during stance phase at baseline condition and immediately after 5 and 10 km of running, **(A)**: forefoot with respect to hindfoot motion; **(B)**: hallux with respect to forefoot motion; **(C)**: hindfoot with respect to tibia motion. Note: FFHFA, forefoot with respect to hindfoot angles; HXFFA, hallux with respect to forefoot angle; HFTBA, hindfoot with respect to tibia angles; DF, dorsiflexion; PF, plantarflexion; SP, supination; PR, pronation; ADD, adduction; ABD, abduction; IV, inversion; EV, eversion; IR, internal rotation; ER, external rotation.

exhibits test statistics for all kinematic parameters at critical points.

3.1.1 Forefoot with Respect to Hindfoot Motion

Through the SPM1d analysis, it was found that FFHFA was significantly different after 5 km of running compared to baseline and 10 km (**Figure 2A**). The larger dorsiflexion and adduction angles during the mid-stance phase and the larger supination throughout the stance phase were found at 5 km. In addition, 10 km of running resulted in relatively smaller dorsiflexion at the early stance phase compared to baseline and 5 km. In the meantime, significantly less plantarflexion was also found after 5 and 10 km of running by comparing the angles at TO with baseline. The critical point differences among conditions can be found in **Table 1**.

3.1.2 Hallux with Respect to Forefoot Motion

As for HXFFA in the sagittal plane, smaller plantarflexion angles were presented during the early to midstance phase (**Figure 2B**) at 10 km of running, and the peak value of plantarflexion also decreased after 10 km of running when compared to baseline and 5 km of running (**Table 2**).

3.1.3 Hindfoot with Respect to Tibia Motion

Similar trends were also found for hindfoot with respect to tibia motion by examining the full-time series of angles (**Figure 2C**), especially in the frontal and transverse planes, 5 km of running led to larger eversion and external rotation angles during the mid-stance phase. A consistent result was also found after 5 km of running when comparing the peak angles, angles at IC and TO instant, and ROM. Additionally, some significant differences were presented at 10 km compared to baseline and 5 km. The critical point differences among conditions are shown in **Table 3**.

3.2 Ground Reaction Forces

The group average and statistics of GRFs during the stance phase are presented in **Table 4**. No significant differences were found among conditions except peak propulsive, with its value

TABLE 1 | Forefoot with respect to hindfoot motion kinematics at baseline and immediately after 5 and 10 km of running.

	Running distance			*p*-values, mean difference (95%CI)		
	Baseline	5 km	10 km	Baseline/5 km	Baseline/10 km	5km/10 km
	Mean (SD)	Mean (SD)	Mean ± SD			
FFHFA (°)						
X						
IC	−1.30 ± 3.88	−0.77 ± 4.63	−1.29 ± 3.47	0.470, −0.53 (−1.43 to 0.38)	1.000, −0.01 (−0.80 to 0.78)	0.458, 0.52 (−0.37–1.40)
TO	−10.55 ± 2.53	−8.11 ± 4.83	−8.54 ± 3.94	**0.007**, −2.45 (−4.33 to −0.57)	**0.013**, −2.01 (−3.69 to −0.34)	1.000, 0.44 (−0.74–1.61)
DF (max)	13.98 ± 6.44	14.14 ± 6.79	13.42 ± 5.45	1.000, −0.16 (−1.24 to 0.92)	0.561, 0.56 (−0.48–1.60)	0.252, 0.72 (−0.29–1.74)
PF(MAX)	−16.35 ± 2.65	−14.96 ± 6.21	−15.46 ± 5.10	0.125, −1.39 (−3.03 to 0.26)	0.278, −0.89 (−2.17 to 0.40)	0.369, 0.50 (−0.29–1.29)
ROM(DF/PF)	30.33 ± 6.30	29.10 ± 7.45	28.88 ± 6.03	0.304, 1.23 (−0.59–3.04)	0.071.1.45 (−0.09–2.98)	1.000, 0.22 (−1.04–1.48)
Y						
IC	11.95 ± 1.84	12.07 ± 1.28	11.52 ± 2.55	1.000, −0.12 (−0.75 to 0.52)	0.172, 0.43 (-0.12–0.99)	0.368, 0.55 (−0.32–1.42)
TO	12.92 ± 2.26	13.38 ± 2.16	12.56 ± 1.74	0.104, −0.46 (−0.98 to 0.07)	0.601, 0.36 (-0.33–1.06)	**0.001**, 0.82 (0.29–1.35)
SP(max)	13.93 ± 2.93	14.41 ± 2.21	13.46 ± 2.17	0.060, −0.48 (−0.98 to 0.01)	0.141, 0.47 (-0.10–1.03)	< **0.001**, 0.95 (0.50–1.40)
ROM(SP/PR)	4.61 ± 1.12	4.64 ± 1.25	4.66 ± 0.82	1.000, −0.04 (−0.46 to 0.39)	1.000, −0.05 (−0.60 to 0.49)	1.000, −0.02 (−0.61 to 0.57)
Z						
IC	14.01 ± 2.07	13.52 ± 2.37	13.70 ± 2.85	0.143, 0.50 (−0.11–1.10)	0.501, 0.31 (−0.24–0.87)	1.000, −0.18 (−0.73 to 0.37)
TO	14.04 ± 2.26	14.40 ± 1.68	13.89 ± 2.42	0.177, −0.37 (−0.83 to 0.10)	1.000, 0.15 (−0.42–0.71)	0.127, 0.51 (−0.10–1.12)
ADD (max)	20.00 ± 3.60	20.66 ± 3.20	19.57 ± 3.54	**0.049**, −0.66 (−1.32 to -0.01)	0.775, 0.43 (−0.50–1.35)	**0.002**, 1.09 (0.34–1.83)
ROM(ADD/ABD)	13.02 ± 2.16	14.04 ± 1.81	12.96 ± 1.92	**0.001**, −1.02 (−1.67 to −0.38)	1.000, 0.06 (−0.96–1.08)	**0.007**, 1.09 (0.24–1.93)

Note: FFHFA, forefoot with respect to hindfoot angles; SD, standard deviation; CI: confidence interval; IC, initial contact; TO, toe-off; DF, dorsiflexion; PF, plantarflexion; SP, supination; PR, pronation; ADD, adduction; ABD, abduction; ROM, range of motion.

TABLE 2 | Hallux with respect to forefoot motion kinematics at baseline and immediately after 5 and 10 km of running.

	Running distance			*p*-values, mean difference (95%CI)		
	Baseline	5 km	10 km	Baseline/5 km	Baseline/10 km	5km/10 km
	Mean (SD)	Mean (SD)	Mean ± SD			
HXFFA (°)						
X						
IC	−5.41 ± 5.37	−4.99 ± 7.34	−4.22 ± 6.78	1.000, −0.41 (−1.86 to 1.04)	0.055, −1.18 (−2.38 to 0.02)	0.420, −0.77 (−2.04 to 0.50)
TO	3.37 ± 4.81	2.28 ± 4.69	3.77 ± 5.12	0.452, 1.10 (−0.77–2.96)	1.000, −0.40 (−2.00 to 1.21)	0.180, −1.49 (−3.42 to 0.43)
DF (max)	21.39 ± 5.52	21.02 ± 4.37	22.28 ± 4.74	1.000, 0.37 (−1.13–1.87)	0.214, −0.89 (−2.09 to 0.31)	0.102, −1.26 (−2.69 to 0.17)
PF(max)	−10.87 ± 4.03	−11.40 ± 5.42	−9.79 ± 5.40	0.739, 0.54 (−0.60–1.67)	0.074, −1.08 (−2.24 to 0.08)	**0.006**, −1.62 (−2.85 to −0.38)
ROM(DF/PF)	32.25 ± 5.02	32.42 ± 3.84	32.06 ± 4.20	1.000, −0.17 (−1.24 to 0.91)	1.000, 0.19 (−1.10–1.48)	1.000, 0.36 (−0.78–1.50)

Note: HXFFA, hallux with respect to forefoot angle; SD, standard deviation; CI: confidence interval; IC, initial contact; TO, toe-off; DF, dorsiflexion; PF, plantarflexion; ROM, range of motion.

decreasing significantly after 10 km compared to 5 km of running.

4 DISCUSSION

This study set out to measure the inter-segment foot kinematics and GRF differences after a continuous 5 and 10 km of running compared to the baseline. Consistent with our first hypothesis, significant kinematic deviations among conditions were found. However, the second hypothesis was partially supported since only the difference in propulsive force was detected.

4.1 Forefoot Motion

By exploring the forefoot motion with respect to rearfoot, it is possible to gain further insight into the plantar dynamic changes during long-distance running. In the sagittal plane, the plantarflexion angle at TO was found to significantly decrease both after 5 and 10 km of running. Although the differences seem relatively small at first glance (2.45° between baseline and 5 km, 2.01° between baseline and 5 km), several studies have revealed that the intricate foot inter-segment movement could have a significant effect on the plantar fascia function (Ferber and Benson, 2011; Michael E Graham et al., 2011; Chang et al., 2014). For instance, a tiny distance change between the forefoot and rearfoot (< 1 mm) would contribute to a 34.8%

TABLE 3 | Hindfoot with respect to tibia kinematics at baseline and immediately after 5 and 10 km of running.

	Running distance			*p*-values, mean difference (95%CI)		
	Baseline	5 km	10 km	Baseline/5 km	Baseline/10 km	5km/10 km
	Mean (SD)	Mean (SD)	Mean ± SD			
HFTBA (°)						
X						
IC	20.96 ± 3.13	23.19 ± 3.71	20.78 ± 4.48	**0.002**, −2.23 (−3.72 to −0.73)	1.000, 0.19 (−1.33–1.70)	**0.002**, 2.41 (0.81–4.02)
TO	−16.03 ± 9.05	−16.66 ± 13.00	−18.08 ± 12.18	1.000, 0.63 (−2.30–3.57)	0.205, 2.05 (−0.68–4.77)	0.077, 1.42 (−0.11–2.94)
DF (max)	34.82 ± 5.59	37.62 ± 5.96	36.98 ± 5.84	< **0.001**, −2.79 (−4.04 to −1.54)	**0.005**, −2.15 (−3.76 to −0.55)	0.976, 0.64 (−0.96–2.24)
PF(max)	−16.29 ± 8.80	−16.78 ± 12.78	−18.23 ± 11.89	1.000, 0.50 (−2.30–3.29)	0.194, 1.94 (−0.61–4.49)	**0.047**, 1.45 (0.01–2.88)
ROM(DF/PF)	51.11 ± 8.38	54.40 ± 11.47	55.20 ± 10.12	**0.031**, −3.29 (−6.35 to −0.24)	**0.001**, −4.10 (−6.64 to −1.56)	0.997, −0.81 (−2.85 to 1.23)
Y						
IC	−2.72 ± 9.85	−7.14 ± 10.33	−1.92 ± 13.82	< **0.001**, 4.42 (1.93–6.91)	1.000, −0.81 (−5.04 to 3.43)	**0.008**, −5.23 (−9.30 to −1.15)
TO	11.86 ± 12.84	6.27 ± 10.31	8.96 ± 13.80	< **0.001**, 5.59 (3.38–7.80)	0.583, 2.90 (−2.56–8.35)	0.325, −2.70 (−6.79 to 1.39)
IV(max)	12.83 ± 13.06	8.14 ± 11.59	10.90 ± 12.35	< **0.001**, 4.70 (2.81–6.58)	0.953, 1.94 (−2.82–6.69)	0.267, −2.76 (−6.70 to 1.18)
EV (max)	−24.54 ± 11.84	−28.92 ± 11.26	−24.75 ± 13.37	< **0.001**, 4.38 (2.02–6.74)	1.000, 0.20 (−2.85–3.25)	**0.019**, −4.18 (−7.81 to −0.54)
ROM(IV/EV)	37.38 ± 11.47	37.06 ± 10.82	35.64 ± 8.49	1.000, 0.31 (−2.86–3.49)	0.543, 1.73 (−1.43–4.89)	0.161, 1.42 (−0.36–3.19)
Z						
IC	4.78 ± 4.87	2.18 ± 4.71	4.70 ± 6.77	**0.001**, 2.60 (0.96–4.24)	1.000, 0.08 (−1.90–2.05)	**0.006**, −2.52 (−4.44 to −0.60)
TO	7.38 ± 9.36	8.81 ± 10.23	6.69 ± 8.82	0.053, −1.43 (−2.86 to 0.01)	0.578, 0.69 (−0.60–1.98)	**0.014**, 2.12 (0.35–3.88)
IR (max)	10.62 ± 5.92	11.40 ± 7.18	9.08 ± 7.46	0.713, −0.78 (−2.39 to 0.84)	0.060, 1.54 (−0.05–3.13)	**0.017**, 2.32 (0.34–4.30)
ER (max)	−18.55 ± 3.32	−22.30 ± 4.70	−22.24 ± 7.36	< **0.001**, 3.75 (2.34–5.17)	< **0.001**, 3.69 (1.55–5.83)	1.000, −0.06 (−2.05 to 1.93)
ROM(IR/ER)	29.17 ± 8.16	33.70 ± 8.87	31.32 ± 10.98	< **0.001**, −4.53 (−6.47 to −2.59)	0.095,−2.15 (−4.55 to 0.26)	0.128, 2.38 (−0.46–5.22)

Note: HFTBA, hindfoot with respect to tibia angles; SD, standard deviation; CI: confidence interval; IC, initial contact; TO, toe-off; DF, dorsiflexion; PF, plantarflexion; IV, inversion; EV, eversion; IR, internal rotation; ER, external rotation; ROM, range of motion.

TABLE 4 | Ground reaction forces at baseline and immediately after 5 and 10 km of running.

	Running distance			*p*-values, mean difference (95%CI)		
	Baseline	5 km	10 km	Baseline/5 km	Baseline/10 km	5km/10 km
GRFs	Mean (SD)	Mean (SD)	Mean ± SD			
First peak vertical (BW)	1.95 ± 0.28	1.99 ± 0.29	2.03 ± 0.26	1.000, −0.04 (−0.15 to 0.08)	0.268, −0.08 (−0.20 to 0.04)	0.837, −0.05 (−0.16 to 0.06)
Second peak vertical (BW)	2.67 ± 0.18	2.66 ± 0.21	2.60 ± 0.27	1.000, 0.01 (−0.05–0.07)	0.229, 0.07 (−0.02–0.15)	0.134, 0.06 (−0.01–0.12)
First VALR (BW/s)	45.64 ± 15.69	48.11 ± 14.04	47.58 ± 11.04	0.684, −2.47 (−7.48 to 2.54)	1.000, −1.94 (−8.04 to 4.16)	1.000, 0.53 (−4.64–5.69)
Second VALR (BW/s)	27.14 ± 4.59	28.14 ± 3.29	27.85 ± 4.53	0.599, −1.00 (−2.90 to 0.91)	1.000, −0.71 (−2.58 to 1.17)	1.000, 0.29 (−1.37–1.96)
Peak braking (BW)	−0.17 ± 0.05	−0.18 ± 0.07	−0.18 ± 0.08	1.000, 0.01 (−0.02–0.04)	1.000, 0.01 (−0.03–0.04)	1.000, −0.01 (−0.03 to 0.03)
Peak propulsive (BW)	0.14 ± 0.07	0.14 ± 0.08	0.12 ± 0.07	0.741, −0.01 (−0.02 to 0.01)	0.443, 0.01 (−0.01–0.03)	**0.005**, 0.02 (0.01–0.03)

***Note**: SD, standard deviation; CI: confidence interval; GRFs, ground reaction forces; VALR, vertical average loading rate; BW, body weight.*

change of plantar fascia strain (Michael E Graham et al., 2011). Also, a change of 1° in arch angle can lead to a plantar fascia tension change of 0.4–0.7 times of body weight during the early stance phase (Ferber and Benson, 2011). Thus, we speculated that the decreased forefoot plantarflexion motion during the stance phase may result in the increased stress and strain of plantar aponeurosis and consequently higher injury risks. In addition, smaller forefoot dorsiflexion angles were found during the early (15–20%) stance phase at 10 km of running compared to baseline and 5 km of running, which indicates that runners may tend to a relative midfoot strike pattern after long-distance running, probably because of compensating for local muscle fatigue (Kim et al., 2018).

Concerning forefoot motion in the frontal plane, decreased supination angles were observed throughout the stance phase after 10 km of running compared to 5 km, which may also correlate with the changes of foot posture after long-distance

running (Mei et al., 2019). Specifically, it has been proved that long-distance running would result in a more pronated foot posture and a redistributed forefoot plantar load with increased pressure under the 2nd and 3rd metatarsal while decreasing under 4th and 5th metatarsals (Bisiaux and Moretto, 2008; Mei et al., 2019). Moreover, the significantly reduced peak forefoot adduction angle and ROM, as well as relatively smaller forefoot adduction during early (15–21%) and mid-stance (37–51%) phase at 10 km of runnimg, could be another possible explanation for the above findings since forefoot adduction is a part of foot supination during the propulsion phase (Levinger et al., 2010). Similar kinematic changes in frontal and transverse planes were also found in individuals with flat arch during walking (Hunt and Smith, 2004). It has been demonstrated that the pronated foot posture after long-distance running could further lead to a reduced arch height (Fukano et al., 2018), which could let the foot move with a relatively "flat arch" pattern and may induce plantar pain during running.

4.2 Hallux Motion

Compared to previous data, a relatively different result of hallux motion was observed in this study. Generally, rearfoot-strike runners would present great hallux dorsiflexion during the early and last stance phase of running because of the rollover mechanism (Samson et al., 2014). However, our findings showed that, although there was no significant difference among conditions, the hallux exhibited considerably smaller dorsiflexion angle both at IC and TO. A possible explanation for this difference may be the narrow forefoot part of footwear due to modern aesthetic needs. Previous research has demonstrated that the insufficient forefoot space (width and height) may limit the ambulatory function of toes, affect its kinematic performance during locomotion, and potentially lead to foot injuries (such as bruised toenails) because of repetitive friction (Runners Connect, 2013; Wallden, 2016; Xiang et al., 2018). Two studies measuring the foot inter-segment kinematics while walking or running barefoot presented normal hallux dorsiflexion during the stance phase (Sun et al., 2018; Xiang et al., 2020a). Therefore, more comparisons concerning the effects of forefoot space of footwear on hallux biomechanics are warranted. In addition, the strike pattern may also contribute to this difference. Although all participants in this study preferred rearfoot strike at the beginning of the long-distance running test, it was demonstrated above that runners may shift to a relative midfoot landing strategy as indicated by the smaller forefoot dorsiflexion angles from early to mid-stance phases. Compared to baseline and 5 km of running, it was also found that the plantarflexion angles decreased during the early stance phase at 10 km of running. Together with the smaller peak propulsive force found after 10 km of running, it was speculated that the toes' dynamic control function, such as gripping, may gradually reduce after long-distance running, which was also consistent with previous findings (Kim et al., 2018; Mei et al., 2018). Nevertheless, more studies concerning the hallux biomechanics during long-distance running are recommended.

4.3 Rearfoot Motion

Most of the distinct effects concerning foot inter-segment kinematics were observed in rearfoot motion. As for the sagittal plane, higher dorsiflexion angles at IC and during the early (0–5%) and mid-late (56–75%) stance phase were presented after 5 km of running, and a higher peak dorsiflexion angle and ROM were presented after both 5 and 10 km of running. Although stride length was not measured in this study, it was previously demonstrated that the increase in rearfoot dorsiflexion resulted in a greater stride length (Sun et al., 2018). Similarly, the decreased dorsiflexion angle at IC and increased peak plantarflexion angle, and larger plantarflexion during the early (15–18%) stance phase may indicate the stride length was reduced again after 10 km of running when compared to 5 km. As muscular fatigue may happen during long-distance running, the lower limb is likely to shift its gait to a shorter but quicker step frequency (Millet et al., 2009; Kim et al., 2018), which could be a possible explanation for the stride length change at 10 km of running.

In the frontal plane, higher eversion angles throughout the stance phase were found after 5 km of running compared to the other two conditions. Previous research provided evidence that increased rearfoot eversion motion would be an injury indicator, which may potentially increase the risk of plantar fasciitis because of excessive use (Ryan B Graham et al., 2011; Chang et al., 2014). Moreover, excessive rearfoot eversion would further lead to excessive midfoot dorsiflexion, and this abnormal kinematic coupling foot motion has been proved a risk factor for lower limb RRI (Takabayashi et al., 2018). In addition, greater internal to external rotation, especially during the mid-late stance (34–75%) phase and consequently increased ROM in the transverse plane, were also observed at 5 km of running. An increase in the rearfoot rotation was demonstrated to be associated with an increase in tibial rotation and then would further affect the proximal joints' function (such as the knee joint) because of the coupling motion (Lundberg et al., 1989; Williams et al., 2001; Levinger et al., 2010). This could also serve as an underlying mechanism for knee injuries after long-distance running, such as iliotibial band syndrome (Aderem and Louw, 2015).

4.4 Ground Reaction Forces

A comparison with previous data also revealed some different results in GRFs in our study. Kim et al. (2018) conducted a systematic review to investigate the effect of long-distance running on lower-limb biomechanical parameters in healthy runners. They summarized that lower vertical GRFs and loading rate would be presented after long-distance running due to the increased mechanical stress with decreased musculoskeletal capacities. However, no significant differences among conditions were found in this study except a lower peak propulsive force at 10 km of running compared to 5 km. The participants' heterogeneity between studies would be the primary explanation for these differences since the fatigue-related changes were speculated to initiate at 10 km of running according to our findings in kinematics. Investigating longer-distance running (such as 20 km) based on participants involved in this study will be performed for

further verification. Moreover, the inconsistent GRF results of this study may also be due to the equipment accuracy and future studies using more precise devices (e.g., insole-type pressure mat) could add insight (Lung et al., 2008; Jung et al., 2014).

4.5 Limitations

Some limitations of this study should be considered. Firstly, the main purpose of the current study was to investigate the effect of long-distance running on foot adaptions, thus many other parameters, such as running surface, running shoes, and gender were not addressed. Secondly, the plantar pressure differences and the repeated stress loading on soft tissue stiffness before and after long-distance running were not measured, which may add more conclusive explanations for the findings of this study (Pu et al., 2018; Duan et al., 2021). Moreover, the muscular fatigue after 10 km of running was only speculated based on previous research results and further investigation about muscle activity before and after running is warranted for verification. In addition, distinct individuals may show different foot kinematic responses during running and a cluster analysis may help find the particular baseline patterns among them (Watari et al., 2021). Lastly, we only investigated the foot kinematic differences during the stance phase as it is the only time for foot–ground interaction. However, the swing phase kinematics shall present more preparatory foot adaptations during long-distance running (Dixon et al., 2011). Further large sample size studies concerning these aspects would reveal more profound knowledge.

5 CONCLUSION

In summary, this study revealed that the foot inter-segment kinematics and GRFs were significantly influenced by long-distance running. Excessive foot motion after 5 km of running may potentially increase the risks of RRI, while 10 km of running changed foot posture, decreased propulsive force, and may also result in high RRI risks because of muscle fatigue. In addition, the forefoot space of footwear may affect foot biomechanics in response to long-distance running, specifically in the hallux region. Findings from the current study give further insight into how inter-segments of foot interact and how GRFs vary during a long-distance running event, adding references for future studies aiming at foot RRI evaluation and prediction.

DATA AVAILABILITY STATEMENT

The original contributions presented in the study are included in the article/Supplementary Material, further inquiries can be directed to the corresponding authors.

ETHICS STATEMENT

The studies involving human participants were reviewed and approved by Ethics Committee in Ningbo University (RAGH20201013). The patients/participants provided their written informed consent to participate in this study.

AUTHOR CONTRIBUTIONS

JL, YS, DS and E-CT developed the concept; JL, YS and E-CT conducted the experiments and the statistical analysis; RX, E-CT, DS, and YG organized the structure and wrote the manuscript; IB, RX, and YG revised the manuscript, and all authors approved the final version.

FUNDING

This study was sponsored by the Open Fund Project of Institute of Human Biomechanics of Ningbo University (CJ-HBIO202107), Ningbo Medical Science and Technology Plan (2020Y14), Public Welfare Science and Technology Project of Ningbo of China (2021S134), and K. C. Wong Magna Fund in Ningbo University.

REFERENCES

Aderem, J., and Louw, Q. A. (2015). Biomechanical Risk Factors Associated with Iliotibial Band Syndrome in Runners: a Systematic Review. *BMC Musculoskelet. Disord.* 16, 7–9. doi:10.1186/s12891-015-0808-7

Balsdon, M. E. R., and Dombroski, C. E. (2018). Reliability of a Multi-Segment Foot Model in a Neutral Cushioning Shoe during Treadmill Walking. *J. Foot Ankle Res.* 11, 1. doi:10.1186/s13047-018-0301-2

Bisiaux, M., and Moretto, P. (2008). The Effects of Fatigue on Plantar Pressure Distribution in Walking. *Gait & Posture* 28, 693–698. doi:10.1016/j.gaitpost.2008.05.009

Chang, R., Rodrigues, P. A., Van Emmerik, R. E. A., and Hamill, J. (2014). Multi-segment Foot Kinematics and Ground Reaction Forces during Gait of Individuals with Plantar Fasciitis. *J. Biomech.* 47, 2571–2577. doi:10.1016/j.jbiomech.2014.06.003

ChinaDaily (2016). Marathon Fever Grips China in 2016. Available at: https://www.chinadaily.com.cn/china/2016-12/26/content_27777895.htm (Accessed April 10, 2021).

Degache, F., Guex, K., Fourchet, F., Morin, J. B., Millet, G. P., Tomazin, K., et al. (2013). Changes in Running Mechanics and spring-mass Behaviour Induced by a 5-hour Hilly Running Bout. *J. Sports Sci.* 31, 299–304. doi:10.1080/02640414.2012.729136

Dempster, J., Dutheil, F., and Ugbolue, U. C. (2021). The Prevalence of Lower Extremity Injuries in Running and Associated Risk Factors: A Systematic Review. *Phys. Activ. Health* 5, 133–145. doi:10.5334/paah.109

Derrick, T. R., Dereu, D., and Mclean, S. P. (2002). Impacts and Kinematic Adjustments during an Exhaustive Run. *Med. Sci. Sports Exerc.* 34, 998–1002. doi:10.1097/00005768-200206000-00015

Dixon, P. C., Tisseyre, M., Damavandi, M., and Pearsall, D. J. (2011). Inter-segment Foot Kinematics during Cross-Slope Running. *Gait & Posture* 33, 640–644. doi:10.1016/j.gaitpost.2011.02.010

Duan, Y., Ren, W., Xu, L., Ye, W., Jan, Y.-K., and Pu, F. (2021). The Effects of Different Accumulated Pressure-Time Integral Stimuli on Plantar Blood Flow in People with Diabetes Mellitus. *BMC Musculoskelet. Disord.* 22 (1), 1–10. doi:10.1186/s12891-021-04437-9

Ferber, R., and Benson, B. (2011). Changes in Multi-Segment Foot Biomechanics with a Heat-Mouldable Semi-custom Foot Orthotic Device. *J. Foot Ankle Res.* 4, 2. doi:10.1186/1757-1146-4-18

Fukano, M., Inami, T., Nakagawa, K., Narita, T., and Iso, S. (2018). Foot Posture Alteration and Recovery Following a Full marathon Run. *Eur. J. Sport Sci.* 18 (10), 1338–1345. doi:10.1080/17461391.2018.1499134

Graham, M. E., Jawrani, N. T., and Goel, V. K. (2011). Evaluating Plantar Fascia Strain in Hyperpronating Cadaveric Feet Following an Extra-osseous Talotarsal Stabilization Procedure. *J. Foot Ankle Surg.* 50, 682–686. doi:10.1053/j.jfas.2011.07.005

Graham, R. B., Costigan, P. A., Sadler, E. M., and Stevenson, J. M. (2011). Local Dynamic Stability of the Lifting Kinematic Chain. *Gait & Posture* 34, 561–563. doi:10.1016/j.gaitpost.2011.06.022

Hulme, A., Nielsen, R. O., Timpka, T., Verhagen, E., and Finch, C. (2017). Risk and Protective Factors for Middle- and Long-Distance Running-Related Injury. *Sports Med.* 47 (5), 869–886. doi:10.1007/s40279-016-0636-4

Hunt, A. E., and Smith, R. M. (2004). Mechanics and Control of the Flat versus normal Foot during the Stance Phase of Walking. *Clin. Biomech.* 19, 391–397. doi:10.1016/j.clinbiomech.2003.12.010

Jung, Y., Jung, M., Lee, K., and Koo, S. (2014). Ground Reaction Force Estimation Using an Insole-type Pressure Mat and Joint Kinematics during Walking. *J. Biomech.* 47 (11), 2693–2699. doi:10.1016/j.jbiomech.2014.05.007

Kim, H. K., Mirjalili, S. A., and Fernandez, J. (2018). Gait Kinetics, Kinematics, Spatiotemporal and Foot Plantar Pressure Alteration in Response to Long-Distance Running: Systematic Review. *Hum. Mov. Sci.* 57, 342–356. doi:10.1016/j.humov.2017.09.012

Kindred, J., Trubey, C., and Simons, S. M. (2011). Foot Injuries in Runners. *Curr. Sports Med. Rep.* 10 (5), 249–254. doi:10.1249/JSR.0b013e31822d3ea4

Levinger, P., Murley, G. S., Barton, C. J., Cotchett, M. P., McSweeney, S. R., and Menz, H. B. (2010). A Comparison of Foot Kinematics in People with normal- and Flat-Arched Feet Using the Oxford Foot Model. *Gait & Posture* 32, 519–523. doi:10.1016/j.gaitpost.2010.07.013

Lundberg, A., Svensson, O. K., Bylund, C., and Selvik, G. (1989). Kinematics of the Ankle/Foot Complex-Part 3: Influence of Leg Rotation. *Foot & Ankle* 9, 304–309. doi:10.1177/107110078900900609

Lung, C.-W., Chern, J.-S., Hsieh, L.-F., and Yang, S.-W. (2008). The Differences in Gait Pattern between Dancers and Non-dancers. *J. Mech.* 24 (4), 451–457. doi:10.1017/S1727719100002562

Matias, A. B., Caravaggi, P., Taddei, U. T., Leardini, A., and Sacco, I. C. N. (2020). Rearfoot, Midfoot, and Forefoot Motion in Naturally Forefoot and Rearfoot Strike Runners during Treadmill Running. *Appl. Sci.* 10 (21), 7811. doi:10.3390/app10217811

Mei, Q., Gu, Y., Sun, D., and Fernandez, J. (2018). How Foot Morphology Changes Influence Shoe comfort and Plantar Pressure before and after Long Distance Running? *Acta Bioeng. Biomech.* 20, 179–186. doi:10.5277/ABB-01112-2018-02

Mei, Q., Gu, Y., Xiang, L., Baker, J. S., and Fernandez, J. (2019). Foot Pronation Contributes to Altered Lower Extremity Loading after Long Distance Running. *Front. Physiol.* 10, 1–12. doi:10.3389/fphys.2019.00573

Millet, G. Y., Morin, J.-B., Degache, F., Edouard, P., Feasson, L., Verney, J., et al. (2009). Running from Paris to Beijing: Biomechanical and Physiological Consequences. *Eur. J. Appl. Physiol.* 107, 731–738. doi:10.1007/s00421-009-1194-3

Milner, C. E., and Brindle, R. A. (2016). Reliability and Minimal Detectable Difference in Multisegment Foot Kinematics during Shod Walking and Running. *Gait & Posture* 43, 192–197. doi:10.1016/j.gaitpost.2015.09.022

Morin, J.-B., Samozino, P., and Millet, G. Y. (2011). Changes in Running Kinematics, Kinetics, and spring-mass Behavior over a 24-h Run. *Med. Sci. Sports Exerc.* 43, 829–836. doi:10.1249/MSS.0b013e3181fec518

Nikolaidis, P. T., Cuk, I., Clemente-Suárez, V. J., Villiger, E., and Knechtle, B. (2021). Number of Finishers and Performance of Age Group Women and Men in Long-Distance Running: Comparison Among 10km, Half-marathon and marathon Races in Oslo. *Res. Sports Med.* 29, 56–66. doi:10.1080/15438627.2020.1726745

Pu, F., Ren, W., Fu, H., Zheng, X., Yang, M., Jan, Y.-K., et al. (2018). Plantar Blood Flow Response to Accumulated Pressure Stimulus in Diabetic People with Different Peak Plantar Pressure: a Non-randomized Clinical Trial. *Med. Biol. Eng. Comput.* 56 (7), 1127–1134. doi:10.1007/s11517-018-1836-x

Runners Connect (2013). What Is the Best Way to Treat Black and Bruised Toenail from Running? Available at: https://runnersconnect.net/toenail-injury-from-running/(Accessed April 10, 2021).

Samson, W., Van Hamme, A., Sanchez, S., Chèze, L., Jan, S. V. S., and Feipel, V. (2014). Foot Roll-Over Evaluation Based on 3D Dynamic Foot Scan. *Gait & Posture* 39, 577–582. doi:10.1016/j.gaitpost.2013.09.014

Song, Y., Liang, M., and Lian, W. (2020). A Comparison of Foot Kinematics between Pregnant and Non-pregnant Women Using the Oxford Foot Model during Walking. *Ijbet* 34, 20–30. doi:10.1504/IJBET.2020.110335

Sun, D., Fekete, G., Mei, Q., and Gu, Y. (2018). The Effect of Walking Speed on the Foot Inter-segment Kinematics, Ground Reaction Forces and Lower Limb Joint Moments. *PeerJ* 6, e5517. doi:10.7717/peerj.5517

Takabayashi, T., Edama, M., Yokoyama, E., Kanaya, C., Inai, T., Tokunaga, Y., et al. (2018). Changes in Kinematic Coupling Among the Rearfoot, Midfoot, and Forefoot Segments during Running and Walking. *J. Am. Podiatr Med. Assoc.* 108 (1), 45–51. doi:10.7547/16-024

Van Gent, R. N., Siem, D., van Middelkoop, M., Van Os, A. G., Bierma-Zeinstra, S. M. A., Koes, B. W., et al. (2007). Incidence and Determinants of Lower Extremity Running Injuries in Long Distance Runners: a Systematic Review * COMMENTARY. *Br. J. Sports Med.* 41 (8), 469–480. doi:10.1136/bjsm.2006.033548

van Poppel, D., van der Worp, M., Slabbekoorn, A., van den Heuvel, S. S. P., van Middelkoop, M., Koes, B. W., et al. (2021). Risk Factors for Overuse Injuries in Short- and Long-Distance Running: A Systematic Review. *J. Sport Health Sci.* 10, 14–28. doi:10.1016/j.jshs.2020.06.006

Vitti, A., Nikolaidis, P. T., Villiger, E., Onywera, V., and Knechtle, B. (2020). The "New York City Marathon": Participation and Performance Trends of 1.2M Runners during Half-century. *Res. Sports Med.* 28, 121–137. doi:10.1080/15438627.2019.1586705

Wallden, M. (2016). Toe-tal Recall - what on Earth Are Our Toes Actually for? *J. Bodywork Mov. Therapies* 20, 418–431. doi:10.1016/j.jbmt.2016.04.011

Watari, R., Suda, E. Y., Santos, J. P. S., Matias, A. B., Taddei, U. T., and Sacco, I. C. N. (2021). Subgroups of Foot-Ankle Movement Patterns Can Influence the Responsiveness to a Foot-Core Exercise Program: A Hierarchical Cluster Analysis. *Front. Bioeng. Biotechnol.* 9, 481. doi:10.3389/fbioe.2021.645710

Williams, D. S., McClay, I. S., Hamill, J., and Buchanan, T. S. (2001). Lower Extremity Kinematic and Kinetic Differences in Runners with High and Low Arches. *J. Appl. Biomech.* 17, 153–163. doi:10.1123/jab.17.2.153

Wolf, P., Stacoff, A., Liu, A., Nester, C., Arndt, A., Lundberg, A., et al. (2008). Functional Units of the Human Foot. *Gait & Posture* 28, 434–441. doi:10.1016/j.gaitpost.2008.02.004

Xiang, L., Mei, Q., Fernandez, J., and Gu, Y. (2018). Minimalist Shoes Running Intervention Can Alter the Plantar Loading Distribution and Deformation of Hallux Valgus: A Pilot Study. *Gait & Posture* 65, 65–71. doi:10.1016/j.gaitpost.2018.07.002

Xiang, L., Mei, Q., Fernandez, J., and Gu, Y. (2020a). A Biomechanical Assessment of the Acute Hallux Abduction Manipulation Intervention. *Gait & Posture* 76, 210–217. doi:10.1016/j.gaitpost.2019.11.013

Xiang, L., Mei, Q., Xu, D., Fernandez, J., and Gu, Y. (2020b). Multi-segmental Motion in Foot during Counter-movement Jump with Toe Manipulation. *Appl. Sci.* 10, 1893. doi:10.3390/app10051893

Zhou, H., and Ugbolue, U. C. (2019). Is There a Relationship Between Strike Pattern and Injury During Running: A Review. *Phys. Activ. Health* 3, 127–134. doi:10.5334/paah.45

Conflict of Interest: The authors declare that the research was conducted in the absence of any commercial or financial relationships that could be construed as a potential conflict of interest.

Publisher's Note: All claims expressed in this article are solely those of the authors and do not necessarily represent those of their affiliated organizations, or those of the publisher, the editors, and the reviewers. Any product that may be evaluated in this article, or claim that may be made by its manufacturer, is not guaranteed or endorsed by the publisher.

frontiers in Bioengineering and Biotechnology

ORIGINAL RESEARCH
published: 08 March 2022
doi: 10.3389/fbioe.2022.818610

The Study of Biomechanics and Clinical Anatomy on a Novel Plate Designed for Posterolateral Tibial Plateau Fractures *via* Anterolateral Approach

Weizhi Ren[1†], Wen Zhang[2†], Shijie Jiang[3], Jian Peng[1], Chang She[1], Liubing Li[1], Yongtao Mao[1], Haibin Zhou[1] and Wei Xu[1]**

[1]Department of Orthopedics, The Second Affiliated Hospital of Soochow University, Suzhou, China, [2]Orthopedic Institute, Soochow University, Suzhou, China, [3]Department of Orthopedics, Changzhou No. 2 People's Hospital, The Affiliated Hospital of Nanjing Medical University, Changzhou, China

OPEN ACCESS

Edited by:
Lizhen Wang,
Beihang University, China

Reviewed by:
Junchao Guo,
National Research Center for Rehabilitation Technical Aids, China
Tianyun Jiang,
Beihang University, China

***Correspondence:**
Wei Xu
13962157016@139.com
Haibin Zhou
13913133393@163.com

[†]These authors have contributed equally to this work and share first authorship

Specialty section:
This article was submitted to Biomechanics, a section of the journal Frontiers in Bioengineering and Biotechnology

Received: 19 November 2021
Accepted: 17 January 2022
Published: 08 March 2022

Citation:
Ren W, Zhang W, Jiang S, Peng J, She C, Li L, Mao Y, Zhou H and Xu W (2022) The Study of Biomechanics and Clinical Anatomy on a Novel Plate Designed for Posterolateral Tibial Plateau Fractures via Anterolateral Approach. Front. Bioeng. Biotechnol. 10:818610. doi: 10.3389/fbioe.2022.818610

There is no consensus about the optimal internal fixation selection for treatment of posterolateral tibial plateau fracture. This study described a novel plate through an anterolateral approach for posterolateral tibial plateau fractures (PTPFs). We evaluated the biomechanical performance of a novel plate and two conventional internal implants and investigated the anatomic feasibility of the novel plate. The fracture models were randomly assigned into six groups: Groups A–C were the model groups of posterolateral split fracture, fixed with the posterior buttress plate, the lateral locking plate, and the novel plate, respectively. Groups D–E were the model groups of posterolateral depression fracture, fixed with the posterior buttress plate, the lateral locking plate, and the novel plate, respectively. We evaluated the biomechanical performance of six model groups by the biomechanical testing and finite element analysis. Progressively increasing axial compressive loads were applied to each synthetic fracture model by using a customized indentor under 250–750 N loads. Meanwhile, we dissected 12 fresh frozen knee specimens and fixed them with the novel plate through the anterolateral approach. We recorded the adjacency of the novel plate to important anatomic structures. Biomechanical testing showed that the novel plate had the least displacement, followed by the posterior buttress plate, and the lateral plate had the most displacement in posterolateral split fracture. There was no significant difference in the displacement between the novel plate and the lateral plate at different loads in posterolateral depression fractures. And the posterior buttress plate showed the most displacement. In the finite element analysis, the maximum stress values of Groups A, B, and C were 383.76, 414.63, and 305.07 MPa under the load of 750 N, respectively. The maximum stress values of Groups D, E, and F were 474.28, 436.31, and 413.4 MPa under the load of 750 N, respectively. In the anatomic study, the placement of the novel plate had a low risk of damage to the important anatomic structures of knee posterolateral corner. The novel plate could be a great choice for the treatment of PTPFs due to better biomechanical performance and easy manipulation.

Keywords: biomechanical study, finite element analysis, clinical anatomy, internal fixation, tibial plateau fracture

1 INTRODUCTION

Tibial plateau fractures are among the most common fractures in knee trauma. The fractures include a wide variety of fracture patterns, and four different quadrants of the tibial plateau may be involved (Xie et al., 2020). Among them, the treatment of posterolateral tibial plateau fracture (PTPF) has been always a challenging problem for orthopedic surgeons (LaPrade et al., 2003; Sassoon et al., 2014; Cho et al., 2017; Hoekstra et al., 2017). It's difficult to identify the PTPF using the antero-posterior radiograph when the posterolateral (PL) fracture line is parallel to the coronal plane (Higgins et al., 2009; Kfuri and Schatzker, 2018). Thus, the PTPF was considered an uncommon fracture in the past, accounting for only 7%–10% of tibial plateau fractures (Connolly, 2005; Solomon et al., 2010; Chen et al., 2014). However, with the widespread use of computed tomography (CT) in recent years, the diagnosis rate of PTPF is higher than previously thought (Wang et al., 2017). Several studies have reported that PTPF accounts for approximately 15% of all tibial plateau fractures (Xiang et al., 2013), and approximately 54.3% of lateral tibial plateau fractures involve the PL column (Yi et al., 2020).

The PTPFs are the result of axial compressive forces combined with valgus stress with the knee in flexion (Xie et al., 2020), which most commonly causes depression fractures because of the convexity of the lateral tibial plateau (Sun et al., 2014). Besides depression fractures, PL column split fracture is a common type (Sun et al., 2014). The PL region of the knee plays a vital role in the flexion stabilization of the knee (Yu et al., 2012). As an intra-articular fracture, tibial plateau fracture requires anatomical reduction and rigid internal fixation. However, the operative treatment of PTPF is complex because of the special anatomical structures of the PL corner of the knee joint, including the fibular head, the fibular collateral ligament, the popliteus tendon, and the peroneal nerve, which impedes the exposure and fixation of the fracture fragments (Heidari et al., 2013; Giordano et al., 2020; Song et al., 2020). Currently, there is no uniform standard for selecting optimal internal fixation to treat PTPFs. The posterior buttress plate through various posterior approaches (He et al., 2013; Berber et al., 2014; Hoekstra et al., 2015; Gavaskar et al., 2016; Liu et al., 2016; Zhang et al., 2016) and the lateral locking plate through the anterolateral or lateral approaches (Hu et al., 2016; Kfuri et al., 2017) are still commonly used fixation methods in clinical practices. Serval results of biomechanical testing had shown that the posterior buttress plate could provide adequate stability in controlling the vertical displacement of PL fragment compared to the lateral locking plate (Zhang et al., 2012; Sun et al., 2018; Hu et al., 2020; Zhang et al., 2020). When the knee is flexed, there is a posterior and distal displacement of the PL fragment. And the posterior buttress could provide strong support for the shear fragment (Chang et al., 2009; Luo et al., 2010). However, the posterior approach could cause iatrogenic injury to the normal structure of the PL knee joint (Heidari et al., 2013; Solomon et al., 2013; Sun et al., 2017). Compared with the posterior approach, the anterolateral approach is a mature surgical method with little risk of injury to important anatomical structures. Some surgeons had successfully used the lateral locking plate to fix PTPFs by a posteriorly positioned through anterolateral or lateral approaches (Sun et al., 2017). However, whether a lateral locking compression plate could provide sufficient stability to the PTPF is still controversial (Sun et al., 2018). The proximal screws of the lateral locking plate are parallel to the coronal fracture line, which is a disadvantage (Cho et al., 2017). And failure cases of PTPF treated by the lateral locking plate were often encountered (Wang et al., 2017).

The fixation options available for PTPFs are relatively single, with distal radial fixation plates or reconstruction plates being used via a posterior approach or a lateral locking compression plate through the anterolateral approach. Sometimes, the safety of the surgical approach and stability of the internal fixation cannot be met simultaneously. Thus, we developed a novel plate (**Figure 1**) through an anterolateral approach for PTPFs and applied for an invention patent in China (Patent No. ZL202010878681.7).

This study compared the biomechanical performance of this novel plate with other that of two conventional internal implants in the fixation of split fracture and depression fracture. Moreover, we performed an anatomical study to investigate the feasibility of clinical application for the novel plate.

2 MATERIALS AND METHODS

2.1 Fracture Models Construction and Fixation

In this study, 48 right synthetic tibias (type 1110; Sybone AG, Swiss) were used to make models of PL tibial plateau fracture with reference to previous studies (Zhang et al., 2012; Sun et al., 2018). The synthetic tibia model was made of a rigid foam cortical shell, which was filled with cancellous material, which was purchased from a single manufacturing batch to ensure the same material property, architecture, and geometry.

2.1.1 Fracture Models of Posterolateral Split Tibial Plateau Fracture

On the basis of the data from the morphological measurements by Sohn et al. (2015) and published literature (Sun et al., 2018), the PL part of the synthetic tibiae was sawed to simulate a PL split fracture. **Figures 2A–C** demonstrate the modeling of a PL split fracture. A thin blade saw was used to perform the osteotomy. Geometrical measurements were measured by Auto CAD software (Auto CAD, 2020; Autodesk, San Rafael, CA, United States). And we made a custom clay mold to assist us in taking the measurements of the PL fragment (**Figure 2B**). Moreover, all geometric measurements and preparations were performed by a single surgeon.

2.1.2 Fracture Models of Posterolateral Depression Tibial Plateau Fracture

Fracture models that simulate the depression fractures of PL tibial plateau were created in synthetic tibial specimens. **Figures 3A–E** demonstrate the modeling of a PL depression fracture, referring

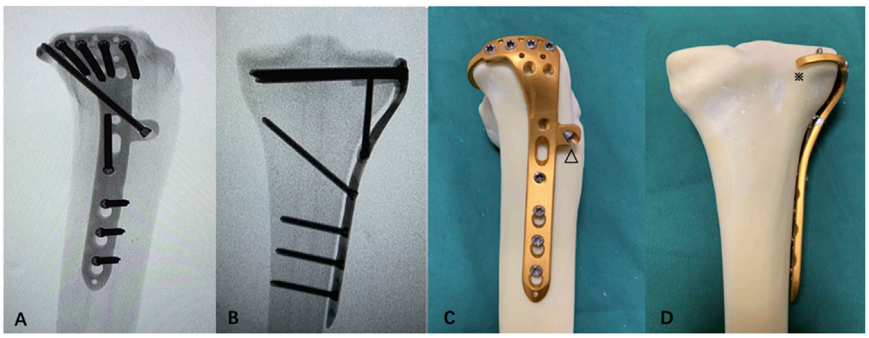

FIGURE 1 | Mock-ups of the novel plate in intact synbones. **(A)** Lateral view of the X-ray image. **(B)** Anteroposterior view of the X-ray image. **(C)** Lateral view of the novel plate. **(D)** Anteroposterior view of the novel plate. The (△) anterior wing and (※) "hoop hook."

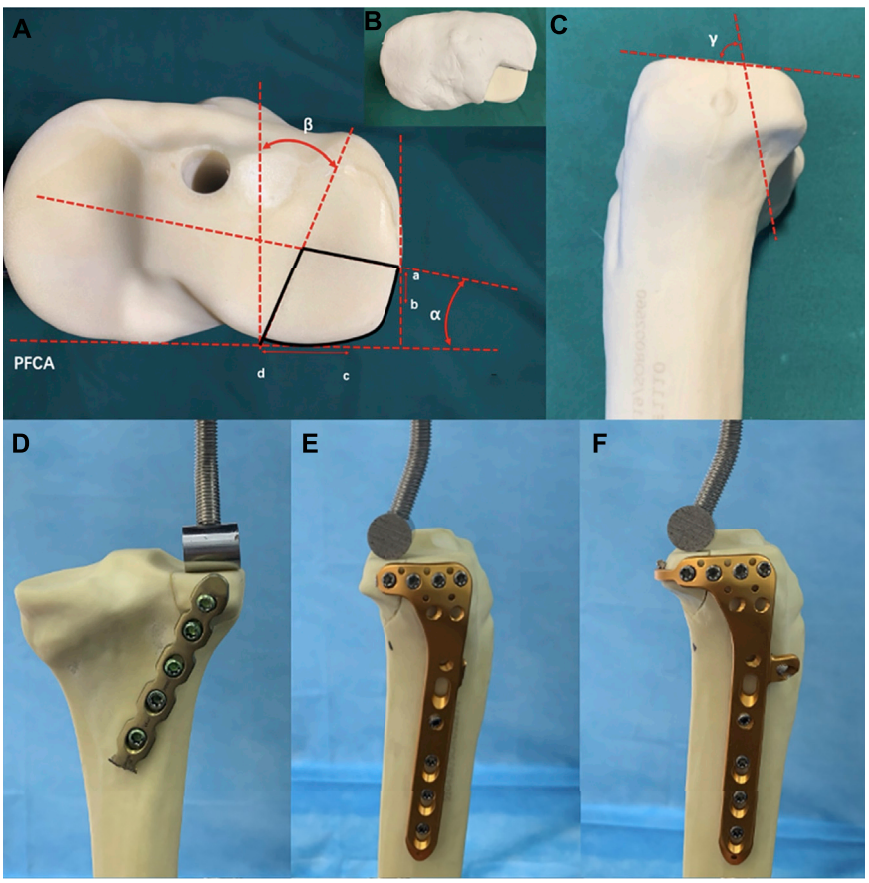

FIGURE 2 | Cranial and lateral views of the posterolateral (PL) split fracture model of tibial plateau and biomechanical test. **(A)** Cranial view. PFCA, posterior femoral condyle axis; point a, lateral exit point of the PL fracture; point b, anterior edge of the articular facet of fibular head; point c, medial edge of the articular facet of fibular head; point d, posterior exit point of the PL fracture; angleα, angle between the lateral fracture line of the PL fragment and the PFCA; angleβ, angle between the medial l fracture line of the PL fragment and the line perpendicular to the PFCA. **(B)** Model made of plastic clay. **(C)** Lateral view. Angle γ, angle between the joint line of the PL fragment with the coronal fracture line [Values of models based on data from the morphological measurements by Sohn et al. (2015)]. **(D)** Fixation of the posterior buttress plate in PL split fracture. **(E)** Fixation of lateral locking plate in the PL split fracture. **(F)** Fixation of novel plate in the PL split fracture.

to the lateral tibial plateau fracture model by previous studies (Welch et al., 2003; Jordan et al., 2016). A 14-mm-diameter depression fragment on the PL tibial plateau was created similarly to the dimension of the PL split fragment. To avoid the adverse effects of an irregular shape of the PL fracture fragment, we used a thin hollow drill to ensure that the shape of the fragment was

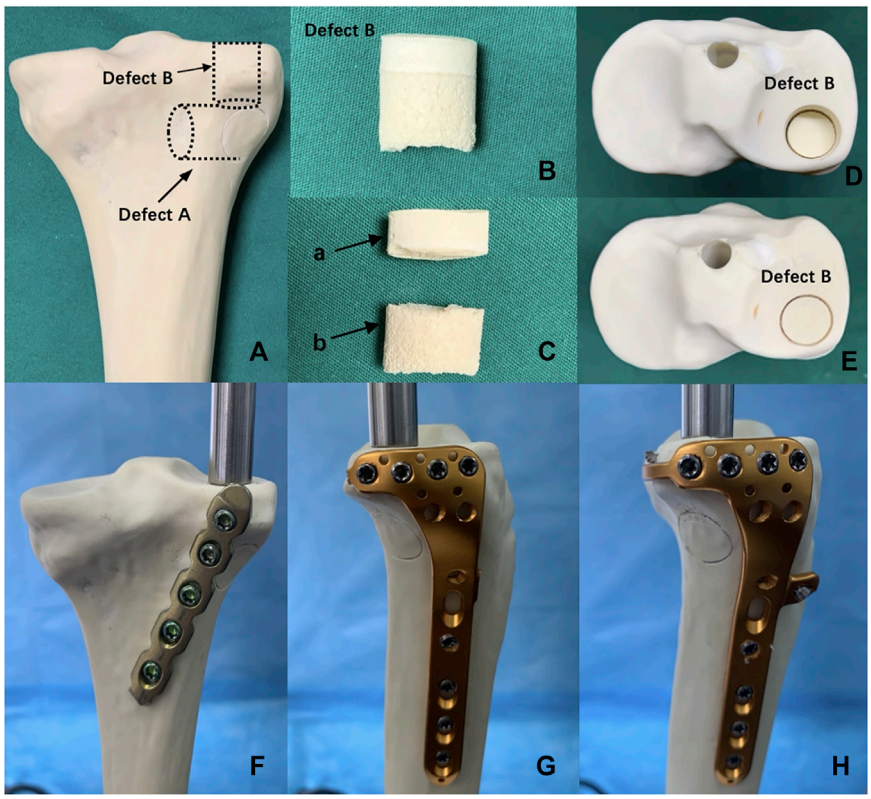

FIGURE 3 | Posterolateral (PL) depression fracture model of tibial plateau and biomechanical test. **(A)** Defect A—15-mm-diameter cylindrical defect in the lateral tibial condyle created by a hollow drill-bit. Defect B—14-mm-diameter cylindrical defect in the PL tibial plateau created by a hollow drill-bit. **(B)** Defect B was put out from tibial plateau. **(C)** Defect B was divided into the two parts, (a) proximal articular surface and (b) distal cancellous bone. **(D)** PL depression fracture model. **(E)** PL depression fracture model was reduced anatomically. **(F)** Fixation of posterior buttress plate in the PL depression fracture. **(G)** Fixation of lateral locking compression plate in the PL depression fracture. **(H)** Fixation of the novel plate in the PL depression fracture.

uniform and regular. First, a cylindrical defect that is 15 mm in diameter (Defect A) was created in the PL tibial condyle far from 15 mm below the tibial plateau surface by using a hollow drill-bit. Second, by using a 14 mm drill bit, a cylindrical defect that is 14 mm in diameter (Defect B) was created within the PL tibial plateau. Defect A and B crossed mutually, and Defect B could be taken out easily. Defect B was divided into two parts, the distal cancellous bone simulating the depression part, and the proximal cortical bone simulating the articular cartilage and subchondral bone. Finally, the removed cancellous and cortical bones were backfilled in sequence to restore anatomical morphology. All geometric measurements and preparations were taken by a single surgeon.

2.1.3 Fracture Fixation Groups

Forty-eight synthetic tibias were randomly assigned to six groups (A–F, eight per group). Groups A to C were the model groups of PL split tibial plateau fractures. Groups D–F were the model groups of PL depression tibial plateau fractures (**Figure 4**). Group A: A posterior five-hole buttress plate (straight, 3.5 mm) was used for the fixation of the PL split fracture. The posterior buttress plate was contoured and implanted from the proximal lateral aspect of the posterior tibia to the distal medial aspect of the tibia. Group B: A lateral locking plate (L-shaped, 3.5 mm) was used for the PL split fracture model, and the transverse arm of the L-shaped plate had four holes. According to previous studies (Hu et al., 2016; Sun et al., 2018), the lateral locking plate was placed as posteriorly as possible to fix the PL fragment with one or at most two screws. Group C: The novel plate (L-shaped, 3.5 mm) was used for PL split fracture model. The novel plate was placed as posteriorly as possible and at the same position as the lateral locking plate. Compared with Group B, the addition of the anterior wing screw and the "hoop hook" of the novel plate fixed the PL split fragment together. Group D: The posterior buttress plate was used for the PL depression fracture model. Group E: A lateral locking plate was used for the PL depression fracture. The lateral locking plate was placed as posteriorly as possible to fix the PL fragment with two screws. Group F: The novel plate was used for the PL depression fracture. The novel plate was also placed as posteriorly as possible and at the same position as the lateral locking plate.

The same manufacturer made the implants to ensure material and design consistency. All fracture models were reduced and fixed by a single orthopedic surgeon.

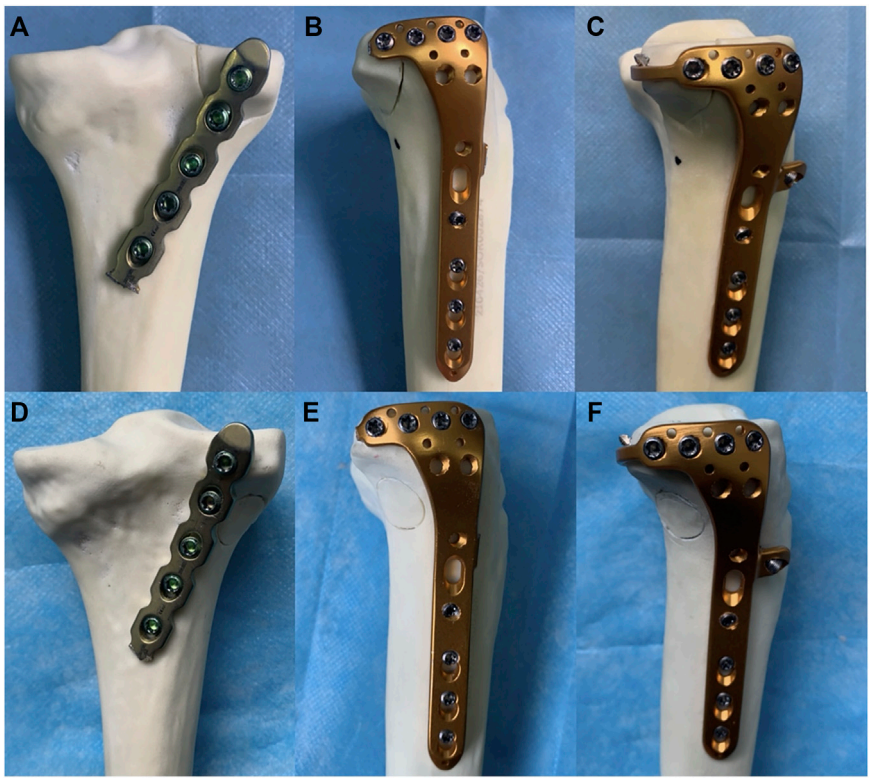

FIGURE 4 | Six different internal fixation models of the posterolateral (PL) fracture. **(A)** The posterior buttress plate fixation in PL split fracture. **(B)** The lateral tibia locking compression plate in PL split fracture. **(C)** The novel plate in PL split fracture. **(D)** The posterior buttress plate fixation in PL depression fracture. **(E)** The lateral tibia locking compression plate in PL depression fracture. **(F)** The novel plate in PL depression fracture.

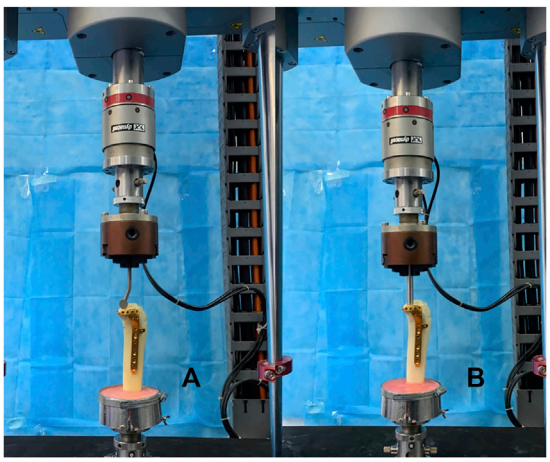

FIGURE 5 | Positioning of synthetic tibia model within the machine. **(A)** Fixation of the novel plate in the posterolateral (PL) split fracture. **(B)** Fixation of the novel plate in the PL depression fracture.

2.2 Biomechanical Testing

Each potted synthetic tibia was placed vertically in a material-testing machine (In-stronE10000, Instron Corporation Norwood, MA, United States) (**Figure 5**). The load was applied to the PL split fragment through a custom T-shaped applicator. The applicator was bent at an angle of 17° so that the angle was parallel to the fracture line in the sagittal plane to simulate the shearing force of the lateral femoral condyle (Feng et al., 2021) (**Figures 2D–F**). Usually, the PL tibial plateau depression fracture was mainly affected by axial forces during normal gait (Jordan et al., 2016). Therefore, for PL depression fracture, an axial load was applied with a custom cylindrical indentor on the PL depression fragment (**Figures 3F–H**). The diameter of the cylinder was slightly smaller than the diameter of the fragment. And the indentor was fixed in advance as the reference location to ensure the models were in the same location.

Biomechanical loading on the knee joint during normal gait is approximately two to three times body weight (Taylor et al., 2004), and the loading ratio of the medial and lateral plateau was approximately 55% and 45%, respectively (Zhao et al., 2007). Therefore, when the human body weight (BW) was set at 60 kg, we chose three different axial peak loads of 250, 500, and 750 N (1–3 times BW) to simulate the loads on the lateral plateau during the state of a single-leg stance. The biomechanical testing was to simulate the static phase for different fixation methods in the material testing machine. After mounting each fracture model, progressively increased axial compressive loads were applied to each model with a load speed of 10 N/s. Axial displacement from the initial position to axial peak loads was continuously captured using Bluehill

TABLE 1 | Properties considered for the materials.

Material	Young's modulus (MPa)	Poisson's ratio
Cortical bone	14000	0.3
Cancellous bone	700	0.3
Plate	110000	0.3
Screw	110000	0.3

software (Instron, Norwood, MA, United States). Load–displacement curves were generated for each model. Moreover, failure form was defined as the situation when the vertical displacement of the PL fragment was 3 mm (Ali et al., 2002). And the maximum peak force was set at 750 N or the force at a displacement of 3 mm for PL fragment. Finally, the displacements at three load levels (250, 500, and 750 N) and failure load were chosen to evaluate the biomechanical stability of three different fixations.

2.3 Statistical Analysis

One-way analysis of variance was performed on the data to determine whether fragment displacement and final failure differed among these fixation models. Fisher's post hoc test and least significant difference criterion were used to correct for multiple group comparisons. The level of significance was set to 0.05 for all statistical tests. All statistical analyses were computed using SPSS version 19.0 software (SPSS, Inc., Chicago, IL, United States).

2.4 Finite Element Analysis

A 30-year-old healthy male volunteer was recruited without a history of knee and systemic disease. By using a 64-row spiral CT scanner, a layer thickness of 0.625 mm CT scan was performed from the knee to the ankle. The CT image was stored in a DICOM format file into the medical three-dimensional reconstruction software Mimics (version 19.0, Materialise, Leuven, Belgium). A three-dimensional model of the tibia was built on the basis of the gray value of the tissue and segmentation of the region. This model was incorporated into software Geomagic-Studio (version 12, Geomagic, NC State, United States) for a smoothing process to correct the three-dimensional model surface. The different parts of finite element model were imported into software Hypermesh (version 2017, Altair, Inc., United States), a meshing tool for finite element analysis, and meshed using quadratic tetrahedral elements Solid187. The tibia was considered isotropic linear elastic and homogeneous. Each model consisted of quadratic tetrahedron elements from 0.5 to 1.0 mm in size. A convergence test was performed on all models to ensure the maximum change was less than 1%. **Table 1** showed the material assignment. The Young's modulus and Poisson's ratio were obtained from the literature (Fan et al., 2008; Qiu et al., 2011; Anwar et al., 2017; Anwar et al., 2018; Huang et al., 2019). The three-dimensional model of the plate and screws was made according to the specifications of the manufacturer using computer-aided design software Creo Parametric (PTC, Inc., United States). All contact conditions between fracture fragments and the implant were defined as frictional contacts. We chose a friction coefficient of 0.4 (Rancourt et al., 1990; Viceconti et al., 2000). The tibia model was imported into software Geomagic Studio (3D system Inc., Rock Hill, SC, United States), and the fracture line was cut to develop the PL tibial plateau split fracture and the PL depression tibial plateau fracture (**Figure 6**). Internal fixations were assembled with fracture models to complete the internal fixation models of the PL tibial plateau fracture by using software Creo Parametric on the basis of the relative data. All contact Group A: A posterior buttress plate was used for the PL split fracture. Group B: A lateral locking compression plate was used for PL split fracture. Group C: The novel plate was used for the PL split fracture. Group D: A posterior buttress plate was used for the PL depression fracture. Group E: A lateral locking compression plate was used for the PL depression fracture. Group F: The novel plate was used for the PL depression fracture. **Table 2** shows the numbers of elements and nodes of the various models in the experiment. The inferior of the distal tibia was fixed in all degrees of freedom. The PL split/depression fragments were compressed using three different loadings (250, 500, and 750 N) with the loading direction parallel to the *Z*-axis of the tibial plateau. All models were analyzed by software ANSYS Mechanical APDL 19.0 (ANSYS, Inc., United States). The finite element analysis was performed simulating a static test for different fixation methods. Moreover, the finite element model was validated with the published data, and the procedure was explained in our previous study (Zhou et al., 2021).

We analyzed the vertical displacement of the PL fragments, the von Mises stress distribution, and the maximum von Mises stress of each internal fixation under axial loads.

2.5 Anatomic Study

Twelve fresh frozen knee specimens were used in this study. None of the knee joints had signs of previous injury, abnormality, or disease. The mean age of the donors was 61.3 years (range: 46–72 years).

Each lower limb was dissected using the anterolateral approach. The incision was made, starting 1 cm proximal to the knee joint line along the midline of the lateral side, toward Gerdy's tubercle, and then down to the lateral side of the tibial tuberosity. Thereafter, a fascial incision was made in the same way as the skin incision. The iliotibial band along the backside was retracted anteriorly and opened to separate the distal fiber bundles from Gerdy's tubercle. Furthermore, the iliotibial band was performed a sharp dissection along the upper edge of the fibular head. The coronary ligament of the meniscus was cut open to visualize the PL tibial plateau. With the knee flexed at 60°, the PL articular surface could be easily visualized by the internal rotation and varus of the tibia. And the plate position could be adjusted to match adequate and optimal anatomic structures through the superior fibular head space. Moreover, the PL tibial plateau was dissected carefully to show the adjacency of the novel plate to important anatomic structures (the popliteus tendon, the common peroneal nerve, lateral inferior genicular artery, and popliteal arteriovenous vessels).

3 RESULTS

3.1 Biomechanical Testing

3.1.1 Posterolateral Split Tibial Plateau Fractures

Table 3 showed the vertical displacement of the PL fragment under three different axial loads. There was a displacement hierarchy of

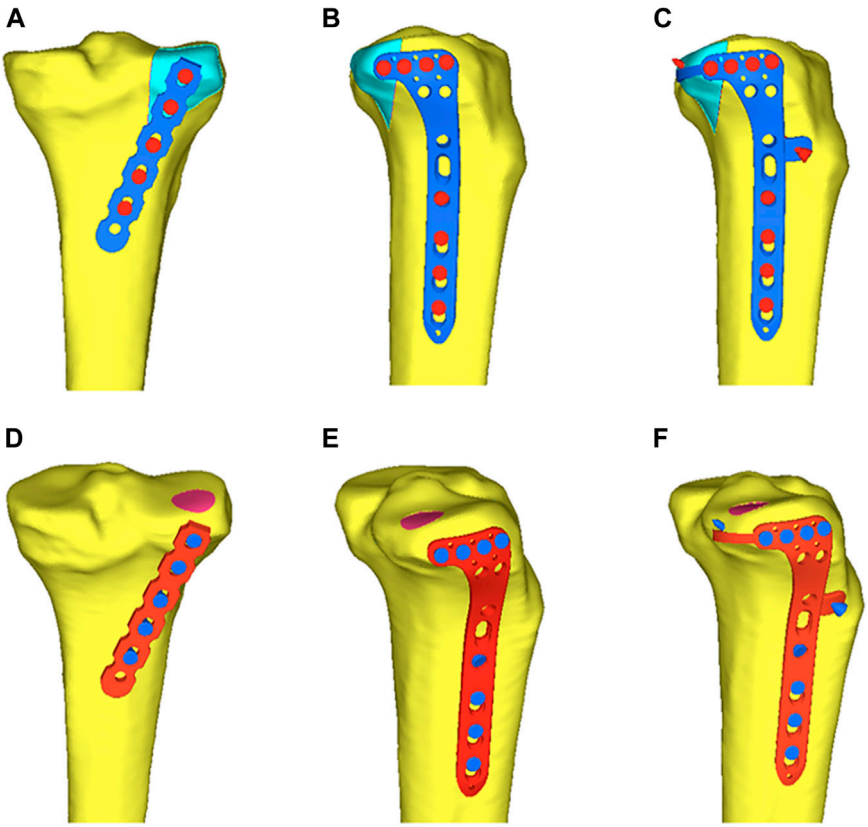

FIGURE 6 | Six different internal fixation after assembly of the finite element model. **(A)** Fixation of the posterior buttress plate in posterolateral (PL) split fracture. **(B)** Fixation of the lateral locking plate in PL split fracture. **(C)** Fixation of the novel plate in the PL split fracture. **(D)** Fixation of the posterior buttress plate in PL depression fracture. **(E)** Fixation of the lateral locking plate in PL depression fracture. **(F)** Fixation of the novel plate in PL depression fracture.

TABLE 2 | Number of nodes and elements for the six models.

Model	Nodes	Elements
Group A	912809	565108
Group B	902541	552457
Group C	945150	591667
Group D	913706	577132
Group E	913248	572768
Group F	945862	591718

TABLE 3 | Vertical displacement of the posterolateral split fracture at three different load levels, load to failure.

Groups	Vertical displacement (mm)			Load to failure (N)
	250 N	500 N	750 N	
A	1.21 ± 0.08	2.17 ± 0.16	3.47 ± 0.40	605.42 ± 34.04
B	1.47 ± 0.10	3.26 ± 0.22	4.85 ± 0.73	431.32 ± 33.01
C	0.96 ± 0.04	1.74 ± 0.08	2.66 ± 0.17	776.71 ± 12.74
P (A-B)[a]	0.001	0.001	0.004	0.001
P (B-C)[a]	0.001	0.001	0.001	0.001
P (C-A)[a]	0.001	0.001	0.001	0.001

[a]*Significant difference (Group A. The posterior buttress plate. Group B. The lateral tibia locking compression plate. Group C. The novel plate).*

the fragment at different load levels in PL split fracture: the novel plate (Group C) had the least displacement, followed by the posterior buttress plate (Group A), and the lateral locking plate (Group B) had the most displacement. The differences among the three groups were statistically significant ($p < 0.001$).

Table 3 showed the failure loads of each specimen. The failure load of Group C was the highest and was significantly higher than that of the other two implants ($p < 0.001$). And there was also a significant difference in the failure load between Groups A and B ($p < 0.001$). The posterior buttress plate (Group A) bore more load than the lateral locking plate (Group B). Failure load was 605.42 ± 34.04 N for the posterior buttress plate (Group A), 431.32 ± 33.01 N for the lateral locking plate (Group B), and 776.71 ± 12.74 N for the novel plate (Group C). This result showed that the novel plate had a better biomechanical advantage over the posterior buttress plate and lateral plate in terms of vertical displacement and failure load for PL split fracture.

3.1.2 Posterolateral Depression Tibial Plateau Fractures

Table 4 showed the vertical displacement of the depression fragment under three different axial loads. The vertical

TABLE 4 | Vertical displacement of the posterolateral depression fracture at three different load levels, load to failure.

Groups	Vertical displacement (mm)			Load to failure (N)
	250 N	500 N	750 N	
D	1.25 ± 0.08	2.13 ± 0.13	2.71 ± 0.14	846.30 ± 52.18
E	0.90 ± 0.09	1.45 ± 0.23	2.28 ± 0.21	1014.95 ± 70.87
F	0.87 ± 0.10	1.38 ± 0.14	2.11 ± 0.07	1034.79 ± 39.05
P (D-E)[a]	0.001	0.001	0.014	0.001
P (E-F)	0.588	0.399	0.236	0.677
P (F-D)[a]	0.001	0.001	0.003	0.006

[a]*Significant difference (Group D. The posterior buttress plate. Group E. The lateral tibia locking compression plate. Group F. The novel plate).*

displacements at 250, 500, and 750 N loads of the novel plate (Group F) and the lateral locking plate (Group E) were significantly smaller than those of the posterior buttress plate (Group D) ($p < 0.05$). Although there was no significantly difference between Groups F and E, there was a hierarchy of vertical displacement of the depression fragment: Group F had the least displacement, Group E had second, and Group D had the most displacement.

Table 4 showed the failure loads of each specimen. Groups E and F had higher failure load, which was significantly higher than that of Group D ($p < 0.05$). The failure load was 846.30 ± 52.18 N for the posterior buttress plate (Group D), 1014.95 ± 70.87 N for the lateral locking plate (Group E), and 1034.79 ± 39.05 N for the novel plate (Group F). The novel plate provided the same biomechanical stability as the lateral locking plate for PL depression tibial plateau fracture, and both were superior to the posterior buttress plate.

3.2 Finite Element Analysis

3.2.1 Posterolateral Split Tibial Plateau Fractures

When an axial load of 750 N was applied to three internal fixations, the maximum displacement in Groups A, B, and C were 0.99, 1.11, and 0.94 mm, respectively (**Figures 7G–I**). The displacement trends of the three different loads (250, 500, and 750 N) were consistent. Moreover, the displacements of the PL split fragment in each of the three groups gradually increased under loads from 250 to 750 N, and **Table 5** showed the displacements of the different loads.

The von Mises stress distribution of the posterior buttress plate (Group A) focused on the two proximal screws in contact with the fracture line and the local area of the plate between the plate and screw (**Figure 7A**). The von Mises stress distribution of the lateral locking plate (Group B) focused on the corner junction of the transverse and longitudinal arms, and the screw was located most posteriorly (**Figure 7B**). The von Mises stress distribution of the novel plate body (Group C) was similar to that of the lateral plate. Moreover, the contact point of the "hoop hook" and the anterior wing screw obtained the stress concentration point (**Figure 7C**). The concentration point of the "hoop hook" was relatively low, thus suggesting that no mechanical damage would be expected in the novel plate. When the load increased, the von Mises stress increased in all three internal fixations. The maximum von Mises stress of Groups A, B, and C were 383.76, 414.63, and 305.07 MPa under an axial load of 750 N, respectively. The von Mises stress distribution was consistent with the increase of the axial loads from 250 to 500 N, and **Table 6** showed the von Mises stress values of different loads. In addition, the maximum von Mises stress in bone of Groups A, B, and C were 76.70, 55.68, and 56.30 MPa under an axial load of 750 N, respectively (**Table 7**). The maximum von Mises stresses in bone by the novel plate and the lateral locking plate were decreased compared to the posterior buttress plate for PL split fracture.

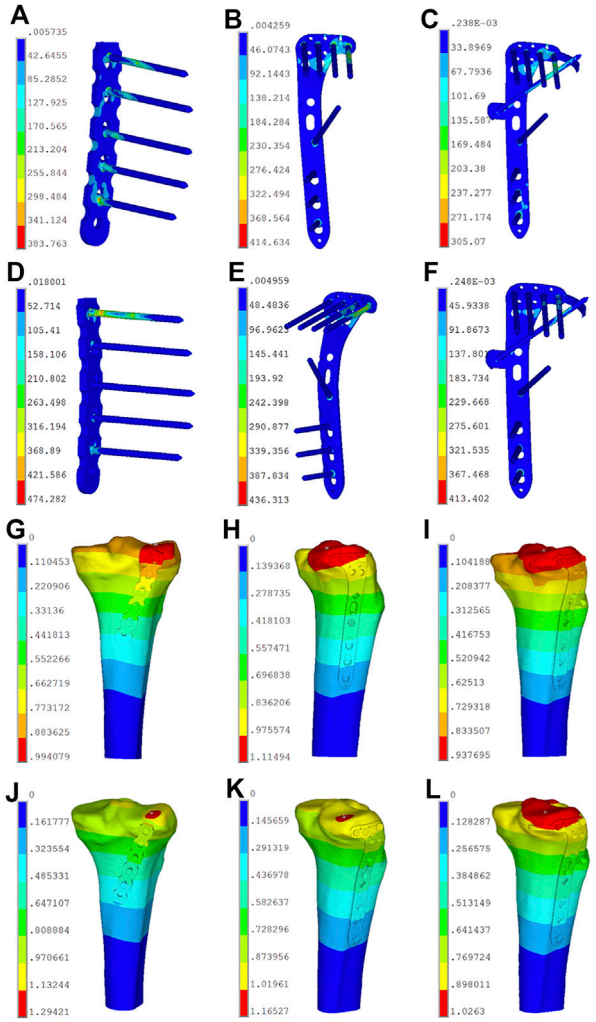

FIGURE 7 | Stress distribution diagram and displacement field of the six finite element models. **(A)** Stress distribution of model A in posterolateral (PL) split fracture. **(B)** Stress distribution of model B in PL split fracture. **(C)** Stress distribution of model C in PL split fracture. **(D)** Stress distribution of model D in PL depression fracture. **(E)** Stress distribution of model E in PL depression fracture. **(F)** Stress distribution of model F in PL depression fracture. **(G)** Displacement field of model A in posterolateral (PL) split fracture. **(H)** Displacement field of model B in PL split fracture. **(I)** Displacement field of model C in PL split fracture. **(J)** Displacement field of model D in PL depression fracture. **(K)** Displacement field of model E in PL depression fracture. **(L)** Displacement field of model F in PL depression fracture.

TABLE 5 | Maximum displacement of the finite element models of posterolateral tibial plateau fracture.

Group	Max displacement (mm)		
	250 N	500 N	750 N
A	0.33	0.66	0.99
B	0.37	0.74	1.11
C	0.31	0.63	0.94
D	0.43	0.86	1.29
E	0.39	0.78	1.17
F	0.34	0.68	1.03

TABLE 6 | Maximum von Mises stress of the finite element models of posterolateral tibial plateau fracture in internal fixation method.

Group	Max von Mises stress (MPa)		
	250 N	500 N	750 N
A	127.92	255.84	383.76
B	138.21	276.42	414.63
C	101.69	203.38	305.07
D	158.09	316.29	474.28
E	145.44	290.88	436.31
F	137.80	275.60	413.40

TABLE 7 | Maximum von Mises stress of the finite element models of posterolateral fracture in bone.

Group	Max von Mises stress (MPa)		
	250 N	500 N	750 N
A	25.57	51.14	76.70
B	18.56	37.12	55.68
C	18.77	37.53	56.30
D	47.97	95.94	143.92
E	24.24	48.49	72.73
F	22.43	44.86	67.29

3.2.2 Posterolateral Depression Tibial Plateau Fractures

When axial loads of 250, 500, and 750 N were applied to three internal fixations, the displacement of the depression fracture fragments with the same load in the novel plate (Group F) was smaller than in the lateral locking plate (Group E) and the posterior buttress plate (Group D). The displacement values in Groups D, E, and F were 1.29, 1.17, and 1.02 mm under an axial load of 750 N, respectively (**Figures 7J–L**). The vertical displacements of the PL depression fragment in each group gradually increased under loads from 250 to 750 N, and **Table 5** showed the displacement values of the different loads.

The von Mises stress distribution of the posterior buttress plate (Group D) mainly focused on the first proximal screw that is in contact with the fracture fragment and the local area of the plate between the plate and screw (**Figure 7D**). The von Mises stress distribution of the lateral locking plate (Group E) mainly focused on the corner junction of the transverse and longitudinal arms (**Figure 7E**). The von Mises stress distribution of the novel plate body (Group F) was also similar to that of the lateral locking plate (**Figure 7F**). However, the maximum von Mises stress of the corner junction of the novel plate body was smaller than that of the lateral locking plate. Moreover, the contact point of the "hoop hook" and the anterior wing screw also obtained the von Mises stress concentration point. The concentration point of the "hoop hook" was relatively low, suggesting that the risk of nail breakage would be low. When the load increased, the von Mises stress increased in all three internal fixation techniques. The maximum von Mises stress values of Groups D, E, and F were 474.28, 436.31, and 413.4 MPa under an axial load of 750 N, respectively. The von Mises stress was consistent with the increase of the axial loads from 250 to 500 N, and **Table 6** showed the maximum von Mises stress values of different loads. Moreover, the maximum von Mises stress in bone of Groups D, E, and F were 143.92, 72.73, and 67.29 MPa under an axial load of 750 N, respectively (**Table 7**). The maximum von Mises stress in bone by the novel plate was decreased compared to the posterior buttress plate and the lateral locking plate for PL depression fracture.

3.3 Anatomic Study

The "hoop hook" of the novel plate was easily fixed to the PL tibial plateau through the superior fibular head space. The common peroneal nerve was identified on the posterior border of the biceps femoris and coursed through the PL aspect of the knee. **Figure 8A** demonstrates that the "hoop hook" and the common peroneal nerve were not in the same plane, and the common peroneal nerve was less likely to be damaged. On the basis of measurement and observation, we found that the mean distance between the tip of the "hoop hook" and popliteal arteriovenous vessels was 10.3 mm (range: 6–15 mm); therefore, the risk of injury to popliteal arteriovenous vessels was considered very low (**Figure 8A**). We carefully dissected the lateral inferior genicular artery. We observed that the lateral inferior genicular artery originated from the popliteal artery, running deep to the lateral collateral ligament at the joint line (**Figure 8B**). Compared with the position of the novel plate, the position of the lateral inferior genicular artery was higher. The average distance from the novel plate to the lateral inferior genicular artery was 8.2 mm (range: 6–12 mm). Therefore, the risk of injury to the lateral inferior genicular artery was also considered low. Moreover, the average distance from the upper edge of the novel plate and the articular surface was 5.3 mm (range: 4–6.2 mm). Additionally, an anterior wing screw of appropriate length was less likely to damage the popliteus tendon (**Figures 8C, D**).

4 DISCUSSION

An increasing number of studies have shown that good long-term outcomes of tibial plateau fracture are associated with anatomic articular reduction and stable fixation (20). However, it is particularly difficult to achieve anatomic reduction and rigid internal fixation in complex tibial plateau fractures, particularly those involving the PL

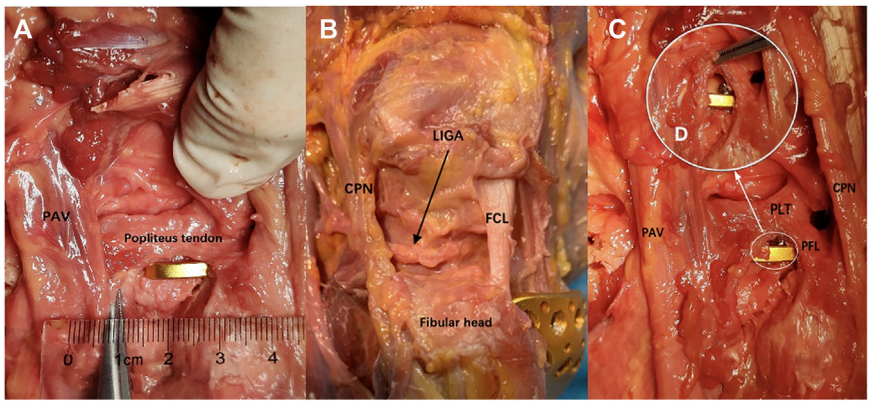

FIGURE 8 | Anatomical study and fixation feasible. **(A)** Measurement of the distance between the tip of the "hoop hook" and PAV. **(B)** The relationship between the novel plate and key structures. **(C)** The relationship between the novel plate and the anterior wing screw. **(D)** Local enlarged view (PLT, the popliteus tendon; PAV, the popliteal arteriovenous vessels; CPN, the common peroneal nerve; LAGA, the lateral inferior genicular artery; FCL, the fibular collateral ligament; PFL, the popliteofibular ligament).

column. The treatment of PTPFs has been one of current hotspots (Sun et al., 2018). Currently, there is no consensus about the optimal internal fixation selection for PTPFs treatment due to the complicated structures of the posterolateral corner of the knee including the fibular head, the fibular collateral ligament, the popliteus tendon, and the peroneal nerve, which impedes the exposure and fixation of the fracture fragments (Heidari et al., 2013; Giordano et al., 2020; Song et al., 2020). The PTPFs treatment was proposed by some experts to use a posterior buttress plate *via* various posterolateral approaches to expose the fracture fragment directly. (Lin et al., 2015) exposed the operation area, repaired the fracture under direct vision through a posterolateral inverted "L" shape approach, and fixed it with a posterior plate fixation. However, the anterior tibial artery perforates through the interosseous membrane is located approximately 4.6 cm below the joint line (Heidari et al., 2013), which means that the safe area for anatomy and the length of the plate is limited (Kfuri and Schatzker, 2018). Lobenhoffer introduced a fibular head osteotomy technique for the PTPFs treatment (Lobenhoffer et al., 1997). The fracture can be exposed fully and fixed with this approach, but it is inevitable to cause iatrogenic injuries on the posterolateral corner of the knee. On the other hand, many surgeons had successfully used lateral plate fixation to manage PTPFs *via* an extend anterolateral or anterolateral supra-fibular-head approach (Hu et al., 2016). Anterolateral operative approaches are relatively simple, and the risk of injury to the neighboring structures is low. Moreover, the lateral locking plate provided good support for depression fracture fragment (Jordan et al., 2016). Sun thought that lateral locking plate fixation was still one of the main trends for the treatment of PTPFs (Sun et al., 2018). However, compared with the posterior buttress plate, the lateral plate used in the PL split fracture fixation is still controversial owing to the weakness of the anti-shear effect (Zhang et al., 2012; Sun et al., 2018). So, there is a great need of PTPFs treatment concerning to low surgical risk, low iatrogenic injury, and rigid fixation.

Currently, studies on the treatment of PTPFs have mainly focused on surgical approaches, and operative fixation devices for the treatment of PTPFs have rarely been reported. The available types of internal fixation are relatively single and limited. In clinical practice, although the anterolateral approach is relatively simple and safe, with a short learning curve, failure cases with PTPFs treatment with the lateral plate fixation are often encountered (Wang et al., 2017). Thus, we designed a novel plate via the anterolateral approach, which could provide adequate support and rigid fixation. The novel plate has a "hoop hook," which is behind the transverse arm of the L-shaped plate, parallel to the articular surface. The "hoop hook" hugs the PL split fragment, which can resist the sliding and posterior displacement of the fracture fragment. And the novel plate has an anterior wing in front of the longitudinal arm of the L-shaped plate and the locking screw into the screw hole of the anterior wing can mount on the "hoop hook," thus combining the anterior wing screw and the "hoop hook" as a whole to fix the PL fragment. The "hoop hook" concept design is similar to the rim plate concept in recent years (Cho et al., 2016; Cho et al., 2017). Compared with the novel plate, the rim plate lacks a plate body that extends to the tibia shaft. Therefore, it is difficult for the rim plate to apply alone when the PL fragment is comminuted and depressed (Cho et al., 2016; Giordano et al., 2020). Meanwhile, the rim plate is usually obtained by pre-bending the distal radius plate, and a thicker plate increases the difficulty of pre-bending. When the depression fracture sometimes extends to the lateral column of tibial plateau, the rim plate is required to combine with other internal fixations, which means a longer operative time is required (Yi et al., 2020). The "hoop hook" of the novel plate is relatively thin, making adjustments relatively simple if necessary, and anatomical design of hook can match the morphological structure of most PL tibial plateau. The design

concept of the anterior wing screw on the novel plate is similar to that of the magic screw (Sun et al., 2017; Sun et al., 2018). An additional screw can be placed, and this screw does not interfere with plate fixations when fixing the PL fragment. The strength of the magic screw fixation with the proximal tibial cortex was weaker than that of the combination fixation of screw and plate. Sun (Sun et al., 2018) proposed that the PTPF fragment would easily lose the reduction following the traditional process by screwing because the fragment was relatively small and had no supporting point. Low support of the magic screw might cause further displacement of the PL fragment of fracture. Interestingly, when the novel plate was used to fix the PL split fragment, we found that the posterior "hoop hook" provided the support for the fragment while hugging the fracture, and the anterior wing screw was placed in a defined thread direction to avoid interference with the proximal screws. Therefore, the anterior wing screw was easier to insert into the PL split fragment. A previous study (Zhang et al., 2012) showed that posterior buttress plating could provide the stronger fixation than lateral locking plate for PL split fracture. According to our biomechanical test, the novel plate showed better biomechanical strength for the PL split fracture than the posterior buttress plate and lateral locking plate. And the result of finite element analysis also showed that there was the least displacement of PL fragment in the novel plate group, and had the similar tendency with the biomechanical testing. Meanwhile we analyzed the maximum von Mises stress and stress distributions through three-dimensional (3D) computational model of the finite element. The novel plate exhibited a significantly lower maximum von Mises stress than the posterior buttress plate and lateral locking plate, although the stress concentration point appeared at the contact point of the "hoop hook" and the anterior wing screw. From another perspective, the stress concentration point indicated the "hoop hook" and the anterior wing screw played a role of resistance in the displacement of the PL fragment. Moreover, the maximum von Mises stress of the stress concentration observed in the "hoop hook" was relatively low compared to the yield strength of 800 MPa in the plate material at 300% body-weight loading; this suggested that no failure risk of mechanics would be expected in the implants.

Compared with PL split fracture, the PL depression fracture, which occurs more frequently in PTPFs, has been conspicuously overlooked. According to previous studies (Giordano et al., 2020; Yi et al., 2020), posterior buttress plating fixation was unsuitable for the PL depression fracture, and our biomechanical test also proved it. Compared with posterior buttress plating, the novel plate and lateral locking plate provided stronger biomechanical supports. This suggested that the strength of the novel plate and locking plate might be more suitable for pure PL depression fractures. Clinically, PL depression fracture of tibial plateau with posterior wall breakage is very common and bone graft is often needed to support the depressed articular surface. If the posterior wall is broken, bone graft would shift to the back side and ineffective bone graft without support to the articular surface would occur. For that matter, the novel plate with hoop hook, which can resist posterior wall displacement, was better than lateral locking plate for posterolateral depression fracture with posterior wall breakage. Furthermore, according to the finite element analysis, the novel plate had balanced stress distribution. And the maximum von Mises stress on the novel plate was relatively lower than lateral locking plate, which meant the risk of the novel plate failure was lower compared with lateral locking plate.

The novel plate was inserted through the lateral incision into the knee joint. This surgery had the advantage of being a low-risk, relatively simple operation. Moreover, the anatomic study showed that the "hoop hook" could be inserted through the superior fibular head space and was enough space from important structures such as major blood vessels and nerves. Therefore, the novel plate had the low risk of iatrogenic injury to the important structures of the PL corner of knee joint. In general, the novel plate showed a good biomechanical property either for posterolateral split fracture or for posterolateral depression fracture, which would have great clinical application.

There are several limitations to this study. First, instead of using human cadaveric bone, which was an ideal test material, we used synthetic tibia in our study. However, synthetic bone provided several advantages over human cadaveric bone. The synthetic tibiae provided standard dimensions and properties between specimens, and the geometrical measurements of the models were obtained from the same mold to ensure the uniformity of the experimental specimens. Second, the biomechanical evaluation in our study was relatively simple; the factors influencing knee stress and stability, including ligaments, muscles, and other soft tissues was not involved in this experiment. Third, the morphology of the PL depression fracture in clinic consists of two typical types: pure depression fracture and depression fracture with posterior plateau rim breakage, with the latter being more common. However, the modeling of the depression fracture with posterior plateau rim breakage is hard to simulate and construct. The effectiveness of the novel plate for depression fracture with plateau rim breakage had not been verified. Further designs of fracture modeling would be required. In addition, the morphology of the PL fracture was various and diverse in clinic, with two typical models, pure split fracture and pure depression fracture, hard to simulate all fracture morphology in clinic. Finally, the biomechanical result of this study must be interpreted as strictly static biomechanical testing, representing only part of the scenario at work and the state of a single-leg stance. The clinical application of the novel plate for PL fracture needed to be further verified.

5 CONCLUSION

The current study showed the novel plate had a good biomechanical advantage for PL tibial plateau fracture. And the finite element analysis suggested the novel plate had balanced stress distribution and low risk of fixation failure. Moreover, the placement of the novel plate had a low risk of damage to the important anatomic structures of the knee posterolateral corner through anterolateral approach. The novel plate may be a great choice for the treatment of PTPFs.

DATA AVAILABILITY STATEMENT

The original contributions presented in the study are included in the article/Supplementary Material, further inquiries can be directed to the corresponding authors.

AUTHOR CONTRIBUTIONS

WX, HZ, WR, and WZ contributed to conception and design of the study. WR and WZ organized the database. WR performed the statistical analysis. WR wrote the first draft of the manuscript. WX, HZ, SJ, and JP wrote sections of the manuscript. All authors contributed to manuscript revision, read, and approved the submitted version.

FUNDING

This work was supported by the Natural Science Foundation of China (Nos. 81874008 and 81472105); the Soochow Program of Health Talent Training (No. GSWS2019010).

REFERENCES

Ali, A. M., El-Shafie, M., and Willett, K. M. (2002). Failure of FIxation of Tibial Plateau Fractures. *J. Orthop. Trauma* 16 (5), 323–329. doi:10.1097/00005131-200205000-00006

Anwar, A., Lv, D., Zhao, Z., Zhang, Z., Lu, M., Nazir, M. U., et al. (2017). Finite Element Analysis of the Three Different Posterior Malleolus Fixation Strategies in Relation to Different Fracture Sizes. *Injury* 48 (4), 825–832. doi:10.1016/j.injury.2017.02.012

Anwar, A., Zhang, Z., Lv, D., Lv, G., Zhao, Z., Wang, Y., et al. (2018). Biomechanical Efficacy of AP, PA Lag Screws and Posterior Plating for Fixation of Posterior Malleolar Fractures: A Three Dimensional Finite Element Study. *BMC Musculoskelet. Disord.* 19 (1), 73. doi:10.1186/s12891-018-1989-7

Berber, R., Lewis, C. P., Copas, D., Forward, D. P., and Moran, C. G. (2014). Postero-Medial Approach for Complex Tibial Plateau Injuries with a Postero-Medial or Postero-Lateral Shear Fragment. *Injury* 45 (4), 757–765. doi:10.1016/j.injury.2013.11.028

Chang, S.-M., Zheng, H.-P., Li, H.-F., Jia, Y.-W., Huang, Y.-G., Wang, X., et al. (2009). Treatment of Isolated Posterior Coronal Fracture of the Lateral Tibial Plateau through Posterolateral Approach for Direct Exposure and Buttress Plate Fixation. *Arch. Orthop. Trauma Surg.* 129 (7), 955–962. doi:10.1007/s00402-009-0829-5

Chen, H.-W., Liu, G.-D., Ou, S., Zhao, G.-S., Pan, J., and Wu, L.-J. (2014). Open Reduction and Internal Fixation of Posterolateral Tibial Plateau Fractures through Fibula Osteotomy-Free Posterolateral Approach. *J. Orthop. Trauma* 28 (9), 513–517. doi:10.1097/bot.0000000000000047

Cho, J.-W., Samal, P., Jeon, Y.-S., Oh, C.-W., and Oh, J.-K. (2016). Rim Plating of Posterolateral Fracture Fragments (PLFs) through a Modified Anterolateral Approach in Tibial Plateau Fractures. *J. Orthop. Trauma* 30 (11), e362–e368. doi:10.1097/bot.0000000000000638

Cho, J.-W., Kim, J., Cho, W.-T., Kim, J.-K., Samal, P., Gujjar, P. H., et al. (2017). Approaches and Fixation of the Posterolateral Fracture Fragment in Tibial Plateau Fractures: A Review with an Emphasis on Rim Plating via Modified Anterolateral Approach. *Int. Orthopaedics (Sicot)* 41 (9), 1887–1897. doi:10.1007/s00264-017-3563-6

Connolly, J. F. (2005). The Posterior Shearing Tibial Plateau Fracture: Treatment and Results via a Posterior Approach. *J. Orthop. Trauma* 19 (7), 508. doi:10.1097/01.bot.0000180355.53196.f1

Fan, Y., Xiu, K., Duan, H., and Zhang, M. (2008). Biomechanical and Histological Evaluation of the Application of Biodegradable Poly-L-Lactic Cushion to the Plate Internal Fixation for Bone Fracture Healing. *Clin. Biomech. (Bristol, Avon)* 23, S7–S16. doi:10.1016/j.clinbiomech.2008.01.005

Feng, J., Gu, Y., You, W., and Rui, G. (2021). A Posterolateral Sheared Fracture of the Tibial Plateau: A Case Presentation. *BMC Musculoskelet. Disord.* 22 (1), 488. doi:10.1186/s12891-021-04373-8

Gavaskar, A. S., Gopalan, H., Tummala, N. C., and Srinivasan, P. (2016). The Extended Posterolateral Approach for Split Depression Lateral Tibial Plateau Fractures Extending into the Posterior Column: 2 Years Follow up Results of a Prospective Study. *Injury* 47 (7), 1497–1500. doi:10.1016/j.injury.2016.04.021

Giordano, V., Pires, R. E., Pimenta, F. S., Campos, T. V. d. O., Andrade, M. A. P. d., and Giannoudis, P. V. (2020). Posterolateral Fractures of the Tibial Plateau Revisited: A Simplified Treatment Algorithm. *J. Knee Surg.* doi:10.1055/s-0040-1721026

He, X., Ye, P., Hu, Y., Huang, L., Zhang, F., Liu, G., et al. (2013). A Posterior Inverted L-Shaped Approach for the Treatment of Posterior Bicondylar Tibial Plateau Fractures. *Arch. Orthop. Trauma Surg.* 133 (1), 23–28. doi:10.1007/s00402-012-1632-2

Heidari, N., Lidder, S., Grechenig, W., Tesch, N. P., and Weinberg, A. M. (2013). The Risk of Injury to the Anterior Tibial Artery in the Posterolateral Approach to the Tibia Plateau: A Cadaver Study. *J. Orthop. Trauma* 27 (4), 221–225. doi:10.1097/BOT.0b013e318271f8f0

Higgins, T. F., Kemper, D., and Klatt, J. (2009). Incidence and Morphology of the Posteromedial Fragment in Bicondylar Tibial Plateau Fractures. *J. Orthop. Trauma* 23 (1), 45–51. doi:10.1097/BOT.0b013e31818f8dc1

Hoekstra, H., Rosseels, W., Luo, C.-F., and Nijs, S. (2015). A Combined Posterior Reversed L-Shaped and Anterolateral Approach for Two Column Tibial Plateau Fractures in Caucasians: A Technical Note. *Injury* 46 (12), 2516–2519. doi:10.1016/j.injury.2015.10.014

Hoekstra, H., Kempenaers, K., and Nijs, S. (2017). A Revised 3-Column Classification Approach for the Surgical Planning of Extended Lateral Tibial Plateau Fractures. *Eur. J. Trauma Emerg. Surg.* 43 (5), 637–643. doi:10.1007/s00068-016-0696-z

Hu, S.-J., Chang, S.-M., Zhang, Y.-Q., Ma, Z., Du, S.-C., and Zhang, K. (2016). The Anterolateral Supra-Fibular-Head Approach for Plating Posterolateral Tibial Plateau Fractures: A Novel Surgical Technique. *Injury* 47 (2), 502–507. doi:10.1016/j.injury.2015.11.010

Hu, S., Chen, S., Chang, S., Xiong, W., and Tuladhar, R. (2020). Treatment of Isolated Posterolateral Tibial Plateau Fracture with a Horizontal Belt Plate through the Anterolateral Supra-Fibular-Head Approach. *Biomed. Res. Int.* 2020, 4186712. doi:10.1155/2020/4186712

Huang, S., Ji, T., and Guo, W. (2019). Biomechanical Comparison of a 3D-Printed Sacrum Prosthesis versus Rod-Screw Systems for Reconstruction after Total Sacrectomy: A Finite Element Analysis. *Clin. Biomech.* 70, 203–208. doi:10.1016/j.clinbiomech.2019.10.019

Jordan, M. C., Zimmermann, C., Gho, S. A., Frey, S. P., Blunk, T., Meffert, R. H., et al. (2016). Biomechanical Analysis of Different Osteosyntheses and the Combination with Bone Substitute in Tibial Head Depression Fractures. *BMC Musculoskelet. Disord.* 17, 287. doi:10.1186/s12891-016-1118-4

Kfuri, M., and Schatzker, J. (2018). Revisiting the Schatzker Classification of Tibial Plateau Fractures. *Injury* 49 (12), 2252–2263. doi:10.1016/j.injury.2018.11.010

LaPrade, R. F., Ly, T. V., Wentorf, F. A., and Engebretsen, L. (2003). The Posterolateral Attachments of the Knee: a Qualitative and Quantitative Morphologic Analysis of the Fibular Collateral Ligament, Popliteus Tendon, Popliteofibular Ligament, and Lateral Gastrocnemius Tendon. *Am. J. Sports Med.* 31 (6), 854–860. doi:10.1177/03635465030310062101

Lin, K.-C., Tarng, Y.-W., Lin, G.-Y., Yang, S.-W., Hsu, C.-J., and Renn, J.-H. (2015). Prone and Direct Posterior Approach for Management of Posterior Column Tibial Plateau Fractures. *Orthopaedics Traumatol. Surg. Res.* 101 (4), 477–482. doi:10.1016/j.otsr.2014.12.021

Liu, G. Y., Xiao, B. P., Luo, C. F., Zhuang, Y. Q., Xu, R.-M., and Ma, W.-H. (2016). Results of a Modified Posterolateral Approach for the Isolated Posterolateral Tibial Plateau Fracture. *Indian J. Orthop.* 50 (2), 117–122. doi:10.4103/0019-5413.177578

Lobenhoffer, P., Gerich, T., Bertram, T., Lattermann, C., Pohlemann, T., and Tscherne, H. (1997). Particular Posteromedial and Posterolateral Approaches for the Treatment of Tibial Head Fractures. *Unfallchirurg* 100 (12), 957–967. doi:10.1007/s001130050218

Luo, C.-F., Sun, H., Zhang, B., and Zeng, B.-F. (2010). Three-Column Fixation for Complex Tibial Plateau Fractures. *J. Orthop. Trauma* 24 (11), 683–692. doi:10.1097/BOT.0b013e3181d436f3

Qiu, T.-X., Teo, E.-C., Yan, Y.-B., and Lei, W. (2011). Finite Element Modeling of a 3D Coupled Foot-Boot Model. *Med. Eng. Phys.* 33 (10), 1228–1233. doi:10.1016/j.medengphy.2011.05.012

Rancourt, D., Shirazi-Adl, A., Drouin, G., and Paiement, G. (1990). Friction Properties of the Interface between Porous-Surfaced Metals and Tibial Cancellous Bone. *J. Biomed. Mater. Res.* 24 (11), 1503–1519. doi:10.1002/jbm.820241107

Sassoon, A. A., Torchia, M. E., Cross, W. W., Cass, J. R., and Sems, S. A. (2014). Fibular Shaft Allograft Support of Posterior Joint Depression in Tibial Plateau Fractures. *J. Orthop. Trauma* 28 (7), e169–e175. doi:10.1097/bot.0000000000000020

Schatzker, J., Castiglia, M., Giordano, V., Fogagnolo, F., Stannard, J., and Kfuri, M. (2017). Extended Anterolateral Approach for Complex Lateral Tibial Plateau Fractures. *J. Knee Surg.* 30 (3), 204–211. doi:10.1055/s-0037-1598077

Sohn, H.-S., Yoon, Y.-C., Cho, J.-W., Cho, W.-T., Oh, C.-W., and Oh, J.-K. (2015). Incidence and Fracture Morphology of Posterolateral Fragments in Lateral and Bicondylar Tibial Plateau Fractures. *J. Orthop. Trauma* 29 (2), 91–97. doi:10.1097/bot.0000000000000170

Solomon, L. B., Stevenson, A. W., Baird, R. P. V., and Pohl, A. P. (2010). Posterolateral Transfibular Approach to Tibial Plateau Fractures: Technique, Results, and Rationale. *J. Orthop. Trauma* 24 (8), 505–514. doi:10.1097/BOT.0b013e3181ccba4b

Solomon, L. B., Stevenson, A. W., Lee, Y. C., Baird, R. P. V., and Howie, D. W. (2013). Posterolateral and Anterolateral Approaches to Unicondylar Posterolateral Tibial Plateau Fractures: a Comparative Study. *Injury* 44 (11), 1561–1568. doi:10.1016/j.injury.2013.04.024

Song, Y., Xiong, Y., Yao, J., Wang, H., Tan, L., Hu, X., et al. (2020). Applied Anatomy and Three-Dimensional Visualization of the Tendon-Bone Junctions of the Knee Joint Posterolateral Complex. *Ann. Anat. - Anatomischer Anzeiger* 229, 151413. doi:10.1016/j.aanat.2019.151413

Sun, H., Luo, C.-F., Shi, H.-P., Yang, G., Zhong, B., Zhang, C.-Q., et al. (2014). Morphological Measurements of the Posterior Surface of the normal Proximal Tibia in a Healthy Chinese Population. *Knee* 21 (2), 567–572. doi:10.1016/j.knee.2012.10.025

Sun, H., Zhu, Y., He, Q.-F., Shu, L.-Y., Zhang, W., and Chai, Y.-M. (2017). Reinforcement Strategy for Lateral Rafting Plate Fixation in Posterolateral Column Fractures of the Tibial Plateau: The Magic Screw Technique. *Injury* 48 (12), 2814–2826. doi:10.1016/j.injury.2017.10.033

Sun, H., He, Q.-F., Zhang, B.-B., Zhu, Y., Zhang, W., and Chai, Y.-M. (2018). A Biomechanical Evaluation of Different Fixation Strategies for Posterolateral Fragments in Tibial Plateau Fractures and Introduction of the 'Magic Screw'. *Knee* 25 (3), 417–426. doi:10.1016/j.knee.2018.03.015

Taylor, W. R., Heller, M. O., Bergmann, G., and Duda, G. N. (2004). Tibio-Femoral Loading during Human Gait and Stair Climbing. *J. Orthop. Res.* 22 (3), 625–632. doi:10.1016/j.orthres.2003.09.003

Viceconti, M., Muccini, R., Bernakiewicz, M., Baleani, M., and Cristofolini, L. (2000). Large-Sliding Contact Elements Accurately Predict Levels of Bone-Implant Micromotion Relevant to Osseointegration. *J. Biomech.* 33 (12), 1611–1618. doi:10.1016/s0021-9290(00)00140-8

Wang, Y., Hu, C., Sun, H., Zhan, Y., and Luo, C. (2017). An Innovative Intra-Articular Osteotomy in the Treatment of Posterolateral Tibial Plateau Fracture Malunion. *J. Knee Surg.* 30 (4), 329–335. doi:10.1055/s-0036-1584922

Welch, R. D., Zhang, H., and Bronson, D. G. (2003). Experimental Tibial Plateau Fractures Augmented with Calcium Phosphate Cement or Autologous Bone Graft. *The J. Bone Jt. Surgery-American Volume* 85 (2), 222–231. doi:10.2106/00004623-200302000-00007

Xiang, G., Zhi-Jun, P., Qiang, Z., and Hang, L. (2013). Morphological Characteristics of Posterolateral Articular Fragments in Tibial Plateau Fractures. *Orthopedics* 36 (10), e1256–1261. doi:10.3928/01477447-20130920-16

Xie, X., Zhan, Y., Wang, Y., Lucas, J. F., Zhang, Y., and Luo, C. (2020). Comparative Analysis of Mechanism-Associated 3-Dimensional Tibial Plateau Fracture Patterns. *J. Bone Jt. Surg.* 102 (5), 410–418. doi:10.2106/jbjs.19.00485

Yi, Z., Hui, S., Binbin, Z., Jianfei, T., Huipeng, S., Jiong, M., et al. (2020). A New Strategy to Fix Posterolateral Depression in Tibial Plateau Fractures: Introduction of a New Modified Frosch Approach and a "Barrel Hoop Plate" Technique. *Injury* 51 (3), 723–734. doi:10.1016/j.injury.2020.01.023

Yu, G.-R., Xia, J., Zhou, J.-Q., and Yang, Y.-F. (2012). Low-Energy Fracture of Posterolateral Tibial Plateau: Treatment by a Posterolateral Prone Approach. *J. Trauma Acute Care Surg.* 72 (5), 1416–1423. doi:10.1097/TA.0b013e318248e7e5

Zhang, W., Luo, C.-F., Putnis, S., Sun, H., Zeng, Z.-M., and Zeng, B.-F. (2012). Biomechanical Analysis of Four Different Fixations for the Posterolateral Shearing Tibial Plateau Fracture. *The Knee* 19 (2), 94–98. doi:10.1016/j.knee.2011.02.004

Zhang, P., Lian, K., Luo, D., Huang, Z., Li, T., and Lin, D. (2016). A Combined Approach for the Treatment of Lateral and Posterolateral Tibial Plateau Fractures. *Injury* 47 (10), 2326–2330. doi:10.1016/j.injury.2016.07.004

Zhang, B.-B., Hu, H., Zhan, S., Mei, J., Zhu, Y., and Luo, C.-F. (2020). Biomechanical Analysis of "Barrel Hoop Plate" Technique for the Posterolateral Fragments of Tibial Plateau Fractures with Different Displacement Tendency. *Injury* 51 (11), 2465–2473. doi:10.1016/j.injury.2020.07.059

Zhao, D., Banks, S. A., Mitchell, K. H., D'Lima, D. D., Colwell, C. W., and Fregly, B. J. (2007). Correlation between the Knee Adduction Torque and Medial Contact Force for a Variety of Gait Patterns. *J. Orthop. Res.* 25 (6), 789–797. doi:10.1002/jor.20379

Zhou, J. H., Rui, Y. L., Zhang, W. X., and Zhang, W. (2021). Analysis on Biomechanical Properties of Anterior Ligament Reinforcement Combined with Screw Fixation for Inferior Tibiofibular Instability. *J. Med. Biomech.* 36, 48–54. [In Chinese, English Abstract]. doi:10.16156/j.1004-7220.2021.01.008

Conflict of Interest: The authors declare that the research was conducted in the absence of any commercial or financial relationships that could be construed as a potential conflict of interest.

Publisher's Note: All claims expressed in this article are solely those of the authors and do not necessarily represent those of their affiliated organizations, or those of the publisher, the editors, and the reviewers. Any product that may be evaluated in this article, or claim that may be made by its manufacturer, is not guaranteed or endorsed by the publisher.

frontiers in Bioengineering and Biotechnology

ORIGINAL RESEARCH
published: 09 March 2022
doi: 10.3389/fbioe.2022.791554

Biomechanical Analysis of a Novel Double-Point Fixation Method for Displaced Intra-Articular Calcaneal Fractures

Miko Lin Lv[1†], Ming Ni[2†], Wanju Sun[2], Duo Wai-Chi Wong[3], Shuren Zhou[4], Yongwei Jia[5] and Ming Zhang[3]*

[1]School of Medical Instrument and Food Engineering, University of Shanghai for Science and Technology, Shanghai, China, [2]Department of Orthopedics, Pudong New Area People's Hospital Affiliated to Shanghai Jiaotong University, Shanghai, China, [3]Department of Biomedical Engineering, Faculty of Engineering, The Hong Kong Polytechnic University, Kowloon, Hong Kong SAR, China, [4]School of Computer and Communication Engineering, Changsha University of Science and Technology, Changsha, China, [5]Department of Spine Surgery, Guanghua Hospital, Shanghai University of Traditional Chinese Medicine, Shanghai, China

OPEN ACCESS

Edited by:
Lizhen Wang,
Beihang University, China

Reviewed by:
Elisabetta M. Zanetti,
University of Perugia, Italy
Qiang Chen,
Southeast University, China

***Correspondence:**
Yongwei Jia
spinejia@163.com

[†]*These authors share first authorship*

Specialty section:
This article was submitted to Biomechanics, a section of the journal Frontiers in Bioengineering and Biotechnology

Received: *08 October 2021*
Accepted: *04 January 2022*
Published: *09 March 2022*

Citation:
Lv ML, Ni M, Sun W, Wong DW-C Zhou S, Jia Y and Zhang M (2022) Biomechanical Analysis of a Novel Double-Point Fixation Method for Displaced Intra-Articular Calcaneal Fractures. Front. Bioeng. Biotechnol. 10:791554. doi: 10.3389/fbioe.2022.791554

The development of minimally invasive procedures and implant materials has improved the fixation strength of implants and is less traumatic in surgery. The purpose of this study was to propose a novel "double-point fixation" for calcaneal fractures and compare its biomechanical stability with the traditional "three-point fixation." A three-dimensional finite element foot model with a Sanders type IIIAB calcaneal fracture was developed based on clinical images comprising bones, plantar fascia, ligaments, and encapsulated soft tissue. Double-point and three-point fixation resembled the surgical procedure with a volar distal radius plate and calcaneal locking plate, respectively. The stress distribution, fracture displacement, and change of the Böhler angle and Gissane's angle were estimated by a walking simulation using the model, and the predictions between the double-point and three-point fixation were compared at heel-strike, midstance, and push-off instants. Double-point fixation demonstrated lower bone stress (103.3 *vs.* 199.4 MPa), but higher implant stress (1,084.0 *vs.* 577.9 MPa). The model displacement of double-point fixation was higher than that of three-point fixation (3.68 *vs.* 2.53 mm). The displacement of the posterior joint facet (0.127 *vs.* 0.150 mm) and the changes of the Böhler angle (0.9° *vs.* 1.4°) and Gissane's angle (0.7° *vs.* 0.9°) in double-point fixation were comparably lower. Double-point fixation by volar distal radius plates demonstrated sufficient and favorable fixation stability and a lower risk of postoperative stress fracture, which may potentially serve as a new fixation modality for the treatment of displaced intra-articular calcaneal fractures.

Keywords: internal fixation, volar distal radial plate, calcaneal locking plate, finite element method, displaced intra-articular calcaneal fracture

INTRODUCTION

Displaced intra-articular calcaneal fractures (DIACFs) are highly disabling injuries usually caused by high-energy trauma (e.g., fall from height) and represent treatment challenges to orthopedic surgeons (Dhillon and Prabhakar, 2017). Recovery after treatment is often prolonged, with poorer functional results compared with other orthopedic conditions (van Tetering and Buckley, 2004). Thus, restoration to preinjury level of functioning is unlikely (Ibrahim et al., 2007). Conservative interventions were once recommended and demonstrated to provide comparable outcomes with operative treatments (Ibrahim et al., 2007). However, several studies have shown that nonoperative interventions often lead to delays in the reconstruction of deformed fractures, leaving patients with painful, stiff feet and permanent disability (Bruce and Sutherland, 2013). Since the mid-1990s, surgical treatment using open reduction and internal fixation (ORIF) was advocated and became the standard treatment for DIACFs, producing anatomical reduction and satisfactory functional outcomes (Sanders, 2000).

ORIF aims to achieve reliable stability by securing three-point fixation (TPF) (**Figure 1A**), i.e., the anterior process, posterior subtalar joint, and calcaneal tuberosity, at the cost of a large incision (Chen et al., 2017). The calcaneal locking plate has been widely adopted in ORIF since it can provide sufficient fixation, as well as a relatively lower risk to the devascularization of fragments (Mostafa et al., 2010). However, ORIF results in a high complication rate of approximately 30% and predisposes patients to serious comorbidities (Shah and Parmar, 2020). Therefore, there is growing interest in developing alternative methods with smaller incisions to minimize soft tissue trauma and resulting complications. Minimally invasive fixation (MIF), which compromises adequate visualization, has emerged and is used increasingly. Shah and Parmar (2020) evaluated MIF *via* the sinus tarsi approach using locking recon plates, demonstrating that MIF led to satisfactory clinical outcomes and a reduced rate of soft tissue-related complications. In addition, Ene et al. (2013) documented the outcome of MIF using the Essex-Lopresti osteosynthesis technique with no reported cases of postoperative wound infection or skin necrosis. In a recent report, the biomechanical characteristics of MIF and ORIF were found to have similar stability performance (Zhang et al., 2020).

MIF could also be achieved by the so-called double-point fixation (DPF) (**Figure 1B**), i.e., the posterior subtalar joint and calcaneal tuberosity. Simon et al. (2015) proposed a locking nail for the treatment of displaced articular fractures through fixed posterior subtalar joint and calcaneal tuberosity. Biomechanical and clinical studies have shown that DPF can reposition the subtalar joint well and satisfy the clinical results (Goldzak et al., 2014). We believe that DPF can also be facilitated by the volar distal radius plate. The slight thickness (1.5 mm) of the plate is advantageous in reducing the risk of soft tissue irritation and infection. The length of the plate is similar to that of the calcaneal tuberosity, and the curved T-shaped design facilitates fixation for the subtalar joint and calcaneal tuberosity. The short limb can fix the posterior subtalar joint with five locking screws, and the long limb can fix the calcaneal tuberosity with three screws. As a proof of concept, it is necessary to know whether the DPF can substantiate sufficient fixation strength for DIACF and not induce exceeding stress.

To this end, the objective of this study was to evaluate the biomechanical performance (in terms of stress distribution, fracture displacements, Böhler angle, and Gissane's angle) of DPF and compare it to that of TPF. We hypothesized that the biomechanical stability of DPF was comparable to that of TPF and thus satisfied the biomechanical demands for secure fixation and could facilitate early weight-bearing rehabilitation. Given a proper model geometry and a set of material properties and boundary conditions, finite element (FE) analysis can provide valuable biomechanical information on the internal environment of the model parts under a preset simulated scenario (Zanetti and Bignardi, 2013; Galbusera et al., 2014; Pascoletti et al., 2018; Scarton et al., 2018; Ün and Çalık, 2019). The evaluation was carried out using FE analysis, which provides a multifunctional platform to evaluate the internal biomechanical environment of the human body and has been widely used to evaluate surgical outcomes, the pathomechanics of surgical complications, and implant design (Wang et al., 2016). In addition, the FE model also facilitates

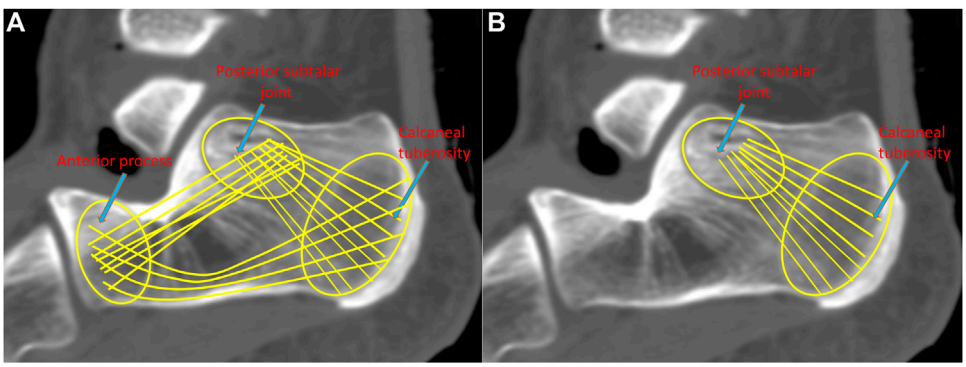

FIGURE 1 | Demonstration of the three-point fixation (TPF) **(A)** and the double-point fixation (DPF) **(B)** mechanisms.

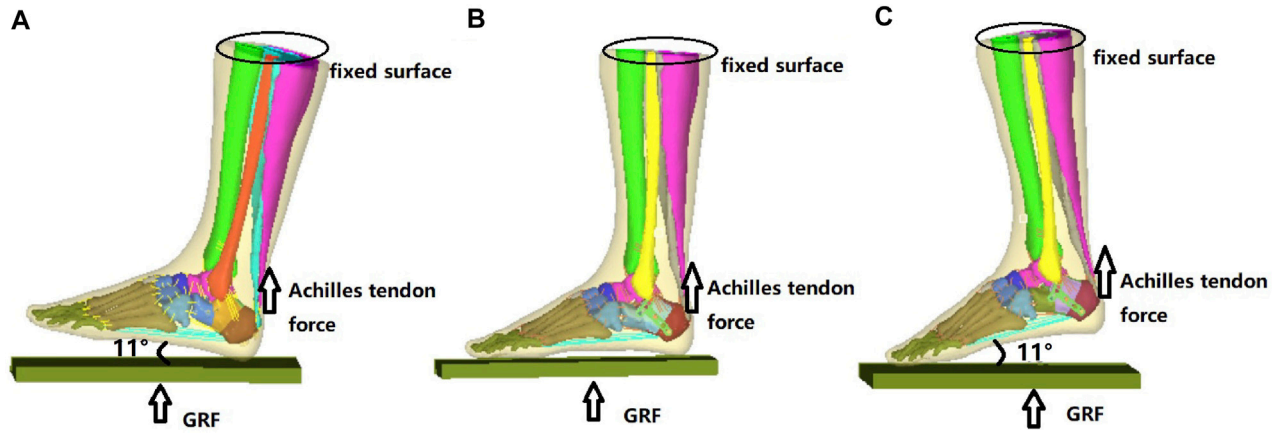

FIGURE 2 | Reconstructed model of the foot-and-ankle complex. **(A)** Reconstructed model geometry. **(B)** Finite element (FE) model after mesh creation. **(C)** Enlarged model view of the double-point fixation (DPF). **(D)** Enlarged model view of the three-point fixation (TPF) (1, anterior process; 2, lateral part of posterior subtar joint; 3, middle part of posterior subtalar joint; 4, sustentaculum tali; 5, calcaneal tuberosity; *x*, medial; *y*, anterior; *z*, superior; GRF, ground reactiono force).

wider investigations of foot deformity, trauma, and rehabilitation (Wang et al., 2016).

MATERIALS AND METHODS

Model Reconstruction

This study was approved by the Ethical Committee of the hospital (no. 2019-16). A 63-year-old female health participant (height, 161 cm; body weight, 64 kg) was recruited as the model participant. Computed tomography (CT) and magnetic resonance imaging (MRI) were performed on the left foot and ankle of the model participant using slice intervals of 1 and 1.25 mm, respectively. The images were integrated and segmented in medical imaging processing software (Mimics 15.0, Materialise, Leuven, Belgium) and reverse engineering software (Geomagic 2015, 3D Systems, Rock Hill, United States), through which the geometry of the foot model was reconstructed.

As shown in **Figure 2A**, the reconstructed model geometry consisted of 26 bones (tibia, fibula, talus, calcaneus, navicular, cuboid, 3 cuneiforms, 5 metatarsals, and 14 proximal and distal phalanges), in addition to the triceps surae (gastrocnemius and soleus), ligament, plantar fascia, and encapsulated soft tissues. A Sanders type IIIAB fracture resembled the reconstructed foot and ankle model by creating fracture gaps of 0.1 mm (Goldzak et al., 2012), which separated the calcaneus into five sections: the anterior process fragment, the sustentacular fragment, the middle and lateral fragments of the posterior subtalar joint, and the tuberosity fragment, as shown in **Figure 2B**.

Two model conditions were created in response to the two surgical conditions. The geometry of the two implants (volar distal radial plate and calcaneal locking plate) was constructed according to the manufacturers' specifications (Depuy Synthes, Raynham, PA, United States) using SolidWorks computer-aided design software (Dassault Systèmes, Vélizy-Villacoublay, France). For DPF, the volar plate was fixed on the posterior joint fragment and calcaneal tuberosity with five 2.4-mm locking screws (S1–S5) and three 2.7-mm locking screws (S6–S8), respectively, as shown in **Figure 2C**. For TPF, the calcaneal plate was fixed onto the anterior fragment (S1–S4), the subtalar joint (S5–S8), and the calcaneal tuberosity (S9–S12) by 3.5-mm locking screws, as shown in **Figure 2D**.

Mesh Creation

The model geometry was exported to Hypermesh 13.0 (Altair, Troy, MI, United States) for mesh creation. Both the plantar fascia and ligament were meshed as two-node truss units, while other parts of the lower limb were assigned four-node three-dimensional distributional stress tetrahedron units (C3D4). For ground, we meshed it with an 8-node reduced integrated hexahedral element (C3D8R).

The FE model of the intact foot comprised 80,311 nodes, 455,104 elements, and 137 truss units. The DPF model comprised 157,672 nodes, 762,929 elements, and 137 truss units, while the TPF model comprised 161,137 nodes, 773,437 elements, and 137 truss units.

Material Properties

As shown in **Table 1**, the material properties were idealized as homogeneous, isotropic, and linearly elastic for the bone, plantar fascia, and ligaments, according to the data from a relevant review (Morales-Orcajo et al., 2016). The hyperelastic material of the encapsulated soft tissue (Morales-Orcajo et al., 2016) and muscle bulk tissue of the gastrocnemius–soleus (Reeves et al., 2005; Yamamura et al., 2014) was specified using a second-order polynomial strain energy potential equation. The plates and screws were assigned a titanium alloy material. None of the bones, soft tissues, or the implant components were pre-strained.

Boundary and Loading Conditions

Three gait instants (i.e., heel strike, midstance, and push-off) were simulated in the FE model. As shown in **Figure 3**, the superior surface of the shank was fixed proximally. Vertical ground

TABLE 1 | Material properties used in the finite element model.

Parts	Young's modulus, *E* (MPa)	Poisson's ratio, *v*	Density (kg/m^3)	Cross-sectional area (mm^2)
Bone	7,300	0.3	1,500	–
Plantar fascia	350	–	937	58.6
Ligament	260	–	937	18.4
Titanium	110,000	0.3	4,540	–
Ground	17,000	0.1	5,000	–
Outer encapsulated soft tissue	Hyperelastic material property with second-order polynomial strain energy potential equation coefficients C_{10} = 0.08556 N mm^{-2}, C_{01} = –0.05841 N mm^{-2}, C_{20} = 0.039 N mm^{-2}, C_{11} = –0.02319 N mm^{-2}, C_{02} = 0.00851 N mm^{-2}, D_1 = 3.65273 mm^2 N^{-1}			
Muscle tissue (gastrocnemius, soleus, and Achilles tendon)	C_{10} = 8.57000 N mm^{-2}, C_{01} = 12.1000 N mm^{-2}, C_{20} = 936.000 N mm^{-2}, C_{11} = 718.000 N mm^{-2}, C_{02} = 480.000 N mm^{-2}, D_1 = 0.00413 mm^2 N^{-1}			

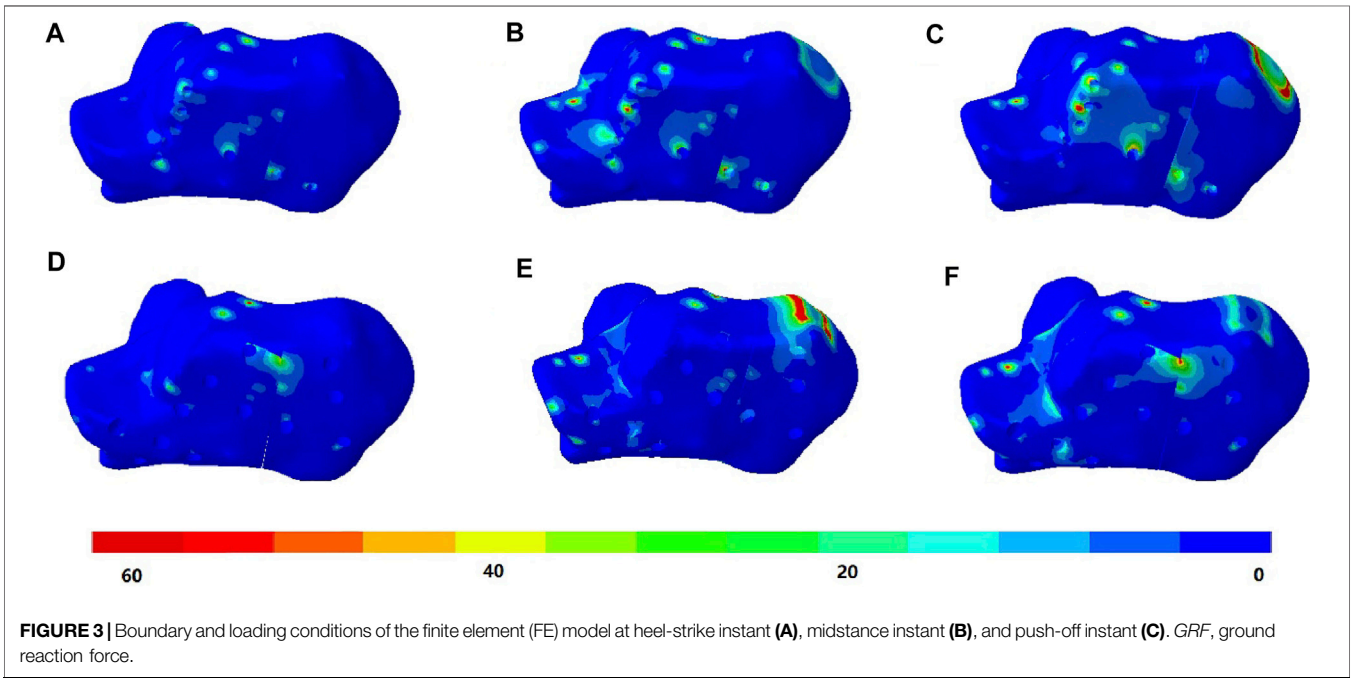

FIGURE 3 | Boundary and loading conditions of the finite element (FE) model at heel-strike instant **(A)**, midstance instant **(B)**, and push-off instant **(C)**. *GRF*, ground reaction force.

reaction forces (GRFs) were applied on the ground plate, which were 704, 608, and 736 N for the three walking stance instants, respectively (Chen et al., 2015; Yu et al., 2016). The magnitude of GRFs corresponded to 110%, 95%, and 115% of body weight. The Achilles tendons were 480, 550, and 1,100 N for the three walking stance instants, respectively (Gefen et al., 2000; Fröberg et al., 2009; Arnold et al., 2010) and were applied at the insertion point of the triceps surae at the calcaneus. The coefficients of friction between the contact pairs ground-to-encapsulated soft tissue, bone fragment-to-screws, and bone fragment-to-bone fragment were 0.6, 0.3, and 0.3, respectively (Dai et al., 2006; Bulaqi et al., 2015). The screws were tied to the plate, and there was no interaction between the bone and the plate. The FE simulation was performed in the commercial FE software package Abaqus (Dassault Systèmes, Vélizy-Villacoublay, France).

Outcome Measures

The primary outcome included the maximum von Mises stress of the calcaneus and implants, in addition to the joint facet displacement, the Böhler angle, and Gissane's angle in three time instants. High stress of the calcaneus and implants implicated the risk of bone breakdown and implant failure, respectively, while the facet displacement and angle measures manifested fracture site stability and the risk of nonunion or malunion.

To measure Böhler's angle, one line was drawn from the highest point of the tuberosity to the highest point of the posterior facet. Another line was drawn from the highest point of the anterior process to the highest point of the posterior facet of the calcaneus. Böhler's angle was measured by the angulation of these two lines. Gissane's angle was measured by the angulation between a line along

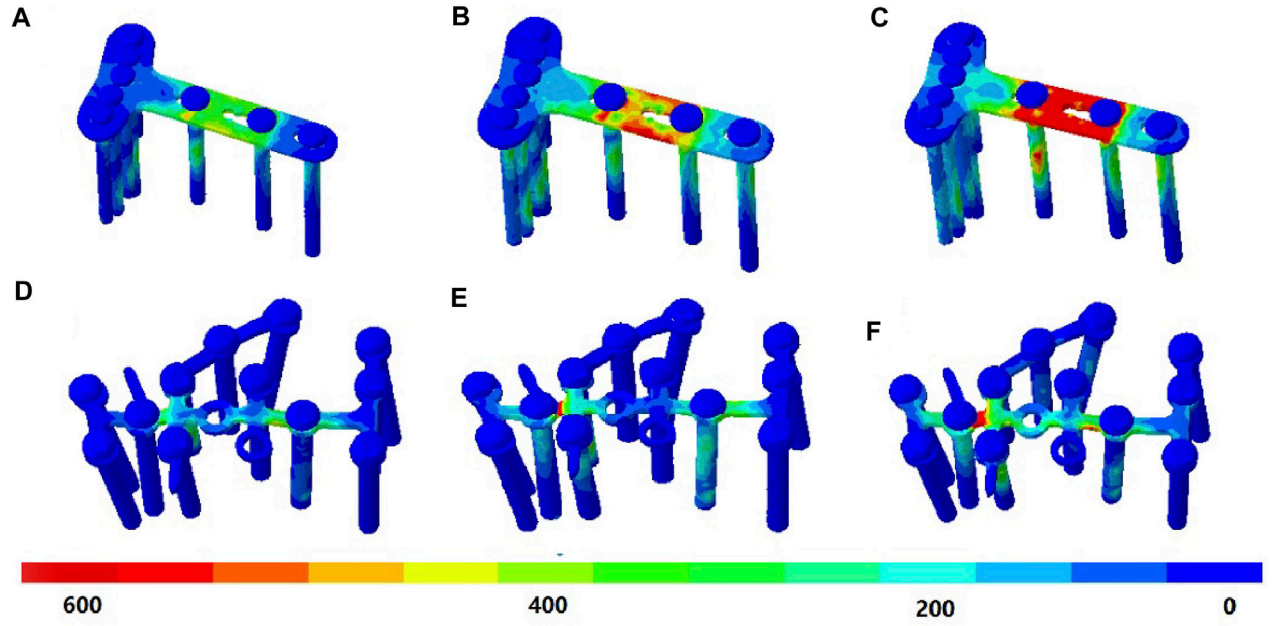

FIGURE 4 | von Mises stress (in megapascal) of the calcaneus bone. **(A)** Condition at heel-strike instant. **(B)** Double-point fixation (DPF) at midstance instant. **(C)** DPF at push-off instant. **(D)** Three-point fixation (TPF) at heel-strike instant. **(E)** TPF at midstance instant. **(F)** TPF condition at push-off instant.

the posterior facet of the calcaneus and another line drawn from the anterior process to the sulcus calcaneus. For the measurement of joint facet displacement, we first selected 10 pairs of nodes from two sides of the fragments according to a protocol (Ni et al., 2016; Ni et al., 2019). The coordinates of the nodes were recorded to calculate the average distance between the 10 pairs of nodes. The displacement of the joint facets was defined as the difference in the average distance before and after load bearing.

RESULTS

FE Model Validation

The model has been validated previously by comparing the plantar pressure distribution of the FE prediction with that measured on the model participant in the existing study (Zhang et al., 2020). The current model essentially has the same model geometry and loading case as that of our existing model, with the exception of the surgery and implant. Given that the deviations in the validation metrics between the FE prediction and measurement were less than 5%, we believed that the FE analysis demonstrated good agreement with the physical measurement and was considered adequately reliable (Wong et al., 2021).

von Mises Stress of Calcaneus

The stress distributions of the DPF and TPF at the heel-strike, midstance, and push-off instants are shown in **Figure 4**. Stress was mainly concentrated at the screw-to-bone interface and in the adjacent soft tissue. The maximum stresses of the calcaneus under DPF were 59.4, 92.7, and 103.3 MPa in the three instants, respectively, which were comparatively lower than those under the TPF condition (121.8, 163.0, and 199.4 MPa), as shown in **Table 2**.

von Mises Stress of Implants

Under the DPF, stress was concentrated in the middle of the long limb, which was located between the two screws, as shown in **Figures 5A–C**. Under the TPF, stress appeared to be more concentrated at the joint of the three limbs (**Figures 5D–F**). As listed in **Table 2**, the maximum stresses of the volar plate were 427.4, 605.9, and 1,084.0 MPa at the heel-strike, midstance, and push-off instants, respectively, which were comparatively larger than those of TPF (210.3, 411.0, and 577.9 MPa).

Reduction and Fixation Conditions

As shown in **Figure 6**, for the DPF, the calcaneus displacement occurred maximally at the internal side of the calcaneal tuberosity and reached a peak value at the push-off instant, which was 3.68 mm. However, the TPF had a maximum displacement of 2.53 mm at the calcaneal tuberosity during the heel strike, which was transferred to the sustentaculum tali during the midstance and push-off instants.

The displacements of the posterior joint facet of the DPF were 0.076, 0.048, and 0.127 mm at the heel-strike, midstance, and push-off instants, respectively, which were less than those of the TPF (0.160, 0.060, and 0.150 mm).

The Böhler angle and Gissane's angle were 31.8° and 128.5°, respectively, in the intact calcaneal model. Both fracture models showed that the Böhler angle decreased while Gissane's angle increased. For both DPF and TPF, the Böhler angle and Gissane's

TABLE 2 | Maximum von Mises stress of the calcaneus and implants under different surgical conditions at different simulated time instants.

Part/time instant	Heel strike (MPa)	Midstance (MPa)	Push-off (MPa)
Volar plate	427.4	605.9	1,084.0
Calcaneal plate	210.3	411.0	577.9
Calcaneus under volar plate fixation (DPF)	59.4	92.7	103.3
Calcaneus under calcaneal plate fixation (TPF)	121.8	163.0	199.4

DPF, double-point fixation; TPF, three-point fixation

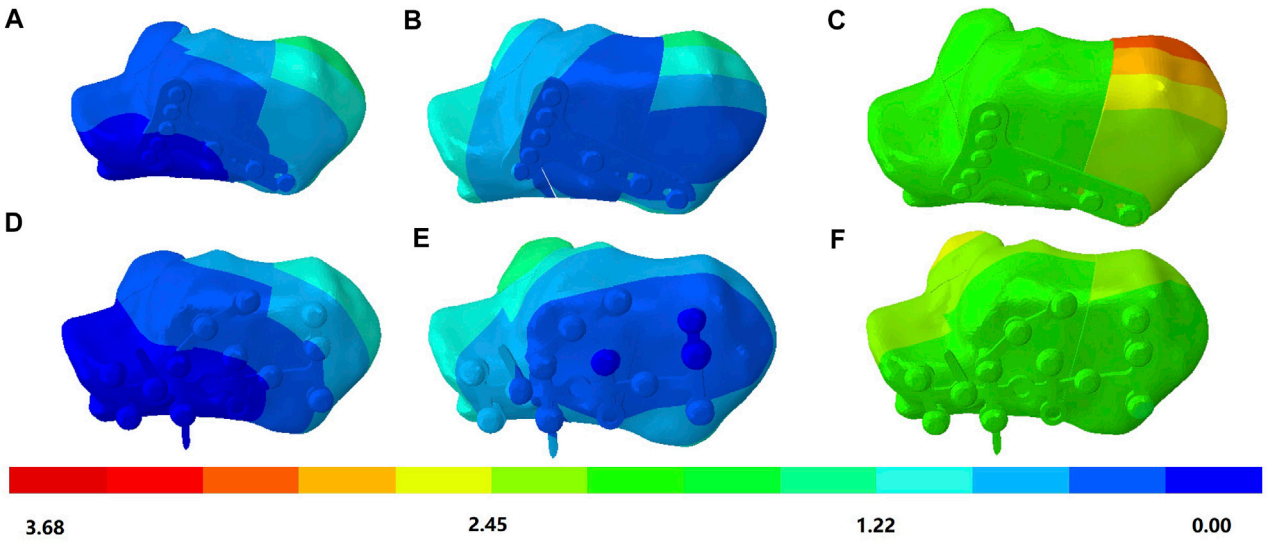

FIGURE 5 | von Mises stress (in megapascal) of the implant. **(A)** Double-point fixation (DPF) at the heel-strike instant. **(B)** DPF at the midstance instant. **(C)** DPF at the push-off instant. **(D)** Three-point fixation (TPF) at the heel-strike instant. **(E)** TPF at the midstance instant. **(F)** TPF at the push-off instant.

angle could meet normal requirements (Su et al., 2013), although MIF demonstrated more change, as shown in **Table 3**.

DISCUSSION

DIACF is the most prevalent mode of calcaneus fracture, accounting for approximately 75% of cases (Marouby et al., 2020). The fracture pattern was classified using the Sanders classification based on the number of fracture lines (Sanders et al., 1993). The fracture lines of DIACF often occur anterior to the posterior joint facet and run through the middle of the calcaneal tuberosity that continues with the upper longitudinal lines and anterior transverse lines (Ni et al., 2021). In this study, we proposed a novel surgical option using a volar plate in the DPF procedure to treat DIACFs. As a proof of concept, a validated FE model of the foot–ankle–shank complex was constructed to evaluate the biomechanical performance of the implant and compare it to that of TPF. The strength of this study was that the reconstructed model considered the geometry of the bones, muscles, and encapsulated soft tissue, while some studies simplify these structures (Gu et al., 2015; Ouyang et al., 2017). As such, the simulation could be comparatively more comprehensive and reliable.

According to our FE predictions, DPF demonstrated adequate stability in treating DIACFs. Firstly, the changes in the Böhler angle and Gissane's angle in the three walking stance instants were small and were within the reported normal range of the calcaneus (Su et al., 2013). Secondly, the maximum displacement of the posterior joint facet was 0.127 mm, which indicated that joint surface collapse and degeneration were unlikely (Potter and Nunley, 2009). Lastly, the maximum stress induced on the calcaneus was 103.3 MPa, which was lower than the yield strength of the bone (Frost, 1997). All these findings supported that there is a low risk of stress fracture and that early weight-bearing rehabilitation is likely possible. On the other hand, the use of volar plates provides several advantages. The small size could facilitate MIF, which decreases incision-induced complications. Moreover, most surgeons are familiar with the volar plate and the surgical procedures, meaning no additional training is required. Wong et al. (2015) commented that interfragmentary compression should be facilitated for healing and to avoid nonunion. In this study, we endeavored to quantify union or nonunion conditions by the displacement of the joint facet, while contact stress between the fragments could be an alternative to demonstrate whether interfragmentary compression could be achieved.

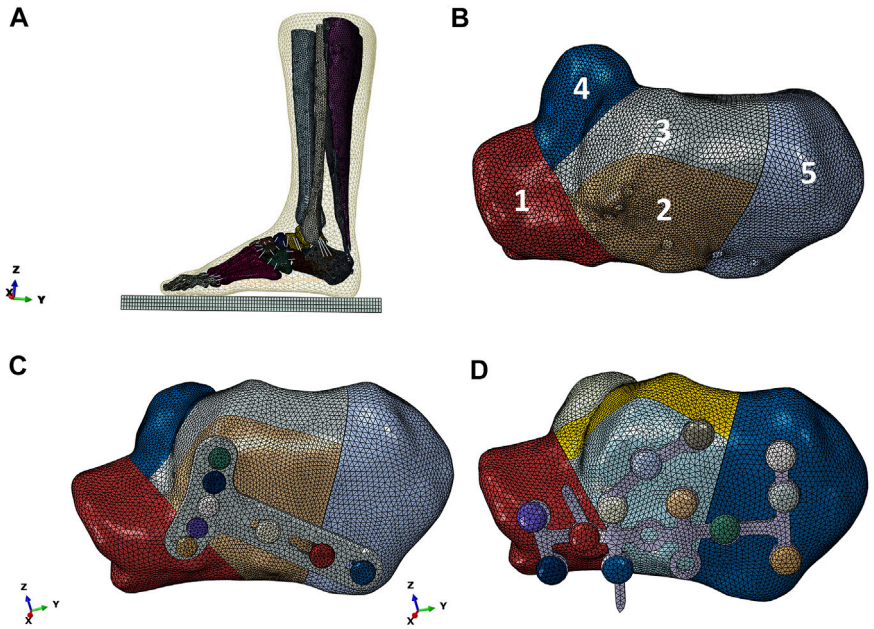

FIGURE 6 | Magnitude of displacement (in megapascal) of the calcaneus and implant simulated with double-point fixation (DPF) at heel-strike instant **(A)**, midstance instant **(B)**, and push-off instant **(C)** and simulated with three-point fixation (TPF) at heel-strike instant **(D)**, midstance instant **(E)**, and push-off instant **(F)**.

TABLE 3 | Posterior joint facet displacement and angles in different surgical conditions.

Parameter	Condition	Heel strike	Midstance	Push-off
Total displacement (mm)	DPF	1.60	1.90	3.68
	TPF	1.22	1.61	2.53
Posterior joint facet fracture displacement (mm)	DPF	0.076	0.048	0.127
	TPF	0.160	0.060	0.150
Böhler angle (°)	DPF	31.6	31.2	30.7
	TPF	31.4	30.5	30.0
Gissane's angle (°)	DPF	129.2	129.6	129.9
	TPF	129.9	130.5	130.7

DPF, double-point fixation; TPF, three-point fixation

The mechanism of DPF coincided with the anatomic and physiological characteristics of the calcaneus. The calcaneus is the largest tarsal bone, with a cortical shell outside and trabecular bones inside. The loading pattern of the calcaneal trabecular structure could be categorized into four groups: the principal compressive group, the principal tensile group, the secondary compressive group, and the secondary tensile group (Gefen and Seliktar, 2004). The principal compressive trabeculae play a major role in resisting the stresses contributed by muscle forces and body weight. It sits on the posterior half of the calcaneus and extends from the posterior facet joint toward the calcaneal tuberosity (Saers et al., 2020), which is the point of fixation in DPF. Inserting the DPF along with the trabecular orientation could maintain the alignment and structure of the principal compressive trabeculae and, thus, could facilitate fracture union and functional recovery.

A previous study showed that DPF using intramedullary nails could provide better stability than its counterparts. Goldzak et al. (2014) conducted calcaneus fixations using calcanail and lateral angular stable plates on cadavers and showed that calcaneus fixation produced threefold less subtalar joint displacement than plate fixation, indicating better stability. Our study was in accordance with the findings of Goldzak and colleagues. In our prediction, DPF using a volar plate induced fewer changes in the Böhler angle and Gissane's angle, as well as the displacement of the posterior joint facet, than TPF. This result could be attributed to the structure of the volar plate, which could fix the posterior subtalar joint by up to five screws. In the mechanism of DPF, the anterior process of the calcaneus was not fixed, and the reduction was maintained by the interfragmentary compression produced by the plantar fascia and intrinsic foot muscles. DPF could be a better option for fixation supported by the minimal change in critical angles.

Posterior joint facet fracture displacement and implant stress were two important factors that manifested fracture stability and implant failure, respectively. From our FE results, the stress

distribution of DPF and TPF demonstrated observable differences. The implant design could be optimized by widening or thickening positions with high stress. A double-support design or additional screws can also be adopted to share the mechanical loading and maintain better stability while compromising the minimally invasive plan. Therefore, DPF can be improved to better reduce the stress concentration of the steel plate.

DPF using a volar plate induced lower stress on the calcaneus than TPF, but higher stress on the implant. This could be due to the principle of load transfer, in which the implants shared and sustained load from the fractured bone. The maximum calcaneal stress in the DPF was less than that in the TPF. In addition, the maximum calcaneal stress in the TPF also exceeded the ultimate stress of calcaneal fracture (Frost, 1997), 199.4 *vs.* 130 MPa, which may reduce the likelihood of postoperative rehabilitation exercise. Our study found that stress was concentrated on the middle but slightly anterior portion of the implant, which was consistent with another study (Ouyang et al., 2017). In addition, concentrated stress was observed adjacent to the calcaneal tuberosity in the DPF. The fracture movement will induce high shear on the plate upon weight bearing, which leads to stress concentration. It should be noted that the stress on the volar plate implant during push-off was alarmingly high and exceeded the ultimate strength of titanium (Sitthiseripratip et al., 2003). This indicated that early weight-bearing rehabilitation should be avoided.

Interfragmentary screw fixation is a simple and effective method to enhance fixation stability and could be supplemented with DPF. Wang et al. (1998) compared the biomechanical stability of the lateral plate with and without interfragmentary screws in the treatment of calcaneal fracture and showed that the lateral plate with interfragmentary screws could sustain a higher load before failure. In addition, locking plates were shown to produce higher stiffness but higher peak stress compared to crossing metallic screws (Ni et al., 2016). Ni et al. (2019) compared the stability among fixations using a locking plate, calcanail, and calcanail with interfragmentary screws (modified calcanail system) for DIACFs. Their findings suggested that adding interfragmentary screws to the calcanail system can effectively enhance the fixation stability and reduce the stress concentration. As such, we anticipated that adding interfragmentary screws would also complement the stability of the volar plate system and reduce the risk of implant fatigue, which requires further investigation.

This study had several limitations. Firstly, the fracture line was reproduced according to previous studies, while the form of the actual fracture could be a variant. Future studies may consider implementing a Monte Carlo approach to generate different forms of fracture models according to their incidence of location (Ni et al., 2021). Secondly, the geometry and material properties were simplified in our simulation. For example, the ligaments and fascia were modeled as one-dimensional truss units, while the mechanical loading and behavior of the muscles were also simplified. Reconstructing the three-dimensional geometry of the plantar fascia and ligaments may facilitate a more comprehensive and accurate simulation outcome (Chen et al., 2020; Peng et al., 2021b). The trabecular core and cortical layer of the bone were not segmented to compromise the complexity, size, and number of bones involved in the whole foot-and-ankle complex structure, which was also a common simplification approach in relevant models (Morales-Orcajo et al., 2016). It should be noted that the simplification may have an apparent influence on the strain of the metatarsals (Trabelsi et al., 2014). In addition, we assumed that the bone and soft tissues were homogeneous and isotropic. Future studies may consider implementing anisotropic properties for soft tissues (Aldieri et al., 2018) and wrapping a skin layer (Wong et al., 2020). For the Achilles tendon force, a previous model often disregarded the geometry of the muscle bulk and applied the force directly on the calcaneus (Chen et al., 2012). We attempted to improve the model by accounting for the material properties of those muscles as passive bulk soft tissue. Some literature constructed a specialized fiber matrix component to resemble both the active and passive mechanical behaviors in the FE model (Yucesoy et al., 2002).

A sensitivity analysis may be conducted to address the variance of model assumption (Wong et al., 2018), while the patient-specific muscle force profile could be obtained by a musculoskeletal model to drive the FE model (Peng et al., 2021a). A sensitivity test on the coefficient of friction between bone fragments could enable the quantification of the biomechanical role of the plate. Our model was previously validated by plantar pressure in an intact state only (Zhang et al., 2020). While direct validation of the fracture model with surgical interventions was the ideal case, validation experiments often came with a paradox of the necessity of simulation if physical experiments could be arranged, along with queries on ethics, feasibility, time, and cost. Wong et al. (2021) suggested providing different modalities of evidence and measurement metrics to enhance the model credibility in the case of indirect or scaled model validation. For example, Ni et al. (2016) constructed a partial model of the calcaneus and validated surgery simulation using a cadaveric experiment with a preset loading condition. Model verification is often targeted to quantify the mesh discretization error. In this study, we determined the mesh size based on an existing model that passed the mesh convergence test (Wong et al., 2018) while ensuring the mesh quality by the mesh creation software (Hypermesh). Lastly, our study was confined to a patient-specific single-subject design such that we viewed our model as typical and representative based on the expertise of the orthopedic surgeon (Wong et al., 2021). Future studies could investigate volar plates with supplementary interfragmentary screw fixation to improve fixation stability and alleviate concentrated implant stress.

In conclusion, we proposed a novel surgical option for DPF with a volar plate in treating DIACFs in this study. The biomechanical performance of DPF was compared to that of TPF using the calcaneal plate system through a computational simulation approach (FE method). The results showed that DPF produced less stress on the calcaneus, less displacement of the fragment, and changes in the Böhler angle and Gissane's angle, which indicated better fixation stability and less risk of stress fractures. Future studies may consider further enhancing the fixation stability and alleviating the concentrated stress at the volar plate by interfragmentary screw fixation.

DATA AVAILABILITY STATEMENT

The original contributions presented in the study are included in the article/Supplementary Material, further inquiries can be directed to the corresponding author.

ETHICS STATEMENT

The studies involving human participants were reviewed and approved by the Ethical Committee of Shanghai Pudong New Area People's Hospital. The patients/participants provided written informed consent to participate in this study.

AUTHOR CONTRIBUTIONS

ML and MN conducted the model reconstruction and simulation and wrote the first draft of the manuscript. MN and WS facilitated the subject recruitment and medical consultation and the image acquisition. DW-CW assisted in troubleshooting on the computer simulation and edited the manuscript. SZ handled the data analysis and visualization. YJ and MZ played a supervisory role, project administration, and funding acquisition. All authors contributed to manuscript revision, read, and approved the submitted version.

FUNDING

This work was supported by the Project of Academic Leader of Health System in Pudong New Area, Shanghai (grant no. PWRd201-05), Key project of NSFC (11732015) and the Science and Technology Planning Project from the Science and Technology Commission of Shanghai Municipality (21410760200). The funder had no role in the design and conduct of the study; collection, management, analysis, and interpretation of the data; preparation, review, or approval of the manuscript; and decision to submit the manuscript for publication.

REFERENCES

Aldieri, A., Terzini, M., Bignardi, C., Zanetti, E. M., and Audenino, A. L. (2018). Implementation and Validation of Constitutive Relations for Human Dermis Mechanical Response. *Med. Biol. Eng. Comput.* 56 (11), 2083–2093. doi:10.1007/s11517-018-1843-y

Arnold, E. M., Ward, S. R., Lieber, R. L., and Delp, S. L. (2010). A Model of the Lower Limb for Analysis of Human Movement. *Ann. Biomed. Eng.* 38 (2), 269–279. doi:10.1007/s10439-009-9852-5

Bruce, J., and Sutherland, A. (2013). Surgical versus Conservative Interventions for Displaced Intra-articular Calcaneal Fractures. *Cochrane Database Syst. Rev.* (1), CD008628. doi:10.1002/14651858.CD008628.pub2

Bulaqi, H. A., Mousavi Mashhadi, M., Safari, H., Samandari, M. M., and Geramipanah, F. (2015). Dynamic Nature of Abutment Screw Retightening: Finite Element Study of the Effect of Retightening on the Settling Effect. *The J. prosthetic dentistry* 113 (5), 412–419. doi:10.1016/j.prosdent.2014.09.017

Chen, C.-H., Hung, C., Hsu, Y.-C., Chen, C.-S., and Chiang, C.-C. (2017). Biomechanical Evaluation of Reconstruction Plates with Locking, Nonlocking, and Hybrid Screws Configurations in Calcaneal Fracture: a Finite Element Model Study. *Med. Biol. Eng. Comput.* 55 (10), 1799–1807. doi:10.1007/s11517-017-1623-0

Chen, T. L.-W., Wong, D. W.-C., Peng, Y., and Zhang, M. (2020). Prediction on the Plantar Fascia Strain Offload upon Fascia Taping and Low-Dye Taping during Running. *J. orthopaedic translation* 20, 113–121. doi:10.1016/j.jot.2019.06.006

Chen, W.-M., Park, J., Park, S.-B., Shim, V. P.-W., and Lee, T. (2012). Role of Gastrocnemius-Soleus Muscle in Forefoot Force Transmission at Heel Rise - A 3D Finite Element Analysis. *J. Biomech.* 45 (10), 1783–1789. doi:10.1016/j.jbiomech.2012.04.024

Chen, Y.-N., Chang, C.-W., Li, C.-T., Chang, C.-H., and Lin, C.-F. (2015). Finite Element Analysis of Plantar Fascia during Walking. *Foot Ankle Int.* 36 (1), 90–97. doi:10.1177/1071100714549189

Dai, X.-Q., Li, Y., Zhang, M., and Cheung, J. T.-M. (2006). Effect of Sock on Biomechanical Responses of Foot during Walking. *Clin. Biomech.* 21 (3), 314–321. doi:10.1016/j.clinbiomech.2005.10.002

Dhillon, M. S., and Prabhakar, S. (2017). Treatment of Displaced Intra-articular Calcaneus Fractures: a Current Concepts Review. *SICOT J.* 3, 59. doi:10.1051/sicotj/2017044

Ene, R., Popescu, D., Panaitescu, C., Circota, G., Cirstoiu, M., and Cirstoiu, C. (2013). Low Complications after Minimally Invasive Fixation of Calcaneus Fracture. *J. Med. Life* 6 (1), 80–83.

Fröberg, Å., Komi, P., Ishikawa, M., Movin, T., and Arndt, A. (2009). Force in the Achilles Tendon during Walking with Ankle Foot Orthosis. *Am. J. Sports Med.* 37 (6), 1200–1207. doi:10.1177/0363546508330126

Frost, H. M. (1997). On Our Age-Related Bone Loss: Insights from a New Paradigm. *J. Bone Miner Res.* 12 (10), 1539–1546. doi:10.1359/jbmr.1997.12.10.1539

Galbusera, F., Freutel, M., Dârselen, L., DâAiuto, M., Croce, D., Villa, T., et al. (2014). Material Models and Properties in the Finite Element Analysis of Knee Ligaments: a Literature Review. *Front. Bioeng. Biotechnol.* 2, 54. doi:10.3389/fbioe.2014.00054

Gefen, A., Megido-Ravid, M., Itzchak, Y., and Arcan, M. (2000). Biomechanical Analysis of the Three-Dimensional Foot Structure during Gait: a Basic Tool for Clinical Applications. *J. Biomech. Eng.* 122 (6), 630–639. doi:10.1115/1.1318904

Gefen, A., and Seliktar, R. (2004). Comparison of the Trabecular Architecture and the Isostatic Stress Flow in the Human Calcaneus. *Med. Eng. Phys.* 26 (2), 119–129. doi:10.1016/j.medengphy.2003.10.003

Goldzak, M., Mittlmeier, T., and Simon, P. (2012). Locked Nailing for the Treatment of Displaced Articular Fractures of the Calcaneus: Description of a New Procedure with Calcanail. *Eur. J. Orthop. Surg. Traumatol.* 22 (4), 345–349. doi:10.1007/s00590-012-0968-1

Goldzak, M., Simon, P., Mittlmeier, T., Chaussemier, M., and Chiergatti, R. (2014). Primary Stability of an Intramedullary Calcaneal Nail and an Angular Stable Calcaneal Plate in a Biomechanical Testing Model of Intraarticular Calcaneal Fracture. *Injury* 45, S49–S53. doi:10.1016/j.injury.2013.10.031

Gu, Z. Q., Pang, Q. J., Yu, X., Chen, L., and Guo, Z. H. (2015). Sustentaculum Tali Screw Fixation for the Treatment of Sanders Type II and III Calcaneal Fractures. *Zhongguo Gu Shang* 28 (1), 31–35.

Ibrahim, T., Rowsell, M., Rennie, W., Brown, A. R., Taylor, G. J. S., and Gregg, P. J. (2007). Displaced Intra-articular Calcaneal Fractures: 15-year Follow-Up of a Randomised Controlled Trial of Conservative versus Operative Treatment. *Injury* 38 (7), 848–855. doi:10.1016/j.injury.2007.01.003

Marouby, S., Cellier, N., Mares, O., Kouyoumdjian, P., and Coulomb, R. (2020). Percutaneous Arthroscopic Calcaneal Osteosynthesis for Displaced Intra-articular Calcaneal Fractures: Systematic Review and Surgical Technique. *Foot Ankle Surg.* 26 (5), 503–508. doi:10.1016/j.fas.2019.07.002

Morales-Orcajo, E., Bayod, J., and Barbosa de Las Casas, E. (2016). Computational Foot Modeling: Scope and Applications. *Arch. Computat Methods Eng.* 23 (3), 389–416. doi:10.1007/s11831-015-9146-z

Mostafa, M. F., El-Adl, G., Hassanin, E. Y., and Abdellatif, M.-S. (2010). Surgical Treatment of Displaced Intra-articular Calcaneal Fracture Using a Single Small Lateral Approach. *Strateg. Trauma limb reconstruction* 5 (2), 87–95. doi:10.1007/s11751-010-0082-z

Ni, M., Lv, M. L., Sun, W., Zhang, Y., Mei, J., Wong, D. W.-C., et al. (2021). Fracture Mapping of Complex Intra-articular Calcaneal Fractures. *Ann. Translational Med.* 9 (4), 333. doi:10.21037/atm-20-7824

Ni, M., Wong, D. W.-C., Mei, J., Niu, W., and Zhang, M. (2016). Biomechanical Comparison of Locking Plate and Crossing Metallic and Absorbable Screws

Fixations for Intra-articular Calcaneal Fractures. *Sci. China Life Sci.* 59 (9), 958–964. doi:10.1007/s11427-016-0010-9

Ni, M., Wong, D. W.-C., Niu, W., Wang, Y., Mei, J., and Zhang, M. (2019). Biomechanical Comparison of Modified Calcanail System with Plating Fixation in Intra-articular Calcaneal Fracture: a Finite Element Analysis. *Med. Eng. Phys.* 70, 55–61. doi:10.1016/j.medengphy.2019.06.004

Ouyang, H., Deng, Y., Xie, P., Yang, Y., Jiang, B., Zeng, C., et al. (2017). Biomechanical Comparison of Conventional and Optimised Locking Plates for the Fixation of Intraarticular Calcaneal Fractures: a Finite Element Analysis. *Comp. Methods Biomech. Biomed. Eng.* 20 (12), 1339–1349. doi:10.1080/10255842.2017.1361938

Pascoletti, G., Cianetti, F., Putame, G., Terzini, M., and Zanetti, E. M. (2018). Numerical Simulation of an Intramedullary Elastic Nail: Expansion Phase and Load-Bearing Behavior. *Front. Bioeng. Biotechnol.* 6, 174. doi:10.3389/fbioe.2018.00174

Peng, Y., Niu, W., Wong, D. W.-C., Wang, Y., Chen, T. L.-W., Zhang, G., et al. (2021a). Biomechanical Comparison Among Five Mid/hindfoot Arthrodeses Procedures in Treating Flatfoot Using a Musculoskeletal Multibody Driven Finite Element Model. *Comp. Methods Programs Biomed.* 211, 106408. doi:10.1016/j.cmpb.2021.106408

Peng, Y., Wong, D. W.-C., Wang, Y., Chen, T. L.-W., Zhang, G., Yan, F., et al. (2021b). Computational Models of Flatfoot with Three-Dimensional Fascia and Bulk Soft Tissue Interaction for Orthosis Design. *Med. Novel Techn. Devices* 9, 100050. doi:10.1016/j.medntd.2020.100050

Potter, M. Q., and Nunley, J. A. (2009). Long-term Functional Outcomes after Operative Treatment for Intra-articular Fractures of the Calcaneus. *The J. Bone Jt. Surgery-American Volume* 91 (8), 1854–1860. doi:10.2106/jbjs.h.01475

Reeves, N. D., Maganaris, C. N., Ferretti, G., and Narici, M. V. (2005). Influence of 90-day Simulated Microgravity on Human Tendon Mechanical Properties and the Effect of Resistive Countermeasures. *J. Appl. Physiol.* 98 (6), 2278–2286. doi:10.1152/japplphysiol.01266.2004

Saers, J. P. P., Ryan, T. M., and Stock, J. T. (2020). Baby Steps towards Linking Calcaneal Trabecular Bone Ontogeny and the Development of Bipedal Human Gait. *J. Anat.* 236 (3), 474–492. doi:10.1111/joa.13120

Sanders, R. (2000). Displaced Intra-articular Fractures of the Calcaneus*. *J. Bone Jt. Surgery-American Volume* 82 (2), 225–250. doi:10.2106/00004623-200002000-00009

Sanders, R., Fortin, P., DiPasquale, T., and Walling, A. (1993). Operative Treatment in 120 Displaced Intraarticular Calcaneal Fractures. *Clin. orthopaedics Relat. Res.* 290 (290), 87–95. doi:10.1097/00003086-199305000-00012

Scarton, A., Guiotto, A., Malaquias, T., Spolaor, F., Sinigaglia, G., Cobelli, C., et al. (2018). A Methodological Framework for Detecting Ulcers' Risk in Diabetic Foot Subjects by Combining Gait Analysis, a New Musculoskeletal Foot Model and a Foot Finite Element Model. *Gait & Posture* 60, 279–285. doi:10.1016/j.gaitpost.2017.08.036

Shah, D., and Parmar, H. (2020). Results of Intra Articular Calcaneal Fractures Treated with Internal Fixation Using Sinus Tarsi Approach. *Int. J. Orthop. Sci.* 6 (1), 280–283. doi:10.22271/ortho.2020.v6.i1e.1874

Simon, P., Goldzak, M., Eschler, A., and Mittlmeier, T. (2015). Reduction and Internal Fixation of Displaced Intra-articular Calcaneal Fractures with a Locking Nail: a Prospective Study of Sixty Nine Cases. *Int. Orthopaedics (Sicot)* 39 (10), 2061–2067. doi:10.1007/s00264-015-2816-5

Sitthiseripratip, K., Van Oosterwyck, H., Vander Sloten, J., Mahaisavariya, B., Bohez, E. L. J., Suwanprateeb, J., et al. (2003). Finite Element Study of Trochanteric Gamma Nail for Trochanteric Fracture. *Med. Eng. Phys.* 25 (2), 99–106. doi:10.1016/s1350-4533(02)00185-6

Su, Y., Chen, W., Zhang, T., Wu, X., Wu, Z., and Zhang, Y. (2013). Bohler's Angle's Role in Assessing the Injury Severity and Functional Outcome of Internal Fixation for Displaced Intra-articular Calcaneal Fractures: a Retrospective Study. *BMC Surg.* 13 (1), 40–48. doi:10.1186/1471-2482-13-40

Trabelsi, N., Milgrom, C., and Yosibash, Z. (2014). Patient-specific FE Analyses of Metatarsal Bones with Inhomogeneous Isotropic Material Properties. *J. Mech. Behav. Biomed. Mater.* 29, 177–189. doi:10.1016/j.jmbbm.2013.08.030

Ün, M. K., and Çalık, A. (2019). Estimation of Depth-dependent Material Properties of Biphasic Soft Tissues through Finite Element Optimization and Sensitivity Analysis. *Med. Eng. Phys.* 74, 73–81. doi:10.1016/j.medengphy.2019.09.019

van Tetering, E. A. A., and Buckley, R. E. (2004). Functional Outcome (SF-36) of Patients with Displaced Calcaneal Fractures Compared to SF-36 Normative Data. *Foot Ankle Int.* 25 (10), 733–738. doi:10.1177/107110070402501007

Wai-Chi Wong, D., Wang, Y., Zhang, M., and Kam-Lun Leung, A. (2015). Functional Restoration and Risk of Non-union of the First Metatarsocuneiform Arthrodesis for Hallux Valgus: a Finite Element Approach. *J. Biomech.* 48 (12), 3142–3148. doi:10.1016/j.jbiomech.2015.07.013

Wang, C.-L., Chang, G.-L., Tseng, W.-C., Yu, C.-Y., and Lin, R.-M. (1998). Strength of Internal Fixation for Calcaneal Fractures. *Clin. Biomech.* 13 (3), 230–233. doi:10.1016/s0268-0033(97)00042-9

Wang, Y., Wong, D. W.-C., and Zhang, M. (2016). Computational Models of the Foot and Ankle for Pathomechanics and Clinical Applications: a Review. *Ann. Biomed. Eng.* 44 (1), 213–221. doi:10.1007/s10439-015-1359-7

Wong, D. W., Wang, Y., Chen, T. L., Yan, F., Peng, Y., Tan, Q., et al. (2020). Finite Element Analysis of Generalized Ligament Laxity on the Deterioration of Hallux Valgus Deformity (Bunion). *Front. Bioeng. Biotechnol.* 8, 571192. doi:10.3389/fbioe.2020.571192

Wong, D. W.-C., Chen, T. L.-W., Peng, Y., Lam, W.-K., Wang, Y., Ni, M., et al. (2021). An Instrument for Methodological Quality Assessment of Single-Subject Finite Element Analysis Used in Computational Orthopaedics. *Med. Novel Techn. Devices* 11, 100067. doi:10.1016/j.medntd.2021.100067

Wong, D. W.-C., Wang, Y., Leung, A. K.-L., Yang, M., and Zhang, M. (2018). Finite Element Simulation on Posterior Tibial Tendinopathy: Load Transfer Alteration and Implications to the Onset of Pes Planus. *Clin. Biomech.* 51, 10–16. doi:10.1016/j.clinbiomech.2017.11.001

Yamamura, N., Alves, J. L., Oda, T., Kinugasa, R., and Takagi, S. (2014). Effect of Tendon Stiffness on the Generated Force at the Achilles Tendon - 3D Finite Element Simulation of a Human Triceps Surae Muscle during Isometric Contraction. *Jbse* 9 (3), 13. doi:10.1299/jbse.13-00294

Yu, J., Wong, D. W.-C., Zhang, H., Luo, Z.-P., and Zhang, M. (2016). The Influence of High-Heeled Shoes on Strain and Tension Force of the Anterior Talofibular Ligament and Plantar Fascia during Balanced Standing and Walking. *Med. Eng. Phys.* 38 (10), 1152–1156. doi:10.1016/j.medengphy.2016.07.009

Yucesoy, C. A., Koopman, B. H. F. J. M., Huijing, P. A., and Grootenboer, H. J. (2002). Three-dimensional Finite Element Modeling of Skeletal Muscle Using a Two-Domain Approach: Linked Fiber-Matrix Mesh Model. *J. Biomech.* 35 (9), 1253–1262. doi:10.1016/s0021-9290(02)00069-6

Zanetti, E. M., and Bignardi, C. (2013). Mock-up in Hip Arthroplasty Pre-operative Planning. *Acta Bioeng. Biomech.* 15 (3), 123–128. doi:10.5277/abb130315

Zhang, H., Lv, M. L., Liu, Y., Sun, W., Niu, W., Wong, D. W.-C., et al. (2020). Biomechanical Analysis of Minimally Invasive Crossing Screw Fixation for Calcaneal Fractures: Implications to Early Weight-Bearing Rehabilitation. *Clin. Biomech.* 80, 105143. doi:10.1016/j.clinbiomech.2020.105143

Conflict of Interest: The authors declare that the research was conducted in the absence of any commercial or financial relationships that could be construed as a potential conflict of interest.

frontiers in Bioengineering and Biotechnology

ORIGINAL RESEARCH
published: 10 March 2022
doi: 10.3389/fbioe.2022.853085

Different Design Feature Combinations of Flatfoot Orthosis on Plantar Fascia Strain and Plantar Pressure: A Muscle-Driven Finite Element Analysis With Taguchi Method

*Yinghu Peng[1,2,3], Yan Wang[1,2], Duo Wai-Chi Wong[1,2], Tony Lin-Wei Chen[1], Shane Fei Chen[1], Guoxin Zhang[1], Qitao Tan[1] and Ming Zhang[1,2]**

[1]Department of Biomedical Engineering, Faculty of Engineering, Hong Kong Polytechnic University, Kowloon, Hong Kong SAR, China, [2]Hong Kong Polytechnic University Shenzhen Research Institute, Shenzhen, China, [3]CAS Key Laboratory of Human-Machine Intelligence-Synergy Systems, Shenzhen Institutes of Advanced Technology Chinese Academy of Sciences, Shenzhen, China

OPEN ACCESS

Edited by:
Lizhen Wang,
Beihang University, China

Reviewed by:
Yaodong Gu,
Ningbo University, China
Chi-Wen Lung,
Asia University, Taiwan

***Correspondence:**
Ming Zhang
ming.zhang@polyu.edu.hk

Specialty section:
This article was submitted to Biomechanics, a section of the journal Frontiers in Bioengineering and Biotechnology

Received: *12 January 2022*
Accepted: *18 February 2022*
Published: *10 March 2022*

Citation:
Peng Y, Wang Y, Wong DW-C, Chen TL-W, Chen SF, Zhang G, Tan Q and Zhang M (2022) Different Design Feature Combinations of Flatfoot Orthosis on Plantar Fascia Strain and Plantar Pressure: A Muscle-Driven Finite Element Analysis With Taguchi Method. Front. Bioeng. Biotechnol. 10:853085. doi: 10.3389/fbioe.2022.853085

Customized foot orthosis is commonly used to modify foot posture and relieve foot pain for adult acquired flexible flatfoot. However, systematic investigation of the influence of foot orthotic design parameter combination on the internal foot mechanics remains scarce. This study aimed to investigate the biomechanical effects of different combinations of foot orthoses design features through a muscle-driven flatfoot finite element model. A flatfoot-orthosis finite element model was constructed by considering the three-dimensional geometry of plantar fascia. The plantar fascia model accounted for the interaction with the bulk soft tissue. The Taguchi approach was adopted to analyze the significance of four design factors combination (arch support height, medial posting inclination, heel cup height, and material stiffness). Predicted plantar pressure and plantar fascia strains in different design combinations at the midstance instant were reported. The results indicated that the foot orthosis with higher arch support (45.7%) and medial inclination angle (25.5%) effectively reduced peak plantar pressure. For the proximal plantar fascia strain, arch support (41.8%) and material stiffness (37%) were strong influencing factors. Specifically, higher arch support and softer material decreased the peak plantar fascia strain. The plantar pressure and plantar fascia loading were sensitive to the arch support feature. The proposed statistics-based finite element flatfoot model could assist the insole optimization and evaluation for individuals with flatfoot.

Keywords: flatfoot, foot orthosis, finite element model, plantar fascia, Taguchi approach

INTRODUCTION

Individuals with flatfoot may demonstrate abnormal foot kinematics, such as excessive rearfoot eversion, collapsed foot arch, valgus forefoot, altered muscle activations, and potential symptoms (e.g., knee pain and foot pain) (Richie Jr, 2007; Cifuentes-De la Portilla et al., 2019; Flores et al., 2019; Zhang and Lu, 2020). In the early stages of the disease, conservative treatments are often prescribed to alleviate foot pain and modify the foot posture (Lee et al., 2005; Arachchige et al., 2019; Peng et al.,

2020; Cen et al., 2021). Foot orthoses, one of the most common conservative treatments, have been widely used to provide support, distribute the foot pressure, correct the flexible misalignment, and constrain the painful joints (Cobb et al., 2011; Telfer et al., 2013; Banwell et al., 2014; Kosonen et al., 2017).

Studies have investigated the effects of foot orthoses on the kinematic and kinetics of flexible flatfoot (Chen Y.-C. et al., 2010; Hurd et al., 2010; Murley et al., 2010; Cobb et al., 2011; Kosonen et al., 2017). Foot orthoses with arch support are common considerations for redistributing plantar foot pressure and relieving foot pain (Cheung and Zhang, 2005). However, the prescribed foot orthoses with enhanced arch support alone cannot reduce the excessive rearfoot eversion. Medial forefoot and rearfoot postings were considered in addition to arch support for more aggressive flatfoot posture correction (Desmyttere et al., 2018). Although previous studies have proposed and tested various foot orthoses for flatfoot, there is a lack of consensus on the foot orthoses design and their configurations on foot kinematics and kinetics (Cobb et al., 2011; Telfer et al., 2013; Banwell et al., 2014; Kosonen et al., 2017). Compared to prefabricated foot orthosis, customized foot orthoses can provide better functional outcomes in hindfoot correction and pain relief due to their consideration in individual variance (Cheung et al., 2011). However, design feature combinations for the customized foot orthosis seriously depended on the experience of a pedorthist, lacking quantitative theoretical support.

Kinematics and kinetics studies were conducted to investigate the effects of orthosis and provide knowledge-based information for flatfoot intervention (Kogler et al., 1995; 1996; Murley et al., 2014). However, although gait analysis could reveal the kinematics changes induced by foot orthosis, the internal foot soft tissue stress loading distribution was hardly obtained (Murley et al., 2014). Meanwhile, cadaver studies and dynamics Magnetic Resonance Imaging (MRI) or biplane fluoroscopy methods had difficulty in analyzing the effects of material sensitivities and experimental setting (Kogler et al., 1995). Compared to these techniques, the finite element (FE) analysis approach offers an alternate approach for internal soft tissue stress investigation, which may be useful in gaining new insights into the mechanisms related to pathomechanics in musculoskeletal systems (Wang et al., 2016).

Foot-ankle complex FE models have been adopted to investigate the effects of orthotic insoles on foot plantar pressure (Cheung and Zhang, 2008; Hsu et al., 2008; Chen W.-M. et al., 2015). One study has predicted an optimal insole to lower the plantar fascia stress and peak plantar pressure (Hsu et al., 2008). Another study also investigated the biomechanical effects of the material hardness and support height and reported that higher arch support increased the long plantar ligament stresses (Su et al., 2017). However, these studies only considered the balanced standing condition, and the effects of foot orthoses on the internal force of flatfoot during walking have not been investigated. Meanwhile, previous studies usually adopted a simplified plantar fascia model and could not demonstrate plantar fascia loading (Cheng et al., 2008; Hsu et al., 2008; Yu et al., 2016). Furthermore, although some studies used detailed three-dimensional plantar fascia (Chen Y.-N. et al., 2015; Akrami et al., 2018), these models ignored the interaction between bulk soft tissue and plantar fascia, which might underestimate the plantar fascia loading, especially for orthosis intervention (Peng et al., 2021b). Meanwhile, previous studies only considered limited design parameters in flatfoot intervention (Su et al., 2017), and systematic investigation of the flatfoot loading

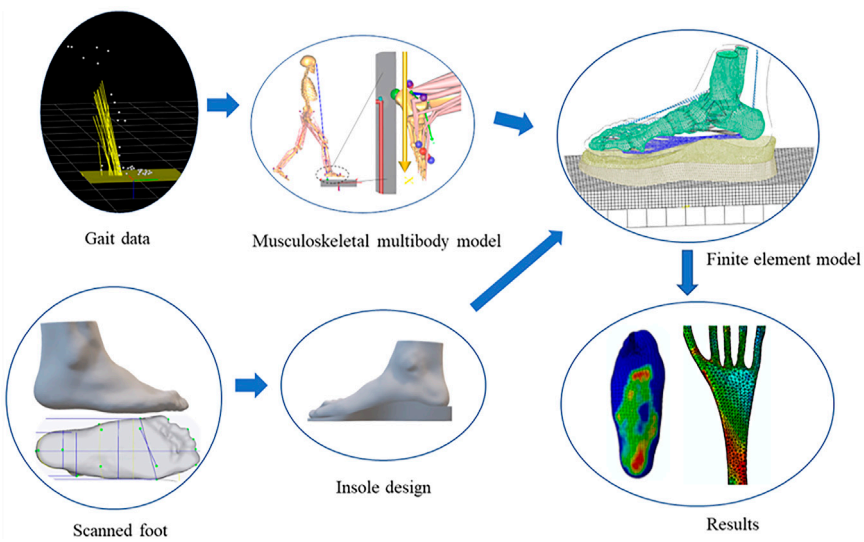

FIGURE 1 | Overview of the foot-ankle complex and insole finite element model. The customized foot orthosis was produced based on the scanned foot surface. Nine design configurations of the foot orthoses were used in the finite element model. Gait data were used as inputs of the musculoskeletal multibody model to calculate the foot muscle forces. The calculated muscles and ground reaction forces were adopted to drive the flatfoot-orthosis finite element model. The foot pressure distribution and plantar fascia strain distribution were predicted based on the muscle-driven foot-ankle complex model.

TABLE 1 | Material properties of the components in the finite element model.

	Elastic modulus (MPa)	Poisson ratio	Cross section (mm^2)
Skin	First-order Ogden hyperelastic model (μ = 0.122 MPa, α = 18, thickness: 2.0 mm)	—	
Bulk soft tissue	Second-order polynomial strain hyperelastic model (C_{10} = 0.8556, C_{01} = −0.05841, C_{20} = 0.03900, C_{11} = −0.02319, C_{02} = 0.00851, D_1 = 3.65273)	—	
Bone	10,000	0.34	—
Ligaments	260	0.4	18.4
Three-dimensional Plantar fascia	350	0.45	—
Midsole	5	0.4	—

Parameters for the material property were based on the same references in our previous work (Peng et al., 2021c).

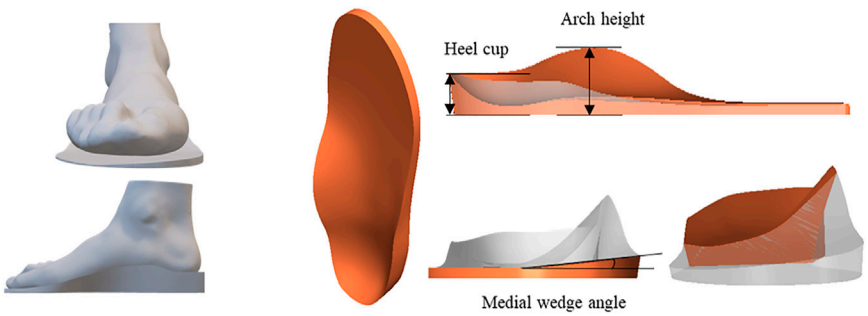

FIGURE 2 | The foot orthosis design parameters, including heel cup, arch support height, and medial wedge angle.

responses to various orthotic design combinations (e.g., arch support heights, medial posting angles, materials, and heel cup height) remains scarce.

This study aimed at determining how the foot-ankle complex responded to various orthoses design combinations. However, all factor and level combinations need to be analyzed and investigated to determine the impact of the multi-factor, which is time-consuming and costly with the conventional testing approach (Karna and Sahai, 2012). The Taguchi method is a widely used multi-factor and multi-level experimental method based on the orthogonal array (Karna and Sahai, 2012). The results of orthogonal experimental design can achieve a balanced comparison of levels of any factor with less effort (Cheung and Zhang, 2008). Taguchi methods' analysis has been used to investigate the sensitivity of the design parameters in FE foot models (Cheung and Zhang, 2008; Zhang et al., 2020). Therefore, this study aims to investigate the effects of foot orthosis parameters on the foot pressure and plantar fascia loading distribution at midstance through the Taguchi approach analysis.

MATERIALS AND METHODS

This study constructed a flatfoot-orthoses FE model with 3D plantar fascia geometry based on foot MRI. The measured ground reaction forces from gait analysis and estimated muscle forces from the musculoskeletal multibody model were used to drive the FE flatfoot model (Peng et al., 2021c). The foot orthoses with four design parameters were adopted in the FE model. Under various foot orthosis design combinations, foot plantar pressure and plantar fascia strain were investigated. More details about the workflow of the customized flatfoot-orthosis modeling can be seen in **Figure 1**. The statistics-based Taguchi method was used to investigate the sensitivity of four design parameters on the plantar fascia strain and plantar pressure.

Flatfoot Finite Element Model Construction

The construction of the flatfoot FE model has been reported in our previous studies (Peng et al., 2021a). A young male adult (27 years old, 175 cm height, and 64 kg weight) was recruited for the FE modeling. The participant had flexible flatfoot with an arch index of 0.30 and a navicular drop of 12 mm for the right foot. This study has been approved by the Human Subject Ethics Sub-Committee of The Hong Kong Polytechnic University (Number: HSEARS20190124008). The three-dimensional geometries of the foot-ankle complex were reconstructed using medical image processing software (Mimics 10.1, Materialise Inc., Belgium), including encapsulated bulk tissue, plantar fascia, and twenty bones. The skin layer was defined as a 2 mm thick membrane encapsulating the bulk soft tissue. The inner foot ligaments were modeled as trusses. The contact properties at the joints were assigned with a frictionless contact algorithm with a non-linear contact stiffness to mimic the articular cartilage (Wong et al., 2018). The finite elements of the foot-ankle complex geometries were created by Abaqus 6.14 (Simulia, Dassault Systemes, France). The bones, the encapsulated bulk

TABLE 2 | Foot orthosis design factors and their levels.

Design factor	Level 1	Level 2	Level 3
Arch support height (mm)	42	45	48
Medial posting inclination (°)	0	2	4
Heel cup height (mm)	14	16	18
Materials (MPa)	3	5	7

tissue, orthosis, shoe, and plantar fascia adopted linear tetrahedral elements (C3D4). The hexahedra elements (C3D8), three-node triangular membrane elements (M3D3), and two-node linear three-dimensional elements (T3D2) were assigned to the ground plate, skin, and linear ligaments. The material properties for the foot-ankle complex were determined from current studies (Chen et al., 2003; Lewis, 2003; Chen W.-M. et al., 2010; Peng et al., 2021c). More detailed information about the material properties is shown in **Table 1**.

Load and Boundary Conditions

The internal foot biomechanics were investigated through the muscle-driven flatfoot FE model at the midstance instant during walking. In this model, the proximal cross section surfaces of the fibula, tibia, and bulk soft tissue were fixed. To control the degree of freedom of the ground plate, one rigid plate was tied beneath the ground plate. The ground reaction forces were applied to the rigid plate, including vertical force (338 N), mediolateral force (6 N in the medial direction), and anteroposterior force (4 N in the posterior direction). In addition, the foot muscles forces for the tibialis anterior (38 N), tibialis posterior (200 N), peroneus brevis (1 N), peroneus longus (0 N), Achilles tendon (gastrocnemius and soleus) (774 N), flexor hallucis longus (95 N), and flexor digitorum longus (26 N) were used as inputs to drive the FE model. The musculoskeletal model was adopted to estimate these muscle forces based on the experimental gait data (Peng et al., 2021a). These simulations were conducted with Abaqus 6.14 (Dassault Systèmes, Vélizy-Villacoublay, France) using the standard static solver. The foot plantar pressures and plantar fascia strain were reported.

Experimental Validation

The muscle-driven flatfoot FE has been validated by comparing the predicted foot pressure with the measurements in our previous studies under barefoot and shod-walking conditions (Peng et al., 2021a; Peng et al., 2021c). The correlation analysis showed that the measurement and prediction were highly associated under barefoot walking ($r = 0.95$, $p < 0.001$) and shod-walking ($r = 0.8$, $p < 0.001$) conditions (Peng et al., 2021a; Peng et al., 2021c).

Parametric Analysis Through Taguchi Method

The customized total contact foot orthosis was produced based on the surface scans of the foot under minimal weight (<5% body weight) condition, in which the arch shape was close to the normal configuration. According to the foot shape, the insole profile was designed in the computer-aided design software, isoleCAD (Nmotion Orthotic Lab, Knoxville, TN, United States). Four design factors, namely, the arch support height (A), the inclination angle of the medial posting (I), heel cup height (H), and material stiffness (M) of insoles, were selected for evaluation. More details of the orthosis configurations are shown in **Figure 2**. Each factor was assigned with three levels (**Table 2**).

In this study, a statistics-based Taguchi method was used to reduce the number of analyses. Nine simulations were required. The insole configurations are shown in an orthogonal array L_9 in **Table 3**. The mechanical responses, namely, peak plantar fascia strain and peak pressures of the forefoot, midfoot, and hindfoot, were predicted by nine FE analyses. The mean effect of each level of the four design factors on the mechanical responses was computed. For example, the mean response of arch support height at level 1 [R (A_1)] on peak forefoot pressure is calculated as the mean pressure over trials 1–3. An analysis of

TABLE 3 | L_9 orthogonal array table (the numbers under design factors indicate the levels assigned to each design factor) and the corresponding FE predicted peak plantar pressures and peak proximal plantar fascia strain for the nine configurations of foot orthosis.

Trial number	Code	Design factor				Plantar pressure (MPa)			Plantar fascia strain (%)
		Arch support	Inclination angle	Heel cup height	Material stiffness	Forefoot	Midfoot	Hindfoot	
		A	I	H	M				
1	$A_1I_1H_1M_1$	1	1	1	1	0.183	0.078	0.04	2.16
2	$A_1I_2H_2M_2$	1	2	2	2	0.184	0.080	0.078	2.03
3	$A_1I_3H_3M_3$	1	3	3	3	0.188	0.096	0.092	2.11
4	$A_2I_1H_2M_3$	2	1	2	3	0.187	0.082	0.051	2.19
5	$A_2I_2H_3M_1$	2	2	3	1	0.18	0.078	0.047	1.73
6	$A_2I_3H_1M_2$	2	3	1	2	0.168	0.109	0.02	1.85
7	$A_3I_1H_3M_2$	3	1	3	2	0.18	0.084	0.058	1.48
8	$A_3I_2H_1M_3$	3	2	1	3	0.17	0.118	0	2.06
9	$A_3I_3H_2M_1$	3	3	2	1	0.164	0.105	0	1.61

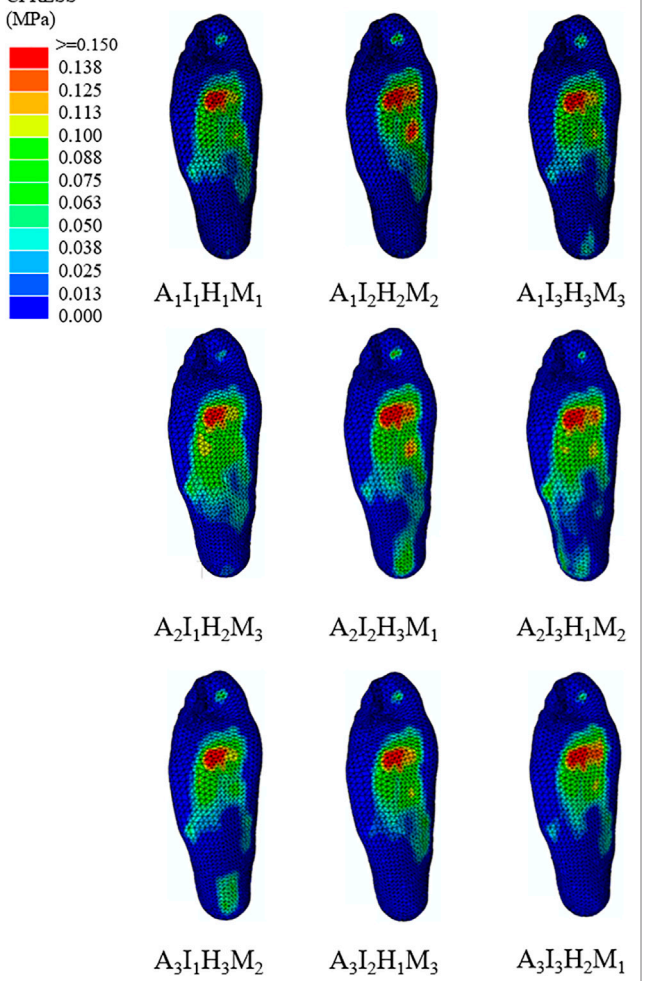

FIGURE 3 | An illustration of the foot pressure distribution among the nine orthoses design configurations.

variance (ANOVA) was performed, calculating the sum of squares of each design factor to determine the sensitivity of each design parameter (Lee and Zhang, 2005). For example, the sum of squares due to arch support height would be equal to

$$[R(A_1) - R_m]^2 + [R(A_2) - R_m]^2 + [R(A_3) - R_m]^2, \quad (1)$$

where R (A_1), R (A_2), and R (A_3) are mean responses of thickness at levels 1–3, respectively. R_m is the overall mean response over nine trials.

RESULTS

Plantar Pressures

The FE predicted foot pressure distributions of the nine different orthotic configurations illustrated in **Figure 3**. The predicted foot plantar pressure was divided into hindfoot, midfoot, and forefoot regions. The peak foot pressures among different orthotic designs occurred in the forefoot region at the midstance instant. The peak foot pressures among three regions for nine orthotic configurations are presented in **Table 3**. The mean effect of each design factor at each of the three levels can be found in **Figure 5**. In general, the foot orthoses with higher arch support and medial inclination angle effectively reduced peak plantar pressure. Meanwhile, using a softer material and lower heel cup also reduced the peak foot pressures. The peak plantar pressure of the midfoot increased with higher arch support, medial inclination angle, and material stiffness. However, the high heel cup height decreased the midfoot pressure. In the hindfoot region, foot orthosis with increased medial inclination angle and arch support reduced the peak pressure, and the latter had a larger reducing effect. However, higher heel cup height and material stiffness increased the peak hindfoot pressures. The material stiffness had less effect on the peak hindfoot pressures, especially in the latter two levels.

The degree of importance for each design factor can be further identified by comparing the sum of squares of the predicted plantar pressure shown in **Table 4**. The geometrical parameters (arch support height, medial posting inclination, and heel cup height) had larger effects on the peak foot pressures than the material stiffness. Specifically, arch support height and medial posting inclination had larger effects on the peak forefoot and midfoot pressures. In contrast, arch support height and heel cup were more important parameters for the peak hindfoot pressures. Among the four design factors, the use of an arch supporting foot orthosis was found to be the most critical design factor for peak foot pressure reduction (45.7%). The medial inclination angle was found to be the second most important factor for peak pressure reduction (25.5%). Then, the rest of the design factors contributed to a much lesser extent in peak pressure reduction with a descending order from heel cup height and insole stiffness. In

TABLE 4 | Analysis of variance of predicted peak plantar pressure in the forefoot, midfoot, and rearfoot and plantar fascia strain for the four-factor and three-level fractional factorial analysis.

Design factor	Sum of squares for plantar pressure and plantar fascia strain			
	Forefoot	Midfoot	Hindfoot	Plantar fascia
Arch support height	9.5×10^{-5} (45.7%)	16.8×10^{-5} (26.7%)	125.5×10^{-5} (47.6%)	7.4×10^{-2} (41.8%)
Medial posting inclination	5.3×10^{-5} (25.5%)	24.1×10^{-5} (38.4%)	7.6×10^{-5} (2.9%)	0.5×10^{-2} (2.7%)
Heel cup height	4.1×10^{-5} (19.7%)	7.3×10^{-5} (11.7%)	99.8×10^{-5} (37.8%)	3.3×10^{-2} (18.5%)
Materials	1.9×10^{-5} (9.1%)	14.5×10^{-5} (23.1%)	30.8×10^{-5} (11.7%)	6.5×10^{-2} (37%)

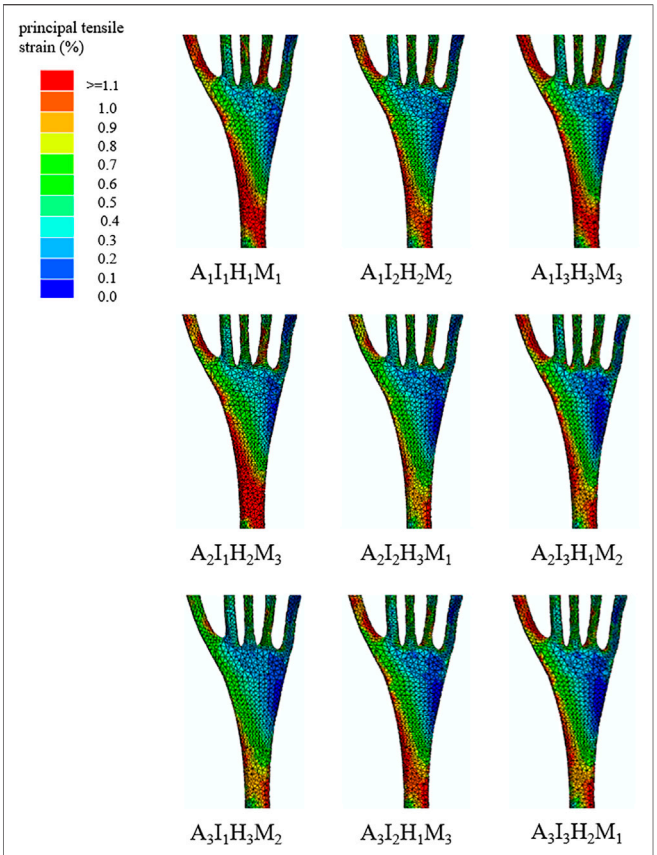

FIGURE 4 | An illustration of the plantar fascia strain distribution among the nine orthoses design configurations.

the midfoot region, the medial posting inclination is the most critical parameter for peak pressure (38.4%). The effects of arch support height and material stiffness are similar (26.7% and 23.1%, respectively). For the hindfoot region, the arch support height had the most effect (47.6%) on the peak hindfoot pressure, followed by heel cup height (37.8%).

Plantar Fascia Strain

The predicted principal tensile strain distributions of plantar fascia among the nine orthotic configurations are illustrated in **Figure 4**. The predicted principal tensile strain distributions of plantar fascia could be divided into the distal, middle, and proximal regions. The peak values in the proximal region among different orthotic designs were reported since plantar fasciitis normally induced pain in the hindfoot region (Cole et al., 2005; Hsu et al., 2008). The peak proximal plantar fascia strain among nine orthotic configurations is presented in **Table 3**.

The mean effect of each design factor at each of the three levels can be found in **Figure 5**. In general, the peak strain of the plantar fascia was decreased with higher arch support, medial inclination angle, and heel cup. The importance degree for each design factor can be further identified by comparing the sum of squares of the predicted plantar fascia strain shown in **Table 4**. Among the four design factors, arch support (41.8%) and material properties (37%) were significant design factors affecting the peak plantar fascia strain more than other factors.

DISCUSSION

This study investigated the influence of four orthosis design parameters (arch support height, medial posting inclination, heel cup height, and material stiffness) configurations on foot pressure and plantar fascia loading at midstance. The sensitivity of the foot orthosis design combinations indicated that the foot orthoses with higher arch support and medial inclination angle were more effective in reducing peak plantar pressure. For the proximal plantar fascia, arch support and material properties were significant design factors affecting the peak plantar fascia strain more than other factors. These results could contribute to the customized foot orthosis optimization in clinical practice for flat-arched individuals with symptoms.

The previous study normally indicated that arch support height was the first choice for individuals with flatfoot (Su et al., 2017; Wahmkow et al., 2017). Customized foot orthoses with arch support design could maintain the medial longitudinal arch, elevate the arch height, and distribute foot pressure during stance and walking conditions (Su et al., 2017; Peng et al., 2021c). This study indicated that foot orthosis with higher arch support effectively reduced peak plantar pressure. The peak foot pressure occurred on the forefoot region, one of the most critical areas of clinical significance (Tang et al., 2015). A previous study also indicated that total contact insole reduced the peak forefoot pressures in flat-arched patients, which may partially account for the positive symptom-relieving outcomes after customized foot orthoses intervention (Tang et al., 2015). However, the increased arch support height inevitably increased the pressure of the medial midfoot area, which could cause pain in the medial midfoot region after long-term excessive loading. Foot orthoses with excessive arch support height could also cause excessive stress on the joint cartilage and ligaments of the foot-ankle complex (Su et al., 2017). Therefore, foot orthoses with higher arch support height should be carefully adopted based on the symptoms of the foot.

Although foot orthoses with arch support could resist the collapse of the medial longitudinal arch, it should also be noted that this design alone cannot effectively modify the excessive rearfoot eversion (Desmyttere et al., 2018). Some studies have adopted additional foot orthoses design parameters, such as medial posting, to correct the foot misalignment and distribute the foot pressure (Kosonen et al., 2017; Desmyttere et al., 2018). In this study, the foot orthosis with medial inclination angle was also effective in reducing peak plantar pressure. Compared to foot orthoses with only arch support, this study adopted an additional medial posting design, which was believed to effectively control the rearfoot eversion (Desmyttere et al., 2018). Although medial posting could control the rearfoot eversion, the excessive medial inclination angle should be avoided as the medial posting can have adverse effects. One study has investigated the dose-response effects of medial posting and found that greater medial posting inclination angle increased the external knee adduction moment (Telfer et al., 2013). The increased knee adduction moment could elevate the risk of medial

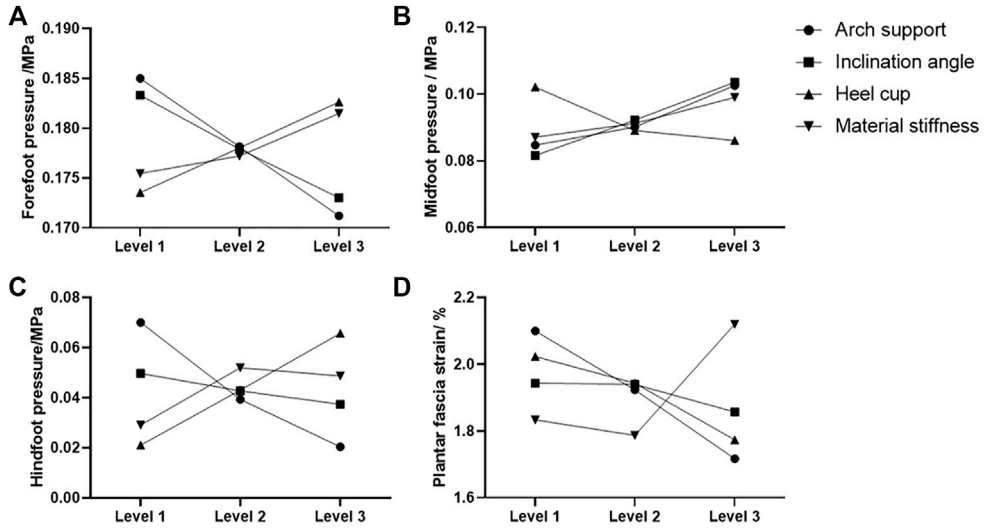

FIGURE 5 | Mean effect of the four design factors at each level on the predicted peak plantar pressure at the **(A)** forefoot, **(B)** midfoot, **(C)** rearfoot regions, and **(D)** predicted proximal plantar fascia strain.

compartment knee osteoarthritis, especially for the elderly (Creaby et al., 2010). In such a case, the clinical symptoms of foot and knee joints should be considered in clinical practice when adopting the medial posting design in the flatfoot intervention.

Different customized orthotic design parameters could be combined to achieve better outcomes, including reduced peak foot pressure and stable foot arch. The material properties can affect foot pressure distribution and medial longitudinal arch stability for customized foot orthoses. Harder insole material can lead to a higher arch height and peak foot pressure (Su et al., 2017). This study also found that stiffer orthoses increased the peak foot pressure. Soft material could be adopted in the specific region to reduce the peak foot pressure in the clinically significant area (Cheng et al., 2021). Meanwhile, the low heel cup can also reduce the peak foot pressure. Therefore, the interaction of the insole shape and materials should be considered in insole optimization for flatfoot patients.

The plantar fascia is one of the most significant passive stabilizers in maintaining the medial longitudinal arch. To identify the plantar fascia loading distribution, this study has adopted the three-dimensional plantar fascia model and considered its interaction with bulk soft tissues, which could withstand the supporting force induced by the ground or insole interface (Peng et al., 2021a; Peng et al., 2021c). The progression of flatfoot deformity could increase the plantar fascia strain and may cause plantar fasciitis (Irving et al., 2006). Previous studies revealed that customized insoles could relieve pain and improve function in runners with running-related overuse injuries (Hirschmüller et al., 2011; Wahmkow et al., 2017). This study indicated that increased arch support could decrease the strain in the proximal region of the plantar fascia. Meanwhile, increased medial posting angle and heel cup height reduced the peak plantar fascia strain in the proximal regions. The influences of arch support height could be more critical than medial posting inclination angle and heel cup height. The reduced plantar fascia strain of the proximal area could account for pain relief in the hindfoot areas (Hsu et al., 2008). The medial posting and heel cup features may be used in conjunction with the arch support design in clinical practice, especially for flat arch individuals with heel pain.

This study has some limitations that should be considered when interpreting the findings and applying them in clinical practice. Firstly, this study adopted the single-subject design for the FE analysis and could ignore the population variability. Because creating a foot-ankle complex involves highly complex boundary and loading conditions, the single-subject models are often used in previous foot-related studies (Wong et al., 2018; Chen et al., 2020; Wong et al., 2020). In this study, we aimed to choose a representative participant of this population to account for the generalizability and endeavored to compromise the external validity issue (Wong et al., 2021). Secondly, the material properties for the specific foot orthoses were the same. Foot orthoses with the same material properties had difficulty achieving reduced foot pressure and stable medial longitudinal arch simultaneously. Future studies could divide the foot orthoses into different regions and adjust material characteristics using different infill rates and patterns with 3D printed techniques. For example, the arch support region could adopt stiffer material, and other regions could adopt softer materials to reduce the peak foot pressure (Cheng et al., 2021). Thirdly, this study has not considered the body weight and foot width when investigating the effects of the arch support height on the foot pressure of the flatfooted participant. Further study should adopt a normalized arch index by simultaneously considering the foot width, foot length, and bodyweight (Lung et al., 2009; Cen et al., 2020). In such a case, the peak pressure could be effectively reduced. Fourthly, this study did not evaluate the foot ligaments stiffness. The foot ligament's laxity could affect the medial longitudinal arch and internal foot loading (Wong et al., 2020). Further simple clinical tests, such as ultrasound evaluation (Chen et al., 2019), could be performed to obtain the level of generalized ligament laxity or hypermobility of the foot, thus facilitating the foot orthoses design.

CONCLUSION

This study investigated the influence of different orthotic design configurations on foot pressure and plantar fascia loading at midstance instant through the muscle-driven FE-orthosis flatfoot model and Taguchi approach. This study adopted a three-dimension plantar fascia geometry, and the interaction between fascia and surrounding soft tissues was considered. The results indicated that the foot orthosis with higher arch support and medial inclination angle was more effective in reducing peak plantar pressure. Meanwhile, medial forefoot posting could be added to modify the forefoot deformity and forefoot pressure. For the proximal plantar fascia, arch support and material properties were more significant design factors for peak plantar fascia strain. Specifically, higher arch support and softer material decreased the peak plantar fascia strain. The statistic-based FE method could provide knowledge-based criteria for designing foot orthosis and fabrication, which can be applied in clinical and commercial settings to treat flatfoot.

DATA AVAILABILITY STATEMENT

The raw data supporting the conclusion of this article will be made available by the authors without undue reservation.

ETHICS STATEMENT

The studies involving human participants were reviewed and approved by the Human Subject Ethics Sub-committee of The Hong Kong Polytechnic University (Number: HSEARS20190124008). The patients/participants provided their written informed consent to participate in this study.

AUTHOR CONTRIBUTIONS

YP, YW, and MZ planned the studies. YW and DW facilitated patient recruitment and the MRI scan. YP, YW, and DW reconstructed the model and conducted the FE analysis. YP, TC, and SC conducted the gait experiment and analysis. TC and SC conducted the muscle force estimation in the musculoskeletal model. GZ and QT handled the data processing and checking. YP conducted the data analysis and wrote the manuscript. MZ obtained funding and supervised the project. All authors contributed to revising and editing the manuscript.

FUNDING

The work was supported by the NSFC granted by the National Natural Science Foundation of China (Grant nos. 11732015 and 11972315).

REFERENCES

Akrami, M., Qian, Z., Zou, Z., Howard, D., Nester, C. J., and Ren, L. (2018). Subject-specific Finite Element Modelling of the Human Foot Complex during Walking: Sensitivity Analysis of Material Properties, Boundary and Loading Conditions. *Biomech. Model. Mechanobiol* 17, 559–576. doi:10.1007/s10237-017-0978-3

Banwell, H. A., Mackintosh, S., and Thewlis, D. (2014). Foot Orthoses for Adults with Flexible Pes Planus: a Systematic Review. *J. Foot Ankle Res.* 7, 23. doi:10.1186/1757-1146-7-23

Cen, X., Gao, L., Yang, M., Liang, M., Bíró, I., and Gu, Y. (2021). Arch-support Induced Changes in Foot-Ankle Coordination in Young Males with Flatfoot during Unplanned Gait Termination. *Jcm* 10, 5539. doi:10.3390/jcm10235539

Cen, X., Xu, D., Baker, J. S., and Gu, Y. (2020). Effect of Additional Body Weight on Arch index and Dynamic Plantar Pressure Distribution during Walking and Gait Termination. *PeerJ* 8, e8998. doi:10.7717/peerj.8998

Chen, T. L.-W., Agresta, C. E., Lipps, D. B., Provenzano, S. G., Hafer, J. F., Wong, D. W.-C., et al. (2019). Ultrasound Elastographic Assessment of Plantar Fascia in Runners Using Rearfoot Strike and Forefoot Strike. *J. Biomech.* 89, 65–71. doi:10.1016/j.jbiomech.2019.04.013

Chen, T. L.-W., Wong, D. W.-C., Peng, Y., and Zhang, M. (2020). Prediction on the Plantar Fascia Strain Offload upon Fascia Taping and Low-Dye Taping during Running. *J. Orthopaedic Translation* 20, 113–121. doi:10.1016/j.jot.2019.06.006

Chen, W.-M., Lee, S.-J., and Lee, P. V. S. (2015a). Plantar Pressure Relief under the Metatarsal Heads - Therapeutic Insole Design Using Three-Dimensional Finite Element Model of the Foot. *J. Biomech.* 48, 659–665. doi:10.1016/j.jbiomech.2014.12.043

Chen, W.-M., Lee, T., Lee, P. V.-S., Lee, J. W., and Lee, S.-J. (2010a). Effects of Internal Stress Concentrations in Plantar Soft-Tissue-A Preliminary Three-Dimensional Finite Element Analysis. *Med. Eng. Phys.* 32, 324–331. doi:10.1016/j.medengphy.2010.01.001

Chen, W.-P., Ju, C.-W., and Tang, F.-T. (2003). Effects of Total Contact Insoles on the Plantar Stress Redistribution: a Finite Element Analysis. *Clin. Biomech.* 18, S17–S24. doi:10.1016/s0268-0033(03)00080-9

Chen, Y.-C., Lou, S.-Z., Huang, C.-Y., and Su, F.-C. (2010b). Effects of Foot Orthoses on Gait Patterns of Flat Feet Patients. *Clin. Biomech.* 25, 265–270. doi:10.1016/j.clinbiomech.2009.11.007

Chen, Y.-N., Chang, C.-W., Li, C.-T., Chang, C.-H., and Lin, C.-F. (2015b). Finite Element Analysis of Plantar Fascia during Walking. *Foot Ankle Int.* 36, 90–97. doi:10.1177/1071100714549189

Cheng, H.-Y. K., Lin, C.-L., Wang, H.-W., and Chou, S.-W. (2008). Finite Element Analysis of Plantar Fascia under Stretch-The Relative Contribution of Windlass Mechanism and Achilles Tendon Force. *J. Biomech.* 41, 1937–1944. doi:10.1016/j.jbiomech.2008.03.028

Cheng, K.-W., Peng, Y., Chen, T. L.-W., Zhang, G., Cheung, J. C.-W., Lam, W.-K., et al. (2021). A Three-Dimensional Printed Foot Orthosis for Flexible Flatfoot: An Exploratory Biomechanical Study on Arch Support Reinforcement and Undercut. *Materials* 14, 5297. doi:10.3390/ma14185297

Cheung, J. T.-M., and Zhang, M. (2005). A 3-dimensional Finite Element Model of the Human Foot and Ankle for Insole Design. *Arch. Phys. Med. Rehabil.* 86, 353–358. doi:10.1016/j.apmr.2004.03.031

Cheung, J. T.-M., and Zhang, M. (2008). Parametric Design of Pressure-Relieving Foot Orthosis Using Statistics-Based Finite Element Method. *Med. Eng. Phys.* 30, 269–277. doi:10.1016/j.medengphy.2007.05.002

Cheung, R. T. H., Chung, R. C. K., and Ng, G. Y. F. (2011). Efficacies of Different External Controls for Excessive Foot Pronation: a Meta-Analysis. *Br. J. Sports Med.* 45, 743–751. doi:10.1136/bjsm.2010.079780

Cifuentes-De La Portilla, C., Larrainzar-Garijo, R., and Bayod, J. (2019). Biomechanical Stress Analysis of the Main Soft Tissues Associated with the Development of Adult Acquired Flatfoot Deformity. *Clin. Biomech.* 61, 163–171. doi:10.1016/j.clinbiomech.2018.12.009

Cobb, S. C., Tis, L. L., Johnson, J. T., Wang, Y. T., and Geil, M. D. (2011). Custom-molded Foot-Orthosis Intervention and Multisegment Medial Foot Kinematics during Walking. *J. Athl Train.* 46, 358–365. doi:10.4085/1062-6050-46.4.358

Cole, C., Seto, C., and Gazewood, J. (2005). Plantar Fasciitis: Evidence-Based Review of Diagnosis and Therapy. *Am. Fam. Physician* 72, 2237–2242.

Creaby, M. W., Wang, Y., Bennell, K. L., Hinman, R. S., Metcalf, B. R., Bowles, K.-A., et al. (2010). Dynamic Knee Loading Is Related to Cartilage Defects and

Tibial Plateau Bone Area in Medial Knee Osteoarthritis. *Osteoarthritis and Cartilage* 18, 1380–1385. doi:10.1016/j.joca.2010.08.013

Desmyttere, G., Hajizadeh, M., Bleau, J., and Begon, M. (2018). Effect of Foot Orthosis Design on Lower Limb Joint Kinematics and Kinetics during Walking in Flexible Pes Planovalgus: A Systematic Review and Meta-Analysis. *Clin. Biomech.* 59, 117–129. doi:10.1016/j.clinbiomech.2018.09.018

Flores, D. V., Mejía Gómez, C., Fernández Hernando, M., Davis, M. A., and Pathria, M. N. (2019). Adult Acquired Flatfoot Deformity: Anatomy, Biomechanics, Staging, and Imaging Findings. *Radiographics* 39, 1437–1460. doi:10.1148/rg.2019190046

Hirschmüller, A., Baur, H., Müller, S., Helwig, P., Dickhuth, H.-H., and Mayer, F. (2011). Clinical Effectiveness of Customised Sport Shoe Orthoses for Overuse Injuries in Runners: a Randomised Controlled Study. *Br. J. Sports Med.* 45, 959–965. doi:10.1136/bjsm.2008.055830

Hsu, Y.-C., Gung, Y.-W., Shih, S.-L., Feng, C.-K., Wei, S.-H., Yu, C.-h., et al. (2008). Using an Optimization Approach to Design an Insole for Lowering Plantar Fascia Stress-A Finite Element Study. *Ann. Biomed. Eng.* 36, 1345–1352. doi:10.1007/s10439-008-9516-x

Hurd, W. J., Kavros, S. J., and Kaufman, K. R. (2010). Comparative Biomechanical Effectiveness of Over-the-counter Devices for Individuals with a Flexible Flatfoot Secondary to Forefoot Varus. *Clin. J. Sport Med.* 20, 428–435. doi:10.1097/jsm.0b013e3181fb539f

Irving, D. B., Cook, J. L., and Menz, H. B. (2006). Factors Associated with Chronic Plantar Heel Pain: a Systematic Review. *J. Sci. Med. Sport* 9, 11–22. doi:10.1016/j.jsams.2006.02.004

Karna, S. K., and Sahai, R. (2012). An Overview on Taguchi Method. *Int. J. Math. Eng. Manag.* 1, 1–7.

Kodithuwakku Arachchige, S. N. K., Chander, H., and Knight, A. (2019). Flatfeet: Biomechanical Implications, Assessment and Management. *The Foot* 38, 81–85. doi:10.1016/j.foot.2019.02.004

Kogler, G., Solomonidis, S., and Paul, J. (1996). Biomechanics of Longitudinal Arch Support Mechanisms in Foot Orthoses and Their Effect on Plantar Aponeurosis Strain. *Clin. Biomech.* 11, 243–252. doi:10.1016/0268-0033(96)00019-8

Kogler, G., Solomonidis, S., and Paul, J. (1995). *In Vitro* method for Quantifying the Effectiveness of the Longitudinal Arch Support Mechanism of a Foot Orthosis. *Clin. Biomech.* 10, 245–252. doi:10.1016/0268-0033(95)99802-9

Kosonen, J., Kulmala, J.-P., Müller, E., and Avela, J. (2017). Effects of Medially Posted Insoles on Foot and Lower Limb Mechanics across Walking and Running in Overpronating Men. *J. Biomech.* 54, 58–63. doi:10.1016/j.jbiomech.2017.01.041

Lee, M. S., Vanore, J. V., Thomas, J. L., Catanzariti, A. R., Kogler, G., Kravitz, S. R., et al. (2005). Diagnosis and Treatment of Adult Flatfoot. *J. Foot Ankle Surg.* 44, 78–113. doi:10.1053/j.jfas.2004.12.001

Lee, W. C. C., and Zhang, M. (2005). Design of Monolimb Using Finite Element Modelling and Statistics-Based Taguchi Method. *Clin. Biomech.* 20, 759–766. doi:10.1016/j.clinbiomech.2005.03.015

Lewis, G. (2003). Finite Element Analysis of a Model of a Therapeutic Shoe: Effect of Material Selection for the Outsole. *Biomed. Mater. Eng.* 13, 75–81.

Lung, C.-W., Yang, S.-W., and Hsieh, L.-F. (2009). Is the Arch Index Meaningful. *Korean J. Sport Biomech.* 19, 187–196. doi:10.5103/kjsb.2009.19.2.187

Murley, G. S., Landorf, K. B., and Menz, H. B. (2010). Do foot Orthoses Change Lower Limb Muscle Activity in Flat-Arched Feet towards a Pattern Observed in normal-arched Feet? *Clin. Biomech.* 25, 728–736. doi:10.1016/j.clinbiomech.2010.05.001

Murley, G. S., Tan, J. M., Edwards, R. M., De Luca, J., Munteanu, S. E., and Cook, J. L. (2014). Foot Posture Is Associated with Morphometry of the Peroneus Longus Muscle, Tibialis Anterior Tendon, and Achilles Tendon. *Scand. J. Med. Sci. Sports* 24, 535–541. doi:10.1111/sms.12025

Peng, Y., Niu, W., Wong, D. W.-C., Wang, Y., Chen, T. L.-W., Zhang, G., et al. (2021a). Biomechanical Comparison Among Five Mid/hindfoot Arthrodeses Procedures in Treating Flatfoot Using a Musculoskeletal Multibody Driven Finite Element Model. *Computer Methods Programs Biomed.* 211, 106408. doi:10.1016/j.cmpb.2021.106408

Peng, Y., Wong, D. W.-C., Chen, T. L.-W., Wang, Y., Zhang, G., Yan, F., et al. (2021c). Influence of Arch Support Heights on the Internal Foot Mechanics of Flatfoot during Walking: A Muscle-Driven Finite Element Analysis. *Comput. Biol. Med.* 132, 104355. doi:10.1016/j.compbiomed.2021.104355

Peng, Y., Wong, D. W.-C., Wang, Y., Chen, T. L.-W., Tan, Q., Chen, Z., et al. (2020). Immediate Effects of Medially Posted Insoles on Lower Limb Joint Contact Forces in Adult Acquired Flatfoot: a Pilot Study. *Ijerph* 17, 2226. doi:10.3390/ijerph17072226

Peng, Y., Wong, D. W.-C., Wang, Y., Chen, T. L.-W., Zhang, G., Yan, F., et al. (2021b). Computational Models of Flatfoot with Three-Dimensional Fascia and Bulk Soft Tissue Interaction for Orthosis Design. *Med. Novel Technology Devices* 9, 100050. doi:10.1016/j.medntd.2020.100050

Richie, D. H., Jr (2007). Biomechanics and Clinical Analysis of the Adult Acquired Flatfoot. *Clin. Podiatric Med. Surg.* 24, 617–644. doi:10.1016/j.cpm.2007.07.003

Su, S., Mo, Z., Guo, J., and Fan, Y. (2017). The Effect of Arch Height and Material Hardness of Personalized Insole on Correction and Tissues of Flatfoot. *J. Healthc. Eng.* 2017, 8614341. doi:10.1155/2017/8614341

Tang, S. F.-T., Chen, C.-H., Wu, C.-K., Hong, W.-H., Chen, K.-J., and Chen, C.-K. (2015). The Effects of Total Contact Insole with Forefoot Medial Posting on Rearfoot Movement and Foot Pressure Distributions in Patients with Flexible Flatfoot. *Clin. Neurol. Neurosurg.* 129, S8–S11. doi:10.1016/s0303-8467(15)30004-4

Telfer, S., Abbott, M., Steultjens, M. P. M., and Woodburn, J. (2013). Dose-response Effects of Customised Foot Orthoses on Lower Limb Kinematics and Kinetics in Pronated Foot Type. *J. Biomech.* 46, 1489–1495. doi:10.1016/j.jbiomech.2013.03.036

Wahmkow, G., Cassel, M., Mayer, F., and Baur, H. (2017). Effects of Different Medial Arch Support Heights on Rearfoot Kinematics. *PLOS ONE* 12, e0172334. doi:10.1371/journal.pone.0172334

Wang, Y., Wong, D. W.-C., and Zhang, M. (2016). Computational Models of the Foot and Ankle for Pathomechanics and Clinical Applications: A Review. *Ann. Biomed. Eng.* 44, 213–221. doi:10.1007/s10439-015-1359-7

Wong, D. W., Wang, Y., Chen, T. L., Yan, F., Peng, Y., Tan, Q., et al. (2020). Finite Element Analysis of Generalized Ligament Laxity on the Deterioration of Hallux Valgus Deformity (Bunion). *Front. Bioeng. Biotechnol.* 8, 571192. doi:10.3389/fbioe.2020.571192

Wong, D. W.-C., Chen, T. L.-W., Peng, Y., Lam, W.-K., Wang, Y., Ni, M., et al. (2021). An Instrument for Methodological Quality Assessment of Single-Subject Finite Element Analysis Used in Computational Orthopaedics. *Med. Novel Technology Devices* 11, 100067. doi:10.1016/j.medntd.2021.100067

Wong, D. W.-C., Wang, Y., Leung, A. K.-L., Yang, M., and Zhang, M. (2018). Finite Element Simulation on Posterior Tibial Tendinopathy: Load Transfer Alteration and Implications to the Onset of Pes Planus. *Clin. Biomech.* 51, 10–16. doi:10.1016/j.clinbiomech.2017.11.001

Yu, J., Wong, D. W.-C., Zhang, H., Luo, Z.-P., and Zhang, M. (2016). The Influence of High-Heeled Shoes on Strain and Tension Force of the Anterior Talofibular Ligament and Plantar Fascia during Balanced Standing and Walking. *Med. Eng. Phys.* 38, 1152–1156. doi:10.1016/j.medengphy.2016.07.009

Zhang, B., and Lu, Q. (2020). A Current Review of Foot Disorder and Plantar Pressure Alternation in the Elderly. *J. Phys. Act. Health* 4. doi:10.5334/paah.57

Zhang, H., Lin Lv, M., Yang, J., Niu, W., Cheung, J. C., Sun, W., et al. (2020). Computational Modelling of Foot Orthosis for Midfoot Arthritis: a Taguchi Approach for Design Optimization. *Acta Bioeng. Biomech.* 22, 75–83. doi:10.37190/abb-01694-2020-03

Conflict of Interest: The authors declare that the research was conducted in the absence of any commercial or financial relationships that could be construed as a potential conflict of interest.

Publisher's Note: All claims expressed in this article are solely those of the authors and do not necessarily represent those of their affiliated organizations or those of the publisher, the editors, and the reviewers. Any product that may be evaluated in this article, or claim that may be made by its manufacturer, is not guaranteed or endorsed by the publisher.

frontiers in Bioengineering and Biotechnology

ORIGINAL RESEARCH
published: 15 March 2022
doi: 10.3389/fbioe.2022.855114

Evaluation of Ankle Fractures in 228 Patients From a Single Center Using Three-Dimensional Computed Tomography Mapping

Jianshuang Zeng[1,2,3], Cheng Xu[2,3], Gaoxiang Xu[2,3], Wupeng Zhang[1,2,3], Daofeng Wang[2,3], Hua Li[2,3], Xuewen Gan[4], Ying Xiong[4], Jiantao Li[2,3], Licheng Zhang[2,3]* and Peifu Tang[1,2,3]**

[1]School of Medicine, Nankai University, Tianjin, China, [2]Senior Department of Orthopedics, The Fourth Medical Center of PLA General Hospital, Beijing, China, [3]National Clinical Research Center for Orthopedics, Sports Medicine and Rehabilitation, Beijing, China, [4]Department of Orthopedics, Yanan Hospital, Kunming Medical University, Kunming, China

OPEN ACCESS

Edited by:
Mohammad Nikkhoo,
Islamic Azad University, Iran

Reviewed by:
Weitao Jia,
Shanghai Jiao Tong University, China
Rui B. Ruben,
Polytechnic Institute of Leiria, Portugal

***Correspondence:**
Jiantao Li
lijiantao618@163.com
Licheng Zhang
zhanglcheng218@126.com
Peifu Tang
pftang301@163.com

Specialty section:
This article was submitted to Biomechanics, a section of the journal Frontiers in Bioengineering and Biotechnology

Received: 14 January 2022
Accepted: 25 February 2022
Published: 15 March 2022

Citation:
Zeng J, Xu C, Xu G, Zhang W, Wang D, Li H, Gan X, Xiong Y, Li J, Zhang L and Tang P (2022) Evaluation of Ankle Fractures in 228 Patients From a Single Center Using Three-Dimensional Computed Tomography Mapping. Front. Bioeng. Biotechnol. 10:855114. doi: 10.3389/fbioe.2022.855114

Purpose: The ankle joint has a complex anatomy structure with many causative factors and various injury mechanisms, and the clinical presentation of ankle fractures is diverse. This study aimed to analyze the characteristics of ankle fractures by applicating three-dimensional fracture line mapping technique.

Methods: A retrospective study was conducted on 228 patients with ankle fractures. Three-dimensional reconstruction was performed by CT images and the fracture reconstruction model was superimposed onto a standard model of the tibiofibula for fracture line drawing. Then the fracture lines were converted into a three-dimensional coordinate point data set. And the fracture line maps as well as the fracture line heat maps were generated in 3-Matic software and Unigraphics NX software, respectively.

Results: The dense area of the fibular fracture lines was located above the tibiofibular joint ligament and wrapped obliquely around the distal fibula from the anterior edge of the fibular neck. The fibular fracture line could be divided into three categories according to the degree of denseness. The dense area of the tibial fracture line is located within the anterior tibial fornix, the anterolateral corner, and the fibular notch. The tibial fracture lines can be classified into four categories according to the density of the fracture lines. The combined medial malleolus + posterior malleolar fracture line situation was found to be not encompassed by the existing AO and Lauge-Hansen (LH) classification systems according to this classification.

Conclusion: The 3D fracture line mapping technique can better reflect the distribution of ankle fracture lines and could help to establish a new ankle fracture typing system in the future.

Keywords: ankle fracture, LH classification, AO classification, 3D mapping, 3DCT

INTRODUCTION

Ankle fractures account for approximately 3.9% of total body fractures (Koval et al., 2005), of which the incidence has a tendency to increase year by year with the aging process of the population and social development. Since the complex anatomical structure of the ankle joint, the various causative factors, and the mechanism of injury containing both vertical extensive force at a strong level and rotational extensive force at a moderate level, ankle fractures are clinically presented in various forms. How to comprehensively and accurately assess ankle fractures, understand fracture injury mechanisms and select appropriate treatment methods are also very important in clinical practice. As the main method to describe the fracture injury pattern, fracture classification is the most scientific, simple, and practical method to analyze the fracture injury mechanism, guide the treatment, and judge the prognosis, which plays a vital role in clinical practice. However, the existing common classification of ankle fractures, the LH and AO classification, are based on plain film diagnosis. However, with the popularization of CT and three-dimensional (3D) CT technology in recent years, the research on ankle fractures in the industry has deepened, and the understanding of fracture morphology, fracture line distribution, fracture pattern, and fracture injury mechanism has become more advanced. In 2000, Hanse reported a special type of posterior fracture of the inferior articular surface of the tibia, which was named "Posterior Pilon fracture" (Sigvaard and Hansen, 2000). The fracture line was distributed in the coronal plane of the posterior malleolus and extended to the anterior medial malleolus. Unlike the traditional posterior malleolus fracture, the fracture fragment was much bigger and proximally displaced, and the articular surface was collapsed without comminuted fracture fragment, which cannot be explained by the existing ankle fracture classification.

Other findings suggest that articular surface collapse is an important factor affecting the prognosis of ankle fractures (Berkes et al., 2013; Hoogendoorn, 2017), and Jan Bartoníček et al. (Bartoníček et al., 2017) summarized the factors related to posterior malleolus prognosis and concluded that there was a significant correlation between bone mass size, articular surface flatness, and ankle stability and the choice of treatment modality and treatment outcome.

However, none of the above is captured by the existing classification system. The 3D fracture line mapping and heatmap is a new technique developed in recent years (Cole et al., 2013; Yang et al., 2018), which can clearly and visually display the distribution and frequency of fracture lines. Nowadays, it has been widely used in various fracture sites, but currently, the studies on ankle fracture are only limited to one part of the ankle fracture (lateral, medial, or posterior malleolar) (Yun et al., 2016; Blom et al., 2019; Peng, 2019; Yu,

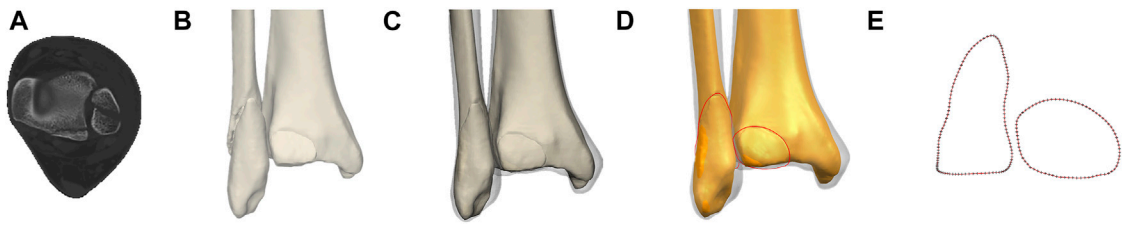

FIGURE 1 | The method used for the mapping of ankle fracture. **(A)** CT image of ankle fracture. **(B)** Major fragments were reconstructed in Mimics software. **(C)** Virtual reduction and registeration with the transparent standard tibiofibular template in 3-matic software. **(D)** Delineation of fracture lines on the template in Unigraphics NX software. **(E)** Dataset extraction of fracture curves in AutoCAD software at 0.1 mm spacing equidistant.

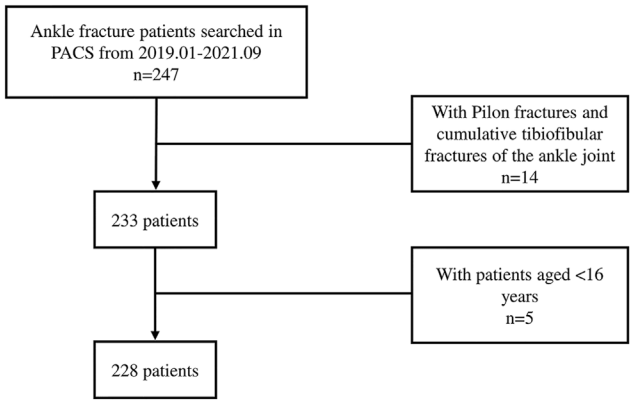

FIGURE 2 | Flowchart illustrates the process of patient inclusion. PACS, Picture Archiving and Communication Systems.

TABLE 1 | Patient characteristics and fracture patterns organized by two primary categories of fracture.

Character	Data (*n* = 228)	Character	Data (*n* = 228)
Female	101	AO classification	
Male	127	A1	6 (3%)
Age	42.6 years (16–87)	A2	13 (6%)
16–40y	42%	A3	11 (5%)
41–70y	51%	B1	49 (21%)
71–above	7%	B2	19 (8%)
LH classification		B3	85 (37%)
SER1	0	C1	13 (6%)
SER2	49 (21%)	C2	10 (4%)
SER3	30 (13%)	C3	3 (1%)
SER4	76 (33%)	Unspecified fracture lines	
SA1	6 (3%)	LH	10 (4%)
SA2	11 (5%)	AO	19 (8%)
PER1	16 (7%)		
PER2	2 (1%)		
PER3	5 (2%)		
PER4	16 (7%)		
PA1	0		
PA2	0		
PA3	6 (3%)		

**LH, Lauge-Hansen; SER, supination-external/eversion rotation; SA, supination-adduction; PA, pronation-abduction; PER, pronation-external rotation; AO, AO/OTA classification.*

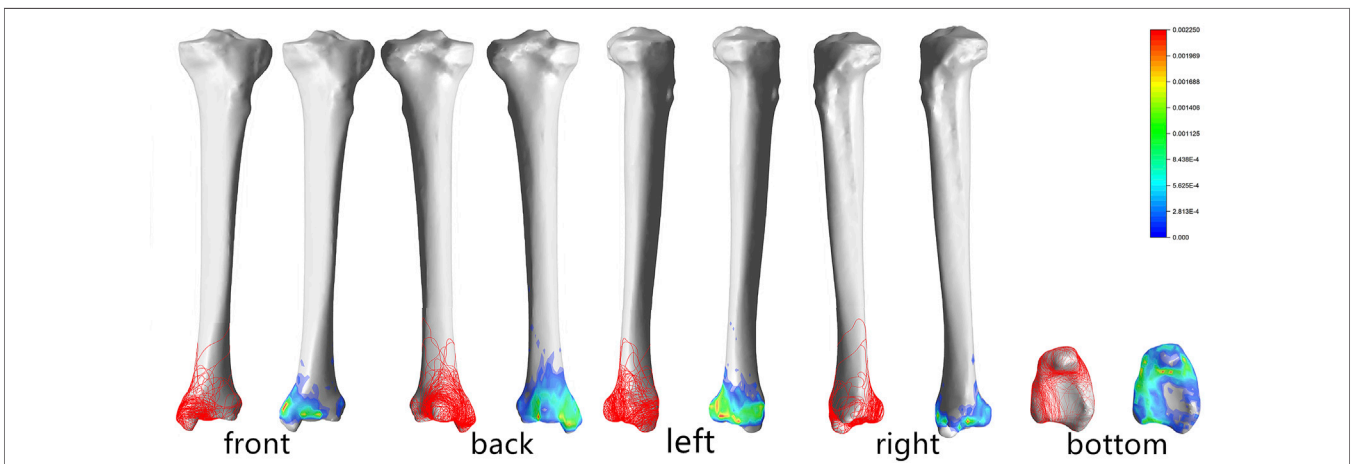

FIGURE 3 | Distribution and hotpots of fractures on tibia: the front view, the back view, the left view, the right view and the bottom view (from left to right). The scale of heatmap represents relative frequency of fracture lines. From the blue area to the red area, the relative frequency gradually increases.

2019; Yu et al., 2021), and there is no relevant study for the whole ankle fracture line. Therefore, this study aims to investigate the characteristics of the overall fracture line distribution in ankle fractures by using 3D CT imaging combined with heatmap techniques to explore the pattern of ankle fractures.

MATERIALS AND METHODS

Study Eligibility Criteria

Inclusion criteria: 1). Patients aged >16 years; 2). With closed ankle fractures; 3). With preoperative CT images from our institution and the CT scan data is qualified for 3D reconstruction.

Exclusion criteria: 1). Patients with pathological fractures; 2). With open fractures; 3). With Pilon fractures and cumulative tibiofibular fractures of the ankle joint; 4). With a previous history of ipsilateral ankle deformity.

CT Technique

All Computed Tomography (CT) examinations were performed using conventional cross-sectional scans and performed on 16-detector row CT scanners (United Imaging uCT 510 [Shanghai, China]). Scanning conditions were as follows: voltage 120 kV, current 150 mA, pitch 0.8–0.9 mm, layer thickness 3 mm, and reconstruction matrix 512 × 512. The scan area was as follows: distal tibiofibular includes ankle

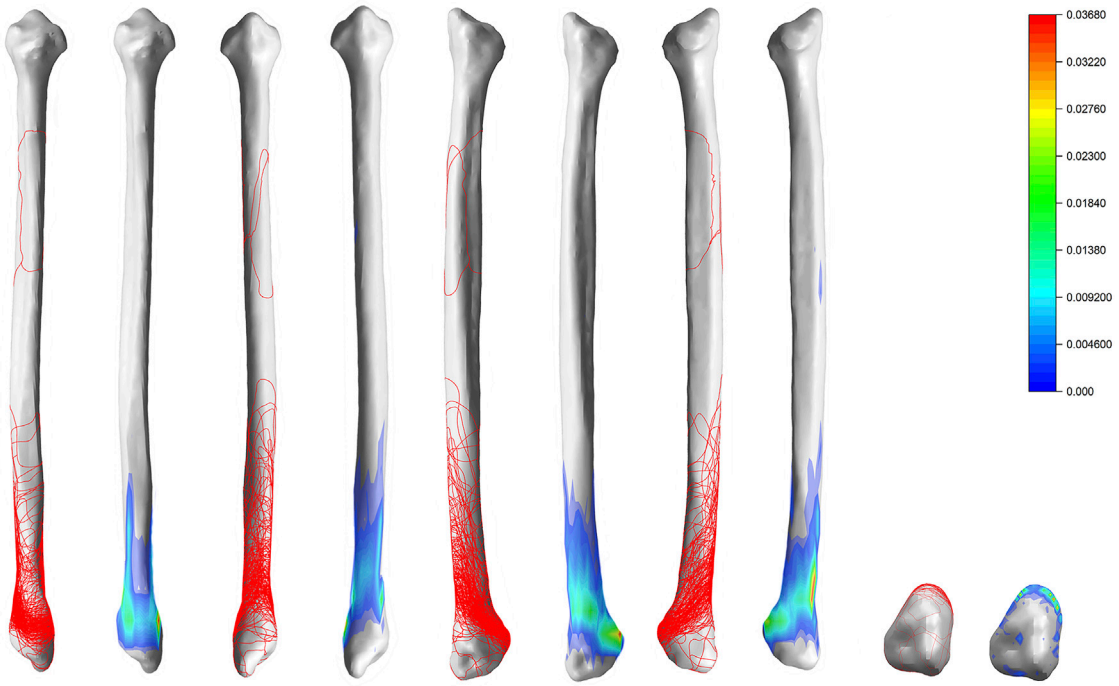

FIGURE 4 | Distribution and hotpots of fractures on fibula: the front view, the back view, the left view, the right view and the bottom view (from left to right). The scale of heatmap represents relative frequency of fracture lines. From the blue area to the red area, the relative frequency gradually increases.

fracture line to mid-metatarsal segment, scan plane parallelling to the cross-section of the tibia.

Fracture Mapping

(1) DICOM (Initial Digital Imaging and Communications in Medicine) data of a healthy male adult have been imported into Mimics 21.0 software (Materialise, Leuven, Belgium) for 3D reconstruction, keeping the intact tibial and fibular as standard templates.
(2) The DICOM data of the selected 228 patients were imported into Mimics 21.0 software (Materialise, Leuven, Belgium) for 3D reconstruction and virtual reduction of the ankle fracture fragment.
(3) Then the registeration between 3D reconstructed fracture model and the standard tibiofibular template being aligned was conducted in 3-Matic 13.0 (Materialise, Leuven, Belgium). The alignment process including rotation, translation and scale adjustment in five fields of view (anterior, posterior, internal, external and inferior tibiofibular articular surfaces).
(4) After the registration, the 3D reconstructed fracture model was imported into Unigraphics NX 12.0 (Siemens PLM Software, Co., Ltd., Plano, TX, United States) together with the tibiofibular standard template, and then the 3D fracture lines were delinated on the skeletal standard template and exported in iges format, grouped according to different fracture classifications.
(5) The same classification of fractures curves were imported into 3-Matic software and overlaid on the tibiofibular standard template to obtain the 3D fracture line distribution map.
(6) Fracture lines dataset was extracted from 3D fracture curves in AutoCAD 2020 (Autodesk Inc., San Rafael, CA, United States) at 0.1 mm spacing equidistant in the form of (x, y, z).
(7) The dataset obtained in step 6 was then imported into Originlab 9.0 (OriginLab, Hampton, MA, United States) to produce and generate heatmap of the fracture line distribution (**Figure 1**).

Data Analysis

A descriptive study was performed to analyze the fracture patterns of patients. The general information was summarized as means ± standard deviations for continuous variables and as frequencies and percentages for categorical variables. The fracture maps illustrated the fracture location, while the heatmap illustrated the spatial differentiation of the fracture lines.

RESULTS

A total of 228 ankle fracture patients (from 2019.01-2021.09) were retrieved from the PACS (Picture Archiving and Communication Systems) of Chinese PLA General Hospital (**Figure 2**). General information and fracture characteristics were summarized in

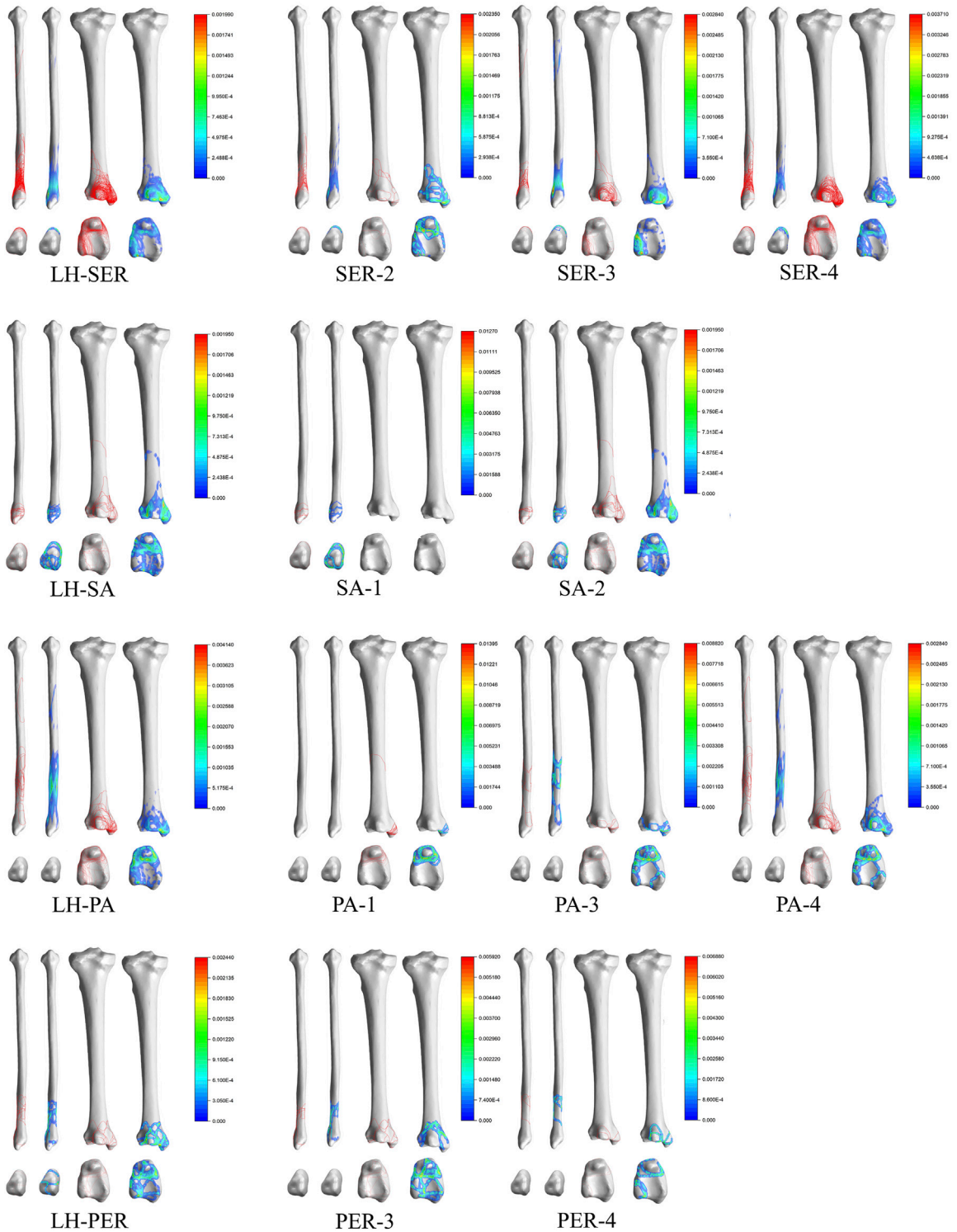

FIGURE 5 | Distribution and hotpots of fractures by Lauge-Hansen classification. The scale of heatmap represents relative frequency of fracture lines. From the blue area to the red area, the relative frequency gradually increases.

Table 1. The cohort of 228 patients (including 127 men, 101 women) had a wide range of ankle fracture types. The highest percentage of fracture type was supination-external/eversion rotation (SER) with 67% in the LH classification, the least was pronation-external rotation (PA) with only 6 patients, and the number of cases of type supination-adduction (SA) and pronation-abduction (PER) was

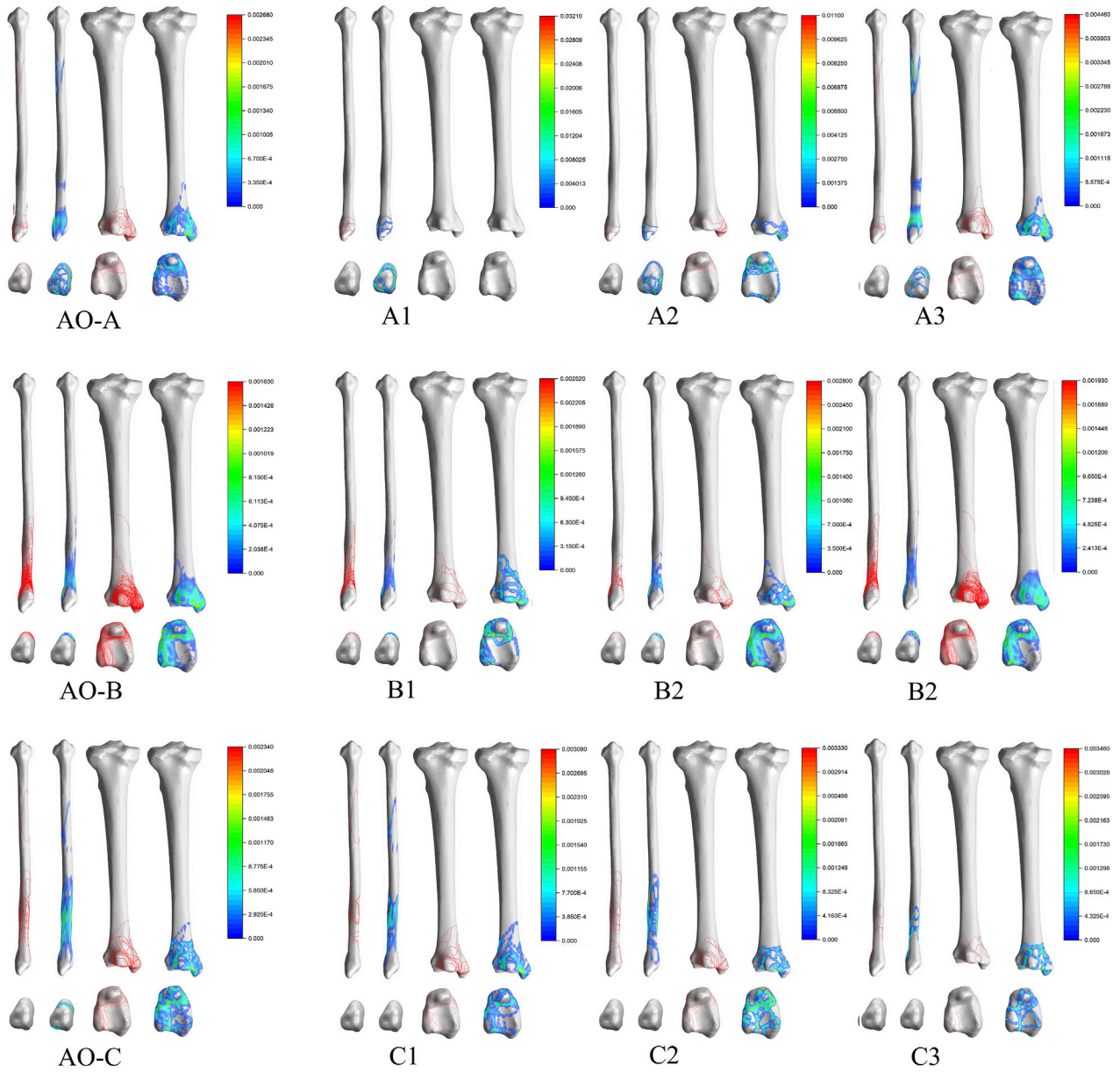

FIGURE 6 | Distribution and hotpots of fractures by AO classification. The scale of heatmap represents relative frequency of fracture lines. From the blue area to the red area, the relative frequency gradually increases.

close to 8% (17 cases) and 17% (39 cases), respectively. The highest percentage of type SER was stage IV with an overall percentage of about 33%. The highest percentage of the AO classification was type B with a high percentage of 66%. The proportion of B1, B2, and B3 was close to 21,8 and 37%, respectively, where the proportion of types A and C was close to 14 and 11%, respectively.

3D Mapping of Tibia Fracture Lines

Front view: The tibial fracture lines were mainly distributed on the lateral surface of the medial malleolus and the anteromedial corner of the tibial fornix. On the heatmap, the hot spots were also on the lateral surface of the medial malleolar and the anteromedial corner of the tibial fornix.

Back view: The fracture lines were distributed around the Volkmann's tuberosity and on the medial malleolar surface, and the hot spot was located at the anteromedial corner of the tibial fornix.

Left view: The fracture lines extended from the anteromedial corner of the tibial fornix to the anterolateral corner of the tibial fornix and from the medial malleolar surface to the tibial fornix. The hot spot was located at the anterolateral corner of the tibial vault.

Right view: The fracture lines were distributed along the fibular notch toward the subtalar articular surface.

TABLE 2 | The method used for the mapping of ankle fracture.

Classification system	Medial malleolus fracture	Medial malleolus + posterior malleolus fracture	Chaput fracture	Posterior malleolus fracture	Total no. of unspecified fracture lines
LH	9	5	2	3	19
AO	0	4	2	4	10

**LH, Lauge-Hansen classification; AO, AO/OTA classification.*

TABLE 3 | A summary of fracture lines of fibula and tibia based on the 3D maps and heatmaps of fracture line distribution.

Anatomic sites	Classification	Description
Fracture lines of fibula	a	Located under the joint tibiofibular ligament and wrapped around the fibular head in a horizontal loop
	b	Located above the tibiofibular joint ligament, with the lowest point located at the anterior edge of the fibula, where the fibular head expands, and travels posteriorly and obliquely to wrap around the distal end of the fibula
	c	Located on the joint tibiofibular ligament and may wrap around the fibular stem in a circular or oblique fashion
Fracture lines of tibia	A	Over the medial malleolar joint surface, sub horizontally encircling the medial malleolar in a circular fashion
	B	surrounding the Volkmann's tuberosity in a ring shape
	C	Similar to type B, but the annular fracture line was larger in diameter and extended upward from the lateral fibular notch of the tibia, crossing the anteromedial corner of the tibial fornix above, behind, and below Volkmann's tuberosity, entering the subtalar articular surface, and running medially along the medial margin of the distal tibia to join the fibular notch fracture
	D	The fracture line run longitudinally from the subtalar articular surface up through the medial or posterior malleolus

Bottom view: A portion of the fracture lines were distributed mainly at the interface between the medial malleolar facet and the subtalar articular facet, while another portion of the fracture line extended downward from the medial sulcus and along the medial edge of the subtalar articular facet. The lesion was located at the lateral edge of the distal lower tibial articular surface (**Figure 3**).

3D Mapping of Fibula Fracture Lines

The fracture lines of the fibula were mainly distributed in a circular pattern, basically symmetrically along with the lower projection of the fibular neck, and traveled obliquely posteriorly past the most pronounced projection of the fibular head to converge just above the posterior edge of the fibula (**Figure 4**).

3D Mapping of L-H Classification

SER: Stage II fracture line is distributed obliquely near the fibular neck. Stage III adds a fracture line wrapped around Volkmann's tuberosity to stage II. The hot spot on stage III is mainly located at the inferior edge of Volkmann's tuberosity. Stage IV adds a circumferential fracture line around the medial malleolar on the basis of stage III.

SA: Stage I fracture line is mainly located on the lower part of the fibular head, and stage II fracture line is mainly located on the surface of the medial malleolar.

PA: Stage I fracture line is mainly distributed in the medial malleolar and is circular through the anteromedial and anterolateral angles of the tibial fornix and the medial surface of the ankle joint. Stage II fracture line is mainly located in the fibular stem. Stage IV mainly crosses the fibular stem and surrounds the Volkmann's tuberosity and the medial malleolar.

PER: There were 0 cases of stage I and stage II in this study. There were only 6 cases of stage III with fracture lines distributed distal to the fibular stem (above the tibiofibular joint ligament), and there was no significant regularity in the distribution of stage III. Stage IV fractures were characterized by a circumferential fracture line extending above the tibiofibular joint and encircling the posterior and medial malleolar (**Figure 5**).

3D Mapping of AO Classification

Type A: Type A1 fracture lines were mainly distributed in the lower part of the fibular head, under the tibiofibular joint ligament, and pass through the enlarged part of the fibular head and surround it in a circular pattern. Type A2 added a circular fracture line around the medial malleolar on the basis of Type A1, with hot spots located mainly on the medial aspect of the medial malleolar, the anteromedial corner of the tibial fornix, and the prominent area below the fibular joint fossa. Type A3 fracture lines were distributed in the lower part of the fibular head, posterior malleolar, and medial malleolar, but no obvious pattern was seen on the heatmap.

Type B: Type B1 fracture lines were obliquely distributed over the tibiofibular joint ligament and around the Volkmann's tuberosity and the medial malleolar. Type B2 was similar to Type B1 in that the tibial fracture line was distributed along the medial edge of the medial malleolar and wrapped around the medial malleolar. Type B3 is similar to Type B2 but is more densely distributed.

Type C: Type C3 fracture lines were distributed closer to the distal fibula than Type C2, and the portion of the fracture line on the tibia was similar to Type C2 (**Figure 6**).

DISCUSSION

As far as the published literature is concerned, although some studies have been conducted to perform fracture line mapping of ankle fractures using fracture line mapping techniques and heatmap techniques, they were limited to medial malleolus

FIGURE 7 | Different colored areas and corresponding letters on the surface of the bones represent the different types summarized in the **Table 3**.

fracture or posterior malleolar fracture. This study is the first to apply 3D fracture line mapping techniques as well as heatmap techniques to analyze ankle fracture patterns.

We analyzed the 10 cases that could not be classified by AO classification and the 19 cases that could not be classified by LH classification. The fracture characteristics that could not be

TABLE 4 | Fracture patterns organized by the method above.

Classification	No.(*n* = 228)	Classification	No.(*n* = 228)
0 + A	18	b + AD	5
0 + AB	4	b + ADB	1
0 + AC	4	b + B	24
0 + ACD	1	b + BD	3
0 + B	6	b + C	4
0 + C	4	b + CA	3
0 + D	5	b + CD	4
a+0	11	b + D	2
a+A	2	b + DA	1
a+AB	1	c+0	2
a+CD	1	c + A	2
a+D	4	c + AB	6
b+0	44	c + ADC	3
b + A	11	c + B	5
b + AB	30	c + BD	1
b + ABD	1	c + CD	2
b + AC	9	c + D	3
b + ACD	1		

**a, b, c represents the corresponding pattern of classification of fracture lines on fibula; A, B, C, D represents the corresponding pattern of classification of fracture lines on tibia.*

classified by LH or AO classification were summarized as follows: 1) All fractures were simple tibial fractures and no fibular fractures. 2) The most involved anatomic site was medial malleolus (14/19 of medial malleolus involvement in LH classification, 4/10 of medial malleolus involvement in AO classification) (**Table 2**).

At present, scholars have made explorations related to the medial or posterior malleolus fracture line course and characteristics, based on which, they have proposed the corresponding classification. For example, Hraguchi et al. (Haraguchi et al., 2006) typed posterior malleolar fractures based on the morphology of posterior malleolar fractures in distal tibial cross-section under CT. They classified posterior malleolar fractures into three types, type I: the fracture fragment was wedge-shaped and involved the posterior external angle of the distal tibial articular surface; type II: the fracture line extended from the fibular notch of the distal tibia to the medial malleolar; type III: small shell type, where one or more small shell-shaped bone fragments were fractured at the posterior edge of the distal tibia. Mangnus et al. (Mangnus et al., 2015), on the other hand, qualitatively analyzed the morphology of posterior malleolar fractures based on the Haraguchi classification and divided the posterior malleolar fracture line into two categories: posterior external oblique (Haraguchi type I and III, both of which were fractures of different degrees caused by the same extensive force) and transverse (fracture line extending medially and involving the posterior malleolus of the medial malleolar; Haraguchi type II fracture).

For medial malleolus fracture, Herscovici et al. proposed a Herscovici classification in 2007 (Herscovici et al., 2007), which classified medial malleolus fracture into four categories A: avulsion fractures of the tip of the internal ankle, mostly involving the anterior malleolus and superficial deltoid ligament, while the deeper layer was more posterior; B: fracture line located between the level of the articular surface and the tip of the internal ankle; C: fracture line and articular surface were at the same level; D: the fracture line was vertical or obliquely directed inward and upward, mostly seen in the posterior rotational inversion type of injury. Less commonly, there was longitudinal instability.

From the reported literature, the fracture line alignment in the case of combined medial + lateral ankle involvement is consistent with the current definition of posterior pilon fracture. A specific type of posterior malleolar fracture with fracture line passing through the posterior malleolar node of the medial malleolar was reported by Pankovich et al. (Pankovich and Shivaram, 1979) in 1979. Ebraheim et al., 1990 named this type of fracture as a posterior collicular fractures of the medial malleolus (Ebraheim et al., 1990). By 2000 Hansen first named such type of fracture as posterior pilon fracture, which was characterized by a large fracture mass with one or more fracture masses and proximal displacement of the fractured mass to form a step, which may be accompanied by posterior or posterior-lateral subluxation of the talus. In 2004 Weber in his paper described 10 cases of posterior malleolar fracture characteristics of the posterior mound of the medial malleolar and proposed the double-contour or flake-fragment sign as the concept that the presence of such sign-on anteroposterior malleolar radiographs predicted extension of the posterior malleolar fracture mass to the posterior medial aspect, i.e., posterior malleolar involvement (Weber, 2004). According to the various existing medial malleolus fracture classifications, although it is possible to type such fractures, for example, type II in the Haraguchi classification and types III and IV in the Bartonícek classification fit the above definition of posterior pilon fracture. However, with the in-depth study of posterior malleolar fractures, it is now generally accepted that posterior pilon fracture is a special type of posterior malleolar fracture, and many scholars are trying to classify posterior pilon fractures. Klammer et al.

(Klammer et al., 2013) divided posterior pilon fractures into three types based on clinical practice: type I accumulated the whole posterior malleolar, and the fractured mass was a long oblique shape with the base toward the posterior lateral side; type II fracture fragment included both posterior medial and posterior-lateral parts; type III was accompanied by anterior malleolus fracture of the medial malleolar. Yu et al. divided posterior pilon fractures into three types based on CT manifestations (Zhang and Yu, 2018), type I was a postero-lateral oblique type with a larger postero-lateral volkmann fracture mass; type II was a fracture line extending to the medial malleolar; type III fracture mass was divided into two parts: posterior medial and posterior lateral. Wang et al. (Lei et al., 2011) divided posterior pilon fractures into two types based on the location of the lateral malleolus fracture lines: type I fracture line was located in the lower tibiofibular union above and the medial posterior malleolar fracture fragment was not connected to the anterior malleolus fracture fragment of the medial malleolar; type II fracture line was located at the level of the inferior tibiofibular union and the medial posterior ankle fracture fragment was connected to the medial malleolar fracture fragment. In 2017, Zhang et al. proposed AGH classification (Zhang, 2017), type I posterior malleolar was a single intact bone block; type II was a posterior malleolar fracture fragment splits along the sagittal plane and was divided into two parts: posterior medial and posterior-lateral; type II b was a posterior malleolar fracture fragment split along the sagittal plane with a comminuted fracture of the posterior malleolar; type III a was fracture with a posterior malleolar fracture line accumulating the anterior malleolus of the medial malleolar and a complete fracture of the medial malleolar but without separation of the millia and posterior malleolus; and type III b was with a posterior malleolar fracture line accumulating the intermalleolar groove and an avulsion fracture of the anterior malleolus with separation of the anterior and posterior malleoli.

Although there have been many studies on classification of medial malleolus fracture, posterior malleolus fracture or posterior pilon fractures involving the entire coronal surface of the posterior malleolar, none of them can fully summarize all their characteristics, such as whether the fracture line is transverse or long oblique, whether it extends posteriorly, and medially to the posterior or anterior mound of the medial malleolar, and whether the fractured mass is 1-part, 2-part, or comminuted. The reason for the lack of uniformity in the understanding of the relevant classification is that the biomechanical mechanisms that lead to fractures involving the posterior malleolar fractures are not understood yet. Most of the currently available explanations for the mechanism of the fracture in question are derived from the analysis and extrapolation of the morphological features of the fracture in question on CT images (Bartoníček et al., 2015; Mason et al., 2017; Yi et al., 2018; Vosoughi et al., 2019). Posterior malleolar fractures have rarely been successfully simulated in biomechanical tests. Of the few relevant reports retrieved, Schaffer (Schaffer and Manoli, 1987), Michelson (Michelson et al., 1997), Stiehl (Stiehl et al., 1992), et al. failed to reproduce a posterior malleolar fractures in their respective experiments, except for a report by Haraguchi (Haraguchi and Armiger, 2020) in 2020 in which a fracture involving the entire posterior tibial margin, corresponding to Haraguchi type II, was reproduced, inferring that the mechanism of formation of this type of fracture as follows: As a result of axial loading of the talus, the posterior lower part of the tibiofibular ligament is torn leading to a posterior malleolar fractures with the formation of fracture fragments.

The uncertainty of the fracture mechanism and the lack of uniformity in the classification have made it difficult to communicate the condition among physicians in the current clinical setting. The fracture lines and the distribution of hot spots on the heatmaps were summarized in **Figures 2**, **3**, and the differences in the sites of different subtypes of fibula fractures in the existing Arbeitsgemeinschaftfür Osteosynthesefragen (AO) classification were also referred hereof, thus we tried to classify the fracture lines of the fibula and tibia into three categories and four categories, by analyzing the fracture map and heatmap, respectively (**Table 3**, **Figure 7**). In the area with the densest distribution of fracture lines (the green ring on the heatmap) in **Figure 4**, we defined it as category b (corresponding to the fibula fracture pattern of type B in the AO classification), then the fracture lines above this area we defined it as category c (corresponding to the fibula fracture pattern of type A in the AO classification), and the fracture lines below this area we defined it as a category a (corresponding to the fibula fracture pattern of type C in the AO classification). In **Figure 3**, the fracture line wrapped around the Volkmann's node and the medial malleolus can be observed in a circular distribution area, and the corresponding green circular hot spot distribution can be observed on the heatmap, which is defined as type B and types A fractures, respectively. Outside the area of the fracture line encircling the Volkmann's tuberosity (type B fracture line), which is the green circle encircling the Volkmann's tuberosity on the heatmap, we can see the presence of an elliptical fracture line with a long axis parallel to the tibial stem, which exceeds the boundary of the type B fracture line. Similarly, outside of the circular fracture line encircling the medial ankle and the corresponding green circular hot spot, a distribution of fracture lines that travel vertically through the medial malleolus can be observed, and we define them as type C and D, respectively.

Following this pattern of fracture line regional division, we reclassified the 228 patients (**Table 4**). A total of 32 combinations were identified, with fibula b being the most common of the single ankle fracture subtypes and fibula b + tibia AB being the most common of the trimalleolar fracture subtypes. Of course, such classification is based solely on the distribution of fracture lines, and it is only an attempt to map the ankle fracture lines in order to include fracture patterns that cannot be identified by Lauge-Hansen (LH) classification and AO classification and to differentiate and name them in order to facilitate communication between physicians about the condition.

The limitations of our study are as follows: Firstly, the number of patients was relatively small; Secondly, the proposed new fracture pattern in the conclusion is subjective, based on the summary of the distribution of ankle fracture lines and the reference to the existing fracture pattern of the fibula in the AO classification, thus lacking the biomechanical mechanism of the corresponding fracture pattern; Thirdly, due to anatomical variability (length of the tibiofibular, the cross-sectional aspect

ratio of the distal tibiofibular, the size of the distal tibial articular surface, and the size of the anatomic structures such as the medial, lateral, and posterior ankle differ from patient to patient), some fracture reconstruction models did not exactly match the standard model of the tibiofibular; Fourthly, existing fracture line depiction techniques could only display the distribution of fracture lines on the surface of the tibiofibular and cannot display the distribution of fracture fractures within the cancellous mass.

CONCLUSION

In this study, the 3D fracture line mapping technique was selected to describe the distribution of fracture lines throughout the ankle (not limited to the posterior or medial malleolar), with an attempt to classify the fibular and tibial fracture lines into three and four categories based on the distribution and density of lines to combine the two classifications to derive the fracture pattern of the ankle, respectively. And an attempt was made to classify 228 patients with ankle fractures using the above new method. The new classification method can include fracture types that cannot be identified by both AO and LH classification and is simple and convenient for physicians to communicate with each other about the patient's condition. It is surely just an attempt to develop a uniform, comprehensive and accurate classification of ankle fractures. To truly develop a classification system that encompasses all ankle fracture types, a larger sample size of ankle fracture patients and an exploration of the biomechanical mechanisms of posterior ankle fractures are required.

DATA AVAILABILITY STATEMENT

The raw data supporting the conclusions of this article will be made available by the authors, without undue reservation.

AUTHOR CONTRIBUTIONS

JZ: Conceptualization, Methodology, Software Validation, Formal analysis, Data Curation, Writing-Original Draft, Visualization. JL: Conceptualization, Methodology, Software Validation, Writing-Review and Editing. GX: Data Curation. WZ: Data Curation. DW: Data Curation. HL: Data Curation. XG: Data Curation. YX: Data Curation. CX: Visualization, Supervision. LZ: Project administration, Writing–Review and Editing. PT: Project administration, Writing–Review and Editing, Funding acquisition.

FUNDING

This work was supported by The 13th Five-year Plan for Key Discipline Construction Project of PLA (A350109).

ACKNOWLEDGMENTS

We thank the associate editor and the reviewers for their help and remarks.

REFERENCES

Bartoníček, J., Rammelt, S., Kostlivý, K., Vaněček, V., Klika, D., and Trešl, I. (2015). Anatomy and Classification of the Posterior Tibial Fragment in Ankle Fractures. *Arch. Orthop. Trauma Surg.* 135 (4), 505–516. doi:10.1007/s00402-015-2171-4

Bartoníček, J., Rammelt, S., and Tuček, M. (2017). Posterior Malleolar Fractures. *Foot Ankle Clin.* 22 (1), 125–145. doi:10.1016/j.fcl.2016.09.009

Berkes, M. B., Little, M. T. M., Lazaro, L. E., Pardee, N. C., Schottel, P. C., Helfet, D. L., et al. (2013). Articular Congruity Is Associated with Short-Term Clinical Outcomes of Operatively Treated SER IV Ankle Fractures. *J. Bone Jt. Surg Am* 95 (19), 1769–1775. doi:10.2106/JBJS.L.00949

Blom, R. P., Meijer, D. T., de Muinck Keizer, R.-J. O., Stufkens, S. A. S., Sierevelt, I. N., Schepers, T., et al. (2019). Posterior Malleolar Fracture Morphology Determines Outcome in Rotational Type Ankle Fractures. *Injury* 50 (7), 1392–1397. doi:10.1016/j.injury.2019.06.003

Cole, P. A., Mehrle, R. K., Bhandari, M., and Zlowodzki, M. (2013). The Pilon Map. *J. Orthop. Trauma* 27 (7), e152–e156. doi:10.1097/BOT.0b013e318288a7e9

Ebraheim, N. A., Savolaine, E. R., Skie, M. C., and Jackson, T. W. (1990). Posterior Collicular Fractures of the Medial Malleolus. *J. Orthopaedic Trauma* 4 (3), 336–338. doi:10.1097/00005131-199004030-00017

Haraguchi, N., and Armiger, R. S. (2020). Mechanism of Posterior Malleolar Fracture of the Ankle. *OTA Int. : open access J. orthopaedic Trauma* 3 (2), e060. doi:10.1097/OI9.0000000000000060

Haraguchi, N., Haruyama, H., Toga, H., and Kato, F. (2006). Pathoanatomy of Posterior Malleolar Fractures of the Ankle. *J. Bone Jt. Surg.* 88 (5), 1085–1092. doi:10.2106/JBJS.E.00856

Herscovici, D., Jr, Scaduto, J. M., and Infante, A. (2007). Conservative Treatment of Isolated Fractures of the Medial Malleolus. *The J. Bone Jt. Surg. Br. volumeBritish volume* 89-B (1), 89–93. doi:10.1302/0301-620X.89B1.18349

Hoogendoorn, J. M. (2017). Posterior Malleolar Open Reduction and Internal Fixation through a Posterolateral Approach for Trimalleolar Fractures. *JBJS Essent. Surg. Tech.* 7 (4), e31. doi:10.2106/JBJS.ST.17.00016

Klammer, G., Kadakia, A. R., Joos, D. A., Seybold, J. D., and Espinosa, N. (2013). Posterior Pilon Fractures. *Foot Ankle Int.* 34 (2), 189–199. doi:10.1177/1071100712469334

Koval, K. J., Lurie, J., Zhou, W., Sparks, M. B., Cantu, R. V., Sporer, S. M., et al. (2005). Ankle Fractures in the Elderly. *J. Orthop. Trauma* 19, 635–639. doi:10.1097/01.bot.0000177105.53708.a9

Lei, W., Zhong-Min, S., Chang-Qing, Z., and Bing-Fang, Z. (2011). Trimalleolar Fracture with Involvement of the Entire Posterior Plafond. *Foot Ankle Int.* 32 (8), 774–781. doi:10.3113/FAI.2011.0774

Mangnus, L., Meijer, D. T., Stufkens, S. A., Mellema, J. J., Steller, E. P., Kerkhoffs, G. M. M. J., et al. (2015). Posterior Malleolar Fracture Patterns. *J. Orthop. Trauma* 29 (9), 428–435. doi:10.1097/BOT.0000000000000330

Mason, L. W., Marlow, W. J., Widnall, J., and Molloy, A. P. (2017). Pathoanatomy and Associated Injuries of Posterior Malleolus Fracture of the Ankle. *Foot Ankle Int.* 38 (11), 1229–1235. doi:10.1177/1071100717719533

Michelson, J., Solocoff, D., Waldman, B., Kendell, K., and Ahn, U. (1997). Ankle Fractures. *Clin. Orthopaedics Relat. Res.* 345 (345), 198–205. doi:10.1097/00003086-199712000-00029

Pankovich, A. M., and Shivaram, M. S. (1979). Anatomical Basis of Variability in Injuries of the Medial Malleolus and the Deltoid Ligament:II. Clinical Studies. *Acta Orthopaedica Scand.* 50 (2), 225–236. doi:10.3109/17453677908989760

Peng, J. (2019). Medial Malleolar Patterns in Ankle Fractures: a Morphology Study Based on Three Dimensional Computed Tomography. *Chin. J. Bone Jt. Surg.* 12 (8), 609–614. doi:10.3969/j.issn.2095-9958.2019.08.08

Schaffer, J. J., and Manoli, A., 2nd (1987). The Antiglide Plate for Distal Fibular Fixation. A Biomechanical Comparison with Fixation with a Lateral

Plate. *J. Bone Jt. Surg.* 69 (4), 596–604. doi:10.2106/00004623-198769040-00017

Sigvaard, T., and Hansen, J. (2000). *Functional Reconstruction of the Foot and Ankle*. Philadelphia: Lippincott Williams & Wilkins, 544.

Stiehl, J. B., Skrade, D. A., and Johnson, R. P. (1992). Experimentally Produced Ankle Fractures in Autopsy Specimens. *Clin. Orthopaedics Relat. Res.* 285 (285), 244–249. doi:10.1097/00003086-199212000-00033

Vosoughi, A. R., Jayatilaka, M. L. T., Fischer, B., Molloy, A. P., and Mason, L. W. (2019). CT Analysis of the Posteromedial Fragment of the Posterior Malleolar Fracture. *Foot Ankle Int.* 40 (6), 648–655. doi:10.1177/1071100719830999

Weber, M. (2004). Trimalleolar Fractures with Impaction of the Posteromedial Tibial Plafond: Implications for Talar Stability. *Foot Ankle Int.* 25 (10), 716–727. doi:10.1177/107110070402501005

Yang, Y., Yi, M., Zou, C., Yan, Z.-k., Yan, X.-a., and Fang, Y. (2018). Mapping of 238 Quadrilateral Plate Fractures with Three-Dimensional Computed Tomography. *Injury* 49 (7), 1307–1312. doi:10.1016/j.injury.2018.05.026

Yi, Y., Chun, D.-I., Won, S. H., Park, S., Lee, S., and Cho, J. (2018). Morphological Characteristics of the Posterior Malleolar Fragment According to Ankle Fracture Patterns: a Computed Tomography-Based Study. *BMC Musculoskelet. Disord.* 19 (1), 51. doi:10.1186/s12891-018-1974-1

Yu, T. (2019). Heatmap Characteristics and Treatment Options of Posterior Malleolus Fractures in Supination-External Rotation Ankle Fracture. *Chin. J. Anat. Clin.* 24 (2), 93–98. doi:10.3760/cma.j.issn.2095-7041.2019.02.002

Yu, T., Zhang, Y., Zhou, H., and Yang, Y. (2021). Distribution of Posterior Malleolus Fracture Lines in Ankle Fracture of Supination-External Rotation. *Orthopaedics Traumatol. Surg. Res.* 107 (6), 103000. doi:10.1016/j.otsr.2021.103000

Yun, Y., Min, Y., and Chang, Z. (2016). Morphologic Characteristics of the Lateral Ankle Fragment: A 3-D Computer Tomography Based Study. *J. Wenzhou Med. Univ.* 46 (010), 730–733. doi:10.3969/j.issn.2095-9400.2016.10.006

Zhang, J. (2017). The Role of AGH Classification for Treatment Strategies of the Posterior Pilon Fractures. *Chin. J. Orthopaedics* 37 (5), 284–290. doi:10.3760/cma.j.issn.0253-2352.2017.05.005

Zhang, M. Z., and Yu, G. R. (2018). Treatment Outcomes of Buttress Plating for Posterior Pilon Fractures. *Foot & Ankle Orthopaedics* 3 (3), 2473011418S0053. doi:10.1177/2473011418S00538

Conflict of Interest: The authors declare that the research was conducted in the absence of any commercial or financial relationships that could be construed as a potential conflict of interest.

frontiers | Frontiers in Bioengineering and Biotechnology

ORIGINAL RESEARCH
published: 14 April 2022
doi: 10.3389/fbioe.2022.890428

Effects of Foot-Core Training on Foot-Ankle Kinematics and Running Kinetics in Runners: Secondary Outcomes From a Randomized Controlled Trial

*Alessandra B. Matias[1], Ricky Watari[1], Ulisses T. Taddei[1], Paolo Caravaggi[2], Rafael S. Inoue[1], Raissa B. Thibes[3], Eneida Y. Suda[1], Marcus F. Vieira[4] and Isabel C. N. Sacco[1]**

[1]Faculdade de Medicina, Physical Therapy, Speech and Occupational Therapy Department, Universidade de São Paulo, Sao Paulo, Brazil, [2]Movement Analysis Laboratory, IRCCS Istituto Ortopedico Rizzoli, Bologna, Italy, [3]Center of Mathematics, Computing and Cognition, Universidade Federal do ABC, Santo André, Brazil, [4]Bioengineering and Biomechanics Laboratory, Federal University of Goiás, Goiás, Brazil

OPEN ACCESS

Edited by:
Lizhen Wang,
Beihang University, China

Reviewed by:
Liang Wang,
Southeast University, China
Tianyun Jiang,
Beihang University, China

***Correspondence:**
Isabel C. N. Sacco
icnsacco@usp.br

Specialty section:
This article was submitted to Biomechanics, a section of the journal Frontiers in Bioengineering and Biotechnology

Received: *05 March 2022*
Accepted: *29 March 2022*
Published: *14 April 2022*

Citation:
Matias AB, Watari R, Taddei UT, Caravaggi P, Inoue RS, Thibes RB, Suda EY, Vieira MF and Sacco ICN (2022) Effects of Foot-Core Training on Foot-Ankle Kinematics and Running Kinetics in Runners: Secondary Outcomes From a Randomized Controlled Trial. Front. Bioeng. Biotechnol. 10:890428. doi: 10.3389/fbioe.2022.890428

This study investigated the effectiveness of an 8-week foot-core exercise training program on foot-ankle kinematics during running and also on running kinetics (impact loads), with particular interest in biomechanical outcomes considered risk factors for running-related injuries in recreational runners. A single-blind, randomized, controlled trial was conducted with 87 recreational runners randomly allocated to either the control (CG) or intervention (IG) group and assessed at baseline and after 8 weeks. The IG underwent foot-core training 3 times/week, while the CG followed a placebo lower-limb stretching protocol. The participants ran on a force-instrumented treadmill at a self-selected speed while foot-segment motion was captured simultaneously with kinetic measurements. After the intervention, there were statistically significant changed in foot biomechanics, such as: IG participants strike the ground with a more inverted calcaneus and a less dorsiflexed midfoot than those in the CG; at midstance, ran with a less plantarflexed and more adducted forefoot and a more abducted hallux; and at push-off, ran with a less dorsiflexed midfoot and a less adducted and more dorsiflexed hallux. The IG runners also had significantly decreased medial longitudinal arch excursion (p = 0.024) and increased rearfoot inversion (p = 0.037). The 8-week foot-core exercise program had no effect on impact (p = 0.129) and breaking forces (p = 0.934) or on vertical loading rate (p = 0.537), but it was positively effective in changing foot-ankle kinematic patterns."

Keywords: running, exercise therapy, rehabilitation research, foot joint kinematics, running injuries, statistical parametric mapping

INTRODUCTION

Running is one of the most popular sports and fitness activities worldwide owing to its simple requirements in terms of gear and ability to be performed indoors or outdoors. However, one of the drawbacks is the high incidence of running-related injuries (RRI), such as patellofemoral pain syndrome, iliotibial band friction syndrome, plantar fasciitis, meniscal injuries and patellar tendinopathy (Van Gent et al., 2007; Kluitenberg et al., 2015). The etiology of RRI is believed to

be multifactorial (Buist et al., 2010; van der Worp et al., 2015; Davis et al., 2017; Dudley et al., 2017) and is generally thought to include the following biomechanical risk factors: altered medial longitudinal arch (MLA) posture (Cowan et al., 1993; Busseuil et al., 1998; Bennett et al., 2001; Williams et al., 2001; Weist et al., 2004; Headlee et al., 2008; Kelly et al., 2015); greater ankle (Messier and Pittala, 1988; Willems et al., 2006; Pohl and Buckley, 2008) or rearfoot (Noehren et al., 2007, 2013; Hein and Grau, 2014; Messier et al., 2018) eversion; and higher loading rates (Hreljac et al., 2000; Milner et al., 2005; Zadpoor and Nikooyan, 2011; Bredeweg et al., 2013; Davis et al., 2016), impact peaks (Bennell et al., 1996; Hreljac et al., 2000; Milner et al., 2005; Davis et al., 2016), and breaking forces (Grimston et al., 1991; Messier et al., 1995; Napier et al., 2018).

Several therapeutic strategies have been implemented in recent decades to minimize RRI incidence, but these have yielded poor outcomes (Buist et al., 2008; Fokkema et al., 2017; Hespanhol et al., 2018). Some of the most commonly adopted therapeutic approaches to reducing RRI are strengthening programs focused on the hip and the core areas—i.e., the "top-down" approach (Powers, 2010; Hott et al., 2015; Palmer et al., 2015). This approach claims that increased hip and core muscle (abdominal and multifidus muscles) strength contribute to the reduction of non-sagittal joint movements and moments, and thus of the loads in the adjacent joints in the lower limbs, which in turn would result in lower risks of RRI (Fredericson and Moore, 2005; Brumitt, 2009; Snyder et al., 2009; Powers, 2010; Hott et al., 2015; Palmer et al., 2015). Although this approach is very popular (Johnston et al., 2003; Fredericson and Moore, 2005; Brumitt, 2009; Willy and Davis, 2011), its beneficial effects in diminishing the incidence and the biomechanical risk factors of RRI (Ceyssens et al., 2019) are yet to be proven (Nigg et al., 2017).

A promising alternative strategy, the so-called "bottom-up" approach, targeted foot core muscles strength (intrinsic and extrinsic foot muscles) (McKeon and Fourchet, 2015a) and biomechanics with the goal of attenuating mechanical loads directly related to RRI (Milner et al., 2005; Warden et al., 2008; Davis et al., 2016). It applies the lumbopelvic core system concept to the foot core system. The lumbopelvic core system is comprised of interacting subsystems (neural, passive and active) that provide relevant sensory input and functional stability for accommodating to changing demands during both static and dynamic activities (McKeon et al., 2015b). The application of this concept to the foot core it is logical as it works just like the trunk core considering that the subsystems in the foot also provide a stable base on which the primary movers of the foot-ankle complex, those with larger cross-sectional areas and moment arms, can act to cause gross motion, and the intrinsic muscles work as the local stabilizers, as they have small cross-sectional areas and small moment arms (McKeon and Fourchet, 2015a; McKeon et al., 2015b). According to the "bottom-up" theoretical assumptions (Tiberio, 1987; Feltner et al., 1994; Hollman et al., 2006; Lucas-Cuevas et al., 2016; Nigg et al., 2017), this approach may potentially change the mechanical or biomechanical response of more proximal joints (knee, hip). The foot is a biomechanically complex structure made of 26 bones, four layers of plantar intrinsic muscles, and several joints, providing the foot with multiple degrees of freedom. Active and passive elements in the foot, such as ligaments and soft tissues, act in synergy to make the foot a mobile adapter capable of receiving and attenuating external loads, and of storing and releasing elastic energy (Kelly et al., 2018; Farris et al., 2019). Hypothetically, a stronger foot structure (stronger foot muscles and improved mechanical properties of passive tissues—tendons, ligaments and joint tissues) and the medial longitudinal arch should better dissipate excessive and cumulative loads through actively supporting changing the function of the foot from a dampener in the early stance to a spring in the late stance (Ker et al., 1987; Taddei et al., 2020a). Some studies demonstrate the benefits of strengthening the foot core muscles and, knowing the intrinsic foot muscle's role in dampening impacts and propelling the body during running (Ker et al., 1987; Kluitenberg et al., 2015; Taddei et al., 2020b), it is logical to think that these roles were also improved with this "bottom-up" training (Feltner et al., 1994; Nigg et al., 1997, 2017; Matias et al., 2016; Baltich et al., 2017; Mølgaard et al., 2018). Thus, we can assume that by reducing shock, cumulative load, better controlling foot-ankle motion and alignment, strengthening the foot muscles resulted in preventing the RRI in the intervention group.

There is some evidence that this approach is effective in preventing RRI and promoting functional gains related to running. A previous proof-of-concept study performed by our group showed that an 8-week foot-core strengthening program increased the intrinsic anatomical cross-sectional area of the foot muscle and the propulsive impulse during running (Taddei et al., 2018) The primary outcome of our single-blind, randomized, controlled trial (RCT) concerning RRI prevention showed that 8 weeks of foot-core training in healthy runners resulted in a 2.42-fold reduction of RRI incidence at the 1-year follow-up compared with a placebo stretching program (Taddei et al., 2020b). There was also a significant correlation between time-to-injury and foot strength gain that all might support the hypothesis-driven mechanism we described, where the stronger the runner's foot, the longer it took the runner to develop an RRI. In this follow-up report of secondary outcomes from that study, we report the effects of the 8-week foot-core exercise training program (Taddei et al., 2020b) on the participants who had their foot-ankle kinematics and running kinetics assessed, with particular interest in the biomechanical outcomes considered to be risk factors for RRI in recreational runners.

MATERIALS AND METHODS

A detailed protocol of the single-blind RCT with two parallel arms has been published elsewhere (Matias et al., 2016). The study was approved by the Ethics Committee of the School of Medicine of the University of São Paulo (18/03/2015, Protocol #031/15), and was registered with clinicaltrials.gov (Identifier NCT02306148).

Participants and Recruitment

Adult recreational runners were recruited through digital social media advertising, posted flyers, and direct contact with runners and running groups in the university surroundings between

August 2015 and August 2017. All participants were RRI-free in the 2 months prior to the baseline assessment, had no experience running barefoot or in minimalist shoes, were without chronic diseases or impairments that could influence running performance, and had run between 20 and 100 km/week for ≥1 year.

Sample Size

In our previous study (Taddei et al., 2018), an a priori sample size was calculated using several kinematic foot outcomes. The fifth metatarsal bone to the ground (V2G), second metatarsal bone to the ground (S2G), first metatarsal bone to the ground (F2G), second to first metatarsal bone divergence in the transverse plane of the foot (S2F), second to fifth metatarsal bone divergence in the transverse plane of the foot (S2V) and the medial longitudinal arch (MLA) required 38, 86, 58, 2,184, 34, and 6 participants, respectively. Based on 80% power and a significance level of 5%, the study indicated that we needed a total of 86 participants for most of the secondary outcomes, and we included 87 participants in the present study as they had their running biomechanics assessed. It was a sample size feasible to obtain from the full sample of the RCT ($n = 119$) and it would be capable of detecting changes in almost all foot biomechanical outcomes, except the one that needed more than two thousand participants, what would make the study unfeasible.

Randomization and Follow-Up Assessments

After the runners' agreement to participate and completion of the baseline questionnaire, they were randomized into either the IG or the CG by using Clinstat software (University of York, Heslington, UK) to generate a randomization list with blocks of eight. The randomization list was developed by an individual who is not part of the research team. The codes for the groups were kept in opaque, sealed envelopes numbered from 1 to 120, and the researchers involved in the allocation and assessments were blind to the group codes and block size. The participants were enrolled and assigned to the interventions by a member of the research group. From the 119 participants included in the full RCT to evaluate RRI incidence over 1-year follow up, the 87 participants that had their running biomechanics assessed were included in the current analysis of secondary outcomes, 41 in the IG and 46 in the CG.

The trial statistician was blind to treatment allocation until the main analysis had been completed. All participants' data were kept confidential before, during, and after the study by encoding their names.

Participants allocated to the IG were given access to 8 weeks of a training program. Participants in the CG were informed about their allocation into the control group and were instructed to perform a 5-minute static stretching protocol (Matias et al., 2016) as a placebo. We instructed the participants to keep their allocation group information strictly personal.

The baseline questionnaire consisted of six sections (demographics, training, running events, Foot Health Status Questionnaire, anthropometrics, and previous RRIs) (**Table 1**). The follow-up questionnaires asked about running routine, adherence to the foot-core training program, and RRIs.

Intervention

The foot-core training program to prevent RRI focused on the foot and ankle muscles, with 12 exercises progressing weekly in volume and difficulty (Matias et al., 2016). Participants in the IG were trained once a week by a physiotherapist and given online access to web-based software developed for this project with descriptions of the exercises and videos to help them perform the same exercises an additional 3×/week, remotely supervised by the same physiotherapist. Each session, either locally or remotely supervised, had a duration of 20–30 min. Gradual and progressive difficulty were offered to the runner, respecting any limitation due to pain, fatigue and/or decrease in performance during execution. The runners in the IG were asked to access the web software daily, entering their data regarding performance of the foot exercise training and ranking their level of difficulty in each exercise from 0 to 10. If the effort score ranged from 0 to 5 and the runner's performance of each exercise was found adequate during the supervised session by the physiotherapist, the exercises increased in difficulty. If the effort score ranged from 6 to 7, the exercise did not increase in difficulty and no progressions were done on that exercise. Thus, the runner remained in the same exercise progression until he/she scored 0 to 5 in that exercise. Finally, if an IG runner reports a score from 8 to 10, the exercise decreased in difficulty, if possible, until the runner was able to perform it without pain or discomfort.

Runners allocated to the CG received a 5-minute placebo warm-up and muscle stretching exercise routine that should be performed immediately before each running practice. The placebo exercises were developed based on the runner's habitual routine warm-up combined with muscle stretching exercises focused on the lower limb's muscles (triceps surae, quadriceps, hamstrings, gluteus) involving both open and closed- kinetic chain exercise. The CG exercises aimed to not have any effect on foot muscles strength and functionality, lower extremity biomechanics or injury prevention. CG runners received weekly feedback and interaction with the physiotherapist through the web-software and calls.

Both groups were instructed to perform their respective exercises 3×/week up to the end of the 1-year follow-up and, to improve adherence to the programs, to register their adherence in the web software. The importance of adhering to the program was reinforced at every contact with the participants. The participants were strongly advised not to engage in any new exercise program during the intervention period.

Measurements

Eighty-seven participants that had their running biomechanics assessed were included in the current analysis of secondary outcomes. Biomechanical data were collected using an eight-camera motion capture system (Vicon Motion System Ltd., Oxford Metrics, UK) for the acquisition of 3D kinematic data at 200 Hz while running. Sixteen reflective skin markers (each 9 mm in diameter) were placed on the shank and foot in accordance with the Rizzoli multi-segment foot model

TABLE 1 | Baseline questionnaire and follow-up.

Questionnaire	Section	Items
Baseline questionnaire	Demographics	Sex
		Age
		Body mass (kg)
		Height (m)
		Body Mass Index (kg/m^2)
	Training	Running experience (years)
		Average running frequency over the last month (times per week)
		Average running distance over the last month (km/week)
		Average pace over the last month (min/km)
	Running events	Member of athletic association (yes)
		Previous participation in running events (yes/no)
		Average participations in running events before
	Foot health status Questionnaire	Eight domains of the questionnaire
	Anthropometrics	Foot posture index
		Cavanagh Rodgers index
	Previous running-related injuries	Running-related injury in previous 12 months (yes/no)
		Location of running injury
Weekly follow-up questionnaires	Training	Running frequency (times/week)
		Running distance (km/week)
	Intervention protocol sessions	Number of foot exercise sessions completed
	New running-related injuries	New running-related injury since filling in previous questionnaire (yes/no)
		Location of new running-related injury
		Time to injury

(Leardini et al., 2007; Portinaro et al., 2014). Following a standing calibration trial, the participants were requested to run barefoot at a self-selected comfortable speed on an AMTI™ force-sensing tandem treadmill (AMTI, Watertown, MA, United States) for the acquisition of ground reaction force data at 1,000 Hz. In order to habituate to the treadmill and to warm up, the participants were instructed to run for 2–3 min before the data collection. A 30-s running trial was recorded at the self-selected comfortable speed after the accommodation period. Heel strike and toe off were identified when the vertical ground reaction force crossed a 30 N threshold. Kinematic and ground reaction force data were filtered using a fourth-order, zero-lag, low-pass Butterworth filter with cut-off frequencies of 10 and 80 Hz, respectively. The outputs of the Rizzoli foot model were calculated by custom-made scripts in Visual3D (Visual3D, C-Motion, Germantown, MD, United States) in accordance with the published definitions (Leardini et al., 2007; Portinaro et al., 2014; Caravaggi et al., 2019). Joint rotations were calculated by using the Joint Coordinate System (Grood and Suntay, 1983) convention. The axes of each joint reference frame were defined as follows: sagittal-plane rotations around the z-axis (medio-lateral); frontal-plane rotations around the x-axis (anterior-posterior); and transverse-plane rotations around the y-axis (vertical). Data were normalized to 0–100% of stance phase.

Outcomes

This study is an analysis of the secondary outcomes from the developed RCT. The primary outcome variable was incidence of RRI in recreational runners over the course of a 1-year follow-up and was published elsewhere (Taddei et al., 2020b). The secondary outcomes were related to foot-ankle kinematics during running and running kinetics which were evaluated 8 weeks after the baseline assessment. The foot time series kinematic variables were 3D MLA (Caravaggi et al., 2019) excursion and rotation angles in the three anatomical planes (Sha-Cal, Cal-Mid, Mid-Met, Cal-Met, and Met-Hal). The following metatarsal bone angles were also assessed: sagittal-plane inclination of F2G, S2G, and V2G and transverse-plane divergence between S2F and between S2V. In addition, kinematic and kinetic biomechanical-related risk factors for RRI were investigated as discrete parameters: rearfoot angle (Sha-Cal frontal angle peaks), MLA ROM (max-min), vertical average loading rate (average slope of the line through the interval between 20 and 80% of the time from the foot contact and the first peak), horizontal breaking forces (maximum posterior force, horizontal component), and vertical impact peak (local maximum vertical force at initial contact).

Statistical Analysis

All analyses used the full set of randomly assigned participants under the intention-to-treat assumption. The generalized linear mixed model (GLMM) method was used for univariate analyses, considering the following as factors: groups (CG and IG); time of assessment (baseline and after 8 weeks); and the interaction effect (time by group), which was our primary outcome comparison. Participants and time were considered as random effects and groups as fixed effects in the GLMM modeling. Q-Q graphs were plotted to verify the adequacy (normality) of each model. Univariate comparisons (main and interaction effects) of the estimated marginal means were adjusted with the Bonferroni correction. The comparisons between the pairs of estimated marginal means were made based on the original scale of each

of the dependent variables of the study. Statistical analyses were performed using the Statistical Package for the Social Sciences (SPSS, IBM; v.26.0), adopting a 5% significance level. Cohen's d effect size was calculated for discrete variables, and effects between 0.2 and 0.5 were considered small, between 0.5 and 0.8 were medium, and above 0.8 were large (Cohen, 1988).

Additionally, to capture features of the entire time series, a vector field analysis of the resultant angles was conducted using one-dimensional statistical parametric mapping (1D-SPM), as described elsewhere (Pataky et al., 2013, 2017). Custom-written MATLAB code (MATLAB 2020a; MathWorks, Natick, United States), using the source code available at http://www.spm1d.org/, was employed in the analysis. The 1D-SPM captures features of the entire time series, rather than a few discrete variables, and can provide additional information. Each component of each time series was interpolated to contain 101 points (0–100% of the stance phase) and organized in an array with two or three corresponding matrices, one for each variable component; 87 rows, one for each subject; and 101 columns. 1D-SPM ANOVA followed by post-hoc SPM t-tests was used for 1D variables (F2G, S2G, V2G, S2F, S2V, and MLA). Paired (for assessment comparisons) and independent (for group comparisons) Hotelling's T2 tests were used for comparison of 3D variables (Sha-Cal, Cal-Mid, Mid-Met, Cal-Met, and Met-Hal) in a 3D vector field SPM analysis, followed by the paired or independent t-test as a post-hoc test with a Sidák correction. The output of SPM provides T2, F, and t values for each sample of the investigated kinematic time series, and the threshold corresponding to the set alpha level (see **Supplementary Figures**). The T2, F, and t values exceeding this threshold (marked as black bars below each figure, e.g., in **Figures 2**, **3**) indicate significant differences in the corresponding portion of the time series (**Figures 2**–**5**).

RESULTS AND DISCUSSION

Baseline assessment data are described in **Table 2**. The participants were randomly assigned to either the control group (CG) or to the 8-week supervised foot-core training group (interventional group, IG) (**Figure 1**). They were on average 40.3 (SD 6.9) years old, and the majority (51.2%) were female (**Table 2**), with a mean running experience of 6.5 (SD 5.7) years, a median Foot Posture Index of 2.0 (8% highly supinated, 26% supinated, 49% normal, 14% pronated, 1% highly pronated). An RRI was reported by 46% of all runners in the 12 months prior to their participation in the study (**Table 2**). An RRI was reported by 46% of all runners in the 12 months prior to their participation in the study (**Table 2**). The mean running volume at baseline was 35.8 (SD 27.6) km/week (**Table 2**). During the follow-up assessments and contact with the runners throughout the study, we certified that they followed our instructions rigorously about any changes in their regular physical activity, such as use of minimalist shoes, barefoot sports, or isolated foot strengthening. All participants reported the modifications on their sports activities, and it was not observed any activities that would modify the biomechanical outcomes. Participants were recommended to maintain their running routine during the study period, which was closely monitored to ensure that participants and groups did not differ significantly in the volume run each week during the 8-week intervention period (all participants: mean volume of 83.72 (SD 59.66) km/week; IG: 77.78 (SD 57.31) km/week, CG: 89.09 (SD 61.90) km/week, $p = 0.40$).

During the 8-week training program, all participants completed a custom online survey regarding new RRIs (if any had occurred) and completed the remote training sessions. The dropout rate was 4.9% (2 participants) in the IG and 2.2% (1 participant) in the CG. Participants in the IG were expected to attend the locally supervised training with the designated researcher once a week. The full protocol lasted 8 weeks, and participants were excluded if they missed two consecutive weekly sessions. The total adherence to the protocol, defined as attendance at the locally supervised training, was 96.7%, where 100% corresponds to all participants attending all sessions ($n = 304$, after excluding three participants from the IG who suffered injuries during the 8 weeks of training). Adherence to the remote intervention sessions performed by the IG was on average 83.5% between 8 and 16 weeks, 68.5% between 16 and 24 weeks, 62.5% between 24 and 32 weeks, and 48.9% between 32 and 40 weeks (12 months). Both groups, IG and CG, evolved quickly in the exercises and achieved the most difficult level of the proposed exercises during the first 8 weeks of sessions.

Of the 87 runners, 20 had sustained an RRI by the 1-year follow-up: 6 of 41 in the IG, and 14 of 46 in the CG (**Figure 1**). Injuries in the IG at 1-year follow-up were shin splint, plantar fasciitis, and calcaneal tendinitis. Injuries in the CG were patellofemoral pain, shin splint, and thigh strain.

The Effect of the Foot-Core Training on Discrete Biomechanical Risk Factors for Running-Related Injuries

The average loading rate, impact, and breaking force peaks were not significantly different between IG and CG at the 8-week follow-up (**Table 3**). These parameters were chosen as secondary outcomes in this study because they have historically been retrospectively and prospectively associated with RRI. Retrospective studies have shown a strong association between higher vertical loading rates and tibial shock with stress fractures in female runners (Milner et al., 2005), greater vertical impact forces and loading rates with overuse RRI (Hreljac et al., 1999), and higher breaking forces in female runners who sustained an injury in a 15-week period (Napier et al., 2018). Furthermore, in prospective studies, higher impacts and loading rates were observed in runners who sustained an RRI in a 2-year period (Davis et al., 2016) and in novice male runners who sustained an injury in a 9-week period (Bredeweg et al., 2013). However, another prospective study did not find differences in loading rates between injured and uninjured collegiate runners at 12 weeks (Kuhman et al., 2016). The etiology of RRI is multifactorial, and the different types of RRI observed in our RCT after 1 year (14 in the CG and six in the IG) were probably generated by multiple RRI mechanisms. However, establishing a direct relationship between this kinetic risk factor and RRIs would

TABLE 2 | Baseline characteristics of participants from the intervention and control groups.

	All participants		Intervention group		Control group	
	N	%/Mean (SD)	N	%/Mean (SD)	N	%/Mean (SD)
N	87		41	47.1%	46	52.9%
Demographics						
Sex (male)	42	48.8%	17	41.5%	25	54.3%
Age (years)		40.3 (6.9)		40.3 (7.7)		40.3 (6.1)
Body mass (kg)		70.5 (13.1)		67.2 (12.1)		73.5 (13.0)
Height (m)		169.3 (8.8)		166.5 (7.6)		171.8 (9.0)
Body Mass Index (kg/m^2)		24.5 (3.2)		24.1 (3.0)		24.8 (3.3)
Training						
Running Experience (years)		6.5 (5.7)		5.9 (5.1)		7.1 (6.2)
Running frequency per week		3.7 (1.0)		3.8 (1.0)		3.6 (1.2)
Running volume per week (km)		35.8 (27.6)		31.7 (22.5)		39.4 (30.8)
Average pace (min/km)		6.58" (1.36)		6.46" (2.36)		6.69" (2.38)
Running event						
Member of athletic association (yes)	38	43.7%	19	46.3%	19	41.3%
Participated in a running event before (yes)	83	95.4%	40	97.6%	43	93.5%
Number of running events before		37.0 (41.7)		29.3 (31.8)		44.0 (47.5)
Anthropometrics						
Foot posture index—median (25th and 75th percentiles)		2.0 (–2.25; 4.0)		2.0 (–3.0; 4.0)		1.0 (–1.0; 4.0)
Cavanagh & Rodgers index (right foot)		0.20 (0.06)		0.22 (0.05)		0.18 (0.07)
Previous RRI						
Previous RRI in previous 12 months (yes)	40	46.0%	20	48.8%	20	43.5%
FHSQ score (0-100 points)						
Foot pain		90.5 (12.7)		89.9 (13.3)		91.6 (12.0)
Foot function		98.2 (6.0)		98.8 (5.0)		97.6 (6.6)
Shoes		74.5 (24.8)		73.4 (26.9)		76.8 (22.3)
General Foot Health		78.4 (22.9)		76.4 (25.0)		80.3 (20.4)
General Health		86.2 (13.4)		87.1 (12.9)		85.1 (13.6)
Physical Activity		95.5 (15.3)		95.1 (15.0)		95.8 (15.3)
Social Activity		87.5 (15.0)		88.4 (14.2)		86.7 (15.5)
Vigor		75.2 (13.5)		74.1 (11.8)		76.1 (14.4)
Running Biomechanics						
Medial Longitudinal Arch ROM (deg)		3.40 (7.39)		6.16 (8.14)		3.59 (7.89)
Sha-Cal Inv (-) Peak (deg)		–3.12 (7.38)		–0.56 (7.42)		–3.30 (8.71)
Sha-Cal Eve (+) Peak (deg)		6.81 (2.82)		6.72 (3.29)		6.89 (2.35)
Vertical Impact Peak (BW)		1.14 (0.49)		1.13 (0.39)		1.21 (0.44)
Vertical Average Load Rate (BW*s^{-1})		75.05 (55.75)		75.19 (46.43)		73.48 (43.17)
Peak Braking Force (BW)		–0.24 (0.06)		–0.24 (0.05)		–0.24 (0.05)

FHSQ, foot health status questionnaire; ROM, range of motion; BW, bodyweight; Eve, eversion; Inv, inversion; RRI, running-related injury; Sha-Cal, calcaneus with respect to the shank joint angles.

be difficult due to the small sample and the accompanying low statistical power.

Despite the IG being 2.42 times less likely to experience an RRI within the 1-year study period following the foot-core intervention (Taddei et al., 2020b), no reduction in loading rates—which are considered a biomechanical-related risk factor (Hreljac et al., 1999; Bredeweg et al., 2013; Davis et al., 2016; Napier et al., 2018)—was observed in the IG after 8 weeks (**Table 3**). In the present study, although changes in running biomechanics were assessed after the 8 weeks of intervention, the RRI incidence was calculated at 1 year. It is possible that the kinematic- and kinetic-related risk factors changed in the intervening time; however, we did not assess running biomechanics at 1 year, but only at 8 weeks. Future studies should further evaluate the effects of specific foot-ankle intervention strategies on the modification of the loading variables associated with RRIs throughout the full trial period and their relationship with the reduction of RRI risk.

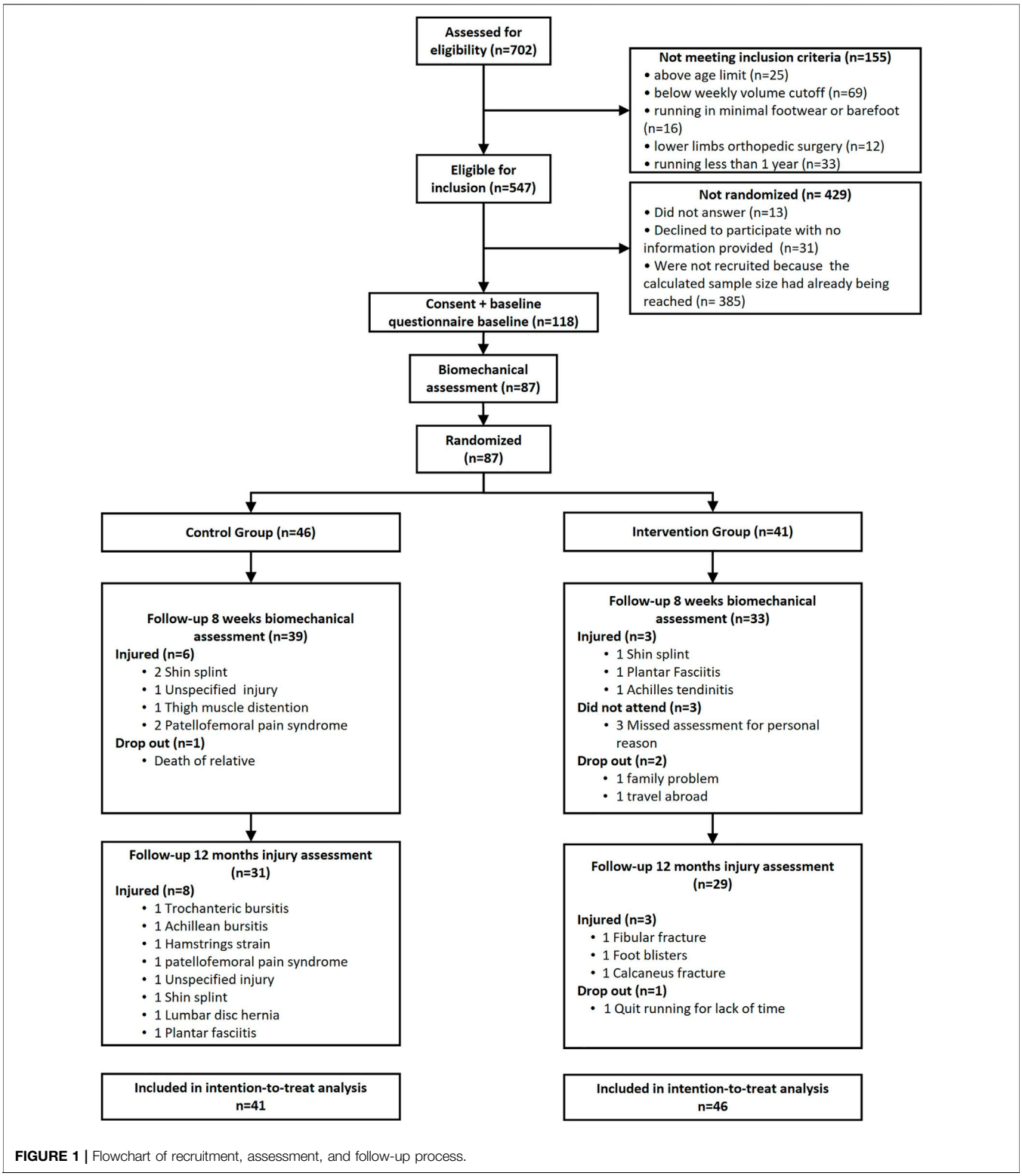

FIGURE 1 | Flowchart of recruitment, assessment, and follow-up process.

The MLA range of motion (ROM) ($p = 0.024$) was significantly lower in the IG than in the CG at week 8 with a small effect size (**Table 3**). In a previous publication, we showed that the foot-core training strengthened some of the intrinsic foot muscles (abductor hallucis, flexor digitorum brevis, abductor digiti minimi, and flexor hallucis brevis) (Taddei et al., 2020a) responsible for sustaining the MLA (Fiolkowski et al., 2003), possibly increasing the resistance to its deformation during

TABLE 3 | Mean (standard deviation) pre- and post-intervention values for kinetic and kinematic biomechanical measures in the experimental groups. *p*-values of the interaction effect (group × time) and Cohen's d effect sizes are presented.

Variable	Intervention group		Control group		Interaction	Cohen's d effect size (95% CI)
	Pre	*Post*	*Pre*	*Post*	*p*	
MLA ROM (deg)	6.16 (8.14)	0.17 (6.86)	3.59 (7.89)	2.88 (5.36)	0.024*	0.45
Sha-Cal Inv (–) Peak (deg)	–0.56 (7.42)	–5.74 (6.31)	–3.30 (8.71)	–3.51 (5.70)	0.037*	0.54
Sha-Cal Eve (+) Peak (deg)	6.72 (3.29)	5.90 (2.95)	6.89 (2.35)	6.39 (1.88)	0.557	0.20
Vertical Impact Peak (BW)	1.13 (0.39)	1.14 (0.55)	1.21 (0.44)	1.09 (0.58)	0.129	0.37
Vertical Average Loading Rate (BW*s^{-1})	75.19 (46.43)	77.17 (57.52)	73.48 (43.17)	72.84 (65.73)	0.537	0.08
Peak Breaking Force (BW)	–0.24 (0.05)	–0.24 (0.07)	–0.24 (0.05)	–0.24 (0.05)	0.934	0.07

*Indicates significant differences.
MLA, medial longitudinal arch; ROM, range of motion; Inv, inversion; Eve, eversion; BW, bodyweight; Sha-Cal, calcaneus with respect to the shank joint angles.

running and thus resulting in a smaller amount of arch collapse in the IG. This is consistent with what was reported by Mulligan and Cook (Mulligan and Cook, 2013), who found a decreased navicular drop after 4 weeks of intrinsic foot muscle training. The MLA should have the capacity to be flexible in response to running loads, allowing foot-joint adjustments to dampen impacts through multiple mechanisms, including stiffness and power absorption, but it must also be rigid enough to allow propulsion in the push-off phase (McDonald et al., 2016). Our foot-core training may have increased the ability of the plantar intrinsic muscles to provide force-dependent alterations in the MLA stiffness and to facilitate efficient foot-to-ground contact during running (Kelly, 2015; Kelly et al., 2018). An actively restricted MLA may help to decrease the mechanical demand on the soft tissues of the foot, such as ligaments, fascia, and tendons, and may result in fewer injuries in these structures, such as plantar fasciitis, which derives from repetitive abnormal strain and loading of the plantar fascia and flattening of the MLA (Wearing et al., 2006; Chang et al., 2014). A further mediation analysis could reveal if the changes observed in MLA behavior in the IG are associated with the reduction of RRI in our RCT (Taddei et al., 2020b). Further research should be conducted to determine how the changes in MLA pattern observed after the training program modify the running performance, because our previous proof-of-concept study showed that the foot-core training increased the vertical impulse during running (Taddei et al., 2020a).

The 8-week foot-core training affected the rearfoot inversion peak [shank-calcaneus (Sha-Cal) angle] as the rearfoot presented with increased inversion to the shank with respect to what was observed in controls with a medium effect size (p = 0.037; **Table 3**). We speculate that this is a consequence of the strengthening of the extrinsic foot-ankle muscles, such as the tibialis posterior, thus promoting the inversion of the calcaneus, resisting eversion during stance phase (Ivanenko et al., 2002; Neptune et al., 2008; Dubbeldam et al., 2013), and stabilizing the MLA (Imhauser et al., 2004; Kelly et al., 2015). The pathomechanics of medial tibial stress syndrome caused by periosteal inflammation is probably linked to excessive fascial traction caused by muscle tension resulting from excessive and/or prolonged pronation. A more inverted calcaneus in the IG may have increased the twisting of the osteoligamentous plate at initial ground contact (Araújo et al., 2019), which could consequently increase the resistance to pronation during the loading phase of running, when this plate tends to untwist. This increased resistance to calcaneus pronation in the IG may have provided the necessary protection for the tibiotalar joint from high traction forces imposed by the evertor and invertor muscles during the stance phase (Lundberg, 1989), resulting in less chance for an injury to occur in the IG than in the CG, whose members presented with more lower-leg RRI (Taddei et al., 2020b).

The Effect of the Foot-Core Training on Foot-Ankle Kinematic Patterns During the Whole Stance Phase of Running.

In order to better describe and measure the complexity of the interaction between foot joints in running, we next explored changes resulting from the intervention in the 24 kinematic time series from the Rizzoli foot model (Phinyomark et al., 2018). We performed a vector analysis of the resultant angles using 1D-SPM to compare the CG and IG (**Supplementary Figures**). This approach does not rely on the experimenter's subjective selection of the appropriate discrete variables, allowing changes to be identified in the whole time series that may have been missed using a discrete-parameter approach.

Sagittal-plane inclination of the metatarsal bones to the ground [first metatarsal bone to the ground (F2G), second metatarsal bone to the ground (S2G), and fifth metatarsal bone to the ground (V2G)] and metatarsal bone divergence in the transverse plane of the foot [second to first (S2F) and second to fifth (S2V)] were not different between the IG and CG after 8 weeks (**Figure 2**, **Supplementary Figures S1–3**). Although our previous proof-of-concept study (Taddei et al., 2020a) showed that the foot-core training increased the muscle volume of the abductor digiti minimi and flexor digitorum brevis, the full RCT did not result in changes in the kinematics of the metatarsal bones. We had expected an increase of F2G, S2G, and V2G as the MLA raised and shortened, but these changes may be very small and difficult to detect with skin markers.

No difference was observed in the kinematics of the first metatarsus-phalangeal (MTP) joint (Met-Hal) between the groups at baseline (**Figures 3A,B** and **Supplementary Figure S4**). After the intervention, the IG presented with increased abduction in the period from 47 to 99% of stance; the first MTP joint retuned to a less adducted (t*2.702, p = 0.003) and

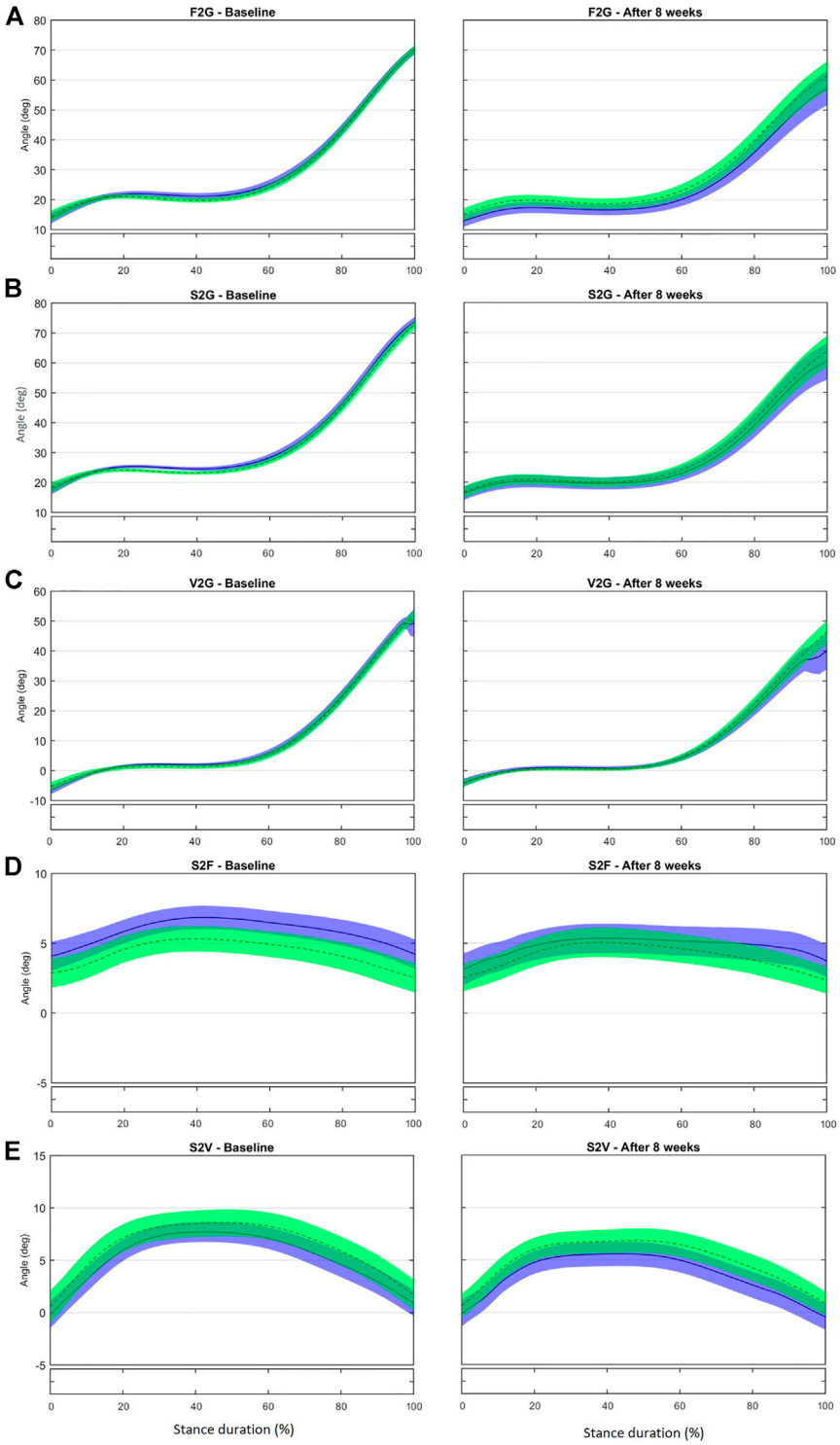

FIGURE 2 | Mean (±1SD) joint rotation angles during normalized stance phase duration of running in the baseline (left) and after 8 weeks of intervention (right). From top to bottom: Sagittal-plane inclination of the first metatarsal bone to the ground **(A)**, of the second metatarsal bone to the ground **(B)**, and of the fifth metatarsal bone to the ground **(C)**; transverse-plane divergence between first and second metatarsal bones **(D)** and between fifth and second metatarsal bones **(E)**. Green, CG group; Blue, IG group. The black bar below the graph represents the time during which the differences between the groups occurred ($p < 0.05$), what was indicated by the SPM {t} statistics.

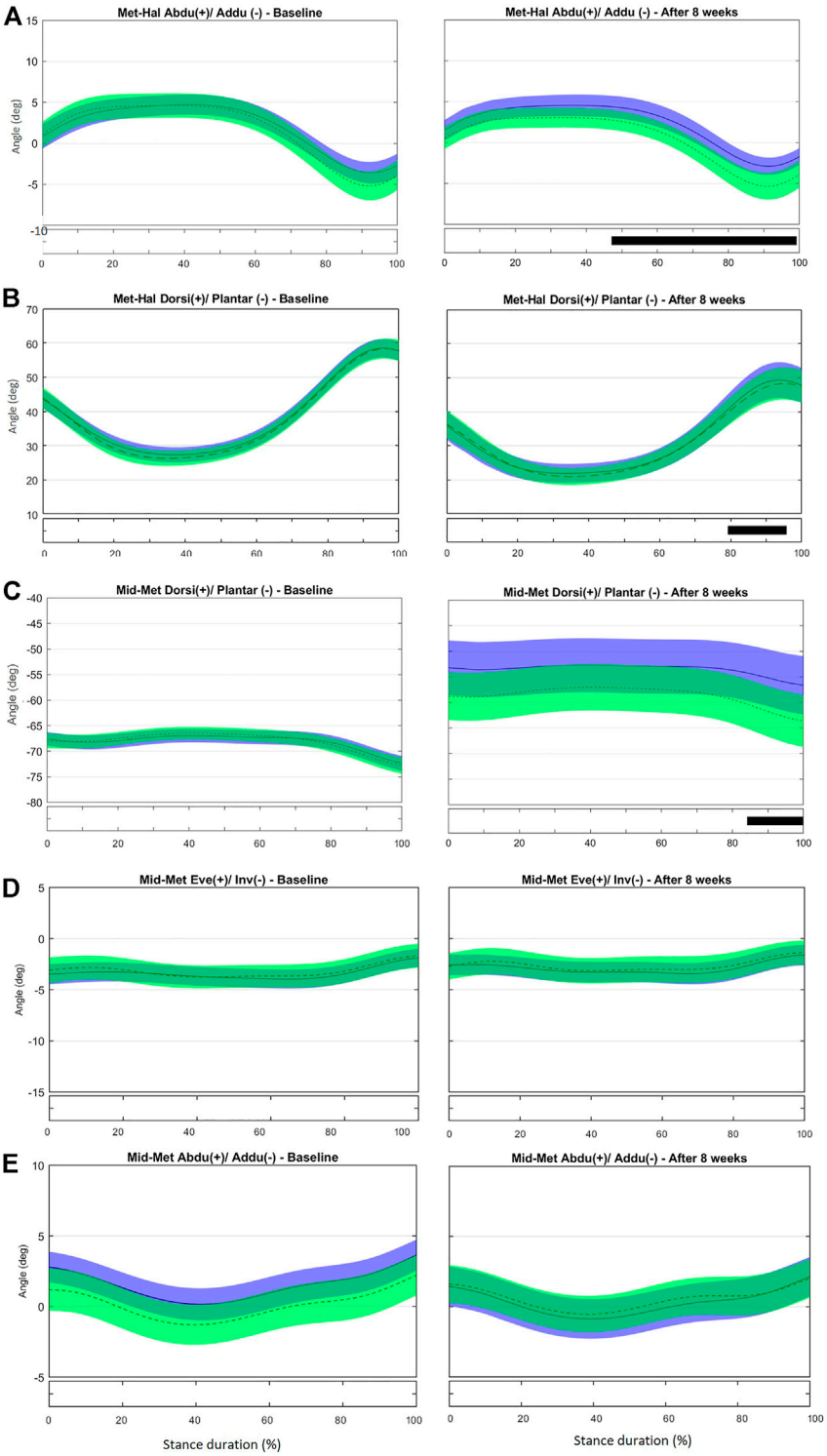

FIGURE 3 | Mean (±1SD) joint rotation angles during normalized stance phase duration of running in the baseline (left) and after 8 weeks of intervention (right). From top to bottom: transverse-plane rotations between hallux and metatarsus **(A)**; sagittal-plane rotations between hallux and metatarsus **(B)**; sagittal-plane rotations between metatarsus and midfoot **(C)**, frontal-plane rotations between metatarsus and midfoot **(D)**, and transverse-plane rotations between metatarsus and midfoot **(E)**. Green, CG group; Blue, IG group. The black bar below the graph represents the time during which the differences between the groups occurred ($p < 0.05$), what was indicated by the SPM{t} statistics.

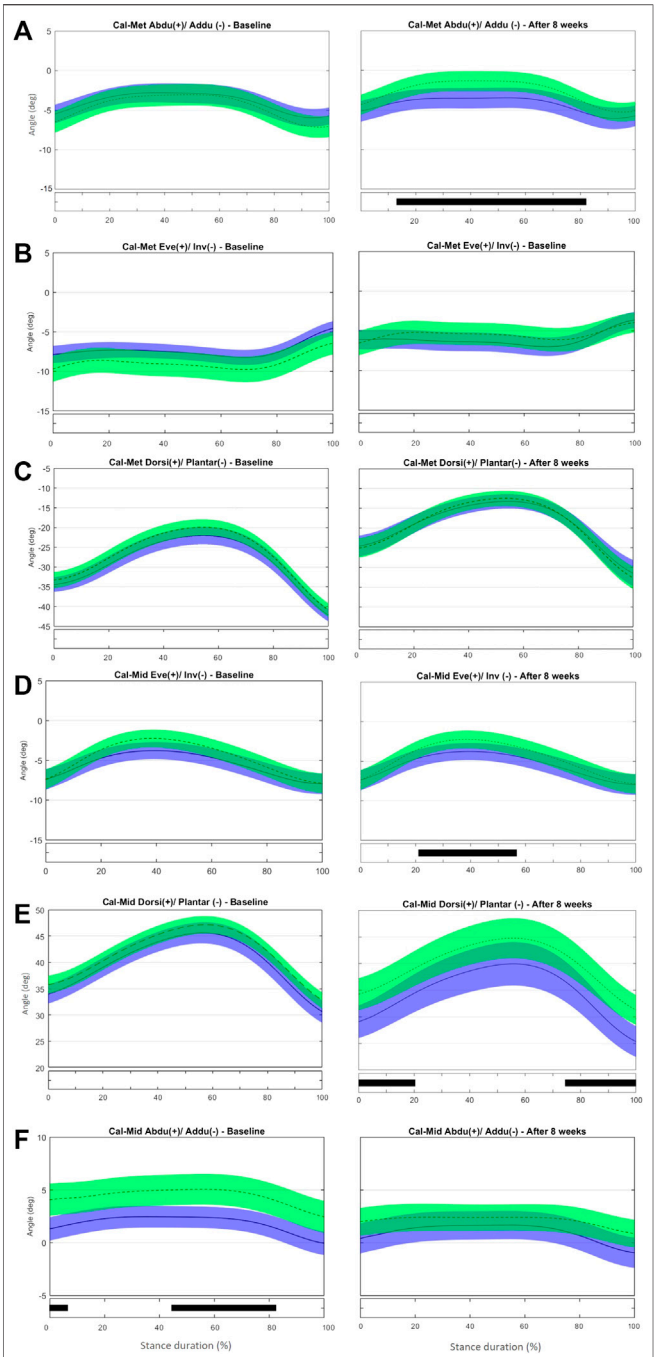

FIGURE 4 | Mean (±1SD) joint rotation angles during normalized stance phase duration of running in the baseline (left) and after 8 weeks of intervention (right). From top to bottom: transverse-plane rotations between metatarsus and calcaneus **(A)**, frontal-plane rotations between metatarsus and calcaneus **(B)**, sagittal-plane rotations between metatarsus and calcaneus **(C)**, frontal-plane rotations between midfoot and calcaneus **(D)**, sagittal-plane rotations between midfoot and calcaneus **(E)**, and transverse-plane rotations midfoot and calcaneus **(F)**. Green, CG group; Blue, IG group. The black bar below the graph represents the time during which the differences between the groups occurred ($p < 0.05$), what was indicated by the SPM{t} statistics.

more dorsiflexed position (t*2.783, $p = 0.003$) at push-off (79–96%) compared with controls (**Figures 3A,B**). Greater hallux abduction may be the consequence of a stronger abductor hallucis due to the intervention. This muscle also acts as a dynamic elevator of the MLA by increasing the tension in the plantar fascia that connects the MTP joint and calcaneus (the windlass mechanism) (Wong, 2007; Caravaggi et al., 2009; Jung et al., 2011a; McDonald et al., 2016). Thus, this greater hallux abduction may also explain the resulting reduction in MLA ROM found in the discrete analysis.

No difference was observed in midfoot-metatarsus (Mid-Met) (**Figures 3C–E**) and calcaneus-metatarsus (Cal-Met) (**Figures 4A–C**) kinematics between the IG and CG at baseline. The intervention had the effect in the sagittal-plane motion of Mid-Met of reducing metatarsal bone plantarflexion from 84 to 100% of stance compared with controls (t*2.764, $p = 0.016$) (**Figure 3C** and **Supplementary Figure S5**). After the foot-core training, the reduction in the Mid-Met plantarflexion toward a dorsiflexion from 84% to push-off may be a consequence of a more fixed position of the midfoot and metatarsal bones relative to the ground at push-off. The position of the midfoot (Cal-Mid) at push-off may have influenced the metatarsal segment (Mid-Met) as in a closed kinetic chain, leading this segment to move in the same direction as the midfoot (Takabayashi et al., 2018), and thus resulting in more dorsiflexion of the first metatarsus-hallux joint (Met-Hal), as discussed previously. After the intervention, Cal-Met adduction increased in the IG relative to the CG from 13 to 82% of stance (t*2.722, $p = 0.008$) (**Figure 4A** and **Supplementary Figure S6**). The concomitant reduction in MLA ROM (discrete analysis) seems to show that the IG developed a "stiffer" foot that behaves like a rigid lever, allowing greater plantarflexion torque to be transmitted to the ground during running (Donatelli, 1985). Further research is needed to determine how these changes in the MLA and Cal-Met patterns affect the running performance. Although Messier et al. (2018) did not find differences in forefoot adduction between injured and uninjured runners in a 2-year prospective study, the present foot-core training changed the metatarsal position and motion during running; a mediation effect analysis should be performed to assess how this change was related to the lower RRI incidence observed in the IG (Taddei et al., 2020b).

At baseline, no difference was observed in frontal- and sagittal-plane midfoot-to-calcaneus angles (Cal-Mid) between the IG and CG. After the training program, the CG showed lower Cal-Mid inversion from 25 to 45% of stance (t*2.704, $p = 0.014$) (**Figure 4D** and **Supplementary Figure S7**). The IG presented a reduced Cal-Mid dorsiflexion at early stance (0–20% of stance; t*2.820, $p = 0.014$) and at push-off (80–100% of stance; t*2.820, $p = 0.013$) compared with controls after 8 weeks (**Figure 4E**). The CG showed a less-abducted Cal-Mid at baseline from 0–0.7% and 44–80% of stance (t*2.630, $p = 0.017$ and $p = 0.015$, respectively). After 8 weeks of training, there was no difference between IG and CG (**Figure 4F**).

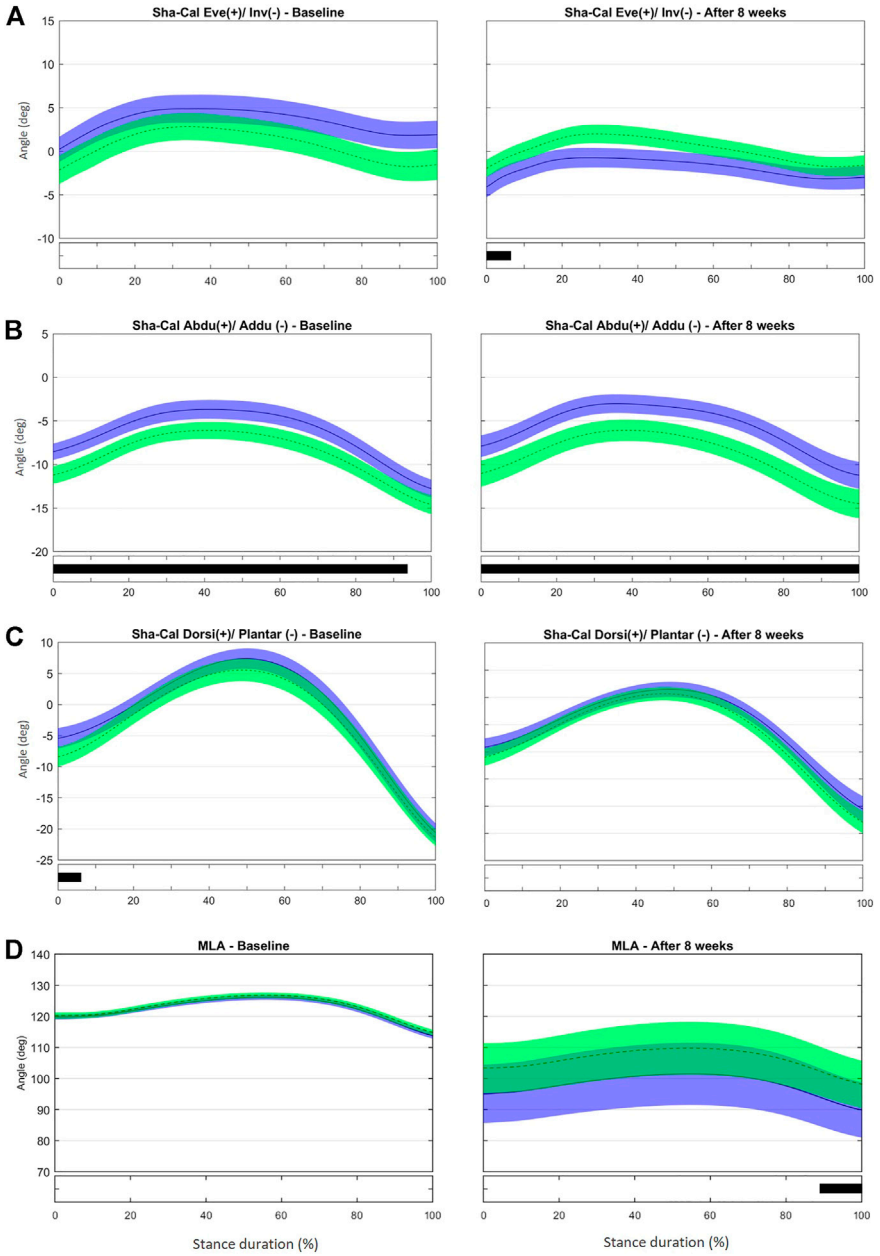

FIGURE 5 | Mean (±1SD) joint rotation angles during normalized stance phase duration of running in the baseline (left) and after 8 weeks of intervention (right). From top to bottom, frontal-plane rotations between calcaneus and shank **(A)**, transverse-plane rotations between calcaneus and shank **(B)**, sagittal-plane rotations between calcaneus and shank **(C)**, and medial longitudinal arch angle **(D)**. Green, CG group; Blue, IG group. The black bar below the graph represents the time during which the differences between the groups occurred ($p < 0.05$), what was indicated by the SPM{t} statistics.

At baseline, no difference between groups was observed in the frontal-plane Sha-Cal. At the 8-week assessment, calcaneus inversion at initial contact (0–6% stance, t* = 1.969, $p = 0.05$, **Supplementary Figure S8**) was greater in the IG than in the CG (**Figure 5A**). This result is consistent with the outcome of the discrete analysis that showed a more inverted rearfoot in the IG. As stated before, a more inverted calcaneus at early stance may help to attenuate the impact forces to the tibiotalar joint and diminish tibia rotation (Deschamps et al., 2019), and thus may have contributed to the reduced RRI incidence in the IG (Bouché and Johnson, 2007).

At baseline, the IG showed a less adducted Sha-Cal than the CG for most of stance duration (0–94% stance, t*2.694, $p < 0.001$), and a significant change was observed after 8 weeks (0–100% stance, t*2.788, $p < 0.001$) (**Figure 5B** and **Supplementary Figure S9**). Because the groups were different for most of the stance duration at baseline and maintained those differences after 8 weeks, the intervention does not seem to be responsible for the changes in

the transverse Sha-Cal pattern observed in the IG after the training. No difference was found in the Sha-Cal sagittal-plane angle between groups after the intervention (**Figure 5C**).

Different from what we found in the discrete analysis; the SPM analysis did not reveal differences between the groups in the MLA excursion during any part of the stance phase after 8 weeks (**Figure 5D** and **Supplementary Figure S3B**]. Both groups presented with more pronounced MLA angles, with large variability in the ROM within each group at late stance, after 8 weeks than at baseline (89–100% stance; $t^* = 2.521$, $p = 0.025$). In addition, both the IG and CG had significantly greater variability in the MLA pattern after 8 weeks. Both protocols (intervention and control) may have affected MLA biomechanics, albeit in different directions, thus making it difficult to determine the differences between the groups. It is notable that a stretching protocol designed as a placebo intervention affected MLA kinematics. We chose a simple stretching protocol as the control because most participants were part of running groups that already had some sort of stretching routine. Because most participants would combine their running practice with muscle stretching, the CG adherence to the protocol was not tracked thoroughly. The stretching exercises resulted in stretching of the Achilles tendon and foot-ankle plantar flexor muscles that may directly influence the calcaneus inclination; this could in turn modify the tension in the plantar fascia and, consequently, the passive support of the MLA (Yeap et al., 2001; DiGiovanni et al., 2003). Thus, the potential changes in the MLA pattern expressed by the increased variability in the CG may be a consequence of the changes in plantar fascia tension and calcaneus position and motion enhanced by the variability in the amount of stretching and also in individual response to the movement. However, another explanation may be considered. According to Pataky et al. (2013), in some cases scalar extraction analysis, based on the extraction of discrete variables that appear to have maximum effect, reaches significance and SPM analysis does not. Comparing discrete variables means, in fact, considering the comparison of only one sample of the entire time series and discarding the remaining samples for the comparisons.

In summary, the IG runners had decreased medial longitudinal arch excursion and increased rearfoot inversion. After the intervention, recreational runners also landed with a more inverted calcaneus in relation to the shank, and a less dorsiflexed midfoot with respect to the calcaneus, than did controls. At midstance, the metatarsus was less plantarflexed relative to the midfoot and more adducted relative to the calcaneus, and the first MTP joint was more abducted in the IG than in the controls. Last, the intervention resulted in a less dorsiflexed midfoot to the calcaneus at push-off, and in a less adducted and more dorsiflexed MTP joint.

Strengths and Limitations

The strengths of our study are the rigorous method for the RCT, its high completion and small dropout rates at follow-up, the adoption of robust statistical models (GLMM and 1D-SPM) that consider the complex non-linear iterations of foot-joint biomechanics, and its large sample size compared with other studies in the same field (Jung et al., 2011b; Goldmann et al., 2013; Baltich et al., 2015; Campitelli et al., 2016; Lucas-Cuevas et al., 2016; Mølgaard et al., 2018).

This study also had some limitations. First, we did not assess running biomechanics at the 1-year follow-up as we did for RRI incidence; thus, we could not draw any conclusions about the causality between RRI incidence and kinetic- or kinematic-related risk factors for RRI affected by our training program. Second, although different RRIs or injury sites are expected to originate from different mechanisms, and enhancing foot strength might be more effective in preventing some types of injuries than others (some of them reduced impact loading, some did not, thus the mean of the group did not show between-group differences), we could not differentiate between different types of RRIs. It is important to note that the most serious RRIs were in runners from CG—stress fractures, which could also be related to the difference in the impact damping mechanisms performed by the musculoskeletal system, more specifically the foot-core, that was not strengthened as in the IG, where those type of RRIs did not occur.

This prevented us from explaining the biomechanical mechanisms for the reduction of RRI incidence in the IG after the intervention. Furthermore, although lower-limb kinematic patterns are similar in over-ground and treadmill running (Fellin et al., 2010; Sinclair et al., 2014), the participants ran barefoot on a treadmill to facilitate kinematic measurements, a condition different from their usual practice. Finally, we observed some differences at baseline in the foot-ankle kinematic patterns that could be related to the previously identified clusters of movement patterns among our population of recreational runners included in this study (Watari et al., 2021). Runners in the different clusters might have responded differently to the training program. If true, this would suggest that the response to the exercise intervention depends on the individual foot biomechanical pattern, which could explain the absence of differences in some discrete and continuous outcomes analyzed.

CONCLUSION

The 8-week foot-core exercise program significantly changed the kinematic patterns of the ankle, tarso-metarsal, midtarsal, and MPT joints and some of the biomechanical risk factors for RRI, such as MLA ROM and rearfoot angle. No effect was observed on impact and breaking forces or on loading rates. After the intervention, recreational runners landed with a significantly less dorsiflexed midfoot, and a more inverted calcaneus compared to controls. At midstance, runners run with a significantly more abducted hallux, a less plantarflexed and more adducted forefoot. And finally, the intervention resulted in a push-off with a significantly less dorsiflexed midfoot, a less adducted and more plantarflexed hallux. Although a further mediation analysis should be performed, the observed changes in foot-joint kinematics may be responsible for the reduction in RRI incidence following the foot-core training program.

DATA AVAILABILITY STATEMENT

The original contributions presented in the study are publicly available. This data can be found here: https://figshare.com/search?q=10.6084%2Fm9.figshare.13484715.

ETHICS STATEMENT

The studies involving human participants were reviewed and approved by the Ethics Committee of the School of Medicine of the University of São Paulo (18/03/2015, Protocol #031/15). The patients/participants provided their written informed consent to participate in this study.

AUTHOR CONTRIBUTIONS

AM, UT and IS were responsible for the conception and design of the study; AM, RW, UT, RI and RT were responsible for data acquisition and data processing; PC and MV for developing tools for the analysis; AM, RW, UT, PC, RI, RT, ES, MV and IS for data analysis and interpretation; and AM and IS for drafting the paper. IS revised the manuscript critically. All authors read, provided feedback and approved the submitted version.

FUNDING

The Sao Paulo Research Foundation (FAPESP) funded the project (2015/14810-0), the fellowship of AM (2016/17077-4, 2017/26844-1), RW (2019/19291-1), PC (2017/23975-8) and ES (2017/15449-4); UT was awarded by Agency Coordination of Improvement of Higher Education Personnel (CAPES, financial code 001). IS and MV are a fellow of the National Council for Scientific and Technological Development (CNPq), Brazil (Process: 304124/2018-4, 304533/2020-3, respectively). The funders do not have any role in the study and do not have any authority over any study activity or in the decision to submit the report for publication.

SUPPLEMENTARY MATERIAL

The Supplementary Material for this article can be found online at: https://www.frontiersin.org/articles/10.3389/fbioe.2022.890428/full#supplementary-material

REFERENCES

Araújo, V. L., Souza, T. R., Magalhães, F. A., Santos, T. R. T., Holt, K. G., and Fonseca, S. T. (2019). Effects of a Foot Orthosis Inspired by the Concept of a Twisted Osteoligamentous Plate on the Kinematics of Foot-Ankle Complex during Walking: A Proof of Concept. *J. Biomech.* 93, 118–125. doi:10.1016/j.jbiomech.2019.06.020

Baltich, J., Emery, C. A., Whittaker, J. L., and Nigg, B. M. (2017). Running Injuries in Novice Runners Enrolled in Different Training Interventions: a Pilot Randomized Controlled Trial. *Scand. J. Med. Sci. Sports* 27, 1372–1383. doi:10.1111/sms.12743

Baltich, J., Maurer, C., and Nigg, B. M. (2015). Increased Vertical Impact Forces and Altered Running Mechanics with Softer Midsole Shoes. *PLoS One* 10, e0125196–11. doi:10.1371/journal.pone.0125196

Bennell, K. L., Malcolm, S. A., Thomas, S. A., Wark, J. D., and Brukner, P. D. (1996). The Incidence and Distribution of Stress Fractures in Competitive Track and Field Athletes. *Am. J. Sports Med.* 24, 211–217. doi:10.1177/036354659602400217

Bennett, J. E., Reinking, M. F., Pluemer, B., Pentel, A., Seaton, M., and Killian, C. (2001). Factors Contributing to the Development of Medial Tibial Stress Syndrome in High School Runners. *J. Orthop. Sports Phys. Ther.* 31, 504–510. doi:10.2519/jospt.2001.31.9.504

Bouche, R. T., and Johnson, C. H. (2007). Medial Tibial Stress Syndrome (Tibial Fasciitis). *J. Am. Podiatr. Med. Assoc.* 97, 31–36. doi:10.7547/0970031

Bredeweg, S. W., Kluitenberg, B., Bessem, B., and Buist, I. (2013). Differences in Kinetic Variables between Injured and Noninjured Novice Runners: A Prospective Cohort Study. *J. Sci. Med. Sport* 16, 205–210. doi:10.1016/j.jsams.2012.08.002

Brumitt, J. (2009). Injury Prevention for High School Female Cross-Country Athletes. *Athl. Ther. Today* 14, 8–12. doi:10.1123/att.14.4.8

Buist, I., Bredeweg, S. W., Bessem, B., van Mechelen, W., Lemmink, K. A. P. M., and Diercks, R. L. (2010). Incidence and Risk Factors of Running-Related Injuries during Preparation for a 4-mile Recreational Running Event. *Br. J. Sports Med.* 44, 598–604. doi:10.1136/bjsm.2007.044677

Buist, I., Bredeweg, S. W., van Mechelen, W., Lemmink, K. A. P. M., Pepping, G.-J., and Diercks, R. L. (2008). No Effect of a Graded Training Program on the Number of Running-Related Injuries in Novice Runners. *Am. J. Sports Med.* 36, 33–39. doi:10.1177/0363546507307505

Busseuil, C., Freychat, P., Guedj, E. B., and Lacour, J. R. (1998). Rearfoot-forefoot Orientation and Traumatic Risk for Runners. *Foot Ankle Int.* 19, 32–37. doi:10.1177/107110079801900106

Campitelli, N. A., Spencer, S. A., Bernhard, K., Heard, K., and Kidon, A. (2016). Effect of Vibram Fivefingers Minimalist Shoes on the Abductor Hallucis Muscle. *J. Am. Podiatr. Med. Assoc.* 106, 344–351. doi:10.7547/14-084

Caravaggi, P., Matias, A. B., Taddei, U. T., Ortolani, M., Leardini, A., and Sacco, I. C. N. (2019). Reliability of Medial-Longitudinal-Arch Measures for Skin-Markers Based Kinematic Analysis. *J. Biomech.* 88, 180–185. doi:10.1016/j.jbiomech.2019.03.017

Caravaggi, P., Pataky, T., Goulermas, J. Y., Savage, R., and Crompton, R. (2009). A Dynamic Model of the Windlass Mechanism of the Foot: Evidence for Early Stance Phase Preloading of the Plantar Aponeurosis. *J. Exp. Biol.* 212, 2491–2499. doi:10.1242/jeb.025767

Ceyssens, L., Vanelderen, R., Barton, C., Malliaras, P., and Dingenen, B. (2019). Biomechanical Risk Factors Associated with Running-Related Injuries: A Systematic Review. *Sports Med.* 49, 1095–1115. doi:10.1007/s40279-019-01110-z

Chang, R., Rodrigues, P. A., Van Emmerik, R. E. A., and Hamill, J. (2014). Multi-segment Foot Kinematics and Ground Reaction Forces during Gait of Individuals with Plantar Fasciitis. *J. Biomech.* 47, 2571–2577. doi:10.1016/j.jbiomech.2014.06.003

Cohen, J. (1988). in *Statistical Power Analysis for the Behavioral Sciences*. Editor L. E. Associates (Academic Press).

Cowan, D. N., Jones, B. H., and Robinson, J. R. (1993). Foot Morphologic Characteristics and Risk of Exercise-Related Injury. *Arch. Fam. Med.* 2, 773–777. doi:10.1001/archfami.2.7.773

Davis, I. S., Bowser, B. J., and Mullineaux, D. R. (2016). Greater Vertical Impact Loading in Female Runners with Medically Diagnosed Injuries: A Prospective Investigation. *Br. J. Sports Med.* 50, 887–892. doi:10.1136/bjsports-2015-094579

Davis, I. S., Rice, H. M., and Wearing, S. C. (2017). Why Forefoot Striking in Minimal Shoes Might Positively Change the Course of Running Injuries. *J. Sport Health Sci.* 6, 154–161. doi:10.1016/j.jshs.2017.03.013

Deschamps, K., Eerdekens, M., Peters, H., Matricali, G. A., and Staes, F. (2019). Multi-segment Foot Kinematics during Running and its Association with Striking Patterns. *Sports Biomech.* 21, 71–84. doi:10.1080/14763141.2019.1645203

DiGiovanni, B. F., Nawoczenski, D. A., Lintal, M. E., Moore, E. A., Murray, J. C., Wilding, G. E., et al. (2003). Tissue-specific Plantar Fascia-Stretching Exercise Enhances Outcomes in Patients with Chronic Heel Pain. *The J. Bone Jt. Surgery-American Volume* 85, 1270–1277. doi:10.2106/00004623-200307000-00013

Donatelli, R. (1985). Normal Biomechanics of the Foot and Ankle. *J. Orthop. Sports Phys. Ther.* 7, 91–95. doi:10.2519/jospt.1985.7.3.91

Dubbeldam, R., Nester, C., Nene, A. V., Hermens, H. J., and Buurke, J. H. (2013). Kinematic Coupling Relationships Exist between Non-adjacent Segments of the

Foot and Ankle of Healthy Subjects. *Gait & Posture* 37, 159–164. doi:10.1016/j.gaitpost.2012.06.033

Dudley, R. I., Pamukoff, D. N., Lynn, S. K., Kersey, R. D., and Noffal, G. J. (2017). A Prospective Comparison of Lower Extremity Kinematics and Kinetics between Injured and Non-injured Collegiate Cross Country Runners. *Hum. Mov. Sci.* 52, 197–202. doi:10.1016/j.humov.2017.02.007

Farris, D. J., Kelly, L. A., Cresswell, A. G., and Lichtwark, G. A. (2019). The Functional Importance of Human Foot Muscles for Bipedal Locomotion. *Proc. Natl. Acad. Sci. U.S.A.* 116, 1645–1650. doi:10.1073/pnas.1812820116

Fellin, R. E., Manal, K., and Davis, I. S. (2010). Comparison of Lower Extremity Kinematic Curves during Overground and Treadmill Running. *J. Appl. Biomech.* 26, 407–414. doi:10.1126/scisignal.2001449.Engineering10.1123/jab.26.4.407

Feltner, M. E., MacRae, H. S., Macrae, P. G., Turner, N. S., Hartman, C. A., Summers, M. L., et al. (1994). Strength Training Effects on Rearfoot Motion in Running. *Med. Sci. Sports Exerc.* 26, 1021–1027. doi:10.1249/00005768-199408000-00014

Fiolkowski, P., Brunt, D., Bishop, M., Woo, R., and Horodyski, M. (2003). Intrinsic Pedal Musculature Support of the Medial Longitudinal Arch: an Electromyography Study. *J. Foot Ankle Surg.* 42, 327–333. doi:10.1053/j.jfas.2003.10.003

Fokkema, T., Vos, R.-J. d., Van Ochten, J. M., van Ochten, J. A., Davis, I. S., Bindels, P. J., et al. (2017). Preventing Running-Related Injuries Using Evidence-Based Online Advice: The Design of a Randomised-Controlled Trial. *BMJ Open Sport Exerc. Med.* 3, e000265–9. doi:10.1136/bmjsem-2017-000265

Fredericson, M., and Moore, T. (2005). Muscular Balance, Core Stability, and Injury Prevention for Middle- and Long-Distance Runners. *Phys. Med. Rehabil. Clin. North America* 16, 669–689. doi:10.1016/j.pmr.2005.03.001

Goldmann, J.-P., Sanno, M., Willwacher, S., Heinrich, K., and Brüggemann, G.-P. (2013). The Potential of Toe Flexor Muscles to Enhance Performance. *J. Sports Sci.* 31, 424–433. doi:10.1080/02640414.2012.736627

Grimston, S. K., Engsberg, J. R., Kloiber, R., and Hanley, D. A. (1991). Bone Mass, External Loads, and Stress Fracture in Female Runners. *Int. J. Sport Biomech.* 7, 293–302. doi:10.1123/ijsb.7.3.293

Grood, E. S., and Suntay, W. J. (1983). A Joint Coordinate System for the Clinical Description of Three-Dimensional Motions: Application to the Knee. *J. Biomech. Eng.* 105, 136–144. doi:10.1115/1.3138397

Headlee, D. L., Leonard, J. L., Hart, J. M., Ingersoll, C. D., and Hertel, J. (2008). Fatigue of the Plantar Intrinsic Foot Muscles Increases Navicular Drop. *J. Electromyogr. Kinesiol.* 18, 420–425. doi:10.1016/j.jelekin.2006.11.004

Hein, T., and Grau, S. (2014). Can Minimal Running Shoes Imitate Barefoot Heel-Toe Running Patterns? A Comparison of Lower Leg Kinematics. *J. Sport Health Sci.* 3, 67–73. doi:10.1016/j.jshs.2014.03.002

Hespanhol, L. C., van Mechelen, W., and Verhagen, E. (2018). Effectiveness of Online Tailored Advice to Prevent Running-Related Injuries and Promote Preventive Behaviour in Dutch Trail Runners: a Pragmatic Randomised Controlled Trial. *Br. J. Sports Med.* 52, 851–858. doi:10.1136/bjsports-2016-097025

Hollman, J. H., Kolbeck, K. E., Hitchcock, J. L., Koverman, J. W., and Krause, D. A. (2006). Correlations between Hip Strength and Static Foot and Knee Posture. *J. Sport Rehabil.* 15, 12–23. doi:10.1123/jsr.15.1.12

Hott, A., Liavaag, S., Juel, N. G., and Brox, J. I. (2015). Study Protocol: A Randomised Controlled Trial Comparing the Long Term Effects of Isolated Hip Strengthening, Quadriceps-Based Training and Free Physical Activity for Patellofemoral Pain Syndrome (Anterior Knee Pain). *BMC Musculoskelet. Disord.* 16, 1–8. doi:10.1186/s12891-015-0493-6

Hreljac, A., Marshall, R. N., and Hume, P. A. (1999). Evaluation of Lower Extremity Overuse Injury Potential in Runners. *Med. Sci. Sports Exerc.* 32, 1635–1641. doi:10.1097/00005768-200009000-00018

Hreljac, A., Marshall, R. N., and Hume, P. A. (2000). Evaluation of Lower Extremity Overuse Injury Potential in Runners. *Med. Sci. Sports Exerc.* 32, 1635–1641. doi:10.1097/00005768-200009000-00018

Imhauser, C. W., Siegler, S., Abidi, N. A., and Frankel, D. Z. (2004). The Effect of Posterior Tibialis Tendon Dysfunction on the Plantar Pressure Characteristics and the Kinematics of the Arch and the Hindfoot. *Clin. Biomech.* 19, 161–169. doi:10.1016/j.clinbiomech.2003.10.007

Ivanenko, Y. P., Grasso, R., Macellari, V., and Lacquaniti, F. (2002). Control of Foot Trajectory in Human Locomotion: Role of Ground Contact Forces in Simulated Reduced Gravity. *J. Neurophysiol.* 87, 3070–3089. doi:10.1152/jn.2002.87.6.3070

Johnston, C. A., Taunton, J. E., Lloyd-Smith, D. R., and McKenzie, D. C. (2003). Preventing Running Injuries. Practical Approach for Family Doctors. *Can. Fam. Physician* 49, 1101–1109.

Jung, D.-Y., Kim, M.-H., Koh, E.-K., Kwon, O.-Y., Cynn, H.-S., and Lee, W.-H. (2011a). A Comparison in the Muscle Activity of the Abductor Hallucis and the Medial Longitudinal Arch Angle during Toe Curl and Short Foot Exercises. *Phys. Ther. Sport* 12, 30–35. doi:10.1016/j.ptsp.2010.08.001

Jung, D.-Y., Koh, E.-K., and Kwon, O.-Y. (2011b). Effect of Foot Orthoses and Short-Foot Exercise on the Cross-Sectional Area of the Abductor Hallucis Muscle in Subjects with Pes Planus: A Randomized Controlled Trial1. *Bmr* 24, 225–231. doi:10.3233/BMR-2011-0299

Kelly, L. A., Cresswell, A. G., and Farris, D. J. (2018). The Energetic Behaviour of the Human Foot across a Range of Running Speeds. *Sci. Rep.* 8, 10576. doi:10.1038/s41598-018-28946-1

Kelly, L. A., Lichtwark, G., Cresswell, A. G., and Cresswell, A. G. (2015). Active Regulation of Longitudinal Arch Compression and Recoil during Walking and Running. *J. R. Soc. Interf.* 12, 20141076. doi:10.1098/rsif.2014.1076

Kelly, L. (2015). In-vivo *Function of Human Plantar Intrinsic Foot Muscles*. doi:10.14264/uql.2015.341

Ker, R. F., Bennett, M. B., Bibby, S. R., Kester, R. C., and Alexander, R. M. (1987). The spring in the Arch of the Human Foot. *Nature* 325, 147–149. doi:10.1038/325147a0

Kluitenberg, B., van Middelkoop, M., Diercks, R., and van der Worp, H. (2015). What Are the Differences in Injury Proportions between Different Populations of Runners? A Systematic Review and Meta-Analysis. *Sports Med.* 45, 1143–1161. doi:10.1007/s40279-015-0331-x

Kuhman, D. J., Paquette, M. R., Peel, S. A., and Melcher, D. A. (2016). Comparison of Ankle Kinematics and Ground Reaction Forces between Prospectively Injured and Uninjured Collegiate Cross Country Runners. *Hum. Mov. Sci.* 47, 9–15. doi:10.1016/j.humov.2016.01.013

Leardini, A., Benedetti, M. G., Berti, L., Bettinelli, D., Nativo, R., and Giannini, S. (2007). Rear-foot, Mid-foot and Fore-Foot Motion during the Stance Phase of Gait. *Gait & Posture* 25, 453–462. doi:10.1016/j.gaitpost.2006.05.017

Lucas-Cuevas, A. G., Baltich, J., Enders, H., Nigg, S., and Nigg, B. (2016). Ankle Muscle Strength Influence on Muscle Activation during Dynamic and Static Ankle Training Modalities. *J. Sports Sci.* 34, 803–810. doi:10.1080/02640414.2015.1072640

Lundberg, A. (1989). Kinematics of the Ankle and Foot: *In Vivo* Roentgen Stereophotogrammetry. *Acta Orthopaedica Scand.* 60, 1–26. doi:10.3109/17453678909154185

Matias, A. B., Taddei, U. T., Duarte, M., and Sacco, I. C. N. (2016). Protocol for Evaluating the Effects of a Therapeutic Foot Exercise Program on Injury Incidence, Foot Functionality and Biomechanics in Long-Distance Runners: a Randomized Controlled Trial. *BMC Musculoskelet. Disord.* 17, 160. doi:10.1186/s12891-016-1016-9

McDonald, K. A., Stearne, S. M., Alderson, J. A., North, I., Pires, N. J., and Rubenson, J. (2016). The Role of Arch Compression and Metatarsophalangeal Joint Dynamics in Modulating Plantar Fascia Strain in Running. *PLoS One* 11, e0152602–16. doi:10.1371/journal.pone.0152602

McKeon, P. O., and Fourchet, F. (2015a). Freeing the Foot. *Clin. Sports Med.* 34 (2), 347–361. doi:10.1016/j.csm.2014.12.002

McKeon, P. O., Hertel, J., Bramble, D., and Davis, I. (2015b). The Foot Core System: a New Paradigm for Understanding Intrinsic Foot Muscle Function. *Br. J. Sports Med.* 49, 290. doi:10.1136/bjsports-2013-092690

Messier, S. P., Edwards, D. G., Martin, D. F., Lowery, R. B., Cannon, D. W., James, M. K., et al. (1995). Etiology of Iliotibial Band Friction Syndrome in Distance Runners. *Med. Sci. Sports Exerc.* 27, 951–960. doi:10.1249/00005768-199507000-00002

Messier, S. P., Martin, D. F., Mihalko, S. L., Ip, E., DeVita, P., Cannon, D. W., et al. (2018). A 2-Year Prospective Cohort Study of Overuse Running Injuries: The Runners and Injury Longitudinal Study (TRAILS). *Am. J. Sports Med.* 46, 2211–2221. doi:10.1177/0363546518773755

Messier, S. P., and Pittala, K. A. (1988). Etiologic Factors Associated with Selected Running Injuries. *Med. Sci. Sports Exerc.* 20, 501–505. doi:10.1249/00005768-198810000-00012

Milner, C. E., Ferber, R., Pollard, C. D., Hamill, J., and Davis, I. S. (2006). Biomechanical Factors Associated with Tibial Stress Fracture in Female

Runners. *Med. Sci. Sports Exerc.* 38, 323–328. doi:10.1249/01.mss.0000183477.75808.92

Mølgaard, C. M., Rathleff, M. S., Andreasen, J., Christensen, M., Lundbye-Christensen, S., Simonsen, O., et al. (2018). Foot Exercises and Foot Orthoses Are More Effective Than Knee Focused Exercises in Individuals with Patellofemoral Pain. *J. Sci. Med. Sport* 21, 10–15. doi:10.1016/j.jsams.2017.05.019

Mulligan, E. P., and Cook, P. G. (2013). Effect of Plantar Intrinsic Muscle Training on Medial Longitudinal Arch Morphology and Dynamic Function. *Man. Ther.* 18, 425–430. doi:10.1016/j.math.2013.02.007

Napier, C., MacLean, C. L., Maurer, J., Taunton, J. E., and Hunt, M. A. (2018). Kinetic Risk Factors of Running-Related Injuries in Female Recreational Runners. *Scand. J. Med. Sci. Sports* 28, 2164–2172. doi:10.1111/sms.13228

Neptune, R. R., Sasaki, K., and Kautz, S. A. (2008). The Effect of Walking Speed on Muscle Function and Mechanical Energetics. *Gait & Posture* 28, 135–143. doi:10.1016/j.gaitpost.2007.11.004

Nigg, B. M., Baltich, J., Federolf, P., Manz, S., and Nigg, S. (2017). Functional Relevance of the Small Muscles Crossing the Ankle Joint - the Bottom-Up Approach. *Ciss* 2. doi:10.15203/ciss_2017.003

Nigg, B. M., Khan, A., Fisher, V., and Stefanyshyn, D. (1998). Effect of Shoe Insert Construction on Foot and Leg Movement. *Med. Sci. Sports Exerc.* 30, 550–555. doi:10.1097/00005768-199804000-00013

Noehren, B., Davis, I., and Hamill, J. (2007). ASB Clinical Biomechanics Award Winner 2006. *Clin. Biomech.* 22, 951–956. doi:10.1016/j.clinbiomech.2007.07.001

Noehren, B., Hamill, J., and Davis, I. (2013). Prospective Evidence for a Hip Etiology in Patellofemoral Pain. *Med. Sci. Sports Exerc.* 45, 1120–1124. doi:10.1249/MSS.0b013e31828249d2

Palmer, K., Hebron, C., and Williams, J. M. (2015). A Randomised Trial into the Effect of an Isolated Hip Abductor Strengthening Programme and a Functional Motor Control Programme on Knee Kinematics and Hip Muscle Strength. *BMC Musculoskelet. Disord.* 16, 1–8. doi:10.1186/s12891-015-0563-9

Pataky, T. C., Robinson, M. A., and Vanrenterghem, J. (2018). A Computational Framework for Estimating Statistical Power and Planning Hypothesis-Driven Experiments Involving One-Dimensional Biomechanical Continua. *J. Biomech.* 66, 159–164. doi:10.1016/j.jbiomech.2017.09.031

Pataky, T. C., Robinson, M. A., and Vanrenterghem, J. (2013). Vector Field Statistical Analysis of Kinematic and Force Trajectories. *J. Biomech.* 46, 2394–2401. doi:10.1016/j.jbiomech.2013.07.031

Phinyomark, A., Petri, G., Ibáñez-Marcelo, E., Osis, S. T., and Ferber, R. (2018). Analysis of Big Data in Gait Biomechanics: Current Trends and Future Directions. *J. Med. Biol. Eng.* 38, 244–260. doi:10.1007/s40846-017-0297-2

Pohl, M. B., and Buckley, J. G. (2008). Changes in Foot and Shank Coupling Due to Alterations in Foot Strike Pattern during Running. *Clin. Biomech.* 23, 334–341. doi:10.1016/j.clinbiomech.2007.09.016

Portinaro, N., Leardini, A., Panou, A., Monzani, V., and Caravaggi, P. (2014). Modifying the Rizzoli Foot Model to Improve the Diagnosis of Pes-Planus: Application to Kinematics of Feet in Teenagers. *J. Foot Ankle Res.* 7, 754. doi:10.1186/s13047-014-0057-2

Powers, C. M. (2010). The Influence of Abnormal Hip Mechanics on Knee Injury: A Biomechanical Perspective. *J. Orthop. Sports Phys. Ther.* 40, 42–51. doi:10.2519/jospt.2010.3337

Sinclair, J., Taylor, P. J., and Vincent, H. (2014). Multisegment Foot Kinematics and Plantar Fascia Strain during Treadmill and Overground Running. *Foot Ankle Online J.* 7. doi:10.3827/faoj.2014.0704.0004

Snyder, K. R., Earl, J. E., O'Connor, K. M., and Ebersole, K. T. (2009). Resistance Training Is Accompanied by Increases in Hip Strength and Changes in Lower Extremity Biomechanics during Running. *Clin. Biomech.* 24, 26–34. doi:10.1016/j.clinbiomech.2008.09.009

Taddei, U. T., Matias, A. B., Duarte, M., and Sacco, I. C. N. (2020b). Foot Core Training to Prevent Running-Related Injuries: A Survival Analysis of a Single-Blind, Randomized Controlled Trial. *Am. J. Sports Med.* 48, 3610–3619. doi:10.1177/0363546520969205

Taddei, U. T., Matias, A. B., Ribeiro, F. I. A., Bus, S. A., and Sacco, I. C. N. (2020a). Effects of a Foot Strengthening Program on Foot Muscle Morphology and Running Mechanics: A Proof-Of-Concept, Single-Blind Randomized Controlled Trial. *Phys. Ther. Sport* 42, 107–115. doi:10.1016/j.ptsp.2020.01.007

Taddei, U. T., Matias, A. B., Ribeiro, F. I. A., Inoue, R. S., Bus, S. A., and Sacco, I. C. N. (2018). Effects of a Therapeutic Foot Exercise Program on Injury Incidence, Foot Functionality and Biomechanics in Long-Distance Runners: Feasibility Study for a Randomized Controlled Trial. *Phys. Ther. Sport* 34, 216–226. doi:10.1016/j.ptsp.2018.10.015

Takabayashi, T., Edama, M., Yokoyama, E., Kanaya, C., and Kubo, M. (2018). Quantifying Coordination Among the Rearfoot, Midfoot, and Forefoot Segments during Running. *Sports Biomech.* 17, 18–32. doi:10.1080/14763141.2016.1271447

Tiberio, D. (1987). The Effect of Excessive Subtalar Joint Pronation on Patellofemoral Mechanics: A Theoretical Model. *J. Orthop. Sports Phys. Ther.* 9, 160–165. doi:10.2519/jospt.1987.9.4.160

van der Worp, M. P., ten Haaf, D. S. M., van Cingel, R., de Wijer, A., Nijhuis-Van Der Sanden, M. W. G., Staal, J. B., et al. (2015). Injuries in Runners; a Systematic Review on Risk Factors and Sex Differences. *PLoS One* 10, e0114937. doi:10.1371/journal.pone.0114937

Van Gent, R. N., Siem, D., van Middelkoop, M., Van Os, a. G., Bierma-Zeinstra, S. M. A., Koes, B. W., et al. (2007). Incidence and Determinants of Lower Extremity Running Injuries in Long Distance Runners: a Systematic Review * COMMENTARY. *Br. J. Sports Med.* 41, 469–480. doi:10.1136/bjsm.2006.033548

Watari, R., Suda, E. Y., Santos, J. P. S., Matias, A. B., Taddei, U. T., and Sacco, I. C. N. (2021). Subgroups of Foot-Ankle Movement Patterns Can Influence the Responsiveness to a Foot-Core Exercise Program: A Hierarchical Cluster Analysis. *Front. Bioeng. Biotechnol.* 9, 1–13. doi:10.3389/fbioe.2021.645710

Wearing, S. C., Smeathers, J. E., Urry, S. R., Hennig, E. M., and Hills, A. P. (2006). The Pathomechanics of Plantar Fasciitis. *Sports Med.* 36, 585–611. doi:10.2165/00007256-200636070-00004

Weist, R., Eils, E., and Rosenbaum, D. (2004). The Influence of Muscle Fatigue on Electromyogram and Plantar Pressure Patterns as an Explanation for the Incidence of Metatarsal Stress Fractures. *Am. J. Sports Med.* 32, 1893–1898. doi:10.1177/0363546504265191

Willems, T. M., De Clercq, D., Delbaere, K., Vanderstraeten, G., De Cock, A., and Witvrouw, E. (2006). A Prospective Study of Gait Related Risk Factors for Exercise-Related Lower Leg Pain. *Gait & Posture* 23, 91–98. doi:10.1016/j.gaitpost.2004.12.004

Williams III, D. S., McClay, I. S., and Hamill, J. (2001). Arch Structure and Injury Patterns in Runners. *Clin. Biomech.* 16, 341–347. doi:10.1016/S0268-0033(01)00005-5

Willy, R. W., and Davis, I. S. (2011). The Effect of a Hip-Strengthening Program on Mechanics during Running and during a Single-Leg Squat. *J. Orthop. Sports Phys. Ther.* 41, 625–632. doi:10.2519/jospt.2011.3470

Wong, Y. S. (2007). Influence of the Abductor Hallucis Muscle on the Medial Arch of the Foot: a Kinematic and Anatomical Cadaver Study. *Foot Ankle Int.* 28, 617–620. doi:10.3113/FAI.2007.0617

Yeap, J. S., Singh, D., and Birch, R. (2001). Tibialis Posterior Tendon Dysfunction: A Primary of Secondary Problem? *Foot Ankle Int.* 22, 51–55. doi:10.1177/107110070102200108

Zadpoor, A. A., and Nikooyan, A. A. (2011). The Relationship between Lower-Extremity Stress Fractures and the Ground Reaction Force: A Systematic Review. *Clin. Biomech.* 26, 23–28. doi:10.1016/j.clinbiomech.2010.08.005

Conflict of Interest: The authors declare that the research was conducted in the absence of any commercial or financial relationships that could be construed as a potential conflict of interest.

frontiers | Frontiers in Bioengineering and Biotechnology

ORIGINAL RESEARCH
published: 05 May 2022
doi: 10.3389/fbioe.2022.893337

A Comparative Study on the Multiscale Mechanical Responses of Human Femoral Neck Between the Young and the Elderly Using Finite Element Method

Haipeng Cen[1], *He Gong*[1]*, *Haibo Liu*[1], *Shaowei Jia*[1], *Xiaodan Wu*[1] *and Yubo Fan*[1,2]

[1]Key Laboratory for Biomechanics and Mechanobiology of Ministry of Education, Beijing Advanced Innovation Center for Biomedical Engineering, School of Biological Science and Medical Engineering, Beihang University, Beijing, China, [2]School of Engineering Medicine, Beihang University, Beijing, China

Background: Femoral neck fracture (FNF) is the most serious bone disease in the elderly population. The multiscale mechanical response is a key to predicting the strength of the femoral neck, assessing the risk of FNF, and exploring the role of mechanosensation and mechanotransmission in bone remodeling, especially in the context of aging bone.

Methods: Multiscale finite element (FE) models of the proximal femur for both young and elderly people were developed. The models included organ scale (proximal femur), tissue scale (cortical bone), tissue element scale (osteon), and cell scale [osteocyte lacuna-canalicular network (LCN) and extracellular matrix (ECM), OLCEM]. The mechanical responses of cortical bone and osteocytes in the mid-femoral neck and the differences in mechanical responses between these two scales were investigated.

Results: The mechanical responses of cortical bone and osteocyte showed significant differences between the elderly and the young. The minimum principal strains and mean SEDs of cortical bone in the elderly were 2.067–4.708 times and 3.093–14.385 times of the values in the young, respectively; the minimum principal strains and mean SEDs of osteocyte in the elderly were 1.497–3.246 times and 3.044–12 times of the values in the young, respectively; the amplification factors of minimum principal strain in the inferior (Inf), anterior (Ant), and posterior (Post) quadrants in the young were 1.241–1.804 times of the values in the elderly, but the amplification factor of minimum principal strain in the superior (Sup) quadrant was 87.4% of the value in the elderly; the amplification factors of mean SED in the young were 1.124–9.637 times of the values in the elderly.

Conclusion: The mass and bone mineral density (BMD) of cortical bone in the femoral neck is closely related to the mechanical response of osteocytes, which provides a new idea for improving cortical bone quality. Perhaps cortical bone quality could be improved by stimulating osteocytes. Quadrantal differences of bone quality in the mid-femoral neck should be considered to improve fracture risk prediction in the future.

Keywords: aging, femoral neck, multiscale finite element models, biomechanical responses, cortical bone, osteocyte lacuna-canalicular network and extracellular matrix (OLCEM)

OPEN ACCESS

Edited by:
Chih-Hsiu Cheng,
Chang Gung University, Taiwan

Reviewed by:
Yinghu Peng,
Hong Kong Polytechnic University, Hong Kong SAR, China
Fei Yan,
Chongqing University Three Gorges Hospital, China

***Correspondence:**
He Gong
bmegonghe@buaa.edu.cn

Specialty section:
This article was submitted to Biomechanics, a section of the journal Frontiers in Bioengineering and Biotechnology

Received: *10 March 2022*
Accepted: *14 April 2022*
Published: *05 May 2022*

Citation:
Cen H, Gong H, Liu H, Jia S, Wu X and Fan Y (2022) A Comparative Study on the Multiscale Mechanical Responses of Human Femoral Neck Between the Young and the Elderly Using Finite Element Method. Front. Bioeng. Biotechnol. 10:893337. doi: 10.3389/fbioe.2022.893337

INTRODUCTION

Femoral neck fracture (FNF) is the most serious bone disease in the elderly due to its high morbidity and mortality, which is a serious threat to the health of the elderly and causes a huge economic burden for patients (Chen et al., 2014; Veronese and Maggi, 2018; Guzon-Illescas et al., 2019). FNF is closely related to the biomechanical response of femoral neck and occurs when the load on the femoral neck exceeds its strength. Therefore, biomechanical characteristics and responses of the femoral neck have always been the focus of research.

Based on engineering principles, the strength of bone depends on the material properties, the morphology, and the loading conditions in terms of magnitude, rate, and direction of applied force (Hart et al., 2017). FNF is believed to be closely related to the geometry of the femur, which has been verified by investigating the geometric parameters of the proximal femur and the recorded incidence of FNF (Faulkner et al., 1993). Subsequently, it was found that bone mineral density (BMD) of the femoral neck measured by dual-energy X-ray absorptiometry (DXA) could evaluate bone quality and predict FNF very well (Rivadeneira et al., 2007). The biomechanical response of femoral neck is to some extent dependent on its geometric shape and BMD, which has been verified in the literature (Carpenter et al., 2011). Previously, strain gauges have been used to measure the surface strain of femoral neck (Cristofolini et al., 2009). However, only the surface strain of femoral neck can be measured at limited locations. With the rapid development of computer technology, finite element method (FEM) has been widely used to study biomechanical responses. FEM can overcome this limitation effectively. The mechanical response of femoral neck was investigated using FEM, and the stress and strain distributions at any position of the femoral neck could be acquired (Kersh et al., 2018).

The aforementioned studies mainly focused on mechanical response analyses at the tissue scale. However, bone has a complex hierarchical structure, including organ scale (whole bone), tissue scale (cortical and cancellous bones), tissue element scale (osteon), and cell scale [osteocyte lacuna-canalicular network (LCN) and extracellular matrix (ECM), OLCEM] (Reznikov et al., 2014). Recently, multiscale FE method has been used to investigate the mechanical responses of bone. From the perspective of biomechanics, multiscale FE models of bone were developed to investigate the mechanical behavior of bone, e.g., organ and tissue two scales FE models of bone [radius and cortical bone (Johnson and Troy, 2017)] and organ, tissue and tissue element three scales FE models of bone [proximal femur, cortical bone and osteon (Ascenzi et al., 2013)]. However, the cell scale is not considered. In fact, the mechanical responses at the cell scale were equally important, as the mechanical responses of osteocytes affected the quality of cortical bone. Bone is a dynamic organ that can change its shape and quality through bone formation and resorption to adapt to the mechanical environment, a process known as bone remodeling (Wolff, 1892). Osteocytes are mechanosensors of bone and play an important role in bone remodeling (Tresguerres et al., 2020). When external force is exerted on femur, the mechanical stimuli are transmitted from the organ scale to the cell scale step by step and ultimately sensed by osteocytes, which then release biochemical signals to activate bone remodeling (Klein-Nulend et al., 2013; Robling and Bonewald, 2020; Tresguerres et al., 2020). Finally, the shape and quality of the bone are changed to adapt to the mechanical environment. Therefore, the mechanical response of osteocytes plays an important role in regulating cortical bone quality. Organ, tissue, tissue element and cell four scales FE models of bone were developed that could investigate the mechanical responses of cortical bone at any regions of interest in our previous study (Cen et al., 2021). In addition, cortical bone loss in the mid-femoral neck occurred in elderly individuals with aging, and it showed heterogeneous changes in different regions (Looker et al., 1998). A quantitative analysis of the structural changes of the femoral neck in 100 women aged 20–90 years showed that cortical bone in the inferior (Inf) quadrant of the femoral neck was relatively thicker and had higher BMD, but it was thinner and had lower BMD in the other three quadrants of the femoral neck (Poole et al., 2010). The differences in cortical bone thickness and BMD among different quadrants of femoral neck caused the mechanical responses to be more complex in the elderly. Now, based on the quadrantal differences in bone quality of the mid-femoral neck, multiscale FE models of bone were developed to investigate the mechanical responses of the mid-femoral neck. The mechanical response analysis of cortical bone is crucial for the prediction of femoral neck strength and the assessment of FNF risk. The mechanical response of osteocytes plays a key role in understanding the regulatory mechanisms of bone remodeling. The comparison of mechanical response between cortical bone and osteocytes was the basis for exploring mechanosensation and mechanotransmission among different scales. However, the mechanical response analysis of femoral neck at the cell scale is scarce, especially in the context of the aging bone.

In this study, multiscale finite element (FE) models of the proximal femur in young and elderly people were developed. The mechanical responses at the tissue and cell scales in the mid-femoral neck, as well as the comparison of mechanical responses between the two scales were investigated. The results have important implications for exploring the relationship of bone quality and the mechanical responses among different scales and provide new insights for the pathogenesis for age-related bone loss.

MATERIALS AND METHODS

In this study, multiscale FE models of the proximal femur for young and elderly individuals were developed based on our previous study (Cen et al., 2021). The models included four scales, i.e., organ scale (proximal femur), tissue scale (cortical bone), tissue element scale (osteon), and cell scale (OLCEM), as shown in **Figure 1**. Differences in morphological and mechanical properties of the proximal femur at different scales between the elderly and young people were considered in the modeling process, especially in the mid-femoral neck region. Finally, the

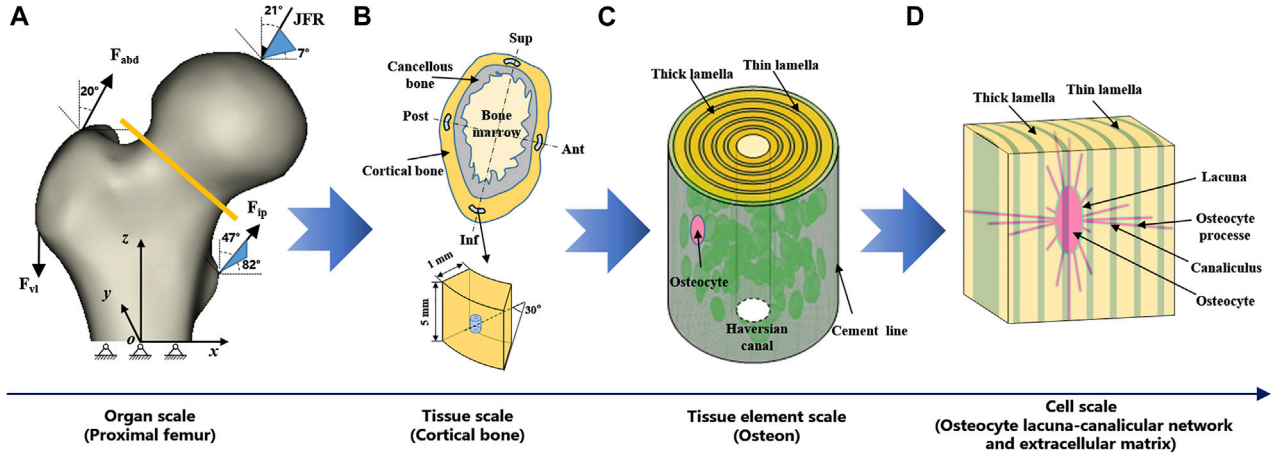

FIGURE 1 | Multiscale FE models of proximal femur. **(A)** organ scale (proximal femur), **(B)** tissue scale (cortical bone), **(C)** tissue element scale (osteon), and **(D)** cell scale (OLCEM). Superior (Sup), Inferior (Inf), Anterior (Ant), Posterior (Post).

TABLE 1 | Detailed element parameters of multiscale FE models.

FEA models	Models types	Number of nodes	Number of elements
Proximal femur	Young	38,148	2,04,622
	Elderly	31,543	1,67,827
Cortical bone	Young	21,033	17,920
	Elderly	21,033	17,920
Osteon	Young	7,88,690	44,76,206
	Elderly	4,23,458	23,53,219
OLCEM	Young	7,30,898	33,41,193
	Elderly	5,40,038	23,25,931

TABLE 2 | Density–elasticity relationships used to determine the orthotropic elastic constants as functions of element ash density ρ_{ash} (g/cm^3) (Enns-Bray et al., 2014).

Elastic constant (MPa)	Cancellous bone	Cortical bone
E_x	$E_z \times 0.47\ \rho^{0.12}$	$0.57 \times E_z$
E_y	$E_z \times 0.76\ \rho^{0.09}$	$0.57 \times E_z$
E_z	$10500\ \rho^{2.29}$	$10500\ \rho^{2.29}$
G_{xy}	$E_z \times 0.26\ \rho^{0.24}$	$0.29 \times E_z$
G_{yz}	$E_z \times 0.29\ \rho^{0.17}$	$0.2 \times E_z$
G_{zx}	$E_z \times 0.45\ \rho^{0.18}$	$0.2 \times E_z$
ν_{xy}	$0.27\ \rho^{-0.09}$	0.37
ν_{yz}	$0.14\ \rho^{-0.16}$	0.3
ν_{zx}	$0.14\ \rho^{-0.07}$	0.3

Note: The subscripts x, y, and z represent the directions along the normal directions of the sagittal, coronal, and transverse planes, respectively.

mid-femoral neck region was divided into four quadrants, i.e., superior (Sup), Inf, anterior (Ant), and posterior (Post). FE models of cortical bone, osteon, and OLCEM were located in the four quadrants of the mid-femoral neck. A similar method of modeling process has been described in our previous study (Cen et al., 2021). Now, a simple modeling process and necessary parameters of the multiscale FE models in this study were introduced here.

Organ Scale FE Model: Proximal Femur

Proximal femur models of the elderly and young were established based on quantitative computed tomography (QCT) data. The models were a quarter of the full femur length for both the young and the elderly, as shown in **Figure 1A**. The models were meshed using Hypermesh 13.0 (Altair Engineering Corp., United States). The element sizes of the models at different scales were determined through a convergence analysis by gradually increasing the size of the elements until the deviations in the estimated strain reached <3%. The detailed element parameters are listed in **Table 1**. The BMD of each element in the proximal femur model was determined based on QCT data, as shown in **Eqs 1**, **2** (Schileo et al., 2008; Cen et al., 2021). The mechanical properties of the models were defined as orthotropic, and 121 discrete material sets were grouped based on the relationship between BMD and elastic constants, as shown in **Table 2** (Enns-Bray et al., 2014). The loading condition of the mid-stance with single limb support in the walking gait was simulated. Three muscle groups (abductors, vastus lateralis, and iliopsoas) and the joint contact force (**Figure 1A**) were considered (Simões et al., 2000; Sangeux, 2019). The distal end of the proximal femur was rigidly constrained. The muscle forces were the average values for adult reported in the literatures (Simões et al., 2000; Diffo Kaze et al., 2017; Sangeux, 2019), and the muscle forces in the elderly were assumed to be 60% of those in the young due to age-related loss of muscle mass and strength (Doherty, 2001; Williams et al., 2002). The joint contact force was assumed to be twice the weight in the mid-stance of gait (Diffo Kaze et al., 2017). The values of the muscle and joint contact forces are listed in **Table 3**. Finally, the FE models were solved using Abaqus 6.14 (Simulia Corp., United States) for standard static analysis.

$$\rho_{QCT} = 0.0008102HU + 0.0026371\ (g/cm^3) \quad (1)$$

$$\rho_{ash} = 0.87719\rho_{QCT} + 0.07895\ (g/cm^3) \quad (2)$$

TABLE 3 | Muscle and joint contact forces in the proximal femur models for the young and the elderly (Simões et al., 2000; Doherty, 2001; Williams et al., 2002; Diffo Kaze et al., 2017; Sangeux, 2019).

Load	Resultant force (N)		Angle (degree)	
	Young	Elderly	α	β
Joint contact force	1,100	1,170	21	7
Abductors	300	180	20	180
Iliopsoas	188	112.8	47	82
Vastus lateralis	292	175.2	180	—

Note: α represents the angle between the load direction and z-axis; β represents the angle between the load direction and x axis.

TABLE 4 | The geometrical parameters of the osteon (Ardizzoni, 2001; Bernhard et al., 2013; Hemmatian et al., 2018).

Parameters	Young (μm)		Elderly (μm)	
Diameter of osteon	239	—	195.6	—
Diameter of Haversian canal	28	—	30	—
Layers of lamellae	—	30	—	24
Thickness of thick lamellae	4.5	—	4	—
Thickness of thin lamellae	1.4	—	1.4	—
Thickness of cement line	3	—	3	—
Number of lacunae	—	202	—	101

Tissue Scale FE Model: Cortical Bone

Cortical bone models were segmented into four quadrants of the mid-femoral neck based on QCT data. The models were simplified as an arc shell of 30°, 5 mm length, and 1 mm thickness for both the young and the elderly, as shown in **Figure 1B**. The models were meshed with a denser mesh using Hypermesh 13.0, and the detailed element parameters are listed in **Table 1**. The models were defined as orthotropic mechanical properties and grouped into 37–68 discrete material sets. The boundary conditions of the cortical bone models were applied using the sub-model method, in which an interpolation of the calculated nodal displacements from the proximal femur models was applied to the peripheral nodes of the cortical bone models. The FE models were solved using Abaqus 6.14 for standard static analysis.

Tissue Element Scale FE Model: Osteon

The osteon models were simplified as hollow cylinders, as shown in **Figure 1C**. The hollow space is the Haversian canal, which is surrounded by concentric lamellae. The outermost layer is the cement line. Each layer of lamellae contained five sub-lamellar layers and was divided into thick and thin lamellae because the orientations of the collagen fibers were different (Weiner et al., 1999). The lacunae were removed from the lamellae using MATLAB software (MathWorks, Natick, MA, United States). The differences in osteon morphology between the elderly and the young were considered in the modeling process, and the geometrical parameters of the osteon models are listed in **Table 4**, including the diameters of the osteon and the Haversian canal, thickness of thick and thin lamellae, and the sizes and densities of lacunae (Ardizzoni, 2001; Bernhard et al., 2013; Hemmatian et al., 2018). The models were meshed using Hypermesh 13.0, and the detailed element parameters are listed in **Table 1**. Numerical homogenization method was used to determine the mechanical properties of the thick and thin lamellae (Vercher et al., 2014; Tian et al., 2019). Differences in mineral content among the four quadrants of the mid-femoral neck in the elderly and young models were considered in the modeling process. That is, the mineral content of lamellae in the Inf quadrant of the mid-femoral neck was the highest and gradually decreased in the Post, Ant, and Sup quadrants. Meanwhile, the mineral content decreased in the four quadrants with aging (Looker et al., 1998; Poole et al., 2010; Bala et al., 2015). Therefore, the mineral contents of lamellae in the osteon models in the Sup, Inf, Ant, and Post quadrants of the mid-femoral neck of the elderly and the young were assumed to be 30%, 34%, 38%, and 42% vs. 36%, 40%, 42%, and 44%, respectively (Looker et al., 1998; Poole et al., 2010). In short, representative volume elements (RVEs) of the mineralized collagen fibrils were developed to determine the stiffness matrices of mineralized collagen fibrils based on the different mineral contents of the four quadrants of the mid-femoral neck in the elderly and young models. Then, the stiffness matrices of the five sub-lamellar layers were calculated through the Lekhnitskii transformation according to the orientations of the collagen fibers. Finally, the stiffness matrices of the thick and thin lamellae with different mineral contents were determined, and are listed in **Table 5**. The detailed process was described in our previous study (Cen et al., 2021). Note that the porosity of the lamellae was no longer introduced as an independent factor affecting the stiffness matrix, but as an influential factor on the mineral content of the lamellae. The material properties of the cement lines were assumed to be isotropic elastic for the young and the elderly models with E = 8 MPa and $\nu = 0.30$ (Beno et al., 2006). The boundary condition of the osteon models was applied using the sub-model method, in which an interpolation of the calculated nodal displacements of the FE model of the cortical bone was applied to the peripheral nodes of the FE model of the osteon. The FE models were solved using Abaqus 6.14 for standard static analysis.

Cell Scale FE Model: OLCEM

The OLCEM models were simplified as cubes for both the young and the elderly, as shown in **Figure 1D**. Each model contained osteocytes, perilacunar matrix (PCM), canaliculi, and ECM. The differences in OLCEM morphology between the elderly and young were considered in the modeling process, such as the sizes of osteocytes and PCM, and numbers of canaliculi and osteocyte processes (Ascenzi et al., 2004; Fratzl et al., 2004; You et al., 2004; Beno et al., 2006; Milovanovic et al., 2013; Buenzli and Sims, 2015). The geometrical parameters of the OLCEM models are listed in **Table 6**. The models were meshed using Hypermesh 13.0, and the detailed element parameters are listed in **Table 1**. The mechanical properties of the PCM and osteocyte were assumed to be isotropic elastic for the young and the elderly models with E = 40.00 kPa, ν = 0.40 and E = 4.47 kPa, ν = 0.30, respectively (Wang et al., 2015). The mechanical properties of thick and thin lamellae in the ECM were the same as those of the lamellae in the osteon models. The submodel boundary condition was also applied to the FE models of the OLCEM by interpolation

TABLE 5 | The stiffness matrices of thick and thin lamellae with different mineral contents.

Mineral content (%)	Stiffness matrices of thin lamellae (MPa)	Stiffness matrices of thick lamellae (MPa)
30	27052 9908 4012 −753 824 −124 23575 3796 −753 203 −293 9692 −94 1 0 5736 −143 251 *symm* 4085 1040 6488	11547 5269 3575 425 −2157 −93 29693 6539 1031 −684 −272 23746 271 −1482 −134 3776 78 24 *symm* 7053 −661 3148
34	30590 11089 4193 −970 889 −124 26109 3954 −970 210 −322 10293 −104 13 −5 6357 −154 284 *symm* 4436 1191 7188	12411 5690 3700 501 −2449 109 33786 7181 1298 −811 −291 26125 329 −1646 −157 4133 86 27 *symm* 7819 −767 3364
36	32410 11693 4308 −1093 906 −130 27353 4043 −1093 216 −325 10595 −115 −3 1 6669 −158 284 *symm* 4614 1257 7516	12850 5926 3774 567 −2581 110 35895 7518 1443 −872 −298 27256 362 −1726 −153 4320 89 31 *symm* 8183 −796 3470
38	34308 12316 4407 −1220 922 −141 28673 4134 −1220 227 −325 10973 −118 −24 10 7008 −162 278 *symm* 4800 1322 7852	13351 6150 3866 −635 −2704 −106 38106 7865 −1594 −941 306 28452 −394 −1816 143 4526 90 32 *symm* 8565 813 3592
40	36048 12885 4512 −1328 927 −146 29915 4229 −1328 233 −324 11353 −123 −28 11 7328 −163 273 *symm* 4974 1377 8154	13832 6370 3967 685 −2809 102 40107 8183 1736 −1001 −309 29589 421 −1910 −138 4724 90 33 *symm* 8913 −833 3714
42	37713 13435 4657 −1419 943 −151 31157 4344 −1419 239 −329 11751 −136 −25 10 7644 −165 275 *symm* 5158 1431 8463	14330 6622 4078 726 −2914 101 42010 8499 1856 −1046 −315 30753 444 −2006 −139 4922 92 35 *symm* 9264 −860 3843
44	40450 14376 4834 −1522 1008 −161 33419 4479 −1522 257 −352 12187 −154 −15 6 8160 −176 295 *symm* 5436 1555 9028	14992 6977 4200 785 −3172 106 45090 8991 2032 −1130 −336 33014 481 −2226 −150 5182 94 38 *symm* 9916 −935 4006

TABLE 6 | The geometrical parameters of the OLCEM models (Ascenzi et al., 2004; Fratzl et al., 2004; You et al., 2004; Beno et al., 2006; Milovanovic et al., 2013; Buenzli and Sims, 2015).

Parameters	Young (μm)	—	Elderly (μm)	—
Semiaxis of lacunae	3.465/7.305/10.405	—	2.145/4.505/5.865	—
Thickness of PCM	0.75	—	0.75	—
Number of canaliculi and osteocyte processes	—	18	—	14
Diameter of canaliculi and osteocyte processes	0.259/0.104	—	0.259/0.104	—
Length of ECM	45	—	45	—

from the osteon models. The FE models were solved using Abaqus 6.14 for standard static analysis.

RESULTS

In this study, multiscale FE models of the proximal femur in young and elderly people were developed. The mechanical responses at the tissue and cell scales in the four quadrants of the mid-femoral neck and the differences in mechanical responses between the two scales were studied. The minimum principal strain and mean SED were analyzed, since the minimum principal strain is one of the most effective way for osteocytes to sense mechanical stimulation (Ascenzi et al., 2013; Vaughan et al., 2013) and the mean strain energy density (SED) is

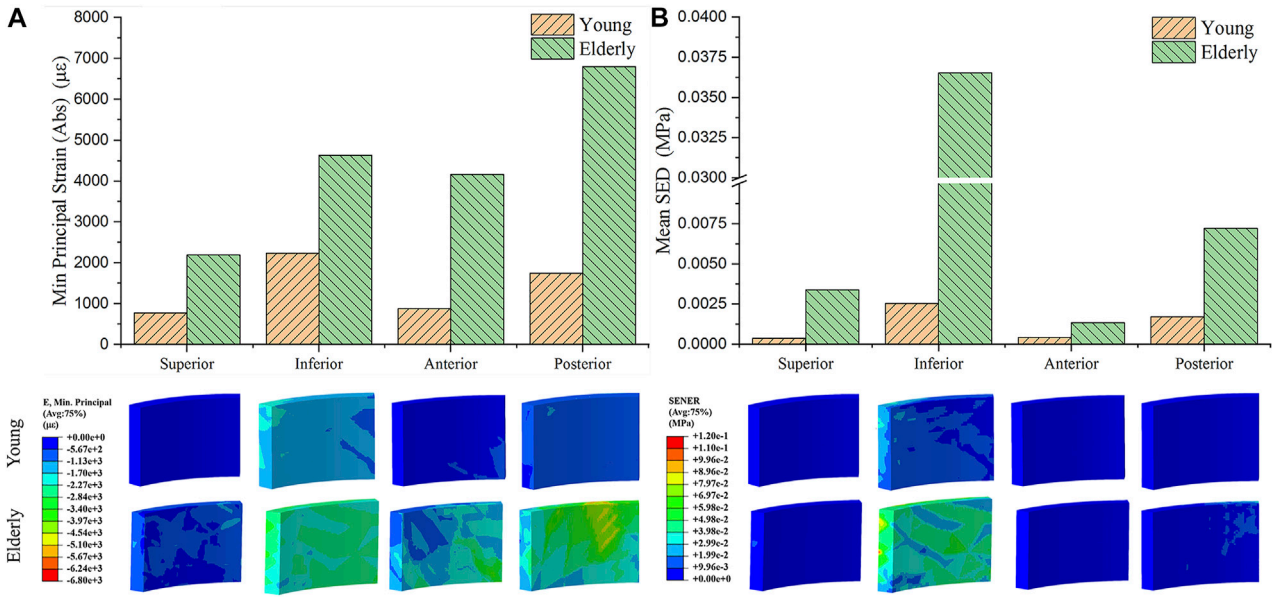

FIGURE 2 | The minimum principal strain **(A)** and SED **(B)** of cortical bone in four quadrants of the mid femoral neck between the young and the elderly models.

considered to be closely related to bone formation (Schulte et al., 2013).

The Minimum Principal Strain and SED Distributions at Tissue Scale

Figure 2 shows the minimum principal strains and SEDs of the cortical bone in four quadrants of the mid-femoral neck in the young and the elderly models. The results showed that the absolute value of the minimum principal strains and mean SEDs of the cortical bone in the elderly were higher than those in the young. Furthermore, the differences in the minimum principal strain and the mean SED of the cortical bone among the four quadrants in the elderly were larger than those in the young. Specifically, the minimum principal strain of the cortical bone in the Post quadrant of the mid-femoral neck was the highest and gradually decreased in the Inf, Ant, and Sup quadrants in the elderly. The highest minimum principal strain of the cortical bone occurred in the Inf quadrant in the young model and gradually decreased in the Post, Ant, and Sup quadrants. Although the mean SEDs of the cortical bone in different quadrants of the mid-femoral neck in the elderly were higher than those in the young, their distribution trends among the four quadrants were consistent. The highest mean SED of cortical bone occurred in the Inf quadrant and gradually decreased in the Post, Sup, and Ant quadrants for both the elderly and young. Two ranges were calculated to quantitatively describe the differences in minimum principal strain and mean SED of cortical bone between the elderly and the young. The lower and upper limits of range were the values of minimum and maximum multiples that were calculated as the corresponding minimum principal strains (or the mean SEDs) in the elderly divided by that in the young, as shown in **Table 7**.

TABLE 7 | The minimum principal strain and mean SED of cortical bone in the elderly and the young.

Absolute values of the minimum principal strain at tissue scale (με)				
Quadrants	**Sup**	**Inf**	**Ant**	**Post**
Elderly	2,193	4,633	4,163	6,803
Young	772.8	2,241	884.3	1,747
Multiples	2.838	2.067[a]	4.708[b]	3.894
Mean SED at tissue scale (kPa)				
Quadrants	**Sup**	**Inf**	**Ant**	**Post**
Elderly	3.39	36.54	1.33	7.21
Young	0.38	2.54	0.43	1.71
Multiples	8.921	14.386[b]	3.093[a]	4.216

[a]*Represent the lower limits of range.*
[b]*Represent upper limits of range.*

The Minimum Principal Strain and SED Distributions at Cell Scale

Figure 3 shows the minimum principal strain and SED of the osteocyte in the four quadrants of the mid-femoral neck in the young and the elderly models. The minimum principal strain and mean SED showed the same distribution trends among the different quadrants of the mid-femoral neck for the young and the elderly. Specifically, the highest minimum principal strain and mean SED of osteocytes occurred in the Inf quadrant, and gradually decreased in the Post, Sup, and Ant quadrants. The absolute value of minimum principal strains and mean SEDs of osteocyte in the elderly were higher than those in the young. Two ranges were calculated to quantitatively describe the differences in minimum principal strain and mean SED of osteocyte between the elderly and the young. The lower and upper limits of range

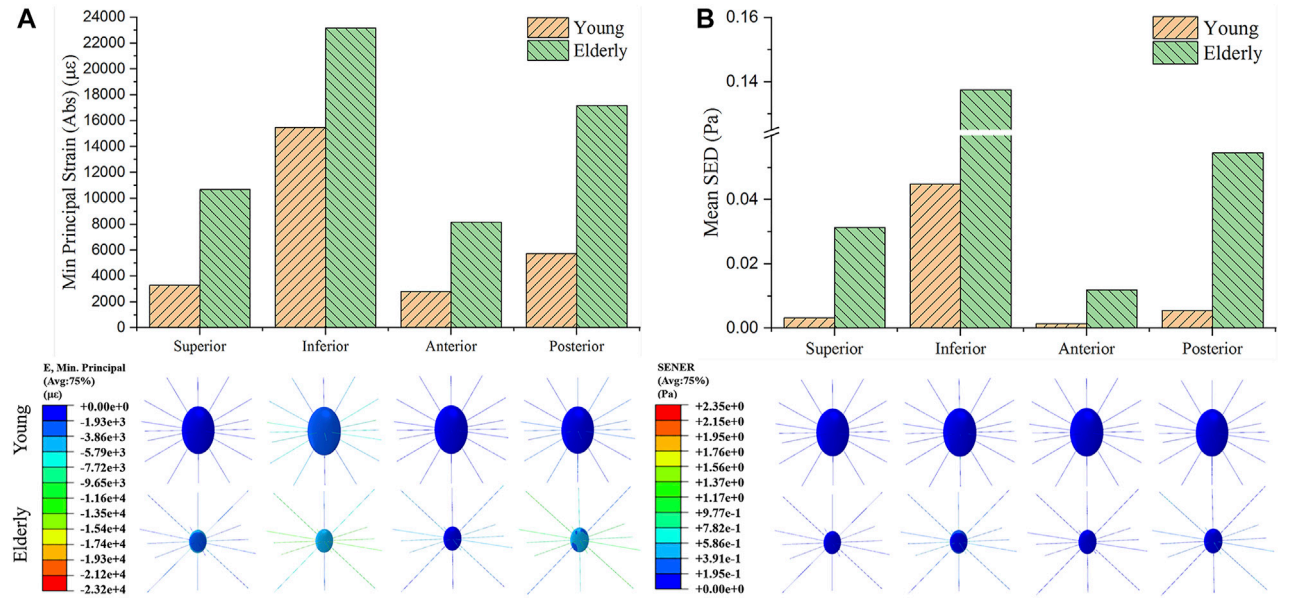

FIGURE 3 | The minimum principal strain **(A)** and SED **(B)** of osteocyte in the four quadrants of the mid-femoral neck between the young and the elderly models.

TABLE 8 | The minimum principal strain and mean SED of osteocytes in the elderly and the young.

Absolute values of the minimum principal strain at cell scale (με)				
Quadrants	**Sup**	**Inf**	**Ant**	**Post**
Elderly	10,670	23,160	8,155	17,180
Young	3,287	15,470	2,808	5,736
Multiples	3.246[b]	1.497[a]	2.904	2.995
Mean SED at cell scale (Pa)				
Quadrants	**Sup**	**Inf**	**Ant**	**Post**
Elderly	0.031	0.137	0.012	0.055
Young	0.003	0.045	0.001	0.005
Multiples	10.333	3.044[a]	12[b]	11

[a]*Represent the lower limits of range.*
[b]*Represent upper limits of range.*

were the values of minimum and maximum multiples that were calculated as the corresponding minimum principal strains (or the mean SEDs) in the elderly divided by that in the young, as shown in **Table 8**.

Comparison of Mechanical Responses Between the Tissue and Cell Scales

To investigate the mechanotransmission between the tissue and cell scales, the strain and SED amplification factors were defined. The minimum principal strain amplification factor was calculated as the minimum principal strain of the osteocytes divided by the minimum principal strain of the cortical bone. The SED amplification factor was calculated as the SED of the ECM divided by that of the cortical bone. **Figure 4** shows the minimum principal strain and SED amplification factors in the young and the elderly models. Because both the minimum principal strain and mean SED at the cell scale were higher than those at the tissue scale, the amplification factors were greater than one. The results revealed that both the amplification factors of minimum principal strain and mean SED showed large differences among the four quadrants of the mid-femoral neck. Most of the amplification factors in the young were higher than those in the elderly, except the amplification factor of minimum principal strain in the Sup quadrant. The amplification factor of minimum principal strain in the Sup quadrant in the young was 87.4% of that in the elderly. Specifically, the peak of the minimum principal strain amplification factor occurred in the Inf quadrant in both the young and the elderly models, and the values of the minimum principal strain amplification factor gradually decreased in the Sup, Post, and Ant quadrants. The mean SED amplification factor of the Inf quadrant was much greater than those of the other quadrants in the young models. The mean SED amplification factors were relatively low in the elderly models. Two ranges were calculated to quantitatively describe the differences in the amplification factors of minimum principal strain and mean SED between the elderly and the young. The lower and upper limits of range were the values of minimum and maximum multiples that were calculated as the corresponding amplification factor of minimum principal strains (or mean SEDs) in the young divided by that in the elderly, as shown in **Table 9**.

DISCUSSION

In this study, multiscale FE models of the proximal femur in young and elderly people were developed. The mechanical responses of cortical bone and osteocytes in the mid-femoral neck and the differences between the two scales were analyzed.

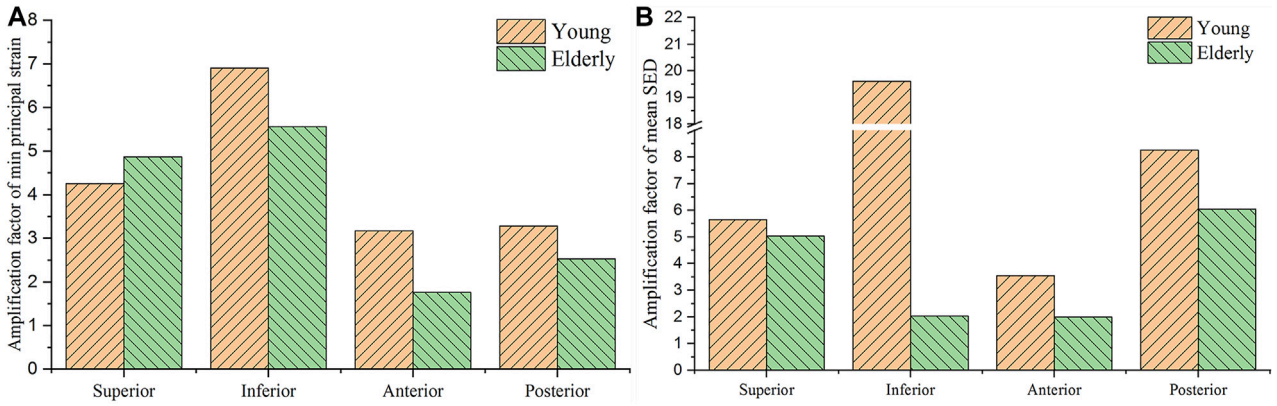

FIGURE 4 | Comparisons of the amplification factors of the minimum principal strain **(A)** and the mean SED **(B)** in the four quadrants of the femoral neck in the young and the elderly.

TABLE 9 | The amplification factors of minimum principal strain and mean SED in the elderly and the young.

Amplification factor of the minimum principal strain				
Quadrants	**Sup**	**Inf**	**Ant**	**Post**
Elderly	4.865	5.563	1.76	2.525
Young	4.253	6.903	3.175	3.283
Multiples	0.874[c]	1.241[a]	1.804[b]	1.300
Amplification factor of the mean SED				
Quadrants	**Sup**	**Inf**	**Ant**	**Post**
Elderly	5.031	2.035	1.989	6.044
Young	5.656	19.612	3.548	8.261
Multiples	1.124[a]	9.637[b]	1.784	1.367

[a]*Represent the lower limits of range.*

[b]*Represent upper limits of range.*

[c]*represents a special value which has been described specially in the main text Section (Section: Comparison of Mechanical Responses Between the Tissue and Cell Scales).*

The mechanical response analysis of cortical bone was crucial for the prediction of femoral neck strength and the assessment of FNF risk. The mechanical response of osteocytes was key to understanding the role of mechanical stimulation in bone remodeling and to exploring the regulatory mechanism of osteocytes in bone remodeling.

The strains and mean SEDs of the cortical bone models in the elderly were higher than those in the young, and significant differences in different quadrants were observed. The minimum principal strains in the Post and Inf quadrants of the mid-femoral neck was greater than those in the Ant and Sup quadrants, which is consistent with the results reported in the literature (Anderson and Madigan, 2013). The differences in mechanical responses among different quadrants were closely related to the anatomical structure, mechanical properties, and loading distribution of the proximal femur. The human hip joint is a ball-and-socket synovial joint formed by an articulation between the acetabulum and the femoral head. The acetabulum tilts forward, outward, and downward, respectively. In the mid-stance of gait, the body weight was transmitted to the femoral head and neck through the hip joint, and then to the femoral shaft. In addition, the muscles attached to the proximal femur produce some constraint forces. Finally, under combined loading, the cortical bone in the Sup quadrant of the mid-femoral neck bore tension. However, the cortical bone in the Inf quadrant is compressed. This was the main reason for the differences in the cortical bone mechanical responses among the different quadrants of the mid-femoral neck.

Generally, cortical bone in the Sup quadrant of the mid-femoral neck is thin and has low BMD. Cortical bone in the Inf quadrant is thick and has high BMD. With increasing age, loss of cortical bone in the Sup and Ant quadrants was more serious than that in the Inf and Post quadrants (Looker et al., 1998; Poole et al., 2010; Johannesdottir et al., 2011). Previous study has found that bone loss in the cortical bones of the mid-femoral neck in four different quadrants caused high strain and SED in the elderly models compared to those in the young models (Cen et al., 2021). This study found that the differences in bone mass and BMD among different quadrants in the elderly models aggravated the differences in cortical bone mechanical responses among different quadrants, which is consistent with the results reported in the literature (Bala et al., 2015; Cen et al., 2021). A numerical simulation study on the mechanical response of femoral neck showed that when the mechanical properties of the proximal femur in the young model were assigned to the mechanical properties of the elderly model, the strain increased by 42% (Anderson and Madigan, 2013). In this study, geometric models of the proximal femur were established based on QCT image data, and the mechanical properties of the proximal femur and cortical bone models were determined by the relationship between the gray value of QCT image data and elastic coefficients. Therefore, the morphologic and bone quality differences in different quadrants of the mid-femoral neck between the elderly and the young could be reflected very well in the FE models of the proximal femur and cortical bone, as shown in **Figures 5A,B,C** respectively. In addition, age-related

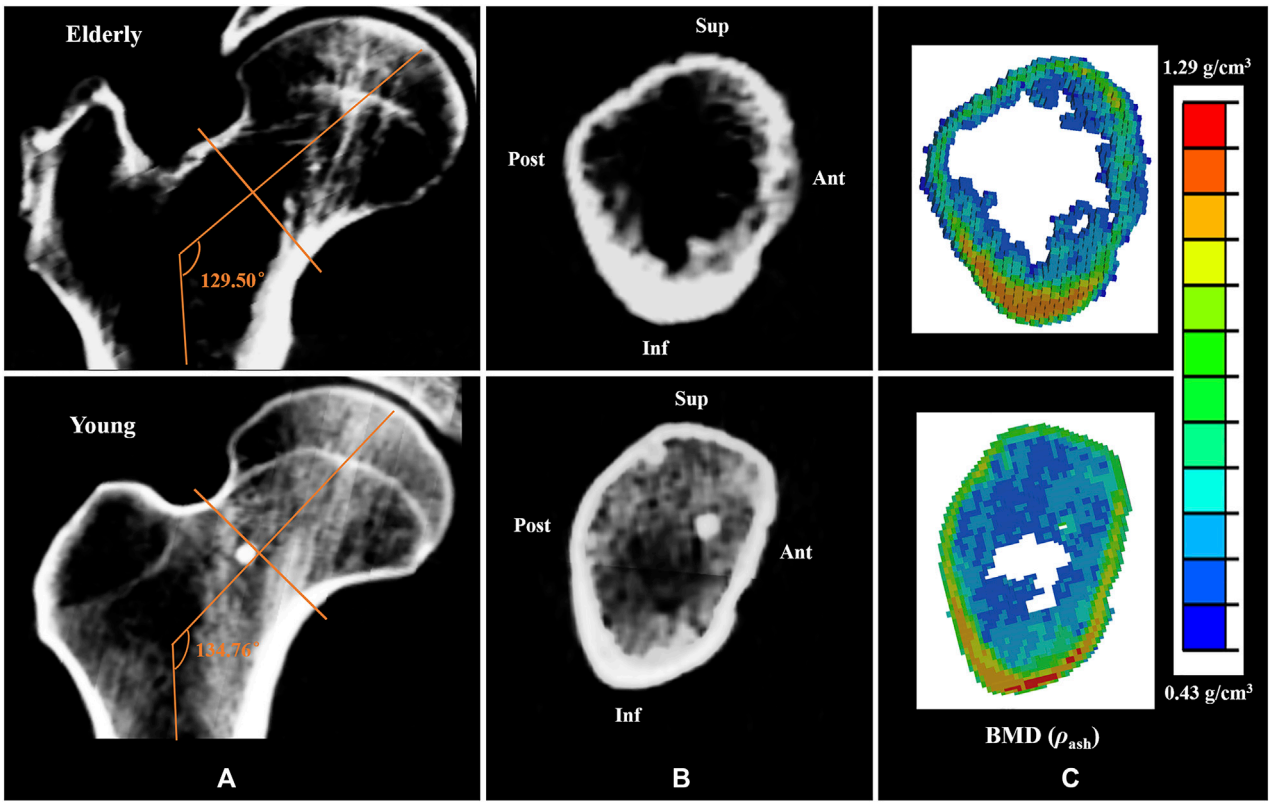

FIGURE 5 | Comparisons of the CT scan slices and the BMD distributions between the elderly and the young. **(A,B)** the CT scan slices of the proximal femur and the mid-femoral neck, **(C)** the BMD distributions of the mid-femoral neck.

loss of muscle mass and strength affects the mechanical response of cortical bone in the mid-femoral neck. Generally, human muscle mass and strength appeared to peak between the ages of 25 and 35, and decline annually, especially after the age of 60, with a rate of about 10% per decade (Doherty, 2001; Williams et al., 2002). One study showed that the constraint force of muscles attached to the proximal femur (abductor, vastus lateralis, and iliopsoas) further reduced the strain levels of the proximal femur (Simões et al., 2000). When the loading of the proximal femur in the young model was applied in the elderly model, the strain increased by 12% compared with that with its own loading (Anderson and Madigan, 2013). Therefore, the special morphology of the proximal femur and inhomogeneity of bone mass and BMD of the cortical bone caused differences in cortical bone mechanical responses among four quadrants of the mid-femoral neck. Furthermore, the inhomogeneous degradation of bone mass and BMD among four quadrants and age-related loss of muscle mass and strength in the elderly models aggravated the differences in mechanical response of cortical bone among quadrants. Those were also the main reason for the differences in the mechanical responses of cortical bone between the elderly and the young.

The mechanical responses at cell scale in the mid-femoral neck also showed quadrant differences. The mechanical response of osteocyte in the Post quadrant was no longer the maximum, but rather in the Inf quadrant. In fact, as mechanosensor of bone, osteocytes can sense mechanical stimuli to regulate bone remodeling, and cell strain is one way for osteocytes to sense mechanical stimuli directly (Klein-Nulend et al., 2013). The mechanical response of osteocytes affects cortical bone quality by regulating the bone remodeling process. An *in vitro* cell culture study showed that only high strain responses can generate biochemical responses in osteocytes (You et al., 2000). In this study, osteocytes in the Inf quadrant of the femoral neck experienced higher strain, and the cortical bone was thicker and had high BMD in the corresponding position. In contrast, osteocytes in the Ant and Sup quadrants of the femoral neck experienced lower strain, and the cortical bone was thinner and had low BMD, as shown in **Figure 5B**. This suggests that the strain response of osteocytes is closely related to cortical bone quality. Moreover, bone loss would decline under high strain environment, and the bone quality would be relatively better. In this study, high strain was mainly localized at the junctions of the osteocyte cell body and the processes, which are considered the most sensitive regions for osteocytes to sense mechanical stimulation (McNamara et al., 2009). Interestingly, integrins are attached to osteocyte processes. Therefore, osteocytes may regulate the bone remodeling

process by adjusting the protein activity after sensing mechanical stimulation at the osteocyte processes.

Although the strain and mean SED of the proximal femur in the elderly models were higher than those in the young models at the tissue and cell scales, the minimum principal strain and mean SED amplification factors in the elderly models were lower than those in the young models. The minimum principal strain amplification factors of the elderly were lower than those in the young models by 19.4%–45.6%. These results indicate that the ability to sense strain stimuli for osteocytes in the elderly was weaker than that in the young. With increasing age, the densities of osteocytes and lacunae, and the number of canaliculi and osteocyte processes decreased (Milovanovic et al., 2013). Meanwhile, osteocytes became much smaller and rounder with aging (Hemmatian et al., 2018). These changes in osteocytes and LCNs were not conducive to sensing and transmitting mechanical stimuli in the elderly (Rath Bonivtch et al., 2007; Hemmatian et al., 2021), which was the main reason for the differences in the mechanical responses of osteocyte between the elderly and the young. Therefore, osteocytes require higher mechanical stimuli to regulate bone remodeling in the elderly. Our results showed that the minimum principal strain of osteocytes and the mean SED of ECM in the elderly were higher than those in the young, which is related to cortical bone loss in four different quadrants of the mid-femoral neck. This indicates that local cortical bone loss can enhance the mechanical response of osteocytes. Perhaps cortical bone quality could be improved by stimulating osteocytes. As a dynamic adaptive biomaterial, bone can change its shape and quality to adapt to the mechanical environment through bone remodeling. Generally, the elderly lack daily activities, and walking is their main activity. Although bone loss appeared at the femoral neck in the elderly, they could adapt to the mechanical environment of walking very well. However, it was difficult for the elderly femoral neck to bear high intensity loading. Therefore, sideways falls are the major cause of FNF in the elderly (Zani et al., 2015). Therefore, bone loss of femoral neck in the elderly was the result of adaptation to daily activities, and appropriate exercise may help improve the bone quality of femoral neck in the elderly.

In this study, a multiscale FE method was used to investigate the mechanical responses of proximal femur, and the differences in morphological and mechanical properties of the proximal femur at different scales between elderly and young people were considered in the modeling process. This study had some limitations. First, the proximal femur and cortical bone models were established based on CT image data from two participants, while only two participants were recruited in this study. Fortunately, the differences in bone morphology and bone quality among different quadrants of the mid-femoral neck between the elderly and young were in line with the characteristics described in the literature (Looker et al., 1998; Poole et al., 2010). Second, parameterized FE models at tissue element and cell scales were developed based on histological studies of human osteons and osteocytes instead of individual real morphologies of participants in this study. At present, it is difficult to acquire the actual morphology of living osteons and osteocytes. In addition, the parameterized model was more conducive to capturing morphological characteristics and comparing the effects of morphological differences on the mechanical responses. However, the assumption of an idealized geometry model may underestimate the strain compared with the real geometry model because the canaliculi and osteocyte processes with irregular shapes can generate stress and strain concentrations more easily than idealized straight cylindrical channels. Third, the validation of our models was limited by current experimental technologies that cannot directly measure the strain and SED of osteons and osteocytes *in vivo*. Fortunately, the strain distributions of the proximal femur and cortical bone models in the mid-femoral neck were in line with the results reported in the literature (Wik et al., 2010; Anderson and Madigan, 2013; Kersh et al., 2018); the strain response of osteocyte in this study was slightly lower than that measured by digital image correlation (DIC) technique (23,160 με vs. 35,000 με) (Nicolella et al., 2006), and was close to the results reported in numerical simulation studies (23,160 με vs. 6,600–26,000 με) (Rath Bonivtch et al., 2007; Verbruggen et al., 2012). New experimental platforms should be developed in future studies to verify the proposed model. Meanwhile, the FE models with the subject-specific joint and muscle forces as the boundary conditions are necessary to investigate the effect of boundary conditions on the mechanical responses in future study. Meanwhile, the sensitive analysis of the boundary conditions will be performed in future study.

CONCLUSION

In this study, multiscale FE models of the proximal femur for young and elderly people were developed, and the mechanical responses of cortical bone and osteocytes in different quadrants of the mid-femoral neck were studied in the mid-stance of gait. The main conclusions are as follows:

1) The mechanical responses of cortical bone models showed significant differences in different quadrants of the mid-femoral neck, which was caused by the special anatomical morphology and inhomogeneous bone mass and BMD of the femoral neck.
2) The degradation of bone mass and BMD causes the minimum principal strains and mean SEDs in the elderly to be higher than those in the young. Inhomogeneous degradation of bone mass and BMD among four quadrants and age-related loss of muscle mass and strength in the elderly aggravated the differences in mechanical response of cortical bone among quadrants.
3) The higher the level of osteocyte mechanical response, the better the cortical bone quality in the mid-femoral neck.
4) The ability of osteocytes to sense strain stimuli in the elderly was weaker than that in the young. The cortical bone loss increased the mechanical response in the mid-femoral neck for the elderly, and enhanced mechanical stimulation of osteocytes.

DATA AVAILABILITY STATEMENT

The original contributions presented in the study are included in the article/Supplementary Material, further inquiries can be directed to the corresponding author.

ETHICS STATEMENT

The studies involving human participants were reviewed and approved by The Ethics Committee of the National Rehabilitation Hospital. The patients/participants provided their written informed consents to participate in this study. Written informed consent was obtained from the individual(s) for the publication of any potentially identifiable images or data included in this article.

AUTHOR CONTRIBUTIONS

Conceptualization: HG and HC; Methodology: HC, HG, and HL; Formal analysis and investigation: HC, SJ, and XW; Writing—original draft preparation: HC; Writing—review and editing: HC and HG; Funding acquisition: HG; Resources: HG and YF; Supervision: HG.

FUNDING

This work is supported by the National Natural Science Foundation of China (No. 11872095), and the Natural Science Foundation of Jilin Province (No. 20200201260JC).

REFERENCES

Anderson, D. E., and Madigan, M. L. (2013). Effects of Age-Related Differences in Femoral Loading and Bone Mineral Density on Strains in the Proximal Femur during Controlled Walking. *J. Appl. Biomech.* 29, 505–516. doi:10.1123/jab.29.5.505

Ardizzoni, A. (2001). Osteocyte Lacunar Size-Lamellar Thickness Relationships in Human Secondary Osteons. *Bone* 28, 215–219. doi:10.1016/S8756-3282(00)00417-8

Ascenzi, M.-G., Kabo, J. M., and Andreuzzi, M. (2004). Mathematical Modeling of Human Secondary Osteons. *Scanning* 26, 25–35. doi:10.1002/sca.4950260105

Ascenzi, M.-G., Kawas, N. P., Lutz, A., Kardas, D., Nackenhorst, U., and Keyak, J. H. (2013). Individual-specific Multi-Scale Finite Element Simulation of Cortical Bone of Human Proximal Femur. *J. Comput. Phys.* 244, 298–311. doi:10.1016/j.jcp.2012.05.027

Bala, Y., Zebaze, R., and Seeman, E. (2015). Role of Cortical Bone in Bone Fragility. *Curr. Opin. Rheumatol.* 27, 406–413. doi:10.1097/BOR.0000000000000183

Beno, T., Yoon, Y.-J., Cowin, S. C., and Fritton, S. P. (2006). Estimation of Bone Permeability Using Accurate Microstructural Measurements. *J. Biomechanics* 39, 2378–2387. doi:10.1016/j.jbiomech.2005.08.005

Bernhard, A., Milovanovic, P., Zimmermann, E. A., Hahn, M., Djonic, D., Krause, M., et al. (2013). Micro-morphological Properties of Osteons Reveal Changes in Cortical Bone Stability during Aging, Osteoporosis, and Bisphosphonate Treatment in Women. *Osteoporos. Int.* 24, 2671–2680. doi:10.1007/s00198-013-2374-x

Buenzli, P. R., and Sims, N. A. (2015). Quantifying the Osteocyte Network in the Human Skeleton. *Bone* 75, 144–150. doi:10.1016/j.bone.2015.02.016

Carpenter, R. D., Sigurdsson, S., Zhao, S., Lu, Y., Eiriksdottir, G., Sigurdsson, G., et al. (2011). Effects of Age and Sex on the Strength and Cortical Thickness of the Femoral Neck. *Bone* 48, 741–747. doi:10.1016/j.bone.2010.12.004

Cen, H., Yao, Y., Liu, H., Jia, S., and Gong, H. (2021). Multiscale Mechanical Responses of Young and Elderly Human Femurs: A Finite Element Investigation. *Bone* 153, 116125. doi:10.1016/j.bone.2021.116125

Chen, I.-J., Chiang, C.-Y. F., Li, Y.-H., Chang, C.-H., Hu, C.-C., Chen, D. W., et al. (2014). Nationwide Cohort Study of Hip Fractures: Time Trends in the Incidence Rates and Projections up to 2035. *Osteoporos. Int.* 26, 681–688. doi:10.1007/s00198-014-2930-z

Cristofolini, L., Juszczyk, M., Taddei, F., and Viceconti, M. (2009). Strain Distribution in the Proximal Human Femoral Metaphysis. *Proc. Inst. Mech. Eng. H.* 223, 273–288. doi:10.1243/09544119JEIM497

Diffo Kaze, A., Maas, S., Arnoux, P.-J., Wolf, C., and Pape, D. (2017). A Finite Element Model of the Lower Limb during Stance Phase of Gait Cycle Including the Muscle Forces. *Biomed. Eng. Online* 16, 138. doi:10.1186/s12938-017-0428-6

Doherty, T. J. (2001). The Influence of Aging and Sex on Skeletal Muscle Mass and Strength. *Curr. Opin. Clin. Nutr. Metabolic Care* 4, 503–508. doi:10.1097/00075197-200111000-00007

Enns-Bray, W. S., Owoc, J. S., Nishiyama, K. K., and Boyd, S. K. (2014). Mapping Anisotropy of the Proximal Femur for Enhanced Image Based Finite Element Analysis. *J. Biomechanics* 47, 3272–3278. doi:10.1016/j.jbiomech.2014.08.020

Faulkner, K. G., Cummings, S. R., Black, D., Palermo, L., Glüer, C.-C., and Genant, H. K. (1993). Simple Measurement of Femoral Geometry Predicts Hip Fracture: The Study of Osteoporotic Fractures. *J. Bone Min. Res.* 8, 1211–1217. doi:10.1002/jbmr.5650081008

Fratzl, P., Gupta, H. S., Paschalis, E. P., and Roschger, P. (2004). Structure and Mechanical Quality of the Collagen-Mineral Nano-Composite in Bone. *J. Mat. Chem.* 14, 2115–2123. doi:10.1039/b402005g

Guzon-Illescas, O., Perez Fernandez, E., Crespí Villarias, N., Quirós Donate, F. J., Peña, M., Alonso-Blas, C., et al. (2019). Mortality after Osteoporotic Hip Fracture: Incidence, Trends, and Associated Factors. *J. Orthop. Surg. Res.* 14, 1–9. doi:10.1186/s13018-019-1226-6

Hart, N. H., Nimphius, S., Rantalainen, T., Ireland, A., Siafarikas, A., and Newton, R. U. (2017). Mechanical Basis of Bone Strength: Influence of Bone Material, Bone Structure and Muscle Action. *J. Musculoskelet. Neuronal Interact.* 17, 114–139.

Hemmatian, H., Bakker, A. D., Klein-Nulend, J., and van Lenthe, G. H. (2021). Alterations in Osteocyte Lacunar Morphology Affect Local Bone Tissue Strains. *J. Mech. Behav. Biomed. Mater.* 123, 104730. doi:10.1016/j.jmbbm.2021.104730

Hemmatian, H., Laurent, M. R., Bakker, A. D., Vanderschueren, D., Klein-Nulend, J., and van Lenthe, G. H. (2018). Age-related Changes in Female Mouse Cortical Bone Microporosity. *Bone* 113, 1–8. doi:10.1016/j.bone.2018.05.003

Johannesdottir, F., Poole, K. E. S., Reeve, J., Siggeirsdottir, K., Aspelund, T., Mogensen, B., et al. (2011). Distribution of Cortical Bone in the Femoral Neck and Hip Fracture: A Prospective Case-Control Analysis of 143 Incident Hip Fractures; the AGES-REYKJAVIK Study. *Bone* 48, 1268–1276. doi:10.1016/j.bone.2011.03.776

Johnson, J. E., and Troy, K. L. (2017). Validation of a New Multiscale Finite Element Analysis Approach at the Distal Radius. *Med. Eng. Phys.* 44, 16–24. doi:10.1016/j.medengphy.2017.03.005

Kersh, M. E., Martelli, S., Zebaze, R., Seeman, E., and Pandy, M. G. (2018). Mechanical Loading of the Femoral Neck in Human Locomotion. *J. Bone Min. Res.* 33, 1999–2006. doi:10.1002/jbmr.3529

Klein-Nulend, J., Bakker, A. D., Bacabac, R. G., Vatsa, A., and Weinbaum, S. (2013). Mechanosensation and Transduction in Osteocytes. *Bone* 54, 182–190. doi:10.1016/j.bone.2012.10.013

Looker, A. C., Wahner, H. W., Dunn, W. L., Calvo, M. S., Harris, T. B., Heyse, S. P., et al. (1998). Updated Data on Proximal Femur Bone Mineral Levels of US Adults. *Osteoporos. Int.* 8, 468–490. doi:10.1007/s001980050093

McNamara, L. M., Majeska, R. J., Weinbaum, S., Friedrich, V., and Schaffler, M. B. (2009). Attachment of Osteocyte Cell Processes to the Bone Matrix. *Anat. Rec.* 292, 355–363. doi:10.1002/ar.20869

Milovanovic, P., Zimmermann, E. A., Hahn, M., Djonic, D., Püschel, K., Djuric, M., et al. (2013). Osteocytic Canalicular Networks: Morphological Implications for Altered Mechanosensitivity. *ACS Nano* 7, 7542–7551. doi:10.1021/nn401360u

Nicolella, D. P., Moravits, D. E., Gale, A. M., Bonewald, L. F., and Lankford, J. (2006). Osteocyte Lacunae Tissue Strain in Cortical Bone. *J. Biomechanics* 39, 1735–1743. doi:10.1016/j.jbiomech.2005.04.032

Poole, K. E., Mayhew, P. M., Rose, C. M., Brown, J. K., Bearcroft, P. J., Loveridge, N., et al. (2010). Changing Structure of the Femoral Neck across the Adult Female Lifespan. *J. Bone Min. Res.* 25, 482–491. doi:10.1359/jbmr.090734

Rath Bonivtch, A., Bonewald, L. F., and Nicolella, D. P. (2007). Tissue Strain Amplification at the Osteocyte Lacuna: A Microstructural Finite Element Analysis. *J. Biomechanics* 40, 2199–2206. doi:10.1016/j.jbiomech.2006.10.040

Reznikov, N., Shahar, R., and Weiner, S. (2014). Bone Hierarchical Structure in Three Dimensions. *Acta Biomater.* 10, 3815–3826. doi:10.1016/j.actbio.2014.05.024

Rivadeneira, F., Zillikens, M. C., De Laet, C. E., Hofman, A., Uitterlinden, A. G., Beck, T. J., et al. (2007). Femoral Neck BMD Is a Strong Predictor of Hip Fracture Susceptibility in Elderly Men and Women Because it Detects Cortical Bone Instability: The Rotterdam Study. *J. Bone Min. Res.* 22, 1781–1790. doi:10.1359/jbmr.070712

Robling, A. G., and Bonewald, L. F. (2020). The Osteocyte: New Insights. *Annu. Rev. Physiol.* 82, 485–506. doi:10.1146/annurev-physiol-021119-034332

Sangeux, M. (2019). "Biomechanics of the Hip during Gait," in *The Pediatric and Adolescent Hip*, 53–71. doi:10.1007/978-3-030-12003-0_3

Schileo, E., Dall'Ara, E., Taddei, F., Malandrino, A., Schotkamp, T., Baleani, M., et al. (2008). An Accurate Estimation of Bone Density Improves the Accuracy of Subject-specific Finite Element Models. *J. Biomechanics* 41, 2483–2491. doi:10.1016/j.jbiomech.2008.05.017

Schulte, F. A., Ruffoni, D., Lambers, F. M., Christen, D., Webster, D. J., Kuhn, G., et al. (2013). Local Mechanical Stimuli Regulate Bone Formation and Resorption in Mice at the Tissue Level. *PLoS One* 8, e62172. doi:10.1371/journal.pone.0062172

Simões, J. A., Vaz, M. A., Blatcher, S., and Taylor, M. (2000). Influence of Head Constraint and Muscle Forces on the Strain Distribution within the Intact Femur. *Med. Eng. Phys.* 22, 453–459. doi:10.1016/S1350-4533(00)00056-4

Tian, W., Qi, L., Chao, X., Liang, J., and Fu, M. (2019). Periodic Boundary Condition and its Numerical Implementation Algorithm for the Evaluation of Effective Mechanical Properties of the Composites with Complicated Micro-structures. *Compos. Part B Eng.* 162, 1–10. doi:10.1016/j.compositesb.2018.10.053

Tresguerres, F. G. F., Torres, J., López-Quiles, J., Hernández, G., Vega, J. A., and Tresguerres, I. F. (2020). The Osteocyte: A Multifunctional Cell within the Bone. *Ann. Anat. - Anatomischer Anzeiger* 227, 151422. doi:10.1016/j.aanat.2019.151422

Vaughan, T. J., Verbruggen, S. W., and McNamara, L. M. (2013). Are All Osteocytes Equal? Multiscale Modelling of Cortical Bone to Characterise the Mechanical Stimulation of Osteocytes. *Int. J. Numer. Meth. Biomed. Engng.* 29, 1361–1372. doi:10.1002/cnm.2578

Verbruggen, S. W., Vaughan, T. J., and McNamara, L. M. (2012). Strain Amplification in Bone Mechanobiology: A Computational Investigation of the *In Vivo* Mechanics of Osteocytes. *J. R. Soc. Interface.* 9, 2735–2744. doi:10.1098/rsif.2012.0286

Vercher, A., Giner, E., Arango, C., Tarancón, J. E., and Fuenmayor, F. J. (2014). Homogenized Stiffness Matrices for Mineralized Collagen Fibrils and Lamellar Bone Using Unit Cell Finite Element Models. *Biomech. Model. Mechanobiol.* 13, 437–449. doi:10.1007/s10237-013-0507-y

Veronese, N., and Maggi, S. (2018). Epidemiology and Social Costs of Hip Fracture. *Injury* 49, 1458–1460. doi:10.1016/j.injury.2018.04.015

Wang, L., Dong, J., and Xian, C. J. (20152015). Strain Amplification Analysis of an Osteocyte under Static and Cyclic Loading: A Finite Element Study. *BioMed Res. Int.* 2015, 1–14. doi:10.1155/2015/376474

Weiner, S., Traub, W., and Wagner, H. D. (1999). Lamellar Bone: Structure-Function Relations. *J. Struct. Biol.* 126, 241–255. doi:10.1006/jsbi.1999.4107

Wik, T. S., Østbyhaug, P. O., Klaksvik, J., and Aamodt, A. (2010). Increased Strain in the Femoral Neck Following Insertion of a Resurfacing Femoral Prosthesis. *J. Bone Jt. Surg. Br. volume* 92-B, 461–467. doi:10.1302/0301-620X.92B3.22592

Williams, G. N., Higgins, M. J., and Lewek, M. D. (2002). Aging Skeletal Muscle: Physiologic Changes and the Effects of Training. *Phys. Ther.* 82, 62–68. doi:10.1053/joca.2001.048310.1093/ptj/82.1.62

Wolff, J. (1892). *Das Gesetz der Transform der Knochen*. Stuttgart, Germany: Dtsch. Medizinische Wochenschrift, 1222–1224.

You, J., Yellowley, C. E., Donahue, H. J., Zhang, Y., Chen, Q., and Jacobs, C. R. (2000). Substrate Deformation Levels Associated with Routine Physical Activity Are Less Stimulatory to Bone Cells Relative to Loading-Induced Oscillatory Fluid Flow. *J. Biomech. Eng.* 122, 387–393. doi:10.1115/1.1287161

You, L.-D., Weinbaum, S., Cowin, S. C., and Schaffler, M. B. (2004). Ultrastructure of the Osteocyte Process and its Pericellular Matrix. *Anat. Rec.* 278A, 505–513. doi:10.1002/ar.a.20050

Zani, L., Erani, P., Grassi, L., Taddei, F., and Cristofolini, L. (2015). Strain Distribution in the Proximal Human Femur during *In Vitro* Simulated Sideways Fall. *J. Biomechanics* 48, 2130–2143. doi:10.1016/j.jbiomech.2015.02.022

Conflict of Interest: The authors declare that the research was conducted in the absence of any commercial or financial relationships that could be construed as a potential conflict of interest.

Publisher's Note: All claims expressed in this article are solely those of the authors and do not necessarily represent those of their affiliated organizations, or those of the publisher, the editors and the reviewers. Any product that may be evaluated in this article, or claim that may be made by its manufacturer, is not guaranteed or endorsed by the publisher.

frontiers | Frontiers in Bioengineering and Biotechnology

ORIGINAL RESEARCH
published: 16 May 2022
doi: 10.3389/fbioe.2022.892760

Influence of Shod and Barefoot Running on the *In Vivo* Kinematics of the First Metatarsophalangeal Joint

Faning Zhang[1], *Dongqiang Ye*[1], *Xini Zhang*[1], *Xiaole Sun*[1], *Shen Zhang*[1,2], *Shaobai Wang*[1,3] *and Weijie Fu*[1,3,4]*

[1]School of Kinesiology, Shanghai University of Sport, Shanghai, China, [2]School of Physical Education and Training, Shanghai University of Sport, Shanghai, China, [3]Key Laboratory of Exercise and Health Sciences of Ministry of Education, Shanghai University of Sport, Shanghai, China, [4]Shanghai Frontiers Science Research Base of Exercise and Metabolic Health, Shanghai University of Sport, Shanghai, China

The biomechanics of the first metatarsophalangeal joint (MTPJ) is affected by different shoe conditions. In the biomechanical research field, traditional skin marker motion capture cannot easily acquire the *in vivo* joint kinematics of the first MTPJ in shoes. Thus, the present study aims to investigate the differences of the first MTPJ's six-degree-of-freedom (6DOF) kinematics between shod and barefoot running by using a high-speed dual fluoroscopic imaging system (DFIS). In total, 15 healthy male runners were recruited. Computed tomography scans were taken from each participant's right foot for the construction of 3D models and local coordinate systems. Radiographic images were acquired at 100 Hz while the participants ran at a speed of 3 m/s ± 5% in shod and barefoot conditions along an elevated runway, and 6DOF kinematics of the first MTPJ were calculated by 3D–2D registration. Paired sample *t*-tests were used to compare the kinematic characteristics of the first MTPJ 6DOF kinematics during the stance phase between shod and barefoot conditions. Compared with barefoot, wearing shoes showed significant changes ($p < 0.05$): 1) the first MTPJ moved less inferior at 50% but moved less superior at 90 and 100% of the stance phase; 2) the peak medial, posterior, and superior translation of the first MTPJ significantly decreased in the shod condition; 3) the extension angle of the first MTPJ was larger at 30–60% but smaller at 90 and 100% of the stance phase; 4) the maximum extension angle and flexion/extension range of motion of the first MTPJ were reduced; and 5) the minimum extension and adduction angle of the first MTPJ was increased in the shod condition. On the basis of the high-speed DFIS, the aforementioned results indicated that wearing shoes limited the first MTPJ flexion and extension movement and increased the adduction angle, suggesting that shoes may affect the propulsion of the first MTPJ and increase the risk of hallux valgus.

Keywords: dual fluoroscopic imaging system, barefoot, shod, first metatarsophalangeal joint, *in vivo* kinematics

OPEN ACCESS

Edited by:
Lizhen Wang,
Beihang University, China

Reviewed by:
Tianyun Jiang,
Beihang University, China
Qichang Mei,
Ningbo University, China

****Correspondence:***
Weijie Fu
fuweijie@sus.edu.cn

Specialty section:
This article was submitted to Biomechanics, a section of the journal Frontiers in Bioengineering and Biotechnology

Received: *09 March 2022*
Accepted: *13 April 2022*
Published: *16 May 2022*

Citation:
Zhang F, Ye D, Zhang X, Sun X, Zhang S, Wang S and Fu W (2022) Influence of Shod and Barefoot Running on the In Vivo Kinematics of the First Metatarsophalangeal Joint. Front. Bioeng. Biotechnol. 10:892760. doi: 10.3389/fbioe.2022.892760

1 INTRODUCTION

Shoes are primarily used to protect the foot from injuries and improve running performance (Wolf et al., 2008; Fuller et al., 2015; Kakouris et al., 2021). In the shod condition, the foot and shoe act together to modulate the mechanical function of the first metatarsophalangeal joint (MTPJ) (Day and Hahn, 2019). In other words, the function of the first MTPJ is influenced by the shoe properties. Previous studies have found that increased midsole bending stiffness would decrease the peak

extension angle and negative work of the first MTPJ (Stefanyshyn and Nigg, 2000; Roy and Stefanyshyn, 2006), thus improving the running economy. The rocker-soled shoes offered a transition with a lower extension angle and decreased peak pressure of the first MTPJ from heel strike to push off during walking (Lin et al., 2013; Menz et al., 2016). However, the effect of shoes on the first MTPJ was not beneficial. Shu et al. (2015) found that habitual barefoot runners have more straight alignment of the first MTPJ than those who are habitually wearing shoes, which suggested that shoe-wearing might increase the risk of hallux valgus. Similarly, a recent study found that compared with the barefoot condition, the medial stress of the first MTPJ was significantly increased in the shod condition, which was related to the process of hallux valgus (Yu et al., 2020). Meanwhile, the stress on the medial capsule of the first MTPJ produced by walking and running with shoes was believed to form a torque to tear the medial side of the joint capsule, which may accelerate the process of hallux valgus (Yu et al., 2020). The aforementioned inconsistent findings might be partially due to the inaccurate kinematics of the first MTPJ obtained in the shod condition.

Most of the previous studies on the first MTPJ were based on skin marker motion capture. While skin marker motion capture provides relatively efficient estimates of joint kinematics, markers move relative to the underlying skeleton, resulting in soft tissue artifacts (Roach et al., 2021). Shultz et al. (2011) found that the translational soft tissue artifact at the calcaneus in the quasi-static position was 12.1 ± 0.3 mm at the toe-off. Roach et al. (2021) found that the positions of the fifth metatarsal skin marker were significantly different from the DFIS-tracked virtual markers during loading and unloading, which may indicate that skin marker motion capture is less accurate during quicker motions. To obtain the joint kinematics more precisely, some studies have carried out experiments by digging holes in shoe surfaces (Wegener et al., 2015), which could eliminate the effect of shoe surfaces, but still could not acquire the real skeletal motion in shod conditions. Although some researchers quantified the first MTPJ movement using intracortical pins (Arndt et al., 2013), this method is invasive and susceptible to infection and may disturb normal movement. In addition, previous studies often focused only on the sagittal movement but fail to explore the transverse movement of the first MTPJ. It may not fully understand the joint kinematics characteristics. Therefore, more accurate techniques should be used to obtain the kinematics of the first MTPJ during shod running.

A high-speed dual fluoroscopic imaging system (DFIS), a noninvasive medical imaging measurement technology, compensates for the limitations of traditional biomechanical methods by dynamically capturing *in vivo* joint motion without being affected by the relative movement of the skin and other soft tissues (Ye et al., 2021). The measuring precision of the DFIS in determining the joint position and capturing the six-degree-of-freedom (6DOF) motion in bony structures is on the sub-millimeter and sub-degree level, which is suitable for exploring the kinematic characteristics of the foot joint (Cross et al., 2017).

The purpose of this study therefore is to investigate the 6DOF kinematic difference of the first MTPJ between shod and barefoot running using the high-speed DFIS. We hypothesized that shoe-wearing limited the 6DOF of the first MTPJ and specifically increased the peak adduction angle in the horizontal plane compared with barefoot.

2 MATERIALS AND METHODS

2.1 Participants

In total, 15 healthy male runners (age: 30.9 ± 7.3 years, height: 172.7 ± 4.4 cm, weight: 70.3 ± 8.4 kg, weekly running volume: 46.4 ± 23.4 km) were recruited. The inclusion criteria were as follows: 1) habitual rear-foot strike runners, 2) right-foot dominant, 3) running more than 20 km per week, and 4) no lower limb injury in the past 6 months. This study was approved by the Institutional Review Board of the Shanghai University of Sport (No. 102772021RT034).

2.2 Instrumentation

2.2.1 Computed Tomography

The 64-row 128-slice spiral CT (SOMATOM, Germany) was used to take the CT images of the subjects' feet at the neutral position of the right foot. The scanning layer thickness and spacing were all 0.6 mm; the voltage was 120 kV; the current was 140 mA; the length, width, and height of the voxel were set as 0.488, 0.488, and 0.625 mm, respectively; and the size of the voxel was 512 × 512 × 256.

2.2.2 High-Speed DFIS

The high-speed DFIS consisted of two pairs of fluoroscopic imaging systems, which were, respectively, composed of two fluorescence emitters that generate X-rays and two image intensifiers that receive and image X-rays, with a diameter of 431.8 mm (**Figure 1**). In this study, the distances between the two fluorescence emitters and the image intensifiers were 132.2 and 128.6 cm, respectively, and the two image intensifiers were positioned at 119.6° to one another. The shooting voltage was 60 kV, the current was 63 mA, the shooting frequency was 100 Hz, the exposure speed was 1/1,000 s, and the image resolution was 1,024 × 1,024 pixels.

2.2.3 Witty–Manual Grating Timing System

A wireless Witty–Manual grating timing system (Microgate, Bolzano, Italy) was used to guarantee the target running speed.

2.2.4 Grating Sensor

An infrared blocking grating sensor (GJ-2004, Changju Electronic Technology, China) was applied to trigger the DFIS while the participants ran through the image volume.

2.3 Data Collection

The participants were asked to wear experimental vests, shorts, and shoes (traditional footwear, heel-to-toe drop: 6 mm; midsole material: TPU, EVA; upper structure: textile fabric; toe box: width, 11 cm, depth, 8 cm, height, 3 cm, size, 9; without any

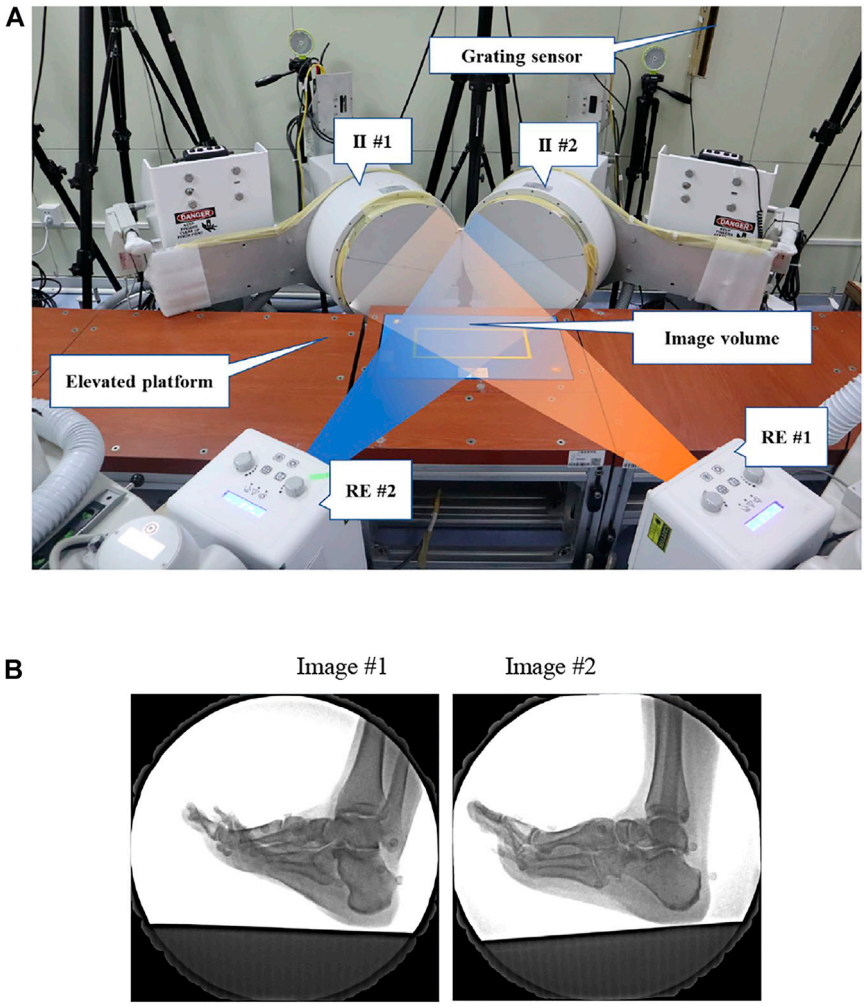

FIGURE 1 | (A) High-speed DFIS setup. Participants ran on an elevated platform. The image intensifiers (II #1 and II #2) processed images created by X-rays from the radiographic emitters (RE #1 and RE #2). **(B)** DFIS images showed the first MTPJ of a participant.

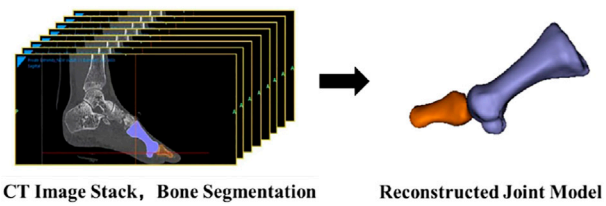

FIGURE 2 | Reconstruction of the first MTPJ.

arch support) before the running experiment. Then, the participants warmed up for 5 min on a treadmill at a speed of 3 m/s. Before initiating the measurement process, several practice trials were performed, so that the participants became familiar with the elevated runway. Radiographic images were acquired at 100 Hz while the participants ran at a speed of 3 m/s ± 5% in shod and barefoot conditions along the elevated runway with their right foot landing within the image volume naturally. One successful trial was collected using high-speed DFIS in each condition (Campbell et al., 2016; Welte et al., 2021), which was guided by the X-ray image quality.

2.4 Data Processing

2.4.1 CT Scans and Reconstruction of the First MTPJ

CT scans were taken from each participant's right foot while they were supine with a neutral ankle position. The first metatarsal and first proximal phalanx were segmented and reconstructed first using the MTPJ bone models in mimics (v. 21.0; Mimics, Materialise, Leuven, Belgium, **Figure 2**).

2.4.2 Establishment of a Coordinate System

Inertial anatomical coordinate systems were generated from the bone meshes, with the origin located at the centroid and the x–y–z-axes aligned along the principal axes of the moment of inertia tensor (Eberly D et al., 1991). A rectangular box was fitted around the first metatarsal that touched the bone model contours

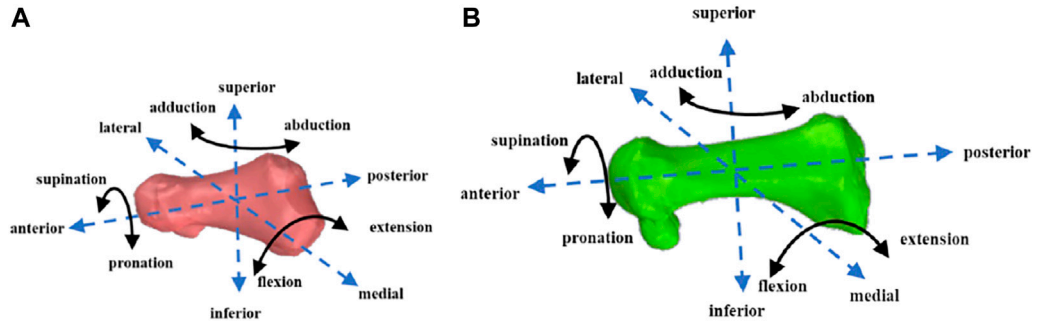

FIGURE 3 | First proximal phalanx **(A)** and first metatarsal **(B)** motion diagram.

in the superior–inferior, medial–lateral, and anterior–posterior directions. It can decrease potential variability in the identification of bony landmarks (Esfandiarpour et al., 2018). The box vertex coordinates were used to calculate the geometric center and the axis of symmetry by the plug-in of the Rhinoceros (v6.0, McNeel & Associates, Seattle, United States). The geometric center of the box was considered the origin of the coordinate system. Moreover, the first metatarsal was considered a symmetrical rigid body of uniform mass, so the axis of symmetry of the skeleton was the principal axis of the moment of inertia tensor. Y-axis was along the principal axis (Eberly D et al., 1991), and x-axis and z-axis were perpendicular to the y-axis, respectively. The x-axis was lateral–medial, the y-axis was anterior–posterior, and the z-axis was superior–inferior (Welte et al., 2021). The coordinate system of the first proximal phalanx was established in the same way.

2.4.3 Definition of 6DOF Kinematics

The 6DOF kinematics of the first MTPJ was defined as the relative motions of the first metatarsal coordinate system with respect to the first proximal phalanx coordinate system. The medial/lateral, anterior/posterior, and superior/inferior directions were aligned with the x-, y-, and z-axes of the coordinate systems, respectively (Welte et al., 2021). Extension/flexion (EX/FL), supination/pronation (SUP/PRO), and abduction/adduction (AB/AD) were determined as rotations around the medial/lateral, anterior/posterior, and superior/inferior axes, respectively (**Figure 3**). The positive values represented anterior translation, lateral translation, superior translation, EX, SUP, and AB, and the negative values corresponded to the opposite.

2.4.5 *In Vivo* Kinematics

Images obtained with high-speed DFIS are subject to distortion when X-ray beams are transformed into visible images (Tersi and Stagni, 2014). Pincushion distortion and magnetic lens distortion are the two major sources of distortion (Wang and Blackburn, 2000). To correct for the distortion, an X-ray image was collected with an "un-distortion" grid (Brainerd et al., 2010). The grid consisted of a perforated piece of aluminum plate with the known size and spacing of each hole. A software program, XMALab, used a distortion-correcting algorithm to correct for any changes to the spacing or size of the holes in the perforated grid (Rohr et al., 2001).

Calibrated fluoroscopic images were then imported into the modeling software (Rhinoceros 6.0, McNeel & Associates, Seattle, United States). The 3D models were also imported into the same software in the virtual 3D environment and were moved and rotated independently at increments of 0.01 mm and 0.01° (Cao et al., 2019). The kinematic results of the first MTPJ were calculated by 3D–2D registration (**Figure 4**). The specific indicators include the range of motion (ROM) at 6DOF, which was defined as the maximum minus the minimum joint angle among all frames; initial contact angle; and peak angle in each DOF. The stance phase was divided into 10 sections with 10% per section. The kinematics of each counterpart section were compared.

2.5 Statistics

The mean and standard deviation for each variable were calculated. The paired sample *t*-test was used to compare the 6DOF data of the first MTPJ under two conditions (SPSS 25.0, IBM, Chicago, United States). The significance level was set as $\alpha = 0.05$.

3 RESULTS

3.1 *In Vivo* Kinematics of the First MTPJ

3.1.1 Joint Translation

Compared with barefoot, the first MTPJ moved less inferior at 50% ($p = 0.032$) but moved less superior at 90% ($p = 0.014$) and 100% ($p = 0.007$) of the stance phase in the shod condition. The anterior translation of the first MTPJ at 20 and 60% and the posterior translation at 90–100% of the stance phase were significantly reduced in the shod condition ($p < 0.05$, **Figure 5**).

3.1.2 Joint Rotation

Compared with barefoot, the EX angle of the first MTPJ was larger at 30–60% but smaller at 90–100% of the stance in the shod condition ($p < 0.05$). The AD angle of the first MTPJ was larger at 10, 20, 50, and 60% of the stance period in the shod condition ($p < 0.05$). There were no significant differences in PRO and SUP of the first MTPJ during the stance phase (**Figure 5**).

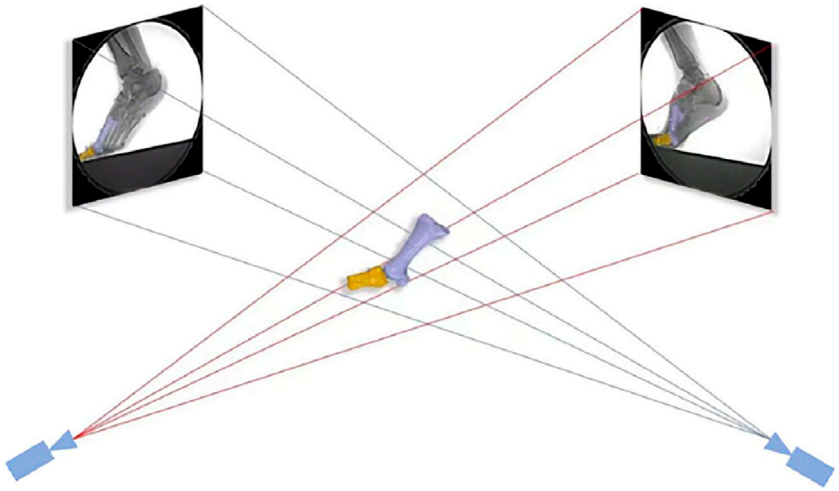

FIGURE 4 | 3D–2D registration. The position of the joint was adjusted by translating and rotating the joint model in the software until the edge of the bones matched the radiographic images.

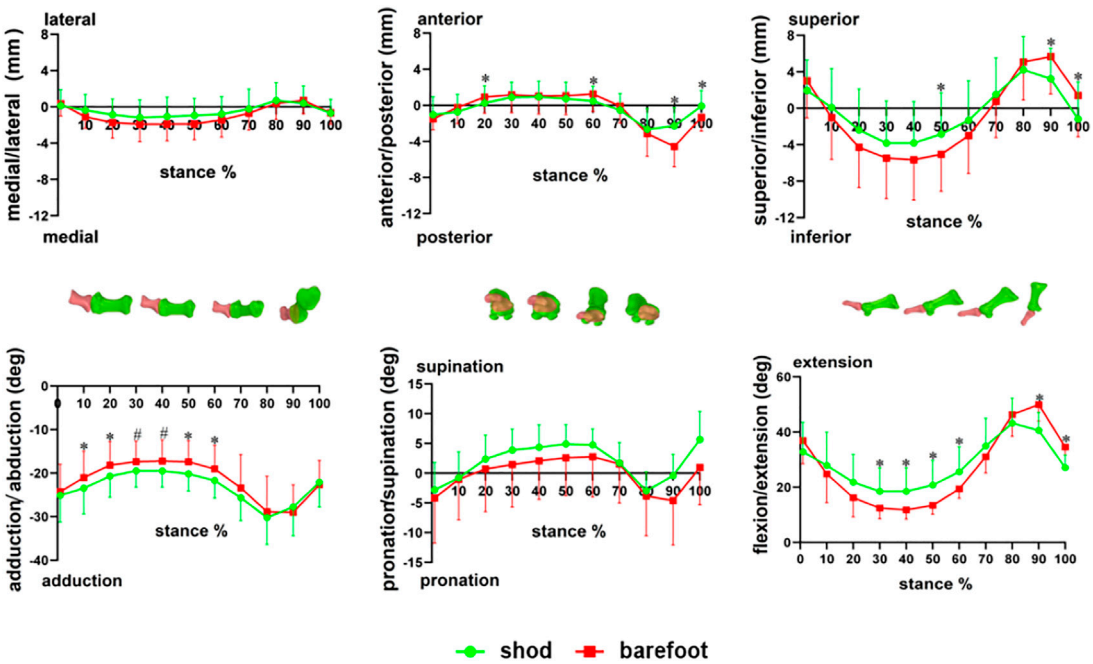

FIGURE 5 | Six degrees of freedom of the first MTPJ during stance. * there are significant differences between the shod and barefoot conditions, $p < 0.05$; # there are different trends between the shod and barefoot conditions, $p < 0.1$.

3.2 Angles and ROM of the First MTPJ

3.2.1 Joint Translation

During the stance phase, the first MTPJ's peak medial ($p = 0.039$), posterior ($p < 0.001$), and superior movement ($p = 0.043$) (**Figure 6**); anterior to posterior ROM ($p = 0.002$) and superior to inferior ROM ($p < 0.001$) were significantly smaller in the shod condition than in the barefoot condition (**Table 1**).

3.2.2 Joint Rotation

Compared with barefoot, the maximum EX of the first MTPJ was smaller ($p < 0.001$), whereas the minimum EX and AD were significantly larger ($p = 0.009$) in the shod condition (**Figure 6**). Meanwhile, the FL/EX ROM in the shod condition was significantly smaller ($p < 0.001$), whereas there were no significant differences in the PRO/SUP and AD/AB ROM (**Table 1**).

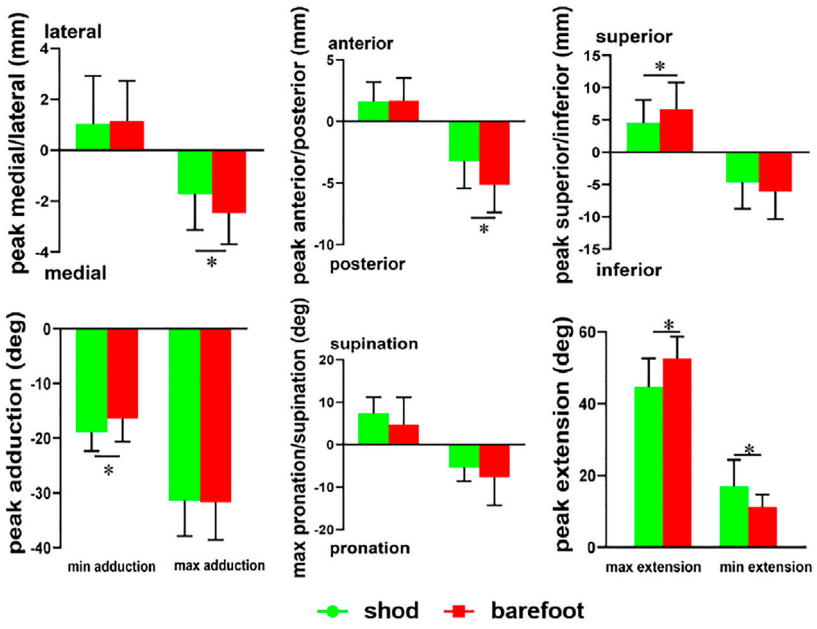

FIGURE 6 | Peak angle of the first MTPJ in shod and barefoot. * compared with barefoot, there are significant differences in the shod condition, $p < 0.05$.

TABLE 1 | Comparison of translation, rotation at initial contact, and ROM of the first MTPJ in shod and barefoot.

	Condition	M/L (mm)	A/P (mm)	S/I (mm)	EX/FL (°)	PRO/SUP (°)	AB/AD (°)
Initial contact	Barefoot	−0.34 ± 1.35	−1.49 ± 1.21	3.03 ± 4.1	36.94 ± 8.47	−4.16 ± 7.62	−24.26 ± 6.3
	Shod	0.14 ± 1.76	−1.04 ± 1.99	1.96 ± 3.34	32.82 ± 10.61	−2.8 ± 4.58	−25.09 ± 6.1
ROM	Barefoot	3.6 ± 1.26	6.82 ± 2.37[a]	12.78 ± 2.47[a]	41.36 ± 6.77[a]	12.35 ± 3.29	15.34 ± 4.62
	Shod	2.76 ± 0.98	4.81 ± 2.27	9.22 ± 2.55	27.68 ± 5.48	12.82 ± 4.07	12.48 ± 4.55

[a]*compared with barefoot, there are significant differences in the shod condition, p < 0.05. M/L: medial/lateral translation; A/P: anterior/posterior translation; S/I: superior/inferior translation; EX/FL: extension/flexion; PRO/SUP: pronation/supination; AB/AD: abduction/adduction; ROM: range of motion; "+": the first MTPJ, medial, anterior, superior translation and extension, supination, abduction; "−": the first MTPJ, lateral, posterior, inferior translation and flexion, pronation, and adduction.*

4 DISCUSSION

This study found that compared with barefoot, the peak medial/posterior/superior translation, the maximum EX angle, and the ROM of the EX were significantly reduced in the shod condition, whereas the minimum EX and AD angle were increased. These results were consistent with the hypothesis that shoe-wearing restricted partial 6DOF movement of the first MTPJ.

The first MTPJ in the sagittal plane was significantly reduced in the shod condition, which was consistent with previous studies (Lin et al., 2013; Wegener et al., 2015; Sichting et al., 2020). Specifically, Wegener et al. (2015) found that shoes reduced the first MTPJ's peak EX during running from 31.5° (barefoot) to 12.6° (shod), and Sichting et al. (2020) found that the EX ROM of the first MTPJ decreased from 27.9 (barefoot) to 19.7 (shod). The minimum EX angle of the first MTPJ in the shod condition was significantly increased. It may partially be due to the toe spring of the footwear, which increased the minimum EX angle during the stance phase (Sichting et al., 2020). In addition, runners exhibited significantly greater medial longitudinal arch compression in the barefoot condition than in the shod condition (Holowka et al., 2022). Thus, the plantarflexion of the first metatarsal was decreased, which might cause the minimum EX angle of the first MTPJ to increase in the shod condition. These results based on skin marker motion capture were consistent with the results of this study which shows that shoes restricted the EX motion of the first MTPJ. However, the minimum and maximum EX angles during the stance phase were larger than those in previous studies using skin marker motion capture. In the study of McDonald et al. (2016), who used skin marker motion capture, the minimum EX of the first MTPJ was close to 0° in barefoot and shod running at 2.7 m/s, whereas the maximum EX was 34.2 ± 3.9° (barefoot) and 30.1 ± 2.8° (shod), which were far smaller than the maximum angle (shod: 44.7 ± 7.9°; barefoot: 52.6 ± 6.0°) in the current study. Midfoot plantarflexion, primarily the first metatarsal, during propulsion is believed to occur due to the windlass mechanism (Wegener et al., 2015). The larger EX angle in the current study might be the result of the plantarflexion of the first metatarsal. However, traditional motion capture methods cannot easily detect the *in vivo* motion of the first metatarsal, thus failing to obtain the most accurate

motion of the first MTPJ. In addition, the EX of the first MTPJ plays an important role in calculating joint dynamics, and the underestimation of FL/EX activity by traditional motion capture methods may have affected the joint dynamic results of previous studies. However, the current research based on high-speed DFIS is still at an early stage. Moreover, we did not calculate the dynamics in this study. Therefore, future studies should compare the differences in the dynamic results of the first MTPJ obtained by DFIS and other motion capture methods.

This study showed that the peak superior translation of the first MTPJ was significantly reduced under the shod condition, which may be related to the anatomical structure of the first MTPJ. Human metatarsal heads are dorsally oriented and mediolaterally broad articular surfaces. The dorsally oriented metatarsal heads in the human forefoot are thought to increase the range of EX motion at the MTPJ by providing more dorsal articular surface area on which the proximal phalangeal base can slide (Fernandez et al., 2016; Sichting et al., 2020) In the current study, the EX trend of the first MTPJ was consistent with the superior/inferior translation trend, which further supported the result of the previous study (Phillips et al., 1996). The shoe limited the flexion and extension of the first MTPJ, thus reducing the ROM of joint translation in the sagittal plane.

In the current study, the AD angle of the first MTPJ in the static CT model of all participants was within 15°–20°, which was consistent with the clinical standard for mild hallux valgus (Coughlin et al., 2002; Xiang et al., 2018). Previous studies have shown that the distance between the first and second MTPJs was generally narrower in habitually shod runners than in habitually barefoot runners. The straight alignment between the first metatarsal and the first proximal phalangeal was disrupted, so habitually shod runners have a higher risk of suffering from hallux valgus (Shu et al., 2015). The first MTPJ straight alignment of participants in this study may have been affected by long-term shoe-wearing running. In addition, the AD angle of the first MTPJ in shod was significantly greater than that in barefoot, which was consistent with our hypothesis. Using finite element simulation, Yu et al. (2020) found that with the increase in the AD angle of the first MTPJ, the stress on the medial joint capsule increased, and the stress on the medial joint capsule was significantly higher under shoe-wearing than barefoot. The positive and negative axial principal stresses formed a combined torque in the medial capsule of the first MTPJ. The medial capsule was damaged by the torque during periodic movement in shod, such as running, indicating that shoe-wearing may induce hallux valgus. By contrast, the first MTPJ had a decreased AD angle and increased AD/AB ROM under the barefoot condition, which meant that the forefoot has more space for movement. Thus, the joint motion in the horizontal plane was increased. Barefoot running could potentially help improve the shape and function of the first MTPJ (D'AoÛt et al., 2009) and then may contribute to the correction of hallux valgus. Although this study was cross-sectional research, the previous study showed that barefoot training could improve the hallux valgus. Xiang et al. (2018) performed a 12-week five-finger shoe running intervention for 15 subjects with mild and moderate hallux valgus and found that the degree of hallux valgus was significantly reduced after the intervention. The five-finger shoe, without any support or cushioning, only protects the skin of the foot and is thought to mimic barefoot conditions (Smith et al., 2015; Holowka et al., 2018). While footwear helps the foot resist external injuries, its relatively small toe space not only limits the movement of the first MTPJ but also makes the medial side subject to external torque during propulsion, potentially accelerating the occurrence and progression of hallux valgus.

In this study, high-speed DFIS provided a new perspective for analyzing the *in vivo* motion characteristics of the first MTPJ during running, but there were still some limitations: only male participants who were used to running in shoes were recruited, and gender differences were not explored. Due to ionizing radiation, only data on one valid aspect were collected. The experimental shoes were traditional running shoes, and the kinematic differences of the first MTPJ under different toe sizes should be explored in future studies. In addition, future studies should further explore the effect of training on the *in vivo* kinematics of the first MTPJ during running by using DFIS.

5 CONCLUSION

On the basis of a high-speed DFIS, the 6DOF kinematic difference of the first MTPJ in the whole stance phase was investigated, which created a more accurate measurement method for studying the movement of the small joint of the foot. The results showed that shoe-wearing limited the extension and joint translation of the first MTPJ and increased the horizontal adduction angle, suggesting that shoes could limit the propulsion effect and ROM of the first MTPJ and might increase the risk of hallux valgus. This finding indicated that shoemakers should increase the capacity of the forefoot movement to lower the risk of injury.

DATA AVAILABILITY STATEMENT

The raw data supporting the conclusion of this article will be made available by the authors, without undue reservation.

ETHICS STATEMENT

The studies involving human participants were reviewed and approved by the Institutional Review Board of the Shanghai University of Sport (No. 102772021RT034). The patients/participants provided their written informed consent to participate in this study.

AUTHOR CONTRIBUTIONS

WF and FZ conceived and designed the review. FZ wrote the manuscript. FZ, DY, XZ, SZ, and XS revised the manuscript. All authors have read and approved the final manuscript.

FUNDING

This research was funded by the National Key Technology Research and Development Program of the Ministry of Science and Technology of China (2019YFF0302100), the National Natural Science Foundation of China (11772201), the "Outstanding Young Scholar" Program of Shanghai Municipal, and the "Dawn" Program of Shanghai Education Commission, China (19SG47).

REFERENCES

Arndt, A., Lundgren, P., Liu, A., Nester, C., Maiwald, C., Jones, R., et al. (2013). The Effect of a Midfoot Cut in the Outer Sole of a Shoe on Intrinsic Foot Kinematics during Walking. *Footwear Sci.* 5 (1), 63–69. doi:10.1080/19424280.2012.740688

Brainerd, E. L., Baier, D. B., Gatesy, S. M., Hedrick, T. L., Metzger, K. A., Gilbert, S. L., et al. (2010). X-ray Reconstruction of Moving Morphology (XROMM): Precision, Accuracy and Applications in Comparative Biomechanics Research. *J. Exp. Zool.* 9999A (5), a–n. doi:10.1002/jez.589

Campbell, K. J., Wilson, K. J., LaPrade, R. F., and Clanton, T. O. (2016). Normative Rearfoot Motion during Barefoot and Shod Walking Using Biplane Fluoroscopy. *Knee Surg. Sports Traumatol. Arthrosc.* 24 (4), 1402–1408. doi:10.1007/s00167-014-3084-4

Cao, S., Wang, C., Zhang, G., Ma, X., Wang, X., Huang, J., et al. (2019). *In Vivo* kinematics of Functional Ankle Instability Patients during the Stance Phase of Walking. *Gait Posture* 73, 262–268. doi:10.1016/j.gaitpost.2019.07.377

Coughlin, M. J., Saltzman, C. L., and Nunley, J. A., 2nd (2002). Angular Measurements in the Evaluation of Hallux Valgus Deformities: A Report of the Ad Hoc Committee of the American Orthopædic Foot & Ankle Society on Angular Measurements. *Foot Ankle Int.* 23 (1), 68–74. doi:10.1177/107110070202300114

Cross, J. A., McHenry, B. D., Molthen, R., Exten, E., Schmidt, T. G., and Harris, G. F. (2017). Biplane Fluoroscopy for Hindfoot Motion Analysis during Gait: A Model-Based Evaluation. *Med. Eng. Phys.* 43, 118–123. doi:10.1016/j.medengphy.2017.02.009

D'AoÛt, K., Pataky, T. C., De Clercq, D., and Aerts, P. (2009). The Effects of Habitual Footwear Use: Foot Shape and Function in Native Barefoot Walkers. *Footwear Sci.* 1 (2), 81–94. doi:10.1080/19424280903386411

Day, E. M., and Hahn, M. E. (2019). Dynamic Angular Stiffness about the Metatarsophalangeal Joint Increases with Running Speed. *Hum. Mov. Sci.* 67, 102501. doi:10.1016/j.humov.2019.102501

Eberly, D., and Lancaster, J. (1991). On Gray Scale Image Measurements: II. Surface Area and Volume. *CVGIP Graph. Models Image Process* 53, 550–562. doi:10.1016/1049-9652(91)90005-5

Esfandiarpour, F., Lebrun, C. M., Dhillon, S., and Boulanger, P. (2018). *In-vivo* Patellar Tracking in Individuals with Patellofemoral Pain and Healthy Individuals. *J. Orthop. Res.* doi:10.1002/jor.23887

Fernandez, P. J., Holowka, N. B., Demes, B., and Jungers, W. L. (2016). Form and Function of the Human and Chimpanzee Forefoot: Implications for Early Hominin Bipedalism. *Sci. Rep.* 6, 30532. doi:10.1038/srep30532

Fuller, J. T., Bellenger, C. R., Thewlis, D., Tsiros, M. D., and Buckley, J. D. (2015). The Effect of Footwear on Running Performance and Running Economy in Distance Runners. *Sports Med.* 45 (3), 411–422. doi:10.1007/s40279-014-0283-6

Holowka, N. B., Gillinov, S. M., Virot, E., and Lieberman, D. E. (2022). Effects of Footwear Cushioning on Leg and Longitudinal Arch Stiffness during Running. *J. Biomech.* 133, 110869. doi:10.1016/j.jbiomech.2021.110869

Holowka, N. B., Wallace, I. J., and Lieberman, D. E. (2018). Foot Strength and Stiffness Are Related to Footwear Use in a Comparison of Minimally- vs. Conventionally-Shod Populations. *Sci. Rep.* 8 (1), 3679. doi:10.1038/s41598-018-21916-7

Kakouris, N., Yener, N., and Fong, D. T. P. (2021). A Systematic Review of Running-Related Musculoskeletal Injuries in Runners. *J. Sport Health Sci.* 10 (5), 513–522. doi:10.1016/j.jshs.2021.04.001

Lin, S.-C., Chen, C. P. C., Tang, S. F. T., Wong, A. M. K., Hsieh, J.-H., and Chen, W.-P. (2013). Changes in Windlass Effect in Response to Different-Shoe and Insole Designs during Walking. *Gait Posture* 37 (2), 235–241. doi:10.1016/j.gaitpost.2012.07.010

McDonald, K. A., Stearne, S. M., Alderson, J. A., North, I., Pires, N. J., and Rubenson, J. (2016). The Role of Arch Compression and Metatarsophalangeal Joint Dynamics in Modulating Plantar Fascia Strain in Running. *Plos One* 11 (4). doi:10.1371/journal.pone.0152602

Menz, H. B., Auhl, M., Tan, J. M., Levinger, P., Roddy, E., and Munteanu, S. E. (2016). Biomechanical Effects of Prefabricated Foot Orthoses and Rocker-Sole Footwear in Individuals with First Metatarsophalangeal Joint Osteoarthritis. *Arthritis Care Res. Hob.* 68 (5), 603–611. doi:10.1002/acr.22743

Phillips, R. D., Law, E. A., and Ward, E. D. (1996). Functional Motion of the Medial Column Joints of the Foot during Propulsion. *J. Am. Podiatr. Med. Assoc.* 86 (10), 474–486. doi:10.7547/87507315-86-10-474

Roach, K. E., Foreman, K. B., MacWilliams, B. A., Karpos, K., Nichols, J., and Anderson, A. E. (2021). The Modified Shriners Hospitals for Children Greenville (mSHCG) Multi-Segment Foot Model Provides Clinically Acceptable Measurements of Ankle and Midfoot Angles: A Dual Fluoroscopy Study. *Gait Posture* 85, 258–265. doi:10.1016/j.gaitpost.2021.02.004

Rohr, K., Stiehl, H. S., Sprengel, R., Buzug, T. M., Weese, J., and Kuhn, M. H. (2001). Landmark-based Elastic Registration Using Approximating Thin-Plate Splines. *IEEE Trans. Med. Imaging* 20 (6), 526–534. doi:10.1109/42.929618

Roy, J.-P. R., and Stefanyshyn, D. J. (2006). Shoe Midsole Longitudinal Bending Stiffness and Running Economy, Joint Energy, and EMG. *Med. Sci. Sports Exerc.* 38 (3), 562–569. doi:10.1249/01.mss.0000193562.22001.e8

Shu, Y., Mei, Q., Fernandez, J., Li, Z., Feng, N., and Gu, Y. (2015). Foot Morphological Difference between Habitually Shod and Unshod Runners. *PLoS One* 10 (7), e0131385. doi:10.1371/journal.pone.0131385

Shultz, R., Kedgley, A. E., and Jenkyn, T. R. (2011). Quantifying Skin Motion Artifact Error of the Hindfoot and Forefoot Marker Clusters with the Optical Tracking of a Multi-Segment Foot Model Using Single-Plane Fluoroscopy. *Gait Posture* 34 (1), 44–48. doi:10.1016/j.gaitpost.2011.03.008

Sichting, F., Holowka, N. B., Hansen, O. B., and Lieberman, D. E. (2020). Effect of the Upward Curvature of Toe Springs on Walking Biomechanics in Humans. *Sci. Rep.* 10 (1), 14643. doi:10.1038/s41598-020-71247-9

Smith, B. S., Burton, B., Johnson, D., Kendrick, S., Meyer, E., and Yuan, W. (2015). Effects of Wearing Athletic Shoes, Five-Toed Shoes, and Standing Barefoot on Balance Performance in Young Adults. *Int. J. Sports Phys. Ther.* 10 (1), 69–74.

Stefanyshyn, D. J., and Nigg, B. M. (2000). Influence of Midsole Bending Stiffness on Joint Energy and Jump Height Performance. *Med. Sci. Sports Exerc* 32 (2), 471–476. doi:10.1097/00005768-200002000-00032

Tersi, L., and Stagni, R. (2014). Effect of Calibration Error on Bone Tracking Accuracy with Fluoroscopy. *J. Biomech. Eng.* 136 (5), 054502. doi:10.1115/1.4027058

Wang, J., and Blackburn, T. J. (2000). The AAPM/RSNA Physics Tutorial for Residents: X-Ray Image Intensifiers for Fluoroscopy. *Radiographics* 20 (5), 1471–1477. doi:10.1148/radiographics.20.5.g00se181471

Wegener, C., Greene, A., Burns, J., Hunt, A. E., Vanwanseele, B., and Smith, R. M. (2015). In-shoe Multi-Segment Foot Kinematics of Children during the Propulsive Phase of Walking and Running. *Hum. Mov. Sci.* 39, 200–211. doi:10.1016/j.humov.2014.11.002

Welte, L., Kelly, L. A., Kessler, S. E., Lieberman, D. E., D'Andrea, S. E., Lichtwark, G. A., et al. (2021). The Extensibility of the Plantar Fascia Influences the Windlass Mechanism during Human Running. *Proc. Biol. Sci.* 288 (1943), 20202095. doi:10.1098/rspb.2020.2095

Wolf, S., Simon, J., Patikas, D., Schuster, W., Armbrust, P., and Doderlein, L. (2008). Foot Motion in Children Shoes: a Comparison of Barefoot Walking with Shod Walking in Conventional and Flexible Shoes. *Gait Posture* 27 (1), 51–59. doi:10.1016/j.gaitpost.2007.01.005

Xiang, L., Mei, Q., Fernandez, J., and Gu, Y. (2018). Minimalist Shoes Running Intervention Can Alter the Plantar Loading Distribution and Deformation of Hallux Valgus: A Pilot Study. *Gait Posture*, 65–71. doi:10.1016/j.gaitpost.2018.07.002

Ye, D., Sun, X., Zhang, C., Zhang, S., Zhang, X., Wang, S., et al. (2021). *In Vivo* Foot and Ankle Kinematics during Activities Measured by Using a Dual Fluoroscopic Imaging System: A Narrative Review. *Front. Bioeng. Biotechnol.* 9, 693806. doi:10.3389/fbioe.2021.693806

Yu, G., Fan, Y., Fan, Y., Li, R., Liu, Y., Antonijevic, D., et al. (2020). The Role of Footwear in the Pathogenesis of Hallux Valgus: A Proof-Of-Concept Finite Element Analysis in Recent Humans and Homo Naledi. *Front. Bioeng. Biotechnol.* 8, 648. doi:10.3389/fbioe.2020.00648

Conflict of Interest: The authors declare that the research was conducted in the absence of any commercial or financial relationships that could be construed as a potential conflict of interest.

Publisher's Note: All claims expressed in this article are solely those of the authors and do not necessarily represent those of their affiliated organizations, or those of the publisher, the editors, and the reviewers. Any product that may be evaluated in this article, or claim that may be made by its manufacturer, is not guaranteed or endorsed by the publisher.

frontiers | Frontiers in Bioengineering and Biotechnology

ORIGINAL RESEARCH
published: 01 June 2022
doi: 10.3389/fbioe.2022.894131

Effects of 4Weeks of High-Definition Transcranial Direct Stimulation and Foot Core Exercise on Foot Sensorimotor Function and Postural Control

Songlin Xiao[1], *Baofeng Wang*[1], *Xini Zhang*[1], *Junhong Zhou*[2,3]* and *Weijie Fu*[1,4,5]*

[1]Key Laboratory of Exercise and Health Sciences of Ministry of Education, Shanghai University of Sport, Shanghai, China, [2]The Hinda and Arthur Marcus Institute for Aging Research, Hebrew SeniorLife, Boston, MA, United States, [3]Harvard Medical School, Boston, MA, United States, [4]School of Kinesiology, Shanghai University of Sport, Shanghai, China, [5]Shanghai Frontiers Science Research Base of Exercise and Metabolic Health, Shanghai University of Sport, Shanghai, China

Objective: This study aimed to examine the effects of 4 weeks of high-definition transcranial direct current stimulation (HD-tDCS) and foot core exercise (FCE) on foot sensorimotor function (i.e., toe flexor strength and passive ankle kinesthesia) and postural control.

Methods: In total, 36 participants were randomly assigned into three groups as follows: HD-tDCS, FCE, and the control group. A total of 12 training sessions were performed over 4 weeks (i.e., three sessions per week) in the laboratory. The HD-tDCS group received 20-min HD-tDCS with a current density of 2 mA, and the FCE group completed short foot exercise, towel curls, toe spread and squeeze, and balance board training. Participants in the control group just maintained the activities what they usually did and did not receive any interventions. Foot muscle strength, passive ankle kinesthesia, and postural control were assessed at baseline and post-intervention.

Results: HD-tDCS induced a greater decrease in the percentage changes in the passive kinesthesia thresholds of ankle inversion ($p < 0.001$) and eversion ($p = 0.013$) than the control group. Compared with the control group, a significant increase in the percentage change in the metatarsophalangeal joint flexor strength was found in the HD-tDCS group ($p = 0.008$) and the FCE group ($p = 0.027$), and a significant increase in the percentage change in toe flexor strength was observed in the FCE group ($p = 0.015$). Moreover, FCE induced a greater reduction in the percent changes in the medial–lateral average center of gravity sway velocity in one-leg standing with eyes open ($p = 0.033$) and the anteroposterior average center of gravity sway velocity in one-leg standing with eyes closed ($p < 0.001$) than control.

Conclusion: This study demonstrated that 4 weeks of HD-tDCS and FCE induced distinct benefits on foot sensorimotor function and the standing postural control performance in healthy young adults. HD-tDCS could improve the metatarsophalangeal joint flexor strength and the passive kinesthesia thresholds of ankle inversion and eversion.

OPEN ACCESS

Edited by:
Lizhen Wang,
Beihang University, China

Reviewed by:
Shuqi Zhang,
Boise State University, United States
Qin "Arthur" Zhu,
University of Wyoming, United States

***Correspondence:**
Junhong Zhou
junhongzhou@hsl.harvard.edu
Weijie Fu
fuweijie@sus.edu.cn

Specialty section:
This article was submitted to Biomechanics, a section of the journal Frontiers in Bioengineering and Biotechnology

Received: *11 March 2022*
Accepted: *25 April 2022*
Published: *01 June 2022*

Citation:
Xiao S, Wang B, Zhang X, Zhou J and Fu W (2022) Effects of 4 Weeks of High-Definition Transcranial Direct Stimulation and Foot Core Exercise on Foot Sensorimotor Function and Postural Control. Front. Bioeng. Biotechnol. 10:894131. doi: 10.3389/fbioe.2022.894131

Meanwhile, FCE could also enhance foot muscle strength and enhance postural control performance in one-leg standing.

Keywords: high-definition transcranial direct current stimulation, foot core exercise, foot sensorimotor function, toe flexor strength, passive ankle kinesthesia, postural control

INTRODUCTION

The foot core system consists of a complex foot structure, including active, passive, and neural subsystems, providing stability and flexibility when coping with changing foot demands (McKeon et al., 2015). During daily weight-bearing activities (e.g., walking), the foot functions by performing force attenuation with loading, transmitting force during propulsion, providing afferent information to accommodate uneven terrain, and maintaining postural control (Kelly et al., 2014; Fraser and Hertel, 2019). The diminished sensorimotor function of the foot and ankle has been linked to poor functional performance and associated with loading-related injuries (Ridge et al., 2019; Kakouris et al., 2021). For example, weakness of the intrinsic foot muscles suggested that inefficient active support of the arch may contribute to injuries, such as plantar fasciitis (Wearing et al., 2006; van Poppel et al., 2021). Thus, strengthening the foot sensorimotor function is critical for addressing degenerative foot-related conditions and maintaining the intact capacity for functional independence in daily activities.

One commonly used strategy of strengthening the foot sensorimotor function is foot core exercise (FCE), which is traditionally described as intrinsic foot muscle flexion exercises, such as towel curls, toe spread-out exercise, and short foot exercise (Lynn et al., 2012; Sulowska et al., 2016; Fraser and Hertel, 2019). Previous studies demonstrated that FCE was able to improve ankle-foot functional performance by activating the plantar intrinsic muscles (Mulligan and Cook, 2013; Hashimoto and Sakuraba, 2014). For example, Mulligan et al. reported that 4 weeks of short foot exercise decreased navicular drop, increased the arch foot index, and improved motor performance during a static unilateral balancing activity in young healthy adults (Mulligan and Cook, 2013).

Moreover, the regulation of the foot core system also depends upon the activation of supraspinal networks, such as the brain cortical networks. Studies have shown the execution of foot movements was associated with the range and magnitude of activation in the sensorimotor cortex including the primary motor cortex (M1), primary sensory cortex (S1), and supplementary motor area (Orr et al., 2008). Nowadays, noninvasive brain stimulation techniques are used to enhance physical performance in healthy individuals, and transcranial direct current stimulation (tDCS) represented the most widely used technique (Angius et al., 2018). Generally, tDCS induced a weak electric direct current applied to the scalp to modulate cortical excitability to improve physical performance (Nitsche and Paulus, 2001). In particular, an early study showed that one session of 20-min tDCS applied over the sensorimotor cortex could enhance toe pinch force in young healthy adults (Tanaka et al., 2009). A recent systematic review has shown that tDCS could ultimately influence the neural circuitry responsible for the neuromechanical regulation of the foot and ankle and then improve their muscle strength and somatosensory function, which indicated that targeting the excitability of the cortical regions may help further augment the foot sensorimotor function (Xiao et al., 2020b). More importantly, such positive effects induced by tDCS may be accumulated in multiple-session interventions to improve performance by remarkably reshaping neuroplasticity (Nitsche et al., 2005). However, the effects of multi-session tDCS on the foot sensorimotor function have not been well examined, especially compared with FCE.

Therefore, this study aimed to examine the effects of 4 weeks of FCE and multi-session high-definition tDCS (HD-tDCS) on foot sensorimotor function and postural control. This study also hypothesized that 4 weeks of FCE and HD-tDCS intervention could result in increasing the foot muscle strength, passive ankle kinesthesia, and postural control as compared with control.

MATERIALS AND METHODS

Participants

The sample size was calculated using *a priori power analysis* with a statistical power of 0.80, a probability level of 0.05, and an effect size f of 0.38 (Yotnuengnit et al., 2018) *via* G*Power 3.1.9.2 software. In total, 10 participants per group were identified as achieving sufficient power. Thus, to account for up to 20 percent attrition, 36 young healthy male adults without the habit of regular exercise were recruited from a university community *via* advertisements and randomly assigned to three groups (n = 12 in each group, **Table 1**) by using a Microsoft Excel random number table. The inclusion criteria were as follows: no history of lower extremity injuries in the past 6 months and not participating in other training programs of tDCS or FCE. The exclusion criteria were as follows: skin allergies and any contraindications to the use of tDCS (e.g., metal-implanted devices in the brain). All participants provided written informed consent as approved by the Institutional Review Board of the Shanghai University of Sport (No.102772021RT035).

Intervention

Given the duration of the intervention in the previous studies (Lynn et al., 2012; Yotnuengnit et al., 2018), participants received

TABLE 1 | Participant demographics.

Group	Age (years)	Height (cm)	Weight (kg)
HD-tDCS group (n = 12)	21.9 ± 2.1	174.9 ± 6.1	69.8 ± 7.6
FCE group (n = 12)	22.7 ± 2.0	173.5 ± 7.1	69.3 ± 13.1
Control group (n = 12)	23.5 ± 1.5	177.5 ± 6.1	75.2 ± 7.1
P	0.135	0.272	0.256

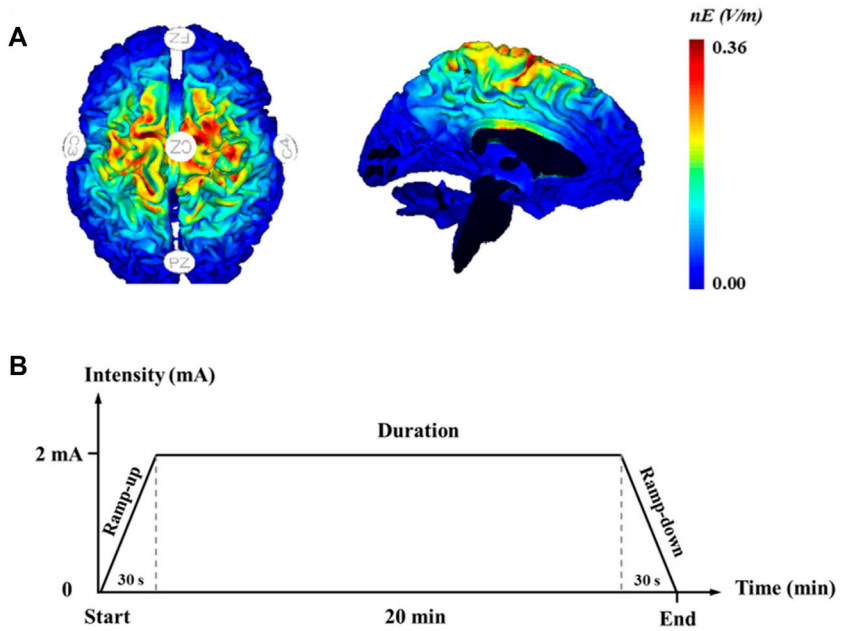

FIGURE 1 | High-definition transcranial direct current stimulation. **(A)** Electrode montages for tDCS and simulated distribution of electrical field in the brain; **(B)** high-definition transcranial direct current stimulation protocol.

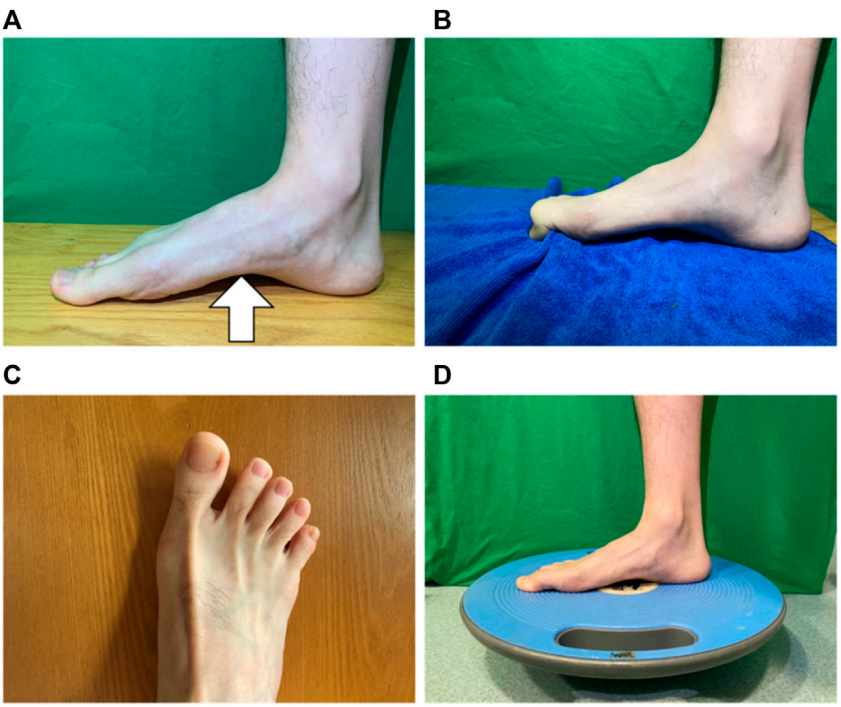

FIGURE 2 | Foot core exercise. **(A)** short foot exercise; **(B)** towel curls; **(C)** toe spread and squeeze; and **(D)** balance board training.

a total of 12 training sessions over 4 weeks (i.e., three sessions per week) in the laboratory in both HD-tDCS and FCE groups. Within each week, at least 1 day of resting was provided between sessions.

The participants in the HD-tDCS group received HD-tDCS, and they were asked not to imagine any foot movements. A 4 × 1 ring-type high-definition tDCS was administered with a battery-driven, wireless multichannel Starstim®

TABLE 2 | Foot core exercise progression.

Training	Week 1	Week 2	Week 3	Week 4
Short foot exercise	two sets of 10 times	two sets of 15 times	two sets of 20 times	three sets of 20 times
Towel curls	three sets of 10 times	three sets of 20 times	three sets of 10 times (0.25 kg)	three sets of 15 times (0.5 kg)
Toe spread and squeeze	two sets of 10 times	two sets of 15 times	two sets of 20 times	three sets of 20 times
Balance board training	two sets of 20 s	two sets of 25 s	two sets of 30 s	three sets of 30 s

neurostimulator system (Neuroelectrics, Barcelona, Spain). The current was delivered using round gel Ag/AgCl electrodes (3.14 cm^2). The anodal electrode was placed over the Cz and surrounded by four return electrodes (i.e., C3, C4, Fz, and Pz) on the basis of 10/20 electroencephalogram brain templates (**Figure 1A**) (Xiao et al., 2020a). The maximum current intensity of this HD-tDCS was set at 2 mA, and the stimulation duration was 20 min. Neuro-modeling results showed that a high and focal electric field induced by this montage effectively penetrated the sensorimotor cortex located along the longitudinal fissure controlling the foot-ankle area (Ma et al., 2020). The current intensity was ramped up from 0 to 2 mA in the initial 30 s at the beginning of the stimulation and ramped down to 0 mA in the last 30 s of the stimulation, as shown in **Figure 1B** (Boonstra et al., 2016). The participants were asked to complete a questionnaire at the end of each stimulation visit to evaluate the potential side effects.

For the FCE group, the training sessions consisted of short foot exercise, towel curls, toe spread and squeeze, and balance board training (**Figure 2**), with the goal to strengthen the intrinsic and extrinsic foot muscles and the functionalities of the foot and ankle (**Table 2**) (Ridge et al., 2019). All participants were verbally instructed, provided with a demonstration, and guided through a single practice trial. Following the instruction, the participants sequentially performed each exercise to the best of their ability barefoot, and one session was completed within 20 min. The participants in the control group did not receive any intervention.

Data Collection

Foot muscle strength, passive ankle kinesthesia, and postural control were assessed at baseline and post-intervention.

The passive kinesthesia threshold of the ankle joint was assessed using an ankle proprioception tester (KP-11, Toshimi, Shandong, China) (Sun et al., 2015). In particular, each participant sat on an adjustable seat with their eyes closed, and the dominant foot was placed on the bottom of the foot pedal. The platform was randomly activated to drive the participant's ankle in plantarflexion, dorsiflexion, inversion, and eversion. After the trigger and the direction of foot movement were confirmed, the participants pressed the stop button immediately. The ankle proprioception testing system showed the angle of the ankle, and then, the research personnel recorded it (i.e., the passive kinesthesia threshold of the ankle joint). The participants completed three trials of the test in each movement direction (i.e., plantarflexion, dorsiflexion, inversion, and eversion) in a randomized order.

The metatarsophalangeal joint (MPJ) flexor strength was measured using an MPJ flexor strength testing system customized and validated by the team (Zhang et al., 2019; Xiao et al., 2020b). Each participant was seated in the system with bare feet. The position and height of the seat were adjusted to make the thighs parallel to the ground, and the knee joint was fixed at 90°. The participants were asked to flex the MPJ and press the pedal for 10 s with maximum force. The peak MPJ flexor strength (N) was then obtained and normalized by the bodyweight of each participant.

The toe flexor strength was measured in a sitting position by using a toe grip dynamometer (T.K.K.3361, Niigata, Japan) (Kurihara et al., 2014; Yamauchi and Koyama, 2015). Each participant was asked to sit on an adjustable seat, and the dominant foot was placed on the dynamometer and fixed with the heel stopper. The participants were asked to flex their toes vigorously for at least 3 s. The peak toe flexor strength (N) was recorded and normalized by the bodyweight of each participant.

In the postural control test, each participant stood barefoot on the balance testing system (Super Balance, Acmeway, Beijing, China) (Xiao et al., 2020a). All participants completed three trials within each of the following conditions: one-leg standing with eyes open (OL_EO) and eyes closed (OL_EC) for 20 s. The system recorded the sway velocity of the CoG in the medial–lateral (ML) and anteroposterior (AP) directions.

Statistics

SPSS 22.0 (SPSS Inc., Chicago, IL, United States) was used to complete the statistical analysis of the training effects for percentage change from baseline to post-intervention during the groups, and all data were expressed by mean ± standard deviation. The Shapiro–Wilk test was used to examine if the outcomes were normally distributed, and Levene's test was used to check homoscedasticity. For normally distributed and homoscedastic data, one-way ANOVA was used to examine if percent changes in each outcome between baseline to post-intervention were significantly different among groups, and the planned contrasts were performed to examine the difference between intervention and control groups. When the data on the outcomes were not normally distributed, a nonparametric test (the Kruskal-Wallis test) was implemented, and the Mann–Whitney U test was used to analyze the difference between intervention and control groups. The significance level was set to $p < 0.05$ for all the analyses.

RESULTS

All participants in the HD-tDCS and FCE groups completed the training sessions, and their data were collected successfully

TABLE 3 | Percentage changes in passive ankle kinesthesia, foot muscle strength, and one-leg standing balance from baseline to post-intervention.

Outcome (%)	HD-tDCS	FCE	Control	*p*-value
Plantarflexion	− 14.03 ± 16.96	− 9.75 ± 21.24	− 6.48 ± 7.28	0.721
Dorsiflexion	− 9.32 ± 13.50	7.17 ± 20.02	4.31 ± 13.62	0.058
Inversion	− 25.15 ± 17.22	− 2.97 ± 16.82	4.85 ± 11.64	**0.001**
Eversion	− 21.46 ± 19.61	− 9.18 ± 17.70	− 2.32 ± 9.06	**0.020**
MPJ flexor strength	13.77 ± 13.97	11.34 ± 14.30	− 0.13 ± 6.25	**0.029**
Toe flexor strength	9.09 ± 13.73	13.13 ± 14.23	0.74 ± 5.28	**0.047**
ML CoG sway velocity in OL_EO	3.18 ± 14.75	− 10.79 ± 16.51	− 1.35 ± 11.82	**0.020**
AP CoG sway velocity in OL_EO	− 0.93 ± 10.97	− 10.96 ± 12.13	− 7.31 ± 17.05	0.323
ML CoG sway velocity in OL_EC	− 4.14 ± 18.13	− 13.71 ± 18.74	0.28 ± 9.49	0.078
AP CoG sway velocity in OL_EC	− 4.92 ± 20.94	− 17.89 ± 12.82	2.18 ± 7.19	**0.003**

Notes: OL_EO, one-leg standing with eyes open; OL_EC, one-leg standing with eyes closed; ML, medial–lateral; AP, anteroposterior; CoG, the center of gravity; HD-tDCS, high-definition transcranial direct current stimulation; MPJ, metatarsophalangeal joint; FCE, foot core exercise. The bold p-value means p < 0.05.

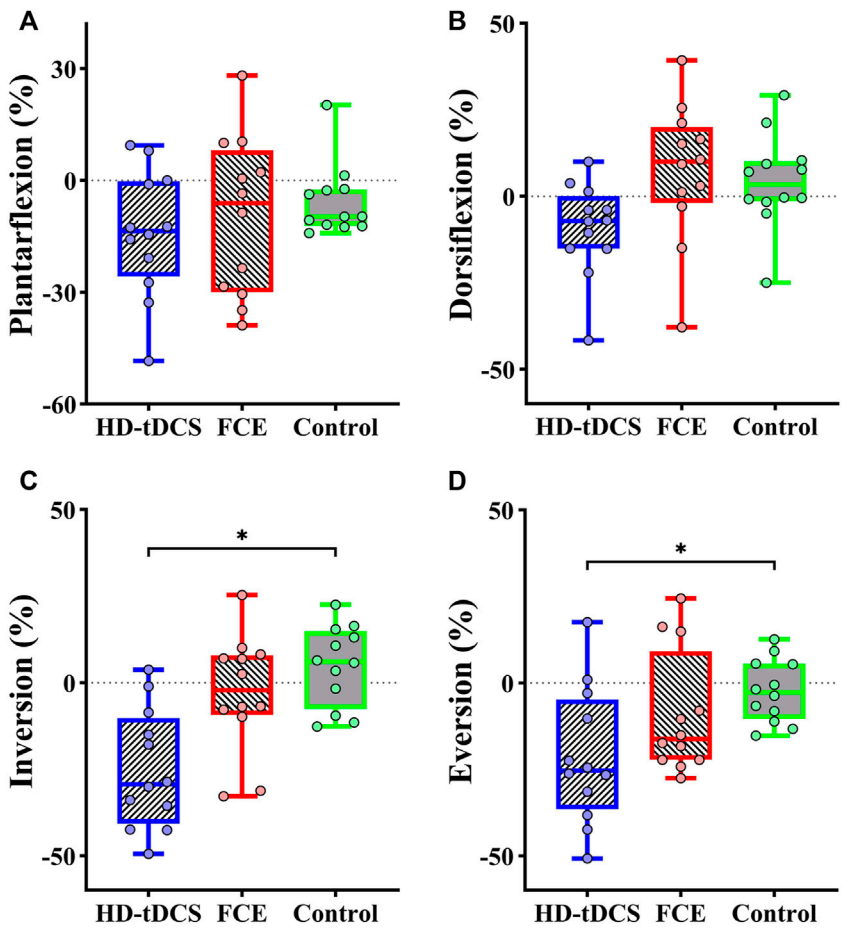

FIGURE 3 | Differences in percent changes in the passive kinesthesia thresholds of **(A)** plantarflexion, **(B)** dorsiflexion, **(C)** inversion, and **(D)** eversion from baseline to post-intervention among groups. HD-tDCS: high-definition transcranial direct current stimulation; FCE: foot core exercise; $^{*}p < 0.05$.

(**Supplementary Table 1**). Twelve participants received 2 mA of HD-tDCS, and no side effects or risk events were reported. No significant differences in demographics (i.e., year, height, and weight) were observed (p = 0.135, 0.272, and 0.256; **Table 1**).Moreover, the passive kinesthesia thresholds of eversion in the FCE group, the ML average CoG sway velocity in OL_EO in the HD-tDCS group, and the AP average CoG sway velocity in OL_EC in the FCE group were not normally distributed and were thus analyzed by a nonparametric test.

Significant differences in the percent changes in the passive kinesthesia thresholds of inversion ($F_{(2, 32)} = 9.210$, $p = 0.001$, and $\eta_p^2 = 0.365$, **Table 3**) and eversion (H = 7.788, p = 0.020) were

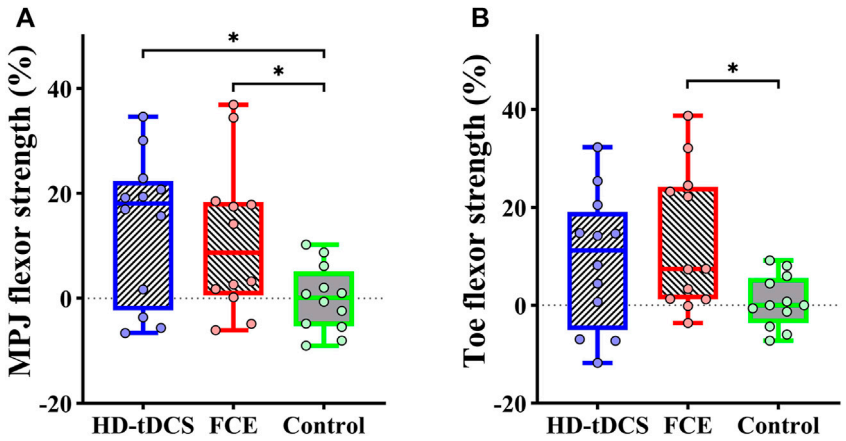

FIGURE 4 | Differences in percent changes in **(A)** the MPJ flexor strength and **(B)** the toe flexor strength from baseline to post-intervention among groups. HD-tDCS: high-definition transcranial direct current stimulation; MPJ: metatarsophalangeal joint; FCE: foot core exercise; $^{*}p < 0.05$.

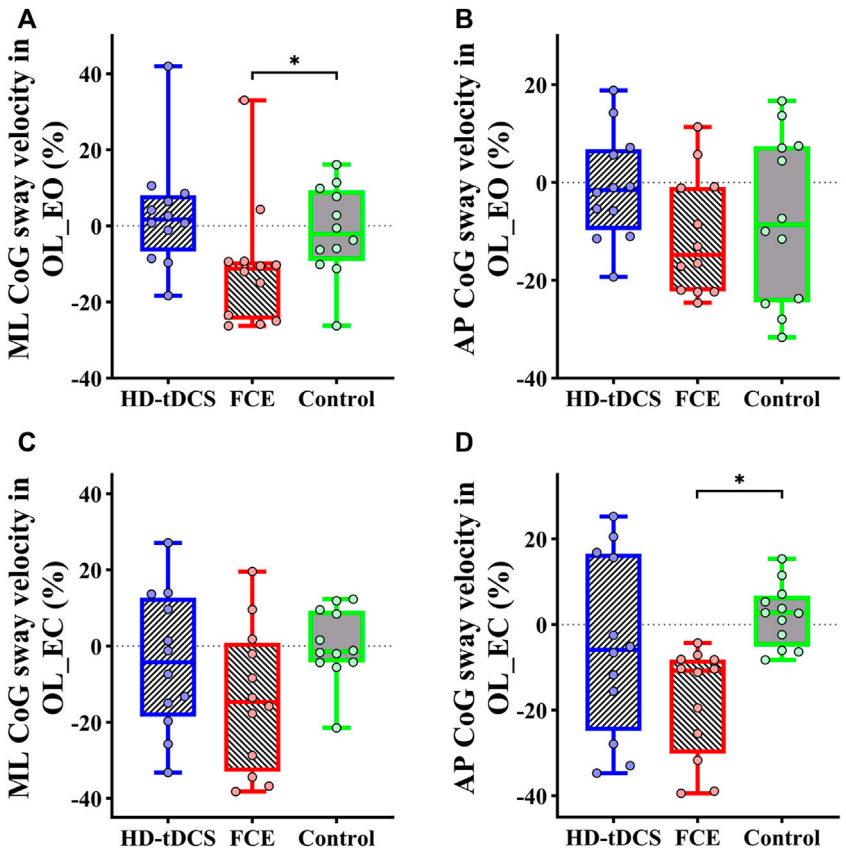

FIGURE 5 | Differences in percent changes in one-leg standing balance from baseline to post-intervention among groups. **(A)** ML CoG sway velocity in OL_EO; **(B)** AP CoG sway velocity in OL_EO; **(C)** ML CoG sway velocity in OL_EC; **(D)** AP CoG sway velocity in OL_EO. OL_EO: one-leg standing with eyes open; OL_EC: one-leg standing with eyes closed; ML: medial–lateral; AP: anteroposterior; CoG, center of gravity; HD-tDCS: high-definition transcranial direct current stimulation; FCE: foot core exercise; $^{*}p < 0.05$.

observed from baseline to post-intervention among groups. Planned contrasts indicated that the HD-tDCS group showed a considerable decrease in the percent change in the passive kinesthesia threshold of inversion ($t = -4.761$ and $p < 0.001$, **Figure 3C**) than the control group. Moreover, the Mann–Whitney U test showed that a greater decrease in

percent change in the passive kinesthesia threshold of eversion was observed in the HD-tDCS group than in the control group (p = 0.013, **Figure 3D**). No significant differences were observed for the percent changes in the passive kinesthesia thresholds of plantar flexion ($F_{(2,\ 32)}$ = 0.331, p = 0.721, and η_p^2 = 0.020, **Figure 3A**) and dorsiflexion ($F_{(2,\ 32)}$ = 3.112, p = 0.058, and η_p^2 = 0.163, **Figure 3B**).

Significant differences in the percent changes in the MPJ flexor strength ($F_{(2,\ 32)}$ = 3.979, p = 0.029, and η_p^2 = 0.199) and toe flexor strength ($F_{(2,\ 32)}$ = 3.372, p = 0.047, and η_p^2 = 0.174) were observed (**Table 3**). Planned contrasts showed that compared with the control group, a significantly higher increase in percentage change in the MPJ flexor strength was demonstrated in the HD-tDCS group (t = 2.814 and p = 0.008, **Figure 4A**) and in the FCE group (t = 2.323 and p = 0.027, **Figures 4A**), significantly greater increase in the percentage change in toe flexor strength was observed in the FCE group (t = 2.569, p = 0.015, **Figure 4B**).

Regarding postural control, significant differences in the percent changes in the ML average CoG sway velocity in OL_EO (H = 7.826 and p = 0.020) and the AP average CoG sway velocity in OL_EC (H = 11.740 and p = 0.003) were observed (**Table 3**). Furthermore, the Mann–Whitney U test showed that compared with the control group, FCE induced a greater decrease in the percent changes in the ML average CoG sway velocity in OL_EO (p = 0.033, **Figure 5A**) and the AP average CoG sway velocity in OL_EC (p < 0.001, **Figure 5D**). Moreover, no significant differences were observed for the percent changes in the AP CoG sway velocity in OL_EO ($F_{(2,\ 32)}$ = 1.172, p = 0.323, and η_p^2 = 0.068, **Figure 5B**) and the ML CoG sway velocity in OL_EC ($F_{(2,\ 32)}$ = 2.762, p = 0.078, and η_p^2 = 0.147, **Figure 5C**).

DISCUSSION

This study explored the effects of FCE and HD-tDCS on foot sensorimotor function (i.e., toe flexor strength and passive ankle kinesthesia) and postural control performance. It is observed here that compared with control, HD-tDCS can significantly decrease the passive kinesthesia thresholds of inversion and eversion and improve MPJ flexor strength; on the other hand, compared with control, FCE can enhance the foot muscle strength and decrease the ML average CoG sway velocity in OL_EO and the AP average CoG sway velocity in OL_EC. These results suggested that compared with FCE, HD-tDCS can at least induce comparable, but to some extent distinct, benefits for foot sensorimotor function, suggesting the intervention of cortical modulation *via* HD-tDCS, may uniquely contribute to the enhancement of foot function and postural control, in addition to the intervention targeting central and peripheral function. Future studies are needed to explicitly examine the potential mechanisms underlying the difference between such benefits from tDCS and FCE.

As a novel "brain training", the current literature provided interesting insights into the potential for tDCS to enhance physical performance, including the sensory function, muscle strength, and balance (Vaseghi et al., 2014; Lattari et al., 2018; de Moura et al., 2019). In this study, the results showed that compared with the control group, the HD-tDCS group demonstrated significantly decreased passive kinesthesia thresholds of ankle inversion and eversion, suggesting that HD-tDCS could improve the sensory perception of the ankle. The previous study showed that tDCS could decrease the vibrotactile threshold of the foot sole when standing and the tactile threshold of the left-center of the distal pulp of the hallux, indicating that tDCS could enhance the ankle-foot somatosensory function (Zhou et al., 2018; Yamamoto et al., 2020). Evidence from neuroimaging studies showed that tDCS increased activation of the left posterior paracentral lobule (including S1) in response to relatively large and easily-perceivable pressure stimuli applied to the right foot sole (Wang et al., 2015). Taken together, these findings suggested that HD-tDCS applied over the sensorimotor cortex can lower the ankle passive kinesthesia thresholds by facilitating the activation of the brain's somatosensory cortical network.

No significant differences were observed in the plantarflexion and dorsiflexion kinesthesia thresholds in the HD-tDCS group. The neutral regulation effect of tDCS may be related to sensory sensitivity, and healthy participants can accurately perceive the trivial changes in ankle plantarflexion and dorsiflexion (Sun et al., 2015). Thus, it is speculated that the available effect of tDCS-induced improvements in the plantarflexion and dorsiflexion kinesthesia may have been limited. In a word, HD-tDCS helped to decrease passive kinesthesia thresholds of inversion and eversion, implying that the ability to cope with lateral slanted terrain could be improved by multiple sessions of HD-tDCS. On the other hand, no such effects were observed in the FCE group. A potential reason is that FCE targets the central and peripheral components in the somatosensory circuit simultaneously, and its benefits oftentimes can only arise chronically, so the current design of FCE of 4 weeks may not be sufficient to induce significant improvement in the function of mechanoreceptors on the feet, and thus in the sensorimotor function.

It was also observed that 4 weeks of HD-tDCS could enhance MPJ flexor strength and FCE could improve foot muscle strength including MPJ flexor strength and toe flexor strength, indicating HD-tDCS and FCE both promote intrinsic foot muscle strength. In general, anodal HD-tDCS alters the resting membrane potential of the targeted neurons to increase cortical excitability, and these effects can sustain about 6 h after receiving HD-tDCS (Nitsche and Paulus, 2001; Kuo et al., 2013). Moreover, this lasting effect induced by tDCS may continuously reduce short-interval intracortical inhibition, assisting in the production of voluntary force output by modulating descending excitatory drive, thereby improving muscle strength (Nitsche et al., 2005; Weier et al., 2012). FCE is one type of intervention that involves the activation of both central and peripheral systems, which can directly strengthen muscle functions. Specifically, exercises (e.g., short foot exercise and towel curls) included in FCE can activate various flexor muscle activities. Towel curls tend to recruit the flexor hallucis and digitorum longus, and short foot exercise targets the plantar intrinsic muscles of the foot. Thus, studies have shown that FCE targeting the foot muscle strengthening can improve and activate the function in the foot muscles, such as abductor hallucis, flexor

digitorum brevis, and flexor hallucis brevis (Fraser and Hertel, 2019; Taddei et al., 2020).

The results of this study also showed that FCE decreased the average CoG sway velocity in one-leg standing balance, which is consistent with previous studies that observed the improvements induced by 4 weeks of short foot exercise in the intrinsic foot muscle performance during a static unilateral balancing activity and in the performance of functional balance task (Mulligan and Cook, 2013). Moreover, short foot exercise and towel curl could decrease the ML center of pressure movement on the dominant limb by a small amount (≈5 mm) during a dynamic-balance test (Lynn et al., 2012). Taken together, our results suggested that FCE is of great promise to improve the postural control performance of one-leg standing. However, no significant differences were observed for the CoG sway velocity in the OL_EO condition. One possible explanation is that visual information has a main effect on the standing balance with eyes open, and thus, maintaining the balance does not need more information integrated by the sensorimotor cortex.

Moreover, no significant improvements in postural control as induced by HD-tDCS were observed. Although a meta-analysis revealed that tDCS applied over M1 appeared to improve postural control, more recent studies also showed significant effects of tDCS targeting M1 on standing postural control (de Moura et al., 2019; Zhou et al., 2021). One possible reason may be that the leg area of M1 is located in parallel to the direction of current flow delivered by tDCS so that only a very small electric field can be generated over M1. Therefore, the excitability of M1 can be increased to a very limited extent, which largely limits the effects of tDCS targeting M1 on standing postural control performance (Zhou et al., 2021). Future studies are highly demanded to optimize the tDCS montages targeting M1 to maximize the activation of this important brain region.

The mechanisms underlying the benefits of HD-tDCS and FCE are distinct, and the dose-response relationship in these two interventions may thus be different. Therefore, one session of FCE may induce a different response from tDCS of the same time length. Future studies implementing multiple assessments in the postural control performance (e.g., assessing every week through the intervention) may provide important knowledge for the dose-response relationships of the two interventions, and then, we can more explicitly examine and compare the efficacy of these two interventions.

This study is of several limitations in addition to the uncertain difference in the dose-response relationship between tDCS and FCE. Only a small sample of male adults was enrolled, future studies with a larger sample size of participants with similar numbers of men and women are needed. Moreover, healthy young adults were recruited, and the effects of HD-tDCS and FCE on foot sensorimotor function and postural control in populations with diminished or impaired foot functionality are worth to be examined. Also, no follow-up assessment was conducted in this study to investigate the lasting effect of the interventions. Finally, the positive effects of HD-tDCS may be limited by a 4-week intervention with a rather long interval (i.e., three sessions weekly). Notably, the focalization degree of HD-tDCS here was not measured quantitatively and should be explicitly assessed in future studies, which can provide helpful knowledge for the design of sensorimotor tDCS.

CONCLUSION

This study demonstrated that 4 weeks of HD-tDCS and FCE induced distinct benefits on foot sensorimotor function and the standing postural control performance in healthy young adults. HD-tDCS could improve foot sensorimotor function including the MPJ flexor strength and passive kinesthesia thresholds of ankle inversion and eversion. Meanwhile, FCE could also strengthen foot muscle strength and enhance postural control performance in one-leg standing. It indicates that for the rehabilitation of the foot sensorimotor function and standing postural control, interventions targeting the peripheral and the central components are both needed. Future studies are warranted to further explore the potential benefits of implementing the combined type of intervention (i.e., interventions combining both FCE and tDCS).

DATA AVAILABILITY STATEMENT

The original contributions presented in the study are included in the article/**Supplementary Material**, further inquiries can be directed to the corresponding authors.

ETHICS STATEMENT

The studies involving human participants were reviewed and approved by the Institutional Review Board of the Shanghai University of Sport. The patients/participants provided their written informed consent to participate in this study.

AUTHOR CONTRIBUTIONS

SX and BW contributed to the study design, data collection, drafting, and revising the manuscript; JZ and WF contributed to supervising the study design, completing data analysis and interpretation, and revising the manuscript; BW and XZ revised the manuscript. All authors have read and approved the final version of the manuscript and agree with the order of the presentation of the authors.

FUNDING

This research was funded by the National Key Technology Research and Development Program of the Ministry of Science and Technology of China (2018YFF0300500), the National Natural Science Foundation of China (11772201 and

119320131), and the "Dawn" Program of Shanghai Education Commission, China (19SG47), the "Outstanding Young Scholar" Program of Shanghai Municipal. JZ is supported by the grant from the National Institutes of Health (1K01AG075180-01).

REFERENCES

Angius, L., Pascual-Leone, A., and Santarnecchi, E. (2018). Brain Stimulation and Physical Performance. *Prog. Brain Res.* 240, 317–339. doi:10.1016/bs.pbr.2018.07.010

Boonstra, T. W., Nikolin, S., Meisener, A.-C., Martin, D. M., and Loo, C. K. (2016). Change in Mean Frequency of Resting-State Electroencephalography after Transcranial Direct Current Stimulation. *Front. Hum. Neurosci.* 10, 270. doi:10.3389/fnhum.2016.00270

de Moura, M. C. D. S., Hazime, F. A., Marotti Aparicio, L. V., Grecco, L. A. C., Brunoni, A. R., and Hasue, R. H. (2019). Effects of Transcranial Direct Current Stimulation (tDCS) on Balance Improvement: a Systematic Review and Meta-Analysis. *Somatosens. Mot. Res.* 36 (2), 122–135. doi:10.1080/08990220.2019.1624517

Fraser, J. J., and Hertel, J. (2019). Effects of a 4-Week Intrinsic Foot Muscle Exercise Program on Motor Function: A Preliminary Randomized Control Trial. *J. Sport Rehabil.* 28 (4), 339–349. doi:10.1123/jsr.2017-0150

Hashimoto, T., and Sakuraba, K. (2014). Strength Training for the Intrinsic Flexor Muscles of the Foot: Effects on Muscle Strength, the Foot Arch, and Dynamic Parameters before and after the Training. *J. Phys. Ther. Sci.* 26 (3), 373–376. doi:10.1589/jpts.26.373

Kakouris, N., Yener, N., and Fong, D. T. P. (2021). A Systematic Review of Running-Related Musculoskeletal Injuries in Runners. *J. Sport Health Sci.* 10 (5), 513–522. doi:10.1016/j.jshs.2021.04.001

Kelly, L. A., Cresswell, A. G., Racinais, S., Whiteley, R., and Lichtwark, G. (2014). Intrinsic Foot Muscles Have the Capacity to Control Deformation of the Longitudinal Arch. *J. R. Soc. Interface.* 11 (93), 20131188. doi:10.1098/rsif.2013.1188

Kuo, H.-I., Bikson, M., Datta, A., Minhas, P., Paulus, W., Kuo, M.-F., et al. (2013). Comparing Cortical Plasticity Induced by Conventional and High-Definition 4 × 1 Ring tDCS: A Neurophysiological Study. *Brain Stimul.* 6 (4), 644–648. doi:10.1016/j.brs.2012.09.010

Kurihara, T., Yamauchi, J., Otsuka, M., Tottori, N., Hashimoto, T., and Isaka, T. (2014). Maximum Toe Flexor Muscle Strength and Quantitative Analysis of Human Plantar Intrinsic and Extrinsic Muscles by a Magnetic Resonance Imaging Technique. *J. Foot Ankle Res.* 7, 26. doi:10.1186/1757-1146-7-26

Lattari, E., Oliveira, B. R. R., Monteiro Júnior, R. S., Marques Neto, S. R., Oliveira, A. J., Maranhão Neto, G. A., et al. (2018). Acute Effects of Single Dose Transcranial Direct Current Stimulation on Muscle Strength: A Systematic Review and Meta-Analysis. *PLoS One* 13 (12), e0209513. doi:10.1371/journal.pone.0209513

Lynn, S. K., Padilla, R. A., and Tsang, K. K. W. (2012). Differences in Static- and Dynamic-Balance Task Performance after 4 Weeks of Intrinsic-Foot-Muscle Training: the Short-Foot Exercise versus the Towel-Curl Exercise. *J. Sport Rehabil.* 21 (4), 327–333. doi:10.1123/jsr.21.4.327

Ma, Y., Yin, K., Zhuang, W., Zhang, C., Jiang, Y., Huang, J., et al. (2020). Effects of Combining High-Definition Transcranial Direct Current Stimulation with Short-Foot Exercise on Chronic Ankle Instability: A Pilot Randomized and Double-Blinded Study. *Brain Sci.* 10 (10), 749. doi:10.3390/brainsci10100749

McKeon, P. O., Hertel, J., Bramble, D., and Davis, I. (2015). The Foot Core System: a New Paradigm for Understanding Intrinsic Foot Muscle Function. *Br. J. Sports Med.* 49 (5), 290. doi:10.1136/bjsports-2013-092690

Mulligan, E. P., and Cook, P. G. (2013). Effect of Plantar Intrinsic Muscle Training on Medial Longitudinal Arch Morphology and Dynamic Function. *Man. Ther.* 18 (5), 425–430. doi:10.1016/j.math.2013.02.007

Nitsche, M. A., Seeber, A., Frommann, K., Klein, C. C., Rochford, C., Nitsche, M. S., et al. (2005). Modulating Parameters of Excitability during and after Transcranial Direct Current Stimulation of the Human Motor Cortex. *J. Physiol.* 568 (Pt 1), 291–303. doi:10.1113/jphysiol.2005.092429

Nitsche, M. A., and Paulus, W. (2001). Sustained Excitability Elevations Induced by Transcranial DC Motor Cortex Stimulation in Humans. *Neurology* 57 (10), 1899–1901. doi:10.1212/wnl.57.10.1899

Orr, E. L. R., Lacourse, M. G., Cohen, M. J., and Cramer, S. C. (2008). Cortical Activation during Executed, Imagined, and Observed Foot Movements. *Neuroreport* 19 (6), 625–630. doi:10.1097/wnr.0b013e3282fbf9e0

Ridge, S. T., Olsen, M. T., Bruening, D. A., Jurgensmeier, K., Griffin, D., Davis, I. S., et al. (2019). Walking in Minimalist Shoes Is Effective for Strengthening Foot Muscles. *Med. Sci. Sports Exerc* 51 (1), 104–113. doi:10.1249/mss.0000000000001751

Sulowska, I., Oleksy, Ł., Mika, A., Bylina, D., and Sołtan, J. (2016). The Influence of Plantar Short Foot Muscle Exercises on Foot Posture and Fundamental Movement Patterns in Long-Distance Runners, a Non-randomized, Non-blinded Clinical Trial. *PLoS One* 11 (6), e0157917. doi:10.1371/journal.pone.0157917

Sun, W., Song, Q., Yu, B., Zhang, C., and Mao, D. (2015). Test-retest Reliability of a New Device for Assessing Ankle Joint Threshold to Detect Passive Movement in Healthy Adults. *J. Sports Sci.* 33 (16), 1667–1674. doi:10.1080/02640414.2014.1003589

Taddei, U. T., Matias, A. B., Ribeiro, F. I. A., Bus, S. A., and Sacco, I. C. N. (2020). Effects of a Foot Strengthening Program on Foot Muscle Morphology and Running Mechanics: A Proof-Of-Concept, Single-Blind Randomized Controlled Trial. *Phys. Ther. Sport* 42, 107–115. doi:10.1016/j.ptsp.2020.01.007

Tanaka, S., Hanakawa, T., Honda, M., and Watanabe, K. (2009). Enhancement of Pinch Force in the Lower Leg by Anodal Transcranial Direct Current Stimulation. *Exp. Brain Res.* 196 (3), 459–465. doi:10.1007/s00221-009-1863-9

van Poppel, D., van der Worp, M., Slabbekoorn, A., van den Heuvel, S. S. P., van Middelkoop, M., Koes, B. W., et al. (2021). Risk Factors for Overuse Injuries in Short- and Long-Distance Running: A Systematic Review. *J. Sport Health Sci.* 10 (1), 14–28. doi:10.1016/j.jshs.2020.06.006

Vaseghi, B., Zoghi, M., and Jaberzadeh, S. (2014). Does Anodal Transcranial Direct Current Stimulation Modulate Sensory Perception and Pain? A Meta-Analysis Study. *Clin. Neurophysiol.* 125 (9), 1847–1858. doi:10.1016/j.clinph.2014.01.020

Wang, Y., Hao, Y., Zhou, J., Fried, P. J., Wang, X., Zhang, J., et al. (2015). Direct Current Stimulation over the Human Sensorimotor Cortex Modulates the Brain's Hemodynamic Response to Tactile Stimulation. *Eur. J. Neurosci.* 42 (3), 1933–1940. doi:10.1111/ejn.12953

Wearing, S. C., Smeathers, J. E., Urry, S. R., Hennig, E. M., and Hills, A. P. (2006). The Pathomechanics of Plantar Fasciitis. *Sports Med.* 36 (7), 585–611. doi:10.2165/00007256-200636070-00004

Weier, A. T., Pearce, A. J., and Kidgell, D. J. (2012). Strength Training Reduces Intracortical Inhibition. *Acta Physiol.* 206 (2), 109–119. doi:10.1111/j.1748-1716.2012.02454.x

Xiao, S., Wang, B., Zhang, X., Zhou, J., and Fu, W. (2020a). Acute Effects of High-Definition Transcranial Direct Current Stimulation on Foot Muscle Strength, Passive Ankle Kinesthesia, and Static Balance: A Pilot Study. *Brain Sci.* 10 (4), 246. doi:10.3390/brainsci10040246

Xiao, S., Wang, B., Zhang, X., Zhou, J., and Fu, W. (2020b). Systematic Review of the Impact of Transcranial Direct Current Stimulation on the Neuromechanical Management of Foot and Ankle Physical Performance in Healthy Adults. *Front. Bioeng. Biotechnol.* 8, 587680. doi:10.3389/fbioe.2020.587680

Yamamoto, S., Ishii, D., Ichiba, N., Yozu, A., and Kohno, Y. (2020). Cathodal tDCS on the Motor Area Decreases the Tactile Threshold of the Distal Pulp of the Hallux. *Neurosci. Lett.* 719, 133887. doi:10.1016/j.neulet.2018.10.032

SUPPLEMENTARY MATERIAL

The Supplementary Material for this article can be found online at: https://www.frontiersin.org/articles/10.3389/fbioe.2022.894131/full#supplementary-material

Yamauchi, J., and Koyama, K. (2015). Influence of Ankle Braces on the Maximum Strength of Plantar and Toe Flexor Muscles. *Int. J. Sports Med.* 36 (7), 592–595. doi:10.1055/s-0034-1396824

Yotnuengnit, P., Bhidayasiri, R., Donkhan, R., Chaluaysrimuang, J., and Piravej, K. (2018). Effects of Transcranial Direct Current Stimulation Plus Physical Therapy on Gait in Patients with Parkinson Disease: A Randomized Controlled Trial. *Am. J. Phys. Med. Rehabil.* 97 (1), 7–15. doi:10.1097/phm.0000000000000783

Zhang, S., Fu, W., and Liu, Y. (2019). Does Habitual Rear-Foot Strike Pattern with Modern Running Shoes Affect the Muscle Strength of the Longitudinal Arch? *Isokinet. Exerc. Sci.* 27 (3), 213–218. doi:10.3233/ies-192139

Zhou, J., Lo, O.-Y., Lipsitz, L. A., Zhang, J., Fang, J., and Manor, B. (2018). Transcranial Direct Current Stimulation Enhances Foot Sole Somatosensation when Standing in Older Adults. *Exp. Brain Res.* 236 (3), 795–802. doi:10.1007/s00221-018-5178-6

Zhou, J., Manor, B., Yu, W., Lo, O. Y., Gouskova, N., Salvador, R., et al. (2021). Targeted tDCS Mitigates Dual-Task Costs to Gait and Balance in Older Adults. *Ann. Neurology* 90 (3), 428–439. doi:10.1002/ana.26156

Conflict of Interest: The authors declare that the research was conducted in the absence of any commercial or financial relationships that could be construed as a potential conflict of interest.

frontiers | Frontiers in Bioengineering and Biotechnology

ORIGINAL RESEARCH
published: 06 June 2022
doi: 10.3389/fbioe.2022.914990

Increased Femoral Anteversion Does Not Lead to Increased Joint Forces During Gait in a Cohort of Adolescent Patients

Nathalie Alexander[1,2], *Reinald Brunner*[3,4,5], *Johannes Cip*[6], *Elke Viehweger*[3,4,5] *and Enrico De Pieri*[3,5]*

[1]Laboratory for Motion Analysis, Department of Paediatric Orthopaedics, Children's Hospital of Eastern Switzerland, St. Gallen, Switzerland, [2]Department of Orthopaedics and Traumatology, Cantonal Hospital St. Gallen, St. Gallen, Switzerland, [3]Laboratory for Movement Analysis, University of Basel Children's Hospital, Basel, Switzerland, [4]Department of Paediatric Orthopaedics, University of Basel Children's Hospital, Basel, Switzerland, [5]Dpartment of Biomedical Engineering, University of Basel, Basel, Switzerland, [6]Department of Paediatric Orthopaedics, Children's Hospital of Eastern Switzerland, St. Gallen, Switzerland

Orthopedic complications were previously reported for patients with increased femoral anteversion. A more comprehensive analysis of the influence of increased femoral anteversion on joint loading in these patients is required to better understand the pathology and its clinical management. Therefore, the aim was to investigate lower-limb kinematics, joint moments and forces during gait in adolescent patients with increased, isolated femoral anteversion compared to typically developing controls. Secondly, relationships between the joint loads experienced by the patients and different morphological and kinematic features were investigated. Patients with increased femoral anteversion (n = 42, 12.8 ± 1.9 years, femoral anteversion: 39.6 ± 6.9°) were compared to typically developing controls (n = 9, 12.0 ± 3.0 years, femoral anteversion: 18.7 ± 4.1°). Hip and knee joint kinematics and kinetics were calculated using subject-specific musculoskeletal models. Differences between patients and controls in the investigated outcome variables (joint kinematics, moments, and forces) were evaluated through statistical parametric mapping with Hotelling T2 and t-tests ($\alpha = 0.05$). Canonical correlation analyses (CCAs) and regression analyses were used to evaluate within the patients' cohort the effect of different morphological and kinematic predictors on the outcome variables. Predicted compressive proximo-distal loads in both hip and knee joints were significantly reduced in patients compared to controls. A gait pattern characterized by increased knee flexion during terminal stance ($KneeFlex_{tSt}$) was significantly correlated with hip and knee forces, as well as with the resultant force exerted by the quadriceps on the patella. On the other hand, hip internal rotation and in-toeing, did not affect the loads in the joints. Based on the finding of the CCAs and linear regression analyses, patients were further divided into two subgroups based $KneeFlex_{tSt}$. Patients with excessive $KneeFlex_{tSt}$ presented a significantly higher femoral anteversion than those with normal $KneeFlex_{tSt}$. Patients with excessive $KneeFlex_{tSt}$ presented significantly larger quadriceps forces on the patella and a larger posteriorly-oriented shear force at the knee, compared to patients with normal $KneeFlex_{tSt}$, but both patients' subgroups presented only limited differences in

OPEN ACCESS

Edited by:
Ching-Chi Hsu,
National Taiwan University of Science and Technology, Taiwan

Reviewed by:
Yaodong Gu,
Ningbo University, China
Dong Sun,
Ningbo University, China

***Correspondence:**
Enrico De Pieri
enrico.depieri@unibas.ch

Specialty section:
This article was submitted to Biomechanics, a section of the journal Frontiers in Bioengineering and Biotechnology

Received: 07 April 2022
Accepted: 13 May 2022
Published: 06 June 2022

Citation:
Alexander N, Brunner R, Cip J, Viehweger E and De Pieri E (2022) Increased Femoral Anteversion Does Not Lead to Increased Joint Forces During Gait in a Cohort of Adolescent Patients. Front. Bioeng. Biotechnol. 10:914990. doi: 10.3389/fbioe.2022.914990

terms of joint loading compared to controls. This study showed that an altered femoral morphology does not necessarily lead to an increased risk of joint overloading, but instead patient-specific kinematics should be considered.

Keywords: femoral torsion, coxa antetorta, musculoskeletal modelling, joint loading, in-toeing, hip internal rotation, knee flexion

INTRODUCTION

Femoral anteversion refers to the twist between the proximal and distal parts of the femur on the transverse plane (Kaiser et al., 2016). The normal amount of torsion depends on age and sex (Hefti, 2000; Jacquemier et al., 2008), starting approximatively at 40° of anteversion at birth, and decreasing to 15–20° during adulthood (Crane, 1959; Fabry et al., 1973). When increased femoral anteversion does not resolve spontaneously during growth and persists during adolescence, it can be associated with disturbances in mobility, such as an in-toeing gait pattern, and represents a frequent reason for consultation with pediatric orthopedic clinicians (Fabry, 2010). There is no consistent definition in the literature of what is considered as pathologically increased femoral anteversion, with values ranging from >30° to 50° (Jani et al., 1979; Cordier and Katthagen, 2000; Hefti, 2000).

Although increased femoral anteversion is often considered a primarily cosmetic problem, it can also be associated with orthopedic and functional problems in pediatric and adolescent patients, who may eventually require surgical intervention. Increased femoral torsion was reported to lead to functional problems, especially concerning high falling frequencies (Leblebici et al., 2019; Mackay et al., 2021) and altered lower-limb kinematics during gait, such as in-toeing and increased hip internal rotation (Bruderer-Hofstetter et al., 2015; Passmore et al., 2018; Alexander et al., 2019; Mackay et al., 2021). Since femoral anteversion measured by computed tomography (CT) scans correlates weakly with hip internal rotation during walking, a complete three-dimensional (3D) gait analysis was recommended when planning a surgical correction of torsional deformities (Radler et al., 2010; Gaston et al., 2011). However, gait deviations due to increased femoral anteversion in otherwise typically developing adolescents often receive little attention as increased femoral anteversion <50° is most of the time not considered for surgery (Tonnis and Heinecke, 1999; Cordier and Katthagen, 2000; Sass and Hassan, 2003; Fabry, 2010). These gait deviations may nevertheless cause future complaints, such as limited function and pain (Mackay et al., 2021). Corrective osteotomies for increased femoral anteversion are usually conducted in patients during adolescence. While femoral derotation osteotomy is a common procedure in patients with cerebral palsy (Dreher et al., 2007; Dreher et al., 2012), the indication is less common in otherwise typically developing children and adolescents (MacWilliams et al., 2016).

Nevertheless, previous studies have also shown an association between femoral anteversion and anterior knee pain (Eckhoff et al., 1997), as the rotational alignment of the limb has a major impact on patellar kinematics (Keshmiri et al., 2016). Powers (2003) and Stevens et al. (2014) reported a correlation of increased femoral anteversion with patellofemoral pain, while increased femoral anteversion is also a known risk factor for patellofemoral instability (Dejour and Le Coultre, 2007). Lower limb torsional malalignment is also one of the major risk factors implicated in the development of overuse injuries (Pagliazzi et al., 2022). Femoral torsional and coronal deformities have previously been correlated with hip pain and labral damage (Tönnis and Heinecke, 1999). A recent meta-analysis of 1756 patients found a positive correlation between increased anteversion and the severity of hip osteoarthritis (Parker et al., 2021). Excessive femoral anteversion was also associated with femoroacetabular impingement (FAI) syndrome (Ito et al., 2001; Audenaert et al., 2012; Ejnisman et al., 2013). Ejnisman et al. (2013) investigated hips with FAI and reported that patients with femoral anteversion greater than 15° were 2.2 times more likely to have labral tears. Furthermore, alterations of the femoral torsional morphology could affect the orientation of the hip intra-articular forces (De Pieri et al., 2021), which could be associated with the spatial distribution of the acetabular cartilage damage observed during adulthood, especially in concomitance with other morphological alterations, such as cam and pincer deformities that characterize FAI syndrome (Pascual-Garrido et al., 2019).

This evidence suggests the need for a more comprehensive understanding of the influence of increased femoral anteversion on hip and knee joint loading. Since surgical corrections are taken into consideration for pediatric and adolescent patients before the onset of secondary orthopedic problems, it is particularly important to investigate potentially pathological joint mechanics in this specific demographic cohort. In order to gain a better understanding of hip and knee joint loading, musculoskeletal modelling can be used to assess intra-articular loads while accounting for both subject-specific morphological and kinematic characteristics (De Pieri et al., 2021). Passmore et al. (2018) compared hip and knee loading using generic and subject-specific musculoskeletal models in a cohort of adolescent patients with increased femoral anteversion and increased tibial torsion, and predicted increased mediolateral patellofemoral joint contact forces when using subject-specific models. In a heterogeneous cohort of 37 healthy and asymptomatic adults (range: −7° retroversion to +38° anteversion), De Pieri et al. (2021) found significant correlations between higher femoral anteversion and higher anterior (swing phase) and medial (loaded stance phase) hip contact forces during gait. Furthermore, modelling patient-specific femoral anteversion was also shown to be particularly important for the analysis of patients affected by cerebral palsy, who often present torsional bony deformities (Kainz et al., 2020; Kainz et al., 2021; Veerkamp

TABLE 1 | Mean (standard deviation) anthropometric data and walking speed for patients and controls, as well as distinct gait variables for patients including (range).

	Patients (n = 42)	Controls (n = 9)	*p*-value
Femoral anteversion [°]	39.6 (6.9) [30–63]	18.7 (4.1) [13–25]	0.000
Midpoint $_{HipRot\ ROM}$ [°]	24.6 (10.5) [0–40]	—	—
Age [years]	12.8 (1.9) [10.3–17.5]	12.0 (3.0) [8.5–16.3]	0.270
Gender [female/male]	26/16	5/4	—
Height [m]	1.56 (0.10) [1.40–1.78]	1.53 (0.18) [1.28–1.77]	0.520
Mass [kg]	44.9 (9.5) [30.8–68.6]	41.8 (12.3) [28.3–63.2]	0.413
Walking speed [m/s]	1.25 (0.11) [0.93–1.50]	1.32 (0.23) [1.06–1.61]	0.142
Specific gait pattern descriptors			
$HipRot_{tSt}$ [°]	14.0 (6.9) [3.4–29.1]	—	—
$KneeFlex_{tSt}$ [°]	15.4 (4.5) [3.3–24.2]	—	—
$FootProg_{tSt}$ [°]	1.9 (5.8) [−11.2–12.7]	—	—

Midpoint $_{HipRot\ ROM}$*, Midpoint of passive hip rotation range of motion (positive value indicate internal rotation);* $HipRot_{tSt}$*, mean hip rotation in terminal stance;* $KneeFlex_{tSt}$*, mean knee flexion in terminal stance;* $FootProg_{tSt}$*, mean foot progression angle in terminal stance.*

et al., 2021). These studies highlight the importance of accounting for subject-specific morphological information in the analysis of joint loads. However, a direct comparison of joint loading between patients with increased femoral anteversion and healthy controls is still lacking in literature, thus not allowing drawing any clinically relevant conclusion regarding the effect of these morphological deviations on joint mechanics and the long-term risk of joint overloading.

In addition to an altered bone morphology, patients with increased femoral anteversion also tend to present altered joint kinematics during gait. Previous studies have shown that these patients tend to walk with a more internally-rotated foot progression angle, increased hip internal rotation, increased hip flexion and greater anterior pelvic tilt. Additionally, an increased knee flexion in mid- and terminal stance was found for some children with increased femoral anteversion (Bruderer-Hofstetter et al., 2015; Passmore et al., 2018; Alexander et al., 2019; Mackay et al., 2021). In general, children with different lower-limb torsional deformities, tend to present kinematic compensatory mechanisms (Alexander et al., 2020; Byrnes et al., 2020). A stratified analysis based on different kinematic gait patterns might help identifying specific subgroups of patients who present a higher risk of joint overloading as a consequence of both altered morphology and kinematics.

It was hypothesized that pediatric and adolescent patients with increased femoral anteversion present increased hip and knee joint contact forces during gait compared to controls, which could be associated with some of the orthopedic complications previously reported for these patients. Furthermore, different loading situations, based on the specific deviations of their gait pattern, were expected. Therefore, the first aim of this study was to investigate lower-limb kinematics and kinetics, as well as intra-articular joint forces during gait in pediatric and adolescent patients with increased femoral anteversion compared to typically developing controls. Secondly, relationships between the joint loads experienced by the patients and different morphological and kinematic features were investigated. Specifically, the effects of femoral anteversion, the midpoint of hip rotational range of motion, and different kinematic characteristics representative of the gait patterns were analyzed through regression analyses. Finally, when potential indicators of joint overload were identified, a further subgroup analysis based on the specific gait pattern was carried out.

METHODS

Participants

Forty-two patients with increased femoral anteversion were retrospectively included from the overall patient pool at the Children's Hospital of Eastern Switzerland (**Table 1**). Patients with CT-confirmed femoral anteversion >30° were included in the study. Femoral anteversion was calculated as the angle between the femoral neck axis and the posterior contour of the femoral condyles (**Figure 1**) (Hernandez et al., 1981) from CT measurements (Somatom Definition AS 64 slices, Siemens Healthineers, Erlangen, Germany). Patients' data were compared to control data of nine healthy children and adolescents collected at the University of Basel Children's Hospital (**Table 1**), for whom normal values of femoral anteversion were confirmed through existing MRI measurements (Siemens Prisma, Siemens Healthineers, Erlangen, Germany) to limit radiation exposure. Exclusion criteria were defined as follows for patients and controls: <8 years or >18 years, leg length discrepancy >1 cm, any kind of foot deformity, tibiofemoral varus/valgus deformity >5°, adiposity (body mass index over 90th percentile), scoliosis or any type of psychomotor or neurological disorder, pathological tibial torsion; additional for controls: pathological femoral anteversion. The study was approved by the regional ethics board (Ethics Committee Northwest Switzerland EKNZ 2021-00015) and written informed consent was provided by all participants and their legal guardians.

Data Collection

Self-reflecting markers were attached according to the PiG-model (Kadaba et al., 1990). Participants walked barefoot at a self-selected normal speed. Lower-limb kinematics and kinetics were collected during gait using a 3-dimensional motion capture system (Vicon Motion Systems Ltd., Oxford, United Kingdom, 200 Hz), and force plates (patients: AMTI, Advanced Mechanical Technology Inc., Watertown, Massachusetts, United States, 1,000 Hz; controls: Kistler

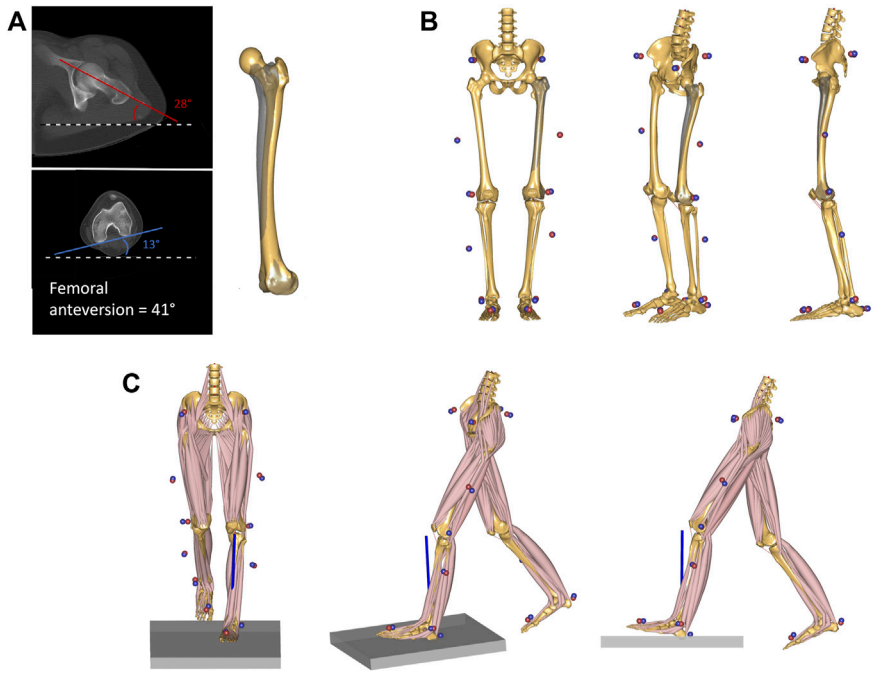

FIGURE 1 | (A) CT-measurement of femoral anteversion in one of the investigated patients. The angle between the horizontal reference (black and white dashed line) and both femoral neck axis (red) and the posterior contour of the femoral condyles (blue) were measured. The femoral anteversion angle is reported as a sum of the two values. The femoral geometry of the musculoskeletal model was then personalized to match the measured torsional value. The original unscaled femoral geometry is shown in shaded grey, while the personalized geometry is shown in solid yellow. **(B)** The model was scaled to match the subject's anthropometrics based on marker data collected during a standing reference trial. The measured markers' data are presented as blue spheres, while the virtual markers attached to the musculoskeletal model are shown as red spheres. **(C)** Kinematic and kinetic analyses during gait were based on the tracking of the measured marker trajectories and the ground reaction forces. An inverse dynamics analysis based on a third-order-polynomial muscle recruitment criterion was performed to calculate required muscle activations, as well as resulting joint moments and contact forces.

Instrumente AG, Winterthur, Switzerland, 1,000 Hz). Proper marker placement was checked using a static and dynamic trial prior to the measurement with a primary focus on the correct placement of the knee and thigh markers. Knee ab-/adduction motion >15° during swing phase indicated imprecise marker placement (Reinschmidt et al., 1997). A minimum of three valid gait cycles were collected, where participants hit the force plates without any visual interruption of the gait cycle.

Clinical examination was further conducted on patients and included amongst others evaluation of hip and knee passive range of motion. Clinical hip rotation is presented as mid-point of hip rotational range of motion (Midpoint $_{HipRot\ ROM}$), which is mid-point between maximal internal and external hip rotation (Kerr et al., 2003). If the Midpoint $_{HipRot\ ROM}$ is positive, hip internal rotation predominates while for negative values hip external rotation predominates.

Musculoskeletal Modelling

Data were first processed using Vicon Nexus (Vicon, Oxford Metrics Ltd., Oxford, United Kingdom). Following, marker trajectories and ground reaction forces (GRF) were filtered using a second-order low-pass Butterworth filter with a cut-off frequency of 5 and 12 Hz, respectively, and used as input for an inverse dynamics analysis in the AnyBody Modelling System (version 7.3, AnyBody Technology A/S, Aalborg, Denmark) (Damsgaard et al., 2006). Personalized models for each subject were created from a detailed generic model of the lower limb (De Pieri et al., 2018), based on a cadaveric dataset (Carbone et al., 2015), scaled to match the overall anthropometrics and the marker data collected during the static standing reference trial (Lund et al., 2015). The geometry of the femur was morphed to include a transversal rotation between the proximal and distal sections, matching the subject's femoral torsion value obtained from the imaging data (De Pieri et al., 2021) (**Figure 1**). The hip joints were modelled as 3-degrees of freedom (DoF) ball-and-socket joints, while knee and talocrural joints were modelled as 1-DoF hinges. The position of the patella was defined as a function of the knee flexion angle, and motion of the subtalar joint was restricted due to the reduced number of markers on the foot segment (one heel and one toe marker). The muscle elements were modelled with a simple muscle model represented by constant strength actuators.

Joint kinematics were computed from the measured marker trajectories and reported according to the International Society for Biomechanics' (ISB) recommendations (Wu et al., 2002). The foot progression angle relative to the direction of gait was also calculated. The orientation of the foot was identified through an axis connecting the heel and the second-metatarsal markers, while the direction of gait was defined as the line connecting

the positions of the heel marker in two consecutive ipsilateral heel strikes.

An inverse dynamics analysis based on a third-order-polynomial muscle recruitment criterion was then performed to calculate required muscle activations and forces, as well as resulting joint moments and contact forces (Andersen, 2021). Hip moments and hip contact forces (HCFs) were calculated in a proximal (pelvis-based) coordinate system according to ISB recommendations (Derrick et al., 2020). Knee moments and knee contact forces (KCFs) were computed in an anatomical tibia-based coordinate system similar to (Grood and Suntay, 1983) based on the bony landmarks of the tibial plateau. The resultant force exerted by the quadriceps muscles on the patella was also computed (De Pieri et al., 2022).

Data Analysis

Gait trials were processed and analyzed through the toolkit AnyPyTools (Lund et al., 2019) in the Python programming language (Python Software Foundation, Wilmington, DE, United States). The analysis was limited to the affected leg for the patients (or the leg with the highest measured femoral anteversion in case of bilateral involvement), while a randomly chosen leg was analyzed for the control group. Joint moments were normalized to body mass, while joint contact forces were normalized to body weight (BW). Average trajectories per subject were then calculated based on the collected walking trials. Kinematic trajectories (angles) were time-normalized to the gait cycle (GC) from foot-strike (0%) to foot-strike (100%) of the leg of interest, and kinetic trajectories (moments and forces) were time-normalized to the stance phase (ST), from foot-strike (0%) to foot-off (100%) of the leg of interest.

Comparison Between Patients and Controls

Differences between patients and controls in anthropometrics, femoral anteversion, clinical examination values, and walking speed were assessed using independent Student's *t*-tests with a significance level set at $\alpha = 0.05$. Moreover, the time profiles of joint kinematics, moments and contact forces were analyzed using statistical parametric mapping (SPM; www.spm1D.org, v0.43) (Pataky, 2012). The three hip joint angles were regarded as a 3D vector field, describing the 3D spatial variation of the kinematic vector trajectory over time. The use of vector field analysis takes into consideration covariance between spatial components, thus reducing errors due to covariation bias (Pataky et al., 2013). Similarly, hip moments, hip contact forces, and knee contact forces were described as 3D vectorial fields. Knee flexion angle, foot progression angle, knee sagittal moment, and the resultant force of the quadriceps acting on the patella were considered as separate 1D time-dependent scalar variables. Comparisons between patients and controls were carried out as SPM-based two-sample Hotelling T2 tests for 3D vector fields and as two-sample, two-tailed t-tests for 1D scalar variables. The output test statistics, SPM(T2) or SPM(t), were evaluated at each point of the gait cycle or stance phase. The significance level was set a priori at $\alpha = 0.05$, and the corresponding critical thresholds T2* and t* were calculated based on the temporal smoothness of the input data through random field theory. In case of 3D vector field analysis, post-hoc scalar t-tests were also conducted using on each separate component, with Bonferroni-corrected significance threshold levels set at $\alpha = 0.05/3 = 0.017$.

Regression Analyses With Morphological and Kinematic Parameters

For the second aim, canonical correlation analyses (CCAs) and regression analyses were used to evaluate within the patients' cohort the effect of different morphological and kinematic predictors on the investigated outcome variables, meaning joint kinematics, moments, and forces during gait. The SPM-based analyses allowed to identify specific intervals of the gait cycle or stance phase in which the outcome variables were correlated with the individual predictors. Femoral anteversion and the clinically assessed Midpoint $_{HipRot\ ROM}$ were used as morphological independent variables for the analyses. Furthermore, three distinct kinematic characteristics were chosen to identify potential relationships between subject-specific gait patterns and the outcome variables. The distinct kinematic gait characteristics were hip internal rotation, knee flexion, and foot progression angle. Synthetic values, defined for each variable as the mean value during terminal stance (31–50% GC), were used as independent variables in the regression analyses: HipRot_{tSt}, KneeFlex_{tSt} and FootProg_{tSt}, respectively (**Table 1**). Finally, walking speed was also included as an independent variable. For each independent variable, SPM-based independent CCAs or scalar linear regressions were used to identify potential correlations with 3D vector fields and 1D scalar outcome variables, respectively. The significance level was set at $\alpha = 0.05$. When a statistically significant correlation was observed between one of the independent variables and a 3D vector fields, post-hoc scalar linear regressions were also conducted on each separate component, with Bonferroni-corrected significance threshold levels set at $\alpha = 0.05/3 = 0.017$.

Subgroup Analysis

In order to further evaluate the clinical meaningfulness of these correlations, the patients were further divided into subgroups based on gait-pattern-specific characteristics whenever a significant correlation between a specific kinematic feature and the joint contact forces was detected. Patients were divided into two subgroups (e.g. based on KneeFlex_{tSt}): one group characterized by values that fell within the normal range of the control data, and one group by values that excessively deviated from this range. The normative range was defined by identifying the mean value during terminal stance across controls. Each patient's mean value during terminal stance was defined as exceeding control data when above/below the control's mean ±1 standard deviation. Differences in anthropometrics, femoral anteversion, clinical examination values, gait speed, and distinct gait characteristics in terminal stance between subgroups were identified using independent Student's *t*-tests. Furthermore, potential differences in joint kinematics, moments, and forces between each subgroup of patients (normal and excessive) and controls, as well as in-between subgroups, were

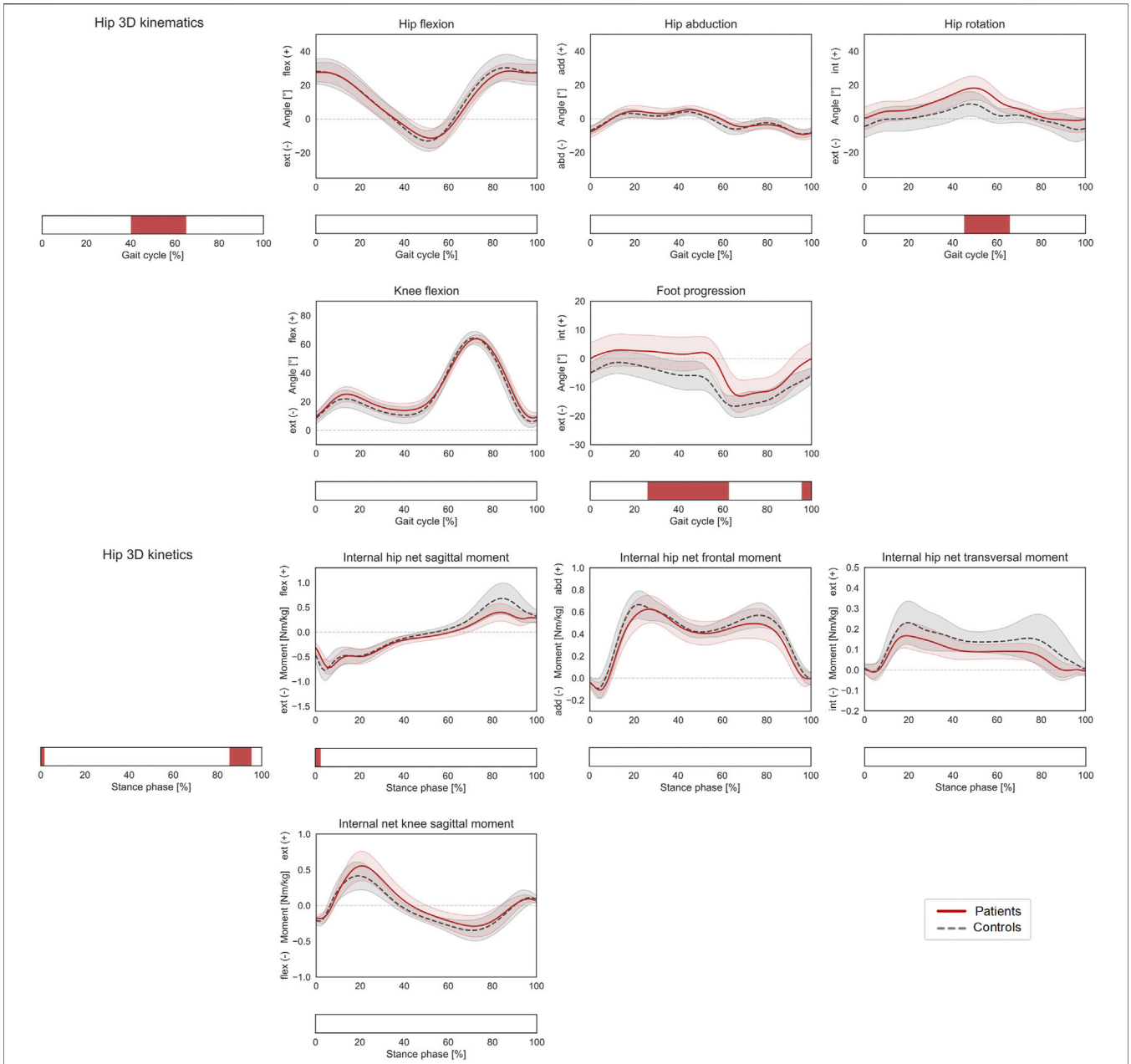

FIGURE 2 | Lower-limb kinematics during the gait cycle (GC) and joint moments during stance phase (ST). Mean ± 1SD hip flexion, hip abduction, hip rotation, knee flexion, and foot progression angles, as well as hip sagittal, frontal, transversal, and knee sagittal moments, are reported as red solid lines for patients, and as grey dashed lines for controls. Intervals of GC or ST with a statistically significant difference in the relevant SPM tests are reported as red bars. Hip joint angles and moments were regarded as a 3D vector fields. 3-dimensional significant differences between patients and controls were analyzed by means of two-sample Hotelling T2 tests and are reported in the leftmost panels. 1D scalar outcome variables, as well as individual components of the vector fields in the post-hoc vectorial analyses, were analyzed by means of two-sample t-tests and intervals characterized by significant differences between the two groups are reported below each subplot.

analyzed through SPM-based two-sample Hotelling T2 tests for 3D vector fields and as two-sample, two-tailed t-tests for 1D scalar variables ($\alpha = 0.05$, with post-hoc Bonferroni-corrected t-tests $\alpha = 0.017$).

In the interest of clarity, for all SPM analyses only statistically significant differences in intervals longer than 2% of the gait cycle or stance phase are discussed.

RESULTS

Comparison Between Patients and Controls

Patients presented a significantly larger femoral anteversion compared controls (+20.9°), while there were no statistically significant differences in terms of age, mass, height, and walking speed (**Table 1**).

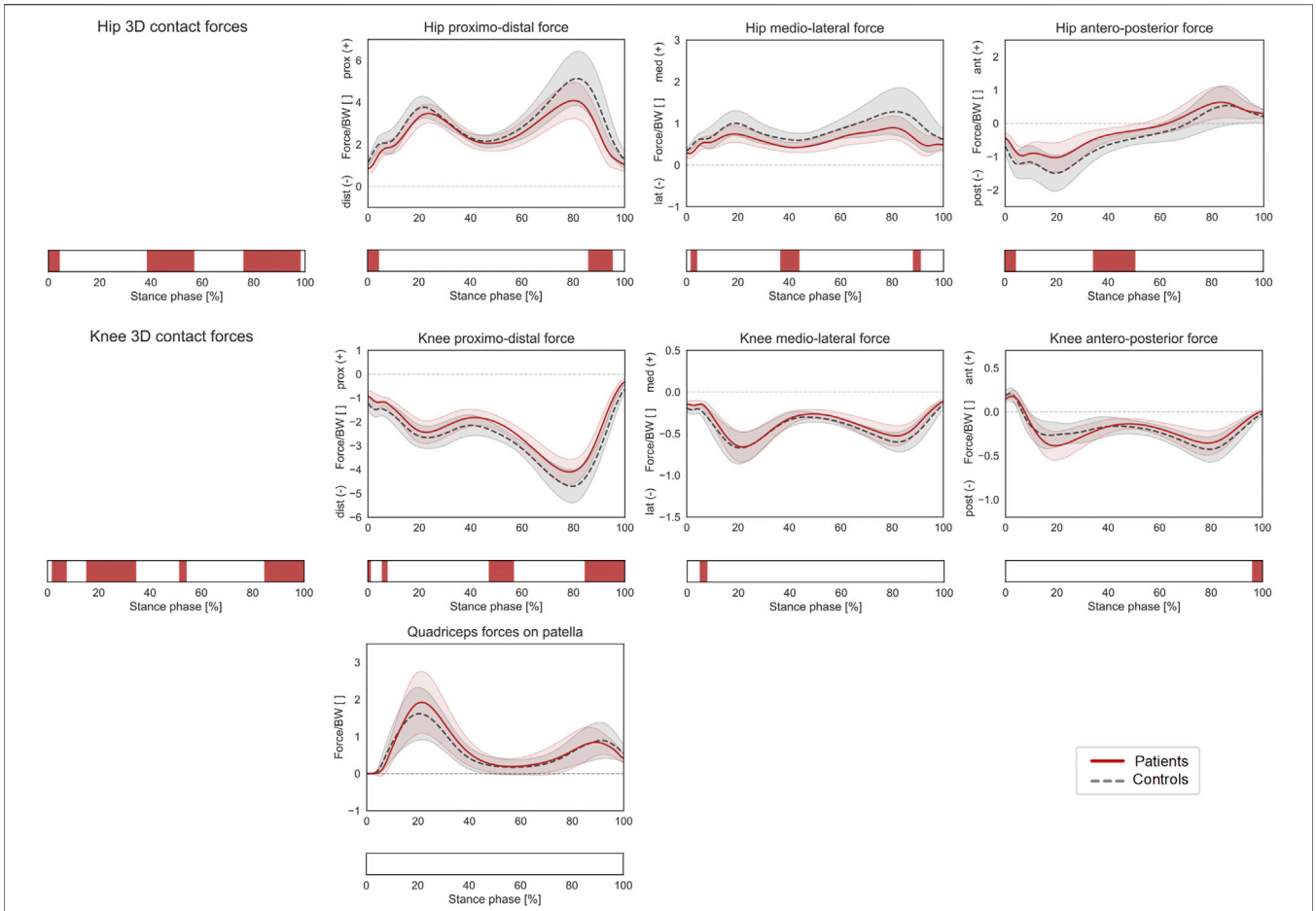

FIGURE 3 | Joint forces during stance phase (ST). Mean ± 1SD hip and knee proximo-distal, medio-lateral, and antero-posterior contact forces, as well as resultant force exerted by the quadriceps muscles on the patella, are reported as red solid lines for patients, and as grey dashed lines for controls. Intervals of ST with a statistically significant difference in the relevant SPM tests are reported as red bars. Knee and hip contact forces were regarded as a 3D vector fields. 3-dimensional significant differences between patients and controls were analyzed by means of two-sample Hotelling T2 tests and are reported in the leftmost panels. The resultant force on the patella, as well as individual components of the vector fields in the post-hoc vectorial analyses, were analyzed by means of two-sample t-tests and intervals characterized by significant differences between the two groups are reported below each subplot.

Patients with increased femoral anteversion walked with significantly different hip 3D kinematics from terminal stance until initial swing (40–65% GC), which was mostly associated with an increased internal hip rotation in patients (post-hoc: 45–66% GC). The gait of the patients was also characterized by a more internally rotated foot progression angle from mid-stance to toe-off as well as in terminal swing (26–63% and 96–100% GC, **Figure 2**). The overall 3D hip joint moments showed significant differences briefly during heel-strike (0–2% ST) as well as in pre swing (86–95% ST), but post-hoc analyses only revealed a significantly lower hip extensor moment at initial contact for patients (0–2% ST). In terms of HCFs, statistically significant 3D differences were observed between the two groups during loading response, mid and terminal stance and pre swing (0–4%, 39–57%, and 76–98% ST). The post-hoc analysis revealed that patients presented lower proximal (0–4% and 86–95% ST), lower medial (2–4%, 37–44%, and 88–91% ST), and lower posterior (0–4% and 34–50% ST) hip joint forces compared to controls. Significant differences were also found in terms of KCFs (2–7%, 15–35%, 52–54%, and 85–100% ST). When looking at the individual force components, patients presented reduced distal (compressive) forces (6–8%, 47–57% and 84–100% ST), but only limited differences in terms of medio-lateral (5–8% ST) and antero-posterior (96–100%) shear components (**Figure 3**).

Regression Analyses With Morphological and Kinematic Parameters

Within the patients' cohort, femoral anteversion was only positively correlated with the knee flexion angle during terminal stance (37–52% GC). Midpoint $_{HipRot\ ROM}$ was significantly correlated with the 3D hip joint angles from terminal stance to initial swing (46–68% GC). The post hoc linear regression analyses indicated a positive correlation between the Midpoint $_{HipRot\ ROM}$ and hip internal rotation (43–69% GC). The foot progression angle also presented a positive correlation

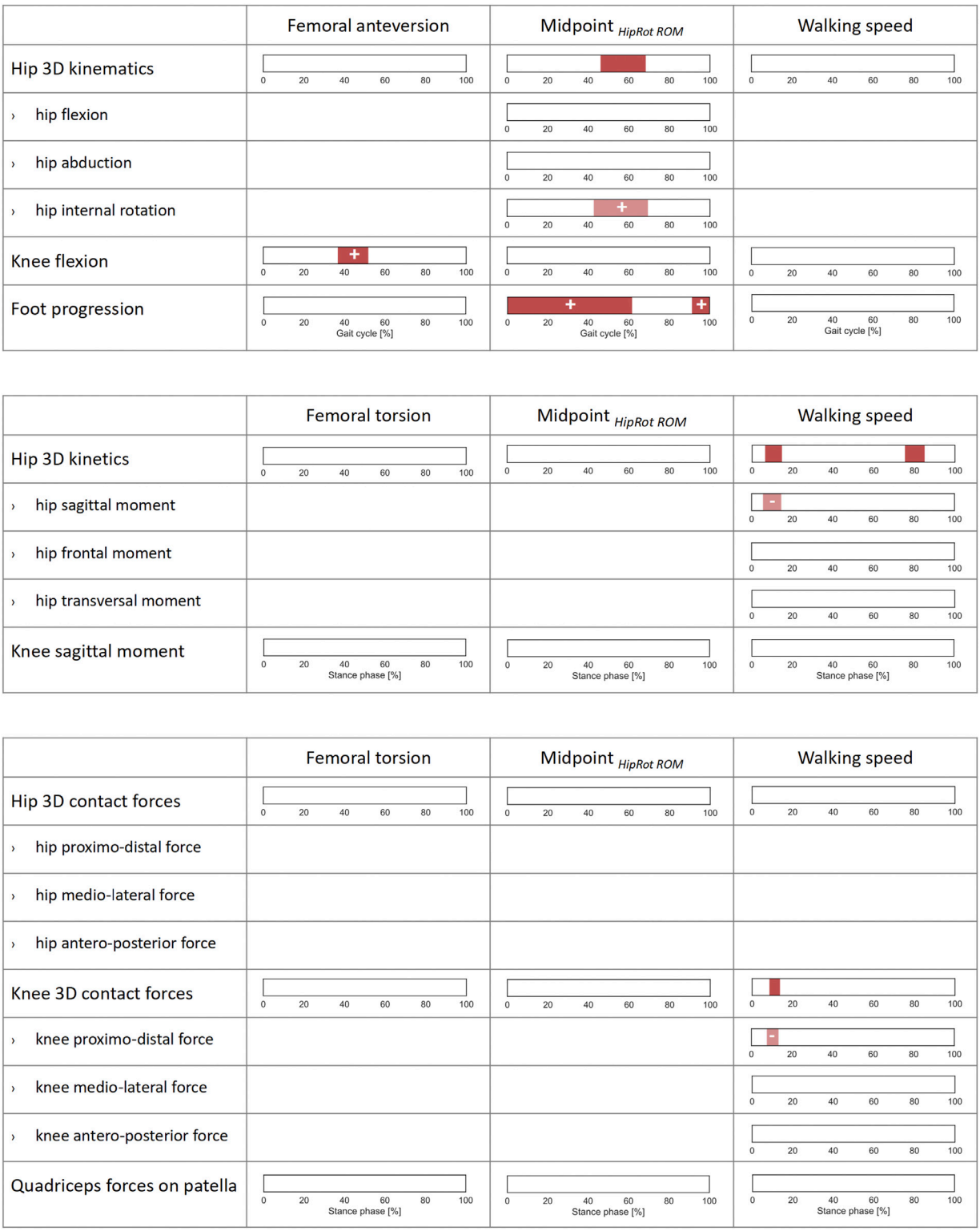

FIGURE 4 | Correlations of lower-limb kinematics, joint moments, and joint forces with femoral anteversion, midpoint of hip rotational range of motion (Midpoint $_{HipRot\ ROM}$), and walking speed across the patients' cohort. SPM canonical correlation analyses (CCAs) or scalar linear regressions were used to identify potential correlations of the 3D vector fields and 1D scalar outcome variables (rows) with the independent predictors (columns). Intervals of the gait cycle for kinematics and intervals of the stance phase for moments and forces which are characterized by a statistically significant correlation in the relevant SPM test are reported as red bars. Post-hoc scalar linear regressions were conducted on the individual components of the vector fields, for which intervals with significant correlations are reported in light red. The sign of the correlation is indicated on each interval for all scalar linear regressions. For a correct interpretation of the directionality of the correlation, the reader is referred to the axes reported in the corresponding graphs in **Figures 1**, **2**.

FIGURE 5 | Correlations of joint kinematics, joint moments, and forces with synthetic gait-pattern-related kinematic descriptors ($HipRot_{tSt}$, $KneeFlex_{tSt}$, $FootProg_{tSt}$, defined, respectively as the mean value of hip rotation, knee flexion, and foot progression during terminal stance) across the patients' cohort. SPM canonical correlation analyses (CCAs) or scalar linear regressions were used to identify potential correlations of the 3D vector fields and 1D scalar outcome variables with the independent predictors. Intervals of the gait cycle for joint kinematics, and intervals of the stance phase for joint moments and forces, characterized by a statistically significant correlation in the relevant SPM test are reported as red bars. Post-hoc scalar linear regressions were conducted on the individual components of the vector fields, for which intervals with significant correlations are reported in light red. The sign of the correlation is indicated on each interval for all scalar linear regressions. For a correct interpretation of the directionality of the correlation, the reader is referred to the axes reported in the corresponding graphs in **Figures 1**, **2**.

TABLE 2 | Anthropometrics and clinical examination for sub-grouping scenario based on knee flexion in terminal stance. Values are presented as means (standard deviation).

Grouping scenario	$KneeFlex_{tSt}$		
	Normal (n = 32)	Excessive (n = 10)	p-value
Femoral anteversion (°)	37.6 (5.7)	44.9 (7.8)	0.030
Height (m)	1.56 (0.11)	1.55 (0.07)	0.452
Mass (kg)	45.3 (10.4)	43.7 (6.3)	0.393
Age (years)	12.8 (1.9)	13.0 (1.9)	0.968
Walking speed (m/s)	1.25 (0.12)	1.25 (0.11)	0.347
Clinical examination			
Hip external rotation (°)	17.2 (12.4)	11.5 (12.0)	0.088
Hip internal rotation (°)	63.4 (14.8)	70 (15.1)	0.773
Midpoint $_{HipRot\ ROM}$ (°)	23.1 (9.9)	29.3 (11.5)	0.279
Hip extension (°)	9.4 (4.0)	9.0 (6.6)	0.921
Hip flexion (°)	136.1 (9.1)	134 (10.2)	0.193
Knee extension (°)	4.5 (4.3)	4.0 (3.2)	0.773
Knee flexion (°)	157.0 (5.8)	158.5 (3.4)	0.538
Popliteal angle (°)	30.6 (16.2)	21.0 (15.6)	0.935

Midpoint $_{HipRot\ ROM}$, Midpoint of passive hip rotation range of motion (positive value indicate internal rotation); $KneeFlex_{tSt}$, mean knee flexion in terminal stance.

from terminal swing throughout stance phase (0–62%, and 91–100% GC). Walking speed correlated with the 3D hip moments during loading response and parts of terminal stance/pre-swing (7–15%, and 75–85% ST). The post-hoc analysis revealed that higher walking speeds were correlated with more extensive moments in the sagittal plane (6–14% ST). No correlation was found with the resulting joint forces (**Figure 4**).

$HipRot_{tSt}$ was correlated with the overall hip 3D kinematics from mid-swing throughout stance phase (0–64% and 79–100% GC). The post hoc linear regression analyses indicated a positive correlation with the hip internal rotation angle itself (0–65% and 79–100% GC). Additionally, $HipRot_{tSt}$ was correlated with the foot progression angle from mid-swing until terminal stance phase (0–56% and 86–100% GC). It was also observed that a more internally rotated hip is correlated with a higher sagittal knee flexion moment during late stance (72–90% ST), however no correlation with joint forces was found (**Figure 5**).

$KneeFlex_{tSt}$ correlated well with the knee flexion angle itself throughout stance phase and in terminal swing (0–58% and 96–100% GC). $KneeFlex_{tSt}$ was correlated with the overall hip 3D kinematics in terminal stance (31–53% GC) with the post hoc linear regression analyses indicating a positive correlation with hip flexion (35–54% GC). In terms of joint kinetics, $KneeFlex_{tSt}$ was positively correlated with the sagittal knee moment (22–33% and 45–93% ST) as well as overall 3D KCFs (35–92% ST) and 3D HCFs (54–76%). The post hoc linear regression analyses indicated that higher values of $KneeFlex_{tSt}$ were associated with larger proximal (compressive) (57–75% ST) and medial (53–75% ST) HCFs, and with more laterally (31–45% ST) and posteriorly oriented (29–76% ST) KCFs. Additionally, $KneeFlex_{tSt}$ was correlated with the quadriceps force on the patella (29–93% ST) (**Figure 5**).

$FootProg_{tSt}$ correlated with the foot progression angle itself throughout most of the gait cycle (0–65% and 70–100% GC), and it also presented a positive correlation with hip internal rotations from terminal stance to initial swing (26–68% GC). No correlation with joint moments or forces were found (**Figure 5**).

Subgroup Analysis

Based on the finding of the CCAs and linear regression analyses, patients were further divided into two subgroups based on $KneeFlex_{tSt}$. Patients with excessive $KneeFlex_{tSt}$ had also significantly higher femoral anteversion than those with normal $KneeFlex_{tSt}$ (**Table 2**). The gait of patients with excessive $KneeFlex_{tSt}$ was characterized by a larger knee flexion at heel contact and from mid stance to pre-swing (0–2% and 25–58% GC), as well as by a more extensive knee sagittal moment from mid stance to pre swing (49–92% ST) (**Figure 6**). In terms of 3D KCFs, significant differences were found between the two groups during terminal stance (52–85% ST). The post-hoc analysis indicated that patients with excessive $KneeFlex_{tSt}$ present significantly larger posterior-oriented shear forces (50–78% ST), in addition to a large overall force exerted by the quadriceps on the patella (46–92% ST).

Compared to healthy controls, patients with excessive $KneeFlex_{tSt}$ walked with a more flexed knee (27–53% GC), a more internally rotated hip (post-hoc: 58–62% GC), a more internally rotated foot progression angle (45–65% GC), and a larger internal knee net extensive moment (23–39% and 49–80% ST). No statistically significant differences were found in terms of HCFs (**Figure 7**), while the 3D KCFs differed significantly between the two groups (2–5%, 20–30% and 86–100% ST). However, the post-hoc analysis only revealed significant differences during pre-swing (91–100% ST) in the proximo-distal component. Despite presenting larger quadriceps forces on the patella, no statistically significant differences compared to controls were found.

On the other hand, patients with a normal $KneeFlex_{tSt}$ walked with more a pronounced hip internal rotation compared to controls (45–65% GC), as well as with an increased foot progression angle (29–62% GC). Statistically significant differences in HCFs were observed during heel strike for the 3D vector field (0–5% ST) as well as for the individual components (proximo-distal: 0–5% ST, medio-lateral 0–5% ST, antero-posterior 0–4%). KCFs also significantly differed in terms of the overall vector field (5–8%, 20–30% and 86–100% ST), the proximo-distal component (5–8% and 84–100% ST), and the medio-lateral component (5–8% ST).

DISCUSSION

This study investigated lower limb joint loads during gait in pediatric and adolescent patients with increased, isolated femoral anteversion. This was done by: 1) comparing patients to typically developing controls; 2) analyzing within the patients' cohort potential correlations between morphological parameters, kinematic gait descriptors, and joint loads; 3) stratifying the patients according to specific features of their gait pattern.

Comparison Between Patients and Controls

The hypothesis that children with increased femoral anteversion present increased joint loads during gait had to be rejected, as the

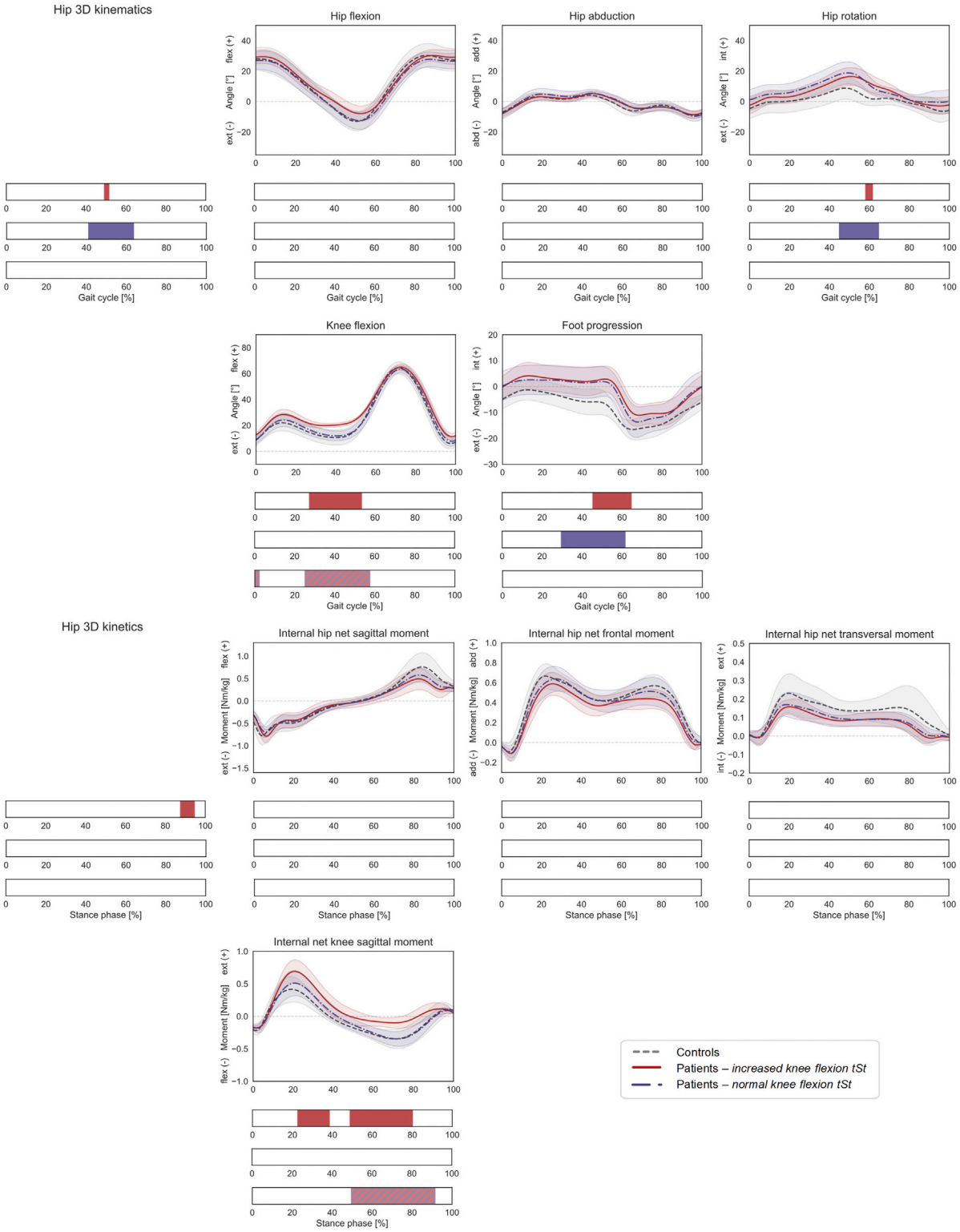

FIGURE 6 | Lower-limb kinematics during the gait cycle (GC) and joint moments during stance phase (ST) with patient stratification according to knee flexion angle during terminal stance ($KneeFlex_{tSt}$). Mean ± 1SD hip flexion, hip abduction, hip rotation, knee flexion, and foot progression angles, as well as hip sagittal, frontal, transversal, and knee sagittal moments, are reported as grey dashed lines for controls, as red solid lines for patients with increased $KneeFlex_{tSt}$, and as blue dashed-dotted lines for patients with normal $KneeFlex_{tSt}$. Intervals of GC or ST with a statistically significant difference in the relevant SPM tests are reported as red bars for the comparison between controls and patients with increased $KneeFlex_{tSt}$, as blue bars for the comparison between controls and patients with normal $KneeFlex_{tSt}$, and

(*Continued*)

FIGURE 6 | as red-and-blue striped bars for the comparison between patients with increased vs. normal KneeFlex$_{tSt}$. Hip joint angles and moments were regarded as a 3D vector fields. 3-dimensional significant differences between patients and controls were analyzed by means of two-sample Hotelling T2 tests and are reported in the leftmost panels. 1D scalar outcome variables, as well as individual components of the vector fields in the post-hoc vectorial analyses, were analyzed by means of two-sample t-tests and intervals characterized by significant differences between the two groups are reported below each subplot.

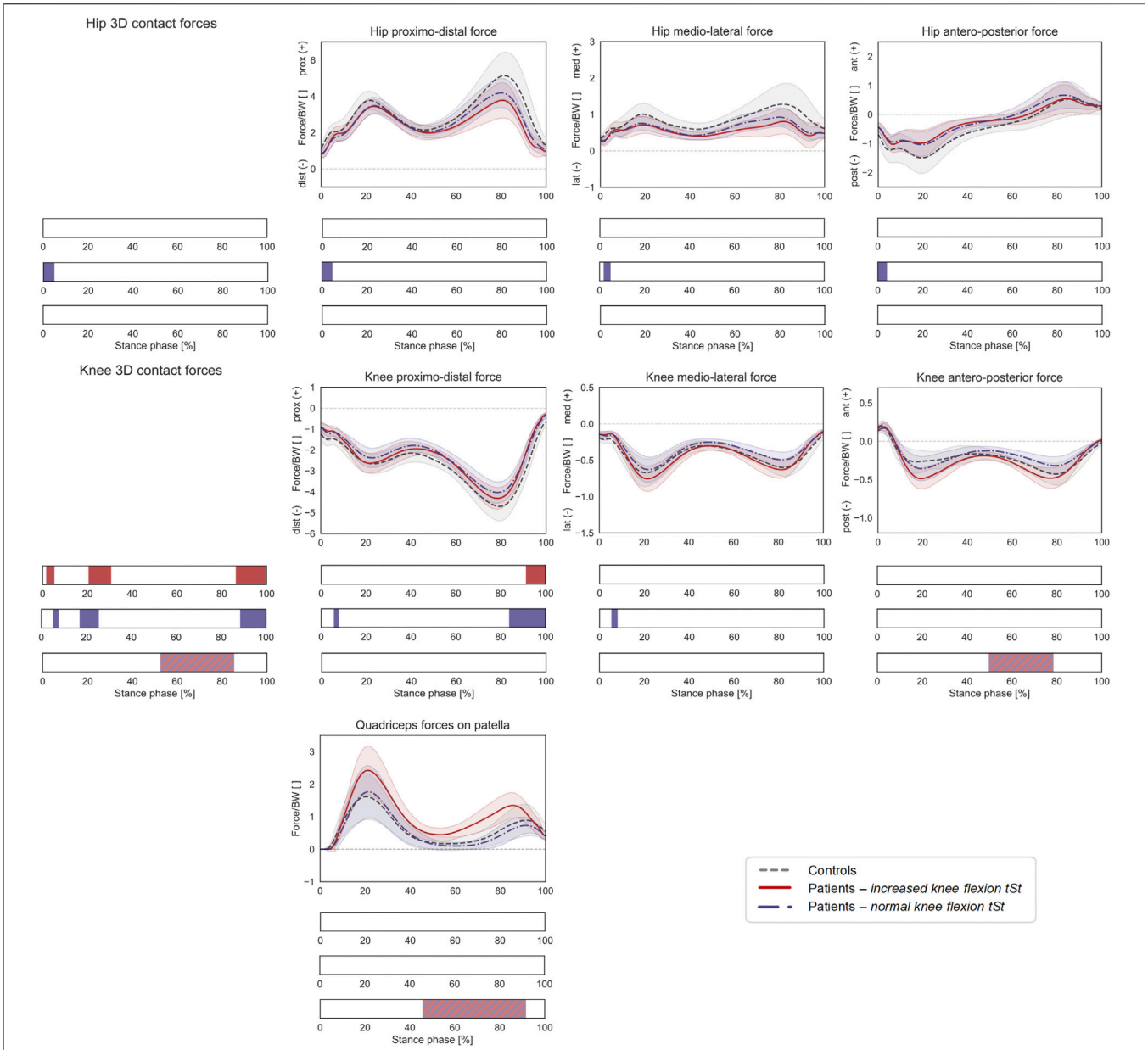

FIGURE 7 | Joint forces during stance phase (ST) with patient stratification according to knee flexion angle during terminal stance (KneeFlex$_{tSt}$). Mean ± 1SD hip and knee proximo-distal, medio-lateral, and antero-posterior contact forces, as well as resultant force exerted by the quadriceps muscles on the patella, are reported as grey dashed lines for controls, as red solid lines for patients with increased KneeFlex$_{tSt}$, and as blue dashed-dotted lines for patients with normal KneeFlex$_{tSt}$. Intervals of ST with a statistically significant difference in the relevant SPM tests are reported as red bars for the comparison between controls and patients with increased KneeFlex$_{tSt}$, as blue bars for the comparison between controls and patients with normal KneeFlex$_{tSt}$, and as red-and-blue striped bars for the comparison between patients with increased vs. normal KneeFlex$_{tSt}$. Knee and hip contact forces were regarded as a 3D vector fields. 3-dimensional significant differences between patients and controls were analyzed by means of two-sample Hotelling T2 tests and are reported in the leftmost panels. The resultant force on the patella, as well as individual components of the vector fields in the post-hoc vectorial analyses, were analyzed by means of two-sample t-tests and intervals characterized by significant differences between the two groups are reported below each subplot.

predicted compressive proximo-distal loads in both hip and knee joints were significantly reduced in patients compared to controls. Significant differences in the 3D HCF and KCF vectors were limited to narrow intervals of the loaded stance phase. Furthermore, the analysis of the individual force components showed limited differences and overall similar trends, suggesting also a similar intra-articular orientation of the joint contact forces in both hip and knee (**Figure 2**).

The overall gait pattern of the investigated cohort of patients, characterized by increased internal hip rotation and in-toeing, is in agreement with previous research focusing on the gait of adolescent patients with increased femoral anteversion (Bruderer-Hofstetter et al., 2015; Passmore et al., 2018; Alexander et al., 2019; Mackay et al., 2021).

Increased internal hip rotation during walking has been previously discussed as a compensatory mechanism to restore the abducting capacity of the hip abductors, which present a reduced abducting lever arm for femoral morphologies characterized by a large anteversion (Arnold et al., 1997; De Pieri et al., 2021). Although the patients included in this study presented an excessive femoral anteversion (range: 30–63°), their gait was not characterized by significant differences in the internal hip net frontal moment compared to controls (**Figure 1**). This suggests that they were able to produce a comparable abduction moment around the hip during gait, and that their overall hip-abductive capacity is not compromised during this activity.

Regression Analyses With Morphological and Kinematic Parameters

Within the patients' cohort, different morphological and kinematic predictors of potential joint over-loading were explored through independent CCAs and regression analyses. A gait pattern characterized by increased knee flexion during terminal stance was found to be significantly correlated with the intra-articular forces acting on hip and knee, as well as with the resultant force exerted by the quadriceps on the patella. In particular, increased KneeFlex_{tSt} is associated with increased medial and proximal (compressive) HCFs, increased lateral and posterior (shear) KCFs, as well as increased quadriceps force on the patella during the loaded stance phase (**Figure 4**). On the other hand, the commonly reported transversal plane gait deviations, HipRot_{tSt} and FootProg_{tSt}, did not affect the loads in the joints. No significant correlations between femoral anteversion and joint loads were found, in contrast to a previous study reporting higher medial HCFs for larger femoral torsional values during stance phase in a cohort of healthy asymptomatic adults (De Pieri et al., 2021).

In terms of kinematics, no significant correlation between femoral anteversion and hip rotation during walking was found. This is in agreement with previous studies showing a weak correlation between femoral anteversion and hip rotation, as a result of a considerable dynamic influence of compensatory mechanisms during walking (Radler et al., 2010; Gaston et al., 2011; Braatz et al., 2013; Mackay et al., 2021; Schranz et al., 2021). Additionally, in case of flat feet, the oblique axis of rotation in the hind foot could lead to hip internal rotation when the foot is loaded (Zafiropoulos et al., 2009), which would have to be further considered for a comprehensive assessment of overall lower-limb alignment. However, in this study only patients without foot deformities were included. However, a significant correlation between femoral anteversion and knee flexion in terminal stance was observed (**Figure 3**).

Midpoint $_{HipRot\ ROM}$ was significantly correlated with hip internal rotation and the foot progression angle. In agreement with Kerr et al. (2003), Midpoint $_{HipRot\ ROM}$ is a better indicator for transversal gait deviations than femoral anteversion. Even though lower-limb kinematics were affected by the Midpoint $_{HipRot\ ROM}$, there was no statistically significant effect on joint loading and the clinical rotational ability did not influence the hip-abductor moment either.

Walking speed was also included as an independent variable in regression analyses, as it is known to influence joint kinematics, kinetics and intra-articular forces during gait (Schwartz et al., 2008; De Pieri et al., 2019; Schreiber and Moissenet, 2019). However, hardly any correlations between kinematics and kinetics were found. Therefore, discussed differences can be accounted on morphological or kinematic gait differences rather than walking speed differences.

The synthetic gait pattern descriptors HipRot_{tSt}, KneeFlex_{tSt} and FootProg_{tSt}, defined as mean values during terminal stance, showed extensive correlations with the corresponding kinematic parameters from which they were derived. HipRot_{tSt} and FootProg_{tSt} were positively correlated with hip rotation and foot progression angles, respectively, through most of the gait cycle, indicating that these are good synthetic indicators for an internally rotated hip and inward foot progression angle during gait. In contrast, KneeFlex_{tSt} is a good indicator for the knee flexion in the loaded stance phase, but not during swing. Furthermore, HipRot_{tSt} was correlated with the foot progression angle, and conversely FootProg_{tSt} was correlated with the hip internal rotation angle, suggesting that these two variables are coupled and representative of a transversal plane kinematic mechanism. A larger KneeFlex_{tSt} on the other hand was also correlated with a larger hip flexion during terminal stance, suggesting that adaptations at multiple joint levels in the sagittal plane can occur. Two different kinematic mechanisms, one in the transversal and one in the sagittal plane, seem therefore to exist. However, the knee sagittal moment during stance was correlated with both HipRot_{tSt} and KneeFlex_{tSt}, suggesting that both transversal and sagittal kinematic deviations can affect sagittal plane functionality.

A reduced efficacy of the plantar flexor-knee extension couple mechanism (Passmore et al., 2018) was previously reported as possible cause for increased knee flexion while in-toeing. Within the investigated cohort however, we could not observe any significant correlation between the foot progression angle and knee flexion in terminal stance, suggesting that, in patients with solely increased femoral anteversion, in-toeing does not impair knee extension during gait. Interestingly, with increasing hip internal rotation the knee flexor moment in terminal stance increased even though with increasing femoral anteversion an increase in knee flexion during terminal stance was found (e.g.

increasing KneeFlex$_{tSt}$ lead to a decreased knee flexor moment). Therefore, hip internal rotation might be a compensatory mechanism to achieve an adequate knee flexor moment in terminal stance. This hypothesis, however, needs further evaluation and even though only patients without foot deformities were included in the current study, the effect of foot kinematics on knee flexion might has to be considered since as, e.g., increased forefoot supination can be linked to several gait parameters (Pothrat et al., 2013).

Subgroup Analysis

When stratifying the patients in two groups according to their knee flexion during terminal stance (the only kinematic parameter showing significance in the regression analyses), patients with excessive KneeFlex$_{tSt}$ presented significantly larger quadriceps forces on the patella and a larger posteriorly-oriented shear force at the knee, compared to patients with normal KneeFlex$_{tSt}$ (**Figure 6**). Nevertheless, both patients' subgroups presented only limited differences in terms of joint loads compared to controls suggesting only limited clinical relevance of different gait patterns in terms of joint loading. Increased quadriceps force on the patella is in line with reported increasing patellofemoral compression forces increasing knee flexion angle (Modenese et al., 2013; Alexander and Schwameder, 2016) and the fact that increased quadriceps force contributes to larger tibiofemoral and patellofemoral joint loadings with increasing knee flexion (Steele et al., 2012). Patients with increased KneeFlex$_{tSt}$ showed significantly reduced knee flexor moments in terminal stance compared to controls as well as patients with normal KneeFlex$_{tSt}$, in contrast to a previous study where the same group of patients was compared to a different control group (Alexander et al., 2019).

In this groups, increased knee flexion in terminal stance was not caused by a decreased knee joint range of motion since patients could achieve full knee extension with a bias towards knee hyper-extension (**Table 2**) as previously reported in the literature (Passmore et al., 2018; Alexander et al., 2019). Furthermore, besides higher femoral anteversion in patients with excessive KneeFlex$_{tSt}$, no differences concerning anthropometrics or clinical examination values were found (**Table 2**).

Limitations and Outlook

Finally, the following limitations should be considered. Patients with increased femoral anteversion were included based on clinical evaluation of hip rotation, which was verified in CT-scans, possibly introducing a selection bias. Only data for a limited number of patients and controls having femoral anteversion verified *via* CT or MRI scans was available. An analysis of a larger and more heterogeneous sample of patients is warranted to further confirm the validity of these findings and potentially identify critical subgroups of patients who might not have been represented in this study. For instance, increased femoral anteversion is a comorbidity commonly observed in patients with cerebral palsy, where the impaired muscular control combined with structural deformities could lead to more pronounced functional impairments (Kainz et al., 2021). Additionally, future studies should also include patients with foot deformities since correlations between flat feet and hip internal rotation have been previously reported (Zafiropoulos et al., 2009) and foot deformities might lead to further gait deviations as well.

Due to the limited number of patients and controls, individual independent regression analyses rather than a multiple regression were performed, thus not allowing assessing any interaction between predictors, which were instead treated as independent variables. Nevertheless, all chosen morphological and gait-pattern-related predictors have a direct applicability in clinical practice, making this analysis a relevant starting point for identifying potential factors associated with a risk of joint overloading in patients with increased femoral anteversion.

Personalized musculoskeletal models accounting for radiographically-measured femoral torsional values were created for all subjects. However, anatomical variations in the neck-shaft angle could also affect the resulting HCFs (Kainz et al., 2020). HCFs were calculated in a proximal (pelvis-based) coordinate system according to ISB recommendations. While this standardization enables comparisons with other studies, calculating HCFs in an anatomically-oriented reference frame according to subject-specific acetabular inclination and version could further reveal intra-patient differences and potentially help identifying critical loading scenarios at the hip. A correct understanding of the orientation of the HCFs in the acetabulum could be even more relevant for activities other than gait, which present substantially different HCFs (Lunn et al., 2020).

Furthermore, simplified ankle and knee joint mechanics, characterized by one DoF in each joint, were implemented in the models, neglecting subtalar version, knee transversal rotation, as well as knee varus or valgus alignment. Bretin et al. (2011) on the other hand showed in a cadaver study that hip internal rotation resulted in valgus deviation of the mechanical axis of the lower limb, and in a shift of the center of force towards the lateral condyle of the knee. Furthermore, quadriceps forces were assessed as an indicator of the loads sustained by the patella, which could however be underestimated for patients who present altered patellar contact mechanics. Future studies should therefore include a more complex multi-DoF model of the femorotibial and femoropatellar joints, including a detailed characterization of the articular contact geometry and the stabilizing passive soft-tissue constraints (Lenhart et al., 2015; Marra et al., 2015; Dejtiar et al., 2020). A more detailed understanding of knee and patellar mechanics could be particularly important in the analysis of patients with miserable malalignment syndrome, in which an increased femoral anteversion and a concomitant outward tibial torsion can cause anterior knee pain, patellar maltracking and instability (Eckhoff, 1994; Eckhoff et al., 1997; Bruce and Stevens, 2004; Stevens et al., 2014; Pagliazzi et al., 2022).

Finally, muscles fascicles were modelled as constant strength actuators, neglecting force-length and force-velocity relationships. Using a Hill-type muscle model would require accurate knowledge of muscle-tendon properties, which were not available for this group of participants, and could have

therefore introduced a bias in the models' predictions (Arnold et al., 2013; Carbone et al., 2016). Future studies should aim at devising experimental protocols to calibrate these properties over subject-specific ranges of motion (Heinen et al., 2016) and consider muscle weakness in the presence of altered femoral morphology (Vandekerckhove et al., 2021).

Based on the current results increased femoral anteversion by itself might not be a problem concerning joint overloading. The effect of femoral torsional deformities should be assessed in a holistic biomechanical analysis of the patient, which accounts for patient-specific kinematics, clinical examination of joint mobility, as well as potentially coexisting bony deformities, such as cam and pincer morphologies, increased tibial torsion, or altered patellar morphology. A static analysis of altered femoral morphology alone is not sufficient for a correct management of the patient, but should rather be framed in a more dynamic assessment that takes into account motion and muscle functionality. Within this context, a patient-specific assessment of joint loads through gait analysis and musculoskeletal modelling represents an important tool for a well-informed management of orthopedic conditions associated with altered bony morphologies. Future studies based on larger datasets and machine learning algorithms could help identifying clinical, anatomical, and movement-related parameters for a rapid and data-driven estimation of joint loading, thus assisting orthopedic clinicians in assessing the patient-specific risks of further orthopedic complications (Burton II et al., 2021; Mouloodi et al., 2021; Xiang et al., 2021).

CONCLUSION

Torsional deformities of the lower limb have been associated with a number of orthopedic complications, leading to the overall assumption in current clinical practice that an altered morphology is problematic. Through the analysis of a cohort of pediatric and adolescent patients with isolated increased femoral anteversion, this study showed that an altered femoral morphology does not always lead to an increased risk of joint overloading. When taking into account both subject-specific morphological and kinematic deviations, the investigated patients presented hip and knee loads within normative values, or even slightly reduced. Increased femoral anteversion by itself might therefore not always be a problem warranting orthopedic intervention. Nevertheless, the presence of other orthopedic problems, such as additional morphological deformities, and their potential interplay with increased femoral anteversion should still be kept in mind in the clinical management of these patients.

DATA AVAILABILITY STATEMENT

The datasets presented in this article are not readily available because of privacy restrictions. Requests to access the datasets should be directed to enrico.depieri@unibas.ch.

ETHICS STATEMENT

The studies involving human participants were reviewed and approved by the Ethics Committee Northwest Switzerland (EKNZ 2021-00015). Written informed consent to participate in this study was provided by the participants' legal guardian/next of kin.

AUTHOR CONTRIBUTIONS

NA and EDP contributed to study conceptualization, project administration, ethics, study design, methodology, data curation, data analysis, data interpretation, and writing. RB and JC contributed to study conceptualization, study design, data interpretation, and writing. EV contributed to data interpretation, and writing. All authors contributed to the article and approved the submitted version.

FUNDING

EDP was partially funded by the University of Basel Research Fund for Excellent Junior Researchers.

ACKNOWLEDGMENTS

The authors would like to thank Claudia Weidensteiner for the analysis of the MRI data of the control subjects and the extraction of the relevant information in terms of bone morphology.

REFERENCES

Alexander, N., and Schwameder, H. (2016). Lower Limb Joint Forces during Walking on the Level and Slopes at Different Inclinations. *Gait Posture* 45, 137–142. doi:10.1016/j.gaitpost.2016.01.022

Alexander, N., Studer, K., Lengnick, H., Payne, E., Klima, H., and Wegener, R. (2019). The Impact of Increased Femoral Antetorsion on Gait Deviations in Healthy Adolescents. *J. Biomechanics* 86, 167–174. doi:10.1016/j.jbiomech.2019.02.005

Alexander, N., Wegener, R., Lengnick, H., Payne, E., Klima, H., Cip, J., et al. (2020). Compensatory Gait Deviations in Patients with Increased Outward Tibial Torsion Pre and Post Tibial Derotation Osteotomy. *Gait Posture* 77, 43–51. doi:10.1016/j.gaitpost.2020.01.011

Andersen, M. S. (2021). "Introduction to Musculoskeletal Modelling," in *Computational Modelling of Biomechanics and Biotribology in the Musculoskeletal System* (Elsevier), 41–80.

Arnold, A. S., Komattu, A. V., and Delp, S. L. (1997). Internal Rotation Gait: a Compensatory Mechanism to Restore Abduction Capacity Decreased by Bone Deformity. *Dev. Med. Child. Neurol.* 39 (1), 40–44. doi:10.1111/j.1469-8749.1997.tb08202.x

Arnold, E. M., Hamner, S. R., Seth, A., Millard, M., and Delp, S. L. (2013). How Muscle Fiber Lengths and Velocities Affect Muscle Force Generation as Humans Walk and Run at Different Speeds. *J. Exp. Biol.* 216 (Pt 11), 2150–2160. doi:10.1242/jeb.075697

Audenaert, E. A., Peeters, I., Vigneron, L., Baelde, N., and Pattyn, C. (2012). Hip Morphological Characteristics and Range of Internal Rotation in Femoroacetabular Impingement. *Am. J. Sports Med.* 40 (6), 1329–1336. doi:10.1177/0363546512441328

Braatz, F., Wolf, S. I., Gerber, A., Klotz, M. C., and Dreher, T. (2013). Do changes in Torsional Magnetic Resonance Imaging Reflect Improvement in Gait after Femoral Derotation Osteotomy in Patients with Cerebral Palsy? *Int. Orthop. (SICOT)* 37 (11), 2193–2198. doi:10.1007/s00264-013-2054-7

Bretin, P., O'Loughlin, P. F., Suero, E. M., Kendoff, D., Ostermeier, S., Hüfner, T., et al. (2011). Influence of Femoral Malrotation on Knee Joint Alignment and Intra-articular Contract Pressures. *Arch. Orthop. Trauma Surg.* 131 (8), 1115–1120. doi:10.1007/s00402-010-1210-4

Bruce, W. D., and Stevens, P. M. (2004). Surgical Correction of Miserable Malalignment Syndrome. *J. Pediatr. Orthop.* 24 (4), 392–396. doi:10.1097/00004694-200407000-00009

Bruderer-Hofstetter, M., Fenner, V., Payne, E., Zdenek, K., Klima, H., and Wegener, R. (2015). Gait Deviations and Compensations in Pediatric Patients with Increased Femoral Torsion. *J. Orthop. Res.* 33 (2), 155–162. doi:10.1002/jor.22746

Burton, W. S., II, Myers, C. A., and Rullkoetter, P. J. (2021). Machine Learning for Rapid Estimation of Lower Extremity Muscle and Joint Loading during Activities of Daily Living. *J. Biomech.* 123, 110439. doi:10.1016/j.jbiomech.2021.110439

Byrnes, S. K., Kunic, D., Rethwilm, R., Böhm, H., Horstmann, T., and Dussa, C. U. (2020). Compensatory Mechanisms in Children with Idiopathic Lower Extremity Internal Rotational Malalignment during Walking and Running. *Gait Posture* 79, 46–52. doi:10.1016/j.gaitpost.2020.03.015

Carbone, V., Fluit, R., Pellikaan, P., Van Der Krogt, M. M., Janssen, D., Damsgaard, M., et al. (2015). TLEM 2.0 - A Comprehensive Musculoskeletal Geometry Dataset for Subject-specific Modeling of Lower Extremity. *J. biomechanics* 48 (5), 734–741. doi:10.1016/j.jbiomech.2014.12.034

Carbone, V., van der Krogt, M. M., Koopman, H. F. J. M., and Verdonschot, N. (2016). Sensitivity of Subject-specific Models to Hill Muscle-Tendon Model Parameters in Simulations of Gait. *J. Biomechanics* 49 (9), 1953–1960. doi:10.1016/j.jbiomech.2016.04.008

Cordier, W., and Katthagen, B.-D. (2000). Femoral Torsional Deformities. *Orthopade* 29 (9), 795–801. doi:10.1007/s001320050528

Crane, L. (1959). Femoral Torsion and its Relation to Toeing-In and Toeing-Out. *J. Bone & Jt. Surg.* 41 (3), 421–428. doi:10.2106/00004623-195941030-00006

Damsgaard, M., Rasmussen, J., Christensen, S. T., Surma, E., and De Zee, M. (2006). Analysis of Musculoskeletal Systems in the AnyBody Modeling System. *Simul. Model. Pract. Theory* 14 (8), 1100–1111. doi:10.1016/j.simpat.2006.09.001

De Pieri, E., Lund, M. E., Gopalakrishnan, A., Rasmussen, K. P., Lunn, D. E., and Ferguson, S. J. (2018). Refining Muscle Geometry and Wrapping in the TLEM 2 Model for Improved Hip Contact Force Prediction. *PLoS One* 13 (9), e0204109. doi:10.1371/journal.pone.0204109

De Pieri, E., Romkes, J., Wyss, C., Brunner, R., and Viehweger, E. (2022). Altered Muscle Contributions Are Required to Support the Stance Limb during Voluntary Toe-Walking. *Front. Bioeng. Biotechnol.* 10, 810560. doi:10.3389/fbioe.2022.810560

De Pieri, E., Friesenbichler, B., List, R., Monn, S., Casartelli, N. C., Leunig, M., et al. (2021). Subject-Specific Modeling of Femoral Torsion Influences the Prediction of Hip Loading during Gait in Asymptomatic Adults. *Front. Bioeng. Biotechnol.* 9, 551. doi:10.3389/fbioe.2021.679360

De Pieri, E., Lunn, D. E., Chapman, G. J., Rasmussen, K. P., Ferguson, S. J., and Redmond, A. C. (2019). Patient Characteristics Affect Hip Contact Forces during Gait. *Osteoarthr. Cartil.* 27 (6), 895–905. doi:10.1016/j.joca.2019.01.016

Dejour, D., and Le Coultre, B. (2007). Osteotomies in Patello-Femoral Instabilities. *Sports Med. Arthrosc. Rev.* 15 (1), 39–46. doi:10.1097/JSA.0b013e31803035ae

Dejtiar, D. L., Dzialo, C. M., Pedersen, P. H., Jensen, K. K., Fleron, M. K., and Andersen, M. S. (2020). Development and Evaluation of a Subject-specific Lower Limb Model with an Eleven-Degrees-Of-Freedom Natural Knee Model Using Magnetic Resonance and Biplanar X-Ray Imaging during a Quasi-Static Lunge. *J. Biomech. Eng.* 142 (6). doi:10.1115/1.4044245

Derrick, T. R., van den Bogert, A. J., Cereatti, A., Dumas, R., Fantozzi, S., and Leardini, A. (2020). ISB Recommendations on the Reporting of Intersegmental Forces and Moments during Human Motion Analysis. *J. biomechanics* 99, 109533. doi:10.1016/j.jbiomech.2019.109533

Dreher, T., Wolf, S., Braatz, F., Patikas, D., and Döderlein, L. (2007). Internal Rotation Gait in Spastic Diplegia-Critical Considerations for the Femoral Derotation Osteotomy. *Gait Posture* 26 (1), 25–31. doi:10.1016/j.gaitpost.2006.07.018

Dreher, T., Wolf, S. I., Heitzmann, D., Swartman, B., Schuster, W., Gantz, S., et al. (2012). Long-term Outcome of Femoral Derotation Osteotomy in Children with Spastic Diplegia. *Gait Posture* 36 (3), 467–470. doi:10.1016/j.gaitpost.2012.04.017

Eckhoff, D. G., Brown, A. W., Kilcoyne, R. F., and Stamm, E. R. (1997). Knee Version Associated with Anterior Knee Pain. *Clin. Orthop. Relat. Res.* 339, 152–155. doi:10.1097/00003086-199706000-00020

Eckhoff, D. G. (1994). Effect of Limb Malrotation on Malalignment and Osteoarthritis. *Orthop. Clin. N. Am.* 25 (3), 405–414. doi:10.1016/s0030-5898(20)31925-8

Ejnisman, L., Philippon, M. J., Lertwanich, P., Pennock, A. T., Herzog, M. M., Briggs, K. K., et al. (2013). Relationship between Femoral Anteversion and Findings in Hips with Femoroacetabular Impingement. *Orthopedics* 36 (3), e293–300. doi:10.3928/01477447-20130222-17

Fabry, G. (2010). Clinical Practice. Static, Axial, and Rotational Deformities of the Lower Extremities in Children. *Eur. J. Pediatr.* 169 (5), 529–534. doi:10.1007/s00431-009-1122-x

Fabry, G., MacEwen, G. D., and Shands, A. R., Jr. (1973). Torsion of the Femur. A Follow-Up Study in Normal and Abnormal Conditions. *J. Bone & Jt. Surg.* 55 (8), 1726–1738. doi:10.2106/00004623-197355080-00017

Gaston, M. S., Rutz, E., Dreher, T., and Brunner, R. (2011). Transverse Plane Rotation of the Foot and Transverse Hip and Pelvic Kinematics in Diplegic Cerebral Palsy. *Gait Posture* 34 (2), 218–221. doi:10.1016/j.gaitpost.2011.05.001

Grood, E. S., and Suntay, W. J. (1983). A Joint Coordinate System for the Clinical Description of Three-Dimensional Motions: Application to the Knee. *J. biomechanical Eng.* 105 (2), 136–144. doi:10.1115/1.3138397

Hefti, F. (2000). Deviations in the Axes of the Lower Extremities. *Orthopade* 29 (9), 814–820. doi:10.1007/s001320050531

Heinen, F., Lund, M. E., Rasmussen, J., and de Zee, M. (2016). Muscle-tendon Unit Scaling Methods of Hill-type Musculoskeletal Models: An Overview. *Proc. Inst. Mech. Eng. H.* 230 (10), 976–984. doi:10.1177/0954411916659894

Hernandez, R., Tachdjian, M., Poznanski, A., and Dias, L. (1981). CT Determination of Femoral Torsion. *Am. J. Roentgenol.* 137 (1), 97–101. doi:10.2214/ajr.137.1.97

Ito, K., Minka-II, M.-A., 2nd, Leunig, M., Werlen, S., and Ganz, R. (2001). Femoroacetabular Impingement and the Cam-Effect. A MRI-Based Quantitative Anatomical Study of the Femoral Head-Neck Offset. *J. Bone Jt. Surg. Br. volume* 83-B (2), 171–176. doi:10.1302/0301-620x.83b2.0830171

Jacquemier, M., Glard, Y., Pomero, V., Viehweger, E., Jouve, J.-L., and Bollini, G. (2008). Rotational Profile of the Lower Limb in 1319 Healthy Children. *Gait Posture* 28 (2), 187–193. doi:10.1016/j.gaitpost.2007.11.011

Jani, L., Schwarzenbach, U., Afifi, K., Scholder, P., and Gisler, P. (1979). Progression of Idiopathic Coxa Antetorta. a) Spontaneous Progression of Idiopathic Coxa Antetorta (Controlled Clinical Study of 148 Patients at the End of Adolescence). *Orthopade* 8 (1), 5–11.

Kadaba, M. P., Ramakrishnan, H. K., and Wootten, M. E. (1990). Measurement of Lower Extremity Kinematics during Level Walking. *J. Orthop. Res.* 8 (3), 383–392. doi:10.1002/jor.1100080310

Kainz, H., Killen, B. A., Wesseling, M., Perez-Boerema, F., Pitto, L., Garcia Aznar, J. M., et al. (2020). A Multi-Scale Modelling Framework Combining Musculoskeletal Rigid-Body Simulations with Adaptive Finite Element Analyses, to Evaluate the Impact of Femoral Geometry on Hip Joint Contact Forces and Femoral Bone Growth. *PLoS One* 15 (7), e0235966. doi:10.1371/journal.pone.0235966

Kainz, H., Wesseling, M., and Jonkers, I. (2021). Generic Scaled versus Subject-specific Models for the Calculation of Musculoskeletal Loading in Cerebral Palsy Gait: Effect of Personalized Musculoskeletal Geometry Outweighs the Effect of Personalized Neural Control. *Clin. Biomech.* 87, 105402. doi:10.1016/j.clinbiomech.2021.105402

Kaiser, P., Attal, R., Kammerer, M., Thauerer, M., Hamberger, L., Mayr, R., et al. (2016). Significant Differences in Femoral Torsion Values Depending on the CT Measurement Technique. *Arch. Orthop. Trauma Surg.* 136 (9), 1259–1264. doi:10.1007/s00402-016-2536-3

Kerr, A. M., Kirtley, S. J., Hillman, S. J., van der Linden, M. L., Hazlewood, M. E., and Robb, J. E. (2003). The Mid-point of Passive Hip Rotation Range Is an Indicator of Hip Rotation in Gait in Cerebral Palsy. *Gait Posture* 17 (1), 88–91. doi:10.1016/S0966-6362(02)00056-5

Keshmiri, A., Maderbacher, G., Baier, C., Zeman, F., Grifka, J., and Springorum, H. R. (2016). Significant Influence of Rotational Limb Alignment Parameters on Patellar Kinematics: an *In Vitro* Study. *Knee Surg. Sports Traumatol. Arthrosc.* 24 (8), 2407–2414. doi:10.1007/s00167-014-3434-2

Leblebici, G., Akalan, E., Apti, A., Kuchimov, S., Kurt, A., Onerge, K., et al. (2019). Increased Femoral Anteversion-Related Biomechanical Abnormalities: Lower Extremity Function, Falling Frequencies, and Fatigue. *Gait Posture* 70, 336–340. doi:10.1016/j.gaitpost.2019.03.027

Lenhart, R. L., Kaiser, J., Smith, C. R., and Thelen, D. G. (2015). Prediction and Validation of Load-dependent Behavior of the Tibiofemoral and Patellofemoral Joints during Movement. *Ann. Biomed. Eng.* 43 (11), 2675–2685. doi:10.1007/s10439-015-1326-3

Lund, M. E., Andersen, M. S., de Zee, M., and Rasmussen, J. (2015). Scaling of Musculoskeletal Models from Static and Dynamic Trials. *Int. Biomech.* 2 (1), 1–11. doi:10.1080/23335432.2014.993706

Lund, M., Rasmussen, J., and Andersen, M. (2019). AnyPyTools: A Python Package for Reproducible Research with the AnyBody Modeling System. *Joss* 4 (33), 1108. doi:10.21105/joss.01108

Lunn, D. E., De Pieri, E., Chapman, G. J., Lund, M. E., Redmond, A. C., and Ferguson, S. J. (2020). Current Preclinical Testing of New Hip Arthroplasty Technologies Does Not Reflect Real-World Loadings: Capturing Patient-specific and Activity-Related Variation in Hip Contact Forces. *J. Arthroplasty* 35 (3), 877–885. doi:10.1016/j.arth.2019.10.006

Mackay, J., Thomason, P., Sangeux, M., Passmore, E., Francis, K., and Graham, H. K. (2021). The Impact of Symptomatic Femoral Neck Anteversion and Tibial Torsion on Gait, Function and Participation in Children and Adolescents. *Gait Posture* 86, 144–149. doi:10.1016/j.gaitpost.2021.03.004

MacWilliams, B. A., McMulkin, M. L., Davis, R. B., Westberry, D. E., Baird, G. O., and Stevens, P. M. (2016). Biomechanical Changes Associated with Femoral Derotational Osteotomy. *Gait Posture* 49, 202–206. doi:10.1016/j.gaitpost.2016.07.002

Marra, M. A., Vanheule, V., Fluit, R., Koopman, B. H., Rasmussen, J., Verdonschot, N., et al. (2015). A Subject-specific Musculoskeletal Modeling Framework to Predict *In Vivo* Mechanics of Total Knee Arthroplasty. *J. Biomech. Eng.* 137 (2), 020904. doi:10.1115/1.4029258

Modenese, L., Gopalakrishnan, A., and Phillips, A. T. M. (2013). Application of a Falsification Strategy to a Musculoskeletal Model of the Lower Limb and Accuracy of the Predicted Hip Contact Force Vector. *J. Biomechanics* 46 (6), 1193–1200. doi:10.1016/j.jbiomech.2012.11.045

Mouloodi, S., Rahmanpanah, H., Gohari, S., Burvill, C., Tse, K. M., and Davies, H. M. S. (2021). What Can Artificial Intelligence and Machine Learning Tell Us? A Review of Applications to Equine Biomechanical Research. *J. Mech. Behav. Biomed. Mater.* 123, 104728. doi:10.1016/j.jmbbm.2021.104728

Pagliazzi, G., De Pieri, E., Kläusler, M., Sangeux, M., and Viehweger, E. (2022). Torsional Deformities and Overuse Injuries: what Does the Literature Tell Us. *EFORT Open Rev.* 7 (1), 26–34. doi:10.1530/eor-21-0092

Parker, E. A., Meyer, A. M., Nasir, M., Willey, M. C., Brown, T. S., and Westermann, R. W. (2021). Abnormal Femoral Anteversion Is Associated with the Development of Hip Osteoarthritis: A Systematic Review and Meta-Analysis. *Arthrosc. Sports Med. Rehabilitation* 3 (6), e2047–e2058. doi:10.1016/j.asmr.2021.07.029

Pascual-Garrido, C., Li, D. J., Grammatopoulos, G., Yanik, E. L., Clohisy, J. C., and Group, A. (2019). The Pattern of Acetabular Cartilage Wear Is Hip Morphology-dependent and Patient Demographic-dependent. *Clin. Orthop. Relat. Res.* 477 (5), 1021–1033. doi:10.1097/CORR.0000000000000649

Passmore, E., Graham, H. K., Pandy, M. G., and Sangeux, M. (2018). Hip- and Patellofemoral-Joint Loading during Gait Are Increased in Children with Idiopathic Torsional Deformities. *Gait Posture* 63, 228–235. doi:10.1016/j.gaitpost.2018.05.003

Pataky, T. C. (2012). One-dimensional Statistical Parametric Mapping in Python. *Comput. Methods Biomechanics Biomed. Eng.* 15 (3), 295–301. doi:10.1080/10255842.2010.527837

Pataky, T. C., Robinson, M. A., and Vanrenterghem, J. (2013). Vector Field Statistical Analysis of Kinematic and Force Trajectories. *J. Biomechanics* 46 (14), 2394–2401. doi:10.1016/j.jbiomech.2013.07.031

Pothrat, C., Authier, G., Viehweger, E., and Rao, G. (2013). Multifactorial Gait Analysis of Children with Flat Foot and Hind Foot Valgus Deformity. *Comput. Methods Biomechanics Biomed. Eng.* 16 (Suppl. 1), 80–81. doi:10.1080/10255842.2013.815982

Powers, C. M. (2003). The Influence of Altered Lower-Extremity Kinematics on Patellofemoral Joint Dysfunction: a Theoretical Perspective. *J. Orthop. Sports Phys. Ther.* 33 (11), 639–646. doi:10.2519/jospt.2003.33.11.639

Radler, C., Kranzl, A., Manner, H. M., Höglinger, M., Ganger, R., and Grill, F. (2010). Torsional Profile versus Gait Analysis: Consistency between the Anatomic Torsion and the Resulting Gait Pattern in Patients with Rotational Malalignment of the Lower Extremity. *Gait Posture* 32 (3), 405–410. doi:10.1016/j.gaitpost.2010.06.019

Reinschmidt, C., van den Bogert, A. J., Nigg, B. M., Lundberg, A., and Murphy, N. (1997). Effect of Skin Movement on the Analysis of Skeletal Knee Joint Motion during Running. *J. Biomechanics* 30 (7), 729–732. doi:10.1016/s0021-9290(97)00001-8

Sass, P., and Hassan, G. (2003). Lower Extremity Abnormalities in Children. *Am. Fam. Physician* 68 (3), 461–468.

Schranz, C., Belohlavek, T., Sperl, M., Kraus, T., and Svehlik, M. (2021). Does Femoral Anteversion and Internally Rotated Gait Correlate in Subjects with Patellofemoral Instability? *Clin. Biomech.* 84, 105333. doi:10.1016/j.clinbiomech.2021.105333

Schreiber, C., and Moissenet, F. (2019). A Multimodal Dataset of Human Gait at Different Walking Speeds Established on Injury-free Adult Participants. *Sci. Data* 6 (1), 111. doi:10.1038/s41597-019-0124-4

Schwartz, M. H., Rozumalski, A., and Trost, J. P. (2008). The Effect of Walking Speed on the Gait of Typically Developing Children. *J. Biomechanics* 41 (8), 1639–1650. doi:10.1016/j.jbiomech.2008.03.015

Steele, K. M., Demers, M. S., Schwartz, M. H., and Delp, S. L. (2012). Compressive Tibiofemoral Force during Crouch Gait. *Gait Posture* 35 (4), 556–560. doi:10.1016/j.gaitpost.2011.11.023

Stevens, P. M., Gililland, J. M., Anderson, L. A., Mickelson, J. B., Nielson, J., and Klatt, J. W. (2014). Success of Torsional Correction Surgery after Failed Surgeries for Patellofemoral Pain and Instability. *Strateg. Trauma Limb Reconstr.* 9 (1), 5–12. doi:10.1007/s11751-013-0181-8

Tönnis, D., and Heinecke, A. (1999). Acetabular and Femoral Anteversion: Relationship with Osteoarthritis of the Hip. *J. Bone & Jt. Surg.* 81 (12), 1747–1770. doi:10.2106/00004623-199912000-00014

Vandekerckhove, I., Wesseling, M., Kainz, H., Desloovere, K., and Jonkers, I. (2021). The Effect of Hip Muscle Weakness and Femoral Bony Deformities on Gait Performance. *Gait Posture* 83, 280–286. doi:10.1016/j.gaitpost.2020.10.022

Veerkamp, K., Kainz, H., Killen, B. A., Jónasdóttir, H., and van der Krogt, M. M. (2021). Torsion Tool: An Automated Tool for Personalising Femoral and Tibial Geometries in OpenSim Musculoskeletal Models. *J. Biomech.* 125, 110589. doi:10.1016/j.jbiomech.2021.110589

Wu, G., Siegler, S., Allard, P., Kirtley, C., Leardini, A., Rosenbaum, D., et al. (2002). ISB Recommendation on Definitions of Joint Coordinate System of Various Joints for the Reporting of Human Joint Motion-Part I: Ankle, Hip, and Spine. *J. biomechanics* 35 (4), 543–548. doi:10.1016/s0021-9290(01)00222-6

Xiang, L., Deng, K., Mei, Q., Gao, Z., Yang, T., Wang, A., et al. (2021). Population and Age-Based Cardiorespiratory Fitness Level Investigation and Automatic Prediction. *Front. Cardiovasc Med.* 8, 758589. doi:10.3389/fcvm.2021.758589

Zafiropoulos, G., Prasad, K. S. R. K., Kouboura, T., and Danis, G. (2009). Flat Foot and Femoral Anteversion in Children-A Prospective Study. *Foot* 19 (1), 50–54. doi:10.1016/j.foot.2008.09.003

Conflict of Interest: The authors declare that the research was conducted in the absence of any commercial or financial relationships that could be construed as a potential conflict of interest.

Publisher's Note: All claims expressed in this article are solely those of the authors and do not necessarily represent those of their affiliated organizations, or those of the publisher, the editors and the reviewers. Any product that may be evaluated in this article, or claim that may be made by its manufacturer, is not guaranteed or endorsed by the publisher.

frontiers | Frontiers in Bioengineering and Biotechnology

ORIGINAL RESEARCH
published: 15 June 2022
doi: 10.3389/fbioe.2022.893840

Compensatory Responses During Slip-Induced Perturbation in Patients With Knee Osteoarthritis Compared With Healthy Older Adults: An Increased Risk of Falls?

Xiping Ren[1,2], Christoph Lutter[2], Maeruan Kebbach[2], Sven Bruhn[3], Qining Yang[4], Rainer Bader[2] and Thomas Tischer[2]*

[1]College of Physical Education and Health Sciences, Zhejiang Normal University, Jinhua, China, [2]Biomechanics and Implant Technology Research Laboratory, Department of Orthopedics, Rostock University Medical Center, Rostock, Germany, [3]Institute of Sport Science, Faculty of Philosophy, University of Rostock, Rostock, Germany, [4]Department of Joint Surgery, The affiliated Jinhua Hospital, Zhejiang University School of Medicine, Jinhua, China

Background: Functional impairment of the knee joint affected by osteoarthritis and loss of muscle strength leads to a significant increase in the number of falls. Nevertheless, little is known about strategies for coping with gait perturbations in patients with knee osteoarthritis (KOA). Thus, this study aimed to examine the compensatory strategies of patients with KOA in response to a backward slip perturbation compared with healthy older adults.

Methods: An automated perturbation program was developed by using D-Flow software based on the Gait Real-time Analysis Interactive Lab, and an induced backward slip perturbation was implemented on nine patients with severe KOA (68.89 ± 3.59 years) and 15 age-matched healthy older adults (68.33 ± 3.29 years). Step length, gait speed, range of motion, vertical ground reaction forces, lower extremity joint angles, and joint moments were computed and analyzed.

Results: Compared with older adults, patients with KOA had significantly lower step length, gait speed, and vertical ground reaction forces in both normal walking and the first recovery step following backward slip perturbations. Inadequate flexion and extension of joint angles and insufficient generation of joint moments predispose patients with KOA to fall. Hip extension angle and flexion moment, knee range of motion, and vertical ground reaction forces are key monitoring variables.

Conclusion: The risk of falls for patients with KOA in response to backward slip perturbations is higher. Patients with KOA should focus not only on quadriceps muscle strength related to knee range of motion but also on improving hip extensor strength and activation through specific exercises. Targeted resistance training and perturbation-based gait training could be better options.

Keywords: musculoskeletal disorders, older adults, treadmill-induced perturbation, slips and falls, compensatory step

OPEN ACCESS

Edited by:
Chih-Hsiu Cheng,
Chang Gung University, Taiwan

Reviewed by:
Ben-Yi Liau,
Hungkuang University, Taiwan
Chich-Haung Richard Yang,
Tzu Chi University, Taiwan

****Correspondence:***
Xiping Ren
renxiping@zjnu.cn

Specialty section:
This article was submitted to Biomechanics, a section of the journal Frontiers in Bioengineering and Biotechnology

Received: *10 March 2022*
Accepted: *30 May 2022*
Published: *15 June 2022*

Citation:
Ren X, Lutter C, Kebbach M, Bruhn S, Yang Q, Bader R and Tischer T (2022) Compensatory Responses During Slip-Induced Perturbation in Patients With Knee Osteoarthritis Compared With Healthy Older Adults: An Increased Risk of Falls? Front. Bioeng. Biotechnol. 10:893840. doi: 10.3389/fbioe.2022.893840

INTRODUCTION

Knee osteoarthritis (KOA) is a highly prevalent degenerative joint disease in older adults (Sharma, 2021), with an incidence that has doubled since the mid-20th century (Wallace et al., 2017). It poses major socioeconomic challenges throughout the world (Cross et al., 2014; Cui et al., 2020).

KOA commonly causes considerable pain (Neogi, 2013) and dysfunction (Alencar et al., 2007). In addition to the direct impairment, these deficiencies are also likely to cause falls during normal walking (Manlapaz et al., 2019; Deng et al., 2021). Falls by themselves can lead to a high burden of musculoskeletal diseases like fractures of the hip, distal radius, and proximal humerus, among others (Lamb et al., 2020). Considering patients with KOA, women with OA have a 25% higher risk of falls and a 20% higher risk of fracture than their peers without OA (Prieto-Alhambra et al., 2013). Moreover, an increase in the number of joints with symptomatic KOA of the lower extremities increases the risk of falling (Doré et al., 2015). Therefore, preventing falls among patients with KOA is a critical but often-overlooked topic. An in-depth understanding of the compensatory response to a slip is fundamental to help fall-prone populations reduce the incidence of falls (Marigold et al., 2003; Gholizadeh et al., 2019). To the best of our knowledge, there is only a limited understanding of compensatory strategies after gait perturbations in patients with KOA, especially for a slip-induced perturbation.

"Slip" is a type of external dynamic perturbation of walking, which can induce a sudden displacement of the base of support (BoS) into the anterior or posterior direction relative to the center of mass (CoM) (Debelle et al., 2020; Lee et al., 2020). Both a single session of slip perturbation training and single-repeated slip training have positive effects on improving dynamic stability (Pai and Bhatt, 2007; Lee et al., 2020). Humans can quickly regain stability and maintain balance from the same type of perturbation (Debelle et al., 2020). The "first-trial effect" has been used to describe the training effects of older adults experiencing the first slip perturbation, suggesting that first-exposure trials generate rapid adaptive effects, and such effects could be maintained for up to a full year (Pai and Bhatt, 2007; Liu et al., 2017). Subsequently, Inkol et al. (2019) found that the first response of a slip perturbation has the largest effect on the gait variables compared with the subsequent perturbations of the same type (Inkol et al., 2019), and the first step following the perturbation is the most important protective postural strategy (Maki and McIlroy, 1997; Melzer et al., 2008). Further, the step length of the first recovery step after a slip perturbation determines the stability of the subsequent steps and is corrected with balance recovery mechanics (Debelle et al., 2021). It has been found that the frequency of backward slip on the oiled surfaces is twice as high as that of the forward slip (Nagano et al., 2013), implying a high risk of falls, yet this perturbation is also most prevalent in daily life (Debelle et al., 2020). However, there is still a lack of research on the effects of backward slip perturbations in people at high risk of falls, such as patients with KOA, and it is unclear how the first step after the perturbation plays a protective role. Therefore, effective monitoring of the first step after a slip perturbation in patients with KOA is crucial.

Moreover, lower extremity joint kinematics and kinetics partially influence the outcome of perturbations and hence play a critical role in understanding the complicated link between gait and slip-induced falls (Karamanidis et al., 2020). The application of joint moments to clinical-pathological gait analysis, such as knee and hip OA, is of increasing interest (Lathrop-Lambach et al., 2014). For example, changes in the magnitude of knee joint moments indicate the progression and severity of OA development (Asay et al., 2018). The quadriceps strength is directly related to knee flexion moment (Lisee et al., 2019), and the medial-lateral load distribution is usually expressed in terms of knee adduction moments (Zeighami et al., 2021). However, few studies have addressed the effect of joint moment application in response to gait perturbations in patients with KOA.

Given the above-mentioned research gap, this study aimed to examine the compensatory strategies of patients with KOA and healthy older adults in response to backward slip perturbations, mainly focusing on comparing the differences and similarities between the first recovery step (Rec1) after the perturbation and the normal gait (Normal), and thus to determine whether patients with KOA are more prone to falls. We developed and implemented a procedure to automatically trigger a slip perturbation and then measure the effects of gait spatiotemporal parameters and the lower extremity kinematics and kinetics on the recovery of dynamic stability. We hypothesized patients with KOA are at higher risk of falls relative to healthy older adults and the protective strategy in the first step following the backward slip perturbation focuses on the effective compensatory effect of the lower extremity.

MATERIALS AND METHODS

Subjects

Nine patients (age: 68.89 ± 3.59 years; body height: 1.69 ± 0.11 m; body mass: 97.53 ± 19.16 kg) with advanced left KOA with persistent pain [Kellgren and Lawrence (K-L) grade 4] and 15 age-matched healthy older adults (age: 68.33 ± 3.29 years; body height: 1.76 ± 0.10 m; body mass: 81.13 ± 13.99 kg) participated in this investigation. The dominant leg was right in all participants. The inclusion criteria for patients with KOA were those who were about to undergo total knee arthroplasty on the left knee within 3 months, and the inclusion criterion for older adults was no lower extremity history of disorders and injuries. Patients with KOA were recruited through the Rostock Orthopedic Clinic, and older adults were recruited from different communities. Written consent was obtained from all participants prior to the measurement. Ethical approval was granted by the committee of the Rostock University Medical Center, Germany (A2019-0231). All measurements were carried out in compliance with the Declaration of Helsinki.

Experimental Protocol

The Gait Real-time Analysis Interactive Lab (GRAIL) (Motek Medical B.V., Houten, Netherlands), which integrates multiple devices, was utilized for the investigation. A 10 infrared cameras

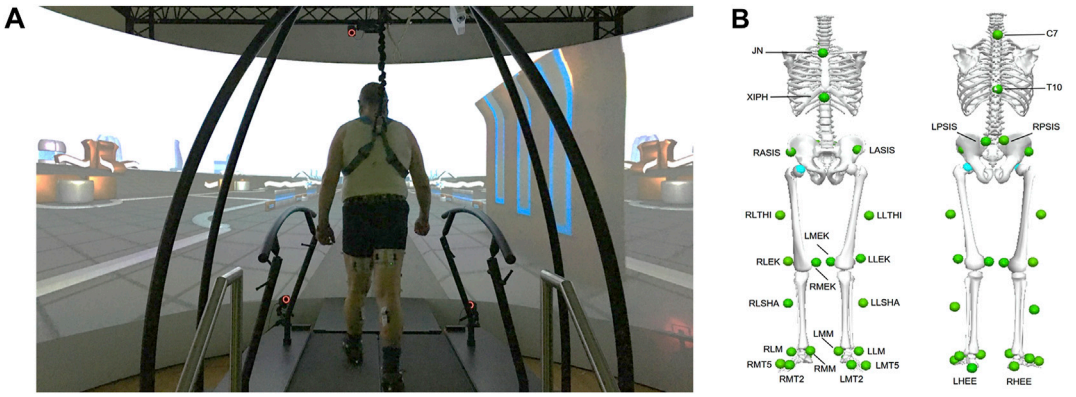

FIGURE 1 | The Gait Real-Time Analysis Interactive Lab (GRAIL) and the industrial-style virtual reality scenario involved in this study **(A)**; front and rear view of marker set used in Human Body Model (v2) with its specific 26 markers (green), which involves the anatomical positions of the lower extremities and trunk **(B)**.

motion capture system (Vicon Bonita B10, Vicon Metrics Ltd., Oxford, United Kingdom) was utilized to track the marker trajectories at 100 Hz, and an embedded treadmill force plate (ForceLink B.V., Culemborg, Netherlands) was used to record the ground reaction forces (GRFs) at 1,000 Hz. The D-flow software (v3.34, Motek Medical B.V.) synchronized all hardware and triggered signals for data collection. Participants felt like they were in an industrial-style virtual reality scenario during the entire measurement (**Figure 1A**).

Prior to the investigation, the subjects' demographic parameters and leg length were recorded and the Timed Up and Go test (TUG) was performed. Subsequently, 26 reflective markers with a diameter of 1.4 cm (**Figure 1B**) were attached to the anatomical landmarks according to the Human Body Model (HBM, v2, Motek Medical B.V.). Self-selected speeds were obtained during the participants' 6-min treadmill familiarization (Meyer et al., 2019; Oudenhoven et al., 2019). In the first trial, normal walking was collected for 2 min. In the second trial, right-side treadmill belt posterior acceleration (to induce a "slip-like" effect) and deceleration (to induce a "trip-like" effect) perturbations were performed (van den Bogaart et al., 2020). Two different types of perturbations were set up in each trial, which were randomly and automatically triggered by a custom program. The acceleration and deceleration intensities were set at 3 m/s^2. The perturbation occurred and lasted for 300 ms after the speed reached a specific value, then returned to normal speed. All perturbations happened at the moment of the right heel strike. Each perturbation occurred at a pseudo-random interval of 15–20 s for a total of six times. There were sufficient breaks to prevent fatigue and knee pain. The whole session took around 15 min for each participant, and each participant successfully completed the measurements. During the entire session, each participant was protected from falling by a harness and was able to cope with the perturbation task and did not grasp the handrails of the treadmill.

Data Processing

The Gait Offline Analysis Tool (GOAT, version 4.1, Motek Medical B.V.) (Oudenhoven et al., 2019; Bahadori et al., 2021) was used for data processing with a built-in HBM computational model, which had been verified previously (Van Den Bogert et al., 2013; Falisse et al., 2018; Flux et al., 2020). The local maximum of the anterior-posterior position of the heel marker relative to the pelvis was used to determine the heel-strike event (Zeni et al., 2008). A second-order low-pass Butterworth filter at 6 Hz was set to filter kinematic data, which were found to be the highest frequency in kinematics related to gait (Winter et al., 1974). To prevent artifacts, GRFs were processed with the same filter cutoff as for kinematics (Bisseling and Hof, 2006; Van Den Bogert et al., 2013). Inverse kinematics and inverse dynamics algorithms were conducted to calculate the gait spatiotemporal parameters, joint angles, and joint moments of the lower extremity by deploying HBM (Van Den Bogert et al., 2013). The joint moments were normalized to the participant's body mass to reduce the confounding effect (Moisio et al., 2003). To compare continuous time series variables, each joint angle and moment was normalized to the percentage of the gait cycle (101 data points, 0%–100%).

For normal walking, 20–25 consecutive strides were averaged for each participant, an approach consistent with previous studies (Kribus-Shmiel et al., 2018; Kroneberg et al., 2019; Riazati et al., 2019). For slip-perturbed walking, only the slip_Rec1 of the first trial was used for analysis (Debelle et al., 2020). In the current study, the focus was on treadmill belt acceleration perturbations in the posterior direction, and only the participants' recovery compensatory strategies in response to slip perturbations were analyzed. The following parameters were processed: step length, gait speed, vertical GRFs (vGRFs), and lower extremity joint angles, joint moments in the sagittal plane. It has been reported that anteroposterior gait perturbations mainly affect parameters in the sagittal plane (Yoo et al., 2019).

Statistical Analyses

Before determining the type of statistical analysis, the normality of the data was assessed by using the Shapiro–Wilk test. Independent and paired sample *t*-tests were utilized for zero-dimensional data analysis of demographic characteristics, leg lengths, TUG scores, step length, gait speed, and peak vGRFs.

TABLE 1 | Basic information of patients with knee osteoarthritis (KOA) and older adults.

Variables	Patients with KOA (n = 9; 4 females)	Older adults (n = 15; 4 females)	p-value
Age (years)	68.89 ± 3.59 [66.13, 71.65]	68.33 ± 3.29 [66.51, 70.15]	0.7020
Body height (m)	1.69 ± 0.11 [1.60, 1.77]	1.76 ± 0.10 [1.71, 1.81]	0.0989
Body mass (kg)	97.53 ± 19.16 [82.81, 112.30]	81.13 ± 13.99 [73.38, 88.88]	0.0242*
BMI (kg/m2)	34.03 ± 3.43 [31.39, 36.67]	26.24 ± 4.83 [23.56, 28.91]	0.0010**
Leg length (m)	0.86 ± 0.09 [0.79, 0.93]	0.93 ± 0.07 [0.89, 0.97]	0.0423*
TUG (s)	15.28 ± 3.96 [12.24, 18.32]	10.32 ± 1.23 [9.64, 11.00]	0.0053**

*The data are presented as the mean ± standard deviation [95% Confidence Interval]. *p < 0.05, **p < 0.01. Abbreviations: BMI, body mass index; TUG, timed up and go test.*

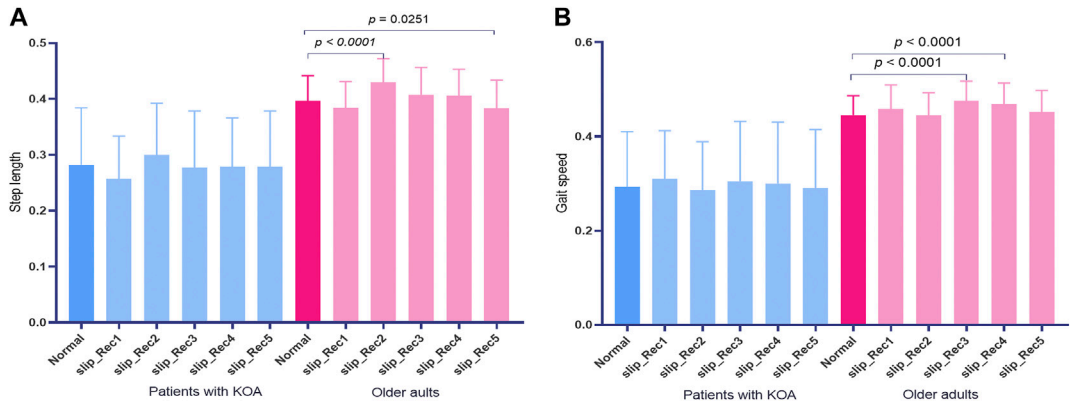

FIGURE 2 | The step length **(A)** and gait speed **(B)** in normal walking (Normal) and the five steps following the perturbation. Blue bars indicate patients with knee osteoarthritis (KOA) and red bars indicate older adults.

One-dimensional time-series statistical analysis of joint angles and joint moments was conducted by using open-source statistical parametric mapping (SPM), which is based on random field theory (Pataky et al., 2015). All statistical analyses were performed by using GraphPad Prism (v8.0.2, GraphPad Software Inc., La Jolla, CA, United States) and Matlab 2018b (The MathWorks Inc., Natick, MA, United States). The significance level was set at $p < 0.05$.

RESULTS

Basic Information of Participants

Demographic characteristics, leg length, and TUG score from the participants are presented in **Table 1**. Body mass ($p = 0.0242$), body mass index (BMI) ($p = 0.0010$), leg length ($p = 0.0423$), and TUG scores ($p = 0.0053$) were significantly different between the patients with KOA and older adults.

Spatiotemporal Parameters and vGRFs

The step length normalized to body height (BH) and gait speed normalized to leg length ($\sqrt{gl_0}$, with $g = 9.81$ m/s^2, l_0, leg length) of Normal and the five consecutive steps following the perturbation are presented in **Figure 2.** There were no changes in step length and gait speed in patients with KOA, while there were significant differences in step length between Normal and slip_Rec2 and slip_Rec5 ($p < 0.0001$ and $p = 0.0251$, respectively) (**Figure 2A**), and significant differences in gait speed between Normal and slip_Rec3 and slip_Rec4 ($p < 0.0001$ and $p < 0.0001$, respectively) (**Figure 2B**).

The step length for Normal was 0.28 ± 0.10 [95% confidence interval (CI) 0.20, 0.36] and 0.40 ± 0.05 [95% CI 0.37, 0.42] for patients with KOA and older adults, while in the slip_Rec1 gait, the values were 0.26 ± 0.08 [95% CI 0.20, 0.32] and 0.38 ± 0.05 [95% CI 0.36, 0.41], respectively. There were no changes in the step length of Normal and slip_Rec1 in patients with KOA and older adults. There were significant differences in the step lengths of Normal ($p = 0.0129$) and slip_Rec1 ($p < 0.0001$) between patients with KOA and older adults (**Figure 3A**). The step length of patients with KOA was significantly smaller than that of older adults.

The gait speeds for Normal and slip_Rec1 between patients with KOA and older adults were 0.29 ± 0.12 [95% CI 0.20, 0.38] and 0.45 ± 0.05 [95% CI 0.42, 047] versus 0.31 ± 0.10 [95% CI 0.23, 0.39] and 0.46 ± 0.05 [95% CI 0.43, 0.49], respectively. There was no significant difference in the same group, whereas there were differences between the groups under the same condition ($p = 0.0016$ for Normal and $p = 0.0021$ for slip_Rec1) (**Figure 3B**). Patients with KOA had a significantly lower gait speed than older adults.

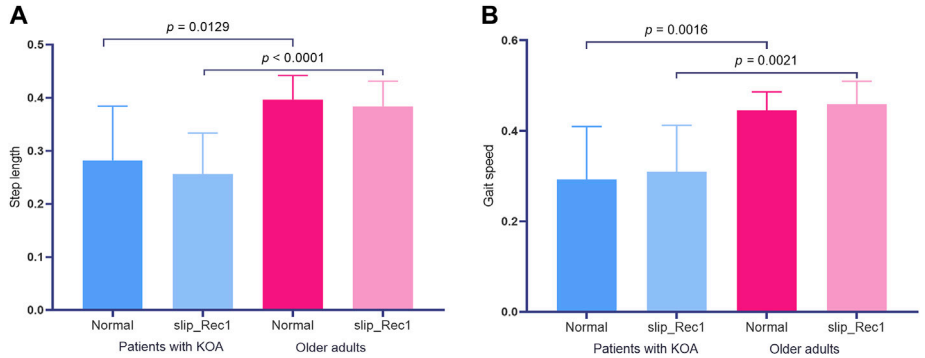

FIGURE 3 | Zero-dimensional statistical analysis of step length **(A)** and gait speed **(B)** between Normal and slip_Rec1 among patients with knee osteoarthritis (KOA) and older adults.

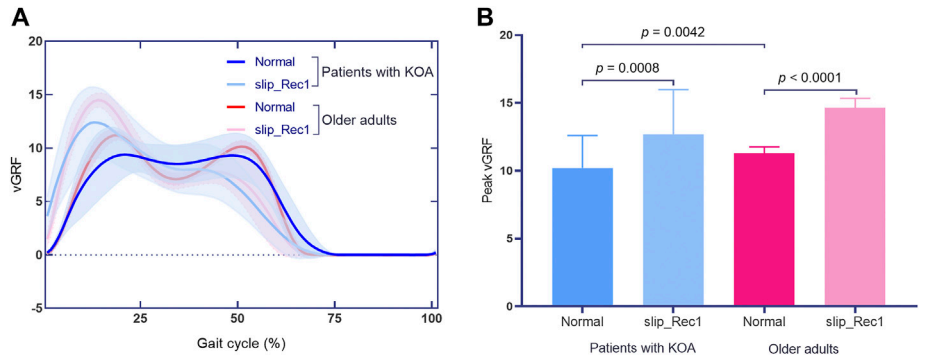

FIGURE 4 | The vertical ground reaction force (vGRF) curves in Normal and slip_Rec1 **(A)**; zero-dimensional statistical analysis of peak vGRFs among patients with knee osteoarthritis (KOA) and older adults **(B)**.

The vGRF normalized to body mass (BM) for Normal and slip_Rec1 in patients with KOA and older adults during the gait cycle are presented in **Figure 4A**. The Normal and slip_Rec1 phases of vGRFs reaching zero in patients with KOA were 71% and 67%, respectively, while these values were 66% and 65% in older adults. Peak vGRFs for Normal and slip_Rec1 in the vertical direction for patients with KOA and older adults were 10.21 ± 2.38 [95% CI 8.38, 12.04] and 12.70 ± 3.29 [95% CI 10.17, 15.22] versus 11.30 ± 0.46 [95% CI 11.05, 11.55] and 14.64 ± 0.70 [95% CI 14.25, 15.02], respectively. There were significant differences between the two conditions in the same group (p = 0.0008 for patients with KOA and $p < 0.0001$ for older adults). The vGRFs significantly increased during slip_Rec1. The increases were 24.39% for patients with KOA and 29.56% for older adults. Patients with KOA showed a significantly smaller value than older adults in Normal (p = 0.0042) (**Figure 4B**). However, such a difference was not observed in slip_Rec1.

Ankle Joint

At the ankle joint, for Normal, patients with KOA showed significantly larger dorsiflexion angles throughout 26.79%–42.6% of the gait cycle (p = 0.003) and smaller plantarflexion angles throughout 56.18%–69.91% of the gait cycle (p = 0.005) than older adults (**Figure 5A**); lower plantarflexion moments throughout 45.77%–56.41% of the gait cycle (p = 0.001) and higher plantarflexion moments throughout 74.67%–77.91% of the gait cycle (p = 0.004) (**Figure 5B**). Nevertheless, for slip_Rec1, there were no significant differences for ankle angle or moment between groups (**Figures 5C,D**). The ankle range of motion (ROM) is presented in **Table 2**, with no significant differences between the two groups for both Normal and slip_Rec1.

Knee Joint

Regarding the knee joint, for Normal, patients with KOA developed significantly smaller extension angles across 0%–8.188% (p = 0.027), 31.23%–48.69% (p = 0.003), and 85.63%–100% (p = 0.007) of the gait cycle (**Figure 6A**), smaller flexion moments across 35.30%–48.90% of the gait cycle (p = 0.005) (**Figure 6B**) than older adults. For slip_Rec1, patients with KOA only developed significantly smaller extension angles across 96.48%–98.18% of the gait cycle (p = 0.048) (**Figure 6C**) and smaller extension moments across 15.47%–18.23% of the gait cycle (p = 0.026) (**Figure 6D**). The knee ROM is presented in **Table 2**, with significant differences between the two groups for both Normal (p = 0.0200) and slip_Rec1 (p = 0.0047).

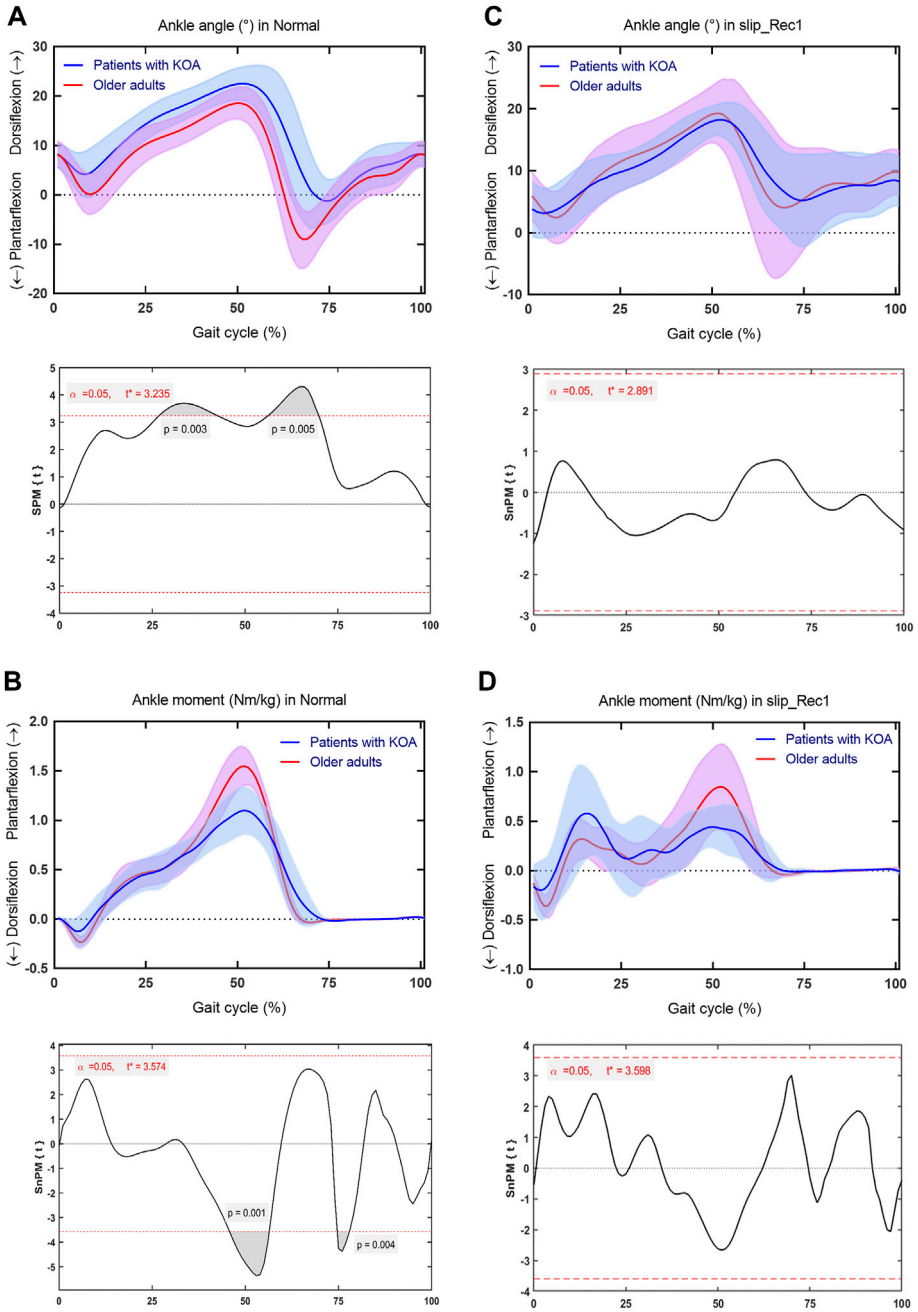

FIGURE 5 | Comparison between patients with knee osteoarthritis (KOA) and older adults for the ankle angle and ankle moment in Normal and slip_Rec1 in the sagittal plane. Ankle angle for patients with KOA and older adults in Normal **(A)**, ankle moment for patients with KOA and older adults in Normal **(B)**, ankle angle for patients with KOA and older adults in slip_Rec1 **(C)**, and ankle moment for patients with KOA and older adults in slip_Rec1 **(D)**. The upper and lower panels present the average and standard deviation of patients with KOA and older adults and the corresponding outcomes of the one-dimensional statistical parametric mapping (SPM) scalar trajectory *t*-test, respectively. For each analysis, the significance level is set at 0.05, and the corresponding t* is presented as the horizontal red dashed line. The *p* values associated with the supra-threshold clusters, denoted as the grey shaded regions, are presented whenever the test statistic continuum SPM{t} or SnPM{t} exceeds the threshold.

Hip Joint

At the hip joint, for Normal, patients with KOA showed significantly smaller extension throughout 26.98%–60.94% of the gait cycle (p = 0.005) and flexion angle throughout 91.18%–99.23% of the gait cycle (p = 0.044) (**Figure 7A**), smaller flexion moments throughout 41.04%–58.24% of the gait cycle (p < 0.001) and larger extension moments throughout 77.17%–84.87% of the gait cycle (p < 0.001) (**Figure 7B**). For slip_Rec1, patients with KOA also showed significantly smaller extension throughout 22.4%–62.01% (p =

TABLE 2 | Ankle, knee, and hip range of motion (ROM) in the sagittal plane.

Variable	Normal		*p*-value	Slip_Rec1		*p*-value
	Patients with KOA	Older adults		Patients with KOA	Older adults	
Ankle ROM (°)	25.96 ± 4.07 [22.84, 29.09]	28.69 ± 3.38 [26.82, 30.57]	0.0900	19.06 ± 4.66 [15.47, 22.64]	22.25 ± 6.99 [18.38, 26.12]	0.2380
Knee ROM (°)	51.34 ± 10.80 [43.04, 59.64]	61.86 ± 4.38 [59.43, 64.28]	0.0200*	42.01 ± 13.22 [31.85, 52.16]	55.45 ± 7.87 [51.09, 59.81]	0.0047**
Hip ROM (°)	37.61 ± 10.96 [29.19, 46.04]	43.64 ± 6.95 [39.80, 47.49]	0.1114	27.64 ± 10.17 [19.82, 35.46]	41.40 ± 10.32 [35.69, 47.12]	0.0043**

*The data are presented as the mean ± standard deviation [95% Confidence Interval]. *p < 0.05, **p < 0.01. Abbreviations: KOA, knee osteoarthritis; Rec1, first recovery step.*

0.002) (**Figure 7C**) and smaller flexion moment throughout 40.23%–52.26% of the gait cycle ($p < 0.001$) (**Figure 7D**). The hip ROM is presented in **Table 2**, with significant differences between the two groups for slip_Rec1 ($p = 0.0043$).

DISCUSSION

This study investigated the compensatory strategies between normal walking and the first recovery step following a backward slip perturbation in patients with KOA compared with age-matched older adults. The novelty of this study is that the adapted gait perturbation procedure induces the mechanism of human falls and quantifies the lower limb response to gait compensation after the onset of a slip perturbation. Our findings indicate that the pathological condition of patients with KOA limits the normal gait pattern compared with older adults. The spatiotemporal parameters, as well as joint kinematics and kinetics of the lower extremities, showed significant differences in response to the perturbed gait, confirming that patients with KOA have a higher risk of falling relative to healthy older adults. Based on the fact that no falls occurred, effective compensatory strategies in the first step following backward slip perturbations might act primarily through lower extremity joints to prevent falls.

In line with previous studies (Debi et al., 2012; Sun et al., 2017; Wiik et al., 2017), patients with KOA showed significantly shorter step lengths relative to older adults in Normal. In this regard, the step length of slip_Rec1 is considered to be a critical element for improving balance recovery after a perturbation, as sufficient step length may help restore balance and may be more effective in avoiding falls (Debelle et al., 2021). In the current study, the step length of slip_Rec1 decreased slightly compared with Normal, even though statistical significance was not reached between Normal and slip_Rec1 in either group. This indicates that the step length is controlled within the effective range after the occurrence of a slip perturbation. Milner et al. (2018) indicated that the purpose of shortening step length in patients with KOA is to reduce knee joint loading, thereby preventing falls (Milner et al., 2018). However, patients with KOA may be at greater risk of falling in response to perturbations relative to older adults, as there was also a significant difference in the step length of slip_Rec1 between the two groups.

Gait speed is a predictor of morbidity in patients with KOA (Alenazi et al., 2021); this factor is related to functional capacity in adults with mobility impairments (Peel et al., 2013). Gait speed reduction has been documented as a risk factor for falls in patients with KOA (Purser et al., 2012; Taş et al., 2014; Gill et al., 2017). In the current study, the gait speed of patients with KOA in Normal was significantly smaller than that of older adults, which is consistent with previous studies (Debi et al., 2012; Queen et al., 2016; Wiik et al., 2017; Vennu and Misra, 2018; Alenazi et al., 2021). The difference between the groups was still present in slip_Rec1, whereas the gait speed of slip_Rec1 did not differ from the Normal gait speed within the groups. This means that both patients with KOA and older adults are within their capabilities for speed control after a backward slip perturbation, and gait speed does not serve as an indicative indicator of their response to the perturbation but may be considered a predictor of increased fall risk in KOA patients compared to healthy older adults. Patients with KOA not only showed lower gait speed, but this also declined over time, even after controlling for BMI and other covariates (Vennu and Misra, 2018; Alenazi et al., 2021). However, in the present study, the difference in BMI between the two groups was significant ($p = 0.001$), which may have contributed to the decrease in gait speed, although no correlation analysis between the two was performed. A large population-based cohort study found that decreased gait speed was significantly and independently associated with BMI in patients with symptomatic KOA (King et al., 2018). On the other hand, knee ROM (Brinkmann and Perry, 1985), quadriceps muscle weakness (Spinoso et al., 2018), and quadriceps tendon stiffness (Ebihara et al., 2021) are factors that influence the gait speed of patients with KOA. Quadriceps tendon stretching (Ebihara et al., 2021) and resistance training (Li et al., 2021) may be effective in improving gait speed. As gait speed increases, step length also increases (Bovi et al., 2011; Fukuchi et al., 2019). Therefore, we strongly recommend that patients with KOA focus on strengthening the quadriceps muscles, regardless of the severity of KOA. This may also be an important part of improving gait stability.

GRFs are a screening tool for rapid detection of abnormal joint loading (Tang et al., 2004) and a key factor in predicting KOA severity (Kotti et al., 2014). Among patients with KOA, the significant reduction in push-off force and push-off impulse during the terminal stance phase makes GRFs abnormal, which leads to an overall decrease in gait speed (Wiik et al., 2017). In addition, it has been shown that vGRFs are lower in patients with severe KOA (Moustakidis et al., 2010). Our results showed that the normalized vGRFs of patients with KOA were significantly lower than that of older adults, regardless of whether it is in Normal or slip_Rec1. Kotti et al. (2014) found that vGRFs reached zero after approximately 73% of the gait cycle in healthy subjects, compared with approximately

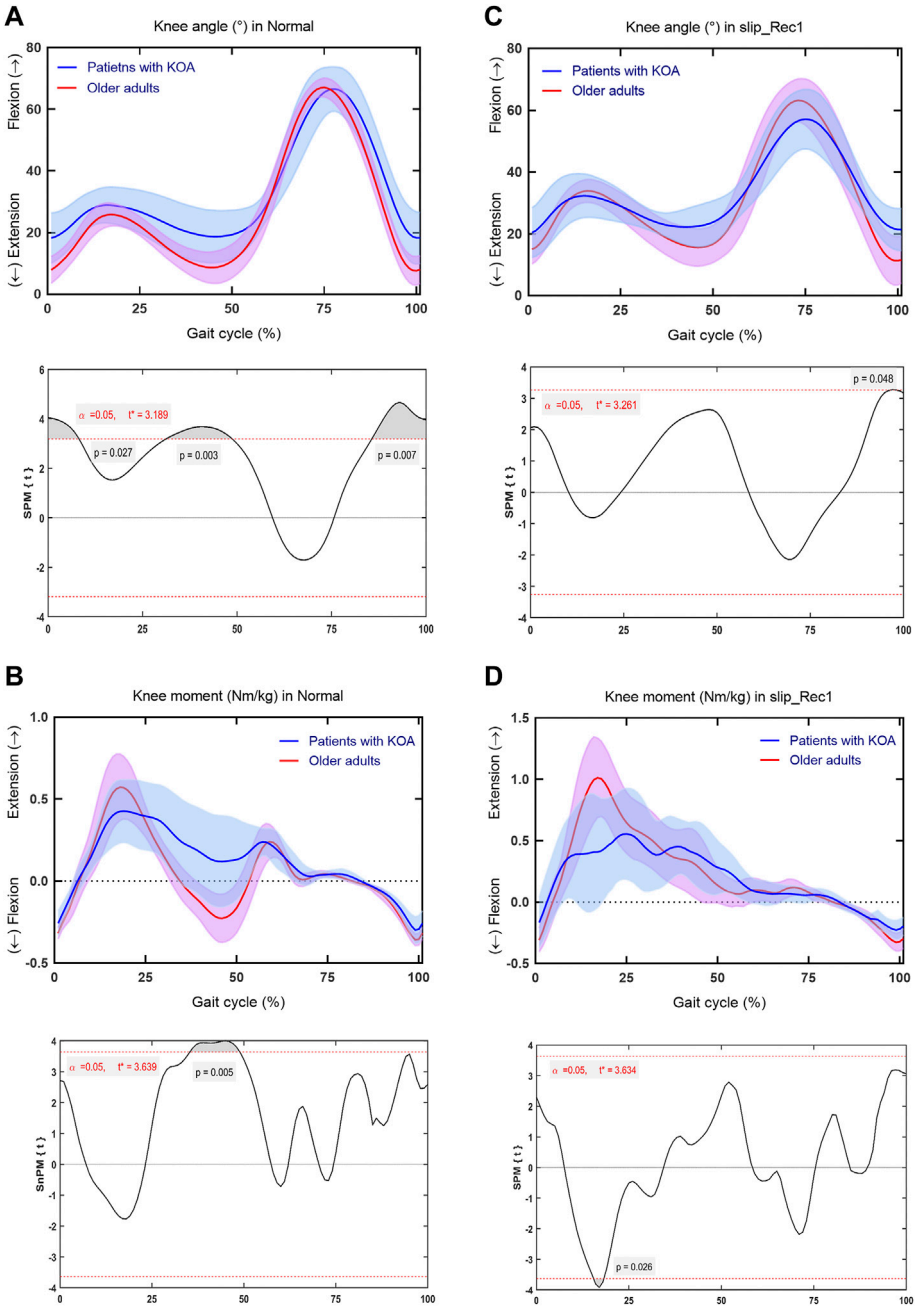

FIGURE 6 | Comparison between patients with knee osteoarthritis (KOA) and older adults for the knee angle and knee moment in Normal and slip_Rec1 in the sagittal plane. Knee angle for patients with KOA and older adults in Normal **(A)**, knee moment for patients with KOA and older adults in Normal **(B)**, knee angle for patients with KOA and older adults in slip_Rec1 **(C)**, and knee moment for patients with KOA and older adults in slip_Rec1 **(D)**. The upper and lower panels present the average and standard deviation of patients with KOA and older adults and the corresponding outcomes of the one-dimensional statistical parametric mapping (SPM) scalar trajectory *t*-test, respectively. For each analysis, the significance level is set at 0.05, and the corresponding t* is presented as the horizontal red dashed line. The *p* values associated with the supra-threshold clusters, denoted as the grey shaded regions, are presented whenever the test statistic continuum SPM{t} or SnPM{t} exceeds the threshold.

71% in patients with KOA (Kotti et al., 2014). The end of the stance phase was the most distinctive difference between the healthy individuals and patients with KOA, with the stance phase being prolonged in healthy subjects compared with patients with KOA (Kotti et al., 2014). Our results appear to be contrary to the above-mentioned study, with the vGRFs reaching zero for older adults (66% in Normal and 65% in slip_Rec1) earlier relative to patients with KOA (71% in Normal and 67% in slip_Rec1). These findings corroborate a previous study (Spinoso et al., 2018). Patients with KOA remain in the

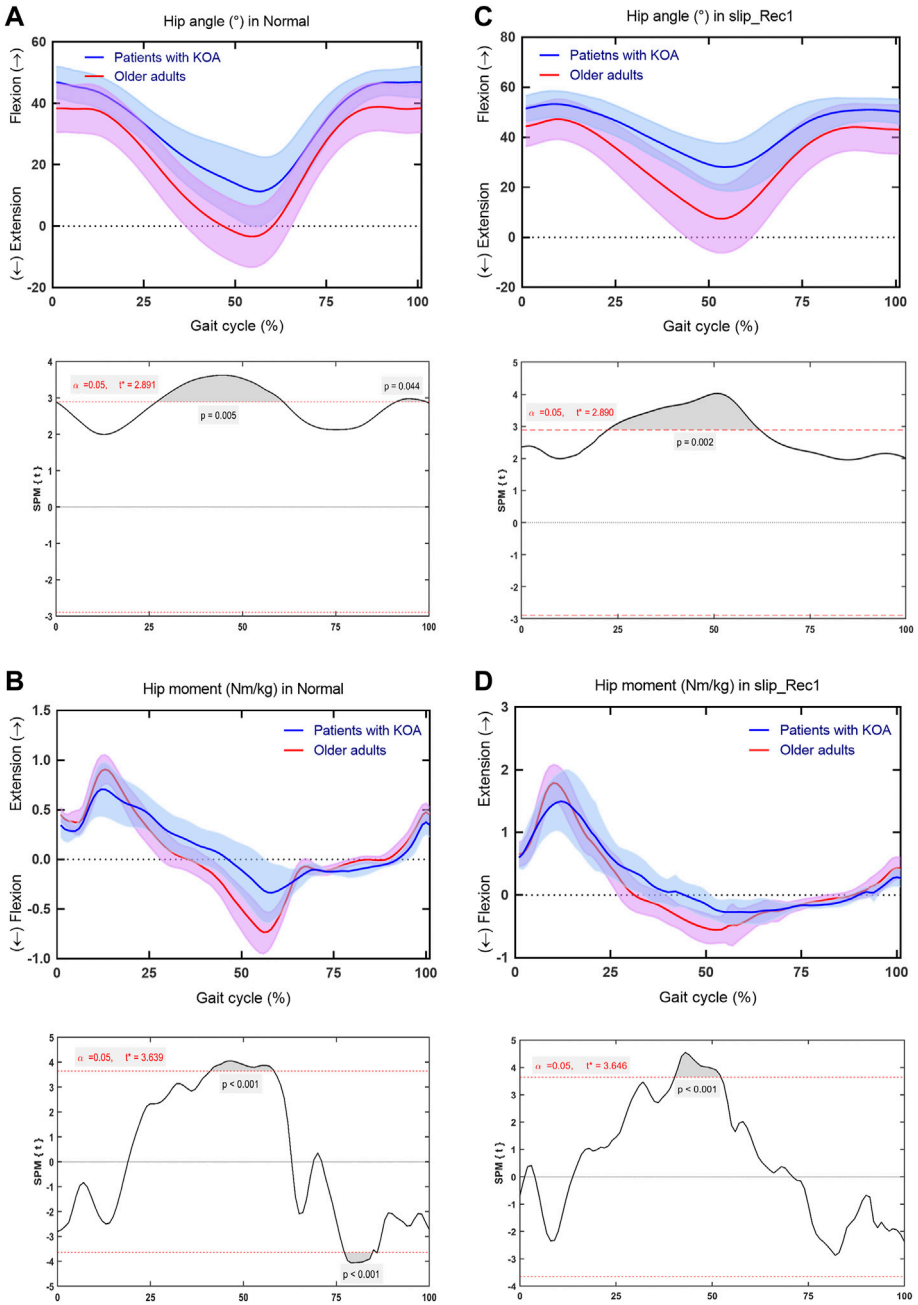

FIGURE 7 | Comparison between patients with knee osteoarthritis (KOA) and older adults for the hip angle and hip moment in Normal and slip_Rec1 in the sagittal plane. Hip angle for patients with KOA and older adults in Normal **(A)**, hip moment for patients with KOA and older adults in Normal **(B)**, hip angle for patients with KOA and older adults in slip_Rec1 **(C)**, and hip moment for patients with KOA and older adults in slip_Rec1 **(D)**. The upper and lower panels present the average and standard deviation of patients with KOA and older adults and the corresponding outcomes of the one-dimensional statistical parametric mapping (SPM) scalar trajectory *t*-test, respectively. For each analysis, the significance level is set at 0.05, and the corresponding t* is presented as the horizontal red dashed line. The *p* values associated with the supra-threshold clusters, denoted as the grey shaded regions, are presented whenever the test statistics continuum SPM{t} or SnPM{t} exceeds the threshold.

stance phase for a longer time, suggesting that the prolonged effect of a minor overload could be comparable to the short effect of intense joint stress (Kirkwood et al., 2011). From a clinical perspective, the negative effects of the prolonged stance phase are joint overload and early fatigue, leading to a gradual increase in joint wear (Spinoso et al., 2018).

Concerning the joint ROM of the lower extremity, only the knee joint ROM was significantly different in both Normal and slip_Rec1. Restricted ROM of knee flexion appears to be an important determinant of locomotor disability in patients with KOA (Steultjens et al., 2000). Knee flexion ROM was lower in patients with KOA than in older adults throughout the stance

phase in the present study, showing decreased flexion angles at the stance phases of loading response and terminal stance phase. This finding enriches the existing literature (Astephen et al., 2008; Zeni and Higginson, 2009; McCarthy et al., 2013). Likewise, the knee flexion moment was decreased and the knee extension moment was increased across the stance phase in patients with KOA, a finding that is comparable to the peak moment values in a previous study (Astephen et al., 2008). This behavior is considered to be a compensatory strategy used by patients with KOA in response to pain (McCarthy et al., 2013). A recent study reported that the activation effect of the quadriceps is improved with an increased knee joint extension moment (Hyodo et al., 2020), which plays a critical role in improving gait speed. This finding is supported by the significant difference between patients with KOA and older adults across the mid-stance phase for slip_Rec1. In our study, there were significant differences in the knee extension angle across the terminal swing phase for both Normal and slip_Rec1, but there were no significant differences of flexion moment. This is in line with a previous study in which the improvement in the knee was attributed to the overactivity of the rectus femoris muscle (McCarthy et al., 2013). From a biomechanical point of view, the strength of the quadriceps might be the main contributor to the difference between patients with KOA and older adults. In both Normal and slip_Rec1, the quadriceps muscle seems to be insufficient to fully extend the knee joint. Thus, it needs to be strengthened and activated effectively to increase the ROM of the knee extensor angles during walking. Therefore, effective training is needed to increase the ROM of the knee extensor angles. In this context, future studies using musculoskeletal multibody simulation are needed to examine the differences between patients with KOA and healthy older adults in quadriceps and other muscle forces (Tischer et al., 2017; Kebbach et al., 2020).

There were significant changes at the ankle angles, particularly across the mid and terminal stance phases and the pre- and initial swing phases in Normal, most notably as a marked lack of plantarflexion in patients with KOA. Correspondingly, for Normal, there were lower ankle plantarflexion moments across the terminal stance phase and the pre- and mid-swing phases in patients with KOA, findings that are consistent with a previous study on ankle plantarflexion moment extremes (Gonçalves et al., 2017). It has been shown that the use of ankle plantar flexors in the later stance phase of the gait cycle in patients with OA could lead to increase knee joint reaction forces (Fisher et al., 1997). Therefore, patients with KOA should try to avoid using ankle plantar flexors during gait to reduce the compressive force on the knee joint.

For Normal, there were significant differences in the hip joint involved in the mid/terminal stance phases and the pre- and terminal swing phases, whereas for slip_Rec1 the differences only involved the mid/terminal stance phases and the pre-swing phase. The main manifestation was an inadequate extension of the hip joint, leading to an insufficient hip flexion moment. Slip-induced falls could be exacerbated by an inability to generate sufficient joint moments (Chandler et al., 1990; Wojcik et al., 1999; Liu and Lockhart, 2009). Apparently, the muscles responsible for hip extension are primarily the gluteus maximus (Neumann, 2010; Alnahdi et al., 2012) and adductor magus (Neumann, 2010). A recent systematic review revealed that patients with KOA have significant hip strength deficits with hip abduction (Deasy et al., 2016); nevertheless, there is no clear result that indicates hip joint strength in the sagittal plane. It could be speculated from our results that adequate joint moments generated in the sagittal plane of the hip joint play a crucial role in both patients with KOA and older adults. This also confirms our hypothesis that relatively weaker hip muscle strength and inadequate activation account for the greater susceptibility to falls in patients with KOA compared with older adults.

Some limitations should be noted. First, the sample size of the KOA group in the current study is relatively small, with only nine patients including both males and females. Small samples may result in reduced statistical power, less reliability, and inflated effect sizes, which in turn may limit the general applicability of the findings (Mullineaux et al., 2001). However, a recent study suggests that a target power of 0.8 involving one-dimensional data effects could be achieved with small to moderate sample sizes (n = 5–40) in biomechanical experiments (Robinson et al., 2021). Therefore, we believe that our study should be feasible. For the follow-up study, we will recruit more patients with similar severity to further confirm our results. Second, we did not consider sex-induced differences in the investigated biomechanical parameters, since Phinyomark et al. (2016) found no significant differences in any discrete gait kinematic variables between KOA and healthy subjects by gender (Phinyomark et al., 2016). Furthermore, we did not directly analyze muscle forces acting in the lower extremity, which is an interesting aspect for future studies.

CONCLUSION

Compared with healthy older individuals, patients with KOA have a higher risk of falling in response to a backward slip perturbation, which could be monitored effectively by key parameters such as hip angle, moment, knee ROM, and vGRFs. Patients with KOA should focus on the strength and activation of the muscles that play a major role in hip extension during gait from another perspective, i.e., the gluteus maximus and adductor magus, etc., and improve hip extension with specific exercises, such as targeted resistance training and perturbation-based stepping state training while focusing on knee-related quadriceps strength. This could be essential in addressing backward slip-induced gait perturbations.

DATA AVAILABILITY STATEMENT

The raw data supporting the conclusion of this article will be made available by the authors, without undue reservation.

ETHICS STATEMENT

The studies involving human participants were reviewed and approved by the committee of the Rostock University Medical

Center, Germany. The patients/participants provided their written informed consent to participate in this study. Written informed consent was obtained from the individual(s) for the publication of any potentially identifiable images or data included in this article.

AUTHOR CONTRIBUTIONS

XR, CL, MK, SB, RB, and TT conceived and designed this study. SB and RB provided the lab and equipment for the entire measurement. XR and CL conducted data collecting, data processing, and analysis. XR, CL, QY, and TT prepared the manuscript. XR, CL, MK, QY, SB, RB, and TT commented, revised the manuscript, and all approved for submission.

FUNDING

This work was jointly funded by Zhejiang Normal University (Jinhua, China) and Biomechanics and Implant Technology Research Laboratory (Rostock, Germany). The GRAIL system was supported by the German Research Foundation (DFG, INST 264/137–1). The funding sources have no role in the study design, data collection, analysis, interpretation of data, the writing of this article or the decision to submit it for publication.

ACKNOWLEDGMENTS

We would like to thank Frank Feldhege for the technical support during data collection.

REFERENCES

Alenazi, A. M., Alqahtani, B. A., Vennu, V., Alshehri, M. M., Alanazi, A. D., Alrawaili, S. M., et al. (2021). Gait Speed as a Predictor for Diabetes Incidence in People with or at Risk of Knee Osteoarthritis: A Longitudinal Analysis from the Osteoarthritis Initiative. *Ijerph* 18, 4414. doi:10.3390/ijerph18094414

Alencar, M. A., Arantes, P. M. M., Dias, J. M. D., Kirkwood, R. N., Pereira, L. S. M., and Dias, R. C. (2007). Muscular Function and Functional Mobility of Faller and Non-faller Elderly Women with Osteoarthritis of the Knee. *Braz J. Med. Biol. Res.* 40, 277–283. doi:10.1590/S0100-879X2007000200016

Alnahdi, A. H., Zeni, J. A., and Snyder-Mackler, L. (2012). Muscle Impairments in Patients with Knee Osteoarthritis. *Sports Health* 4, 284–292. doi:10.1177/1941738112445726

Asay, J. L., Erhart-Hledik, J. C., and Andriacchi, T. P. (2018). Changes in the Total Knee Joint Moment in Patients with Medial Compartment Knee Osteoarthritis over 5 Years. *J. Orthop. Res.* 36, 2373–2379. doi:10.1002/jor.23908

Astephen, J. L., Deluzio, K. J., Caldwell, G. E., and Dunbar, M. J. (2008). Biomechanical Changes at the Hip, Knee, and Ankle Joints during Gait Are Associated with Knee Osteoarthritis Severity. *J. Orthop. Res.* 26, 332–341. doi:10.1002/jor.20496

Bahadori, S., Williams, J. M., and Wainwright, T. W. (2021). Lower Limb Kinematic, Kinetic and Spatial-Temporal Gait Data for Healthy Adults Using a Self-Paced Treadmill. *Data Brief* 34, 106613. doi:10.1016/j.dib.2020.106613

Bisseling, R. W., and Hof, A. L. (2006). Handling of Impact Forces in Inverse Dynamics. *J. Biomechanics* 39, 2438–2444. doi:10.1016/j.jbiomech.2005.07.021

Bovi, G., Rabuffetti, M., Mazzoleni, P., and Ferrarin, M. (2011). A Multiple-Task Gait Analysis Approach: Kinematic, Kinetic and EMG Reference Data for Healthy Young and Adult Subjects. *Gait Posture* 33, 6–13. doi:10.1016/j.gaitpost.2010.08.009

Brinkmann, J. R., and Perry, J. (1985). Rate and Range of Knee Motion during Ambulation in Healthy and Arthritic Subjects. *Phys. Ther.* 65, 1055–1060. doi:10.1093/ptj/65.7.1055

Chandler, J. M., Duncan, P. W., and Studenski, S. A. (1990). Balance Performance on the Postural Stress Test: Comparison of Young Adults, Healthy Elderly, and Fallers. *Phys. Ther.* 70, 410–415. doi:10.1093/ptj/70.7.410

Cross, M., Smith, E., Hoy, D., Nolte, S., Ackerman, I., Fransen, M., et al. (2014). The Global Burden of Hip and Knee Osteoarthritis: Estimates from the Global Burden of Disease 2010 Study. *Ann. Rheum. Dis.* 73, 1323–1330. doi:10.1136/annrheumdis-2013-204763

Cui, A., Li, H., Wang, D., Zhong, J., Chen, Y., and Lu, H. (2020). Global, Regional Prevalence, Incidence and Risk Factors of Knee Osteoarthritis in Population-Based Studies. *EClinicalMedicine* 29-30, 100587. doi:10.1016/j.eclinm.2020.100587

Deasy, M., Leahy, E., and Semciw, A. I. (2016). Hip Strength Deficits in People with Symptomatic Knee Osteoarthritis: A Systematic Review with Meta-Analysis. *J. Orthop. Sports Phys. Ther.* 46, 629–639. doi:10.2519/jospt.2016.6618

Debelle, H., Harkness-Armstrong, C., Hadwin, K., Maganaris, C. N., and O'Brien, T. D. (2020). Recovery from a Forward Falling Slip: Measurement of Dynamic Stability and Strength Requirements Using a Split-Belt Instrumented Treadmill. *Front. Sports Act. Living* 2, 82. doi:10.3389/fspor.2020.00082

Debelle, H., Maganaris, C. N., and O'Brien, T. D. (2021). Biomechanical Mechanisms of Improved Balance Recovery to Repeated Backward Slips Simulated by Treadmill Belt Accelerations in Young and Older Adults. *Front. Sports Act. Living* 3, 1–15. doi:10.3389/fspor.2021.708929

Debi, R., Mor, A., Segal, G., Debbi, E. M., Cohen, M. S., Igolnikov, I., et al. (2012). Differences in Gait Pattern Parameters between Medial and Anterior Knee Pain in Patients with Osteoarthritis of the Knee. *Clin. Biomech.* 27, 584–587. doi:10.1016/j.clinbiomech.2012.02.002

Deng, Z. h., Xu, J., Long, L. j., Chen, F., Chen, K., Lu, W., et al. (2021). Association between Hip and Knee Osteoarthritis with Falls: A Systematic Review and Meta-analysis. *Int. J. Clin. Pract.* 75. doi:10.1111/ijcp.14537

Doré, A. L., Golightly, Y. M., Mercer, V. S., Shi, X. A., Renner, J. B., Jordan, J. M., et al. (2015). Lower-extremity Osteoarthritis and the Risk of Falls in a Community-Based Longitudinal Study of Adults with and without Osteoarthritis. *Arthritis Care & Res.* 67, 633–639. doi:10.1002/acr.22499

Ebihara, B., Mutsuzaki, H., Fukaya, T., and Iwai, K. (2021). Interpretation of Causal Relationship between Quadriceps Tendon Young's Modulus and Gait Speed by Structural Equation Modeling in Patients with Severe Knee Osteoarthritis. *J. Orthop. Surg. Hong. Kong)* 29, 230949902110340–230949902110347. doi:10.1177/23094990211034003

Falisse, A., Van Rossom, S., Gijsbers, J., Steenbrink, F., van Basten, B. J. H., Jonkers, I., et al. (2018). OpenSim Versus Human Body Model: A Comparison Study for the Lower Limbs During Gait. *J. Appl. Biomech.* 34, 496–502. doi:10.1123/jab.2017-0156

Fisher, N. M., White, S. C., Yack, H. J., Smolinski, R. J., and Pendergast, D. R. (1997). Muscle Function and Gait in Patients with Knee Osteoarthritis before and after Muscle Rehabilitation. *Disabil. Rehabilitation* 19, 47–55. doi:10.3109/09638289709166827

Flux, E., van der Krogt, M. M., Cappa, P., Petrarca, M., Desloovere, K., and Harlaar, J. (2020). The Human Body Model versus Conventional Gait Models for Kinematic Gait Analysis in Children with Cerebral Palsy. *Hum. Mov. Sci.* 70, 102585. doi:10.1016/j.humov.2020.102585

Fukuchi, C. A., Fukuchi, R. K., and Duarte, M. (2019). Effects of Walking Speed on Gait Biomechanics in Healthy Participants: A Systematic Review and Meta-Analysis. *Syst. Rev.* 8, 1–11. doi:10.1186/s13643-019-1063-z

Gholizadeh, H., Hill, A., and Nantel, J. (2019). Effect of Arm Motion on Postural Stability when Recovering from a Slip Perturbation. *J. Biomechanics* 95, 109269. doi:10.1016/j.jbiomech.2019.07.013

Gill, S. V., Hicks, G. E., Zhang, Y., Niu, J., Apovian, C. M., and White, D. K. (2017). The Association of Waist Circumference with Walking Difficulty Among Adults with or at Risk of Knee Osteoarthritis: the Osteoarthritis Initiative. *Osteoarthr. Cartil.* 25, 60–66. doi:10.1016/j.joca.2016.07.011

Gonçalves, G. H., Sendín, F. A., da Silva Serrão, P. R. M., Selistre, L. F. A., Petrella, M., Carvalho, C., et al. (2017). Ankle Strength Impairments Associated with

Knee Osteoarthritis. *Clin. Biomech.* 46, 33–39. doi:10.1016/j.clinbiomech.2017.05.002

Hyodo, K., Kanamori, A., Kadone, H., Takahashi, T., Kajiwara, M., and Yamazaki, M. (2020). Gait Analysis Comparing Kinematic, Kinetic, and Muscle Activation Data of Modern and Conventional Total Knee Arthroplasty. *Arthroplasty Today* 6, 338–342. doi:10.1016/j.artd.2020.03.011

Inkol, K. A., Huntley, A. H., and Vallis, L. A. (2019). Repeated Exposure to Forward Support-Surface Perturbation during Overground Walking Alters Upper-Body Kinematics and Step Parameters. *J. Mot. Behav.* 51, 318–330. doi:10.1080/00222895.2018.1474336

Karamanidis, K., Epro, G., McCrum, C., and König, M. (2020). Improving Trip- and Slip-Resisting Skills in Older People: Perturbation Dose Matters. *Exerc. Sport Sci. Rev.* 48, 40–47. doi:10.1249/JES.0000000000000210

Kebbach, M., Darowski, M., Krueger, S., Schilling, C., Grupp, T. M., Bader, R., et al. (2020). Musculoskeletal Multibody Simulation Analysis on the Impact of Patellar Component Design and Positioning on Joint Dynamics after Unconstrained Total Knee Arthroplasty. *Materials* 13, 2365. doi:10.3390/ma13102365

King, L. K., Kendzerska, T., Waugh, E. J. E., and Hawker, G. A. G. (2018). Impact of Osteoarthritis on Difficulty Walking: A Population-Based Study. *Arthritis Care Res.* 70, 71–79. doi:10.1002/acr10.1002/acr.23250

Kirkwood, R. N., Resende, R. A., Magalhães, C. M. B., Gomes, H. A., Mingoti, S. A., and Sampaio, R. F. (2011). Aplicação da análise de componentes principais na cinemática da marcha de idosas com osteoartrite de joelho. *Rev. Bras. Fisioter.* 15, 52–58. doi:10.1590/S1413-35552011000100007

Kotti, M., Duffell, L. D., Faisal, A. A., and McGregor, A. H. (2014). The Complexity of Human Walking: A Knee Osteoarthritis Study. *PLoS ONE* 9, e107325. doi:10.1371/journal.pone.0107325

Kribus-Shmiel, L., Zeilig, G., Sokolovski, B., and Plotnik, M. (2018). How Many Strides Are Required for a Reliable Estimation of Temporal Gait Parameters? Implementation of a New Algorithm on the Phase Coordination Index. *PLoS ONE* 13, e0192049–16. doi:10.1371/journal.pone.0192049

Kroneberg, D., Elshehabi, M., Meyer, A.-C., Otte, K., Doss, S., Paul, F., et al. (2019). Less Is More - Estimation of the Number of Strides Required to Assess Gait Variability in Spatially Confined Settings. *Front. Aging Neurosci.* 10, 1–13. doi:10.3389/fnagi.2018.00435

Lamb, S. E., Bruce, J., Hossain, A., Ji, C., Longo, R., Lall, R., et al. (2020). Screening and Intervention to Prevent Falls and Fractures in Older People. *N. Engl. J. Med.* 383, 1848–1859. doi:10.1056/nejmoa2001500

Lathrop-Lambach, R. L., Asay, J. L., Jamison, S. T., Pan, X., Schmitt, L. C., Blazek, K., et al. (2014). Evidence for Joint Moment Asymmetry in Healthy Populations during Gait. *Gait Posture* 40, 526–531. doi:10.1016/j.gaitpost.2014.06.010

Lee, A., Bhatt, T., Liu, X., Wang, Y., Wang, S., and Pai, Y.-C. (2020). Can Treadmill Slip-Perturbation Training Reduce Longer-Term Fall Risk upon Overground Slip Exposure? *J. Appl. Biomechanics* 36, 298–306. doi:10.1123/JAB.2019-0211

Li, S., Ng, W. H., Abujaber, S., and Shaharudin, S. (2021). Effects of Resistance Training on Gait Velocity and Knee Adduction Moment in Knee Osteoarthritis Patients: a Systematic Review and Meta-Analysis. *Sci. Rep.* 11, 1–11. doi:10.1038/s41598-021-95426-4

Lisee, C., Birchmeier, T., Yan, A., and Kuenze, C. (2019). Associations between Isometric Quadriceps Strength Characteristics, Knee Flexion Angles, and Knee Extension Moments during Single Leg Step Down and Landing Tasks after Anterior Cruciate Ligament Reconstruction. *Clin. Biomech.* 70, 231–236. doi:10.1016/j.clinbiomech.2019.10.012

Liu, J., and Lockhart, T. E. (2009). Age-related Joint Moment Characteristics during Normal Gait and Successful Reactive-Recovery from Unexpected Slip Perturbations. *Gait Posture* 30, 276–281. doi:10.1016/j.gaitpost.2009.04.005

Liu, X., Bhatt, T., Wang, S., Yang, F., Pai, Y.-C., and Clive) (2017). Retention of the "First-Trial Effect" in Gait-Slip Among Community-Living Older Adults. *GeroScience* 39, 93–102. doi:10.1007/s11357-017-9963-0

Maki, B. E., and McIlroy, W. E. (1997). The Role of Limb Movements in Maintaining Upright Stance: The "Change-In-Support" Strategy. *Phys. Ther.* 77, 488–507. doi:10.1093/ptj/77.5.488

Manlapaz, D. G., Sole, G., Jayakaran, P., and Chapple, C. M. (2019). Risk Factors for Falls in Adults with Knee Osteoarthritis: A Systematic Review. *PM&R.* 11, 745–757. doi:10.1002/pmrj.12066

Marigold, D. S., Bethune, A. J., and Patla, A. E. (2003). Role of the Unperturbed Limb and Arms in the Reactive Recovery Response to an Unexpected Slip during Locomotion. *J. Neurophysiology* 89, 1727–1737. doi:10.1152/jn.00683.2002

McCarthy, I., Hodgins, D., Mor, A., Elbaz, A., and Segal, G. (2013). Analysis of Knee Flexion Characteristics and How They Alter with the Onset of Knee Osteoarthritis: A Case Control Study. *BMC Musculoskelet. Disord.* 14. doi:10.1186/1471-2474-14-169

Melzer, I., Elbar, O., Tsedek, I., and Oddsson, L. I. (2008). A Water-Based Training Program that Include Perturbation Exercises to Improve Stepping Responses in Older Adults: Study Protocol for a Randomized Controlled Cross-Over Trial. *BMC Geriatr.* 8, 1–13. doi:10.1186/1471-2318-8-19

Meyer, C., Killeen, T., Easthope, C. S., Curt, A., Bolliger, M., Linnebank, M., et al. (2019). Familiarization with Treadmill Walking: How Much Is Enough? *Sci. Rep.* 9, 1–10. doi:10.1038/s41598-019-41721-0

Milner, C. E., Meardon, S. A., Hawkins, J. L., and Willson, J. D. (2018). Walking Velocity and Step Length Adjustments Affect Knee Joint Contact Forces in Healthy Weight and Obese Adults. *J. Orthop. Res.* 36, 2679–2686. doi:10.1002/jor.24031

Moisio, K. C., Sumner, D. R., Shott, S., and Hurwitz, D. E. (2003). Normalization of Joint Moments during Gait: A Comparison of Two Techniques. *J. Biomechanics* 36, 599–603. doi:10.1016/S0021-9290(02)00433-5

Moustakidis, S. P., Theocharis, J. B., and Giakas, G. (2010). A Fuzzy Decision Tree-Based SVM Classifier for Assessing Osteoarthritis Severity Using Ground Reaction Force Measurements. *Med. Eng. Phys.* 32, 1145–1160. doi:10.1016/j.medengphy.2010.08.006

Mullineaux, D. R., Bartlett, R. M., and Bennett, S. (2001). Research Design and Statistics in Biomechanics and Motor Control. *J. Sports Sci.* 19, 739–760. doi:10.1080/026404101317015410

Nagano, H., Sparrow, W. A., and Begg, R. K. (2013). Biomechanical Characteristics of Slipping during Unconstrained Walking, Turning, Gait Initiation and Termination. *Ergonomics* 56, 1038–1048. doi:10.1080/00140139.2013.787122

Neogi, T. (2013). The Epidemiology and Impact of Pain in Osteoarthritis. *Osteoarthr. Cartil.* 21, 1145–1153. doi:10.1016/j.joca.2013.03.018

Neumann, D. A. (2010). Kinesiology of the Hip: A Focus on Muscular Actions. *J. Orthop. Sports Phys. Ther.* 40, 82–94. doi:10.2519/jospt.2010.3025

Oudenhoven, L. M., Booth, A. T. C., Buizer, A. I., Harlaar, J., and van der Krogt, M. M. (2019). How Normal Is Normal: Consequences of Stride to Stride Variability, Treadmill Walking and Age when Using Normative Paediatric Gait Data. *Gait Posture* 70, 289–297. doi:10.1016/j.gaitpost.2019.03.011

Pai, Y.-C., and Bhatt, T. S. (2007). Repeated-slip Training: An Emerging Paradigm for Prevention of Slip-Related Falls Among Older Adults. *Phys. Ther.* 87, 1478–1491. doi:10.2522/ptj.20060326

Pataky, T. C., Vanrenterghem, J., and Robinson, M. A. (2015). Zero- vs. One-Dimensional, Parametric vs. Non-parametric, and Confidence Interval vs. Hypothesis Testing Procedures in One-Dimensional Biomechanical Trajectory Analysis. *J. Biomechanics* 48, 1277–1285. doi:10.1016/j.jbiomech.2015.02.051

Peel, N. M., Kuys, S. S., and Klein, K. (2013). Gait Speed as a Measure in Geriatric Assessment in Clinical Settings: A Systematic Review. *Journals Gerontology - Ser. A Biol. Sci. Med. Sci.* 68, 39–46. doi:10.1093/gerona/gls174

Phinyomark, A., Osis, S. T., Hettinga, B. A., Kobsar, D., and Ferber, R. (2016). Gender Differences in Gait Kinematics for Patients with Knee Osteoarthritis. *BMC Musculoskelet. Disord.* 17, 1–12. doi:10.1186/s12891-016-1013-z

Prieto-Alhambra, D., Nogues, X., Javaid, M. K., Wyman, A., Arden, N. K., Azagra, R., et al. (2013). An Increased Rate of Falling Leads to a Rise in Fracture Risk in Postmenopausal Women with Self-Reported Osteoarthritis: A Prospective Multinational Cohort Study (GLOW). *Ann. Rheum. Dis.* 72, 911–917. doi:10.1136/annrheumdis-2012-201451

Purser, J. L., Golightly, Y. M., Feng, Q., Helmick, C. G., Renner, J. B., and Jordan, J. M. (2012). Slower Walking Speed Is Associated with Incident Knee Osteoarthritis-Related Outcomes. *Arthritis Care Res.* 64, a–n. doi:10.1002/acr.21655

Queen, R. M., Sparling, T. L., and Schmitt, D. (2016). Hip, Knee, and Ankle Osteoarthritis Negatively Affects Mechanical Energy Exchange. *Clin. Orthop. Relat. Res.* 474, 2055–2063. doi:10.1007/s11999-016-4921-1

Riazati, S., Caplan, N., and Hayes, P. R. (2019). The Number of Strides Required for Treadmill Running Gait Analysis Is Unaffected by Either Speed or Run Duration. *J. Biomechanics* 97, 109366. doi:10.1016/j.jbiomech.2019.109366

Robinson, M. A., Vanrenterghem, J., and Pataky, T. C. (2021). Sample Size Estimation for Biomechanical Waveforms: Current Practice,

Recommendations and a Comparison to Discrete Power Analysis. *J. Biomechanics* 122, 110451. doi:10.1016/j.jbiomech.2021.110451

Sharma, L. (2021). Osteoarthritis of the Knee. *N. Engl. J. Med.* 384, 51–59. doi:10.1056/NEJMCP1903768

Spinoso, D. H., Bellei, N. C., Marques, N. R., and Navega, M. T. (2018). Quadriceps Muscle Weakness Influences the Gait Pattern in Women with Knee Osteoarthritis. *Adv. Rheumatol.* 58, 26. doi:10.1186/s42358-018-0027-7

Steultjens, M. P. M., Dekker, J., Van Baar, M. E., Oostendorp, R. A. B., and Bijlsma, J. W. J. (2000). Range of Joint Motion and Disability in Patients with Osteoarthritis of the Knee or Hip. *Rheumatology* 39, 955–961. doi:10.1093/rheumatology/39.9.955

Sun, J., Liu, Y., Yan, S., Cao, G., Wang, S., Lester, D. K., et al. (2017). Clinical Gait Evaluation of Patients with Knee Osteoarthritis. *Gait Posture* 58, 319–324. doi:10.1016/j.gaitpost.2017.08.009

Tang, S. F., Chen, C. P., Chen, M. J., Pei, Y.-C., Lau, Y.-C., and Leong, C.-P. (2004). Changes in Sagittal Ground Reaction Forces after Intra-articular Hyaluronate Injections for Knee osteoarthritis11No Commercial Party Having a Direct Financial Interest in the Results of the Research Supporting This Article Has or Will Confer a Benefit upon the Author(s) or upon Any Organization with Which the Author(s) Is/are Associated. *Archives Phys. Med. Rehabilitation* 85, 951–955. doi:10.1016/j.apmr.2003.08.095

Tas, S., Güneri, S., Baki, A., Yildirim, T., Kaymak, B., and Erden, Z. (2014). Effects of Severity of Osteoarthritis on the Temporospatial Gait Parameters in Patients with Knee Osteoarthritis. *Acta Orthop. Traumatol. Turc* 48, 635–641. doi:10.3944/AOTT.2014.13.0071

Tischer, T., Geier, A., Lenz, R., Woernle, C., and Bader, R. (2017). Impact of the Patella Height on the Strain Pattern of the Medial Patellofemoral Ligament after Reconstruction: a Computer Model-Based Study. *Knee Surg. Sports Traumatol. Arthrosc.* 25, 3123–3133. doi:10.1007/s00167-016-4190-2

van den Bogaart, M., Bruijn, S. M., van Dieën, J. H., and Meyns, P. (2020). The Effect of Anteroposterior Perturbations on the Control of the Center of Mass during Treadmill Walking. *J. Biomechanics* 103, 109660. doi:10.1016/j.jbiomech.2020.109660

Van Den Bogert, A. J., Geijtenbeek, T., Even-Zohar, O., Steenbrink, F., and Hardin, E. C. (2013). A Real-Time System for Biomechanical Analysis of Human Movement and Muscle Function. *Med. Biol. Eng. Comput.* 51, 1069–1077. doi:10.1007/s11517-013-1076-z

Vennu, V., and Misra, H. (2018). Evaluation of Gait Speed over Time in Adults with Arthritis: Data from the Osteoarthritis Initiative. *Indian J. Rheumatol.* 13, 154–158. doi:10.4103/injr.injr_34_18

Wallace, I. J., Worthington, S., Felson, D. T., Jurmain, R. D., Wren, K. T., Maijanen, H., et al. (2017). Knee Osteoarthritis Has Doubled in Prevalence since the Mid-20th Century. *Proc. Natl. Acad. Sci. U.S.A.* 114, 9332–9336. doi:10.1073/pnas.1703856114

Wiik, A. V., Aqil, A., Brevadt, M., Jones, G., and Cobb, J. (2017). Abnormal Ground Reaction Forces Lead to a General Decline in Gait Speed in Knee Osteoarthritis Patients. *Wjo* 8, 322–328. doi:10.5312/wjo.v8.i4.322

Winter, D. A., Sidwall, H. G., and Hobson, D. A. (1974). Measurement and Reduction of Noise in Kinematics of Locomotion. *J. Biomechanics* 7, 157–159. doi:10.1016/0021-9290(74)90056-6

Wojcik, L. A., Thelen, D. G., Schultz, A. B., Ashton-Miller, J. A., and Alexander, N. B. (1999). Age and Gender Differences in Single-step Recovery from a Forward Fall. *Journals Gerontology Ser. A Biol. Sci. Med. Sci.* 54, M44–M50. doi:10.1093/gerona/54.1.M44

Yoo, D., Seo, K.-H., and Lee, B.-C. (2019). The Effect of the Most Common Gait Perturbations on the Compensatory Limb's Ankle, Knee, and Hip Moments during the First Stepping Response. *Gait Posture* 71, 98–104. doi:10.1016/j.gaitpost.2019.04.013

Zeighami, A., Dumas, R., and Aissaoui, R. (2021). Knee Loading in OA Subjects Is Correlated to Flexion and Adduction Moments and to Contact Point Locations. *Sci. Rep.* 11, 1–9. doi:10.1038/s41598-021-87978-2

Zeni, J. A., and Higginson, J. S. (2009). Differences in Gait Parameters between Healthy Subjects and Persons with Moderate and Severe Knee Osteoarthritis: A Result of Altered Walking Speed? *Clin. Biomech.* 24, 372–378. doi:10.1016/j.clinbiomech.2009.02.001

Zeni, J. A., Richards, J. G., and Higginson, J. S. (2008). Two Simple Methods for Determining Gait Events during Treadmill and Overground Walking Using Kinematic Data. *Gait Posture* 27, 710–714. doi:10.1016/j.gaitpost.2007.07.007

Conflict of Interest: The authors declare that the research was conducted in the absence of any commercial or financial relationships that could be construed as a potential conflict of interest.

frontiers | Frontiers in Bioengineering and Biotechnology

ORIGINAL RESEARCH
published: 20 June 2022
doi: 10.3389/fbioe.2022.920462

A Framework for Determining the Performance and Requirements of Cable-Driven Mobile Lower Limb Rehabilitation Exoskeletons

Rajan Prasad[1], *Marwan El-Rich*[1,2]*, *Mohammad I. Awad*[1,2,3], *Irfan Hussain*[1,3], *H.F. Jelinek*[2,4,5], *Umer Huzaifa*[6] *and Kinda Khalaf*[2,4]

[1]Department of Mechanical Engineering, Khalifa University of Science Technology and Research, Abu Dhabi, United Arab Emirates, [2]Health Engineering Innovation Center, Khalifa University of Science Technology and Research, Abu Dhabi, United Arab Emirates, [3]Khalifa University Center for Autonomous Robotic Systems (KUCARS), Khalifa University of Science Technology and Research, Abu Dhabi, United Arab Emirates, [4]Department of Biomedical Engineering, Khalifa University of Science Technology and Research, Abu Dhabi, United Arab Emirates, [5]Center for Biotechnology, Khalifa University of Science Technology and Research, Abu Dhabi, United Arab Emirates, [6]School of Computing, DePaul University, Chicago, IL, United States

OPEN ACCESS

Edited by:
Ching-Chi Hsu,
National Taiwan University of Science and Technology, Taiwan

Reviewed by:
Anand Kumar Mishra,
Cornell University, United States
Shu-Yu Jhou,
National Taiwan University of Science and Technology, Taiwan

***Correspondence:**
Marwan El-Rich
marwan.elrich@ku.ac.ae

Specialty section:
This article was submitted to Biomechanics, a section of the journal Frontiers in Bioengineering and Biotechnology

Received: *14 April 2022*
Accepted: *30 May 2022*
Published: *20 June 2022*

Citation:
Prasad R, El-Rich M, Awad MI, Hussain I, Jelinek HF, Huzaifa U and Khalaf K (2022) A Framework for Determining the Performance and Requirements of Cable-Driven Mobile Lower Limb Rehabilitation Exoskeletons. Front. Bioeng. Biotechnol. 10:920462. doi: 10.3389/fbioe.2022.920462

The global increase in the number of stroke patients and limited accessibility to rehabilitation has promoted an increase in the design and development of mobile exoskeletons. Robot-assisted mobile rehabilitation is rapidly emerging as a viable tool as it could provide intensive repetitive movement training and timely standardized delivery of therapy as compared to conventional manual therapy. However, the majority of existing lower limb exoskeletons continue to be heavy and induce unnecessary inertia and inertial vibration on the limb. Cable-driven exoskeletons can overcome these issues with the provision of remote actuation. However, the number of cables and routing can be selected in various ways posing a challenge to designers regarding the optimal design configuration. In this work, a simulation-based generalized framework for modelling and assessment of cable-driven mobile exoskeleton is proposed. The framework can be implemented to identify a 'suitable' configuration from several potential ones or to identify the optimal routing parameters for a given configuration. For a proof of concept, four conceptual configurations of cable-driven exoskeletons (one with a spring) were developed in a manner where both positive and negative moments could be generated for each joint (antagonistic configuration). The models were analyzed using the proposed framework and a decision metric table has been developed based on the models' performance and requirements. The weight of the metrics can be adjusted depending on the preferences and specified constraints. The maximum score is assigned to the configuration with minimum requirement or error, maximum performance, and *vice versa*. The metric table indicated that the 4-cable configuration is a promising design option for a lower limb rehabilitation exoskeleton based on tracking performance, model requirements, and component forces exerted on the limb.

Keywords: lower limb rehabilitation, cable-driven exoskeleton, performance analysis, generalized framework, link-based model, tracking

INTRODUCTION

According to World Health Organization (WHO), stroke is the second leading cause of mortality and the third leading cause of long-term disability worldwide (Johnson et al., 2016). In 2020, 13.7 million people around the world had their first stroke, and five and a half million consequently lost their lives (Learn about stroke, 2022). In general, up to 74% of stroke survivors have physical, cognitive, and emotional challenges leading them to become dependent in activities of daily living (ADL). Movement impairment post-stroke most often affects the upper or lower limb on one side of the body resulting in hemiparetic gait (Sheffler and Chae, 2015) which induces compensatory motion on the healthy, contralateral limb (Balaban and Tok, 2014). In hemiparetic gait, various spatiotemporal parameters, including velocity, step and stride length, stance on the paretic limb, and cadence are significantly compromised (Sheffler and Chae, 2015). This alteration primarily stems from impairment in motor control, muscle spasticity, and degraded strength, as well as abnormal muscle synergistic activation and interaction (Li et al., 2018). Moreover, the duration of the double support phase (DSP) and that of the paretic limb swing phase increase to maintain stability during walking. These changes in kinematic and spatiotemporal parameters often lead to asymmetric gait (Figueiredo et al., 2015) and result in further difficulties to complete ADL.

Rehabilitation improves ADL of stroke survivors and helps them walk independently by primarily focusing on regaining optimal muscle and nervous system function towards functional gait restoration. Stroke rehabilitation should start as early as possible. It should be repetitive and intensive, task-oriented, proportional to the patient's functional status, and designed to encourage and motivate the patient with the help of feedback (Winstein et al., 2016). Due to its multiple potential advantages over manual therapy, including automated, accurate, repetitive intervention, and the potential for tele and home rehabilitation solutions, robotic rehabilitation has recently been at the forefront of stroke rehabilitation research (Unluhisarcikli et al., 2011; Chen et al., 2013; Riener, 2016). Robots not only could provide task-based high intensity, repetitive functional movement training, but could also offer continuous and objective quantitative movement assessment, as well as economical solutions for large-scale use (Dao and Yamamoto, 2018). The last decade has witnessed an increasing focus on exoskeletons and rehabilitation devices. A remarkable number of powered and portable (autonomous power supply) lower-limb exoskeletons were designed to serve as assistive devices for ADL attainment as well as gait rehabilitation. The majority of these rehabilitation devices could be categorized as a tethered power supply (stationary (treadmill-based, or footplate-based); moving (over ground-based)); and portable (autonomous power supply). Most devices function by actuating joints directly (i.e., LOKOMAT (Riener, 2016), ANdROS (Unluhisarcikli et al., 2011), AIRGAIT (Dao and Yamamoto, 2018), and AGoRA (Sanchez-Manchola et al., 2018), etc.) where the actuators are mounted *via* links near the joints and the actuator along with the link induces both inertia and inertial vibration to the attached stroke-affected limb. Furthermore, direct actuation at the joint level requires strong structural support on the acting and reacting parts, which renders these systems heavy and bulky. In such designs, the system also tends to be less transparent as it compensates for the user as well as for the component (support and actuators) weights. In the direct actuation approach, the knee joint is assumed as a pin joint, which oversimplifies its biomechanics and may induce unnecessary moments (Wang et al., 2014) at the joint. Importantly, safety issues need to be taken into consideration when placing an actuator directly at a physiological joint, as the device closely interacts with the human body and any misalignment may induce undesired moments or torques, which could compromise the safety and comfort of the user.

Lower limb exoskeletons with remote actuator locations (distant from the joint), not only enhance the human interaction safety and function of the exoskeleton but also reduce the inertial vibration at the joint (Grosu et al., 2018). However, reducing or compensating alone for the exoskeleton's structural weight is not sufficient for restoring natural gait due to dominant inertial vibrations (Jin et al., 2017). Thus, to restore natural gait more closely, both weight and inertia-induced vibrations need to be minimized. Cable-driven rehabilitation devices (CDRD) were introduced to overcome these limitations (Bryson and Agrawal, 2014; Jin et al., 2015; Alamdari and Krovi, 2016; Witte et al., 2017). For Example, employing Bowden cables as transmission elements facilitate the remote location of the actuators and minimize the inertia and inertial vibration on the impaired limb as well as the need for strong structural support. Actuating *via* cables acts in a similar manner to an end effector (actuated by exerting force/moments at the end) and hence mitigates the burden of exact joint alignment.

C-ALEX (Jin et al., 2015) is an example of a 4 cable-driven rehabilitation device in which cables are routed through multiple cuffs mounted on the lower limb. An optimization-based strategy distributes the cable tensions to ensure that they are always taut, within the specified limit, and meet the required joint torque requirement at the joint. The robot employs both PD (proportional-derivative) and force-field controller to track the user's ankle motion during training. Experiments on healthy subjects revealed that C-ALEX assisted users to track the desired motion of the limb with the selected ankle trajectory. Kirby et al. (Witte et al., 2017) designed and tested a cable-driven knee rehabilitation exoskeleton using a powerful tethered testbed. The rehabilitator had a lightweight structure (0.76 kg) achieved by mounting the actuators and control accessories on a testbed which transmitted power to the rehabilitator *via* two cables allowing for rapid design modification in design. Although the device showed its potential as a knee rehabilitator, rehabilitating the knee joint alone was sufficient to regain a healthy gait trajectory in stroke patients. Bryson et al. (Bryson and Agrawal, 2014) analyzed a 3 DOFs robot leg actuated device using 4 cables to identify the optimal parameters most commonly associated with performance, such as cable routing and configuration. The configuration fulfilling the design requirements based on the analysis was used in designing the cable-driven robot. Aliakbar et al. (Alamdari and Krovi, 2016) designed a 4 cable-driven lower limb rehabilitation exoskeleton

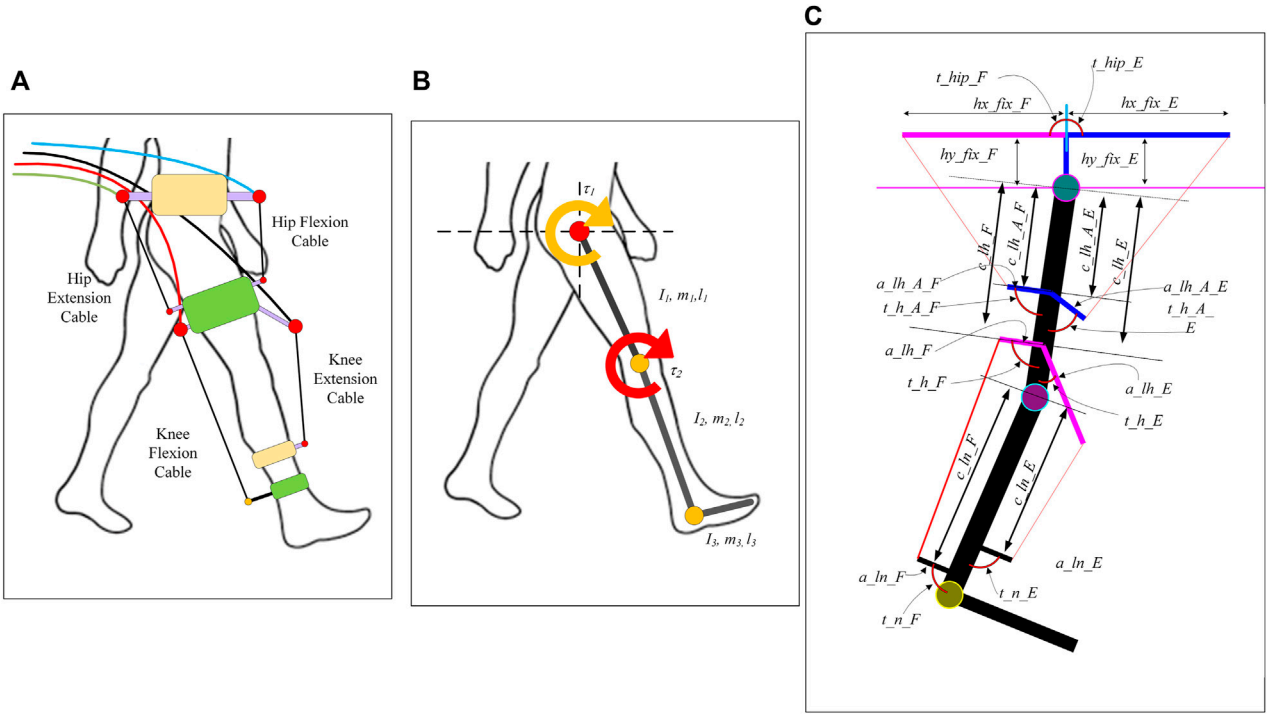

FIGURE 1 | Conceptual cable driven model **(A)**, 2 link-based model of lower limb **(B)**, and transformation of conceptual cable driven exoskeleton model into the link-based model **(C)**.

which tracked the lower limb joints and positions, employing a (PD) controller and force field controller respectively. The cables were routed from the fixed frame (attached to the treadmill) to the lower limb, where one cable was assigned for the hip and knee joint while the remaining cables were assigned for ankle tracking. The design constrained the overall device mobility along with the routing and configurability of cables.

Although it is well accepted that CDRD has immense potential in robotic rehabilitation, the optimal cable routing(s) and configuration toward enhancing design options and human safe interaction and comfort remain elusive. In the literature, cable configurations which meet the desired performance specifications and objectives while minimizing the system requirements have not been fully achieved, and there continues to be a lack of generalized methodology of modelling to accommodate a variety of configurations and routings. In this work, we purpose a generalized methodology/framework to evaluate the feasibility of various routings and configuration-based designs of cable-driven exoskeletons and provide metrics to help in selecting the suitable configuration for an optimal design based on the specified constraints.

MODELLING OF CABLE DRIVEN EXOSKELETONS

In our previous work (Prasad et al., 2022), we proposed a generalized framework for modelling a cable-driven exoskeleton. The proposed model can test the feasibility and performance of a variety of configurations and routing of cables. However, the framework assumed the hip cuff to be oriented at a fixed angle to the pelvis. In the current study, the framework has been extended to accommodate the hip cuff at any angle. This adaptation makes the model more realistic, modular, and configurable. Furthermore, a three-variable definition-based strategy was selected to fully define any cuff on the user's body. The framework assumes the lower limb as a 2-link model (thigh and shank) with the foot being fixed perpendicular to the shank (**Figure 1**). Exoskeleton assistance is provided only during the swing phase of the motion assuming that the person can continue the stance phase on their own. For the sake of simulation, the leg is assumed to be suspended in air replicating the swing phase.

The equation of motion formulated in MATLAB using Euler-Lagrange can be written as:

$$M(\theta)\ddot{\theta} + C\left(\theta, \dot{\theta}\right)\dot{\theta} + G(\theta) = \tau \tag{1}$$

Where $M(\theta)$ represents the inertial matrix (2 × 2), $C(\theta, \dot{\theta})$ represents the Coriolis component (2 × 1), $G(\theta)$ represents the Gravitational components (2 × 1), and τ represents the torques on the joints.

Generalized Cuff Parameters

The model was created such that any cuff placed on the user's limb (either pelvis, thigh, or shank) can be defined using three

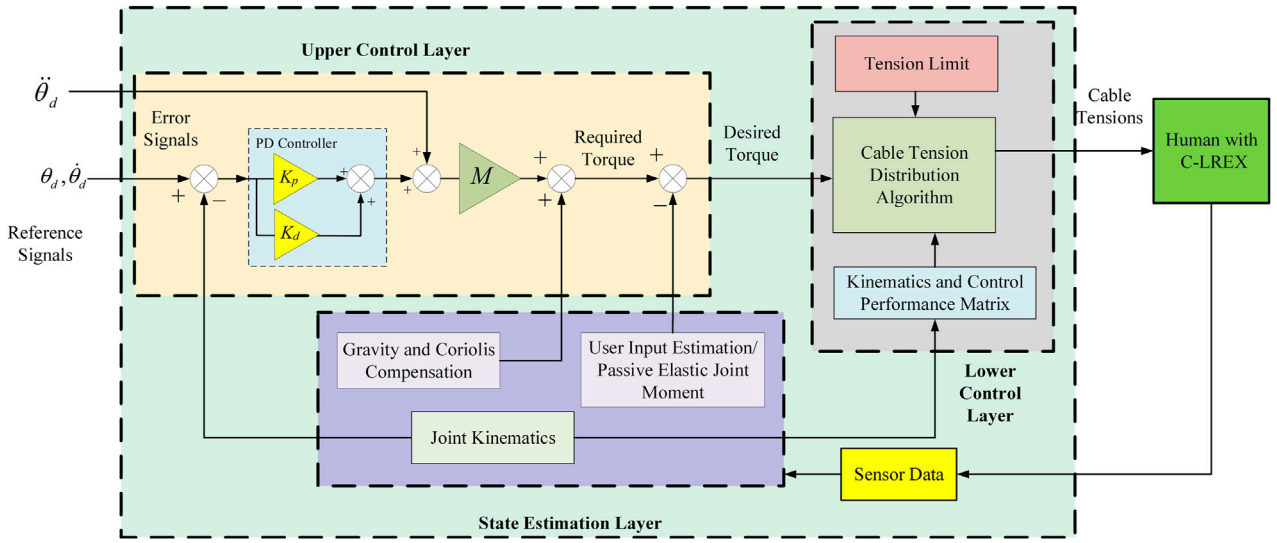

FIGURE 2 | Generalized control strategy.

parameters as shown in **Figure 1C**. ***F*** and ***E*** represent the posterior (back) and anterior (front) sides of the leg. The measured angles are assumed positive in the clockwise direction.

The three defined parameters are

1) The distance of the cuff from the nearest joint (hip for thigh and pelvis, knee for shank cuffs).
2) The length of the cuff.
3) The angle of the cuff from the attached limb part (measured by viewing from the cuff to the nearest joint).

For example, the shank cuff on the posterior side can be fully defined using three parameters *c_ln_F, a_ln_F, and t_n_F* respectively. All the other cuffs can be defined similarly.

Control System

The controller used in this study is an impedance controller where a PD controller is employed to estimate the desired torque based on the errors, similar to controllers used in orthoses (impedance control) reported in (Unluhisarcikli et al., 2011) (Riener et al., 2005) (Tucker et al., 2015). The desired trajectory during motion is tracked using a three-layer control algorithm based on the 2-link model. **Figure 2** depicts the generalized control strategy with the all-control layers. C-LREX stands for the Cable driven Lower limb Rehabilitation Exoskeleton.

Upper Control Layer

The upper control layer is responsible for generating the desired torque required for tracking the next step based on the current motion step. It can employ various controllers such as PID (proportional—integral-derivative), MPC (model predictive control), SMC (sliding mode control), etc. In the current controller, PD-based feedback linearization was used to transform the error dynamics system into an exponentially stable system and is defined as: $\tau = M(K_p e + K_d \dot{e} + \ddot{\theta}_d) + C\dot{\theta} + G$ Where K_p and K_d are diagonal matrices $K_p = diag(K_{p1}, K_{p2})$, $K_d = diag(K_{d1}, K_{d2})$ With this feedback linearization, the error dynamics can be written as: $K_p e + K_d \dot{e} + \ddot{e} = 0$.

The above feedback linearization yields the required torque to track the trajectory. The passive elastic joint moment is considered as the user's voluntary contribution during walking and is subtracted from the required torque to estimate the desired torque, which is then re-distributed among the cables *via* the cable tension distribution module.

State Estimation Layer

The state estimation layer is responsible for identifying current angles, angular velocities, inertial and other matrices (*M, C, G*), as well as the user's voluntary input based on the sensor's data. The sensor data may include kinematics, kinetics, or both depending on the requirements (angle, angular velocity, angular acceleration, and cable tension). The matrices are calculated using kinematics data and the 2-link model equations listed in **Eq. 1**. At present, the model considers passive elastic joint moment as the user's voluntary input during the motion. The anthropometric data required for the model is obtained using Winter's (Winter 2009) model based on the user's height and weight.

The active joint moment accounts for the active muscle contribution while the passive joint moment includes the contribution of passive muscles as well as other passive structures, such as ligaments and joint capsules. The moment is exerted to the distal segment about the joint center from the proximal segment. In literature, a double exponential-based model has been widely adopted with joint kinematics to predict the passive elastic joint (Riener and Edrich, 1999, 2013; Amankwah et al., 2004; Whittington et al., 2008). Apart from the double exponential-based model, some other models,

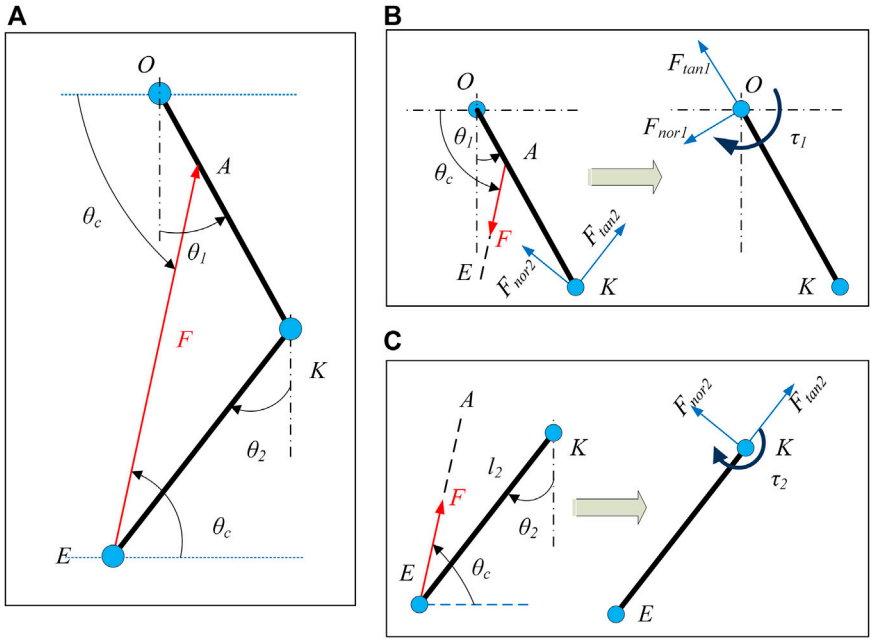

FIGURE 3 | Two link model with applied cable tension **(A)**, Force to Torque mapping for shank **(C)**, and Force to Torque mapping for thigh **(B)**. F_{tan} and F_{nor} represent the compressive and shear forces respectively induced on the joints. Subscripts 1 and 2 represent the hip and knee joints respectively.

such as those combining linear and exponential-based functions, have also been proposed (Hines et al., 2018). The study conducted by (Gasparutto et al., 2018) with models proposed in the literature (Riener and Edrich, 1999; Amankwah et al., 2004) found that the passive elastic joint moment predicted by both models are somehow similar in pattern and alignment with the literature data, suggesting that these models can be used even though they are a non-subject-specific. In this study, the passive elastic joint moments were estimated based on the model in work (Riener and Edrich, 1999).

Lower Control Layer

The lower control layer interacts directly with the exoskeleton and is responsible for generating the desired control effect by distributing various tensions among the cables based on the capability and limitation of the system at that instant of motion.

Control Performance Matrix Estimation

The C-LREX employs cables to generate the required torque at the hip and/or knee joints and the relationship between the cable tension and the torque generated can be derived by either using the principle of virtual work (as derived in work (Jin et al., 2015)) or *via* vector algebra methods. Both methods yield the same output, however, the vector algebra approach provides shear and compressive forces that act at the joints while calculating the torques induced *via* the cables.

The cable tension vector is projected onto the shank and thigh vectors to find the tangential and normal component of the force as shown in **Figure 3**. The projection of the cable tension vector ($\overrightarrow{EA}$) along the shank vector provides the tangential component of the force, while the orthogonal component of ($\overrightarrow{EA}$) provides the normal force component. The torque on the joint that is caused by the cable tension can be estimated using the cross-product of the distance vector and the force vector.

$$\overrightarrow{F_{\tan 2}} = \left(proj_{\widehat{EK}}\widehat{EA}\right) = \left(\frac{\left(\widehat{EA}\bullet\widehat{EK}\right)}{\left\|\widehat{EK}\right\|^2}\widehat{EK}\right)$$

$$\overrightarrow{F_{nor2}} = \left(\widehat{EA} - proj_{\widehat{EK}}\widehat{EA}\right) = \left(\widehat{EA} - \frac{\left(\widehat{EA}\bullet\widehat{EK}\right)}{\left\|\widehat{EK}\right\|^2}\widehat{EK}\right)$$

$$\overrightarrow{\tau_2} = \left(\overrightarrow{KE} \times \widehat{EA}\right) \tag{2}$$

Where, $\widehat{EA}$ *and* $\widehat{EK}$ are the unit vector along the $\overrightarrow{EA}$ *and* $\overrightarrow{EK}$ direction, respectively.

Similarly, the equivalent force components and torque on the hip joint can be estimated as:

$$\overrightarrow{F_{\tan 1}} = \left(proj_{\widehat{KO}}\overrightarrow{F_{\tan 2}}\right) + \left(proj_{\widehat{KO}}\overrightarrow{F_{nor2}}\right) + \left(proj_{\widehat{KO}}\widehat{AE}\right)$$

$$\overrightarrow{F_{nor1}} = \overrightarrow{F_{\tan 2}} - \left(proj_{\widehat{KO}}\overrightarrow{F_{\tan 2}}\right) + \overrightarrow{F_{nor2}} - \left(proj_{\widehat{KO}}\overrightarrow{F_{nor2}}\right) + \widehat{AE} - \left(proj_{\widehat{KO}}\widehat{AE}\right)$$

$$\overrightarrow{\tau_1} = \left(\overrightarrow{OK} \times \overrightarrow{F_{\tan 2}}\right) + \left(\overrightarrow{OK} \times \overrightarrow{F_{nor2}}\right) + \left(\overrightarrow{OA} \times \widehat{AE}\right) \tag{3}$$

In **Eqs 2**, **3**, the actual values of force and torque are obtained by multiplying the outcomes of the equations with the magnitude of the applied cable tension. In **Eqs 2**, **3**, the force magnitude is unknown for a given cable routing configuration.

Thus, the relation between torque and force can be written as:

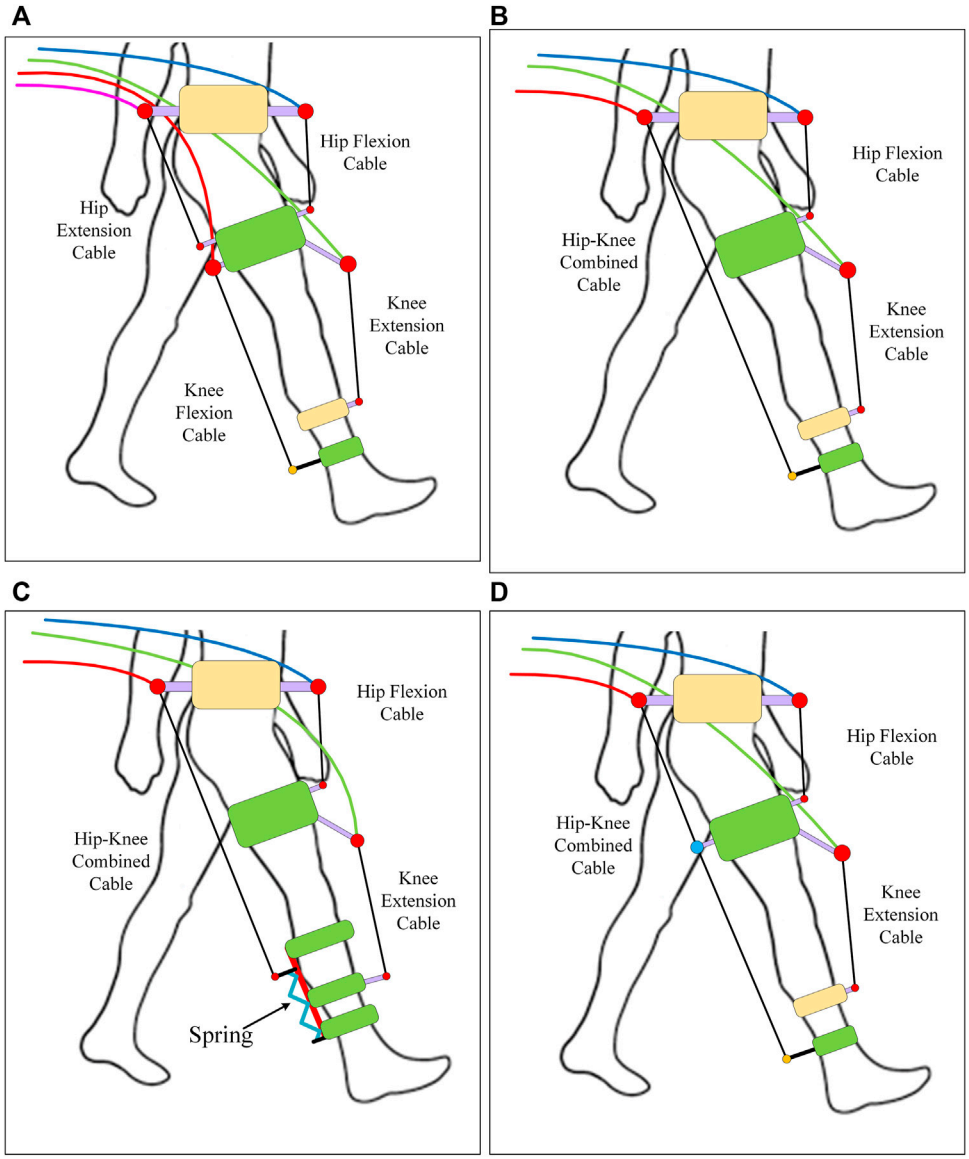

FIGURE 4 | Conceptual models: **(A)** Configuration 1 **(B)** Configuration 2, **(C)** Configuration 3, and **(D)** Configuration 4.

$$\tau = \begin{bmatrix} \tau_1 \\ \tau_2 \end{bmatrix} = \begin{bmatrix} B_1 \\ B_2 \end{bmatrix} F = B^T F \tag{4}$$

Where, $B^T = [\, B_1 \quad B_2 \,]^T$ is the control performance matrix that maps the cable tension F to the hip joint and knee joint torque and is dependent on the kinematics of the C-LREX at any instant.

In general, C-LREX employs a combination of cables to generate the desired control effect. The dimension of matrix $\boldsymbol{B}$ depends on the number of the cables. For example, using 3 separate cables, the control performance matrix ($\boldsymbol{B}$) can be written from **Eq. 4** as:

$$F = [\, F_1 \quad F_2 \quad F_3 \,]^T, \tau = [\, \tau_1 \quad \tau_2 \,]^T$$

$$B = [\, J_1 \quad J_2 \quad J_3 \,]^T = \begin{bmatrix} J_{11} & J_{21} & J_{31} \\ J_{12} & J_{22} & J_{32} \end{bmatrix}^T, \; B \in \mathbb{R}^{3\times2}, J \in \mathbb{R}^{2\times1}$$

Cable Tension Distribution Algorithm

The cable tension can be distributed either in a priority-based order or in an optimized order. The priority-based algorithm gives full priority to knee control allocation and then to hip control allocation in a single operational step. While the optimization-based algorithm distributes overall control based on a defined objective function in an iterative approach. **Supplementary Figure S1** layout the cable tension distribution algorithm based on the priority approach and optimization.

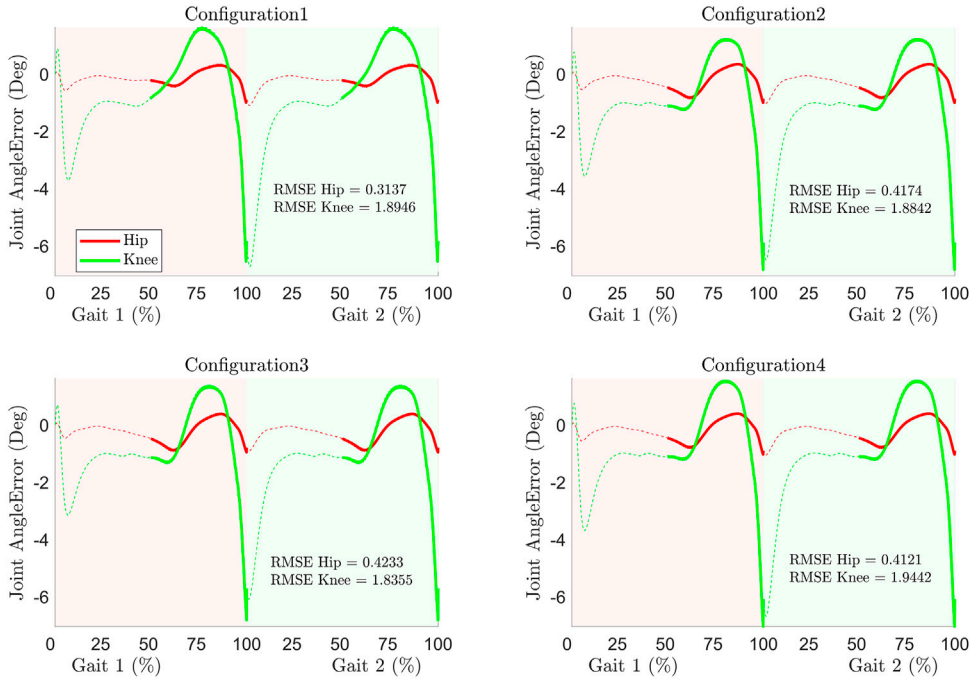

FIGURE 5 | Joint angle error and RMSE during tracking.

The number of inputs and outputs for the control distribution is not always the same (depends on the number of cables) and results in a rectangular control performance matrix. Depending on the number of cables, the system could be either overdrive (if the number of outputs is greater than the input) or underdrive (if the number of outputs is less than the number of inputs). The tension in each cable for a given torque requirement must be coordinated in such a way that either the cable generates the exact torque or less than the required torque while utilizing the full potential features of the configuration and actuators. Since the control performance matrix (***B***) is not square, the values of the corresponding tensions in the cable cannot be determined easily as the inverse of ***B*** does not exist. Thus, it is essential to form an optimized control allocation strategy, although, optimization-based distribution requires additional resources. In the case where constraints are not tightly aligned, and faster distribution is required, a priority-based control allocation approach can be implemented.

The objective function for optimization can be defined in different ways. **Eq. 4** can be transformed into a simple optimization problem as:

$$\begin{cases} \tau = BF \\ F_{\min} \le F \le F_{\max} \end{cases} \tag{5}$$

Where $F_{\min}$ *and* $F_{\max}$ are the lower and upper bounds for the values of cable tension(s).

To solve the above problem, MATLAB-based *find minimum of constrained nonlinear multivariable function (fmincon)* function can be implemented. The objective function is defined as the minimization of allocated control to the actuators as:

$$\min_{F} \left(FF^T\right) \quad s.t. \begin{cases} \tau = BF \\ F_{\min} \le F \le F_{\max} \end{cases} \tag{6}$$

Based on the previous work reported in the literature (refer to (Prasad et al., 2020) for detailed formulation and solution), the simple optimization problem (**Eq. 6**) can be converted into a quadratic programming (QP) problem. QP objective function is defined as a hybrid objective function (combination of error minimization and control minimization) and is transformed to have a final form as a standard QP function in **Eq. 7**. The solution is obtained either by employing MATLAB QP solver or the algorithm described (Prasad et al., 2020).

$$\min_{F}\left(\frac{1}{2}F^T HF + f^T F\right) \quad s.t. \{AF \le D \tag{7}$$

Where $A = \begin{bmatrix} -I & I \end{bmatrix}^T$, $D = \begin{bmatrix} -F_{\min} & F_{\max} \end{bmatrix}^T$, ***H*** is the Hessian matrix and ***f*** is the gradient matrix calculated from the hybrid objective function.

CONCEPTUAL MODELS

The modelling approach described in the previous section outlines a generalized framework that can be exploited to assess the viability of CDRD, identify the model requirements, and compare their performances. This section focuses on the implementation of the generalized framework to develop a decision metric that can be used to select a suitable cable

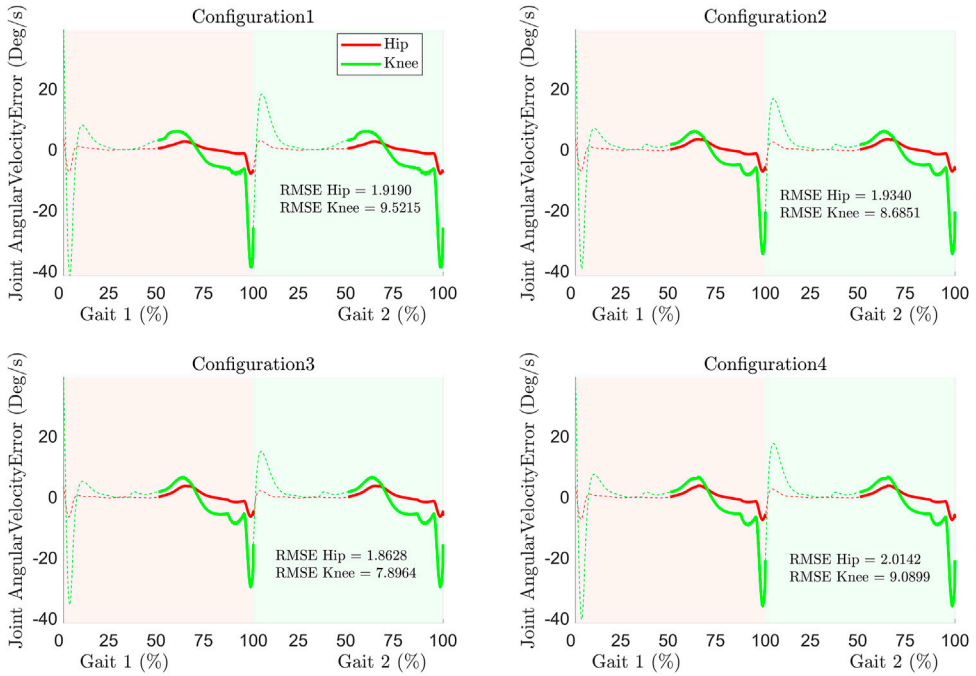

FIGURE 6 | Joint angular velocities error and RMSE during tracking.

routing configuration among a group of alternative configurations. Throughout the literature, a 4-cable configuration has been most often adopted for a mobile cable-driven rehabilitation device. However, other configurations can also meet similar performance requirements. The number of cable configurations that can be generated remains therefore elusive and depends on multiple factors such as design requirements, power constraints, performance requirements, and so on.

Selection of the Conceptual Models

The optimal exoskeleton/rehabilitation device applies the required torques on the hip and knee joints and satisfies the required coordination between the motion of the limb and joints to achieve the desired gait patterns. Hence, to track the desired motion, the cables need to be configured in a manner such that each joint can generate the required joint moment (either independently or in relation with other joints) in both flexion and extension directions (if only sagittal motion is considered). Failure to provide the moment in either direction at either joint (the hip or knee joint) will result in poor coordination and thus lead to a higher deviation from the desired trajectory ((Prasad et al., 2022)). To accomplish this, the cables must be arranged in an antagonistic configuration where 2 cables (either individually or combined) act at a joint in opposite directions to provide flexion and extension torque. Four examples of conceptual models capable of generating torque on joints in antagonistic configurations are selected (**Figure 4**) for demonstration in this study. Since springs are passive energy storing elements which can alter the energy cycle of a system, a spring was added to the 3-cable model to study its effect on the performance and requirements of the model (**Figure 4C**).

Configuration 1: 4 cables where 2 cable acts for each joint (hip and knee) separately in antagonistic configuration. Configuration 2: 3 cables where the posterior cables of configuration are combined as one acting from pelvis to shank. Configuration 3: an extension of configuration 2 where spring is attached to the shank cuff that allows movement along the shank only depending on the magnitude of applied cable tension. Configuration 4: 3 cables where the combined Hip-Knee cable is routed through the thigh cuff and thus acts as two cables with the same cable tension.

Modelling of the Spring

A second-order spring with stiffness and damping coefficients is used in the model (**Eq. 8**). The spring is attached to the posterior shank cuff from the foot side as shown in **Figure 4C**.

$$ms^2 + bs + k = F \tag{8}$$

Where, ***m, b,*** *and* ***k*** represent mass, damping coefficient, and spring stiffness respectively. ***F*** is the force applied to the spring.

The spring is allowed to slide along the shank direction only in an upward/downward direction. The stiffness and damping constants are assumed as 500N/m and 10 N-s/m respectively. A dead-end (max stretchable length) of the spring is defined to simulate a physical stop or spring stop end.

Simulating the Conceptual Models

The conceptual models (in **Figure 4**) are transformed into a link-based model with cuff parameters as shown in **Figure 1**. The link-based

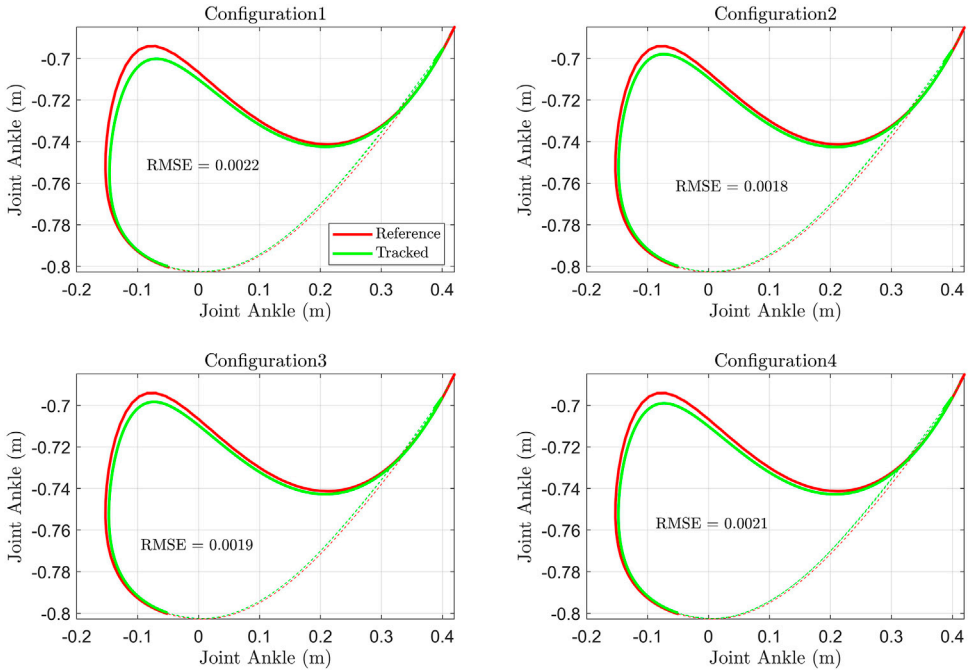

FIGURE 7 | Ankle joint position (Hip joint as reference) and RMSE of the ankle distance tracking error.

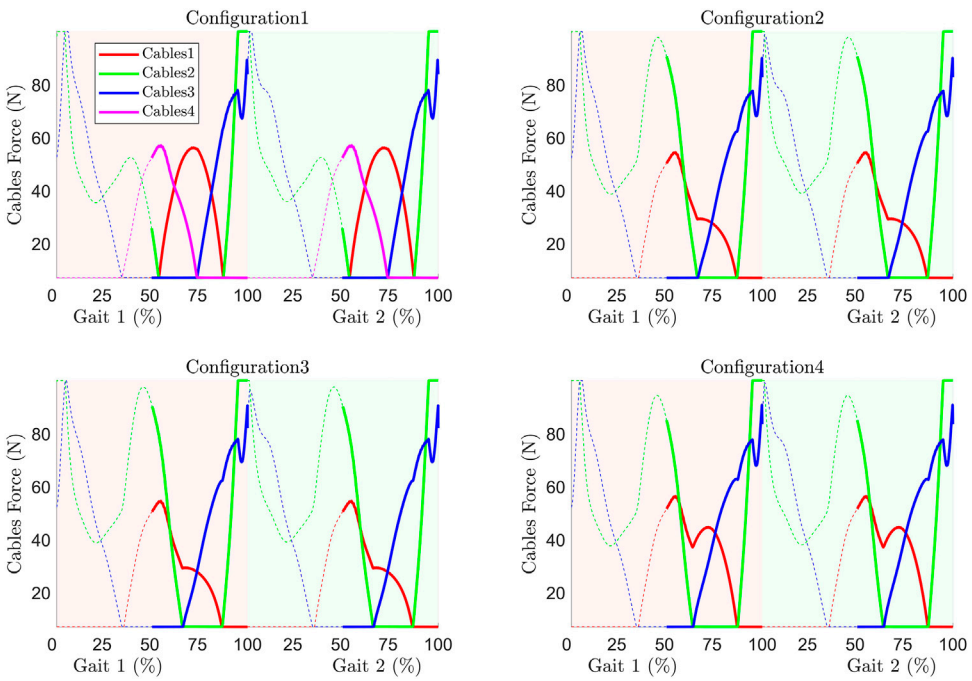

FIGURE 8 | Cable tension requirement during trajectory tracking.

model is the same for all configurations (**Figure 1B**) while the number of cables only altered the number of cuffs (**Figure 1C**). The cuff parameters are kept the same for all configurations. The healthy reference trajectory is adopted from Fukuchi (Fukuchi et al., 2018) with a gait cycle time of 3.48 s of overground walking (plotted in **Supplementary Figure S2**). The maximum and minimum allowable cable tensions are set to 100N and 7N respectively, to ensure that the tension is within the desired

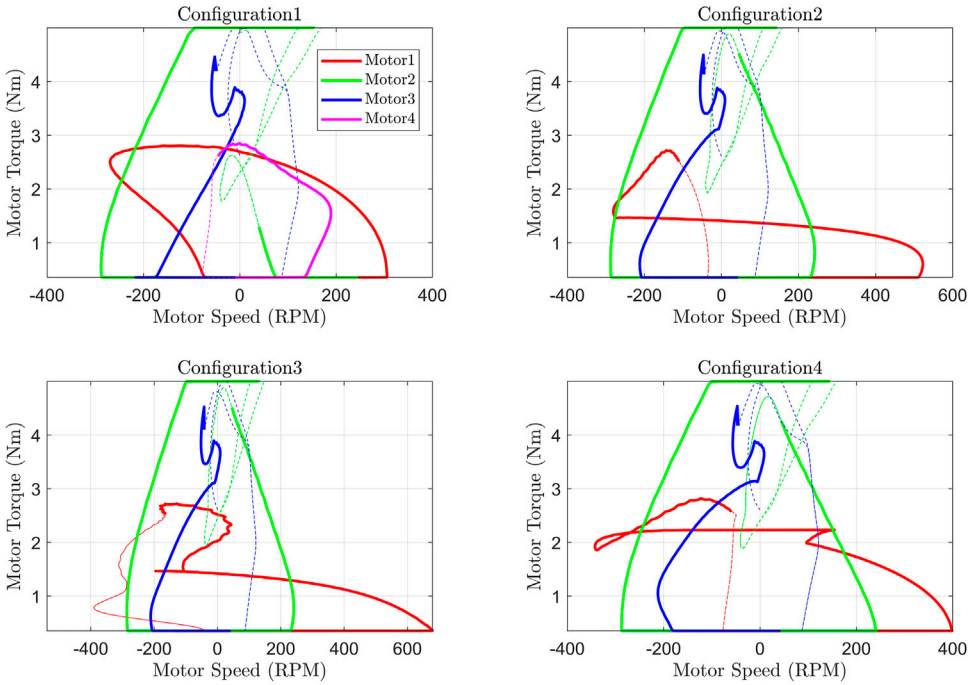

FIGURE 9 | Motor torque versus speed curve.

range and the cable is always taut. Based on the assumptions and simplifications, a *MATLAB* model was developed and simulated to track the healthy gait trajectories (performances) and the requirements were analyzed. The models were simulated for 2 gait cycles.

DECISION METRICS DEVELOPMENT

The conceptual model's performance and the requirements during tracking are analyzed and developed as metrics to help in the decision-making process. Further information, such as the exertion of the component forces on the joints due to cable tension, is also included as additional metrics. Throughout the results, the solid line represents the swing phase, and the dashed line represents the stance phase of the gait cycle.

Performance Analysis

Performance is one of the key metrics which plays a critical role in decision-making. Performance parameters, such as joint angle and angular velocity tracking, tracking error, root mean square error (RMSE), and ankle trajectory can be used to assess the performance of the models.

Joint Angle Error

The error in tracking the joint angle in all configurations and its RMSE (in degree) are shown in **Figure 5**. As depicted in the figure, the maximum error does not exceed 7° (in the knee joint at the transition between gait cycles (around 100% of the first gait cycle) while its counterpart in the hip joint is less than 1°. The tracking performance in each case is reasonable. The RMSE in the tracking for each model indicates that configuration 1 has better tracking than others for the hip joint while configuration 3 has better tracking for the knee joint.

Joint Angular Velocity Error

Similar to joint angle error, the joint angular velocity error during tracking (**Figure 6**) revealed a higher error in the knee joint in contrast to the hip joint. At the start of the gait cycle, the errors are higher due to the assumption of zero initial velocity. Furthermore, the errors are higher at the transition between the gait cycle (around 100% of the first gait cycle). The velocity requirement of the knee joint during the swing phase is higher and leads to higher inertial torque contribution. Since C-LREX has limited capability to exert torque (due to predefined cable tension range), the system fails to exert the required higher amount of torque and thus results in a higher error at the end of gait cycles. Nevertheless, the 3 cables configuration with spring demonstrated the least maximum velocity error. The RMSE (degree/s) of the joint velocity error (**Figure 6**) revealed that the 3 cables configuration outperforms others due to the spring contribution. The addition of a spring increased the flexibility of the attached cuff and contributed to additional velocity.

Ankle Position Tracking

The tracking of the ankle position (hip joint as origin) during tracking and the RMSE of the error of the distance of the ankle joint from the hip joint (hip as reference) are shown in **Figure 7**. The tracking in configurations 2 and 3 is superior to others. The 4-cable configuration has a higher error in tracking ankle

TABLE 1 | The area under Torque-Speed Curve (Total Power Requirement of each motor).

Config/Motor	Motor1	Motor2	Motor3	Motor4	Sum
Config 1	30.6	55.5	16.7	21.8	124.6
Config 2	9.5	26.3	76.1	—	111.9
Config 3	38.6	26.5	72.0	—	137.0
Config 4	18.0	72.7	28.0	—	118.8

position. The RMSE revealed that configuration 2 is tracking the ankle position more closely than other configurations.

Requirement Analysis

The requirements to meet the above tracking performances in each configuration differ due to the different number of cables and routings. Requirements such as cable tension, motor torque, motor speed, motor power, and total power requirements can be analyzed to assess the configuration.

Cable Tension

The cable tension(s) in each configuration is shown in **Figure 8**. The tension requirement in all configurations except for configuration 1 is higher in general throughout the gait cycle. Configurations 2 and 3 have a similar trend of cable tension distribution.

Cable Force Versus Cable Velocity Curve (Actuator Requirement Curve)

The cable tension versus cable linear velocity (in **Supplementary Figure S3**) curve combines two requirements (tension and velocity) for a given cable of a configuration to meet the tracking performance. Since the cable tension is provided by the motor, this plot is important in the identification of actuators/motors. The cable tension can be converted into motor torque assuming a suitable cable roller diameter (assumed as a 5 cm radius in this study) attached to the motor. Similarly, the cable's linear velocity can be transformed into motor speed (RPM) *via* the same roller diameter. The plots in **Supplementary Figure S3** can be transformed into Torque-vs-Speed curves of the motor (actuator requirement curve) as shown in **Figure 9**. The area under these curves yields the total power requirement of each motor and the sum of the area under the curve is the total power required of the respective configuration, as listed in **Table 1**. The maximum torque requirement in each configuration is the same (due to the fixed max tension limit), but the speed requirement is different. Configuration 1 has the least speed requirement of the motor while configuration 3 has the highest (due to the spring contribution). The higher speed requirement results in a higher power requirement of the motor and thus a bigger size of the motor.

C-LREX Power Requirements

The number of cables corresponds to the number of motors in a configuration. The power requirements of the motor of each configuration (**Supplementary Figure S4**) are limited to 16 W; however, the patterns, as well as the number of motors in some configurations, are different. Since the number of the motors included in the exoskeleton will increase/decrease the power demand during the gait cycle, the sum of the individual motor's power requirement is estimated to analyze the power demand pattern of the C-LREX and is shown in **Figure 10** along

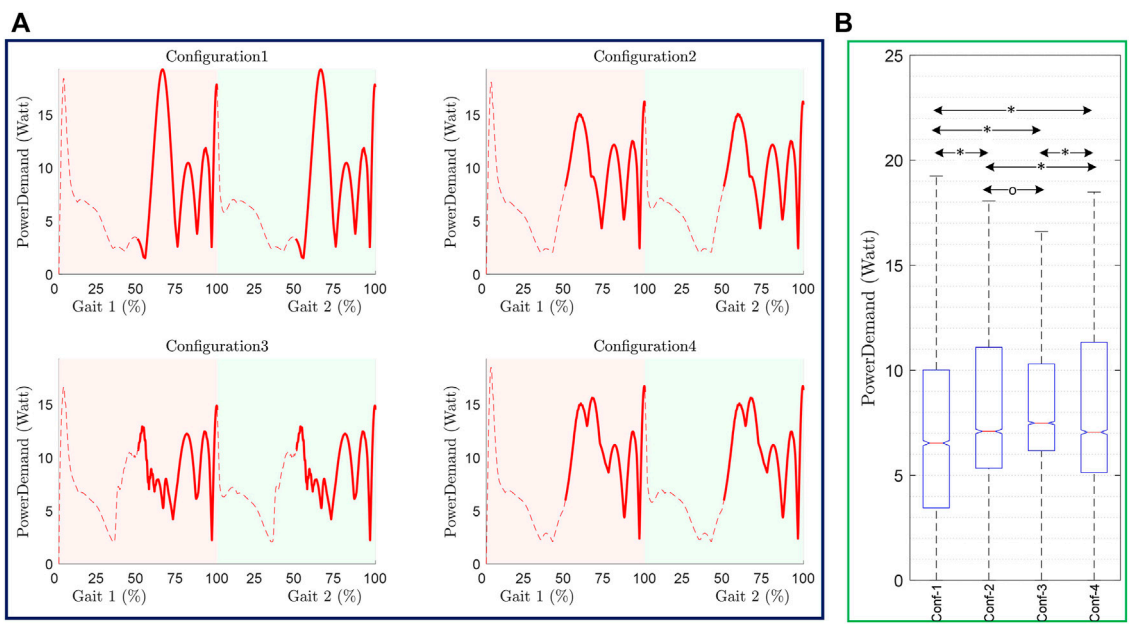

FIGURE 10 | Power demand in C-LREX throughout Gait cycle **(A)** and one-way ANOVA analysis **(B)**. The pairwise significant difference and no significance between the configurations are marked as '*', and 'o' respectively. *p*-value less than 0.05 is taken as a significant difference.

TABLE 2 | Statistical analysis of Power demand of C-LREX in each configuration.

	Configuration	Mean ± Std	ANOVA	
			F	*p*
Power Demand	Config 1	7.44 ± 4.65	59.83	0.00
	Config 2	7.97 ± 3.83		
	Config 3	8.03 ± 2.95		
	Config 4	8.32 ± 4.12		

with its statistical analysis (one-way ANOVA). The *p-value* in **Figure 10B** is less than 0.05 indicating that data are significantly different from each other. It was observed that configuration 3 has the highest total power requirement (**Table 1**) at least peak power demand (**Figure 10**). Configuration 1 has the highest peak power demand with a higher standard deviation (**Table 2**), while the mean peak power demand is the least among all configurations. Employing the spring has reduced the peak power demand and standard deviation, however with a higher median power demand in contrast to the configuration without a spring with 3 cables.

Additional Metrics

Apart from the performance and the model requirements, it is also important to analyse and minimize the force exerted by the system on the user limb joints to ensure human-robot interaction, comfort, and safety. In general, a configuration should exert the least possible additional forces to meet the performance specification.

Joint Component Forces

In this section, the joint compressive and shear forces resulting from the cable tensions were studied. These forces depend on the cable tensions and joint kinematics, and they vary with the gait cycle as shown in **Figure 11**. Configuration 1 exerts the least shear and compressive force on the knee joint compared to all other configurations while almost similar shear forces occur at the hip joint. Configuration 2 and 3 yields similar compressive and shear forces on the joints due to their similar cable tensions. The spring facilitates the movement of the posterior shank cuff in configuration 3 in contrast to configuration 2, however, it doesn't alter the cable angle significantly and thus results in similar cable tension as well as component forces.

Selecting a "Suitable" Configuration

Based on the metrics above and the design constraints, a suitable candidate from the four configurations studied here can be identified. For instance, in terms of performance (i.e., angle, angular velocity, and ankle position tracking), all the configurations are acceptable. On other hand, whilst considering the cable tension distribution throughout the cycle, configuration 1 is the "best", however, it requires 4 motors as compared to the other configurations where 3 motors meet the demands. Furthermore, in terms of motor requirements, configuration 1 requires 4 motors with less power (thus smaller size) compared to others with 3 motors of higher power specification (thus bigger size). The higher power requirement is due to higher speed demand since the maximum torque is the same for all the configurations.

Similarly, for the total power required for the different configurations, configuration 2 is the 'best'. The inclusion of spring has increased the power requirement by 22.43% while configuration 4 holds a reasonable position with a 6.16% higher requirement compared to configuration 2 (**Table 1**). In terms of individual motor power requirements, all configurations require less than 16 W. However, for peak power demand at a given instant of the motion, configuration 1 demands the highest peak power while other configurations without the spring remain close to configuration 1. The spring in configuration 3 results in the lowest peak power demand despite the maximum total power required throughout the gait cycle.

In terms of force exerted by the device on the lower limb joints, configuration 1 produces the minimum force and is hence the preferred configuration. Configuration 1 with 4 cables is 'preferable' among all configurations despite requiring 4 motors due to the following:

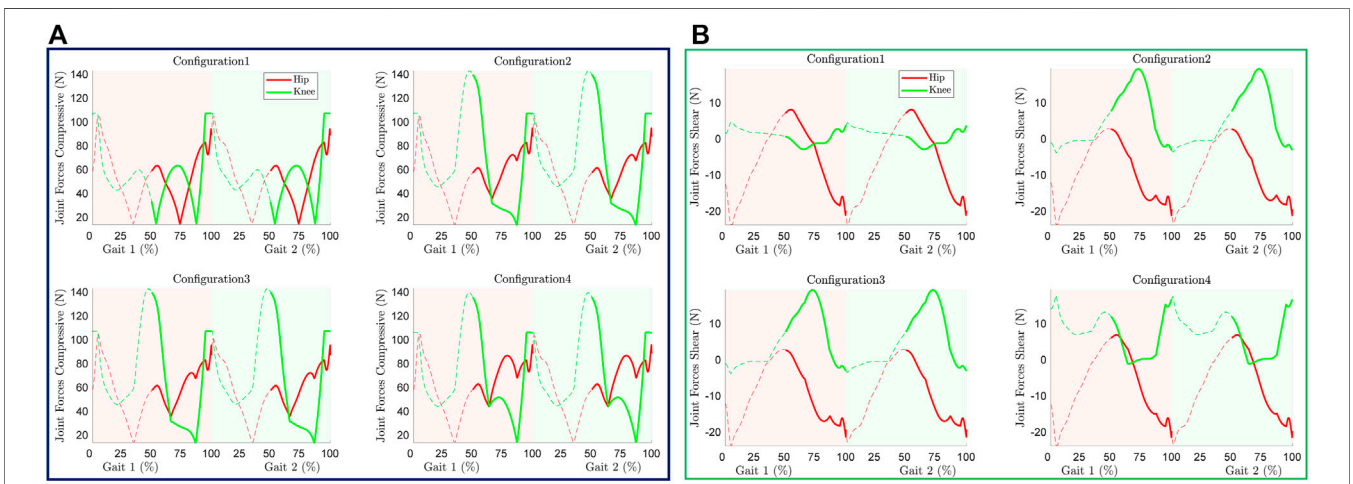

FIGURE 11 | Joint component forces induced due to cable tension **(A)** Compressive, **(B)** Shear.

TABLE 3 | General metric table for decision making.

Metric names		Weights	Score			
			Config 1	Config 2	Config 3	Config 4
Angle Error		20	20	18	20	16
Angular Velocity Error		20	16	18	20	16
Ankle Position Error		10	8	10	9	8
Cable Tension		5	5	3	3	3
Motor Torque *vs*. Speed (T-S) Curve		5	5	3.5	2	4
Area under T-S curve		10	8	10	7	9
Power Demand		10	7	9	10	8
Component Forces	Shear	10	10	7	7	8
	Compressive	10	10	7	7	8
Total Score		100	89	85.5	85	80

1) The motors required are of less power and similar specification unlike other demanding higher power motors with different specifications.
2) The forces exerted by the device on the user's limb are minimal.
3) The cable tension peak remains minimal throughout the gait cycle (except at the end of the gait cycle which is similar in all configurations).
4) The tracking performance is similar to other configurations.

Generating the Metrics Table

Based on the discussed metrics, a table was developed to help identify the most 'suitable' configuration for exoskeleton development. A suitable weight is assigned to each metric and can be adjusted depending on the priority and/or constraints given in terms of performance, model requirements, etc. The score assigned in the table is based on the performances and requirements as observed above. The minimum error during tracking, minimum requirements, and higher performances are given maximum scores and vice versa.

Configuration 1 has the highest score (**Table 3**) and is considered the most "suitable" configuration in this study. The addition of a spring improves the joint angular velocity tracking in configuration 3, however, the overall score is less than the 3-cable configuration without a spring (Configuration 2).

The metric-based identification methodology can be implemented to find the best cable routing of a configuration by creating multiple cases with different cable routing parameters (cuffs parameters). An optimization problem with the combination of the metrics as the objective function can be solved to find the optimal cuff parameters.

Identifying Motor Specification or Selecting Configuration Based on Available Motor

The actuator torque versus speed curve (T-S diagram) plotted in **Figure 9** can be utilized to identify the motor specifications for the selected configuration. For an instant, the motors required to track the trajectory in configuration 1 are required to have the capability of generating 5 Nm torque at 300 RPM. Similarly, the plot can also be utilized in a reverse manner to select the configuration where a predefined motor specification (for example a certain torque at a certain speed), is provided. Assuming a motor capable of providing 5 Nm torque at 420 RPM is provided as a constraint, **Figure 9** can serve as a baseline to find the suitable configuration based on the provided motor/actuator specifications (configurations 1 and 4).

CONCLUSION

Cable driven rehabilitation devices are promising and capable of reshaping the field of robotic rehabilitation due to multiple advantages over traditional link-based devices. These include lightweight, exertion of negligible inertia and inertial vibration on the impaired limb, remote actuation capability, flexible routing and reconfiguration options, and flexibility in terms of exact joint alignment. Despite these benefits, the optimal number of cables and cable configurations to achieve the best performance remains elusive.

We have developed a generalized methodology/framework to model and assess cable-driven exoskeletons based on various metrics. The model assumes the lower limb as a two link-pendulum with the foot attached perpendicularly to the shank. The voluntary contribution of the user limb is assumed to be the only passive elastic joint moment. The proposed framework can be used to study different cable configurations, identify the suitable one and its associated optimal routing parameters, and estimate the required motor specifications to meet the tracking performance under specified constraints (such as pre-specified actuator T-S specifications). For proof of concept, four different configurations of a conceptual CDRD model that can apply the joint torque in an antagonistic arrangement were studied as potential models to develop a stroke rehabilitation lower limb exoskeleton. A spring was incorporated into one of the models to study the possibility of alteration in the model's energy requirements along with other performance and requirements. A decision metric was developed based on the performance, requirements, and resulting forces applied to the joints to serve as a qualitative tool for the selection of a "suitable" configuration. Simulation of the conceptual configurations revealed that the 4-cable configuration is "suitable" for a lower limb exoskeleton development, as it generates minimum cable tension distribution, requires smaller individual motor power

requirements, and produces a lower component force on the limb joints, as compared to the other configurations. The incorporation of spring in configuration 3 tended to increase the total power requirement of the CDRD (however at the lowest peak power demand pattern) but improved the overall tracking performance.

Some of the limitations of the current modelling approach include considering only the sagittal plane motion, assuming the user's limb contribution as passive elastic joint moment only and assisting the user during the swing phase of the gait cycle. Moreover, the proposed framework is open to parameter adjustments including cuffs, cable tensions, springs, routing, etc., to meet the specified design objectives. Future work includes the extension of the current work to accommodate knee and hip abduction/adduction and cable routings in the frontal plane. Furthermore, the actual user limb contribution can be incorporated into the model instead of the passive elastic joint moment only if the impaired gait kinematic/kinetic trajectory is known.

DATA AVAILABILITY STATEMENT

The original contributions presented in the study are included in the article/**Supplementary Material**, further inquiries can be directed to the corresponding author.

AUTHOR CONTRIBUTIONS

RP: Conceptualization, simulating, data interpretation, result discussion, writing. KK: Editing, data interpretation, discussion on the result. MA: Data interpretation, result discussion. IH: Data interpretation, result discussion. HJ: Editing, data interpretation, result discussion. UH: Conceptualization, Data interpretetion, result discussion. ME: Conceptualization, editing, Data interpretation, result discussion. All authors approved the submitted version of the manuscript.

FUNDING

This publication is based upon work supported by the Khalifa University of Science and Technology under Award RC2-2018-022 (HEIC).

SUPPLEMENTARY MATERIAL

The Supplementary Material for this article can be found online at: https://www.frontiersin.org/articles/10.3389/fbioe.2022.920462/full#supplementary-material

REFERENCES

Alamdari, A., and Krovi, V. (2016). Design and Analysis of a Cable-Driven Articulated Rehabilitation System for Gait Training. *J. Mech. Robot.* 8. 051018-1, –051018-12. doi:10.1115/1.4032274

Amankwah, K., Triolo, R. J., and Kirsch, R. (2004). Effects of Spinal Cord Injury on Lower-Limb Passive Joint Moments Revealed Through a Nonlinear Viscoelastic Model. *Jrrd* 41, 15. doi:10.1682/JRRD.2004.01.0015

Balaban, B., and Tok, F. (2014). Gait Disturbances in Patients with Stroke. *PM&R* 6, 635–642. doi:10.1016/j.pmrj.2013.12.017

Bryson, J. T., and Agrawal, S. K. (2014). Analysis of Optimal Cable Configurations in the Design of a 3-DOF Cable-Driven Robot Leg. Proceedings of the ASME Design Engineering Technical Conference American Society of Mechanical Engineers (ASME), 1–9. doi:10.1115/DETC2014-34656

Chen, G., Chan, C. K., Guo, Z., and Yu, H. (2013). A Review of Lower Extremity Assistive Robotic Exoskeletons in Rehabilitation Therapy. *Crit. Rev. Biomed. Eng.* 41, 343–363. doi:10.1615/CritRevBiomedEng.2014010453

Dao, Q.-T., and Yamamoto, S.-i. (2018). Modified Computed Torque Control of a Robotic Orthosis for Gait Rehabilitation. 40th Annual International Conference of the IEEE Engineering in Medicine and Biology Society (EMBC). IEEE, 1719–1722. doi:10.1109/EMBC.2018.8512608

Figueiredo, J., Santos, C. P., and Moreno, J. C. (2015). Assistance and Rehabilitation of Gait Disorders Using Active Lower Limb Orthoses. IEEE 4th Portuguese Meeting on Bioengineering (ENBENG). IEEE, 1–6. doi:10.1109/ENBENG.2015.7088837

Fukuchi, C. A., Fukuchi, R. K., and Duarte, M. (2018). A Public Dataset of Overground and Treadmill Walking Kinematics and Kinetics in Healthy Individuals. *PeerJ* 6, e4640. doi:10.7717/peerj.4640

Gasparutto, X., Jacquelin, E., and Dumas, R. (2018). Contribution of Passive Actions to the Lower Limb Joint Moments and Powers During Gait: A Comparison of Models. *Proc. Inst. Mech. Eng. H.* 232, 768–778. doi:10.1177/0954411918785661

Grosu, S., Rodriguez–Guerrero, C., Grosu, V., Vanderborght, B., and Lefeber, D. (2018). Evaluation and Analysis of Push-Pull Cable Actuation System Used for Powered Orthoses. *Front. Robot. AI* 5, 1–11. doi:10.3389/frobt.2018.00105

Hines, M. G., Tillin, N. A., Luo, J., and Lee, R. Y. W. (2018). Passive Elastic Contribution of Hip Extensors to Joint Moments During Walking in People with Low Back Pain. *Clin. Biomech.* 60, 134–140. doi:10.1016/j.clinbiomech.2018.10.012

Jin, X., Cui, X., and Agrawal, S. K. (2015). Design of a Cable-Driven Active Leg Exoskeleton (C-ALEX) and Gait Training Experiments with Human Subjects. IEEE International Conference on Robotics and Automation (ICRA). IEEE, 5578–5583. doi:10.1109/ICRA.2015.7139979

Jin, X., Cai, Y., Prado, A., and Agrawal, S. K. (2017). Effects of Exoskeleton Weight and Inertia on Human Walking. IEEE Int. Conf. Robotics Automation (ICRA) (IEEE), 1772–1777. doi:10.1109/ICRA.2017.7989210

Johnson, W., Onuma, O., Owolabi, M., and Sachdev, S. (2016). Stroke: A Global Response Is Needed. *Bull. World Health Organ.* 94, 634–634A. doi:10.2471/BLT.16.181636

Learn about stroke (2022). *World Stroke Organ*. Available at: https://www.world-stroke.org/world-stroke-day-campaign/why-stroke-matters/learn-about-stroke (Accessed April 10, 2022).

Li, S., Francisco, G. E., and Zhou, P. (2018). Post-Stroke Hemiplegic Gait: New Perspective and Insights. *Front. Physiol.* 9, 1–8. doi:10.3389/fphys.2018.01021

Prasad, R., Ma, Y., Wang, Y., and Zhang, H. (2020). Hierarchical Coordinated Control Distribution and Experimental Verification for Six-Wheeled Unmanned Ground Vehicles. *Proc. Institution Mech. Eng. Part D J. Automob. Eng.* 235. 1. doi:10.1177/0954407020940823

Prasad, R., Khalaf, K., Awad, M. I., Hussain, I., Jelinek, H. F., Huzaifa, U., et al. (2022). "A Generalized Framework for the Assessment of Various Configurations of Cable-Driven Mobile Lower Limb Rehabilitation Exoskeletons," in 2022 12th International Conference on Biomedical Engineering and Technology (ICBET 2022). Tokyo, Japan. April 20–23, 2022. New York, NY, USA: ACM, 8. doi:10.1145/3535694.3535716

Riener, R., and Edrich, T. (1999). Identification of Passive Elastic Joint Moments in the Lower Extremities. *J. Biomechanics* 32, 539–544. doi:10.1016/S0021-9290(99)00009-3

Riener, R., and Edrich, T. (2013).Passive Elastic Joint Moments in the Lower Extremity, Proceedings of the 19th Annual International Conference of the IEEE Engineering in Medicine and Biology Society. "Magnificent Milestones and Emerging Opportunities in Medical Engineering" (Cat. No.97CH36136). Chicago, IL, USA. IEEE, 1717–1720. doi:10.1109/IEMBS.1997.757053

Riener, R., Lunenburger, L., Jezernik, S., Anderschitz, M., Colombo, G., and Dietz, V. (2005). Patient-Cooperative Strategies for Robot-Aided Treadmill Training:

First Experimental Results. *IEEE Trans. Neural Syst. Rehabil. Eng.* 13, 380–394. doi:10.1109/TNSRE.2005.848628

Riener, R. (2016). "Technology of the Robotic Gait Orthosis Lokomat," in *Neurorehabilitation Technology*. Second Edition (Cham: Springer International Publishing), 395–407. doi:10.1007/978-3-319-28603-7_19

Sanchez-Manchola, M., Gomez-Vargas, D., Casas-Bocanegra, D., Munera, M., and Cifuentes, C. A. (2018). *Development of a Robotic Lower-Limb Exoskeleton for Gait Rehabilitation: AGoRA Exoskeleton*. Colombia: IEEE ANDESCON IEEE, 1–6. doi:10.1109/ANDESCON.2018.8564692

Sheffler, L. R., and Chae, J. (2015). Hemiparetic Gait. *Phys. Med. Rehabilitation Clin. N. Am.* 26, 611–623. doi:10.1016/j.pmr.2015.06.006

Tucker, M. R., Olivier, J., Pagel, A., Bleuler, H., Bouri, M., Lambercy, O., et al. (2015). Control Strategies for Active Lower Extremity Prosthetics and Orthotics: A Review. *J. NeuroEngineering Rehabilitation* 12, 1. doi:10.1186/1743-0003-12-1

Unluhisarcikli, O., Pietrusinski, M., Weinberg, B., Bonato, P., and Mavroidis, C. (2011). Design and Control of a Robotic Lower Extremity Exoskeleton for Gait Rehabilitation. IEEE/RSJ International Conference on Intelligent Robots and Systems. San Francisco. 25-30 September 2011. IEEE, 4893–4898. doi:10.1109/IROS.2011.6048649

Wang, D., Lee, K.-M., Guo, J., and Yang, C.-J. (2014). Adaptive Knee Joint Exoskeleton Based on Biological Geometries. *IEEE/ASME Trans. Mechatron.* 19, 1268–1278. doi:10.1109/TMECH.2013.2278207

Whittington, B., Silder, A., Heiderscheit, B., and Thelen, D. G. (2008). The Contribution of Passive-Elastic Mechanisms to Lower Extremity Joint Kinetics During Human Walking. *Gait Posture* 27, 628–634. doi:10.1016/j.gaitpost.2007.08.005

Winstein, C. J., Stein, J., Arena, R., Bates, B., Cherney, L. R., Cramer, S. C., et al. (2016). Guidelines for Adult Stroke Rehabilitation and Recovery. *Stroke* 47, e98–e169. doi:10.1161/STR.0000000000000098

Winter, D. A. (2009). *Biomechanics and Motor Control of Human Movement*. Hoboken, NJ, USA: John Wiley & Sons. doi:10.1002/9780470549148

Witte, K. A., Fatschel, A. M., and Collins, S. H. (2017). Design of a Lightweight, Tethered, Torque-Controlled Knee Exoskeleton, International Conference on Rehabilitation Robotics (ICORR). IEEE, 1646–1653. doi:10.1109/ICORR.2017.8009484

Conflict of Interest: The authors declare that the research was conducted in the absence of any commercial or financial relationships that could be construed as a potential conflict of interest.

Publisher's Note: All claims expressed in this article are solely those of the authors and do not necessarily represent those of their affiliated organizations, or those of the publisher, the editors and the reviewers. Any product that may be evaluated in this article, or claim that may be made by its manufacturer, is not guaranteed or endorsed by the publisher.

frontiers | Frontiers in Bioengineering and Biotechnology

ORIGINAL RESEARCH
published: 28 June 2022
doi: 10.3389/fbioe.2022.917675

Effects of Barefoot and Shod on the *In Vivo* Kinematics of Medial Longitudinal Arch During Running Based on a High-Speed Dual Fluoroscopic Imaging System

Wanyan Su[1], *Shen Zhang*[1,2]*, *Dongqiang Ye*[1], *Xiaole Sun*[1], *Xini Zhang*[1] and *Weijie Fu*[1,3,4]*

[1]School of Kinesiology, Shanghai University of Sport, Shanghai, China, [2]School of Physical Education and Training, Shanghai University of Sport, Shanghai, China, [3]Key Laboratory of Exercise and Health Sciences of Ministry of Education, Shanghai University of Sport, Shanghai, China, [4]Shanghai Frontiers Science Research Base of Exercise and Metabolic Health, Shanghai University of Sport, Shanghai, China

OPEN ACCESS

Edited by:
Lizhen Wang,
Beihang University, China

Reviewed by:
Yaodong Gu,
Ningbo University, China
Tsung-Yuan Tsai,
Shanghai Jiao Tong University, China

***Correspondence:**
Shen Zhang
zhangshen0708@163.com
Weijie Fu
fuweijie@sus.edu.cn

Specialty section:
This article was submitted to Biomechanics, a section of the journal Frontiers in Bioengineering and Biotechnology

Received: *11 April 2022*
Accepted: *20 May 2022*
Published: *28 June 2022*

Citation:
Su W, Zhang S, Ye D, Sun X, Zhang X and Fu W (2022) Effects of Barefoot and Shod on the In Vivo Kinematics of Medial Longitudinal Arch During Running Based on a High-Speed Dual Fluoroscopic Imaging System. Front. Bioeng. Biotechnol. 10:917675. doi: 10.3389/fbioe.2022.917675

Shoes affect the biomechanical properties of the medial longitudinal arch (MLA) and further influence the foot's overall function. Most previous studies on the MLA were based on traditional skin-marker motion capture, and the observation of real foot motion inside the shoes is difficult. Thus, the effect of shoe parameters on the natural MLA movement during running remains in question. Therefore, this study aimed to investigate the differences in the MLA's kinematics between shod and barefoot running by using a high-speed dual fluoroscopic imaging system (DFIS). Fifteen healthy habitual rearfoot runners were recruited. All participants ran at a speed of 3 m/s ± 5% along with an elevated runway in barefoot and shod conditions. High-speed DFIS was used to acquire the radiographic images of MLA movements in the whole stance phase, and the kinematics of the MLA were calculated. Paired sample t-tests were used to compare the kinematic characteristics of the MLA during the stance phase between shod and barefoot conditions. Compared with barefoot, shoe-wearing showed significant changes ($p < 0.05$) as follows: 1) the first metatarsal moved with less lateral direction at 80%, less anterior translation at 20%, and less superiority at 10–70% of the stance phase; 2) the first metatarsal moved with less inversion amounting to 20–60%, less dorsiflexion at 0–10% of the stance phase; 3) the inversion/eversion range of motion (ROM) of the first metatarsal relative to calcaneus was reduced; 4) the MLA angles at 0–70% of the stance phase were reduced; 5) the maximum MLA angle and MLA angle ROM were reduced in the shod condition. Based on high-speed DFIS, the above results indicated that shoe-wearing limited the movement of MLA, especially reducing the MLA angles, suggesting that shoes restricted the compression and recoil of the MLA, which further affected the spring-like function of the MLA.

Keywords: dual fluoroscopic imaging system, barefoot, shod, medial longitudinal arch, *in vivo* kinematics

1 INTRODUCTION

Given the increased investigation and analysis of running biomechanics, the function and material of running shoes, such as cushioned shoes, have been developed (Hannigan and Pollard, 2020; Fu et al., 2021; Li et al., 2022). Running shoes were designed to attenuate impact forces *via* the viscose-elastic midsole (Nigg et al., 2003; Bishop et al., 2006), which can be compressed and rebounded during the loading and unloading periods of the running cycle (Baltich et al., 2015), thus effectively avoiding lower limb injuries caused by repeated high-intensity impact loads (Nigg et al., 2003; Sun et al., 2020; Kakouris et al., 2021).

During running, the foot is an important structure connecting the ground to the body, adapting to the running surface, affecting energy absorption and transfer (Welte et al., 2018). The medial longitudinal arch (MLA) allows the foot to function in a spring-like manner which is crucial in energy storage and release (Lynn et al., 2012). During the early and mid-stance phases, MLA compresses and lowers its height, whereas mechanical energy is absorbed and stored in the elastic structures of the MLA (Ker et al., 1987). During propulsion, the dorsiflexion (DF) of the first metatarsophalangeal joint tightened the plantar fascia (Hicks, 1954; Bolgla and Malone, 2004), thus, the MLA is shortened, and height is increased, accompanied by the elastic rebound of soft tissue and release of 17% mechanical energy (Ker et al., 1987; Kelly et al., 2015). The deformation of MLA directly affects the arch-spring behavior and the energetics of the foot.

From the perspective of MLA function, wearing shoes limit the DF of the metatarsophalangeal joint before initial contact during gait, it may further restrict the elongation of the MLA during impact, attenuates the magnitude of MLA deformation, and subsequently affect the MLA's ability to absorb shock (Wegener et al., 2015; Welte et al., 2018). Moreover, the long-term wearing of cushioned shoes leads to over-reliance on the shoes to absorb shock rather than the foot intrinsic muscles and tendons, which may potentially weaken the foot intrinsic muscle and spring-like function of MLA (Lieberman et al., 2010; Davis, 2014).

Knowing the accurate movement of MLA inside a shoe may contribute to further understanding of the influence of shoes on MLA during running. In previous studies, the trajectories of reflective markers with motion capture systems were used to measure MLA movement. However, the relative movement between the marker and the bone may cause soft tissue artifacts (STA), which cannot accurately reflect bone movement (Shultz et al., 2011). Intracortical pins can eliminate the effects of STA, but they are an invasive and infectious procedure for the human body (Arndt et al., 2013). A high-speed dual fluoroscopic imaging system (DFIS), combined with fluoroscopic imaging, medical imaging, and 3D-2D model registration technologies, can transcend the limitations of traditional biomechanical motion capture methods, that capture and quantify the dynamic movement of bones *in vivo* without STA and invasion (Ye et al., 2021). Moreover, a few studies recently published have used DFIS to measure skeletal foot kinematics *in vivo* during walking (Balsdon et al., 2016; Phan et al., 2018; Balsdon et al., 2019; Phan et al., 2019). DFIS has been used to measure the relative movement of the tibiotalar to subtalar joints (Phan et al., 2018) and midtarsal joint locking (Phan et al., 2019) and MLA angle (Balsdon et al., 2016; Balsdon et al., 2019) during walking. Given the above, the application of DFIS in the field of biomechanics provides a new perspective for accurate analysis of the *in vivo* kinematics of the foot. However, in contrast to this study that using high-speed DFIS, previous studies were based on normal DFIS. No studies to date have used high-speed DFIS to quantify the movement of the MLA under shod and barefoot conditions during running. This study based on high-speed DFIS may provide insights into the accurate movement of the MLA and a reference for future assessment of the potential association between abnormal MLA movement and injury.

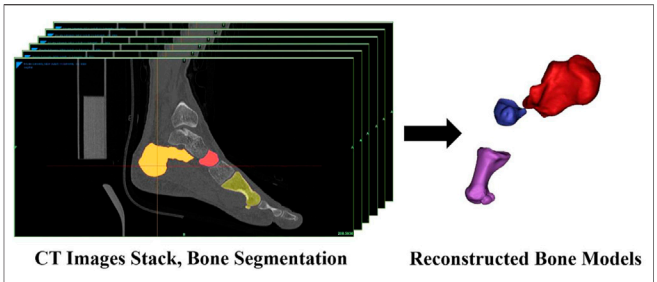

FIGURE 1 | Reconstruction of the first metatarsal, navicular, and calcaneus.

Thus, this study aimed to investigate the *in vivo* kinematics of the MLA during running in barefoot and shod conditions using high-speed DFIS. We hypothesized that compared with barefoot, wearing shoes limits the six degrees of freedom (6DOF) movement of the MLA.

2 METHODS

2.1 Participants

Fifteen healthy male participants (29.1 ± 6.9 years, 173.0 ± 4.5 cm, 71.7 ± 7.3 kg, and 38.8 ± 16.6 km/week) were included in the study. Sample size estimation by G*power (Version 3.1.9.6, Kiel University, Kiel, Germany) indicated that a minimum sample size of 15 participants was required to achieve a minimum effect size of 0.8 (significance level: 0.05, statistical power: 0.8). The inclusion criteria were habitual rearfoot strike runners and absence of pain and injury in the lower limbs for at least 3 months before enrollment in the study. All participants were right foot dominant (dextropedal). All participants provided informed consent, and the study protocol, including computed tomography (CT) scan and high-speed DFIS, was approved by the Institutional Review Board at Shanghai University of Sport, Shanghai, China (Approval No.102772021RT034).

2.2 Computed Tomography Scanning and Three-Dimensional Bone Modeling

All participants underwent CT scanning (SOMATOM, Germany) of their right foot for the creation of the 3D model used in postprocessing. A brace was used to fix the ankle and foot in a neutral position with the participants in the supine position during CT scanning. The main CT scanning parameters were as follows: thickness, 0.6 mm; voltage, 120 kV; current, 140 mA; image matrix, 512 × 512 × 256 pixels. The voxel length, width, and height were set as 0.488, 0.488, and 0.625 mm, respectively. The scanning scale ranged from 10 cm above the ankle joint to the end of the toes (Cao et al., 2019).

All CT images were subsequently imported into a 3D reconstruction software (v.21.0; Mimics, Materialise, Leuven, Belgium). The models of the first metatarsal, calcaneus, and navicular bones were reconstructed *via* threshold and region growth in Mimics (**Figure 1**). According to previous studies, we used the first metatarsal, navicular, and calcaneus to quantify the movement of the MLA (Simon et al., 2006; Tome et al., 2006; Bandholm et al., 2008; Balsdon et al., 2016; Welte et al., 2021).

2.3 Establishment of a Coordinate System

The three orthonormal axes (xyz) were aligned with the XYZ axes of the global coordinate system at the zero-loading condition on the level surface, and the inertial anatomical coordinate systems were generated from the bone meshes with the origin located at the centroid (Eberly et al., 1991; Negishi et al., 2022). The coordinate system axes were re-labeled such that the x-, y-, and z-axes more closely represented the lateral, anterior, and superior (Welte et al., 2021). We quantified the changes in the positions of the bones base on their origins.

2.4 Data Collection

The high-speed DFIS consisted of two pairs of fluorescence emitters that can generate X-rays and two image intensifiers (diameter: 431.8 mm) that can receive and image X-rays. In terms of precision, DFIS demonstrated a bias range of −0.16–0.13 mm and −0.05–0.13°, a precision range of 0.05–0.86 mm and 0.06–0.69°, and an overall dynamic root-mean-squared average error of 0.59 mm and 0.71° in static and dynamic trials (Cross et al., 2017). In this study, the distances between the two fluorescence emitters and between image intensifiers were 132.2 and 128.6 cm, respectively. The two image intensifiers were positioned at 119.6° to one another. The shooting voltage was 60 kV, the current was 63 mA, and the shooting frequency was 100 Hz. The exposure speed was 1/1000 s, and the image resolution was 1024 × 1024 pixels. Due to the limited range of high-speed DFIS acquisition, only right foot was investigated during data collection.

All participants were provided with a pair of running shoes (traditional footwear, heel-to-toe drop: 6 mm, midsole material: TPU and EVA; without any arch support) before the running experiment. Then, all participants warmed up for 5 min on a treadmill at a speed of 3 m/s. Before initiating the measurement, the participants could practice with and without shoes several times, so that the participants were familiar with the elevated runway under footwear and barefoot conditions for eliminating the effect of practice. During the test, they ran at a speed of 3 m/s ± 5% in barefoot and shod conditions along an elevated runway with their right foot landing within the X-ray volume. Each trial was supervised by the experimenter to ensure that the participants landed naturally. According to the study of Shetty and Bendall (2011), the stance phase was defined as the phase from foot strike to toe-off. The moment that the vertical ground reaction force was larger than 15 N was used to define the "heel-strike" (Welte et al., 2018). The force plate was synchronized with the DFIS *via* a custom synchronized trigger device. During running, the body of the participants blocked the infrared blocking grating sensor and triggered the high-speed DFIS and force plate to collect the data during the stance phase. One successful trial was collected using high-speed DFIS in each condition (Campbell et al., 2016; Welte et al., 2021), guided by the X-ray image quality (**Figure 2**).

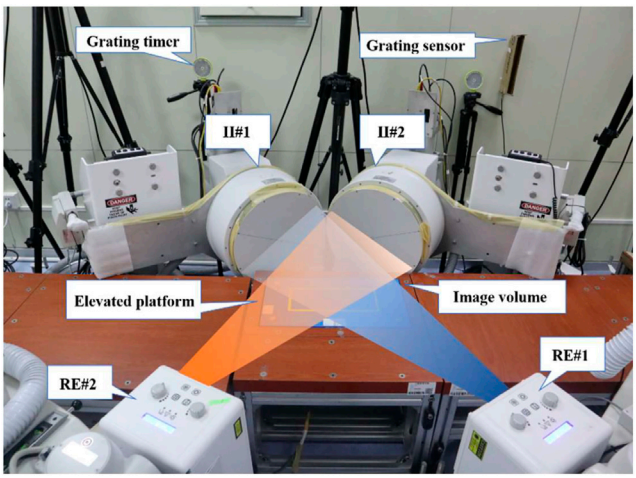

FIGURE 2 | High-speed DFIS set-up. Participants ran on an elevated platform. Image intensifiers (II#1 and II#2) processed images created by X-rays from the radiographic emitters (RE#1 and RE#2).

2.5 Data Processing

Images obtained with high-speed DFIS were subjected to distortion when X-ray beams were transformed into visible images (Gronenschild, 1999; Tersi and Stagni, 2014). Pincushion and magnetic lens distortions were the two major sources of distortion (Wang and Blackburn, 2000). For calibration, an X-ray image was collected with an undistorted grid (Brainerd et al., 2010), which consisted of a perforated piece of aluminum plate with a known size and spacing of each hole. An X-ray-specific software (XMALab, Brown University, United States) was used to correct for any changes in the spacing or size of the holes in the perforated grid *via* a distortion-correcting algorithm (Rohr et al., 2001).

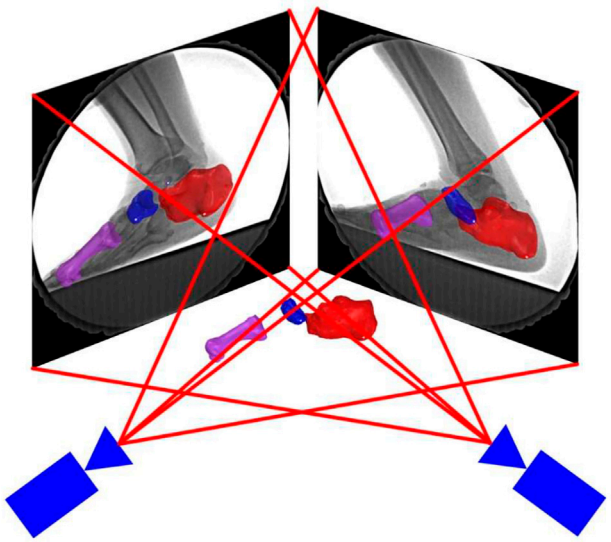

FIGURE 3 | 3D–2D registration. Bone positions were adjusted by translation and rotating the bone models in the software until the edge of the bones matched with the radiographic images.

The corrected fluoroscopic images and 3D models of the first metatarsal, navicular, and calcaneus were transferred to the 3D to 2D scientific rotoscoping software (Rhinoceros 6.0, 142 McNeel & Associates, Seattle, United States). The software created a 3D virtual environment of the experiment on a computer (**Figure 3**).

2.6 Parameters

The kinematic results of the MLA were calculated by 3D to 2D registration. The specific indicators included the range of motion (ROM), which was defined as the maximum minus the minimum value among all frames, initial contact value, and peak value. The stance phase was divided into 10 sections with 10% per section. The stance phase was divided into an early stance (0–20%), mid-stance (20–55%), and propulsion (55–85%) (Welte et al., 2021). The kinematics of each counterpart section were compared. The execution time of the joint kinematics during the stance period was standardized *via* an interpolation algorithm in MATLAB (R2018a, MathWorks, Natick, United States).

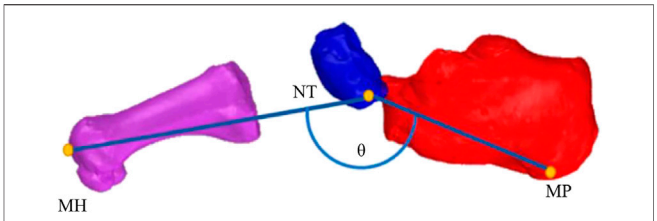

FIGURE 5 | Bones and landmarks defining the MLA angle (θ).

2.6.1 Definition of Six Degrees of Freedom Kinematics

The 6DOF kinematics of the MLA was defined as the relative movement of the first metatarsal coordinate system with respect to the calcaneus coordinate system (Kelly et al., 2015; Welte et al., 2021). The medial/lateral, anterior/posterior, and superior/inferior directions were aligned with the x-, y-, and z-axes of the coordinate systems, respectively (Wu et al., 2002). Plantar flexion/dorsiflexion (PF/DF), inversion/eversion (IR/ER), and abduction/adduction (AB/AD) were determined as rotations around the medial/lateral, anterior/posterior, and superior/inferior axes, respectively (Wu et al., 2002). The positive values represented anterior translation, lateral translation, superior translation, DF, IR, and AB, and the negative values corresponded to the opposite (**Figure 4**).

2.6.2 Medial Longitudinal Arch Angle

Similar to the MLA measurement used by Tome et al. (2006), landmarks, including the medial process of the calcaneus (MP), navicular tuberosity (NT), and the most distal point on the first metatarsal head (MH), were used to quantify the angle representing the MLA angle. A custom algorithm was used to calculate the spatial vector angles, which represented the MLA angles (θ), using vectors from NT to the MP ($NTMP$) and the NT to the first MH ($NTMH$) in the 3D space (Balsdon et al., 2016). A large MLA angle represents a low (flattened) arch height, and a small MLA angle denotes a high (raised) arch height (**Figure 5**).

2.7 Statistics

The mean and standard deviation for each variable were calculated. All variables were normally distributed as indicated by the Shapiro-Wilk test. Paired sample t-test was used to

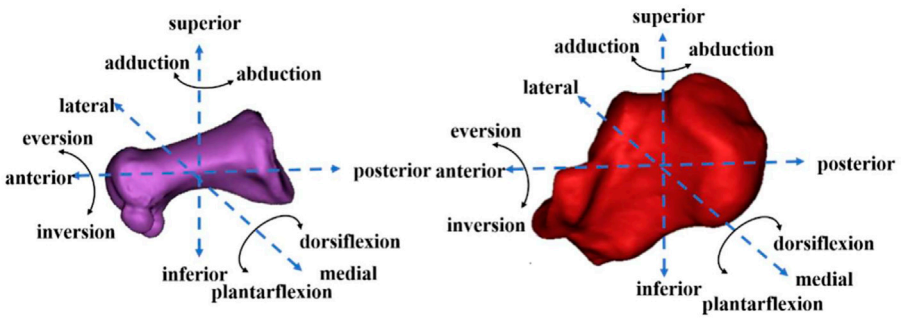

FIGURE 4 | First metatarsal (left) and calcaneus (right) motion diagram.

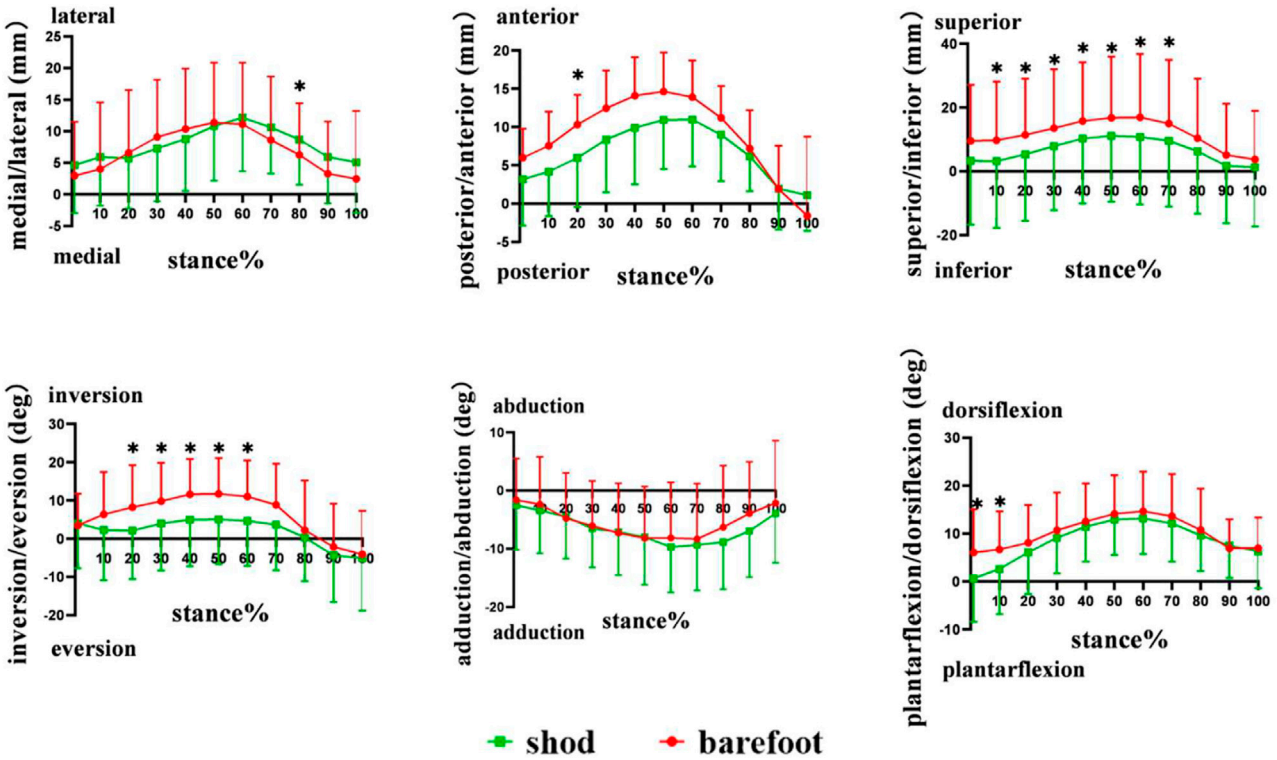

FIGURE 6 | 6DOF movement of the first metatarsal relative to the calcaneus during the stance phase. *: significant differences between the shod and barefoot conditions, $p < 0.05$.

compare the 6DOF data of the MLA and MLA angles under two conditions (SPSS 25.0, IBM, Chicago, United States). The significance level was set as $\alpha = 0.05$.

3 RESULTS

3.1 Translation of the First Metatarsal Relative to the Calcaneus

Compared with barefoot, the lateral translation at 80% ($p = 0.046$) and the anterior translation at 20% ($p = 0.029$) of the stance phase were smaller in the shod condition. The superior translation at 10% ($p = 0.010$), 20% ($p = 0.015$), 30% ($p = 0.017$), 40% ($p = 0.027$), 50% ($p = 0.031$), 60% ($p = 0.022$) and 70% ($p = 0.022$) of the stance phase was significantly reduced in the shod condition (**Figure 6**).

During the stance phase, no significant differences were observed in the initial contact value, peak value, and ROM in the translation of the first metatarsal relative to the calcaneus between shod and barefoot conditions (**Figure 7**) (**Table 1**).

3.2 Rotation of the First Metatarsal Relative to the Calcaneus

Compared with barefoot, the IR angles were smaller at 20% ($p = 0.033$), 30% ($p = 0.049$), 40% ($p = 0.032$), 50% ($p = 0.021$), and 60% ($p = 0.014$), and the DF angles were reduced at initial contact ($p = 0.002$) and 10% ($p = 0.010$) of the stance phase in the shod condition. No significant differences were observed in AB and AD angles during the stance phase (**Figure 6**).

Compared with barefoot, the IR/ER ROM in the shod condition was significantly smaller ($p = 0.044$). No significant differences were noticed in the peak value of PF/DF, IR/ER, and AD/AB angles between the shod and barefoot conditions (**Figure 7**) (**Table 1**).

3.3 *In Vivo* Kinematic of the Medial Longitudinal Arch Angles

Compared with barefoot, the MLA angles were significantly smaller at initial contact ($p = 0.004$), 10% ($p < 0.001$), 20% ($p < 0.001$), 30% ($p = 0.001$), 40% ($p = 0.001$), 50% ($p = 0.001$), 60% ($p = 0.016$), and 70% ($p = 0.043$) of the stance phase in the shod condition (**Figure 8**). The MLA angle at the initial contact ($p = 0.004$), maximum angle ($p = 0.002$), and ROM ($p < 0.001$) in the shod condition were significantly smaller, whereas no significant difference was observed between the shod and barefoot conditions at the minimum angle (**Figure 9**) (**Table 2**).

4 DISCUSSION

The study showed that compared with the barefoot, the medial, anterior, superior translation, and IR, DF angles of the first

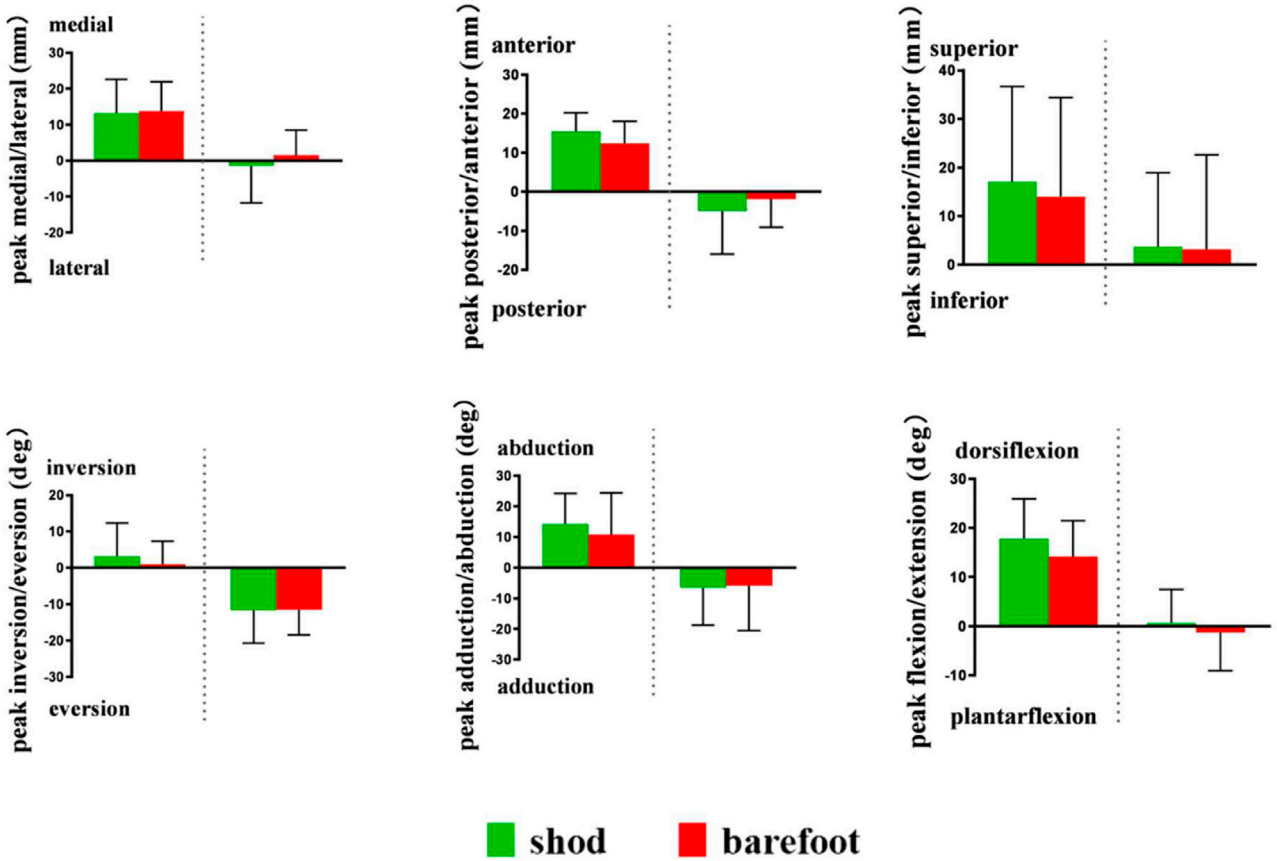

FIGURE 7 | Peak translation and rotation of the first metatarsal relative to calcaneus in shod and barefoot conditions. *: significant differences between the shod and barefoot conditions, $p < 0.05$.

TABLE 1 | Comparison of translation, rotation at initial contact, and ROM of the first metatarsal relative to the calcaneus in shod and barefoot conditions.

	Condition	M/L (mm)	A/P (mm)	S/I (mm)	PF/DF (°)	IR/ER (°)	AB/AD (°)
Initial contact	barefoot	2.96 ± 8.51	5.99 ± 3.79	9.51 ± 17.57	6.05 ± 9.01*	3.48 ± 8.23	−1.61 ± 7.09
	shod	4.65 ± 7.60	3.15 ± 6.01	3.28 ± 20.00	0.63 ± 9.02*	4.03 ± 11.73	−2.51 ± 7.68
ROM	barefoot	14.68 ± 4.35	20.38 ± 11.2	19.31 ± 7.06	17.10 ± 4.90	20.89 ± 9.94*	14.87 ± 3.53
	shod	12.15 ± 2.25	14.73 ± 6.87	15.81 ± 5.49	15.96 ± 4.98	16.45 ± 9.09*	12.54 ± 3.31

**: compared with barefoot, significant differences existed in the shod condition, p < 0.05. M/L, medial/lateral translation; A/P, anterior/posterior translation; S/I, superior/inferior translation; PF/DF, plantarflexion/dorsiflexion; IR/ER, inversion/eversion; AB/AD, abduction/adduction; ROM, range of motion; "+": the first metatarsal medial, anterior, superior translation and DF, IR, and AB; "-": the first metatarsal lateral, posterior, inferior translation, and PF, ER, and AD.*

metatarsal relative to the calcaneus were reduced in the shod condition at early and mid-stances. The study also revealed that compared with barefoot, the MLA angles at the initial contact, maximal MLA angle, ROM of MLA angles, and MLA angles from early to mid-stances were reduced. These results were consistent with the first hypothesis, which states that shoe wearing restricts partial 6DOF movement of the first metatarsal relative to the calcaneus. Inconsistent with the study hypothesis, no significant differences were observed in the minimal MLA angles between shod and barefoot conditions.

Compared with the barefoot condition, the maximal MLA angle and the ROM of MLA angles were significantly reduced in the shod condition, which partly coincide with the results of previous studies (Kelly et al., 2016; Holowka et al., 2021). Kelly et al. (2016) reported that running with shoes led to a reduction in the magnitude of MLA compression and recoil. Holowka et al. (2021) discovered that compared with barefoot, running with viscose-elastic midsole shoes reduced the ROM of MLA angles. These results based on skin-marker motion capture were consistent with the findings of this study, that is, shoes restricted the MLA movement in the sagittal plane, indicating that shoe wearing limited the compression and recoil of the MLA. The MLA may be affected by the compressive stiffness of footwear, and footwear compressive stiffness and MLA stiffness are related through an in-series spring system, such as the

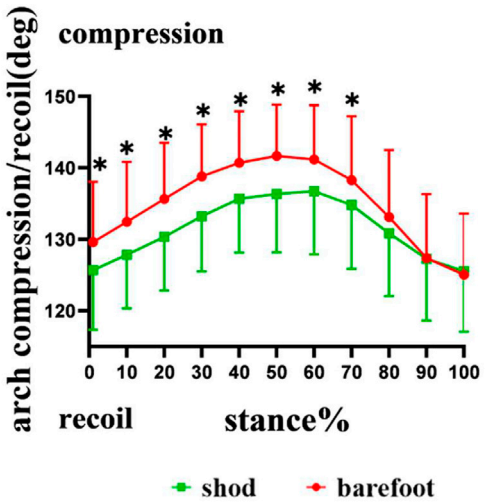

FIGURE 8 | MLA compression and recoil during the stance phase. *: significant differences existed between the shod and barefoot conditions, $p < 0.05$.

leg–surface relationship (Kelly et al., 2016). The in-series spring system is believed to maintain the constant overall stiffness; more compliant footwear should cause individuals to increase their MLA stiffness during running (Butler et al., 2003). Compared with wearing shoes that are more compliant, barefoot running is in direct contact with the stiff ground. Therefore, to maintain the constant overall stiffness, the human body increased the MLA stiffness under shod conditions and achieved the adjustment by decreasing the compression of MLA. MLA stiffness is defined as the ability to resist compression during loading and is commonly associated with arch height (Noro et al., 2021). Both extremes of MLA height have been associated with an increased risk of foot injuries, with both overly-stiff and overly-compliant arched thought to be poor shock absorbers (Simkin et al., 1989). Additionally, high-arched individuals with larger MLA stiffness were more likely to develop tibial and femoral stress fractures (Williams et al., 2001). The compression and recoil of MLA are related to the storage and release of elastic energy during running. Ker et al. (1987) identified the MLA as an elastic storage-return mechanism and estimated that approximately 17% of the mechanical work of running can be stored and returned through the compression and recoil of the MLA over the stance phase. Accordingly, we hypothesized that the reduced compression and recoil of the MLA may influence the spring-like function of MLA and limit the stored and released elastic energy.

This study, based on high-speed DFIS, observed the movement of the first metatarsal with respect to the calcaneus during running under barefoot and shod conditions. This study showed no significant differences in the peak lateral/medial, anterior/posterior, and inferior/superior translation and PF/DF, AB/AD, and IR/ER in the movement of the first metatarsal relative to the calcaneus between barefoot and shod conditions. However, in the early and mid-stances, the metatarsal anterosuperior was smaller in the shod condition compared with the barefoot. Noh et al. (2015) believed that given the decreased displacement of the metatarsal, muscle activation of the plantar flexors, such as flexor digitorum brevis muscle (FDB), which insert onto the bone, was increased. In line with the results, Kelly et al. (2016) observed that compared with barefoot, the compression and recoil of the MLA reduced, and peak FDB activation was greater when running with shoes. According to previous studies, the magnitude of MLA compression decreased accompanied by an increased muscle activation due to the replacement of the spring-like function of the MLA with muscle work, which may increase the metabolic cost (Alexander, 1991; Stearne et al., 2016; Cigoja et al., 2021). Stearne et al. (2016) observed that limiting the MLA compression by the use of custom insoles, which restricted arch compression to 20 and 40%, resulted in increases of 1 and 2.5% in metabolic energy cost, respectively. Perl et al. (2012) also revealed a significant 3% increase in metabolic costs for traditional shoe wearing compared with

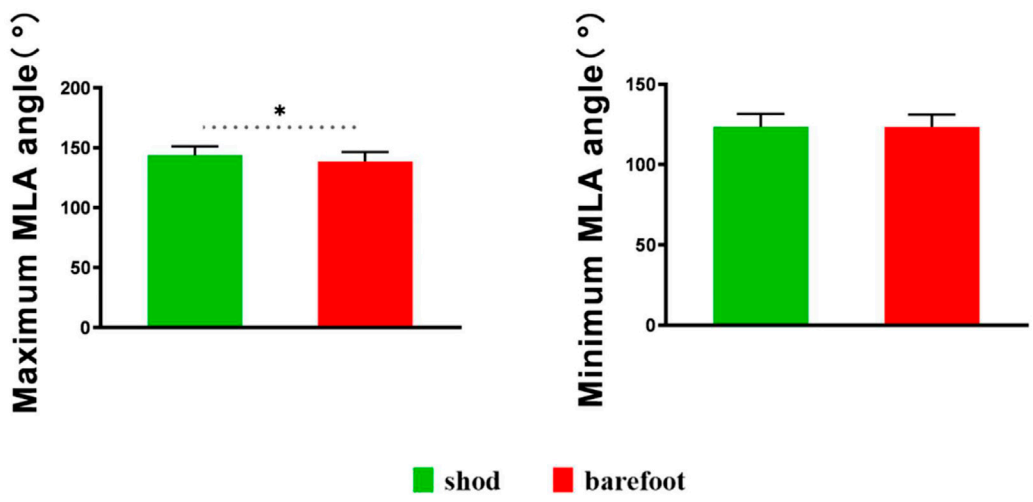

FIGURE 9 | Maximum and minimum MLA angles in shod and barefoot conditions. *: significant differences existed between the shod and barefoot conditions, $p < 0.05$.

TABLE 2 | Comparison of MLA angle at initial contact and ROM of MLA angle in shod and barefoot conditions.

	Condition	MLA angle (°)
Initial contact	barefoot	129.62 ± 8.43*
	shod	126.13 ± 7.67*
ROM	barefoot	20.32 ± 4.20*
	shod	15.01 ± 3.98*

**: compared with barefoot, significant differences existed in the shod condition,* $p < 0.05$.

minimalist shoes that were similar to barefoot running. Although metabolic costs and muscle activation were not directly measured in this study, combining the results of this and previous research, we agreed with the opinion that shoe wearing may increase metabolic costs compared with barefoot running.

It has been shown that wearing minimal shoes (used to mimic barefoot running) is associated with increases in intrinsic foot muscle size and MLA height (Lieberman et al., 2010; Lieberman, 2012). Miller et al. (2014) and Johnson et al. (2016) randomly assigned participants to wear minimal shoes or traditional shoes for weeks of running, and both found that participants in the minimal shoes group were significantly increased in cross-sectional area (CSA) of abductor hallucis muscles than in the traditional shoes group. Miller et al. (2014) also found that CSA of abductor digiti minimi muscles was larger and MLA height was higher in the minimal shoes group. Similar to these studies, Chen et al. (2016) found that overall foot muscle volume was larger in the minimal shoes group but not in the traditional shoes group. These studies suggested that wearing minimal footwear for the long term can help increase foot strength and MLA height. Conversely, shoe-wearing may be associated with weaker intrinsic foot muscles that may potentially lower MLA, further collapsing the foot.

Based on high-speed DFIS, this study revealed that compared with barefoot, MLA angle at the initial contact and maximal MLA angle were significantly smaller in the shod condition. However, Kelly et al. (2016) reported differences in the maximal and minimal angles between shod and barefoot running; however, the MLA angle at initial contact was similar for both conditions. We hypothesized that the differences between this study and those of previous research were mainly due to the different methods of measuring the MLA angle. Previous studies on the measurement of MLA angle were mostly based on infrared motion-capture techniques and referred to the Rizzoli foot model, which defines the MLA angle as the 2D angle between the projections of two vectors on the sagittal plane of the foot, thus simulating X-ray image-based clinical measurements of the MLA (Leardini et al., 2007; Portinaro et al., 2014). In this study, we defined the MLA angle as the angle between two 3D vectors. Caravaggi et al. (2021) observed that during the dynamic task, the variability of the 3D angle was consistently lower than the 2D angle, which was projected to the sagittal plane, suggesting that the 3D angle reflected the deformation of the MLA more accurately. Therefore, this study, based on high-speed DFIS, may observe the movement of the MLA more accurately.

This study encountered several limitations. Only male runners were recruited, and gender differences were not explored. All participants were habitual shoe-wearing runners, and when immediately transitioning from shod to barefoot running, this transition may lead to a decreased local dynamic stability (Ekizos et al., 2017). In addition, future studies should further explore the effect of training on the *in vivo* kinematics of the MLA during running based on high-speed DFIS.

5 CONCLUSION

The study investigated the MLA angle and the 6DOF movement of the first metatarsal relative to the calcaneus in the whole stance phase, which provided valuable insights into the MLA kinematic under barefoot and shod conditions during running and lend more accurate information of MLA in the whole stance phase. The results showed that shoe wearing restricted partial 6DOF movement of the MLA, especially reducing the magnitude of MLA compression and recoil, suggesting that shoes limited the spring-like function of the MLA. The restricted spring-like function of the MLA may affect the storage and release of elastic energy during running.

DATA AVAILABILITY STATEMENT

The original contributions presented in the study are included in the article/supplementary material, further inquiries can be directed to the corresponding authors.

ETHICS STATEMENT

The studies involving human participants were reviewed and approved by the Institutional Review Board at Shanghai University of Sport, Shanghai, China. The patients/participants provided their written informed consent to participate in this study.

AUTHOR CONTRIBUTIONS

WF, SZ, and WS conceived and designed the review. WS wrote the manuscript. WS, DY, XS, XZ, and SZ revised the manuscript. All authors have read and approved the final manuscript.

FUNDING

This research was funded by the National Key Technology Research and Development Program of the Ministry of Science and Technology of China (2019YFF0302100), the National Natural Science Foundation of China (11772201), the "Outstanding Young Scholar" Program of Shanghai Municipal, and the "Dawn" Program of Shanghai Education Commission, China (19SG47).

REFERENCES

Alexander, R. M. (1991). Energy-saving Mechanisms in Walking and Running. *J. Exp. Biol.* 160, 55–69. doi:10.1242/jeb.160.1.55

Arndt, A., Lundgren, P., Liu, A., Nester, C., Maiwald, C., Jones, R., et al. (2013). The Effect of a Midfoot Cut in the Outer Sole of a Shoe on Intrinsic Foot Kinematics during Walking. *Footwear Sci.* 5 (1), 63–69. doi:10.1080/19424280.2012.740688

Balsdon, M., Dombroski, C., Bushey, K., and Jenkyn, T. R. (2019). Hard, Soft and Off-The-Shelf Foot Orthoses and Their Effect on the Angle of the Medial Longitudinal Arch. *Prosthet. Orthot. Int.* 43 (3), 331–338. doi:10.1177/0309364619825607

Balsdon, M. E. R., Bushey, K. M., Dombroski, C. E., LeBel, M.-E., and Jenkyn, T. R. (2016). Medial Longitudinal Arch Angle Presents Significant Differences between Foot Types: A Biplane Fluoroscopy Study. *J. Biomech. Eng.* 138 (10). doi:10.1115/1.4034463

Baltich, J., Maurer, C., and Nigg, B. M. (2015). Increased Vertical Impact Forces and Altered Running Mechanics with Softer Midsole Shoes. *PLoS One* 10 (4), e0125196. doi:10.1371/journal.pone.0125196

Bandholm, T., Boysen, L., Haugaard, S., Zebis, M. K., and Bencke, J. (2008). Foot Medial Longitudinal-Arch Deformation during Quiet Standing and Gait in Subjects with Medial Tibial Stress Syndrome. *J. Foot Ankle Surg.* 47 (2), 89–95. doi:10.1053/j.jfas.2007.10.015

Bishop, M., Fiolkowski, P., Conrad, B., Brunt, D., and Horodyski, M. (2006). Athletic Footwear, Leg Stiffness, and Running Kinematics. *J. Athl. Train.* 41 (4), 387–392.

Bolgla, L. A., and Malone, T. R. (2004). Plantar Fasciitis and the Windlass Mechanism: A Biomechanical Link to Clinical Practice. *J. Athl. Train.* 39 (1), 77–82.

Brainerd, E. L., Baier, D. B., Gatesy, S. M., Hedrick, T. L., Metzger, K. A., Gilbert, S. L., et al. (2010). X-ray Reconstruction of Moving Morphology (Xromm): Precision, Accuracy and Applications in Comparative Biomechanics Research. *J. Exp. Zool.* 9999A (5), a–n. doi:10.1002/jez.589

Butler, R. J., Crowell, H. P., 3rd, and Davis, I. M. (2003). Lower Extremity Stiffness: Implications for Performance and Injury. *Clin. Biomech.* 18 (6), 511–517. doi:10.1016/s0268-0033(03)00071-8

Campbell, K. J., Wilson, K. J., LaPrade, R. F., and Clanton, T. O. (2016). Normative Rearfoot Motion during Barefoot and Shod Walking Using Biplane Fluoroscopy. *Knee Surg. Sports Traumatol. Arthrosc.* 24 (4), 1402–1408. doi:10.1007/s00167-014-3084-4

Cao, S., Wang, C., Zhang, G., Ma, X., Wang, X., Huang, J., et al. (2019). *In Vivo* kinematics of Functional Ankle Instability Patients during the Stance Phase of Walking. *Gait Posture* 73, 262–268. doi:10.1016/j.gaitpost.2019.07.377

Caravaggi, P., Rogati, G., Leardini, A., Ortolani, M., Barbieri, M., Spasiano, C., et al. (2021). Accuracy and Correlation between Skin-Marker Based and Radiographic Measurements of Medial Longitudinal Arch Deformation. *J. Biomechanics* 128, 110711. doi:10.1016/j.jbiomech.2021.110711

Chen, T. L. W., Sze, L. K. Y., Davis, I. S., and Cheung, R. T. H. (2016). Effects of Training in Minimalist Shoes on the Intrinsic and Extrinsic Foot Muscle Volume. *Clin. Biomech.* 36, 8–13. doi:10.1016/j.clinbiomech.2016.05.010

Cigoja, S., Fletcher, J. R., and Nigg, B. M. (2022). Can Changes in Midsole Bending Stiffness of Shoes Affect the Onset of Joint Work Redistribution during a Prolonged Run? *J. Sport Health Sci.* 11, 293–302. doi:10.1016/j.jshs.2020.12.007

Cross, J. A., McHenry, B. D., Molthen, R., Exten, E., Schmidt, T. G., and Harris, G. F. (2017). Biplane Fluoroscopy for Hindfoot Motion Analysis during Gait: A Model-Based Evaluation. *Med. Eng. Phys.* 43, 118–123. doi:10.1016/j.medengphy.2017.02.009

Davis, I. S. (2014). The Re-emergence of the Minimal Running Shoe. *J. Orthop. Sports Phys. Ther.* 44 (10), 775–784. doi:10.2519/jospt.2014.5521

Eberly, D., Lancaster, J., and Alyassin, A. (1991). On Gray Scale Image Measurements. *CVGIP Graph. Models Image Process.* 53 (6), 550–562. doi:10.1016/1049-9652(91)90005-5

Ekizos, A., Santuz, A., and Arampatzis, A. (2017). Transition from Shod to Barefoot Alters Dynamic Stability during Running. *Gait Posture* 56, 31–36. doi:10.1016/j.gaitpost.2017.04.035

Fu, F., Levadnyi, I., Wang, J., Xie, Z., Fekete, G., Cai, Y., et al. (2021). Effect of the Construction of Carbon Fiber Plate Insert to Midsole on Running Performance. *Materials* 14 (18), 5156. doi:10.3390/ma14185156

Gronenschild, E. (1999). Correction for Geometric Image Distortion in the X-Ray Imaging Chain: Local Technique versus Global Technique. *Med. Phys.* 26 (12), 2602–2616. doi:10.1118/1.598800

Hannigan, J. J., and Pollard, C. D. (2020). Differences in Running Biomechanics between a Maximal, Traditional, and Minimal Running Shoe. *J. Sci. Med. Sport* 23 (1), 15–19. doi:10.1016/j.jsams.2019.08.008

Hicks, J. H. (1954). The Mechanics of the Foot. Ii. The Plantar Aponeurosis and the Arch. *J. Anat.* 88 (1), 25–30.

Holowka, N. B., Gillinov, S. M., Virot, E., and Lieberman, D. E. (2022). Effects of Footwear Cushioning on Leg and Longitudinal Arch Stiffness during Running. *J. Biomechanics* 133, 110869. doi:10.1016/j.jbiomech.2021.110869

Johnson, A., Myrer, J., Mitchell, U., Hunter, I., and Ridge, S. (2016). The Effects of a Transition to Minimalist Shoe Running on Intrinsic Foot Muscle Size. *Int. J. Sports Med.* 37 (2), 154–158. doi:10.1055/s-0035-1559685

Kakouris, N., Yener, N., and Fong, D. T. P. (2021). A Systematic Review of Running-Related Musculoskeletal Injuries in Runners. *J. Sport Health Sci.* 10 (5), 513–522. doi:10.1016/j.jshs.2021.04.001

Kelly, L. A., Lichtwark, G. A., Farris, D. J., and Cresswell, A. (2016). Shoes Alter the Spring-like Function of the Human Foot during Running. *J. R. Soc. Interface.* 13 (119), 20160174. doi:10.1098/rsif.2016.0174

Kelly, L. A., Lichtwark, G., and Cresswell, A. G. (2015). Active Regulation of Longitudinal Arch Compression and Recoil during Walking and Running. *J. R. Soc. Interface.* 12 (102), 20141076. doi:10.1098/rsif.2014.1076

Ker, R. F., Bennett, M. B., Bibby, S. R., Kester, R. C., and Alexander, R. M. (1987). The Spring in the Arch of the Human Foot. *Nature* 325 (7000), 147–149. doi:10.1038/325147a0

Leardini, A., Benedetti, M. G., Berti, L., Bettinelli, D., Nativo, R., and Giannini, S. (2007). Rear-foot, Mid-foot and Fore-Foot Motion during the Stance Phase of Gait. *Gait Posture* 25 (3), 453–462. doi:10.1016/j.gaitpost.2006.05.017

Li, J., Song, Y., Xuan, R., Sun, D., Teo, E.-C., Bíró, I., et al. (2022). Effect of Long-Distance Running on Inter-segment Foot Kinematics and Ground Reaction Forces: A Preliminary Study. *Front. Bioeng. Biotechnol.* 10, 833774. doi:10.3389/fbioe.2022.833774

Lieberman, D. E. (2012). What We Can Learn about Running from Barefoot Running: an Evolutionary Medical Perspective. *Exerc Sport Sci. Rev.* 40 (3), 63–72. doi:10.1097/JES.0b013e31824ab210

Lieberman, D. E., Venkadesan, M., Werbel, W. A., Daoud, A. I., D'Andrea, S., Davis, I. S., et al. (2010). Foot Strike Patterns and Collision Forces in Habitually Barefoot versus Shod Runners. *Nature* 463 (7280), 531–535. doi:10.1038/nature08723

Lynn, S. K., Padilla, R. A., and Tsang, K. K. W. (2012). Differences in Static- and Dynamic-Balance Task Performance after 4 Weeks of Intrinsic-Foot-Muscle Training: The Short-Foot Exercise versus the Towel-Curl Exercise. *J. Sport Rehabil.* 21 (4), 327–333. doi:10.1123/jsr.21.4.327

Miller, E. E., Whitcome, K. K., Lieberman, D. E., Norton, H. L., and Dyer, R. E. (2014). The Effect of Minimal Shoes on Arch Structure and Intrinsic Foot Muscle Strength. *J. Sport Health Sci.* 3 (2), 74–85. doi:10.1016/j.jshs.2014.03.011

Negishi, T., Nozaki, S., Ito, K., Seki, H., Hosoda, K., Nagura, T., et al. (2022). Three-dimensional Innate Mobility of the Human Foot on Coronally-Wedged Surfaces Using a Biplane X-Ray Fluoroscopy. *Front. Bioeng. Biotechnol.* 10, 800572. doi:10.3389/fbioe.2022.800572

Nigg, B. M., Stefanyshyn, D., Cole, G., Stergiou, P., and Miller, J. (2003). The Effect of Material Characteristics of Shoe Soles on Muscle Activation and Energy Aspects during Running. *J. Biomechanics* 36 (4), 569–575. doi:10.1016/s0021-9290(02)00428-1

Noh, B., Masunari, A., Akiyama, K., Fukano, M., Fukubayashi, T., and Miyakawa, S. (2015). Structural Deformation of Longitudinal Arches during Running in Soccer Players with Medial Tibial Stress Syndrome. *Eur. J. Sport Sci.* 15 (2), 173–181. doi:10.1080/17461391.2014.932848

Noro, H., Miyamoto, N., Mitsukawa, N., and Yanagiya, T. (2021). No Association of Plantar Aponeurosis Stiffness with Medial Longitudinal Arch Stiffness. *Int. J. Sports Med.* 42 (10), 945–949. doi:10.1055/a-1373-5734

Perl, D. P., Daoud, A. I., and Lieberman, D. E. (2012). Effects of Footwear and Strike Type on Running Economy. *Med. Sci. Sports Exerc* 44 (7), 1335–1343. doi:10.1249/MSS.0b013e318247989e

Phan, C.-B., Nguyen, D.-P., Lee, K. M., and Koo, S. (2018). Relative Movement on the Articular Surfaces of the Tibiotalar and Subtalar Joints during Walking. *Bone & Jt. Res.* 7 (8), 501–507. doi:10.1302/2046-3758.78.BJR-2018-0014.R1

Phan, C.-B., Shin, G., Lee, K. M., and Koo, S. (2019). Skeletal Kinematics of the Midtarsal Joint during Walking: Midtarsal Joint Locking Revisited. *J. Biomechanics* 95, 109287. doi:10.1016/j.jbiomech.2019.07.031

Portinaro, N., Leardini, A., Panou, A., Monzani, V., and Caravaggi, P. (2014). Modifying the Rizzoli Foot Model to Improve the Diagnosis of Pes-Planus: Application to Kinematics of Feet in Teenagers. *J. Foot Ankle Res.* 7 (1), 754. doi:10.1186/s13047-014-0057-2

Rohr, K., Stiehl, H. S., Sprengel, R., Buzug, T. M., Weese, J., and Kuhn, M. H. (2001). Landmark-based Elastic Registration Using Approximating Thin-Plate Splines. *IEEE Trans. Med. Imaging* 20 (6), 526–534. doi:10.1109/42.929618

Shetty, N., and Bendall, S. (2011). (i) Understanding the Gait Cycle, as it Relates to the Foot. *Orthop. Trauma* 25 (4), 236–240. doi:10.1016/j.mporth.2011.04.009

Shultz, R., Kedgley, A. E., and Jenkyn, T. R. (2011). Quantifying Skin Motion Artifact Error of the Hindfoot and Forefoot Marker Clusters with the Optical Tracking of a Multi-Segment Foot Model Using Single-Plane Fluoroscopy. *Gait Posture* 34 (1), 44–48. doi:10.1016/j.gaitpost.2011.03.008

Simkin, A., Leichter, I., Giladi, M., Stein, M., and Milgrom, C. (1989). Combined Effect of Foot Arch Structure and an Orthotic Device on Stress Fractures. *Foot Ankle* 10 (1), 25–29. doi:10.1177/107110078901000105

Simon, J., Doederlein, L., McIntosh, A. S., Metaxiotis, D., Bock, H. G., and Wolf, S. I. (2006). The Heidelberg Foot Measurement Method: Development, Description and Assessment. *Gait Posture* 23 (4), 411–424. doi:10.1016/j.gaitpost.2005.07.003

Stearne, S. M., McDonald, K. A., Alderson, J. A., North, I., Oxnard, C. E., and Rubenson, J. (2016). The Foot's Arch and the Energetics of Human Locomotion. *Sci. Rep.* 6, 19403. doi:10.1038/srep19403

Sun, X., Lam, W. K., Zhang, X., Wang, J., and Fu, W. (2020). Systematic Review of the Role of Footwear Constructions in Running Biomechanics: Implications for Running-Related Injury and Performance. *J. Sports Sci. Med.* 19 (1), 20–37.

Tersi, L., and Stagni, R. (2014). Effect of Calibration Error on Bone Tracking Accuracy with Fluoroscopy. *J. Biomech. Eng.* 136 (5), 054502. doi:10.1115/1.4027058

Tome, J., Nawoczenski, D. A., Flemister, A., and Houck, J. (2006). Comparison of Foot Kinematics between Subjects with Posterior Tibialis Tendon Dysfunction and Healthy Controls. *J. Orthop. Sports Phys. Ther.* 36 (9), 635–644. doi:10.2519/jospt.2006.2293

Wang, J., and Blackburn, T. J. (2000). The AAPM/RSNA Physics Tutorial for Residents. *Radiographics* 20 (5), 1471–1477. doi:10.1148/radiographics.20.5.g00se181471

Wegener, C., Greene, A., Burns, J., Hunt, A. E., Vanwanseele, B., and Smith, R. M. (2015). In-shoe Multi-Segment Foot Kinematics of Children during the Propulsive Phase of Walking and Running. *Hum. Mov. Sci.* 39, 200–211. doi:10.1016/j.humov.2014.11.002

Welte, L., Kelly, L. A., Kessler, S. E., Lieberman, D. E., D'Andrea, S. E., Lichtwark, G. A., et al. (2021). The Extensibility of the Plantar Fascia Influences the Windlass Mechanism during Human Running. *Proc. R. Soc. B* 288 (1943), 20202095. doi:10.1098/rspb.2020.2095

Welte, L., Kelly, L. A., Lichtwark, G. A., and Rainbow, M. J. (2018). Influence of the Windlass Mechanism on Arch-Spring Mechanics during Dynamic Foot Arch Deformation. *J. R. Soc. Interface.* 15 (145), 20180270. doi:10.1098/rsif.2018.0270

Williams, D. S., III, McClay, I. S., and Hamill, J. (2001). Arch Structure and Injury Patterns in Runners. *Clin. Biomech.* 16 (4), 341–347. doi:10.1016/s0268-0033(01)00005-5

Wu, G., Siegler, S., Allard, P., Kirtley, C., Leardini, A., Rosenbaum, D., et al. (2002). ISB Recommendation on Definitions of Joint Coordinate System of Various Joints for the Reporting of Human Joint Motion-Part I: Ankle, Hip, and Spine. *J. Biomechanics* 35 (4), 543–548. doi:10.1016/s0021-9290(01)00222-6

Ye, D., Sun, X., Zhang, C., Zhang, S., Zhang, X., Wang, S., et al. (2021). *In Vivo* Foot and Ankle Kinematics During Activities Measured by Using a Dual Fluoroscopic Imaging System: A Narrative Review. *Front. Bioeng. Biotechnol.* 9, 693806. doi:10.3389/fbioe.2021.693806

Conflict of Interest: The authors declare that the research was conducted in the absence of any commercial or financial relationships that could be construed as a potential conflict of interest.

Publisher's Note: All claims expressed in this article are solely those of the authors and do not necessarily represent those of their affiliated organizations, or those of the publisher, the editors and the reviewers. Any product that may be evaluated in this article, or claim that may be made by its manufacturer, is not guaranteed or endorsed by the publisher.

frontiers | Frontiers in Bioengineering and Biotechnology

ORIGINAL RESEARCH
published: 04 July 2022
doi: 10.3389/fbioe.2022.891940

Study of Mechanical Behavior in Epiphyseal Fracture Treated by Reduction and Cement Injection: No Immediate Post-Operative Weight-Bearing but Only Passive and Active Mobilization Should be Advised

A. Moufid[1,2], *P. Bokam*[2,3], *G. Harika-Germaneau*[3,4], *M. Severyns*[2], *L. Caillé*[2], *V. Valle*[2], *T. Vendeuvre*[1,2] *and A. Germaneau*[2]*

[1]Department of Orthopaedic Surgery and Traumatology, University Hospital, Poitiers, France, [2]Institut Pprime UPR 3346, CNRS—Université de Poitiers—ISAE-ENSMA, Poitiers, France, [3]Unité de Recherche Clinique Pierre Deniker, Centre Hospitalier Henri Laborit, Poitiers, France, [4]CERCA UMR 7295, CNRS—Université de Poitiers, Poitiers, France

OPEN ACCESS

Edited by:
Mohammad Nikkhoo,
Islamic Azad University, Iran

Reviewed by:
Kamran Hassani,
Islamic Azad University, Iran
Rui B. Ruben,
Polytechnic Institute of Leiria, Portugal

***Correspondence:**
A. Germaneau
arnaud.germaneau@univ-poitiers.fr

Specialty section:
This article was submitted to Biomechanics, a section of the journal Frontiers in Bioengineering and Biotechnology

Received: 08 March 2022
Accepted: 25 May 2022
Published: 04 July 2022

Citation:
Moufid A, Bokam P, Harika-Germaneau G, Severyns M, Caillé L, Valle V, Vendeuvre T and Germaneau A (2022) Study of Mechanical Behavior in Epiphyseal Fracture Treated by Reduction and Cement Injection: No Immediate Post-Operative Weight-Bearing but Only Passive and Active Mobilization Should be Advised. Front. Bioeng. Biotechnol. 10:891940. doi: 10.3389/fbioe.2022.891940

The development of new percutaneous treatment techniques using a balloon for the reduction and cement for the stabilization for tibial plateau fractures (TPF) are promising. The biomechanical changes brought by the cement in the periarticular fracture are unknown. The objective of this study was to provide elements of understanding of the bone behavior in an epiphyseal fracture treated with cementoplasty and to define the modifications brought about by the presence of this cement in the bone from both an architectural and biomechanical point of view.

In vitro animal experimentation was conducted. Bones samples were prepared with a cavity created with or without cancellous compaction, aided by balloon expansion following the same protocol as in the treatment of TPF. A uniaxial compression test was performed with various speeds and by using Heaviside Digital Image Correlation to measure mechanical fields. Preliminary finite element models were constructed with various boundary conditions to be compared to our experimental results.

The analysis of the images permits us to obtain a representative load vs. time response, the displacement fields, and the strain distribution for crack initiation for each sample. Microcracks and discontinuity began very early at the interface bone/cement. Even when the global behavior was linear, microcracks already happened. There was no strain inside the cement. The finite element model that matched our experiments had no link between the two materials.

In this work, the use of a novel correlation process highlighted the biomechanical role of the cement inside the bone. This demonstrated that there is no load transfer between bone and cement. After the surgery, the cement behaves like a rigid body inside the cancellous bone (same as a screw or plate). The cement provides good reduction and primary stabilization (mini-invasive approach and good stress distribution), permitting the patient to

undergo rehabilitation with active and passive mobilization, but no weight-bearing should be authorized while the cortical bone is not consolidated or stabilized.

Keywords: Tibial plateau fractures (TPF), PMMA cement, cancellous bone, strain distribution, balloon kyphoplasty, interface

1 INTRODUCTION

Tibial plateau fractures (TPF) are known to be arthrogenic (Honkonen, 1995; Rademakers et al., 2007). They result from high-energy injuries in young people and low-energy injuries in over-weight and elderly people (Cole et al., 2009). The gold standard treatment remains an open reduction and osteosynthesis using a plate and screws (Krause et al., 2018) which means that at the time of total knee prosthesis, the knee would have undergone at least three surgeries: the osteosynthesis, then the removal of the plate, and the prosthesis which increases the risk of infection and complication (Suzuki et al., 2011). That is why the development of new percutaneous techniques using a balloon for reduction and cement for stabilization are promising (Vendeuvre et al., 2013; Belaid et al., 2018).

PMMA cement has been used in orthopedic surgery since the 1960s (Charnley). Its initial use allowed for the sealing of joint prostheses (Smith, 2005). Since 1984, new fields of use have emerged with a standalone application in the field of traumatology in the spine, and since 2010, in different anatomical localizations (calcaneus and tibial plateau) (Vendeuvre et al., 2013; Smith, 2005; Prod'homme et al., 2018). This new approach allows minimally invasive management, reducing postoperative complications and immobilization time. The vertebral metastatic fracture were the first beneficiaries of PMMA cement in the 1980s (Onimus and Bertin, 1982). Considering the good results in the medium term, its use tends to become more democratic in some teams, even in the treatment of young patients, raising new questions: what is its role in consolidation? What tolerance is there in the long term? What biomechanical effect does it produce? Is it stable enough to permit weight-bearing? Is it stable enough to permit active and passive mobilization? What role does it play after consolidation? How does the human body react cytologically, histologically, and biomechanically to the presence of this cement initially and once the fracture has consolidated? Up to the present, no study has answered all these questions.

Animal experimentation is the only way to quantify the effects of time on the bone with cement in an organic environment after consolidation. The first step is to provide an element of understanding *in vitro* to ensure the feasibility of the *in vivo* study and to uncover a basic understanding for future *in vivo* experiments.

Measurements of the displacements and strains in bone and cement are needed to characterize and understand the biomechanical modifications that imply the presence of cement in the bone at the time of the fracture and after consolidation.

Formerly, the main source of measuring the strain in soft tissues (Larrabee, 1986; Nagarkatti et al., 2001) and hard tissues (Yang et al., 2011) was by using strain gauges and extensometers. However, gauges can be too large when compared to the scale at which strain gradients are evaluated in tissues (Nicolella et al., 2001; Väänänen et al., 2013). The extensometers sometimes can damage the bone. When the computational side is considered, particularly finite element (FE) analysis, there was a total reliance on experimental data as an input and result validation. Therefore, the alternative is optical measurement techniques such as holographic interferometry and speckle interferometry although they are quite sensitive to minute displacement fields. In such a predicament, digital image correlation (DIC) (Schreier et al., 2009) turned out to be an assuring optical technique in the biomechanical field (Bay, 1995; Bay et al., 1999). However, there are some limitations such as lack of accuracy and precision due to correlation errors, substantial noise, out-of-plane movements of the surface during testing, and uncertainty problems in the vicinity of the crack junction. An improved DIC method (Heaviside-based DIC) was developed and used on bone tissue to compensate for these limitations (Valle et al., 2015). In addition, finite element methods were used recently to study the microdamage in the bone distribution in the cancellous bone and bone interface (Tozzi et al., 2012; Srinivasan et al., 2017). However, no works so far have reported on the mechanical understanding of the bone–cement interface in the field of traumatology.

Therefore, the objective of this study was to provide elements of understanding of the bone behavior on an epiphyseal fracture treated with cementoplasty to measure the mechanical effects of cement injection on adjacent bone structures and to know if it would be possible to advise weight bearing or simple passive and active mobilization postoperatively. For that, we had to define the modifications brought about by the presence of this cement in the bone under compressive stress from both an architectural and biomechanical point of view using Heaviside-based DIC to evaluate displacement fields and identification of multiple cracks.

2 MATERIALS AND METHODS

2.1 Specimen Preparation

Metaphyso-epiphyseal bone from a 6-month calf knee was used. The bone samples were cleaned of flesh and tissues. Metaphyseal regions with a good amount of cancellous bone were chosen. We reproduced the protocol of preparation and injection identical to that used to treat the cortico-spongious fracture. The first step was to dig a hole with a square tip, and then two kinds of samples were prepared. In three samples, a balloon was inflated (2ml and 500PSI of pressure), then the created cavity was filled with PMMA cement with a texture similar to the one used in the

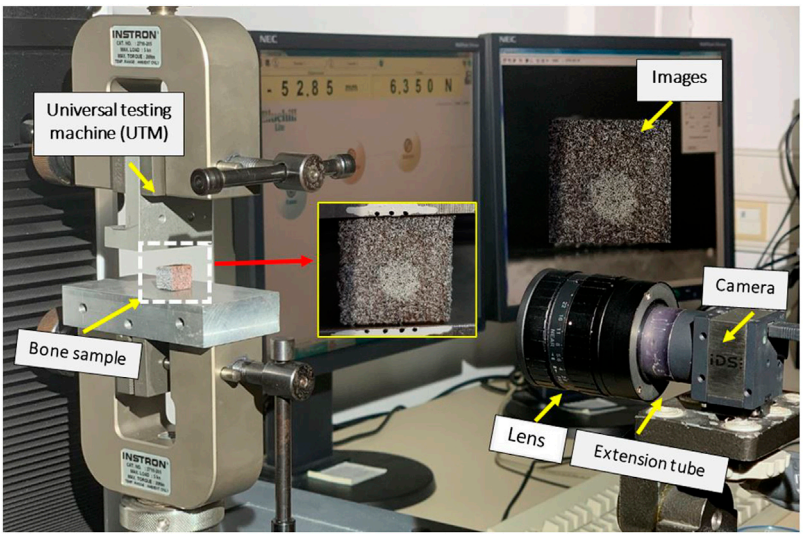

FIGURE 1 | Uniaxial compression test with speckle pattern on bone sample and markers on the support.

TABLE 1 | Strain rates used for compression tests.

	Strain rate (mm/min)		
Sample with balloon	0.001	0.05	0.1
Sample without balloon	0.001	0.05	0.1

surgical treatment of the fracture. In three other samples, the cavity was just enlarged using a drill bit of 6 mm and then filled the same way the samples with the balloon were. Cubic samples were extracted using a mechanical saw with the dimension of $15*15*10mm^3$.

Samples were preserved from degradation and stored in a refrigerator (−20°C). Before mechanical testing and before cement injection, the samples were washed with normal saline commixed with ethanol and dried in an oven at approximately 40°C to abstract moisture content (Voor et al., 2004). A speckle pattern was made on all samples using paint spray as shown in **Figure 1**.

2.2 Mechanical Experiment

The mark-tracking technique was used to measure imposed strain from markers deposed on the supports precisely. The surface of the specimen was colored by spraying white spots on a black opaque layer to increase the contrast and create a random distribution of gray levels (**Figure 1**). Uniaxial compression testing was performed using an Instron universal testing machine (5 kN). The compression tests were conducted under displacement control at three different strain rates (Shim et al., 2005) (**Table 1**) until cracks or damage in the sample were observed.

Continuous images were recorded every 2 s during the compression test (**Figure 1**). The loading stopped when the curve dropped from the maximum load.

2.3 Heaviside Digital Image Correlation (H-DIC)

In the present work, we use a novel technique (Heaviside DIC) based on Digital Image Correlation, adapted to measure the presence of cracks. This method was described in a previous article with an application in rock mechanics (Valle et al., 2015) or analysis of cracks in bone tissue (Bokam et al., 2020). H-DIC is an extension of the classic DIC method, for which we recall that the correlation function S is described as **Eq. (1)**

$$S\left(u, v, \frac{\partial u}{\partial x}, \frac{\partial u}{\partial y}, \frac{\partial v}{\partial x}, \frac{\partial v}{\partial y}\right), \tag{1}$$

and the kinematical transformation is defined [**Eq. (2)**] by simple in-plane translations $\underline{U} = (u, v)$ and the first gradients **Eq. (2)**

$$\frac{\partial \underline{U}}{\partial \underline{X}} = \left(\frac{\partial u}{\partial x}, \frac{\partial u}{\partial y}, \frac{\partial v}{\partial x}, \frac{\partial v}{\partial y}\right)$$
$$\underline{x} = \underline{\varphi}\,(\underline{X}) = \underline{X} + \underline{U} + \frac{\partial \underline{U}}{\partial \underline{X}}\left(\underline{X} - \underline{X_0}\right), \tag{2}$$

where x designates the final configuration and X, the initial one.

The solution corresponding to the optimal kinematical transformation between initial and final configurations of a deformed specimen is computed by minimization of the correlation function S [**Eq. (1)**]. Initial values need to be calculated using a minimization process to ensure an optimization starts near the global solution.

To accurately measure the displacements in presence of a crack in the subset, the kinematical field was enriched by adding a Heaviside function $\underline{H}'$ (Valle et al., 2015) as shown in **Eq. (3)**

$$\underline{x} = \underline{\varphi}\,(\underline{X}) = \underline{X} + \underline{U} + \frac{\partial \underline{U}}{\partial \underline{X}}\left(\underline{X} - \underline{X_0}\right) + \underline{H}'\left(\underline{X} - \underline{X_0}\right). \tag{3}$$

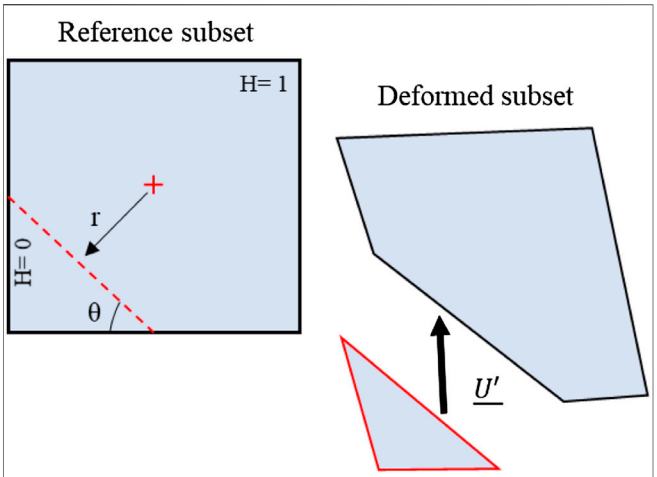

FIGURE 2 | Heaviside function effect on a subset defining the discontinuity for the H-DIC process (Valle et al., 2015).

In the first part of the above representation, the terms of a Taylor development issued from the classical DIC can be retrieved, and the second part, which corresponds to the Heaviside term as illustrated in **Figure 2**, cuts the subset into two parts. This representation can be formulated as a classical DIC analysis on two separate sub-domains D_1 and D_2 as shown in **Eq. (4)**

$$\begin{cases} \varphi_1(\underline{X}) = \underline{X} + \underline{U_1} + \dfrac{\partial U}{\partial X}\left(\underline{X} - \underline{X_0}\right) \text{on domain } D_1 \ (H=0) \\ \varphi_2(\underline{X}) = \underline{X} + \underline{U_2} + \dfrac{\partial U}{\partial X}\left(\underline{X} - \underline{X_0}\right) \text{on domain } D_2 \ (H=1) \end{cases}, \tag{4}$$

where r and θ define the position and the orientation of the two-dimensional Heaviside function $\underline{H'}$.

The optimized solution S is formulated as shown in **Eq. (5)**

$$S\left(u, v, \frac{\partial u}{\partial x}, \frac{\partial v}{\partial x}, \frac{\partial u}{\partial y}, \frac{\partial v}{\partial y}, u', v', \theta, r\right), \tag{5}$$

with $\underline{U}' = (u', v')$ the jump vector and $H(\underline{X} - \underline{X_0}) = H(r, \theta)$ defining a right line in a circular base and using the representation in **Figure 2**.

Parameters $(u, v, \frac{\partial u}{\partial x}, \frac{\partial v}{\partial x}, \frac{\partial u}{\partial y}, \frac{\partial v}{\partial y}, u', v', \theta, r)$ are optimized in a single process, and all subsets are enriched. When there is no discontinuity present in the subset, the optimization gives a jump $\underline{U}'$ near zero and automatically deactivates the Heaviside term.

The optimization process, based on a descending gradient algorithm, was employed to retrieve the displacement for each subset. Moreover, the algorithm implemented in "Massive Parallel Computation" with a GPU card allows high-speed and high-resolution analysis.

2.4 Finite Element (FE) Analysis

To obtain a better understanding of bone behavior when filled with PMMA cement and to dispose of stress analysis, we built a preliminary FE model from the comparison with the displacement and strain of experimental results. We used the same geometry we had in our samples without a balloon. The sample was discretized in two parts, a cement cylinder inside the cubic cancellous bone sample. The quality of the mesh was evaluated from a convergence study to verify the optimal mesh parameters. The resulting mesh was composed of four-noded tetrahedral elements (mean edge length, 0.5 mm). The experimental boundary conditions were mimicked as realistically as possible in the FE simulations (**Table 2**). The mechanical properties of materials are given in **Table 3**. The Young modulus of the cement (PMMA material) and of the cancellous bone was evaluated from experimental tests (Vendeuvre et al., 2019).

The FE simulations were performed using ANSYS® software (release 16.1, ANSYS, Inc., United States).2.5.

3 RESULTS

3.1 Displacement-Load Curves

Individual results for the six cases, that is, cement/cancellous interface with a balloon and without a balloon with a strain rate of 0.001 mm/min, 0.05 mm/min, and 0.1 mm/min are presented here. The compression loading conditions (as shown in **Figure 1**) were chosen to mimic real-time loading of tibial fractures, especially for type I (split), II (split and depression), and type-III (depression) of Schatzker classification (Schatzker et al., 1979).

A representative load vs. displacement response for the six bone specimens is shown in **Figure 3**. Incremental loading of the specimens was then continued until the final fracture and digital images were recorded to identify the incremental crack growth.

3.2 Displacement Field

An image of the specimen was recorded prior to the loading (reference step) and at each loading step of the displacement (every 2 s during the loading). These images were later used for computing the displacement fields using the H-DIC method at every load step. Some illustrations of displacement fields are shown in **Figure 4** from a few load steps. Analysis was conducted by H-DIC with a subset size of 48*48 pixels used for all the computations for identifying discontinuity and for measuring displacement.

TABLE 2 | Boundary conditions used for FE analysis.

Model 1	Model 2
Two materials bonded Zero imposed displacement on the lower face Load applied on the upper face	No separation contacts without friction between two materials

TABLE 3 | Material properties used for FE analysis.

Property	Cancellous bone	PMMA
Young modulus (MPa)	150	2500
Poisson ratio	0.3	0.3

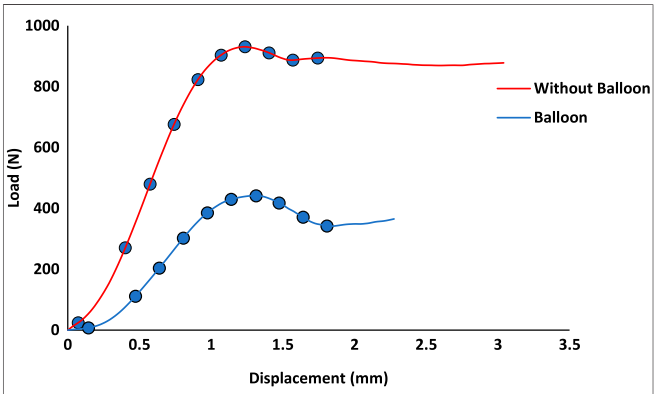

FIGURE 3 | Load–displacement curve for a sample with a 1 mm/min loading condition, with and without a balloon. The circles on the curve represent the loading steps that were chosen to analyze using H-DIC.

With the proposed H-DIC method, the discontinuities were observed both near and far from the crack with variation in the gradient values throughout the boundaries in both X and Y directions. The enriched Heaviside function was very efficient at giving results for the zone influenced by fractures. The accuracy of the gradients in the horizontal U_x component and vertical U_y component were well retrieved in H-DIC. The displacement fields according to both directions show the absence of displacement inside the cement compared to the cancellous bone where there was the maximum displacement. The cement behaved like a rigid body inside a material that is far less stiff.

3.3 Strain Distribution and Crack Identification

Figure 5 shows the equivalent strain fields for the sample with and without a balloon for 1 mm/min at the bone/cement interface. For the same strain gradient value, successive loading steps were considered to identify the discontinuity from the initial state to the final fracture. The strain maps resulting from H-DIC demonstrated clear localization of the crack and reliable evolution of the μcrack until a final fracture was observed in the interface between cement and cancellous bone.

We see clearly in **Figure 5** that the discontinuity has been initiated between bone and cement. Even if we were still were in the linear part of the curve (**Figure 3**), there were already discontinuities and even the beginning of cracks. So, there was a clear discontinuity between both materials which led to the degradation, when it occurs, of the cancellous bone alone.

Figure 6 shows the equivalent strain in different localizations in the specimen. The two configurations were compared (with the balloon, in black, and without the balloon, in red). For cancellous bone, we had a similar strain initially and after the fracture. The strain increased abruptly in the specimen in both cases.

In cement, for both specimens, the strain was almost the same with a slight increase after the fracture. In the interface, in the specimen without a balloon, the strains were very high from the beginning and were almost constant with a slight increase after a fracture. However, in specimens with a balloon, the strain increased as the load increased even after the fracture.

3.4 Which Finite Element Model Matches the Experiment

The results of displacement fields from the two different models are shown in **Figure 7** for a compression loading of 500 N. The most relevant model in terms of displacement and strain was the model without a link between the two materials. In this model, as in our experimentation, a discontinuity of mechanical behavior occurred at the interface, involving a slight heterogeneous displacement of the cement part.

4 DISCUSSION

4.1 Mechanical Behavior of Cement/Bone Tissue Interface

The identification of mechanical fields and cracks in the cement/cancellous bone interface was important to understand the biomechanical behavior of the bone filled with cement in the

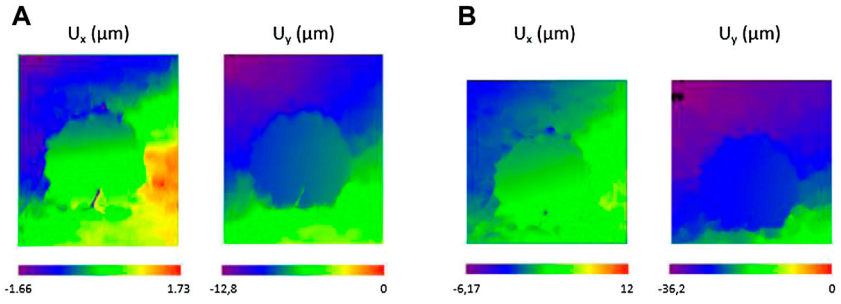

FIGURE 4 | Examples of displacement fields for a sample without a balloon at **(A)** 0.66 mm and **(B)** 1.33 mm of imposed displacement (loading speed: 1 mm/min).

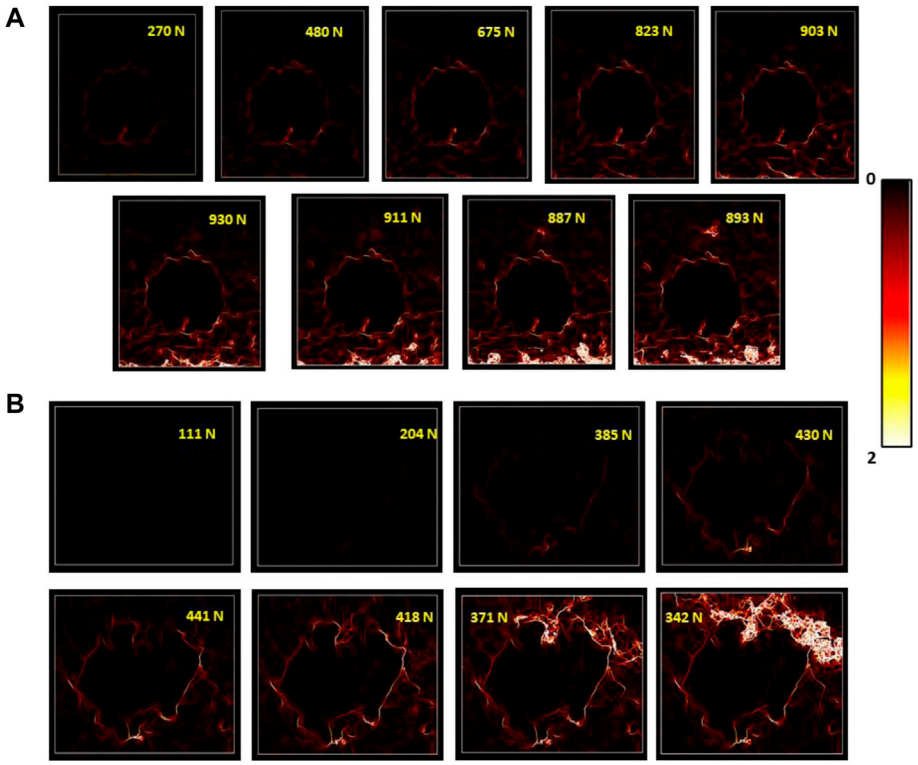

FIGURE 5 | Evolution of equivalent strain fields obtained from the DIC method for consecutive loading steps for **(A)** sample without a balloon and **(B)** with a balloon.

treatment of tibial plateau fracture treated by tuberoplasty. No similar work, especially corresponding to the cement/cancellous interface fracture, has been reported earlier using digital image correlation. A clear evolution of the fracture line could be observed between the interfaces from the initial to the final state. It demonstrated the discontinuity between both materials that begin early but caused cracks and fracture after a linear behavior. This demonstration was carried out with the use of a novel correlation process: H-DIC. There is no equivalent method available in the literature to analyze bone tissues during continuous loading. With the help of H-DIC, it was possible to identify and localize fracture zone, multiple fracture lines, and multiple µcracks even at a very low strain gradient and with good accuracy.

4.2 Same Curves Without Cement but Crack Initiation and Propagation Identical to the Cancellous–Cortical Interface

In a recent work (Bokam et al., 2020), a compression test using H-DIC correlation showed the behavior of different configurations of bone without cement (**Figure 8**). The load vs. time plot is illustrated in **Figure 8**.

In our present work, the load versus time plot is similar to the one of cancellous bone without cement and without cortical. However, the initiation and propagation of the cracks were more similar to the configuration of sample 3 with cancellous–cortical interface (**Figure 9**).

4.3 Speed and Balloon Contribution

During a tibial plateau fracture, there is a fracture in the cortical bone and compaction of the cancellous bone below. To reduce the fracture during tuberoplasty, a balloon is inflated, inducing compaction of the cancellous bone around the balloon (Vendeuvre et al., 2013; Belaid et al., 2018). To be as close to reality as possible, we decided to create a cavity using compaction due to the inflation of the balloon.

The results of our study showed no difference in the initiation of the cracks that occurred at the cement–bone interface, and no difference in the displacement map with no displacement in the cement. We obtained the same results of variation of the level of load needed to fail, to modify the speed of loading. These results are explained by a deterioration of the bone's mechanical properties by compacting the cancellous bone.

But the compaction induced a modification of bone density, and the contrast between cement and healthy cancellous was far lower which explained the results we show in **Figure 7**. With balloon and bone compaction, there was a transfer of strain carried out without changes of behavior at the interface compared to the group without a balloon. This explains the fact that in samples with a balloon, the discontinuity began later in the linear part of the curve. Whereas, without balloon samples, the first cracks which indicate the discontinuity appeared very early in the experiment, when we were still in the very beginning of the linear part.

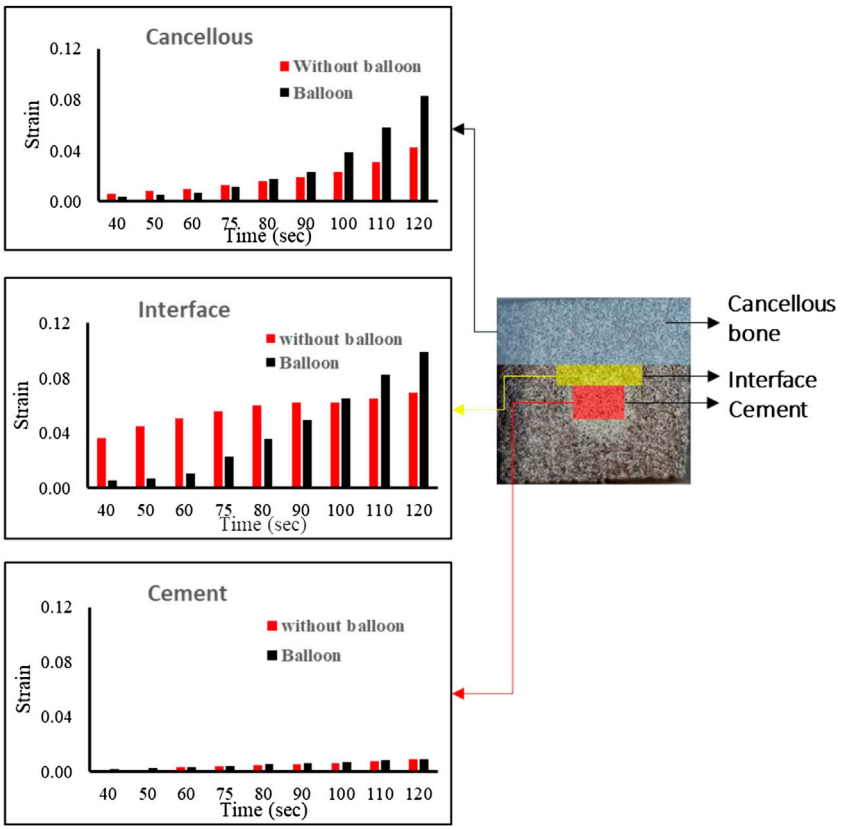

FIGURE 6 | Strain variation in different zones for a sample without the balloon and with the balloon.

4.4 Which Biomechanical Model and Clinical Relevance

Surgeons use the cement thinking that it will create a link with the different cancellous bone fragments (as in model 1 in **Figure 7**). They do not know if the mechanical properties of the cement permit weight-bearing on the operated foot. With the contact model used, the experiment demonstrated that the most relevant model would be model 2 (where cement and bone were not bonded). The FE approach provided stress analysis showing a higher stress concentration in the bone around the cement with model 2 (**Figure 10**). In future works, an evolutionary model with bonded contact with bone and cement, which could debond above some stress limits, is important to better answer this issue.

In addition, the load needed to obtain a crack, which in real life means a bone fracture, is far under the load observed in the knee for a 75 kg male person while walking (Bergmann et al., 2014). Our work demonstrated that for the cement to provide good reduction and primary stabilization (Vendeuvre et al., 2013; Belaid et al., 2018), permitting the patient to undergo rehabilitation with active and passive mobilization, no weight-bearing should be authorized while the bone is not consolidated. These results were very interesting because it differed from some works showing that the stabilization of spine fracture with kyphoplasty was sufficient to stabilize the fracture, permitting the patient to walk 12 h after the surgery without any brace (Germaneau et al., 2016).

Two parameters could play a role to improve adhesion between bone and cement: the pressure of injection and the present viscosity of the injection. During surgery, cement is injected with pressure and with high viscosity to limit the leakage. An experimental biomechanical study with the variation of these two parameters must be performed to provide significant inputs concerning the optimal way to inject the cement. In addition, in the future, FE analysis on the treatment of tibial plateau fracture using adequate biomechanical characteristics with no contact bonding between both materials should be made to study the linear behavior before discontinuity.

4.5 Limitations

Owing to the aforementioned results, the present study has some limitations. The experiments have been performed using 2D image analyses that only provide surface strain measurements. A volume approach with X-ray micro-computed tomography analysis to measure the displacement fields by H-Digital Volume Correlation (H-DVC) (Valle et al., 2018) could provide a better understanding of the microstructure mechanical behavior in bone tissues and particular volume crack detection between

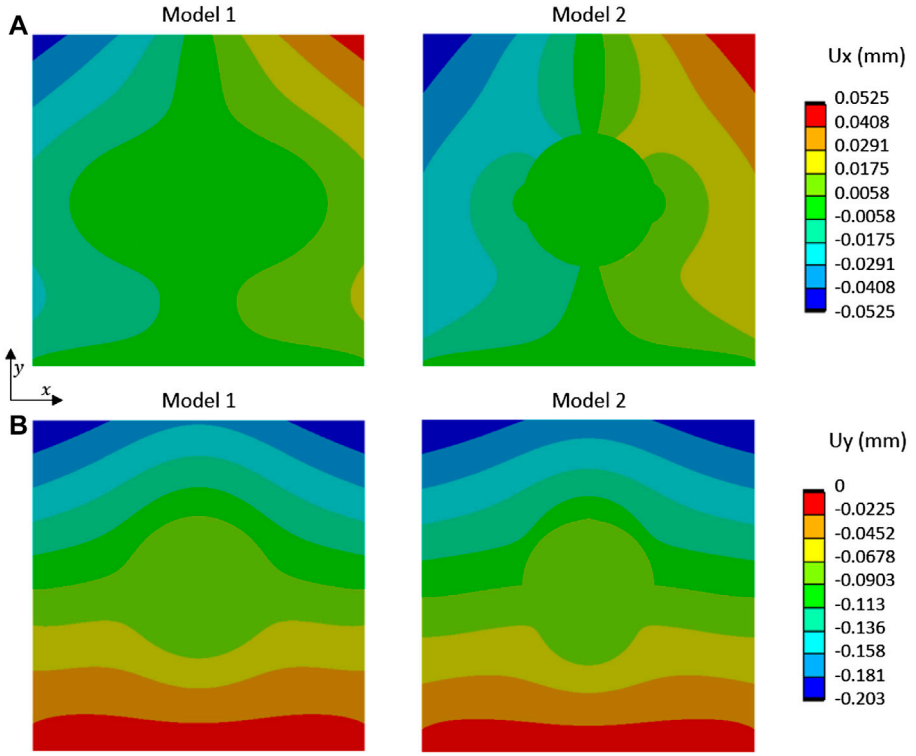

FIGURE 7 | Displacement fields, **(A)** U_x and **(B)** U_y, from FE simulation of compression tests for two models (Model 1: cement and cancellous bone were bonded; Model 2: cement and cancellous bone were not bonded without separation) and loading of 500 N.

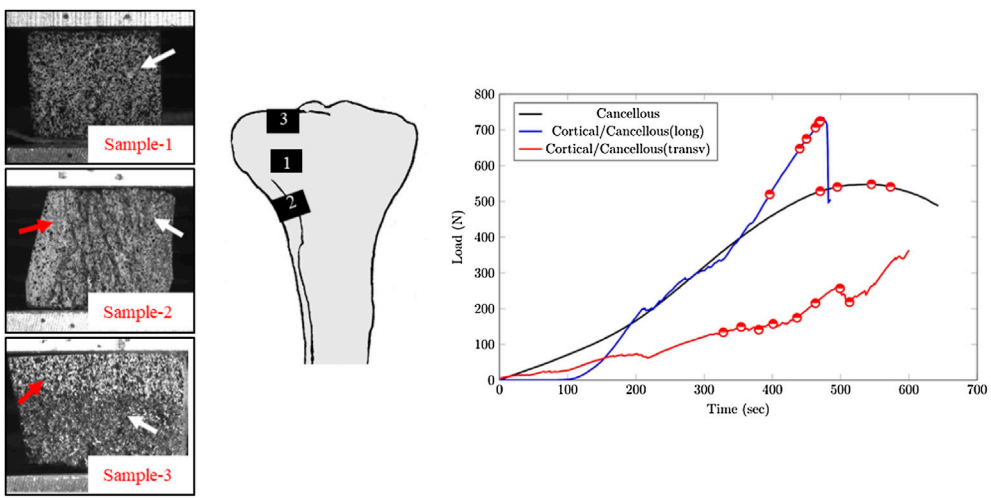

FIGURE 8 | Load vs. time plot for different sample configurations: Sample 1—cancellous bone, Sample 2—cortical/cancellous in a longitudinal orientation, and Sample 3—tibial plateau in a transverse orientation.

bone and cement. This will be the next step of the present work. On the other hand, DVC analyses were performed with a limited number of static load steps making crack apparition and crack propagation difficult. Therefore, a 2D analysis with H-DIC would be very interesting for detecting microcracks, crack initiation, and propagation for various loading conditions without interrupting the loading. 2D *in vitro* analysis also allows highlighting the relevant static load steps for future 3D analysis. Moreover, in the present study, only a macro-scale sample (cuboid shape) was used as a first test, whereas, in the future, more experiments on the whole bone sample should be performed to improve the finite element model of bone treatment by tuberoplasty. Concerning FE

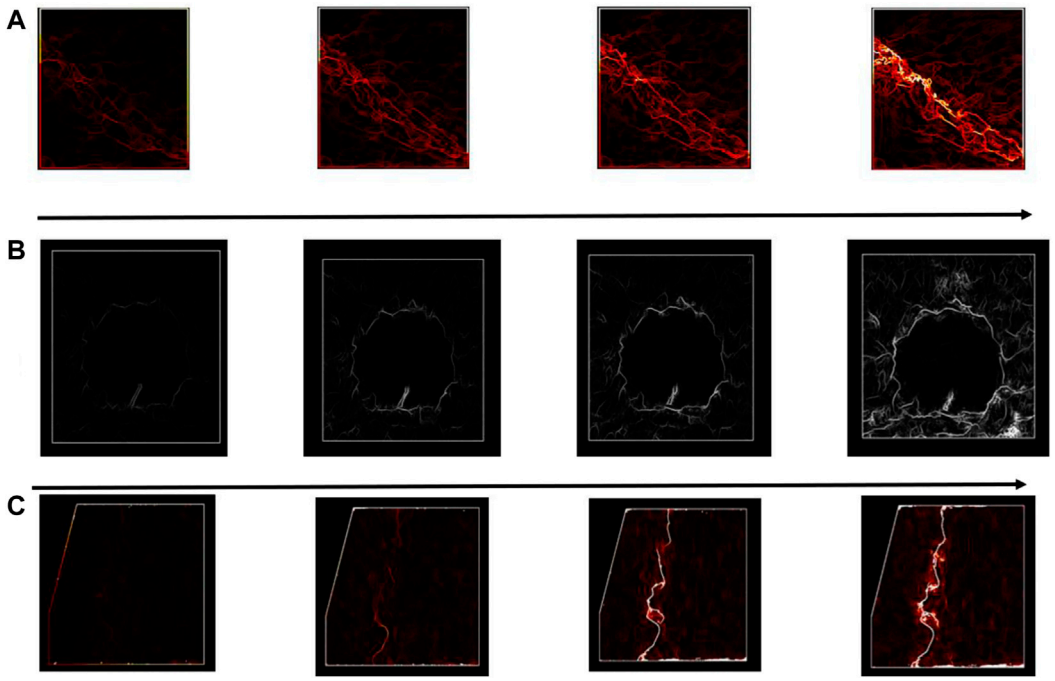

FIGURE 9 | Equivalent strain displacement comparison for consecutive loading steps between different configurations for **(A)** cancellous bone, **(B)** cancellous–cement sample, and **(C)** cancellous–cortical samples, respectively.

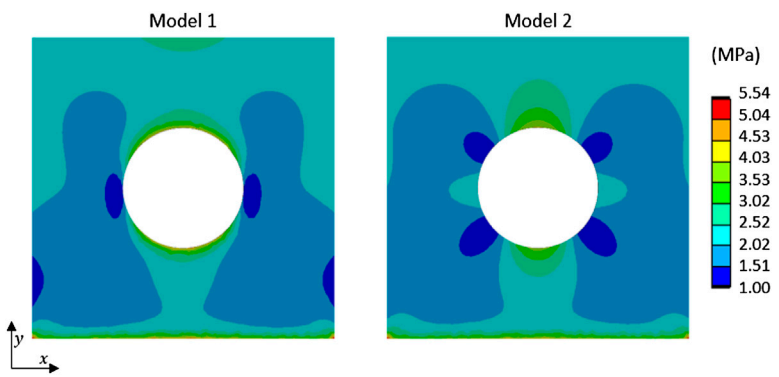

FIGURE 10 | Equivalent stress fields from FE simulation of compression test for two models (Model 1: cement and cancellous bone were bonded; Model 2: cement and cancellous bone were not bonded without separation) and loading of 500 N.

analysis, we considered two contact models: bonded and without friction. An evolutionary model with bonded contact between bone and cement which could debond above some stress limits could be future work to complete the local analysis of mechanical effects of cement injection.

5 CONCLUSION

In this work, experiments were performed to study the bone's mechanical behavior when filled with PMMA cement. Several parameters have been studied by using a novel correlation process highlighting the biomechanical role of the cement inside the bone. This demonstrated that there is a discontinuity of load transfer between bone and cement. After the surgery, the cement behaves like a rigid body inside the cancellous bone (same as a screw or plate). With balloon inflation and bone compaction, there was a transfer of strain carried out without changes of behavior at the interface, compared to specimens without the balloon. FE analysis has been performed and compared to other experiments. This approach underlined a higher stress concentration when there is no link between bone and cement.

The cement provides good reduction and primary stabilization with its large contact area with the bone (minimally invasive

approach and good stress distribution), permitting the patient to undergo rehabilitation with active and passive mobilization, but no weight-bearing should be authorized while the cortical bone is not consolidated or stabilized.

DATA AVAILABILITY STATEMENT

The raw data supporting the conclusions of this article will be made available by the authors, without undue reservation.

AUTHOR CONTRIBUTIONS

Conceptualization: A.M, P.B, T.V, V.V, and A.G; methodology: P.B, V.V, L.C, A.M, and A.G; software: V.V, P.B, L.C, and A.G; validation: AM, P.B, and A.G; resources: A.G, V.V, G.H-G, and T.V; writing—original draft preparation: A.M, P.B, L.C, V.V, T.V, and A.G; writing—review and editing: A.M, P.B, L.C, G.H-G, M.S, T.V, V.V, and A.G; supervision: A.G, T.V, G.H-G, and V.V; and project administration: A.G, T.V, and V.V. All authors have read and agreed to the published version of the manuscript.

REFERENCES

Bay, B. K., Smith, T. S., Fyhrie, D. P., and Saad, M. (1999). Digital Volume Correlation: Three-Dimensional Strain Mapping Using X-Ray Tomography. *Exp. Mech.* 39, 217–226. doi:10.1007/BF02323555

Bay, B. K. (1995). Texture Correlation: A Method for the Measurement of Detailed Strain Distributions within Trabecular Bone. *J. Orthop. Res.* 13, 258–267. doi:10.1002/jor.1100130214

Belaid, D., Vendeuvre, T., Bouchoucha, A., Brémand, F., Brèque, C., Rigoard, P., et al. (2018). Utility of Cement Injection to Stabilize Split-Depression Tibial Plateau Fracture by Minimally Invasive Methods: A Finite Element Analysis. *Clin. Biomech.* 56, 27–35. doi:10.1016/j.clinbiomech.2018.05.002

Bergmann, G., Bender, A., Graichen, F., Dymke, J., Rohlmann, A., Trepczynski, A., et al. (2014). Standardized Loads Acting in Knee Implants. *PloS One* 9 (1), e86035. doi:10.1371/journal.pone.0086035

Bokam, P., Germaneau, A., Rigoard, P., Vendeuvre, T., and Valle, V. (2020). Evaluation of Fracture Properties of Cancellous Bone Tissues Using Digital Image Correlation/wedge Splitting Test Method. *J. Mech. Behav. Biomed. Mater.* 102, 103469. doi:10.1016/j.jmbbm.2019.103469

Cole, P., Levy, B., Watson, J. T., and Schatzker, J. (2009). "Tibial Plateau Fractures," in *Skeletal Trauma: Basic Science Management and Reconstruction* (Philadelphia, PA: Saunders Elsevier), 2201–2287. doi:10.1016/b978-1-4160-2220-6.10056-8

Germaneau, A., Vendeuvre, T., Saget, M., Doumalin, P., Dupré, J. C., Brémand, F., et al. (2016). A Novel Approach for Biomechanical Spine Analysis: Mechanical Response of Vertebral Bone Augmentation by Kyphoplasty to Stabilise Thoracolumbar Burst Fractures. *J. Mech. Behav. Biomed. Mater.* 59, 291–303. doi:10.1016/j.jmbbm.2016.02.002

Honkonen, S. E. (1995). Degenerative Arthritis after Tibial Plateau Fractures. *J. Orthop. Trauma* 9 (04), 273–277. doi:10.1097/00005131-199509040-00001

Krause, M., Müller, G., and Frosch, K.-H. (2018). Chirurgische Zugänge bei Tibiakopffrakturen. *Unfallchirurg* 121 (7), 569–582. doi:10.1007/s00113-018-0515-6

Larrabee, W. F. (1986). A Finite Element Model of Skin Deformation. *Laryngoscope* 96, 399–405. doi:10.1288/00005537-198604000-00012

Nagarkatti, D. G., McKeon, B. P., Donahue, B. S., and Fulkerson, J. P. (2001). Mechanical Evaluation of a Soft Tissue Interference Screw in Free Tendon Anterior Cruciate Ligament Graft Fixation. *Am. J. Sports Med.* 29, 67–71. doi:10.1177/03635465010290011601

Nicolella, D. P., Nicholls, A. E., Lankford, J., and Davy, D. T. (2001). Machine Vision Photogrammetry: A Technique for Measurement of Microstructural Strain in Cortical Bone. *J. Biomechanics* 34, 135–139. doi:10.1016/S0021-9290(00)00163-9

Onimus, M., and Bertin, D. (1982). Surgical Stabilisation of Metastatic Fractures of the Spine. *Rev. Chir. Orthop. Reparatrice Appar. Mot.* 68 (6), 369–378.

Prod'homme, M., Pour Jafar, S., Zogakis, P., and Stutz, P. (2018). A Novel Minimally Invasive Reduction Technique by Balloon and Distractor for Intra-articular Calcaneal Fractures: A Report of 2 Cases. *Case Rep. Orthop.* 2018, 1–8. doi:10.1155/2018/7909184

Rademakers, M. V., Kerkhoffs, G. M. M. J., Sierevelt, I. N., Raaymakers, E. L. F. B., and Marti, R. K. (2007). Operative Treatment of 109 Tibial Plateau Fractures: Five- to 27-Year Follow-Up Results. *J. Orthop. Trauma* 21 (01), 5–10. doi:10.1097/BOT.0b013e31802c5b51

Schatzker, J., McBroom, R., and Bruce, D. (1979). The Tibial Plateau Fracture. The Toronto Experience 1968--1975. *Clin. Orthop. Relat. Res.* 138, 94–104.

Schreier, H., Orteu, J.-J., and Sutton, M. A. (2009). *Image Correlation for Shape, Motion and Deformation Measurements. Basic Concepts, Theory and Applications*. Rochester NY: Springer, 341. doi:10.1007/978-0-387-78747-3

Shim, V. P. W., Yang, L. M., Liu, J. F., and Lee, V. S. (2005). Characterisation of the Dynamic Compressive Mechanical Properties of Cancellous Bone from the Human Cervical Spine. *Int. J. Impact Eng.* 32, 525–540. doi:10.1016/j.ijimpeng.2005.03.006

Smith, D. C. (2005). The Genesis and Evolution of Acrylic Bone Cement. *Orthop. Clin. N. Am.* 36 (1), 1–10. doi:10.1016/j.ocl.2004.06.012

Srinivasan, P., Miller, M. A., Verdonschot, N., Mann, K. A., and Janssen, D. (2017). A Modelling Approach Demonstrating Micromechanical Changes in the Tibial Cemented Interface Due to *In Vivo* Service. *J. Biomechanics* 56, 19–25. doi:10.1016/j.jbiomech.2017.02.017

Suzuki, G., Saito, S., Ishii, T., Motojima, S., Tokuhashi, Y., and Ryu, J. (2011). Previous Fracture Surgery Is a Major Risk Factor of Infection after Total Knee Arthroplasty. *Knee Surg. Sports Traumatol. Arthrosc.* 19 (12), 2040–2044. doi:10.1007/s00167-011-1525-x

Tozzi, G., Zhang, Q.-H., and Tong, J. (2012). 3D Real-Time Micromechanical Compressive Behaviour of Bone-Cement Interface: Experimental and Finite Element Studies. *J. Biomechanics* 45 (2), 356–363. doi:10.1016/j.jbiomech.2011.10.011

Väänänen, S. P., Amin Yavari, S., Weinans, H., Zadpoor, A. A., Jurvelin, J. S., and Isaksson, H. (2013). Repeatability of Digital Image Correlation for Measurement of Surface Strains in Composite Long Bones. *J. Biomechanics* 46, 1928–1932. doi:10.1016/j.jbiomech.2013.05.021

Valle, V., Bokam, P., Germaneau, A., and Hedan, S. (2018). New Development of Digital Volume Correlation for the Study of Fractured Materials. *Exp. Mech.* 59, 1–15. doi:10.1007/s11340-018-0415-2

Valle, V., Hedan, S., Cosenza, P., Fauchille, A. L., and Berdjane, M. (2015). Digital Image Correlation Development for the Study of Materials Including Multiple Crossing Cracks. *Exp. Mech.* 55, 379–391. doi:10.1007/s11340-014-9948-1

Vendeuvre, T., Babusiaux, D., Brèque, C., Khiami, F., Steiger, V., Merienne, J.-F., et al. (2013). Tuberoplasty: Minimally Invasive Osteosynthesis Technique for Tibial Plateau Fractures. *Orthop. Traumatology Surg. Res.* 99 (4 Suppl. l), S267–S272. doi:10.1016/j.otsr.2013.03.009

Vendeuvre, T., Dupré, J.-C., Courat, N., Léglise, A., Hesser, F., Brémand, F., et al. (2019). Assessment of PMMA Mechanical Properties versus Time Polymerization

to Optimize Fracture Stabilizations. *Comput. Methods Biomechanics Biomed. Eng.* 22, S494–S496. doi:10.1080/10255842.2020.1714994

Voor, M. J., White, J. E., Grieshaber, J. E., Malkani, A. L., and Ullrich, C. R. (2004). Impacted Morselized Cancellous Bone: Mechanical Effects of Defatting and Augmentation with Fine Hydroxyapatite Particles. *J. Biomechanics* 37, 1233–1239. doi:10.1016/j.jbiomech.2003.12.002

Yang, P. F., Brüggemann, G. P., and Rittweger, J. (2011). What Do We Currently Know from *In Vivo* Bone Strain Measurements in Humans? *J. Musculoskelet. Neuronal Interact.* 11, 8–20.

Conflict of Interest: The authors declare that the research was conducted in the absence of any commercial or financial relationships that could be construed as a potential conflict of interest.

Publisher's Note: All claims expressed in this article are solely those of the authors and do not necessarily represent those of their affiliated organizations, or those of the publisher, the editors, and the reviewers. Any product that may be evaluated in this article, or claim that may be made by its manufacturer, is not guaranteed or endorsed by the publisher.

frontiers | Frontiers in Bioengineering and Biotechnology

BRIEF RESEARCH REPORT
published: 06 July 2022
doi: 10.3389/fbioe.2022.914137

Subject-Specific 3D Models to Investigate the Influence of Rehabilitation Exercises and the Twisted Structure on Achilles Tendon Strains

Alessia Funaro[1], Vickie Shim[2], Marion Crouzier[1], Ine Mylle[1] and Benedicte Vanwanseele[1]*

[1]Human Movement Biomechanics Research Group, KU Leuven, Leuven, Belgium, [2]Auckland Bioengineering Institute, University of Auckland, Auckland, New Zealand

The Achilles tendon (AT) is the largest tendon of the human body and has a primary role in locomotor activities. The complex structure of the AT includes twisting of three sub-tendons, non-uniform tissue deformations and differential triceps surae muscle forces. The main aim of this study was to investigate the impact of commonly used rehabilitation exercises (walking on heels, walking on toes, unilateral heel rise, heel drop with extended knee and heel drop with the knee bent) and different twists on AT strains. 3D freehand ultrasound based subject-specific geometry and subject-specific muscle forces during different types of rehabilitation exercises were used to determine tendon strains magnitudes and differences in strains between the sub-tendons. In addition, three Finite Element models were developed to investigate the impact of AT twist. While walking on heels developed the lowest average strain, heel drop with knee bent exhibited the highest average strain. The eccentric heel drop resulted in higher peak and average strain, compared to concentric heel rise for all the three models. The isolated exercises (heel rise and heel drop) presented higher average strains compared to the functional exercises (walking tasks). The amount of twist influences the peak strains but not the average. Type I consistently showed highest peak strains among the five rehabilitation exercises. The ranking of the exercises based on the AT strains was independent of AT twist. These findings might help clinicians to prescribe rehabilitation exercises for Achilles tendinopathy based on their impact on the AT strains.

Keywords: achilles tendon, fascicle twist, sub-tendon morphology, tendon strain, finite element modeling, rehabilitation exercises

OPEN ACCESS

Edited by:
Mohammad Nikkhoo, Islamic Azad University, Iran

Reviewed by:
Kirsten Albracht, University of Applied Sciences Aachen, Germany
Weijie Fu, Shanghai University of Sport, China

****Correspondence:***
Alessia Funaro
alessia.funaro@kuleuven.be

Specialty section:
This article was submitted to Biomechanics, a section of the journal Frontiers in Bioengineering and Biotechnology

Received: *06 April 2022*
Accepted: *20 June 2022*
Published: *06 July 2022*

Citation:
Funaro A, Shim V, Crouzier M, Mylle I and Vanwanseele B (2022) Subject-Specific 3D Models to Investigate the Influence of Rehabilitation Exercises and the Twisted Structure on Achilles Tendon Strains. Front. Bioeng. Biotechnol. 10:914137. doi: 10.3389/fbioe.2022.914137

1 INTRODUCTION

The Achilles tendon (AT) plays a major role during weight-bearing locomotor activities by sustaining loads up to 7.7 times bodyweight (Komi et al., 1992) and transfers the generated muscle force from the triceps surae to the calcaneus. Despite being the strongest and thickest tendon of the human body (Maffulli, 1999), the AT is very susceptible to injuries. Achilles tendinopathy is one of the most common foot and ankle overuse injuries (Sobhani et al., 2013), with a prevalence of up to 9.5% and 11.8% in athletic (Lopes et al., 2012) and non-athletic populations (Albers et al., 2016), respectively.

The AT is mechanosensitive, so the exposure to loading leads to changes in its mechanical properties. Loading of the tendon causes complex internal tissue strains which, in turn, induces tendon remodeling. Wang et al. (2015) demonstrated that a certain loading regime might create a proper (internal) mechanical environment, able to reverse early-stage pathological changes in Achilles tendinopathy patients. Consequently, insights into the effect of these exercises on the tendon strain can serve as a guide for progression in rehabilitation, since an appropriate biomechanical environment can facilitate the rehabilitation process of the AT through an optimal loading dose.

Currently, exercise-based therapy with load management is the treatment of choice in clinical practice, to reduce aggravating loads and to introduce pain-relieving loads (Cook and Purdam, 2014). Different rehabilitation protocols were proposed including a variety of eccentric exercises (Alfredson et al., 1998), a combination of eccentric and concentric exercises (Silbernagel et al., 2001) and a combination of more functional exercises (Mascaró et al., 2018). However, there is still little clinical or mechanistic evidence for isolating the eccentric component (Malliaras et al., 2013). In addition, up to 40% of the patients don't respond to the classical treatment schemes (Maffulli et al., 2008) and it remains unknown if these rehabilitation programs provide an optimal stimulus for healing (Lysholm and Wiklander, 1987) or they are just pain relievers. The progression of exercises is currently mostly based on the subjective feeling of pain rather than the objective tendon loading, which is the driving factor for tissue regeneration. Previous studies attempted to rank the rehabilitation exercises according to AT load. Recently, studies by Baxter et al. (2021) and Devaprakash et al. (2022) developed an exercise progression that incrementally increases AT load. However, in both studies, the AT loading was estimated by external measures, with motion capture in conjunction with ground reaction force data or surface electromyography, which don't account for the tendon geometry or material properties and cannot describe the internal tendon load. During force production, the tendon strain is governed by the muscle forces but also by the 3D geometry of the AT, which is complex (Edama et al., 2016; Pękala et al., 2017). Tendon fibers originate from triceps surae: the soleus (SOL) and the two heads (medialis, GM and lateralis, GL) of the gastrocnemius muscle, forming three individual sub-tendons (Pękala et al., 2017). Based on the degree of twist, three types of twisted structures have been identified: Type I (least), Type II (moderate) and Type III (extreme) (Pękala et al., 2017). Since the AT arises from three muscles, it will be subjected to three muscles forces and therefore behaves as three partially independent sub-tendons, leading to significant sliding between adjacent sub-tendons. This sliding has been previously reported *in vivo* within healthy AT using ultrasound imaging (Bogaerts et al., 2017), and is thought to reduce the stress within the tendon (Thorpe et al., 2015).

Finite element (FE) models of the AT allow us to investigate the effects of variations in tendon geometry and material properties on local tendon stress and strain. Handsfield et al. (2017) demonstrated that the amount of intra-tendon sliding and tendon twist plays a role on the relationship between muscle forces and tendon behaviour. Shim et al. (2018) further showed that the AT experiences non-uniform tissue deformation between tendon regions when sub-tendons geometry and tendon twist were included in their FE model. This was further confirmed by the fact that varying overall tendon twist in such models showed to impact tendon fascicle length, strain and energy storage (Knaus and Blemker, 2021). The main limitation of these previous studies is that the three sub-tendons were not included in the AT models (Hansen et al., 2017) or, if included, only two sub-tendons were considered (soleus and gastrocnemius) (Shim et al., 2019; Handsfield et al., 2020). In studies that considered the three sub-tendons (Handsfield et al., 2017; Knaus and Blemker, 2021; Yin et al., 2021), the focus was on the analysis of more static exercises. To compare the effect of typical exercises from rehabilitation protocols for Achilles tendinopathy, one needs to use a FE model which includes all three sub-tendons, subject-specific geometry and muscle forces.

Therefore, the aim of this study was to develop and implement FE models including subject-specific geometry and muscle forces during a selection of common rehabilitation exercises to investigate the different types of exercises and the effect of twist on the AT strain. Accordingly, we included exercises to compare eccentric vs. concentric, isolated vs. functional and exercises variation with differential muscle forces. Then, investigating the influence of the type of twist on AT strains could provide insights into potential reasons for subject-specific responses to treatment. Because the different executions of the exercises are expected to redistribute the muscle forces, we hypothesized that they would change the tendon strains. Specifically, we hypothesized that the ranking of the exercises would start from eccentric and concentric exercises, moving towards more functional exercises, as recommended by previous rehabilitation protocols (Mascaró et al., 2018). We also hypothesized that an increase in the degrees of tendon twist would reduce the tendon strain.

2 MATERIALS AND METHODS

A subject-specific geometry of the free tendon as well as the triceps surae muscle forces during the rehabilitation exercises were obtained from one female participant (age = 29 years, weight = 56 kg, height = 174 cm). The participant did not report any (previous) injuries to the AT or foot and ankle complex, nor a systemic disease affecting the collagenous tissue and provided written informed consent before participation.

2.1 Generic Model Geometry

To allow the consistent definition of the three sub-tendons within subject-specific FE models, we created first a generic template mesh. This mesh was generated from an initial geometry, obtained by segmentation of images from one healthy male subject (age = 22 years, weight = 64 kg, height = 180 cm) recorded by 3DfUS images, defining the outer geometry of the tendon. Three different types of twist were then created using Materialise 3-matic (Materialise NV, Leuven, Belgium). The tendon model was divided into three sub-tendons. Different

twist angles were applied that resulted in three twisted structures that corresponded with the classification of the AT twist (Type I, Type II, and Type III) described by Pękala et al. (2017). The sub-tendons geometries were meshed into 8-nodes hexahedral solid elements. A mesh convergence study was performed to refine the mesh until the Principal Effective Lagrange strains reached an asymptote.

2.2 Constitutive Models

The tendon models were represented as an incompressible, transversely isotropic hyperelastic material (Weiss et al., 1996). The uncoupled strain energy function can be written as in **Eq. 1**:

$$\Psi = F_1\left(\tilde{I}_1, \tilde{I}_2\right) + F_2\left(\tilde{\lambda}\right) + \frac{K}{2}[ln(J)]^2 \quad (1)$$

Here, $\tilde{I}_1$ and $\tilde{I}_2$ are the first and second invariants of the deviatoric version of the right Cauchy-Green deformation tensor. $\tilde{\lambda}$ is the deviatoric part of the stretch along the fiber direction, and $J = \det(F)$ is the Jacobian of the deformation. This strain energy density function consists of two parts: F_1 represents the material response of the isotropic ground substance matrix, while F_2 represents the contribution from the collagen fibers. F_1 was described as a Neo-Hookean model and it was equal to $\frac{C_1(I_1-3)}{2}$. The resulting fiber stress from the fibers was expressed using the piecewise function in **Eq. 2**:

$$\tilde{\lambda}\frac{\partial F_2}{\partial \tilde{\lambda}} = \begin{cases} 0 & \tilde{\lambda} \le 1 \\ C_3\left(e^{C_4\left(\tilde{\lambda}-1\right)} - 1\right) & 1 < \tilde{\lambda} < \lambda_m \\ C_5\tilde{\lambda} + C_6 & \tilde{\lambda} \ge \lambda_m \end{cases} \quad (2)$$

Here, λ_m is the strain at which the fibers are straightened, C_3 is the scaling of the exponential stress, C_4 is the rate of the uncrimping of the fibers and C_5 is the Young's modulus of the straightened fibers. C_6 is determined from the requirement that the stress is continuous at λ_m. The values of the material properties that were used for the models were obtained from previous studies (Hansen et al., 2017; Knaus and Blemker, 2021) and can be found in the **Supplementary Material**. The constitutive models implemented in FEBio Studio (Maas et al., 2012) as "*trans iso Mooney-Rivlin*" were used in this study.

2.3 Model Fascicles

The model sub-tendons fascicles were defined in FEBio (Maas et al., 2012): a local fiber direction (a_0) was defined for each element to represent the tendon fascicle structure (Knaus and Blemker, 2021). For each 3D sub-tendon, fibers were directed from the proximal cross-section to the distal cross-section. In this way, the local fibers resulted in different fascicle twist angles in each model, as described in the literature (Pękala et al., 2017).

2.4 Subject-Specific Volume Reconstruction and Segmentation From Freehand Three-Dimensional Ultrasound

A conventional 2D ultrasound machine with a linear transducer (ArtUS, UAB Telemed, Vilnius, Lithuania) was used to record images of the AT. The ultrasound machine was combined with an optical motion tracking system (Optitrack NaturalPoint, United States) to generate a 3D reconstruction of the AT during rest. During the acquisition, the participant was positioned prone with a fixated foot and a neutral ankle angle. The 2D ultrasound images were transformed into the global coordinate system using 3D Slicer (Version 4.11.20210226) to create a reconstructed 3D volume. After computing a 3D volume reconstruction, the AT was manually outlined using the reconstructed 2D images, and the corresponding borders were interpolated to generate a 3D mesh of the tendon. The tendon geometry of the subject-specific mesh was reconstructed.

TABLE 1 | The estimated peak muscle forces during the rehabilitation exercises, applied on each sub-tendon and used as boundary conditions for the finite element analysis. The unit of the muscle forces is Newton (N).

Exercise	GM force (N)	GL force (N)	SOL force (N)
Heel walk	108.8	78.9	180.2
Toe walk	328.4	154.7	702.3
Unirise	721.4	164.1	576.0
Unidrop	982.8	422.5	91.4
Unidrop Bent	351.7	84.6	1589.6

2.5 Subject-Specific Muscle Force Estimation

The participant came to the Movement and posture Analysis Laboratory Leuven (Belgium) for a single session and started with a 5-min warm-up on a stationary bicycle. The participant completed five repetitions of five rehabilitation exercises in a randomized order: walking on heels (heel walk), walking on toes (toe walk), unilateral heel rise (unirise), heel drop with extended knee (unidrop) and heel drop with knee bent (unidrop bent). Description of the execution of the exercises can be found in the **Supplementary Material**. In between trials, the participant was given a minimum of 30 s of rest before moving on to the next trial.

An extended Plug-in Gait marker set including 34 retroreflective markers, of which the trajectories were recorded using ten infrared cameras (Vicon, Oxford Metrics, Oxford, United Kingdom) at a sampling rate of 150 Hz, were placed on anatomical landmarks to obtain kinematic data. Ground reaction force data was measured from the participant's dominant leg using a force plate embedded in the walkway. A modified generic musculoskeletal model (OpenSim gait2392 model) (Delp et al., 1990) with 6 degrees of freedom and 43 Hill-type muscle-tendon actuators per leg was scaled in OpenSim 3.3 (OpenSim, Stanford, CA, United States) and joint kinematics were then computed using a Kalman Smoothing algorithm (De Groote et al., 2008). Next, an inverse dynamic approach was used to calculate the joint moments. SOL, GM, and GL muscle forces were then estimated using a dynamic optimization method by minimizing the sum of squared muscle activations (De Groote et al., 2016). The muscle forces at the time of peak total muscle force during each exercise were used as boundary conditions in the FE model (**Table 1**).

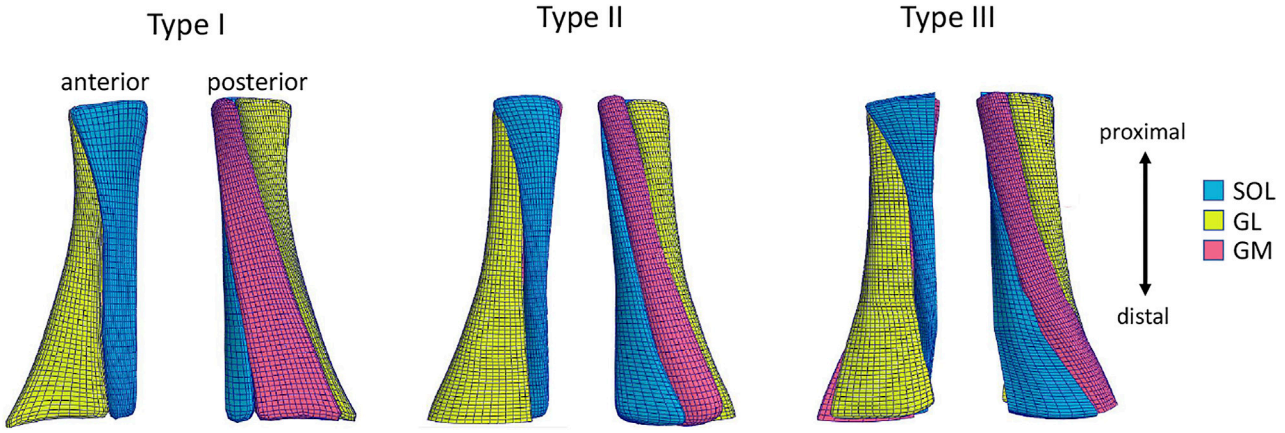

FIGURE 1 | Anterior and posterior view of the Achilles free tendon geometries representing the three types of twist: Type I (least), Type II (moderate), Type III (extreme). Each 3D tendon model was divided in three sub-tendons, each one arising from one of the three triceps surae muscles: the soleus (SOL) and the two heads (medialis, GM and lateralis, GL) of the gastrocnemius muscle.

2.6 Creation of a Subject-Specific FE Model With Free-form Deformation

Subsequently, the template mesh containing three sub-tendons was customized to the subject-specific geometry obtained with the subject's 3DfUS image. We used the free-form deformation method (Fernandez et al., 2018), which morphs an underlying mesh by embedding it inside a host mesh. This allows the nodes on the external surface of the given mesh to match the subject's geometry while the internal nodes of the mesh are also deformed using the same transformation. In this way, it was possible to obtain three subject-specific free AT geometries, representing the three twists described in the literature (Pękala et al., 2017) (**Figure 1**). The length of the 3D geometry was 40 mm and the volume was 1,136 mm^3 on average between twisted geometries.

2.7 Subject-Specific Model Boundary Conditions

The contact between the three sub-tendons was defined as frictionless sliding (Knaus and Blemker, 2021). The distal end of the three models was fixed. Different rehabilitation exercises were simulated by applying muscle forces (**Table 1**) as nodal loads to the proximal faces of each sub-tendon. The nodal displacements were constrained to move only in the distal-proximal direction to mimic the constraints provided by fascia tissues that hold the sub-tendons together.

2.8 Strain Analysis

To quantitatively analyze strain distribution patterns during the different exercises, two different analysis were performed. Firstly, we examined the peak and average of the maximum principal strain, in the mid-portion of the tendon (defined as the center third of the AT models), to identify the differences between different types of rehabilitation exercises (**Figure 2B**). We also analyzed the peak and average of the maximum principal strain in the mid-portion of each sub-tendon, to examine the non-uniform deformations of such sub-tendons (**Figure 3**). Secondly, we examined the distribution of the maximum principal strain and location of the peak maximum principal strain in the whole free tendon, to characterize the overall strain patterns between different twist types and exercises (**Figure 2A**).

3 RESULTS

3.1 Effect of Task Type on Tendon Strains

3.1.1 The Effect of Bending the Knee During Unilateral Heel Drop

Bending the knee during the heel drop exercise (unidrop bent) redistributed the muscle force and increased the peak strain by 0.392 for Type I, 0.242 for Type II and 0.298 for Type III, and the average strain by 0.046 for Type I, 0.018 for Type II and 0.02 for Type III, in the mid-portion (**Figure 2B**). Bending the knee also had an effect on the difference in tendon strain between sub-tendons in the mid-portion. SOL sub-tendon showed the greatest strains compared to GM and GL sub-tendons when the knee was bent. During unidrop, GM sub-tendon showed the largest strains followed by SOL and GL sub-tendons (**Figure 3**). This was observable for all types of twists.

3.1.2 Eccentric Versus Concentric Exercises

Unidrop exercise resulted in higher peak (Type I: 0.317 vs. 0.213, Type II: 0.174 vs. 0.121, Type III: 0.184 vs. 0.129) and average strain (Type I: 0.096 vs. 0.088, Type II: 0.058 vs. 0.054, Type III: 0.06 vs. 0.054), in the mid-portion, compared to concentric unirise for all the three models (**Figure 2B**). The type of exercises also had an effect on difference in tendon strains between sub-tendons. During both unirise and unidrop, the largest peak and average strains were observed in the GM sub-tendon for all types of twist, but the difference of the strains between GM and SOL sub-tendons increased for the eccentric heel drop (**Figure 3**).

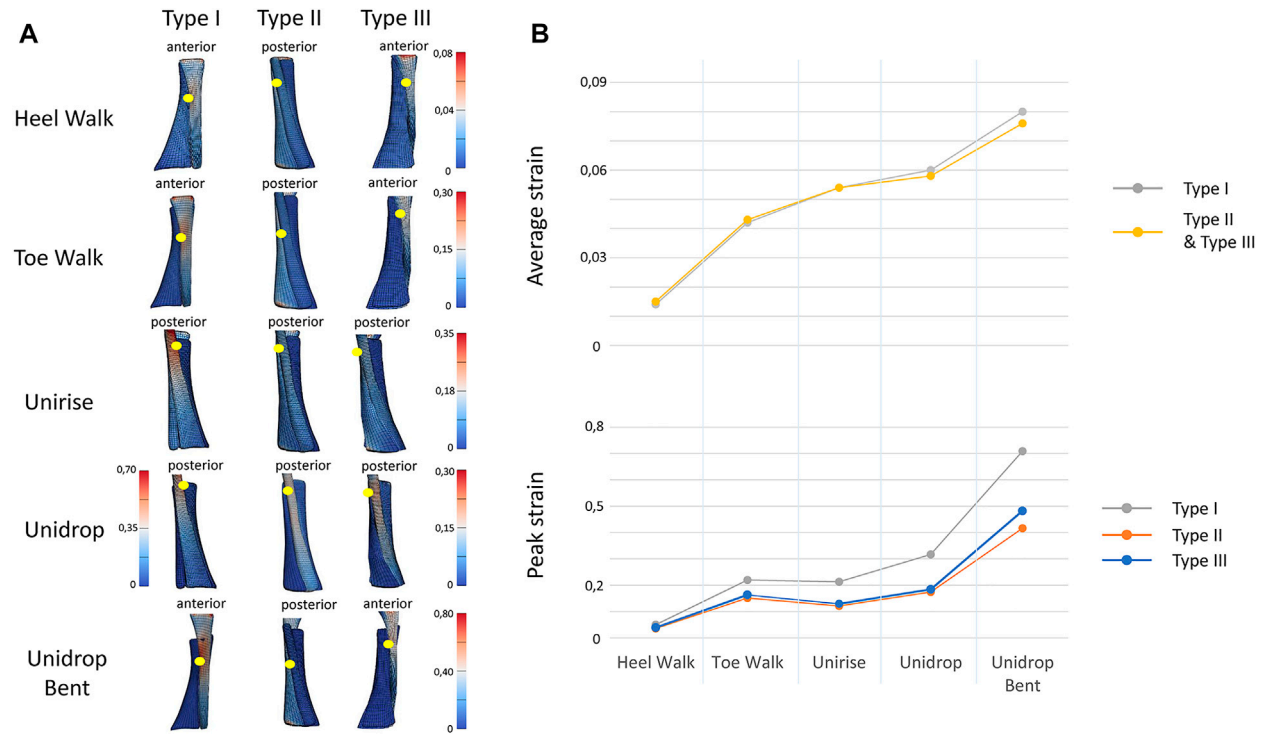

FIGURE 2 | (A). View of the distribution of the maximum Lagrange strain for the three types of twist and for all the five rehabilitation exercises. The yellow dots indicate the location of the peak strain. **(B)** Trend of the peak and average of the maximum Lagrange strain for all the types of twist and all the rehabilitation exercises, in the mid-portion of the tendon models. In average strain, Type I and Type II strain are described with the same line, since the values are the same.

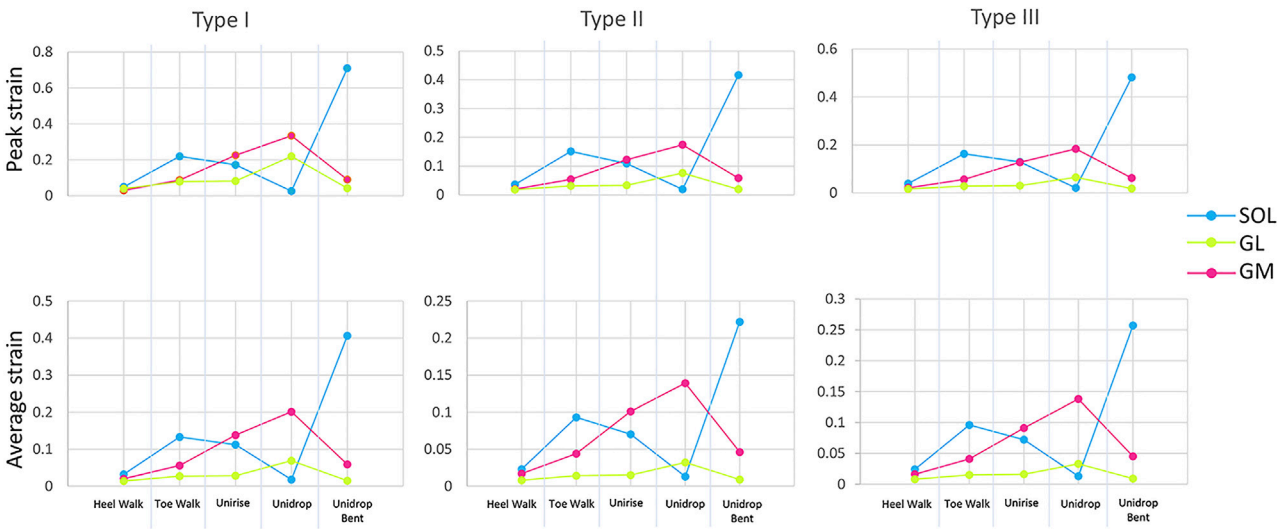

FIGURE 3 | Peak and average of the maximum Lagrange strain at the mid-portion of each sub-tendon, soleus (SOL), gastrocnemius medialis (GM) and gastrocnemius lateralis (GL), for all the five rehabilitation exercises and twist.

3.1.3 Isolated Versus Functional Exercises

The isolated exercises (unirise and unidrop) presented higher average strains compared to the functional exercises (walking tasks), in the mid-portion of the AT (**Figure 2B**). However, toe walk showed higher peak strain than unirise, for all types of twist (Type I: 0.220 and 0.213, Type II: 0.151 and 0.121, Type III: 0.163

and 0.129, peak strains, for toe walk and unirise, respectively). The type of exercises had also an effect in the difference in tendon strains between sub-tendons, in the mid-portion. While during the functional exercises the highest strains were observed in the SOL sub-tendon, during the isolated exercises the highest strains were in the GM sub-tendon. The difference in strains of the sub-tendons increased going from the functional exercises to the isolated ones (**Figure 3**).

3.2 Ranking of the Rehabilitation Exercises Based on Tendon Strains

The ranking of the exercise is independent of the twist of the tendon. Starting from the lowest average strain in the mid-portion of the AT models, the ranking of the rehabilitation exercises was: heel walk, toe walk, unirise, unidrop and unidrop bent, which exhibited the highest average strains (**Figure 2B**).

3.3 Effect of the Twist on Tendon Strains and Peak Value Location

The amount of twist influences the peak strains but not the average strains nor the ranking of the rehabilitation exercises. Type I consistently showed higher peak strains than the other two types, regardless of the type of rehabilitation exercise. Type II showed the lowest peak strains, for all the rehabilitation exercises. The location of the peak strain differed among the three different types of twist and exercises (**Figure 2A**). The twist didn't have any effect on the difference in the sub-tendons strain: the trend of both peak and average strains for each sub-tendon among the rehabilitation exercises was the same when comparing the three types of twist.

4 DISCUSSION

This study assessed the effect of different types of rehabilitation exercises on tendon strains, and ranked them based on the average strain in the mid-portion of the tendon (**Figure 2B**). Although the tendon strains follow changes in the muscle forces, this study shows the potential to use subject-specific FE models to provide information on the specific location of high strains within the free tendon and determine the effect of different twist types. Based on the ranking of the rehabilitation exercises, to gradually increase the tendon strain, it should be recommended to start with heel walk, followed by toe walk, unirise, unidrop and finally to unidrop bent. The type of tendon twist influences the peak strains but not the average. Type I consistently showed highest peak strains among the five rehabilitation exercises.

The original eccentrics-only approach in Achilles tendinopathy rehabilitation (Stanish et al., 1986) was extended by Alfredson et al. (1998) with the inclusion of eccentric exercises with a knee bent, to activate the SOL muscle more and cause a redistribution of the muscle force. Our results showed that bending the knee not only redistributes the muscle forces but also increased both the peak and average strain in the AT by approximately 2%. In addition, the location of the highest strain also moves from more proximal to the mid-portion. This variety in location of the peak strain might be beneficial for the loading of the tendon. However, from these results it is clear that bending the knee strains the tendon more and might need to be included in a later stage of the rehabilitation program. The eccentrics-only approach has also been enriched by other contraction modes. For example, Silbernagel et al.(2001) recommended the combination of eccentric and concentric exercises. The current study was able to demonstrate that during unirise (concentric contraction), lower average strain are observed compared to unidrop (eccentric contraction). If the rehabilitation aims to minimize tendon strain during the initial phase of treatment, our result suggests that rehabilitation should start with concentric exercises and gradually move towards eccentric exercises. More recently, functional exercises to promote speed and energy storage and release, especially towards the end of the rehabilitation program, were introduced (Mascaró et al., 2018). In contrast to our hypothesis, our results show that functional exercises (walking tasks) developed lower average strains compared to the isolated exercises (heel rise and heel drop), suggesting that these functional exercises could be included early in the rehabilitation program.

Our results also clearly show that the type of exercise influences the location of the peak and average tendon strain: these changes, together with the location of the tendinopathy, could be considered to prescribe the correct exercises. For example, comparing the walking tasks with the isolated extended knee exercises, the location of the peak moves from the mid-portion to the proximal side of the tendon. Furthermore, while the functional exercises and the unidrop bent displayed the highest strains in the SOL sub-tendon, the isolated exercises with extended knees did in the GM sub-tendon. This finding may also explain the occurrence of the failure of a single sub-tendon, resulting in a partial tear in the AT (Śmigielski, 2008).

The complexity of the *in vivo* behavior of the AT is well known. Our results corroborates the non-uniform deformations observed *in vivo* (Bojsen-Møller et al., 2004; Arndt et al., 2012; Franz et al., 2015), demonstrating varying tendon strain distribution during the rehabilitation exercises. Using a subject-specific FE model that contains the sub-tendons structure and their relative sliding, we found that going from concentric to eccentric exercise, the difference in strain increases between sub-tendons, and consequently the non-uniform tissue deformations in the AT increase for the eccentric exercises. This difference in strain between sub-tendons increases even more when the heel drop is performed with a knee bent. Ideally, based on these observations, it would be possible to define which exercises stimulates the intra-tendon sliding.

The AT twist has been listed as a contributing factor in Achilles tendinopathy (Bojsen-Møller et al., 2004), but little is known since the twist cannot be quantified *in vivo*. By simulating the three twist types, our study showed that the twist of the sub-tendons influences the peak tendon strains and its location, but not the ranking of the exercises or the average strain. Similar to Shim et al. (2018), the current work found that the least twisted geometry showed the highest peak strain. As peak strain might

cause micro-damage to the tendon, this finding suggests that Type I may not be an optimal geometry and may place individuals more at risk of injury. In addition, differently than the other twist types, the highest strain for this tendon type is located in the mid-portion of the tendon for some exercises, which is also the most frequent location of tendon thickening and pain. Unfortunately, Type I is also the twist which most commonly occurs in the individuals (Edama et al., 2015; Pękala et al., 2017). Furthermore, our results showed that the average strain is not influenced by the twist, since the three twisted models showed very similar values of the average strain in the mid-portion, for the different rehabilitation exercises. It is known from previous literature (Pizzolato et al., 2019) that the AT can experience positive adaptation when exposed to strains within a specific range (Wang et al., 2015) or "sweet spot " The identified "sweet spot" to maintain and promote tendon health (Pizzolato et al., 2019) is 5%–6% tendon strain. Based on our average strain results, the unirise and unidrop exercises fall within this range. However, caution must be taken when interpreting these results, considering the complicated Achilles sub-tendon structure and the above-mentioned sliding mechanism. The inter-individual differences in triceps surae force distribution (Crouzier et al., 2020) and the AT material properties (Yin et al., 2021) need to be taken into account when targeting the "sweet spot." All these parameters will inherently generate different internal tendon strain distribution. However, to our knowledge, there are no studies investigating strains yet, taking into account the inter-individual differences in Achilles tendinopathy patients. FE modeling represents a promising method for estimating AT strain, as it allows to consider morphological and material properties of different individuals. A future challenge would be to design personalized exercise programs to promote tendon strain within the "sweet spot," based on FE models results. In this way, the clinical efficacy of exercise-based rehabilitation should improve.

There are some limitations of this study. First, we didn't include subject-specific material properties and friction between sub-tendons. To answer the current research question, this didn't seem crucial. However future developments of the FE model will need to take subject-specific material properties and friction into account. Secondly, the ranking of the rehabilitation exercises was solely based on one subject. As such, caution is required in interpreting the outcome since different geometry and exercise executions may influence the AT strains. Therefore, a more comprehensive study including patients with tendinopathy is needed to confirm our findings and providing general guidelines for the prescription of the rehabilitation exercises. However, the study showed the potential of the application of FE models for estimation of AT strains, taking into account a subject-specific geometry. Indeed, since the AT behavior is complex and affected by individual tendon morphology (Yin et al., 2021), a subject-specific morphology should be preferred rather than a general one when modelling the AT for evaluation of the strains.

In conclusion, the AT models developed in this study were able to quantify tendon strain distribution during different type of rehabilitation exercises for Achilles tendinopathy, and the impact of the twisted geometry. Based on average tendon strain in the mid-portion, the rehabilitation exercises ranking was independent of the AT twist. While heel walk developed the lowest average strain, unidrop bent exhibited the highest average strain in the mid-portion of the AT. The eccentric unidrop exercise resulted in higher peak and average strain compared to concentric unirise, for all the three models. The isolated exercises (unirise and unidrop) presented higher average strains compared to the functional exercises (walking tasks). The amount of twist influences the peak strains but not the average. Type I consistently showed highest peak strains among the five rehabilitation exercises. This study was a first step towards future work to design biomechanically informed rehabilitation protocols and provide clinicians with a better guide to prescribe rehabilitation exercises based on their impact on the AT strain.

DATA AVAILABILITY STATEMENT

The raw data supporting the conclusion of this article will be made available by the authors, without undue reservation.

ETHICS STATEMENT

The studies involving human participants were reviewed and approved by KU/UZ Leuven. The patients/participants provided their written informed consent to participate in this study.

AUTHOR CONTRIBUTIONS

AF, VS, and BV contributed to conception and design of the study. AF developed the model geometries, performed the free-form deformation and FE modelling and analysis. AF wrote the first draft of the manuscript. VS wrote a section of the manuscript. IM performed volume reconstruction and segmentation, and muscle force estimation. IM wrote a section of the manuscript. All authors contributed to manuscript revision, read, and approved the submitted version.

FUNDING

Grant No: C24M/20/053, Research Council KU Leuven.

ACKNOWLEDGMENTS

The authors would like to thank the Research Council KU Leuven for providing financial support to this project.

SUPPLEMENTARY MATERIAL

The Supplementary Material for this article can be found online at: https://www.frontiersin.org/articles/10.3389/fbioe.2022.914137/full#supplementary-material

REFERENCES

Albers, I. S., Zwerver, J., Diercks, R. L., Dekker, J. H., and Van den Akker-Scheek, I. (2016). Incidence and Prevalence of Lower Extremity Tendinopathy in a Dutch General Practice Population: A Cross Sectional Study. *BMC Musculoskelet. Disord.* 17. doi:10.1186/s12891-016-0885-2

Alfredson, H., Pietilä, T., Jonsson, P., and Lorentzon, R. (1998). Heavy-Load Eccentric Calf Muscle Training for the Treatment of Chronic Achilles Tendinosis. *Am. J. Sports Med.* 26 (3), 360–366. doi:10.1177/03635465980260030301

Arndt, A., Bengtsson, A.-S., Peolsson, M., Thorstensson, A., and Movin, T. (2012). Non-uniform Displacement within the Achilles Tendon during Passive Ankle Joint Motion. *Knee Surg. Sports Traumatol. Arthrosc.* 20 (9), 1868–1874. doi:10.1007/s00167-011-1801-9

Baxter, J. R., Corrigan, P., Hullfish, T. J., O'Rourke, P., and Silbernagel, K. G. (2021). Exercise Progression to Incrementally Load the Achilles Tendon. *Med. Sci. Sports Exerc.* 53 (1), 124–130. doi:10.1249/MSS.0000000000002459

Bogaerts, S., De Brito Carvalho, C., Scheys, L., Desloovere, K., D'hooge, J., Maes, F., et al. (2017). Evaluation of Tissue Displacement and Regional Strain in the Achilles Tendon Using Quantitative High-Frequency Ultrasound. *Plos One* 12 (7), e0181364. doi:10.1371/journal.pone.0181364

Bojsen-Møller, J., Hansen, P., Aagaard, P., Svantesson, U., Kjaer, M., and Magnusson, S. P. (2004). Differential Displacement of the Human Soleus and Medial Gastrocnemius Aponeuroses during Isometric Plantar Flexor Contractions *In Vivo*. *J. Appl. Physiology* 97 (5), 1908–1914. doi:10.1152/japplphysiol.00084.2004

Cook, J. L., and Purdam, C. R. (2014). The Challenge of Managing Tendinopathy in Competing Athletes. *Br. J. Sports Med.* 48 (7), 506–509. doi:10.1136/bjsports-2012-092078

Crouzier, M., Tucker, K., Lacourpaille, L., Doguet, V., Fayet, G., Dauty, M., et al. (2020). Force-sharing within the Triceps Surae: An Achilles Heel in Achilles Tendinopathy. *Med. Sci. Sports Exerc.* 52, 1076–1087. doi:10.1249/MSS.0000000000002229

De Groote, F., De Laet, T., Jonkers, I., and De Schutter, J. (2008). Kalman Smoothing Improves the Estimation of Joint Kinematics and Kinetics in Marker-Based Human Gait Analysis. *J. Biomechanics* 41 (16), 3390–3398. doi:10.1016/j.jbiomech.2008.09.035

De Groote, F., Kinney, A. L., Rao, A. V., and Fregly, B. J. (2016). Evaluation of Direct Collocation Optimal Control Problem Formulations for Solving the Muscle Redundancy Problem. *Ann. Biomed. Eng.* 44 (10), 2922–2936. doi:10.1007/s10439-016-1591-9

Delp, S. L., Loan, J. P., Hoy, M. G., Zajac, F. E., Topp, E. L., and Rosen, J. M. (1990). An Interactive Graphics-Based Model of the Lower Extremity to Study Orthopaedic Surgical Procedures. *IEEE Trans. Biomed. Eng.* 37 (8), 757–767. doi:10.1109/10.102791

Devaprakash, D., Graham, D. F., Barrett, R. S., Lloyd, D. G., Obst, S. J., Kennedy, B., et al. (2022). Free Achilles Tendon Strain During Selected Rehabilitation, Locomotor, Jumping, and Landing Tasks. *J. Appl. Physiol.* 132 (4), 956–965. doi:10.1152/japplphysiol.00662.2021

Edama, M., Kubo, M., Onishi, H., Takabayashi, T., Inai, T., Yokoyama, E., et al. (2015). The Twisted Structure of the Human Achilles Tendon. *Scand. J. Med. Sci. Sports* 25 (5), e497–e503. doi:10.1111/sms.12342

Edama, M., Kubo, M., Onishi, H., Takabayashi, T., Yokoyama, E., Inai, T., et al. (2016). Structure of the Achilles Tendon at the Insertion on the Calcaneal Tuberosity. *J. Anat.* 229 (5), 610–614. doi:10.1111/joa.12514

Fernandez, J., Zhang, J., Shim, V., Munro, J. T., Sartori, M., Besier, T., et al. (2018). "Musculoskeletal Modelling and the Physiome Project," in *Multiscale Mechanobiology of Bone Remodeling and Adaptation*. Editor P. Pivonka (Cham: Springer International Publishing), 123–174. doi:10.1007/978-3-319-58845-2_3

Franz, J. R., Slane, L. C., Rasske, K., and Thelen, D. G. (2015). Non-uniform *In Vivo* Deformations of the Human Achilles Tendon during Walking. *Gait Posture* 41 (1), 192–197. doi:10.1016/j.gaitpost.2014.10.001

Grävare Silbernagel, K., Thomeé, R., Thomeé, P., and Karlsson, J. (2001). Eccentric Overload Training for Patients with Chronic Achilles Tendon Pain - A Randomised Controlled Study with Reliability Testing of the Evaluation Methods. *Scand. J. Med. Sci. Sports* 11 (4), 197–206. doi:10.1034/j.1600-0838.2001.110402.x

Handsfield, G. G., Greiner, J., Madl, J., Rog-Zielinska, E. A., Hollville, E., Vanwanseele, B., et al. (2020). Achilles Subtendon Structure and Behavior as Evidenced from Tendon Imaging and Computational Modeling. *Front. Sports Act. Living* 2, 70. doi:10.3389/fspor.2020.00070

Handsfield, G. G., Inouye, J. M., Slane, L. C., Thelen, D. G., Miller, G. W., and Blemker, S. S. (2017). A 3D Model of the Achilles Tendon to Determine the Mechanisms Underlying Nonuniform Tendon Displacements. *J. Biomechanics* 51, 17–25. doi:10.1016/j.jbiomech.2016.11.062

Hansen, W., Shim, V. B., Obst, S., Lloyd, D. G., Newsham-West, R., and Barrett, R. S. (2017). Achilles Tendon Stress Is More Sensitive to Subject-specific Geometry Than Subject-specific Material Properties: A Finite Element Analysis. *J. biomechanics* 56, 26–31. doi:10.1016/j.jbiomech.2017.02.031

Knaus, K. R., and Blemker, S. S. (2021). 3D Models Reveal the Influence of Achilles Subtendon Twist on Strain and Energy Storage. *Front. Bioeng. Biotechnol.* 9, 1–10. doi:10.3389/fbioe.2021.539135

Komi, P. V., Fukashiro, S., and Järvinen, M. (1992). Biomechanical Loading of Achilles Tendon during Normal Locomotion. *Clin. Sports Med.* 11 (3), 521–531. doi:10.1016/S0278-5919(20)30506-8

Lopes, A. D., Hespanhol, L. C., Yeung, S. S., and Costa, L. O. P. (2012). What Are the Main Running-Related Musculoskeletal Injuries? A Systematic Review. *Sports Med.* 42 (10), 891–905. doi:10.2165/11631170-000000000-00000

Lysholm, J., and Wiklander, J. (1987). Injuries in Runners. *Am. J. Sports Med.* 15 (2), 168–171. doi:10.1177/036354658701500213

Maas, S. A., Ellis, B. J., Ateshian, G. A., and Weiss, J. A. (2012). FEBio: Finite Elements for Biomechanics. *J. Biomechanical Eng.* 134 (1). doi:10.1115/1.4005694

Maffulli, N. (1999). Current Concepts Review - Rupture of the Achilles Tendon*. *JBJS* 81 (7). doi:10.2106/00004623-199907000-00017

Maffulli, N., Walley, G., Sayana, M. K., Longo, U. G., and Denaro, V. (2008). Eccentric Calf Muscle Training in Athletic Patients with Achilles Tendinopathy. *Disabil. Rehabilitation* 30 (20–22), 1677–1684. doi:10.1080/09638280701786427

Malliaras, P., Barton, C. J., Reeves, N. D., and Langberg, H. (2013). Achilles and Patellar Tendinopathy Loading Programmes. *Sports Med.* 43 (4), 267–286. doi:10.1007/s40279-013-0019-z

Mascaró, A., Cos, M. À., Morral, A., Roig, A., Purdam, C., and Cook, J. (2018). Load Management in Tendinopathy: Clinical Progression for Achilles and Patellar Tendinopathy. *Apunts. Med. l'Esport* 53 (197), 19–27. doi:10.1016/j.apunts.2017.11.005

Pękala, P. A., Henry, B. M., Ochała, A., Kopacz, P., Tatoń, G., Młyniec, A., et al. (2017). The Twisted Structure of the Achilles Tendon Unraveled: A Detailed Quantitative and Qualitative Anatomical Investigation. *Scand. J. Med. Sci. Sports* 27, 1705–1715. doi:10.1111/sms.12835

Pizzolato, C., Lloyd, D. G., Zheng, M. H., Besier, T. F., Shim, V. B., Obst, S. J., et al. (2019). Finding the Sweet Spot via Personalised Achilles Tendon Training: The Future Is within Reach. *Br. J. Sports Med.* 53 (1), 11–12. doi:10.1136/bjsports-2018-099020

Shim, V. B., Handsfield, G. G., Fernandez, J. W., Lloyd, D. G., and Besier, T. F. (2018). Combining In Silico and *In Vitro* Experiments to Characterize the Role of Fascicle Twist in the Achilles Tendon. *Sci. Rep.* 8 (1), 1–12. doi:10.1038/s41598-018-31587-z

Shim, V. B., Hansen, W., Newsham-West, R., Nuri, L., Obst, S., Pizzolato, C., et al. (2019). Influence of Altered Geometry and Material Properties on Tissue Stress Distribution under Load in Tendinopathic Achilles Tendons - A Subject-specific Finite Element Analysis. *J. Biomechanics* 82, 142–148. doi:10.1016/j.jbiomech.2018.10.027

Śmigielski, R. (2008). Management of Partial Tears of the Gastro-Soleus Complex. *Clin. Sports Med.* 27 (1), 219–229. doi:10.1016/j.csm.2007.10.005

Sobhani, S., Dekker, R., Postema, K., and Dijkstra, P. U. (2013). Epidemiology of Ankle and Foot Overuse Injuries in Sports: A Systematic Review. *Scand. J. Med. Sci. Sports* 23 (6), 669–686. doi:10.1111/j.1600-0838.2012.01509.x

Stanish, W. D., Rubinovich, R. M., and Curwin, S. (1986). Eccentric Exercise in Chronic Tendinitis. *Clin. Orthop. Relat. Res.* 208, 65–68. doi:10.1097/00003086-198607000-00014

Thorpe, C. T., Godinho, M. S. C., Riley, G. P., Birch, H. L., Clegg, P. D., and Screen, H. R. C. (2015). The Interfascicular Matrix Enables Fascicle Sliding and Recovery in Tendon, and Behaves More Elastically in Energy Storing Tendons. *J. Mech. Behav. Biomed. Mater.* 52, 85–94. doi:10.1016/j.jmbbm.2015.04.009

Wang, T., Lin, Z., Ni, M., Thien, C., Day, R. E., Gardiner, B., et al. (2015). Cyclic Mechanical Stimulation Rescues Achilles Tendon from Degeneration in a Bioreactor System. *J. Orthop. Res.* 33 (12), 1888–1896. doi:10.1002/jor.22960

Weiss, J. A., Maker, B. N., and Govindjee, S. (1996). Finite Element Implementation of Incompressible, Transversely Isotropic Hyperelasticity. *Comput. Methods Appl. Mech. Eng.* 135 (1), 107–128. doi:10.1016/0045-7825(96)01035-3

Yin, N.-H., Fromme, P., McCarthy, I., and Birch, H. L. (2021). Individual Variation in Achilles Tendon Morphology and Geometry Changes Susceptibility to Injury. *eLife* 10, e63204. doi:10.7554/eLife.63204

Conflict of Interest: The authors declare that the research was conducted in the absence of any commercial or financial relationships that could be construed as a potential conflict of interest.

frontiers | Frontiers in Bioengineering and Biotechnology

ORIGINAL RESEARCH
published: 06 July 2022
doi: 10.3389/fbioe.2022.874074

Derivation of the Gait Deviation Index for Spinal Cord Injury

Diana Herrera-Valenzuela[1,2]*, *Isabel Sinovas-Alonso*[1,2], *Juan C. Moreno*[3], *Ángel Gil-Agudo*[2] *and Antonio J. del-Ama*[4]

[1]International Doctoral School, Rey Juan Carlos University, Madrid, Spain, [2]Biomechanics and Technical Aids Unit, National Hospital for Paraplegics, Toledo, Spain, [3]Neural Rehabilitation Group, Cajal Institute, CSIC–Spanish National Research Council, Madrid, Spain, [4]School of Science and Technology, Department of Applied Mathematics, Materials Science and Engineering and Electronic Technology, Rey Juan Carlos University, Madrid, Spain

The Gait Deviation Index (GDI) is a dimensionless multivariate measure of overall gait pathology represented as a single score that indicates the gait deviation from a normal gait average. It is calculated using kinematic data recorded during a three-dimensional gait analysis and an orthonormal vectorial basis with 15 gait features that was originally obtained using singular value decomposition and feature analysis on a dataset of children with cerebral palsy. Ever since, it has been used as an outcome measure to study gait in several conditions, including spinal cord injury (SCI). Nevertheless, the validity of implementing the GDI in a population with SCI has not been studied yet. We investigate the application of these mathematical methods to derive a similar metric but with a dataset of adults with SCI (SCI-GDI). The new SCI-GDI is compared with the original GDI to evaluate their differences and assess the need for a specific GDI for SCI and with the WISCI II to evaluate its sensibility. Our findings show that a 21-feature basis is necessary to account for most of the variance in gait patterns in the SCI population and to provide high-quality reconstructions of the gait curves included in the dataset and in foreign data. Furthermore, using only the first 15 features of our SCI basis, the fidelity of the reconstructions obtained in our population is higher than that when using the basis of the original GDI. The results showed that the SCI-GDI discriminates most levels of the WISCI II scale, except for levels 12 and 18. Statistically significant differences were found between both indexes within each WISCI II level except for 12, 20, and the control group ($p < 0.05$). In all levels, the average GDI value was greater than the average SCI-GDI value, but the difference between both indexes is larger in data with greater impairment and it reduces progressively toward a normal gait pattern. In conclusion, the implementation of the original GDI in SCI may lead to overestimation of gait function, and our new SCI-GDI is more sensitive to larger gait impairment than the GDI. Further validation of the SCI-GDI with other scales validated in SCI is needed.

Keywords: gait deviation index (GDI), spinal cord injury (SCI), gait impairment, three-dimensional (3D) kinematic gait data, walking index for spinal cord injury (WISCI), singular value decomposition

OPEN ACCESS

Edited by:
Lizhen Wang,
Beihang University, China

Reviewed by:
João Abrantes,
Universidade Lusófona, Portugal
Fuhao Mo,
Hunan University, China

***Correspondence:**
Diana Herrera-Valenzuela,
dherrerav@externas.sescam.jccm.es

Specialty section:
This article was submitted to Biomechanics, a section of the journal Frontiers in Bioengineering and Biotechnology

Received: *11 February 2022*
Accepted: *24 May 2022*
Published: *06 July 2022*

Citation:
Herrera-Valenzuela D, Sinovas-Alonso I, Moreno JC, Gil-Agudo Á and del-Ama AJ (2022) Derivation of the Gait Deviation Index for Spinal Cord Injury. Front. Bioeng. Biotechnol. 10:874074. doi: 10.3389/fbioe.2022.874074

1 INTRODUCTION

Walking is an extraordinarily complex task requiring integration of the entire nervous system, making gait susceptible to a variety of underlying neurologic abnormalities, such as spinal cord injuries (SCIs). Incidence rates of SCI vary across countries between 10.4 and 83 new cases per million inhabitants per year (Wyndaele and Wyndaele, 2006), with a global prevalence between 236 and 1,009 per million (Cripps et al., 2011). From these, more than 95% experience mobility impairments resulting from the injury (Aspaym, Federación Nacional, 2012), which affects their quality of life. The average age when subjects experience an SCI is 33 years, and men are more affected than women with a 3.8:1 ratio (Wyndaele and Wyndaele, 2006). Therefore, although the incidence is considered low, the personal but also the social and economic consequences of spinal cord damage can be severe.

The overall objectives of rehabilitation in SCI are to increase personal independence and quality of life minimizing the socio-economic burden. Still, regardless of the severity of the SCI, the time after lesion or age at the time of injury, the restoration of walking is given high priority (Ditunno et al., 2008).Gait improvement in SCI following rehabilitation is assessed using different procedures, metrics, and tools: on the one hand, validated clinical tests on overall gait function, such as categorical and spatiotemporal-related walking and balance assessment measures such as the Walking Index for Spinal Cord Injury (WISCI) (Dittuno et al., 2001), the 10-meter walk test (10MWT) (Van Hedel et al., 2008), the timed up and go test (TUGT) (Podsiadlo and Richardson, 1991), the 6 min walking test (6MWT) (Brooks et al., 2003), and the Berg balance scale (BBS) (Berg, 1989) (Wyndaele and Wyndaele, 2006); on the other hand, tests of motor function and spasticity assessment, such as the lower extremity motor score (LEMS) and the modified Ashworth scale (MAS), respectively; and finally, instrumental techniques including dynamometry and three-dimensional gait analysis (3DGA). The latter is the most comprehensive and precise technology to analyze gait that allows to objectively assess lower limb kinematics and kinetics, thus providing a powerful tool for quantifying gait impairment and, therefore, to assist decision-making for clinicians (Patrick, 2003; Baker, 2006; Baker et al., 2016; Murphy et al., 2019; Sinovas-Alonso et al., 2021).

The main feature of 3DGA is that it provides a large amount of data describing the spatiotemporal gait parameters, together with three-dimensional (3D) pelvis, thigh, leg, and foot kinematics, as well as hip, knee, and ankle joint kinematics and kinetics during a gait cycle, along with specific values for each one of the gait phases and events (Gage, 1991). This extensive information, usually presented with many graphs and tables, is often both difficult and impractical to be understood by clinicians (Whittle, 1996; Patrick, 2003). Therefore, it is recognized that clinical interpretation of the 3DGA results needs to be facilitated to increase its usefulness in clinical settings. One way to achieve this goal is to develop and implement straightforward, easy to interpret metrics that merge data from 3DGA and yield a metric —or set of metrics— that describe overall gait deficits. One such metric is the Gait Deviation Index (GDI), which is a dimensionless multivariate measure of overall gait pathology represented as a single score that indicates the gait deviation from a normal gait pattern average (Schwartz and Rozumalski, 2008). It is calculated upon the kinematics of pelvis and hip in the three planes in space, knee, and ankle in the sagittal plane and foot progression angle.

Originally, a dataset with more than 6,000 strides of children with cerebral palsy (CP) was built to develop the GDI (Schwartz and Rozumalski, 2008). Based on these data, the authors derived a set of independent joint rotation patterns, referred to as gait features, so that, when combined linearly, high-quality reconstructions of gait curves can be obtained. In order to select the least amount of features needed to represent the whole CP gait profile dataset, they considered two criteria: 1) the set of features selected must account for at least 95% of the overall variance of the whole dataset, and 2) they must provide high-fidelity reconstructions of any gait curve with respect to the original curve. Applying these criteria, the authors found that 15 features out of 459 were enough to account for 98% of the total variance of the whole dataset and allowed to reconstruct the gait curves with 98% fidelity on average. These 15 features were organized into a matrix used as an orthonormal basis to calculate the representation of any gait curve. Afterward, to obtain the GDI, the Euclidean distance between this representation and the average of a set of control strides that may be introduced by the user, is calculated, representing the deviation of a gait pattern from a control group of typically developing (TD) children. Last, this value is scaled to improve the interpretability of the index, so that every 10 points of GDI below 100 correspond to one standard deviation away from the control pattern, whereas a score ≥100 represents a gait without any pathology (Schwartz and Rozumalski, 2008).

Ever since, that 15-feature basis originally developed from data of children with CP has been widely used to calculate the GDI across different conditions, including post-stroke hemiparetic gait (Correa et al., 2017; Guzik and Drużbicki, 2020), Duchenne muscular dystrophy (Sienko Thomas et al., 2010), Parkinson's disease (Galli et al., 2012; Speciali et al., 2013), arthritis (Broström et al., 2013; Esbjörnsson et al., 2014; Kobsar et al., 2019; Bazarnik-Mucha et al., 2020), lower limb amputations (Eshraghi et al., 2014; Kark et al., 2016), degenerative spinal pathologies (Mar et al., 2019; Trivedi et al., 2021; Zhou et al., 2021), genetic disorders (Ito et al., 2020; Mindler et al., 2020), congenital disorders (Eriksson et al., 2015; Garman et al., 2019), the effect of the Covid-19 on physical function (Ito et al., 2021), and mostly in CP (Schwartz and Rozumalski, 2008; Molloy et al., 2010; Cimolin et al., 2011; Sagawa et al., 2013; Massaad et al., 2014; Wilson et al., 2015; Malt et al., 2016; Ito et al., 2019; Rasmussen et al., 2019).

The GDI has therefore become a clinically relevant score partly because it is easy to interpret and compute. Nevertheless, the basis provided in Schwartz and Rozumalski (2008) has proven to account for the variance in gait patterns and to reconstruct gait vectors with high fidelity, only in pediatric CP population. Significant differences in gait patterns among pediatric and adult population have been described (Cupp et al., 1999; Ganley and

Powers, 2005; Bleyenheuft et al., 2012), as well as both clinical and biomechanical differences among the different neurological disorders. Furthermore, when applied only to CP, differences in GDI were found between adult and pediatric population (Maanum et al., 2012). Actually, the authors in the original work of the development of the index suggested that the methodology could be used in other sets of data (Schwartz and Rozumalski, 2008) but instead of developing a new basis for each condition, the articles found in the literature implement the GDI using the original basis regardless of the population. Therefore, straightforward application of the GDI derived in Schwartz and Rozumalski (2008) in other populations than pediatric CP can lead to a misleading interpretation of the gait data.

To date, no studies have attempted to validate the GDI in SCI. To our knowledge, only two articles have investigated its application under this condition (Hwang et al., 2021; Sinovas-Alonso et al., 2022). One of them uses the index to quantify and characterize gait patterns in ambulatory children and adolescents with transverse myelitis with respect to a normal gait pattern (Hwang et al., 2021). In this work, the difference in gait between patients and TD children was assessed with the GDI, without addressing the discriminative validity of the scale within different levels of impairment. The work presented in Sinovas-Alonso et al. (2022) compared the GDI and the WISCI II, showing limited discriminative properties of the GDI in SCI because there were statistically significant differences in the GDI values only between levels 13, 19, 20, and the control group. Therefore, the applicability of the GDI to SCI population that leads to discriminate the heterogeneity of gait impairment is still an open question calling for investigation.

The main objective of this article is to investigate the application of the mathematical methodology behind the GDI (Schwartz and Rozumalski, 2008) to a dataset of adults with SCI, resulting in the new SCI-GDI. Then, an evaluation of the differences between new SCI-GDI with the original GDI is presented, assessing the need for a specific GDI for SCI. Last, the relationship between our SCI-GDI and the WISCI II, the most validated scale in SCI developed specifically for this population (Sinovas-Alonso et al., 2021), is further presented to investigate the differences between the GDI and our novel SCI-GDI in terms of stratification and sensitivity to walking impairment with respect to a validated scale.

2 MATERIALS AND METHODS

2.1 Participants

A dataset containing the kinematic data from 3D gait analysis of patients with SCI was used in this study. The 3DGA were conducted between August 2019 and July 2021 at the Biomechanics and Technical Aids Unit of the National Hospital for Paraplegics of Toledo, Spain. Patients aged ≥16 years old with diagnosis of SCI, regardless of the etiology, time since injury, injury level, or injury severity were included. A total of 302 strides from patients aged between 16 and 70 years old (33.91 ± 17.86), with injury levels between C1 and L5 and the ASIA impairment scale (AIS) C to D were gathered. The ratio of males to females of the dataset is 3.25:1. The detailed demographic and clinical characteristics of the sample are presented in **Table 1**. In addition, a control group with the 3D kinematic gait data of 446 strides from adults without gait pathologies was collected. These healthy volunteers (HV) were between 18 and 63 years old (35.10 ± 15.41), and the ratio of females to males was 1.63:1.

All patients and HV signed an informed consent to perform the gait analysis. The study protocol was approved by the local bioethics committee (Clinical Research Ethics Committee at Complejo Hospitalario Universitario de Toledo, no. 823) and conformed to the Declaration of Helsinki.

2.2 Experimental Procedure

A Codamotion® motion capture system (Charnwood Dynamics Ltd, United Kingdom) was used to capture 3D kinematic gait data. The standard protocol with 22 active markers placed on the lower limbs (Charnwood Dynamics Limited, 2004), three scanners, and two force platforms Kistler 9286A (Kistler Group, Switzerland) in the center of a 10-meter walkway were used. Post-processing was performed using the software ODIN v. 2.02 (Codamotion Ltd., England, United Kingdom). The subjects were asked to walk barefoot at a comfortable speed with the minimum external assistance required. Five complete gait cycles were recorded and time-normalized. For patients who were not able to complete five trials, at least three cycles were gathered.

2.3 Overview of the Calculation of the Gait Deviation Index

The GDI derivation procedure was described in detail in Schwartz and Rozumalski (2008). The calculation is based on a matrix with kinematic data from several walking strides where each column vector is a stride represented by nine joint angles of a whole gait cycle extracted at 2% increments: three planes for the pelvis and hip, knee flex/extension, ankle dorsi/plantarflexion, and foot progression angle. Singular value decomposition (SVD) of the matrix is computed to obtain its singular values and singular vectors. Using the latter, referred herein as gait features, the authors build an orthonormal basis that is both optimal to maximize the variance accounted for (VAF) of the whole dataset, and useful to reconstruct gait data. When multiplying the first m-vectors of this basis by any gait vector, an m^{th} order approximation of the vector is obtained, therefore forming a vectorial basis. The accuracy of this reconstruction is calculated with its projection onto the original vector, normalized by the original gait curve. Two criteria were used to find out the minimum m features needed to form a reduced order basis such that it represented the whole CP dataset; first, these first m features accounted for 98% of the total variance of the original dataset, and second, the accuracy of the m^{th} order reconstructed curves was 98% on average. The authors in Schwartz and Rozumalski (2008) found that 15 features were sufficient to form the reduced order basis. Last, using the approximation of a gait vector obtained with this basis, its Euclidean distance with

TABLE 1 | Demographic and clinical characteristics of the samples in the train and validation datasets.

Characteristic	Type	Train (n = 302)	Validation (n = 72)
Age	16–25	156	52
	26–40	32	0
	41–60	79	10
	>60	35	10
AIS	A	0	10
	C	36	10
	D	256	36
	Cauda equina	10	10
	N.A. (congenital)	0	6
Time since injury	6 months (incl.) or less	58	10
	6 months (excl.) to 1 year (incl.)	40	0
	1 (excl.) to 5 years (incl.)	86	26
	More than 5 years	92	30
	Congenital	26	6
Injury level	C1–C8	153	0
	T1–T6	12	26
	T7–T12	68	20
	L1–L5	69	20
	N.A. (Congenital)	0	6
WISCI II level	12	2	0
	13	6	0
	15	18	10
	16	65	26
	18	12	6
	19	87	0
	20	112	30

an average gait vector from a control group is calculated and scaled to obtain the GDI.

2.4 Data Analysis

An overview of the data analysis performed is presented in this section. The detailed description of each step is found on the following subsections. Henceforth, all data analysis was performed with Matlab R2019a (The MathWorks, Inc., Natick, MA, United States).

Using the dataset described previously, the first step of the data analysis was the computation of what we call the SCI-GDI basis, that is, the optimal reduced order orthonormal basis to reconstruct gait data of SCI with high fidelity and to account for most of the variance of the SCI dataset (data analysis details in **Section 2.4.1**). Once the SCI basis is formed with the sufficient amount of gait features m, in order to assess the appropriateness of computing the GDI in adult population with SCI using the original GDI basis, developed using a dataset of pediatric patients with CP (Schwartz and Rozumalski, 2008), we compared the quality of the reconstructions of the whole SCI dataset obtained with three bases: our SCI-GDI basis, the original GDI basis comprises 15 gait features (Schwartz and Rozumalski, 2008), and the first 15 features of our SCI-GDI basis. From the three bases, the latter was used to compare the fidelity of the reconstructions of the same order as those obtained with the original GDI basis. **Figure 1** shows a diagram of the steps followed to obtain these three bases. In addition, to assess the generalizability of the new SCI basis in foreign data, we computed the quality of reconstruction in a set of strides not used during the computation of the SCI basis.

Afterward, we calculated the SCI-GDI of the dataset using our basis and compared it with the WISCI II scale, to assess the stratification of gait impairment and discriminative properties of the new index (data analysis details in **Section 2.4.2**). To our knowledge, there is only one work published that studies the relationship of the GDI with a scale developed specifically for SCI and validated in this population, which is the WISCI II (Sinovas-Alonso et al., 2022). We did not perform comparisons with other validated metrics in SCI, such as 10MWT, 6MWT, TUGT, or the BBS because these were not available. Last, we compared and correlated the GDI with the SCI-GDI in our dataset to find out whether there is an actual difference between both indexes when computed in the same set of SCI subjects, in order to recommend one index over the other in this specific population of adults with SCI (data analysis details in **Section 2.4.3**).

2.4.1 Computation of the Spinal Cord Injury-Gait Deviation Index Basis

In this work, 302 strides from SCI patients were used to form a matrix to compute the reduced order optimal basis. We refer to this data as our train dataset. We performed a grid search considering values of m between 10 and 30 to find the minimum features needed to form the optimal reduced order SCI basis with the two criteria explained at the end of **Section 2.3**. We also considered the percentage of gait vectors of the whole dataset reconstructed with a fidelity ≥95%, a parameter reported

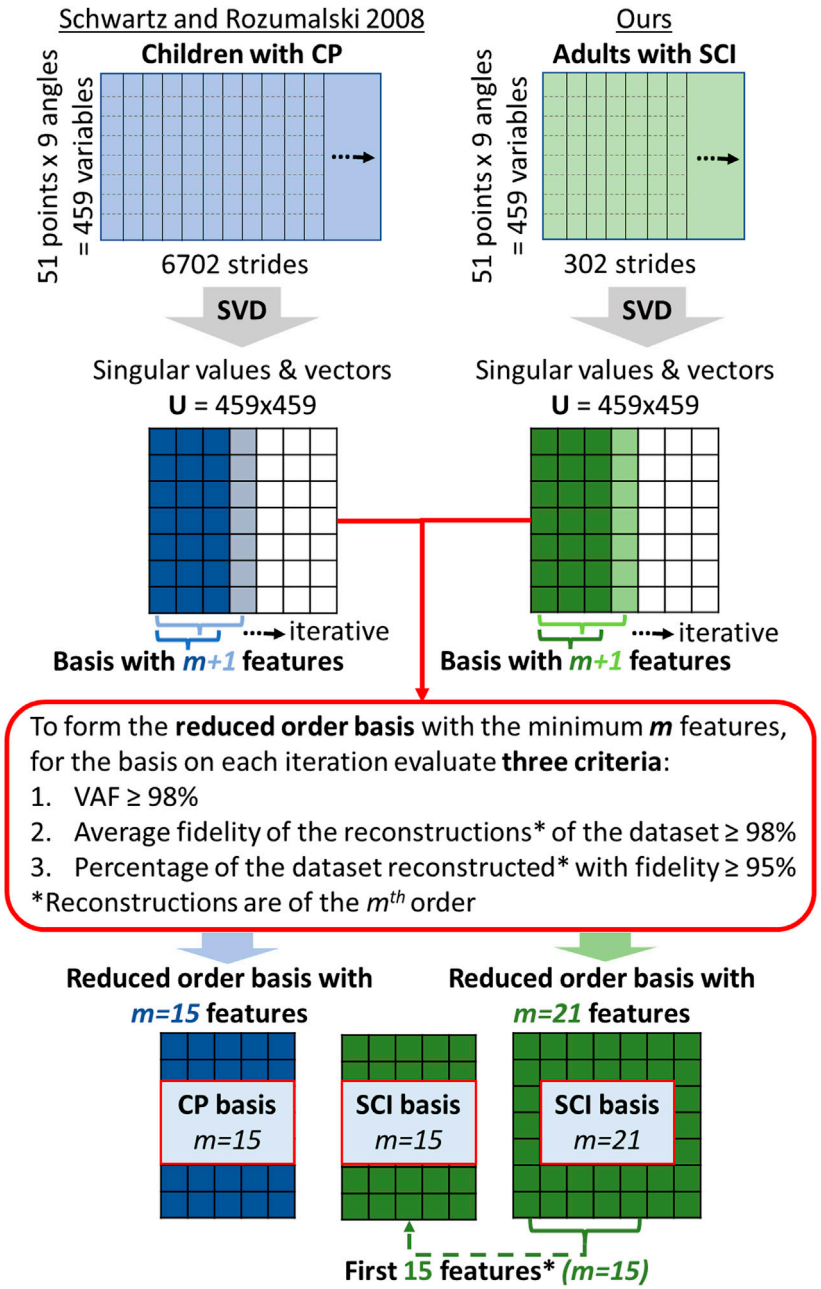

FIGURE 1 | Diagram showing the steps followed to obtain the three reduced order bases compared in this article. The column on the left, with matrices in blue, represents the process followed in the original article by Schwartz and Rozumalski (2008), whereas the green matrices on the right correspond to the steps performed in this work, using SCI gait data. Note that the reduced order SCI basis with 15 features, located in the middle at the bottom of the diagram is merely the set of the first 15 features of the 21-feature reduced order SCI basis. We compare the results of the three criteria in red when using this basis because the number of features in the basis determines the order of the reconstructions of the gait curves. Thus, it is fair to compare the quality of the reconstructions of the same order.

in the original work of the derivation of the GDI (Schwartz and Rozumalski, 2008). Although our dataset could be considered small to perform Feature Analysis, especially when compared to the 6000-stride dataset of the original GDI work, it is possible to obtain reliable, high-quality solutions with small datasets if the communalities between the features are high because accurate recovery of population structure may be obtained with a small sample; thus, the size of the dataset will have little impact on the quality of the result (MacCallum et al., 1999). Communality is related to the VAF criteria previously defined in this work because it is defined as the proportion of the variance of the variable that is accounted for by the features (Hogarty et al., 2005). Therefore, to consider the validity of our dataset in this task, we performed a Monte Carlo cross-validation with 10 iterations to assess the

TABLE 2 | Comparison of the quality of reconstruction of the whole dataset when using our SCI basis with $m = 21$, our SCI basis with $m = 15$ and the basis of the original GDI derived for children with CP with $m = 15$ (Schwartz and Rozumalski 2008).The best results in terms of average fidelity of the reconstructions and percentage of vectors reconstructed with a fidelity ≥95% are obtained with our m = 21 basis, followed by our basis built using only the first 15 features.

Basis (n° of features)	Set	VAF	Average fidelity of reconstruction	% of gait vectors reconstructed with average fidelity ≥95 (%)
SCI basis ($m = 21$)	Train	98.27%	97.99% ± 1.54%	97.86
	Validation		94.74% ± 4.88%	72.22
SCI basis ($m = 15$)	Train	97.11%	96.58% ± 2.49%	83.11
	Validation		92.40% ± 6.64%	52.78
CP basis ($m = 15$) (10)	Train	N/A	93.13% ± 5.51%	44.70
	Validation		90.73% ± 7.81%	40.28

VAF, variance accounted for; SCI, spinal cord injury; CP, cerebral palsy; N/A, not applicable.

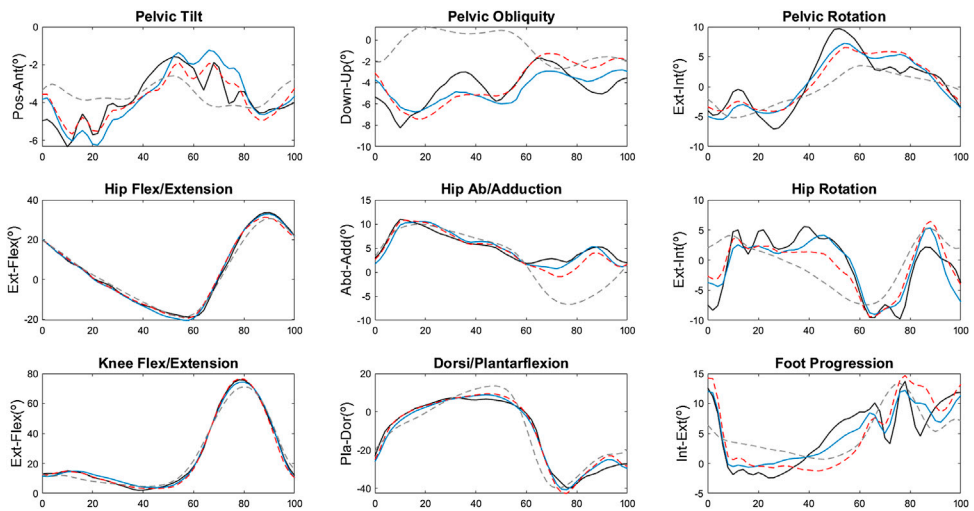

FIGURE 2 | Kinematic reconstructions of a validation stride using the three bases. The black line is the original curve, the blue line is the result when using the SCI basis with $m = 21$, the red dashed line corresponds to the reconstruction with the SCI basis with $m = 15$, and the gray dashed line is the reconstruction with the CP basis (Schwartz and Rozumalski 2008). For all nine angles, the reconstructions with the original CP basis provide the largest deviation from the original curve.

stability of the result. On each iteration, five percent of the data was randomly removed before computing the SVD and a surrogate model was built. With each model, the three criteria were assessed to find the minimum m features that allowed fulfilling each criterion: VAF≥98%, average fidelity of the reconstructions ≥98%, and percentage of the dataset reconstructed with fidelity ≥95%. Small differences between the m values found on each run indicated similarity between the models and stable results (MacCallum et al., 1999).

Moreover, we compared these results with the quality of the 15th order reconstructions of all the gait vectors in the dataset using the basis provided in Schwartz and Rozumalski (2008), built with 15 features from CP patients, and also with the reconstructions obtained with the first 15 features of the basis calculated with our SCI dataset. Furthermore, to validate the generalizability of the new basis built from SCI gait data, a validation set was built with 72 additional strides that were not used to calculate the basis. These were reconstructed and compared using the three bases, and the reconstruction fidelity was assessed with the same criteria used in the train set, allowing to compare the quality of the reconstructions in foreign data.

2.4.2 Comparison Between the Spinal Cord Injury-Gait Deviation Index and the Walking Index for Spinal Cord Injury II Scale

The SCI-GDI was calculated for each stride of both patients and HV using the reduced order orthonormal basis built in this work. Control group data, used as the reference gait pattern to compute the gait deviation, was collected at National Hospital for Paraplegics, as described in **Section 2.1**, following the same procedure used with the patients. Each gait analysis study had an associated WISCI II level, according to the walking impairment of the patient when recording the study. SCI-GDI data were grouped according to the corresponding WISCI II level, and HV data were considered as an additional set. The dataset included WISCI II levels 12, 13, 15, 16, 18, 19, and 20. Normal

TABLE 3 | Descriptive statistics of the SCI-GDI values within each WISCI II level. Numbers in parentheses indicate statistically significant differences found with an ANOVA ($p < 0.05$). The values marked with * indicate statistically significant differences found only in the SCI-GDI but not with the original GDI (Sinovas-Alonso, Herrera-Valenzuela, et al., 2022).

WISCI II	No. strides	Mean ± S.D. SCI-GDI	Minimum SCI-GDI	Maximum SCI-GDI	Normally distributed (K–S test)
C (12, 13, 15, 16, 18, 19, 20)	446	100.0 ± 10.0	72.2	126.5	True
20 (12, 13, 15, 16, 18, 19, C)	112	77.7 ± 15.8	53.8	120.8	True
19 (12, 13, 15, 16, 18, 20, C)	87	67.0 ± 8.4	51.7	95.0	True
18 (13, 19, 20, C)	12	54.7 ± 5.1	42.0	59.2	True
16 (13, 15*, 19, 20, C)	65	59.3 ± 10.8	41.0	80.2	True
15 (13, 16*, 19, 20, C)	18	52.6 ± 6.6	44.8	66.2	True
13 (12, 15, 16, 18, 19, 20, C)	6	42.7 ± 1.9	40.7	44.9	True
12 (13, 19, 20, C)	2	52.4 ± 3.5	49.9	54.8	True

WISCI II, Walking Index for Spinal Cord Injury II; SCI-GDI, gait deviation index for spinal cord injury; S.D., standard deviation; C, control; K–S Test, Kolmogórov–Smirnov test.

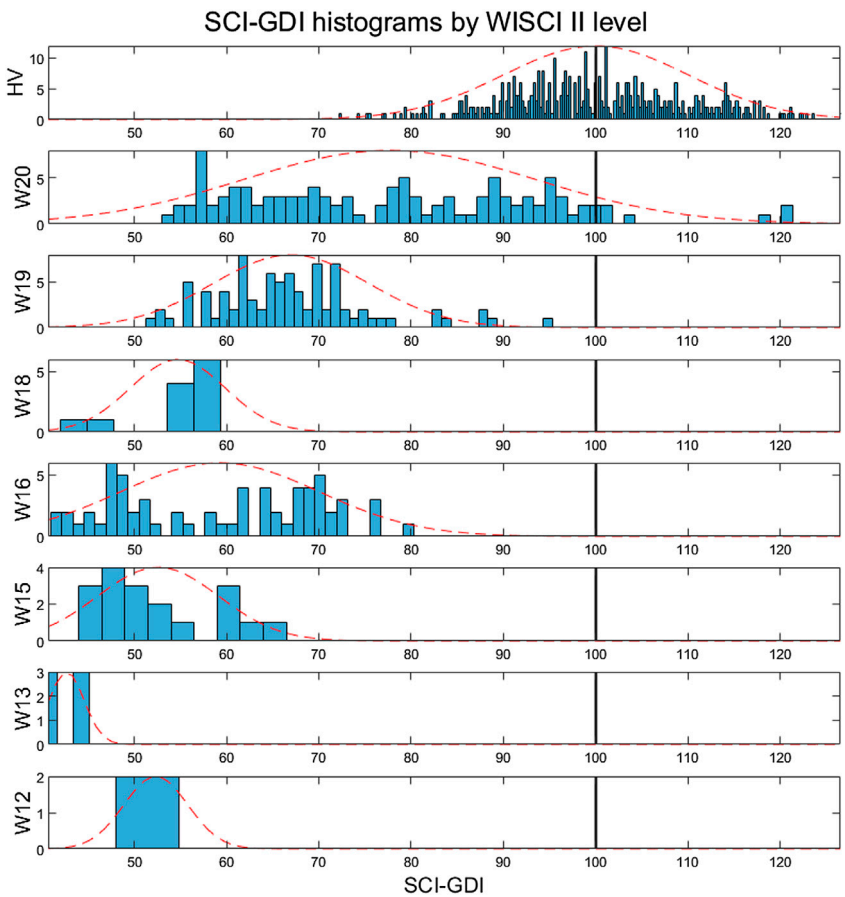

FIGURE 3 | Histograms of the SCI-GDI stratified by the WISCI II level (12–20 and control). The dotted line represents the normal distribution curve fitted to the data within each level. The vertical black line indicates the control mean.

distribution for each group was assessed with Kolmogorov–Smirnov tests ($p < 0.05$).

To facilitate the analysis, a histogram of the SCI-GDI data comprised within each WISCI II level was calculated with a normal distribution curve fitted to its mean and standard deviation. A stratified result of the histograms was expected, in accordance with the ordinal nature of the WISCI II scale. Afterward, one-way ANOVA tests were performed between the SCI-GDI values of each pair of WISCI II levels to identify differences among groups ($p < 0.05$). In addition, a Kendall's Tau-b correlation was run between both scales to assess their relationship.

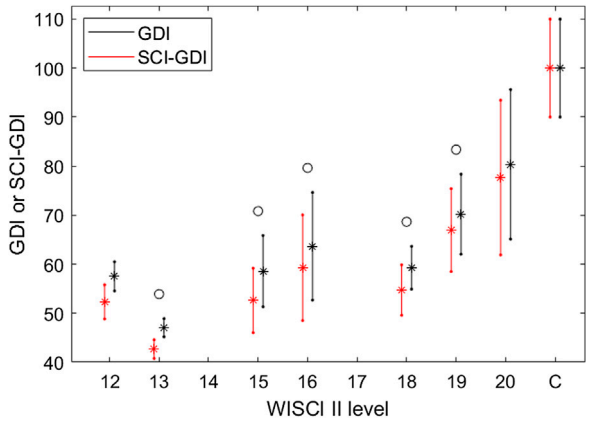

FIGURE 4 | Average ± one standard deviation for GDI (black) and SCI-GDI (red) for each WISCI II level. In all levels, GDI values are greater than SCI-GDI values. WISCI II levels with a statistically significant difference between both indexes are marked with a circle.

2.4.3 Comparison and Correlation Between the Spinal Cord Injury-Gait Deviation Index and the Gait Deviation Index

To seek differences between the original GDI, calculated from a basis derived from a CP pediatric population (Schwartz and Rozumalski, 2008), and the SCI-GDI, both indexes were calculated for each stride of the dataset using the HV data gathered in our institution. The results were grouped according to the WISCI II level of the sample. Normal distribution for each group was assessed with Kolmogorov–Smirnov tests ($p < 0.05$). Consequently, one-way ANOVA tests were performed between each pair of equivalent WISCI II levels to identify differences among groups ($p < 0.05$). In addition, to study the relationship between both indexes, Pearson's correlation and linear regression were calculated between both GDI values using the whole dataset.

3 RESULTS

3.1 Computation of the Spinal Cord Injury-Gait Deviation Index Basis

The Monte Carlo cross-validation demonstrated stable results in terms of differences no larger than one in the minimum number of features necessary to build the basis, according to the criteria defined. On average, 19.3 ± 0.5 features were sufficient to account for 98% of variance of the dataset. Nevertheless, 21.0 ± 0.0 features were necessary to reconstruct the vectors of the dataset with an average fidelity of 98%. At m = 21, 97.9 ± 0.4% of the whole dataset was reconstructed with a fidelity of at least 95%. Therefore, m = 21 was set as the minimum number of features to build the basis to represent the whole SCI gait dataset.

The comparison of the quality of reconstruction of the whole dataset when using our SCI basis with m = 21, our SCI basis with m = 15 and the basis of the original GDI derived for children with CP with m = 15 is presented in **Table 2**. The best results in terms of average fidelity of the reconstructions and percentage of vectors reconstructed with a fidelity ≥95% were obtained with our m = 21 basis, followed by our basis built using only the first 15 features. Less than 50% of the dataset was reconstructed with a quality of at least 95% when using the basis provided in Schwartz and Rozumalski (2008). Note that it was not possible to calculate the VAF with the original GDI basis because the singular values of the original dataset are not publicly available. In the validation set, the results for all criteria followed the same pattern when using each type of basis but all scores were lower than those obtained in the train dataset. In **Figure 2**, we present the reconstructions obtained with the three bases on a sample of the validation dataset with a SCI-GDI of 55.59 and a GDI of 60.03.

3.2 Comparison Between the Spinal Cord Injury-Gait Deviation Index and the Walking Index for Spinal Cord Injury II Scale

The results showed that the SCI-GDI is normally distributed across all WISCI II levels and in the HV group. **Table 3** presents the distribution of the data, the mean and the standard deviation of the SCI-GDI values comprised in each WISCI II level. There is a trend of increasing SCI-GDI with a decreasing level of functional limitation in WISCI II levels 13 to 20 and in the control group, except in level 18, with an average SCI-GDI lower than the average on level 16. This can be easily seen in **Figure 3** that shows the histograms of the SCI-GDI stratified by WISCI II level. Statistically significant differences were found between control group, levels 13, 19 and 20 with all other groups, and additionally, between levels 15 and 16. In essence, all the levels had statistically significant differences except from 12 to 18 (see **Table 3**). Furthermore, both SCI-GDI and WISCI II have a strong, positive correlation of 0.460, which is statistically significant, according to Kendall's coefficient of rank correlation (p = 1.63e-26) (Botsch, 2011).

3.3 Comparison and Correlation Between the Spinal Cord Injury-Gait Deviation Index and the Gait Deviation Index

Both SCI-GDI and GDI are normally distributed across all WISCI II levels and in the control group, according to the KS tests. When comparing the GDI and SCI-GDI values within each WISCI II level (**Figure 4**), statistically significant differences were found between all levels except for 12, 20, and the control group. For all levels, average GDI was greater than average SCI-GDI and followed the same pattern among adjacent WISCI levels (**Figure 4**). Furthermore, a strong linear correlation between both GDI and SCI-GDI was found (r = 0.993) (**Figure 5**), although both deviate at lower values.

4 DISCUSSION

The main objective of this article was to derive a specific GDI applicable to SCI (SCI-GDI). Our hypothesis was that, since the

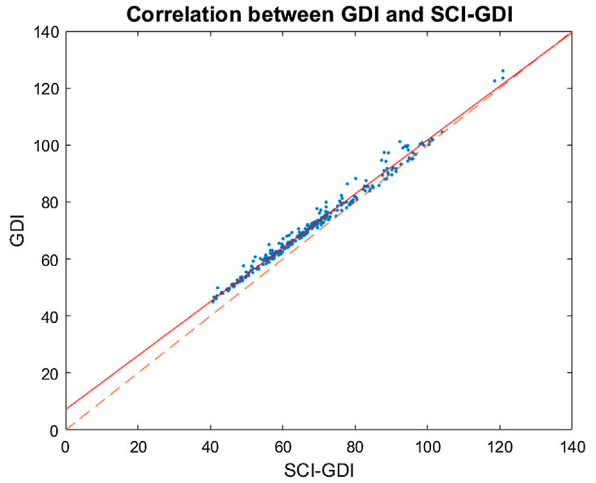

FIGURE 5 | Strong linear correlation between GDI and SCI-GDI was found ($r = 0.993$). The linear regression between both indexes, represented by the continuous line, is given by the equation $SCI\_GDI = 1.0573 * GDI - 7.5915$. The dashed line indicates the 1:1 axis. For all the samples, GDI values are larger than SCI-GDI values. The difference between both indexes is larger in data with greater impairment and it reduces progressively toward a normal gait pattern.

GDI was obtained from a database of children with CP, the application to SCI would not correctly represent the gait impairments of this population. To this extent, we derived a GDI following the methodology originally proposed (Schwartz and Rozumalski, 2008) to a gait database of adults with SCI to obtain the SCI-GDI, studied the correlation of our SCI-GDI with the WISCI II, and compared the GDI and the SCI-GDI to assess their differences.

Although our dataset to compute the reduced order SCI basis contained fewer number of steps than the original one, there is no rule of thumb to define the minimum size that a dataset should have to perform SVD and feature selection given an initial number of features (Bandalos and Boehm-Kaufman, 2009). Different recommendations stated in the literature and some studies demonstrate that it is feasible to obtain quality solutions with small datasets if certain conditions are met, like having data with high communalities (MacCallum et al., 1999; Hogarty et al., 2005; Mundfrom et al., 2005). During the process of finding the number of gait features necessary to form our optimal reduced order SCI basis, a high variables-to-factors ratio and stable results with variations of at most one feature in the Monte Carlo cross-validation suggested that our dataset is large enough to represent robustly the variety of gait patterns within the population of SCI comprised in the data, by using linear combinations of the information. Nevertheless, a larger dataset would be recommendable, given the number of features of the original matrix in which SVD is performed.

Regarding the process of defining the minimum number of features to form the reduced order basis, our results showed that $m = 19$ was enough to account for at least 98% of the variance comprised in the dataset, indicating high communalities in the data, and suggesting that the size of our dataset is acceptable to be used in this study. Two more features are necessary ($m = 21$) to reconstruct the curves within the dataset with an average fidelity of 98%. This difference is understandable because the first criterion was calculated with the singular values of the PCA while the second one depended on the singular vectors. In addition, at $m = 21$, almost 98% of the whole dataset was reconstructed with a fidelity of at least 95%, only 1% less than the results presented by Schwartz and Rozumalski (2008) in the original derivation of the GDI in CP. Therefore, we defined $m = 21$ to build our SCI basis because both criteria must be fulfilled in order to build a basis that represents the whole dataset. It is important to note that these results indicate that six features or more are necessary to represent the variety of gait in SCI when compared to the 15 features that were sufficient in CP (Schwartz and Rozumalski, 2008). These results suggest a larger variance in the kinematics of gait in SCI when compared to CP, which may be related to the heterogeneity of the clinical forms of incomplete SCI depending on the level of injury and AIS. Hence, the original 15-feature basis of the GDI may not account for the variety or reconstruct with enough precision gait vectors in SCI.

In this regard, the results presented in **Table 2** show that when calculating the quality of the reconstructions obtained with the original basis of the GDI (Schwartz and Rozumalski, 2008) on our train dataset, fidelity drops from an "ideal" value reported in Schwartz and Rozumalski (2008) of 98–93% and most importantly, only 44.70% of the dataset is reconstructed with a fidelity of at least 95%. These findings support the fact that the implementation of the GDI in SCI is not recommended because the dataset used to derive the GDI basis was a pediatric CP population and there are differences in the etiology of the neurological impairment, clinical consequences related to function and maturity of gait between adults and children that cause differences in gait patterns among populations. Indeed, even when using only the first 15 features of our SCI basis, the average fidelity of reconstruction is 1.41% lower when compared to our SCI basis with 21 features, but only 83.11% of the dataset is reconstructed with high quality, which is almost twice the value obtained with the CP basis. This means that even when using a basis built with data of adults with SCI, 15 features are not enough to represent and reconstruct with accuracy the whole dataset, but are better than using the 15 features from the original CP basis.

The results obtained using the validation dataset follow the same pattern, supporting the previous findings and indicating that results are not due to an overfitting to our dataset. Nevertheless, we highlight the fact that all the values obtained when using the validation dataset are lower than the corresponding results in the train dataset, suggesting that using more train data would be recommended to obtain a SCI basis that provides more generalizable results, as reflected by smaller differences in performance when evaluating the criteria in both sets.

Moreover, the reconstruction of a single sample of the validation set with a large level of gait deviation (WISCI II = 18, SCI-GDI = 53.47, and GDI = 60.43) in **Figure 2** shows that the reconstructions obtained with the CP basis are poorly related to the original vector, whereas reconstructions with the SCI basis

with 15 features have a better quality and the most accurate results are obtained with our 21st order reconstructions. It is also noteworthy that pelvic movement in the three axes is poorly reconstructed in all cases. We hypothesize this might be because the pelvis is the most complicated segment to model accurately and with reliability during a 3DGA (O'Sullivan et al., 2010). The anatomical landmarks used to place or align the pelvic markers on most motion capture systems, including the Codamotion, are the anterior and posterior superior iliac spines. These are bony protuberances in the pelvis covered with adipose tissue; therefore, the markers cannot be placed accurately on the subjects (C-Motion Wiki Documentation, 2019) and are prone to soft tissue artefacts (Langley et al., 2019). Based on these markers, the position of the pelvis is estimated; thus, the sources of error propagate from marker positioning to the computation of the kinematics of the segment. The improvement of the register of the pelvis during 3DGA is out of the scope of this article, but the issues for precisely estimating the position of the pelvis during a 3DGA are common to any capture, and therefore it is a limitation present in any 3DGA, and not only applicable to the calculation of the GDI or the SCI-GDI. Although it is not stated in the work by Schwartz and Rozumalski (2008), in their **Figure 2** it seems they identified similar difficulties in achieving precise pelvic representations. On the contrary, kinematics in the sagittal plane for the knee, hip, and ankle have more precise reconstructions in the three examples. The angles that are better reconstructed might be more useful in attempts to derive indexes that use less variables than the nine used in the GDI.

In other respects, the comparison between the SCI-GDI and the WISCI II scale showed the stratification expected in levels 13 to 20 and in the control group, except in level 18 (see **Figure 3**), similarly to the results obtained when using the GDI (Sinovas-Alonso et al., 2022). Nevertheless, an important difference is that only in the SCI-GDI, levels 15 and 16 showed a statistical difference, unlike in GDI (see **Table 3**). Therefore, the SCI-GDI provides a better discrimination of more WISCI II levels when compared to the GDI. The new index managed to discriminate all the levels comprised in the dataset except for 12 and 18, which have few data, especially level 12. Therefore, the SCI-GDI provides a good discrimination of most WISCI II levels between 13 and 20. We hypothesize that level 18 is hard to discriminate first because there are few data in this level, and second because it indicates the use of braces to improve functionality, which blocks differently hip, knee, and ankle joints, depending on the nature of the orthosis, imposing a less-physiological gait pattern. Asking a patient who usually uses braces to walk without them, even in short distances like during a 3DGA, increases considerably the difficulty of the task, highlighting the impairment of gait with respect to the normal pattern. That might be why impairment as measured by the GDI is increased in level 18 with respect to level 16, and that does not include the use of braces but the use of crutches that affect mostly gait kinetics instead of kinematics. Moreover, the strong, positive correlation found between both scales ($\tau_B = 0.460$) show that they are related and measure gait impairment while at the same time, with a τ_B value far from a perfect correlation, representing different aspects of gait pathology. Furthermore, the comparison between the GDI and SCI-GDI demonstrated that both indexes are statistically different (see **Figure 4**) for all the WISCI II levels analyzed that include any type of walking assistance, supporting the importance of using a gait deviation index derived from a proper sample, in essence, a SCI adult population. Level 12 is not analyzed in detail because it is poorly represented with only two samples.

The results shown in **Figure 4** indicate that walking impairment is less penalized by the GDI when compared to the SCI-GDI. This is congruent with the findings stated previously in our work because if the CP basis covers a smaller variance on gait patterns and provides low quality reconstructions on SCI, the GDI calculated from a SCI gait vector using this basis might be based on a poorer representation of the original SCI vector and therefore, less penalized than when the vector is better reconstructed and includes the alterations present in the gait curves. Furthermore, the similar patterns between both deviation indexes across all WISCI II levels presented in **Figure 4** and the strong linear correlation ($r = 0.993$) support that our SCI-GDI represents the same aspects of gait impairment as the GDI. The linear relationship between both indexes presented in **Figure 5** show clearly that in higher values of GDI, the differences between GDI and SCI-GDI reduce. Thus, the application of the GDI in SCI could provide misleading information about the dimension of the gait impairment, especially in patients with greater neurological damage. Therefore, our SCI-GDI is more sensitive to larger gait impairment than the GDI, but the difference between both indexes reduces progressively towards normal gait. These findings are congruent with the statistical differences found between both indexes for all WISCI II levels except for level 20 (see **Figure 4**), corresponding to individuals that do not require any assistance to walk. This makes sense because no difference in the degree of gait impairment is identified in subjects that do not need assistance to walk.

Our study had several limitations. First, as mentioned before, even though the computation of the SCI-GDI basis showed stable results, using a larger dataset would allow us to verify that our results (number of features m, VAF and reconstruction percentages) indeed remain independently of the number of strides in the database. Other limitations inherent to the SCI pathology is that due to the high variability of gait impairment in SCI ,which depends on several factors such as the neurological level of injury (NLI), the severity of the injury according to the AIS and the time since onset of injury, there is no topographic classification of SCI to assess an ordinal level of gait impairment, unlike other neurological pathologies such as CP (Gage, 1991). Therefore, it is not possible to compare or validate the SCI-GDI with neither the AIS nor the NLI. Even though we only compared the SCI-GDI with the WISCI II due to data availability, a more balanced distribution of the data within the WISCI II levels was desirable. In this regard, our

study lacks data of other gait tests or scales validated in SCI, like the 6MWT, TUG, 10MWT, or BBS, to further validate the SCI-GDI. Such validation will also reinforce the need of developing specific GDIs for each condition instead of implementing the pediatric CP-based GDI to several populations without sufficient validation. Centers with gait datasets from other pathologies than CP (Schwartz and Rozumalski, 2008) and SCI (this work) can reproduce this methodology to develop specific gait deviation indexes for their specific pathologies.

In spite of these limitations, the SCI-GDI can be applied in any person with a SCI regardless of the severity or neurological level of injury, from 16 to 70 years old in both men and women. The most important changes in gait kinematics occur during adolescence, and gait is considered mature and steady afterward, with few changes (Cupp et al., 1999). Children have different gait kinematics than adults (Ganley and Powers, 2005) that are constantly changing through ages, and in elderly, around the age of 60–70, significant changes in gait are also reported (Prince et al., 1997). In addition, after an SCI is chronic, changes in gait are reduced mostly to those related to rehabilitation outcomes and are covered by the data included in our dataset. Likewise, the small differences in gait kinematics between men and women that are mostly present in the frontal plane of the pelvis and hip (Bruening et al., 2015) are not as conditioning as the gait limitations after an SCI, allowing the application of the SCI-GDI regardless of sex. We intentionally captured a wide variety of gait data of SCI with different severity, neurological level of injury, time since injury onset, sex, and age, to capture the largest variety in gait patterns we had access to, and guarantee that the SCI-GDI could properly represent any of these patterns. This leads us to suggest the implementation of the SCI-GDI in adults with SCI from 16 to 70 years old, using the electronic addendum provided in the **Supplementary Material**.

5 CONCLUSION

The SCI-GDI is calculated using a 21-feature vectorial basis derived from gait data of adult population with SCI, instead of the 15-feature basis used for the original GDI. Our index has better discriminative properties of more WISCI II levels than the original GDI when applied to adults with SCI and conforms to the stratification of gait impairment of the WISCI II scale. In addition, the SCI-GDI is more sensitive to larger gait impairment than the GDI, but its sensitivity decreases with less impaired gait function. Indeed, the implementation of the original GDI in SCI may lead to overestimation of gait function. The SCI basis also allows building higher-quality reconstructions of gait curves when compared to the original GDI basis. Although further validation of the index with other scales used in SCI would be of interest, we recommend its implementation in adults with SCI. It can be easily computed using the electronic addendum provided in the **Supplementary Material**.

DATA AVAILABILITY STATEMENT

An electronic addendum is provided in the **Supplementary Material** to implement the SCI-GDI. Detailed instructions to compute the index are provided in the same file. The novelty of this article with respect to the original development of the GDI (Schwartz and Rozumalski, 2008) is the 21st feature SCI basis calculated. Therefore, the addendum provided has the same structure that the one provided to compute the GDI, but with our SCI basis.

ETHICS STATEMENT

The studies involving human participants were reviewed and approved by the Local Ethics Committee of University Hospital Complex of Toledo, Spain. Written informed consent to participate in this study was provided by the participants' legal guardian/next of kin.

AUTHOR CONTRIBUTIONS

DH-V, AJd-A, AG-A, and IS-A conceived the study. IS-A registered the data. DH-V analyzed the data. DH and AJd-A wrote the manuscript. DH-V, AJd-A, and IS contributed to the interpretation and discussion of study results. AJd-A obtained funding. All authors revised, improved, and approved the final version of the manuscript. All authors have read and agreed to the published version of the manuscript.

FUNDING

This research has been supported by the TAILOR project: "Modular robotic and neuroprosthetic customizable systems for the assistance of pathological gait," funded by Agencia Estatal de Investigación on 2018 call (reference RTI 2018-097290-B-C31).

ACKNOWLEDGMENTS

The authors acknowledge Dr. Ana de los Reyes Guzmán who helped registering the data. In addition, they acknowledge all the patients and healthy volunteers who accepted voluntarily to be part of this study.

SUPPLEMENTARY MATERIAL

The Supplementary Material for this article can be found online at: https://www.frontiersin.org/articles/10.3389/fbioe.2022.874074/full#supplementary-material

REFERENCES

Aspaym, Federación Nacional (2012). *Análisis sobre la Lesión Medular en España*. Toledo: Federación Nacional Aspaym.

Baker, R., Esquenazi, A., Benedetti, M. G., and Desloovere, K. (2016). Gait Analysis: Clinical Facts. *Eur. J. Phys. Rehabil. Med.* 52 (4), 560–574.

Baker, R. (2006). Gait Analysis Methods in Rehabilitation. *J. Neuroeng Rehabil.* 3 (4), 4. doi:10.1186/1743-0003-3-4

Bandalos, D., and Boehm-Kaufman, M. (2009). "Four Common Misconceptions in Exploratory Factor Analysis," in *Statistical and Methodological Myths and Urban Legends* (New York: Routledge), 61–87.

Bazarnik-Mucha, K., Snela, S., Szczepanik, M., Jarmuziewicz, A., Guzik, A., WoliŃska, O., et al. (2020). Three-dimensional Analysis of Gait in Children and Adolescents with Juvenile Idiopathic Arthritis. *Acta Bioeng. Biomech.* 22, 35–45. doi:10.37190/abb-01511-2019-02

Berg, K. (1989). Measuring Balance in the Elderly: Preliminary Development of an Instrument. *Physiother. Can.* 41, 304–311. doi:10.3138/ptc.41.6.304

Bleyenheuft, C., Detrembleur, C., Bleyenheuft, C., and Detrembleur, C. (2012). Kinematic Covariation in Pediatric, Adult and Elderly Subjects: Is Gait Control Influenced by Age? *Clin. Biomech.* 27, 568–572. doi:10.1016/j.clinbiomech.2012.01.010

Botsch, R. (2011). *Chapter 12. Significance and Measures of Association*. Aiken: University of South Carolina Aiken.

Brooks, D., Solway, S., and Gibbons, W. J. (2003). ATS Statement on Six-Minute Walk Test. *Am. J. Respir. Crit. Care Med.* 167, 1287. doi:10.1164/ajrccm.167.9.950

Broström, E. W., Esbjörnsson, A., von Heideken, J., Larsson, P., Wretenberg, P., and Iversen, M. (2013). Change in Gait Deviation Index after Anti-tumour Necrosis Factor-α Treatment in Individuals with Rheumatoid Arthritis: a Pilot Study. *Scand. J. Rheumatol.* 42, 356–361. doi:10.3109/03009742.2013.776102

Bruening, D. A., Frimenko, R. E., Goodyear, C. D., Bowden, D. R., and Fullenkamp, A. M. (2015). Sex Differences in Whole Body Gait Kinematics at Preferred Speeds. *Gait Posture* 41, 540–545. doi:10.1016/j.gaitpost.2014.12.011

C-Motion Wiki Documentation (2019). *Coda Pelvis*. c-motion.com. Available at: https://www.c-motion.com/v3dwiki/index.php?title=Coda_Pelvis (Accessed January 21, 2022)

Charnwood Dynamics Limited (2004). *CODA Cx1 User Guide*. Rothley: Charnwood Dynamics Limited.

Cimolin, V., Galli, M., Vimercati, S. L., and Albertini, G. (2011). Use of the Gait Deviation Index for the Assessment of Gastrocnemius Fascia Lengthening in Children with Cerebral Palsy. *Res. Dev. Disabil.* 32, 377–381. doi:10.1016/j.ridd.2010.10.017

Correa, K. P., Devetak, G. F., Martello, S. K., de Almeida, J. C., Pauleto, A. C., and Manffra, E. F. (2017). Reliability and Minimum Detectable Change of the Gait Deviation Index (GDI) in Post-stroke Patients. *Gait Posture* 53, 29–34. doi:10.1016/j.gaitpost.2016.12.012

Cripps, R. A., Lee, B. B., Wing, P., Weerts, E., Mackay, J., and Brown, D. (2011). A Global Map for Traumatic Spinal Cord Injury Epidemiology: towards a Living Data Repository for Injury Prevention. *Spinal Cord.* 49, 493–501. doi:10.1038/sc.2010.146

Cupp, T., Oeffinger, D., Tylkowski, C., and Augsburger, S. (1999). Age-related Kinetic Changes in Normal Pediatrics. *J. Pediatr. Orthop.* 19, 475–478. doi:10.1097/01241398-199907000-00010

Dittuno, P., Dittuno Jr, J., and Dittuno, J. F. (2001). Walking Index for Spinal Cord Injury (WISCI II): Scale Revision. *Spinal Cord.* 39, 654–656. doi:10.1038/sj.sc.3101223

Ditunno, P. L., Patrick, M., Stineman, M., and Ditunno, J. F. (2008). Who Wants to Walk? Preferences for Recovery after SCI: A Longitudinal and Cross-Sectional Study. *Spinal Cord.* 46 (7), 500–506. doi:10.1038/sj.sc.3102172

Eriksson, M., Bartonek, Å., Pontén, E., and Gutierrez-Farewik, E. M. (2015). Gait Dynamics in the Wide Spectrum of Children with Arthrogryposis: a Descriptive Study. *BMC Musculoskelet. Disord.* 16, 384. doi:10.1186/s12891-015-0834-5

Esbjörnsson, A., Rozumalski, A., Iversen, M., Schwartz, M., Wretenberg, P., and Broström, E. (2014). Quantifying Gait Deviations in Individuals with Rheumatoid Arthritis Using the Gait Deviation Index. *Scand. J. Rheumatol.* 43, 124–131. doi:10.3109/03009742.2013.822095

Eshraghi, A., Abu Osman, N. A., Karimi, M., Gholizadeh, H., Soodmand, E., and Abas, W. A. B. W. (2014). Gait Biomechanics of Individuals with Transtibial Amputation: Effect of Suspension System. *PLOS ONE* 9, e96988. doi:10.1371/journal.pone.0096988

Gage, J. (1991). *Gait Analysis in Cerebral Palsy*. Oxford: Blackwell Scientific Publications Ltd.

Galli, M., Cimolin, V., De Pandis, M. F., Schwartz, M. H., and Albertini, G. (2012). Use of the Gait Deviation Index for the Evaluation of Patients with Parkinson's Disease. *J. Mot. Behav.* 44, 161–167. doi:10.1080/00222895.2012.664180

Ganley, K. J., and Powers, C. M. (2005). Gait Kinematics and Kinetics of 7-Year-Old Children: a Comparison to Adults Using Age-specific Anthropometric Data. *Gait Posture* 21, 141–145. doi:10.1016/j.gaitpost.2004.01.007

Garman, C. R., Graf, A., Krzak, J., Caudill, A., Smith, P., and Harris, G. (2019). Gait Deviations in Children with Osteogenesis Imperfecta Type I. *J. Pediatr. Orthop.* 39, e641–e646. doi:10.1097/bpo.0000000000001062

Guzik, A., and Drużbicki, M. (2020). Application of the Gait Deviation Index in the Analysis of Post-stroke Hemiparetic Gait. *J. Biomechanics* 99, 109575. doi:10.1016/j.jbiomech.2019.109575

Hogarty, K. Y., Hines, C. V., Kromrey, J. D., Ferron, J. M., and Mumford, K. R. (2005). The Quality of Factor Solutions in Exploratory Factor Analysis: the Influence of Sample Size, Communality, and Overdetermination. *Educ. Psychol. Meas.* 65 (2), 202–226. doi:10.1177/0013164404267287

Hwang, M., Flanagan, A., Graf, A., Kruger, K. M., Scullion, N., Tayne, S., et al. (2021). Gait Characteristics in Youth with Transverse Myelitis. *Top. Spinal Cord. Inj. Rehabil.* 27, 38–48. doi:10.46292/sci20-00048

Ito, T., Noritake, K., Sugiura, H., Kamiya, Y., Tomita, H., Ito, Y., et al. (2019). Association between Gait Deviation Index and Physical Function in Children with Bilateral Spastic Cerebral Palsy: A Cross-Sectional Study. *J. Clin. Med.* 9, 28. doi:10.3390/jcm9010028

Ito, T., Sugiura, H., Ito, Y., Noritake, K., and Ochi, N. (2021). Effect of the COVID-19 Emergency on Physical Function Among School-Aged Children. *Ijerph* 18, 9620. doi:10.3390/ijerph18189620

Ito, Y., Ito, T., Kurahashi, N., Ochi, N., Noritake, K., Sugiura, H., et al. (2020). Gait Characteristics of Children with Williams Syndrome with Impaired Visuospatial Recognition: a Three-Dimensional Gait Analysis Study. *Exp. Brain Res.* 238, 2887–2895. doi:10.1007/s00221-020-05946-0

Kark, L., Odell, R., McIntosh, A. S., and Simmons, A. (2016). Quantifying Prosthetic Gait Deviation Using Simple Outcome Measures. *Wjo* 7, 383–391. doi:10.5312/wjo.v7.i6.383

Kobsar, D., Charlton, J. M., and Hunt, M. A. (2019). Individuals with Knee Osteoarthritis Present Increased Gait Pattern Deviations as Measured by a Knee-specific Gait Deviation Index. *Gait Posture* 72, 82–88. doi:10.1016/j.gaitpost.2019.05.020

Langley, B., Page, R., and Greig, M. (2019). The Influence of Different Pelvic Technical Marker Sets upon Hip Kinematics during Gait. *Gait Posture* 71, 74–78. doi:10.1016/j.gaitpost.2019.04.012

Maanum, G., Jahnsen, R., Stanghelle, J., Sandvik, L., Larsen, K., and Keller, A. (2012). Face and Construct Validity of the Gait Deviation Index in Adults with Spastic Cerebral Palsy. *J. Rehabil. Med.* 44, 272–275. doi:10.2340/16501977-0930

MacCallum, R. C., Widaman, K. F., Zhang, S., and Hong, S. (1999). Sample Size in Factor Analysis. *Psychol. Methods* 4, 84–99. doi:10.1037/1082-989x.4.1.84

Malt, M. A., Aarli, Å., Bogen, B., and Fevang, J. M. (2016). Correlation between the Gait Deviation Index and Gross Motor Function (GMFCS Level) in Children with Cerebral Palsy. *J. Children's Orthop.* 10, 261–266. doi:10.1007/s11832-016-0738-4

Mar, D., Lieberman, I., and Haddas, R. (2019). The Gait Deviation Index as an Indicator of Gait Abnormality Among Degenerative Spinal Pathologies. *Eur. Spine J.* 29 (10), 2591–2599 doi:10.1007/s00586-019-06252-2

Massaad, A., Assi, A., Skalli, W., and Ghanem, I. (2014). Repeatability and Validation of Gait Deviation Index in Children: Typically Developing and Cerebral Palsy. *Gait Posture* 39, 354–358. doi:10.1016/j.gaitpost.2013.08.001

Mindler, G. T., Kranzl, A., Stauffer, A., Haeusler, G., Ganger, R., and Raimann, A. (2020). Disease-specific Gait Deviations in Pediatric Patients with X-Linked Hypophosphatemia. *Gait Posture* 81, 78–84. doi:10.1016/j.gaitpost.2020.07.007

Molloy, M., McDowell, B. C., Kerr, C., and Cosgrove, A. P. (2010). Further Evidence of Validity of the Gait Deviation Index. *Gait Posture* 31, 479–482. doi:10.1016/j.gaitpost.2010.01.025

Mundfrom, D. J., Shaw, D. G., and Ke, T. L. (2005). Minimum Sample Size Recommendations for Conducting Factor Analyses. *Int. J. Test.* 5 (2), 159–168. doi:10.1207/s15327574ijt0502_4

Murphy, A. T., Kravtsov, S., Sangeux, M., Rawicki, B., and New, P. W. (2019). Utilizing Three Dimensional Clinical Gait Analysis to Optimize Mobility Outcomes in Incomplete Spinal Cord Damage. *Gait Posture* 74, 53–59. doi:10.1016/j.gaitpost.2019.08.001

O'Sullivan, K., Clifford, A., and Hughes, L. (2010). The Reliability of the CODA Motion Analysis System for Lumbar Spine Analysis: a Pilot Study. *Physiother. Pract. Res.* 31, 16–22. doi:10.3233/ppr-2010-31104

Patrick, J. H. (2003). The Case for Gait Analysis as Part of the Management of Incomplete Spinal Cord Injury. *Spinal Cord.* 41, 479–482. doi:10.1038/sj.sc.3101524

Podsiadlo, D., and Richardson, S. (1991). The Timed "Up & Go": A Test of Basic Functional Mobility for Frail Elderly Persons. *J. Am. Geriatrics Soc.* 39, 142–148. doi:10.1111/j.1532-5415.1991.tb01616.x

Prince, F., Corriveau, H., Hébert, R., and Winter, D. A. (1997). Gait in the Elderly. *Gait Posture* 5, 128–135. doi:10.1016/s0966-6362(97)01118-1

Rasmussen, H. M., Pedersen, N. W., Overgaard, S., Hansen, L. K., Dunkhase-Heinl, U., Petkov, Y., et al. (2019). Gait Analysis for Individually Tailored Interdisciplinary Interventions in Children with Cerebral Palsy: a Randomized Controlled Trial. *Dev. Med. Child. Neurol.* 61, 1189–1195. doi:10.1111/dmcn.14178

Sagawa, Y., Watelain, E., De Coulon, G., Kaelin, A., Gorce, P., and Armand, S. (2013). Are Clinical Measurements Linked to the Gait Deviation Index in Cerebral Palsy Patients? *Gait Posture* 38, 276–280. doi:10.1016/j.gaitpost.2012.11.026

Schwartz, M. H., and Rozumalski, A. (2008). The Gait Deviation Index: a New Comprehensive Index of Gait Pathology. *Gait Posture* 28, 351–357. doi:10.1016/j.gaitpost.2008.05.001

Sienko Thomas, S., Buckon, C. E., Nicorici, A., Bagley, A., McDonald, C. M., and Sussman, M. D. (2010). Classification of the Gait Patterns of Boys with Duchenne Muscular Dystrophy and Their Relationship to Function. *J. Child. Neurol.* 25, 1103–1109. doi:10.1177/0883073810371002

Sinovas-Alonso, I., Gil-Agudo, Á., Cano-de-la-Cuerda, R., and del-Ama, A. J. (2021). Walking Ability Outcome Measures in Individuals with Spinal Cord Injury: A Systematic Review. *Ijerph* 18 (18), 9517. doi:10.3390/ijerph18189517

Sinovas-Alonso, I., Herrera-Valenzuela, D., Cano-de-la-Cuerda, R., de-los-Reyes-Guzmán, A., del-Ama, A. J., and Gil-Agudo, Á. (2022). Application of the Gait Deviation Index to Study Gait Impairment in Adult Population with Spinal Cord Injury: Comparison with the Walking Index for Spinal Cord Injury Levels. *Front. Hum. Neurosci.* 16, 826333. doi:10.3389/fnhum.2022.826333

Speciali, D. S., Oliveira, E. M. d., Santos, N. M. d., Pereira, F. V., Fracini, A. C., Fukuda, T. Y., et al. (2013). Use of the Gait Deviation Index and Spatiotemporal Variables for the Assessment of Dual Task Interference Paradigm. *J. Bodyw. Mov. Ther.* 17, 19–27. doi:10.1016/j.jbmt.2012.03.001

Trivedi, J., Srinivas, S., Trivedi, R., Davidson, N., Munigangaiah, S., Bruce, C., et al. (2021). Preoperative and Postoperative, Three-Dimensional Gait Analysis in Surgically Treated Patients with High-Grade Spondylolisthesis. *J. Pediatr. Orthop.* 41, 111–118. doi:10.1097/bpo.0000000000001721

Van Hedel, H. J. A., Wirz, M., and Dietz, V. (2008). Standardized Assessment of Walking Capacity after Spinal Cord Injury: The European Network Approach. *Neurological Res.* 30, 61–73. doi:10.1179/016164107x230775

Whittle, M. (1996). *Gait Analysis. An Introduction*. Oxford: Butterworth-Heinemann.

Wilson, N. C., Signal, N., Naude, Y., Taylor, D., and Stott, N. S. (2015). Gait Deviation Index Correlates with Daily Step Activity in Children with Cerebral Palsy. *Archives Phys. Med. Rehabilitation* 96, 1924–1927. doi:10.1016/j.apmr.2015.05.024

Wyndaele, M., and Wyndaele, J.-J. (2006). Incidence, Prevalence and Epidemiology of Spinal Cord Injury: What Learns a Worldwide Literature Survey? *Spinal Cord.* 44 (9), 523–529. doi:10.1038/sj.sc.3101893

Zhou, C., Xia, H., Yin, J., and Zheng, Y. (2021). Three-dimensional Gait Quantitative Analysis in Postoperative Rehabilitation of Lumbar Degenerative Diseases: a Self-Controlled Before-After Study. *Am. J. Transl. Res.* 13, 6913–6920.

Conflict of Interest: The authors declare that the research was conducted in the absence of any commercial or financial relationships that could be construed as a potential conflict of interest.

frontiers | Frontiers in Bioengineering and Biotechnology

TYPE Systematic Review
PUBLISHED 23 August 2022
DOI 10.3389/fbioe.2022.890118

OPEN ACCESS

EDITED BY
Mohammad Nikkhoo,
Islamic Azad University, Iran

REVIEWED BY
Yaodong Gu,
Ningbo University, China
Ahmed Imran,
Ajman University, United Arab Emirates

*CORRESPONDENCE
Pan Liu,
2264137208@qq.com
Changqing Jiang,
jcq-006@163.com

†These authors have contributed equally to this work and share first authorship

‡These authors have contributed equally to this work

SPECIALTY SECTION
This article was submitted to Biomechanics, a section of the journal Frontiers in Bioengineering and Biotechnology

RECEIVED 05 March 2022
ACCEPTED 14 July 2022
PUBLISHED 23 August 2022

CITATION
Guo W, Wan T, Tan H, Fan G, Gao X, Liu P and Jiang C (2022), Anterior cruciate ligament deficiency versus intactness for outcomes in patients after unicompartmental knee arthroplasty: a systematic review and meta-analysis. *Front. Bioeng. Biotechnol.* 10:890118. doi: 10.3389/fbioe.2022.890118

Anterior cruciate ligament deficiency versus intactness for outcomes in patients after unicompartmental knee arthroplasty: a systematic review and meta-analysis

Weiming Guo[1†], Teng Wan[1†], Haifeng Tan[2†], Gang Fan[1], Xiaoyu Gao[2], Pan Liu[2*‡] and Changqing Jiang[1*‡]

[1]Department of Sports Medicine, Huazhong University of Science and Technology Union Shenzhen Hospital, The 6th Affiliated Hospital of Shenzhen University Health Science Center, Shenzhen, China, [2]Hengyang Medical College, University of South China, Hengyang, Hunan, China

Objective: The unicondylar knee arthroplasty (UKA) procedure is primarily indicated for osteoarthritis of the knee. Anterior cruciate ligament (ACL) defects have long been considered a contraindication to UKA. However, recent clinical studies have found that ACL defects do not affect postoperative outcomes in UKA. To elucidate whether ACL defects affect postoperative outcomes in UKA, we performed a systematic review and Meta-analysis of observational cohort studies comparing the effects of ACL defects and intactness on surgical outcomes in UKA.

Methods: In this study, we used "Anterior Cruciate Ligament", "Anterior Cruciate Ligament Injuries" and "Arthroplasty, Replacement, Knee" as the subject terms according to PICOS principles. These subject terms and the corresponding free texts were used to conduct a systematic search in the three major databases PubMed, Embase and Cochrane on December 9, 2021. The main study variables included age, gender, region, definition of ACL defect and diagnosed diseases. The study used a random effect model to pool the effect of 95% CIs. To explore the sources of heterogeneity and to test the stability of the results, a sensitivity analysis was performed.

Results: The systematic review found no significant differences in postoperative clinical outcomes in the elderly population when unicondylar replacement was performed in the setting of multiple factors such as injury, defects, longitudinal tear, and synovial bursa injury defined as ACL deficiency. The primary clinical outcomes included postoperative revision, Tegner activity score, and Oxford Knee Score (OKS). After statistical meta-analysis, postoperative outcomes such as postoperative revision (OR, 1.174; 95% CIs, 0.758–1.817) and Tegner activity score (OR, -0.084; 95% CIs, -0.320–0.151) were not statistically different.

Conclusion: There was no difference in postoperative revision rates and functional outcomes such as Tegner activity score between the ACL-deficient group compared with the ACL-intact group. For the present results, it is not advisable to consider ACL deficiency as a contraindication of UKA.

KEYWORDS

anterior cruciate ligament, surgery, meta, unicompartmental arthroplasty, knee

Introduction

Osteoarthritis is currently the most common type of arthritis in the world and is one of the leading causes of pain, disability and increased socioeconomic costs worldwide (Bijlsma et al., 2011; Glyn-Jones et al., 2015). The pathology is characterized by degenerative changes in the bones, cartilage, menisci, ligaments and synovial tissues of the joints, and patients usually suffer from irregular chronic pain, which seriously affects their quality of life (Braun and Gold, 2012; Goldring and Goldring, 2016). The prevalence of knee osteoarthritis appears to be higher compared to other types of osteoarthritis (Bliddal and Christensen, 2009). Current research suggests that the rising incidence of knee osteoarthritis in the population is closely related to the aging of the population and the obesity epidemic (Bijlsma et al., 2011; Heidari, 2011). UKA is now a common treatment modality for many patients with knee osteoarthritis (Wilson et al., 2019). Compared to total knee arthroplasty (TKA), it has the advantages of less injury and faster recovery, but a higher revision rate (Murray and Parkinson, 2018). ACL rupture and injury are often caused by degenerative changes in the knee joint and are also likely to occur in young and active individuals (Louboutin et al., 2009). In addition, drastic biomechanical changes in the knee joint during sports and accidents can also lead to ACL (Larwa et al., 2021). A ruptured and defective ACL will result in anterior tibial translation and abnormal shearing forces to the posterior medial aspect of the knee (Filbay and Grindem, 2019). Further progression may also lead to degenerative tears of the posterior horn of the medial meniscus, thereby affecting joint stability (Frobell et al., 2010).

The current study shows that knee osteoarthritis and ACL deficits can be causally linked across age groups, which makes the two symptoms often appear together, especially after ACL damage, and patients have a significantly higher incidence of knee osteoarthritis (Friel and Chu, 2013; Mancuso et al., 2016; Cinque et al., 2018). Combined ACL reconstruction and UKA is one of the accepted treatment modalities for ACL defects combined with osteoarthritis. This treatment modality has performed better for younger patients with a mean of 2 years of follow-up, but longer-term observational studies are lacking (Volpin et al., 2018; Tecame et al., 2019). It is also of concern that ligament reconstruction, while it may help improve joint stability and functional prognosis, may also mean that TKA is more likely to be performed later than in the general population (Leroux et al., 2014). And as the need for TKA continues to increase in youngers, ACL reconstruction has been found to increase the risk of reoperation for TKA due to the need to remove the implant (Leroux et al., 2014; Watters et al., 2017). This suggests that ACL reconstruction combined with UKA treatment may also have long-term risks. In contrast, resection of the ACL has been found to have no impact on clinical outcomes such as maximum knee extension or overall limb alignment for TKA surgery (Hoogeslag et al., 2019). The scope of applicability of UKA needs to be further evaluated. Past studies have shown a clear association between ACL defects and failure of UKA surgery, which may be due to aseptic loosening of the tibial prosthesis in the early postoperative period (Goodfellow et al., 1988; Kozinn and Scott, 1989). Additionally, clinical studies have shown an increased failure rate of both fixed-axis and mobile-axis UKA procedures for ACL defects (Deschamps and Lapeyre, 1987; Goodfellow et al., 1988). Therefore, ACL defects or injuries have been considered a contraindication to UKA. However, given the advantages of UKA over TKA surgery, such as more bone reserves, less surgical injury, and faster recovery, patients with ACL defects still take this procedure (Price et al., 2001). In 2004, a study suggested that UKA was indicated in the absence of a history of knee instability in the setting of ACL deficiency (Engh and Ammeen, 2004). This view was supported by a clinical study in 2014 (Engh and Ammeen, 2014). A retrospective study highlighted that ACL deficiency was not a contraindication to UKA and that fixed-axis lateral UKA had been successful in patients with ACL deficiency (Plancher et al., 2014). A study in 2019 showed no significant differences in kinetic and kinematic outcomes between conventional UKA and ACL-deficient UKA (Suter et al., 2019). Notably, several post-UKA follow-up surveys have shown no significant difference in mean 3- or 5-years follow-up prosthesis survival rates between patients with ACL defects and those with intact ACLs (Boissonneault et al., 2013; Engh and Ammeen, 2014; Kikuchi et al., 2021). Recent studies have revealed no difference in postoperative revision and functional scores between ACL-deficient and intact patients undergoing UKA (Kikuchi et al., 2021; Plancher et al., 2021). This suggests that ACL defects may not be related to the loosening of the prosthesis after UKA surgery and that the suitability of ACL-deficient patients for UKA treatment remains controversial.

This study will perform a meta-analysis and systematic review of the impact of ACL defects and ACL integrity on clinical outcomes such as postoperative revision, Tegner activity score and OKS in patients. This study will explore whether ACL defects are contraindication to UKA, which will inform clinicians' choice of surgical approach in the case of patients with ACL defects from an evidence-based medicine perspective.

Methods

Results are reported using Preferred Reporting Items for Systematic Reviews and Meta-Analyses 2020 (PRISMA 2020) (Page et al., 2021).

Search strategy

A systematic search of PubMed, Embase, and the Cochrane Library was conducted up to 12/09/2021. All medical subject headings and corresponding free texts were taken from the "Mesh Database". Published research on other related topics was used to ensure the comprehensiveness and rationality of the terms used. The medical subject heading terms were used including "Anterior Cruciate Ligament" "Anterior Cruciate Ligament Injuries" "Arthroplasty, Replacement, Knee". In addition, the reference lists of retrieved papers and reviews related to the impact of ACL status on UKA were screened to try to avoid possible omissions. Corresponding authors were not contacted for additional data. There were no language restrictions for the literature search (Supplementary Appendix S1).

Study selection

Each of the 2 authors independently screened the articles and cross-checked the finalized ones. In case of disagreement on the inclusion and exclusion of a few articles, a third author made the final decision. In the first stage, we screened titles, and then in the second stage, we performed the abstract and full-text screening. Studies meeting the following criteria were included: (Glyn-Jones et al., 2015): study design: retrospective observational studies; (Bijlsma et al., 2011); participants: patients who underwent UKA surgery, with and those without ACL defects, mainly including fragile and broken ACL, tears, non-functionality, complete absence and synovial damage; (Braun and Gold, 2012); Outcomes: Postoperative revision due to prosthetic loosening, imaging findings of transilluminated bands, and wear of the lateral osteoarthrosis, Tegner activity score, and OKS, for which odds ratio (OR) or standard mean difference (SMD), and the corresponding 95% confidence intervals (CIs) were provided as the effect measures. Studies that did not compare ACL deficiencies with complete studies, non-original articles such as reviews, duplicate cohorts, and studies that did not report primary outcomes were excluded.

Data extraction and quality assessment

Two authors independently extracted the following information from each study: 1) study characteristics, authors, year of publication, and study design; 2) study population characteristics, such as total number of knees with UKA, age, and sex ratio of participants in each group; 3) intervention characteristics, such as definition of ACL deficits; 4) clinical outcomes such as postoperative revision, Tegner activity score, and OKS and their mean follow-up time. The final decision on disagreement was made by a third senior author. Quality scores were derived by applying the Newcastle Ottawa Scale. A score of less than or equal to 7 is considered a low risk of bias (Supplementary Appendix Table S3).

Statistical analysis

The primary outcome analyzed was postoperative revision, defined as conversion from UKA to TKA or otherwise. Secondary outcomes included Tegner activity score and OKS. we extracted adjusted effect estimates. During continuous data extraction, some studies were reported as medians, which we converted to mean and standard deviation form by arithmetic (Wan et al., 2014; Luo et al., 2018). Stata software (15.1 version) was used to perform the data analysis. Meta-analysis of outcomes reported by three or more studies was performed by using a random effects model. Binary variables were reported with odds ratio (OR) and continuous variables were reported with standard mean difference (SMD). We applied an algorithm to combine SMDs for multiple ACL deficiency-related subgroups (Cumpston et al., 2019). ORs converted to logs were combined using the generalized inverse variance method and random effects models and effect estimates and their 95% confidence intervals are reported. I^2 values above 50% indicate significant heterogeneity (Higgins et al., 2003). Begg's test was not performed because the number of included studies was less than 10.

Results

Search results

The search yielded a total of 1748 articles. After excluding 1734 articles, the remaining 14 articles were evaluated for

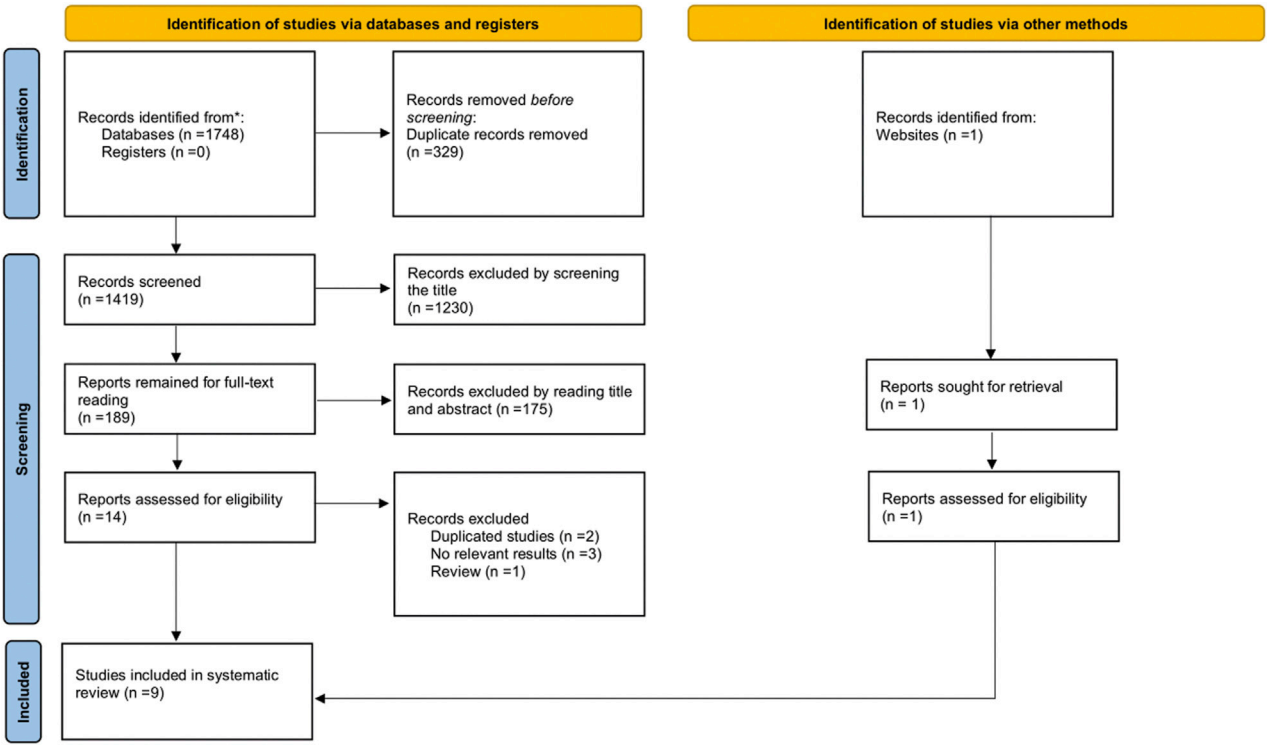

FIGURE 1
Flowchart of study selection based on PRISMA guidelines.

eligibility. In addition, a keyword search on Google Scholar was conducted to obtain 1 eligible paper. We excluded one review, two duplicate cohort studies, and three studies that did not report a relevant outcome. Ultimately, we included nine studies (Hernigou and Deschamps, 2004a; Gulati et al., 2009; Boissonneault et al., 2013; Engh and Ammeen, 2014; Hamilton et al., 2016; Pegg et al., 2016; Liu et al., 2020; Kikuchi et al., 2021; Plancher et al., 2022). The search and screening process is detailed in the PRISMA flow diagram (Figure 1).

Study characteristics

The nine included studies were all retrospective cohort studies two studies were conducted before 2010. The included studies were carried out in five countries across the three continents, including United States, the United Kingdom, France, China, and Japan. In these studies, one study did not report the gender proportion of participants, two studies had less than 50% female participants, and one study had more than 70% female participants. in reporting about UKA, three studies were conducted with less than 100 UKAs. Regarding the definition of ACL defect, one study did not report the definition of ACL, and one study found ACL defects in the post operative period. In terms of results reporting, eight studies reported outcomes related to postoperative revision, five studies reported Tegner activity scores, and four studies reported OKS. About Follow-up time, The mean follow-up time for the primary outcome of the studies was less than 10 years (Supplementary Tables S1, S2). In addition, all included studies were considered to be at low risk of bias based on NOS scores (Supplementary Appendix Table S3).

Analysis of outcome measures

Postoperative Revision (Hernigou and Deschamps, 2004a; Gulati et al., 2009; Boissonneault et al., 2013; Engh and Ammeen, 2014; Hamilton et al., 2016; Liu et al., 2020; Kikuchi et al., 2021; Plancher et al., 2022) was defined as having undergone a second surgery due to implant loosening or surgical failure. Outcomes associated with postoperative revision were reported in one article, of which two reported loosening of the implant, one reported postoperative posterolateral joint wear status, and six reported postoperative revision. There was no statistical difference in postoperative revision rates between intact and

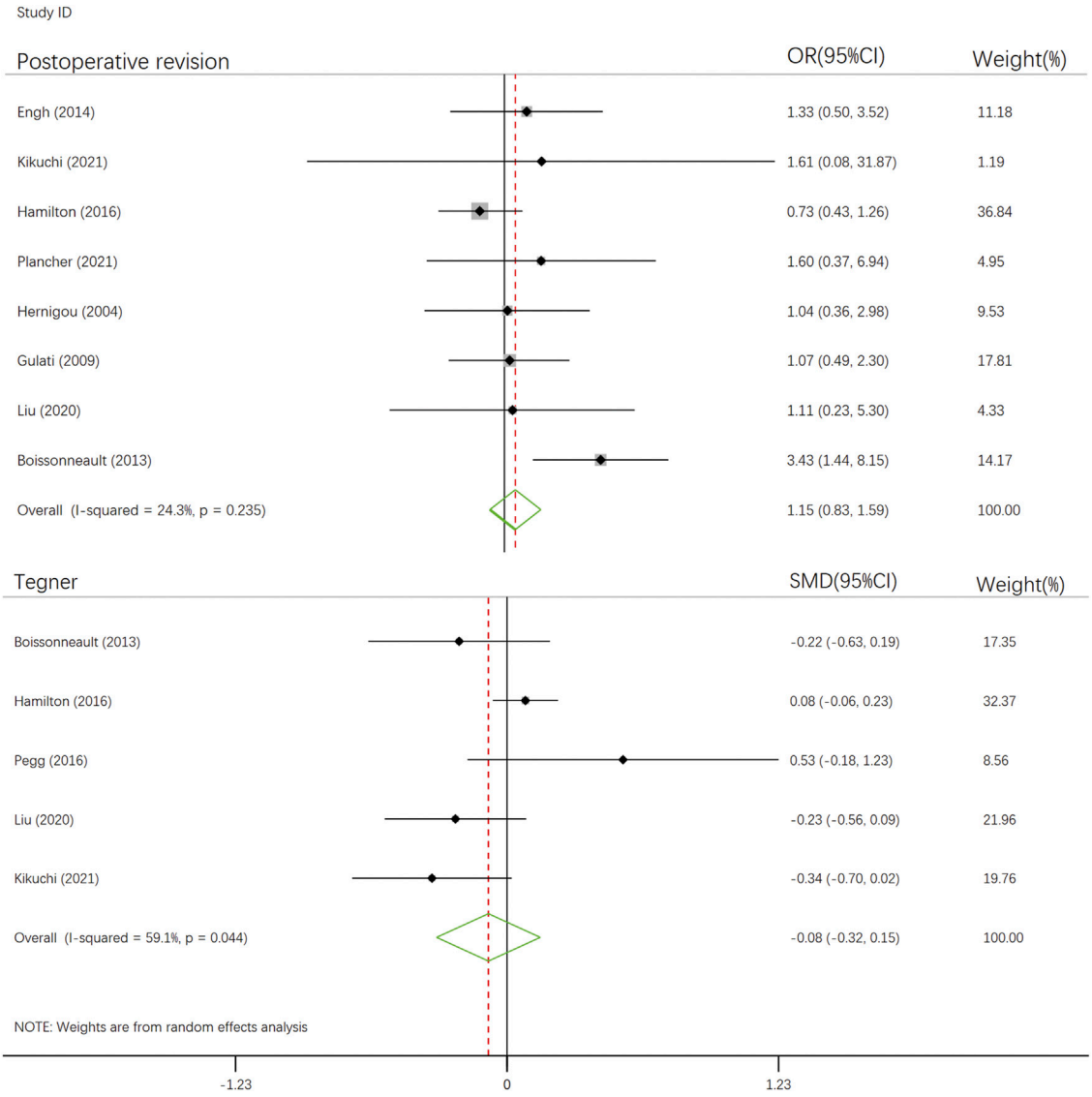

FIGURE 2
The forest plot for relationship between anterior cruciate ligament defect and postoperative outcomes after UKA.

defective ACLs (OR, 1.15; 95% CI, 0.83–1.59; *p*-value, 0.235). Sensitivity analysis showed stability of this combined result by excluding studies before 2010 (OR, 1.19; 95% CI, 0.81–1.74; *p*-value, 0.101), two Asian studies (OR, 1.15; 95% CI, 0.82–1.60; *p*-value, 0.101), studies with less than 50% and more than 70% of women (OR, 0.94; 95% CI, 0.65–1.37; *p*-value, 0.737), studies with less than 100 UKAs (OR, 0.95; 95% CI, 0.65–1.38; *p*-value, 0.833), studies with age of participants more than 70 years old (OR, 1.16; 95% CI, 0.82–1.63; *p*-value, 0.407) and studies with follow-up less than 5 years (OR, 0.92; 95% CI, 0.61–1.39; *p*-value, 0.737). (Figure 2 and Supplementary Appendix Table S2).

Tegner activity score (Boissonneault et al., 2013; Hamilton et al., 2016; Pegg et al., 2016; Liu et al., 2020; Kikuchi et al., 2021) is a numerical scale (ranging from 0 to 10) used to assess work and physical activity levels (Tegner and Lysholm, 1985). Five articles reported on the Tegner activity score. According to the delineation and interpretation of SMD outcome indicators by Patrick Schober et al. (Andrade, 2020; Schober et al., 2021), there was no statistical difference in the postoperative follow-up Tegner activity score between ACL-intact and ACL-deficient group (SMD, -0.084; 95% CI, -0.320–0.151; *p*-value, 0.482). After excluding studies from Asia (SMD, 0.056; 95% CI, -0.222–0.334; *p*-value, 0.692), studies with lower 50 and higher 70 percentages of women (SMD, -0.042, 95% CI, -0.346–0.262; *p*-value, 0.786), studies with lower numbers of 100 UKAs (SMD, -0.127; 95% CI, -0.412–0.158; *p*-value, 0.382) and studies with

follow-up longer than 10 years (SMD, -0.175; 95% CI, -0.435–0.084, *p*-value, 0.185), the result remained stable.

OKS (Boissonneault et al., 2013; Hamilton et al., 2016; Pegg et al., 2016; Kikuchi et al., 2021) is a patient-reported questionnaire that measures pain and daily activities (ranging from 0 to 48 points) (Dawson et al., 1998). Four articles reported OKS. Because of the paucity of reports on OKS and the possibility that direct merging of the data may yield unconvincing outcomes, here we only performed a qualitative systematic review of the results of the four studies rather than a quantitative synthetic analysis. Of the four studies, only one showed a moderate difference (SMD, -0.47; 95% CI, -1.17–0.24), and no significant effect of ACL deficiency on patients' OKS scores after unicondylar knee arthroplasty was found in the remaining three studies. Considering the low sample size (2.38%) of the four studies included in this study combined, the confidence level of its findings is relatively low. The analysis of the above results shows that the defect of anterior cruciate ligament does not seem to be a risk factor for revision rate or functional recovery after UKA.

Discussion

Principal findings

This systematic review and meta-analysis showed that ACL defects and integrity do not affect the survival and functional scores of the prosthesis after UKA. This suggests that ACL defects are not a contraindication to UKA. The results of this study, which underwent systematic review of multiple outcome variables and Meta-analysis, showed no difference in postoperative revision rates, Tegner activity scores, and OKS between patients with ACL defects and intact patients undergoing UKA. The heterogeneity of the Meta-analysis results for postoperative revision (I^2 = 24.3%) was low, suggesting a reliable result. In contrast, the Meta-analysis results of the Tegner activity score had significant heterogeneity (I^2 = 59.1%), and the results need to be treated with caution. As for the OKS scores, only one of the included studies showed differences, but the results were not sufficiently convincing due to sample size limitations.

Potential mechanisms

Common reasons for postoperative revision of UKA include progression of osteoarthritis, aseptic loosening, and bearing dislocation (Mohammad et al., 2018). During UKA, avoiding overfill is considered the most important factor in preventing the progression of osteoarthritis (Heyse et al., 2016). Studies on cadaver legs have also demonstrated that the overfilling causes a series of kinematic changes that can make knee valgus more severe and even lead to high strains of the medial collateral ligament (Heyse et al., 2016; Heyse et al., 2017). While overcorrection of valgus has also been shown to result in narrowing of the lateral joint space, causing an increased risk of UKA revision (Hernigou and Deschamps, 2004b; Khamaisy et al., 2016). A meta-analysis showed that Asian patients had a higher rate of revision after UKA compared to Western patients for a higher frequency of both deep knee flexion and internal femoral flexion, making the knee environment more susceptible to soft tissue imbalance (Ro et al., 2018).

Aseptic loosening is thought to be caused by small movements between the implant surface and the bone, which leads to fibrous membrane formation, trabecular microdamage and bone marrow edema, usually indicated by the presence of radiolucent lines on imaging (Fritz et al., 2015; Kleeblad et al., 2018a). A prospective study showed that the use of pulsed lavage significantly reduced the incidence of aseptic loosening, possibly due to deeper penetration of the bone cement into the lavaged cancellous bone, enhancing the strength of the cement interface and reducing micromovements (Clarius et al., 2009). This was also confirmed by 3D analysis and CT scans of the cemented implant interface in the cadaveric UKA tibia (Schlegel et al., 2011; Jaeger et al., 2013). Mechanisms of bearing dislocation include deep knee flexion, injury, and turning during sleep, and these events usually occur suddenly and are difficult for patients to detect (Fujii et al., 2015; Kawaguchi et al., 2019). As with aseptic loosening, the rate of dislocation is higher in Asian patients than in Western patients (Kim et al., 2014; Ro et al., 2018). We found that in studies conducted in Asia, the majority of those who underwent revision were due to loosening of the implanted prosthesis, whereas in study populations in Europe and the United States, the majority of patients who underwent revision were due to progression of knee osteoarthritis or trauma of unknown origin, which is consistent with previous findings.

We found only 23% of female patients in a cohort that showed significant difference in revision rates (Boissonneault et al., 2013). Another study had an only 11.1% percentage of female patients, showed significant difference in revision rates, but the same results did not appear in the Tegner score (Pegg et al., 2016). In addition, a systematic review and a joint national registry of arthroplasty showed a higher rate of revision of UKA in younger, more active people (Liddle et al., 2014; Kleeblad et al., 2018b). High levels of activity increase the risk of implant loosening due to wear and tear and may negatively impact revision rates (Naal et al., 2007) (63). Differences in exercise levels between patients of different ages and genders may be related to the heterogeneity of postoperative revision rates in UKA.

Implications

Our meta-analysis provides an important reference for the choice of surgical approach for ACL-deficient patients with knee

osteoarthritis. In the case of ACL deficiency, clinicians will likely be faced with three options, first to perform a single UKA, second to perform simultaneous ACL reconstruction and UKA, and last to perform TKA. In the case of ACL deficiency, our and other studies have shown that UKA and simultaneous ACL reconstruction are appropriate for active young adults, while isolate UKA is a reasonable option for older patients with reduced mobility (Mancuso et al., 2016; Ventura et al., 2017). The use of this procedure is still limited to elderly patients without knee instability. While fixed-bearing UKA compensates for the anterior-posterior stability of a single UKA in patients with ACL defects, rotational stability remains a prerequisite for its use (Zumbrunn et al., 2020). Some systematic reviews have shown that ACL reconstruction and UKA in ACL-deficient patients with knee instability and isolated medial septal pain are also beneficial in improving postoperative function and clinical outcomes (Volpin et al., 2018; Albo et al., 2021; El-Husseini et al., 2021). Due to the lack of reliable data to guide clinicians, physicians can consider the appropriate surgical option to use depending on the patient's ACL injury, age and severity of knee osteoarthritis, etc.

Research gaps

Compared to current studies, high-quality data from randomized controlled trials comparing ACL deficits with UKA outcomes are still lacking. More studies are needed to develop the assessment of other outcomes or scoring indicators such as postoperative recovery, OKS and so on. There are still some shortcomings in this study, including the lack of outcome indicators and sample size, as well as not covering patients of all ages. In this study, the average age of all the people involved is over 60 years old, but the incidence of ACL injury is very high in the process of teenagers' sports, and the incidence of post traumatic arthritis (PTOA) is as high as 87% (Shelbourne and Stube, 1997), this also makes it impossible for this study to show whether ACL defects have an impact on young patients after single UKA. Besides, the long-term follow-up results of ACL reconstruction combined with UKA are still lacking (Tian et al., 2016; Legnani et al., 2021).

In future clinical research, we should recruit more patients, extend the follow-up time, define outcomes with more occurrences (including the use of compound outcomes), or combine the above methods to meet the sample size required to achieve the efficacy of the test. In addition, most of the studies included in this study were retrospective cohort studies with short-to medium-term follow-up, and longer follow-up or higher-level prospective studies are still needed to provide solid evidence-based medical evidence for the choice of clinical surgical modality. However, in future prospective studies, the problem of patients not wanting to undergo surgery or not wanting to risk conservative treatment may arise, which will cause some difficulties in the research (Smith et al., 2014).

Conclusion

This systematic review and meta-analysis yielded no difference in the primary clinical outcome such as postoperative revision, Tegner activity score and OKS in ACL-deficient and UKA-intact patients. Thus, it is advisable for UKA to be performed in elderly patients with ACL deficiency. This would further expand the applicability of UKA and facilitate the reduction of patient injury, cost, and improvement of their quality of life compared to TKA.

Data availability statement

The original contributions presented in the study are included in the article/Supplementary Material, further inquiries can be directed to the corresponding authors.

Author contributions

TW and CJ conceived and designed the experiments. TW performed the experiments. TW and HT contributed reagents/material/analysis tools. TW, HT, XG, and CJ wrote the manuscript. TW, PL, and WG performed reference collection and data management. HT, GF, and WG performed statistical analyses. TW, PL, and CJ revised the manuscript.

Conflict of interest

The authors declare that the research was conducted in the absence of any commercial or financial relationships that could be construed as a potential conflict of interest.

Publisher's note

Supplementary material

The Supplementary Material for this article can be found online at: https://www.frontiersin.org/articles/10.3389/fbioe.2022.890118/full#supplementary-material

References

Albo, E., Campi, S., Zampogna, B., Torre, G., Papalia, G. F., Diaz Balzani, L. A., et al. (2021). Results of simultaneous unicompartmental knee arthroplasty and anterior cruciate ligament reconstruction: A systematic review. *J. Clin. Med.* 10 (19), 4290. doi:10.3390/jcm10194290

Andrade, C. (2020). Mean difference, standardized mean difference (SMD), and their use in meta-analysis: As simple as it gets. *J. Clin. Psychiatry* 81 (5), 20f13681. doi:10.4088/jcp.20f13681

Bijlsma, J. W., Berenbaum, F., and Lafeber, F. P. (2011). Osteoarthritis: An update with relevance for clinical practice. *Lancet* 377 (9783), 2115–2126. doi:10.1016/s0140-6736(11)60243-2

Bliddal, H., and Christensen, R. (2009). The treatment and prevention of knee osteoarthritis: A tool for clinical decision-making. *Expert Opin. Pharmacother.* 10 (11), 1793–1804. doi:10.1517/14656560903018911

Boissonneault, A., Pandit, H., Pegg, E., Jenkins, C., Gill, H. S., Dodd, C. A., et al. (2013). No difference in survivorship after unicompartmental knee arthroplasty with or without an intact anterior cruciate ligament. *Knee Surg. Sports Traumatol. Arthrosc.* 21 (11), 2480–2486. doi:10.1007/s00167-012-2101-8

Braun, H. J., and Gold, G. E. (2012). Diagnosis of osteoarthritis: Imaging. *Bone* 51 (2), 278–288. doi:10.1016/j.bone.2011.11.019

Cinque, M. E., Dornan, G. J., Chahla, J., Moatshe, G., and LaPrade, R. F. (2018). High rates of osteoarthritis develop after anterior cruciate ligament surgery: An analysis of 4108 patients. *Am. J. Sports Med.* 46 (8), 2011–2019. doi:10.1177/0363546517730072

Clarius, M., Hauck, C., Seeger, J. B., James, A., Murray, D. W., and Aldinger, P. R. (2009). Pulsed lavage reduces the incidence of radiolucent lines under the tibial tray of oxford unicompartmental knee arthroplasty: Pulsed lavage versus syringe lavage. *Int. Orthop.* 33 (6), 1585–1590. doi:10.1007/s00264-009-0736-y

Cumpston, M., Li, T., Page, M. J., Chandler, J., Welch, V. A., Higgins, J. P., et al. (2019). Updated guidance for trusted systematic reviews: A new edition of the Cochrane handbook for systematic reviews of interventions. *Cochrane Database Syst. Rev.* 10, Ed000142. doi:10.1002/14651858.ed000142

Dawson, J., Fitzpatrick, R., Murray, D., and Carr, A. (1998). Questionnaire on the perceptions of patients about total knee replacement. *J. Bone Jt. Surg. Br. Vol* 80 (1), 63–69. doi:10.1302/0301-620x.80b1.0800063

Deschamps, G., and Lapeyre, B. (1987). Rupture of the anterior cruciate ligament: A frequently unrecognized cause of failure of unicompartmental knee prostheses. Apropos of a series of 79 Lotus prostheses with a follow-up of more than 5 years. *Rev. Chir. Orthop. Reparatrice Appar. Mot.* 73 (7), 544–551.

El-Husseini, T. F., Ahmed, M. A., and Sadek, Y. A. (2021). Outcomes of combined unicompartmental knee replacement and anterior cruciate ligament reconstruction: A systematic review. *QJM Int. J. Med.* 114 (1), hcab104.023. doi:10.1093/qjmed/hcab104.023

Engh, G. A., and Ammeen, D. (2004). Is an intact anterior cruciate ligament needed in order to have a well-functioning unicondylar knee replacement? *Clin. Orthop. Relat. Res.* (428), 170–173. doi:10.1097/01.blo.0000148895.78766.8a

Engh, G. A., and Ammeen, D. J. (2014). Unicondylar arthroplasty in knees with deficient anterior cruciate ligaments. *Clin. Orthop. Relat. Res.* 472 (1), 73–77. doi:10.1007/s11999-013-2982-y

Filbay, S. R., and Grindem, H. (2019). Evidence-based recommendations for the management of anterior cruciate ligament (ACL) rupture. *Best. Pract. Res. Clin. Rheumatol.* 33 (1), 33–47. doi:10.1016/j.berh.2019.01.018

Friel, N. A., and Chu, C. R. (2013). The role of ACL injury in the development of posttraumatic knee osteoarthritis. *Clin. Sports Med.* 32 (1), 1–12. doi:10.1016/j.csm.2012.08.017

Fritz, J., Lurie, B., and Potter, H. G. (2015). MR imaging of knee arthroplasty implants. *Radiographics* 35 (5), 1483–1501. doi:10.1148/rg.2015140216

Frobell, R. B., Roos, E. M., Roos, H. P., Ranstam, J., and Lohmander, L. S. (2010). A randomized trial of treatment for acute anterior cruciate ligament tears. *N. Engl. J. Med. Overseas. Ed.* 363 (4), 331–342. doi:10.1056/nejmoa0907797

Fujii, T., Matsui, Y., Noboru, M., Inagaki, Y., Kadoya, Y., and Tanaka, Y. (2015). Meniscal bearing dislocation of unicompartmental knee arthroplasty with faint symptom. *Case Rep. Orthop.* 2015, 1–5. doi:10.1155/2015/217842

Glyn-Jones, S., Palmer, A. J., Agricola, R., Price, A. J., Vincent, T. L., Weinans, H., et al. (2015). Osteoarthritis. *Lancet* 386 (9991), 376–387. doi:10.1016/S0140-6736(14)60802-3

Goldring, S. R., and Goldring, M. B. (2016). Changes in the osteochondral unit during osteoarthritis: Structure, function and cartilage-bone crosstalk. *Nat. Rev. Rheumatol.* 12 (11), 632–644. doi:10.1038/nrrheum.2016.148

Goodfellow, J. W., Kershaw, C. J., Benson, M. K., and O'Connor, J. J. (1988). The Oxford Knee for unicompartmental osteoarthritis. The first 103 cases. *J. Bone Jt. Surg. Br. Vol* 70 (5), 692–701. doi:10.1302/0301-620x.70b5.3192563

Gulati, A., Chau, R., Pandit, H. G., Gray, H., Price, A. J., Dodd, C. A., et al. (2009). The incidence of physiological radiolucency following Oxford unicompartmental knee replacement and its relationship to outcome. *J. Bone Jt. Surg. Br. Vol* 91 (7), 896–902. doi:10.1302/0301-620x.91b7.21914

Hamilton, T. W., Pistritto, C., Jenkins, C., Mellon, S. J., Dodd, C. A., Pandit, H. G., et al. (2016). Unicompartmental knee replacement: Does the macroscopic status of the anterior cruciate ligament affect outcome? *Knee* 23 (3), 506–510. doi:10.1016/j.knee.2016.01.013

Heidari, B. (2011). Knee osteoarthritis prevalence, risk factors, pathogenesis and features: Part I. *Casp. J. Intern. Med.* 2 (2), 205–212.

Hernigou, P., and Deschamps, G. (2004). Alignment influences wear in the knee after medial unicompartmental arthroplasty. *Clin. Orthop. Relat. Res.* 423, 161–165. doi:10.1097/01.blo.0000128285.90459.12

Hernigou, P., and Deschamps, G. (2004). Posterior slope of the tibial implant and the outcome of unicompartmental knee arthroplasty. *J. Bone Jt. Surg.* 86 (3), 506–511. doi:10.2106/00004623-200403000-00007

Heyse, T. J., El-Zayat, B. F., De Corte, R., Scheys, L., Chevalier, Y., Fuchs-Winkelmann, S., et al. (2016). Balancing UKA: Overstuffing leads to high medial collateral ligament strains. *Knee Surg. Sports Traumatol. Arthrosc.* 24 (10), 3218–3228. doi:10.1007/s00167-015-3848-5

Heyse, T. J., Slane, J., Peersman, G., Dworschak, P., Fuchs-Winkelmann, S., and Scheys, L. (2017). Balancing mobile-bearing unicondylar knee arthroplasty *in vitro*. *Knee Surg. Sports Traumatol. Arthrosc.* 25 (12), 3733–3740. doi:10.1007/s00167-016-4241-8

Higgins, J. P., Thompson, S. G., Deeks, J. J., and Altman, D. G. (2003). Measuring inconsistency in meta-analyses. *BMJ Clin. Res. ed).* 327 (7414), 557–560. doi:10.1136/bmj.327.7414.557

Hoogeslag, R. A. G., Brouwer, R. W., Boer, B. C., de Vries, A. J., and Huis in 't Veld, R. (2019). Acute anterior cruciate ligament rupture: Repair or reconstruction? Two-year results of a randomized controlled clinical trial. *Am. J. Sports Med.* 47 (3), 567–577. doi:10.1177/0363546519825878

Jaeger, S., Seeger, J. B., Schuld, C., Bitsch, R. G., and Clarius, M. (2013). Tibial cementing in UKA: A three-dimensional analysis of the bone cement implant interface and the effect of bone lavage. *J. Arthroplasty* 28 (9), 191–194. doi:10.1016/j.arth.2013.05.014

Kawaguchi, K., Inui, H., Taketomi, S., Yamagami, R., Kono, K., Nakazato, K., et al. (2019). Meniscal bearing dislocation while rolling over in sleep following Oxford medial unicompartmental knee arthroplasty. *Knee* 26 (1), 267–272. doi:10.1016/j.knee.2018.10.015

Khamaisy, S., Zuiderbaan, H. A., van der List, J. P., Nam, D., and Pearle, A. D. (2016). Medial unicompartmental knee arthroplasty improves congruence and restores joint space width of the lateral compartment. *Knee* 23 (3), 501–505. doi:10.1016/j.knee.2016.02.012

Kikuchi, K., Hiranaka, T., Kamenaga, T., Hida, Y., Fujishiro, T., and Okamoto, K. (2021). Anterior cruciate ligament deficiency is not always a contraindication for medial unicompartmental knee arthroplasty: A retrospective study in nondesigner's Japanese hospital. *J. Arthroplasty* 36 (2), 495–500. doi:10.1016/j.arth.2020.08.024

Kim, S. J., Postigo, R., Koo, S., and Kim, J. H. (2014). Causes of revision following Oxford phase 3 unicompartmental knee arthroplasty. *Knee Surg. Sports Traumatol. Arthrosc.* 22 (8), 1895–1901. doi:10.1007/s00167-013-2644-3

Kleeblad, L. J., van der List, J. P., Zuiderbaan, H. A., and Pearle, A. D. (2018). Larger range of motion and increased return to activity, but higher revision rates following unicompartmental versus total knee arthroplasty in patients under 65: A systematic review. *Knee Surg. Sports Traumatol. Arthrosc.* 26 (6), 1811–1822. doi:10.1007/s00167-017-4817-y

Kleeblad, L. J., Zuiderbaan, H. A., Burge, A. J., Amirtharaj, M. J., Potter, H. G., and Pearle, A. D. (2018). MRI findings at the bone-component interface in symptomatic unicompartmental knee arthroplasty and the relationship to radiographic findings. *HSS Jrnl.* 14 (3), 286–293. doi:10.1007/s11420-018-9629-1

Kozinn, S. C., and Scott, R. (1989). Unicondylar knee arthroplasty. *J. Bone Jt. Surg.* 71 (1), 145–150. doi:10.2106/00004623-198971010-00023

Larwa, J., Stoy, C., Chafetz, R. S., Boniello, M., and Franklin, C. (2021). Stiff landings, core stability, and dynamic knee valgus: A systematic review on documented anterior cruciate ligament ruptures in male and female athletes. *Int. J. Environ. Res. Public Health* 18 (7), 3826. doi:10.3390/ijerph18073826

Legnani, C., Muzzi, S., Peretti, G. M., Borgo, E., and Ventura, A. (2021). Anterior cruciate ligament reconstruction combined to partial knee replacement in active

patients with ACL deficiency and knee osteoarthritis. *Phys. Sportsmed.* 49 (1), 12–17. doi:10.1080/00913847.2020.1795558

Leroux, T., Ogilvie-Harris, D., Dwyer, T., Chahal, J., Gandhi, R., Mahomed, N., et al. (2014). The risk of knee arthroplasty following cruciate ligament reconstruction: A population-based matched cohort study. *J. Bone Jt. Surg.* 96 (1), 2–10. doi:10.2106/jbjs.m.00393

Liddle, A. D., Judge, A., Pandit, H., and Murray, D. W. (2014). Adverse outcomes after total and unicompartmental knee replacement in 101, 330 matched patients: A study of data from the national joint registry for england and wales. *Lancet* 384 (9952), 1437–1445. doi:10.1016/s0140-6736(14)60419-0

Liu, S., Zhou, G., Chen, X., Xiao, K., Cai, J., and Liu, X. (2020). Influence of anterior cruciate ligament defect on the mid-term outcome of fixed-bearing unicompartmental knee arthroplasty. *Chin. J. Tissue Eng. Res.* 25 (6), 860–865.

Louboutin, H., Debarge, R., Richou, J., Selmi, T. A., Donell, S. T., Neyret, P., et al. (2009). Osteoarthritis in patients with anterior cruciate ligament rupture: A review of risk factors. *Knee* 16 (4), 239–244. doi:10.1016/j.knee.2008.11.004

Luo, D., Wan, X., Liu, J., and Tong, T. (2018). Optimally estimating the sample mean from the sample size, median, mid-range, and/or mid-quartile range. *Stat. Methods Med. Res.* 27 (6), 1785–1805. doi:10.1177/0962280216669183

Mancuso, F., Dodd, C. A., Murray, D. W., and Pandit, H. (2016). Medial unicompartmental knee arthroplasty in the ACL-deficient knee. *J. Orthop. Traumatol.* 17 (3), 267–275. doi:10.1007/s10195-016-0402-2

Mohammad, H. R., Strickland, L., Hamilton, T. W., and Murray, D. W. (2018). Long-term outcomes of over 8, 000 medial oxford phase 3 unicompartmental knees-a systematic review. *Acta Orthop.* 89 (1), 101–107. doi:10.1080/17453674.2017.1367577

Murray, D. W., and Parkinson, R. W. (2018). Usage of unicompartmental knee arthroplasty. *bone & Jt. J.* 100-b (4), 432–435. doi:10.1302/0301-620x.100b4.bjj-2017-0716.r1

Naal, F. D., Fischer, M., Preuss, A., Goldhahn, J., von Knoch, F., Preiss, S., et al. (2007). Return to sports and recreational activity after unicompartmental knee arthroplasty. *Am. J. Sports Med.* 35 (10), 1688–1695. doi:10.1177/0363546507303562

Page, M. J., Moher, D., Bossuyt, P. M., Boutron, I., Hoffmann, T. C., Mulrow, C. D., et al. (2021). PRISMA 2020 explanation and elaboration: Updated guidance and exemplars for reporting systematic reviews. *BMJ Clin. Res. ed)* 372, n160. doi:10.1136/bmj.n160

Pegg, E. C., Mancuso, F., Alinejad, M., van Duren, B. H., O'Connor, J. J., Murray, D. W., et al. (2016). Sagittal kinematics of mobile unicompartmental knee replacement in anterior cruciate ligament deficient knees. *Clin. Biomech. (Bristol, Avon.* 31, 33–39. doi:10.1016/j.clinbiomech.2015.10.004

Plancher, K. D., Briggs, K. K., Brite, J. E., and Petterson, S. C. (2022). The lawrence D. Dorr surgical techniques & technologies award: Patient Acceptable symptom state. *J. Arthroplasty* 37 (8), S710-S715. doi:10.1016/j.arth.2022.01.081

Plancher, K. D., Brite, J. E., Briggs, K. K., and Petterson, S. C. (2021). Patient-acceptable symptom state for reporting outcomes following unicompartmental knee arthroplasty : A matched pair analysis comparing UKA in ACL-deficient versus ACL-intact knees. *bone & Jt. J.* 103-b (8), 1367–1372. doi:10.1302/0301-620x.103b8.bjj-2021-0170.r1

Plancher, K. D., Dunn, A. S., and Petterson, S. C. (2014). The anterior cruciate ligament-deficient knee and unicompartmental arthritis. *Clin. Sports Med.* 33 (1), 43–55. doi:10.1016/j.csm.2013.08.006

Price, A. J., Webb, J., Topf, H., Dodd, C. A., Goodfellow, J. W., and Murray, D. W. (2001). Rapid recovery after oxford unicompartmental arthroplasty through a short incision. *J. Arthroplasty* 16 (8), 970–976. doi:10.1054/arth.2001.25552

Ro, K. H., Heo, J. W., and Lee, D. H. (2018). Bearing dislocation and progression of osteoarthritis after mobile-bearing unicompartmental knee arthroplasty vary between asian and western patients: A meta-analysis. *Clin. Orthop. Relat. Res.* 476 (5), 946–960. doi:10.1007/s11999.0000000000000205

Schlegel, U. J., Siewe, J., Delank, K. S., Eysel, P., Puschel, K., Morlock, M. M., et al. (2011). Pulsed lavage improves fixation strength of cemented tibial components. *Int. Orthop.* 35 (8), 1165–1169. doi:10.1007/s00264-010-1137-y

Schober, P., Mascha, E. J., and Vetter, T. R. (2021). Statistics from A (agreement) to Z (z score): A guide to interpreting common measures of association, agreement, diagnostic accuracy, effect size, heterogeneity, and reliability in medical research. *Anesth. Analg.* 133 (6), 1633–1641. doi:10.1213/ane.0000000000005773

Shelbourne, K. D., and Stube, K. C. (1997). Anterior cruciate ligament (ACL)-deficient knee with degenerative arthrosis: Treatment with an isolated autogenous patellar tendon ACL reconstruction. *Knee Surg. Sports Traumatol. Arthrosc.* 5 (3), 150–156. doi:10.1007/s001670050043

Smith, T. O., Postle, K., Penny, F., McNamara, I., and Mann, C. J. (2014). Is reconstruction the best management strategy for anterior cruciate ligament rupture? A systematic review and meta-analysis comparing anterior cruciate ligament reconstruction versus non-operative treatment. *Knee* 21 (2), 462–470. doi:10.1016/j.knee.2013.10.009

Suter, L., Roth, A., Angst, M., von Knoch, F., Preiss, S., List, R., et al. (2019). Is ACL deficiency always a contraindication for medial UKA? Kinematic and kinetic analysis of implanted and contralateral knees. *Gait posture* 68, 244–251. doi:10.1016/j.gaitpost.2018.11.031

Tecame, A., Savica, R., Rosa, M. A., and Adravanti, P. (2019). Anterior cruciate ligament reconstruction in association with medial unicompartmental knee replacement: A retrospective study comparing clinical and radiological outcomes of two different implant design. *Int. Orthop.* 43 (12), 2731–2737. doi:10.1007/s00264-019-04341-x

Tegner, Y., and Lysholm, J. (1985). Rating systems in the evaluation of knee ligament injuries. *Clin. Orthop. Relat. Res.* 198, 42–49. doi:10.1097/00003086-198509000-00007

Tian, S., Wang, B., Wang, Y., Ha, C., Liu, L., and Sun, K. (2016). Combined unicompartmental knee arthroplasty and anterior cruciate ligament reconstruction in knees with osteoarthritis and deficient anterior cruciate ligament. *BMC Musculoskelet. Disord.* 17, 327. doi:10.1186/s12891-016-1186-5

Ventura, A., Legnani, C., Terzaghi, C., Iori, S., and Borgo, E. (2017). Medial unicondylar knee arthroplasty combined to anterior cruciate ligament reconstruction. *Knee Surg. Sports Traumatol. Arthrosc.* 25 (3), 675–680. doi:10.1007/s00167-015-3808-0

Volpin, A., Kini, S. G., and Meuffels, D. E. (2018). Satisfactory outcomes following combined unicompartmental knee replacement and anterior cruciate ligament reconstruction. *Knee Surg. Sports Traumatol. Arthrosc.* 26 (9), 2594–2601. doi:10.1007/s00167-017-4536-4

Wan, X., Wang, W., Liu, J., and Tong, T. (2014). Estimating the sample mean and standard deviation from the sample size, median, range and/or interquartile range. *BMC Med. Res. Methodol.* 14, 135. doi:10.1186/1471-2288-14-135

Watters, T. S., Zhen, Y., Martin, J. R., Levy, D. L., Jennings, J. M., and Dennis, D. A. (2017). Total knee arthroplasty after anterior cruciate ligament reconstruction: Not just a routine primary arthroplasty. *J. Bone Jt. Surg.* 99 (3), 185–189. doi:10.2106/jbjs.16.00524

Wilson, H. A., Middleton, R., Abram, S. G. F., Smith, S., Alvand, A., Jackson, W. F., et al. (2019). Patient relevant outcomes of unicompartmental versus total knee replacement: Systematic review and meta-analysis. *BMJ* 364, l352. doi:10.1136/bmj.l352

Zumbrunn, T., Schütz, P., von Knoch, F., Preiss, S., List, R., and Ferguson, S. J. (2020). Medial unicompartmental knee arthroplasty in ACL-deficient knees is a viable treatment option: *In vivo* kinematic evaluation using a moving fluoroscope. *Knee Surg. Sports Traumatol. Arthrosc.* 28 (6), 1765–1773. doi:10.1007/s00167-019-05594-0

frontiers | Frontiers in Bioengineering and Biotechnology

TYPE Original Research
PUBLISHED 28 September 2022
DOI 10.3389/fbioe.2022.855870

OPEN ACCESS

EDITED BY
Ching-Chi Hsu,
National Taiwan University of Science and Technology, Taiwan

REVIEWED BY
Mariska Wesseling,
Delft University of Technology, Netherlands
Wenxin Niu,
Tongji University, China

*CORRESPONDENCE
Benjamin J. Fregly,
fregly@rice.edu

SPECIALTY SECTION
This article was submitted to Biomechanics, a section of the journal Frontiers in Bioengineering and Biotechnology

RECEIVED 16 January 2022
ACCEPTED 01 September 2022
PUBLISHED 28 September 2022

CITATION
Vega MM, Li G, Shourijeh MS, Ao D, Weinschenk RC, Patten C, Font-Llagunes JM, Lewis VO and Fregly BJ (2022), Computational evaluation of psoas muscle influence on walking function following internal hemipelvectomy with reconstruction. *Front. Bioeng. Biotechnol.* 10:855870. doi: 10.3389/fbioe.2022.855870

Computational evaluation of psoas muscle influence on walking function following internal hemipelvectomy with reconstruction

Marleny M. Vega[1], Geng Li[1], Mohammad S. Shourijeh[1], Di Ao[1], Robert C. Weinschenk[2], Carolynn Patten[3,4,5], Josep M. Font-Llagunes[6,7], Valerae O. Lewis[8] and Benjamin J. Fregly[1]*

[1]Rice Computational Neuromechanics Lab, Department of Mechanical Engineering, Rice University, Houston, TX, United States, [2]Department of Orthopaedic Surgery, University of Texas Southwestern Medical Center, Dallas, TX, United States, [3]Biomechanics, Rehabilitation, and Integrative Neuroscience (BRaIN) Lab, UC Davis School of Medicine, Sacramento, CA, United States, [4]UC Davis Center for Neuroengineering and Medicine, University of California, Davis, CA, United States, [5]VA Northern California Health Care System, Martinez, CA, United States, [6]Biomechanical Engineering Lab, Department of Mechanical Engineering and Research Centre for Biomedical Engineering, Universitat Politècnica de Catalunya, Barcelona, Spain, [7]Health Technologies and Innovation, Institut de Recerca Sant Joan de Déu, Esplugues de Llobregat, Spain, [8]Department of Orthopaedic Oncology, University of Texas MD Anderson Cancer Center, Houston, TX, United States

An emerging option for internal hemipelvectomy surgery is custom prosthesis reconstruction. This option typically recapitulates the resected pelvic bony anatomy with the goal of maximizing post-surgery walking function while minimizing recovery time. However, the current custom prosthesis design process does not account for the patient's post-surgery prosthesis and bone loading patterns, nor can it predict how different surgical or rehabilitation decisions (e.g., retention or removal of the psoas muscle, strengthening the psoas) will affect prosthesis durability and post-surgery walking function. These factors may contribute to the high observed failure rate for custom pelvic prostheses, discouraging orthopedic oncologists from pursuing this valuable treatment option. One possibility for addressing this problem is to simulate the complex interaction between surgical and rehabilitation decisions, post-surgery walking function, and custom pelvic prosthesis design using patient-specific neuromusculoskeletal models. As a first step toward developing this capability, this study used a personalized neuromusculoskeletal model and direct collocation optimal control to predict the impact of ipsilateral psoas muscle strength on walking function following internal hemipelvectomy with custom prosthesis reconstruction. The influence of the psoas muscle was targeted since retention of this important muscle can be surgically demanding for certain tumors, requiring additional time in the operating room. The post-surgery walking predictions emulated the most common surgical scenario encountered at MD Anderson Cancer Center in Houston. Simulated post-surgery psoas strengths included 0% (removed), 50% (weakened), 100% (maintained), and 150% (strengthened) of the pre-surgery

value. However, only the 100% and 150% cases successfully converged to a complete gait cycle. When post-surgery psoas strength was maintained, clinical gait features were predicted, including increased stance width, decreased stride length, and increased lumbar bending towards the operated side. Furthermore, when post-surgery psoas strength was increased, stance width and stride length returned to pre-surgery values. These results suggest that retention and strengthening of the psoas muscle on the operated side may be important for maximizing post-surgery walking function. If future studies can validate this computational approach using post-surgery experimental walking data, the approach may eventually influence surgical, rehabilitation, and custom prosthesis design decisions to meet the unique clinical needs of pelvic sarcoma patients.

KEYWORDS

orthopedic biomechanics, neuromusculoskeletal modeling, computational modeling, predictive simulation, treatment optimization, optimal control, pelvic sarcoma, internal hemipelvectomy surgery

Introduction

Over the past few decades, surgical treatment of pelvic sarcomas has improved considerably with limb-preserving internal hemipelvectomy frequently being possible in place of limb-sacrificing external hemipelvectomy to achieve local control of cancerous tumors (Aljassir et al., 2005). When limb salvage is possible, the orthopedic oncologist must choose between three surgical options: 1) no reconstruction, 2) allograft reconstruction, or more recently, 3) custom prosthesis reconstruction (Figure 1). For all three options, when the hip joint and numerous muscles are removed to achieve clear margins around the tumor, restoration of normal ambulatory function can be challenging. Even when the hip joint must be sacrificed, patients who receive no reconstruction typically ambulate well post-surgery and benefit from a reduced complication rate compared to the other two options (Gupta et al., 2020). However, the recovery time is on the order of 6 months, and the resulting leg-length discrepancy is uncomfortable, requires a shoe lift, and often results in scoliosis due to altered gait mechanics. Patients who receive allograft reconstruction with total hip replacement typically achieve a post-surgery ambulatory function that is closer to normal since leg shortening and medialization are avoided. However, the recovery time is on the order of a year or more, and there is a high risk of complications and additional surgery due to the relatively short lifespan of the alloprosthesis (Beadel et al., 2005). The goals of custom prosthesis reconstruction with a total hip replacement are to maximize post-surgery ambulatory function and minimize recovery time. Though custom prosthesis reconstruction has the best clinical potential, the design of durable custom prostheses remains challenging, with a three-year survival rate of less than 70% (Sun et al., 2011).

Based on the potential benefits of custom prosthesis reconstruction, orthopedic implant companies and academic researchers have started to design and implant custom pelvic prostheses that include a total hip replacement (Hilton et al., 2017; Dion et al., 2018; Bai et al., 2019; Babazadeh Naseri et al.,

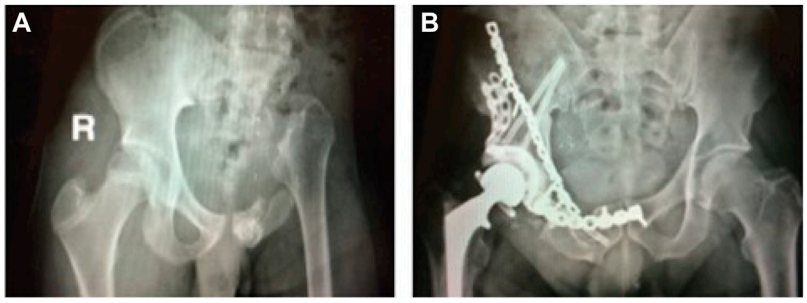

FIGURE 1
(A) Sample x-ray image of a pelvic cancer patient who received internal hemipelvectomy surgery with no reconstruction. **(B)** Sample x-ray image of a pelvic cancer patient who received internal hemipelvectomy surgery with allograph reconstruction and a total hip replacement. Images courtesy of Dr. Valerae Lewis, MD Anderson Cancer Center patient education DVD.

2021). Custom pelvic prostheses are designed using patient-specific three-dimensional pelvis geometric models developed from a CT scan of the patient's pelvis (Chen et al., 2020). Since the shape of the custom prosthesis normally recapitulates the removed bony anatomy, an implicit design assumption is that mimicking the original anatomy will produce the best post-surgery ambulatory function. However, anatomic reconstruction may not produce the best post-surgery function in other areas of the body when numerous muscles are injured or removed. For example, a reverse shoulder prosthesis switches the ball and shallow socket between the humerus and scapula to improve mechanical stability by accounting for missing or impaired rotator cuff muscles (Gutiérrez et al., 2007). Thus, it is possible that a non-anatomic custom pelvic prosthesis design could achieve better functional outcomes than current anatomic designs. Regardless, the current custom prosthesis design process does not account for the post-surgery loading patterns that the prosthesis and remaining bone will experience, which could help explain why prosthesis durability is not as high as desired. Furthermore, the current design process provides no means for predicting how different surgical or rehabilitation decisions (e.g., retention or removal of the psoas muscle, strengthening the psoas if retained) will affect the patient's post-surgery ambulatory function.

One option for predicting the complex interaction between custom pelvic prosthesis design, internal hemipelvectomy surgical decisions, post-surgery muscle and hip contact forces, and post-surgery ambulatory function is to use patient-specific neuromusculoskeletal models. In recent years, such models have been used to predict various gait impairments due to stroke (Meyer et al., 2016; Sauder et al., 2019), weakened muscles (Falisse et al., 2019), cerebral palsy (Falisse et al., 2020), and knee osteoarthritis (Fregly et al., 2007). Fregly et al. (2007) predicted a personalized gait modification that minimized an external indicator of medial knee contact force for an individual with medial knee osteoarthritis. The study predicted that subtle gait modifications could reduce the external indicator by an amount comparable to high tibial osteotomy surgery. For an individual post-stroke, Meyer et al. (2016) predicted how the subject would walk at his fastest comfortable speed in excellent agreement with experimental measurements. Sauder et al. (2019) predicted a personalized fast functional electrical stimulation (FastFES) training prescription for an individual post-stroke to improve propulsive force symmetry. The study predicted that optimal muscle selection and stimulation timing could produce a 23% improvement in propulsive force symmetry compared to the standard FastFES prescription. Falisse et al. (2019) predicted various clinical gait deficiencies caused by muscle strength deficits and a lower limb prosthesis that reproduced experimentally observed walking mechanics and energetics. Falisse et al. (2020) also predicted the walking function of a child with cerebral palsy. The study found that the crouch gait pattern observed experimentally was primarily due to altered muscle-tendon properties rather than spasticity or reduced complexity in neuromuscular control. Despite growing predictive simulation capabilities, only a few studies have used them to optimize surgical or rehabilitation treatment decisions (Fregly et al., 2007; Falisse et al., 2019; Pitto et al., 2019; Sauder et al., 2019), and none have explored computational treatment design for individuals receiving internal hemipelvectomy surgery with custom prosthesis reconstruction.

As a first step toward developing such capabilities for internal hemipelvectomy surgery, this study used predictive walking simulations to investigate the effect of post-surgery psoas strength on walking function when custom prosthesis reconstruction is chosen. The simulated surgery mimicked the most common surgical decisions made at MD Anderson Cancer Center in Houston, Texas, under the assumption that the custom prosthesis with total hip replacement was designed to recapitulate the missing pelvic bony anatomy. The computer simulations used a personalized neuromusculoskeletal model of a healthy subject to which the most common surgical decisions were applied. These decisions dictated which lower back and hip muscles were retained and which were removed from the model. To investigate the impact of the operated side psoas muscle on post-surgery walking function, we changed the strength of the psoas from 0% (removed) to 50% (weakened), 100% (pre-surgery), and 150% (strengthened) of its pre-surgery strength. We quantified the impact of the psoas on walking function by calculating stride length, stride time, stance width, spatial symmetry, temporal symmetry, cost of transport, and metabolic cost, along with gait kinematics and kinetics, for all post-surgery walking predictions. The predictive walking simulations provide insight into the potential importance of retaining the psoas muscle for improving post-surgery walking function.

Methods

Experimental data collection

Experimental walking data collected previously from a healthy male subject (age 47 years, height 1.7 m, mass 66.7 kg) were used for this study. Data collection was approved by the University of Florida Institutional Review Board, and the subject gave informed consent. Full body marker-based motion capture, ground reaction, and surface and fine-wire electromyographic (EMG) (Table 1, 26 channels from the right leg only) data were collected simultaneously at different walking speeds using a split-belt instrumented treadmill with belts tied. Walking speeds ranged from 1.0 m/s (slower than self-selected) to 1.4 m/s (self-selected) in increments of 0.1 m/s. A highly symmetric representative walking cycle (defined as heel strike to heel strike of the right foot) collected at self-selected speed was chosen for subsequent analysis. Additional experimental data were collected for static

TABLE 1 Right leg muscles from which surface or fine-wire (*) EMG data were collected.

*Adductor longus
Adductor magnus
Gluteus maximus lateralis
Gluteus maximus medius
Gluteus medius
*Sartorius
Semimembranosus
Semitendinosus
Biceps femoris long head
Rectus femoris
Tensor fascia latae
Gracilis
*Biceps femoris short head
Vastus lateralis
Vastus medialis
*Vastus intermedius
Gastrocnemius medialis
Gastrocnemius lateralis
Tibialis anterior
*Tibialis posterior
*Extensor hallucis longus
*Flexor hallucis longus
Peroneus longus
Soleus
*Extensor digitorum longus
*Flexor digitorum longus

standing and isolated lower body joint motion trials. The static standing trial was collected for model scaling purposes. Isolated joint motion trials were collected for each knee and ankle to personalize the model's lower body joint axes. All functional axes for the joint of interest were exercised during each isolated joint motion trial (Reinbolt et al., 2005, 2008). Pre-existing CT scan data from the subject's pelvis were also obtained to personalize the pelvis geometry and both hip joints of the scaled generic musculoskeletal model.

Experimental movement data were filtered using published methods. Ground reaction and marker motion data were low-pass filtered using a fourth-order zero-phase lag Butterworth filter with a cut-off frequency of $7/t_f$ Hz (Hug, 2011), where t_f is the period of the gait cycle being processed (Meyer et al., 2017). On average, this variable cut-off frequency caused data collected at a normal walking speed to be filtered at approximately 6 Hz. EMG data were high-pass filtered (40 Hz), demeaned, rectified, and low-pass filtered using a fourth-order zero-phase lag Butterworth filter with a cut-off frequency of $3.5/t_f$ Hz (Meyer et al., 2016). EMG amplitude for each muscle was normalized to the maximum value over all trials. All data were resampled to 101 time points per gait cycle (Meyer et al., 2017).

Generic model creation

A generic full-body OpenSim musculoskeletal model (Rajagopal et al., 2016) (henceforth called the "base model") was enhanced with additional hip and lower back muscles so that walking function could be predicted following internal hemipelvectomy surgery (Figure 2). The base model possessed 40 Hill-type muscle-tendon actuators per leg and 37 degrees of freedom (DOFs), including a 3 DOF lower back joint, 3 DOF shoulder joints, 1 DOF elbow joints, 3 DOF hip joints, 1 DOF knee joints, 2 DOF ankle joints, and 1 DOF toes joints. The pronation-supination angle of each forearm and the flexion-extension and inversion-eversion angles of each wrist were locked to reduce the number of DOFs to 31.

The hip and lower back muscles added to the base model were taken from two other published generic OpenSim models (Arnold et al., 2005; Bruno et al., 2015). The first was an earlier full-body model (Arnold et al., 2005) that contributed three small hip muscles (i.e., gemelli, pectineus, and quadratus femoris) to each leg of the base model, thereby allowing it to generate the hip internal-external rotation moments required for walking. Since the kinematic structure and bone geometry of the earlier full-body model were identical to those of the base model, the earlier model did not need to be scaled before the six hip muscles were transferred to the base model. The second generic model was a spine model (Bruno et al., 2015) that contributed 68 muscles to each side of the base model's lower back joint, allowing it to generate the lower back moments required to keep the trunk upright during walking. These muscles included the rectus abdominis, internal oblique, external oblique, erector spinae, multifidus, and quadratus lumborum. Additionally, the psoas was modeled as a hybrid of both models to obtain a physiologically realistic representation that actuated all three degrees of freedom at the hip and lumbar joints. The origin locations and multi-headed psoas muscle from (Bruno et al., 2015) were combined with the wrapping objects and second to fourth insertion locations from (Arnold et al., 2005). Since the bone geometry of the spine model did not match that of the base model, bony landmarks on the pelvis, spine, and ribcage of the spine model and base model were identified in NMS Builder (Valente et al., 2017) and used to determine the affine transformation that mapped the muscle attachments in the spine model onto the base model. The affine transformation and virtual palpation of lower back muscle origins and insertions were performed in accordance with a codified workflow (Modenese et al., 2018). After transfer, muscle attachment locations were adjusted slightly such that the

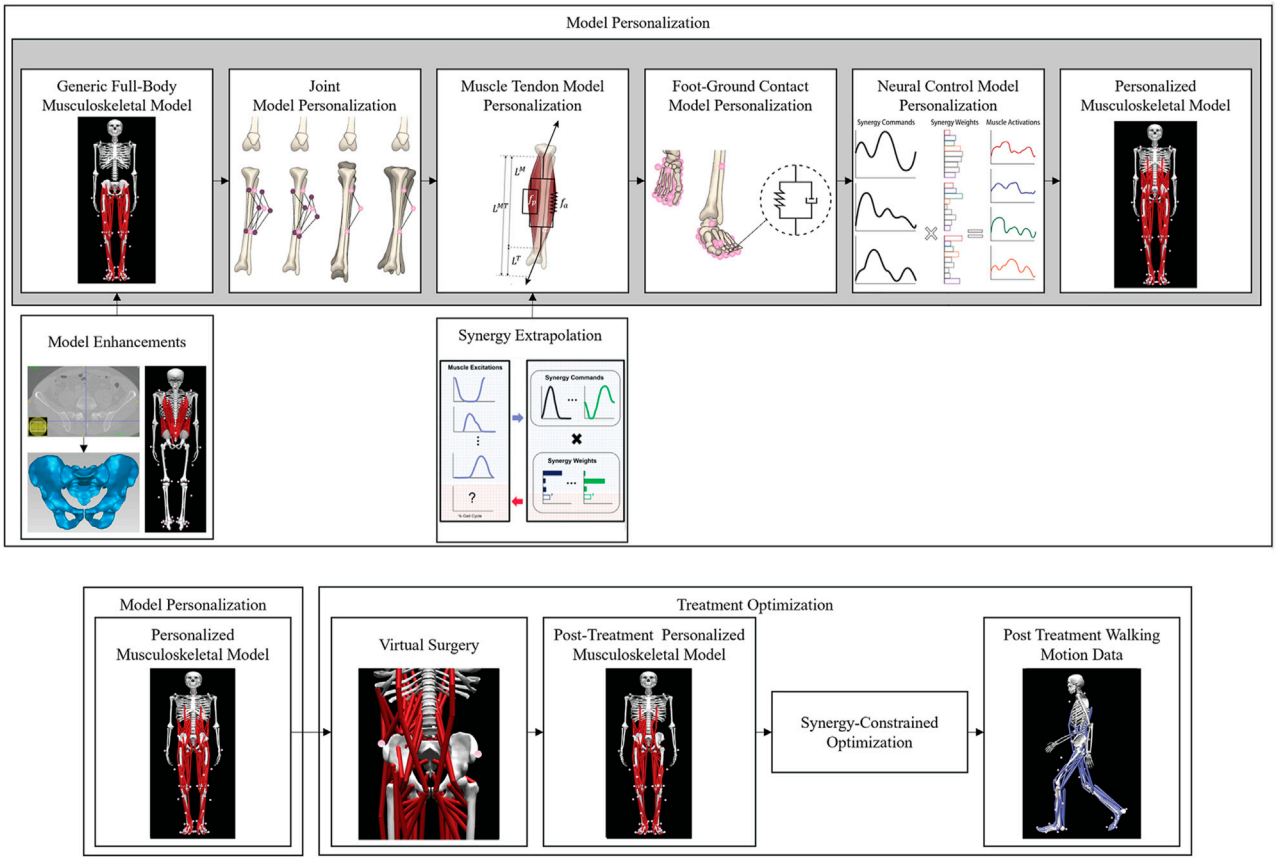

FIGURE 2
Overview of the computational processes used for model personalization and treatment optimization. Top row: Model personalization process. Bottom row: Treatment optimization process.

origin and insertion of each muscle head were on the appropriate bone surface. The resulting base model with added hip and lower back muscles possessed 246 Hill-type muscle-tendon actuators.

To simplify the computational prediction of post-surgery walking motions, we performed a model reduction process to minimize the number of heads representing each lower back muscle. The goal was to find the minimum number of original heads with modified peak isometric strength values such that the reduced set of heads produced the same moment-generating behavior as the original heads. This goal was achieved by analyzing all possible combinations of retained heads that spanned the original anatomic range and possessed approximately equal spacing between heads. For each combination, an optimization was performed to identify new peak isometric strength values for the retained heads such that the root-mean-square error between new and original lower back moments was minimized. Lower back moments were calculated for original and retained heads by setting muscle activations equal to one and placing the model in 1,000 random poses selected using Latin hypercube sampling, where the upper and lower bounds for lower back joint angles were chosen to be slightly larger than the joint ranges of motion calculated from the subject's walking data. For each multiple-head muscle, the combination of retained heads with new peak isometric strength values that most closely matched the moments generated by the original heads was chosen for use in the base model. The resulting reduced model (henceforth called the "enhanced base model") possessed 148 (74 per side) Hill-type muscle-tendon actuators spanning the lower back, hips, knees, and ankles, where 90 muscles (45 per side) actuated the lower extremities and 58 muscles (29 per side) actuated the lower back. Of particular relevance for the present study, the number of heads representing the psoas muscle was reduced from 11 to 3.

Personalized model calibration

We followed the first three steps of the four-step model personalization process described in (Meyer et al., 2016;

Sauder et al., 2019) to develop a subject-specific walking model (Figure 2). The fourth step involving neural control model personalization was modified as described in the next subsection due to the lack of EMG data for the left leg and all lower back muscles. Prior to running our model personalization process, we scaled the enhanced base model to match the dimensions of the experimental subject using the OpenSim Scale Model tool and the subject's static standing trial data. Next, the pelvis geometry in the scaled model was replaced with subject-specific pelvis geometry constructed by segmenting the subject's pelvic CT scan data. Finally, muscle attachment points on the new pelvis geometry were minimally adjusted using NMS Builder (Valente et al., 2017) such that each attachment point was moved to a bone surface. The scaled enhanced base model with the subject-specific pelvis geometry was used for the subsequent model personalization process.

The first step in the model personalization process was joint model personalization. This step involved adjusting the functional axes of the ankle and knee joints in both legs such that the motion of surface markers placed on the model reproduced experimentally measured surface marker motions as closely as possible (van den Bogert et al., 1994; Reinbolt et al., 2005). The adjustment process was formulated as a two-level non-linear optimization problem, where the outer level adjusted joint positions and orientations in their respective segment frames, while the inner level performed repeated OpenSim Inverse Kinematics analyses to calculate root-mean-square errors between model and experimental marker coordinates using the current guess for the joint parameters. The Inverse Kinematics analyses used experimental marker motion data from the isolated ankle and knee motion trials to calibrate each functional axis using a sufficiently large joint range of motion. Since subject-specific pelvis geometry was used for this study, the hip joint locations in the pelvis were defined directly from the pelvis geometry rather than through a functional calibration process.

The second step in the model personalization process was muscle-tendon model personalization. This step involved creating an EMG-driven model of the subject's right leg (the leg for which EMG data were available), where the inputs to the model were processed EMG signals and lower extremity joint positions and velocities, and the outputs were the net joint moments generated at the ankle, knee, and hip. Prior to constructing the EMG-driven model, we created surrogate models of the subject's muscle-tendon lengths, velocities, and moment arms as a function of lower extremity joint angles and angular velocities (Menegaldo et al., 2004; Sartori et al., 2012; Meyer et al., 2016, 2017). The surrogate models permitted faster and more reliable calculation of these muscle-tendon geometric quantities than possible by repeatedly calling the OpenSim Muscle Analysis tool. To personalize the muscle-tendon force-generating properties of the right leg muscles, we used a modified version of a published EMG-driven model calibration process (Meyer et al., 2017) to adjust two types of model parameters: EMG-to-activation parameters (electromechanical delays, activation dynamics time constants, activation non-linearization shape factors, and EMG scale factors), and rigid tendon Hill-type muscle model parameters (optimal muscle fiber lengths and tendon slack lengths). Parameter adjustment was performed via non-linear optimization such that the net joint moments produced by the model at the ankle, knee, and hip for walking trials from all available speeds reproduced experimental net joint moments found from OpenSim Inverse Dynamics analyses as closely as possible. Muscle peak isometric strength values were estimated from subject height and weight using published regression relationships derived from MR measurements of lower extremity muscle volumes (Handsfield et al., 2014). Since EMG data were not available for two large (iliacus and psoas) and three small (piriformis, gemelli, and quadratus femoris) hip muscles, we used synergy extrapolation (Ao et al., 2020; Ao et al., 2022) to estimate the missing EMG signals for these muscles.

The third step in the model personalization process was foot-ground contact model personalization. This step involved calibrating the stiffness, damping, and frictional properties of non-linear viscoelastic contact elements placed on a grid across the bottom of each foot such that the contact elements reproduced experimentally measured ground reaction forces and moments as closely as possible. For each foot, the contact element grid was divided into a rear foot and toes grid to permit flexion of the toes segment within the foot model. Each contact element generated a normal force using a linear spring with non-linear damping (Hunt and Crossley, 1975) and a shear force using a continuous stick-slip friction model (Jackson et al., 2016; Meyer et al., 2016). Contact model properties were calibrated for the representative walking cycle using GPOPS-II, a direct collocation optimal control solver (Patterson and Rao, 2014). The calibration process used the full-body model and produced a near-periodic simulated walking motion that matched experimental marker motion for both feet, full body joint angles, lower limb and lower back joint moments, and ground reaction forces and moments as closely as possible while simultaneously satisfying full-body skeletal dynamics (Table 2).

Muscle activation estimation

Due to the lack of EMG data for the left leg and lower back muscles, neural control model personalization required performing two novel tasks to estimate the missing muscle activations. Both tasks utilized experimental data from the representative walking cycle. The first novel task involved estimating the missing left leg muscle activations from the

TABLE 2 Overview of direct collocation optimal control problem formulations used for model personalization and treatment optimization.

Model personalization

	Cost Function	Constraints	Static Parameters	Controls
Foot-ground contact model calibration	Track experimental foot marker positions, full-body joint angles, ground reactions, and lower body and back joint moments; Minimize joint jerk	Satisfy skeletal dynamics; Enforce joint angle periodicity	Foot-ground contact model parameters	Joint jerk
Neural control model calibration	Track experimental full-body joint angles, ground reactions, lower body and back joint moments, and muscle activations; Minimize joint jerk	Satisfy skeletal dynamics; Match inverse dynamic lower body and back joint moments using synergy controls; Enforce unit magnitude synergy vectors; Enforce ground reaction and joint angle periodicity	Synergy vector weights	Synergy activations; Joint jerk
Neuromusculoskeletal model verification	Minimize joint jerk	Satisfy skeletal dynamics; Match inverse dynamic lower body joint and lumbar joint moments using synergy controls; Enforce ground reaction and joint angle periodicity	None	Synergy activations; Joint jerk
Strengthening or weakening the psoas muscle	Track synergy activations, track upper body joint angles, minimize joint jerk	Satisfy skeletal dynamics; Match inverse dynamic lower body and back joint moments using synergy controls; Enforce ground reaction and joint angle periodicity; Enforce bounds on muscle activations	None	Synergy activations; Joint jerk

available right leg muscle activations (see Supplementary Material). First, all muscle-tendon model properties for the right leg were transferred to the left leg. Second, periodicity was imposed on the right leg muscle activations output by activation dynamics in the EMG-driven model. Third, the periodic muscle activations were duplicated for two consecutive gait cycles and fitted with a Fourier series. Fourth, the Fourier-fitted right leg muscle activations were time-shifted by half a cycle to develop an initial estimate of the left leg muscle activations. Fifth, non-linear optimization was used to modify the left leg muscle activations as little as possible such that the ankle, knee, and hip moments generated by left leg muscles matched the corresponding inverse dynamic moments as closely as possible. For each left leg muscle, the optimization modified an activation scale factor, time delay, and aperiodicity term to improve the fit of the left leg muscle moments from inverse dynamics.

The second novel task involved estimating the missing lower back muscle activations (except for psoas) while simultaneously imposing a synergy structure on the muscle activations for each side (Shourijeh and Fregly, 2020). Prior to estimating the missing muscle activations, we minimally adjusted the initial values of optimal muscle fiber length and tendon slack length for each lower back muscle such that every muscle operated on the ascending region of its normalized force-length curve with a maximum normalized length close to one. After this adjustment, non-linear optimization was used to estimate the unknown trunk muscle activations, assuming the activations on each side of the body were generated using a synergy structure (see Supplementary Material). The cost function tracked lower back joint inverse dynamic moments, minimized lower back muscle activations squared, and required muscle heads from the same lower back muscle to have similar activation patterns. The time-varying synergy activations were extracted by decomposing the lower extremity muscle activations using non-negative matrix factorization. The design variables were the time-invariant synergy vector weights for the lower back muscles, where each weight was associated with a corresponding extracted synergy activation. Six synergies were required on each side of the body (Ivanenko et al., 2004) to achieve the best match of inverse dynamic joint moments (all root-mean-square errors <2.5 Nm) and leg muscle activations (98% total variability accounted for).

Once right and left side synergies defining the muscle activations for both legs and the lower back were available, the time-varying synergy activations and associated time-invariant synergy vectors were adjusted slightly to produce a dynamically consistent full-body walking motion that closely reproduced all available data. Synergy adjustments for the representative walking cycle were found using GPOPS-II (Patterson and Rao, 2014), where the cost function tracked experimental full-body joint angles, lower limb and lower back joint moments, experimental ground reaction forces and moments, and experimental and estimated muscle activations. Path constraints were added to satisfy skeletal dynamics and ensure that model-predicted joint moments from inverse dynamics matched muscle-predicted joint moments from

synergy-constructed muscle activations. A terminal constraint enforced joint angle periodicity (Table 2).

Pre-surgery walking verification

The predictive capability of the final personalized model was verified by performing a predictive walking optimization that closely reproduced all experimental data and estimated muscle activations for the representative walking cycle with fixed final time. The verification process involved solving two direct collocation optimal control problems using GPOPS-II. The goal of the first problem was to show that the personalized model could closely reproduce a) experimental full-body joint motions, b) experimental lower back and leg muscle moments, c) experimental ground reaction forces and moments, and d) experimental and estimated muscle activations simultaneously. All of these quantities were tracked in the cost function, which also included a joint jerk minimization term due to the use of an inverse formulation for skeletal dynamics (van Den Bogert et al., 2011; Meyer et al., 2016; Sauder et al., 2019; Febrer-Nafría et al., 2020). The six synergy activations on each side were used as the controls, and the six associated synergy vectors per side were assumed to remain unchanged (Supplementary Figures S1, S2). Path constraints enforced a dynamically consistent solution by eliminating residual forces and torques acting on the pelvis and a kinetically consistent solution by ensuring that joint moments generated by the synergy-constructed muscle activations matched those produced by inverse skeletal dynamics. A terminal constraint enforced joint angle and ground reaction force near-periodicity (Table 2).

The goal of the second problem was to show that the personalized model could reproduce the joint motions, joint moments, ground reactions, and muscle activations found by the first problem simply by tracking the synergy activations produced by the first problem with free final time. The cost function also included minimization of joint jerk and the same path and terminal constraints as the first problem (Table 2). Verification was considered to be successful once the second problem could closely predict the results and final time of both the first problem and the experimental walking motion (Supplementary Table S1).

Post-surgery walking prediction

A free final time direct collocation optimal control problem was formulated to predict post-surgery walking function for different assumptions about post-surgery psoas strength representative of real-life surgical and rehabilitation scenarios (Figure 2). The optimal control problem assumed that a) the modeled subject's recovery had plateaued, b) pre-surgery synergy activations for each side changed only minimally to produce the predicted post-surgery walking motion (Meyer et al., 2016; Pitto et al., 2018; Sauder et al., 2019), c) post-surgery walking speed matched the pre-surgery self-selected speed of 1.4 m/s, d) the modeled subject received a custom prosthesis that reproduced the original pelvis and hip anatomy, and e) lower back and hip muscles removed from the right (assumed operated) side of the model (Table 3) corresponded to the most common surgical scenario encountered at MD Anderson Cancer Center in Houston, Texas. Notably, this surgical scenario involves resection of all operated side hip abductor muscles. Muscle removal emulated a worst-case clinical scenario in which all resected muscles were either not reattached or reattached but had no remaining biomechanical function. Four different post-surgery walking predictions were generated for assumed ipsilateral post-surgery psoas strengths of 0%, 50%, 100%, and 150% of pre-surgery strength. Zero percent represented surgical removal of the

TABLE 3 Muscles included in the enhanced base OpenSim musculoskeletal model. Muscles listed in bold text were removed from the operated side of the model when generating post-surgery walking predictions.

Adductor brevis	Gracilis
Adductor Longus	**Iliacus**
Adductor Magnus	Pectineus
Adductor Magnus (distal)	Peroneus Brevis
Adductor Magnus (ischial)	Peroneus Longus
Adductor Magnus (middle)	Piriformis
Adductor Magnus (proximal)	Psoas
Biceps Femoris Long Head	**Quadratus Femoris**
Biceps Femoris Short Head	**Rectus Femoris**
Extensor Digitorium Longus	**Sartorius**
Extensor Hallucis Longus	Semimembranosus
Flexor Digitorium Longus	Semitendinosus
Flexor Hallucis Longus	Soleus
Gastrocnemius Lateral Head	**Tensor Fascia Latae**
Gastrocnemius Medial Head	Tibialis Anterior
Gemelli	Tibialis Posterior
Gluteus Maximus	Vastus Lateralis
Gluteus Maximus (inferior)	Vastus Medialis
Gluteus Maximus (middle)	Vastus Intermedius
Gluteus Maximus (superior)	Rectus Abdominus
Gluteus Medius	**Internal Oblique**
Gluteus Medius (anterior)	**External Oblique**
Gluteus Medius (middle)	**Quadratus Lumborum**
Gluteus Medius (posterior)	**Multifidus**[a]
Gluteus Minimus	**Erector Spinae**[a]
Gluteus Minimus (anterior)	
Gluteus Minimus (middle)	
Gluteus Minimus (posterior)	

[a]A few heads of these muscles remain.

psoas on the operated side, while 50%, 100%, and 150% represented different potential rehabilitation outcomes when the psoas is retained. These strength values were implemented by changing the peak isometric strength of the ipsilateral psoas muscle. Apart from the addition of free final time, removal of the specified muscles, and inclusion of a path constraint bounding all muscle activations to be between 0 and 1, the optimal control problem formulation was identical to that of the final verification problem (Table 2).

To quantify the impact of post-surgery psoas strength on predicted post-surgery walking function, we compared multiple clinical walking measures predicted by each of the four optimizations. These included the cost of transport, metabolic cost, stride length, stride time, spatial symmetry, temporal symmetry, and stance width. Cost of transport (CoT) (J/kg*m) is defined as the metabolic cost expended to move a unit of body mass a unit of distance. Metabolic cost is defined as the energy consumed by the body during a given activity, in this case, a single walking cycle. Based on a previous study (Arones et al., 2020), we used Bhargava's model to calculate the metabolic cost (Bhargava et al., 2004). Stride length is defined as the distance between two consecutive heel strikes of the same foot. Stride time is defined as the time between two consecutive heel strikes of the same foot. Spatial symmetry is defined as the ratio between step length on the operated side and stride length,

$$Spatial\ symmetry = \frac{Operated\ Step\ Length}{Stride\ Length}$$

where step length is defined as the distance between heel strike of one foot and heel strike of the opposite foot. A spatial symmetry value of 0.5 represents perfect symmetry. If the operated foot takes a longer step than does the non-operated foot, then the spatial symmetry value will be less than 0.5. Similarly, if the non-operated foot takes a longer step than does the operated foot, then the spatial symmetry value will be greater than 0.5. Temporal symmetry is defined as the ratio between step time on the operated side and stride time,

$$Temporal\ Symmetry = \frac{Operated\ Step\ Time}{Stride\ Time}$$

where step time is defined as the time between heel strike of one foot and heel strike of the opposite foot. A temporal symmetry value of 0.5 represents perfect symmetry. If the step time for the operated foot is longer than that of the non-operated foot, then the temporal symmetry value will be less than 0.5. Similarly, if the step time for the non-operated foot is longer than that of the operated foot, then the temporal symmetry value will be greater than 0.5.

Stance width is defined as the side-to-side distance between the heel on one foot and the heel on the other foot when each foot is flat on the ground.

Results

Out of the four post-surgery walking predictions, only the 100% and 150% treatment options successfully converged to a complete gait cycle (heel strike to heel strike of the operated foot). Relative to pre-surgery, the CoT, metabolic cost, spatial and temporal symmetry, and step length decreased while the stance width increased when operated side psoas strength was maintained at its pre-surgery value (100%) (Table 4). However, when the operated side psoas was strengthened above its pre-surgery value (150%), spatial symmetry, stride length, and stance width returned close to pre-surgery values (Table 4). Additionally, cost of transport decreased, metabolic cost increased, and temporal symmetry remained unchanged as post-surgery psoas strength was increased. Both walking predictions possessed a large lateral trunk lean to the operated side (Figures 3, 4), with comparable changes in stride time regardless of post-surgery psoas status.

Predicted joint angles were similar across some joints and substantially different for others between the two successful post-surgery walkng conditions (Table 5; Figure 5). For the operated leg, increased hip extension was observed during toe-off for both post-surgery conditions and during swing phase for the 100% Fmax case. The 100% Fmax case had an increase in hip abduction over the entire gait cycle, while the 150% Fmax had an increase in hip abduction during stance phase and hip adduction during swing phase. For hip rotation, the 100% Fmax case exhibited increased internal rotation over the entire gait cycle, while the 150% Fmax case had increased external rotation during stance phase and increased internal rotation during swing. Knee flexion decreased for the 100% Fmax case during swing phase. At the ankle, the 150% Fmax case had an increase in dorsiflexion during early stance phase and late swing phase. For ankle rotation, the 100% Fmax case exhibited increased eversion over the entire gait cycle, while the 150% Fmax case had increased inversion during stance and increased eversion during swing phase. For the non-operated leg, both post-surgery predictions exhibited increased hip adduction, decreased knee flexion, and increased ankle inversion during swing phase. Additionally, the 150% Fmax case had increased ankle eversion during stance phase. For the lower back, the lumbar bending increased toward the operated side over the entire gait cycle. Although differences in lumbar rotation between the post-surgery conditions were not large in magnitude, the 150% Fmax case displayed pronounced swaying between operated and non-operated sides over the gait cycle.

Predicted lower body joint moments had several large differences compared to pre-surgery walking (Table 6; Figure 6). For the operated leg, the most notable differences were at the hip, where hip abduction and internal rotation moments were close to zero throughout the gait cycle. The hip extension moment followed a similar pattern as pre-

TABLE 4 Comparison of experimental pre-surgery and predicted post-surgery clinical gait measures. Psoas strength is indicated as percent of pre-surgery value

Condition	Psoas strength	CoT $(\frac{J}{kg^*m})$	Metabolic cost (J)	Spatial symmetry	Temporal symmetry	Stance width (m)	Stride length (m)	Stride time (s)
Pre-Surgery	100%	5.98	620	0.49	0.50	0.082	1.55	1.06
Post-Surgery	150%	5.52	571	0.51	0.47	0.071	1.55	1.10
	100%	5.75	548	0.42	0.47	0.23	1.43	1.05

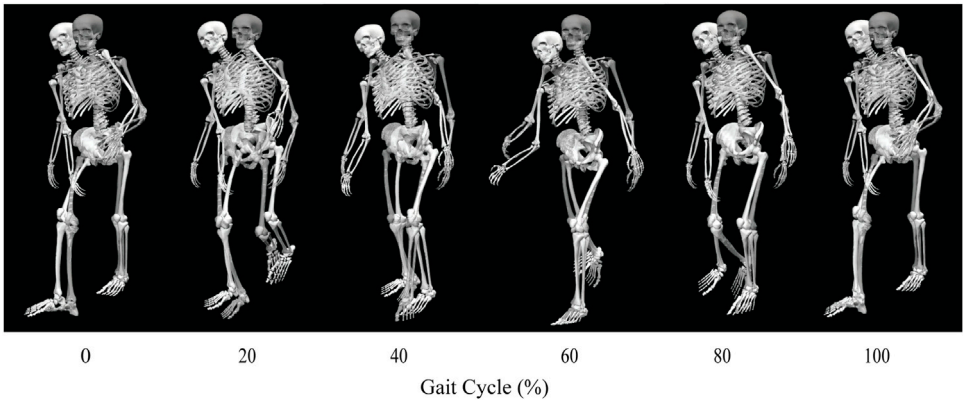

FIGURE 3
Animation strip comparing the subject's experimental walking motion (translucent skeleton) to his predicted walking motion when post-surgery operated side psoas strength was 100% of its pre-surgery value (opaque skeleton).

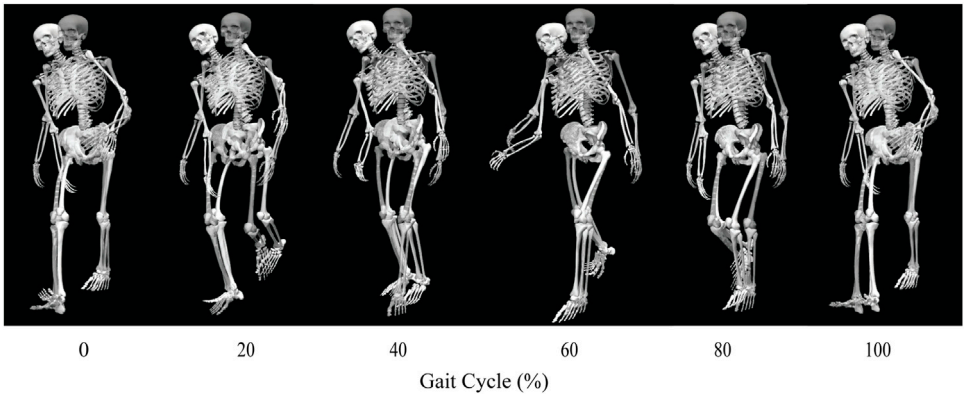

FIGURE 4
Animation strip comparing the subject's experimental walking motion (translucent skeleton) to his predicted walking motion when post-surgery operated side psoas strength was 150% of its pre-surgery value (opaque skeleton).

surgery but with a decreased hip flexion moment. In addition, peak knee extension moments decreased during stance phase. For the non-operated leg, both post-surgery predictions produced hip flexion, adduction, and internal rotations that followed similar trajectories to those observed experimentally. The largest differences were an increase in hip extension moment

TABLE 5 Root-mean-square (RMS) differences between pre-surgery and predicted post-surgery joint angles. Percentage of Fmax indicates the percent of pre-surgery psoas peak isometric strength used to generate the post-surgery walking prediction.

	RMS difference (deg)	
Joint angle	**150% Fmax**	**100% Fmax**
Pelvis Tilt	3.99	4.48
Pelvis List	10.44	13.27
Pelvis Rotation	12.56	12.12
Operated Hip Flexion	5.59	12.54
Operated Hip Adduction	16.09	20.72
Operated Hip Rotation	17.03	14.36
Operated Knee Flexion	9.04	18.13
Operated Ankle Dorsiflexion	8.73	6.79
Operated Ankle Inversion	12.01	25.59
Non-operated Hip Flexion	4.71	4.19
Non-operated Hip Adduction	10.64	12.18
Non-operated Hip Rotation	6.15	6.03
Non-operated Knee Flexion	11.72	8.66
Non-operated Ankle Dorsiflexion	6.24	5.80
Non-operated Ankle Inversion	20.41	15.97
Lumbar Extension	4.78	4.37
Lumbar Bending	18.72	16.02
Lumbar Rotation	8.09	7.15

during swing, an increase in hip abduction moment during toe-off and early stance, and a time shift in peak hip internal moment. Similarly, the peak knee extension moment time-shifted for both successful post-surgery conditons, but increased in magnitude for the 100% Fmax case. The ankle plantarflexion moment increased during late stance and early swing. Lastly, the lower back bending moment increased toward the non-operated side throughout the gait cycle.

In general, the muscle activations produced by the 100% Fmax and 150% Fmax post-surgery walking predictions shared similar characteristics to pre-surgery activations (Supplementary Figures S3–S6). Predicted muscle activations for the operated leg and trunk were comparable to pre-surgery activations with small increases in all three psoas branches, gastrocnemius lateralis, soleus, and the remaining multifidus and erector spinae muscles during late stance phase. Similarly, the muscle activations predicted for the non-operated leg and trunk were similar to pre-surgery activations for both post-surgery conditions, with the exception of small activation increases for iliacus, soleus, piriformis, and tensor fasciae latae.

Analogous to the minimal changes observed in muscle activations, the synergy activations for both post-surgery walking predictions exhibited similar behavior (Table 7, Supplementary Figures S7, S8).

Discussion

This study used a personalized neuromusculoskeletal model and direct collocation optimal control to predict the impact of ipsilateral psoas muscle strength on post-surgery walking function following internal hemipelvectomy surgery with custom prosthesis reconstruction. The post-surgery walking prediction problem was formulated to emulate the most common surgical scenario encountered at MD Anderson Cancer Center in Houston, Texas, assuming a custom prosthesis design that recapitulated the original pelvis bony anatomy and hip center location. In addition to removing from the model the same muscles removed surgically, we investigated post-surgery psoas strengths ranging from 0% (removed) to 50% (weakened), 100% (maintained), and 150% (strengthened) of pre-surgery value. For each of the four post-surgery walking situations, a range of clinical gait measures were calculated, including stride length, stride time, step width, spatial symmetry, temporal symmetry, cost of transport, and metabolic cost. Of the four treatment options, only the 100% and 150% scenarios produced successful post-surgery walking predictions. When the strength of the operated side psoas muscle was maintained at its pre-surgery value, the predicted gait pattern exhibited features observed clinically post-surgery (e.g., increased stance width and lateral trunk lean) to accommodate the lack of hip abductor muscles. Interestingly, when the strength of the operated side psoas was increased above its pre-surgery value, stance width, stride length, and spatial symmetry returned to pre-surgery values and the cost of transport decreased. Overall, our post-surgery walking predictions suggest that retention and strengthening of the psoas muscle on the operated side may have a clinically important impact on post-surgery walking ability, at least for the most common surgical scenario involving complete resection of all hip abductor muscles. Other common surgical scenarios, including the second most common scenario at MD Anderson Cancer Center, retain all of the hip abductor muscles, and the influence of the psoas muscle on post-surgery walking function for these scenarios has not yet been investigated.

There are several possible explanations for the inability of the optimal control solver to find a solution for the 0% and 50% Fmax treatment conditions. First, the psoas muscle may play a more critical role in walking than originally anticipated. When post-surgery psoas strength was 100% or 150% of its pre-surgery value, predicted psoas muscle force increased (Supplementary Figures S9) during late stance phase and early swing phase, resulting in a hip flexion moment that was nearly as large as before surgery and a corresponding hip extension angle that was slightly increased. The model was therefore able to use the operated side psoas muscle to swing the operated leg forward to achieve a post-surgery walking pattern that was similar to pre-

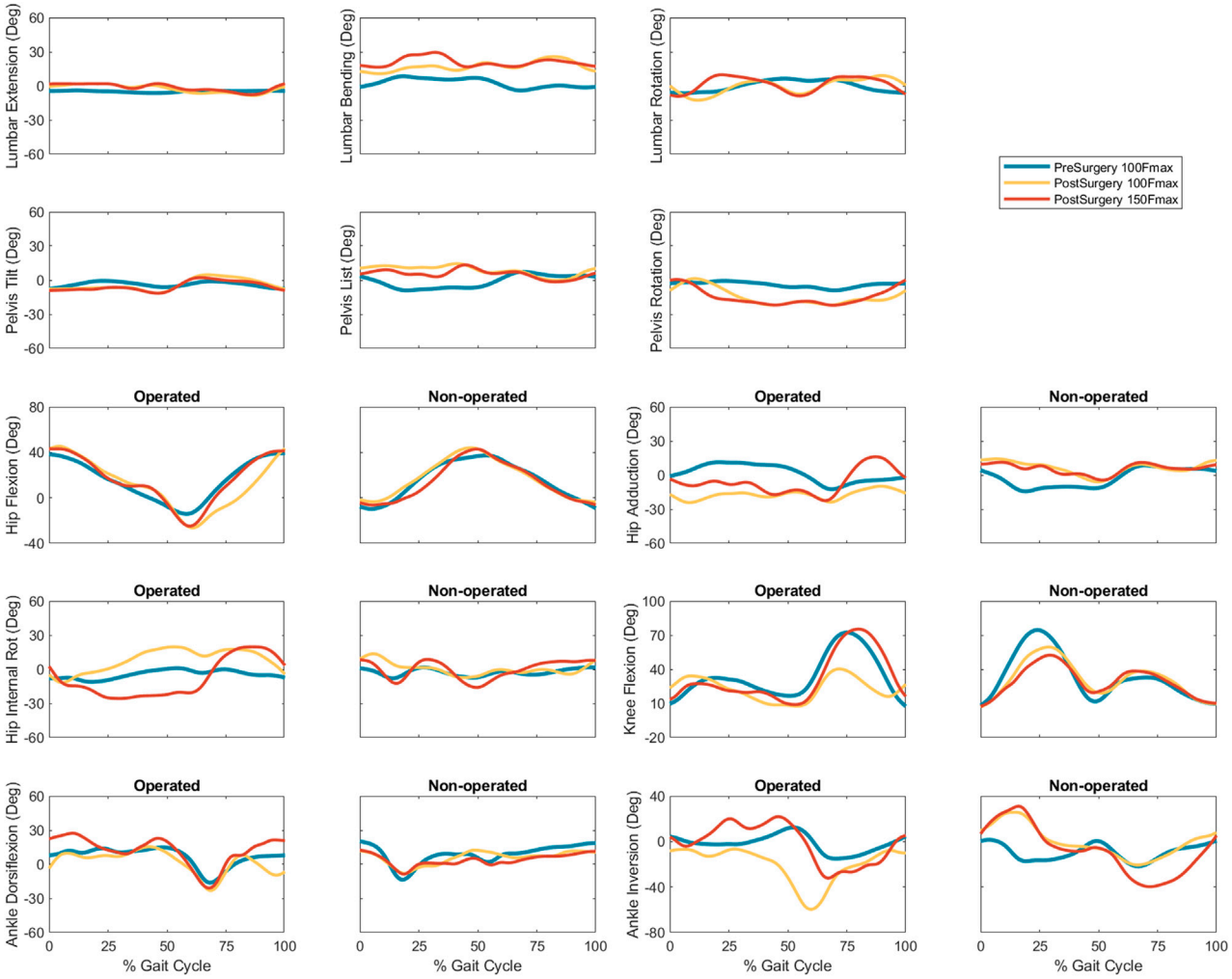

FIGURE 5
Experimental pre-surgery and predicted post-surgery joint angles for post-surgery psoas strengths of 100%, and 150% of the pre-surgery value. The gait cycle begins with operated leg heel strike.

surgery. Increasing psoas muscle force appears to be metabolically efficient as the cost of transport decreased when post-surgery operated side psoas strength was increased. In contrast, the model lost the ability to complete a full gait cycle when the operated side psoas muscle was either removed or weakened to 50% of its pre-surgery strength, supporting the conclusion that retention of the operated side psoas muscle may be important for maintaining post-surgery walking function. Second, the synergy structure used to predict post-surgery muscle activations may have imposed unrealistic limitations on psoas muscle recruitment. It is possible that following surgery, the synergy vectors coupling muscle activations would be changed such that the psoas could be recruited more heavily without increasing the recruitment of other muscles. Third, hip and lower back muscles taken down during surgery are often reattached to neighboring soft tissue and may still contribute somewhat to walking function. However, reattached muscles may or may not be enervated, and their new attachments may or may not provide mechanical benefits, making it difficult to assess their contribution to post-surgery walking function. A future study should investigate how assumptions about the remaining function of reattached muscles impact post-surgery walking predictions.

Overall, our post-surgery walking predictions exhibited similar gait characteristics to those observed clinically. Compared to pre-surgery, the post-surgery gait patterns exhibited increased stance width through a more lateral foot placement on the operated side, and increased trunk lean toward

TABLE 6 Root-mean-square (RMS) differences between pre-surgery and predicted post-surgery joint moments. Percentage of Fmax indicates the percent of pre-surgery psoas peak isometric strength used to generate the post-surgery walking prediction.

	RMS difference (Nm)	
Joint moment	**150% Fmax**	**100% Fmax**
Operated Hip Flexion	18.07	19.07
Operated Hip Adduction	19.43	21.70
Operated Hip Rotation	51.66	54.54
Operated Knee Flexion	24.91	24.29
Operated Ankle Dorsiflexion	10.56	11.09
Operated Ankle Inversion	9.13	7.91
Non-operated Hip Flexion	23.30	24.05
Non-operated Hip Adduction	19.59	21.81
Non-operated Hip Rotation	20.20	16.79
Non-operated Knee Flexion	28.51	22.61
Non-operated Ankle Dorsiflexion	4.78	11.16
Non-operated Ankle Inversion	9.53	7.49
Lumbar Extension	8.76	8.49
Lumbar Bending	39.04	39.01
Lumbar Rotation	10.95	7.89

the operated side. These changes redirected the line of action of the operated side ground reaction force vector through the hip center and up to the center of mass of the trunk, thereby eliminating any ground reaction force moment arm about the hip center. These biomechanical changes allowed the model to accommodate the removal of all hip abductor muscles by eliminating the need for any muscle-generated hip abduction moment.

Though no published experimental studies have reported changes in gait kinematics following internal hemipelvectomy with reconstruction, our predicted increases in stance width and lateral trunk lean were consistent with and larger than, respectively, clinical observations made at MD Anderson Cancer Center in Houston. Several factors may be contributing to this outcome. First, predicted activations for the trunk muscles may have been too low. The synergy-based optimization used to estimate trunk muscle activations essentially ran static optimization with a synergy structure to constrain the solution, and static optimization is known to underestimate muscle co-contraction. Second, reattached trunk muscles may have a substantial contribution to trunk muscle stability. As noted earlier, muscles taken down during surgery are often reattached to neighboring soft tissue, and these reattachments may be especially effective for trunk muscles. Third, the assumed post-surgery optimal muscle fiber lengths and tendon slack lengths of trunk muscles on both sides of the body may have been inaccurate. Changes in these properties alter where a muscle operates on its normalized force-length curve, and it is possible that the body adapts these properties following surgery to place the trunk muscles into a more favorable operating range. This hypothesis is supported by the observation that trunk muscles on the non-operated side produced little to no active force and large passive force from being stretched, while trunk muscles on the operated side produced minimal active force and no passive force from becoming slack due to trunk lean. Future research should investigate the impact of modifying lower trunk muscle-tendon properties on predicted post-surgery walking function. In addition, modifying the spine model to include an additional joint in the thoracic region would allow the shoulders to remain level, as observed clinically, while still allowing the model to lean toward the operated side.

Although both post-surgery simulations predicted two common gait features observed clinically, some of the predicted joint motions were slightly abnormal for this patient population. When post-surgery psoas strength was maintained, the hip internally rotated and the ankle everted more than normal over the entire gait cycle. Similarly, when post-surgery psoas strength was increased, the non-operated leg exhibited increased ankle inversion during swing phase and eversion during stance phase. These abnormal movement patterns may have helped the model compensate for the large number of removed muscles on the operated side. However, this compensatory mechanism could have also resulted from our assumption that the synergy vectors remained fixed and only the synergy activations were allowed to change post-surgery. Since the synergy structure was formulated to control the trunk and legs together, changing a single synergy activation affected multiple muscles. For example, since synergies 2 and 3 possess the largest psoas synergy vectors weights (Supplementary Figures S1, S2, Supplementary Figures S7, S8), increasing these synergy activations also increased muscle activations for other muscles with sizeable weights in the same synergy vectors, including soleus, gastrocnemius lateralis, gastrocnemius medialis, peroneus longus, and peroneus brevis, all of which contribute to subtalar rotation. Similarly, key hip rotation muscles were also affected, including iliacus and tensor fascia latae. Therefore, the abnormal gait features observed in the predicted post-surgery walking motions may be a product of our synergy-controlled problem formulation.

The neural control assumption that the synergy vectors remain fixed and the corresponding synergy activations change as little as possible to produce a new motion has been tested experimentally in only two previous studies (Meyer et al., 2016; Pitto et al., 2018) involving a different patient population than the one here. Thus, this assumption may not be appropriate for the present clinical application involving orthopedic cancer surgery. This hypothesis is supported by the findings of Falisse et al., 2020 (Falisse et al., 2020), who used gait-related performance criteria (e.g., muscle fatigue, energy expenditure) in their optimization cost function to predict a crouch gait

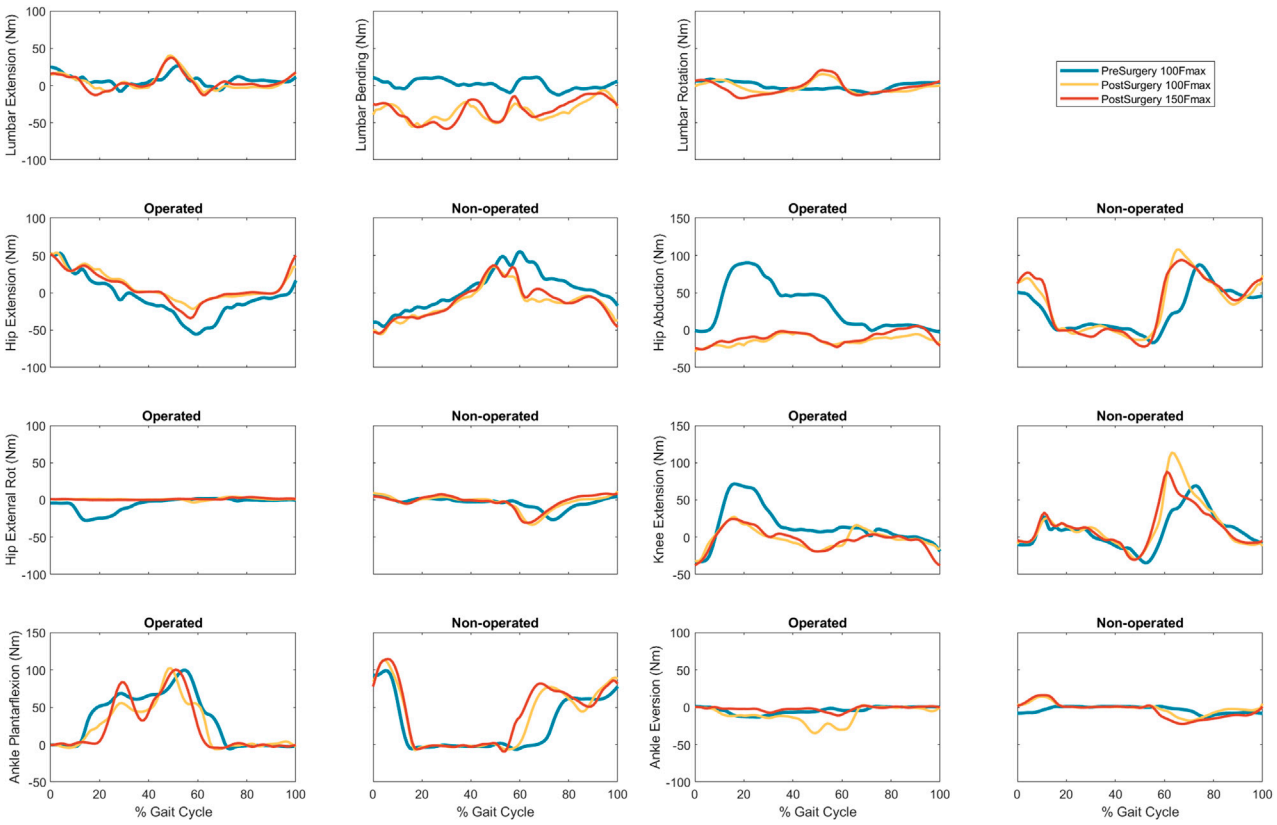

FIGURE 6
Experimental pre-surgery and predicted post-surgery joint moments for post-surgery psoas strengths of 100%, and 150% of the pre-surgery value. The gait cycle begins with operated leg heel strike.

pattern using a model of a child with cerebral palsy. Addressing this important issue will require collecting pre- and post-surgery gait data, including video motion capture, ground reaction, and EMG data, from the same patient. Then a personalized model can be constructed for both the pre- and post-surgery situations, and the extent to which the synergy vectors remain unchanged between the two can be evaluated. If the assumption of unchanged synergy vectors turns out to be invalid, such data sets would permit exploration of alternative neural control hypotheses to identify one that works for this particular clinical problem. Any new neural control hypotheses would need to be validated on pre- and post-surgery data sets collected from multiple patients receiving internal hemipelvectomy surgery.

This study represents our initial foray into predicting walking function following internal hemipelvectomy surgery. We decided to focus this initial study specifically on the psoas muscle since its influence on post-surgery walking function is debated among orthopedic oncologists. Since retention of the psoas muscle requires extra time in the operating room, which increases the risk of complications, investigating its importance to post-surgery walking function is a valuable effort. Though these initial post-surgery walking predictions are imperfect, they are still a significant step forward in using computational modeling and simulation to identify optimal surgical, rehabilitation, and even custom prosthesis design decisions for individuals receiving internal hemipelvectomy surgery with or without reconstruction.

Our study possesses several important limitations related to the personalized neuromusculoskeletal model and computational solution approach. First, operated leg EMG data had to be mirrored to the non-operated leg. The mirroring process implicitly assumed that operated and non-operated leg kinematics and kinetics were similar, which was a reasonable assumption for a normal healthy walking cycle. Second, several missing non-operated leg EMG signals had to be estimated. Though previous studies demonstrated that comparable synergy-based EMG estimation methods could predict one missing EMG signal with excellent reliability (Ao et al., 2020; Ao et al., 2022), extension of this methodology to multiple missing EMG signals has yet not been validated. Third, the generic base OpenSim model had to be constructed by combining two different published OpenSim models, one of

TABLE 7 Root-mean-square (RMS) differences between pre-surgery and predicted post-surgery synergy activations. Percentage of Fmax indicates the percent of pre-surgery psoas peak isometric strength used to generate the post-surgery walking prediction.

		RMS difference (unitless)	
Side	**Synergy no.**	**150% Fmax**	**100% Fmax**
Non-operated	1	0.057	0.062
	2	0.065	0.057
	3	0.056	0.067
	4	0.063	0.051
	5	0.057	0.061
	6	0.067	0.068
Operated	1	0.048	0.054
	2	0.067	0.068
	3	0.060	0.064
	4	0.068	0.068
	5	0.067	0.066
	6	0.065	0.048

which had to be modified further to reduce its complexity. Despite our best efforts at combining the two models, it is possible that some trunk muscle lines of action are less accurate than desired. Fourth, even with considerable reduction in the number of trunk muscles, the computation time required to generate each post-surgery walking prediction was large, ranging from 8 to 11 h. Future research efforts will explore ways to reduce computation time to a matter of minutes rather than hours. Fifth, as is the case with any gradient-based optimization, the potential existed for finding a solution that was a local minimum. To minimize the possibility of entrapment in a local minimum, we ran each post-surgery optimal control problem with different initial guesses and reported the solution with the smallest objective function value (Ackermann and van den Bogert, 2010). Sixth (and probably the biggest limitation), no directly comparable post-surgery walking data were available for validation purposes from either the subject modeled in this study (a healthy volunteer) or previous studies. The closest experimental data are from a case study reported by Wingrave and Jarvis 2018 (Wingrave and Jarvis, 2018), which measured post-surgery walking function of a single patient following internal hemipelvectomy. Unlike in our computational study, the patient in that study was not reconstructed with a custom prosthesis, and no list of resected muscles was included, making comparison with our computational predictions infeasible. As noted earlier, it will be critical for future research efforts to measure walking function both before and after internal hemipelvectomy surgery with custom prosthesis reconstruction so that post-surgery walking predictions generated from pre-surgery walking data and the implemented surgical decisions can be validated.

In conclusion, this study used a patient-specific neuromusculoskeletal model to predict post-surgery walking function following internal hemipelvectomy surgery with custom prosthesis reconstruction for different assumptions about post-surgery psoas muscle strength on the operated side. Simulated post-surgery psoas strengths included 0% (removed), 50% (weakened), 100% (maintained), and 150% (strengthened) of the pre-surgery value. However, only the 100% and 150% treatment options successfully converged to a complete gait cycle. When the strength of the psoas was maintained, key clinical post-surgery gait features were observed, including increased stance width, decreased stride length, and increased lumbar bending toward the operated side. Furthermore, when the psoas was strengthened above its pre-surgery level, stance width and stride length returned to pre-surgery values. These results suggest that retention and strengthening of the psoas muscle on the operated side may be important for maximizing post-surgery walking function, at least for the most common surgical scenario involving resection of operated side hip abductor muscles. Other common surgical scenarios retain all of the hip abductors, and thus the influence of the psoas on post-surgery walking function for these scenarios requires further investigation. Future studies comparing computationally predicted and experimentally measured post-surgery walking function for different surgical scenarios will be needed to evaluate and refine our predictive simulation process. Once validated, this computational approach could ultimately influence surgical, rehabilitation, and implant design decisions to meet the unique clinical needs of individual pelvic sarcoma patients.

Data availability statement

The raw data supporting the conclusions of this article will be made available by the authors, without undue reservation.

Ethics statement

The studies involving human participants were reviewed and approved by the institutional review boards of the University of Florida and Rice University. The patients/participants provided their written informed consent to participate in this study.

Author contributions

CP and BF collected the experimental walking data. MV performed joint model personalization, foot-ground contact model personalization, neural control model personalization, pre-surgery walking verification, and post-surgery walking predictions, prepared figures, and drafted the manuscript. GL processed the experimental walking data, created the enhanced base model, generated patient-specific pelvis geometry, and generated

operated leg and trunk muscle activations. MS performed muscle reduction on the enhanced base model. DA calibrated the EMG-driven model with synergy extrapolation to estimate missing EMG signals. RW identified the most common internal hemipelvectomy surgical scenario performed at MD Anderson Cancer Center in Houston, Texas. JF-L provided input on optimal control problem formulations. VL defined the clinical problem to investigate, provided clinical background information, and clinically assessed the post-surgery walking predictions. BF acquired funding and supervised the overall study. MV and BF analysed data. MV, MS, VL, and BF interpreted the results of the walking predictions. All authors revised and approved the manuscript.

Funding

This work was conducted with support from the Cancer Prevention and Research Institute of Texas (grant RR170026 to BF), the National Science Foundation (Graduate Research Fellowship to MV), and the United States Department of Veterans Affairs (Research Career Scientist Award—Rehabilitation R&D #N9274S to CP).

Conflict of interest

The authors declare that the research was conducted in the absence of any commercial or financial relationships that could be construed as a potential conflict of interest.

Publisher's note

All claims expressed in this article are solely those of the authors and do not necessarily represent those of their affiliated organizations, or those of the publisher, the editors and the reviewers. Any product that may be evaluated in this article, or claim that may be made by its manufacturer, is not guaranteed or endorsed by the publisher.

Supplementary material

The Supplementary Material for this article can be found online at: https://www.frontiersin.org/articles/10.3389/fbioe.2022.855870/full#supplementary-material

References

Ackermann, M., and van den Bogert, A. J. (2010). Optimality principles for model-based prediction of human gait. *J. Biomech.* 43, 1055–1060. doi:10.1016/J.JBIOMECH.2009.12.012

Aljassir, F., Beadel, G. P., Turcotte, R. E., Griffin, A. M., Bell, R. S., Wunder, J. S., et al. (2005). Outcome after pelvic sarcoma resection reconstructed with saddle prosthesis. *Clin. Orthop. Relat. Res.* 438, 36–41. Available at: https://journals.lww.com/clinorthop/Fulltext/2005/09000/Outcome_after_Pelvic_Sarcoma_Resection.9.aspx. doi:10.1097/00003086-200509000-00009

Ao, D., Shourijeh, M. S., Patten, C., and Fregly, B. J. (2020). Evaluation of synergy extrapolation for predicting unmeasured muscle excitations from measured muscle synergies. *Front. Comput. Neurosci.* 14, 588943. doi:10.3389/FNCOM.2020.588943

Ao, D., Vega, M. M., Shourijeh, M. S., Patten, C., and Fregly, B. J. (2022). EMG-driven musculoskeletal model calibration with estimation of unmeasured muscle excitations via synergy extrapolation. *Front. Bioeng. Biotechnol.* 10. doi:10.3389/fbioe.2022.962959

Arnold, A. S., Anderson, F. C., Pandy, M. G., and Delp, S. L. (2005). Muscular contributions to hip and knee extension during the single limb stance phase of normal gait: a framework for investigating the causes of crouch gait. *J. Biomech.* 38, 2181–2189. doi:10.1016/J.JBIOMECH.2004.09.036

Arones, M. M., Shourijeh, M. S., Patten, C., and Fregly, B. J. (2020). Musculoskeletal model personalization affects metabolic cost estimates for walking. *Front. Bioeng. Biotechnol.* 8, 588925. doi:10.3389/FBIOE.2020.588925

Babazadeh Naseri, A., Dunbar, N. J., Baines, A. J., Akin, J. E., Higgs, C. F., III, and Fregly, B. J. (2021). Heterogeneous material mapping methods for patient-specific finite element models of pelvic trabecular bone: a convergence study. *Med. Eng. Phys.* 96, 1–12. doi:10.1016/J.MEDENGPHY.2021.07.012

Bai, L., Gong, C., Chen, X., Sun, Y., Zhang, J., Cai, L., et al. (2019). Additive manufacturing of customized metallic orthopedic implants: Materials, structures, and surface modifications. *Met. (Basel).* 9, 1004. doi:10.3390/MET9091004

Beadel, G. P., McLaughlin, C. E., Wunder, J. S., Griffin, A. M., Ferguson, P. C., and Bell, R. S. (2005). Outcome in two groups of patients with allograft-prosthetic reconstruction of pelvic tumor defects. *Clin. Orthop. Relat. Res.* 438, 30–35. Available at: https://journals.lww.com/corr/Fulltext/2005/09000/Outcome_in_Two_Groups_of_Patients_with.8.aspx. doi:10.1097/01.blo.0000180048.43208.2f

Bhargava, L. J., Pandy, M. G., and Anderson, F. C. (2004). A phenomenological model for estimating metabolic energy consumption in muscle contraction. *J. Biomech.* 37, 81–88. doi:10.1016/s0021-9290(03)00239-2

Bruno, A. G., Bouxsein, M. L., and Anderson, D. E. (2015). Development and validation of a musculoskeletal model of the fully articulated thoracolumbar spine and rib cage. *J. Biomech. Eng.* 137, 081003. doi:10.1115/1.4030408

Chen, G., Muheremu, A., Yang, L., Wu, X., He, P., Fan, H., et al. (2020). Three-dimensional printed implant for reconstruction of pelvic bone after removal of giant chondrosarcoma: a case report. *J. Int. Med. Res.* 48, 030006052091727–300060520917275. doi:10.1177/0300060520917275

Dion, C., Pollock, M., Howard, J., Somerville, L., and Lanting, B. (2018). Surgical outcomes of 3d printed musculoskeletal metal implants: A systematic review. *J. Musculoskelet. Res.* 21, 1840001. doi:10.1142/S0218957718400018

Falisse, A., Serrancolí, G., Dembia, C. L., Gillis, J., Jonkers, I., and De Groote, F. (2019). Rapid predictive simulations with complex musculoskeletal models suggest that diverse healthy and pathological human gaits can emerge from similar control strategies. *J. R. Soc. Interface* 16, 20190402. doi:10.1098/rsif.2019.0402

Falisse, A., Pitto, L., Kainz, H., Hoang, H., Wesseling, M., Van Rossom, S., et al. (2020). Physics-based simulations to predict the differential effects of motor control and musculoskeletal deficits on gait dysfunction in cerebral palsy: A retrospective case study. *Front. Hum. Neurosci.* 14, 40. doi:10.3389/FNHUM.2020.00040

Febrer-Nafría, M., Pallarès-López, R., Fregly, B. J., and Font-Llagunes, J. M. (2020). Comparison of different optimal control formulations for generating dynamically consistent crutch walking simulations using a torque-driven model. *Mech. Mach. Theory* 154, 104031. doi:10.1016/J.MECHMACHTHEORY.2020.104031

Fregly, B. J., Reinbolt, J. A., Rooney, K. L., Mitchell, K. H., Chmielewski, T. L., and Rooney, K. L. (2007). Design of patient-specific gait modifications for knee osteoarthritis rehabilitation. *IEEE Trans. Biomed. Eng.* 54, 1687–1695. doi:10.1109/TBME.2007.891934

Gupta, S., Griffin, A. M., Gundle, K., Kafchinski, L., Zarnett, O., Ferguson, P. C., et al. (2020). Long-term outcome of iliosacral resection without reconstruction for primary bone tumours. *Bone Jt. J.* 102-B, 779–787. doi:10.1302/0301-620X.102B6.BJJ-2020-0004

Gutiérrez, S., Greiwe, R. M., Frankle, M. A., Siegal, S., and Lee, W. E. (2007). Biomechanical comparison of component position and hardware failure in the reverse shoulder prosthesis. *J. Shoulder Elb. Surg.* 16, S9–S12. doi:10.1016/J.JSE.2005.11.008

Handsfield, G. G., Meyer, C. H., Hart, J. M., Abel, M. F., and Blemker, S. S. (2014). Relationships of 35 lower limb muscles to height and body mass quantified using MRI. *J. Biomech.* 47, 631–638. doi:10.1016/J.JBIOMECH.2013.12.002

Hilton, T., Campbell, N., and Hosking, K. (2017). Additive manufacturing in orthopaedics: Clinical implications. *SA Orthop. J.* 16, 63–67. doi:10.17159/2309-8309/2017/V16N2A9

Hug, F. (2011). Can muscle coordination be precisely studied by surface electromyography? *J. Electromyogr. Kinesiol.* 21, 1–12. doi:10.1016/J.JELEKIN.2010.08.009

Hunt, K. H., and Crossley, F. R. E. (1975). Coefficient of restitution interpreted as damping in vibroimpact. *J. Appl. Mech.* 42, 440–445. doi:10.1115/1.3423596

Ivanenko, Y. P., Poppele, R. E., and Lacquaniti, F. (2004). Five basic muscle activation patterns account for muscle activity during human locomotion. *J. Physiol.* 556, 267–282. doi:10.1113/JPHYSIOL.2003.057174

Jackson, J. N., Hass, C. J., and Fregly, B. J. (2016). Development of a subject-specific foot-ground contact model for walking. *J. Biomech. Eng.* 138. doi:10.1115/1.4034060

Menegaldo, L. L., De Toledo Fleury, A., and Weber, H. I. (2004). Moment arms and musculotendon lengths estimation for a three-dimensional lower-limb model. *J. Biomech.* 37, 1447–1453. doi:10.1016/j.jbiomech.2003.12.017

Meyer, A. J., Eskinazi, I., Jackson, J. N., Rao, A. V., Patten, C., and Fregly, B. J. (2016). Muscle synergies facilitate computational prediction of subject-specific walking motions. *Front. Bioeng. Biotechnol.* 4, 77. doi:10.3389/FBIOE.2016.00077

Meyer, A. J., Patten, C., and Fregly, B. J. (2017). Lower extremity EMG-driven modeling of walking with automated adjustment of musculoskeletal geometry. *PLoS One* 12, e0179698. doi:10.1371/journal.pone.0179698

Modenese, L., Montefiori, E., Wang, A., Wesarg, S., Viceconti, M., and Mazzà, C. (2018). Investigation of the dependence of joint contact forces on musculotendon parameters using a codified workflow for image-based modelling. *J. Biomech.* 73, 108–118. doi:10.1016/J.JBIOMECH.2018.03.039

Patterson, M. A., and Rao, A. V. (2014). GPOPS-II: A MATLAB software for solving multiple-phase optimal control problems using hp-adaptive Gaussian quadrature collocation methods and sparse nonlinear programming. *ACM Trans. Math. Softw.* 41, 1–37. doi:10.1145/2558904

Pitto, L., Kaat, D., Guy, M., Catherine, H., Friedl, D. G., and Ilse, J. (2018). O 109 – post-treatment muscle coordination patterns during gait are highly similar to pre-treatment ones in CP children. *Gait Posture* 65, 228–229. doi:10.1016/J.GAITPOST.2018.06.144

Pitto, L., Kainz, H., Falisse, A., Wesseling, M., Van Rossom, S., Hoang, H., et al. (2019). SimCP: A simulation platform to predict gait performance following orthopedic intervention in children with cerebral palsy. *Front. Neurorobot.* 13, 54. doi:10.3389/fnbot.2019.00054

Rajagopal, A., Dembia, C. L., DeMers, M. S., Delp, D. D., Hicks, J. L., and Delp, S. L. (2016). Full-body musculoskeletal model for muscle-driven simulation of human gait. *IEEE Trans. Biomed. Eng.* 63, 2068–2079. doi:10.1109/TBME.2016.2586891

Reinbolt, J. A., Schutte, J. F., Fregly, B. J., Il, B., Haftka, R. T., George, A. D., et al. (2005). Determination of patient-specific multi-joint kinematic models through two-level optimization. *J. Biomech.* 38, 621–626. doi:10.1016/j.jbiomech.2004.03.031

Reinbolt, J. A., Haftka, R. T., Chmielewski, T. L., and Fregly, B. J. (2008). A computational framework to predict post-treatment outcome for gait-related disorders. *Med. Eng. Phys.* 30, 434–443. doi:10.1016/J.MEDENGPHY.2007.05.005

Sartori, M., Reggiani, M., van den Bogert, A. J., and Lloyd, D. G. (2012). Estimation of musculotendon kinematics in large musculoskeletal models using multidimensional B-splines. *J. Biomech.* 45, 595–601. doi:10.1016/j.jbiomech.2011.10.040

Sauder, N. R., Meyer, A. J., Allen, J. L., Ting, L. H., Kesar, T. M., and Fregly, B. J. (2019). Computational design of FastFES treatment to improve propulsive force symmetry during post-stroke gait: A feasibility study. *Front. Neurorobot.* 13, 80. doi:10.3389/FNBOT.2019.00080

Shourijeh, M. S., and Fregly, B. J. (2020). Muscle synergies modify optimization estimates of joint stiffness during walking. *J. Biomech. Eng.* 142, 011011. doi:10.1115/1.4044310

Sun, W., Li, J., Li, Q., Li, G., and Cai, Z. (2011). Clinical effectiveness of hemipelvic reconstruction using computer-aided custom-made prostheses after resection of malignant pelvic tumors. *J. Arthroplasty* 26, 1508–1513. doi:10.1016/J.ARTH.2011.02.018

Valente, G., Crimi, G., Vanella, N., Schileo, E., and Taddei, F. (2017). nmsBuilder: Freeware to create subject-specific musculoskeletal models for OpenSim. *Comput. Methods Programs Biomed.* 152, 85–92. doi:10.1016/J.CMPB.2017.09.012

van den Bogert, A. J., Smith, G. D., and Nigg, B. M. (1994). *In vivo* determination of the anatomical axes of the ankle joint complex: An optimization approach. *J. Biomech.* 27, 1477–1488. doi:10.1016/0021-9290(94)90197-X

van Den Bogert, A. J., Blana, D., and Heinrich, D. (2011). Implicit methods for efficient musculoskeletal simulation and optimal control. *Procedia IUTAM* 2, 297–316. doi:10.1016/J.PIUTAM.2011.04.027

Wingrave, A., and Jarvis, H. (2018). The importance of the rehabilitation program following an internal hemipelvectomy and reconstruction with limb salvage – gait analysis and outcomes: a case study. *Disabil. Rehabil.* 41, 2066–2070. doi:10.1080/09638288.2018.1457090

frontiers | Frontiers in Bioengineering and Biotechnology

TYPE Original Research
PUBLISHED 26 October 2022
DOI 10.3389/fbioe.2022.899799

OPEN ACCESS

EDITED BY
Ching-Chi Hsu,
National Taiwan University of Science and Technology, Taiwan

REVIEWED BY
AmirAli Jafarnezhadgero,
University of Mohaghegh Ardabili, Iran
Yaodong Gu,
Ningbo University, China

*CORRESPONDENCE
Jingguang Qian,
2867996025@qq.com

†These authors have contributed equally to this work and share the first authorship

SPECIALTY SECTION
This article was submitted to Biomechanics, a section of the journal Frontiers in Bioengineering and Biotechnology

RECEIVED 19 March 2022
ACCEPTED 10 October 2022
PUBLISHED 26 October 2022

CITATION
Chen L, Jiang Z, Yang C, Cheng R, Zheng S and Qian J (2022), Effect of different landing actions on knee joint biomechanics of female college athletes: Based on opensim simulation. *Front. Bioeng. Biotechnol.* 10:899799. doi: 10.3389/fbioe.2022.899799

Effect of different landing actions on knee joint biomechanics of female college athletes: Based on opensim simulation

Liang Chen[1,2†], Ziang Jiang[2,3†], Chen Yang[1†], Rongshan Cheng[2,3], Size Zheng[4] and Jingguang Qian[1*]

[1]Department of Sports Science, Nanjing Sport Institute, Nanjing, China, [2]Department of Orthopaedic Surgery, Shanghai Ninth People's Hospital, Shanghai Jiao Tong University School of Medicine, Shanghai, China, [3]School of Biomedical Engineering and Med-X Research Institute, Shanghai Jiao Tong University, Shanghai, China, [4]School of Mechanical Engineering, Zhejiang University, Hangzhou, China

Background: The anterior cruciate ligament (ACL) is one of the most injurious parts of the knee in the biomechanical environment during landing actions. The purpose of this study was to compare the lower limb differences in movement patterns, muscle forces and ACL forces during drop landing (DL), drop vertical jump (DVJ) and forward vertical jump (FVJ).

Methods: Eleven basketball and volleyball female college athletes (Division II and I) were recruited. Landing actions of DL, DVJ and FVJ, kinematics and dynamics data were collected synchronously using a motion capture system. OpenSim was used to calculate the ACL load, knee joint angle and moment, and muscle force.

Results: At initial contact, different landing movements influenced knee flexion angle; DL action was significantly less than FVJ action (p = 0.046). Different landing actions affected quadriceps femoris forces; FVJ was significantly greater than DL and DVJ actions (p = 0.002 and p = 0.037, respectively). However, different landing movements had no significant effects on other variables (knee extension moment, knee valgus angle and moment, hamstring and gastrocnemius muscle forces, and ACL forces) (p > 0.050).

Conclusion: There was no significant difference in the knee valgus, knee valgus moment, and the ACL forces between the three landing actions. However, knee flexion angle, knee extension moments sagittal factors, and quadriceps and gastrocnemius forces are critical factors for ACL injury. The DL action had a significantly smaller knee flexion angle, which may increase the risk of ACL injury, and not recommended to assess the risk of ACL injuries. The FVJ action had a larger knee flexion angle and higher quadriceps femoris forces that were more in line with daily training and competition needs. Therefore, it is

Abbreviations: ACL, Anterior Cruciate Ligament; CMC, Computer Muscle Control; DL, Drop Landing; DOF, Degree of Freedom; DVJ, Drop Vertical Jump; EMG, Electromyography; FD, Forward Dynamics; FVJ, Forward Vertical Jump; IC, Initial Contact; IK, Inverse Kinematics; LESS, Landing Error Scoring System; MKF, Maximum Knee Flexion; RRA, Residual Reduction Algorithms; SPM, Para-metric Mapping; SPM{F}, Para-metric Mapping Characteristics with F Statistics

recommended to use FVJ action in future studies on risk assessment of ACL injuries and injury prevention in female college athletes.

KEYWORDS

landing test movements, ACL, opensim, knee joint, biomechanics

Introduction

The anterior cruciate ligament (ACL) injuries in female athletes are four to six times higher compared to male athletes (Agel et al., 2005). Mainly, ACL injuries are classified as non-contact injuries and usually occur in landing, plant-and-cut, and twisting actions (Meyer and Haut, 2008). Landing is one of the everyday sports actions in basketball, volleyball, and other sports activities (Fort-Vanmeerhaeghe et al., 2016). The previous studies reported that overly small knee or hip flexion, overly large knee valgus angle, extension moment, the valgus moment might be leading causes of ACL injuries (Chappell et al., 2002; Kernozek et al., 2005). Further, the muscle reaction forces such as excessively high quadriceps muscle force and low hamstring muscle contraction force can also contribute to the ACL injury during landing in professional female athletes.

Currently, the landing test actions in risk assessment of ACL injury mainly include drop landing (DL) (Decker et al., 2003; Kernozek et al., 2005), drop vertical jump (DVJ) (Cortes et al., 2007), and forward vertical jump (FVJ) (Padua et al., 2004). Wenxin et al. (Niu et al., 2013) reported the dynamic postural stability and the influence mechanism of muscle activities during DL from 30cm, 52cm, and 72 cm. Satoshi et al. reported the effects of multi-task interference on the biomechanics of the lower limb during the DVJ while Hossein et al. compared the lower limb differences in movement patterns, muscle forces, and ACL forces during DVJ (Mokhtarzadeh et al., 2017; Imai et al., 2022). Padua et al. (2009) use FVJ as a standard action for Landing Error Scoring System (LESS) testing and treated it as one of the most efficient ones for ACL injury risk tests. These tasks are functionally relevant to athletic performance and execution of these complex skills requires well-trained and coordinated movement. However, most previous studies used only one test protocol, which also led to some differences in the findings of the different studies, which may be related to the different task requirements of the test movements, thus changing the human movement pattern. In addition, these studies extensively used the inverse dynamics method to qualitatively and quantitatively determine the risk factors of ACL injury during exercise (Bennett et al., 2008; Padua et al., 2009; Blackburn et al., 2013; Mokhtarzadeh et al., 2017; Bulat et al., 2019; Imai et al., 2022). Although the calculation process and experimental method are unified, significant divergence still exists in the estimated ACL load (Bennett et al., 2008; Blackburn et al., 2013) due to limitations in the experimental object and the algorithm. Blackburn et al. (2013) calculated the peak value of anterior tibial shear force during DL action (30 cm height) through inverse dynamics, and it was about 0.7BW, while the result of Bennett et al. (2008) reported only about 0.4BW under the same method and landing action. However, some studies demonstrated that muscle forces are one of the main determinants of the dynamic load of the knee ligaments, and the ligaments balance the anterior tibial shear force during landing (Dürselen et al., 1995; Anderson and Pandy, 2003; Bennett et al., 2008; Blackburn et al., 2013). The quadriceps and hamstring muscle groups make function during landing is critical in determining the load experienced by the knee joint structures and therefore fundamental to understanding ACL injuries. Therefore, estimating the ACL load during landing by calculating anterior tibial shear forces through the inverse dynamic method has limitations affecting the accurate evaluation of the risk factors of ACL injury.

The simulation technology plays an essential role in complex biomechanical problems (Reinbolt et al., 2011), and it can simulate the mechanisms of the musculoskeletal system during human motion through an optimization framework of forward and reverse analysis (Rajagopal et al., 2016). Many studies have demonstrated that the simulation optimization method of the OpenSim musculoskeletal numerical simulation system is superior to the traditional inverse dynamics or mathematical methods (Delp et al., 2007; Seth et al., 2018; Yu et al., 2020). Recently, Huiyu et al. reported the effects of different footwear on lower limb kinematics, kinetics, and muscle forces in walking and running movements by OpenSim (Zhou et al., 2021). It is also considered one of the most widely used software for kinematic and dynamic analysis in complex actions such as running, jumping, and landing (Kar and Quesada, 2012; Mokhtarzadeh et al., 2017; Zhou et al., 2021; Renganathan, 2022), while providing validated platforms for exploring the nerve-muscle performance in dynamic activities. Although there are studies that assessed the risk of ACL injury under landing test actions in female athletes (Decker et al., 2003; Kernozek et al., 2005), there are no reports on quantified ACL loads in parallel with the three landing actions (DL, DVJ and FVJ). This research explored the differences and relationships of ACL load, knee angle, joint moment, and muscle forces in three landing test actions of professional female athletes using the OpenSim system. Further, it provided a theoretical basis for selecting appropriate landing assessment movements and ACL injury prevention.

Accordingly, we hypothesize as follows: 1) the differences in the knee angle, moment, and muscle forces of the three test

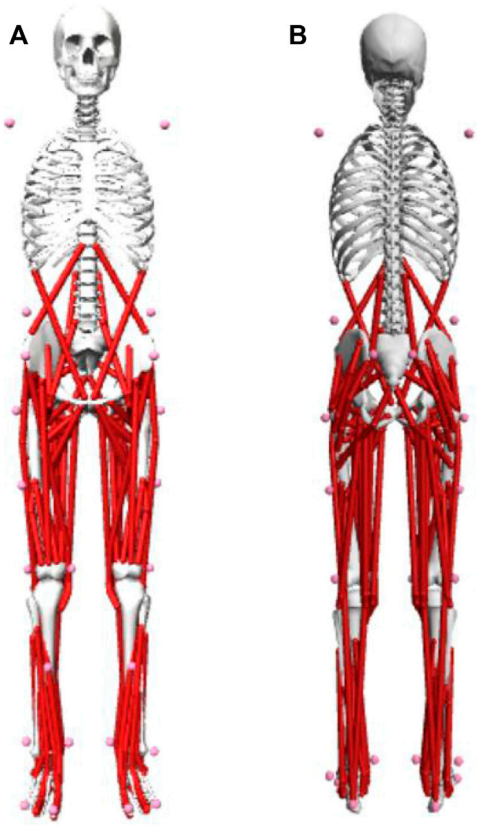

FIGURE 1
Schematic representation of the placements of the marker. **(A)** The front vision of the marker set; **(B)** the back vision of the marker set.

actions. 2) ACL injury had a higher risk for DL action than for DVJ and FVJ.

Materials and methods

Subjects selection

The sample size was calculated according to a previous study protocol (Decker et al., 2003; Fagenbaum and Darling, 2003; Cortes et al., 2007). Eleven female athletes (4 division I basketball players and 7 division II volleyball players) from the Nanjing Sports Institute were recruited (age: 21.7 ± 0.7 years; height: 171.5 ± 4.6 cm; weight: 63.1 ± 9.0 kg). The inclusion criteria were no history of lower limb injury and not engaged in strenuous exercise within 48 h before the experiment. All the participants had greater than 10 years' sufficient training and competition experience on sports. Subjects have all given written informed consent for participation and were familiar with the experiment process.

Experiment process

Twenty-eight 14 mm infrared-reflective markers were firmly secured on each participant to characterize the anatomical bone landmarks. Bone landmarks included acromion, the highest point of the iliac spine, anterior superior iliac spine, posterior superior iliac spine, greater trochanter, medial and lateral femoral condyle, medial and lateral malleolus, heel, the first and the fifth metatarsal, as shown in Figure 1. The markers were pasted on bilateral bone landmarks to ensure the complete capture of the participants' actions. Four additional markers were secured in the middle of the thigh and shank bilaterally to prevent the loss of a marker while capturing. An experienced researcher manually located anatomical bone landmarks through the skin surface and pasted each marker. The methodology of pasting markers was primarily based on the study of Kar and Quesada (2012). However, certain modifications were done according to the modelling coordinate points guide in Visual3D inverse dynamics software (Visual3D, C-Motion, Inc., United States).

The trajectories of markers were captured during the landing process by 12 Vicon motion capture cameras (200 Hz, Vicon Motion Analysis Inc., Vantage 5, Oxford, United Kingdom). Two fully integrated three-dimensional force platforms (1000 Hz, AMTI, Watertown, Massachusetts, United States) synchronously captured the dynamic ground-reaction force signal with the motion capture system. Surface electromyography (EMG) data were collected using a Telemetered system, was used to collect muscle activations. The surface electrodes were applied to the participant's dominant limb over the muscle bellies of the rectus femoris, vastus lateralis, biceps femoris, and tibialis posterior.

Before the experiment, each participant was well instructed on the movement performance for the assessment, instructions and cadence which were standardized according to the experimental protocol (Decker et al., 2003; Padua et al., 2004; Kernozek et al., 2005; Cortes et al., 2007). Participants completed the following tasks in sequence: (1) DL: the participants were instructed to jump forward from a block 30 cm high with arms akimbo and land with their feet on two separate force platforms. (2) DVJ: the take-off process was similar to DL. After the first landing, participants were instructed to perform a maximal vertical jump coherently. (3) FVJ: the block was 70 cm away from the force platform. Participants were instructed to land on the center of the force platform and perform a maximal vertical jump coherently after the first landing (Figure 2). All the subjects were asked to warm up in each self-select activities before the experiment started and practiced the three landing actions until be familiar with the test movements and process. The formal experiment was preceded and followed by a 5-min rest period.

Participants performed the three landing actions until three valid trials were recorded, and the final result was based on the average of three valid trials. A trial was acceptable when the participant jumped from the block without falling due to loss of

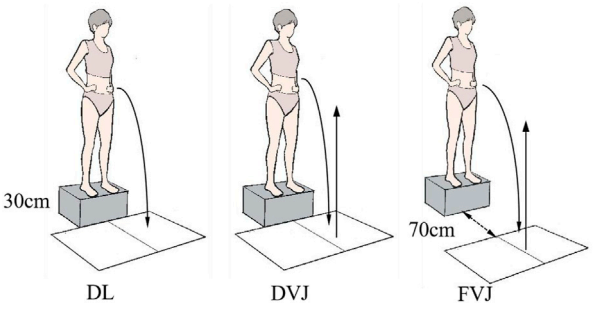

FIGURE 2
DL, DVJ and FVJ landing test action.

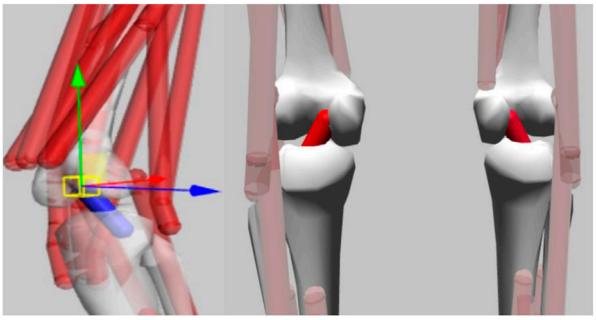

FIGURE 3
Gait2392 model with ACL model imported in OpenSim.

balance. Further, the trial was invalid if their hands did not remain akimbo or the feet did not land separately on two different force platforms.

Primary data process

The kinematics and dynamics data of the trials were filtered using a low-pass filter (Butterworth 4th order) and run with a cutoff frequency of 10 Hz for the motion capture system and 100 Hz for force signal in the inverse dynamics software, Visual3D (Koltermann et al., 2018).

Firstly, a 4th-order band-pass filter between 10 and 450 Hz was applied to the EMG data, before it was full-wave-rectified. Finally, the Root Mean Square RMS was calculated. The data from the initial contact (IC) phase to the maximum knee flexion (MKF) phase were selected for processing. The data from the dominant side of the athletes were analyzed in three landing test actions. Knee kinematics, dynamics, and muscle forces data of the three landing actions were temporally standardized in Origin 2019b software. Raw data were interpolated to 101 data points, and 0% represented the touching moment, and 100% represented the maximum flexion moment of the knee joint. The direction of the joint angle and moment was defined as positive sagittal knee extension; frontal knee valgus is positive.

Statistical analysis

The biomechanical parameters of the lower limbs from three landing test actions were analyzed in SPSS (Version 20.0., IBM Corp., Armonk, NY, United States). Data were tested for normality and equal variance before the analysis. If the data met normal distribution assumptions and equal variances, analysis of variance was used (one-way ANOVA), and nonparametric Kruskal–Wallis test was used when the variance was not homogeneous. The post-hoc comparison was performed by the least significant difference (LSD) test of mean values. The effect size is represented by a partial eta square (η^2), and p-value < 0.05 was considered significant. Statistical Parametric Mapping (SPM) was also applied in the comparison of the kinematic and dynamic result in the process of three actions performance which was a one-dimensional methodology for the topological analysis of smooth continuum changes associated with experimental intervention (Pataky, 2012). The significance level of the SPM{F} characteristics of the test for joint angles, joint moments, and muscle forces was set at $\alpha = 0.05$, while F statistics are considered as the aforementioned family of linear statistical tests. All the Statistical analysis was performed in MALTLAB (MATLAB R2018a, The MathWorks, MA, United States).

Biomechanical data analysis

This study used a simplified generic Gait2392 musculoskeletal model in OpenSim (OpenSim 4.1, Stanford, California, United States), with 12 bony segments, 92 muscles, and 23 degrees of freedom (Kainz et al., 2016). This study mainly focused on the ACL load and the variation between the knee joint variables in three landing test actions. Therefore, the ACL model was introduced into the original Gait2392 model, and the degree of freedom (DOF) on the frontal plane of the knee joint was also added. The generalized coordinates, physiological parameters and the DOF function of ACL were referred to the verified results (Kar and Quesada, 2012; Kar and Quesada, 2013) (Figure 3).

The musculoskeletal model was scaled (Scaling) to generate the real anthropometry, and the Inverse Kinematics (IK) calculation module from the Visual3D was input into the OpenSim. The inverse simulation of the three landing actions was achieved through the OpenSim Residual Reduction Algorithms (RRA), Computer Muscle Control (CMC), and Forward Dynamics (FD) tool (Figure 4). The dependent variables such as the knee biomechanical parameters, muscle

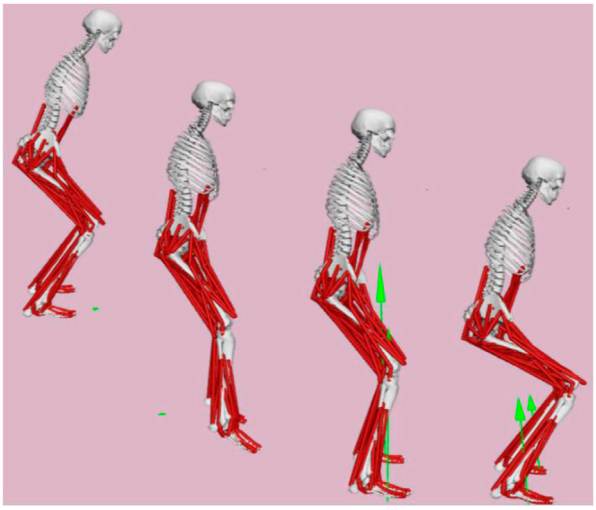

FIGURE 4
Schematic of the OpenSim simulation results. Note: Since the main bearing stage of ACL during landing occurs from the IC to MKF, the simulation results of the three landing test actions in this study were taken during the IC-MKF (0%–100%) stage (Panel).

forces and ACL load were calculated while time was used as the independent variable.

The muscle forces calculated in our study are as follows: Quadriceps femoris (rectus femoris, vastus lateralis, vastus medialis and vastus intermedius), Hamstring (biceps femoris lh, biceps femoris sh, semitendinosus and semimembranosus), Gastrocnemius (medial, gastrocnemius, lateral gastrocnemius and soleus).

Results

As shown in Figure 5, Calculated four muscle activations and their corresponding measured EMGs were also in good agreement qualitatively. As shown in Table 1 and Figure 6, One-way ANOVA showed that different landing actions had significant effects on the knee flexion angle at IC ($p = 0.046$). A subsequent test showed that the knee flexion angle of the DL action was less than the FVJ action. One-way ANOVA showed that different landing movements had affected quadriceps femoris forces at IC. Secondary tests showed that the quadriceps femoris forces under the FVJ action were significantly greater than the DL and DVJ actions ($p = 0.002$ and $p = 0.037$, respectively). Knee extension moment, knee valgus angle, knee valgus moment, hamstring muscle forces, gastrocnemius muscle forces, and ACL forces had no significant effects ($p > 0.05$).

As shown in Figure 6, The SPM{F} showed that different landing actions had significant effects on the knee flexion moment at IC-MKF from 11% to 21% ($\alpha = 0.05$, $F = *7.42$). The SPM{F} showed that different landing actions had significant effects on the quadriceps femoris forces at IC-MKF from 0% to 41% ($\alpha = 0.05$, $F^* = 5.40$). The SPM{F} showed that different landing actions had significant effects on the gastrocnemius muscle forces at IC-MKF from 0% to 100% ($\alpha = 0.05$, $F^* = 4.81$). Knee flexion angle, knee valgus angle, knee valgus moment, hamstring muscle forces, and ACL forces had no significant effects ($\alpha = 0.05$, $F^*>4.47$).

Discussion

The influence of different landing test actions on anterior cruciate ligament load

The objective of this study was to investigate the differences and relationships of ACL load, knee angle, joint moment, and muscle forces in three landing test actions. We first hypothesized the differences in the knee angle, moment, and muscle forces of the three test actions. The results of our study partly agree with our hypotheses.

The risk factors for ACL injury are mainly reported in the sagittal plane (Hashemi et al., 2011), such as excessive small knee flexion angle or excessive large knee extension moment. In our study, The ANOVA and SPM also found that differences in the knee flexion angle and knee extension moment.

The ACL load decreases with the increase of knee flexion angle in knee motion (Markolf et al., 1995). Therefore, an increase in the knee flexion angle while landing helps absorb part of the energy and effectively reduces the ACL load, thus reducing the risk of ACL injury (Decker et al., 2003; Kernozek et al., 2005; Cortes et al., 2007). This study found that the ACL load decreased when the knee flexion angle increased during the three landing actions. However, the participants experienced more knee flexion angle in the FVJ group than in the DVJ group, but the FVJ group suffered a higher ACL load than the DVJ group. Previous studies reported that the large extension moment and valgus moments of the landing process might significantly increase the ACL load (Lohmander et al., 2007). In this study, the peak values of knee extension and knee valgus moments of the FVJ group were higher than the DVJ group, which could be one of the reasons for the difference in ACL load in the two landing actions. The FVJ action seems the most applicable to athletes out of three landing test actions (Cortes et al., 2007). However, ACL load in the DL group was the highest compared to the DVJ and FVJ groups, which could be due to the smaller passive knee flexion angle in the IC phase of the DL action compared to the other two actions. As previously reported, ACL load will be effectively reduced when the knee flexion angle exceeds 60°. Hence, the ground reaction force will increase by 68N with each degree

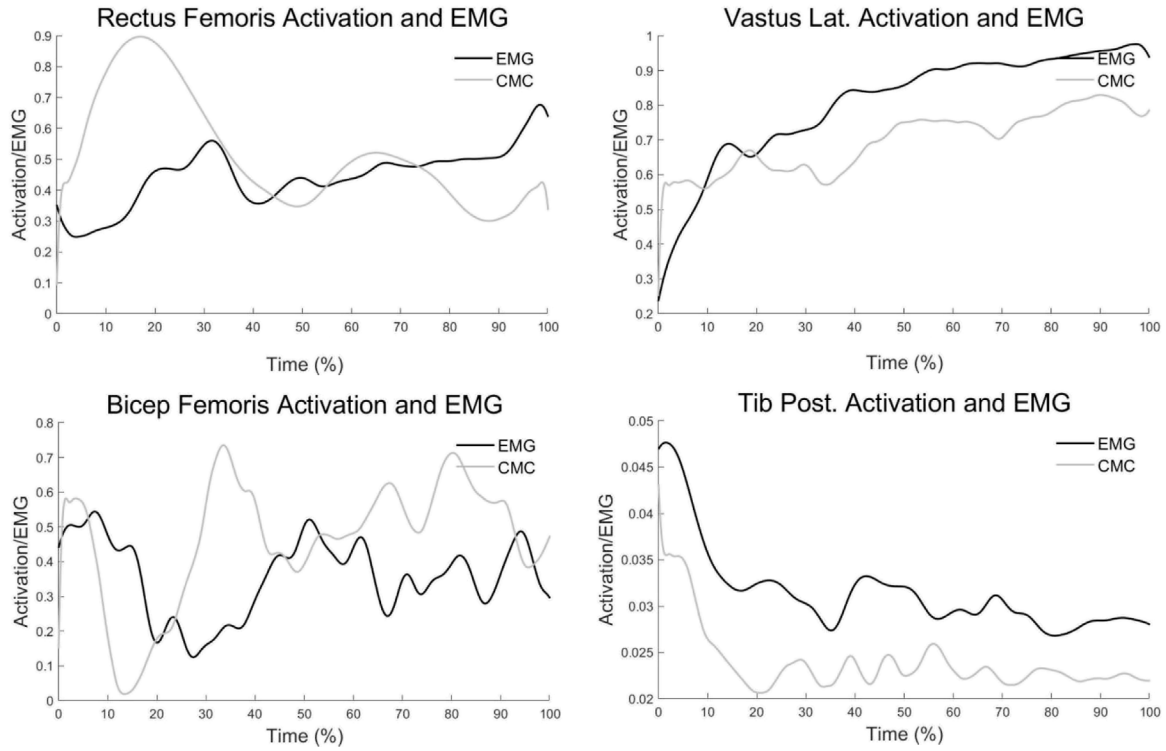

FIGURE 5
Comparisons between EMG signal and muscle activation estimated from CMC in OpenSim.

TABLE 1 Statistics of knee variables from the IC phase of three landing actions performed by 11 subjects.

Variables	Mean ± SD_DL	Mean ± SD_DVJ	Mean ± SD_FVJ	*p*-value	η^2
Knee flexion angle (°)[c*]	−55.56 ± 7.23	−57.91 ± 7.58	−61.77 ± 4.53	0.05	0.14
Knee flexion moment (N/kg)	0.26 ± 0.32	0.45 ± 0.99	0.84 ± 1.58	0.87	0.06
Knee valgus angle (°)	2.49 ± 4.48	1.51 ± 3.82	1.81 ± 4.00	0.85	0.01
Knee valgus moment (N/kg)	0.03 ± 0.06	−0.02 ± 0.11	0.00 ± 0.17	0.81	0.03
Quadriceps femoris forces (N/BW)[a*c*]	3.29 ± 1.90	5.27 ± 1.38	6.37 ± 2.58	0.00	0.31
Hamstring muscle forces (N/BW)	0.49 ± 0.43	0.49 ± 0.69	1.40 ± 1.48	0.26	0.18
Gastrocnemius muscle forces (N/BW)	1.45 ± 0.45	1.50 ± 0.35	0.83 ± 0.67	0.28	0.28
ACL forces (N/BW)	2.71 ± 0.37	2.64 ± 0.40	2.67 ± 0.36	0.44	0.01

(1) a* indicates a significant difference between DL, and DVJ; b* indicates a significant difference between DVJ, and FVJ; and c* indicates a significant difference between DL, and FVJ. (2) The unit of joint moment data was N/kg which was standardized according to the body mass (kg). The muscle forces and ACL, load were standardized in N/BW, according to body weight (BW). (3) While $\eta^2 = 0.01$ is a small effect, $\eta^2 = 0.06$ is a medium effect, and $\eta^2 = 0.14$ is a large effect.

reduction of the knee flexion angle (Gerritsen et al., 1995), which could be the reason for the higher ACL load and injury risk of DL action to a certain extent.

Some studies suggested that the risk factors measured in the frontal plane, such as the angle and moment of the knee joint valgus in landing, can cause higher ACL load during the landing process (Bendjaballah et al., 1997; Kar and Quesada, 2012; Kar and Quesada, 2013). The ACL load increases to almost six folds when the valgus angle is 5° (Bendjaballah et al., 1997), and when the angle exceeds 8°, the knee valgus angle poses a significant risk of ACL injury (Kar and Quesada, 2013). However, the maximum knee valgus angle of DL action was approximately 7° during the IC phase. The first peak value of the knee extension moment, knee valgus angle and moment were all within the range of 30% of the IC-MKF phase (Figure 6), which was similar to the phenomenon described by Kar et al. (Decker et al., 2003;

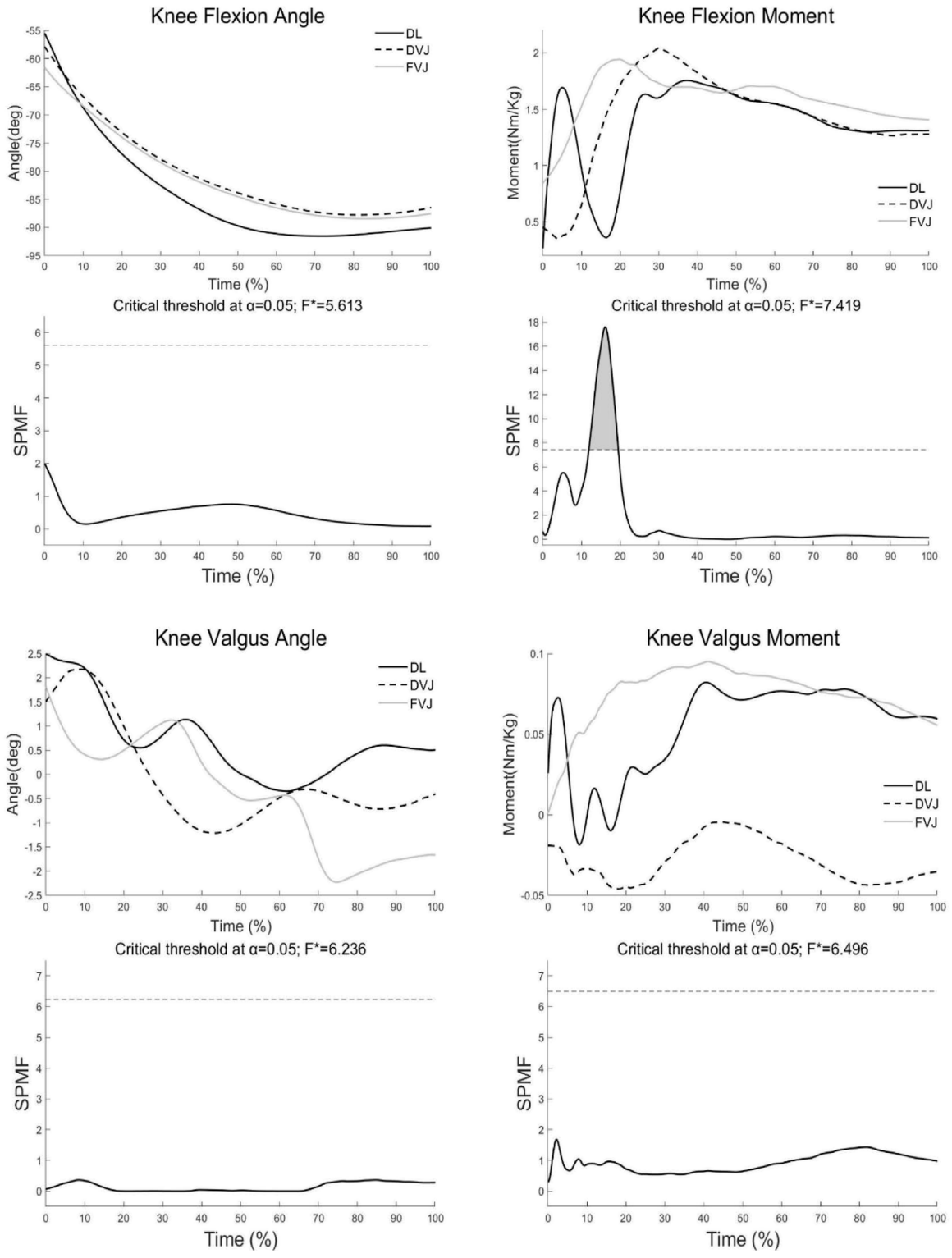

FIGURE 6
Ensemble average and SPM{F} evaluation of right knee variables against percentage time obtained from 11 subjects participating in the three landing actions.

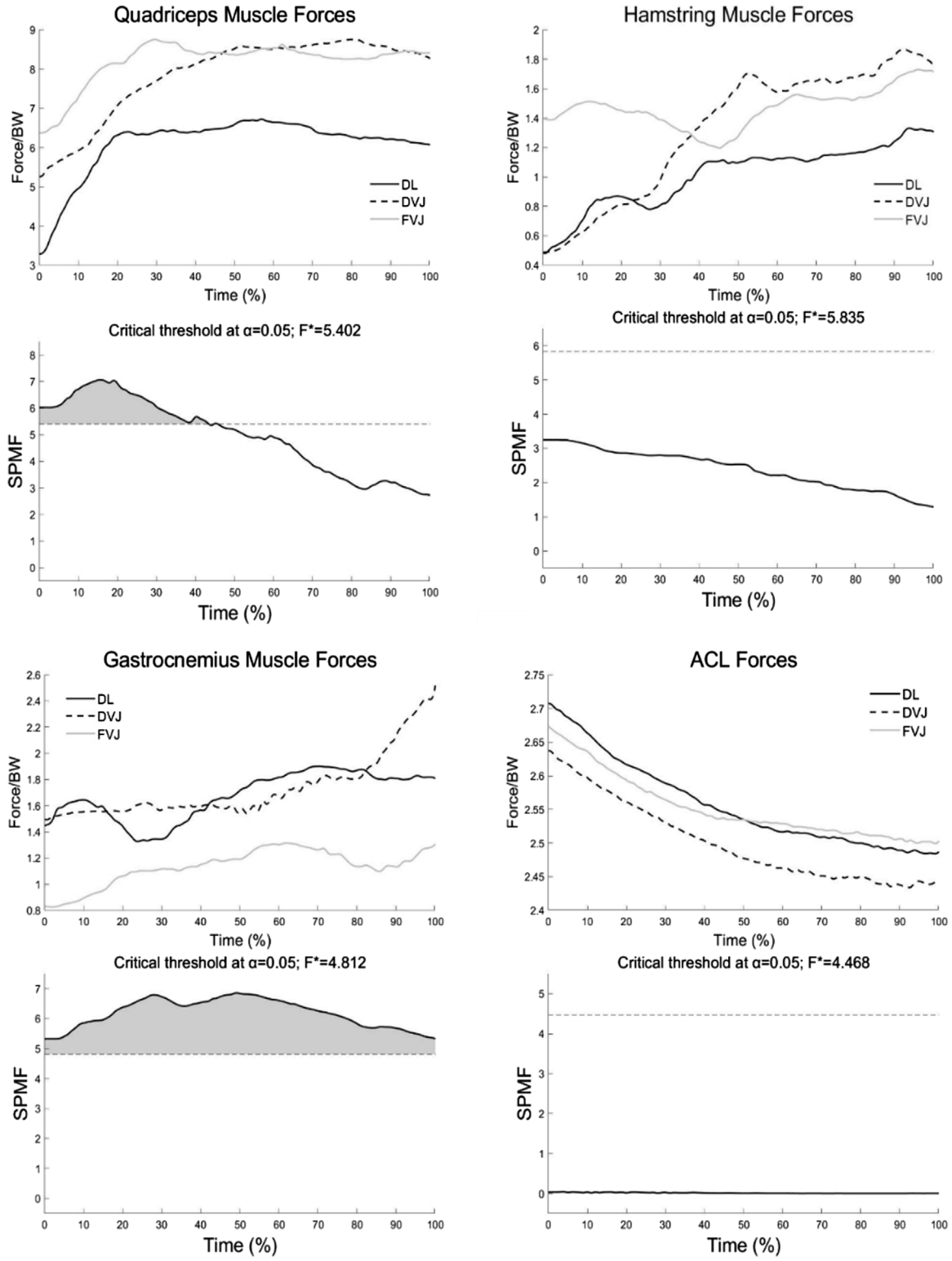

FIGURE 6b
(continued)

Cortes et al., 2007). This phenomenon described that the risk factors measured in the frontal plane, such as valgus angle and moment, also contribute to ACL load, but significantly lower than those measured in the sagittal plane. This study showed that none of the three actions had a maximum of 8° and did not pose a risk of injury to the ACL. Hence, the factors measured in the frontal plane, such as the knee valgus angle and moment, may contribute to the ACL load, but the factors measured in the sagittal plane, such as the knee flexion and extension moment, are the primary risk factors of ACL injury.

The muscle forces characteristics in different landing actions

The ACL load also depends on muscle forces (Anderson and Pandy, 2003; Hootman et al., 2007). Previous studies reported that the knee extension moment caused by the contraction of the quadriceps femoris could increase the tibial anterior shear force, increasing the ACL load and injury risk (Fagenbaum and Darling, 2003; Alentorn-Geli et al., 2009; Boden et al., 2010). In this study, the quadriceps femoris muscle forces and knee extension moment were highest in the FVJ group and followed by the DVJ and DL groups (Figure 6 and Table 1). The greater knee extension moment and quadriceps femoris muscle forces reported in the FVJ group may be due to the neuromuscular control strategy. The FVJ action needs more distance from the force plates and reaches the maximum vertical jump height immediately after landing Theoretically, the FVJ action should produce larger quadriceps femoris forces, which increases the tibial anterior shear force causing a higher ACL load. Thus, FVJ action may cause a higher ACL injury risk than the other two actions (Fagenbaum and Darling, 2003; Alentorn-Geli et al., 2009; Boden et al., 2010). However, the ACL load of the FVJ action was not the highest in this study. This phenomenon is explicable with the discovery that the ACL load caused by quadriceps femoris tension begins to decrease when the knee flexion angle exceeds 45° and remains little or no impact on ACL load when it exceeds 60° (Arms et al., 1984). According to kinematics results, the knee flexion angle of the three landing actions exceeded 55°; specifically, the FVJ action reached over 60°, which may be why there was no significant difference between the ACL load in the three landing actions during the IC phase.

Further, this may also be related to the contraction of the hamstrings and gastrocnemius muscles. Studies have shown (Bendjaballah et al., 1997) that the posterior shearing force of the tibia due to the contraction of the gastrocnemius and hamstring muscles effectively reduces the load on the ACL when the knee flexion angle is greater than 22°. In our study, the SPM{F} test found differences in gastrocnemius forces between the three actions. DL and DVJ have higher gastrocnemius muscle forces at IC, which provides the ankle joint a greater range of motion to slow the impact of the ground, reducing the risk of ACL injury (Leppänen et al., 2017). The hamstring muscle forces was higher during FVJ maneuvers because FVJ's larger knee flexion angle increases the activation level of the hamstring muscles (Brazen et al., 2010). Increased knee flexion angle (>30°) on landing attracts more hamstring contraction to participate in coordination (Leppänen et al., 2017), which effectively reduces ACL tension, decreasing the risk of ACL injury. Therefore, a larger knee flexion angle during landing effectively reduces the quadriceps femoris forces. At the same time, it can effectively reduce the ACL load with the coordinated contraction of the hamstring and the gastrocnemius muscles reducing the risk of ACL injury.

Screening of landing test action

Our second hypothesized that the risk of injury is higher in DL than in DVJ and FVJ. This study showed that the DL action demonstrated a smaller knee flexion angle and greater valgus angle than DVJ and FVJ actions in the IC phase. The relatively unnatural landing action may increase the risk of ACL injury. Therefore, DL action has a higher ACL injury risk than DVJ and FVJ actions, and it is not recommended to use as a test action for ACL injury risk assessment. The FVJ action has higher requirements from the body, which showed a large knee angle, moment and muscle forces during landing, which is more suitable for the actual training and competition conditions. In summary, the FVJ action should be the test action for ACL injury risk assessment. A previous study has also recognized the effectiveness of the FVJ action in ACL injury risk assessment (Cortes et al., 2007).

Limitations

Previous studies reported that females have a smaller knee flexion angle than males during the IC phase of the landing (Chappell et al., 2002; Yu et al., 2006). Therefore, using a gender unified landing test is vital in ACL injury risk assessment. However, the difference in the ACL load of three landing test actions was insignificant because the experimental subjects had been professionally trained. Since the subjects in this study were all division II and I basketball and volleyball athletes, the neuromuscular control strategies and landing protection awareness may differ from the normal females. Therefore, a buffered landing strategy may be selected to reduce the risk of ACL injury with unawareness, which can be one of the limitations of this study. Secondly, subjects' hands were in akimbo during the three landing test actions, which may affect the maximum vertical jump height of DVJ and FVJ action. Nevertheless, this pose unifies the posture during jumping and is widely used during landing tests in previous studies (Meyer and Haut, 2008; Fort-Vanmeerhaeghe et al., 2016).

Conclusion

Our study indicated minimal differences in knee valgus, knee valgus moment, ACL forces between the three landing actions. However, knee flexion angle, knee extension moments sagittal factors, and quadriceps and gastrocnemius forces are critical factors for ACL injury. This study also revealed that DL action had a significantly smaller knee flexion angle, which may increase the risk of ACL injury, and it is not recommended for risk assessment of ACL injuries. The FVJ action showed a larger knee flexion angle, mobilizing more quadriceps femoris forces, and the moving patterns were relatively similar to the needs of daily training and competition. Therefore, it is recommended to use FVJ action for future studies on ACL injury risk assessment and injury prevention in female college athletes.

Data availability statement

The raw data supporting the conclusions of this article will be made available by the authors, without undue reservation.

Ethics statement

The patients/participants provided their written informed consent to participate in this study. Written informed consent was obtained from the individual(s) for the publication of any potentially identifiable images or data included in this article.

Author contributions

All authors listed have made a substantial, direct, and intellectual contribution to the work and approved it for publication.

Funding

This study was sponsored by National Natural Science Foundation of China (No. 31270998).

Conflict of interest

The authors declare that the research was conducted in the absence of any commercial or financial relationships that could be construed as a potential conflict of interest.

Publisher's note

All claims expressed in this article are solely those of the authors and do not necessarily represent those of their affiliated organizations, or those of the publisher, the editors and the reviewers. Any product that may be evaluated in this article, or claim that may be made by its manufacturer, is not guaranteed or endorsed by the publisher.

References

Agel, J., Arendt, E. A., and Bershadsky, B. (2005). Anterior cruciate ligament injury in national collegiate athletic association basketball and soccer: A 13-year review. *Am. J. Sports Med.* 33 (4), 524–531. doi:10.1177/0363546504269937

Alentorn-Geli, E., Myer, G. D., Silvers, H. J., Samitier, G., Romero, D., Lazaro-Haro, C., et al. (2009). Prevention of non-contact anterior cruciate ligament injuries in soccer players. Part 1: Mechanisms of injury and underlying risk factors. *Knee Surg. Sports Traumatol. Arthrosc.* 17 (7), 705–729. doi:10.1007/s00167-009-0813-1

Anderson, F. C., and Pandy, M. G. (2003). Individual muscle contributions to support in normal walking. *Gait posture* 17 (2), 159–169. doi:10.1016/s0966-6362(02)00073-5

Arms, S. W., Pope, M. H., Johnson, R. J., Fischer, R. A., Arvidsson, I., and Eriksson, E. (1984). The biomechanics of anterior cruciate ligament rehabilitation and reconstruction. *Am. J. Sports Med.* 12 (1), 8–18. doi:10.1177/036354658401200102

Bendjaballah, M., Shirazi-Adl, A., and Zukor, D. (1997). Finite element analysis of human knee joint in varus-valgus. *Clin. Biomech.* 12 (3), 139–148. doi:10.1016/s0268-0033(97)00072-7

Bennett, D. R., Blackburn, J. T., Boling, M. C., McGrath, M., Walusz, H., and Padua, D. A. (2008). The relationship between anterior tibial shear force during a jump landing task and quadriceps and hamstring strength. *Clin. Biomech.* 23 (9), 1165–1171. doi:10.1016/j.clinbiomech.2008.05.005

Blackburn, J. T., Norcross, M. F., Cannon, L. N., and Zinder, S. M. (2013). Hamstrings stiffness and landing biomechanics linked to anterior cruciate ligament loading. *J. Athl. Train.* 48 (6), 1062–1772. doi:10.4085/1062-1050-48.4.1

Boden, B. P., Sheehan, F. T., Torg, J. S., and Hewett, T. E. (2010). Noncontact anterior cruciate ligament injuries: Mechanisms and risk factors. *Am. Acad. Orthop. Surg.* 18 (9), 520–527. doi:10.5435/00124635-201009000-00003

Brazen, D. M., Todd, M. K., Ambegaonkar, J. P., Wunderlich, R., and Peterson, C. (2010). The effect of fatigue on landing biomechanics in single-leg drop landings. *Clin. J. Sport Med.* 20 (4), 286–292. doi:10.1097/jsm.0b013e3181e8f7dc

Bulat, M., Korkmaz Can, N., Arslan, Y. Z., and Herzog, W. (2019). Musculoskeletal simulation tools for understanding mechanisms of lower-limb sports injuries. *Curr. Sports Med. Rep.* 18 (6), 210–216. doi:10.1249/jsr.0000000000000601

Chappell, J. D., Yu, B., Kirkendall, D. T., and Garrett, W. E. (2002). A comparison of knee kinetics between male and female recreational athletes in stop-jump tasks. *Am. J. Sports Med.* 30 (2), 261–267. doi:10.1177/03635465020300021901

Cortes, N., Onate, J., Abrantes, J., Gagen, L., Dowling, E., and Van Lunen, B. (2007). Effects of gender and foot-landing techniques on lower extremity kinematics during drop-jump landings. *J. Appl. biomechanics* 23 (4), 289–299. doi:10.1123/jab.23.4.289

Decker, M. J., Torry, M. R., Wyland, D. J., Sterett, W. I., and Richard Steadman, J. (2003). Gender differences in lower extremity kinematics, kinetics and energy absorption during landing. *Clin. Biomech.* 18 (7), 662–669. doi:10.1016/s0268-0033(03)00090-1

Delp, S. L., Anderson, F. C., Arnold, A. S., Loan, P., Habib, A., John, C. T., et al. (2007). OpenSim: Open-source software to create and analyze dynamic simulations of movement. *IEEE Trans. Biomed. Eng.* 54 (11), 1940–1950. doi:10.1109/tbme.2007.901024

Dürselen, L., Claes, L., and Kiefer, H. (1995). The influence of muscle forces and external loads on cruciate ligament strain. *Am. J. Sports Med.* 23 (1), 129–136. doi:10.1177/036354659502300122

Fagenbaum, R., and Darling, W. G. (2003). Jump landing strategies in male and female college athletes and the implications of such strategies for anterior cruciate

ligament injury. *Am. J. Sports Med.* 31 (2), 233–240. doi:10.1177/03635465030310021301

Fort-Vanmeerhaeghe, A., Gual, G., Romero-Rodriguez, D., and Unnitha, V. (2016). Lower limb neuromuscular asymmetry in volleyball and basketball players. *J. Hum. Kinet.* 50, 135–143. doi:10.1515/hukin-2015-0150

Gerritsen, K. G., van den Bogert, A. J., and Nigg, B. M. (1995). Direct dynamics simulation of the impact phase in heel-toe running. *J. biomechanics* 28 (6), 661–668. doi:10.1016/0021-9290(94)00127-p

Hashemi, J., Breighner, R., Chandrashekar, N., Hardy, D. M., Chaudhari, A. M., Shultz, S. J., et al. (2011). Hip extension, knee flexion paradox: A new mechanism for non-contact ACL injury. *J. biomechanics* 44 (4), 577–585. doi:10.1016/j.jbiomech.2010.11.013

Hootman, J. M., Dick, R., and Agel, J. (2007). Epidemiology of collegiate injuries for 15 sports: Summary and recommendations for injury prevention initiatives. *J. Athl. Train.* 42 (2), 311.

Imai, S., Harato, K., Morishige, Y., Kobayashi, S., Niki, Y., Sato, K., et al. (2022). Effects of dual task interference on biomechanics of the entire lower extremity during the drop vertical jump. *J. Hum. Kinet.* 81 (1), 5–14. doi:10.2478/hukin-2022-0001

Kainz, H., Modenese, L., Lloyd, D., Maine, S., Walsh, H., and Carty, C. (2016). Joint kinematic calculation based on clinical direct kinematic versus inverse kinematic gait models. *J. biomechanics* 49 (9), 1658–1669. doi:10.1016/j.jbiomech.2016.03.052

Kar, J., and Quesada, P. M. (2013). A musculoskeletal modeling approach for estimating anterior cruciate ligament strains and knee anterior–posterior shear forces in stop-jumps performed by young recreational female athletes. *Ann. Biomed. Eng.* 41 (2), 338–348. doi:10.1007/s10439-012-0644-y

Kar, J., and Quesada, P. M. (2012). A numerical simulation approach to studying anterior cruciate ligament strains and internal forces among young recreational women performing valgus inducing stop-jump activities. *Ann. Biomed. Eng.* 40 (8), 1679–1691. doi:10.1007/s10439-012-0572-x

Kernozek, T. W., Torry, M. R., Van Hoof, H., Cowley, H., and Tanner, S. (2005). Gender differences in frontal and sagittal plane biomechanics during drop landings. *Med. Sci. Sports Exerc.* 37 (6), 1003–1012.

Koltermann, J. J., Gerber, M., Beck, H., and Beck, M. (2018). Validation of various filters and sampling parameters for a COP analysis. *Technologies* 6 (2), 56. doi:10.3390/technologies6020056

Leppänen, M., Pasanen, K., Kujala, U. M., Vasankari, T., Kannus, P., Ayramo, S., et al. (2017). Stiff landings are associated with increased ACL injury risk in young female basketball and floorball players. *Am. J. Sports Med.* 45 (2), 386–393. doi:10.1177/0363546516665810

Lohmander, L. S., Englund, P. M., Dahl, L. L., and Roos, E. M. (2007). The long-term consequence of anterior cruciate ligament and meniscus injuries: Osteoarthritis. *Am. J. Sports Med.* 35 (10), 1756–1769. doi:10.1177/0363546507307396

Markolf, K. L., Burchfield, D. M., Shapiro, M. M., Shepard, M. F., Finerman, G. A. M., and Slauterbeck, J. L. (1995). Combined knee loading states that generate high anterior cruciate ligament forces. *J. Orthop. Res.* 13 (6), 930–935. doi:10.1002/jor.1100130618

Meyer, E. G., and Haut, R. C. (2008). Anterior cruciate ligament injury induced by internal tibial torsion or tibiofemoral compression. *J. biomechanics* 41 (16), 3377–3383. doi:10.1016/j.jbiomech.2008.09.023

Mokhtarzadeh, H., Ewing, K., Janssen, I., Yeow, C. H., Brown, N., and Lee, P. V. S. (2017). The effect of leg dominance and landing height on ACL loading among female athletes. *J. biomechanics* 60, 181–187. doi:10.1016/j.jbiomech.2017.06.033

Niu, W., Zhang, M., Fan, Y., and Zhao, Q. (2013). Dynamic postural stability for double-leg drop landing. *J. Sports Sci.* 31 (10), 1074–1081. doi:10.1080/02640414.2012.762600

Padua, D. A., Marshall, S. W., Beutler, A. I., DeMaio, M., Onate, J. A., Yu, B., et al. (2004). Sex comparison of jump landing kinematics and technique. *Med. Sci. Sports Exerc.* 36 (5), S348. doi:10.1249/00005768-200405001-01666

Padua, D. A., Marshall, S. W., Boling, M. C., Thigpen, C. A., Garrett, W. E., and Beutler, A. I. (2009). The landing error scoring system (LESS) is a valid and reliable clinical assessment tool of jump-landing biomechanics: The JUMP-ACL study. *Am. J. Sports Med.* 37 (10), 1996–2002. doi:10.1177/0363546509343200

Pataky, T. C. (2012). One-dimensional statistical parametric mapping in Python. *Comput. methods biomechanics Biomed. Eng.* 15 (3), 295–301. doi:10.1080/10255842.2010.527837

Rajagopal, A., Dembia, C. L., DeMers, M. S., Delp, D. D., Hicks, J. L., and Delp, S. L. (2016). Full-body musculoskeletal model for muscle-driven simulation of human gait. *IEEE Trans. Biomed. Eng.* 63 (10), 2068–2079. doi:10.1109/tbme.2016.2586891

Reinbolt, J. A., Seth, A., and Delp, S. L. (2011). Simulation of human movement: Applications using OpenSim. *Procedia Iutam* 2, 186–198. doi:10.1016/j.piutam.2011.04.019

Renganathan, G. (2022). *Effect of wearing running shoes on lower limb kinematics by using OpenSim simulation software*. Multidisciplinary Digital Publishing Institute.

Seth, A., Hicks, J. L., Uchida, T. K., Habib, A., Dembia, C. L., Dunne, J. J., et al. (2018). OpenSim: Simulating musculoskeletal dynamics and neuromuscular control to study human and animal movement. *PLoS Comput. Biol.* 14 (7), e1006223. doi:10.1371/journal.pcbi.1006223

Yu, B., Lin, C.-F., and Garrett, W. E. (2006). Lower extremity biomechanics during the landing of a stop-jump task. *Clin. Biomech.* 21 (3), 297–305. doi:10.1016/j.clinbiomech.2005.11.003

Yu, J., Zhang, S., Wang, A., Li, W., et al. (2020). "Human gait analysis based on OpenSim, " in 2020 International Conference on Advanced Mechatronic Systems (ICAMechS). IEEE, 278–281.

Zhou, H., Xu, D., Quan, W., Liang, M., Ugbolue, U. C., Baker, J. S., et al. (2021). A pilot study of muscle force between normal shoes and bionic shoes during men walking and running stance phase using opensim. *Actuators* 10 (10), 274. doi:10.3390/act10100274

frontiers | Frontiers in Bioengineering and Biotechnology

TYPE Original Research
PUBLISHED 03 February 2023
DOI 10.3389/fbioe.2023.918013

OPEN ACCESS

EDITED BY
Mohammad Nikkhoo,
Islamic Azad University, Iran

REVIEWED BY
Robert Salzar,
University of Virginia, United States
Kamran Hassani,
Islamic Azad University, Iran

*CORRESPONDENCE
Spyros Masouros,
smas@imperial.ac.uk

SPECIALTY SECTION
This article was submitted to Biomechanics, a section of the journal Frontiers in Bioengineering and Biotechnology

RECEIVED 11 April 2022
ACCEPTED 02 January 2023
PUBLISHED 03 February 2023

CITATION
Rebelo EA, Grigoriadis G, Carpanen D, Bull AMJ and Masouros S (2023), Stature and mitigation systems affect the risk of leg injury in vehicles attacked under the body by explosive devices.
Front. Bioeng. Biotechnol. 11:918013.
doi: 10.3389/fbioe.2023.918013

Stature and mitigation systems affect the risk of leg injury in vehicles attacked under the body by explosive devices

Eduardo A Rebelo, Grigoris Grigoriadis, Diagarajen Carpanen, Anthony M. J. Bull and Spyros Masouros*

Department of Bioengineering, Imperial College London, London, United Kingdom

A finite-element (FE) model, previously validated for underbody blast (UBB) loading, was used here to study the effect of stature and of mitigation systems on injury risk to the leg. A range of potential UBB loadings was simulated. The risk of injury to the leg was calculated when no protection was present, when a combat boot (Meindl Desert Fox) was worn, and when a floor mat (IMPAXX^{TM}), which can be laid on the floor of a vehicle, was added. The risk of injury calculated indicates that the floor mat provided a statistically significant reduction in the risk of a major calcaneal injury for peak impact speeds below 17.5 m/s when compared with the scenarios in which the floor mat was not present. The risk of injury to the leg was also calculated for a shorter and a taller stature compared to that of the nominal, 50th percentile male anthropometry; shorter and taller statures were constructed by scaling the length of the tibia of the nominal stature. The results showed that there is a higher risk of leg injury associated with the short stature compared to the nominal and tall statures, whereas the leg-injury risk between nominal and tall statures was statistically similar. These findings provide evidence that the combat boot and the floor mat tested here have an attenuating effect, albeit limited to a range of possible UBB loads. The effect of stature on injury has implications on how vehicle design caters for all potential anthropometries and indeed gender, as women, on average, are shorter than men. The results from the computational simulations here complement laboratory and field experimental models of UBB, and so they contribute to the improvement of UBB safety technology and strategy.

KEYWORDS

blast injury, anthropometry, combat boots, finite element modeling, foot and ankle, high loading rate, protection, mitigation

1 Introduction

In recent conflicts, explosive devices have caused damage to numerous land vehicles and resulted in a range of injuries to their occupants (Kempinski and Murphy, 2012; McGuire et al., 2019). The transmission of the blast loading through the vehicle, primarily through the floor, termed underbody blast (UBB), can result in difficult-to-treat ankle, foot, and leg injuries that present significant morbidity (Asensio and Trunkey, 2008; Ramasamy et al., 2013).

In order to minimize the severity of these blast injuries, mitigation strategies have included the targeted redesign of armored vehicles and the development of mobile personal protection systems (Ramasamy et al., 2009; Kamel, 2019). An energy-dissipating structure that has been used between the encroaching floor and the occupant's feet is a floor mat; indeed, it has been

shown in physical experiments that floor mats are able to attenuate load under impact (Newell et al., 2013).

Furthermore, whilst in the civilian automotive setting it is known that stature and gender may affect the severity of leg injury (Crandall et al., 1996; Welsh et al., 2003; Malczyk et al., 2013; Hu et al., 2017; Ammori and Abu-Zidan, 2018), there have been no such studies for UBB. Stature can vary substantially amongst vehicle occupants; the height of 180 American soldiers was found to vary between 1.53 and 1.76 m for women and 1.52 and 1.93 m for men (Darter et al., 2012).

The use of anthropomorphic test devices (ATDs) is limited in terms of both relevance to UBB loading and variability in stature alike, and experimental testing with cadaveric tissue is limited in terms of the number of tests that can be conducted across a range of potential UBB loading. Computational modeling, however, offers a realistic alternative to simulating UBB. Therefore, this study aimed to use a validated lower limb finite-element (FE) model of UBB to quantify the protection offered by vehicle-design mitigation represented by a floor mat and assess the influence of stature on injury risk.

2 Methods

An FE model of the lower limb developed in PATRAN (v2018, MSC. Software, Santa Ana, CA, United States), solved in Dytran (v2018, MSC. Software, Santa Ana, CA, United States), and validated for UBB-related loading conditions was used (Rebelo et al., 2021) (Figure 1). Briefly, the FE model is of a cadaveric lower limb with anthropometry close to that of the 50th percentile American male (height = 1.727 m; weight = 72.6 kg). The model response was compared against that of laboratory-based UBB tests conducted at two independent laboratories. The computational signals were found to be within the experimental corridors and, when experimental corridors were not available, acceptably close in magnitude to values reported in these studies. A version of the validated model incorporated a combat boot, specifically a UK-size 10 Meindl Desert Fox combat boot (Lukas Meindl GmbH & Co., Germany). Briefly, the combat boot used is made up of three layers, namely, insole, midsole, and outsole, and a cardboard insert that structurally supports the insole and allows integration with the lower layers. Simulations were run across a range of UBB-related loading conditions, and the amount of protection offered by the boot was quantified.

Here, two sets of UBB simulations were set up. The first one incorporated the IMPAXX™ foam between the loading plate representing the vehicle's floor and the sole of the combat boot in the original, baseline model. IMPAXX™ is a commercial foam available for use in vehicle floors as a floor mat. It is a closed cell foam, which was modeled using the FOAM2 material model and a material stress–strain field (Slik et al., 2006).

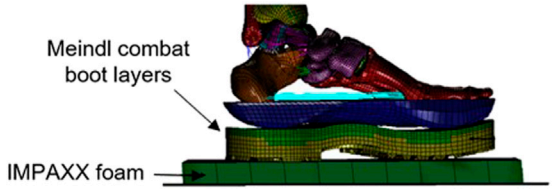

FIGURE 1
Distal part of the finite-element model developed previously by Rebelo et al. (2021) and used here to study the effect of the IMPAXX floor mat and stature on injury.

The second set of simulations was of two statures representing a shorter and a taller stature to that used in the baseline model, which was considered to be a medium, average stature (tibia length = 386 mm) (Figure 2). The objective was to assess the effect of stature alone on the risk of foot-and-ankle injury. In order to obtain the geometry of the short and tall statures, the lower limb of the baseline, medium stature model was scaled. The length of the tibia was used for scaling as it has been shown to correlate well with stature (Duyar and Pelin, 2003). Scaling was achieved in HyperMesh (Altair, v2014, CA, United States) using the relationship established by Duyar and Pelin (2003). All meshes were morphed linearly with the same scaling factor. The relative position between components (bones) was kept, and the cortical thickness of all tarsal bones remained unaltered. All other model parameters, including the material properties, were not changed. The combat boot and floor mat were included in all simulations.

UBB-representative vehicle-floor velocity profiles with peak velocities ranging from 5 to 17.5 m/s and time to peak between 1.5 and 9 ms were applied to the loading plate (Rebelo et al., 2021) (Supplementary Table S1). These profiles were triangular in shape, consisting of a section in which the loading velocity increased until the peak velocity reached at the time to peak velocity and a second section in which the velocity decreased to zero with the same slope as it increased to peak velocity. The peak force at the proximal end of the tibia was the output variable of interest; this was used to calculate the risk of injury based on the injury risk curve of Chirvi et al. (2017). Additionally, deformation was monitored in order to quantify the deformation pattern of the foot-and-ankle complex.

The student's *t*-test was used to compare between groups. The statistical analysis was performed in MATLAB (R2019a, MathWorks Inc., Natick, MA) using a script that included the *t* test2 (x,y) function. A two-sample *t*-test was conducted to verify whether the means of normal distributions were equal for a 5% significance level.

3 Results

The normal density distribution function fits of peak tibial force response for the bare foot, combat boot, and combat boot with IMPAXX™ models were significantly different from one another (Figure 3A). The normal density distribution function fit for the smaller stature was shown to be significantly different from both baseline and taller statures (Figure 3B), whereas baseline and taller statures were statistically similar. All resultant forces and associated calcaneal injury risks predicted by the simulations and used to generate Figure 3 are available in Supplementary Table S1.

The compression of the combat boot layers can be used as a surrogate marker for the resulting severity of the insult (see Supplementary Figures S1, S2). For acceleration profiles with a peak impact speed of 11.25 m/s, there was a straightening of the combat boot layers, and the layer compression at the heel site was at the order of 16% at 7 m/s. For acceleration profiles with a peak impact speed of 17.5 m/s, the compression of the combat boot layers at the heel site was 43%; the calcaneus translated distally, and plantar tissue deformation was observed. In the simulation case including the IMPAXX™ floor mat, limited deformation to the combat boot

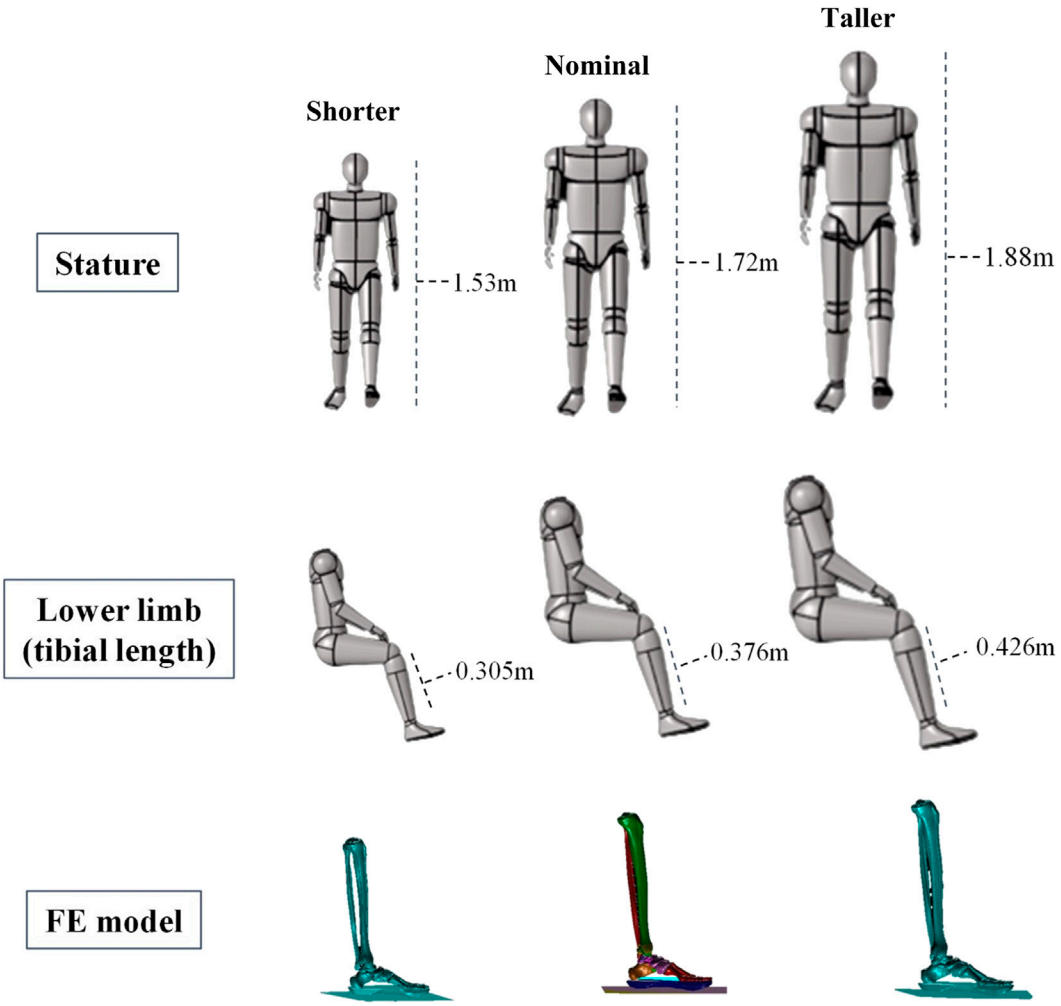

FIGURE 2
Short, nominal, and tall statures used for the anthropometric study. They were selected based on the military stature interval reported by Darter et al. (2012).

structure was observed along with less compression of the combat boot layers when compared with the simulations without the floor mat for a wide range of loading inputs.

4 Discussion

This study explored the effect of stature, a floor mat, and a combat boot on leg injury risk across a range of UBB loading using a previously developed FE model validated for UBB-relevant loading.

The incorporation of the Meindl combat boot resulted in a decrease between 18% and 24% in the force transmitted to the leg for peak impact speeds above 11.25 m/s, which is within the range of previous studies that explored loading attenuation to the tibia from the use of combat boots (Manseau and Keown, 2005; Geurts et al., 2006; North Atlantic Treaty Organisation RTO-TR-HFM-090, 2007; Newell et al., 2012; Kamel, 2019).

Longer times to peak were found to be associated with a larger floor-mat compression and a reduction in the force transmitted to the leg. Although the peak forces were reduced with this protective system in comparison with the configuration without it, the specific floor mat did not offer an effective reduction in injury risk for loading with peak velocities above 11.25 m/s.

The response of the FE model had been shown previously in comparison with that from physical experiments across a range of UBB-loading encompassing anatomical variability (Rebelo et al., 2021). The introduction of the IMPAXX™ floor mat in the model expectedly changed the resulting response; albeit there are no experimental data against which comparisons can be made, the response did not change to an extent that would render the model invalid. This gives confidence that the observations with the incorporation of the IMPAXX™ floor mat are reasonable. A limitation is that the representation of the IMPAXX™ floor mat is simplified to maintain efficient simulation run times. This simplification is likely to have resulted in an underestimation of load attenuation since it does not account for all cellular deformation modes and their effects on energy absorption.

The results of this study are specific to the type and model of the combat boot and floor mat used. It is likely that there are differences in levels of attenuation between different types of combat boot and floor

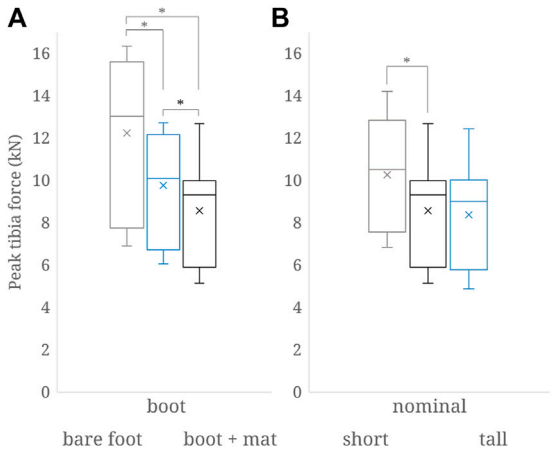

FIGURE 3
Comparison of peak tibia force distributions between **(A)** original, baseline model and mitigation represented by the combat boot (data from (Rebelo et al., 2021)) and the combat boot and the IMPAXX floor mat; **(B)** short, tall, and the nominal stature all with a combat boot and the floor mat. Statistical significance ($p < .05$) using the Student's t-test between the distributions is noted with the asterisk.

mat. The FE model used here can be utilized to establish the level of attenuation of specific designs of the combat boot or floor mat across the range of UBB loading.

The findings of this study indicate that there is a higher risk of calcaneal injury associated with short statures than medium and tall statures (Figure 3B). Force data for the tall stature are slightly, but not statistically, significantly higher than those of the medium stature. There was, however, a reduction in injury risk for a major calcaneal injury across all loading cases for the taller stature (Supplementary Table S1). There are no epidemiological data on appropriate resolution in military populations against which one could compare these findings. Short statures and some very tall statures, however, have been shown to be of higher risk of lower leg injury than a medium stature in road-traffic frontal collisions in epidemiological (Dischinger et al., 1995; Crandall et al., 1996; Welsh et al., 2003; Austin 2012) and in computational studies (Hu et al., 2017). When appreciating the differences between military and civilian vehicle seating, loading direction, and loading rate, the effect of stature on the risk of lower leg injury found in this study is similar to that reported for road-traffic frontal collisions.

This study used the force at the proximal tibia as the metric, or injury criterion, to quantify the risk of injury to the calcaneus, according to the curves by Chirvi et al. (2017) developed from cadaveric experiments. Although other metrics could have been considered, such as strain in the calcaneus, the data by Chirvi et al. (2017) are the most reliable to date that are specific to UBB loading. Furthermore, the small change in long-bone cortical thickness during morphing to generate the taller and shorter statures would not have affected the force measured at the proximal tibia; this, combined with the fact that cortical thickness in the tarsal bones and material properties remained unaltered, means that the differences in injury risk seen between statures can be attributed to the changes in stature alone.

The influence of stature on the risk of UBB injury can be considered in the context of assessing injury tolerance for men compared to women in UBB. It is well established that women have, on average, shorter statures than their male counterparts (Duyar and Pelin, 2003) and so, based on the findings here, are at a higher risk of leg injury. This corroborates with road-traffic frontal collision research (Dischinger et al., 1995; Crandall et al., 1996; Welsh et al., 2003; Austin 2012, Ammori and Abu-Zidan, 2018); Austin (2012) reported 4–7 times higher odds for female drivers to present a leg fracture, and Dischinger et al. (1995) reported a 20% risk of lower limb fractures for females compared to 13% for male drivers with most injuries sustained at the foot and ankle; they also report that, when grouped by stature, the smaller statures were at a higher risk of leg injury than taller statures. Of course, there are biological and anatomical differences between genders other than stature that may contribute to differences in the risk of lower leg injury. The injury–risk curve used in this study to assess the risk of calcaneal fracture had been developed using male specimens exclusively (Chirvi et al., 2017). Cadaveric studies that have included gender as a covariate, such as that of Mildon et al. (2018) on the risk for a foot and ankle fracture in UBB, have all shown that, on average, women have a lower tolerance to injury than men.

Despite no relevant epidemiological data on women in the military, to date, to corroborate laboratory findings, the overwhelming evidence of experimental and computational UBB injury models is that women are at a higher risk of foot and ankle injury than men. This, combined with the findings of road-traffic frontal collision research, to date, supports that military-vehicle design mitigation strategies should consider stature as a risk factor.

In summary, a validated FE model was used to investigate the effect of the combat boot, floor mat, and stature on the risk of foot and ankle injury in UBB. The findings suggest that shorter individuals are at a higher risk of leg injury than taller individuals in UBB. A combat boot and a floor mat were shown to have a variable attenuating efficiency depending on the UBB loading characteristics, but they were shown to reduce the risk of leg injury for UBB loading with a peak floor velocity under 17.5 m/s. The versatility and efficiency of the FE model compared to expensive and laborious experimental tests render it a powerful tool toward improving UBB safety technology and strategy.

Data availability statement

The original contributions presented in the study are included in the article/Supplementary Material; further inquiries can be directed to the corresponding author.

Author contributions

AB and SM conceived the study. ER, GG, AB, and SM designed the study. ER developed the finite-element models with contributions from GG and DC. ER ran all simulations, analyzed the data, and drafted the manuscript. All authors reviewed, edited, and approved the submitted version.

Conflict of interest

The authors declare that the research was conducted in the absence of any commercial or financial relationships that could be construed as a potential conflict of interest.

Publisher's note

Supplementary material

The Supplementary Material for this article can be found online at: https://www.frontiersin.org/articles/10.3389/fbioe.2023.918013/full#supplementary-material

SUPPLEMENTARY FIGURE S1
Deformation plots for simulation configurations **(A)** unreformed, **(B)** sim 1; 5 m/s in 1.5 ms, **(C)** sim 6; 11.5 m/s in 1.5 ms, and **(D)** sim 11; 17.5 m/s in 1.5 ms, all with the combat boot and without the floor mat.

SUPPLEMENTARY FIGURE S2
Deformation plots for simulation configurations **(A)** unreformed, **(B)** sim 1; 5 m/s in 1.5 ms, **(C)** sim 6; 11.5 m/s in 1.5 ms, and **(D)** sim 11; 17.5 m/s in 1.5 m/s, all with the combat boot and the IMPAXX™ floor mat.

SUPPLEMENTARY TABLE S1
Raw data per simulation with which Figure 3 was produced. The input in the simulation was a triangular pulse defined by the maximum velocity (vmax) and the time to maximum velocity or time to peak (TTP). The output from the simulations was the tibial peak force (Fmax). The peak force was then used to look up the risk of a minor or a major calcaneal injury on Chirvi et al.'s injury risk curve.

References

Ammori, M. B., and Abu-Zidan, F. M. (2018). The biomechanics of lower limb injuries in frontal-impact road traffic collisions. *Afr. Health Sci.* 18 (2), 321–332. doi:10.4314/ahs.v18i2.17

Asensio, J. A., and Trunkey, D. (2008). *Current therapy of trauma and surgical critical care*. Amsterdam Netherlands: Elsevier Health Sciences.

Austin, R. (2012). Lower extremity injuries and intrusion in frontal crashes. *Natl. Highw. Traffic Saf. Adm.* 23 (4).

Chirvi, S., Pintar, F., Yoganandan, N., Banerjee, A., Schlick, M., Curry, W., et al. (2017). Human foot-ankle injuries and associated risk curves from under body blast loading conditions. *Stapp Car Crash J.* 61, 157–173. doi:10.4271/2017-22-0006

Crandall, J. R., Martin, P. G., Bass, C. R., Pilkey, W. D., Dischinger, P. C., Burgess, A. R., et al. (1996). Foot and ankle injury: The roles of driver anthropometry, footwear and pedal controls. *Annu. Proc. Assoc. Adv. Automot. Med.* 40, 1–18.

Darter, B. J., Goffar, S. L., Ellwein, J. C., Snell, R. M., Tomalis, E. A., Shaffer, S. W., et al. (2012). Physical performance assessment in military service members. *J. Am. Acad. Orthop. Surg.* 20, 42–47. doi:10.5435/JAAOS-20-08-S42

Dischinger, C., Kerns, T., and Kufera, J. (1995). Lower extremity fractures in motor vehicle collisions: The role of driver gender and height. *Accid. Analysis Prev.* 27 (4), 601–606. doi:10.1016/0001-4575(95)00002-h

Duyar, I., and Pelin, C. (2003). Body height estimation based on tibia length in different stature groups. *Am. J. Phys. Anthropol.* 122, 23–27. doi:10.1002/ajpa.10257

Geurts, J., Van Der Horst, M., Leerdam, P. J., Bir, C., Van Dommelen, H., and Wismans, J. (2006). "Occupant safety: Mine detonation under vehicles a numerical lower leg injury assessment," in Proceedings of the 2006 International IRCOBI Conference on the Biomechanics of Impact, Madrid (Spain), September 2006, 373–376.

Hu, J., Zhang, K., Fanta, A., Jones, M. L. H., Reed, M. P., Neal, M., et al. (2017). "Stature and body shape effects on driver injury risks in frontal crashes: A parametric human modelling study," in Proceedings of the Conference proceedings International Research Council on the Biomechanics of Injury, IRCOBI, Cambridge England, October 2017, 656–667.

Kamel, H. (2019). Review of design techniques of armored vehicles for protection against blast. doi:10.1115/IMECE2019-10227

Kempinski, B., and Murphy, C. (2012). *Technical challenges of the U.S. Army's ground combat vehicle program: working paper 2012–15*. Washington, DC: Working paper series, Congressional Budget Office.

Malczyk, A., Müller, I., Eßers, S., and Hänsel, M. (2013). Effects of seating position of short stature drivers in frontal impacts. *IRCOBI Conf.* 2013, 842–853.

Manseau, J., and Keown, M. (2005). Development of an assessment methodology for lower leg injuries resulting from anti-vehicular blast landmines. *Solid Mech. its Appl.* 124. doi:10.1007/1-4020-3796-1_4

McGuire, R., Hepper, A., and Harrison, K. (2019). From Northern Ireland to Afghanistan: Half a century of blast injuries. *J. R. Army Med. Corps.* 165, 27–32. doi:10.1136/jramc-2017-000892

Mildon, P. J., White, D., Sedman, A. J., Dorn, M., and Masouros, S. D. (2018). Injury Risk of the Human Leg Under High Rate Axial Loading. *Hum. Factors Mech. Eng. Def. Saf.* 2 (1), 5. doi:10.1007/s41314-018-0009-x

North Atlantic Treaty Organisation RTO-TR-HFM-090 (2007). Test methodology for protection of vehicle occupants against Aanti-vehicular landmine effects. doi:10.14339/RTO-TR-HFM-090

Newell, N., Masouros, S. D., Pullen, A. D., and Bull, A. M. J. (2012). The comparative behaviour of two combat boots under impact. *Inj. Prev.* 18, 109–112. doi:10.1136/ip.2010.031344

Newell, N., Masouros, S. D., and Bull, A. M. J. (2013). "A comparison of MiL-Lx and hybrid-III responses in seated and standing postures with blast mats in simulated under-vehicle explosions," in Proceedings of the IRCOBI Conf, Gothenburg in Sweden, 135–144.

Ramasamy, A., Hill, A. M., Hepper, A. E., Bull, A. M., and Clasper, J. C. (2009). Blast mines: Physics, injury mechanisms and vehicle protection. *J. R. Army Med. Corps* 155, 258–264. doi:10.1136/jramc-155-04-06

Ramasamy, A., Hill, A. M., Masouros, S., Bull, A. M. J., Gibb, I., Phillip, R., et al. (2013). Outcomes of IED foot and ankle blast injuries. *J. Bone Jt. Surg. - Ser. A* 95, e25. doi:10.2106/JBJS.K.01666

Rebelo, E., Grigoriadis, G., Bull, A. M. J., and Masouros, S. (2021). An experimentally validated finite-element model of the lower limb to investigate the efficacy of blast-mitigation systems. *Front. Bioeng. Biotechnol.* 9, 665656. doi:10.3389/fbioe.2021.665656

Slik, G., Vogel, G., and Chawda, V. (2006). Material model validation of a high efficient energy absorbing foam. 5th LS-DYNA Forum, (June).

Welsh, R., Morris, A., and Clift, L. (2003). "The effect of height on injury outcome for drivers of European passenger cars," in Annual Proceedings/Association for the Advancement of Automotive Medicine. (Association for the Advancement of Automotive Medicine) 47, 401–416.

Frontiers in
Bioengineering and Biotechnology

Accelerates the development of therapies, devices, and technologies to improve our lives

A multidisciplinary journal that accelerates the development of biological therapies, devices, processes and technologies to improve our lives by bridging the gap between discoveries and their application.

Discover the latest Research Topics

See more →

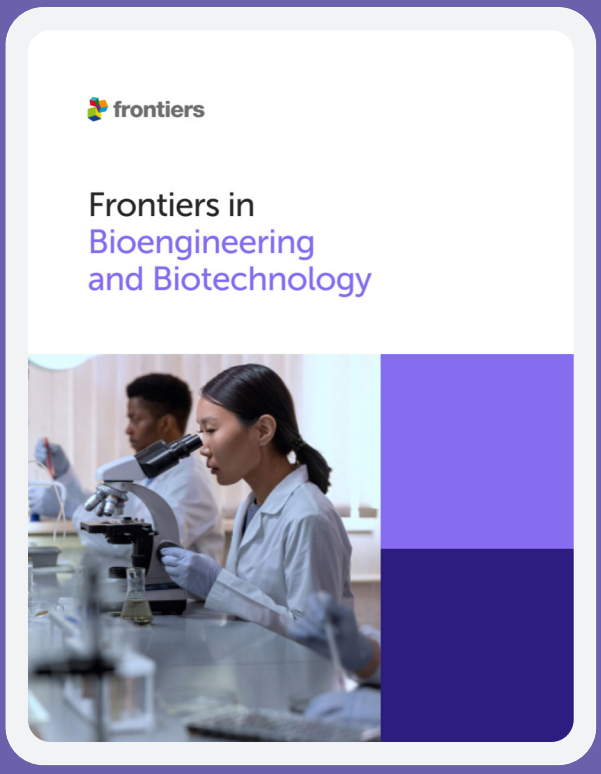

Frontiers

Avenue du Tribunal-Fédéral 34
1005 Lausanne, Switzerland
frontiersin.org

Contact us

+41 (0)21 510 17 00
frontiersin.org/about/contact